Lecture Notes in Electrical Engineering 458

Zhidong Deng
Editor

Proceedings of 2017 Chinese Intelligent Automation Conference

Springer

Lecture Notes in Electrical Engineering

Volume 458

"Lecture Notes in Electrical Engineering (LNEE)" is a book series which reports the latest research and developments in Electrical Engineering, namely:

- Communication, Networks, and Information Theory
- Computer Engineering
- Signal, Image, Speech and Information Processing
- Circuits and Systems
- Bioengineering

LNEE publishes authored monographs and contributed volumes which present cutting edge research information as well as new perspectives on classical fields, while maintaining Springer's high standards of academic excellence. Also considered for publication are lecture materials, proceedings, and other related materials of exceptionally high quality and interest. The subject matter should be original and timely, reporting the latest research and developments in all areas of electrical engineering.

The audience for the books in LNEE consists of advanced level students, researchers, and industry professionals working at the forefront of their fields. Much like Springer's other Lecture Notes series, LNEE will be distributed through Springer's print and electronic publishing channels.

More information about this series at http://www.springer.com/series/7818

Zhidong Deng
Editor

Proceedings of 2017 Chinese Intelligent Automation Conference

Springer

Editor
Zhidong Deng
Tsinghua University
Beijing
China

ISSN 1876-1100 ISSN 1876-1119 (electronic)
Lecture Notes in Electrical Engineering
ISBN 978-981-10-6444-9 ISBN 978-981-10-6445-6 (eBook)
https://doi.org/ 10.1007/978-981-10-6445-6

Library of Congress Control Number: 2017951987

Printed on acid-free paper

This Springer imprint is published by Springer Nature
The registered company is Springer Nature Singapore Pte Ltd.
The registered company address is: 152 Beach Road, #21-01/04 Gateway East, Singapore 189721, Singapore

Contents

Design of a Simulation System for Cross-Eye Dynamic Jamming

Zhang Yang, Shi Chuan and Dai Huanyao

1 Introduction

In modern air defense and anti-missile defense system, monopulse radar is widely used in missile guidance and azimuth tracking. Multi-point source jamming is the most effective way to interference monopulse radar, which can be divided into towed jamming and coherent jamming [1]. One of the most typical engineering implementation methods of coherent jamming is the cross-eye technique. In this paper, a cross-eye dynamic jamming simulation system is designed based on the cross-eye dynamic jamming principle, which lays a foundation for the later engineering realization.

2 Cross-Eye Jamming Principles

Cross-eye jamming uses two or more jamming radiation sources spatially spaced to transmit simulated radar echoes, which satisfy certain condition on some parameters such as power or phase. The local special radiation field of the space point where the phase center of the radar signal is synthesized with each transmitted signal. The wavefront of this radiation field is locally distorted at the location of the radar to produce illusion, and the radar based on the plane wavefront detection is mistaken for that the radiation source is in another false position [2].

Figure 1 shows a cross-eye jamming schematic. The cross-eye jammer consists of two separate jammers with a spacing L. The receiving antenna R1 is in the same position as the transmitting antenna J2 and the receiving antenna R2 is in the same position as the transmitting antenna J1. The two receiving antennas receive the

Z. Yang (✉) · S. Chuan · D. Huanyao
Luoyang Electronic Equipment Test Center, Luoyang 471003, China
e-mail: zhangyhappy@163.com

Z. Deng (ed.), *Proceedings of 2017 Chinese Intelligent Automation Conference*,
Lecture Notes in Electrical Engineering 458,
https://doi.org/10.1007/978-981-10-6445-6_1

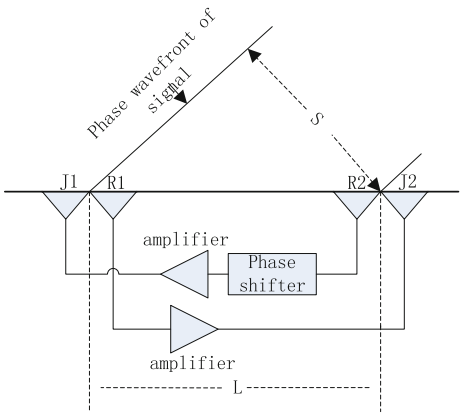

Fig. 1 Working principle schematic of cross-eye jamming

radar signal at the same time. The signal received by the antenna R1 is transmitted from the antenna J2 after passing through the amplifier. The signal received by the antenna R2 is inverted 180° and then transmitted from the antenna J1 after passing through the amplifier. The amplitude and phase of forward signal are controlled accurately, so that the amplitude of signal which reaches the radar antenna array are the same, and the phase are opposite. Because of this, the composite signal will produce phase wavefront distortion.

Figure 2 shows the cross-eye jamming space geometric relation. The location of the two jamming sources is as shown in the Fig. 2. L is the distance between the two jamming sources. R is the distance that the monopulse radar seeker to the location of the center of the two jamming sources. Assuming that the equisignal axis is pointing at 0°, θ_r is the angle between the target and the equisignal axis, θ_e is the angle between the two jamming point sources and the center of the monopulse radar antenna.

Assuming that when the radar signals transmitted across arrive at the center point of the monopulse radar antenna, the signal amplitude ratio is b, and arrival phase difference is ϕ. So indication tracking error angle θ_i of the monopulse radar is described as follow.

$$\theta_i = \frac{\theta_e}{2} \cdot \frac{1 - b^2}{1 + b^2 + 2b\cos(\phi)} \tag{1}$$

If the amplitude is the same, that is, b = 1, then $\theta_i = 0$. At this time, the radar tracking error angle is zero and the tracking antenna beam points to the baseline center of the two jamming sources.

If two coherent jamming sources is inverted, ϕ = 180°, then $\theta_i = \theta_e \frac{1+b}{1-b}$. If the magnitude of two jamming sources is adjacent, that is b → 1. Then the radar tracking error angle rises sharply, and the tracking antenna beam points will remove off the baseline of the two jamming sources. Therefore, the cross-eye jamming can be implemented on decoying monopulse radar, to protect the real goal.

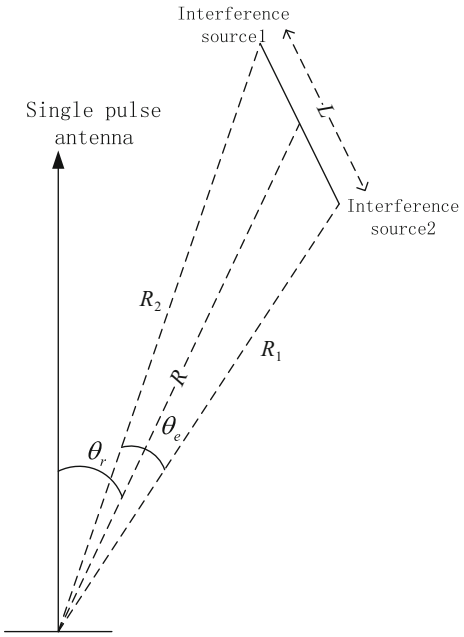

Fig. 2 Space geometric relation of cross-eye jamming

3 Cross-Eye Dynamic Jamming Method

The effectiveness of cross-eye jamming is strictly dependent on the precise control of the signal amplitude ratio and phase difference of the two jamming signal. However, in the practical engineering application, it is very difficult to realize the high precision phase and amplitude control between the two sources. So it causes that conventional method cannot achieve the desired effect. Therefore, a cross-eye dynamic jamming method based on power regulation is proposed in literature [3].

Compared with the conventional cross-eye static jamming method, the cross-eye dynamic jamming method allures its main beam deviate from the target through controlling the two jamming sources power in real time. The method is simple and reduces precision requirements for the jamming amplitude, which can achieve a better interference effect. Cross-eye dynamic jamming power control mode is divided into two modes: single cycle and multi-cycle.

Figure 3 shows the single-cycle jamming power control. In Fig. 3a, initially, the transmitter R1 is switched on and the power remains constant. The transmitter R2 remains off. The main beam of monopulse radar will point to the jamming source 1. Then, the transmitter R2 is switched on and the power of transmitter R2 increases linearly from a low power state. When the powers of the two transmitters are equal, the power of the transmitter R2 is kept constant while the power of the transmitter R1 decreases linearly until it is turned off. Single cycle power control mode shown in Fig. 3b is similar with Fig. 3a.

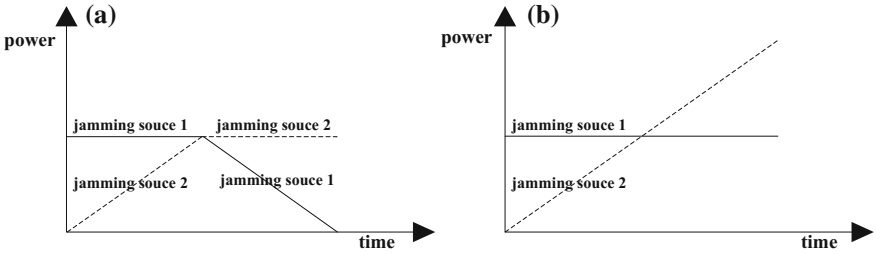

Fig. 3 Schematic of single cycle jamming power control

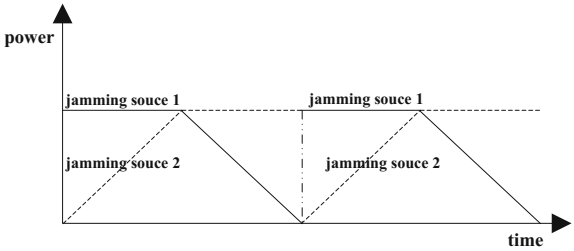

Fig. 4 Schematic of multi-cycle jamming power control

Figure 4 shows the multi-cycle jamming power control. First, the single cycle power control is performed once. When the power of transmitter R1 is reduced to zero, the transmitter R1 is restarted and a constant transmission power is maintained. At the same time, the transmitter 2 turns to the off state. Then the transmitter 2 is switched on, and its power increases linearly from a low power state. That is, the next cycle of jamming power control process starts.

The tracking error curves of the monopulse radar under the two control modes above are given in literature [3]. From the error curves, it is can be seen that in these two mode along with the power ratio of two jamming sources increasing, the monopulse radar stable tracking point gradually deviates from the direction of the visual axis and the deviation amount tends to increase.

4 Cross-Eye Dynamic Jamming Simulation System Design

Based on the principle of cross-eye jamming and the implementation process of cross-eye dynamic jamming, a cross-eye dynamic jamming simulation system is designed.

4.1 System Design Scheme [4, 5]

The system mainly consists of two antennas with a distance of L, two circulators, two signal receiving modules, two digital frequency storage modules, a jamming decision control unit and two transmitters, which is as shown in Fig. 5.

1. Signal receiving module

The jamming system receives the monopulse radar tracking signal through two antennas. Both antennas are capable of transmitting and receiving signals. The distance between the two antennas is much longer than the wavelength of the signal emitted by the monopulse radar. As shown in Fig. 6, the receiver module mainly completes amplification, mixing, filtering and other pre-processing for the receiving signal.

2. Digital frequency storage module [6, 7]

The digital frequency storage module converts analog input signal into a sequential digital signal, and stores it in a memory. The digital signal can be read out of the memory when necessary and converts it into an analog signal to output.

As shown in Fig. 7, because the digital frequency storage needs a lower frequency, it is necessary to perform the up or down conversion processing when the signal need to be stored. The two received signals are down-converted to intermediate frequency signal. Under the control of DSP, they are sent into the A/D, which are transformed into a sequence of digital signals. Then the digital signals are stored in respective memories. The DSP control D/A conversion module 1 reads the digital signal in the memory 2 and the D/A conversion module 2 reads the digital signal in the memory 1. Thus the transmission conversion of the signal is completed.

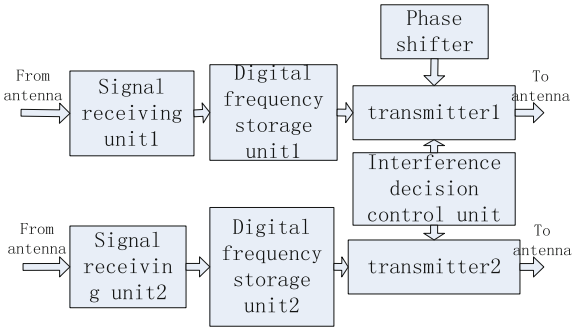

Fig. 5 System design scheme

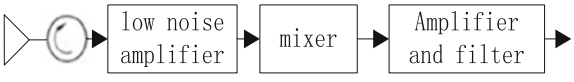

Fig. 6 Signal receiving module

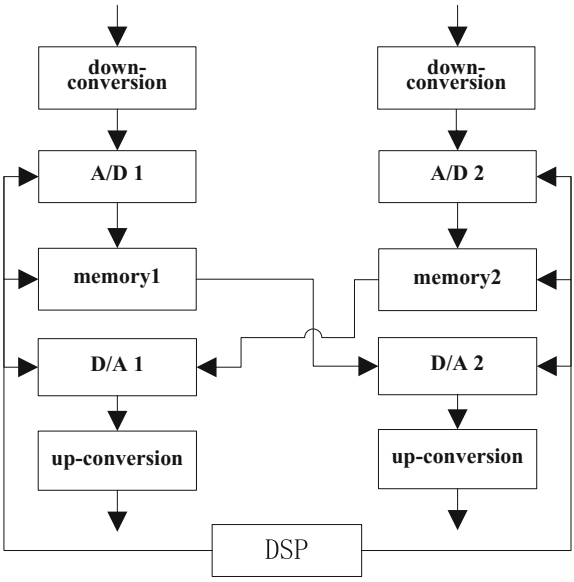

Fig. 7 Digital frequency storage module

3. Jamming decision control module

The jamming decision control module selects the transmitter power control mode according to the jamming instruction of the outside world, and control the change of the power of the two transmitters in real time.

As shown in Fig. 8, the power amplifier microcontrollers of jamming decision control module select the transmitter power control mode according to the external jamming command. The power detection unit detects the transmission power from the transmitter and sends it to the power amplifier microcontroller. The power amplifier microcontroller compares the current transmission power of the two transmitters and adjusts the transmitter output power in real time using the gain control module according to the power control mode.

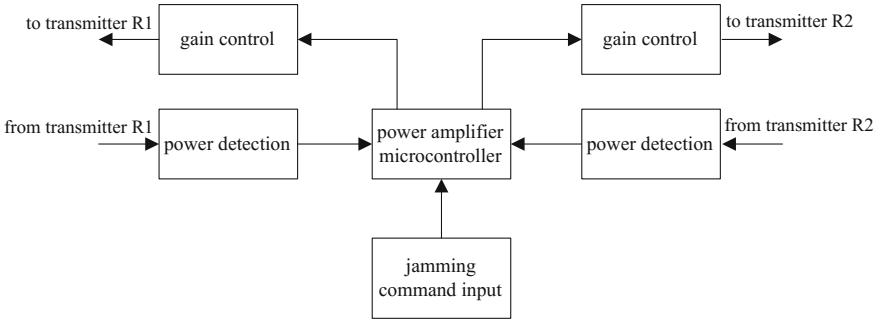

Fig. 8 Jamming decision control module

Power detection unit: It mainly samples power signal at transmitter power amplifier output. Then it carries the spectrum shift and reduces the data sampling rate. At last it will send the digital signal after sampling to power amplifier microcontroller unit. As the RF signal transmitted from transmitter, have a higher sampling rate requirements for the A/D devices. RF A/D chip AD9233 [8] can be chosen based the related literatures.

Power amplifier microcontroller unit: The jamming command input module controls the two pins of the power amplifier microcontroller unit. Power control mode is selected according to the high and low level of the pin. The power calculation and the gain control coefficient calculation are carried on. If pin 1 is high, it is single-cycle control mode. If pin 2 is high, it is multi-cycle control mode. If both pins are low, power control is not used and cross-eye static jamming is put in practice.

Gain control unit: According to the output of power amplifier microcontroller unit, the gain control unit can achieve automatic adjustment of the transmission power gain, which can be achieved using digital attenuator [9–11].

The principle of the switch resistance absorber type attenuator is shown in Fig. 9. A single attenuation unit consists of two SPDT switches and a fixed attenuator. Vn is the control voltage to control SPDT. 1 means through, while 0 means attenuation. Ln is the attenuation of a single SPDT switches in the straight-through path, which connects two SPDT switches directly. The other path is connected with a fixed attenuator. When the path is switched on, the attenuation is the insertion is the sum of the insertion loss of the two switches and the attenuation Xn of the fixed attenuator. A plurality of attenuating units of different attenuation are cascaded and combined to form a digital attenuator.

The six bit digital attenuator HMC472 of Hittite Company with a control range of 31.5 dB and operating frequency from DC to 3000 MHz can complete 0.5 dB control step. A 0.25 dB switch resistance absorber type attenuator is added in series, then only one bit digital control, 0.25 dB attenuation step can be achieved. Cascade mode can be used in attenuation aspect to achieve the maximum attenuation of 63.5 dB. Digital switches can be also used to increase the amount of attenuation. Such as HMC346, the attenuation of which is 32 dB, so its maximum attenuation is 63.75 dB.

The pin level of digital attenuator and digital switches is controlled through Power amplifier microcontroller unit to achieve the attenuation control. The control codes are shown in Table 1. When all control levels are L, the maximum attenuation value of attenuator is a 63.75 dB. However, taking into account the insertion

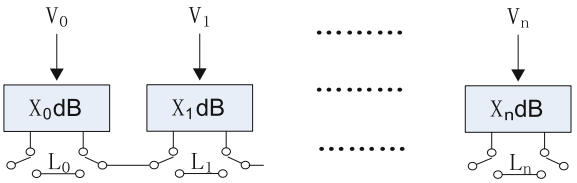

Fig. 9 The switch resistance absorber type attenuator principle

Table 1 Control truth table

Input level									Attenuation value (dB)
Switch resistance absorber type attenuator	HMC472						HMC346		
V0	V1	V2	V3	V4	V5	V6	V1	V2	
H	H	H	H	H	H	H	H	H	0
L	H	H	H	H	H	H	H	H	0.25
…	…	…	…	…	…	…	…	…	…
H	L	L	L	L	L	L	H	H	31.5
L	L	L	L	L	L	L	H	H	31.75
L	H	H	H	H	H	H	L	L	32
L	L	L	L	L	L	L	L	L	63.75

loss actual value of the digital attenuator HMC425, digital switch HMC346 and so on is about 7 dB, so the maximum attenuation of the whole attenuator is about 70.75 dB.

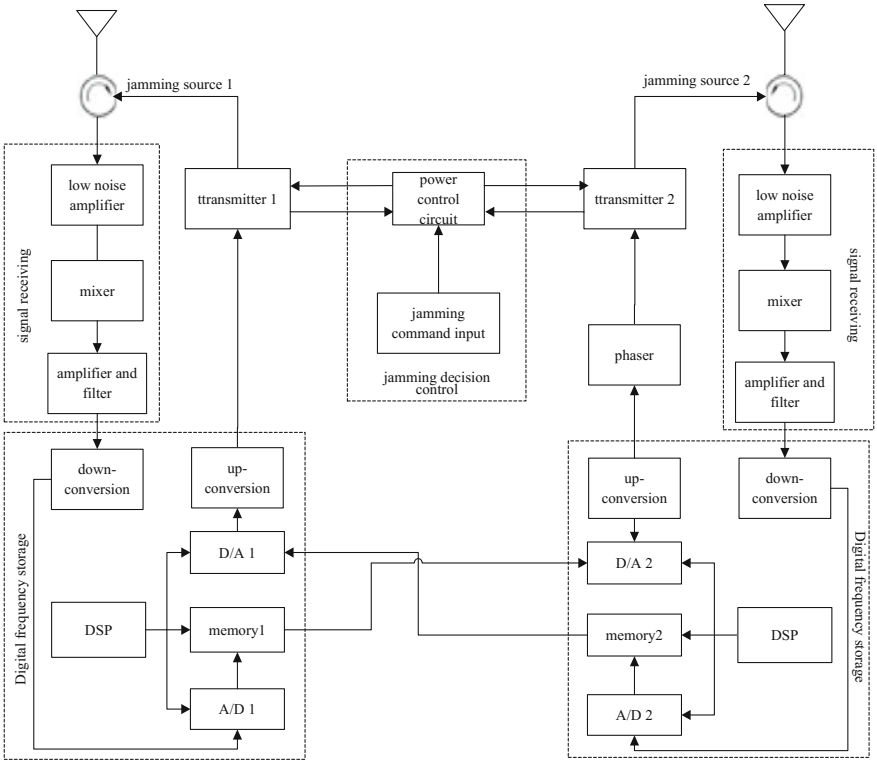

Fig. 10 Structure schematic diagram of the cross-eye dynamic jamming system

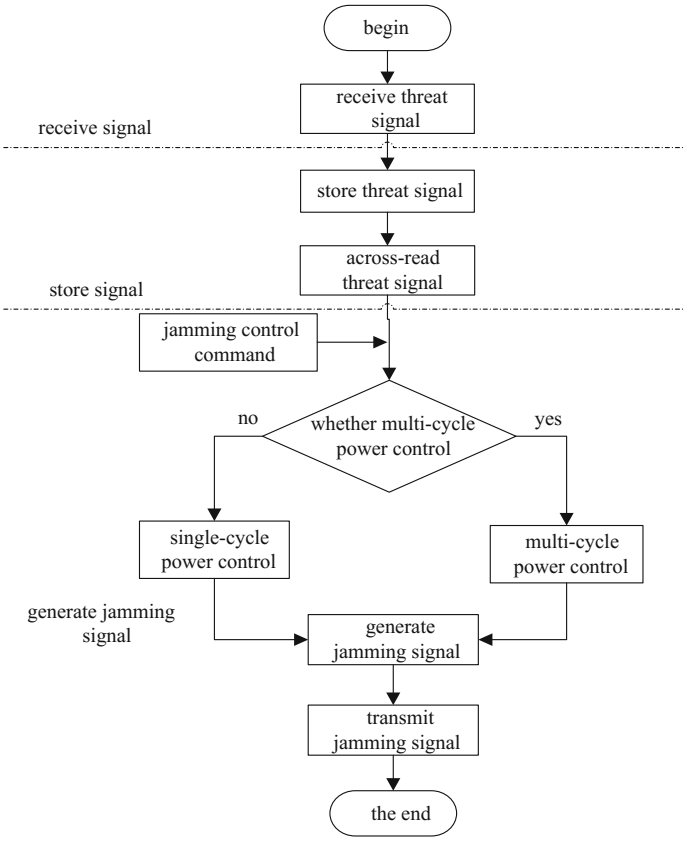

Fig. 11 Work flow of the cross-eye dynamic jamming system

4.2 System Work Flow

Figure 10 shows a cross-eye dynamic jamming system structure diagram. Figure 11 shows the cross-eye dynamic jamming e system work flow.

1. Receive signal

The jamming device receives the monopulse radar tracking signal through two antennas. The two received threat signals are sent to the respective signal receiving modules through the circulator. The pretreatments such as amplification, mixing, filtering are actualized to threat signals by receiving module. Then the signals processed are sent into respective digital storage unit.

2. Store the signal

The input signals of the signal receiving module are received. Then they are converted into digital signals and stored it in the respective memory. Under the control

of the digital signal processor, the signals stored are across-read. One of the signals is sent to the transmitter after up-converted. Another one is sent to the transmitter after 180° phase shift through the phase shifter.

3. Generate jamming signals

The jamming control command is input from outside. The system determines whether multi-cycle power control. If yes, the jamming decision control module performs multi-cycle power control mode, else performs single-cycle power control mode. Two transmitters under the real-time control of the jamming decision control module, transmits the two jamming signals which are opposite phase through the antennas to target. So cross-eye dynamic jamming to monopulse radar seeker tracking system is realized.

5 Conclusion

Aiming at the problem that the control for phase and amplitude of two-point source is difficult in cross-eye jamming, and the jamming effect is not good. A cross-eye dynamic jamming system is designed according to the cross-eye dynamic jamming method based on power control. The system chooses commercial products devices, whose level is relatively mature, the cost is low. It can greatly reduce the complexity of the jamming device and development costs. It lays the foundation for the project to achieve in the future.

References

1. Shang Z, Bai W, FU X (2013) Effective countermeasure of dual-source jamming to initiative target-seeking missile. Mod Def Technol 41:102–105 (in Chinese)
2. Wang H, Zhang Y (2007) A new method to realize cross-eye jamming technique. Shipboard Electron Countermeasure 30:23–25 (in Chinese)
3. Zhao R (2013) Dynamic jamming analysis for monopulse radar angle tracking system. In: Aerospace electronic warfare annual conference proceedings, pp 413–418 (in Chinese)
4. Zhang M, Wang X (2006) Radar System. Publishing House of Electronics Industry, Beijing (in Chinese)
5. Zhao G (1999) Radar confrontation theory. Xi'an University of Electronic Science and Technology Press, Xi'an(in Chinese)
6. Yang W (2011) Design and research of radar jamming simulator. Technol Found Natl Def 11:53–55 (in Chinese)
7. Yang H, Wang G (2011) Missile-borne self-screen jamming technique of mono-pulse radar based on DRFM. Aerosp Electron Warf 1:6–9 (in Chinese)
8. Chui H, Gao J, Qu X (2011) Design and implementation of a power feedback control system for digital shortwave transmitters. Telecommun Eng 8:70–72 (in Chinese)

9. Zhao F, Qi H, Zhao H, Chai S, Mao J (2011) Design and integration of the front end RF for the radiation radar multi-target simulator. Mod Radar 1:70–72 (in Chinese)
10. Deng Y, Zhu L (2010) Design and implementation of a small step power digital attenuator. J Microwaves 8:314–316 (in Chinese)
11. HMC472LP4 Datasheet

Design and Implementation of Real-Time Data Exchange Software of Maneuverable Command Automation System

Shi Chuan, Zhang Yang and Zhou Yuefei

1 Introduction

Command automation system provides an effective means of command under the conditions of information technology, it has been hailed as the "central nervous system" and "force multiplier" of the command, so command automation system confrontation determines the success of information confrontation [1]. For the rapidly changing situation, maneuverable command automation system can better adapt to the requirements motor performance and rapid response capability under real situation.

Maneuverable command automation system carries on the network exchange and data communication with external system or equipments through encipherment/decryption [2, 3]. There are many kinds of hardware maneuverable command automation system. The communication means and the frequency band are different. The interface is complex and the data throughput is large. In order to ensure the continuous and reliable operation and the proper performance of the system, there must be a stable real-time and high-efficiency data exchange system to guarantee the various types of information transmission, processing and other functions to achieve stability between hardware equipments. This paper designs and implements a real-time data exchange software for mobile maneuverable automation system based on requirement analysis using dynamic multi-threading and multicasting technology. It solves the problem of congestion and collapse caused by the large amount of data flooding, which have achieved good results in the test.

S. Chuan (✉) · Z. Yang
Luoyang Electronic Equipment Test Center, Luoyang 471003, China
e-mail: shi__chuan@163.com

Z. Yuefei
The Army of 66135, Beijing 100000, China

Z. Deng (ed.), *Proceedings of 2017 Chinese Intelligent Automation Conference*,
Lecture Notes in Electrical Engineering 458,
https://doi.org/10.1007/978-981-10-6445-6_2

2 Software Requirements Analysis

According to the needs of a certain task, the maneuverable command automation system is mainly to achieve information collection, transmission, processing automation, and support decision-making and in the process, which could ensure that the command of commander to the participants and equipments. Its real-time data exchange software needs to complete the real-time data exchange among the working groups, and accomplish the tasks of complex data communication, transmission, processing, display and control.

Based on the analysis of actual demand and technical, the real-time data exchange software should have the following functions:

1. Data access and distribution: This function can forward the external data to the application seat of the system through internal and external network bridging way.
2. Protocol analysis and recording: This function can achieve the original data protocol analysis, and record the access data efficiently and completely. It can be distributed deployment and realize multiple backup to ensure data security.
3. Data processing and display: This function can complete the two-dimensional track display, data fusion and other required data preprocessing. It also can achieve the real-time display of variety target information and situation.

3 Software System Design

3.1 Structure Design

According to the system functional requirements analysis, the real-time data exchange software is divided into four configuration items: data access and distribution, protocol analysis and conversion, data recording, data processing and display. The main work flow of the real-time data exchange software applied to the maneuverable command automation system is as follows: Data access and distribution configuration item receives the external data, and send them to protocol analysis and conversion configuration item to finish the protocol conversion, and to data recording configuration item to finish data recording. Then the various types of data after analysis will be output in different directions. Data processing and display configuration item preprocesses the received data. The data results processed can be displayed visually based on the requirements. The structure design of this software is shown in Fig. 1.

(1) Data access and distribution configuration item includes the parameter configuration module and data scheduling module.

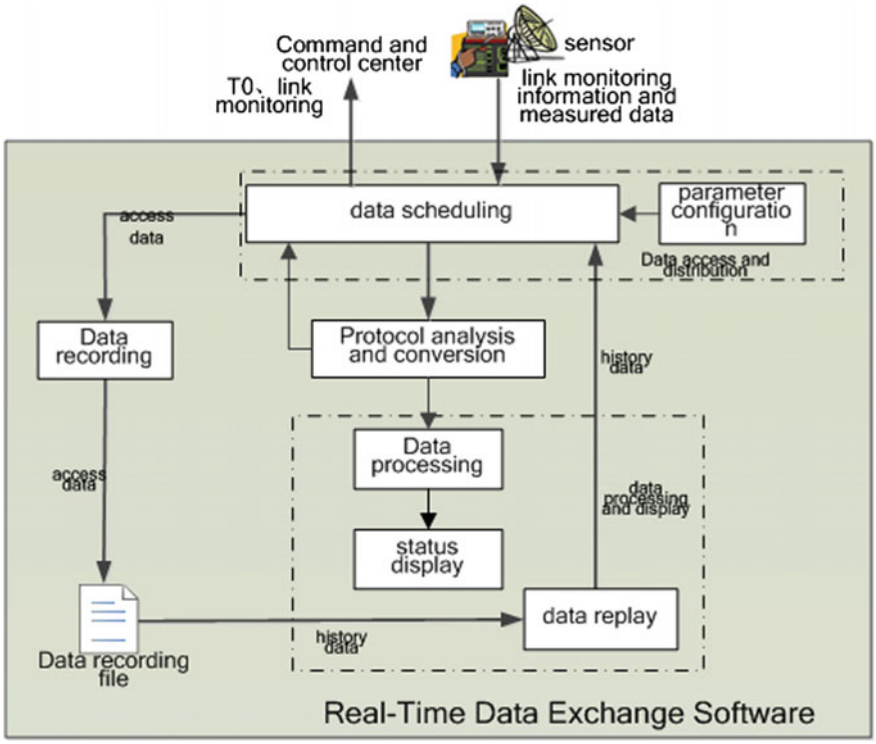

Fig. 1 Software structure design

Parameter configuration module mainly provides data distribution configuration table, operation and maintenance interface and API interface.

Data scheduling module mainly receives all the data sent from the system outside of the system and the data packets from the internal software. It checks the legitimacy of the received data and rejects the illegal data. Through configuring, it can finish the directional transmission and multicast transmission of the received data in the system.

(2) Protocol analysis and conversion configuration item mainly finishes the send and receive protocol conversion of the data send by outside system. The external protocol format is converted to internal protocol format, which will be sent to system internal software for follow-up processing. It also finishes the send and receives protocol conversion of the data send by internal system. The internal protocol format is converted to external protocol format, which will be sent to system external software to ensure the entire data requirements.

(3) Data record configuration item carries out efficient and complete record on the received data. Data scheduling module will receive all the data sent through the private forwarding channel to the data recording module. These dates will be

recorded by the data recording module in accordance with a custom format. Data recording module can be distributed deployment and achieves multi-backup, which ensure data security.

(4) Data processing and display configuration items include data processing module, status display module and data reproduction module.

The data processing module mainly processes the received data in real time. The status display module has the function of state display of system and each device. It can display the state information in real time. The data replay module is used to replay the data afterwards. The recorded data can be sent to the internal network according to the selected data interval, and the software in the system can be driven to run, which is help for the process analysis.

3.2 *Software Running Process*

Real-time data exchange software running process is shown in Fig. 2.

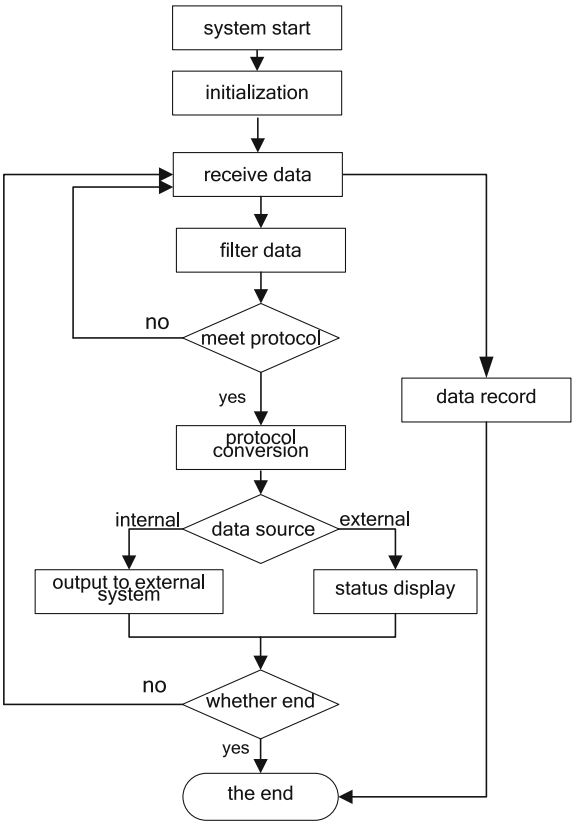

Fig. 2 Real-time data exchange software running flowchart

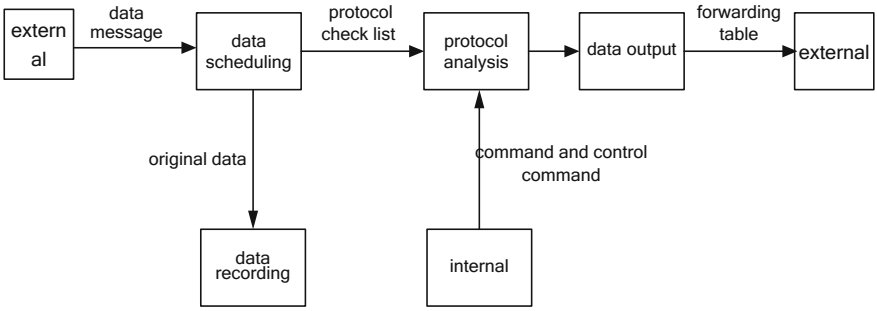

Fig. 3 Real-time data processing and management interface diagram

After the system starts, the system is initialized, and the parameter configuration is read, which includes the source IP address and port number, the destination IP address and port number, the address and device mapping table, the data distribution frequency, etc. Then the data is received. There are two operations for data at the same time. One is to record data directly, which is used for data analysis. The other one is to filter the data received. The data which do not meet the protocol will be discarded. The data which meet the protocol will be carried protocol conversion. According to different sources, the data will be output to different locations. The internal data received is output to external system. The external data received will be sent to status display module for real-time display. If the end has not been selected, the system is waiting for receiving data again. If the end has been selected, the software is end of operation.

3.3 Software Interface Design

Software interface design is shown in Fig. 3. All of the interface types are real-time data transmission. The operating states are normal. According to the interface connection the software data flow can be found out.

4 The Key Technologies and Solutions

4.1 Dynamic Multithreaded Programming

A thread is a single sequential control flow in a program that contains separate stack and CPU register states. Each thread shares all the process resources, including files opened, signal identifiers, and memory allocated dynamically, etc. Multi-threaded is that multiple threads are running simultaneously to complete different work in a

process, in which there is a main thread. If multiple tasks need to be dealt with at the same time, the use of multi-threaded is the ideal choice [4, 5].

Real-time data exchange software in the multi-channel real-time data processing applications, will transform a data packet received into a number of different formats of messages and forwarded to multiple destination addresses, in which case the use of dynamic multi-threaded approach can improve the system efficacy. According to the source address, the main thread can determine whether to open a new thread. If the source address is a new address, a new thread will be opened to receive and manage data send by this new source address. If there is no information of the source address for a long time, the thread corresponding to this source address will be deleted. So that system resources can be released in real-time. In high frequency data transmission of multiple data sources, dynamic multi-threaded approach can effectively improve the system operating efficiency and reduce congestion and other phenomena.

4.2 Multicast Planning

Multicast is a communication mode that enables point-to-multipoint network connectivity between the sender and each receiver. If a sender simultaneously transmits the same data to multiple receivers, only one copy of the same packet is replicated. Hosts can request to join or exit a group from a router. Hosts in the same group can receive all data of the group. Routers and switches in the network selectively copy and transmit data, and only transmit data to the group host, so that the data can be transferred to multiple groups in one time, and not affect the external host communication. Multicast improves data transmission efficiency and reduces the possibility of congestion in the backbone network [6–8].

In order to avoid network congestion caused by multi-channel high-speed data, real-time data exchange software groups the network nodes according to the data stream type. For example, the related information to measurement data of equipment 1 is assigned to a group 1 for transmission; command information is assigned to a group 2 for transmission; telemetry and remote control information is assigned to a group 3 for transmission. According to the data stream type, the network nodes are grouped, so that certain types of information can be propagated only among specific nodes, which do not affect the data transmission and reception of other nodes. The application of multicast technology improves the efficiency of the network, reduces the network congestion and improves the stability of the system.

4.3 Protocol Conversion

Because each equipment and the command system use different the real-time data information, it is need to convert protocol of the data when each equipment

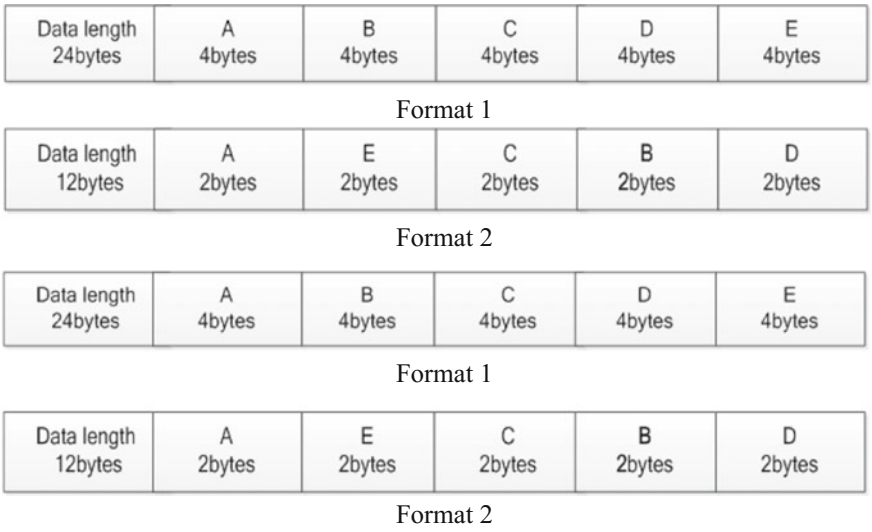

Fig. 4 Format conversion diagram

information is sharing. Specific conversions are as follows: The same information is described by two different structural forms and sequences. For example, there are five fields of A, B, C, D, and E, whose information are described in the following two ways, as shown in Fig. 4.

The information fields A, B, C, D and E in the format 1 are defined as INT data types. Each information field in the format 2 is defined as the short data type. In the data exchange process, it is need to do the following processing.

(1) After the serial data packet is received from the network, it is copied into the structure of format 1.
(2) According to the definition of the structure, the data of each information field is read.
(3) The data type of each information is converted from INT data type to short data type corresponding to the information field of format 2.
(4) The information is rearranged according to the format 2 structure.
(5) The data after the reorganization is copied into the data packet to sent from the network.

5 Software System Implementation

According to the analysis and design, the software is completed using VC++ as the programming language. The software is deployed in a maneuverable mobile command automation system. Figure 5 shows two-dimensional situation display

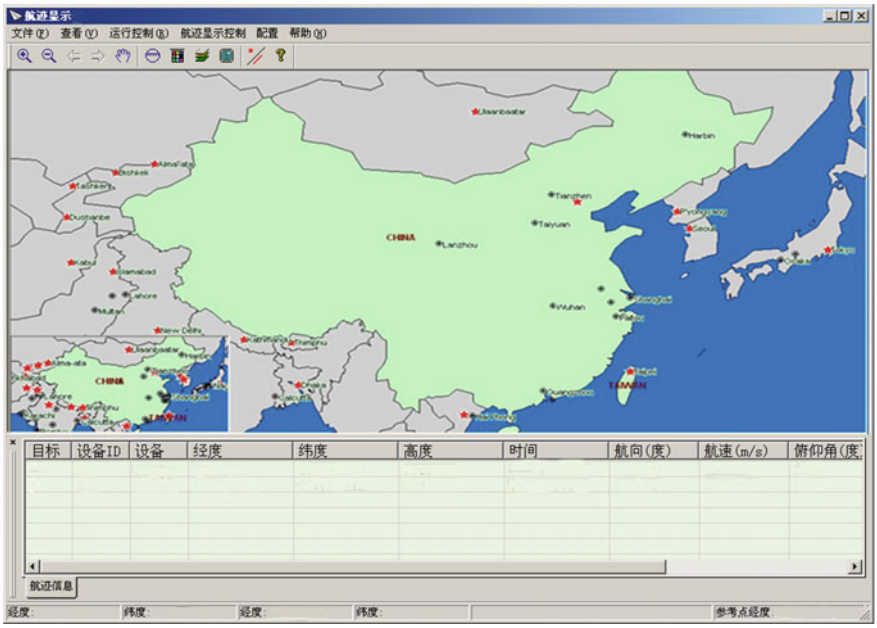

Fig. 5 Two-dimensional situation display

Fig. 6 Target information measurement results

interface in the real-time data exchange software. Figure 6 shows the target information measurement results displayed by the real-time data exchange software. The target information received is consistent with the target equipment state. The

simulation results show that the software can receive and display 25 batches and 100 targets track information correctly and in real time. There is no congestion and collapse when large amount of data is processed. The data records are established correctly in the background and good results are obtained.

6 Concluding Remarks

Based on multicast technology and dynamic multi-thread technology, a real-time data exchange software for maneuverable command automation system is designed and realized in this paper, which greatly improves the data throughput and greatly reduces the congestion in data transmission process, etc. It is proves through a application that the real-time data exchange and processing ability of the software can withstand the test of high-speed and large-flow data, and the software guarantee the completion of the task successfully.

References

1. Xiong Y, Teng ZP, Zheng HL (2006) Distributed artillery command automation system based on movable agent. Fire Control Command Control 31(1):52–54 (in Chinese)
2. Wang Y (2005) EMC design of the maneuverable C4I system. Fire Control Command Control 30(3):96–98 (in Chinese)
3. Wand SL, Dou B, Yand YM (2008) Power supply design for the motorized command automotive system. Mob Power Veh 4:8–10 (in Chinese)
4. Zhu HT, Yao M, Cai TY et al (2011) Multi-thread programming for image display of navigational radar. Mod Electron Technol 34(12):108–110 (in Chinese)
5. Hu M (2008) Windows network programming technology. Science Press, Beijing (in Chinese)
6. Huang K, Guo S (2011) Application of IP multicast in radar data processing. Electron Design Eng 19(17):16–18 (in Chinese)
7. Chen J, Chen W (2001) Visual C++ network advanced programming. People's Posts and Telecommunications Press, Beijing (in Chinese)
8. Gong LF, Ma Q, Pan CD (2007) Research on optimizing performance of multicast network. Comput Modernization 11:78–83 (in Chinese)

Active Fault Tolerant Control for Flexible Spacecraft with Sensor Faults Using Adaptive Integral Sliding Mode

Zhifeng Gao, Bing Han, Moshu Qian and Jing Zhao

1 Introduction

The attitude control system is one of the most important problem in spacecraft design. In modern space related missions, there is a high demand on safety, reliability and performance of spacecraft. In the past few years, the attitude control of spacecraft has attracted extensive interests and attentions by many scientists and engineers, many important results have been reported in the published academic journals [1, 2]. For the high-accuracy attitude control performance of flexible spacecraft, all kinds of advanced attitude control schemes are proposed recently, such as an adaptive fuzzy sliding mode controller is designed in [3] for the attitude stabilization of networked flexible spacecraft with parameter uncertainty and time delay, such that the tracking stability of the closed loop attitude system can be guaranteed. In [4], the attitude regulation control problem is studied for the flexible spacecraft. A dynamic disturbance compensator and a novel robust Lyapunov-based controller are designed.

The above mentioned studies focus on modeling uncertainty, disturbance and vibration to flexible appendages and do not consider the unknown faults. However, faults caused by actuators, sensors or other components, frequently occur in practice attitude control systems, which will deteriorate its performance or even shut-down of the system. Therefore, research into fault tolerant control (FTC) for attitude system has been recognized as one of the important aspects in seeking

Z. Gao (✉) · B. Han · J. Zhao
College of Automation, Nanjing University of Posts and Telecommunications, Nanjing 210023, People's Republic of China
e-mail: gaozhifeng@njupt.edu.cn

M. Qian
College of Electrical Engineering and Control Science, Nanjing Tech University, Nanjing 211800, People's Republic of China
e-mail: moshu_qian@126.com

Z. Deng (ed.), *Proceedings of 2017 Chinese Intelligent Automation Conference*, Lecture Notes in Electrical Engineering 458,
https://doi.org/10.1007/978-981-10-6445-6_3

solution to an improved reliability of spacecraft. In the literature, the categories of FTC and be divide into active and passive methods [5]. Passive FTC is just an extension of robust control. Active FTC needs the feedback from the fault information. The designed controller changes in an active way according to the effects of fault. In [6], A novel fault tolerant attitude tracking control scheme is developed for flexible spacecraft with partial loss of actuator effectiveness fault. a modified fault tolerant control law based on adaptive sliding mode and neural network is proposed. In [7], a FTC method is given to the spacecraft attitude maneuvering control systems against actuator complete failure using feedback controller. In, recent years, sliding mode control has been widely applied for design of FTC as an effective control method to compensate for faults in control system. Until now, to the best of our knowledge, the fault tolerant control problem of spacecraft in sensor faulty case has not been fully investigated yet, which remains challenging and motivates us to do this study.

Inspired by the above background, an active FTC scheme is proposed for a flexible spacecraft attitude systems with unknown sensor faults. Compared to the existing literature, the main contributions of this paper are: (i) Sensor fault can be transformed into the actuator fault form without strict conditions and coordinate. (ii) The proposed approach can achieve the FTC task without fault detection module, which brings convenience FTC design in aerospace Engineering.

2 Problem Statement

The dynamics behavior of flexible spacecraft can be described by Zhang et al. [8],

$$J\ddot{\theta} + \delta^T \ddot{\eta} = u \tag{2.1}$$

$$\ddot{\eta} + D\dot{\eta} + K\eta + \delta\ddot{\theta} = 0 \tag{2.2}$$

where $J \in R^{3\times3}$ is the total inertia matrix of the spacecraft, θ is the attitude angle, which includes roll θ_x, yaw θ_y and pitch θ_z. $\eta \in R^{n\times3}$ stands for the coupling matrix between elastic and rigid dynamics, n is the number of the elastic modes connected to the rigid body, $u \in R^{3\times1}$ is the control torques generating from the flywheels orthogonally mounted on board. D and $K \in R^{n\times n}$ are the damping matrix, stiffness matrix of the appendages and, respectively.

By introducing state variable $x = \begin{bmatrix} \theta & \dot{\theta} \end{bmatrix}^T$, the state space model of flexible spacecraft attitude dynamics with sensor faults is described by,

$$\dot{x} = (A + \Delta A)x + Bu + Bd \tag{2.3}$$

$$y = Cx + f_s \tag{2.4}$$

where $A = \begin{bmatrix} 0 & I_{3\times 3} \\ 0 & 0 \end{bmatrix}$, $B = \begin{bmatrix} 0 \\ (J - \delta^T\delta)^{-1} \end{bmatrix}$, $C = \begin{bmatrix} I_4 \\ 0 \end{bmatrix}^T$, $\Delta A = MFE$ is a real time-varying matrices representing parameter uncertainty with M, E being known real constant matrices of appropriate dimensions, and F is an unknown real time-varying matrix satisfying the following inequality $F^TF < I_4$, $d = \delta^T(D\dot{\eta} + K\eta)$ is the disturbance vector caused by elastic vibration of flexible appendages, which satisfies $\|d\| \le d_0$ and d_0 is a unknown positive scalar. $f_s(t) \in R^{4\times 4}$ represents the unknown sensor faults.

Before ending this section, we recall the following assumptions and lemmas, which will be essential to realize the active FTC design later.

Assumption 1 The sensor fault satisfies the following norm bounded constraint: $\|f_s\| \le l$ and $\|\dot{f}_s\| \le l_d$, l and l_d are two unknown positive scalars.

Lemma 1 Hao et al. [9] *consider the following linear system,*

$$\dot{x} = Ax + B\omega \tag{2.5}$$

$$y = Cx + D\omega \tag{2.6}$$

If there exist a positive scalar γ and a symmetric positive define matrix P, such that the following inequality holds,

$$\begin{bmatrix} A^TP + PA & PB & C^T \\ B^TP & -\gamma^2 I & D^T \\ C & D & -I \end{bmatrix} < 0 \tag{2.7}$$

then above system is stable with a given disturbance attenuation level γ.

3 Sensor Fault Estimation Scheme

In this section, a sensor fault estimation approach will be developed. For this purpose, define a new state variable $z \in R^{4\times 4}$, which can be acheived by passing the faulty system output (2.4) through the following virtual filter.

$$\dot{z} = -A_f z + A_f y \tag{3.1}$$

where $A_f \in R^{4\times 4}$ is the parameter matrix and it is Hurwitz.

Let $\bar{x} = [x \quad z]^T$, the original faulty system (2.3) and (2.4) can be transformed into the following augment system,

$$\dot{\bar{x}} = (A_a + \Delta A_a)x + B_a u + B_a d + B_a f_s \tag{3.2}$$

$$z = C_a \bar{x} \tag{3.3}$$

where

$$A_a = \begin{bmatrix} A & 0_{6\times4} \\ A_f C & -A_f \end{bmatrix} \quad \Delta A_a = \begin{bmatrix} \Delta A & 0_{6\times4} \\ 0_{4\times6} & 0_{4\times4} \end{bmatrix} \quad B_a = \begin{bmatrix} B \\ 0_{4\times3} \end{bmatrix} \quad D_a = \begin{bmatrix} 0_{6\times4} \\ A_f \end{bmatrix}$$

$C_a = \begin{bmatrix} 0_{6\times4} \\ I_4 \end{bmatrix}^T$. After transformation by this way, the original sensor fault can be treated as actuator fault in system (3.2) and (3.3). The estimated value of sensor fault can be obtained by the above designed adaptive fault estimation observer,

$$\dot{\hat{\bar{x}}} = A_a \hat{\bar{x}} + B_a u + D_a \hat{f}_s + L(z - \hat{z}) \tag{3.4}$$

$$\dot{\hat{f}}_s = KR(z - \hat{z}) - \sigma K \hat{f}_s \tag{3.5}$$

where $\hat{\bar{x}}$, $\hat{f}_s$ and $\hat{z}$ are the estimation of $\bar{x}$, f_s and z respectively. L is the designed observer gain matrix. K is a positive define weighting matrix, σ is a positive constant scalar and satisfies $\sigma > \lambda_{\max}(K^{-1})$.

Denoting $e_x = \bar{x} - \hat{\bar{x}}$, $e_f = f_s - \hat{f}_s$, in the following, the fist main result is given in the form of Theorem 1.

Theorem 1 *Based on the proposed observer* (3.4) and (3.5), *the estimation error dynamics are uniformly ultimately bounded, if there exists asymmetric positive definite matrix* P_1 *and a matrix* Q *with appropriate dimensions such that*

$$P_1 D_a = C_a^T R \tag{3.6}$$

$$\begin{bmatrix} P_1 A + A^T P - Q C_a - C_a^T Q^T & P_1 M & P_1 B_a \\ M^T P_1 & -\varepsilon I & 0 \\ B_a^T P_1 & 0 & -\varepsilon I \end{bmatrix} > 0 \tag{3.7}$$

The observer gain can calculated by $L = P_1^{-1} Q$. The estimation errors are bounded and converge with a exponential rate greater than $e^{-\frac{k}{h}}$ to the residual set $\Omega : \left\{ e_x, e_f | \lambda_{\min}(P_1) \|e_x\|^2 + \lambda_{\min}(K^{-1}) \left\|e_f\right\|^2 \le \frac{\delta h}{k} \right\}$.

Proof Choosing a Lyapunov candidate function as follows,

$$V_1 = e_x^T P_1 e_x + e_f^T P_1 e_f \tag{3.8}$$

Under the Assumption 1 and some constraints mentioned above, it is easily obtained that, $2 e_f K^{-1} \dot{f}_s \le \lambda_{\max}(K^{-1})(\left\|e_f\right\|^2 + l_d^2)$, $2\sigma e_f^T f_s \le \sigma(\left\|e_f\right\|^2 + l^2)$, $2 e_x^T P_1 \Delta A x \le \frac{1}{\varepsilon} e_x^T P_1 B_a B_a^T P_1^T e_x + \varepsilon d^T d$.

Then, the derivative of (3.8) satisfies the following inequality relationship,

$$\dot{V}_1 \leq -k(\|e_x\|^2 + \|e_f\|^2) + \delta \tag{3.9}$$

where $k = \min(\lambda_{\max}(\Gamma), \sigma - \lambda_{\max}(K^{-1}))$, $\delta = \lambda_{\max}(K^{-1})l_d^2 + \sigma l^2 + \varepsilon\|x\|^2 + \varepsilon d_0^2$, $\Gamma = -(A_a - LC_a)^T P_1 - P_1(A_a - LC_a) - \frac{1}{\varepsilon}P_1 MM^T P_1^T - \frac{1}{\varepsilon}P_1 B_a B_a^T P_1^T$.

Noting that $V_1 \leq h(\|e_x\|^2 + \|e_f\|^2)$, $h = \max(\lambda_{\max}(P_1), \lambda_{\max}(K_1^{-1}))$, and substituting it into (3.9), it yields $\dot{V}_1 \leq -\frac{k}{h}V_1 + \delta$, which implies that Theorem 1 holds. This completes the proof.

4 Fault Tolerant Controller Design and Stability Analysis

In this section, the compensated output signal $y_c = y - \hat{f}_s$ is used to construct a integral sliding surface as follow,

$$s = G(y_c - y_c(t_0) + \int_{t_0}^{t} y_c(\tau)d\tau) \tag{4.1}$$

where $G = (CB)^+ - Y(I - (CB)(CB)^+)$ and Y is an arbitrary matrix. t_0 represents the initial time of the attitude system.

The designed controller is composed of a linear and a nonlinear part as follows,

$$u = u_l + u_n \tag{4.2}$$

where $u_l = Ny_c$, $u_n = -(\hat{\rho} + \lambda)\frac{s}{\|s\|}$, $\dot{\hat{\rho}} = \frac{1}{v}\|s\|$. N is the designed matrix, λ is a constant scalar and $\hat{\rho}$ is the estimation of the unknown term $\rho = l_d + \|G\|\|\dot{e}_f\| + \|G + N\|\|e_f\|$. $v > 0$ is a constant adaptation gain.

Theorem 2 *If there exist a symmetric matrix P_2 and output feedback gain N satisfy the following linear matrix inequality,*

$$[\Xi]_{34\times 34} < 0 \tag{4.3}$$

where $\Xi_{11} = (\varphi A - BGC)P_2 + P_2(\varphi A - BGC)^T$, $\varphi = I - BGC$, $\Xi_{12} = -BG + BN$, $\Xi_{13} = -BG$, $\Xi_{14} = P_2$, $\Xi_{15} = \varphi M$, $\Xi_{16} = \Xi_{18} = P_2 C^T$, $\Xi_{17} = BN$, $\Xi_{22} = \Xi_{33} = -\gamma_2^2 I$, $\Xi_{28} = I$, $\Xi_{44} = \Xi_{55} = -\mu_2^{-1}I$, $\Xi_{66} = \Xi_{77} = \Xi_{88} = -I$, $\Xi_{i,j}$ are null for others. The asymptotical stability of the system can be guaranteed.

Proof When the system has the ideal sliding mode motion on the sliding surface, i.e. $\dot{s} = 0$, the equivalent control can be designed as,

$$u_{eq} = -G(C(A + \Delta A + I)x + CBd + \dot{e}_f + e_f) + u_n \tag{4.4}$$

Substituting (4.4) into (2.3), the sliding dynamics can be obtained,

$$\dot{x} = ((I - BGC)(A + \Delta A) - BGC + BNC)x + \bar{B}\omega \tag{4.5}$$

$$y_c = Cx + \bar{D}\omega \tag{4.6}$$

where $\omega = [\, e_f \quad \dot{e}_f \,]^T$, $\bar{B} = [\, B(N - G) \quad -BG \,]^T$ and $\bar{D} = [\, I \quad 0 \,]^T$.

By applying Lemma 1 to (4.5) and (4.6), Schur complement and some calculations, the linear matrix inequality condition (4.3) can be obtained.

Consider the following Lyapunov function candidate,

$$V_2 = \frac{1}{2}(s^T s + v\tilde{\rho}^2) \tag{4.7}$$

where $\tilde{\rho} = \rho - \hat{\rho}$ is the adaptive estimation error.

Its derivative follows from (4.2) that,

$$\dot{V}_2 \leq (\varepsilon\|x\| - \lambda)\|s\| \tag{4.8}$$

where $\varepsilon = \|GCA\| + \|GC\| + \|NC\| + \|GCM\|\|E\|$. Choosing $\lambda > \varepsilon\beta$ with a given scalar β, then $\dot{V}_2 < 0$. Which means that the system will be stably even in faulty conditions. This completes the proof.

5 Simulation Example

In this section, the good performance of the proposed active fault tolerant control approach is verified by considering a flexible spacecraft attitude control system model which is given by Zhang et al. [8]. Suppose that the sensor fault occurs on the first measurement channel at 10 s and the fault is a time-varying signal. Namely, $f_s = [\, f_1 \quad 0_{1\times 3} \,]^T$. The expressions of fault is described as $f_s = 0.8\sin(0.9t)$, when $t > 10s$.

Firstly, Fig. 1 provides evidence that our dynamic sensor estimation scheme has excellent fault estimation capability. Furthermore, the simulation is performed with classical output feedback control strategy. Figure 2a shows the bad effect of sensor fault on the flexible spacecraft attitude system. From Fig. 2b, with the implement of the active FTC scheme designed in this paper, it is not difficult to find that the effect of sensor fault to the closed-loop attitude systems is removed.

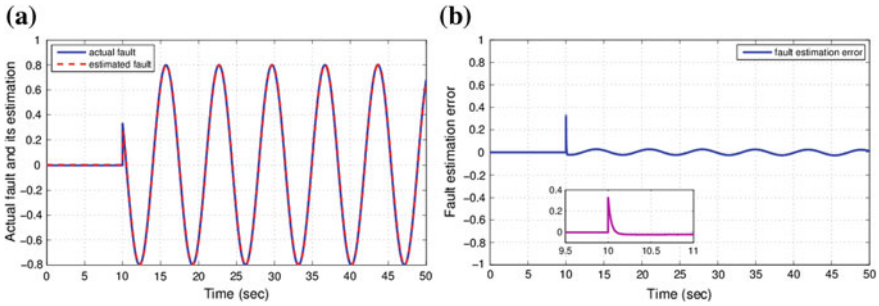

Fig. 1 Sensor fault estimation result (**a**) and its error (**b**)

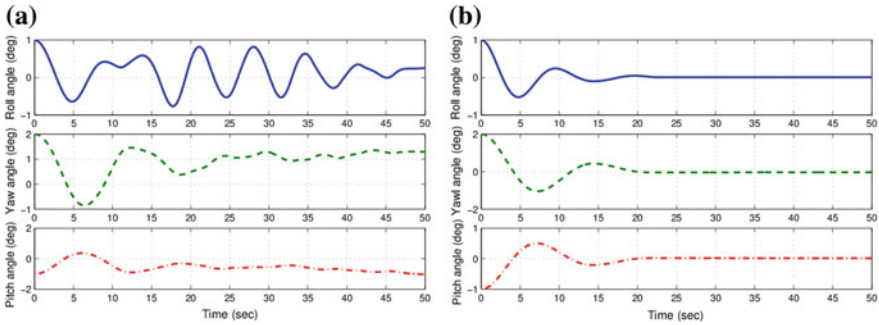

Fig. 2 Attitude angle responses in sensor faulty case using classical output feedback control (**a**) and using active FTC approach designed in this paper (**b**)

6 Conclusion

In this paper, an active FTC strategy for flexible spacecraft under sensor fault case is designed. The sensor fault is transformed into actuator fault form of an augment system and fault estimation is achieve based on an adaptive observer. By applying adaptive integral sliding mode, a FTC controller is proposed, which can ensure the attitude system normal operation although sensor fault occurs. In the finally, simulation results show the excellent performance of our approach.

Acknowledgements This work is supported by NNSF under Grant (61304106, 61403195), the Natural Science Foundation of Jiangsu Province, China (SBK2014042586), the Fundamental Research Funds for the Central Universities (NJ20160051), the Graduate Innovation Research Foundation of Jiangsu Province (1166).

References

1. Zou AM, Ruiter AJD, Kumar KD (2016) Distributed finite-time velocity-free attitude coordination control for spacecraft formations. Automatica 67:46–53
2. Ruiter AJD (2016) Observer-based adaptive spacecraft attitude control with guaranteed performance bounds. IEEE Trans Autom Control 61(10):3146–3151
3. Dong C, Xu L, Chen Y, Wang Q (2009) Networked flexible spacecraft attitude maneuver based on adaptive fuzzy sliding mode control. Acta Astronaut 65:1561–1157
4. Zhong C, Chen Z, Guo Y (2017) Attitude control for flexible spacecraft with disturbance rejection. IEEE Trans Aerosp Electron Syst 53(1):101–110
5. Lan JL, Patton RJ (2016) A new strategy for integration of fault estimation within fault-tolerant control. Automatica 69:48–59
6. Xiao B, Hu QL, Zhang YM (2012) Adaptive Sliding mode fault tolerant attitude tracking control for flexible spacecraft under actuator saturation. IEEE Trans Control Syst Technol 20 (6):1605–1612
7. Zhao D, Yang H, Jiang B, Wen L (2016) Attitude stabilization of a flexible spacecraft under actuator complete failure. Acta Astronaut 123:129–136
8. Zhang R, Qiao JZ, Li T, Guo L (2014) Robust fault-tolerant control for flexible spacecraft against partial actuator failures. Nonlinear Dyn 76:1753–1760
9. Hao LY, Park JH, Ye D (2016) Fuzzy logic systems-based integral sliding mode fault-tolerant control for a class of uncertain non-linear systems. IET Control Theory Appl 10(3):300–311

Method of Detection Optimization Based on Vector Electric Field Multi-electrode Gradient Information

Jianjun Liu, Chao Wu, Guoyu Cui, Zheng Wang, Yubo Wang, Guofeng Pan, Guohua Liu, Chengbo Hu, Yongling Lu and Xujie He

1 Introduction

In the operation of power system, substation operation and maintenance of the substation bear the operation and maintenance management, switching operation and accident handling and other important work, that is to ensure grid security, stability and economic performance of the executor [1]. In the substation operation environment, it is very difficult to calculate the electric field around the space for complicated substation equipment layout. Currently according to the char acteristics of the three-dimensional distribution of electric field. In this paper powered equipment is simply treated to calculate the distribution of power-frequency electrical equipment around the distribution with the calculation method of partition segment processing [1]. Because the result accuracy is not high and the method ca nnot carry on the field strength data real-time computation in the course of moving the job. In this paper, a new detection method combining scene 3D and vector electric field gradient information is proposed, which can realize accurate detection of voltage level, distance and azimuth. This method realizes the accurate detection

J. Liu (✉) · C. Wu · G. Cui · Z. Wang · Y. Wang · G. Liu · X. He
State Grid Key Laboratory of Power Industrial Chip Design and Analysis Technology, Beijing Smart-Chip Microelectronics Technology Co., Ltd, C-3, Dongsheng Science and Technology Park, No.66, Xixiaokou Rd, Haidian District, Beijing, China
e-mail: liujianjun@sgitg.sgcc.com.cn

G. Pan
Microelectronics Technology Institute, Heibei University of Technology, No.27 Guangrong Road, Hongqiao District, Tianjin, China
e-mail: pgf@hebut.edu.cn

C. Hu · Y. Lu
Jiangsu Electric Power Research Institute, No.1, Pawier Road, Jiangning District, Nanjing, Jiangsu, China
e-mail: 15105182955@163.com

Z. Deng (ed.), *Proceedings of 2017 Chinese Intelligent Automation Conference*, Lecture Notes in Electrical Engineering 458,
https://doi.org/10.1007/978-981-10-6445-6_4

of the voltage level information by acquiring the field strength information of the surrounding live equipment and using the multi-directional electrode gradient detection method to process the collected raw data. At the same time the method of calculating the electric field detection is optimized by using the compression—aware greedy reconstruction algorithm so as to improve the accuracy of the electric field gradient voltage level detection judgment.

2 Principle of Near-Field Detection

The commonly used calculation method of the power frequency electric field intensity of the bus-bar and the surrounding electric equipment is to derive the three-dimensional charge system and the electric field coefficient of the working environment of the surrounding charged body using the simulated charge method [2]. Figure 1 shows the Cartesian coordinate system when calculating the power frequency electric field. Considering the ground effect, the image charge method is used. The asymmetric mirror image method is used without considering the influence of the earth. This paper assumes that the simulated charge coordinate is Q_0 (x_0, y_0, z_0).

When the influence of the earth is not considered, this paper takes the coordinate point (x, y, z). The point of charge is evaluated from the relation:

$$V = \frac{Q_0}{4\pi\varepsilon R} \tag{1}$$

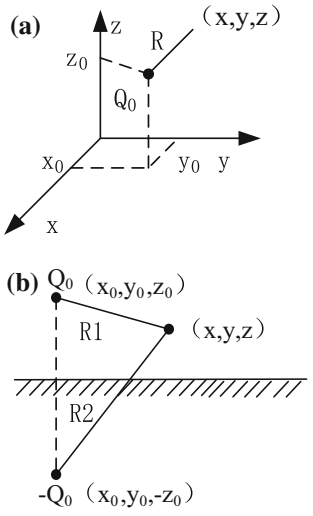

Fig. 1 Cartesian coordinate system **a** coordinate when mirroring is not considered **b** coordinate when mirroring is considered

The potential coefficient of a single point charge:

$$P = \frac{1}{4\pi\varepsilon R} \tag{2}$$

$$R = \sqrt{(x - x_0)^2 + (\mathrm{y} - y_0)^2 + (z - z_0)^2}$$

After the simulation of electric charge it can be determined at any point within the region of a electric field strength:

$$\boldsymbol{E} = -\nabla V = -\sum_{a=1}^{n} (\nabla P_{ao}) Q_0 = \sum_{a=1}^{n} F_{a0} Q_0 \tag{3}$$

N is the number of simulated charges, $\boldsymbol{F}a0$ is the electric field intensity vector coefficient.

According to the above situation, single point charge electric field strength coefficient is calculated using the following formulas:

$$F_x = -\frac{\partial p}{\partial x} = \frac{1}{4\pi\varepsilon}\frac{x - x_0}{R^3} \tag{4}$$

$$F_y = -\frac{\partial p}{\partial y} = \frac{1}{4\pi\varepsilon}\frac{y - y_0}{R^3} \tag{5}$$

$$F_z = -\frac{\partial p}{\partial z} = \frac{1}{4\pi\varepsilon}\frac{z - z_0}{R^3} \tag{6}$$

When the impact of the earth is taken into account, the spatial region at any point (x, y, z) potential and strength coefficient:

$$V = \frac{Q_0}{4\pi\varepsilon}\left(\frac{1}{R_1} - \frac{1}{R_2}\right) \tag{7}$$

$$P = \frac{1}{4\pi\varepsilon}\left(\frac{1}{R_1} - \frac{1}{R_2}\right) \tag{8}$$

Electric field intensity factor:

$$F_x = -\frac{\partial p}{\partial x} = \frac{1}{4\pi\varepsilon}\left(\frac{x - x_0}{R_1^3} - \frac{x - x_0}{R_2^3}\right) \tag{9}$$

$$F_y = -\frac{\partial p}{\partial y} = \frac{1}{4\pi\varepsilon}\left(\frac{y - y_0}{R_1^3} - \frac{y - y_0}{R_2^3}\right) \tag{10}$$

$$F_z = -\frac{\partial p}{\partial z} = \frac{1}{4\pi\varepsilon}\left(\frac{z - z_0}{R_1^3} - \frac{z - z_0}{R_2^3}\right) \tag{11}$$

$$R_1 = \sqrt{(x - x_0)^2 + (\mathrm{y} - y_0)^2 + (z - z_0)^2}\, R_2 = \sqrt{(x - x_0)^2 + (\mathrm{y} - y_0)^2 + (z + z_0)^2}$$

CSM could simulate the field strength of the power frequency field generated by the bus, but cannot well simulate field strength of insulator and suspension conductor equipment in substation. Boundary element method (BEM) can solve the problem of bracketing, which can reduce the dimension of the problem and improve the accuracy of the calculation when comparing the field strength of the substation equipment [3, 4].

In this paper, CSM and BEM algorithm are combined to calculate the field strength of the charged carriers in the substation; CSM is used to simulate the field strength generated by the bus. BEM is used to simulate the field strength generated by other equipment in substation.

2.1 The Establishment of Simulated Charge Equations

The (electrode) n analog charge points Q_j (j = 1, 2, … , n) is setted outside field; N potential matching points are selected on the electrode surface of a given potential boundary condition that the potential value φ_{0j} (j = 1, 2, … , n) on each matching point is known [5]. According to the superposition theorem, the points corresponding to all n matching points can be calculated from the following formulas [5]:

$$\begin{cases} \boldsymbol{P_{11}Q_1 + P_{12}Q_2 + \cdots + P_{1n}Q_n = \varphi_{01}} \\ \boldsymbol{P_{21}Q_1 + P_{22}Q_2 + \cdots + P_{2n}Q_n = \varphi_{02}} \\ \cdots \\ \boldsymbol{P_{n1}Q_1 + P_{n2}Q_2 + \cdots + P_{nn}Q_n = \varphi_{0n}} \end{cases} \tag{12}$$

P_{ij} called potential coefficients is the potential value produced by the j-th unit charge at the i-th matching point, which is related to the type and position of the j-th analog charge and the dielectric constant of the i-th matching point. but regardless of the charge value of the j-th analog charge. When the electric field data of the charged object in the substation is calculated, the charge value of the simulated charge can be calculated by Gaussian column principal component elimination method Q_j (j = 1, 2, …, n) [6].

2.2 The Verification and Determination of Analog Charge Value

The simulated charge data can not directly calculate the potential or electric field strength at any point in the field. It is necessary to check whether the potential generated by these analog charges satisfies the boundary conditions of the non-matching points on the electrode surface [7]. In this paper, m potential calibration points are selected in the middle of two adjacent points matching points, and the potential of each potential calibration point is calculated with the simulation charge.

$$\varphi_k = P_{k1}Q_1 + P_{k2}Q_2 + \cdots + P_{kn}Q_n \quad (k = 1, 2, \ldots, m) \tag{13}$$

φ_k (k = 1, 2, …, m) of each potential checkpoint is compared with a given known potential value φ_{0k} (k = 1, 2, …, m) to determine whether or not the meeting following condition.

$$|\varphi_k - \varphi_{0k}| \leq \Delta \quad (k = 1, 2, \ldots, m) \tag{14}$$

Δ is the calculation error determined by the operator, the charge value of the simulation charge can be solved by formula (12), and the electric potential or electric field strength can be calculated at any point in the field by applying these analog charges [5]. If formula (14) is not satisfied, the type, position, and number of analog charges for the first hypothesis should be adjusted appropriately and recalculate formulas (12) and (13) until meet formula (14) [7].

3 Calculation Method of Electric Field Gradient Based on Algorithm Optimization

In this paper, in order to increase the accuracy of the multi-electrode electric field gradient detection calculation, the pre-processing of the original data of the electric field is increased, and the calculation method of the electric field gradient detection is optimized by using the compression-aware greedy reconstruction algorithm to calculate the voltage level, Distance information [8].

The overall input of the algorithm is the original data collected by the electric field detection collector, which is the electric field raw data collected by 8 multi-electrode multi-position electrode detecting devices.

The overall output of the algorithm is the electric field detection result, including: distance, azimuth, voltage grade information.

Algorithm design principles: making full use of the advantages and characteristics of multi-electrode detection to detection of electric field strength. In the voltage level detection, according to electric field gradient information generated by

multi-electrode detection equipment, so as to analyze voltage level. The algorithm flow chart shown as Fig. 2:

In Fig. 2 when the field strength detection data frame arrives, data preprocessing is performed first, and then the field strength detection is performed. If the field strength data is null, the algorithm is exited directly, then the next frame data is ready to be processed. If the field strength is found in turn to determine the voltage level, distance calculation, azimuth decision. In the preprocessing section of the field data, individual electrode measurements may be abnormal due to hand touch or other conductors, contact of the charged body, and complex environment. So the singular value detection is used to exclude data abnormal results [9].

In this paper, the spatiotemporal distribution test is used to identify the normal, mutation, trend and abnormal conditions, which can identify the mutation value,

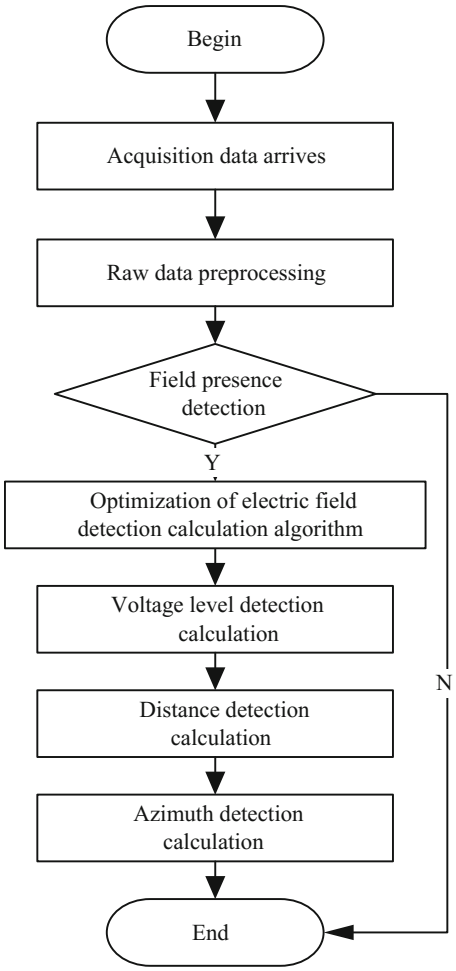

Fig. 2 Electric field intensity data processing flow

trend value and abnormal value [6]. The main basis for the inspection is based on the comparison of the previous field measurements with the previous measured value, the characteristic value (maximum value, minimum value). So needing to count this $\boldsymbol{Y_i}$, the previous measurement $\boldsymbol{Y_{i-1}}$, $\boldsymbol{Y_{max}}$ occurred in the maximum and minimum $\boldsymbol{Y_{min}}$ [6].

(1) When the difference between the measured value $\boldsymbol{Y_i}$ and the previous measured value $\boldsymbol{Y_{i-1}}$ is greater than 3 times the observed error v, then the value is the mutation value:

$$|Y_i - Y_{i-1}| \geq 3\sigma \tag{15}$$

(2) Trend identification: When the measured value and the basic environment of the same amount of the difference between the previous measurement is greater than 3 times the error in observation, the measured trend of change:

$$|Y_i - Y_{i-1}| \geq 3\sigma \tag{16}$$

At this time there is *a* tendency to change the measured value, the rate of change can be calculated.

(3) Abnormal value recognition: If $\boldsymbol{Y_{min}} \leq \boldsymbol{Y_i} \leq \boldsymbol{Y_{max}}$, then the measured value is normal, otherwise abnormal.

In this paper, the compression perception theory is applied to the electric field gradient detection algorithm, which is used to calculate the inverse problem of power frequency electric field. The method requires only a small number of electric field strength monitoring points to be randomly deployed in the monitoring area. The field-source parameters and the field-intensity distribution cloud map are obtained by the compression-aware greedy reconstruction algorithm by the electric field monitoring points randomly arranged in the monitoring area [5]. Simulation results show that the compression-aware greedy reconstruction algorithm can reconstruct the distribution of the intensity distribution. Specific steps are as follows:

(1) compression sampling process:

Assuming that the sensor node coordinates in the *m*-th grid are (x_m, y_m). The element $\boldsymbol{\Phi} \in \boldsymbol{R}^{M\times N}(M << N)$ in the measurement matrix $\varphi_{m,n}$ is:

$$\varphi_{m,n} = \boldsymbol{E}_{m,n}, 1 \leq m \leq M, \quad 1 \leq n \leq N \tag{17}$$

In the above formula, $\boldsymbol{E}_{\mathrm{m,n}}$ is the field strength of the simulated charge located in the *n*th grid measured by the sensor node in the *m*-th grid, and can be obtained by the formula (13).

In this paper, the system's compression sampling process can be described by the following formula:

$$\begin{bmatrix} y_1 \\ y_2 \\ M \\ y_M \end{bmatrix} = \begin{bmatrix} E_{1,1} & E_{1,2} & L & E_{1,N} \\ E_{2,1} & E_{2,2} & L & E_{2,N} \\ M & M & & M \\ E_{M,1} & E_{M,2} & L & E_{M,N} \end{bmatrix} \begin{bmatrix} x_1 \\ x_2 \\ M \\ x_N \end{bmatrix} \tag{18}$$

In the above equation, $x_n = q$ ($1 \leq n \leq N$) when there is an equivalent positive charge +q in the nth grid; $x_n = q$ ($1 \leq n \leq N$) when there is an equivalent negative charge −q; No equivalent charge when $x_n = 0$; Assuming that the equivalent number of simulated charges is K, the sparse degree of N-dimensional vector $\boldsymbol{X}$ is K. The measurement result of the sensor $\boldsymbol{Y}$ is the product of the measurement matrix and the sparse vector $\boldsymbol{X}$, and the physical meaning of the element y_m ($1 \leq m \leq M$) of $\boldsymbol{Y}$ is the sum of the field strengths of all equivalent analog charges at that point [8].

$$\boldsymbol{Y}_{M\times 1} = \boldsymbol{E}_{M\times N}\boldsymbol{X}_{N\times 1} \tag{19}$$

In the above equation, $\boldsymbol{Y}$ represents the compression sampling process, that is, $\boldsymbol{Y}$ measurement result process. Compression-aware reconstruction is the process of reconstructing the sparse vector $\boldsymbol{E}$ according to $\boldsymbol{Y}$ and $\boldsymbol{E}$.

(2) The algorithm of electric field cloud diagram greedy reconstruction

In this paper, the main idea of the design of greedy algorithm is used for the characteristics of the inverse problem of power frequency electric field. The greedy reconstruction algorithm of electric field cloud image is designed by using the analogue charge equivalent model. If the substation equipment parameters and spatial distribution of a priori data, the equivalent charge in the grid position should be further defined to improve algorithm performance and operation speed. Greedy reconstruction algorithm design is shown as below [6]:

Input: Measuring matrix $\boldsymbol{E}_{M\times N}$, measurement result $\boldsymbol{Y}_{M\times 1}$, output: reconstructed signal $\hat{\boldsymbol{X}}$.

(1) Initializing the matching margin $\boldsymbol{y}' = \boldsymbol{y}$, reconstructing the results $\hat{\boldsymbol{X}} = 0$, all the grid N is the number of the support collection;
(2) The following optimization problem is solved: where $\boldsymbol{z}$ is a column vector with sparse degree of 1 (only the i-th element has the value $\boldsymbol{z_i}$ and the remaining elements are 0). In this paper, the equivalent electric charge is discretized. The physical meaning is that there are z_i equivalent unit simulation charges at the i-th grid, if $\boldsymbol{z_i}$ is positive, $\boldsymbol{z_i}$ is positive charge; if z_i is negative, $\boldsymbol{z_i}$ is negative charge. If there is a priori knowledge of the equivalent charge distribution, then i and $\boldsymbol{z_i}$ need to satisfy the following a priori constraints [10].

$$\begin{aligned} \boldsymbol{z} &= \arg\max \frac{\langle \boldsymbol{y}', \boldsymbol{E}\boldsymbol{z} \rangle}{\|\boldsymbol{E}\boldsymbol{z}\|_2} \\ 1 \leq i \leq N, \quad -M &\leq z_i \leq M \end{aligned} \tag{20}$$

(3) If $z \neq 0$, then $\boldsymbol{y}' = \boldsymbol{y}' - \boldsymbol{E}z$, $\hat{\boldsymbol{X}} = \hat{\boldsymbol{X}} + z$, so the support set minus the current grid and jumping to step 2;
(4) Signal reconstruction ends. The result is $\hat{\boldsymbol{X}}$.

In the above algorithm, the approximation and margin updating are carried out by finding the correlation between the residual $\boldsymbol{y}'$ and each atom in the measurement matrix, to ensure that each iteration is optimal, and the maximum number of iterations is N.

4 Experiment and Analysis of Electric Field Gradient Data Detection

In this paper, 110 kV transformer substation equipment for experiments is selected. The optimized data is processed by the optimized multi-pole electric field gradient detection algorithm. The electric field tester and the Matlab tool are used to compare and analyze the processed data, the results are as follows:

A live carrier of 110 kV substation is selected and Charged field electric field gradient data are processed by the above-mentioned optimization algorithm. The cross-section is obtained. The field distribution of X-axis and Y-axis are shown as Figs. 3, 4 and 5. The carrier equipment is 1.5 m above the ground. The X-axis ranges from −3.3 to 3.3 m and the Y-axis ranges from −7.5 to 7.5 m. The origin is at the center of the interval, and the Z-axis represents the magnitude of the field strength in units of V/m.

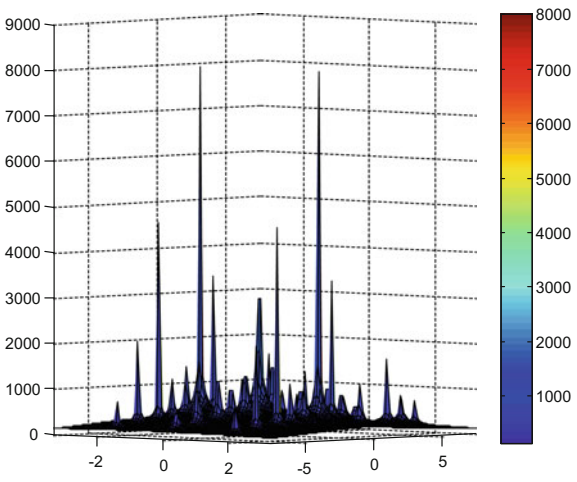

Fig. 3 Field strength distribution of 110 kV substation

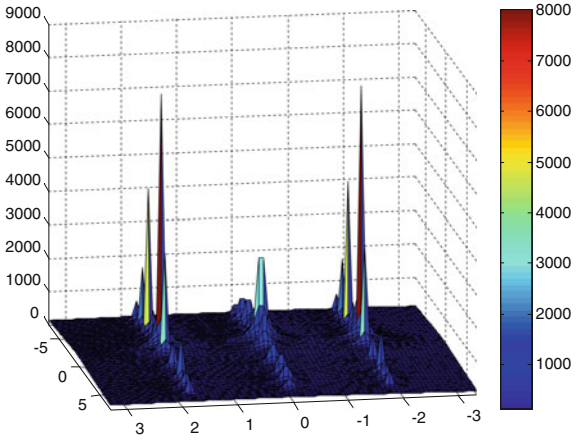

Fig. 4 Field strength distribution of 110 kV substation with X-axis angle

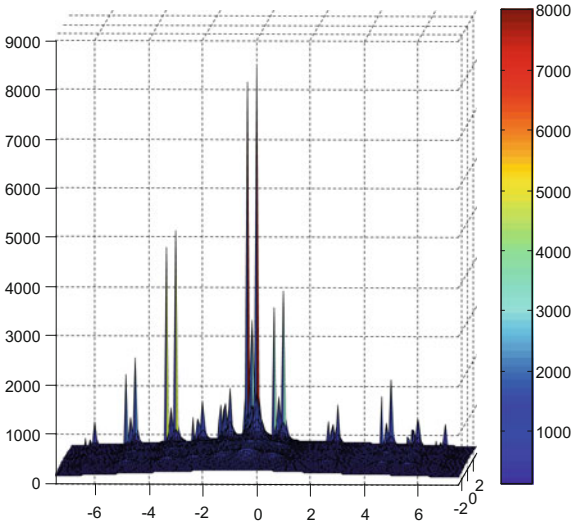

Fig. 5 Field distribution of 110 kV substation in Y-axis direction

In Figs. 3, 4 and 5, the result of three—dimensional field strength simulation shows that due to the mutual offset effect of the superposition field strength, the maximum field strength appears near the middle position.

Through detecting the field intensity distribution from the same direction in different directions, the result shows that the gradients can only be identified by the multi-layer electrode stacking, and the gradient recognition can be realized only for single-level sensors. The biggest advantage is the ability to determine the voltage level.

In this paper, the greedy matching algorithm (GMP) is simulated in Matlab according to the data parameters shown in Table 1. The results of the different reconstruction algorithms shown in Fig. 6 are obtained, by comparing the

Table 1 Main simulation data parameters

Simulation parameters	Parameter variable	Parameter value
The divided number of meshes	N	196
Number of sensors	M	49
The number of simulated charges	K	1–20

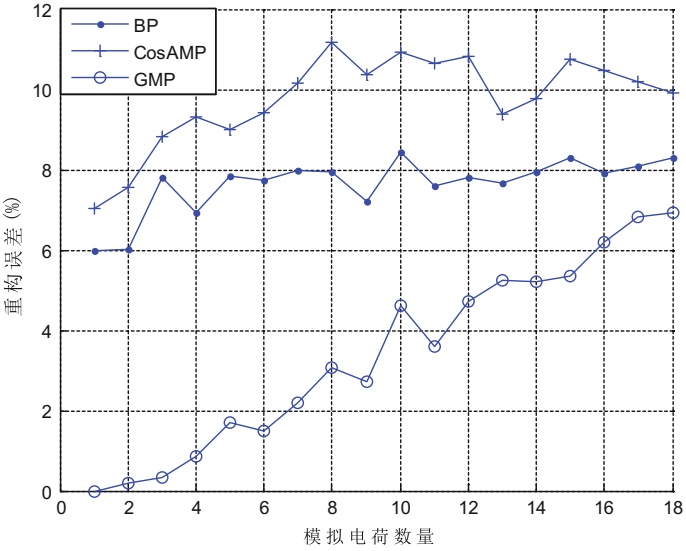

Fig. 6 Reconstruction error comparison of different reconstruction algorithms

simulation results with the BP (L1-Magic) algorithm [11] and the CosAMP algorithm. In the simulation process, the selected monitoring area is 50 m × 50 m rectangular area, the simulation parameters are selected as shown in Table 1. General requirement is $M > 2K$, the best is $4K \sim 6K$, the original signal can be a better reconstruction [11].

The results show that compared with the reconstruction error term of BP (L1-Magic) algorithm [11], CosAMP algorithm and the greedy matching algorithm (GMP) proposed in this paper, under the condition of M = 49, K = 1–18, SNR = 20 dB, the improved compression perception greedy reconstruction algorithm (GMP) can improve the accuracy of reconstruction error. For the 196 grid, the compression-aware greedy reconstruction algorithm can reconstruct the distribution of the source parameters and the distribution of the field strength with only 49 measurements.

5 Conclusion

In this paper, the method of calculating the gradient information of multi-electrode electric field is optimized by combining the idea of compression-conscious reconstruction, the original data is preprocessed at the initial stage of the electric field information collection of the charged carrier in the substation. The results are verified by using the electric field strength detection tool and Matlab simulation shows that the optimization algorithm of multi-electrode electric field gradient information detection and analysis, which incorporates the idea of compression perception and reconstruction, can effectively improve the detection ability of the charged conductor voltage level and the response speed and accuracy of the electric field around the charged body, and improve the safety of the staff working in the environment of complex electric field environment.

Acknowledgements State Grid Corporation of Science and Technology Project (526816160024).

References

1. Lee BY, Park JK, Myung SH, Min SW, Kim ES (1997) An effective modelling method to analyze the electric field around transmission lines and substations using a generalized finite line charge. IEEE Trans Power Delivery 12(3):1143–1150
2. Takuma T, Ikeda T, Kawamoto T (1981) Calculation of ion flow fields of hvdc transmission lines by the finite element method. IEEE Power Eng Rev PAS-100(12):4802–4810
3. Takuma T, Kawamoto T (1987) A very stable calculation method for ion flow field of hvdc transmission lines. IEEE Trans Power Delivery 2(1):189–198
4. Krajewski W (2004) Numerical modelling of the electric field in HV substations. IEE Proceedings-Science, Meas Technol 151(4):267–272
5. Du Z, Ruan J, Gan Z, Ruan X, Rong R, Nie L et al (2012) Three-dimensional numerical simulation of power frequency electromagnetic field inside and outside substation. Power Syst Technol 36(4):229–235 (in Chinese)
6. Ye Q, Wen Y, Mo R, Huang T, Zhang G, Liu X et al (2012) Calculation of power frequency electromagnetic field within substation by moment method and actual measured results. Power Syst Technol 36(2):189–194 (in Chinese)
7. Li N, Peng Z, Du J, Fan C (2012) Simulate calculation and distribution of power frequency electric filed in uhv substations. High Voltage Eng 38(9):2178–2188 (in Chinese)
8. Fisch D, Gruber T, Sick B (2011) Swiftrule: mining comprehensible classification rules for time series analysis. IEEE Trans Knowl Data Eng 23(5):774–787
9. Candes EJ, Romberg J, Tao T (2004) Robust uncertainty principles: exact signal reconstruction from highly incomplete frequency information. IEEE Trans Inf Theory 52 (2):489–509
10. Tropp JA, Wright SJ (2009) Computational methods for sparse solution of linear inverse problems. Proc IEEE 98(6):948–958
11. Zhu Y, Yin J (2013) Study on application of multi-kernel learning relevance vector machines in fault diagnosis of power transformers. Proc Csee 33(22):68–74 (in Chinese)

Nonlinear Control Strategy of Split-Capacitor-Type Shunt Active Power Filter Based on EL Model

Yu Zhang, Qiming Cheng, Yinman Cheng, Fengren Tan, Jie Gao and Deqing Yu

1 Introduction

The Split-Capacitor-type Shunt Active Power Filter (2C SAPF) can be widely used in low-to-medium-power applications of three-phase four-wire system because its cost is lowest [1]. At present, a number of linear strategies for SAPF have been reported in the literature, but the mathematical model of SAPF is nonlinear [2]. In this paper, a nonlinear Passivity-Based Control (PBC) strategy based on EL model is used to achieve globally stable operation of 2C SAPF, which satisfies the current harmonic limits as specified by IEEE-519 [3, 4] and effectively maintains the stability of the DC bus voltage. The principle and comparison with the traditional strategies reveal the merits of the proposed strategy.

2 Modeling of 2C SAPF

The circuit in Fig. 1 is the considered system used to derive the model of 2C SAPF. Selecting the current flowing through the inductor (L_f), the different and the total DC bus voltage (ΔV_{dc} and $\sum V_{dc}$) as state variables, the Kirchhoff's law is used to

Y. Zhang · Q. Cheng (✉) · F. Tan · J. Gao · D. Yu
College of Automation Engineering,
Shanghai University of Electric Power, Shanghai 200090, China
e-mail: chengqiming@sina.com

Y. Cheng (✉)
College of Electronics and Information Engineering,
Tongji University, Shanghai 201804, China
e-mail: chengyinman@hotmail.com

Z. Deng (ed.), *Proceedings of 2017 Chinese Intelligent Automation Conference*,
Lecture Notes in Electrical Engineering 458,
https://doi.org/10.1007/978-981-10-6445-6_5

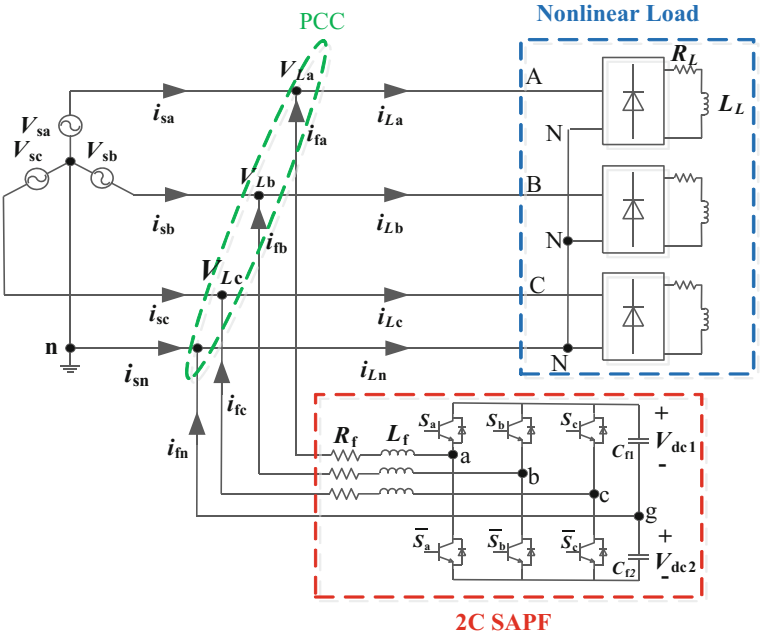

Fig. 1 The equivalent circuit of 2C SAPF

determine the mathematical model of 2C SAPF in *abc* stationary coordinate as shown in (2.1).

$$\begin{cases} L_f \dot{i}_{fa} = S_a \sum V_{dc} - R_f i_{fa} - V_{La} - (\sum V_{dc} - \Delta V_{dc})/2 \\ L_f \dot{i}_{fb} = S_b \sum V_{dc} - R_f i_{fb} - V_{Lb} - (\sum V_{dc} - \Delta V_{dc})/2 \\ L_f \dot{i}_{fc} = S_c \sum V_{dc} - R_f i_{fc} - V_{Lc} - (\sum V_{dc} - \Delta V_{dc})/2 \\ C_f \Delta \dot{V}_{dc} = -(i_{fa} + i_{fb} + i_{fc}) \\ C_f \sum \dot{V}_{dc} = i_{fa} + i_{fb} + i_{fc} - 2(S_a i_{fa} + S_b i_{fb} + S_c i_{fc}) \end{cases} \tag{2.1}$$

where ΔV_{dc}, $\sum V_{dc}$ and C_f are given by: $\Delta V_{dc} = V_{dc1} - V_{dc2}$, $\sum V_{dc} = V_{dc1} + V_{dc2}$, $C_f = C_{f1} = C_{f2}$. And the switching function S_j (for j = a, b, c) is defined as:

$$S_j = \begin{cases} 1, S_j \text{ is on and } \bar{S}_j \text{ is off} \\ 0, S_j \text{ is off and } \bar{S}_j \text{ is on} \end{cases} \tag{2.2}$$

In the future work, the *dq*0 approach is used to describe the control strategy of 2C SAPF. Therefore, the mathematical model in (2.1) can be transformed into (2.3) by using equal power transformation.

$$\begin{cases} L_{\mathrm{f}}\dot{i}_{\mathrm{fd}} = S_{\mathrm{d}}\sum V_{\mathrm{dc}} - R_{\mathrm{f}}i_{\mathrm{fd}} - V_{Ld} + \omega L_{\mathrm{f}}i_{\mathrm{fq}} \\ L_{\mathrm{f}}\dot{i}_{\mathrm{fq}} = S_{\mathrm{q}}\sum V_{\mathrm{dc}} - R_{\mathrm{f}}i_{\mathrm{fq}} - V_{Lq} - \omega L_{\mathrm{f}}i_{\mathrm{fd}} \\ L_{\mathrm{f}}\dot{i}_{\mathrm{f0}} = (S_0 - \sqrt{3}/2)\sum V_{\mathrm{dc}} - R_{\mathrm{f}}i_{\mathrm{f0}} - V_{L0} + \sqrt{3}\Delta V_{\mathrm{dc}}/2 \\ C_{\mathrm{f}}\Delta\dot{V}_{\mathrm{dc}}/2 = -\sqrt{3}i_{\mathrm{f0}}/2 \\ C_{\mathrm{f}}\sum\dot{V}_{\mathrm{dc}}/2 = -S_{\mathrm{d}}i_{\mathrm{fd}} - S_{\mathrm{q}}i_{\mathrm{fq}} - (S_0 - \sqrt{3}/2)i_{\mathrm{f0}} \end{cases} \tag{2.3}$$

where, ω is the angular frequency of the power supply.

Letting us choose $x = [x_1, x_2, x_3, x_4, x_5]^{\mathrm{T}} = [i_{\mathrm{fd}}, i_{\mathrm{fq}}, i_{\mathrm{f0}}, \Delta V_{\mathrm{dc}}, \sum V_{\mathrm{dc}}]^{\mathrm{T}}$, and then rewriting (2.3) into the form of EL equation [5], as shown in (2.4).

$$\boldsymbol{M}\underline{\boldsymbol{x}} + \boldsymbol{J}\boldsymbol{x} + \boldsymbol{R}\boldsymbol{x} = \boldsymbol{u} \tag{2.4}$$

where $\boldsymbol{M}$, $\boldsymbol{J}$, $\boldsymbol{R}$ and $\boldsymbol{u}$ are given by:

$$\boldsymbol{M} = \mathrm{diag}\{L_{\mathrm{f}}, L_{\mathrm{f}}, L_{\mathrm{f}}, C_{\mathrm{f}}/2, C_{\mathrm{f}}/2\}, \quad \boldsymbol{R} = \mathrm{diag}\{R_{\mathrm{f}}, R_{\mathrm{f}}, R_{\mathrm{f}}, 0, 0\},$$

$$\boldsymbol{J} = \begin{bmatrix} 0 & -\omega L_{\mathrm{f}} & 0 & 0 & -S_{\mathrm{d}} \\ \omega L_{\mathrm{f}} & 0 & 0 & 0 & -S_{\mathrm{q}} \\ 0 & 0 & 0 & -\sqrt{3}/2 & -(S_0 - \sqrt{3}/2) \\ 0 & 0 & \sqrt{3}/2 & 0 & 0 \\ S_{\mathrm{d}} & S_{\mathrm{q}} & (S_0 - \sqrt{3}/2) & 0 & 0 \end{bmatrix} \quad \boldsymbol{u} = \begin{bmatrix} -V_{Ld} \\ -V_{Lq} \\ -V_{L0} \\ 0 \\ 0 \end{bmatrix} \tag{2.5}$$

3 Principle and Design of PBC Based on EL Model

The proposed strategy is based on passivity-based method. The main idea is that of proving that the total increased energy of the system is less than that of the external injection.

Assuming that the storage energy of the 2C SAPF is given as:

$$H(\boldsymbol{x}) = \boldsymbol{x}^{\mathrm{T}}\boldsymbol{M}\boldsymbol{x}/2 \tag{3.1}$$

The system is globally asymptotically stable if $H(\boldsymbol{x})$ satisfies the following inequality:

$$\dot{H}(\boldsymbol{x}) \leq \boldsymbol{u}^{\mathrm{T}}\boldsymbol{y} - Q(\boldsymbol{x}) \tag{3.2}$$

where, the $Q(\boldsymbol{x})$ is positive. Based on (2.4) and (3.1), $H(\boldsymbol{x})$ derivative can be expressed as:

$$\dot{H}(\boldsymbol{x}) = \boldsymbol{x}^{\mathrm{T}}\boldsymbol{M}\dot{\boldsymbol{x}} = \boldsymbol{x}^{\mathrm{T}}(\boldsymbol{u} - \boldsymbol{J}\boldsymbol{x} - \boldsymbol{R}\boldsymbol{x}) = \boldsymbol{u}^{T}\boldsymbol{x} - \boldsymbol{x}^{T}\boldsymbol{R}\boldsymbol{x} \tag{3.3}$$

From (3.2) and (3.3), we can see that if we choose $\boldsymbol{y} = \boldsymbol{x}$, $Q(\boldsymbol{x}) = \boldsymbol{x}^{\mathrm{T}}\boldsymbol{R}\boldsymbol{x}$, the 2C SAPF is globally asymptotically stable.

In order to achieve the purpose of PBC, that is to make each controlled variable gradually reach its expected value, the definition of the error of $\boldsymbol{x}$ is given as: $\boldsymbol{x}_{\mathrm{eg}} = \boldsymbol{x} - \boldsymbol{x}_{\mathrm{ref}} = [i_{\mathrm{fd}} - i_{\mathrm{fd}}^{*}, i_{\mathrm{fq}} - i_{\mathrm{fq}}^{*}, i_{\mathrm{f0}} - i_{\mathrm{f0}}^{*}, \Delta V_{\mathrm{dc}}, \sum V_{\mathrm{dc}} - \sum V_{\mathrm{dc}}^{*}]^{\mathrm{T}}$, where i_{fd}^{*}, i_{fq}^{*}, and i_{f0}^{*} are the reference currents extracted from the nonlinear load, and $\sum V_{\mathrm{dc}}^{*}$ is the reference voltage of $\sum V_{\mathrm{dc}}$. The equilibrium points of the system are found to be: $\boldsymbol{x}_{\mathrm{eg}} = 0$. Then, based on (2.4), we can get:

$$\boldsymbol{M}\dot{\boldsymbol{x}}_{\mathbf{eg}} + \boldsymbol{J}\boldsymbol{x}_{\mathbf{eg}} + \boldsymbol{R}\boldsymbol{x}_{\mathbf{eg}} = \boldsymbol{u} - (\boldsymbol{M}\dot{\boldsymbol{x}}_{\mathbf{ref}} + \boldsymbol{J}\boldsymbol{x}_{\mathbf{ref}} + \boldsymbol{R}\boldsymbol{x}_{\mathbf{ref}}) \tag{3.4}$$

Assuming that the error energy storage function of the 2C SAPF is given as:

$$H_{\mathrm{eg}}(\boldsymbol{x}) = \boldsymbol{x}_{\mathbf{eg}}^{\mathrm{T}}\boldsymbol{M}\boldsymbol{x}_{\mathbf{eg}} \Big/ 2 \tag{3.5}$$

As long as the $H_{\mathrm{eg}}(\boldsymbol{x})$ converges to 0, the $\boldsymbol{x}_{\mathbf{eg}}$ can converge to 0, and at this time, we can achieve the purpose of PBC.

In an attempt to increase the speed of convergence, the damping injection method can be used to speed up the system's energy dissipation, so as to increase the speed of the system's response. The injected damping dissipation can be expressed as:

$$\boldsymbol{R}_{\mathbf{d}}\boldsymbol{x}_{\mathbf{eg}} = (\boldsymbol{R} + \boldsymbol{R}_{\mathbf{a}})\boldsymbol{x}_{\mathbf{eg}} \tag{3.6}$$

where, the form of $\boldsymbol{R}_{\mathrm{a}}$ is the same as that of $\boldsymbol{R}$, is given as: $\boldsymbol{R}_{\mathrm{a}} = \mathrm{diag}\{r_{\mathrm{a1}}, r_{\mathrm{a2}}, r_{\mathrm{a3}}, 0, 0\}$. Then, (3.4) becomes:

$$\boldsymbol{M}\dot{\boldsymbol{x}}_{\mathbf{eg}} + \boldsymbol{R}_{\mathbf{d}}\boldsymbol{x}_{\mathbf{eg}} = \boldsymbol{u} - (\boldsymbol{M}\dot{\boldsymbol{x}}_{\mathbf{ref}} + \boldsymbol{J}\boldsymbol{x} + \boldsymbol{R}\boldsymbol{x}_{\mathbf{ref}} - \boldsymbol{R}_{\mathbf{a}}\boldsymbol{x}_{\mathbf{eg}}) \tag{3.7}$$

In an effort to ensure the global asymptotic stability of the 2C SAPF, letting us choose the control law of hybrid PBC as:

$$\boldsymbol{u} = \boldsymbol{M}\dot{\boldsymbol{x}}_{\mathbf{ref}} + \boldsymbol{J}\boldsymbol{x} + \boldsymbol{R}\boldsymbol{x}_{\mathbf{ref}} - \boldsymbol{R}_{\mathbf{a}}\boldsymbol{x}_{\mathbf{eg}} \tag{3.8}$$

At this time, based on (3.5), (3.7) and (3.8), the derivative of $H_{\mathrm{eg}}(\boldsymbol{x})$ satisfies:

$$\dot{H}_{\mathrm{eg}}(\boldsymbol{x}) = \boldsymbol{x}_{\mathbf{eg}}^{\mathrm{T}}\boldsymbol{M}\dot{\boldsymbol{x}}_{\mathbf{eg}} = -\boldsymbol{x}_{\mathbf{eg}}^{\mathrm{T}}\boldsymbol{R}_{\mathbf{d}}\boldsymbol{x}_{\mathbf{eg}} < 0 \tag{3.9}$$

Then, based on (3.9), the switching function on $dq0$-frame can be deduced as:

$$\begin{cases} S_{\mathrm{d}} = \frac{V_{Ld} - \omega L_{\mathrm{f}} i_{\mathrm{fq}} + R_{\mathrm{f}} i_{\mathrm{fd}}^{*} - r_{\mathrm{a1}}(i_{\mathrm{fd}} - i_{\mathrm{fd}}^{*})}{\sum V_{\mathrm{dc}}} \\ S_{\mathrm{q}} = \frac{V_{Lq} + \omega L_{\mathrm{f}} i_{\mathrm{fd}} + R_{\mathrm{f}} i_{\mathrm{fq}}^{*} - r_{\mathrm{a2}}(i_{\mathrm{fq}} - i_{\mathrm{fq}}^{*})}{\sum V_{\mathrm{dc}}} \\ S_{0} = \frac{2V_{L0} - \sqrt{3}\Delta V_{\mathrm{dc}} + 2R_{\mathrm{f}} i_{\mathrm{f0}}^{*} - 2r_{\mathrm{a3}}(i_{\mathrm{f0}} - i_{\mathrm{f0}}^{*})}{2\sum V_{\mathrm{dc}}} + \frac{\sqrt{3}}{2} \end{cases} \tag{3.10}$$

At this time, according to (2.3) and (3.10), we can get:

$$\begin{cases} i_{\mathrm{fd}}^{*} = i_{\mathrm{fd}} + \frac{L_{\mathrm{f}}}{R_{\mathrm{f}} + r_{\mathrm{a1}}} \dot{i}_{\mathrm{fd}} \\ i_{\mathrm{fq}}^{*} = i_{\mathrm{fq}} + \frac{L_{\mathrm{f}}}{R_{\mathrm{f}} + r_{\mathrm{a2}}} \dot{i}_{\mathrm{fq}} \\ i_{\mathrm{f0}}^{*} = i_{\mathrm{f0}} + \frac{L_{\mathrm{f}}}{R_{\mathrm{f}} + r_{\mathrm{a3}}} \dot{i}_{\mathrm{f0}} \end{cases} \tag{3.11}$$

It's easy to see that the control law of PBC of (3.8) can make the compensating current completely decoupled.

From (2.1) and (2.3), it can be seen that the compensating current and DC bus voltage is closely related, so a regulation of the DC bus voltage is required. In order to keep ΔV_{dc} stable at 0 and $\sum V_{\mathrm{dc}}$ stable at $\sum V^{*}$ dc, an outer control loop is designed by a suitable PI regulator. The output of the ΔV_{dc} controller is added to the d-component harmonic current i_{Ldh} and the output of the $\sum V_{\mathrm{dc}}$ controller is added to the 0-component harmonic current i_{L0h} as shown in Fig. 2.

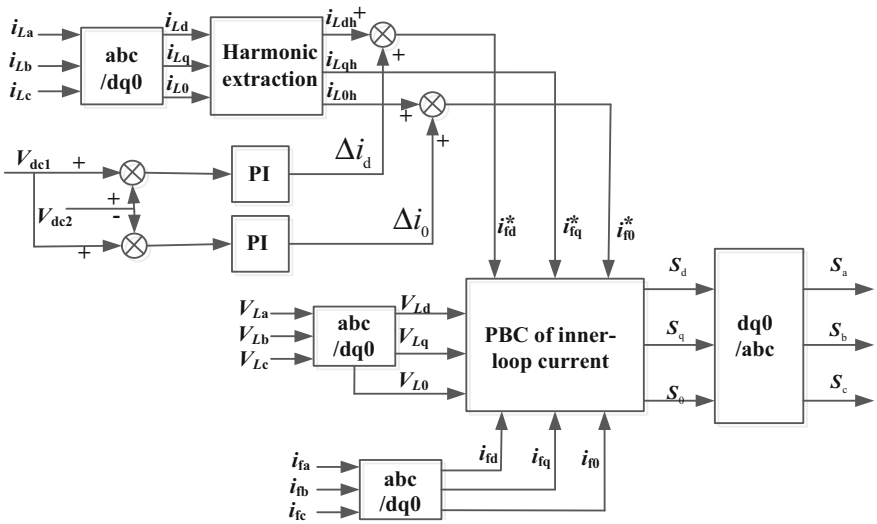

Fig. 2 Block diagram of the proposed control scheme

4 Simulation Results

To verify the merits of the proposed strategy, a system of 2C SAPF based on this and traditional strategy is simulated under the Matlab/Simulink environment, and the THD of the source current under varying load and unbalanced voltage source conditions is taken as the performance index. The simulation parameters are: the nonlinear load R_L = 5 Ω, L_L = 20 mH; filter inductor and resistance L_f = 5 mH, R_f = 0.3 Ω; capacitor of DC bus C_f = 5 mF; $\sum V_{dc}^*$ = 800 V; injection damping $r_{a1} = r_{a2} = r_{a3}$ = 600 Ω; the simulation time is 0.55 s.

Figure 3 shows the transient responses of 2C SAPF that adopted the proposed strategy for a 100% step increase and decrease of the load at t_1 = 0.2 s and

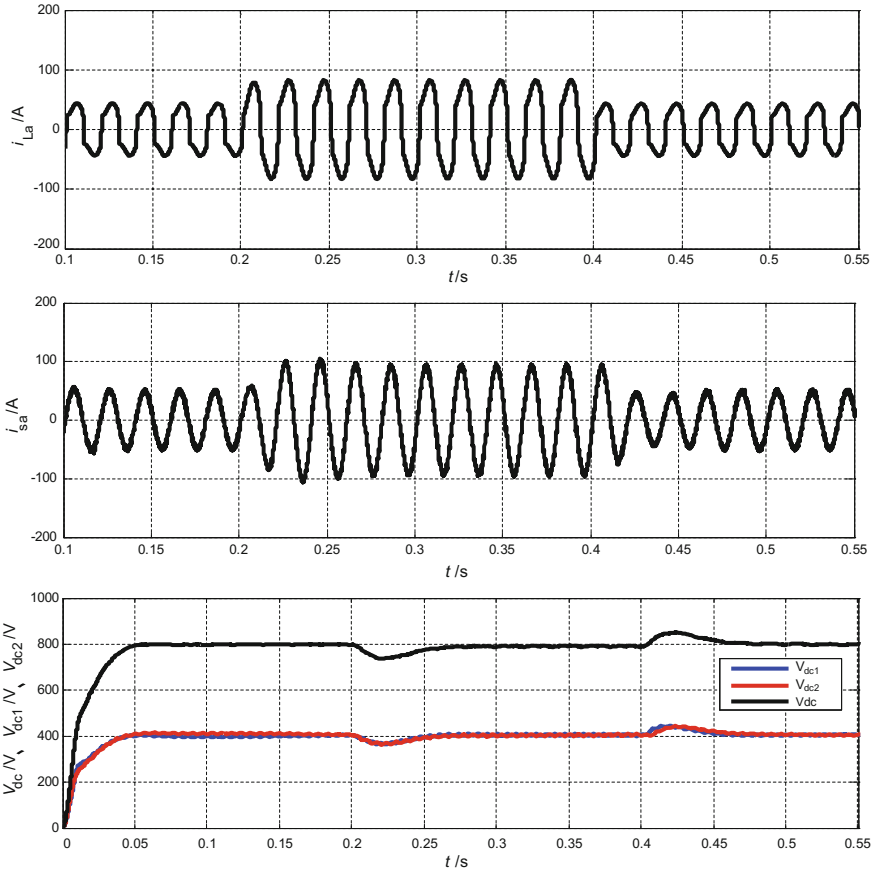

Fig. 3 Dynamic response of the 2C SAPF

t_2 = 0.4 s, respectively. It can be seen that both the supply current and the DC bus voltage exhibit a fast transient response under this sudden variation of load, achieving stable operation of the 2C SAPF.

Figure 4 shows the steady-state simulation results of 2C SAPF that adopted the proposed strategy before and after compensation when the phase of supply voltage is 0°, −90°, 60°, respectively. The corresponding THD of the supply current has reduced from 24.89 to 2.50, 2.32, 2.60%, which shows the effectiveness of the proposed strategy.

Figure 5 shows the simulation results of 2C SAPF that adopted the proposed and traditional strategy before and after compensation at b-phase grounding. The corresponding THD of the supply current using the proposed strategy has reduced from 24.89 to 3.04, 2.67, 2.90%, while using traditional strategy in each phase of THD decreased to 6.72, 7.58 and 6.62% respectively. In addition, the results further show that compared with traditional strategy, the time of reaching steady state can be reduced from 0.1 to 0.05 s when using the proposed strategy. They both show the availability and significant advantage of the proposed strategy.

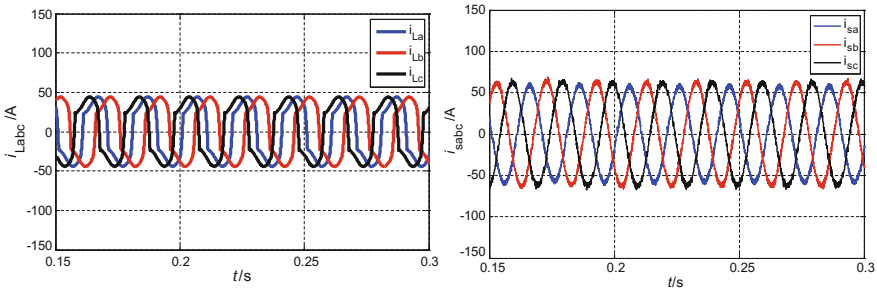

(a) Current supply before compensation (b) Current supply after compensation

Fig. 4 Response of 2C SAPF when the phase of power supply is unbalanced

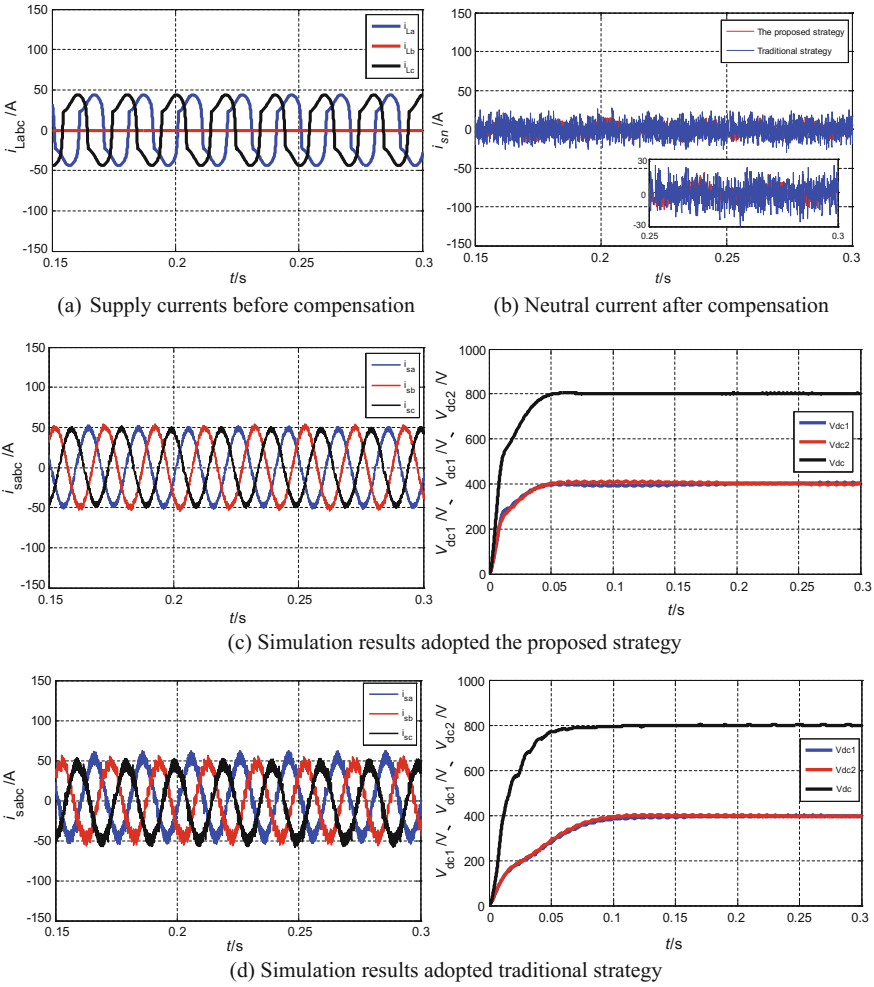

(a) Supply currents before compensation

(b) Neutral current after compensation

(c) Simulation results adopted the proposed strategy

(d) Simulation results adopted traditional strategy

Fig. 5 Response of 2C SAPF at b-phase grounding

5 Conclusion

A hybrid PBC strategy for 2C SAPF has been proposed and implemented in this paper. The observed performance has demonstrated the ability of the proposed strategy of 2C SAF to compensate the current harmonics effectively under varying loads and unbalanced power supply. It has also been shown that the proposed strategy has a faster and better dynamic response than traditional strategy and is able to keep the THD of the supply currents well below the mark of 5% specified in the IEEE-519 standard.

Acknowledgements This work was supported by the National Natural Science Foundation of China (61573239) and the Key Science and Technology Plan of Shanghai Science and Technology Commission (14110500700).

References

1. El-Habrouk M, Darwish MK, Mehta P (2000) Active power filters: a review. IEE Electr Power Appl 147(5):403–413
2. Guzman R, de Vicuna L, Morales J et al (2016) Model-based control for a three-phase shunt active power filter. IEEE Trans Ind Electron 62(7):3998–4007
3. Peng FZ (2011) Harmonic sources and filtering approaches. IEEE Ind Appl Mag 7(4):18–25
4. Hua CC, Li CH, Lee CS (2009) Control analysis of an active power filter using Lyapunov candidate. IET Power Electron 2(4):325–334
5. Mehrasa M, Lesan S, Emeni SNH, et al (2009) Passivity-based control with dual lagrangian model of four-wire three-level three-phase NPC voltage-source rectifier. Compatibility and power electronics. IEEE, pp 411–418

Evolution of Cooperation in Spatial Prisoner's Dilemma Game Based on Incremental Learning

Xiaowei Zhao, Zhenzhen Xu, Xu Han, Linlin Tian and Xiujuan Xu

1 Introduction

Cooperation among agents is critical in the field of agents' artificial intelligence (AI) and multi-agent systems (MAS). Many works have been done for cooperative target observation [1], foraging [2], and peer-to-peer systems [3]. Coordination is important to improve the performance of the entire system; and cooperation is the first step of coordination [4]. In such system, each agent can make the decision whether to cooperate (C) or defect (D) with other agents based on their past interactions and its decision making system. Evolutionary games, such as prisoner's dilemma (PD) [5], have been used widely to model a solution for the question of why and how intelligent agents successfully evolve cooperation instead of defection within their systems. Many researches [6, 7] have discussed network reciprocity, which is one of the five fundamental mechanisms that Nowak has classified [7] in 2006. Network reciprocity based on graph theory provides a very natural and convenient model to describe the spatial structure of cooperation evolutionary groups. Based on network reciprocity, individuals play games with their neighbors on an underlying network and copy a successful strategy among neighbors. The mechanism is simple but it still seems plausible for explaining why cooperation survives in many real complex systems [6].

It is well accepted that the cooperation dynamics on graph, deriving from the individual strategy-updating rules [6, 8]. Some models have been widely adopted [6], such as replication [9], imitation [10], and learning [11]. Among the learning

X. Zhao · Z. Xu · L. Tian · X. Xu (✉)
School of Software Technology, Dalian Economic and Technological Development Zone, Dalian University of Technology, 321 TuQiang Street, Dalian, China
e-mail: xjxu@dlut.edu.cn

X. Zhao · X. Han
Institute of Systems Engineering, Dalian University of Technology, No. 2 Linggong Road, Ganjingzi District, Dalian, Liaoning, China

Z. Deng (ed.), *Proceedings of 2017 Chinese Intelligent Automation Conference*, Lecture Notes in Electrical Engineering 458,
https://doi.org/10.1007/978-981-10-6445-6_6

strategies, imitation mechanisms account for a large proportion of these rules, in which an individual will choose a neighbor with higher payoff and follows its strategy. Based on social psychology, individuals' cognitive processes are quite influenced by social environment and individuals update knowledge through their social interactions with others [12, 13]. On the other hand, many researches have been conducted regarding strategy update rules, but how strategies are actually adopted and spread is still unclear. In recent experimental research, it has been found that individuals do not necessarily follow the imitate-the-best rule (best-take-over, BTO).

Based on the above consideration, alternative formulations of strategy-updating rules exploring how strategies are adopted by individuals and spread on the network is worth to research. In this paper, we propose the strategy-updating rule as an incremental learning process to address mentioned issues. Under our strategy-updating rule, each individual refreshes its decision according to original strategy (self-opinion) and new strategy learnt from one of neighbors (social-opinion). In a social and economic context, it is natural that individuals hesitate to imitate exactly the other's strategy, even though it may be the best performant strategy. As for the strategies, it is conventional to use 2 persons and 2 competing strategies, namely cooperation (C) and defection (D). There are some considerable evidences that the cooperative strategies are usually continuous; in other word, individuals often cooperate with some specific probability besides choosing a pure strategy [14]. Thus, we propose a continuous version of strategy update rules, by introducing the willingness to cooperate.

In this paper, we investigate the evolution of cooperation based on incremental learning on network in the continuous prisoner's dilemma game (CPD). Our results may shed some light on the underlying mechanisms of agents' evolutionary behavior within multi-agent systems. The structure of this paper is as follows. In the next chapter, an introduction of the simulation model is given. In the third chapter, the result and analysis are provided. Finally, we give conclusion in the fourth part.

2 Model Description

In this paper, we adopt the matrix of PD game with one parameter r. We set $S = 0$ and $R = 1$, so the pay-off matrix is shown as formula (2.1), where $r = c/b$ ($r \in [0, 1]$) represents the ratio of cost to benefit of the altruistic behavior.

$$M = \begin{bmatrix} R & S \\ T & P \end{bmatrix} = \begin{bmatrix} 1 & 0 \\ 1+r & r \end{bmatrix}. \tag{2.1}$$

As a CPD game, a real number s_i ($s_i \in [0, 1]$) is adopted to represent continuous strategy. If the strategy is fully cooperation (or defection), $s_i = 1$ (or $= 0$). If an individual adopt partial cooperation strategy, s_i is between 0 and 1. Suppose that an

individual's strategy is p and his opponent uses strategy q, its income can be calculated by formula (2.2) [14].

$$\pi(p,q) = (R - S - T + P)pq + (S - P)p + (T - P)q + P \tag{2.2}$$

When $p = 0$ or 1 and $q = 0$ or 1, $\pi(D,\ C) = T$, $\pi(D,\ D) = P$, $\pi(C,\ C) = R$, $\pi(C,\ D) = S$. Thus, the formula (2.2) can also be used to calculate the income of discrete strategy. In this paper, the population is placed on a square-lattice network and the length of the side is L ($L = 50$). We use Newman neighbor, which means each individual sits in a single grid with 4 neighbors and can interact with its every single neighbor. At the initial stage, the individual strategy is a random real number between [0, 1] which is evenly distributed on the network.

In this paper, we consider weighted average as the way to update individual strategy. Instead of individual choosing the best neighbor as a role model and follow it strategy, each individual updates her strategy as follows: an individual i plays PD game with its neighbors in time step t and calculates total payoff P_i according to formula (2.1). Suppose individual i knows payoffs of N_l neighbors ($N_l = 1, 2, 3, 4$) and chooses the individual j as the learning model with highest payoff P_j. If $P_j > P_i$, the individual i will update its strategy $s_i(t + 1)$ in time step $t + 1$ according to the formula (2.3)

$$\begin{aligned} s_i(t+1) &= s_i(t) + \alpha\big(s_j(t) - s_i(t)\big) * \Phi_i(t) \\ \Phi_i(t) &= \tanh\big[\beta\big(P_j - P_i\big)\big] \end{aligned} \tag{2.3}$$

The parameter $\alpha(\alpha \in [0, 1])$ can be viewed as a factor of resistance to imitation or as a measure of resistance. When $\alpha = 1$, there is no resistance, individuals will try to copy the strategy of their neighbors. On the other hand, when $0 < \alpha < 1$, the individuals gradually learn from their partner. The parameter β can be viewed as a factor of payoff sensitivity. When $\beta \to 0$, individuals are numb for the difference of payoffs with others. When $\beta \to \infty$, individuals are sensitive for the difference of payoffs with others, and more willing to update their strategies.

3 Result and Analysis

Based on the model proposed in the second chapter, we use numerical simulations to test how the incremental learning influences on the evolution of cooperation in lattice population. We examine two parameters:

1. The resistance rate α;
2. The payoff sensitivity parameter β.

In the following simulation experiment, all the statistical results are collected when the system arrives at quasi-equilibrium and all the results are average of 50 independent runs. We use the fraction of cooperation of the system as the indicator

to describe system average cooperation level, which is defined as $f_C = \sum_{i \in N} s_i / N$ (N is the number of population).

First of all, we research correlations between fc and $\alpha - r$ under different N_l when $\beta = 3000$ (Fig. 1). As can been seen, both α and r have a great influence on cooperation evolution. According to its general trend, fc will decrease with increasing r and deceasing α in Fig. 1. Especially when $N_l = 1$ (Fig. 1a), the influence of α is particularly large. When $\alpha = 1$ ($\alpha = 0.05$), fc is very low (high). On the other hand, when $N_l = 4$ (Fig. 1d), the influence of α is quite tiny. From Fig. 1 we can also observe that fc reaches the maximum value at $\alpha = 0.1$ in all figures of Fig. 1.

In order to compare the influence situation when β is tiny, we research correlations between fc and $\alpha - r$ under when $\beta = 0.3$ (see Fig. 2.). As can been seen, when β is tiny, the influence of α is quite small compared with Fig. 1. According to its general trend, fc will increase with deceasing α in all figures of Fig. 2 except Fig. 2d. From Figs. 1 and 2, we can draw the basic conclusion that N_l plays the significant role in our model and the difference is prominent with different α and β. In order to further analyze these issues, we study the influence of α and β separately. Experimental results are shown in Figs. 3 and 4.

From Fig. 3, we can see that the difference of the influence of β is particularly large between $N_l = 1$ and $N_l = 4$. According to its general trend, fc will increase

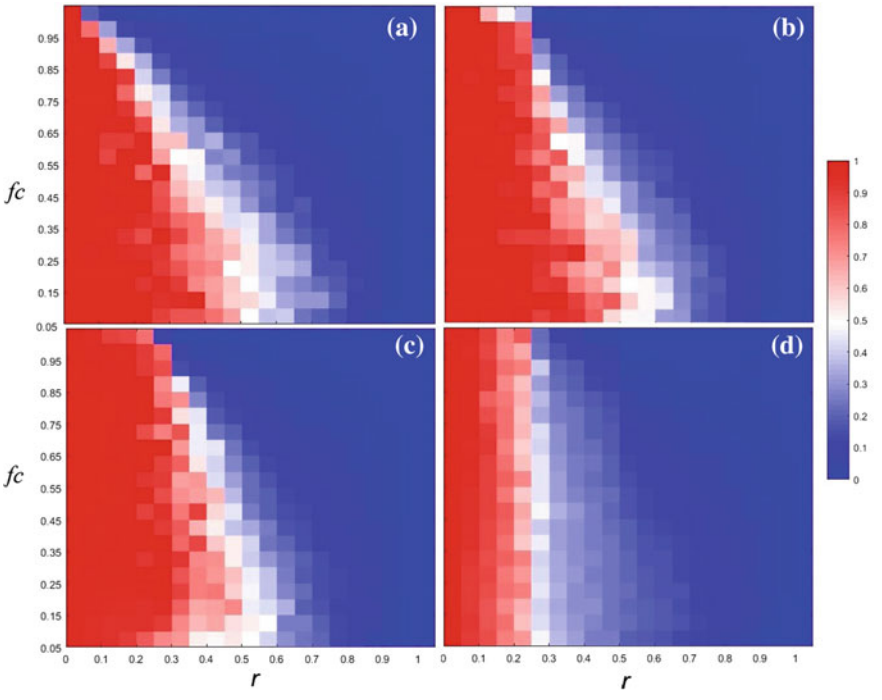

Fig. 1 Correlations between fc and $\alpha - r$ under different N_l when $\beta = 3000$. **a** $N_l = 1$; **b** $N_l = 2$; **c** $N_l = 3$; **d** $N_l = 4$

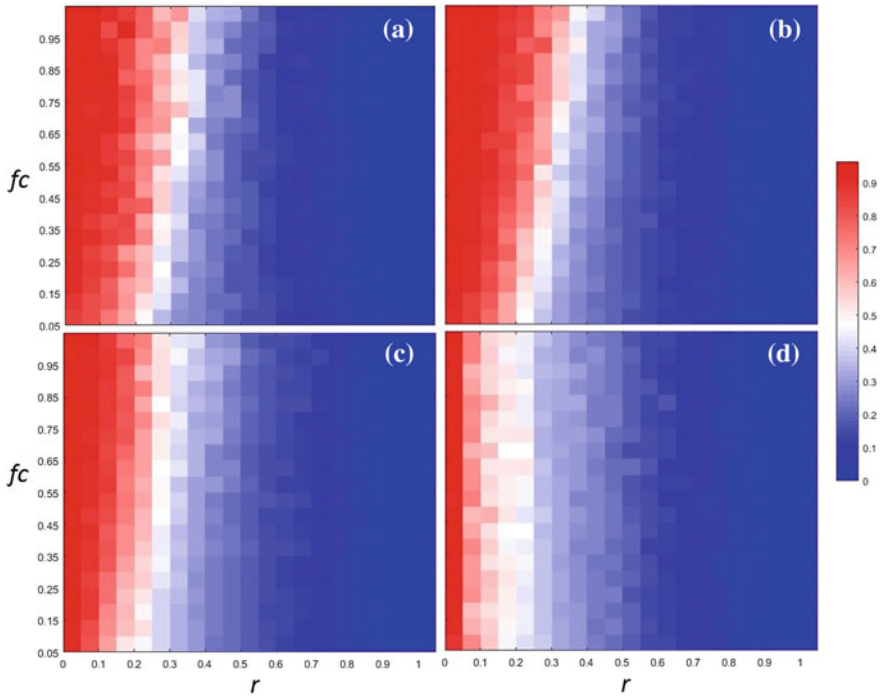

Fig. 2 Correlations between fc and $\alpha - r$ under different N_l when $\beta = 0.3$. **a** $N_l = 1$; **b** $N_l = 2$; **c** $N_l = 3$; **d** $N_l = 4$

with increasing β when $N_l = 4$ if $r = 0.1$, which means high sensibility of payoff could enhance cooperation when individuals know much information of their neighbors if the temptation of cheating is low. If $r = 0.5$, fc will decrease with increasing β when $N_l = 4$. On the contrary, when $N_l = 1$, fc will increase steadily at beginning and drop after $\beta > 5$. Especially when $\alpha = 1$ and $N_l = 1$ (Fig. 3c), fc drops fast after $\beta = 10$ which makes the gap of fc between $N_l = 1$ and $N_l = 4$ quite large.

As shown in Fig. 4, the difference of the influence of α is particularly large for different N_l. According to its general trend, fc will increase with increasing α when $\beta = 0.3$, and fc will decrease with increasing α when $\beta = 3000$. The influence of α is much smaller when $N_l = 4$ compared with $N_l = 1, 2, 3$, which means the evolution is more steady when individuals know much information of their neighbors. It is quite noticeable that when $\beta = 3000$ (see Fig. 4b), fc reaches the peak (almost full cooperation) when $N_l = 1, 2$. This is a unusual result because cooperators could hardly survive based on BTO strategy-updating rule under the same setting of circumstance.

From the above simulations, we can draw the conclusion that the incremental learning rule can enhance cooperation dramatically when individual has small value of α or β. It means the higher resistance to imitate others or lower payoff sensitivity

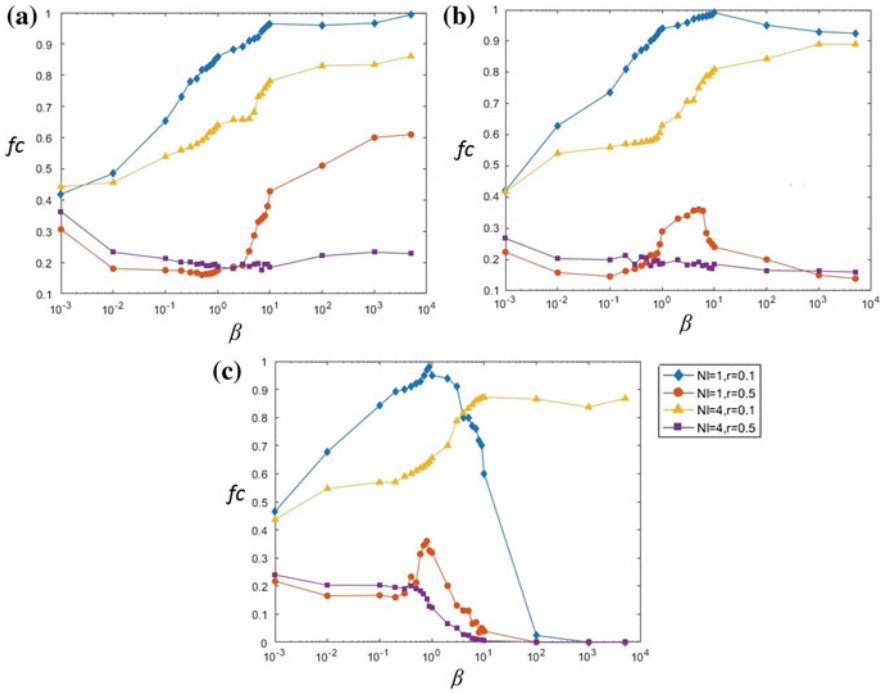

Fig. 3 Correlations between *fc* and β under different α. **a** $\alpha = 0.1$; **b** $\alpha = 0.5$; **c** $\alpha = 1$

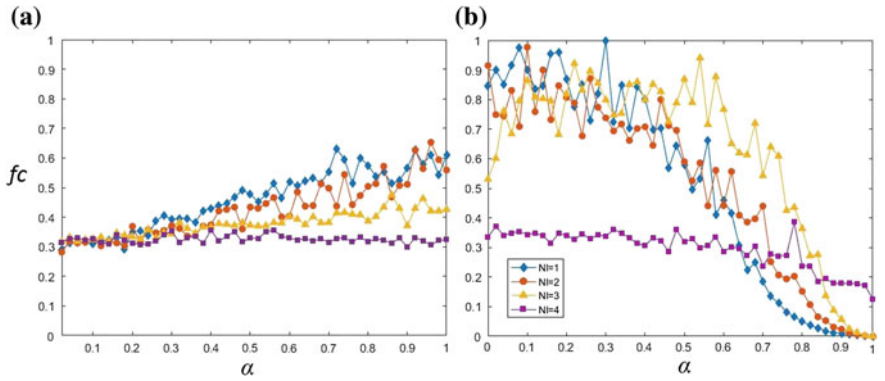

Fig. 4 Correlations between *fc* and α under different β, $r = 0.3$. **a** $\beta = 0.3$; **b** $\beta = 3000$

can both promote cooperative strategies surviving and spreading. We also notice that the incremental learning rule has greater influence when individual obtains fewer information of neighbors' payoff. In order to explain the reason behind, we investigate the evolution of population's strategies with time changing (see Fig. 5). As can be seen in Fig. 5a, b, when $N_l = 1$, the smaller value of α or β can make the

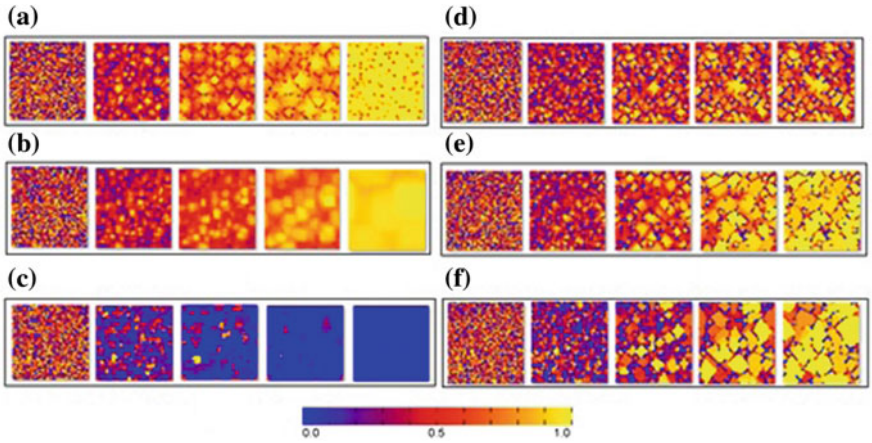

Fig. 5 Snapshots of population strategies with different α and β, $r = 0.1$. **a** $\alpha = 1$, $\beta = 0.3$, $N_l = 1$; **b** $\alpha = 0.2$, $\beta = 3000$, $N_l = 1$; **c** $\alpha = 1$, $\beta = 3000$, $N_l = 1$; **d** $\alpha = 1$, $\beta = 0.3$, $N_l = 4$; **e** $\alpha = 0.2$, $\beta = 3000$, $N_l = 4$; **f** $\alpha = 1$, $\beta = 3000$, $N_l = 4$

effect of gradual learning instead of adopting other's strategy directly. This can generate mid-strategy between complete C and complete D. It has been proved that mid-strategy can promote cooperation. If both α or β have bigger values, the strategy-updating rule becomes the take-over rule in which cooperators cannot survive without enough payoff information of neighbors (Fig. 5c). As can be seen in Fig. 5d–f, when $N_l = 4$, the individuals obtain enough payoff information of neighbors and the influence of α or β become much weaker. In such system, the evolution of cooperation is deriving from the structure of network.

4 Conclusions and Future Work

In this paper, we propose a strategy-updating rule based on incremental learning process for CPD game. Each individual refreshes its decision according to self-strategy and new strategy learnt from one of neighbors. The results show the incremental learning rule can enhance cooperation dramatically when individual has higher resistance to imitate others or lower payoff sensitivity. It is also find that the incremental learning rule has greater influence when individual obtains fewer information of neighbors' payoff. The reason is the incremental learning process can generate mid-strategy between complete cooperation and defection which can promote cooperation dramatically. Our results may shed some light on how cooperative strategies are actually adopted and spread in spatial network.

Acknowledgements This work is partly supported by National Natural Science Foundation of China under grant No. 61300087, No. 61702076 and No. 61502069; "the Fundamental Research Funds for the Central Universities" under grant No. DUT17RW131.

References

1. Luke S, Sullivan K, Panait L, Balan G (2005) Tunably decentralized algorithms for cooperative target observation. In Proceedings of the fourth international joint conference on Autonomous agents and multiagent systems. ACM, pp 911–917
2. Gheorghe M, Holcombe M, Kefalas P (2001) Computational models of collective foraging. BioSystems 61(2):133–141
3. Camorlinga S, Barker K, Anderson J (2004) Multiagent systems for resource allocation in peer-to-peer systems. In Proceedings of the winter international symposium on Information and communication technologies. Trinity College, Dublin, pp 1–6
4. Tanimoto J (2007) A study on a difference of dynamics between discrete and continuous strategies of a multi player game having linear payoff structure. Ipsj J 48(7):2372–2376
5. Axelrod R (1984) The evolution of cooperation. Basic books, New York
6. Szabó G, Fath G (2007) Evolutionary games on graphs. Phys Rep 446(4):97–216
7. Nowak MA (2006) Five rules for the evolution of cooperation. Science 314(5805):1560–1563
8. Du J, Wu B, Altrock PM, Wang L (2014) Aspiration dynamics of multi-player games in finite populations. J R Soc Interface 11(94):20140077
9. Bendor J, Swistak P (1995) Types of evolutionary stability and the problem of cooperation. Proc Natl Acad Sci 92(8):3596–3600
10. Szolnoki A, Perc M, Danku Z (2008) Making new connections towards cooperation in the prisoner's dilemma game. EPL (Europhys Lett) 84(5):50007
11. Macy MW, Flache A (2002) Learning dynamics in social dilemmas. Proc Natl Acad Sci 99 (suppl 3):7229–7236
12. Marchiori D, Warglien M (2008) Predicting human interactive learning by regret-driven neural networks. Science 319(5866):1111–1113
13. Traulsen A, Semmann D, Sommerfeld RD, Krambeck HJ, Milinski M (2010) Human strategy updating in evolutionary games. Proc Natl Acad Sci 107(7):2962–2966
14. Zhong W, Kokubo S, Tanimoto J (2012) How is the equilibrium of continuous strategy game different from that of discrete strategy game? BioSystems 107(2):88–94

A Novel Continuous Feedback Control for Rapidly Exponentially Stabilisation of Mechanical Systems

Tian Shi and Zhongbo Sun

1 Introduction

Rapidly exponential stability of nonlinear systems has the advantage of providing a guarantee on the accelerated time it takes for the nonlinear system to converge to a equilibrium. Actually, under some suitable conditions, the existence of a Lyapunov function with properties is equivalent to stability in the sense of Lyapunov, asymptotic stability, or exponential stability of state equilibrium point [1, 2]. Furthermore, once a Lyapunov function was constructed, a domain of attraction could be estimated. However, the estimate region is very conservative. Recently, Lyapunov methods have been studied a further surge of interest in the nonlinear systems field through powerful tools for obtaining them as sum of squares and here, we will mention the following works, for instance, [3–6]. In [7–9], Sontag and Artestein proposed control Lyapunov function for nonlinear control systems respectively. Without loss of generality, if there exists a control law such that the derivative of Lyapunov function is negative definite, then the state of nonlinear control systems converge to zero. However, when we use the control Lyapunov approach to analyze the stability of nonlinear systems, the controller must be constructed before. In order to satisfy the property of negative definite for control Lyapunov function, the inequalities should holds. Nevertheless, this will lead to a small attractive region. In order to enlarge the domain of attraction, this motivates our present study.

T. Shi · Z. Sun
College of Humanities & Sciences of Northeast Normal University,
130117 Changchun, China

Z. Sun (✉)
Department of Control Engineering, Changchun University of Technology,
Changchun 130012, China
e-mail: zhongbosun2012@163.com

Z. Deng (ed.), *Proceedings of 2017 Chinese Intelligent Automation Conference*,
Lecture Notes in Electrical Engineering 458,
https://doi.org/10.1007/978-981-10-6445-6_7

This work deals with design of rapidly exponential stabilizing control techniques for nonlinear mechanical systems with control input. In this paper, a new Lyapunov uniform framework for rapidly exponential stabilization of fully actuated mechanical systems is developed. The Lyapunov function is constructed as a quadratic function with an accelerated parameter. The motivation of this function is that when the value of Lyapunov function is zero vector, the generalized states converge to the desired states in accelerated time. According to the continuous feedback control law for generalized forces, the vectors converge to the zero vectors in accelerated time. Therefore, the states of nonlinear mechanical systems converge to the equilibrium in accelerated time duration.

This paper is organized as follows: Sect. 2 gives the main result on rapidly exponentially stabilization of nonlinear mechanical systems using a continuous Lyapunov function. Section 3 states two numerical simulation results for inverted pendulum on a cart and two link planar manipulator. The results illustrate the stability of this rapidly exponentially continuous feedback stabilization technique in comparison to finite time and asymptotically stabilizing continuous feedback techniques. Finally, Sect. 4 develops a summary of the main conclusions of this paper and future works.

2 Rapidly Exponentially Stabilization of Nonlinear Mechanical Systems

In this paper, we will consider the nonlinear mechanical systems as follows:

$$M(q)\ddot{q} + C(q,\dot{q})\dot{q} + G(q) = F(q,\dot{q})$$

where $M(q)$ is a positive definite inertia matrix, and $C(q,\dot{q})$ is the time derivative of the inertia matrix, and $G(q)$ is a gravity matrix, and $F(q,\dot{q})$ is the non-conservative forces.

In this section, a new constructive approach to obtain rapidly exponentially stabilization techniques is developed for nonlinear mechanical systems. There are two steps for this method. First, a novel continuous function of the states is constructed that ensure that when the continuous function converges to zero, the state of nonlinear mechanical systems converges to zero as well. Second, a new continuous Lyapunov function is constructed to guarantee the rapidly exponentially stability of the nonlinear mechanical systems. The two subsections are described as following in details.

2.1 Rapidly Exponentially Stabilization of Nonlinear Mechanical Systems

In the first step of the rapidly exponentially stabilization process, a novel function is developed that ensures the generalized coordinate vectors of nonlinear mechanical systems converge to zero. Furthermore, assume that the desired equilibrium to be stabilized is the origin, namely, the generalized coordinate vector. Now, we will construct a function with some properties as follows.

Proposition 1 *Let* $l(q,v): Q \times R^n \rightarrow R^n$ *be a function that has the following properties:*

$l(q,v)$ *is linear in* $v = \dot{q}, l(q,v)$ *is continuous in* q,

$l(q,v) = (0,0) \Rightarrow q(t) = 0$, *for* $t \rightarrow \infty$.

These properties guarantee that the state of nonlinear mechanical systems $(q,v) \in Q \times R^n$ converge to zero in accelerated time when $l(q,v) = (0,0)$.

According to the nonlinear mechanical systems, we can construct a novel function as follows

$$l(q,v) = v + \frac{\kappa q}{\varepsilon}, \kappa > 0, \varepsilon \in (0,1) \tag{1}$$

Due to the Eq. (1), we have an important Lemma 1 as follows.

Lemma 1 *If* $l(q,v)$ *is defined by* (1) *where* $v = \dot{q}$, *then* $l(q,v)$ *satisfies the properties in Proposition* 1.

Proof In order to prove the Lemma 1, we will consider the following candidate Lyapunov function $V(q) = \frac{1}{2} q^T q$.

In order to evaluate on the submanifold $l(q,v) = (0,0)$, where $l(q,v)$ is given by Eq. (1), we will adopt the time derivative of candidate Lyapunov function. Therefore, we have

$$\dot{V}(q) = q^T v = -\frac{\kappa}{\varepsilon} q^T q = -\frac{2\kappa}{\varepsilon} V \leq -CV, \tag{2}$$

where constant $C \in (0, \infty)$. From the inequality (2), we can see that $\dot{V}(q) = \frac{1}{2} q^T q = \frac{1}{2} \|q\|^2$.

The second step of the constructive approach is shown in the following Sect. 2.2. According to a new Lyapunov function, we obtain a rapidly exponentially stabilization technique for nonlinear mechanical systems.

2.2 Rapidly Exponentially Stabilization of Nonlinear Mechanical Systems with Input Forces

In the second step of this rapidly exponentially stabilization approach is considered for nonlinear mechanical systems with input forces. Without loss of generality, a novel vector of generalized input forces is obtained for nonlinear mechanical systems. Furthermore, we will construct a new Lyapunov function with positive definite property. Moreover, the Lyapunov function satisfies the properties listed in Proposition 1. Now, the Lyapunov function is constructed as follows

$$\upsilon(q,v) = \frac{1}{2} l(q,v)^T l(q,v) \tag{3}$$

According to the above candidate Lyapunov function, we can use it to obtain the rapidly exponentially stabilization technique.

Theorem 1 *Consider the nonlinear mechanical systems with the following continuous feedback control law given by*

$$f(q,v) = -\frac{\gamma}{2} l(q,v) - \frac{\kappa}{\varepsilon} v$$

where $\gamma > 0, \kappa > 0, \varepsilon \in (0,1)$*, Moreover,* $l(q,v)$ *is defined by Eq.* (1)*, then the nonlinear mechanical systems is rapidly exponential stable.*

Proof In order to prove the Theorem 1, we will consider the following candidate Lyapunov function $\upsilon(q,v) = \frac{1}{2} l(q,v)^T l(q,v)$. Due to evaluate on the submanifold $l(q,v) = (0,0)$, we will take the time derivative of candidate Lyapunov function (3). Thereby, we obtain

$$\dot{\upsilon}(q,v) = l(q,v)^T \dot{l}(q,v) = l(q,v)^T \left[f(q,v) + \frac{\kappa}{\varepsilon} v \right] = -\gamma V$$

Hence, $\dot{\upsilon}(q,v) = -\gamma V \leq -CV, C \in (0,\infty)$.

3 Numerical Simulation Results

In this section, we will report some numerical results obtained from the inverted pendulum on a cart and two link planar manipulator model [10]. The results show that the continuous feedback controller of this paper is feasible and effective.

3.1 Inverted Pendulum on a Cart

In this subsection, an inverted pendulum on a cart nonlinear mechanical system is considered. In general, this system has two degrees of freedom. The mathematical model is described as follows:

$$M(q) = \begin{bmatrix} m_c + m_p & m_p d\cos\theta \\ m_p d\cos\theta & I + m_p d^2 \end{bmatrix}, C(q,\dot{q}) = \begin{bmatrix} 0 & -m_p d\dot{\theta}\cos\theta \\ 0 & 0 \end{bmatrix}$$
$$G(q) = \begin{bmatrix} 0 \\ -m_p g d\sin\theta \end{bmatrix}, F_c = \begin{bmatrix} f_c(t) \\ \tau_c(t) \end{bmatrix}, F_{NC}(q,v) = \begin{bmatrix} 0 \\ 0 \end{bmatrix}, \tag{4}$$

where m_c and m_p are the mass of the cart and the pendulum respectively. I represents the center of mass of pendulum inertia, and d is a distance between the center of mass and the pendulum pivot, and g is gravity acceleration. $f_c(t)$ and $\tau_c(t)$ are non-conservative forces. The parameters are the same with literature [10], in this paper, we will omit it. In Fig. 1, the horizontal displacement of the cart converges to zero in about 6 s using the finite time stable scheme, whereas it takes the asymptotic stable about 9 s to converge to zero.

From Fig. 1, we can see that the rapidly exponentially stable control law is better than the asymptotic stable control law and finite time control law at the beginning. That is to say, the rapidly exponentially stabilization is suit to real time control systems. From Fig. 2, it is easy can be seen that the time for the finite time stable controller shows that the rotational displacement of the pendulum converges to zero after about 6 s. Whereas the rapidly exponentially controller shows that the rotational displacement of the pendulum converges to zero after about 5 s and the asymptotic controller need about 9 s. Figure 3 shows that the velocity of the cart

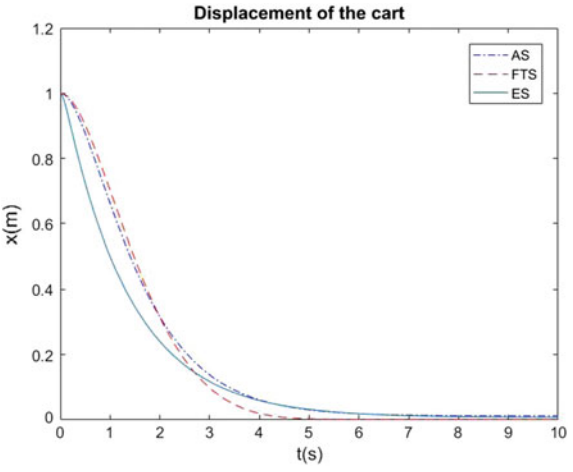

Fig. 1 Displacement of the cart

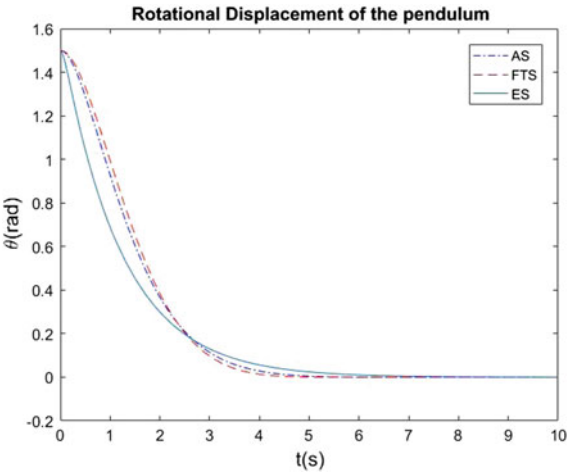

Fig. 2 Rotational displacement of the pendulum

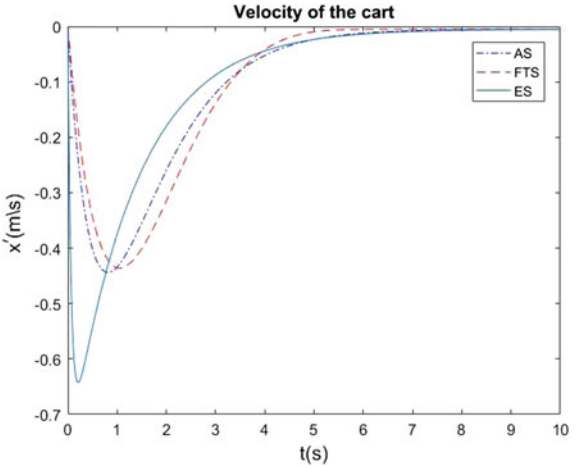

Fig. 3 Velocity of the cart

over the time. From the figure, we can see that the rapidly exponentially stable controller is better than the others. Figure 4 shows that the rate of change of the rotational displacement.

3.2 Two Link Planar Manipulator System

In this subsection, a two-link planar manipulator system of nonlinear mechanical system is considered. The mathematical model is described as follows:

$$M(q)\ddot{q} + C(q,\dot{q})\dot{q} + G(q) = F(q,\dot{q}).$$

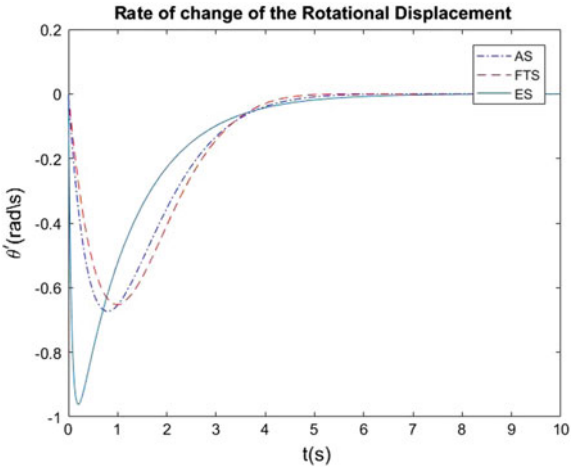

Fig. 4 Rate of change of the rotational displacement

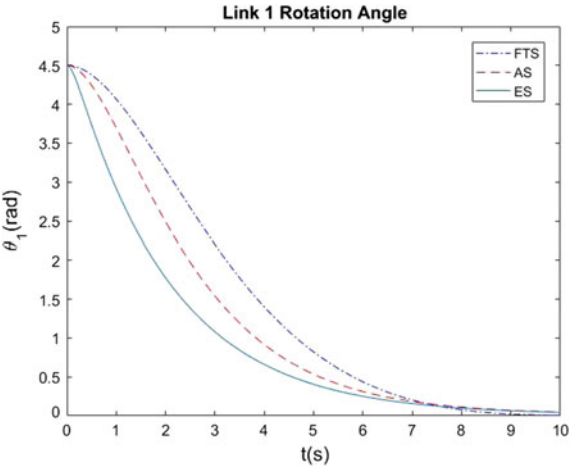

Fig. 5 Link 1 rotation angle

The nonlinear model is of the form given by the following equations

$$M(q) = \begin{bmatrix} (m_1+m_2)d_1^2 + m_2 d_2^2 + 2m_2 d_1 d_2 \cos\theta_2 & m_2\left(d_2^2 + d_1 d_2 \cos\theta\right) \\ m_2\left(d_2^2 + d_1 d_2 \cos\theta\right) & m_2 d_2^2 \end{bmatrix},$$

$$C(q,\dot{q}) = -m_2 d_1 d_2 \dot{\theta}_2 \sin\theta_2 \begin{bmatrix} 2 & 1 \\ 1 & 0 \end{bmatrix}, \quad F_c = \begin{bmatrix} \tau_1(t) \\ \tau_2(t) \end{bmatrix}, \quad F_{NC} = \begin{bmatrix} 0 \\ 0 \end{bmatrix},$$

$$G(q) = g \begin{bmatrix} (m_1+m_2)d_1 \cos\theta_1 + m_2 d_2 \cos(\theta_1+\theta_2) \\ m_2 d_2 \cos(\theta_1+\theta_2) \end{bmatrix}.$$

This nonlinear model assumes that the non-conservative forces acting on the system are the control input torques. Figure 5 shows that the link 1 rotation angle

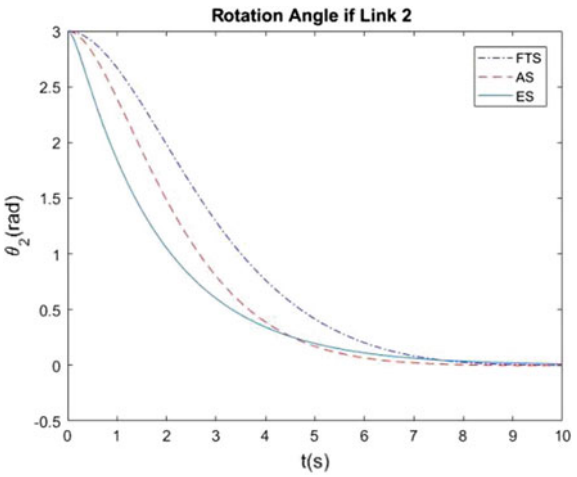

Fig. 6 Link 2 rotation angle

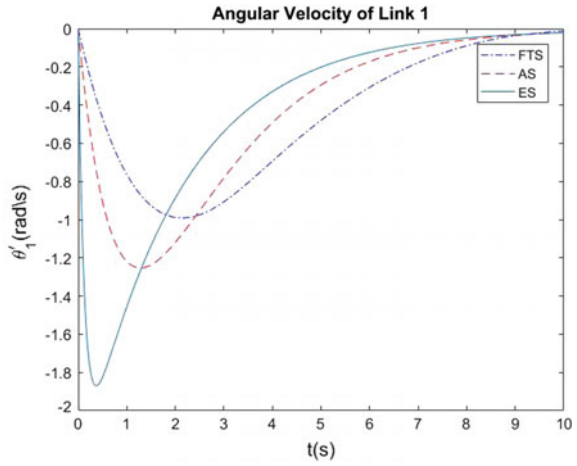

Fig. 7 Angular velocity of link 1

versus time. From the Fig. 5, we can see that the rapidly exponentially stable controller is better than the other controllers. It is shows that the continuous feedback controller of this paper is fit to the real time control systems. Figure 6 shows that the link 2 rotation angle versus time. From Fig. 6, we can see that the state of nonlinear mechanical systems converge to equilibrium about 9 s.

However, at the beginning, the rapidly exponentially controller is better than the others. Figure 7 represents angular velocity of link 1 and Fig. 8 shows that angular velocity of link 2. From Figs. 7 and 8, we can see that the states of mechanical systems converge to equilibrium at 8 s.

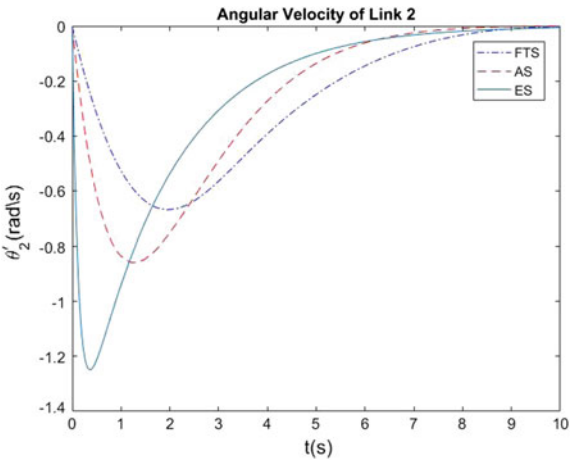

Fig. 8 Angular velocity of link 2

4 Conclusion and Future Work

In this paper, a novel approach of continuous feedback control law is developed for nonlinear mechanical systems. According to the vector value function, some properties are satisfied that ensure when this vector value function converges to zero, the state of nonlinear mechanical systems converges to the desired state in accelerated time. Therefore, due to the vector value function, a new Lyapunov function is constructed for nonlinear mechanical systems. Moreover, a continuous feedback control law is used to obtain rapidly exponential stability in accelerated time. Numerical results are illustrated on two classical nonlinear mechanical systems, for instance, an inverted pendulum on a cart and a planar two-link manipulator. Furthermore, comparisons with asymptotic stability and finite time stability for both examples show that the rapidly exponentially stabilization scheme has superior convergence rate while requiring lower control effort. Future work will generalize such rapidly exponentially stabilizing control schemes to multi-body systems.

References

1. Khalil HK (2002) Nonlinear systems, 3rd edn. Prentice-Hall, Upper Saddle River
2. Sontag ED (1998) Mathematical control theory: deterministic finite dimensional systems, vol 6. Springer, New York
3. Tan W, Packard A (2008) Stability region analysis using polynomial and composite polynomial Lyapunov functions and sum-of-squares programming. IEEE Trans Autom Control 53(2):565–571
4. Wang Z, Liu X, Liu K, Li S, Wang H (2016) Backstepping-based Lyapunov function construction using approximate dynamic programming and sum of square techniques. IEEE Trans Cybern 99. doi:10.1109/TCYB.2016.2574747

5. Guelton K, Manamanni N, Duong CC, Koumba-Emianiwe DL (2013) Sum-of-squares stability analysis of Takagi-Sugeno systems based on multiple polynomial Lyapunov functions. Int J Fuzzy Syst 15(1):1–8
6. Topcu U, Packard A, Seiler P (2008) Local stability analysis using simulations and sum-of-squares programming. Automatica 44(10):2669–2675
7. Liberzon D, Sontag ED, Wang Y (2002) Universal construction of feedback laws achieving ISS and integral-ISS disturbance attenuation. Syst Control Lett 46:111–127
8. Sontag E (1989) A 'universal' construction of Artstein's theorem on nonlinear stabilization. Syst Control Lett 13:117–123
9. Artstein Z (1983) Stabilization with relaxed controls. Nonlinear Anal Theory Methods Appl 7(11):1163–1173
10. Sanyal Amit K, Bohn Jan (2015) Finite-time stabilisation of simple mechanical systems using continuous feedback. Int J Control 88(4):783–791

Semantic Relation Driven SVM-Based Function Recognition for 3D Shape Components

Lingling Zi and Xin Cong

1 Introduction

The semantic knowledge of 3D shapes could reflect the human's perception of shape functions and the knowledge on functional description plays a very important role in shape analysis and understanding. Therefore, functional recognition of 3D shape becomes a hot issue that needs to be solved urgently. And the component-based function recognition technique is one of the main solutions. Feng et al. [1] proposed a junction-aware shape component descriptor to obtain functional semantics. Léon et al. [2] presented a high-level signature method to capture the functional semantics of shape component. Laga et al. [3] proposed the component-aware similarity measure approach. The above methods make full use of the function relations between shape components to achieve the task of function recognition. To further improve the accuracy of functional recognition, the methods combining semantic information with the structure of components are proposed recently. For example, the modal function transformation based on shape matching pairs of shape components [4] and a rule-based expert system for inferring functional annotation [5] were proposed. And the compositional model combining shape and appearance [6] also have good performance for functional recognition. However, they show unsatisfactory results for these shapes, which have large geometric and topological variations. So, it is necessary to propose a new approach to improve the accuracy of function recognition of 3D shapes.

In this paper, we present a semantic relation driven SVM-based 3D shape components function recognition approach(SDFR) to solve the problem of reorganizing functional components under large scale deformations. The main contributions of the proposed approach are as follows. (1) The shape segmentation

L. Zi (✉) · X. Cong
School of Electronic and Information Engineering,
Liaoning Technical University, Huludao 125105, China
e-mail: lingling19812004@126.com

Z. Deng (ed.), *Proceedings of 2017 Chinese Intelligent Automation Conference*,
Lecture Notes in Electrical Engineering 458,
https://doi.org/10.1007/978-981-10-6445-6_8

scheme based on approximate convexity decomposition is proposed to identify shape components with independent semantics. (2) A semantic calculation method based on component context relations is proposed to qualitatively measure semantic relations between the obtained shape components, which has stability for shapes with large geometric and topological variations. (3) The functional classification method using SVM is performed to achieve the task of shape recognition. In a word, SDFR integrates the advantages of semantic information and shape structure to improve the accuracy of function recognition for 3D shapes, especially for shapes with large-scale deformation.

The rest of the paper is structured as follows. Section 2 presents the framework of SDFR. Section 3 illustrates the implementation of SDFR. Section 4 presents experimental work to demonstrate our approach. The last section concludes the paper.

2 The Overview of SDFR

Let $\{S_1, S_2, \ldots, S_n\} \in S$ denotes the three-dimensional shape set, $\{p_1, p_2, \ldots, p_m\} \in P$ denotes the independent component set for $S_i(S_i \in S)$, and $\{c_1, c_2, \ldots, c_m\} \in C$ denote the corresponding component label of functional category. The aim of proposed SDFR is to retrieve the shape component which has the same functional category with p_t, and p_t is one of components for test shape S_t. Figure 1 shows the framework of SDFR and it consists of three steps.

Specifically, the shape segmentation scheme based on approximate convexity decomposition is presented and it uses the contour dissimilarity and boundary attributes of convexity to effectively divide each 3D shape into multiple combinations of components with different function semantics, i.e. $\cup_{i=1}^{N} p_i = S_i(S_i \in S)$. Then, for $\forall p_i(p_i \in S_p)$ and $\forall p_j(p_j \in S_q)$, the semantic calculation method based on context relations of the obtained components is proposed to quantify the semantic similarity between p_i and p_j, which could maintain stability for shape components with large scale deformation. Finally, according to the obtained semantic similarity of shape components, the function recognition method using SVM is adopted to determine the functional label for each component.

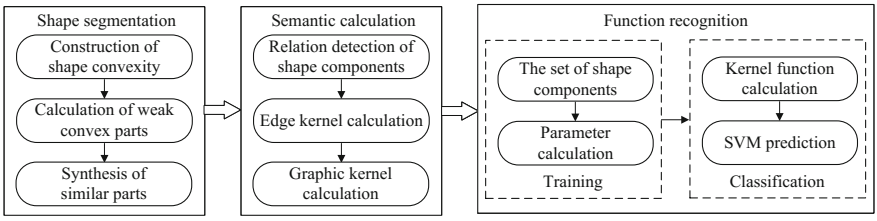

Fig. 1 The framework of SDFR method

3 The Implementation of SDFR

In this section, we elaborate the critical steps in the process of SDFR implementation. The proposed method is to address the problem of automatic recognition in the presence of significant geometric and topological variations of 3D shapes.

3.1 Shape Segmentation of 3D Shapes

In the light of the visual perception characteristics of human for the complex shapes, 3D shapes can be decomposed into multiple combinations with different semantic components and to achieve this task [7], the approximation convexity decomposition technology can be adopted to complete shape segmentation [8, 9]. On this basis, the segmentation scheme contains construction of shape convexity, calculation of weak convex parts and synthesis of similar parts.

Firstly, S_i is divided into the approximate bump set by using the over-segmented method. Based on the extracted bumps from the set, the shape convexity is constructed and the initial block set $BS = \{BS_1, BS_2, \ldots, BS_n\}$ is captured by using the graph-based clustering method.

Secondly, the convex rank for $BS_i (BS_i \in BS)$ is computed using (1):

$$R(BS_i) = |VI(BS_i)|/|BS_i|^2 \tag{1}$$

where $VI(BS_i)$ is the set of all pairs of points in BS_i that are in a line-of-sight, *i.e.* $(i, j) \in VI(BS_i)$ $(i \in BS_i, j \in BS_i)$. The weakly convex set $W = \{W_1, W_2, \ldots, W_m\}$ is obtained by descending $R(BS_i)$ and the weakly convex parts with similar visible properties are merged to inform a new set $W = \{W_1, W_2, \ldots, W_{m'}\}$.

Finally, the geometrical features of the parts are described using the contour dissimilarity and the boundary attributes of the convex set, and the weak convex components with similar geometric features are synthesized. The contour dissimilarity of parts can be computed using EMD, shown in (2).

$$dist(W_i, W_j) = E(h_i, h_j) \tag{2}$$

where h_i and h_j are histogram of shape diameter function for W_i and W_j, respectively.

The boundary attributes can be computed by the convexity of the seams, shown in (3).

$$\begin{aligned} VS_{i,j} &= \{(\boldsymbol{\omega}_p, \boldsymbol{\omega}_q) : \boldsymbol{\omega}_p \in W_i, \boldsymbol{\omega}_q \in W_j, (\boldsymbol{\omega}_p, \boldsymbol{\omega}_q) \in NG_k, \theta(\mathbf{n}_p, \mathbf{n}_q) \leq \pi\} \\ AS_{i,j} &= \{(\boldsymbol{\omega}_p, \boldsymbol{\omega}_q) : \boldsymbol{\omega}_p \in W_i, \boldsymbol{\omega}_q \in W_j, (\boldsymbol{\omega}_p, \boldsymbol{\omega}_q) \in NG_k, \theta(\mathbf{n}_p, \mathbf{n}_q) > \pi + \varsigma\} \end{aligned} \tag{3}$$

In (3), $VS_{i,j}$ and $AS_{i,j}$ denote the convex seam and concave seam between W_i and W_j, respectively. ω_p denotes the sampling point with direction $-\mathbf{n}_p$ in D_i. $\theta(\mathbf{n}_p, \mathbf{n}_q)$ denotes the angle between $\mathbf{n}_p$ and $\mathbf{n}_q$, ζ denotes the adjustment threshold, and NG_k denotes the neighbor graph combined by seams. W_i and W_j are merged when they satisfy the distance condition, shown in (4).

$$|NS_{i,j}|/|AS_{i,j}| \geq \eta, dist(W_i, W_j)/\max(dist(W_i, W_j)) \leq \sigma \tag{4}$$

where η and σ are merge thresholds. Then the independent component set P for shapes can be obtained.

3.2 Semantic Calculation of Shape Components

When the geometrical features and topological structure of 3D shapes change greatly, we find that the semantic relations of the shape part maintain relatively stable and this can be applied to the problem of functional classification.

Given graph $G(V, E)$ denotes component relations of 3D shapes, V denotes the nodes of shape component, and E denotes the different type relations among the nodes. Then the problem of functional classification is changed to the problem of graphic kernel calculation and obtained graphic kernel $\boldsymbol{\Psi}$ quantifies the semantic similarity of the function of the shape components.

Combining geometric features of component with context relations between nodes, $\boldsymbol{\Psi}$ is computed by using (5)

$$\psi^l(G_p, G_q, p_A, p_B) = \begin{cases} \psi_N(p_A, p_B) \times \sum\limits_{\substack{p_s \in AN_{Gp}(p_A) \\ p_{s'} \in AN_{Gq}(p_B)}} \psi_E(e, e')\psi^{l-1}(G_p, G_q, p_s, p_{s'}), & l > 0 \\ \psi_N(p_A, p_B), \quad l = 0 \end{cases} \tag{5}$$

In (5), l denotes the length of graph path, G_p and G_q are the relation graph for shape S_p and S_q, respectively. $p_A \in G_p$, $p_B \in G_q$, $AN(x)$ denotes all adjacent nodes for x in G, e and e' are the edges which connect between p_A and p_s, p_B and p_s. Ψ_N denotes the node kernel, which reflects the similarity geometric characteristics of the two components, and it is calculated by using shape description operator based on Euler distance, shape size based on unit sphere and the principal direction feature based on PCA. Ψ_E denotes the edge kernel, which reflects the context of different nodes, shown in (6).

$$\boldsymbol{\Psi}_E(\boldsymbol{e_p}, \boldsymbol{e_q}) = \boldsymbol{R}(\boldsymbol{e_p}, \boldsymbol{e_q}) \tag{6}$$

Which $e_p \in E_p$ and $e_q \in E_q$, R denotes the context relation between e_p and e_q, *i.e.* if there is the relation between e_p and e_q, $R(e_p, e_q)$ is 1, otherwise is 0.

The contextual semantic relations between shape parts are divided into two sorts: the basic relations and the derivation relations. The basic relations mainly contain inclusion relation, symmetry relation, horizontal support relation, side connection relation and adjacency relation. The definitions are shown as follows.

Definition 1 Inclusion relation. If the overlap of bounding boxes of p_1 and p_2 is over 50%, then there is the inclusion relation between them, denoted as $IN(p_1, p_2) = 1$.

Definition 2 Symmetry relation. If there are rotational symmetry, translation symmetry or reflection symmetry between p_1 and p_2, then there is the symmetry relation between them, denoted as $SYR(p_1, p_2) = 1$.

Definition 3 Horizontal support relation. If the contact surface of p_1 is perpendicular to the gravity vector of p_2, there is the horizontal support relation between them, denoted as $HR(p_1, p_2) = 1$.

Definition 4 Side connection relation. If the normal of contact area of p_1 is perpendicular to the symmetrical spindle of p_2, then there is the side connection relation between them, denoted as $SCR(p_1, p_2) = 1$.

Definition 5 Adjacency relation. If p_1 and p_2 have a common vertex or the bounding boxes of them are overlapping, then there is the adjacency relation between them, denoted as $AR(p_1, p_2) = 1$.

Based on the above the basic relations, the derivation relations are designed to capture the underlying context semantic information, which are shown as follows.

Rule 1 If $SYR(p_1, p_2) = 1$ and $SYR(p_2, p_3) = 1$, then $SYR(p_1, p_3) = 1$.
Rule 2 If $HR(p_1, p_2) = 1$ and $SYR(p_2, p_3) = 1$, then $HR(p_1, p_3) = 1$.
Rule 3 If $SCR(p_1, p_2) = 1$ and $SYR(p_2, p_3) = 1$, then $SCR(p_1, p_3) = 1$.

3.3 Function Recognition Using SVM

Since the methods using SVM are better than many traditional classification methods in the terms of controlling over-fitting, the efficiency of calculation and classification accuracy, function recognition using SVM could be used to establish functional semantic classifiers and it contains two steps, training and classification. In the training phase, we set $\boldsymbol{\Psi}$ as the kernel function, and use it to calculate the support vectors and the optimal parameters. In the testing phase, we segment the 3D shape to obtain the set of shape components, calculate the Kernel function, and predict the function labels of shape components by using the optimal parameters.

4 Experiments Results and Discussion

We used the experimental data from Princeton University database [10] and the COSEG dataset [11], which contain four types of 3D shapes (candlesticks, birds, planes, and ants). Experiments were performed using Matlab platform. For each type of shapes, half of the samples in the data set were randomly selected as the training set and the other half were the test set. In the experiments, the normal adjustment parameter ζ was 0.05, the weak convex component merging thresholds and η and σ were 0.8 and 0.15 respectively.

Since that functional recognition depends on the high-level semantics of shape classification, we use the classification error rate to verify the accuracy of function recognition for each components of 3D shapes. The lower the index of the classification error rate, the higher the accuracy of the function recognition.

Figure 2 shows the comparison results of classification error rates using by semantic corresponding method GCFR [3] and the proposed method, which show that SDFR obtains the lower classification error rates for each shape component of each shape. The main reason is that the semantic calculation method based on the context relations could improve the recognition accuracy of the functional semantic classification.

To further measure the effect of functional recognition, we computed the component matching accuracy. For any type of shapes, the artificial label of component can be marked as its corresponding to the matrix, denoted as $M = m_{ij}$ ($i, j = 1, \ldots, N$). N is the total number of components contained in this shapes. If the component j has the same functional label as the component i, then $m_{ij} = 1$, otherwise $m_{ij} = 0$. $AC(p,q) = \Sigma_i \in {}_p m_{i\varphi(i)}/N_p$ measures the component matching accuracy of the shape class. Where p and q represent the two shapes, respectively. For component i in p,

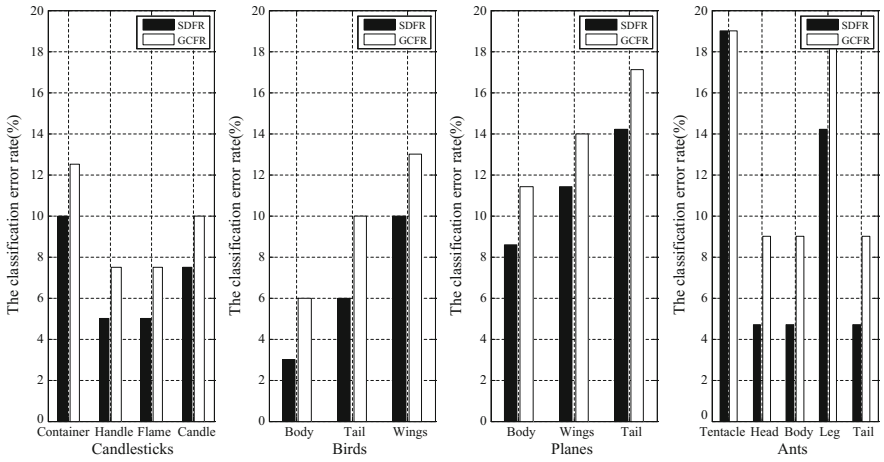

Fig. 2 Comparisons of classification error rates using by GCFR and SDFR

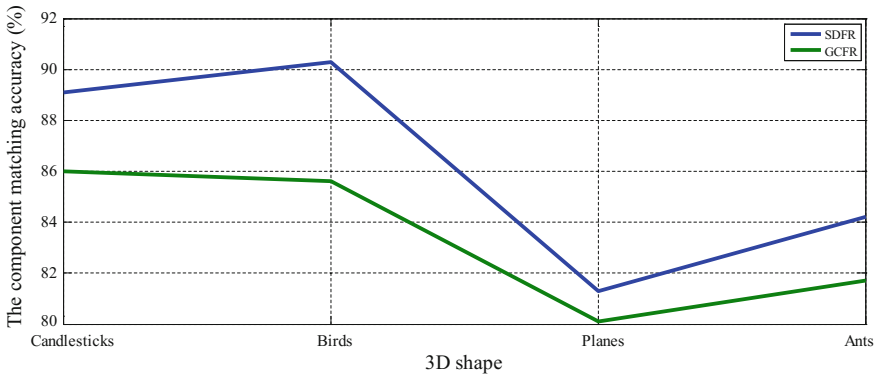

Fig. 3 Comparisons of matching accuracy of shape components

$\varphi(i)$ is the component of q that has the same functional label as i, and N_p is the total number of components in P. If the functional labels of all the components in p are the same as the functional labels in q, the value is 1, and if no function label is classified correctly, the value is 0. Figure 3 shows the average matching accuracy of the components obtained using the proposed method and GCFR. It can be seen that the matching accuracy obtained by using SDFR method is higher than that of GCFR.

5 Conclusions

The diversity of geometrical features and topologies of different 3D shapes leads to the identification of shape components with different apparent is a challenging problem. The semantic relations between shape components contain potential structural information, which could provide valuable observations for statistical methods. On this basis, we change the recognition problem into the prediction problem, and propose the SDFR method. The innovations of this method are shown as follows. (1) The shape segmentation based on approximate convexity decomposition is proposed, which decomposes the shape into shape components with different semantics. (2) A semantic calculation method based on context relations is proposed to quality the functional similarity. (3) SVM classifier with functional semantic similarity as kernel function is constructed to effectively predict the functional semantics of different shape components. The experimental results show that the method has good recognition effect and high recognition accuracy.

Acknowledgements This work is supported by the National Natural Science Foundation of China (61702241, 61602227); The Foundation of the Education Department of Liaoning Province (L2015225, LJYL019) and the Doctoral Starting up Foundation of Science Project of Liaoning Province (201601365).

References

1. Feng J, Liu Y, Gong L (2015) Junction-aware shape descriptor for 3D articulated models using local shape-radius variation. Sig Process 112:4–16
2. Léon V, Bonneel N, Lavoué G et al (2016) Continuous semantic description of 3D meshes. Comput Graph 54:47–56
3. Laga H, Mortara M, Spagnuolo M (2013) Geometry and context for semantic correspondences and functionality recognition in man-made 3D shapes. ACM Trans Graph 32(5) (Article 150)
4. Kuang Z, Li Z, Qian L et al (2015) Modal function transformation for isometric 3D shape representation. Comput Graph 46:209–220
5. Daniela X, Berta C, Rubén F (2015) A rule-based expert system for inferring functional annotation. Appl Soft Comput 35:373–385
6. Wang J, Yuille A (2015) Semantic part segmentation using compositional model combining shape and appearance. In: Proceedings of the IEEE conference on computer vision and pattern recognition, pp 1788–1797
7. Aubry M, Maturana D, Efros AA et al (2014) Seeing 3D chairs: exemplar part-based 2D-3D alignment using a large dataset of CAD models. In: Proceedings of the IEEE conference on computer vision and pattern recognition, pp 3762–3769
8. Asafi S, Goren A, Cohen-Or D (2013) Weak convex decomposition by lines-of-sight. Comput Graph Forum 32(5):23–31
9. Kaick OV, Fish N, Kleiman Y et al (2014) Shape segmentation by approximate convexity analysis. ACM Trans Graph 34(1):1–11
10. Chen X, Golovinskiy A, Funkhouser T (2009) A benchmark for 3D mesh segmentation. ACM Trans Graph 28(3):341–352
11. COS.(2012). The shape coseg dataset. http://web.siat.ac.cn/yunhai/ssl/ssd.htm

Quantitative Analysis of Shear Mark Based on Maximum Lyapunov Exponent Algorithm

Bingcheng Wang and Chang Jing

1 Introduction

The surface topography has unsteady stochastic characteristics. This fact has been discovered by Sayles et al. in the 1970s. The problem of surface topography recognition is studied by time series analysis [1] on the basis of stochastic process theory. The analysis of the two-dimensional profile curve and the three-dimensional surface are treated as one-dimensional signals and three-dimensional signals [2]. In the research of past 20 years, some progress is made in this field. Wang and other researchers wrote the paper [3], etc. results. The achievements show that the time series have been applied in the study of surface topography.

The surface profile curve of shearing marks is treated as one-dimensional signals. The maximum Lyapunov exponent is applied to the study of surface characteristics analysis of shearing marks. The analysis method of surface characteristics of shearing marks based on maximum Lyapunov exponent is proposed. The basis of the reasonable calculation of the maximum Lyapunov exponent is the determination of delay time τ and the embedded dimension d in the phase space reconstruction of time series. Therefore in this paper the determination of these two quantities is analyzed emphatically. The delay time of different time series is determined by mutual information function method. The minimum embedding dimension d is determined according to the improved false neighbor method which is proposed by Cao [4]. The correlation dimension is calculated for the surface profile curve of shearing marks [5, 6] on the basis. The research provides a method of analysis for surface characteristics recognition of shearing marks.

B. Wang (✉)
Center Laboratory for Forensic Science, Shenzhen University, Shenzhen, China
e-mail: wbc8631@163.com

C. Jing
Department of Technology, Guangdong Police College, Guangzhou, China
e-mail: wbc8636@163.com

Z. Deng (ed.), *Proceedings of 2017 Chinese Intelligent Automation Conference*,
Lecture Notes in Electrical Engineering 458,
https://doi.org/10.1007/978-981-10-6445-6_9

2 Experimental Conditions and Data Acquisition

Scissors, wire cutters and wire clippers are used as shearing tools to shear the lead wires. Several samples of shearing marks are made. The samples are observed under the stereo microscope. The samples which can reflect the stability characteristics of the shearing marks are chosen to be collected digitally.

In the experiment, the shearing marks are collected digitally by using Austria Infinite Focus auto-zoom three-dimensional surface topography measurement device. A three-dimensional shearing mark is stored in computer. In this experiment, the objective magnification is 10 times and the sampling resolution is 1.1 μm. The stable part of the mark characteristic is marked by the application software. The profile curve which is perpendicular to the marks surface is obtained. Profile curve which is perpendicular to the mark surface formed by scissors, wire cutters, wire clippers are shown in Fig. 1.

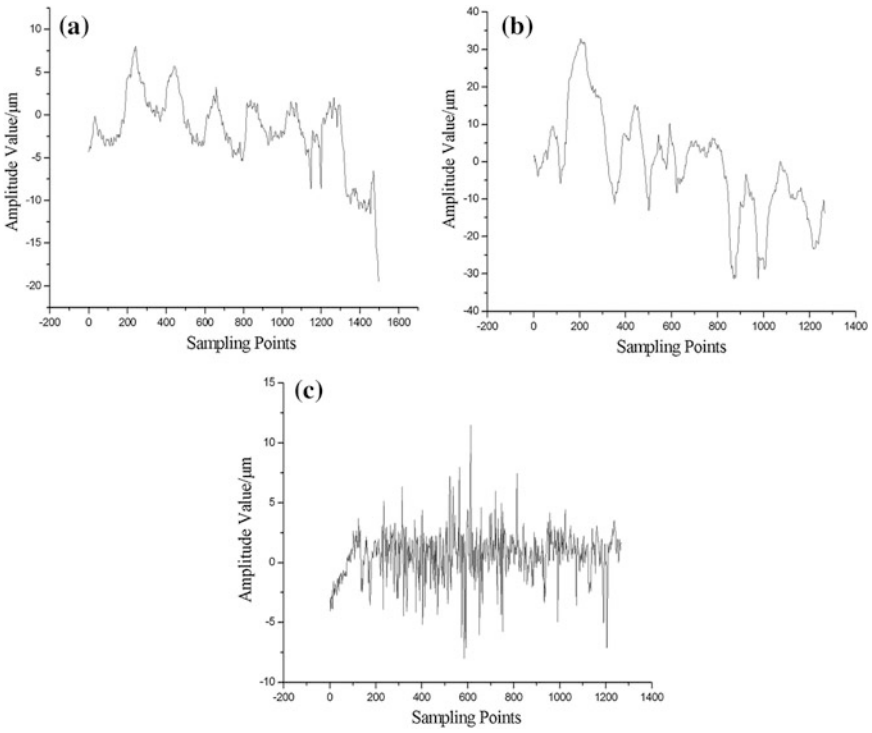

Fig. 1 Three kinds of profile curves

3 Two Parameter Determination in Restructuring of Phase Space

The delay time τ is one of the two important parameters of phase space reconstruction. In order to make the reconstructed phase space fully reflect the system dynamic characteristics, two parameters must be properly selected. When the selection of delay time τ is too big or too small, the dynamic characteristic of system is unable to reflect and the calculated chaotic characteristics may be inaccurate or even incorrect. In this paper, the delay time τ is determined by using mutual information function method.

Supposes the observation time series is $\{x_n\}$, and then observes the mutual information of variables between n and $n+1$ time, the definition is:

$$I(\tau) = \sum_{n=1}^{N} p(x_n, x_{n+\tau}) \ln[p(x_n, x_{n+\tau})/p(x_n)p(x_{n+\tau})] \tag{1}$$

In the formula, $p(x_n)$, $p(x_{n+\tau})$ and $p(x_n, x_{n+\tau})$ are the probability. The function value of the time series $\{x_n\}$ is obtained. Draw the curve under the coordinate system of $I(\tau) - \tau$. The value of τ, which corresponding to the first minimum point, is the time delay.

The delay time τ of phase space reconstruction of three kinds of profile curves is calculated by formula (1) according to determine principles of delay time τ—the mutual information function method.

It can be seen from Fig. 2 the delay time τ of the phase space reconstruction is different with different profile curves.

Embedding dimension d is one of the important parameters of the phase space reconstruction. The improved false neighbour method which is proposed by Cao has no subjective parameters in determining the embedding dimension d. It is suitable the high-dimensional dynamic system and the small data quantity. The random signals can be distinguished and the signals can be determined. The principle is:

Suppose the time series is $\{x_n\} n = 1, 2, \ldots, N$, the delay time τ is determined by formula (1), and then a time vector is constructed, such as $X_i(d) = \{x_i, x_{i+\tau}, \ldots, x_{i+(d-1)\tau}\}\, i = 1, 2, \ldots, N - (d-1)\tau$. The d is embedding dimension. A quantity $\beta(i, d)$ is introduced refers to the false neighbour method, and to order:

$$\beta(i,d) = \frac{\left\|X_i(d+1) - X_{n(i,d)}(d+1)\right\|}{\left\|X_i(d) - X_{n(i,d)}(d)\right\|} \quad i = 1, 2, \ldots, N - d\tau \tag{2}$$

In formula (2) $\|X_k(d) - X_l(d)\| = \max\limits_{0 \le j \le m-1} \left\|x_{k+j\tau} - x_{l+j\tau}\right\|, n(i,d)$ is an integer, the size is $1 \le n(i,d) \le N - d\tau, X_{n(i,d)}(d)$, is the nearest point of $X_i(d)$ in the reconstruction d space.

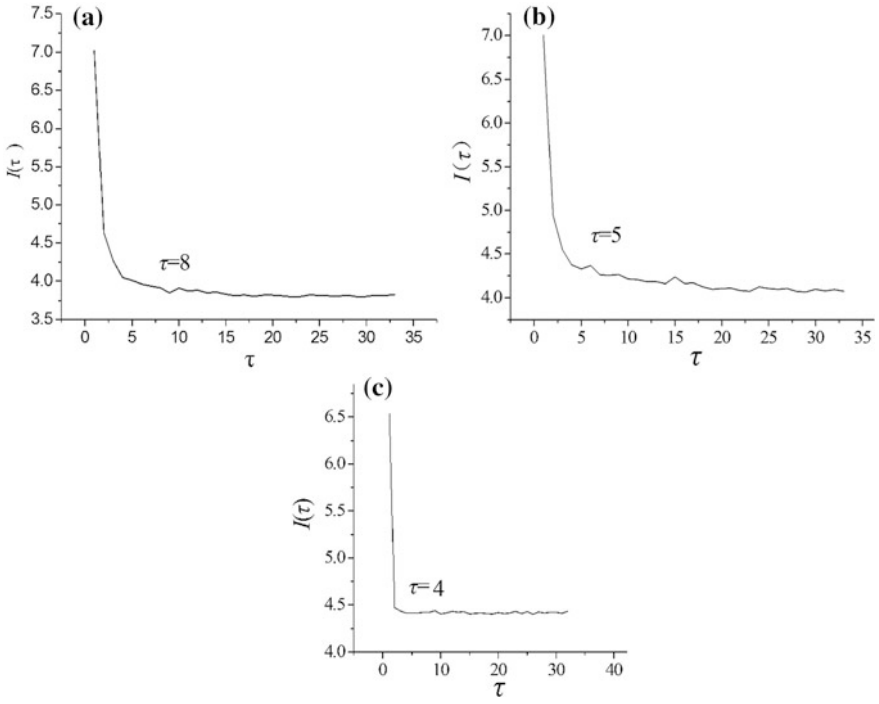

Fig. 2 Delay time τ of different profile curves

In order to avoid that different threshold of distance of two neighbor points have to select the different threshold of distance of two neighbor points, an average value of all parameters $n(i, d)$ is defined, it is:

$$E(d) = \frac{1}{N - d\tau} \sum_{i=1}^{N-d\tau} \beta(i.d) \tag{3}$$

It can be seen by formula (3), the function value $E(d)$ is only related to the embedded dimension d and the delay time τ, obviously, when the delay time τ is given, the function changes is changed only with the embedding dimension d, therefore $E_1(d)$ is defined:

$$E_1(d) = E(d+1)/E(d) \tag{4}$$

Draw the curve under $E_1(d) - d$ coordinate system; the $E_1(d)$ value does not change with the increase of d, the d corresponding to is the minimum embedding dimension.

The minimum embedding dimension d is determined according to the improved false neighbor method which is proposed by Cao. The minimum embedding

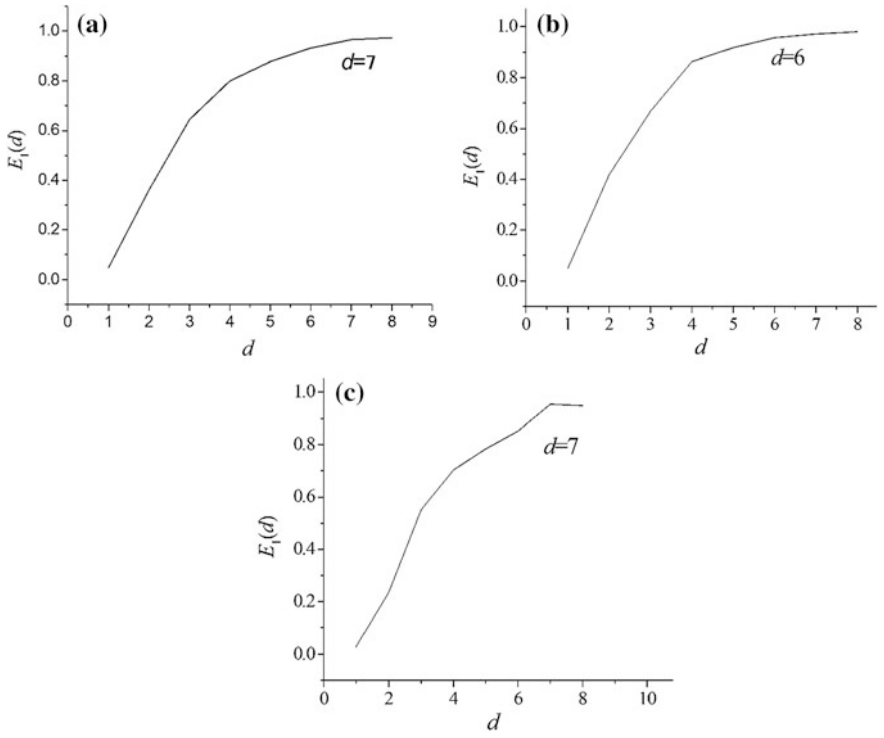

Fig. 3 The minimum embedding dimension of three profile curves

dimension of phase space reconstruction of three kinds of profile curves are calculated by formula (4). Figure 3 shows the minimum embedding dimension of three kinds of profile curves using the method of Cao.

It can be seen from Fig. 3, the embedding dimension of phase space reconstruction is different with different profile curves.

4 Calculating of Maximum Lyapunov Exponent of Profile Curves

A well-known and widely used method of computing the largest Lyapunov exponent, also known as direct method, is proposed by Wolf et al. [7]. Wolf algorithm is often used for experimental data analysis. And another direct method is proposed by Sato et al. [5], which is very similar to the Wolf algorithm; this algorithm is very simple in the calculation of a few parameters. At the logarithmic scale, the average doubling increases of adjacent track distance is studied by the prediction error, it is defined as follows:

$$p(k) = \frac{1}{Nt_s}\sum_{n=1}^{N}\log_2\left(\frac{\left\|X^{n+k} - X^{nn+k}\right\|}{\left\|X^{n} - X^{nn}\right\|}\right) \tag{5}$$

The curve is plotted under the $p(k) - k$ coordinates, and the slope of the straight part is the largest Lyapunov exponent.

Figure 4 shows the maximum Lyapunov exponent estimated by formula (5) for different profile curves.

Figure 4 shows the maximum Lyapunov exponent for different profile curves. It can be seen from Fig. 4, the maximum Lyapunov exponent is different with different profile curves.

The reciprocal of the largest Lyapunov exponent is defined as the quantitative index of the mark surface profile curve, the expression is:

$$f = 1/\lambda \tag{6}$$

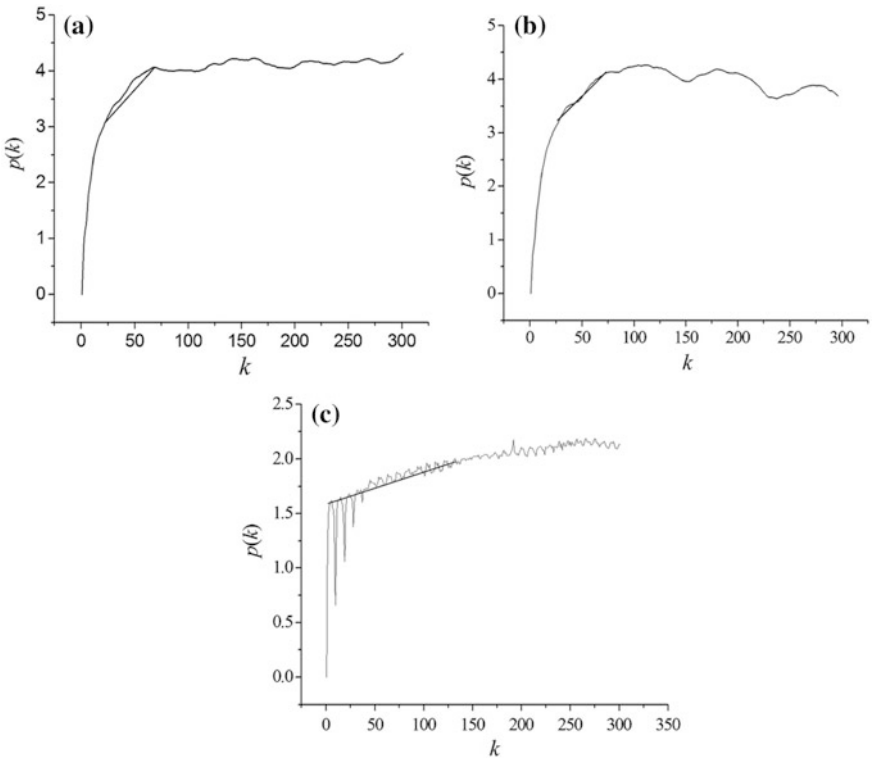

Fig. 4 the maximum Lyapunov exponent of different profile curves

Table 1 Calculating of largest Lyapunov exponent of different profile curves

	Sample a	Sample b	Sample c
Delay time	8	5	4
Embedding dimension	7	6	7
Maximum Lyapunov exponent	0.0280	0.0192	0.0031
Quantitative indexes	35.72	52.08	322.58

Formula (6) can be used to calculate the quantitative index of the trace surface, as shown in Table 1.

The maximum Lyapunov exponent and the quantitative index of different mark surface profile curves are shown in Table 1. It can be seen from the calculation results, the maximum Lyapunov exponents and the quantitative indexes are different with different profile curves.

5 Conclusions

The embedded dimension d and the delay time τ are two important parameters of phase space reconstruction. In order to make the reconstructed phase space fully reflect the chaotic characteristics of the system, these two parameters must be properly selected. It is also the prerequisite and basis for the accurate calculation of chaotic characteristic quantities such as such as maximum Lyapunov exponent. It can be seen that the embedding dimension and delay time are different with different profile curves according to the analysis of three kinds of profile curves.

The maximum Lyapunov exponent of three profile curves is calculated based on the appropriate selection of embedded dimension and delay time. The parameter can reflect the dynamic characteristics of the nonlinear system, and it can be used to analyze and identify the surface characteristics of shearing marks. The maximum Lyapunov exponent and the quantitative indexes are different with different surface of marks. It can be quantitatively marked surface topography characteristics.

Therefore, the maximum Lyapunov exponent and the quantitative indexes can be used to describe the characteristics of nonlinear system. It can be used to analyze and identify the surface characteristics of shearing marks. It provides a method to analyze the surface features of shearing marks.

Acknowledgements This work is supported by the Nature Science Fund of China (NSFC), No.: 61571307.

References

1. Lv J, Lu J, Chen S (2002) Analysis and application of chaotic time series. Wuhan University Press, China
2. Wang A, Yang C (2002) The calculation methods for the fractal characteristics of surface topography, China. Mech Eng 13(8):714–718 (in Chinese)
3. Wang A, Yang C (2001) Application of wavelet transform to evaluate the mechanical surface topography. Chin J Mech Eng 37(8):65–74 (in Chinese)
4. Cao LY (1977) Practical method for determining embedding dimension of a scalar time series. Physica D 110(5):43–50
5. Li YX, Gao MZ, Ma K (2014) Developments in calculation theory of fractal dimension of rough surface. Adv Math 41(4):P397–408 (in Chinese)
6. Wang BC, Wang ZY, Jing C (2015) Study on examination method of striation marks based on fractal theory. Appl Mech Mater 740:553–556
7. Su YW, Chen W, Zhu AB et al (2014) Contact and wear simulation fractal surfaces. J Xian Jiaotong Univ 47(7):P52–55 (in Chinese)

Design and Production of a 3D Printing Robot Hand with Three Underactuated Fingers

Licheng Wu, Tianyi Lan and Xiali Li

1 Introduction

Robot hand is an important part of the robot, most functions are achieved through hand operation. On one hand, Robot hand generally should have more joint freedom for a better and high anthropomorphic performance. On the other hand, in order to reduce the difficulty of control and the volume and weight of robot hand, it is necessary to minimize the number of drives. Designing robot finger with underactuated mechanism can drive these two requirements and allow robot finger to grasp objects with different shapes and sizes adaptively. At the same time, the underactuated robot finger has a lower control difficulty and production cost, and the feature of self-adaptive grasping is also suitable for envelope grasping and strong grasping [1], so the underactuated finger mechanism becomes an important aspect of the robot hand.

The tendon drive and the link drive are two main types of underactuated finger, but link drive is better than the tendon drive [2]. Paper [3] proposes a number of underactuated fingers based on link drive, which uses combination of the linear spring and the torsion spring to achieve a passive mechanical limit of the free joint. The link drive finger has many advantages such as large output force, strong load capacity, compact structure and so on.

At present, domestic and foreign research institutions have developed a number of link drive robot hands. For example, the SARAH underactuated hand (Fig. 1a) developed by the Canadian MD ROBOTICS company and the University of Laval has been successfully applied in the International Space Station [4, 5]; The underactuated robot hand designed by Nazarbayev University [6] (Fig. 1b); The MPJ hand developed by Tsinghua University and Beihang University in 2016

L. Wu (✉) · T. Lan · X. Li
Minzu University of China, Zhongguancun South Street 27,
Beijing 100081, China
e-mail: wulicheng@tsinghua.edu.cn

Z. Deng (ed.), *Proceedings of 2017 Chinese Intelligent Automation Conference*,
Lecture Notes in Electrical Engineering 458,
https://doi.org/10.1007/978-981-10-6445-6_10

(a) SARAH Hand (b) Nazarbayev University hand (c) MPJ Hand

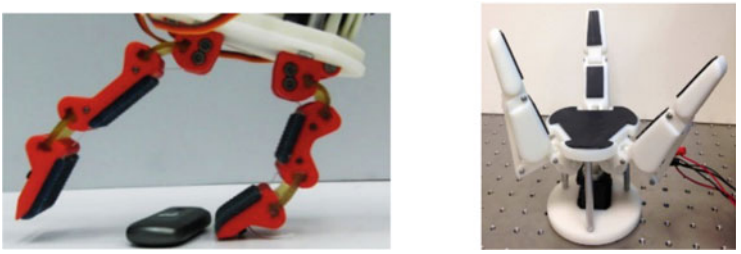

(d) Open Hand (e) National University of Singapore hand

Fig. 1 The robot hand of domestic and foreign institutions

(Fig. 1c) also uses the link drive mechanism [7]. But there also exists many problems such as complex institutions, large size, high cost of manufacturing and maintenance [3].

The cost of the prototype with machining is high, and it is not conducive to update the parts in design process. Producing parts by 3D printing not only greatly reduces the costs, but also increases the flexibility of the design, which is easy to update parts at any time. At present, more and more research institutions chose 3D printing to manufacture prototypes, such as Open Hand [8] designed by Yale University (Fig. 1d), The underactuated robot hand designed by Nazarbayev University (Fig. 1b) The robot hand designed by National University of Singapore [9] (Fig. 1e).

In this paper, we design a finger based on a new type of underactuated link mechanism proposed by the research group and a 3-finger hand with large grasping force, compact structure, simple mechanism and large grasping range. And the robot hand is produced by 3D printing in order to reduce cost. And we consider the characteristics of 3D printing in the design of parts, which can avoid adding supports for improving the accuracy of parts and saving cost. Finally we make grasping experiments to verify the rationality of the design.

2 Full Rotation Joint-Linkage Underactuated Finger and Its Improvement

The designed finger of this paper is a kind of full rotation joint-linkage underactuated finger proposed by research group [10, 11]. As shown in Fig. 2a, the finger mechanism consists of eight links and two springs. Link 1 is the base, Links 2, 6, 8 respectively represent phalanx 1, 2 and 3. Points A, B, C, D, D, E, F, G, H are rotational joints. Spring 1 is fixed between link 3 and link 4 while Spring 2 is fixed between link 5 and link 7. The motor is mounted on point B to drive link 3.

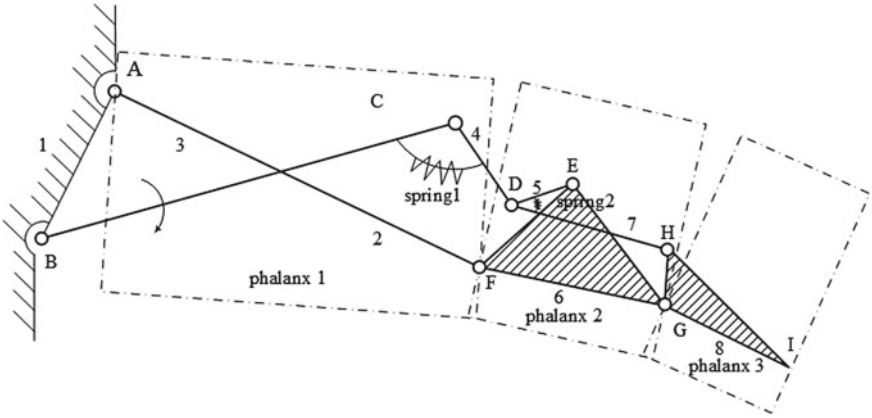

(a) Full rotation joint-linkage underactuated finger

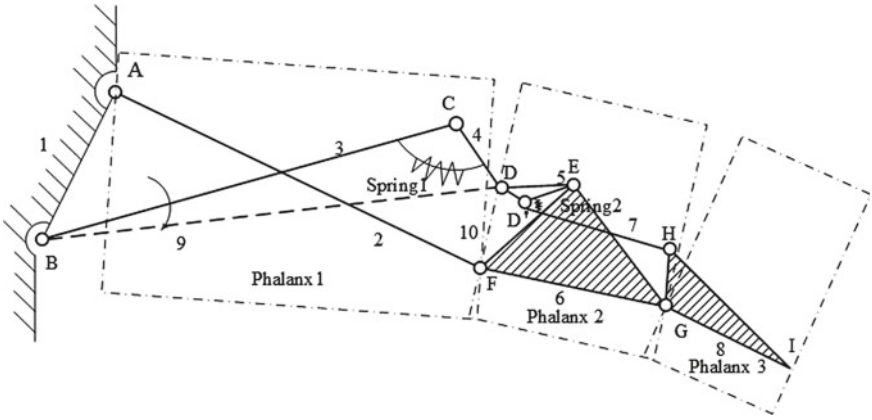

(b) Underactuated finger after improving

Fig. 2 Finger mechanism

It is found that CD link is easy to contact with the shaft that fixed DE link, which significantly reduces the grasping range of the finger. In order to avoid the situation, we change DE link from straight link to triangular link DD′E (Fig. 2b), and it can avoid above situation and allow links to remain inside during the movement.

3 Three Finger Robot Hand Design

3.1 Finger Design

In this paper, the hand can be divided into fingers and the palm. The main function of fingers is to grasp the object while the palm is to determine the distribution position of fingers. The size of fingers and each phalanxes are designed according to the ratio of 1:1 simulated by human index finger [12]. The sizes of each phalanxes are as shown in Table 1. We design the 3D model of finger (Fig. 3) according to the finger mechanism (Fig. 2b). Where A and B are fixed points, points E, F, G whose relative positions with the joints are fixed are connected with the phalanxes by the shaft.

The finger connecting link mechanism BCADE and ED′H are relatively independent by using the triangular link DD′E. As long as the relative position between E and second phalanxes is constant, the relative distance between points D and E does not affect the relative trajectory of the point D′ with the second phalanxes in motion, that is, the relative motion trajectory of point D′ and the second phalanxes is point E as the center of the circle, ED′ radius of the arc. In a similar way, the relative distance between points D′ and E does not affect the relative trajectory of point D with the first phalanxes in motion. So the use of triangular link DD′E not only can solve the problem if link mechanism can hide inside the fingers, but also increase the flexibility of finger design.

In order to ensure that the finger has underactuated characteristic, the elastic deformation of spring 2 should be in an increasing state during the motion when

Table 1 Size of phalanxes

Parts	Phalanx 1 (AF)	Phalanx 2 (FG)	Phalanx 3 (GI)
Length (mm)	47.0	22.0	25.0

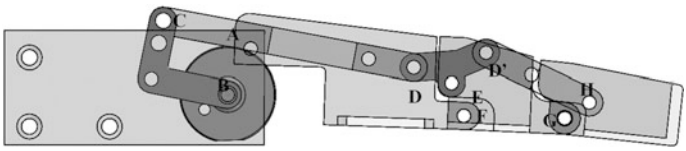

Fig. 3 Finger model

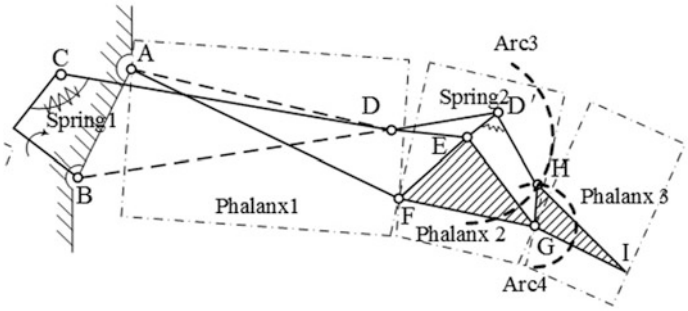

Fig. 4 The trajectory of point H

Table 2 Size of links

Parts	AB	BC	CD	D′E	DE	D′H	HG
Length (mm)	11.2	21.4	55.6	10.0	8.9	25.0	5

second phalanx contacts the object. The second phalanx will no longer move after it contacts object, and third phalanx continues to move, then the trajectory of point H (Fig. 4) should be G as the center, the initial distance of GH as radius. At the same time, the angle change between ED′ and D′H determines the elastic deformation of spring 2, and the elastic deformation of spring increases as ∠ED′H increases. ED′ and D′H are fixed in length, the greater the distance of EH, the greater the ∠ED′H. In the unconstrained state, the trajectory of H-point should be E as the center, the initial distance of EH as radius. In order to ensure that the distance EH is increasing during motion, the part of arc 4 should be on right side of arc 3 in order to keep EH growing during motion. The simulation results show that the size of link in Table 2 meets above conditions.

3.2 Grasping Simulation for Finger (Fig. 5)

In order to verify the design rationality and properties of the finger, we use Solidworks to simulate. We put 10 mm diameter cylindrical object in the root of fingers, where points 1, 2, 3 are contact points for phalanxes and object. It is simulated that the finger designed can achieve good motion coherence and stability grasping. And the finger can produce 5 times of hand grasping force by using the small electromotor which means the finger can produce a larger grasping force.

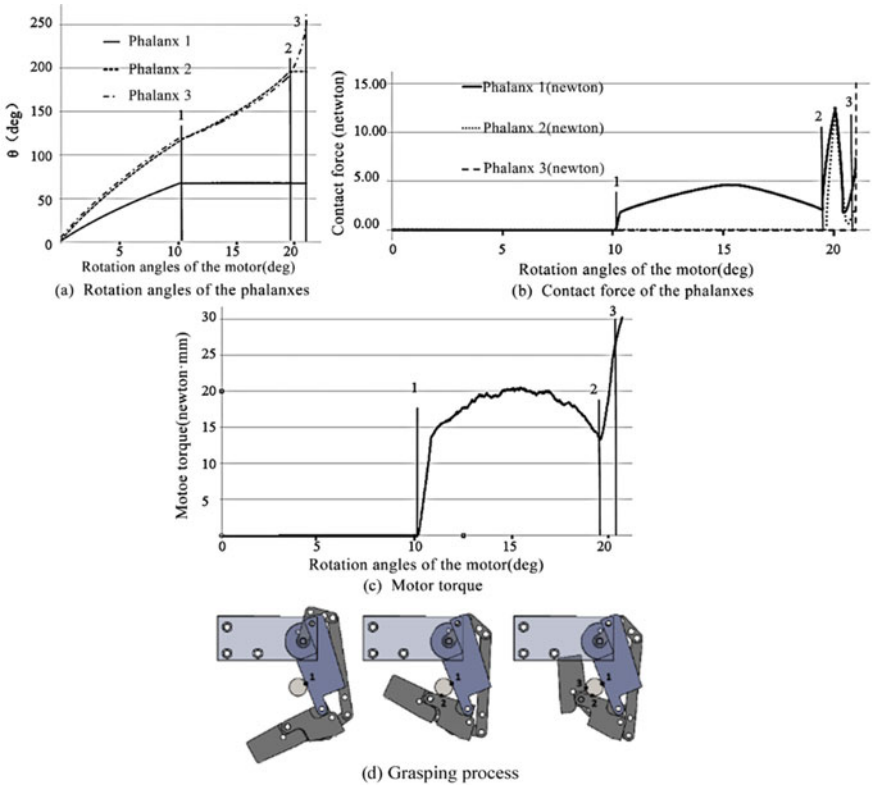

Fig. 5 Changing curve and process of grasping

3.3 Palm Design

In order to meet the needs of grasping, we design a robot palm which can change finger's Position, and a finger displacement device at the bottom of the palm, which can flexibly adjust the finger Position.

The robot hand consists of three fingers and a palm, we can see the palm design program in Fig. 6a. Finger 1 and 2 can be driven by a pair of gears to achieve the rotation and finger 3 position is fixed. As finger 1, 2 can be free to turn, the hand can achieve six kinds of main grasp mode combined with the main mode of human grasp (Fig. 6b). We can see 3D design of the robot hand in Fig. 7, the robot hand has 10° of freedom, 4 input drivers, each finger has a drive motor, while the palm is equipped with a dive motor which is placed in the bottom of the palm.

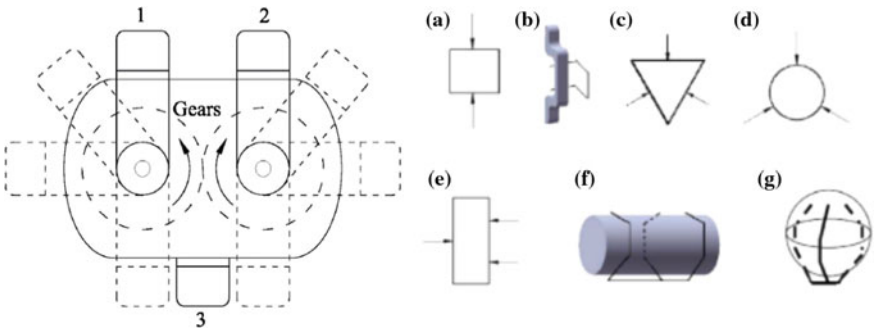

(a) Plam design (b) Main grasping mode

Fig. 6 Palm design and the main grasping mode

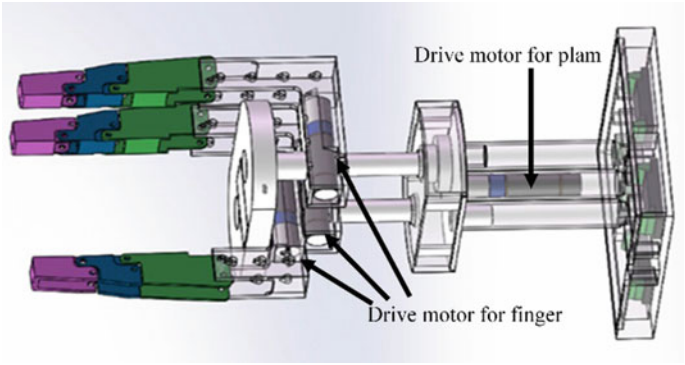

Fig. 7 Assembly diagram of robot hand

4 The Production of Robot Hand by 3D Printing and Experiments

In order to ensure the efficiency of the robot hand, some of the necessary gears still use standard machining metal gears to ensure the accuracy and strength, which can still reduce costs effectively. The parts of hand are produced by 3D printing except for gears, screws, optical axis and springs. We finally produce a higher accuracy prototype hand in this way, while the costs are significantly reduced.

The performances of robot hand on grasping different objects are shown in Fig. 8a–c are the performance respectively on grasping the larger (232 mm × 63 mm), medium (97 mm × 38 mm), small (81 mm × 19 mm) cylindrical objects; Fig. 8d is the performance on grasping the irregular columnar object; Fig. 8e, f are the performance on grasping the larger (Diameter 136 mm),

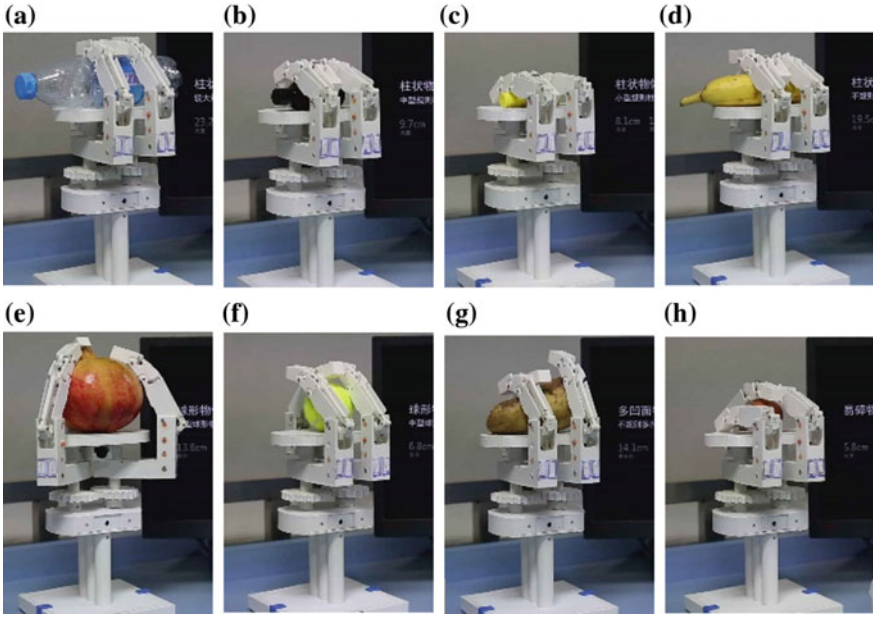

Fig. 8 The results about grasping different objects by robot hand

medium (Diameter 68 mm) spherical objects; Fig. 8g is the performance on grasping the Irregular multi-concave object; Fig. 8h is the performance on grasping the Fragile objects such as raw egg.

In order to verify the reliability of grasping, we make a greater rocking test after the grasping is completed. The results show that the robot hand can make a stable grasping (Experimental video can be seen in [13]). We also make the experiment for raw eggs (Fig. 8h), the results show that the robot hand can grasp raw egg stablely while make any damage to it, which means it has good underactuated characteristics, the mechanism is reasonable and parameters of springs are moderate.

5 Conclusion

In this paper, a kind of linkage underactuated mechanical finger is improved. The rationality of the size design is verified by simulation. The palm of a robot hand is designed, which can change the relative position between the fingers, increase the grasping range. And we design the parts of the hand by Solidworks, the design also meets 3D printing principles, which has advantages such as low cost, flexible design and so on. And we make experiments to verify the performance of the hand

produced by 3D printing. The results show that the robot hand can grasp the objects with different sizes stablely, and verify the rationality of the design and the feasibility of making robot hand by 3D printing.

Acknowledgements This work was funded by the National Nature Science Foundation of China projects No. 51375504 and 61602539.

References

1. Wu L, Yang G, Sun Z (2011) Review on underactuated finger mechanism. J Cent South Univ (Sci Technol) 42(1):417–422
2. Ceccarelli M (2004) Fundamentals of mechanics of robotic manipulation. Springer 241–298
3. Ceccarelli M, Tavolieri C, Lu Z (2006) Design considerations for underactuated grasp with a one D.O.F. anthropomorphic finger mechanism. In: Proceedings of IEEE/RSJ international conference on intelligent robots and systems, 2006, pp 1611–1616
4. Gosselin Clement M (2006) Adaptive robotic mechanical systems: a design paradigm. J Mech Des 128:192
5. Birglen L, Gosselin CM (2006) Geometric design of three-phalanx underactuated fingers. J Mech Des 128:356
6. Omarkulov N, Telegenov K, Zeinullin M, Begalinova A, Shintemirov A (2015) Design and analysis of an underactuated anthropomorphic finger for upper limb prosthetics. Eng Med Biol Soc 2474–2477
7. Luo C, Yang S, Zhang W, Ren Z, Liang J (2016) MPJ hand: a self-adaptive underactuated hand with flexible fingers of multiple passive joints. In: 2016 international conference on advanced robotics and mechatronics (ICARM), 2016
8. Dollar AM, Ma RR (2014) An underactuated hand for efficient finger-gaiting-based dexterous manipulation. In: Proceedings of the 2014 IEEE, international conference on robotics and biomimetics, 5–10 Dec 2014, pp 2214–2219
9. Telegenov K, Tlegenov Y, Shintemirov A (2015) A low-cost open-source 3-d-printed three-finger gripper platform for research and educational purposes. Access IEEE 3:638–647
10. Licheng Wu, Carbone Giuseppe, Ceccarelli Marco (2009) Designing an underactuated mechanism for a 1 active DOF finger operation. Mech Mach Theory 44(2):336–348
11. Wu L, Ceccarelli M (2009) A numerical simulation for design and operation of an underactuated finger mechanism for LARM hand. In: Mechanics based design of structures and machines, Jan 2009, pp 86–112
12. Huo S, Fan S, Zhao C (2009) Measurement of fingers' width and length of every segment in human. Progr Anat Sci 9(4):326–328 (in Chinese)
13. https://v.qq.com/x/page/s03552roa46.html

The Simulation of a Linkage Underactuated Finger on Grasping Performance

Licheng Wu, Tianyi Lan and Xiali Li

1 Introduction

The underactuated mechanical fingers who have little driver have some advantages such as simple structure, easy control and low manufacturing cost. And the underactuated mechanical fingers also have the good adaptive ability, which are good at enveloping grasp [1]. At present, the mainstream of the underactuated mechanical fingers are divided into two types, which are tendon drive and link drive. Linkage underactuated mechanical fingers have many advantages such as large output force, high load capacity, compact structure and so on. From the overall grasping effect, the performance of the link drive is better than the tendon drive [2]. At present, there are some literatures, such as paper [3], has a comprehensive simulated analysis on the grasping stability and mechanical properties of the tendon driven fingers in the process of grasping. Since the developing time is not longer, the analysis of the linkage underactuated fingers is still simple at present. Paper [4] only analyzed the contact force between the fingers and the objects, but the scope of the grab and others were not mentioned. Paper [5] which has added the stability of the fingers grab analysis, was not discussed the fingers stable grasping scope. Paper [6] estimated the fingers' stable grasping scope, but did not analyze the relationship between grasping force and output torque. The overall analyses of linkage underactuated finger are important to test all aspects of the finger grasping performance and the finger design rationality, so it is necessary to proceed a comprehensive simulated analysis.

This paper simulates a linkage underactuated finger and analyzes the underactuated properties in the grasping process, motion coherence, mechanical property and so on, and the links whether inside the fingers in the process of the whole movement or not. And the paper also makes the quantitative analysis of the

L. Wu (✉) · T. Lan · X. Li
Minzu University of China, Zhongguancun South Street 27, Beijing 100081, China
e-mail: wulicheng@tsinghua.edu.cn

Z. Deng (ed.), *Proceedings of 2017 Chinese Intelligent Automation Conference*,
Lecture Notes in Electrical Engineering 458,
https://doi.org/10.1007/978-981-10-6445-6_11

grasping scope and performance, so as to test the performance and rationality of the designed finger.

2 Full Rotation Joint-Linkage Underactuated Finger

The simulated finger of this paper is a kind of full rotation joint-linkage underactuated finger proposed by research group [7, 8]. In Fig. 1, the finger mechanism consists of eight links and two springs. Link 1 is the base, Links 2, 6, 8 respectively represent phalanx 1, phalanx 2 and phalanx 3. Points A, B, C, D, D, E, F, G, H are rotational joints. Spring 1 is fixed between link 3 and link 4 while Spring 2 is fixed between link 5 and link 7. The motor is mounted on the point B to drive link 3. Link DD'E uses a triangular structure (referenced in Fig. 2) to connect link DH and CD. The size of the overall finger and each phalanx are designed according to the ratio of 1:1 simulated by human index finger [9]. The designed sizes of each link bar and the phalanxes are as shown in Table 1.

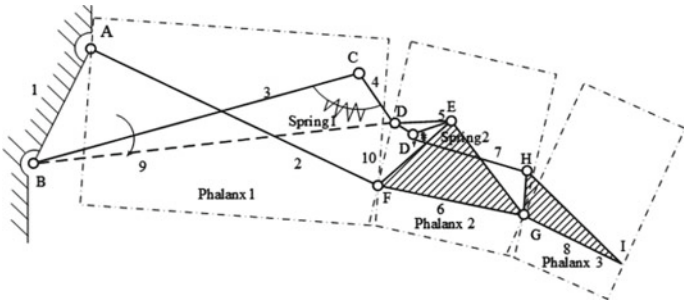

Fig. 1 The mechanism of full rotation joint-linkage underactuated finger

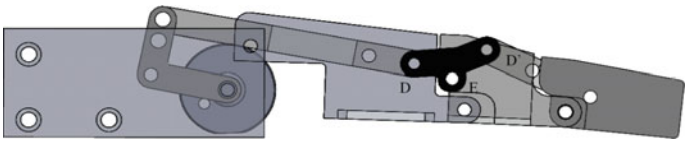

Fig. 2 Finger diagram and the position of link DD'E (Pureblack link)

Table 1 The size of link and phalanx

Part	AB	BC	CD	D'E	DE	D'H	HG	(AF)	(FG)	(GI)
Length (mm)	11.2	21.4	55.6	10.0	8.9	25.0	5.0	47.0	22.0	25.0

3 The Process and Results of Simulation

3.1 Settings of Simulation Parameter

The 3D model of finger is created by SolidWorks, and all parts of grasp are analyzed by the MOTION module. This paper simulates the process of grasping a variety of objects of different radius, which can be used to determine the radius of objects in grasping process. At the same time, the paper simulates grasping process of two different radius cylinders, and analyzes their changing curve of phalanx angle in each grasping process, torque motor and contact force.

Because the movement of the finger during the motion simulation is slow, the inertial force is not considered. And this paper only concerns the contact force between the finger and objects, and ignores the friction between joints. In order to make the movement of the finger easier to observe, the rotational speed of the driving link (BC) is taken as 1 rad/s in all the simulations in this paper.

It is estimated that the elastic coefficient of spring 1 is 2.00 N/mm and the damping coefficient is 10.00 N/(mm/s); the elastic coefficient of spring 2 is 1.00 N/mm and the damping coefficients 0.20 N/(mm/s). Finger can move stablely under this parameter. The recovery coefficient between the finger and object is set to 0, which means the contact between finger and object is the completely inelastic collision.

3.2 Grasping Performance of Finger on Different Size Objects

This paper stimulates grasping process of smaller object and bigger object. The finger has good envelope grasping performance on the object whose diameter equals to 0.106 times (i.e. 10 mm) of the finger length (excluding the base). And the finger can grasp the object whose diameter equals to 0.851 times (i.e. 80 mm) of the finger length (excluding the base) effectively.

In the following, the grasping process of these two kinds of cylinders in different position is emphatically simulated. And this paper uses the analysis of the coherence, grasping force changing curve, final grasping force, the relationship between grasping force of the finger and the motor output torque to analyze and verify the performance of the finger.

3.3 Grasping Performance of Finger on Smaller Object

In Fig. 3, the Cartesian coordinate is established with point B as the origin, and the horizontal extension direction of the finger is X axis. The simulation is divided into

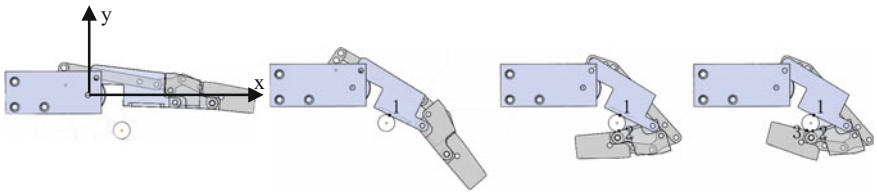

Fig. 3 Grasping process of cylinder with a diameter of 10 mm at the easy grasping position

two situations, one is that the object locates in easy grasping position, another named limit position is that the object locates in difficult grasping position. The easy grasping position is that phalanx 1 near the middle of the phalanx bottom, and in the position where the finger can touch the object by rotating small angle. Limit position refers to the position where the object is in the phalanx root.

3.3.1 Grasping Performance of Finger on Smaller Object at Easy Grasping Position

The object grasped is a rigid cylinder with a diameter of 10 mm, and the coordinate of the center of the circle is in the easy grasping position at (19.98–20.90 mm). Grasping process are as shown in Fig. 3, and point 1, 2, 3 are the contact points between phalanxes and object.

In Fig. 3, the finger envelops the object by contacting with the object gradually. In Fig. 4a, the final rotation angles of phalanxes 1, 2, 3 are 26.51°, 162.01° and 194.5°. Point 1, 2, 3 refered in Fig. 6 are the contact points between phalanxes and object. The contact points between each phalanx and object constitute a static grasping of the object. It can be seen that phalanxes have no abrupt change of angular displacement during the grasping process, and the finger movement is stable. As the result, the finger shows good motion coherence and stability in the simulation.

In Fig. 4b, when phalanx 1 touches the object, the contact force between phalanx 1 and object increases rapidly, and then increases gradually, at which point the other phalanxes do not contact with the cylinder. When the phalanx 2 contacts the object, the contact force between phalanx 2 and object increases rapidly. When phalanx 3 contacts the object, the contact force between phalanx 3 and object increases as the motor torque increases. The motor torque is not setted while the rotational speed of the drive is setted in the simulation process. Therefore the motor torque is constantly changing while keeping the rotational speed of the drive is 1 rad/s. After the completion of the grasp, if the motor torque continues to increase to 29.00 N mm, the grasp will complete with the contact force of phalanxes are 4.80, 1.61 and 4.89 N. During the grasping process, the contact force of phalanx 1 in the individual contact with the object increases first and then decreases because of the displacement of spring 1 increases in this process and a portion of the energy is

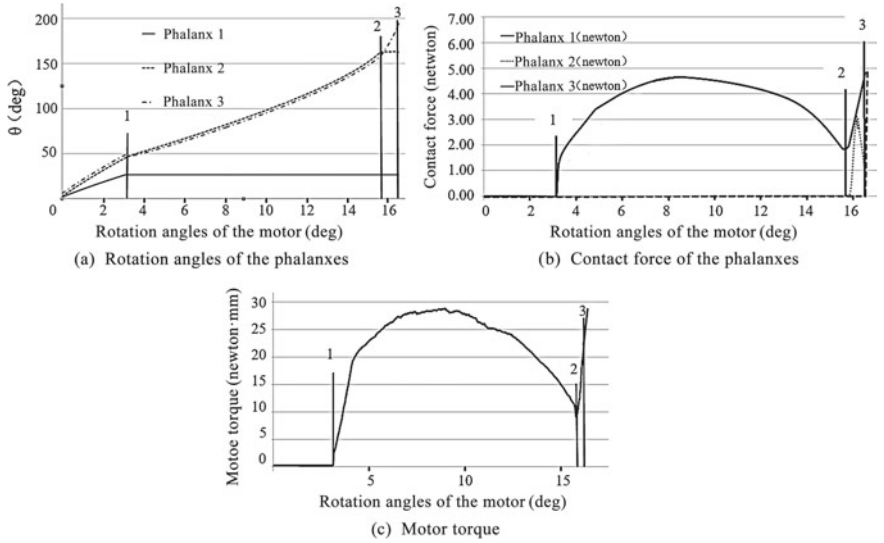

Fig. 4 Changing curve of cylinder with a diameter of 10 mm at easy grasping position

stored in spring 1. The contact force of phalanx 1 increases rapidly after phalanx 2 contacts object because phalanx 1, 2 are distributed on both sides of the object which amounts to opposite side clamping state. The contact force of the phalanx 2 first increases and then decreases, because the spring 2 stores part of the energy during the movement.

In Fig. 4c, since the mass of the finger is not considered, the initial motor torque is 0, and the motor torque increases as the finger contacts object. Phalanx 2 contacts object at position 2, and then the motor torque rises until phalanx 3 touches the object. Generally small DC micro-motor output torque is about 3000 N mm. If the maximum output torque is used, the force of the finger on the object can be about 500 N while general adult male finger force is about 100 N [10], and the Tendon-drive finger force is about 50 N [4, 11]. Therefore the finger can generate a large grasp force.

3.3.2 Grasping Performance of Finger on Smaller Object at Limit Position

The object grasped is a rigid cylinder with a diameter of 10 mm, and the coordinate of the circle center (The coordinate system is the same as Fig. 3) is in the easy grasping position at (−2.88, −26.17 mm). The finger envelops the object by contacting with the object gradually. The final rotation angles of phalanxes are 67.83°, 196.24° and 264.50°. It can be seen that phalanxes have no abrupt change during the grasping process. So it shows a good motion coherence and stability in simulation.

When phalanx 1 touches the object, the contact force between phalanx 1 and object increases rapidly, and then increases gradually, at which point other phalanxes do not contact with the cylinder. When phalanx 2 contacts object, the contact force between phalanx 2 and object increases rapidly. When phalanx 3 contacts object, the contact force between phalanx 3 and object increases as the motor torque increases. After the completion of the grasping, if the motor torque continues to increase to 30.40 N mm, the grasp will complete with the contact force of the phalanxes are 7.50, 2.17 and 15.00 N.

3.4 Grasping Performance of Finger on Bigger Object

Because the cylinder with a diameter of 80 mm is large relative to the finger, the position of cylinder has little effect on grasping effect, so this paper simulates only one position of the cylinder with a diameter of 80 mm.

The coordinate of the center of the circle (The coordinate system is the same as Fig. 3) is in the position at (58.98, −50.11 mm), where the finger can touch the object by rotating small angle, and the first contact point is on phalanx 1. Grasping process are as shown in Fig. 6, and points 1, 2, 3 are the contact points.

In Fig. 5a, the final rotation angles of phalanxes are 8.60°, 38.72° and 64.52°. In Fig. 5b, if the motor torque continues to increase to 8.87 N mm, the contact force will complete on 0.10, 0.16 and 1.08 N. The contact force between phalanx 1 and

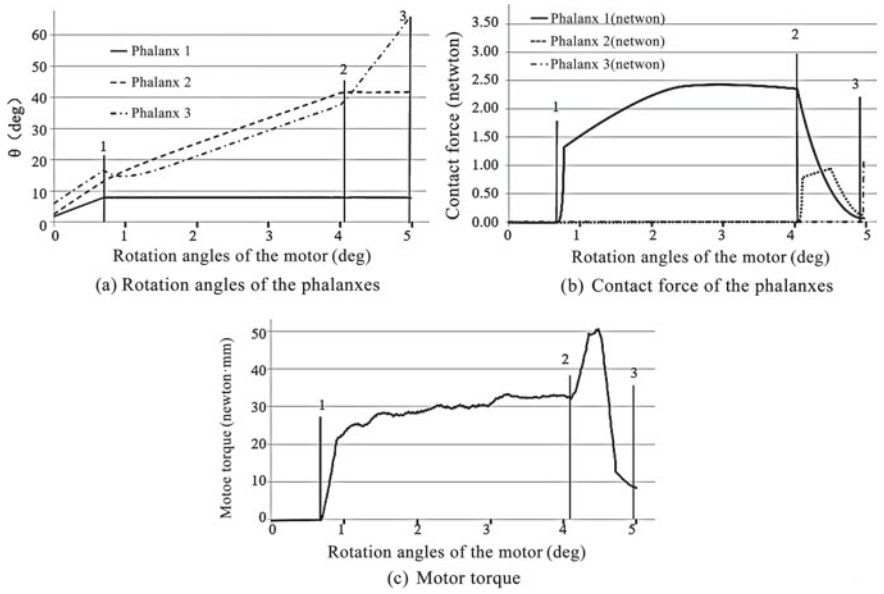

Fig. 5 Changing curve of cylinder with a diameter of 80 mm

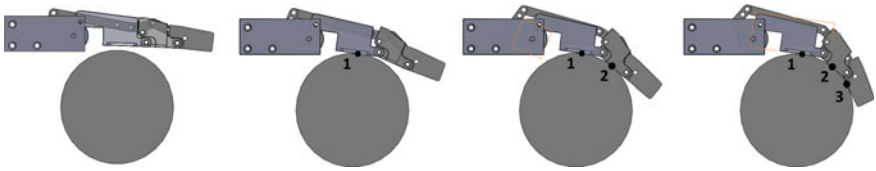

Fig. 6 Grasping process of cylinder with a diameter of 80 mm

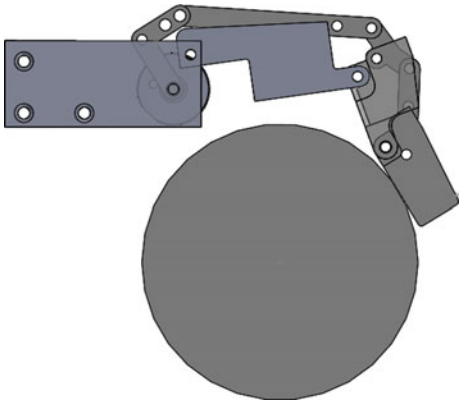

Fig. 7 Roll-back phenomenon

object after phalanx 2 contacts object becomes small because spring 1 stores a part of the energy, and the contact force between phalanx 2 and object becomes smaller when phalanx 3 contacts object because spring 2 stores a part of the energy (Fig. 6).

The motor torque continues to rise after phalanx 2 contacts the object until phalanx 3 contacts the object. However, the motor torque drops when phalanx 3 contacts the object. The reason is that the object relative to the finger is bigger, which triggers Roll-back phenomenon [12] as the root phalanx tends to separate from the object in the case of increasing the grasp force. In Fig. 7, if the rotation is continued, the phalanx will separate from the object.

4 Conclusion

This paper uses Solidworks to simulate the grasp operation of the finger with different situation, which can be used to analyze the range of the grasping, the underactuated characteristic, the coherence of motion and the mechanical property. It is simulated that the finger designed by the mechanism according to Fig. 1 can achieve good motion coherence and stability grasping. The finger can make suitable capability for grasping the cylinders whose diameter can vary from 0.106 to 0.851 respecting to finger length which means it has a large grasping range. And it can produce 5 times of hand grasping force by using small electromotor which means it

can produce a larger grasping force. In Figs. 3 and 6, links are maintained within the phalanxes in grasping process which means the finger has a compact structure in whole process. The rationality of design is validated through the simulation. And the important data of finger such as grasping range and grasping force are obtained.

Acknowledgements This work was funded by the National Nature Science Foundation of China projects No. 51375504 and 61602539.

References

1. Wu L, Yang G, Sun Z (2011) Review on underactuated finger mechanism. J Cent South Univ (SciTechnol) 42(1):417–422
2. Ceccarelli M (2004) Fundamentals of mechanics of robotic manipulation. Springer, Berlin, pp 241–298
3. Liu Y, Feng F, Gao Y (2014) HIT prosthetic hand based on tendon-driven mechanism. J Cent South Univ 21(5):1778–1791
4. Petković D, Iqbal J, Shamshirband S, Gani A (2014) Kinetostatic analysis of passively adaptive robotic finger with distributed compliance. Advances in Mechanical Engineering 6:145648
5. Wang T, Yin J (2016) A type of underactuated finger mechanism design and statics analysis for picking fruit. J Agric Mechanization Res 112–114 (in Chinese)
6. Luo M, Mei T, Wang X, Yu Y (2004) Grasp characteristics of an underactuated robothand. In: Proceedings of the 2004 IEEE international conference on robotics and automation, New Orleans, LA, April 2004, pp 2236–2241
7. Wu L, Carbone G, Ceccarelli M (2009) Designing an underactuated mechanism for a 1 active DOF finger operation. Mech Mach Theor 44(2):336–348
8. Wu L, Ceccarelli M (2009) A numerical simulation for design and operation of an underactuated finger mechanism for LARM hand. Mech Based Des Struct Mach 37(1):86–112
9. Huo S, Fan S, Zhao C (2009) Measurement of fingers' width and length of every segment in human. Prog Anat Sci 9(4) (in Chinese)
10. Jiang Z, Wang S, Liao J, Liu H, Li X (2010) Test of grip and pinch strengths of 111 healthy university students in Fujian Province. J Clin Rehabilitative Tissue Eng Res 14(50):9452–9456
11. He Y (2014) Research on one underactuated three-finger dexterous hand driven by tendon. HarbinInstitute of Technology, Harbin (in Chinese)
12. Birglen L, Gosselin C (2004) kinetostatic analysis of underactuated fingers. IEEE Trans Robot Autom 20(2):211–221

EnhanEigen: A New Comprehensive Trust Model for Peer-to-Peer Network

Xiali Li, Qiao Gao, Licheng Wu, Xun Sun and Songting Deng

1 Introduction

Different from the client/server model, peer-to-peer network has no central server and the peers are equally privileged, equipotent participants in the application. Peers share some resources such as processing power, disk storage or network bandwidth. Each peer can act as both server and client. It can request the service or respond to some requesting some resource [1–4].

Peer-to-peer networks have proven to be an effective way of sharing data and have been used in large scale file sharing system (Napster, Kazaa, Gnutella, eMule) [5], ecommerce [6, 7], instant messaging systems [8], distinct picture archiving and communication system (PACS) archives [9], cloud service selection [10, 11] and so on. Because of the open, anonymous nature of peer-to-peer network and their current level of popularity, users are increasingly concerned about defending attacks and threatens from malicious peers [12]. The notion trust is derived from psychology and sociology [13] and defined as a subjective expectation an entity has about another's future behavior [14, 15]. In trust model, peers gather information about other peers by using their network [16].

The trust model in eBay system is typically centralized structured and use central server to store and manage all user feedback scores and worthiness of the peers [17]. It is successful global reputation model. However, peers will not have any centralized authority to manage distribute reputation information. PeerTrust [18] is a coherent adaptive trust model based on a transaction-based feedback system. EigenTrust [19] proposed an algorithm which used global trust value to decrease inauthentic files downloading in peer-to-peer file sharing network. EigenTrust significantly decrease the number of unauthentic files on the network and can

X. Li · Q. Gao · L. Wu (✉) · X. Sun · S. Deng
Minzu University of China, Beijing 100081, China
e-mail: wulicheng@tsinghua.edu.cn

Z. Deng (ed.), *Proceedings of 2017 Chinese Intelligent Automation Conference*,
Lecture Notes in Electrical Engineering 458,
https://doi.org/10.1007/978-981-10-6445-6_12

identify malicious peers. PowerTrust [20] used a trust overlay network to model the trust and generate the global trust value on the base of considering the power-law distribution of peer feedbacks. GossipTrust [21] is the extension of PowerTrust, proposed a gossip-based reputation system to aggregate global trust scores fast.

2 EnhanEigen Model

In the EnhanEigen trust model, each node stores the local trust values of all the other nodes of the entire network. After every transaction, the global trust value of the nodes will be updated by iterative calculation. We put forward two new parameters *MP* and *FCP* for each node to serve as the new evaluation criterion on judging the feedbacks. The comprehensive trust value is aggregated by the local trust value, global trust value, *MP* and *FCP*.

2.1 Local Trust Value

When two nodes in the network finish one transaction, we assume peer *i* downloads file *f* from peer *j*. The model asks the requiring party to evaluate the serving party's service. Each node in the network saves the local trust value for all other nodes in the entire net. The local trust value s_{ij} is calculated by the following equation

$$s_{ij} = sat(i,j) - unsat(i,j) \tag{2.1}$$

where *sat*(*i, j*) is the number of the times *i* feels satisfied with *j* in all the transactions, and *unsat*(*i, j*) is the number of the times *i* feels unsatisfied with *j* in all the transactions. If *i* offers satisfied evaluation on *j*, then add 1 to *sat*(*i, j*); otherwise add 1 to *unsat*(*i, j*).

To avoid malicious peers from giving higher value than the authenticity to the malicious peers, or giving lower value than the authenticity to the good peers, we make the local trust value normalization by the following equation

$$c_{ij} = \max((s_{ij}), 0) \Big/ \sum_{j} \max((s_{ij}), 0) \tag{2.2}$$

where c_{ij} is the normalized local trust value.

2.2 Global Trust Value

If peer i needs to know peer k's global trust value, it will firstly get peer k's credibility from all the nodes which transact with peer k directly, then combine the

credibility with these nodes' own local credibility (from i's perspective) to finally work out k's global trust value t_{ik}. If we use matrix to represent it, we can get the following

$$\overrightarrow{t} = c^T \cdot \overrightarrow{c_i} \tag{2.3}$$

where c represents the matrix in which the element is $c(ij)$, c^T is the vector of the global trust value t_{ik}.

If peer i get peer k's global trust value by n times transitive inquiring its friends, we can get the global trust value by the following equation

$$\vec{t} = (c^T)^n \vec{c}_i \tag{2.4}$$

Introduce the pre-trusted peers, which never harm the network and has the preset trust value, then the global trust value is calculated by the following question

$$\vec{t}^{k+1} = a(c^T)\vec{t}^{k} + (1-a)\vec{p} \tag{2.5}$$

where a is a constant that is between 0 and 1, $\vec{p}$ is the vector of pre-trusted value.

2.3 Malicious Percent (MP) and Feedback Consistency Percent (FCP)

EnhanEigen model uses the local trust value and global trust value concept of EigenTrust model. Apart from the global trust value, we introduce two parameters Malicious Percent (*MP*) and Feedback Consistency Percent (*FCP*) to help evaluate the trust value of one peer and filter the malicious and cheating peers in the network. The meaning of (*MP*) and (*FCP*) is illustrated in the following.

MP is the probability at which node i provides malicious service

$$MP_i = M_i / Tran_i \tag{2.6}$$

where M_i is the number of node i providing malicious services and $Tran_i$ is the number of node i providing all services.

FCP is defined as the following

$$FCP_i = Con_i / Recv_i \tag{2.7}$$

where $Recv_i$ is the number of i playing the roles of requiring peer.

2.4 Comprehensive Trust

Supposing node i finally select node j as its download source and successfully finishes file downloading in peer-to-peer file sharing network, now node i should offer its assessment to node j. The comprehensive trust value F_i are calculated by the following

$$F_i = \alpha t_i + \beta FCP_i - \gamma MP_i \tag{2.8}$$

where t_i is the global trust value of node i, FCP_i is feedback consistency rate of node i, MP_i is the probability at which node i provides malicious service. α, β, γ satisfies that α plus β plus γ equals 1.

Analyze the comprehensive trust value of good nodes, feedback cheating nodes and malicious slandering nodes respectively. Results are showed in the Table 1.

2.5 Resistance on the Malicious and Feedback Cheating Peers

In the peer-to-peer file sharing network, the following cooperative cheating behaviors may exist. Feedback cheating nodes (or malicious nodes) slander good nodes, feedback cheating nodes raise malicious nodes (or vice versa), feedback cheating nodes raise themselves, malicious nodes raise themselves. The model proposed in this paper make strict judgment both on the raising behavior from cooperative cheating nodes and slandering behavior on good nodes, which can dramatically reduce the possibility to succeed in feedback-cheating.

2.6 Enhanced Probabilistic Peer Selection Algorithm

Malicious nodes offers malicious service, such as uploading untrue files. Supposing node i requires to download file f, it finally receives a responding node set S. Accordingly, let G be the set of the global trust value of these n nodes, g_i is the global trust value of node i. Then we divide set G into two subset A and B.

The Enhanced Probabilistic Peer Selection Algorithm is described in the following.

Table 1 Comprehensive trust values of three kinds of nodes

	FCP	MP	F
G peers	High	Low	High
FC peers	Low	Low	Relatively high
MM peers	Low	Low	Relatively high

if $t_i = 0$, then we get the following set T

$$T = \{t_i \,|t_i \subseteq B \cap MP_i \leq \varnothing \cap \varnothing \; is \; a \; \text{constant}\} \tag{2.9}$$

We choose t_i as the download source at the probability of 10%.

If $t_i \neq 0$, then we choose the node i from set A as the download source at the probability p

$$p = g_i \Big/ \sum_{j=1}^{A} g_i \tag{2.10}$$

This model adds MP to help assess the peer trust. There are two kinds of peers whose global trust value can be 0. One is that who offer malicious service and the other is the new adding peers in the net. EigenTrust choosing 10% of these nodes is to help new nodes establish their global trust value. At the same time 10% of these peers can maintain the balance between malicious peers and new entry peers. This can prevent malicious peers from getting big chance to upload false files.

3 Experiment and Analysis

We use java programming language to implement a peer-to-peer file sharing system in which EigenTrust model and EnhanEigen model are both used. To validate the performance of resisting cooperative-cheating, we divide experiment into two parts, one part is for MM peers and the other part is for FC peers. The parameters of the trust model are set as Table 2. To prevent the possible impacts on the simulation results for unreasonable files allocation, each file at least is owned by one good peer and each node has the same probability of requiring download files.

Each experiment is performed in the condition of 10 different distribution of files. In each distributing environment the model will loop 10 times. Thus each experiments finish 100 times files sharing. The reason that MP takes $\phi = 0.1$ as its threshold value is that type G nodes also have the probability (<10%) of offering malicious files, $\phi = 0.1$ is proper.

Table 2 Value of different parameters

	Total nodes	Total files	Total transactions	Preset trust nodes	MP thresh	α	β	γ
Value	50	300	10,000	5	0.1	0.2	0.5	0.3

3.1 MM Peers Experiments

In this experiment, we compared the performance of EnhanEigen and EigenTrust model from successful transactions ratio, algorithm execution time and false feedbacks adopted by the network at different malicious and slandering nodes percentage of the total nodes.

Figure 1 shows that EnhanEigen model performs better in defense against attacks from type MM than EigenTrust model. For EigenTrust model, at each percentage of MM nodes interval [0.1, 0.3], [0.3, 0.5], [0.5, 0.7], [0.7, 0.9], the success ratio curve has a slope approximately. But for EnhanEigen, the curve has only a little change. Even when MM nodes account for 90% of all the nodes in the net, the successful ratio is still near 90%. Figure 2 shows that the algorithm execution time at different malicious and slandering nodes ratio of the two models. For the two models, there are a inflection point (about at 50%) of the percentage of malicious and slandering peers. Figure 3 show false feedback adopted by network at different proportion of MM nodes. When MM nodes accounts for less than 50%, the EnhanEigen model can't influence the net hardly.

3.2 FC Peers Experiments

For cooperative cheating experiment, each time MP nodes and FC nodes account for half of all malicious nodes. Namely, each time we will let equivalent FC nodes raise MP nodes and slander other G nodes.

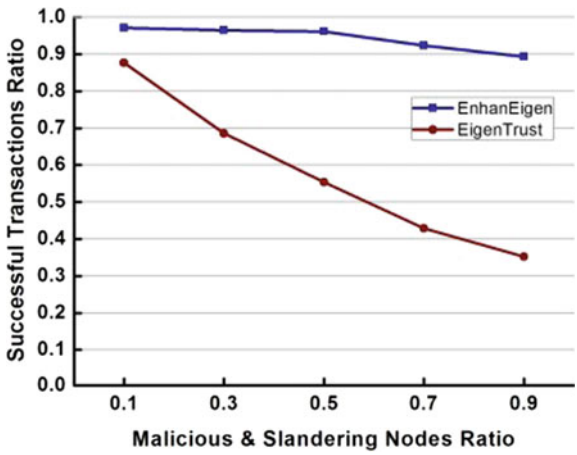

Fig. 1 Successful transactions ratio in different MM ratio

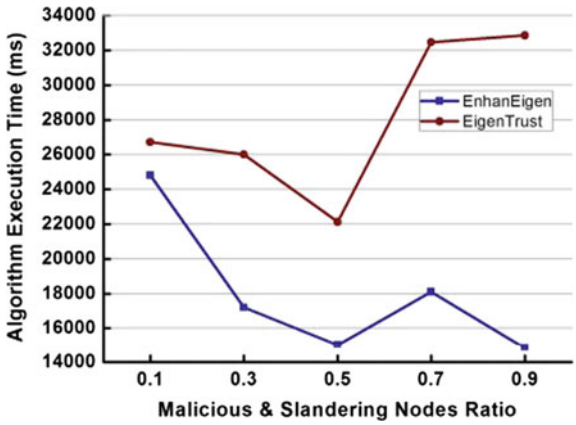

Fig. 2 Algorithm execution time at different MM peers

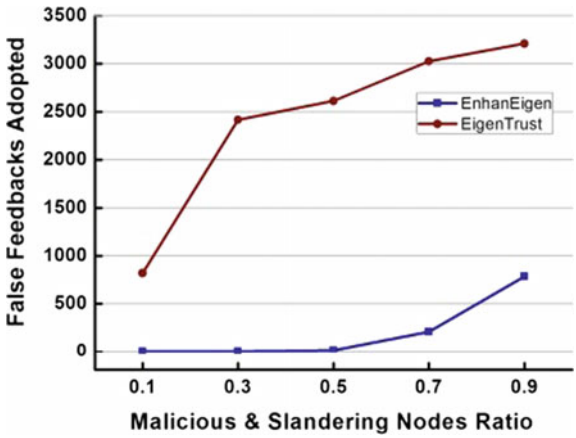

Fig. 3 False feedbacks adopted at different MM peers ratio

Figure 4 show that the two models have the inflection point at about 70 proportion of the cooperative cheating nodes. Before this point, the two curves are slopping and the EnhanEigen model slopes gently. After the point, the two curves all rise. It is obviously that EnhanEigen model plays better than Eigen Trust in defense against cooperative cheating. Figure 5 shows the algorithm execution time contrast between the two models. EnhanEigen model does not have obvious advantages on the algorithm execution time at different cooperative cheating peers. Figure 6 show false feedback adopted by network at different proportion of cooperative cheating nodes. EnhanEigen model adopted much fewer false feedbacks than EigenTrust.

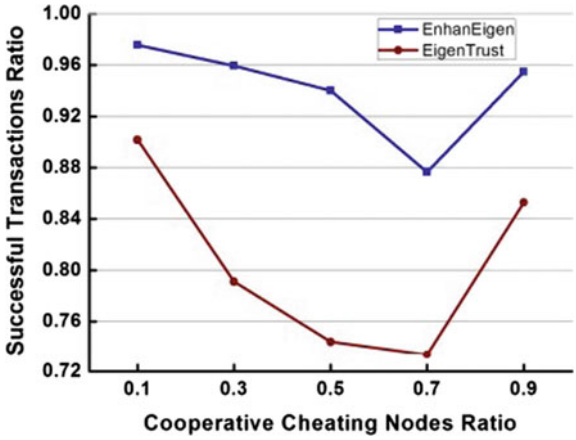

Fig. 4 Successful transactions ratio at different FC peers ratio

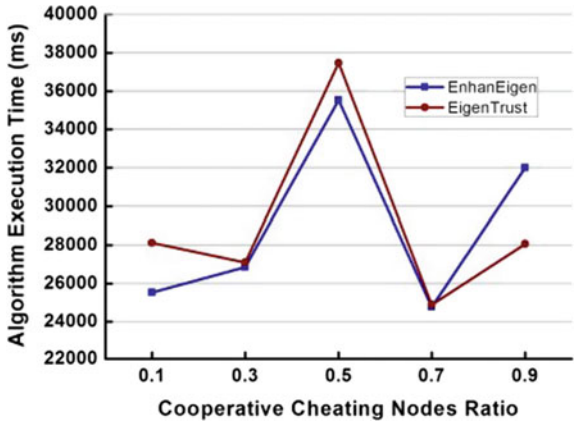

Fig. 5 Algorithm execution time at different FC peers ratio

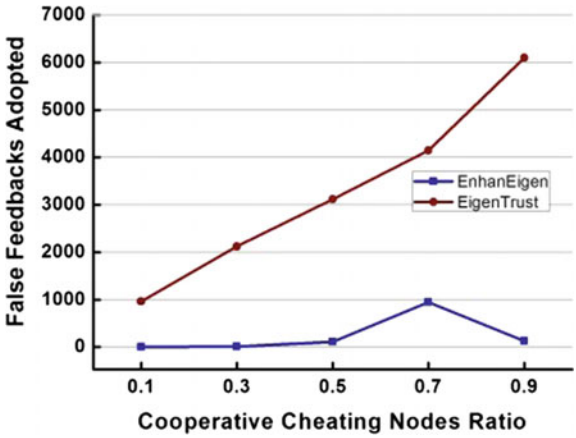

Fig. 6 False feedbacks adopted at different FC peers ratio

4 Conclusion

EnhanEigen trust model propose comprehensive trust value and enhanced probabilistic peer selection algorithm to overcome the shortages that previous trust models can't effectively judge the feedback authenticity and resist cooperative feedback cheating peers. This comprehensive trust is aggregated by local trust value, global trust value, Malicious Percent (MP) and Feedback Consistency Percent (FCP). *MP* and *FCP* are used to filter the malicious peers when selecting peers providing service. Experiments validate that new trust model can distinguish and judge the authenticity of feedbacks, resist the cooperative attacks from malicious peers and feedback cheating peers effectively.

Acknowledgements This paper is supported by the National Science Foundation (Granted number is 61602539 and 51375504).

References

1. Yang M, Yang Y (2014) Applying network coding to peer-to-peer file sharing. IEEE Trans Comput 63(8):1938–1950
2. Dharanipragada J, Chennai J, Haridas H (2012) Stabilizing peer-to-peer systems using public cloud: a case study of peer-to-peer search. In: Proceedings of 11th international symposium on parallel and distributed computing (ISPDC), IEEE, Munich, Germany, pp 135–142
3. Haase P, Siebes R, van Harmelen F (2008) Expertise based peer selection in peer-to-peer networks. Knowl Inf Syst 15(1):75–107 (Periodical style)
4. Schollmeier PR (2001) A definition of peer-to-peer networking for the classification of peer-to-peer architectures and applications. In: Proceedings of the first international conference on peer-to-peer computing, IEEE, Linkoping, Sweden, pp 101–102
5. Yu J, Li M (2008) CBT: a proximity-aware peer clustering system in large-scale BitTorrent-like peer-to-peer networks. Comput Commun 31(3):591–602 (Periodical style)
6. Feigenbaum J, Parkes DC, David M (2009) Computational challenges in e-commerce. Commun ACM 52(1):70–74 (Periodical style)
7. Beatty P, Reay I, Dick S, Miller J (2011) Consumer trust in e-commerce web sites: a meta-study. ACM Comput Surv 43(14):1–46 (Periodical style)
8. Hoffman K, Zage D, Nita-Rotaru C (2009) Expertise-based peer selection in peer-to-peer networks. A survey of attack and defense techniques for reputation systems. ACM Comput Surv 42(1):1–31 (Periodical style)
9. Oliveira L (2012) Clustering of distinct PACS archives using a cooperative peer-to-peer network. Comput Methods Programs Biomed 108(3):1002–1011 (Periodical style)
10. Fan W-J, Yang S-L, Perros H, Pei J (2015) A multi-dimensional trust-aware cloud service selection mechanism based on evidential reasoning approach. Int J Autom Comput 12 (2):208–219
11. Noor TH, Sheng QZ, Zeadally S, Yu J (2013) Trust management of services in cloud environments: obstacles and solutions. ACM Comput Surv 46(1):12
12. Hughes D, Coulson G, Walkerdine J (2005) Free riding on Gnutella revisited: the bell tolls. IEEE Distrib Syst Online 6(6):1–18
13. Marsh SP (1994) Formalising trust as a computational concept. Ph.D. dissertation, University of Stirling, UK

14. Mui L (2003) Computational models of trust and reputation: agents, evolutionary games, and social networks. Ph.D. dissertation, Massachusetts Institute of Technology, USA
15. Mui L, Mohtashemi M, Andhalberstadt A (2002) A computational model of trust and reputation. In: Proceedings of the 35th Hawaii international conference on system sciences (HICSS02), IEEE, Los Alamitos, Canada, pp 188–196
16. Sherchan W, Nepal S, Paris C (2013) A survey of trust in social networks. ACM Comput Surv 45(4):1–33
17. Stoica I, Morris R, karger D, Kaashoek F, Balakrishnan H (2001) Chord: a scalable peer-to-peer lookup service for internet applications. In: Proceedings of special interest group on data communication, ACM, California, USA. Availabe: http://www.cse.iitb.ac.in/dbms/Data/Courses/CS632/2010/Papers/chord.pdf
18. Xiong L, Liu L (2004) PeerTrust: supporting reputation based trust for peer-to-peer electronic communities. IEEE Trans Knowl Data Eng 16(7):843–857
19. Kamvar SD, Schlosser MT, Garcia-Molina H (2003) The EigenTrust algorithm for reputation management in P2P networks. In: Proceedings of the 12th international conference on world wide web, New York, USA, pp 640–651
20. Zhou R, Hwang K (2007) PowerTrust: a robust and scalable reputation system for trusted peer-to-peer computing. IEEE Trans Parallel Distrib Syst 18(5):1–14
21. Zhou R, Hwang K, Cai M (2008) GossipTrust for fast reputation aggregation in peer-to-peer networks. IEEE Trans Knowl Data Eng 20(9):1282–1295

A Rubber Polymerization Conversion Soft Sensor Model Based on Improved ANFIS

Shi-wei Gao

1 Introduction

Synthetic rubber industry is an important part of national production. As one of the most important parameters in the production of synthetic rubber, polymerization conversion determines the efficiency of rubber production and product quality. The conversion is usually measured off-line in the laboratory; the sampling period is generally 6–8 h. It can be seen that due to the longer sampling period, it is very difficult to analyze the data of the device in real time. Therefore, if the conversion can be measured online in real time, production plant can be adjusted according to the on-line measurement data. However, due to technical and economic reasons, it is difficult to create an online analyzer for analyzing conversion rate.

The industrial production process is complicated, which makes it difficult to use many detection instruments for direct detection. For these indicators, the soft sensing technology is widely used in the research and testing. The soft-sensing technology chooses a set of auxiliary variables that are both closely related and easily measured according to some optimal criterion. It is the core of the soft sensing technology to combine the measurable variables with the non-measurable variables. In order to design a reliable soft sensor model, the most important is to establish a simple and robust dynamic mathematical model. Many mathematical techniques have been used to develop models in soft-sensing technology, including physical models, gray-box models, neural networks, fuzzy logic systems. In this paper, an improved modelling method based on neuro-fuzzy technology is proposed.

S. Gao (✉)
Department of Electric & Electronic Engineering, Lanzhou Petrochemical College of Vocational Technology, Lanzhou 730060, China

Z. Deng (ed.), *Proceedings of 2017 Chinese Intelligent Automation Conference*, Lecture Notes in Electrical Engineering 458,
https://doi.org/10.1007/978-981-10-6445-6_13

2 Conversion On-Line Detection

Polymerization is glue mixture of components, and is influenced by many factors. In the case where the polymer composition is constant, the greater the conversion, the more the polymer is formed, so the density is also greater. The conversion rate can be considered by detecting the density of the system, so the key to the success of the system is the density detection. We use the conventional method to measure the density of information. In accordance with the law of fluid mechanics, when the medium flow in the vertical pipe, the pressure difference between any two points composed of two parts, namely static pressure and friction resistance, in which the static depend on the density when the pressure difference in the two measuring point is fixed.

Based on the previous research, we do not simply use the field parameters to build a mathematical model directly, but to combine the field analyzer design with the measurement model of multiple measurement points. A large-scale analyzer is installed on the site pipeline to obtain the targeted raw data, and the conversion rate of the synthetic rubber is calculated by the mathematical model. Therefore, the on-line detection of conversion rate is based on the correspondence between the conversion rate and the mortar density, combined with other parameters to measure the synthetic rubber conversion rate. The analyzer is designed to measure the density of mortar for the purpose of measuring the density.

The selection of auxiliary variables of the model is an important step in constructing a mathematical model and is a preliminary step in carrying out regression analysis or other identification steps. It is necessary to select enough variables to fully reflect the characteristics of the system. However, too many variables can lead to an increase in the complexity of the identification model.

Due to the complexity of the network structure and the complexity of the sample, the phenomenon of overfitting is easy to appear and the generalization ability is low. If the statistical principle is applied to the neural network modeling process, it will effectively improve the simulation performance of the model. Firstly, the principal component analysis (PCA) is used to analyze the existing data and then apply it to the neural network. The PCA simplifies the structure of the neural network model, improves the convergence speed and precision, reduces the over-fitting of the neural network and enhances the generalization ability.

Based on the theoretical analysis and simulation test, the field parameters associated with the conversion rate are chosen as the auxiliary variables of the model. The six signals, such as vertical differential pressure, horizontal differential pressure, ambient temperature, stirring electric power, pipeline pressure and cement temperature, were selected as the key parameters. In the same device, the measurement results of each detection point can be used as the key parameter of other detection points.

3 Neural Fuzzy System

After selecting the auxiliary variables, the next step is to establish the mathematical model. The linear method to establish the model in the complex conditions difficult to meet the site requirements. Here, we use neural fuzzy system to establish mathematical model.

The method based on fuzzy logic does not need accurate mathematical model in dealing with the problem. The fuzzy inference system can make full use of human experience by storing important contents in the rule base and membership function. Fuzzy system does not include learning algorithms. It often takes a long time to find an acceptable system by adjusting the parameters of the fuzzy system by experiment or expert knowledge. Neural networks do not depend on human experience. It uses a learning rule and a given training set to gradually form a set of parameters to obtain the desired functional behavior. However, since the knowledge of the system is distributed throughout the network, it is difficult to extract the structural knowledge from the configuration or weight of the neural network. At the same time, because the hidden layer of the neural network is opaque to the user, the structure and size of the network is still a problem to be solved.

It can be seen that fuzzy systems and neural networks are complementary technologies. The neural network extracts knowledge from the controlled system, and the fuzzy system usually uses the linguistic information from the expert. The collaboration of fuzzy logic and neural network makes the system capable of learning, high level thinking and reasoning. The neuro fuzzy system has fast and accurate learning ability, good generalization ability, as well as excellent interpretation ability, and the ability to accommodate both data and existing expert knowledge, so that it can be widely used in the field of engineering and science [1–4].

The combination of the fuzzy system has promoted the development of the artificial intelligence system, and has produced many methods, such as GARIC, ANFIS, FUN, NEFCON, SOFIN and so on. Among them, the most widely used is ANFIS, compared with other algorithms, ANFIS has higher training speed, effective learning ability, and simple structure. Is also considered to be the best algorithm in function approximation. Adaptive Network-based Fuzzy Inference System (ANFIS) is a multi-layer adaptive network-based fuzzy inference system. It consists of 5 layers, using a hybrid learning model to adjust the fuzzy inference system structure parameters [5–8]. For simplicity, consider a simple fuzzy system with two inputs and one output. Suppose the rule base has two rules:

Rule1: IF x_1 is A_1 and x_2 is B_1

Then $y_1 = p_1x_1 + q_1x_2 + r_1$

Rule2: IF x_1 is A_2 and x_2 is B_2

Then $y_2 = p_2x_1 + q_2x_2 + r_2$

Figure 1 shows a two input, one output ANFIS architecture. The functions of each node are as follows:

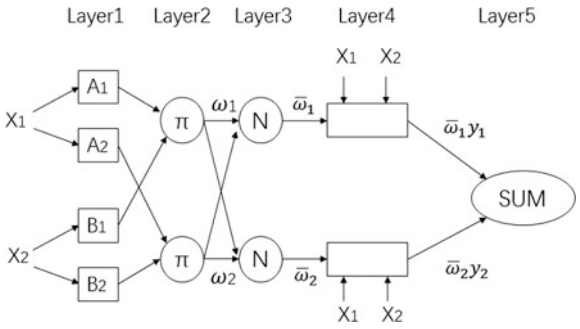

Fig. 1 ANFIS architecture

Layer1: The nodes are adaptive. It is responsible for the fuzzification of the input signal. The membership functions of the input variables are used as node functions. The parameters of this layer are called prerequisite parameters, and the output of each node is:

$$O_{1,i} = \mu A_i(x_1), \quad i = 1, 2$$

$$O_{1,i} = \mu B_{i-2}(x_2), \quad i = 3, 4$$

where x_1, x_2 are inputs to the fuzzy system, A_i or B_i is the fuzzy set associated with the node. In other words, the output of this layer is the value of the membership function of the premises. A_i or B_i can be described by a bell-shaped function:

$$\mu A_i(x) = \frac{1}{1 + \left(\frac{x - c_i}{a_i}\right)^{b_i}}$$

$(a_i,\ b_i,\ c_i)$ is called the premise parameter, the shape of the membership function changes with the change of these parameters, in fact, the membership function can take any piecewise continuous function, such as trapezoidal function or trigonometric function.

Layer2: The nodes are fixed, and the output represents the firing strengths of the rules. Each node performs fuzzy AND operation with the algebraic product,

$$O_{2,i} = \omega_i = \mu A_i(x_1) \times \mu B_i(x_2), \quad i = 1, 2$$

The output of each node represents the credibility of a rule.

Layer3: Node is fixed, the output representing normalized firing strengths. The output of this layer is called the firing strength. The *i*th node strength is:

$$O_{3,i} = \overline{\omega}_i = \frac{\omega_i}{\omega_1 + \omega_2}, \quad i = 1, 2$$

Layer4: The node is fixed and the output is the sum of all input signals, each node in this layer has node function:

$$O_{4,i} = \overline{\omega}_i y_i = \overline{\omega}_i (p_i x_1 + q_i x_2 + r_i), \quad i = 1, 2$$

$\{p_i, q_i, r_i\}$ is the set of consequent parameter.

Layer5: Node is adaptive. The node function is obtained by Layer 1 for a first-order model, and the parameter is the defuzzification of the consequent parameter, it calculates the sum of all incoming signals as the total output:

$$O_{5,i} = Y = \sum_i \overline{\omega}_i y_i$$

Given the premise parameters, the ANFIS output can be expressed as a linear combination of the consequent parameters:

$$\begin{aligned} y &= \frac{\omega_1}{\omega_1 + \omega_2} y_1 + \frac{\omega_2}{\omega_1 + \omega_2} y_2 = \overline{\omega}_1 y_1 + \overline{\omega}_2 y_2 \\ &= \overline{\omega}_1 (p_1 x_1 + q_1 x_2 + r_1) + \overline{\omega}_2 (p_2 x_1 + q_2 x_2 + r_2) = A\theta \end{aligned}$$

The elements of column vector θ form a set of consequent parameters $\{p_1, q_1, r_1, p_2, q_2, r_2\}$. If there are t pairs of input and output data pairs, and given prerequisite parameters, the least squares method (LMS) can be used to make $\|A\theta - y\|^2$ is the best estimate of the consequent parameter vector, $\widehat{\theta}$:

$$\widehat{\theta} = \left(A^T A\right)^{-1} A^T y$$

Then the estimated output of ANFIS is calculated according to the identification result of the consequent parameter $\widehat{\theta}$: $y = A\widehat{\theta}$.

Fuzzy system has the ability to capture human experience or knowledge. Due to the fuzziness and subjectivity of human thinking and linguistic, it is impossible for human experts to describe all possible situations of the system accurately. Especially when the system is complex. This is why the learning based methods (such as neural networks) are introduced into fuzzy system.

The more prior knowledge is used in the fuzzy system, the neural network can learn and extract more hidden information from the system observation. Although the neuro fuzzy system has many advantages, but also has its shortcomings. First of all, it is necessary to ensure that the quality of human knowledge or experience data better, and secondly, when the dimension of the system increases, the size of the

neural fuzzy model is also exponential growth. This makes it difficult to apply the high dimensional neural fuzzy system.

Because of the characteristics of the feedforward network, the hybrid neural fuzzy model cannot effectively capture the dynamic characteristics of the process. There have been some studies on recurrent neural networks to solve this problem. However, because of the complex network structure of the recurrent neural network, it is difficult to train compared with the feed-forward network. The enormous amount of computation makes it difficult to be applied in practice. Therefore, some studies have constructed a recursive fuzzy neural network with internal feedback for control and recognition systems. In this paper, a new neural fuzzy network is introduced, through a feedback loop, the system output is introduced, so that the system can memorize the previous state characteristics and estimate the output state with the current and previous states. The dynamic characteristics of the system are obtained by the feedback loop, as shown in Fig. 2.

By introducing a feedback connection, the system can remember the previous state, and use the previous and current state to calculate the new output value. From the practical point of view, the embedded feedback time delay is time variant, which can produce different dynamic behaviors, which is helpful to improve the prediction ability. Then the output at the moment is:

$$y(t) = f[y(t-1), \ldots, y(t-N), X(t-1), \ldots, X(t-M)]$$

This makes it possible to train a hybrid neuro-fuzzy system via the output delay elements.

4 Simulation Study

For a styrene-butadiene rubber plant, 3 months of production history data were collected. The simulation is carried out after filtering and normalization. Compared with the artificial measurement data, the results are shown in Fig. 3.

It can be seen that the trend of on-line estimated data is in good agreement with the trend of the conversion rate of the material polymerized mortar. Through the

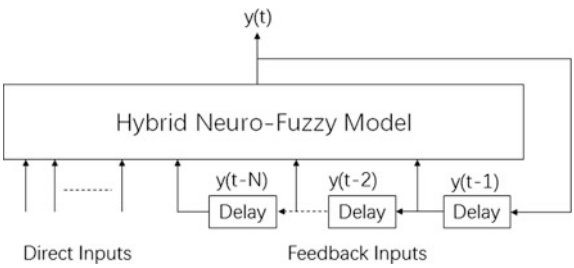

Fig. 2 The feedback neuro-fuzzy system

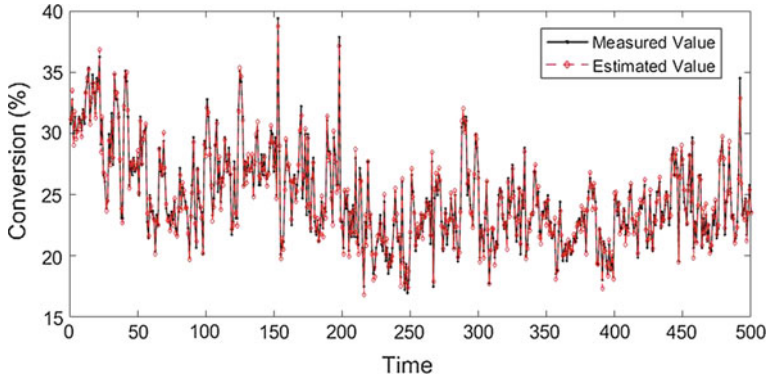

Fig. 3 Comparison of measured data and estimated data

practical application in industrial field, the on-line detection system can meet the actual needs of process control.

The next step is to compare the ANFIS method with the feedback and the ANFIS method without the feedback process. the results are shown in Fig. 4.

The model performance is measured using the following statistical indicators to provide a numerical description of the goodness of the estimates. One of the most common indicators used with hybrid models is the root mean square error (RMSE). This is calculated according to equation:

$$RMSE = \sqrt{\frac{1}{T}\sum_{i=1}^{T}(K_i - L_i)^2}$$

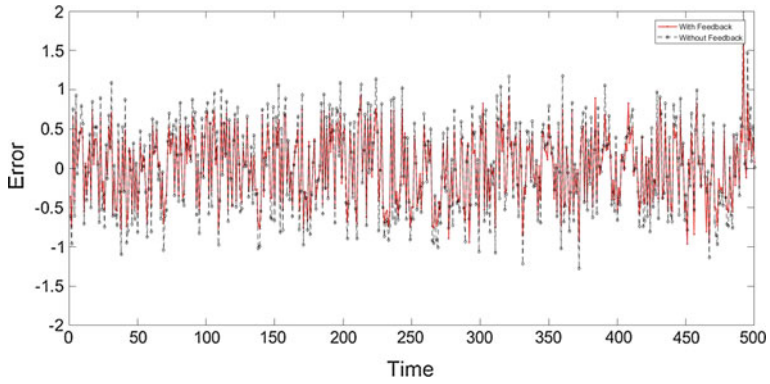

Fig. 4 Error comparison of with feedback and without feedback

The root mean square errors were 0.45 and 0.58 respectively by using feedback and without feedback ANFIS method. It can be seen that the feedback improves the prediction ability.

5 Conclusion

In this paper, a fuzzy neural network model is used to study the conversion of styrene butadiene rubber. A soft sensor model based on improved ANFIS is proposed. The simulation results show that the modified algorithm can realize the accurate analysis of the conversion rate, which can make up for the shortcomings of off-line analysis of the current laboratory, by providing real-time continuous conversion of online data analysis. By providing real-time, continuous on-line conversion data, production process operators and technicians can grasp the progress of polymerization more accurately, control polymerization depth, and smooth device operation.

References

1. Mellit A, Kalogirou SA (2006) Neuro-fuzzy based modelling for photovoltaic power supply system. In: First international power and energy conference, pp 89–93
2. Yildirim Y, Bayramoglu M (2006) Adaptive neuro-fuzzy based modelling for prediction of air pollution daily levels in the City of Zonguldak. Chemosphere 63(9):1575–1582
3. Ayata T, Cam E, Yildiz O (2007) Adaptive neuro-fuzzy inference system (ANFIS) application to investigate potential use of natural ventilation in new building designs in turkey. Energy Convers Manage 48(5):1472–1479
4. Abdulhamit S (2007) Application of adaptive neuro-fuzzy inference system for epileptic seizure detection using feature extraction. Comput Biol Med 37(2):227–244
5. Jassar S, Liao Z, Zhao L (2009) Impact of data quality on predictive accuracy of ANFIS based soft sensor models. Proc World Congr Eng Comput Sci 2:1001–1006
6. Caydas U, Hascalik A, Ekici S (2009) An adaptive neuro-fuzzy inference system (ANFIS) model for wire-EDM. Expert Syst Appl 36(8):6135–6139
7. Mitra P, Maulik S, Chowdhury SP et al (2007) ANFIS based automatic voltage regulator with hybrid learning algorithm. In: 42nd international universities power engineering conference, pp 397–401
8. Kakar M, Nystrom H, Aarup L et al (2005) Respiratory motion prediction by using the adaptive neuro-fuzzy inference system (ANFIS). Phys Med Biol 50(19):4721–4728

Initial Attitude Estimation and Installation Errors Calibration of the IMU for Plane by SINS/CNS Integration

Weiping Yuan, Mingzhen Gui and Xiaolin Ning

1 Introduction

Strapdown inertial navigation system (SINS) has been widely used in various types of aircrafts, for the advantages of completely autonomy and high rate of output. The accuracy of initial alignment and calibration of the IMU installing errors greatly affect the overall navigation accuracy [1]. The initial alignment is the process of determining the initial values of attitude of the system. Installation errors mean that the IMU incorrectly installs on the plane, which can cause the existence of an additional interference acceleration in accelerator output and gyros drift in gyro output and finally lead to navigation errors.

Celestial navigation system (CNS) can provide accurate attitude information, whose navigation accuracy is not relate to time and distance, but strongly depends on the accuracy of measurements [2]. Research on the initial alignment has been carried on the past. Lei [3] proposed a fast initial alignment for SINS method which combines Extended States Observers (ESO) with Kalman filters. Using this method, the speed of initial alignment is more quickly and characters such as high accurate and robust are possessed. However, this fast initial alignment, with low observability, cannot calibrate the installation errors. Sun [4] proposed an online calibration method of marine SINS aided by CCD star sensor. This method could estimate the gyro drift and accelerometer bias quickly and accurately, but it does not take installation errors into account on the navigation result.

The initial alignment of the SINS and the calibration of the IMU installing errors are difficult problems under the environment of autonomous navigation. However, considering the complementary characteristics of SINS and CNS, the SINS initial alignment and calibration can be accomplished by combing both of them [5].

W. Yuan (✉) · M. Gui · X. Ning
School of Instrument Science & Opto-electronics Engineering,
Beihang University, Beijing 100191, People's Republic of China
e-mail: yuan_1166@sina.com

Z. Deng (ed.), *Proceedings of 2017 Chinese Intelligent Automation Conference*,
Lecture Notes in Electrical Engineering 458,
https://doi.org/10.1007/978-981-10-6445-6_14

A method using a single inflight star sighting to estimate the initial attitude and calibrate the IMU installing errors is presented in this paper. To make all state variables observable, the outputs of IMU are also added to the measurement variables, and an unscented Kalman filter is used to fuse the data of SINS and CNS.

2 Principles of SINS and CNS

Coordinate frames which including earth-centered inertial frame (i-frame), earth-fixed frame (e-frame), the navigation frame (n-frame), the plane body frame (b-frame), IMU coordinate frame (p-frame), and the star sensor frame (s-frame) used in this paper are shown in Fig. 1.

2.1 Principle of SINS and Influence of Installation Errors

A full inertial navigation system mainly consists of the corresponding SINS mechanization and an inertial measurement unit (IMU), which typically includes three orthogonal accelerometers and three orthogonal gyroscopes. Angular rates and linear accelerations measured by the IMU are transformed to the n-frame and are used to determine the position, velocity and attitude of the plane. SINS attitude initialization is called alignment, which is the process of determining the initial values of the coordinate transformation from the body frame to the navigation frame in SINS. In the SINS, the IMU is directly mounted on the plane, which is assumed to coincide with the body frame under ideal conditions. However, due to the existence of installation errors, the existence of an additional interferential acceleration in accelerator output and gyro drift in gyros output are induced, which can lead to navigation errors. The installation errors matrix of IMU can be represented by three small angles ϑ_x, ϑ_y and ϑ_z [6].

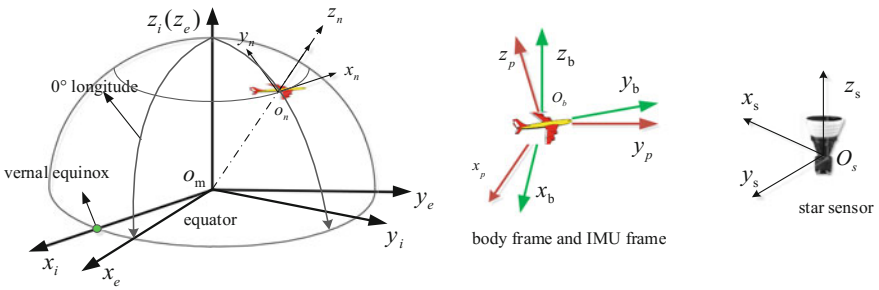

Fig. 1 Reference frame

$$\boldsymbol{C}_b^p = \left(\boldsymbol{C}_p^b\right)^T = \boldsymbol{I} + \Delta\boldsymbol{C}_b^p \approx \begin{bmatrix} 1 & \vartheta_z & -\vartheta_y \\ -\vartheta_z & 1 & \vartheta_x \\ \vartheta_y & -\vartheta_x & 1 \end{bmatrix} \tag{1}$$

In the IMU frame, $\tilde{\boldsymbol{w}}_{ib}^b, \tilde{\boldsymbol{f}}^b$ are the actual output value of the gyroscope and accelerometer respectively. $\boldsymbol{w}_{ib}^b, \boldsymbol{f}^b$ represent ideal output value of the gyroscope and accelerometer respectively. The measurement errors of gyro and accelerometer can be expressed as

$$\begin{cases} \delta\boldsymbol{w}_{ib}^n = \boldsymbol{C}_b^n \delta\boldsymbol{w}_{ib}^b = \boldsymbol{C}_b^n\left(\tilde{\boldsymbol{w}}_{ib}^b - \boldsymbol{w}_{ib}^b\right) = \boldsymbol{C}_b^n\left(\boldsymbol{C}_b^p - \boldsymbol{I}\right)\boldsymbol{w}_{ib}^b \\ \delta\boldsymbol{f}^n = \boldsymbol{C}_b^n \delta\boldsymbol{f}^b = \boldsymbol{C}_b^n\left(\tilde{\boldsymbol{f}}^b - \boldsymbol{f}^b\right) = \boldsymbol{C}_b^n\left(\boldsymbol{C}_b^p - \boldsymbol{I}\right)\boldsymbol{f}^b \end{cases} \tag{2}$$

where $\boldsymbol{C}_b^n$ is the plane's attitude matrix, which can be defined using sequence of rotations 2-1-3 as

$$\begin{aligned} \boldsymbol{C}_n^b &= (\boldsymbol{C}_b^n)^{\mathrm{T}} \\ &= \begin{bmatrix} \cos\theta\cos\psi - \sin\theta\sin\varphi\sin\psi & -\cos\varphi\sin\psi & \sin\theta\cos\psi + \cos\theta\sin\varphi\sin\psi \\ \cos\theta\sin\psi + \sin\theta\sin\varphi\cos\psi & \cos\varphi\cos\psi & \sin\theta\sin\varphi - \cos\theta\sin\varphi\cos\psi \\ -\sin\theta\cos\varphi & \sin\varphi & \cos\theta\cos\varphi \end{bmatrix} \end{aligned} \tag{3}$$

where θ, φ, ψ are pitch, roll and yaw angles, respectively.

2.2 Principle of CNS

Stars always move in the regular way, thus their positions at a specific time can be obtained exactly. CNS is mainly composed of the star sensor and the star image processing software. After preprocessing of the original star image captured by star sensor, the starlight unit vector in the s-frame $\mathbf{s}_s$ can be obtained [7]. At the same time, When the number of stars observed is more than three, the transformation matrix ($\boldsymbol{C}_b^i$) from the b-frame to i-frame can be calculated. Also, the starlight unit vector expressed in the earth-centered inertial frame $\mathbf{s}_i$ can be acquired after star image pattern recognition as follows [8].

$$\mathbf{s}_i = \begin{bmatrix} \cos\Delta\cos R_A & \cos\Delta\sin R_A & \sin\Delta \end{bmatrix}^T \tag{4}$$

where Δ, R_A represent the declination and right ascension of the star respectively.

3 System Models

3.1 State Model

Due to the stationary of the plane, the altitude velocity component is ignored, and the SINS error equation in the navigation frame is used as state model, which can be written as [9]

$$\begin{cases} \dot{\boldsymbol{\phi}} = \boldsymbol{\phi} \times \boldsymbol{\omega}_{in}^{n} + \delta\boldsymbol{\omega}_{in}^{n} - \boldsymbol{C}_{b}^{n}\delta\boldsymbol{\omega}_{ib}^{b} - \boldsymbol{C}_{b}^{n}\boldsymbol{\varepsilon} \\ \delta\dot{\boldsymbol{v}}_{n} = -\boldsymbol{\phi} \times \boldsymbol{f}^{n} + \boldsymbol{C}_{b}^{n}\delta\boldsymbol{f}^{b} - 2\boldsymbol{\omega}_{ie}^{n} \times \delta\boldsymbol{v}_{n} + \boldsymbol{C}_{b}^{n}\nabla \\ \dot{\boldsymbol{\varepsilon}} = 0 \\ \dot{\nabla} = 0 \\ \dot{\boldsymbol{\vartheta}} = 0 \end{cases} \tag{5}$$

where $\boldsymbol{\phi} = [\,\phi_E \quad \phi_N \quad \phi_U\,]^T$ is the misalignment angle. $\delta\boldsymbol{v}_n = [\,\delta v_E \quad \delta v_N\,]^T$ is the velocity error. $\boldsymbol{\varepsilon} = [\,\varepsilon_x \quad \varepsilon_y \quad \varepsilon_z\,]^T$ is the gyro drift. $\nabla = [\,\nabla_x \quad \nabla_y \quad \nabla_z\,]^T$ is the accelerometer bias. $\boldsymbol{f}^n$ is the projection of the output of accelerometers in the n-frame.

$\boldsymbol{\omega}_{ie}^{n} = [0, \omega_{ie}\cos L, \omega_{ie}\sin L\,]^T$ is the earth rotation rate denoted in the n-frame. Assure state vector $\boldsymbol{X}$, Eq. (5) can be expressed as

$$\dot{\boldsymbol{X}} = f(\boldsymbol{X}) + \boldsymbol{W} \tag{6}$$

where $\boldsymbol{W}$ is the process noise.

3.2 Measurement Model

To make all state variables observable, the horizontal velocity errors, starlight vector and outputs of IMU are chosen as the measurement variables.

(1) **Horizontal Velocity Errors**

When the plane is stationary, the horizontal velocities calculated by the SINS are velocity errors. Using this velocity errors as measurements, the measurement equation can be expressed as follows.

$$\delta \mathbf{v}_n = [\delta v_E, \delta v_N]^{\mathrm{T}} = \begin{bmatrix} 0 & 0 & 0 & 1 & 0 & 0 & 0 & 0 & 0 & 0 & 0 & 0 & 0 & 0 \\ 0 & 0 & 0 & 0 & 1 & 0 & 0 & 0 & 0 & 0 & 0 & 0 & 0 & 0 \end{bmatrix} \mathbf{X} \quad (7)$$

(2) **Starlight Vector**

According to the principle of CNS, the starlight vector can be obtained in i-frame and s-frame. Therefore the measurement equation can be expressed as follows.

$$\boldsymbol{s}_s = \boldsymbol{C}_b^s \boldsymbol{C}_n^b \boldsymbol{C}_{n'}^{n} \boldsymbol{C}_e^n \boldsymbol{C}_i^e \boldsymbol{s}_i \quad (8)$$

(3) **Output of Accelerometers**

$$\tilde{\boldsymbol{f}}_{ib}^b = \boldsymbol{C}_b^p \boldsymbol{C}_n^b \boldsymbol{g}_n + \nabla \quad (9)$$

where $\boldsymbol{g}_n = [\,0 \quad 0 \quad g\,]^T$ is the local gravity vector. According to Eqs. (7), (8) and (9), the measurement using $\boldsymbol{Z} = [\delta \mathbf{v}, \mathbf{s}_s, \tilde{\boldsymbol{f}}_{ib}^b]^T$ can be expressed as

$$\boldsymbol{Z} = h(\boldsymbol{X}) + \boldsymbol{V} \quad (10)$$

where $\boldsymbol{V}$ is the measurement noise. Because the measurement model (10) is nonlinear, the Unscented Kalman Filter (UKF) [10, 11] is implemented to fuse SINS and CNS data in this study. The block diagram of alignment and installation errors calibration by SINS/CNS integration method based on UKF is shown in Fig. 2.

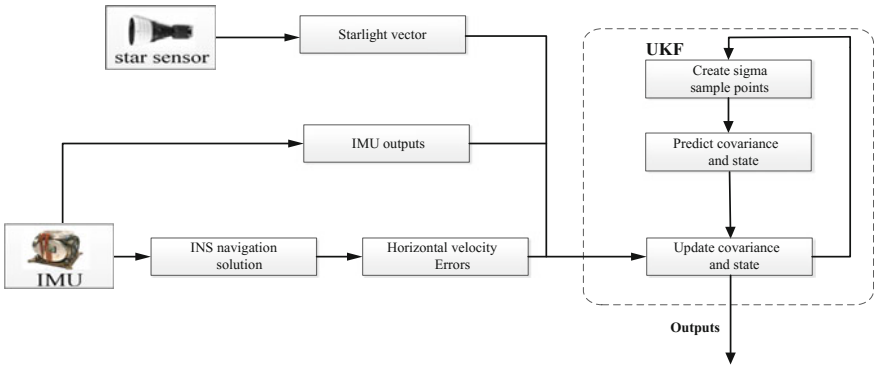

Fig. 2 Workflow of alignment and installation errors calibration by SINS/CNS integration algorithm

4 Results and Discussion

4.1 Simulation Condition

Simulations are performed to verify the feasibility of this method. In the following simulations, the plane keeps stationary, and the initial conditions are defined as: longitude 116°E, latitude 40°N. The initial pitch, yaw and roll angles are 0°, 20° and 0°, and its initial attitude errors of pitch angle, yaw angle and roll angle are all 10″. The parameters of IMU are: the drifts and random drifts of each gyro are chosen as 0.005°/h and 0.001°/h, and the biases and random biases of each accelerometer are chosen as 50 and 10 ug, with its frequency as 100 Hz. The accuracy of the star sensor is 3″ (1σ) and its frequency is 5 Hz. The total running time is 5 min and the filtering period is 1 s.

4.2 Simulation Results

The estimation of attitude and its error are shown in Fig. 3, it can be seen that the curve of estimated attitude converges rapidly from the start. During the filtering period, the mean estimation errors in pitch, yaw and roll are 0.8858″, 0.9232″ and 0.8369″, respectively. The maximum error in attitude is 6.18″, which is much better than that of tradition method. From this result, we can see that this method can accurately estimate the attitude of the plane.

Figure 4 shows the results of accelerometer and gyroscope errors estimated by this SINS/CNS integration method. The estimation curves of accelerometer and gyroscope converge quickly, which suggests that it can accurately estimate the gyroscope drifts and accelerometer biases. Figure 5 illustrates the estimation result of the IMU installing errors. As indicated in this figure, the estimated values of

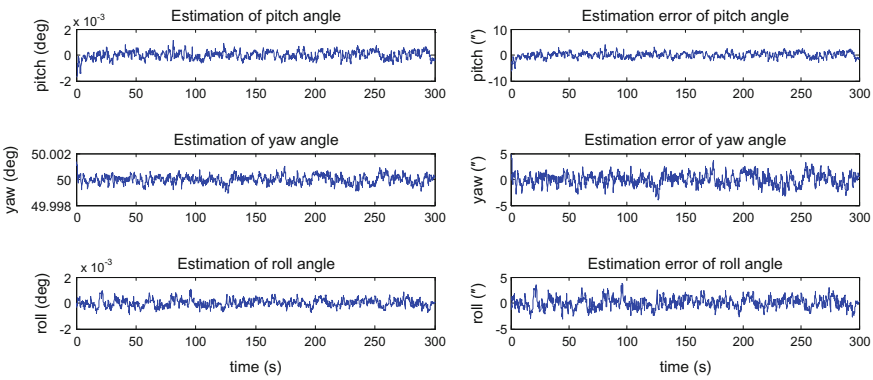

Fig. 3 The estimation of attitude and its error

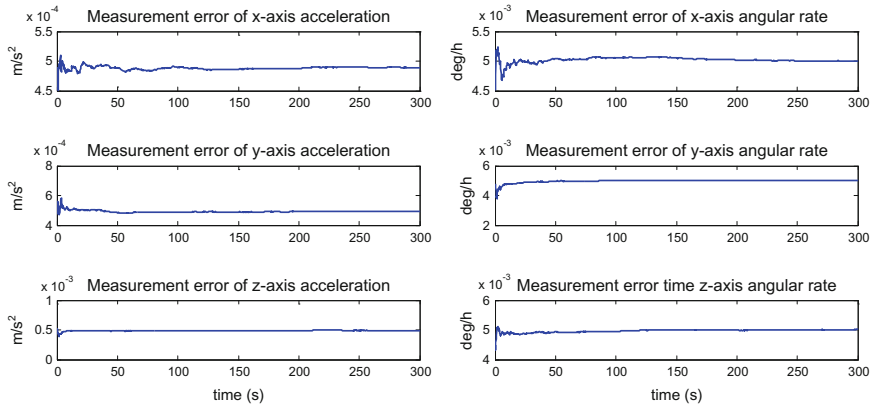

Fig. 4 The estimation of accelerometer and gyro errors

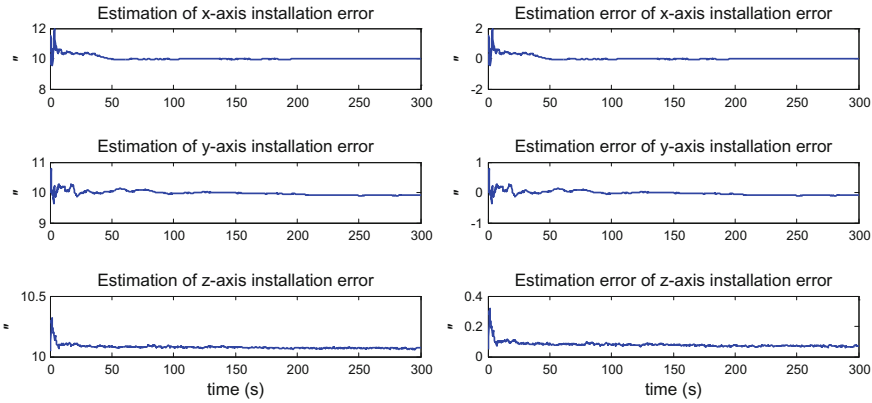

Fig. 5 The estimation of installation errors

installation errors in three directions converge to 9.98″, 9.91″, 10.07″, which are very close to the true value 10″, 10″, and 10″. The maximum estimation errors of installation errors is 2″. From these figures, it is clear that the initial attitude estimation and installation errors calibration by SINS/CNS integration method developed in this paper is able to accurately estimate the accelerometer and gyroscope errors. Furthermore, it can also estimate the installation errors of the IMU effectively.

5 Conclusion

In the paper, an initial attitude estimation and installation errors calibration of the IMU for plane by SINS/CNS integration method is presented, which could solve the problems of SINS initial alignment and IMU calibration at the same time. The IMU installing errors are considered and its corresponding state equation is established. To make all state vectors observable, all original information provided by the sensors of the SINS and the CNS are used as measurements. The maximum error in attitude is 6.18″, which indicates that both the inertial sensors' biases in the SINS and the installation errors of the IMU are estimated effectively. It should be noted that the proposed approach can be also applied to other carrier with a series of sensors.

References

1. Titterton D, Weston J (2004) Strapdown inertial navigation technology. Aerosp Electron Syst Mag IEEE 20:33–34
2. Sigel DA, Wettergreen D (2007) Star tracker celestial localization system for a lunar rover. In: IEEE/RSJ international conference on intelligent robots and systems, pp 2851–2856
3. Lei XL, Song JL, Zhou YL (2005) Fast initial alignment for strapdown inertial navigation system. J Chin Inertial Technol 655–657:1009–1015 (in Chinese)
4. Gao W, Lin XC, Wang QY, Ben YY (2012) FOG on-line calibration assisted by CCD star sensor. Syst Eng Electron 34:1680–1684
5. Kuritsky MM, Goldstein MS (1990) Inertial navigation. Springer, New York
6. Song N, Cai Q, Yang G, Yin H (2013) Analysis and calibration of the mounting errors between inertial measurement unit and turntable in dual-axis rotational inertial navigation system. Measur Sci Technol 24:5002
7. Rufino G, Accardo D (2003) Enhancement of the centroiding algorithm for star tracker measure refinement. Acta Astronaut 53:135–147
8. Yoon H, Lim Y, Bang H (2011) New star-pattern identification using a correlation approach for spacecraft attitude determination. J Spacecraft Rockets 48:182–186
9. Titterton D, Weston J (2005) Strapdown inertial navigation technology. Aerosp Electron Syst Mag IEEE 20:33–34
10. Julier SJ, Uhlmann JK (1999) New extension of the Kalman filter to nonlinear systems. Proc SPIE Int Soc Opt Eng 3068:182–193
11. Julier S, Uhlmann J, Durrant-Whyte HF (2000) A new method for the nonlinear transformation of means and covariances in filters and estimators. IEEE Trans Autom Control 45:477–482

An Improved Heuristic Algorithm for the Order Planning of Steelmaking Production

Liangliang Sun, Sisi Li, Yuanwei Qi and Tianmu Ma

1 Introduction

Daily planning for steel production is a short-time plan which is used by iron and steel company to organize and command the daily production. It makes the tasks that stipulated by company's annual operating plan combined with specific users' order and specific production conditions, then decomposes implemented in the form of scheduling, and makes full use of the company's various resources to produce products which can meet users' requirements balance and stably, finally achieving the best economic benefits. When company makes a POP, they should consider all kinds of realistic production conditions, coordinate all production stages overall balance. It is also a process finding the potential of production, overcoming all kinds of bottleneck, and improving the production efficiency for a company; POP clears the work goals in each stage of production, and the production in various aspects carried out according to a predetermined schedule, which ensures that company configures various factors of production effectively and organize balanced production rhythmically. Then the company needs to implement appropriate production task sequentially to each production processes by taking both the market conditions in different stages and production conditions into consideration. To ensure this activity being conducted orderly, we need to make a production scheduling, which is the specific implementation plan of the company's annual production plan. According to the provisions of annual tasks which is used to be a gist of the daily production and operation of company's organization in various

L. Sun (✉) · S. Li · Y. Qi
Department of Information and Control Engineering, Shenyang Jianzhu University, No. 9 Hunnan Road, 110168 Hunnan, Shenyang, China
e-mail: swinburnsun@163.com

T. Ma
Department of Information and Control Engineering, Northeastern University, No. 3 Culture Road, 110819 Heping, Shenyang, China

Z. Deng (ed.), *Proceedings of 2017 Chinese Intelligent Automation Conference*, Lecture Notes in Electrical Engineering 458,
https://doi.org/10.1007/978-981-10-6445-6_15

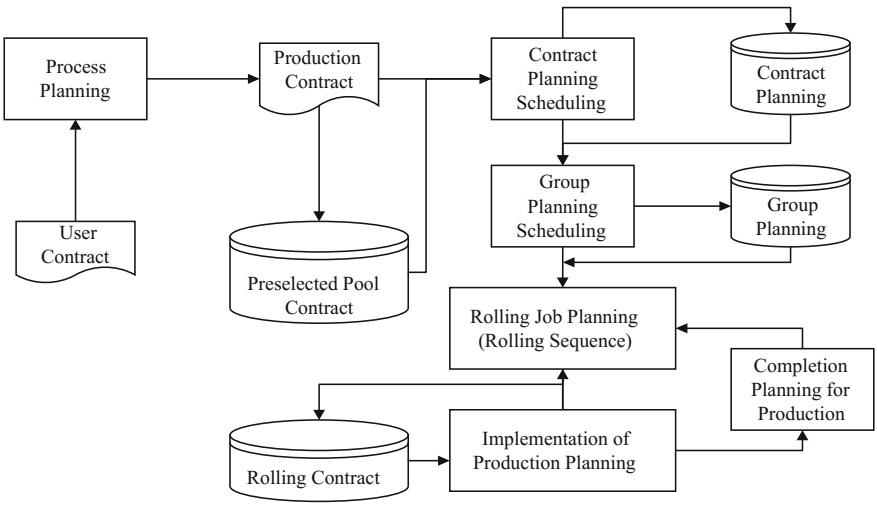

Fig. 1 The plant structure of steel plant

production processes within a relatively short operating time (quarter, month, week, classes), and the specific ordering requirements. As is shown in Fig. 1.

2 Literature Review

In the aspect of batch planning, the charge model targets calcine volume or penalty of calcine volume, and reasonable range of level difference for steel is set as constraint; the cast model targets maximum number of continuous casted charges, taking the life of continuous casting [1] tundish, mould life and level difference of steel as constraints. Model for rolling plan aims at minimizing the penalty of three dimensional skipping for slab and the amount of rolling kilometers, taking width skipping of rolling, width skipping, thickness skipping, longest kilometers of rolling and kilometers for rolling with the same width as constraints. However, order planning is just capacity planning which does not consider reasonability of batch planning.

In terms of application, the Raache steel plant of Rautaraukioy Corporation in Finland produced 2100 thousand tons of steel annually. CPMIS is exploited to shorten deliver date, simplify production from processing raw materials to sending hot rolled products. The Gwangyang steel plant of Pohang Iron and Steel Company exploited systematic Computer Management System which carries out processing melted iron and rolling them. After the system was put into operation, good economic benefits were obtained. Because the specific production technology processes of iron and steel industries differ from each other, and many kinds of difference exist in production management, it is extremely difficult to reuse and

promote this system. Therefore, most choose to develop again, which causes extremely waste for labor and financial sources, affecting the informatization progress of iron and steel enterprises tremendously. For this purpose, developing a planning and scheduling system [5] based on open architecture to meet the requirements of multifarious production job processes and provide a general and scalable decision processing platform for daily production scheduling problems of iron and steel enterprise, has become an important direction for research.

3 Problem Description

For the problem mentioned above, in this section, the POP problem is formulated. Section 3.1 describes the month planning for POP, Subsection 3.2 introduces the period planning.

3.1 Month Planning

For the problem of month planning, $\boldsymbol{K}$ denotes number of orders in preselected pool and $\boldsymbol{J}$ is the number of units for processes; $\boldsymbol{k}$ is the production order number, $\boldsymbol{k} = \mathbf{1}, \mathbf{2}, \ldots, \boldsymbol{K}$; $\boldsymbol{j}$ denotes the processing number, $\boldsymbol{j} = \mathbf{1}, \mathbf{2}, \ldots, \boldsymbol{J}$; $\boldsymbol{T}$ is the planning prospect stage. In this problem, there are two weight coefficients, $\boldsymbol{P_1}$ is the weight coefficient of target one and $\boldsymbol{P_2}$ is the weight coefficient of target two. Here, $\boldsymbol{W_k}$ is the ordering weight (ton) of the k-th order, $\boldsymbol{w_k}$ is the priority coefficient of order $\boldsymbol{k}$; $\boldsymbol{P_{kj}}$ is the processing time of the k-th order in the j-th process; the decision variables are $\boldsymbol{x_{kjt}}$, if contract $\boldsymbol{k}$ produced in the $\boldsymbol{j}$ process on time $\boldsymbol{t}$, $\boldsymbol{x_{kjt}} = 1$, otherwise 0. The objective function of the entire order month plan is the weighted sums of the two goals that mentioned above:

$$\max\left(P_1 \sum_{k=1}^{K}\sum_{j=1}^{J}\sum_{t=1}^{T} x_{kjt}P_{kj} + P_2 \sum_{k=1}^{K} \cdot\omega_k W_k \sum_{j=1}^{J}\sum_{t=1}^{T} x_{kjt}\right) \tag{3.1}$$

Thus, the objective function of the order month plan has been built. Next, let we discuss that what conditions should the model of order month plan be into ensure the objective function is right.

3.1.1 Capacity Constraints for Month Planning

As has been analyzed above, the order month plan shall satisfy the production capacity of the current month. Plans beyond the capacity of this month or not reach the capacity of this month are all unfeasible. In the production process of the iron and steel, main procedures are: steelmaking process, continuous casting process and

hot-rolling process [2], therefore, capacity constraints of the month plan are composed by these three section, which can be expressed by mathematical formula:

$$\sum_{k=1}^{K} x_{kjt} \le L \cdot R_{jt} \quad \begin{matrix} j=1,2,\ldots,J \\ t=1,2,\ldots,T \end{matrix} \tag{3.2}$$

In formula: $\boldsymbol{R_{jt}}$ is the production capacity of j-th process at t-th stage, the unit is hour, $\boldsymbol{L}$ is the load coefficient is more than 1.

3.1.2 Processing Time Constraints for Month Planning

Management for the production of iron and steel enterprise is typical process industry. Production for each stage must be carried out after finishing the previous stage. Therefore, the time requirements among processes must be considered when modeling the order month planning. The mathematical expression of the time constraints among processes is as follows:

$$\tau_{kj}^{\min} \le \sum_{t=EFkj}^{LF_{kj}} t \cdot xk_{kjt} - \sum_{t=EFkj-1}^{LF_{kj-1}} t \cdot xk_{(j-1)} \le \tau_{kj}^{\max} \quad \begin{matrix} k=1,2,\ldots,K \\ j=1,2,\ldots,J \end{matrix} \tag{3.3}$$

In formula, the definition of $\boldsymbol{K}$ and $\boldsymbol{k}$ is the same as defined in the objective function; EF_{kj} is the earliest completion time of order in $\boldsymbol{k}$ process; LF_{kj} is the latest completion time of order $\boldsymbol{k}$ in process $\boldsymbol{j}$; τ_{kj}^{max} is the maximal interval time between the finish of process $\boldsymbol{k}$ and the beginning of process $\boldsymbol{j}-1$ for order $\boldsymbol{k}$; τ_{kj}^{min} is the minimal interval time between the finish of process $\boldsymbol{k}$ and the beginning of process $\boldsymbol{j}-1$ for order $\boldsymbol{k}$;P_{kj} is the processing time of the t-th order in process $\boldsymbol{j}$.

3.1.3 Variety Constraints for Month Planning

In the modeling of order month plan, we provide variety constraints for further. When solving the model, to keep a proportion balance among varieties on basis of productivity. Expressed by mathematical formula, this constraint is described by:

$$\varphi_p^{min} \cdot \sum_{k=1}^{K} x_{kjt} \cdot W_k \le \sum_{k \in \Omega_p} x_{kjt} \cdot W_k \le \varphi_p^{max} \cdot \sum_{k=1}^{K} x_{kjt} \cdot W_k \tag{3.4}$$

In formula, the definition of $\boldsymbol{K}$ and $\boldsymbol{k}$ is the same as defined in the objective function; φ_p^{min} is the lower bound of order which belongs to variety $\boldsymbol{p}$ accounting for total order amount in the order month plan and φ_p^{max} is the upper bound of order which belongs to variety $\boldsymbol{p}$ accounting for total order amount in the order month planning.

3.2 Period Planning

Unit capacity constraints of each period assign the completion time of every process to day. Order period plan should solve the following problems: First, make reasonable arrangement according to the feasible order. Second, overall consideration for the reasonable collocation of warm-up materials and staple materials. Third, make a computational framework of DHCR, CCR and HCR within half of the period. The goal of order period plan is to produce as many orders as possible for every day in the current period. Also, order with high priority should be produced first, then we can get two goals of the order period plan model.

For the period planning, the same as month planning, K is the number of orders in this period; j is the number of process units; k is production order number, $k = 1, 2, \ldots, K$; j is the process number, $j = 1, 2, \ldots, J$; T is the planning prospect stage; P_1 is the weight coefficient of target one and P_2 is the weight coefficient of target two. w_k is the priority coefficient of order k; P_{kj} is the processing time of the k-th order in the j-th process; the decision variables are x_{kjt}, if contract k produced in the j process on time t, $x_{kjt} = 1$, otherwise 0. The objective function of the entire order month plan is the weighted sums of the two goals that mentioned above. In formula, G_1 is the ability used for unit at each stage, its mathematical expression is:

$$G_1 = \max\left(P_1 \sum_{k=1}^{K} \sum_{j=1}^{J} \sum_{t=1}^{T} x_{kjt} P_{kj}\right) \tag{3.5}$$

G_2 is the orders with higher priority weight coefficient have priority to carry out, its mathematical expression is:

$$G_2 = \max\left(P_2 \sum_{k=1}^{K} \cdot \omega_k W_k \cdot \sum_{j=1}^{J} \sum_{t=1}^{T} x_{kjt}\right) \tag{3.6}$$

3.2.1 Capacity Constrains for Period Planning

Capacity constrains are the uppermost in the order month plan, thus, the same as order month plan, order period plan should also consider the capacity constraints, but the time range of capacity constrains for order period plan is limited in ten days, which is more closer to practical production and has a great significance to production. The mathematical expression of capacity constrains in the order period plan is given by:

$$\sum_{k=1}^{K} x_{kjt} P_{kj} \leq L \cdot R_{jt} \quad \begin{matrix} j=1,2,\ldots,J \\ t=1,2,\ldots,T \end{matrix} \tag{3.7}$$

In formula, The definition of $\boldsymbol{x_{kjt}}$, $\boldsymbol{W_k}$, $\boldsymbol{K}$ and $\boldsymbol{k}$ is the same as defined in the objective function; $\boldsymbol{R_{jt}}$ is production capacity of the j-th process at t-th stage, the unit is hour; $\boldsymbol{L}$ is load coefficient is more than 1.

3.2.2 Varieties Constraints for Period Planning

In the varieties of order month plan, we have analyzed the request that the rolling unit has for varieties, so there is no more analysis. Considering the variety constraints in the order month plan is rightly the reflection of integrated planning idea. The mathematical expression of variety constraints is described as:

$$\varphi_p^{min} \cdot \sum_{k=1}^{K} x_{kjt} \cdot W_k \leq \sum_{k \in \Omega_P} x_{kjt} \cdot W_k \leq \varphi_p^{max} \cdot \sum_{k=1}^{K} x_{kjt} \cdot W_k \tag{3.8}$$

In formula, $\boldsymbol{x_{kjt}}$, $\boldsymbol{W_k}$, $\boldsymbol{K}$ and $\boldsymbol{k}$ is defined similarly in the objective function; φ_p^{min}, the lower bound of order, which belongs to variety $\boldsymbol{p}$ accounting for total order amount in the order period plan. φ_p^{max} is the upper bound of order which belongs to variety $\boldsymbol{p}$ accounting for total order amount in the order period plan.

3.2.3 Time Constraints Among Processes

In order period plan, time constraints among processes are more important, because it is directly connected with whether the production can be carried out normally. A certain order shall not arrange the production of next process before arranging the production process of steelmaking. The mathematical expression of time constraints among processes is given by:

$$\tau_{kj}^{\min} \leq \left(\sum_{t=EF_{kj}}^{LF_{kj}} t \cdot x_{kjt} - P_{kj} + 1 \right) - \sum_{t=EF_{kj-1}}^{LF_{kj-1}} t \cdot x_{k(j-1)t} \leq \tau_{kj}^{\max} \quad \begin{matrix} k=1,2,\ldots,K \\ j=1,2,\ldots,J \end{matrix} \tag{3.9}$$

4 Solution of Steelmaking and Continuous Casting Planning

Based on Heuristic Algorithm adopted in this system, the principle in solving model is to use local search strategy according to the knowledge obtained from technical background. Because the mathematical structure of the month planning and period planning is the same. Here we show the period order planning solution, the month planning solution is the same as period solution. The exactly steps are as follows:

Algorithm Design

Step 1 Input plan formulation time;
Step 2 Initialize unit capacity constraints;
Step 3 Select the orders which satisfy the time limits;
Step 4 Select emergency orders and tardiness orders, and classify the two orders as carbon steel or stainless steel;
Step 5 Classify the residual orders as carbon steel or stainless steel;
Step 6 Take period as unit and search every kind of orders in order of steelmaking, continuous casting and hot rolling;
Step 7 Record feasible solutions which satisfy the requirements of capacity and variety;

The same as order month plan, the order period plan builds the optimization model of order period plan according to the background of production process, and based on the model, adopting Heuristic Algorithm based on rules to solve model. The scheduling process of order period plan is given by:

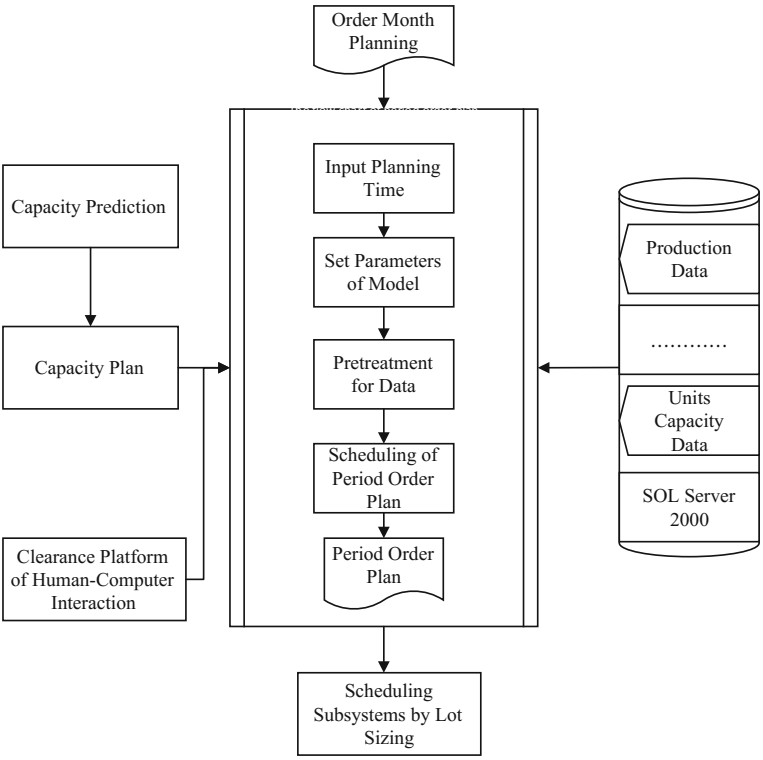

Fig. 2 The flow chart of period order plan

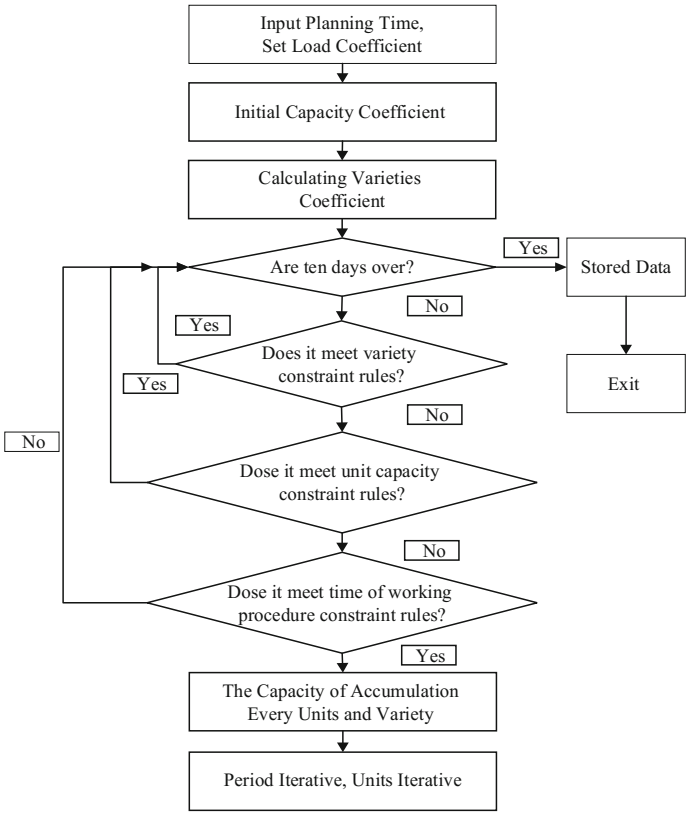

Fig. 3 The arithmetic of order period plan

Step 8 If there is available productivity, return to step6;
Step 9 If there is order, return to step 6;
Step 10 Save results;

The flow chart of period order plan and the arithmetic of order period plan are as shown in Figs. 2 and 3.

5 Computer Experiments Based on Actual Production Data

For the month planning optimization, numerical results for the optimize plan is tested based on one of the largest steelmaking company in China. Simulation method [6] use three different order data, based on the coefficients 1.5, the scheduling results is shown in Table 1. From the results, we can see that the

Table 1 A part of results of order month plan

Contract number	Width of order	Thickness of order	Length of order	Due date	Feeding period
I800287B02	1800	8	8000	2004-10-09	2004-08-01
I800293C01	1250	5	4000	2004-10-10	2004-08-01
I800304A01	1600	7	6000	2004-10-06	2004-08-01
I800331A01	1490	4	2415	2004-10-10	2004-08-01
I800335A01	1250	4.5	2500	2004-10-07	2004-08-01
I800336A01	1010	2.75	2000	2004-10-09	2004-08-01
I800336C01	1350	4.75	2250	2004-10-07	2004-08-01

Table 2 The optimization results of period planning

Load coefficient	Number of scheduled slabs	Number of unscheduled slabs	Scheduling rate	Production utilization rate	
1.5	2490	121	0.9536	Steelmaking	97%
				Continuous casting	89%
				Warm-up rolling	90%
1.5	2051	127	0.9516	Steelmaking	97%
				Continuous casting	90%
				Warm-up rolling	89%

establishment of the month plan order model is corresponding to site production, and its algorithm is correct and efficient. For the period planning, data simulation [5] takes advantage of actual production data of steel in shanghai to simulate either. Simulation method is to adopt a month order to schedule the orders which are planned to complete within month over three periods, adopting 1.5 load coefficients for each period plan. The results are shown in Table 2. We can see that data from a certain steel mill are adopted to schedule the order month plan, the order period plan and the half period batch plan. Models whether have variety constraints or not will be calculated respectively by the algorithm.

Combined the algorithm with the data in one of the largest steelmaking company, we moved the steelmaking month [4] forward to period planning optimization system, as shown in Fig. 4 and future 5, the interface of the developed system. The application example shows this optimize scheduling method is useful, especially for the complex scheduling problem of large-scaled steel plant Fig. 5.

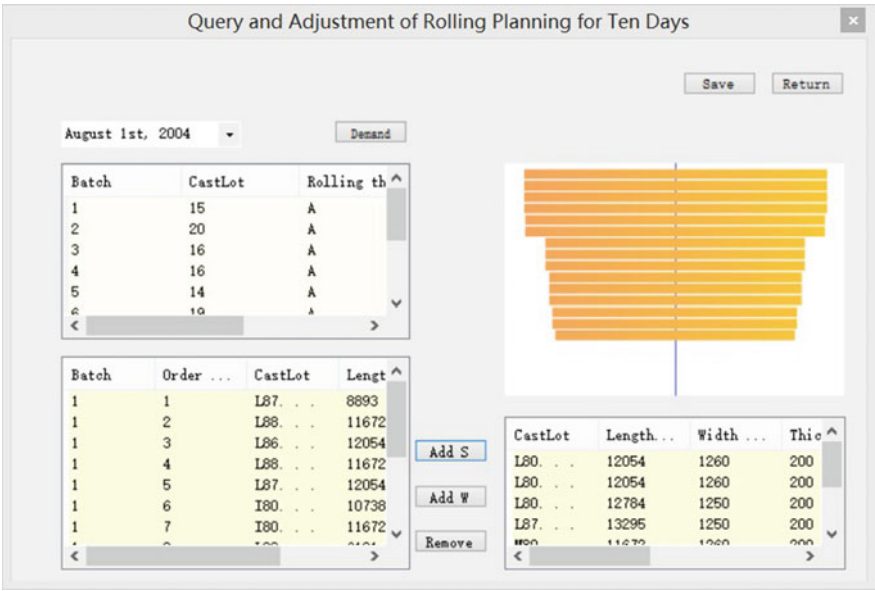

Fig. 4 The roll unit without restrict

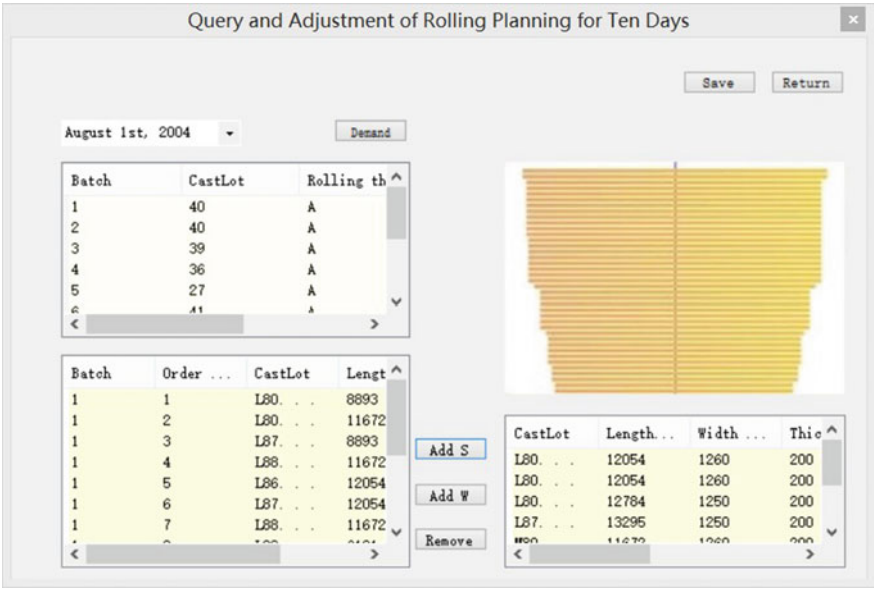

Fig. 5 The rolled unit with restrict

6 Conclusions

In this paper, a two-stage [3] mathematical model from scheduling the monthly plan to the order period plan is built up and an improved heuristic algorithm for steel production plan is proposed. The related system developed is applied in one the Chinese biggest steelmaking plant. Its implementation has several benefits and numerical results has shown that it works effectively in the steelmaking production.

References

1. Tang L, Liu J, Rong A, Yang Z (2000) A mathematical programming model for scheduling steelmaking-continuous casting production. Euro J Oper Res 120(2):423–435
2. Li J, Xiao X, Tang Q, Floudas CA (2012) Production scheduling of a large-scale steelmaking continuous casting process via unit-specific event-based continuous-time models: Short-term and medium-term scheduling. Ind Eng Chem Res 51(21):7300–7319
3. Tan Y, Huang YL, Liu SX (2013) Two-Stage mathematical programming approach for steelmaking process scheduling under variable electricity price. J Iron Steel Res Int 20(7):1–8
4. Liu M (2009) A survey of data-based production scheduling methods. Acta Automatica Sinica 35(6):785–806
5. Bekker J (2001) Discrete-event simulation in steel manufacturing: a case study. In: Proceedings of the international conference on competitive manufacturing, Stellenbosch, South Africa, pp 469–476
6. Li XF, Xu LY, Shao HH, Ren DX (2002) Flexible simulating and scheduling system for steel-making and continuous-casting process and critical problems. J Syst Simul 14(2): 207–211

Adaptive Fuzzy Dynamic Surface Control for AUVs via Backstepping

Shijun Wang, Haisheng Yu, Lin Zhao, Yumei Ma and Jinpeng Yu

1 Introduction

In recent years, AUVs have attracted more and more attention. This is not only due to broad applications of AUVs, such as oceanographic surveys, ocean exploration, and deep sea inspections, but also due to several superiorities of AUV systems, such as high efficiency, good robustness, and large service areas [1, 2]. AUV can bring its own energy, it has no physical connection with the mother ship, and there is no need for human intervention. However, since the AUV systems are highly nonlinear and multivariable, it is still a hot and difficult task to achieve the excellent control property. The researchers have developed many nonlinear control methods such as sliding mode control [3, 4], neural network control [5, 6], backstepping control [7] and so on to achieve high performance control for AUV systems.

The AUV systems have nonlinear functions and many uncertain parameters. One of the most effective approaches to control the systems with parameter uncertainties, the backstepping approach has received significant attention. The advantage of such a control method is by decomposing the complex high order system into several subsystems and introducing the virtual control signals into every subsystems to simplify the control design procedure. Meanwhile, by choosing a suitable Lyapunov function, the control inputs can be derived systematically. However, in the traditional backstepping control, the virtual control function is easy to cause the "explosion of complexity" [8] in continuous derivative calculation. D. Swaroop et al. proposed the dynamic surface control (DSC), using the first-order low pass filter to process the virtual control function. In [8], the DSC technique has been extended to deal with nonlinear systems in which the uncertainties are considered to be linear with unknown constant parameters. Adaptive fuzzy control technique

S. Wang · H. Yu · L. Zhao · Y. Ma · J. Yu (✉)
School of Automation and Electrical Engineering, Qingdao University,
Qingdao 266071, China
e-mail: yjp1109@126.com

Z. Deng (ed.), *Proceedings of 2017 Chinese Intelligent Automation Conference*,
Lecture Notes in Electrical Engineering 458,
https://doi.org/10.1007/978-981-10-6445-6_16

provides a systematic algorithm to solve the tracking control problems of nonlinear systems with unknown parameters, in which the fuzzy logic systems are applied to approximate the unknown nonlinear functions [9].

In this paper, in order to study the position tracking control of the second-order system of AUV, an adaptive fuzzy DSC approach via backstepping is presented. The fuzzy logic systems are applied to deal with the nonlinearities and the DSC approach is utilized to solve the problem of "explosion of complexity". Compared with the traditional backstepping, the main advantages of the proposed control procedure are stated as follows: (1) By using fuzzy logic systems, the designed controllers can cope with the nonlinearity with parameter uncertainties; (2) The DSC approach can solve the problem of "explosion of complexity", and it is able to reduce the computational burden as well as make the proposed method more effective in realistic project applications.

2 Problem Formulation

AUVs have a variety of forces in the underwater movement, these forces include: gravity, buoyancy, hydrodynamic force, thrust, environmental interference, etc. So AUVs have a complex movement under the action of these forces. In order to control the AUVs effectively, we need to establish the mathematical model of AUVs firstly.

The AUV should be equipped with a sensor suite to receive the (relative) position information from its neighbor and determine its own position and orientation in the inertial reference frame. Assume that the AUV has fixed attitudes [10]. The translational dynamics of the AUV can be written as [11]:

$$\begin{cases} \dot{\mathbf{q}} = \mathbf{L}(\Theta)\mathbf{v} \\ \mathbf{J}\dot{\mathbf{v}} = -\mathbf{D}(\mathbf{v}) - \mathbf{g}(\Theta) + \boldsymbol{\mu} \end{cases} \tag{2.1}$$

where $\mathbf{q} = [x, y, z]^T$, $\Theta = [\eta, \sigma, \varsigma]^T$ denote position and attitude (described by Euler angles, i.e., roll η, pitch σ, and yaw ζ angles) vectors in the inertial reference frame, respectively, $\mathbf{L}(\Theta)$ is the kinematic transformation matrix from the body-fixed reference frame to the inertial reference frame, $\mathbf{v} = [u, v, w]^T$ is translational velocity vector in the body-fixed reference frame, $\mathbf{J}$ is the inertia matrix, $\mathbf{D}(\mathbf{v})$ is the damping matrix, $\mathbf{g}(\Theta)$ is the restoring force vector, and $\boldsymbol{\mu} = [X, Y, Z]^T \in R^3$ is the control force vector. For an angle $\alpha \in R$, denote $s_\alpha = \sin\alpha$, $c_\alpha = \cos\alpha$ for brevity. In detail,

$$\mathbf{L}(\Theta) = \begin{bmatrix} c_\zeta c_\sigma & -s_\zeta c_\eta + s_\eta s_\sigma c_\zeta & s_\zeta s_\eta + s_\sigma c_\zeta c_\eta \\ s_\zeta c_\sigma & c_\zeta c_\eta + s_\eta s_\sigma s_\zeta & -c_\zeta s_\eta + s_\sigma s_\zeta c_\eta \\ -s_\sigma & s_\eta c_\sigma & c_\eta c_\sigma \end{bmatrix} \tag{2.2}$$

$\mathbf{D}(\mathbf{v}) = \text{diag}\{d_{L_1} + d_{Q_1}|u|, d_{L_2} + d_{Q_2}|v|, d_{L_3} + d_{Q_3}|w|\}$, $\mathbf{J} = \text{diag}[j_1, j_2, j_3]$, $j_i, d_{L_i}, d_{Q_i} > 0, i = 1, 2, 3$ and $\mathbf{g}(\boldsymbol{\Theta}) = [(K - C)s_\alpha, -(K - C)c_\alpha s_\eta, -(K - C)c_\alpha s_\eta]^T$, where K and C represent the gravitational and buoyancy forces, respectively. For brevity, we denote $\mathbf{L} = \mathbf{L}(\boldsymbol{\Theta}), \mathbf{D} = \mathbf{D}(\mathbf{v}), \mathbf{g} = \mathbf{g}(\boldsymbol{\Theta})$. Note that $\mathbf{L}\mathbf{L}^{\mathbf{T}} = \mathbf{I_3}$. For calculation convenience, several notations can be constructed as:

$$x_1 = \mathbf{q}, \quad x_2 = \dot{\mathbf{q}} \tag{2.3}$$

Define $f_1(\sigma, \mathbf{v}) = \dot{\mathbf{L}}\mathbf{v} - \mathbf{L}\mathbf{J}^{-1}\mathbf{D}\mathbf{v} - \mathbf{L}\mathbf{J}^{-1}\mathbf{g}$, then, the original model can be transformed into

$$\dot{x}_1 = x_2, \ \dot{x}_2 = f_1(\sigma, \mathbf{v}) + \bar{\boldsymbol{\mu}}. \tag{2.4}$$

With $\bar{\boldsymbol{\mu}} = \mathbf{L}\mathbf{J}^{-1}\bar{\boldsymbol{\mu}}$.

3 Fuzzy Adaptive DSC Design

This section is devoted to provide the DSC approach with fuzzy approximation to construct controllers for AUV systems [12].

Step 1: Define the tracking error variable $e_1 = x_1 - x_{1d}$ with x_{1d} being the desired position signal. For the first subsystem of (2.4), choose the Lyapunov function candidate as $V_1 = \frac{1}{2}e_1^2$. Then, $\dot{V}_1 = e_1\dot{e}_1 = e_1(x_2 - \dot{x}_{1d})$.

Design the virtual control as

$$\alpha_1 = -k_1 e_1 + \dot{x}_{1d}. \tag{3.1}$$

With $k_1 > 0$ being the control gain. At present stage, we introduce a new variable α_{1d} and a time constant ξ_1, and then let α_1 pass through a first-order filter to obtain α_{1d} as

$$\xi_1\dot{\alpha}_{1d} + \alpha_{1d} = \alpha_1, \alpha_{1d}(0) = \alpha_1(0). \tag{3.2}$$

Construct $e_2 = x_2 - \alpha_{1d}$. From (3.1) and (3.2), we can obtain

$$\dot{V}_1 = e_1 e_2 + e_1(\alpha_{1d} - \alpha_1 + \alpha_1) - e_1\dot{x}_{1d} = -k_1 e_1^2 + e_1 e_2 + e_1(\alpha_{1d} - \alpha_1). \tag{3.3}$$

Step 2: Similarly, choose $V_2 = V_1 + \frac{1}{2}e_2^2$, we get

$$\begin{aligned} \dot{V}_2 &= \dot{V}_1 + e_2(f_1(\sigma, \mathbf{v}) + \bar{\boldsymbol{\mu}} - \dot{x}_{1d}) \\ &= -k_1 e_1^2 + e_1 e_2 + e_1(\alpha_{1d} - \alpha_1) + e_2(f_1(\sigma, \mathbf{v}) + \bar{\boldsymbol{\mu}} - \dot{x}_{1d}). \end{aligned} \tag{3.4}$$

According to the approximation property of FLSs in [13], the fuzzy logic system is introduced as: $f_2(Z) = f_1(\sigma, \mathbf{v}) - \dot{x}_{1d} = W_2^T S_2(Z) + \delta_2(Z), Z = [x_1, x_2, x_{1d}, \dot{x}_{1d}]^T$ with $\delta_2[Z]$ being the approximation error and satisfies $|\delta_2| \leq \varepsilon_2$. Nevertheless, ε_2 is considered to be an unknown positive constant. By using a straightforward calculation, we can get the following inequality:

$$e_2 f_2 \leq \frac{1}{2l_2^2} e_2^2 \|W_2\|^2 S_2^T S_2 + \frac{1}{2} l_2^2 + \frac{1}{2} e_2^2 + \frac{1}{2} \varepsilon_2^2. \tag{3.5}$$

At this step, we construct the virtual control function as

$$\bar{\boldsymbol{\mu}} = -k_2 e_2 - \frac{1}{2l_2^2} e_2^2 \hat{\omega} S_2^T S_2 - e_1 - \frac{1}{2} e_2. \tag{3.6}$$

Substituting (3.5) and (3.6) into (3.4) yields

$$\dot{V}_2 \leq -k_1 e_1^2 - k_2 e_2^2 + \frac{1}{2l_2^2} e_2^2 \left(\|W_2\|^2 - \hat{\omega} \right) S_2^T S_2 + \frac{1}{2} l_2^2 + \frac{1}{2} \varepsilon_2^2 + e_1(\alpha_{1d} - \alpha_1). \tag{3.7}$$

Define $\omega = \|W_2\|^2$, $\tilde{\omega} = \hat{\omega} - \omega$. $\hat{\omega}$ is the estimated value of ω. Then, we have

$$\dot{V}_2 \leq -k_1 e_1^2 - k_2 e_2^2 - \frac{1}{2l_2^2} e_2^2 \tilde{\omega} S_2^T S_2 + \frac{1}{2} l_2^2 + \frac{1}{2} \varepsilon_2^2 + e_1(\alpha_{1d} - \alpha_1). \tag{3.8}$$

Define $h = \alpha_{1d} - \alpha_1$. The following equations can be obtained:

$$\dot{h} = -\frac{\alpha_{1d} - \alpha_1}{\xi_1} - \dot{\alpha}_1 = -\frac{h}{\xi_1} + E. \tag{3.9}$$

With $E = \dot{\alpha}_1$. Choose the following Lyapunov function: $V = V_2 + \frac{1}{2} h^2 + \frac{\tilde{\omega}^2}{2r_1}$ with r_1 being positive constant. According to (3.8) and (3.9), the time derivative of V can be written as:

$$\begin{aligned} \dot{V} &\leq -k_1 e_1^2 - k_2 e_2^2 - \frac{1}{2l_2^2} e_2^2 \tilde{\omega} S_2^T S_2 + \frac{1}{2} l_2^2 + \frac{1}{2} \varepsilon_2^2 + e_1(\alpha_{1d} - \alpha_1) + h\dot{h} + \frac{\tilde{\omega}}{r_1} \dot{\tilde{\omega}} \\ &= -k_1 e_1^2 - k_2 e_2^2 + \frac{1}{2} l_2^2 + \frac{1}{2} \varepsilon_2^2 + e_1 h + h\dot{h} + \frac{\tilde{\omega}}{r_1} \left(\dot{\tilde{\omega}} - \frac{r_1}{2l_2^2} e_2^2 S_2^T S_2 \right). \end{aligned} \tag{3.10}$$

By use of (3.9), we construct the adaptive laws as:

$$\dot{\hat{\omega}} = \frac{r_1}{2l_2^2} e_2^2 S_2^T S_2 - m_1 \hat{\omega} \tag{3.11}$$

with m_1 and l_2 being positive constants.

Remark 1 Fuzzy logic systems can deal with the unknown system parameters and make the controller's structure quite simpler which makes the proposed scheme more appropriate to real world applications [14].

4 Stability Analysis

To confirm the stability of the proposed control scheme, substituting (3.11) into (3.10), one has

$$\dot{V} \leq -k_1 e_1^2 - k_2 e_2^2 + \frac{1}{2} l_2^2 + \frac{1}{2} \varepsilon_2^2 + e_1 h + h\dot{h} - \frac{m_1}{r_1} \tilde{\omega}\hat{\omega}. \tag{4.1}$$

By [15, 16], $|E|$ has a maximum E_M on compact set $|\Omega|$, $|E| \leq E_M$. Hence, $h\dot{h} \leq -\frac{h^2}{\xi_1} + |E_M||h| \leq -\frac{h^2}{\xi_1} + \frac{1}{2\varsigma} E_M^2 h^2 + \frac{\varsigma}{2}$ with $\varsigma > 0$. With Young's inequality, the following formula can be obtained: $e_1 h \leq \frac{1}{4} h^2 + e_1^2$, $-\tilde{\omega}\hat{\omega} \leq -\frac{\tilde{\omega}^2}{2} + \frac{\omega^2}{2}$.

Then, (4.1) can be rewritten as

$$\begin{aligned} \dot{V} \leq & -(k_1 - 1)e_1^2 - k_2 e_2^2 - \frac{m_1 \hat{\omega}^2}{2r_1} \\ & - \left[\frac{1}{\xi_1} - \left(\frac{1}{4} + \frac{1}{2\varsigma} E_M^2\right)\right] h^2 + \frac{1}{2} l_2^2 + \frac{1}{2} \varepsilon_2^2 + \frac{m_1 \omega^2}{2r_1} + \frac{\varsigma}{2} \leq -a_0 V + b_0 \end{aligned} \tag{4.2}$$

where $a_0 = \min\left\{2(k_1 - 1), 2k_2, m_1, 2\left[\frac{1}{\xi_1} - \left(\frac{1}{4} + \frac{1}{2\varsigma} E_M^2\right)\right]\right\}$ and $b_0 = \frac{1}{2} l_2^2 + \frac{1}{2} \varepsilon_2^2 + \frac{m_1 \omega^2}{2r_1} + \frac{\varsigma}{2}$.

(4.2) indicates that

$$V(t) \leq \left(V(t_0) - \frac{b_0}{a_0}\right) \mathrm{e}^{-a_0(t - t_0)} + \frac{b_0}{a_0} \leq V(t_0) + \frac{b_0}{a_0}, \quad \forall \geq t_0. \tag{4.3}$$

$e_i (i = 1, 2)$ and ω are in the compact set $\Omega = \left\{(e_i, \tilde{\omega}) | V(t_0) + \frac{b_0}{a_0}, \forall \geq t_0\right\}$.

So, all variables in this closed-loop system are bounded. Specifically, by using (4.3), one has $\lim_{t \to \infty} e_1^2 \leq \frac{2b_0}{a_0}$.

Remark 2 From the expressions of a_0 and b_0, the tracking error can be very small by choosing sufficiently large r_1 and small enough ε_2 and l_2 after the parameters

ς,ξ_1,k_i and m_1 are defined. The control precision can be improved by selecting k_i, but the computational load will increase as well. Moreover, the choice of smaller ξ_1 decreases the tracking error, but increases the magnitude of the dynamic surface derivatives.

5 Simulation Results

This simulation is run for AUV system with the parameters:

$$\mathbf{J} = \text{diag}\{175.4, 140.8, 140.8\},$$
$$\mathbf{D} = \text{diag}\{120 + 90|u|, 90 + 90|v|, 150 + 120|w|\},$$

$$K = 1148N, \quad C = 1108N, \quad \eta = \pi/5, \quad \sigma = -\pi/10, \quad \zeta = \pi/12.$$

We assume the AUV is static at $t = 0$ and its initial position is

$$\mathbf{q}(\mathbf{0}) = [-25.5, 17.7, -9.4]^T.$$

The dynamic surface controllers are utilized for this system and the control parameters are selected as:

$$k_1 = 200, \quad k_2 = 140, \quad \xi_1 = 0.001, \quad r_1 = 0.05, \quad m_1 = 0.028, \quad l_2 = 0.65.$$

The fuzzy membership functions are chosen as:

$$\rho_{F_i^l} = \exp\left[-\frac{(x+l)^2}{2}\right], \quad l \in N,\ l \in [-5, 5].$$

The desired signals are selected as:

$$x_{1d} = [x_d, y_d, z_d]^T = \begin{bmatrix} 0.5\sin(t) + \sin(05t), \sin(0.5t) + \cos(0.5t), \\ \cos(0.5t) + 0.5\cos(t) \end{bmatrix}^T.$$

Because AUVs are free in the underwater movement, the simulation is carried out from x, y, z axis respectively. This makes the simulation results more obvious. Figure 1 displays the tracking effect of x phase, Fig. 2 displays the tracking effect of y phase, and Fig. 3 displays the tracking effect of z phase. And Fig. 4 presents the error between x_1 and x_{1d}. It can be observed from Figs. 1, 2, 3 and 4 that the position signal of the AUV can be quickly adjusted to the desired signal. It is obvious that the controller is bounded and the fuzzy adaptive DSC approach developed in this paper can achieve a satisfied control performance.

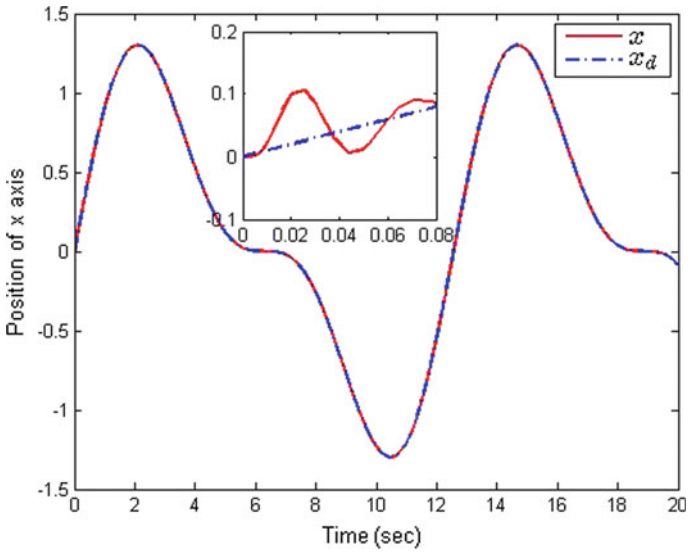

Fig. 1 x and x_d

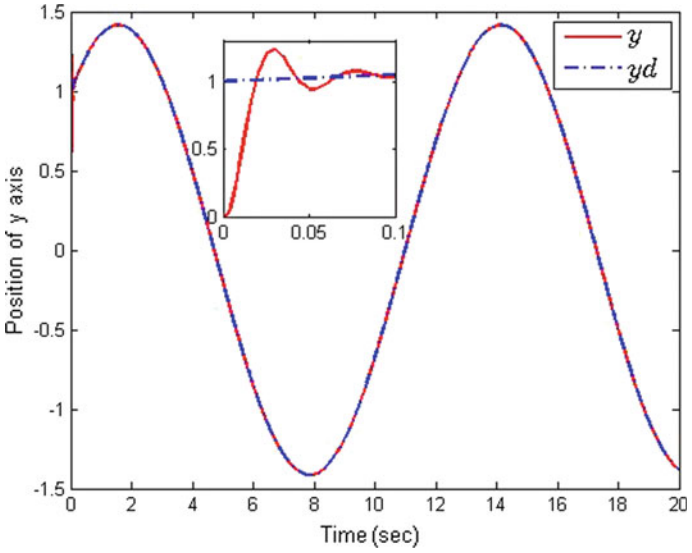

Fig. 2 y and y_d

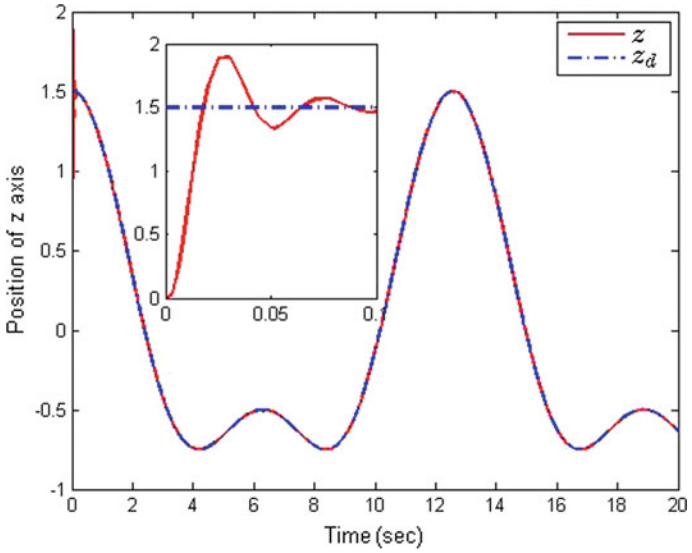

Fig. 3 z and z_d

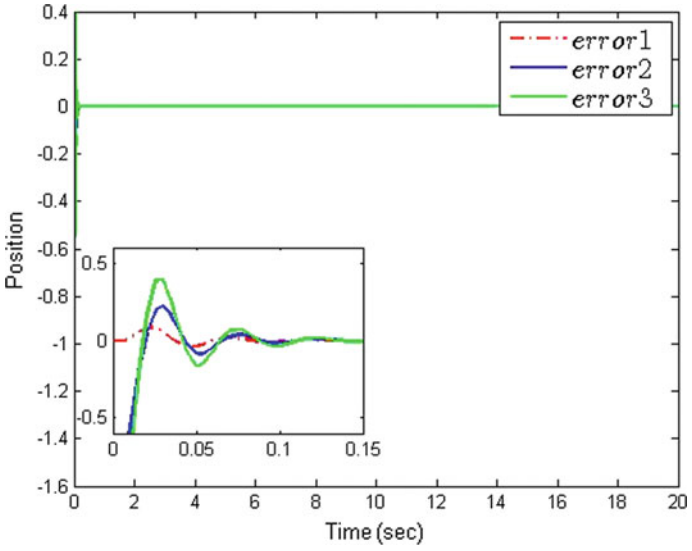

Fig. 4 The tracking error of x_1 and x_{1d}

6 Conclusions

The DSC technique based on adaptive fuzzy approximation is developed for AUVs, which can eliminate the influences from the parameter uncertainties. The present method can also guarantee that the tracking errors converge into a small neighborhood of the origin. Compared with the traditional adaptive controller, the control method is simple in structure and easy to be realized in Engineering. Simulation results show the usefulness of the proposed method.

Acknowledgements This work was partially supported by the Natural Science Foundation of China (61573204, 61501276, 61603204, 61573203), Qingdao Postdoctoral Application Research Project (2015120), Qingdao Application Basic Research Project (16-5-1-22-jch) and Taishan Scholar Special Project Fund.

References

1. Li S, Wang X (2013) Finite-time consensus and collision avoidance control algorithms for multiple AUVs. Automatica 49(11):3359–3367
2. Wang X, Li S, Shi P (2014) Distributed finite-time containment control for double-integrator multiagent systems. IEEE Trans Cybern 44(9):1518–1528
3. Song F, Smith SM (2000) Design of sliding mode fuzzy controllers for an autonomous underwater vehicle without system model. Oceans 2(2):835–840
4. Guo J, Chiu FC et al (2003) Design of a sliding mode fuzzy controller for the guidance and control of an autonomous underwater vehicle. Ocean Eng 30(16):2137–2155
5. Zhang L, Pang Y, Su Y, Liang Y (2008) HPSO-based fuzzy neural network control for AUV. Control Theory Technol 6(3):322–326
6. Zhao L, Jia Y (2016) Neural network-based adaptive consensus tracking control for multi-agent systems under actuator faults. Int J Syst Sci 47(8):1931–1942
7. Liu Y (2011) Autonomous underwater vehicle control based on adaptive backstepping method. Syst Eng Electron 33(3):638–642
8. Yip P, Hedrick J (1998) Adaptive dynamic surface control: a simplified algorithm for adaptive backstepping control of nonlinear systems. Int J Control 71(5):959–979
9. Yu J, Shi P et al (2015) Observer and command filter-based adaptive fuzzy output feedback control of uncertain nonlinear systems. IEEE Trans Ind Electron 62(9):5962–5970
10. Piovan G, Shames I, Fidan B et al (2008) On frame and orientation localization for relative sensing networks. In: IEEE conference on decision & control, vol 49(1), pp 2326–2331
11. Fossen TI (2002) Marine control systems: guidance, navigation and control of ships, rigs and underwater vehicles. Marine Cybern
12. Yu J, Shi P et al (2015) Neural network-based adaptive dynamic surface control for permanent magnet synchronous motors. IEEE Trans Neural Networks Learn Syst 26(3): 640–645
13. Wang L, Mendel J (1992) Fuzzy basis functions, universal approximation, and orthogonal least-squares learning. IEEE Trans Neural Networks 3(5):807–814
14. Yu J, Shi P, Yu H, Chen B, Lin C (2015) Approximation-based discrete-time adaptive position tracking control for interior permanent magnet synchronous motors. IEEE Trans Cybern 45(7):1363–1371

15. Yu J, Chen B, Yu H (2011) Adaptive fuzzy tracking control for the chaotic permanent magnet synchronous motor drive system via backstepping. Nonlinear Anal Real World Appl 12 (1):671–681
16. Yu J, Chen B, Yu H (2010) Position tracking control of induction motors via adaptive fuzzy backstepping. Energy Convers Manage 51(11):2345–2352

Self-organized Task Allocation in a Swarm of E-puck Robots

Qiaoyu Li, Xiaolong Yang, Yuying Zhu and Jianlei Zhang

1 Introduction

The study on task allocation behaviors realized by self-organization receives much attention nowadays, which has a wide range of applications in artificial intelligence and engineering areas. Division of labor, where thousands of individuals in nature perform specific tasks can be seen as the hallmark of insect societies [1–3]. Daily experience tells us that the division of labor is a common phenomenon, in which different sub-tasks may require different effort or cost with others [4, 5]. Group behaviors achieved by self-organization, can be seen as a result from local interactions without central control or global information exchange.

Most mechanisms for promoting effective task allocation results have been proposed. Among these mechanisms, an often-used approach is based on thresholds of tasks, where the switching of the agents' strategy choices are related with the threshold value [6, 7]. This consideration is closely related with the hints provided by the observation from animal societies. The settings of threshold is on the strength of feeling a stimulus which describes the "degree of urgency" of a task to be performed [7]. It is thus understandable that larger stimulus of a task will attract more agents to engage in the task performing. Besides, many works have made their contributions in the study of division of labor. The study in [8] focuses on a foraging task including two sub-tasks, called harvest and store. Robinson [9] investigate the potential ways for effective task allocation, by setting a scenario where the employed robots collect the randomly distributed objects to accumulate them in a cluster. Michael J.B. Krieger et al. use robots to simulate agents to conduct a foraging task by employing the method based on the thresholds [10], where the strategy switching occurs when a given parameter in the surroundings

Q. Li · X. Yang · Y. Zhu · J. Zhang (✉)
Department of Automation, College of Computer and Control Engineering,
Nankai University, Tianjin, China
e-mail: jianleizhang@nankai.edu.cn

Z. Deng (ed.), *Proceedings of 2017 Chinese Intelligent Automation Conference*,
Lecture Notes in Electrical Engineering 458,
https://doi.org/10.1007/978-981-10-6445-6_17

reaches a threshold. The works by Sendova-Franks and Franks [11] provide an equation which is helpful for calculating the instantaneous rate of energy, which is fundamental to the strategy choices of foraging robots in their study.

In the collective systems, collaboration dilemmas usually describe the scenario where the conflicts between the best decision of an individual and that of the group arise [12]. Rational agents, who attempt to maximize their own benefits, may thus attempt to free-ride on the others—benefiting from the contributions of others without offering their own to the group. In investigating this problem the often-used tool for modelling the dilemma is evolutionary game theory [13–15]. In other words, cost and benefits are the key factors for tasks, which will influence individual's choice. From the perspective of game theory and benefits-maximizing pursuit of rational agents, division of labor, can be seen as a particular or further developed form of cooperation. The effective distribution of sub-tasks execution will result a better performance of the system, though different group members may bear unequal costs for the sub-tasks [16, 17].

By feat of game theory, we study the collective behaviors in the form of tasks by a swarm of robots whose personalities are described by their strategies. Then, assumptions made on the robotic platform make these results rather interesting from a theoretical perspective. A single robot is equivalent to an individual in the game theory. The robot task selection can be seen as a game situation. The task assignment of multi-robot system is to select the most effective task by each robot according to the certain goal in a game state. In this paper, we will study the relationship between agents' payoff and agents' cooperative level in different state and try to find some rules which are useful for agents to execute task effectively.

The paper is organized as follows. Section 2 describes the experimental platform design. Sections 3 and 4 is contributed to introduce experimental setup. Section 5 displays the experimental results. Finally in the last section concluding comments are given.

2 Experimental Platform Design

The experiment platform includes two parts: hardware platform and software platform. The hardware platform consists of a host computer, two USB cameras, 4 E-puck robots and an experiment Table (240 cm*240 cm). The host computer is responsible for image processing, running game and path planning algorithm. The USB camera can catch the real-time position information of the robots (Fig. 1).

The software platform includes three modules: target location and recognition module, communication module, and algorithm module. The target recognition and recognition module is mainly responsible for robots' localization. It uses openCV [2], a visual library, to implement the recognition of color marks on robots, which contains position information of robots. The communication module is based on the Bluetooth communication. The algorithm module is divided into two parts: game algorithm, path planning and obstacle avoidance algorithm. Game algorithm is

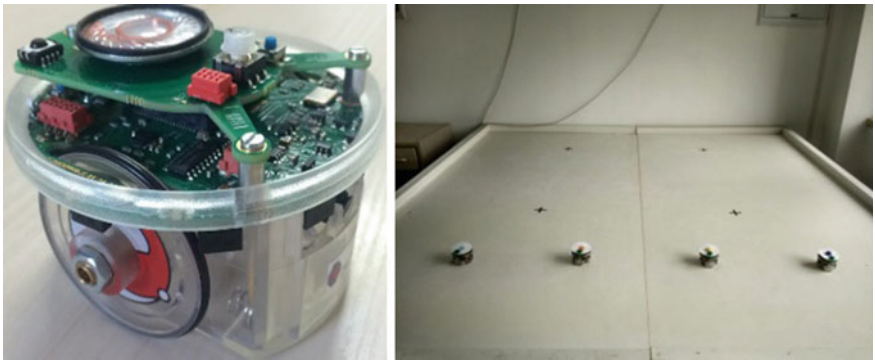

Fig. 1 *Left* the used E-puck robot; *right* settings of the experiment platform

mainly responsible for robots' decision-making and payoff calculation. Path planning [1] and obstacle avoidance algorithm refers to leading robots to run from the current location to the target location, and meanwhile avoid collision with obstacles in the planned route.

3 Experimental Setup

Here 4 E-puck robots are employed for performing the collective task, whose maneuverability and intelligence improves their applicability. It has a pair of driving wheels and their real-time position and angle are available. The experiment settings are: (1) initial position: 4 robots are randomly scattered at the experimental table. (2) initially target site: to increase the conflicts between the robots, robots' initial target site is randomly selected. (3) objects: to move towards the 4 target sites which can form some spatial pattern, such as the square shown in Fig. 2. (4) conflicts: the conflicts for selecting the same site is adjusted by the evolutionary game theory, where strategy choices are endowed with the robots.

4 The Individual Behavior of Robots

Searching state: Robots randomly select a target site in the initial state. When the robot approaches the target site within a certain range, she will check whether the target site has been occupied. If not, robot continues to move to the chosen target. Otherwise, robot must determine whether to give up the target (already has been occupied by others) or not. Insisting on this site will face potential conflicts with the robots who have already been in the site. The results of conflicts depend on the

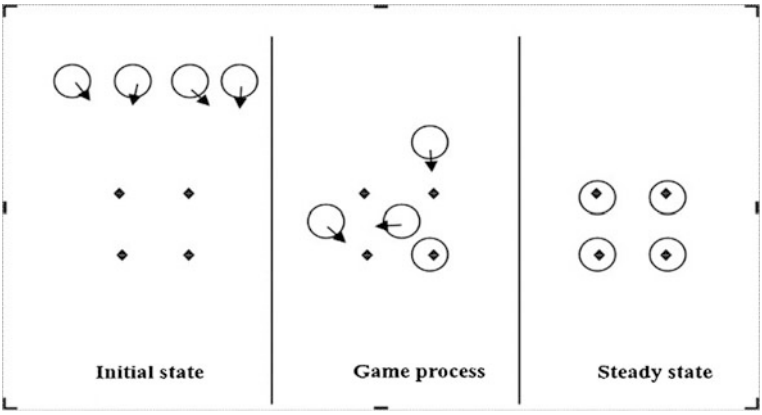

Fig. 2 The illustration about the evolving process of the multi-robots. Initially, robots randomly select the target site. Conflicts results for one site depend on the strategy choices of robots

strategy choice (cooperation or defection) of the involved robots. Whereas giving up the target, means the robot run to another site instead. The above process until it stops at a target position.

Occupation state: Robot that has stopped at the target point is on the Occupation state. The robot on the occupation state checks if any other robot is approaching to the target site occupied by itself. When other robots are coming to fight for the target point, the robot will determine whether to leave. If robot gives up the occupied site, it turns to search state.

Robot's payoffs and cost: The collected payoff is related to the task choice and the completion of the chosen tasks. If the robots can finally form the specified spatial pattern, the collective task succeeds. Successful task will bring robots a payoff denoted by b. Failed task will bring nothing to the group members. To perform the task, the consumed energy of E-puck robots is related to time and distance. Besides, the time and distance needed to achieve a steady state in performing the tasks are noteworthy indicators. And, they can help us to measure how the employed method influences the collaboration behaviors. Therefore, the robots' payoffs are described by,

$$\boldsymbol{R} = \boldsymbol{b} - \boldsymbol{\omega_1 e^{t/\alpha}} + \boldsymbol{\omega_2 e^{d/\beta}} \tag{1}$$

Here $b = 100$ for successful task, and $b = 0$ for failed one. t is the time that robot spends on the task. d is the distance that robot runs for the task. α and β are scale factors.

For a robot suiting on the chosen target, she faces two choices when another robot gets close to her site: cooperation or defection. Here, we employ $\boldsymbol{P_{sea}}$ to describe the probability that robot chooses to be a cooperator who will leave the current site and choose a new target. $\boldsymbol{P_{occ}}$ describes the probability that the focal robot chooses to be a defector who will stay in her current target.

5 Experiment Results

In collecting the experiment results, our focus is put on three main parameters: the success rate of the tasks, the performance index and the payoffs of robots. The success rate is fraction of successfully-performed tasks in the whole experiments. The performance index is the number of appointed sites which are occupied by robots in experiments. If all the sites are occupied by the robots, i.e. they finally self-organize into the specified shape, the value of the performance index will be 4. If only two robots steadily situate in the specified sites, while other two sites are empty, the value of the performance index will be 2. The payoffs are collected and calculated by the $\boldsymbol{R} = \boldsymbol{b} - \omega_1 e^{t/\alpha} + \omega_2 e^{d/\beta}$.

Figure 3 clearly shows that the success rate reaches the highest for the settings: $\boldsymbol{P_{sea}} = \mathbf{1}$ and $\boldsymbol{P_{occ}} = \mathbf{0}$ or $\boldsymbol{P_{sea}} = \mathbf{0}$ and $\boldsymbol{P_{occ}} = \mathbf{1}$. It means that, if the robots in the searching state will leave the already occupied site and choose a new target (i.e. to be a cooperator), meanwhile the robots who occupied this site will stay (i.e. to be a defector), what will benefit the success performing of the specified tasks. In the same way, if the robots in the searching state will insist in occupying the already occupied site, meanwhile the occupants leave this site which causes conflicts, this will promote the successful performance of the tasks. The reason lies on the fact

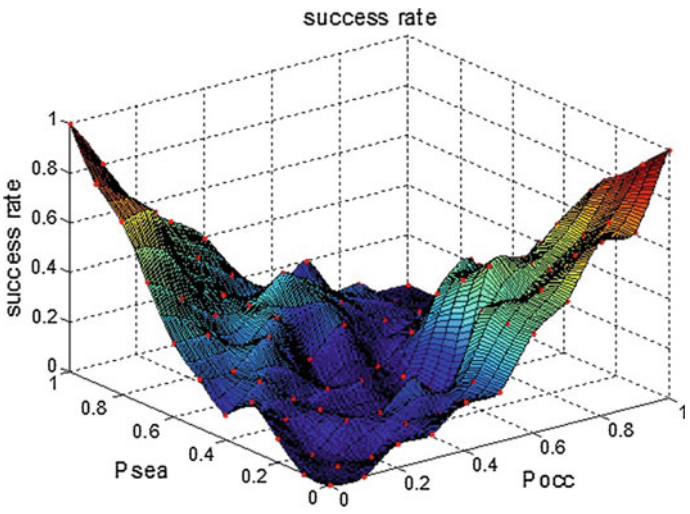

Fig. 3 The success rate of the robotics in performing tasks as a combination function of P_{sea} and P_{occ}. When conflicts for one site occur, P_{sea} is the probability that robot chooses to be a cooperator who will leave the current site and choose a new target. Similarly, P_{occ} describes the probability that the focal robot chooses to be a defector who will stay in her current target, when conflicts for one site occur. Here, it is clear that the success rate reaches the highest for the settings: $P_{sea} = 1$ and $P_{occ} = 0$ or $P_{sea} = 0$ and $P_{occ} = 1$

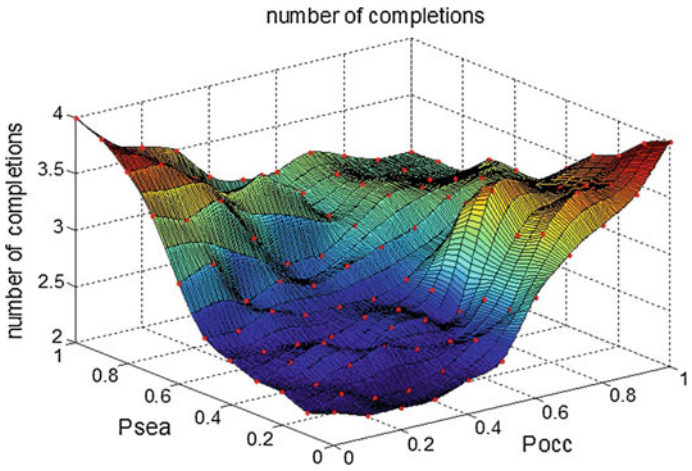

Fig. 4 The fraction of number of completions (i.e. performance index) as a function of P_{sea} and P_{occ}. The number of completions describes the number of robots who stay at a target position when task ends. It is clear that high number of completions means the close to success. As the figure above depicted, the number of completions is low when P_{sea} and P_{occ} are at a low level. It reaches the highest when $P_{sea} = 1$, $P_{occ} = 0$ or $P_{sea} = 0$, $P_{occ} = 1$. The number of completions is low when P_{sea} and P_{occ} are at a low level. The number of completions is high when P_{sea} and P_{occ} are at a high level

that, the cooperation-cooperation will make it be easier for the appearance of vacant sites. While the defection-defection will lead the system to evolve into a state of an infinite loop where the two robots conflict with one site.

Figure 4 suggests that the number of completions reaches a higher level for the settings of larger $\boldsymbol{P_{sea}}$ or larger $\boldsymbol{P_{occ}}$. It means that, larger cooperation probability of the robots will help more specified sites to be occupied by robots. Notably, it is irrespective of the state of robots, either in the searching state or occupation state. Thus, the performance of tasks is closely related with the strategy choice of the robots. However, the successful performance of tasks depends on more limited conditions. To facilitate the understanding, Fig. 5 provides the general view of the gaming process.

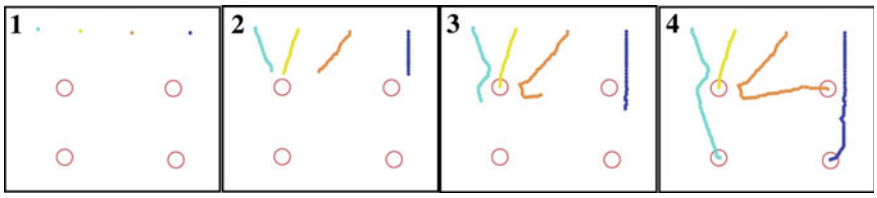

Fig. 5 The process for performing the aggregation task in the robotic swarm. *1* Robots settings at the initial state. *2* Robots are moving to the chosen targets. *3* The conflicts for a site. *4* The steady state where no one changes her choice

6 Conclusions

Conflicts of interest and self-adjustment are pivotal elements in studying the problem of task allocation or division of labor in a swarm of agents. Different from the traditional approach, we employ the evolutionary game theory to study the self-organization of individual behaviors among E-puck robots. Experiment results show that robots can gain the highest payoffs under the following conditions: robots cooperate when being in the searching state and defect in the occupied state, robots defect in the searching state and cooperate in the occupied state. The coordination driven by strategy choice can help us get more hints about the solutions for the effective division of labor among selfish agents. The successful performance of the collective task can be better realized by the agents with rationality and selfishness.

References

1. Agassounon W, Martinoli A, Goodman R (2001) A scalable, distributed algorithm for allocating workers in embedded systems. IEEE international conference on systems 5(2):3367–3373
2. Brutschy A, Pini G, Pinciroli C, Birattari M, Dorigo M (2014) Self-organized task allocation to sequentially interdependent tasks in swarm robotics. Auton Agent Multi-Agent Syst 28 (1):101–125
3. Campo A, Dorigo, M (2007) Efficient multi-foraging in swarm robotics. European conference on advances in artificial life, vol 4648 LNAI. Springer, Berlin, pp 696–705
4. Duarte A, Weissing FJ, Pen I, Keller L (2011) An evolutionary perspective on self-organized division of labor in social insects. Annu Rev Ecol Evol Syst 42(1):91–110
5. Gerdes J, Becker MHG, Key G, Cattoretti G, Sanders HW, Smith AG et al (1992) Letters to the editor. J Pathol 168(1):85–87
6. Karsai I, Wenzel JW (1998) Productivity, individual-level and colony-level flexibility, and organization of work as consequences of colony size. Proc Natl Acad Sci U S A 95(15): 8665–8669
7. Kreiger M, Billeter J (2000) The call of duty: self-organized task allocation in a population of up to twelve mobile robots. Robot Auton Syst 30(1):65–84
8. Wilson EO (1978) Caste and ecology in the social insects. Monogr Popul Biol 12(3):1
9. Robinson GE (1992) Regulation of division of labor in insect societies. Annu Rev Entomol 37(1):637
10. Seeley TD (1989) The honey bee colony as a superorganism. Am Sci 77(6):546–553
11. Sendova-Franks A, Franks NR (1993) Task allocation in ant colonies within variable environments (a study of temporal polyethism: experimental). Bull Math Biol 55(1):75–96
12. Stewart AJ, Plotkin JB (2016) Small groups and long memories promote cooperation. Sci Rep 6(s 1–3): 26889
13. Stivala A, Kashima Y, Kirley M (2016) Culture and cooperation in a spatial public goods game. Phys Rev E 94(3–1):032303
14. Van den Berg P, Molleman L, Weissing FJ (2015) Focus on the success of others leads to selfish behavior. Proc Nat Acad Sci U S A 112(9):2912–2917

15. Xu Z, Zhang J, Zhang C, Chen Z (2016) Fixation of strategies driven by switching probabilities in evolutionary games. Europhys Lett 116(5):58002
16. Zhang J, Chen Z (2016) Contact-based model for strategy updating and evolution of cooperation. Physa D Nonlinear Phenom 323–324(2):27–34
17. Zhang J, Zhang C, Cao M, Weissing FJ (2015) Crucial role of strategy updating for coexistence of strategies in interaction networks. Phys Rev E Stat Nonlin Soft Matter Phys 91 (4):042101

A New Circuit Design for Chaotic Oscillator

Wenjing Hu

1 Introduction

In recent years, the chaos theory is deeply studied in various fields. Due to the extreme sensitivity of chaotic systems to initial parameters, they can be used for weak signal detection and extraction. In the chaotic systems known, Duffing oscillator is more suitable for detecting sinusoidal signal, which is the current research hot spot in many fields, such as exploration seismology, unmanned plane inspection, etc. [1–6]. However, most of the materials are limited to pure numerical simulation, and the Duffing circuit has not been studied in depth.

There are fewer simulation Duffing circuits, but they are only adequate for very low frequencies. Such as reference [7]. Simulation results showed that with the increase of ω, it is more and more inconsistent with the theoretical analysis. The signal frequency is limited to about 1 Hz.

In order to solve this problem, we establish a new Duffing equation suitable for high frequency by a time-scale transformation, based on it, we design a new Duffing circuit for low to high frequency signals, and effectively solve the instantaneous saturation problem of the circuit. We also introduce the operational block diagram and design process for the important circuit unit. At last we study its initial sensitivity at high frequency $\omega = 10^6$ rad/s (159,155 Hz) by Multisim software. Simulation results show that the circuit is very sensitive to weak sinusoidal signals. It provides the basis for the practical application of Duffing oscillator.

W. Hu (✉)
School of Electrical Engineering of Shandong University,
Jingshi Road 17923, Jinan 250061, China
e-mail: hwj@sdu.edu.cn

Z. Deng (ed.), *Proceedings of 2017 Chinese Intelligent Automation Conference*,
Lecture Notes in Electrical Engineering 458,
https://doi.org/10.1007/978-981-10-6445-6_18

2 A New Method to Establish Duffing Circuit

As we know, the commonly used Duffing equation to design circuit is

$$\begin{cases} \frac{dy_1}{dt} = y_2 \\ \frac{dy_2}{dt} = r\cos\ \omega t - ky_2 + y_1^3 - y_1^5 \end{cases} \tag{1}$$

where k is the damping ratio, generally let $k = 0.5$ [1], y_1^3–y_1^5 is the nonlinear restoring force, $r\cos\omega t$ is the forced periodic term, ω is the angular speed. If k is fixed, With the increase of r, the system experiences the homoclinic orbit, period doubling bifurcation, chaos, the chaotic critical state (chaos, but on the verge of changing to the large-scale periodic state), until r is greater than a threshold r_d, the system enters the large-scale periodic state [2]. By observing the complete different phase trajectories between the chaotic state and the large-scale periodic state, we can identify the weak sinusoidal signals [4, 5].

According to the minikev method, only in the case of low frequency, stable invariant manifolds and unstable invariant manifolds in the Poincare map of the Eq. (1) will intersect, then homoclinic intersections appear [1]. So the Duffing system may enter the chaos. But if the frequency is higher, the system can not enter the chaotic state. To solve above problem, we make a time scale transformation for (1), and obtain a new Duffing system as

$$\begin{cases} \frac{dy_1}{dt} = \omega y_2 \\ \frac{dy_2}{dt} = \omega(r\ \cos(\omega t) - 0.5y_2 + y_1^3 - y_1^5) \end{cases} \tag{2}$$

In the new phase space, the phase velocities y_1 and y_2 increase ω times. As long as we change the value of the ω in (2), it can be adapted to different frequencies.

Equation (2) is a new Dufffing system to be used in this paper. According to it, we will design a new type of Duffing circuit. For convenience, we rewrite (2) in integral form. let $r = \sqrt{2}f$, where f is the root mean square (RMS) value, then use $\sqrt{2}f\ \sin\omega t$ to replace the forced periodic term in (2), finally integrate it on both sides and get [2].

$$\begin{cases} y_1 = \int \omega y_2 dt + C_1 \\ y_2 = \int \omega(\sqrt{2}f\ \sin\ \omega t - 0.5y_2 + y_1^3 - y_1^5)dt + C_2 \end{cases} \tag{3}$$

where C_1 and C_2 are integral constants. If $y_1(t_0) = y_1(0) = 0$, $y_2(t_0) = y_2(0) = 0$, C_1 and C_2 are both zero. Before integration, y_2 and $(\sqrt{2}f\ \sin\omega t - 0.5y_2 + y_1^3 - y_1^5)$ are multiply by ω at first respectively. When ω is large, such as ω is 10^6 rad/s, the value of the integral item will be very large. In the design of the circuit, even we can achieve a 10^6 amplification by a high magnification amplifier, but because the

amplifier's supply voltage is generally ±15 V, the circuit will be instantaneous saturation. To solve this problem, we do integral calculation at first, and then multiply by ω, so (3) becomes

$$\begin{cases} y_1 = \omega \int_0^t y_2 dt \\ y_2 = \omega \int_0^t (\sqrt{2} f \ \sin \omega t - 0.5 y_2 + y_1^3 - y_1^5) dt \end{cases} \tag{4}$$

If we let the circuit do the integral at first and then multiply by ω, the corresponding voltages will be reduced ω times, and then magnified ω times. Thus the circuit can successfully avoid the momentary saturation. The circuit established according to (4) is a new type of Duffing circuit, which can be achieved by devices such as op amps.

3 Detailed Design of the Duffing Circuit

We draw an overall operational block diagram which can show the function of each unit circuits as shown in Fig. 1. For convenience, the labels of elements in Figures in this paper are consistent. To illustrate the proportional coefficient K of the inverting amplifier 1# and 2# in Fig. 1, an integrator is first introduced as shown in Fig. 2. Its input and output voltages meet the following relationship

$$U_0 = -\frac{1}{RC} \int_0^t U_i dt \tag{5}$$

The output voltage U_o is proportional to the integral of the input voltage U_i with a proportion coefficient of $-1/(RC)$. Therefore, R_1C_1 and $R_{15}C_2$ in Fig. 1 are introduced by taking into account of this proportional coefficient. As long as the R_1C_1 and $R_{15}C_2$ are appropriately adjusted, the circuit can achieve signal detection

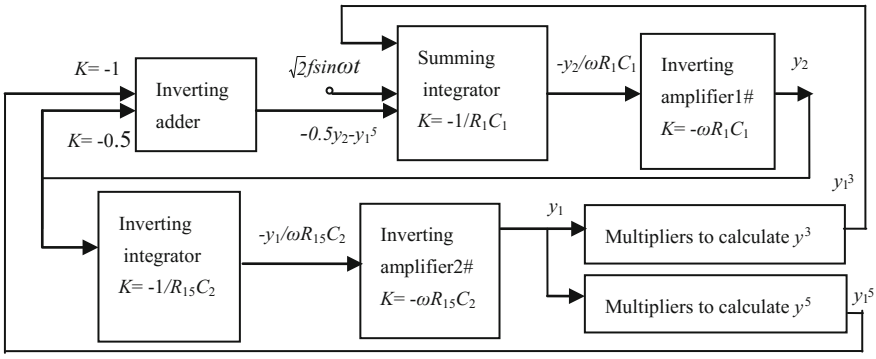

Fig. 1 Operational block diagram

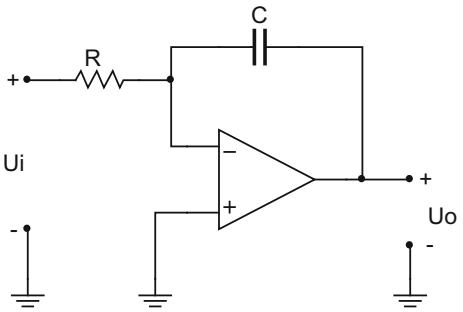

Fig. 2 Analog integrator

from low to high frequency. For example, we let $\omega = 10^6$ rad/s ($f = 159{,}155$ Hz), the magnification of the inverting amplifier 1# $K_1 = R_1C_1\omega$. The closed-loop magnification of single-stage op amp is generally less than 100. Here let $K_1 = 10$, then

$$R_1C_1 = k_1/\omega = 1/10,00,000 = 10^{-5} \tag{6}$$

Let $K_2 = 1$, where K_2 is the amplification of the inverting amplifier 2#, we obtain

$$R_{15}C_2 = k_2/\omega = 1/10,00,000 = 10^{-6} \tag{7}$$

So we can select the appropriate R_{15} and C_2 according to (7). Unit circuits include the summing integrator, inverting integrator, inverting adder, inverting amplifier 1# and 2# and multipliers. Here we introduce the design of the inverting integrator in detail. The summing integrator design is similar to the inverting integrator. Others are conventional design [8]. The integrator is shown in Fig. 3, and its integral relationship is expressed as

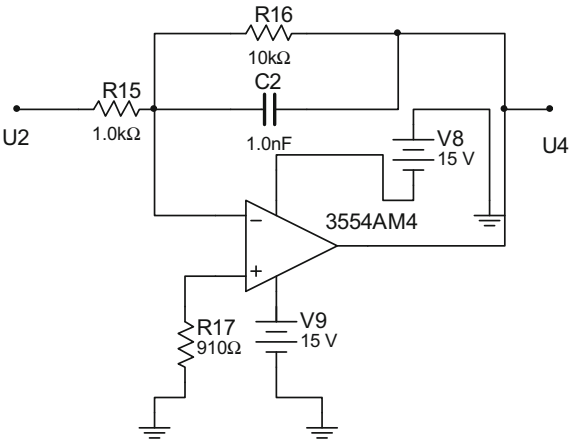

Fig. 3 Inverting integrator

$$U_4 = -\int_0^t U_2 dt \tag{8}$$

From (7), we know the time constant $\tau_f = R_{15}C_2 = 10^{-6}$ s, τ_f is determined by the closed-loop magnification K_2 of the inverting amplifier 2#. If the maximum output of the amplifier is V_{om}, and its input is a sinusoidal signal, according to the design principle of the integrator, $R_{15}C_2$ must meet the relationship $V_{om} \geq r/R_{15}C_2\omega$.

For the Duffing circuit, r is generally less than 2, the op amp DC power supply voltage is generally ±15 V, V_{om} is usually about 70% of the supply voltage, so it is generally ±10 V, thus $R_{15}C_2 \geq 1.9 \times 10^{-7}$. The value of $R_{15}C_2$ is 10^{-6}, which is satisfied the above requirements. Here choose $R_{15} = 1.0$ kΩ, $C_2 = 1.0$ nF. In conventional design, R_{16} is 10 times of R_{15}, Here let $R_{16} = 10$ kΩ.

In Fig. 4, ω_f is the intersection of the ideal integrator amplitude-frequency characteristic and the horizontal axis, Its value $\omega_f = 1/R_{15}C_2 = 10^6$ rad/s.

ω_{of} is the frequency corresponding to the intersection of the ideal integrator amplitude-frequency characteristic and the open-loop amplitude-frequency characteristic of the op amp, and $\omega_{0f} = \omega_f/A_0$.

($\omega_{0f} \sim \omega_c$) is the normal working section of the integrator. Here let the open-loop voltage magnification of the op amp $A_0 = 10^5$, then

$$\omega_{0f} = \frac{\omega_f}{A_0} = \frac{10^6}{10^5} = 10 \text{ rad/s} \tag{9}$$

Since the cutoff frequency $\omega_0 > \omega_{of} = 10$ rad/s, ω_0 is at least 10 rad/s. Therefore, the unity gain bandwidth $\omega_c = A_0\omega_0 = 10^6$ rad/s. ω_c is at least 10^6 rad/s, namely $\omega_c > 10^6$ rad/s.

Duffing circuit often works in the large signal state. The key specification for its instantaneous response is the slew rate S_r. When the input signal is a sine wave, the maximum slope of the waveform should be less than the slew rate of the op amp.

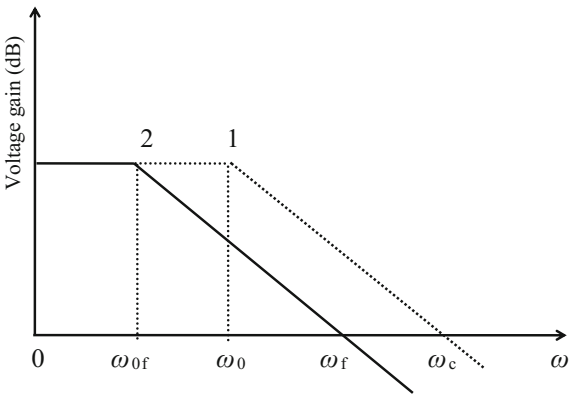

Fig. 4 Amplitude frequency characteristics of the integrator. 1—Open loop amplitude frequency characteristic of operational amplifiers. 2—Amplitude frequency characteristics of ideal integrator

If input voltage $u_i = r\cos\omega t$, the collector voltage of the amplifier output stage is

$$u_o = -\frac{1}{R_{15}C_2}\int_0^t r\cos(\omega t)dt = \frac{-r}{R_{15}C_2\omega}\sin\omega t \tag{10}$$

The slope of u_o is

$$\frac{du_0}{dt} = \frac{-r}{R_{15}C_2}\cos\omega t \tag{11}$$

The maximum slope of u_o is $r/R_{15}C_2$. Since r is less than 2, so the maximum slew rate is $S_{rmax} > r/R_{15}C_2 = 2\times10^6$ V/s. Therefore, the selected op amp should have a slew rate greater than 2×10^6 V/s. Here we emphasize that the slew rate design is very important, but easy to be ignored. If the slew rate is not appropriate, the circuit can not work properly at all. In summary, the selected op amp will be that its cutoff frequency ω_0 is greater than 10 rad/s, unity gain bandwidth ω_c is greater than 10^6 rad/s, open-loop voltage amplification A_0 is 10^5, slew rate is greater than 2×10^6 V/s. Here we choose 3554 AM as the op amp.

4 Circuit Simulation

A new Duffing circuit is as shown in Fig. 5. Its simulations are done by Multisim software [9]. In Fig. 5, V_1 is a sinusoidal voltage source, multipliers are A_1–A_4, and other elements are selected from the Multisim device library. The output voltage U_2 of the 3554AM2 corresponds to y_2, and the output voltage U_5 of the 3554AM5 corresponds to y_1 in Eq. (4). Timing diagrams and phase plane orbit diagrams can be observed by connecting the B-channel of oscilloscope XSC1 to voltage U_5 and A-channel to voltage U_2. If the input signal source V_1 is

$$u = r\sin\omega t = \sqrt{2}f\sin\omega t \tag{12}$$

where r changes between 0 and 1 V, and correspondingly EMS f varies between 0 and 0.707 V, ω is 10^6 rad/s. Since the power supply in Multisim appears as EMS values, it is convenient to change f for voltage adjustment. In addition, the oscilloscope scale is that each division represents 500 mV in phase plane orbit diagrams.

When f is from 0 to 1, from simulation results we know the system experiences the periodic oscillation, homoclinic orbit, chaos, and finally large-scale periodic state. In particular, when $f = 0.52556171$ V, the system appears as a critical chaotic state, as shown in Fig. 6a. If the power supply EMS value increases 0.00000001 V, namely $f = 0.52556172$ V, the circuit is from the chaotic state to large-scale periodic state, as shown in Fig. 6b.

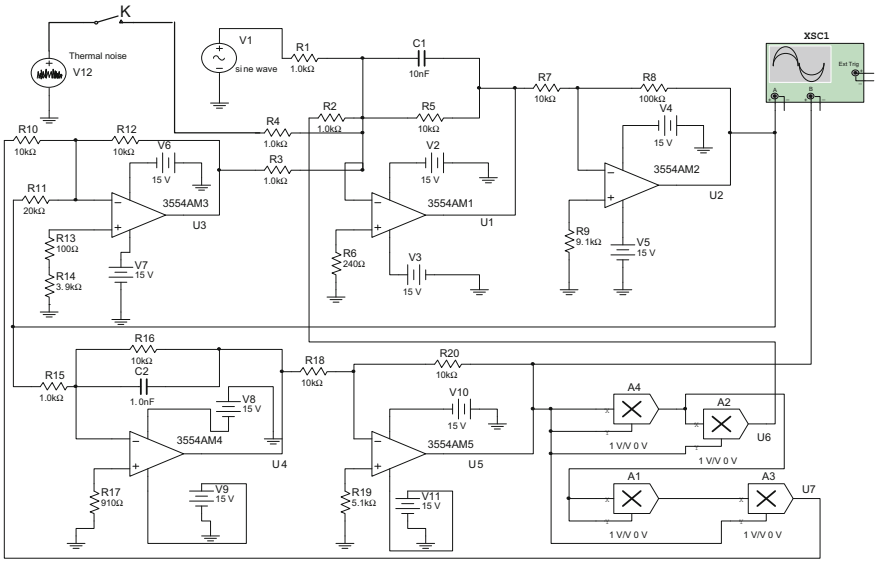

Fig. 5 New Duffing chaotic circuit

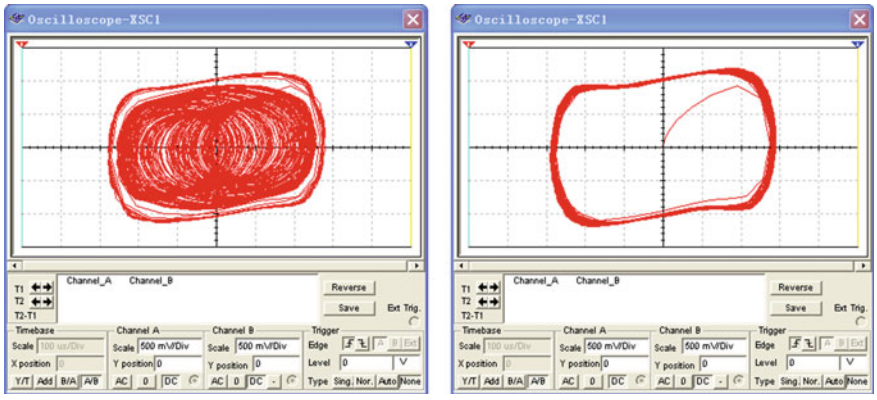

(a) f=0.5255617V, chaos (b) f=0.52556172, large-scale periodic state

Fig. 6 Phase plane orbit diagrams and timing diagrams of U_5

Simulation results show that this new Duffing circuit has the extreme sensitivity to the initial condition. Thus it has the prerequisite to detect weak sinusoidal signals at high frequency.

5 Summary

Since the common Duffing circuit is limited to low frequency signals, this paper proposes a new type of Duffing detection circuit which effectively avoids instantaneous saturation at high-frequency. If the op amp performance is good enough, it can realize the wide frequency detection from low frequency to high frequency by adjusting the parameters of several elements.

It also gives a circuit operational block diagram, and then according to the block diagram, gives the detailed design of the main unit circuit.

We make simulations on the new Duffing chaotic circuit by the Multisim software. Phase plane orbit diagrams and timing diagrams are observed by the oscilloscope. Simulation results prove that the circuit is a chaotic system and has the extreme sensitivity to the initial condition. Therefore it has the prerequisite to detect weak sinusoidal signals at high frequency.

References

1. Li Y, Yang B (2004) Chaotic oscillator detection. Electronics Industry Press, Beijing (in Chinese)
2. Wang W, Li Q, Zhao G (2008) Novel approach based on chaotic oscillator for machinery fault diagnosis. Measurement 41(2):904–911
3. Hu W, Liu Z (2010) Study of metal detection based on chaotic theory. In: *Proceedings of 8th world congress on intelligent control and automation*, 2309–2314
4. Zhang S, Li Y (2007) A new method for detecting line spectrum of ship-radiated noise using Duffing oscillator. Chin Sci Bull 52(14):1906–1912
5. Wang Y, Jiang W, Zhao J (2008) A new method of weak signal detection using Duffing oscillator and its simulation research. Acta Physica Sinica 57(1):2053–2059 (in Chinese)
6. Gao J (2004) Weak signal detection. Tsing Hua University Press, Beijing (in Chinese)
7. Wang Y, Xiao Z (1999) Simulation and experimental study on the chaos circuit of Duffing oscillator. J Circuits Syst 965:325–329 (in Chinese)
8. Gao J, Yang H (1989) The analysis of operational amplifiers application. Beijing Institute of Technology Press, Beijing (in Chinese)
9. Xiong W, Hou C (2005) Mutisim7 circuit design and simulation application. Shanghai Jiaotong University Press, Shanghai (in Chinese)

Manifold Regularized Discriminative Canonical Correlation Analysis for Semi-supervised Data

Hao Wu and Xudong Zhou

1 Introduction

CCA is a powerful tool for dimensionality reduction and it is also a shallow technique in the area of multi-view representation learning [1]. During those years, a large number of multi-view representation learning algorithms have been presented, such as multi-view sparse coding [2], and multi-modal restricted Boltzmann machines [3]. CCA plays a fundamental role in many algorithms which can provide a better understanding for various approaches and specific applications.

CCA is a feature extraction algorithm. However, it can only use paired samples information which may results in the constraint of extracting discriminative features for recognition [4]. To tackle those shortcomings on CCA, Sun et al. [5] proposed the discriminative canonical correlation analysis (DCCA) for supervised multi-view data, this method can make use of the class information of the samples. Although DCCA work well in supervised case, the labeled samples are limited in reality. It is generally known that we can use a small number of labeled information and a large number of unlabeled information to improve performance [6, 7] in semi-supervised learning. There are great interest and success on graph based semi-supervised learning algorithms [7–9], which have been widely used in face recognition [10], data mining [11], audio-visual human recognition [12].

In this paper, our purpose is to improve the recognition ability in semi-supervised learning. Blaschko et al. [13] proposed the semi-supervised Laplacian regularization of KCCA, which can find high variance directions along the data manifold. By introducing this idea into the DCCA model, we propose a method, called Manifold Regularized Discriminative Canonical Correlation Analysis for Semi-supervised Data (MRDCCA). MRDCCA can both include class information inferred from labeled samples and estimate intrinsic geometrical

H. Wu · X. Zhou (✉)
College of Information Engineering, Yangzhou University, Yangzhou 225127, China
e-mail: xdzhou@yzu.edu.cn

Z. Deng (ed.), *Proceedings of 2017 Chinese Intelligent Automation Conference*,
Lecture Notes in Electrical Engineering 458,
https://doi.org/10.1007/978-981-10-6445-6_19

structures by using Laplacian regularized framework [14]. So our algorithm can not only utilize the advantages of DCCA but also preserve the manifold structure, ultimately leading to the improvement of recognition performance.

2 Discriminative Canonical Correlation Analysis

DCCA is a method of combined feature extraction for multi-modal recognition.

Suppose $\overline{X} = [\overline{x}_1, \overline{x}_2, \ldots, \overline{x}_n] = [\overline{x}_1^{(1)}, \ldots, \overline{x}_{n1}^{(1)}, \ldots, \overline{x}_1^{(c)}, \ldots \overline{x}_{nc}^{(c)}] \in \Re^p$, $\overline{Y} = [\overline{y}_1, \overline{y}_2, \ldots, \overline{y}_n] = [\overline{y}_1^{(1)}, \ldots \overline{y}_{n1}^{(1)}, \ldots, \overline{y}_1^{(c)}, \ldots, \overline{y}_{nc}^{(c)}] \in \Re^q$, they belong to c classes. w_x and w_y are two sets of projection vectors for $\overline{X}$ and $\overline{Y}$. The objective function of DCCA is as follows:

$$\begin{aligned} &\max_{wx,wy} \quad w_x^T \overline{X} A \overline{Y}^T w_y \\ &s.t. \quad w_x^T \overline{X}\overline{X}^T w_x = 1, w_y^T \overline{Y}\overline{Y}^T w_y = 1 \end{aligned} \tag{1}$$

where $A = \begin{bmatrix} I_{n1\times n1} & & & \\ & \ddots & & \\ & & I_{ni\times ni} & \\ & & & \ddots \\ & & & I_{nc\times nc} \end{bmatrix} \in \Re^{n\times n}$ is a symmetric, positive semi-definite, blocked diagonal matrix, and $rank(A) = c$. $I_n = [1, \ldots, 1] \in R^n$.

3 Manifold Regularized Discriminative Canonical Correlation Analysis

DCCA can maximize with-in class correlations and minimize between-class correlations at the same time [15]. However, when there are no sufficient training samples, we need introduce a regularizer [9] to overcome the overfitting problems.

We want to make full use of both labeled and unlabeled data information to improve the recognition rate, so we introduce Laplacian regularization terms into Eq. (1) which can include essential manifold structure. Specifically, we use all the data to construct a graph that contains the nearest neighbor information which is used to provide a discrete approximation of manifold. We also add smoothness penalty coefficients on the graph to balance the model complexity and the empirical loss. So, our model can be summarized as follows:

$$\begin{aligned} &\max_{w_x,w_y} w_x^T \overline{X} A \overline{Y}^T w_y \\ &s.t. w_x^T \overline{X}\overline{X}^T w_x + \alpha w_x^T X L X^T w_x = 1 \\ &w_y^T \overline{Y}\overline{Y}^T w_y + \beta w_y^T Y L Y^T w_y = 1 \end{aligned} \tag{2}$$

where $X = [\overline{X}, \widehat{X}]$, $Y = [\overline{Y}, \widehat{Y}]$. $\overline{X} = [\overline{x}_1, \overline{x}_2, \ldots, \overline{x}_{ni}] \subseteq X$, $\overline{Y} = [\overline{y}_1, \overline{y}_2, \ldots, \overline{y}_{ni}] \subseteq Y$.$\overline{X}$ and $\overline{Y}$ are labeled sets which definition are consistent with Eq. (1). $\widehat{X}$ and $\hat{Y}$ are unlabeled sets.α and β are smoothness penalty coefficients. $L = D - W$. L is the Laplacian matrix. D is a diagonal matrix and its entries are row (or column) sums of W. W is a similarity matrix. A possible way of defining W_{ij} is as follows:

$$W_{ij} = \exp(-norm(x_i - x_j)/2t^2) \tag{3}$$

If nodes i and j are connected, put weight $W_{ij} = \exp(-norm(x_i - x_j)/2t^2)$. To solve this optimization problem, some algebraic steps are given as follows. Firstly, we can construct a Lagrange equation according to Eq. (2):

$$\begin{aligned} L = w_x^T \overline{X} A \overline{Y}^T w_y - \frac{\lambda_1}{2}\left(w_x^T \overline{X}\overline{X}^T w_x + \alpha w_x^T X L X^T w_x - 1\right) \\ - \frac{\lambda_2}{2}\left(w_y^T \overline{Y}\overline{Y}^T w_y + \beta w_y^T Y L Y^T w_y - 1\right) \end{aligned} \tag{4}$$

Then, we calculate the partial derivatives of w_x and w_y:

$$\begin{aligned} \frac{\partial L}{\partial w_x} &= \overline{X} A \overline{Y}^T w_y - \lambda_1\left(\overline{X}\overline{X}^T w_x + \alpha X L X^T w_x\right) \\ \frac{\partial L}{\partial w_y} &= \overline{Y} A \overline{X}^T w_x - \lambda_2\left(\overline{Y}\overline{Y}^T w_y + \beta Y L Y^T w_y\right) \end{aligned} \tag{5}$$

Next, we make the partial derivatives equal to 0 and we can obtain that:

$$\begin{aligned} \overline{X} A \overline{Y}^T w_y &= \lambda_1\left(\overline{X}\overline{X}^T w_x + \alpha X L X^T w_x\right) \\ \overline{Y} A \overline{X}^T w_x &= \lambda_2\left(\overline{Y}\overline{Y}^T w_y + \beta Y L Y^T w_y\right) \end{aligned} \tag{6}$$

Then, both sides of Eq. (6) are multiplied by w_x^T and w_y^T:

$$\begin{aligned} w_x^T \overline{X} A \overline{Y}^T w_y &= \lambda_1\left(w_x^T \overline{X}\overline{X}^T w_x + \alpha w_x^T X L X^T w_x\right) \\ w_y^T \overline{Y} A \overline{X}^T w_x &= \lambda_2\left(w_y^T \overline{Y}\overline{Y}^T w_y + \beta w_y^T Y L Y^T w_y\right) \end{aligned} \tag{7}$$

According to Eq. (7), we can easily achieve that $\lambda_1 = \lambda_2 = \lambda$. Finally, Eq. (6) is converted into the following equation:

$$\begin{pmatrix} 0 & \overline{X}A\overline{Y}^T \\ \overline{Y}A\overline{X}^T & 0 \end{pmatrix} \begin{pmatrix} w_x \\ w_y \end{pmatrix} = \lambda \begin{pmatrix} \overline{X}\overline{X}^T + \alpha XLX^T & 0 \\ 0 & \overline{Y}\overline{Y}^T + \beta YLY^T \end{pmatrix} \begin{pmatrix} w_x \\ w_y \end{pmatrix} \quad (8)$$

We make $M\,\text{Prime} = \begin{pmatrix} 0 & \overline{X}A\overline{Y}^T \\ \overline{Y}A\overline{X}^T & 0 \end{pmatrix}$, $R\,\text{Prime} = \begin{pmatrix} \overline{X}\overline{X}^T + \alpha XLX^T & 0 \\ 0 & \overline{Y}\overline{Y}^T + \beta YLY^T \end{pmatrix}$, $W = \begin{pmatrix} w_x \\ w_y \end{pmatrix}$. Then, we can obtain $M\,\text{Prime}\ W = \lambda R\,\text{Prime}\ W$, this problem can be transformed into a generalized eigenvalue decomposition problem, those eigenvalues are shown in descending order: $\lambda_1 \geq \lambda_2 \geq \lambda_3 \geq \cdots \geq \lambda_r$, λ_r represents the minimum eigenvalue. The corresponding eigenvectors are $w_x = (w_{x1}w_{x2}\ldots w_{xr})$ and $w_y = (w_{y1}w_{y2}\ldots w_{yr})$.

4 Experimental Results

In this section, we compare the recognition abilities of the proposed method MRDCCA with CCA and DCCA on different data sets. We use the nearest neighborhood classifier to estimate the recognition rates of these three methods. In our algorithm, the coefficients t_1 and t_2 are chosen by searching the parameter space: $[2^{-10}, 2^{-8}, 2^{-6}, \ldots, 2^6, 2^8, 2^{10}]$. Two balancing coefficients α and β, which are optimized by searching in the range $\alpha, \beta \in [2^{-8}, 2^{-6}, \ldots, 2^{16}, 2^{18}, 2^{20}]$. Several experiments are carried out to show the effectiveness of our proposed MRDCCA method.

4.1 Multiple Features Database

Multiple Features database includes features of handwritten numerals ('0'–'9', total 10 classes). In detail, each class contains two hundred samples, each sample includes six groups of feature sets which are contour correlation characteristics, flourier coefficient, Karhunen-Loève expansion coefficient, morphological characteristics, pixel average and Zernike moment. The name and the dimension of those features are (fac, 216), (fou, 76), (kar, 64),(mor, 6), (pix, 240) and (zer, 47) respectively.

In this experiment, we choose two feature sets to construct the X and Y set, thus there are totally 15 feature combination modes. For training set, we choose ten samples from each class randomly. In each class, the number of labeled samples is 3. Then we arbitrary select 100 samples from remaining data set which are used to do the test. The recognition rates of X set and Y set are calculated respectively. For

each feature combination mode, the results of experiments are carried out 10 times randomly. The average recognition rates are recorded at Table 1. The best performances are highlighted in bold.

Table 1 lists the results of three methods. It can be seen that: in the 15 combination modes, the recognition rates of our method are better than CCA and DCCA in all combination modes. Obviously, MRDCCA has the best performance.

In the above experiment, we have shown that our MRDCCA approach outperforms both CCA and DCCA methods. We also expect our algorithm can use more unsupervised information, so we evaluate the accuracies of these three methods which are drawn on Fig. 1.

Figure 1 shows the experimental results improve as the number of labeled training samples increases on Multiple Features database. As can be seen, when the number of labeled samples is less, the recognition rates are obviously better than both CCA and DCCA, so our algorithm can take the advantages of unlabeled training samples.

4.2 Face Databases

In order to further test the recognition performance of MRDCCA compared with CCA and DCCA methods, the face recognition experiments are carried out on Yale and ORL face databases.

Table 1 Performance comparison on multiple features in UCI

Different kinds of combinations		The recognition rates of three methods					
		CCA		DCCA		MRDCCA	
		X	Y	X	Y	X	Y
fac	fau	0.763	0.490	0.737	0.539	**0.852**	**0.703**
fac	kar	0.759	0.595	0.738	0.631	**0.859**	**0.823**
fac	mor	0.445	0.601	0.546	0.608	**0.813**	**0.641**
fac	pix	0.758	0.712	0.737	0.770	**0.859**	**0.857**
fac	zer	0.618	0.569	0.732	0.616	**0.850**	**0.697**
fou	kar	0.649	0.643	0.596	0.607	**0.704**	**0.845**
fou	mor	0.381	0.615	0.431	0.615	**0.667**	**0.627**
fou	pix	0.643	0.688	0.594	0.752	**0.706**	**0.847**
fou	zer	0.520	0.598	0.545	0.613	**0.712**	**0.720**
kar	mor	0.322	0.615	0.406	0.615	**0.772**	**0.632**
kar	pix	0.774	0.789	0.709	0.781	**0.861**	**0.869**
kar	zer	0.521	0.607	0.575	0.619	**0.862**	**0.706**
kar	pix	0.615	0.382	0.615	0.499	**0.638**	**0.794**
kar	zer	0.595	0.436	0.614	0.485	**0.635**	**0.686**
pix	zer	0.619	0.616	0.742	0.615	**0.845**	**0.712**

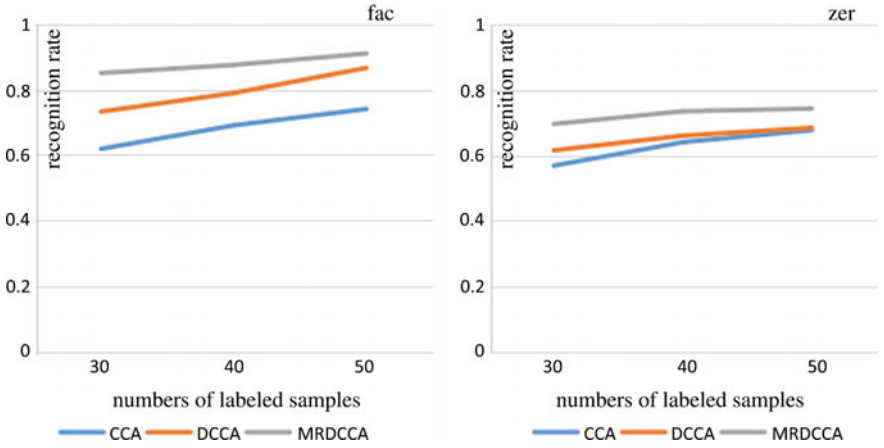

Fig. 1 Performance comparison on Multiple Features database with different number of labeled training samples

The Yale face database is provided by the Yale Center for Computational Vision and Control. It totally has 165 gray level images of 15 person, 11 pictures for each person. Those images contain variations in facial expression, lighting condition and so on. We selected 6 pictures from each person for training randomly. In those 6 pictures, 2 or 3 pictures are labeled and the other unlabeled. Then the remaining 5 pictures from each person are used to do the test set.

The ORL face database, contains images of 40 person, and everyone has ten images which are taken at different times varying the light conditions, different facial expressions and facial details (glasses/no glasses). The same as Yale database, we also arbitrary choose 6 pictures from each person for training, in those 6 pictures, 2 or 3 pictures are labeled, then the remaining 4 pictures are used to test.

We use the Daubechies orthogonal wavelet transform [16] two times, then selecting the low frequency component of the dataset as another data set Y. Obviously, to eliminate small sample problem, we first use PCA to reduce the dimension. Those experiments are also performed for 10 times randomly, then the average recognition rates are recorded at Tables 2 and 3. The best performances are highlighted in bold.

The recognition results are shown in Tables 2 and 3. We evaluate the performance of different number of labeled training samples on face databases. Obviously, we can see that our method outperforms both CCA and DCCA, this is due to the fact that, our algorithm can make use of the underlying face manifold structure.

Table 2 Performance comparison on face database (Yale)

Three methods	The recognition rates			
	Number of labeled samples			
	2		3	
	X	Y	X	Y
CCA	0.507	0.525	0.557	0.589
DCCA	0.587	0.560	0.672	0.588
MRDCCA	**0.652**	**0.681**	**0.765**	**0.761**

Table 3 Performance comparison on face database (ORL)

Three methods	The recognition rates			
	Number of labeled samples			
	2		3	
	X	Y	X	Y
CCA	0.726	0.733	0.815	0.822
DCCA	0.758	0.741	0.820	0.852
MRDCCA	**0.806**	**0.831**	**0.878**	**0.909**

5 Conclusion

Based on CCA and DCCA, we propose a new dimensionality reduction method called Manifold Regularized Discriminative Canonical Correlation Analysis for Semi-supervised Data. MRDCCA takes the idea of geometric localization into consideration. Using this method, we can not only utilize the advantages of DCCA method to maximize the discriminating power, but also preserve the intrinsic structure by introducing Laplacian regularization terms. Experiments on a series of databases show the proposed method can effectively improve the recognition performance.

Acknowledgements This project is supported by National Natural Science Foundation of China (Grant No. 6161154034).

References

1. Li Y, Yang M, Zhang Z (2016) Multi-view representation learning: a survey from shallow methods to deep methods
2. Liu W, Tao D, Cheng J, Tang Y (2014) Multiview hessian discriminative sparse coding for image annotation. Comput Vis Image Underst 118(1):50–60
3. Srivastava N, Salakhutdinov R (2014) Multimodal learning with deep boltzmann machines. J Mach Learn Res 15(8):1967–2006
4. Zhou XD, Chen XH, Chen SC (2012) Combined-feature-discriminability enhanced canonical correlation analysis. Pattern Recog Artif Intell 25(2):285–291
5. Sun T, Chen S, Yang J, Shi P (2008) A novel method of combined feature extraction for recognition. In: Eighth IEEE international conference on data mining. IEEE Computer Society, pp 1043–1048

6. Zhu X (2005) Semi-supervised learning literature survey. *Computer*. Science 37(1):63–77
7. Zhu X, Ghahramani Z, Lafferty J (2003) Semi-supervised learning using Gaussian fields and harmonic functions. In: Twentieth international conference on international conference on machine learning. AAAI Press, pp 912–919
8. Belkin M, Niyogi P, Sindhwani V (2004) Manifold regularization: a geometric framework for learning from examples. J Mach Learn Res 7(1):2399–2434
9. Cai D, He X, Han J (2007) Semi-supervised discriminant analysis. In: IEEE, international conference on computer vision. IEEE, pp 1–7
10. Lu XL (2015) Research of face recognition algorithm based on semi-supervised learning method. University of Electronic Science and Technology, Chengdu (in Chinese)
11. Kong YQ (2009) Studies on semi-supervised learning and its applications. Jiangnan University, Wuxi (in Chinese)
12. Feng W, Xie L, Zeng J, Liu ZQ (2009) Audio-visual human recognition using semi-supervised spectral learning and hidden markov models. J Vis Lang Comput 20 (3):188–195
13. Blaschko MB, Lampert CH, Gretton A (2008) Semi-supervised Laplacian regularization of Kernel canonical correlation analysis. In: European conference on machine learning and knowledge discovery in databases. Springer, Berlin, pp 133–145
14. Yin M, Gao J, Lin Z (2016) Laplacian regularized low-rank representation and its applications. IEEE Trans Pattern Anal Mach Intell 38(3):504–517
15. Peng Y (2008) Locality discriminative canonical correlation analysis algorithm. Comput Eng Appl 44(21):126–129
16. Sun TK (2006) Research on enhanced canonical correlation analysis with applications. University of Aeronautics & Astronautics, Nanjing (in Chinese)

Robust Dual Stage Control for Inertially Stabilized Platform

Jiangpeng Song, Di Zhou, Guangli Sun and Chunning Li

1 Introduction

Inertially stabilized platforms (ISP) mounted on moving vehicles are used to stabilize and point optical-electronic sensors or payload such as cameras, telescopes and so on [1, 2]. Although two-axis gimbal stabilization platform is widely applied in the field of ISP, other electromechanical configurations of ISP are also considered to improve the control performance. In this paper, a dual-stage control system are proposed to improve the control performance without an increase of the system volume.

Dual-stage structured control systems have been used in the field of hard disk drives (HDD). Similar to HDD, the main purpose of dual-stage system of ISP is increasing servo-bandwidth and tracking accuracy. The control method varies from decoupled or sequential single-input-single-output (SISO) classical frequency shaping design techniques [3, 4], to those methodologies that utilize multivariable optimal control design techniques, such as LQG/LTR [5] and robust synthesis [6].

Chao et al. [7] proposed a new H_∞ control and repetitive controller design for the dual-stage lens actuator in optical disk drives, where the dual stage system is simplified as single-input single-output (SISO). Huang et al. [8] proposed a robust mixed H_2/H_∞ controller for HDD, in which H_2 controller is introduced for tracking performance optimization and H_∞ norm bounds is considered for the stability robustness.

In this paper, by considering the obvious difference of the model uncertainties and the bandwidths between the two stages, a robust H_∞ controller is presented for

J. Song (✉) · D. Zhou
School of Astronautics, Harbin Institute of Technology,
Harbin 150001, China
e-mail: jjh_sjp@163.com

J. Song · G. Sun · C. Li
Tianjin Jinhang Technical Physics Institute, Airport Economic Zone
Zhonghuan, West Road 58, Tianjin 300308, China

Z. Deng (ed.), *Proceedings of 2017 Chinese Intelligent Automation Conference*,
Lecture Notes in Electrical Engineering 458,
https://doi.org/10.1007/978-981-10-6445-6_20

the dual stage stabilized platform, which can effectively improve the tracking performance and guarantee overall stability.

2 Plant Modelling

The dual-stage stabilized platform in this paper consists of two stages: the coarse stage derived by a DC direct drive motor and the fine stage derived by a secondary voice-coil-motor (VCM) which is placed in the optical path as micro-scan lens(MSL).

2.1 MSL Modelling

Figure 1 shows the structure form of the MSL mounted in the optical path. A compliant mechanism fabricated by the flexure hinges is used to amplify and transmit the VCM displacement.

The linear dynamic model of MSL can be simplified as a mass–spring–damper system model, and expressed as

$$\begin{bmatrix} \dot{\eta} \\ \ddot{\eta} \end{bmatrix} = \begin{bmatrix} 0 & 1 \\ -\frac{k_f}{m_f} & -\frac{c_f}{m_f} \end{bmatrix} \begin{bmatrix} \eta \\ \dot{\eta} \end{bmatrix} + \begin{bmatrix} 0 \\ \frac{K_f}{m_f R_f} \end{bmatrix} u_f + \begin{bmatrix} 0 \\ -\frac{1}{m_f} \end{bmatrix} d_f \tag{1}$$

where u_f is the input voltage, η is the translation displacement, m_f, c_f, k_f represent the equivalent mass, damping coefficient and stiffness respectively, d_f denotes the lumped extern disturbance in the MSL.

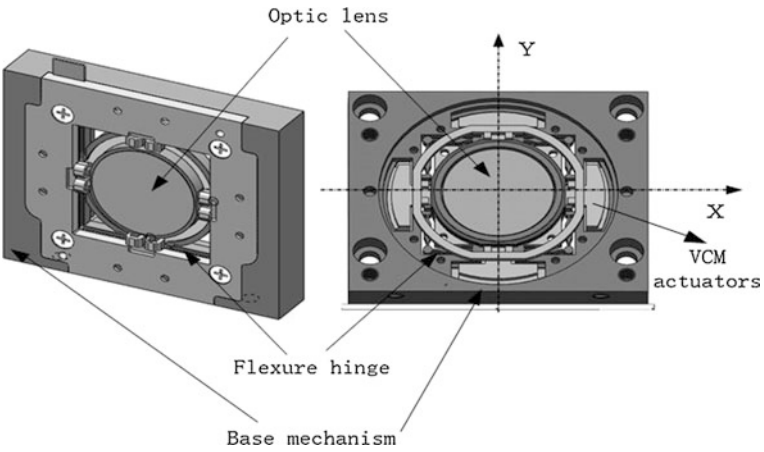

Fig. 1 The mechanical structure of MSL

In order to improve the damping effect of the MSL, the inner loop damping controller of MSL is first designed by using the embedded displacement transducer before the dual-stage controller design.

$$\begin{bmatrix} \dot{\eta} \\ \ddot{\eta} \end{bmatrix} = \begin{bmatrix} 0 & 1 \\ -\omega_f^2 & -2\delta_f\omega_f \end{bmatrix} \begin{bmatrix} \eta \\ \dot{\eta} \end{bmatrix} + \begin{bmatrix} 0 \\ A_f \end{bmatrix} u_f + \begin{bmatrix} 0 \\ -A_f \end{bmatrix} \bar{d}_f \tag{2}$$

where ω_f, δ_f and A_f are the natural frequency, the damping ratio and the equivalent gain, respectively. $\bar{d}_f$ is the equivalent lumped unknown disturbance for MSL.

The system parameters ω_f, δ_f and A_f of the MSL can be obtained from the frequency response of the damping MSL by a dynamic signal analyze, yielding

$$\omega_f = 119.5 \text{ Hz}, \quad \delta_f = 0.63, \quad A_f = 1.6 \text{ rad/V}$$

The high-frequency system modelling of the MSL is treated as unstructured uncertainties.

2.2 A Two-Axis Gimbaled Platform Modelling

A two axis gimbaled mechanical structure can be depicted as in Fig. 2. And the corresponding gimbal dynamics state space model can be written as Eq. (3).

$$\begin{bmatrix} \dot{\theta}_y \\ \ddot{\theta}_y \end{bmatrix} = \begin{bmatrix} 0 & 1 \\ 0 & -\frac{K_t K_e}{J_S R} \end{bmatrix} \begin{bmatrix} \theta_y \\ \dot{\theta}_y \end{bmatrix} + \begin{bmatrix} 0 \\ \frac{K_t}{J_S R} \end{bmatrix} u_{my} - \begin{bmatrix} 0 \\ \frac{1}{J_S} \end{bmatrix} d_{ly} \tag{3}$$

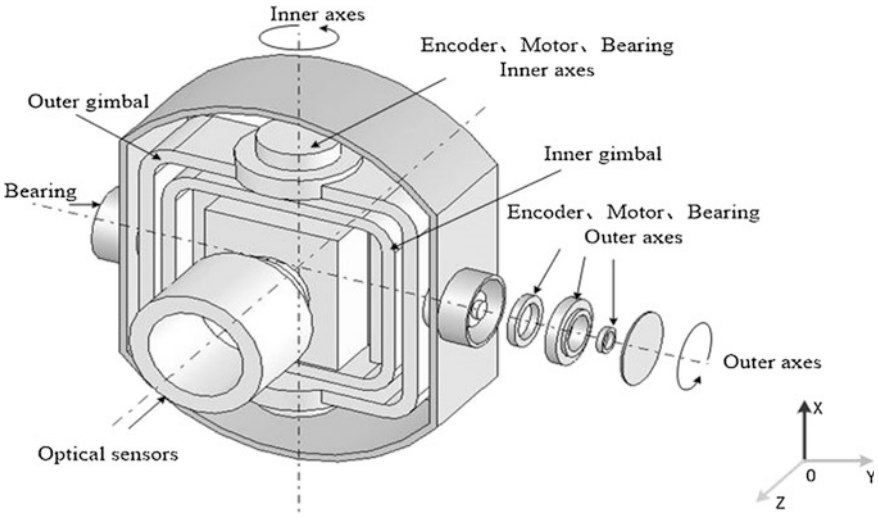

Fig. 2 Structure of a two axis gimbaled configuration

where u_{my} denotes control voltage input, R denotes the motor resistance. d_{ly} denotes lumped unknown disturbances, the scalars K_e and K_t are the amplifier gain and the motor force constant, respectively.

The system parameters J_s, K_t, K_e and R of the gimbal can be obtained from the frequency response of the damping MSL by a dynamic signal analyze, yielding

$$J_s = 0.0027 \text{ kg m}^2, \quad K_t = 0.11 \text{ Nm/A}, \quad K_e = 0.11 \text{ V/(rad/s)}, \quad R = 10\ \Omega$$

Similar to the MSL, the high-frequency gimbal modeling are treated as unstructured uncertainties.

2.3 A Dual-Stage Platform Modelling

In the dual-stage platform, the MSL is mounted on an two-axis gimbaled platform. Based on the dynamic modeling mentioned above, the dual-stage platform dynamic modeling can be derived ignoring unstructured uncertainties as follows.

$$\begin{bmatrix} \dot{\theta} \\ \ddot{\theta} \\ \dot{\eta} \\ \ddot{\eta} \end{bmatrix} = \begin{bmatrix} 0 & 1 & 0 & 0 \\ 0 & -\frac{k_t k_e}{J_S R} & 0 & 0 \\ 0 & 0 & 0 & 1 \\ 0 & 0 & -\omega_f^2 & -2\delta_f \omega_f \end{bmatrix} \cdot \begin{bmatrix} \theta \\ \dot{\theta} \\ \eta \\ \dot{\eta} \end{bmatrix} + \begin{bmatrix} 0 & 0 \\ \frac{k_t}{J_S R} & 0 \\ 0 & 0 \\ 0 & A_f \end{bmatrix} \cdot \begin{bmatrix} u_{my} \\ u_f \end{bmatrix} + \begin{bmatrix} 0 & 0 \\ -\frac{1}{J_S} & 0 \\ 0 & 0 \\ 0 & -A_f \end{bmatrix} \cdot \begin{bmatrix} d_{Ly} \\ \bar{d}_f \end{bmatrix} \tag{4}$$

The structure of the dual stage system is illustrated in Fig. 3. From Fig. 3, it can be seen that the dual stage control system can be regarded as a coupled multiple input and multiple output (MIMO) system. The control problem for the dual stage system can be converted into the standard robust H_∞ design problem.

3 Robust Controller Design

An H_∞ controller is designed next for a dual-stage servo system as shown in Fig. 4. where P_{gimb} and P_{vcm} are the nominal plants of the coarse gimbal stage and fine VCM stage, respectively. K_{gimb} and K_{vcm} are the designed controllers respectively. The position y_T is a combination of the gimbal output y_g and VCM output y_{vcm}.

The framework of the standard H_∞ problem are shown in Fig. 5.

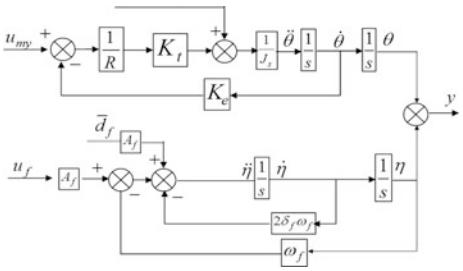

Fig. 3 Structure of the dual stage control system

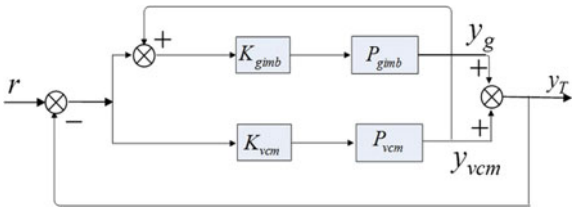

Fig. 4 Block diagram of the dual stage platform

Where K is the H_∞ controller to be designed. The weighting functions W_{gimb_un} and W_{vcm_un} denote the independent multiplicative uncertainties for the two stages, respectively. W_e and W_{g_e} reflects the requirements on control objective. W_{gimbal_U} and

W_{vcm_U} does some restrictions on the control or actuator signals, respectively; W_{g_n} and W_{vcm_n} are chosen to be very small to avoid ill-conditioning in the computation.

By establishing the structure of Fig. 5 in MATLAB, a stable two-input-two-output controller K is obtained using MATLAB robust control toolbox with the input/output transfer function satisfying $\|T_{z\omega}\|_\infty \leq 0.7$.

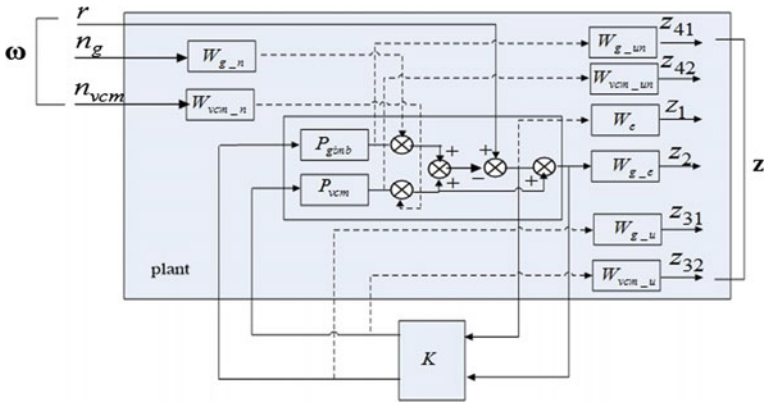

Fig. 5 The framework of the standard H_∞ controller

4 Simulation Analysis

To illustrate the frequency separation of the two stage system obtained by the designed dual stage controller, the closed loop bandwidth of the coarse stage and the fine stage are given in Fig. 6, respectively.

It can be seen from Fig. 8 that, the coarse stage channel has been limited in the low frequency region below 10 Hz, the fine stage has been limited in high frequency region from 10 to 110 Hz.

Figure 7 shows the step response performance. It can be seen that the step response steady state error is 0.07° while the coarse stage is 0.35°.

Figure 8 shows the sinusoidal signal tracking performance of the dual control system under the sinusoidal input of 5°/0.3 Hz.

From Fig. 8a, it can be seen that the maximum tracking error is 0.013° under the sinusoidal input of 5°/0.3 Hz, while that of the coarse stage is 0.035°. The gimbal coarse stage actuator has a large moving range while the VCM fine stage has a small moving range. Therefore the contribution from each stage is properly allocated.

To verify the performance under extern disturbances, the reference inputs of system is selected as the sinusoidal motion with 5°/0.3 Hz and a sinusoidal motion with 2°/2 Hz is also introduced as the extern disturbance motion.

From Fig. 9, it can be seen that the maximum tracking error is 0.06°, while that of the coarse stage is 0.58°. This result reflects the effectiveness of the proposed controller to overcome extern disturbances.

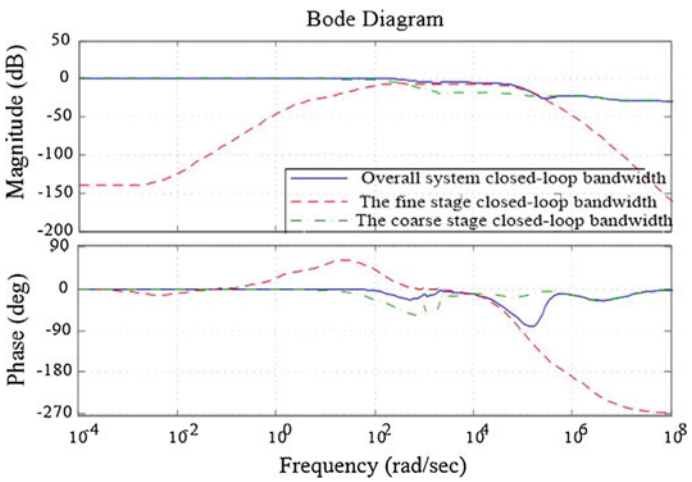

Fig. 6 Simulated bode diagram of the dual stage control system

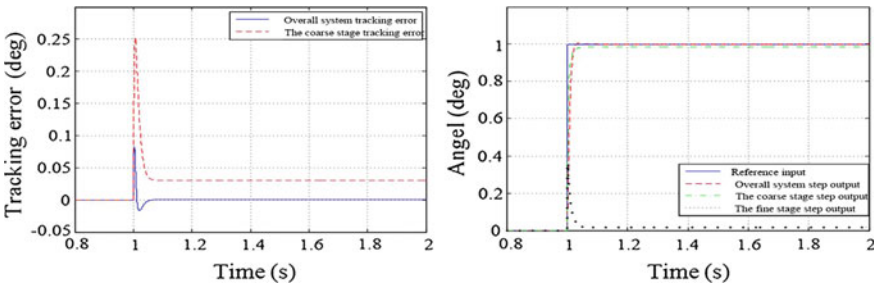

(a) Simulation results of step response steady state errors

(b) Simulation results of step response outputs

Fig. 7 The step response performance of the dual stage control system

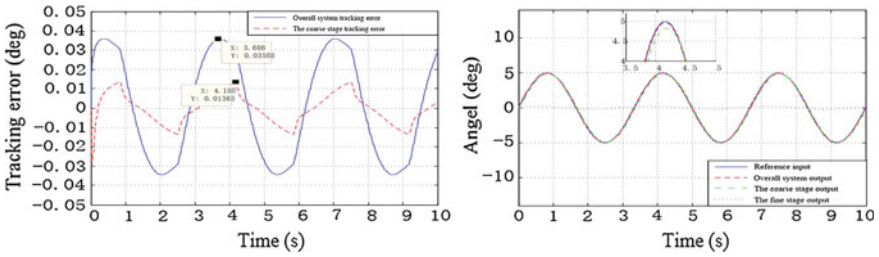

(a) Simulation results of sinusoidal tracking errors

(b) Simulation results of signal tracking outputs

Fig. 8 The sinusoidal signal tracking performance of the dual stage control system

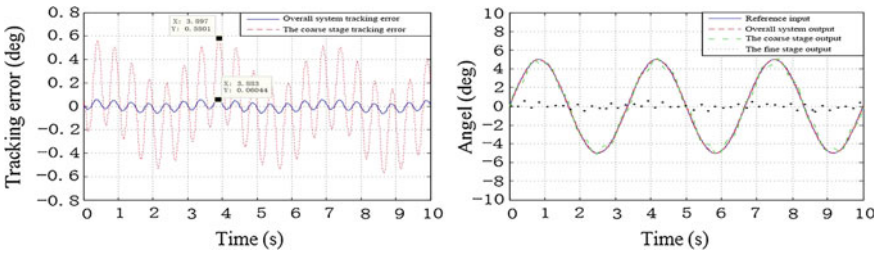

(a) Simulation results of sinusoidal tracking errors

(b) Simulation results of signal tracking outputs

Fig. 9 The sinusoidal signal tracking performance of the dual stage control system

5 Conclusions

In this paper, the robust H_∞ MIMO systematic design method for guaranteeing tracking performance and overall stability is presented, based on the frequency separation design of two stages by considering the difference between the two stages.

The effectiveness of the designed controllers are finally validated based on the simulation results. The resulting closed-loop bandwidth of the coarse stage achieves at 10 Hz, while the fine stage achieves a higher closed-loop bandwidth at 110 Hz. The step response steady state error of the overall system is 0.07°, while that of the coarse stage is 0.35°. The maximum tracking error of the overall system is 0.01° under the sinusoidal input, while that of the coarse stage is 0.14°.

References

1. Hilkert J (2008) Inertially stabilized platform technology. IEEE Control Syst Mag 28(1):26–46
2. Michael KM (2008) Inertially stabilized platforms for optical imaging systems. IEEE Control Syst Mag 28(1):47–64
3. Bo Jie H, Gao JS, Zhou YF (2012) The development of an ultra-precision dual-stage based on a master-slave control system. In: International conference on computer distributed control and intelligent environmental monitoring. IEEE 2012, pp 727–730
4. Nagel WS, Clayton GM, Leang KK (2016) Master-slave control with hysteresis inversion for dual-stage nanopositioning systems. In: American control conference, pp 655–660
5. Hu X et al (1999) Discrete-time LQG/LTR dual-stage controller design and implementation for high track density HDDs. In: American control conference. IEEE 1999, pp 4111–4115
6. Rotunno M, De Callafon RA, Talke FE (2003) Comparison and design of servo controllers for dual-stage actuators in hard disk drives. IEEE Trans Magnetics 39(5):2597–2599
7. Chao CP, Liao LD, Lin HH et al (2010) Robust dual-stage and repetitive control designs for an optical pickup with parallel cantilever beams powered by piezo-actuation. Microsyst Technol 16(1):317–331
8. Huang X et al (2004) Design and analysis of a dual-stage disk drive servo system using an instrumented suspension. In: American control conference. Proceedings of the IEEE 2004, vol 1, pp 535–540

Directed Graph-Based Adaptive Attitude Cooperative Control for Fractionated Spacecraft

Zhaoming Li and Jiejuan Wang

1 Introduction

The concept of fractionated spacecraft is conceived by optimally decomposing the functional units including payload, communication, energy, navigation, calculation process, etc. of a traditional spacecraft into multiple modular spacecrafts. Each modular spacecraft carries different functions and resources related to the tasks [1–3]. The fractionated spacecraft system finishes specific tasks by constructing a big virtual spacecraft through physical separation, free-flying cluster, wireless information exchange and wireless energy exchange in the mode of functional coordination and resource sharing. Cooperative attitude maneuver is an important way of attitude maneuver for fractionated spacecraft, and also is the basis for finishing payload tasks. Therefore, it is necessary to study the cooperative control of attitude maneuver among modular spacecrafts.

A kind of robust adaptive controller without decoupling was designed for certain small satellites [4]. However, this kind of controller is based on the consideration that the external disturbance is unknown constant quantity. An adaptive spacecraft attitude controller was designed by using back-stepping method [5] with the presentation of clear design steps. However, the influence of external disturbance is not taken into consideration. Both the abovementioned methods consider single spacecraft control rather than multi-spacecraft cooperative control. Ren et al. [6–8] investigated the distributed cooperative control strategy based on local information exchange for multi-agent formation systems. Then, they presented the second-order consensus protocol which considers the system state and differential

Z. Li (✉)
Equipment Academy, Huairou Institute, Bayi Road. 1, Beijing 101416, China
e-mail: lizhaomingzbxy@163.com

J. Wang
China Luoyang Electronic Equipment Test Center, Luoyang 471003, China

Z. Deng (ed.), *Proceedings of 2017 Chinese Intelligent Automation Conference*,
Lecture Notes in Electrical Engineering 458,
https://doi.org/10.1007/978-981-10-6445-6_21

state. Furthermore, aiming at the typical Euler–Lagrange system, they proposed the consistency algorithm, which considers various non-linear factors including saturation. To solve the problem of distributed spacecraft attitude synchronization, a method of attitude coordination and tracking control based on information consistency was presented [9]. This method is used to solve attitude synchronization problems among distributed satellites by designing information transmission models among satellites. However, this method also fails to take the influence of external disturbance into account.

By summarizing the above researches, this paper proposes a kind of distributed adaptive attitude cooperative controller based on the graph theory and the consistency theory so as to solve the attitude cooperative control problem of fractionated spacecraft. This method uses one parameter to comprehensively represent the uncertainty of moment of inertia of modular spacecraft, followed by the online evaluation using the designed adaptive law. Meanwhile, compensation term is designed in the controller to offset the influence of disturbance torque. The simulation results validate that this controller can realize the cooperative tracking of desired attitude.

2 Mathematical Models for Modular Spacecraft

There are various forms of attitude parameters for spacecraft. Since the modified Rodriguez parameter (MRP) has no nuisance parameter, it does not need to solve complex constraint equations and meanwhile can reduce the influence of singularity. Therefore, this paper adopts the MRP to describe attitude. The MRP of the ith modular spacecraft is defined as follows [10]:

$$r_i = (r_{i1}, r_{i2}, r_{i3})^{\mathrm{T}} = e_i \tan\frac{\Phi_i}{4} \tag{1}$$

where, e_i and Φ_i are the Euler rotation axis and Euler angle of the ith modular spacecraft, respectively. Rigid body dynamic equation is utilized to describe the attitude dynamics of the modular spacecraft whose attitude dynamics and kinematics equation are presented as follows:

$$\boldsymbol{J}_i\dot{\boldsymbol{\omega}}_i + \boldsymbol{\omega}_i^{\times}\boldsymbol{J}_i\boldsymbol{\omega}_i = \boldsymbol{T}_{iu} + \boldsymbol{T}_{id} \tag{2}$$

$$\dot{\boldsymbol{r}}_i = \boldsymbol{G}_i(\boldsymbol{r}_i)\boldsymbol{\omega}_i \tag{3}$$

where, $\boldsymbol{J}_i \in \mathbf{R}^{3\times 3}$ is the moment of inertia of the ith modular spacecraft; $\boldsymbol{\omega}_i \in \mathbf{R}^3$ denotes the angular velocity; $\boldsymbol{T}_{iu} \in \mathbf{R}^3$ is the control torque and $\boldsymbol{T}_{id} \in \mathbf{R}^3$ presents the space disturbance torque. $\boldsymbol{G}_i(\boldsymbol{r}_i) = \frac{1}{2}\left[\left(\frac{1-\boldsymbol{r}_i^{\mathrm{T}}\boldsymbol{r}_i}{2}\right)\boldsymbol{I} + \boldsymbol{r}_i\boldsymbol{r}_i^{\mathrm{T}} + \boldsymbol{r}_i^{\times}\right]$, and $\boldsymbol{r}_i^{\times}$ is a cross-product matrix in the size of 3×3. $\boldsymbol{G}_i(\boldsymbol{r}_i)$ presents the following properties.

$$\boldsymbol{r}_i^{\mathrm{T}}\boldsymbol{G}_i(\boldsymbol{r}_i) = \left[\frac{1+\boldsymbol{r}_i^{\mathrm{T}}\boldsymbol{r}_i}{4}\right]\boldsymbol{r}_i^{\mathrm{T}} \tag{4}$$

Suppose that the desired MRP and the desired angular velocity of the ith modular spacecraft are $\boldsymbol{r}_{id}$ and $\boldsymbol{\omega}_{id}$ separately. The error of MRP and error of angular velocity are denoted as $\boldsymbol{r}_{ie} = \boldsymbol{r}_i - \boldsymbol{r}_{id}$ and $\boldsymbol{\omega}_{ie} = \boldsymbol{\omega}_i - \boldsymbol{C}_i\boldsymbol{\omega}_{id}$, respectively, in which $\boldsymbol{C}_i$ is the direction cosine matrix of transformation. By substituting these parameters into Formula (2), we can obtain the error dynamics and kinematics equations:

$$\boldsymbol{J}_i\dot{\boldsymbol{\omega}}_{ie} = -\boldsymbol{\omega}_i^{\times}\boldsymbol{J}_i\boldsymbol{\omega}_i + \boldsymbol{J}_i(\boldsymbol{\omega}_{ie}^{\times}\boldsymbol{C}_i\boldsymbol{\omega}_{id} - \boldsymbol{C}_i\dot{\boldsymbol{\omega}}_{id}) + \boldsymbol{T}_{iu} + \boldsymbol{T}_{id} \tag{5}$$

$$\dot{\boldsymbol{r}}_{ie} = \boldsymbol{G}_i(\boldsymbol{r}_{ie})\boldsymbol{\omega}_{ie} \tag{6}$$

Assumption 1 Since the precise value of the moment of inertia of the ith modular spacecraft is impossible to be obtained owing to the factors including rotation of payloads, $\boldsymbol{J}_i$ is considered as a constant in the range of $0 \le \|\boldsymbol{J}_i\| \le c_{iJ}$. Modular spacecraft is mainly subjected to disturbances including solar radiation torque and space environment disturbance torque. Suppose $0 \le \|\boldsymbol{T}_{id}\|^2 \le d_i$, c_{iJ} and $d_i \in \mathbf{R}$ are unknown constants.

3 Design of an Adaptive Cooperative Controller

Lemma 1 [11]: *If a positive definite function $V(t)$ satisfies the following in equation:*

$$\dot{V}(t) \le -\xi V(t) + \chi(t) \tag{7}$$

where, ξ presents a positive constant. For $\forall t > 0$, there exists $\chi(t) > 0$. If $\chi(t) = C$ is a constant, the system is considered to be globally uniform and boundedly stable. The adaptive cooperative controller is designed to $\lim_{t\to\infty}\|\boldsymbol{r}_{ie}\| = 0$ and $\lim_{t\to\infty}\|\boldsymbol{\omega}_{ie}\| = 0$. To describe the communication topology among modular spacecrafts, define cooperative error variable as follows.

$$\begin{aligned}\boldsymbol{e}_i &= \boldsymbol{\omega}_{ei} + \lambda_i\boldsymbol{G}^{-1}(\boldsymbol{r}_{ei})\left[\sum_{j=1}^{n} a_{ij}(\boldsymbol{r}_i - \boldsymbol{r}_j) + \boldsymbol{r}_{ei}\right] \\ &= \boldsymbol{\omega}_{ei} + \lambda_i\boldsymbol{G}^{-1}(\boldsymbol{r}_{ei})\left[\sum_{j=1}^{n} a_{ij}(\boldsymbol{r}_{ei} - \boldsymbol{r}_{ej}) + \boldsymbol{r}_{ei}\right]\end{aligned} \tag{8}$$

where, $\lambda_i > 0 \in \mathbf{R}$ presents design parameters. By performing derivation to Formula (8), we acquire:

$$\dot{\boldsymbol{e}}_i = \dot{\boldsymbol{\omega}}_{ei} + \lambda_i \dot{\boldsymbol{G}}^{-1} \left[\sum_{j=1}^{n} a_{ij}(\boldsymbol{r}_{ei} - \boldsymbol{r}_{ej}) + \boldsymbol{r}_{ei} \right] + \lambda_i \boldsymbol{G}^{-1} \left[\sum_{j=1}^{n} a_{ij}(\dot{\boldsymbol{r}}_{ei} - \dot{\boldsymbol{r}}_{ej}) + \dot{\boldsymbol{r}}_{ei} \right] \tag{9}$$

Suppose $\boldsymbol{\xi}_i = \lambda_i \dot{\boldsymbol{G}}^{-1} \left[\sum_{j=1}^{n} a_{ij}(\boldsymbol{r}_{ei} - \boldsymbol{r}_{ej}) + \boldsymbol{r}_{ei} \right] + \lambda_i \boldsymbol{G}^{-1} \left[\sum_{j=1}^{n} a_{ij}(\dot{\boldsymbol{r}}_{ei} - \dot{\boldsymbol{r}}_{ej}) + \dot{\boldsymbol{r}}_{ei} \right]$, we gain the following formula after substituting $\boldsymbol{\xi}_i$ into Formula (9) and multiplying the two sides of the formula by $\boldsymbol{J}_i$.

$$\boldsymbol{J}_i \dot{\boldsymbol{e}}_i = -\omega_i^{\times} \boldsymbol{J}_i \boldsymbol{\omega}_i + \boldsymbol{J}_i (\boldsymbol{\omega}_{ei}^{\times} \boldsymbol{C}_i \boldsymbol{\omega}_d - \boldsymbol{C}_i \dot{\boldsymbol{\omega}}_d) + \boldsymbol{T}_{ui} + \boldsymbol{T}_{di} + \boldsymbol{J}_i \boldsymbol{\xi}_i \tag{10}$$

To simply Formula (10) and clarify the structure of the controller, let $\boldsymbol{\varepsilon}_i = \boldsymbol{\omega}_{ei}^{\times} \boldsymbol{C}_i \boldsymbol{\omega}_d - \boldsymbol{C}_i \dot{\boldsymbol{\omega}}_d + \boldsymbol{\xi}_i$ and then substitute it into Formula (10).

$$\boldsymbol{J}_i \dot{\boldsymbol{e}}_i = -\boldsymbol{\omega}_i^{\times} \boldsymbol{J}_i \boldsymbol{\omega}_i + \boldsymbol{J}_i \boldsymbol{\varepsilon}_i + \boldsymbol{T}_{ui} + \boldsymbol{T}_{di} \tag{11}$$

The matrix and parameter vector are defined as follows:

$$\boldsymbol{P}_i = \begin{bmatrix} \varepsilon_{i1} & \omega_{i2}\omega_{i3} & -\omega_{i2}\omega_{i3} & \varepsilon_{i2} + \omega_{i1}\omega_{i3} & \varepsilon_{i3} - \omega_{i1}\omega_{i2} & \omega_{i3}^2 - \omega_{i2}^2 \\ -\omega_{i1}\omega_{i3} & \varepsilon_{i2} & \omega_{i1}\omega_{i3} & \varepsilon_{i1} - \omega_{i2}\omega_{i3} & \omega_{i1}^2 - \omega_{i3}^2 & \varepsilon_{i3} + \omega_{i1}\omega_{i2} \\ \omega_{i1}\omega_{i2} & -\omega_{i1}\omega_{i2} & \varepsilon_{i3} & \omega_{i2}^2 - \omega_{i1}^2 & \varepsilon_{i1} + \omega_{i2}\omega_{i3} & \varepsilon_{i2} - \omega_{i1}\omega_{i3} \end{bmatrix} \tag{12}$$

$$\boldsymbol{\theta}_i = [\, J_{i11} \quad J_{i22} \quad J_{i33} \quad J_{i12} \quad J_{i13} \quad J_{i23} \,]^{\mathrm{T}} \tag{13}$$

Then Formula (11) is converted to:

$$\boldsymbol{J}_i \dot{\boldsymbol{e}}_i = \boldsymbol{P}_i \boldsymbol{\theta}_i + \boldsymbol{T}_{ui} + \boldsymbol{T}_{di} \tag{14}$$

The uncertainty of the moment of inertia is mainly reflected by the parameter $\boldsymbol{\theta}_i$, therefore, adaptive online evaluation needs to be performed on this parameter. The control law and adaptive law are designed as follows:

$$\boldsymbol{T}_{ui} = -\boldsymbol{P}_i \hat{\theta}_i - \rho_i \boldsymbol{e}_i - \gamma_i \boldsymbol{e}_i \tag{15}$$

$$\dot{\hat{\theta}}_i = \beta_i \boldsymbol{P}_i^{\mathrm{T}} \boldsymbol{e}_i \tag{16}$$

where, ρ_i and $\gamma_i > 0 \in \mathbf{R}$ are design parameters and $\beta_i \in \mathbf{R}^{6\times 6}$ shows the positive definite symmetric matrix. $\gamma_i e_i$ is designed to compensate the T_{id} in Formula (2) and Formulas (15) and (16) can be used to realize the control aim. The controller is proved to be stability, and the process of proof is omitted here due to the length of the paper.

4 Simulation Example and Result Analysis

To verify the validity of the designed controller in this paper, the cooperative attitude tracking control for fractionated spacecraft is simulated based on Matlab/Simulink. Suppose that there are four modular spacecrafts in the cluster, and the communication topology among the modular spacecrafts is shown in Fig. 1 where the values on the edges represent weights. Based on the abovementioned graph theory, we can obtain the corresponding information including the adjacent matrix.

Suppose the initial uncertainty of the moment of inertia of modular spacecraft is $\boldsymbol{\theta}_i = [5 \quad 10 \quad 10 \quad 0.05 \quad 0.05 \quad 0.05]^{\mathrm{T}}$, the simulation is performed for 30 s. Suppose the desired MRP is $\boldsymbol{r}_d = [0.02 \sin 0.5t,\ 0.03 \sin 0.3t,\ 0.06 \cos 0.3t]^{\mathrm{T}}$. Figures 2, 3, 4 and 5 demonstrate the simulation results. It can be observed from the

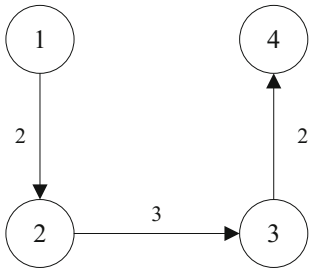

Fig. 1 Directed topology among the four modular spacecrafts

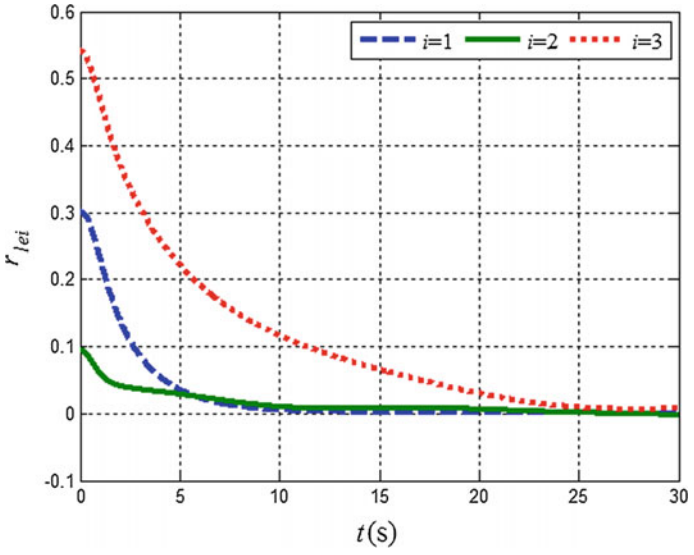

Fig. 2 The error of MRP of module 1

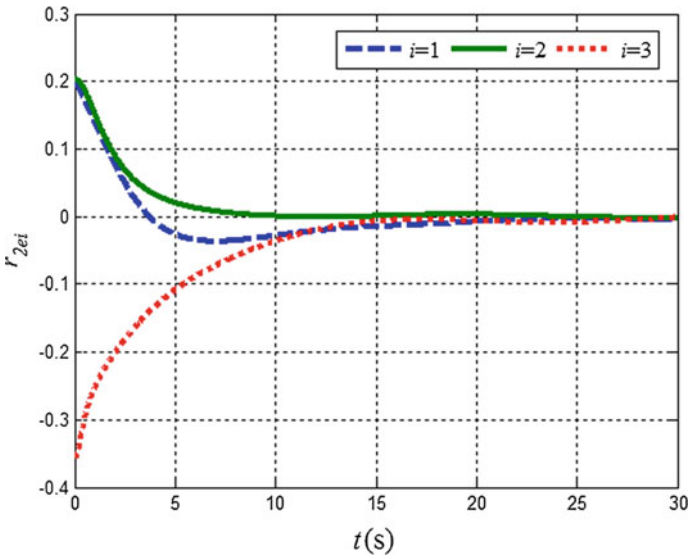

Fig. 3 The error of MRP of module 2

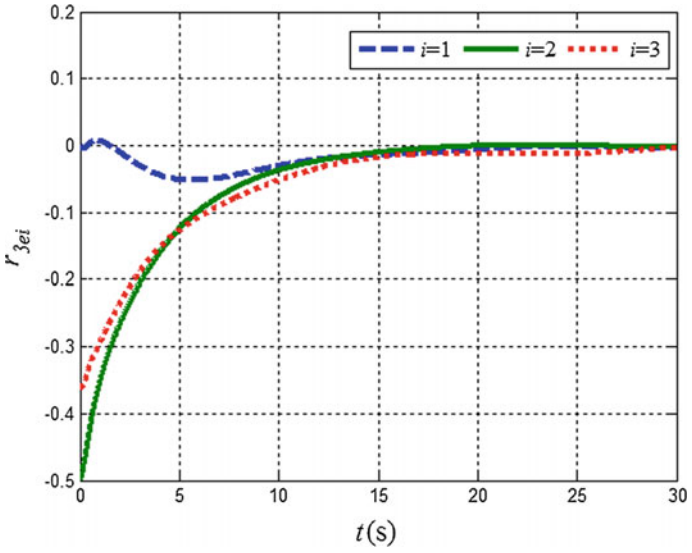

Fig. 4 The error of MRP of module 3

results that, the four modular spacecrafts cooperatively track the desired MRP at 25 s. As can be seen, the controller presents strong robustness to external disturbance and high tracking precision. By comparing the figures, the cooperativity of the modular spacecraft 1 is weaker than the other three. Meanwhile, the

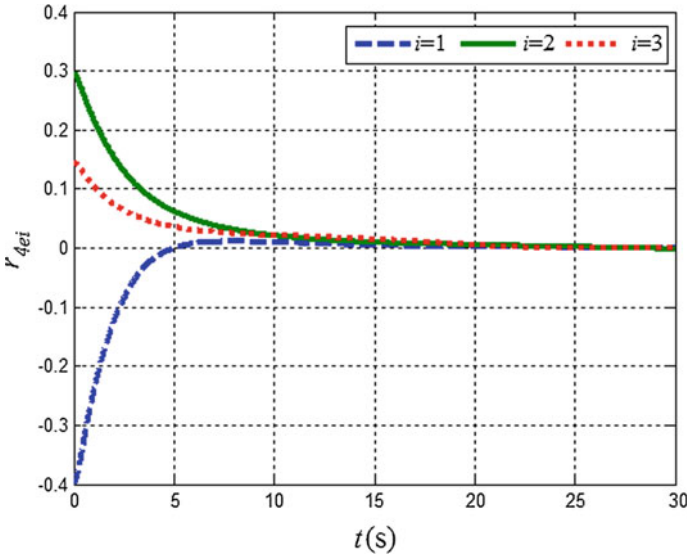

Fig. 5 The error of MRP of module 4

communication topology figure shows that the modular spacecraft 1 does not acquire attitude information from the other three modular spacecrafts, that is, the modular spacecraft 1 is located on the top of the sole directed spanning tree in Fig. 1.

5 Conclusions

Aiming at the attitude cooperative control of fractionated spacecraft, this paper designs a distributed adaptive attitude cooperative controller based on the graph theory and consistency theory. This controller is designed by considering the uncertainty of moment of inertia of modular spacecraft and the influence of external disturbance torque. Firstly, the MRP and Euler equation of motion are used to describe the attitude of modular spacecraft; meanwhile, the kinetic equation of attitude error of the modules is derived. Then, the directed graph is applied to demonstrate the communication topology among modular spacecrafts. Next, a distributed cooperative controller is designed based on the consistency theory, followed by the online evaluation of the unknown moment of inertia by using the designed adaptive law. The controller designed in this paper presents simple structure and can be operated easily. Moreover, the final simulation results indicate that this controller can realize cooperative maneuver of module attitude and shows certain robustness to the external disturbance.

References

1. Yao W, Chen X, Zhao Y (2012) A fractionated spacecraft system assessment tool based on lifecycle simulation under uncertainty. Chin J Aeronaut 25:71–82 (in Chinese)
2. O'Neill MG, Annalisa L et al (2011) Assessing fractionated spacecraft value propositions for earth imaging space missions. J Spacecraft Rockets 48(6):975–985
3. Hu M, Zeng G, Dang Z (2012) Nonlinear feedback control of fractionated spacecraft electromagnetic formation flying in low-Earth orbit. Chin J Space Sci 32(3):417–423 (in Chinese)
4. Zhang L, Shaoju W, Jin G (2009) Design of three-axis stable robust adaptive attitude control of microsatellites. Chin J Space Sci 29(1):29–33 (in Chinese)
5. Ma GF, Zhang HB, Hu QL (2012) Backstepping-based relative-attitude control for the leader-follower spacecrafts. Control Theory Appl 29(6):798–802 (in Chinese)
6. Ren W (2010) Distributed cooperative attitude synchronization and tracking for multiple rigid bodies. IEEE Trans Control Syst Technol 18(2):383–392
7. Ren W (2009) Distributed leaderless consensus algorithms for networked Euler-Lagrange systems. Int J Control 82(11):2137–2149
8. Ren W, Atkins E (2007) Distributed multi-vehicle coordinated control via local information exchange. Int J Robust Nonlinear Control 17:1002–1033
9. Chen ZM, Wang HN, Liu HY (2010) Research on distributed satellite attitude synchronization based on information consensus. J Astronaut 31(10):2283–2287
10. Schaub H, Junkins JL (1996) Stereographic orientation parameters for attitude dynamics: a generalization of the rodrigues parameters. J Astronaut Sci 44(1):1–19
11. Qu Z, Dawson D, Doisey J (1994) A new class of robust control law for tracking of robots. Int J Rob Res 13(4):355–363

Research on Sensorless Control of PMSM Based on a Novel Sliding Mode Observer

Xiaqing Zhu

1 Introduction

The permanent magnet synchronous motor (PMSM) has many advantages such as high efficiency, small size, fast response and high reliability. It is widely used in many driving fields, such as machine tools, industrial robots and other occasions, also in many special occasions has also been more and more attention, such as in aerospace, and special machine tools. At the same time, PMSM has been paid more and more attention in many special occasions, such as in the aviation, aerospace, and special machine tools, etc. [1]. The precise control of PMSM requires the position and speed information of the rotor, but the installation of position and speed sensor increases the volume and cost of the motor, also increases the inertia of the bearing, affects the static and dynamic performance of the system, and reduces the robustness of the system. At the same time, due to the special restrictions of many special occasions, such as the installation space, high reliability requirements, the application of permanent magnet synchronous motor has been a certain limit [2]. Therefore, in recent years, sensorless control technology of permanent magnet synchronous motor and speed sensorless technology has become a hot research topic at home and abroad [3]. The main methods are as following: (1) the speed estimation method based on slip frequency; (2) speed estimation method based on magnetic field orientation; (3) speed estimation method based on adaptive control; (4) speed estimation method based on observer. Among them, the observer method is the most popular one, and the traditional sliding mode observer is one of the most popular methods. But the traditional sliding mode observer is the first to estimate the back EMF of the motor, The position and velocity information of the motor is obtained by the relationship between the back EMF [4] and the rotor position of the motor. Due to the existence of the sliding mode, the system has a

X. Zhu (✉)
Shandong Yingcai University, Jinan 250104, China
e-mail: xiaqing_zhu@126.com

Z. Deng (ed.), *Proceedings of 2017 Chinese Intelligent Automation Conference*,
Lecture Notes in Electrical Engineering 458,
https://doi.org/10.1007/978-981-10-6445-6_22

serious chattering. At the same time, the counter electromotive force is obtained by filtering the high frequency signal through the low pass filter, so there is a phase lag, so the phase compensation is needed, which increases the complexity of the system. In this paper, a new type of sliding mode observer is designed. The Sigmoid function is introduced to eliminate the chattering of sliding mode, and the filter and phase compensation are also reduced. Finally, the feasibility and effectiveness of the sensorless control strategy of PMSM based on the new sliding mode observer is verified by experiment simulation.

2 Mathematical Model of PMSM

Under the premise of not affecting the control performance, neglecting the saturation of the magnetic circuit core and the hysteresis and eddy current losses, Assuming that the induced EMF waveform is a sine wave in the winding, the current equation in coordinate system of permanent magnet synchronous motor [5] is

$$\frac{d}{dt}\begin{bmatrix} i_\alpha \\ i_\beta \end{bmatrix} = \begin{bmatrix} R_s/i_d & \varpi_e(L_d - L_q) \\ 0 & -R_s/i_d \end{bmatrix}\begin{bmatrix} i_\alpha \\ i_\beta \end{bmatrix} - \frac{1}{L_d}\begin{bmatrix} e_\alpha \\ e_\beta \end{bmatrix} + \frac{1}{L_d}\begin{bmatrix} u_\alpha \\ u_\beta \end{bmatrix} \tag{1}$$

Among it $\begin{bmatrix} e_\alpha \\ e_\beta \end{bmatrix} = \left[(L_d - L_q)(\omega_e i_d - i_q) + \omega_e \psi_f\right]\begin{bmatrix} -\sin\theta_e \\ \cos\theta_e \end{bmatrix}$

The voltage equation in the d-q rotating coordinate system is

$$\begin{bmatrix} u_d \\ u_q \end{bmatrix} = \begin{bmatrix} R_s + DL_d & \omega_e L_q \\ \omega_e L_d & R_s + DL_q \end{bmatrix}\begin{bmatrix} i_d \\ i_q \end{bmatrix} + \begin{bmatrix} 0 \\ \omega_e \psi_f \end{bmatrix} \tag{2}$$

The electromagnetic torque equation is

$$T_e = \frac{3}{2} P \psi_a i_q \tag{3}$$

Form in: are d, q axis voltage; are d, q axis current; are d, q axis inductance; is stator resistance; is electric angular velocity for rotor; D for differential operators; is permanent magnet and stator flux linkage; is electromagnetic torque; is motor load torque; P is the polar logarithm of the motor; J is moment of inertia for motor.

3 Design of a New Type of Sliding Mode Observer

According to the traditional sliding mode observer design (Fig. 1), the state equation of the traditional sliding mode observer is

$$\begin{aligned} i_\alpha &= -\frac{R}{L}i_\alpha - \frac{1}{L}Z_\alpha + \frac{1}{L}u_\alpha \\ i_\beta &= -\frac{R}{L}i_\beta - \frac{1}{L}Z_\beta + \frac{1}{L}u_\beta \end{aligned} \tag{4}$$

$$\begin{aligned} Z_\alpha &= k_{sw} sign(\hat{i}_\alpha - i_\alpha) \\ Z_\beta &= k_{sw} sign(\hat{i}_\beta - i_\beta) \end{aligned} \tag{5}$$

Form in: is the sliding mode coefficient; is the Bang Bang controller.

In situations requiring high precision the output value e_α, e_β of the low pass filter can not meet the requirements, so it cannot be directly used. Because the estimated value of the counter electromotive force contains a large amount of deviation and high frequency chattering, the observer is needed to be improved. In order to obtain a better observation effect, a sliding mode observer for PMSM system is developed in this paper. An improved Sigmoid function is introduced, and a new type of sliding mode observer is designed [2]. The schematic diagram is shown in Fig. 2. The equation of the current observer model is

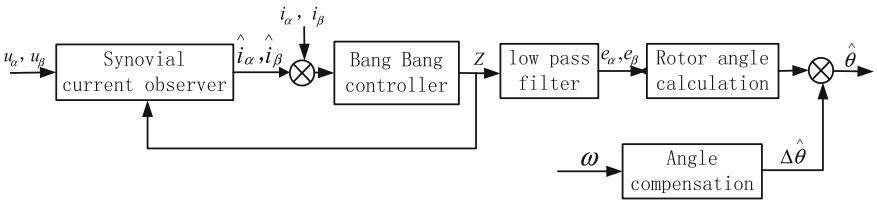

Fig. 1 Structure of traditional sliding mode observer

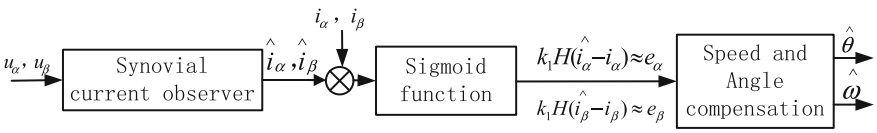

Fig. 2 Structure of a new type of sliding mode observer

$$\begin{aligned}\dot{\hat{i}}_\alpha &= -\frac{R}{L}\hat{i}_\alpha + \frac{1}{L}u_\alpha - \frac{1}{L}k_1 H(\hat{i}_\alpha - i_\alpha)\\ \dot{\hat{i}}_\beta &= -\frac{R}{L}\hat{i}_\beta + \frac{1}{L}u_\beta - \frac{1}{L}k_1 H(\hat{i}_\beta - i_\beta)\end{aligned} \tag{6}$$

Form in: k_1 is the observer gain; H is the *sign*( ) function [3, 5]. Its role is to use continuous control instead of the original discontinuous control. A is greater than zero in the real number, and it can be adjusted according to the actual situation. The sliding surface of the sliding mode observer is defined as

$$\begin{aligned}s_n &= \left[s_\alpha, s_\beta\right]\\ s_\alpha &= \hat{i}_\alpha - i_\alpha\\ s_\beta &= \hat{i}_\beta - i_\beta\end{aligned} \tag{7}$$

When the system arrives at the sliding surface, $S_n = 0$.
Using the formula (6) minus the equation of state can get the following formula

$$\begin{aligned}\frac{d}{dt}(\hat{i}_\alpha - i_\alpha) &= -\frac{R}{L}(\hat{i}_\alpha - i_\alpha) + \frac{1}{L}e_\alpha - \frac{1}{L}k_1 H(\hat{i}_\alpha - i_\alpha)\\ \frac{d}{dt}(\hat{i}_\beta - i_\beta) &= -\frac{R}{L}(\hat{i}_\beta - i_\beta) + \frac{1}{L}e_\beta - \frac{1}{L}k_1 H(\hat{i}_\beta - i_\beta)\end{aligned} \tag{8}$$

The sliding mode condition is substituted into the above formula, Well:

$$\begin{aligned}e_\alpha &= k_1 H(\hat{i}_\alpha - i_\alpha)\\ e_\beta &= k_1 H(\hat{i}_\beta - i_\beta)\end{aligned} \tag{9}$$

After the counter electromotive force is obtained, the rotor speed and the position of the motor can be calculated according to the counter electromotive force of the motor. As with the traditional sliding mode observer, the speed and position of the motor can be obtained by the formula (10) and (11).

$$\hat{\theta}_e = -\tan^{-1}\left(\frac{e_\alpha}{e_\beta}\right) \tag{10}$$

$$\hat{\omega}_e = \frac{d\hat{\theta}_e}{dt} \tag{11}$$

4 Simulation Test

In order to verify the feasibility and effectiveness of the proposed PMSM sensorless control strategy based on a novel sliding mode observer, a PMSM is choosed, motor parameters as shown in Table 1.

Simulation experiment was carried out using the Matlab/Simulink design simulation block diagram. The vector control of PMSM is adopted in this system, Which $i_{dref} = 0$, the PI controller is used in both of the speed loop and current loop.

(1) Simulation test under no load condition

The PMSM is running under the no-load condition, and the motor runs at a given speed 400 r/min. The permanent magnet synchronous motor is running under the no-load condition, and the motor runs at a given speed 400 r/min. The observation experiment of the motor speed, the counter electromotive force and rotor position can be completed, and the data collection of the motor operation is carried out. The simulation results are shown in Figs. 3 and 4.

Figure 3 simulation waveforms of the actual value and the estimated value of the motor speed based on the sliding mode observer control system. From the simulation results, at the starting stage of the motor, the initial value of the counter electromotive force is zero and the starting value is small. The error of the estimated speed of the motor is larger in the initial stage. And at the starting stage, because of the fixed speed in the simulation system for a fixed value, there is no amount of buffer, so that the estimated value of the motor starting current reverse drag phenomenon. After stable operation, it can be seen that the motor speed from the sliding mode observer is relatively smooth, and the observer can quickly track the speed change. The speed estimation error is very small in the stable stage. Figure 4 simulation waveforms of actual value and estimated value of the motor rotor position in the system. The simulation results show that the observation accuracy of the motor position is higher, and the position error of the motor is very small.

(2) Simulation test under loading condition

The PMSM starts under no-load condition, when it runs to the time of 0.1 s, the motor with the load 5 N m is added to the motor. The motor runs at the speed of 400 r/min, and the information of the torque, motor speed and rotor position is observed.The simulation results are shown in Figs. 5 and 6. Figure 5 speed

Table.1 Parameters of motor system

Parameters of PMSM	Parameter values
Stator winding resistance	0.975 Ω
Mutual inductance of stator winding	0.006 H
Pairs of magnetic pole	4
Moment of inertia	0.0015 kgm^2
EMF constant	0.215
Viscous friction coefficient	0.0037

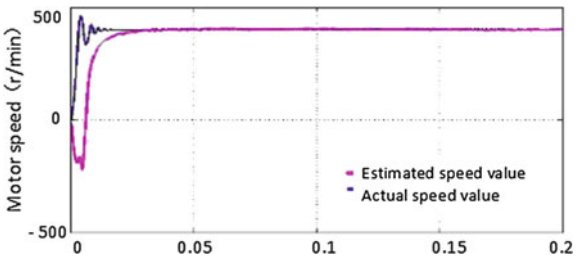

Fig. 3 Actual value and estimated value of motor speed under no-load condition

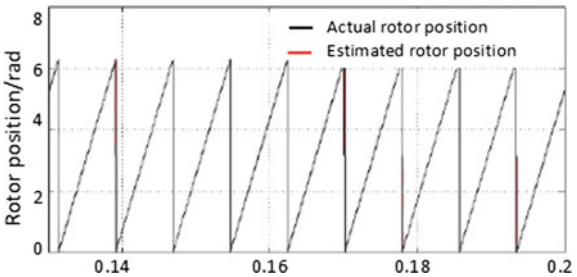

Fig. 4 Actual value and the estimated value of the rotor position under no-load condition

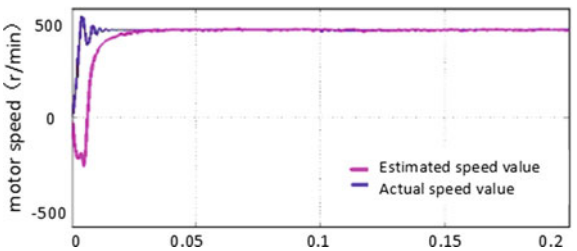

Fig. 5 Actual value and the estimated value of the motor speed under the condition of loading

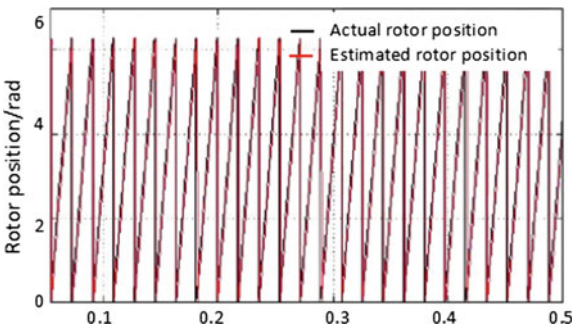

Fig. 6 Actual value and the estimated value of the rotor position under the condition of loading

simulation waveform, we can see that the design of the sliding mode observer under the loading conditions, the system can still get a better estimate of the speed. The simulation results are close to the results of the no-load condition, and can achieve

good control effect. Figure 6 after 0.1 s motor rotor position simulation waveform of the loading system. When the load is abrupt, the position error has a slight increase, and then quickly returns to the stable stage, the observation accuracy is still very high.

5 Conclusion

In this paper, based on the analysis of the traditional sliding mode observer, the Sigmoid function is introduced into the sliding mode observer, a new type of sliding mode observer is designed and the PMSM sensorless control strategy based on the observer is proposed. Simulation results show that the novel sliding mode observer overcomes the buffeting problem existing in the conventional sliding mode observer and reduces the filter links and phase compensation link, simplifies the traditional sliding mode observer. It achieves a higher degree of accuracy of the position and speed of PMSM estimation. The results show that the proposed method is feasible and effective for PMSM sensorless control strategy.

Acknowledgements This paper is supported by the young science foundation project of National Natural Science Foundation of China (61503226) and the natural science project (16YCYBZR02).

References

1. Wang Q, Zhang C, Zhang X (2008) Variable-structure MRAS speed identification for permanent magnet synchronous motor. Proc CSEE 29(9):71–75
2. Eom W, Kang I, Lee J (2013) Enhancement of the speed response of PMSM sensorless control using an improved adaptive sliding mode observer. In: IEEE Conference on Industrial Electronics, pp 188–191
3. Paponpen K, Konghirun M (2012) An improved sliding mode observer for speed sensorless vector control drive of PMSM. In: IEEE Conference on Power Electronics and Motion Control, vol 2, pp 1–5
4. Xu D, HE Y (2010) Motor control. Zhejiang University press, Hangzhou, pp 90–120 (in Chinese)
5. Vaclavek P, Blaha P (2007) Synchronous machine drive observability analysis for sensorless control design. In: Proceedings of the IEEE International Conference on Control Applications, pp 1113–1117

Ship Three-Axis Turntable Control Based on Fuzzy Inference Variable Universe

Huixuan Fu, Yuan Li, Zhongliang Zhang and Yuchao Wang

1 Introduction

The three-axis turntable is used to simulate the navigation attitude. Three-axis including roll axis, pitching axis and bow thruster, are driven by three DC torque motor. Compared with the general flight test turntable, its running speed is relatively low, the rotation of each axis is smaller, the set frequency and amplitude is lower [1, 2], so the low-speed performance is the main performance index of ship turntable. With the improvement of turntable precision and low speed performance requirements, high accuracy turntable control [3, 4], improving the speed of rotary table control system performance is to become more important.

At present, many domestic and foreign scholars have done a lot of research on the turntable performance problems, they generally considered the turntable performance is mainly affected by the friction torque of the driving motor, especially the turntable will crawl phenomenon at low speed, seriously affecting the low-speed performance of turntable [5]. In order to reduce the impact of friction, a traditional double-loop PID controller has designed [6]. However, during the operation of the turntable system, the frictional torque changes with external factors such as inertia, mechanical wear, lubrication and temperature. Due to the low speed friction torque and the complicated nonlinear factors of the turntable system, it is difficult to solve this problem by traditional control methods based on precise mathematical model.

The variable universe fuzzy control algorithm means that the universe of the fuzzy control system can be changed with the error, without changing the number of the control rules, to the universe of the allergic error [7]. The fuzzy logic controller based on variable universe fuzzy controller does not need too much universe expert knowledge, only need to know the general trend of the rule [8].

H. Fu · Y. Li · Z. Zhang · Y. Wang (✉)
College of Automation, Harbin Engineering University,
Nantong Street 145, Harbin, India
e-mail: wangyuchao@hrbeu.edu.cn

Z. Deng (ed.), *Proceedings of 2017 Chinese Intelligent Automation Conference*,
Lecture Notes in Electrical Engineering 458,
https://doi.org/10.1007/978-981-10-6445-6_23

According to the characteristics of ship motion, a variable universe fuzzy controller for ship three-axis turntable has been designed. The simulation results showed that the method can improve the turntable performance and control accuracy.

2 Establishment of Turntable and Friction Model

At low speeds, the most important effect on turntable performance is the friction disturbance torque. In order to facilitate the modeling and analysis of friction, a simplified stribeck friction model is used as follows [9]:

$$T_f = \begin{cases} T_m \mathrm{sgn}(\dot{\theta}) + [(T_m - T_c)/e \\ -(T_m - T_c)/\dot{\theta}_s + K_v]\dot{\theta} & if \ |\dot{\theta}| < \dot{\theta}_s \\ T_c + K_v \cdot \dot{\theta} & if \ |\dot{\theta}| \geq \dot{\theta}_s \end{cases} \tag{1}$$

The linear transformation is as follows:

$$f = \begin{cases} (T_m - T_c)/e - \\ (T_m - T_c)/\dot{\theta}_s + K_v & if \ |\dot{\theta}| < \dot{\theta}_s \\ K_v \cdot \dot{\theta} & if \ |\dot{\theta}| \geq \dot{\theta}_s \end{cases} \tag{2}$$

$$T_f = T_m + f\dot{\theta} = T_m + f\,\omega \tag{3}$$

The friction model is substituted to get the direct torque motor model with friction disturbance, as shown in Fig. 1.

The figure U_a shows the input DC voltage, I_a is the armature current, R_a is the armature resistance, L_a is the armature inductance, T_L is the load torque, T_m is the maximum static friction torque, f is the linear friction coefficient, J is the motor shaft inertia, θ is the angle value, T_c is Coulomb friction torque, T_ε is the external force, $\dot{\theta}_s$ is the speed, K_v is the viscosity constant.

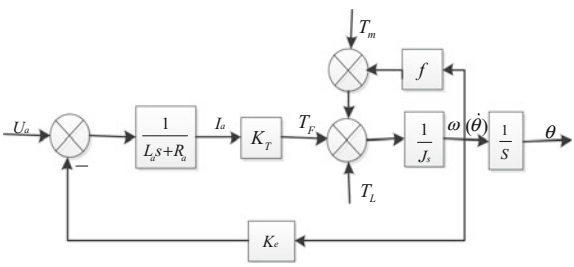

Fig. 1 Single axis turntable model with friction disturbance

3 Turntable Fuzzy Control Strategy for Variable Universe

According to the characteristics and the feasibility of the ship motion, the variable universe fuzzy control based on fuzzy inference is used to design the control system of the turntable azimuth axis system. The system has two main controller module, one controller module determines the input and output of the universe extension factor, the other determines the control output, the input is both determines by the position error e of the turntable and the error rate ec [10]. Figure 2 is the principle block diagram of variable universe fuzzy control system.

Three-axis turntable input variables in e universe for $X_1 = [-E, E]$, the universe of another input variable ec is $X_2 = [-EC, EC]$, the universe of output variable u is $Y = [-U, U]$. The fuzzy division of X_i is $A = \{ A_{ij}\}$, the fuzzy division of Y is $B = \{ B_j\}$, fuzzy control rules are as follows [11]:

$$If\ e\ is\ A_{1j}\ and\ ec\ is\ A_{2j}\ then\ u\ is\ B_j \tag{4}$$

The peak point of A_{ij} is x_{ij} the peak point of B_j is y_j the algorithm based on fuzzy control is essentially a piecewise interpolation function, and the interpolation function is $F(e, ec)$, then the above rule can be transformed into the following formula:

$$u(e, ec) = F(e, ec) \triangleq \sum \prod A_{ij}(x_i) y_j \tag{5}$$

The input and output universe changes expressed as follows:

$$X_1(x) = [-\alpha(x)E, \alpha(x)E] \quad X_2(x) = [-\beta(x)Ec, \beta(x)Ec] \quad Y(x) = [-\gamma(x)U, \gamma(x)U] \tag{6}$$

In formula (6), X_1, X_2, Y are the initial universe, $X_1(x)$, $X_2(x)$, $Y(x)$ are the variable universe.$\alpha(x)$, $\beta(x)$, $\gamma(x)$ respectively for the input variables e, ec, universe scaling factor, u is output variables.

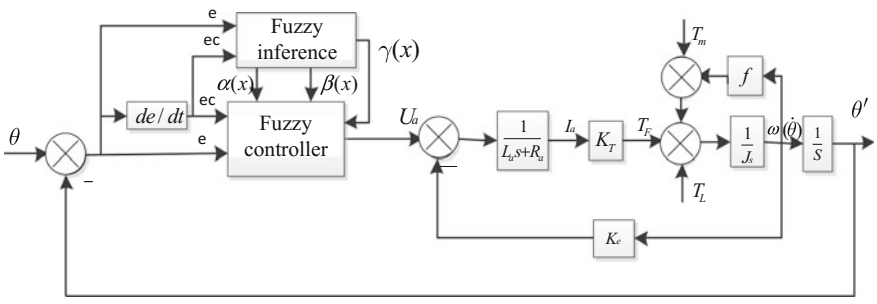

Fig. 2 Functional block diagram of turntable FI-VUFC system

The initial control rules $R(0) = R$, the initial field $X_1 = [-E, E]$, $X_2 = [-EC, EC]$, $Y = [-U, U]$, on the basis of the linear basis are $\{A_i\}_{(1 \le i \le p)}$, $\{B_j\}_{(1 \le j \le q)}$, $\{C_{ij}\}_{(1 \le i \le p, 1 \le j \le q)}$, the peak value of $-E = x_{11} < x_{12} < \cdots < x_{1p} = E$, $-EC = x_{21} < x_{22} < \cdots x_{2p} = EC$, $-U = y_{11} < y_{12} < \cdots < y_{pq} = U$, so that $x_{1i}(0) = x_{1i}$, $x_{2j}(0) = x_{2j}$,$y_{ij}(0) = y_{ij}$, membership functions are defined as $A_i(x_1(k), k)$, $B_j(x_2(k), k)$, the following steps are get the dual input single output controller:

Step 1. Initialize Input $x_1(0) \in X_1$, $x_2(0) \in X_2$ to get the output:

$$y(1) = F(x_1(0), x_2(0)) = \sum_{i=1}^{p} \sum_{j=1}^{q} A_i(x_1(0)) B_j(x_2(0)) y_{ij}(0) \tag{7}$$

Step 2. The y(1) is applied to the controlled object to get the output of the system, and then feedback to the system and reference input, the controller input $x_1(1)$, $x_2(1)$

$$x_{1i}(1) = \alpha(x(1)) x_{1i}(0) \tag{8}$$

$$x_{2j}(1) = \beta(x_1(1), x_2(1)) x_{2j}(0) \tag{9}$$

$$y_{ij}(1) = F(x_{1i}(1), x_{2j}(1)) = \sum_{s=1}^{p} \sum_{t=1}^{q} A_s(x_{1i}(1)) B_t(x_{2j}(1)) y_{st}(0) \tag{10}$$

Step K. The y(k) is applied to the controlled object to get the output of the system, and then feedback to the system and reference input, the controller input $x_1(k)$, $x_2(k)$. Similarly:

$$x_{1i}(k) = \alpha(x_1(k)) x_{1i}(0) \tag{11}$$

$$x_{2j}(k) = \beta(x_1(k), x_2(k)) x_{2j}(0) \tag{12}$$

$$y_{ij}(k) = F(x_{1i}(k), x_{2j}(k)) = \sum_{s=1}^{p} \sum_{t=1}^{q} A_s(x_{1i}(k)) B_t(x_{2j}(k)) y_{st}(0) \tag{13}$$

From the above formula, the adaptive fuzzy control strategy of the double input and single output are:

$$y(k+1) = \sum_{s=1}^{p}\sum_{t=1}^{q}\sum_{i=1}^{p}\sum_{j=1}^{q} A_i(x_1(k)/\alpha(x_1(k)))\cdot$$
$$A_s(\alpha(x_1(k)x_{1i}(0))\cdot \quad B_j(x_2(k)/\beta(x_1(k),x_2(k)))\cdot \quad B_t(\beta(x_1(k),x_2(k))x_{2j}(1)y_{st}(0) \tag{14}$$

when $x_1(k) \to 0$, $x_2(k) \to 0$, $y(k+1) \to 0$.

4 Scaling Factor Selection

The core of variable universe is the selection of scaling factor. The size of the scaling factor determines the shape of the universe. It directly affects the performance of variable universe fuzzy control. According to the definition, scaling factor meet the following conditions [11]:

(1) Scaling factor based on function model

According to the definition and properties, the scaling factor is expressed as a function of the output variable. The commonly input and output scaling factor s are as follows [6]:

$$\alpha(x) = \left(\frac{|x|}{E}\right)^{\tau},\ \tau > 0 \quad \alpha(x) = 1 - \lambda\ \exp(-kx^2)$$
$$\gamma(x,y) = \left(\frac{|x|}{E}\right)^{\tau_1}\left(\frac{|y|}{Ec}\right)^{\tau_2},\ 0 < \tau_1, \tau_2 < 1 \tag{15}$$

The formula above is a practical mathematical model derived from the relationship between fuzzy rules and scaling factor, and it can be used as a general conclusion. Because of this, the fixed function model is used to describe the uncertainty of the change of the scaling factor, which will cause a certain deviation.

(2) Scaling factor based on fuzzy inference

The scaling factor based on fuzzy inference is to adjust the flexibility factor by another fuzzy control. The input universe extension factor is only related to *e ec*, which is divided into fuzzy *NB*, *NM*, *NS*, *ZO*, *PS*, *PM*, *PB*. To input universe scaling factor $\alpha(x)$, $\beta(x)$ for *B*, *M*, *S*, *Z*, respectively, represent "universe to adjust", "universe to small adjustment", "on the field to zero adjustment" are as follows.

The new universe is $[-E', E']$, $[-EC', EC']$, $[-U', U']$, the fuzzy control of output control is divided into *NB*, *NM*, *NS*, *ZO*, *PS*, *PM*, *PB*. On the basis of this universe, the fuzzy rules of the output control quantity of the variable universe fuzzy controller are Table 1.

Table 1 Fuzzy rules of output control

ec/e	NB	NM	NS	ZO	PS	PM	PB
NB	NB	NB	NM	NM	MS	NS	ZO
NM	NB	NM	NM	NS	NS	ZO	PS
NS	NM	NM	NS	NS	ZO	PS	PS
ZO	NM	NS	NS	ZO	PS	PS	PM
PS	NS	NS	ZO	PS	PS	PM	PM
PM	NS	ZO	PS	PS	PM	PM	PB
PB	ZO	PS	PS	PM	PM	PB	PB

5 Simulation Analysis

The parameter values of the azimuth axis of the turntable are respectively:

$L_a = 0.02$, $R_a = 12.1$, $K_T = 4.11$, $K_e = 4.11$

Considering the friction disturbance torque of the turntable, according to the friction model established in the second section, the empirical data $T_m = 2\ N \cdot m$, $T_c = 1.5\ N{\cdot}m$, $\dot{\theta}_s = 0.05$, $K_v = 0.4$. The simulation curves of the turntable are as shown in Fig. 3.

In Fig. 3, the blue curve is Stribeck nonlinear friction torque curve, and the red curve is a linear friction torque curve drawn by the piecewise function model. It can be seen from the curve that the linear curve is better than the real value of the friction torque model, and it can be used for simulation analysis.

The rotation inertia of the azimuth axis of the turntable is $J = 1$. In order to compare the control effect of the variable universe fuzzy controller, a simulation model of PID control and a simulation model of fuzzy PID are established respectively. The results of the three controllers are compared under light load and load respectively.

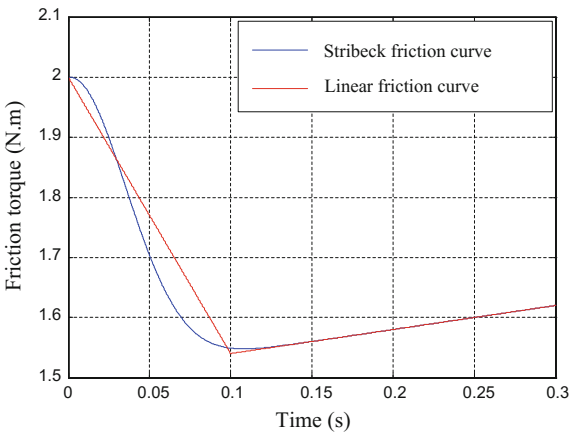

Fig. 3 Friction disturbance moment of turntable

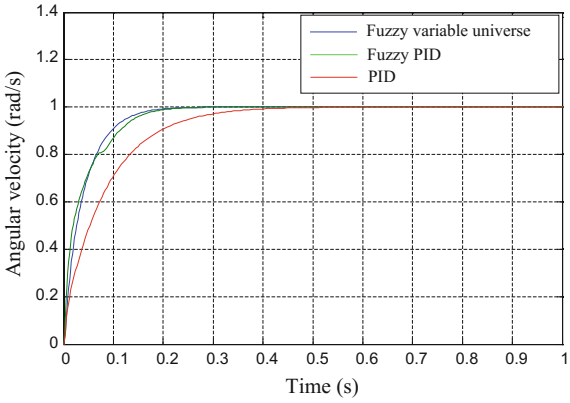

Fig. 4 Control system step response in fractional load of three different control strategies

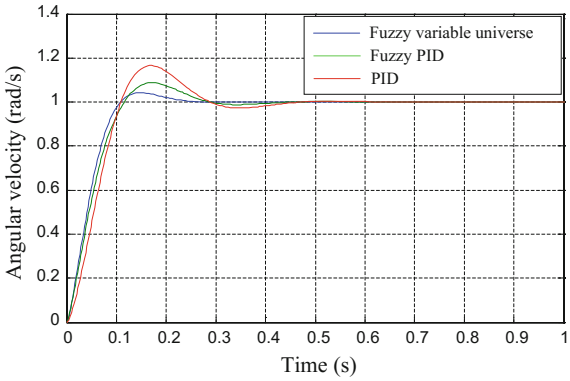

Fig. 5 Control system step response in heavy load of three different control strategies

The input is $r(t) = 1(t)$, under the interference of the linear friction torque shown in Fig. 3, the inertia $J = 1$, simulated under the condition of fractional load, the three control strategies angular velocity simulation results are shown in Fig. 4.

Other conditions do not change, so that the moment of inertia $J = 5$, the simulation results of the simulation of their respective angular load, as follows.

As can be seen form Figs. 4 and 5, in the low speed conditions, three kinds of control strategy performance is not the same, the conventional double loop PID algorithm has a long dynamic response process, the adjusting time is long and there are some static error, a greater overshoot under load. Fuzzy PID has a better dynamic performance, but there are some overshoot and the low speed performance is not so good. The low speed response curve of the fuzzy variable universe control algorithm is good, the response time is fast, the overshoot is small and the static precision is high. Compared with the previous three control strategies, the fuzzy control algorithm has better low-speed performance. From the different load conditions, the fuzzy variable universe control algorithm is better than the fuzzy PID control algorithm and PID algorithm.

6 Conclusions

This paper designed a variable universe fuzzy controller for ship three-axis turntable. According to the low speed characteristics of the marine turntable, the fuzzy control based on the fuzzy inference is used to realize the variable universe. Compared with the PID algorithm and fuzzy PID algorithm, the variable universe fuzzy control based on fuzzy reasoning has good low-speed and fastness, and the adaptability is also good when the load changes which verifies the superiority of variable universe fuzzy control in low speed control for turntable.

Acknowledgements This work is supported by the National Natural Science Foundation of China (Grant No. 51409064, No. 51409062).

References

1. Liu S, Zhang Y, Yu C et al (2012) Three-dimensional fuzzy control for ship electric propulsion turbine. Proc CSEE 32(3):117–122
2. Shunqing Ren, Guangcheng Ma, Changhong Wang (2005) Axis intersection measurement of three-axis turntable with two crosshair targets. J Harbin Inst Technol 12(3):250–254
3. Liang L, Cui D, Zhang S (2010) Research on moment coupling and compensation control of three-axis ship motion simulation turntable, advanced design and manufacture II, pp 625–628
4. Oner Y, Cetin E, Ozturk HK et al (2009) Design of a new three-degree of freedom spherical motor for photovoltaic-tracking systems. Renew Energy 34(12):2751–2756
5. Guo X, Wang Q, Li G et al (2011) Adaptive fuzzy control for permanent magnet spherical motor based on friction compensation. Proc CSEE 31(15):75–79
6. YU Z, Zeng M, Qiao D et al (2008) Complex control for friction compensation in DC motors. Electr Mach Control 12(5):539–543
7. Wu TZ, Juang Y-T (2008) Design of variable structure control for fuzzy nonlinear systems. Expert Syst Appl 35:1496–1503
8. Li H, Miao Z, Lee ES (2002) Variable universe stable adaptive fuzzy control of a nonlinear system. Comput Math Appl 44:799–815
9. Boulkroune A, Tadjine M, M'Saad M et al (2010) Fuzzy adaptive controller for MIMO nonlinear systems with known and unknown control direction. Fuzzy Sets Syst 161:82–797
10. He N, Gao Q, Jiang C et al (2013) Variable universe fuzzy control on nearspace vehicle. Control Eng China 20(1):121–123
11. Li H, Miao Z, Wang J (2002) Variable universe stable adaptive fuzzy controller for nonlinear system. Sci China 32(2):211–223

A Method of Fault Diagnosis Based on DE-DBN

Yajun Wang, Jia Zhang and Fang Deng

1 Introduction

With the development of science and technology, it becomes difficult to deal with modern complex equipment with the traditional methods of fault diagnosis. As a new kind of multi-layer neural network learning algorithm, deep learning has been paid more and more attention due to its remarkable advantages in dealing with complex problems. DBN [1], as one of the classical algorithms of deep learning, has successfully solved such problems as information retrieval, dimension reduction, fault classification and so on, with its excellent feature extraction and training algorithm. Since 2013, Tamilselvan et al. [2], who first applied DBN to aircraft engine fault diagnosis, there are more and more domestic and foreign scholars began to pay attention to this area and made a lot of research results. But as a new research direction of fault diagnosis, there are still many problems to be solved at present. This paper raises two problems in fault diagnosis field: training complexity and fault diagnosis precision. Firstly, DBN, as a deep neural network, requires a long training time, so it is a very time-consuming and labor-intensive task to adjust the parameters of the neural network during training; Secondly, deep model is a non-convex function, so the theoretical research in this field is extremely difficult. How to improve the generalization ability of deep model by combining the existing mature optimization theory with DBN is a problem worthy of discussion. This paper introduces the DE algorithm to try to solve the above problems and get a better effect.

Y. Wang · J. Zhang · F. Deng (✉)
School of Automation, Beijing Institute of Technology, Beijing 100081, China
e-mail: dengfang@bit.edu.cn

Y. Wang · J. Zhang · F. Deng
Key Laboratory of Intelligent Control of Complex System, Beijing 100081, China

Z. Deng (ed.), *Proceedings of 2017 Chinese Intelligent Automation Conference*,
Lecture Notes in Electrical Engineering 458,
https://doi.org/10.1007/978-981-10-6445-6_24

In order to solve the TE chemical process fault diagnosis with massive and highly cross-correlation data, this paper proposes a fault diagnosis method based on DE-DBN. Firstly, we use the DBN model to achieve the fault diagnosis of the TE process. Then we introduce the DE algorithm to optimize the training of the basic DBN model in two aspects. Finally, through a lot of simulation experiments, the validity and feasibility of the algorithm are verified in fault diagnosis field.

2 Deep Belief Networks

DBN is a multi-layer perceptron neural network composed of a series of Restricted Boltzmann Machine (RBM). Each RBM is composed of two layers of network, namely the visual layer ($\boldsymbol{V}$) and the hidden layer ($\boldsymbol{H}$). The layers are connected by the weight $\boldsymbol{W}$ and there is no connection in the layer. The data can be converted to each other by the RBM rule through the activation function. After the input data is transformed by the lower layer of the RBM, its output is regarded as the input of the higher layer of the RBM. The data is transmitted layer by layer, so that the features of the higher layer are more abstract and more capable of representation than the lower layer. This is the main idea of greedy layer-wise pre-training of DBN [3], and also the main reason that DBN can be identified directly through the original fault data. The last layer is generally a classifier. And this paper chooses the soft-max as the classifier, which can classify the whole network by original data and adjust the whole deep network weights by the cost function. This is the backward fine-tuning for discrimination [4, 5].

In summary, DBN learning process consists of two parts: forward pre-training the stacked RBM by greedy layer-wise way and backward fine-tuning the entire network to achieve ideal performance. Because of the large amount of computation in the parameter update, this paper uses a fast learning algorithm for RBM, namely contrastive divergence (CD). When using training data to initialize the first visual layer (v_0), we only need to use k (usually k = 1) steps of Gibbs sampling to get a good approximation. So it is also named CD-k algorithm [6]. Furthermore, the momentum factor is added to the parameter update, and the training speed is accelerated by combining the previous gradient value [7]. At the same time, this paper also introduces the weight decay factor so that the weight can be updated with a large penalty item, which can avoid the over-fitting of the deep model [8]. BP algorithm is a typical representative learning algorithm in machine learning, so this paper choose it as the supervised way to fine-tuning the entire DBN. The All training process is shown in Fig. 1.

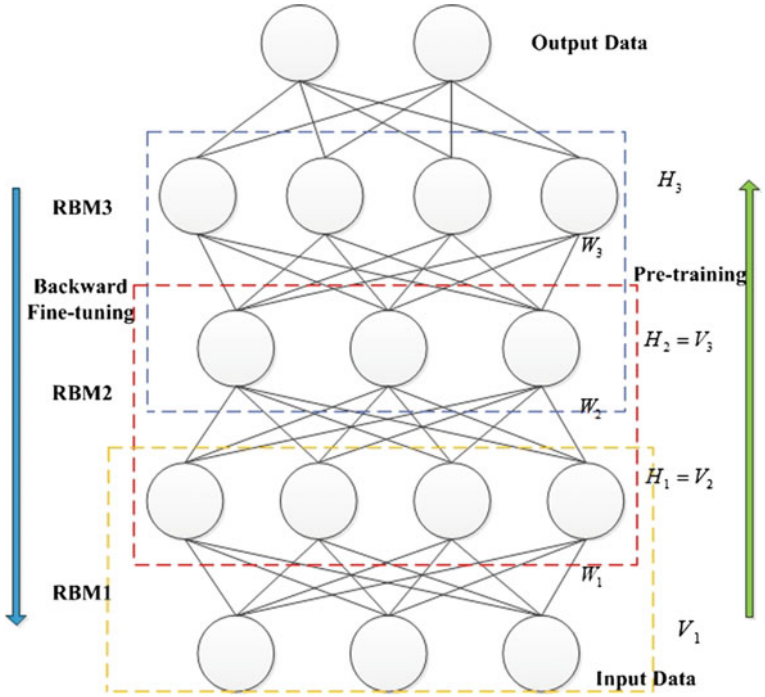

Fig. 1 DBN structure

3 DBN Model Based on DE Algorithm

3.1 The Process Classical DE Algorithm

DE was proposed by Storm et al. in 1995. As with other evolutionary algorithms, DE is a stochastic model that simulates the evolution of organisms, which means that those individuals who adapt to the environment is preserved by repeated iterations [9]. Compared with the other evolutionary algorithm, DE preserves the population-based global search strategy and reduces the complexity of genetic operations by using real coding, simple mutation based on difference and one-to-one competitive survival strategy. Meanwhile, the unique memory ability of DE makes it possible to dynamically track the current search situation to adjust its search strategy. So it has strong global convergence ability and robustness, and does not need to use the feature information of the problem. So it has good optimization performance. Obviously, it has better optimization performance than other evolutionary algorithms. The following is the basic process of the DE algorithm:

1. Initialize the population. Initialize the population randomly:

$$\begin{gathered}\left\{x_i(0)|x_{j,i}^L \le x_{j,i}(0) \le x_{j,i}^U,\ i=1,2,\ldots NP;\ j=1,2\ldots,D\right\} \\ x_{j,i}(0) = x_{j,i}^L + rand(0,1) \times (x_{j,i}^U - x_{j,i}^L)\end{gathered} \tag{1}$$

   where $x_i(0)$ denotes the ith individual of the generation zero in the population, $x_{j,i}(0)$ denotes the jth sequence of the ith individual, NP denotes the population size, rand (0, 1) denotes the random number uniformly distributed in the interval (0,1).
2. Mutation. The population is transformed by using the difference strategy.

$$v_i(g+1) = x_{r_1}(g) + F \times (x_{r_2}(g) - x_{r_3}(g)) \tag{2}$$

   where F is the mutation operator, $x_i(g)$ represents the ith individual in the gth generation population, and $r_1 \neq r_2 \neq r_3 \neq i$.
3. Crossover. Cross between the gth generation $\{x_i(g)\}$ and $\{v_i(g+1)\}$:

$$u_{j,i}(g) = \begin{cases} v_{j,i}(g+1) & if\ rand(0,1) \le CR \\ x_{j,i}(g) & otherwise \end{cases} \tag{3}$$

   where CR is the crossover operator.
4. Selection. DE uses the greedy algorithm to select individuals into the next generation:

$$x_i(g+1) = \begin{cases} v_i(g+1) & if\ f(u_i(g+1)) \le f(x_i(g+1)) \\ x_i(g+1) & otherwise \end{cases} \tag{4}$$

3.2 Hyper-parameter Learning of DBN Based on DE

In DBN training process, its hyper-parameters (such as learning rate, number of hidden nodes and so on) need to be tested many times in order to roughly determine a better value. It costs considerable time and effort on hyper-parameter adjustment of DBN training. In order to solve the problem, this paper uses the DE algorithm to learn the hyper-parameters of DBN [10].

According to Fig. 1 and parameter updating rule, this paper constructs $X = [m_1, m_2, \ldots m_n, \eta, \lambda, \alpha]$ as the individual vector in the DE algorithm. $m_1, m_2, \ldots m_n$ is the number of units in DBN hidden layer, learning rate $\eta \in (0,1)$, weight decay factor $\lambda \in (0,1)$ and momentum factor $\alpha \in (0,1)$. Population size NP generally takes 5D–10D (D is the dimension of X). The process of DBN hyper-parameter learning based on DE algorithm is shown in Table 1.

Table 1 Hyper-parameter learning process

Algorithm 2: DBN hyper-parameter learning based on DE
Input: Training and test sample set; Mutation operator F; Crossover operator CR; population size NP; Max_Epoch; test accuracy threshold $P_{\max}$; The dimension of the hyper-parameter vector D and its boundary value $X_{\min}, X_{\max}$. Output: Optimized hyper-parameter individual vector

Training process
epoch = 1
For i = 1, 2 … NP
Initialize the super-parameter vector according to Eq. (1)
EndFor
While $(P \leq P_{\max})$ or (epoch $\leq$ Epoch)
For i = 1,2…NP
According to Eq. (2), we get the hyper-parameter individual vector of mutation
For j = 1,2,…D
According to Eq. (3), the elements in the individual vector are selected with certain crossover probability CR.
EndFor (A new candidate individual vector is formed by the selected elements)
According to Eq. (4), the original and candidate individual vectors are used to train the DBN model, and the new individual vectors are selected by comparing the test accuracy of the two DBN.
EndFor (obtain a new population)
epoch = epoch + 1
Calculate the highest test accuracy of the new population
EndWhile

3.3 Optimization of DBN Network Parameters Based on DE

The performance of DBN depends on the quality of the deep model network parameters. Optimizing DBN network parameters with DE can improve the convergence speed and generalization performance of the DBN. The algorithm process is shown in Table 2.

4 Experiments in TE Process

4.1 TE Process Introduction and Data Preprocess

The TE process was proposed by Tennessee-Eastman, USA, and its main purpose was to provide a realistic industrial process for evaluating process diagnosis. The whole process mainly has five operating units: reactor, condenser, compressor, separator and stripper. Process monitoring includes four steps, i.e. fault detection,

Table 2 Optimization process of DBN network parameters

Algorithm 3: Optimization of DBN Network Parameters Based on DE
Input: Training and test sample set; Mutation operator F; Crossover operator CR; population size NP; Maximum number of iterations M; test accuracy threshold P; the hyper-parameter Table 2 (continued) vector X obtained in Sect. 3.2. Output: The test accuracy

Training process
m = 1
The DBN model was trained with the hyper-parameters X
For i = 1, 2 … NP
The above DBN model trained by X can obtain a set of better DBN network parameters (a set of optimal weights and bias). The initial population is generated by adding random deviations of the normal distribution to the optimal parameters, which will greatly reduce the scope of search and improve the reconstruction effect.
EndFor
While $(P \leq P_{\max})$ or $(m \leq M)$
For i = 1, 2 … NP
According to Eq. (2), the mutational DBN network parameters are obtained
For j = 1,2,…D
According to Eq. (3), the elements in the parameters vector are selected with certain crossover probability CR.
EndFor(A new candidate individual vector is formed by the selected elements)
According to Eq. (4), the original and candidate individual vectors are used to initializing the DBN parameters, and the new individual vectors are selected by comparing the test accuracy of the accuracy of two DBN
EndFor(obtain a new population)
m = m + 1
Calculate the highest test accuracy of the new population
EndWhile

fault identification, fault diagnosis and recovery process. Here we put TE process as the research platform to research fault diagnosis [11].

The fault diagnosis data of TE process can be downloaded from the http://web.mit.edu/braatzgroup/links.html. The fault data is obtained by the TE simulation system, which is sampled once every 3 min, and finally obtains the 960 sets of training samples and the 480 sets of test samples. Each sample consists of 22 faults and each set of samples contains 52 features.

The magnitude of the 52 features values observed in the TE process is not at the same level, which will affect the results of the data analysis. So it is necessary to perform data normalization processing to eliminate the dimensional effect between the feature quantities. The Z-score normalization method is used in this paper.

$$x_p = \frac{x_u - \mu}{\sigma} \tag{5}$$

where x_p denotes the preprocessed data, x_u denote the original data, μ, σ respectively denote the mean and standard deviation of the original data. The processed data are in accordance with the standard normal distribution, i.e., the mean is 0 and the standard deviation is 1.In this paper, after processing 52 features by Z-score method, it can improve the efficiency of DBN training.

4.2 Experiments

4.2.1 DBN Hyper-parameter Optimization Based on DE

According to the model training process in 3.2 and after several experiments, the results of hyper-parameters of DBN model based on DE algorithm for TE process fault diagnosis are as shown in Table 3.

As can be seen from Table 3, when the number of layers is 3, the accuracy of fault diagnosis is the highest. Thus this paper chooses the parameters of 3L to train the DBN model.

4.2.2 DBN Parameters Optimization Based on DE

According to Sect. 3.3, the DBN model is trained by using the hyper-parameters in Sect. 4.2.1, and then the network parameters of DBN are optimized by DE algorithm. In order to prove the superiority of this method, we choose basic DBN, DBN based on PSO (PSO-DBN) and multi-layer perceptron (MLP) as the comparison [12]. The maximum number of iteration for DE and PSO in PSO-DBN and DE-DBN is set to 100, and the error rate threshold is set to 4%. After several experiments, TE process fault diagnosis accuracy and training time as shown in Table 4.

Table 3 The result of hyper-parameter optimization

Number of the hidden layer	1L	2L	3L	4L
Test accuracy (%)	85.66	87.35	90.17	88.63
Hyper-parameters	$m = 350$ $\eta = 0.11$ $\lambda = 0.001$ $\alpha = 0.6$	$m_1 = 210$ $m_2 = 200$ $\eta = 0.11$ $\lambda = 0.0005$ $\alpha = 0.7$	$m_1 = 220$ $m_2 = 150$ $m_3 = 100$ $\eta = 0.10$ $\lambda = 0.0001$ $\alpha = 0.9$	$m_1 = 200$ $m_2 = 150$ $m_3 = 90$ $m_4 = 50$ $\eta = 0.20$ $\lambda = 0.00007$ $\alpha = 0.9$

Table 4 The result of DBN parameters optimization

	Accuracy (%)	Training time (s)
Basic DBN	90.17	493
MLP	81.30	464
PSO-DBN	93.60	937
DE-DBN	96.00	773

From Table 4, it can be seen that under the same training samples and test samples, the accuracy of the fault diagnosis of the basic DBN and MLP is 90.17 and 81.30% respectively, the training time is 492 and 464 s respectively, the former is much higher than the latter, but the training time is longer than the latter. Compared with the basic DBN, MLP model has a short training time in the process of fault diagnosis, but the accuracy rate is low, which is far from the requirement of fault identification accuracy. Compared with the basic DBN, PSO-DBN will make the fault diagnosis accuracy of the model increase by 2.43%, but need to spend nearly twice the training time. This shows that PSO-DBN can improve the accuracy of fault diagnosis, but the cost of time is great. Compared with the basic DBN, the accuracy of the DE-DBN model is improved by 5.83% but the more time spent is 309 s. Based on the analysis, it is shown that the DBN model can improve the accuracy of fault diagnosis compared with MLP model; And DE-DBN can not only improve the accuracy of fault diagnosis, but also take into account the training efficiency of the model, which proves the superiority of the algorithm.

5 Conclusion

In order to improve the accuracy of fault diagnosis, this paper proposes a DE-DBN algorithm. From the experimental results we can see that the main conclusions of this paper are three points: Firstly, compared with MLP, DBN are more suitable for diversity, non-linear, high-dimensional fault diagnosis under the large data background; Secondly, compared with the basic DBN model, the addition of PSO and DE algorithm makes the fault diagnosis accuracy of DBN model higher, which can improve the performance of the model to a certain extent; At last Compared with PSO algorithm, DE has better training robustness, faster training speed and fewer parameters to be initialized when establishing the training model. Furthermore, the influence of the parameters on the model is relatively smaller. These results make the DE-DBN model better than PSO-DENs in fault diagnosis accuracy and training time.

Acknowledgements This project is partly supported by Beijing NOVA Program, xx2016B027.

References

1. Hinton GE, Salakhutdinov RR (2006) Reducing the dimensionality of data with neural networks. Science 313(5786):504
2. Tamilselvan P, Wang P (2013) Failure diagnosis using deep belief learning based health state classification. Reliab Eng Syst Safety 115(7):124–135
3. Bengio Y, Lamblin P, Popovici D et al (2007) Greedy layer-wise training of deep networks. Adv Neural Inf Process Syst MIT Press 19:153–160
4. Hinton GE, Sejnowski TJ (1986) Learning and relearning in Boltzmann machines. MIT Press 1:282–317
5. Bengio Y (2009) Learning deep architectures for AI. Found Trends® in Mach Learn 2(1): 1–55
6. Hinton G (2002) Training products of experts by minimizing contrastive divergence. Neural Comput 14(8):1771–1800
7. Sutskever I, Martens J, Dahl G E et al (2013) On the importance of initialization and momentum in deep learning ICML (3)28:1139–1147
8. Hinton GE (2012) A practical guide to training restricted boltzmann machines. Momentum 9 (1):599–619
9. Storn R, Price K (1997) Differential evolution—a simple and efficient heuristic for global optimization over continuous spaces. J Global Optim 11(4):341–359
10. Rosa G, Papa J, Costa K et al (2016) Learning parameters in deep belief networks through firefly algorithm. In: IAPR Workshop on artificial neural networks in pattern recognition on Springer International Publishing, pp 138–149
11. Rusinov LA, Vorobiev NV (2013) Kurkina V V (2013) Fault diagnosis in chemical processes and equipment with feedbacks. Chemometr Intell Lab Syst 126(126):123–128
12. Shao H, Jiang H, Zhang X et al (2015) Rolling bearing fault diagnosis using an optimization deep belief network. Meas Sci Technol 26(11):11500

Detection of High Throughput Droplet in Microfluidic System

Yiming Yao, Minkai Li and Xiaojuan Chen

1 Introduction

Microfluidic chip, also known as the chip laboratory, refers to the biological and chemical fields involved in the sample preparation, reaction, separation, detection and other basic operating unit integrated or basically integrated into a few square centimeters of chips, by the micro-channel The formation of a network that controls the flow of fluids throughout the system and is used to replace the various functions of conventional biological or chemical laboratories [1–3]. Development so far, microfluidic chip technology has begun to be applied in different areas of life sciences [4]. Recently, droplet-based microfluidics has attracted more and more attention. Compared with micro-channels, micro-droplets have the following advantages: smaller size, higher flux, faster heat transfer, more flexible transport and fixation, and the formation of a relatively stable and controllable droplet microenvironment; In particular, in microfluidic chips, a large number of micro-droplets can be produced in a short time [5, 6]. Thus, in many high-throughput analysis in the field of chemistry and biology, micro-droplets are used as reactors for large-scale screening of reaction conditions (such as protein crystallization, DNA analysis, etc.), Or used to wrap in a wide variety of particles (including cells, Bacteria, etc.) for various biological studies [7–9]. For these applications, it is necessary to build a device or system based on a droplet microfluidic chip. In these devices or systems, people often need real-time understanding of micro-droplet information (size, morphology, movement speed, frequency of generation, etc.) [10, 11].

Y. Yao (✉) · M. Li · X. Chen
School of Electrical and Electronic Engineering,
Shanghai Institute of Technology, 200000 Shanghai, China
e-mail: 704866830@qq.com

Z. Deng (ed.), *Proceedings of 2017 Chinese Intelligent Automation Conference*,
Lecture Notes in Electrical Engineering 458,
https://doi.org/10.1007/978-981-10-6445-6_25

To this end, this study has implemented a device and method for observing micro-droplets to facilitate the observation of high-throughput micro-droplets, to obtain information about micro-droplets and to reduce costs.

2 Experimental Design

The droplet microfluidic real-time detection system constructed by this study consists of droplet generation system and digital image system. The droplet generation system is composed of nitrogen cylinders, micro-pumps, microfluidic chips and other experimental devices. The droplet generation system is used to generate droplets and the resulting droplets are used for droplet detection experiments. The digital image system includes a microscope, a CCD camera (QImaging Retiga 2000R). The digital image system is used to observe the process of droplet generation experiments and then image collection, image processing and so on (Fig. 1).

2.1 Experimental Principle

The camera model used in this paper is QImaging Retiga 2000R, the exposure time of the camera is set to 100 μs, because the exposure time is set very small, the droplets do not move during this time, so can clearly shoot the droplets.

The high-throughput micro-droplets in the microfluidic chip are usually highly repetitive, as shown in Fig. 2: the micro-droplets in the microfluidic chip have a

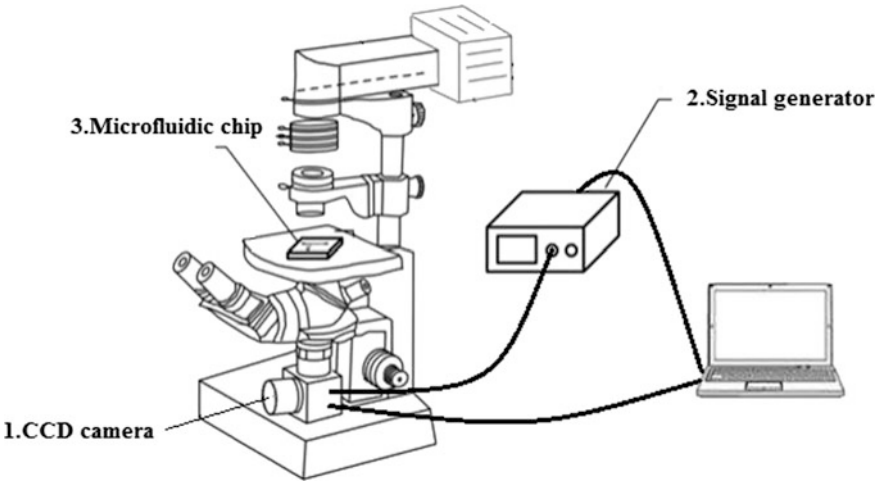

Fig. 1 Digital image system

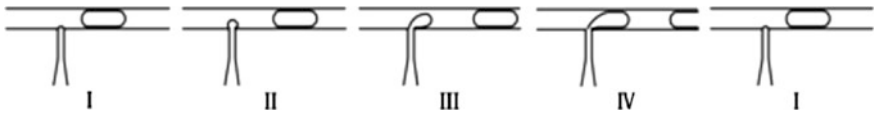

Fig. 2 Droplet cycle diagram

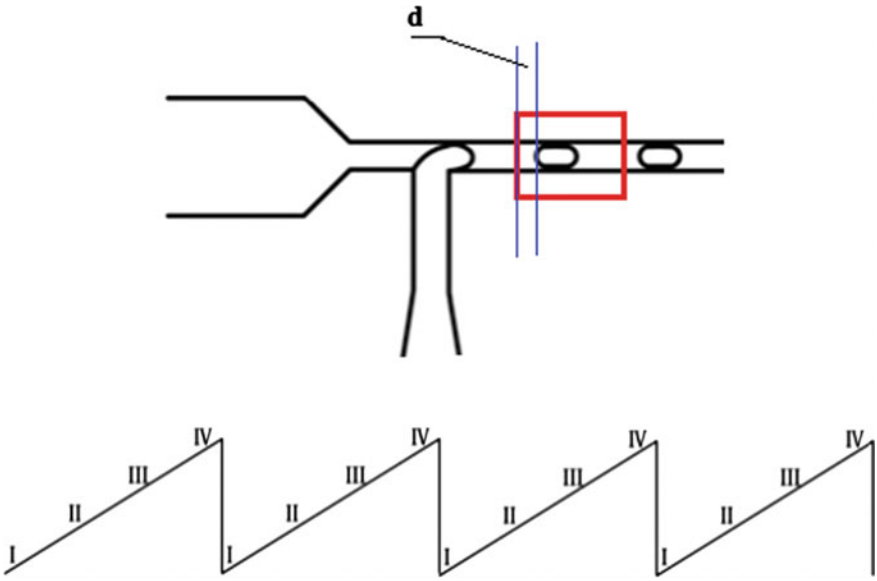

Fig. 3 Droplets and periodic signal

strong periodicity; for convenience of description, a droplet. The cycle is divided into I, II, III, IV state. In the droplet microfluidic, the four states are circulated in turn to reflect the periodicity of the droplets.

As shown in Fig. 3, select red areas for observation, The distance between the red boundary and the droplet is the ordinate, and the time is the abscissa, you can get a periodic signal.

The CCD camera is set to hardware trigger, the trigger frequency range is 5–30 Hz. Adjust the trigger frequency of the signal generator. When the trigger frequency is an integer multiple of the droplet generation frequency, the droplet position of each frame is the same.

As shown in Fig. 4, when the droplet position of each frame is the same, the droplet generation frequency f_n and the trigger $f_{droplets}$ frequency satisfy the formula, as below:

$$f_{\text{droplets}} = Nf_n \tag{1}$$

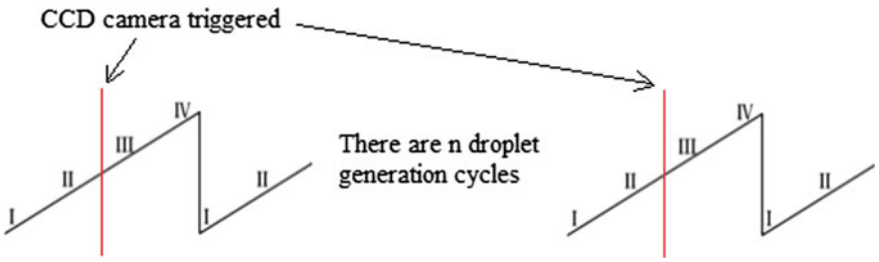

Fig. 4 Camera triggered and droplet generation cycles

Fig. 5 Template recognition

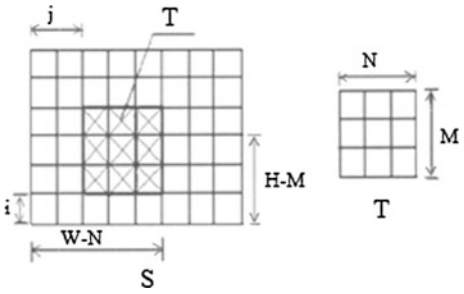

From small to large adjustment signal generator trigger signal, the frequency f_n, f_{n+1} of the stationary droplets in succession are obtain, as below:

$$f_{\text{droplets}} = (N+1)f_{n+1} \tag{2}$$

Calculate the actual frequency of the resulting droplet f_{droplets}:

$$f_{\text{droplets}} = \frac{f_{n+1}f_n}{f_n - f_{n+1}} \tag{3}$$

2.2 Template Recognition

The template matching is based on the known template image T in the search map S translation, find the region with the largest similarity to the template [12], and record the coordinates, the template cover under the search map called subgraph $S_{i,\ j}$, as shown in Fig. 5.

Where i, j are the coordinates under the search graph, m, n is the coordinates under the template, M, N is the height and width of the template, W, H is the width and height of the search image [13]. When the template T and subgraph S exactly match, D(i, j) is 0. After searching in search S, find the minimum $D_{\min}(i, j)$, the

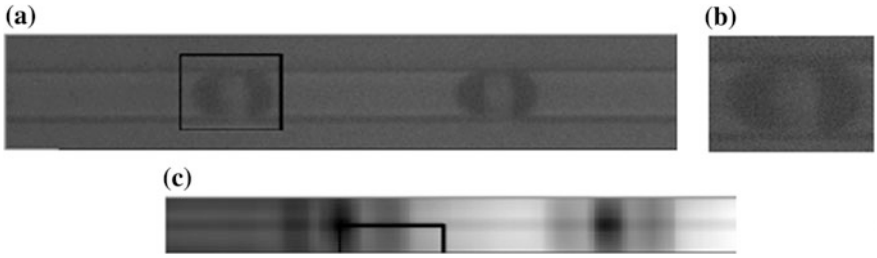

Fig. 6 The result of Template recognition microdroplets

corresponding sub-graph S is matching aims. The squared difference matching is selected according to the actual situation [14, 15], as below:

$$\mathrm{D}(i,j) = \sum_{m=0}^{M-1} \sum_{n=0}^{N-1} [S(m+i, n+j) - T(m,n)]^2 \tag{4}$$

If the D_{min}(i, j) is less than a threshold (this paper is based on the size of the template and the actual situation is 3,800,000), then the template is considered to be the same as the corresponding search area. Each frame takes the leftmost droplet as the target droplet. As shown in Fig. 6, (a) is a subgraph, (b) is a template, and (c) is a normalized display of the D(i, j) result matrix.

3 Programming

The trigger frequency is adjusted by computer and signal generator communication. From 5 to 30 Hz step 1 Hz to adjust the frequency of the signal generator. Each frame is stored 10 times at 600 ms intervals. Each frame takes the leftmost droplet as the target droplet. The target droplets are taken from two successive frames to calculate the distance between the target droplets. The distance calculated for each frequency is summed and the average is calculated to find the minimum of distances. The frequency of droplets can be determined by finding two adjacent minimum values (Fig. 7).

4 Experiment

In the experiment, the pressure of water and oil is 8 Pa. From 25 to 30 Hz step 0.05 Hz to adjust the frequency of the signal generator, each frame is stored 10 times at 600 ms intervals. The droplet displacement mean for each frequency

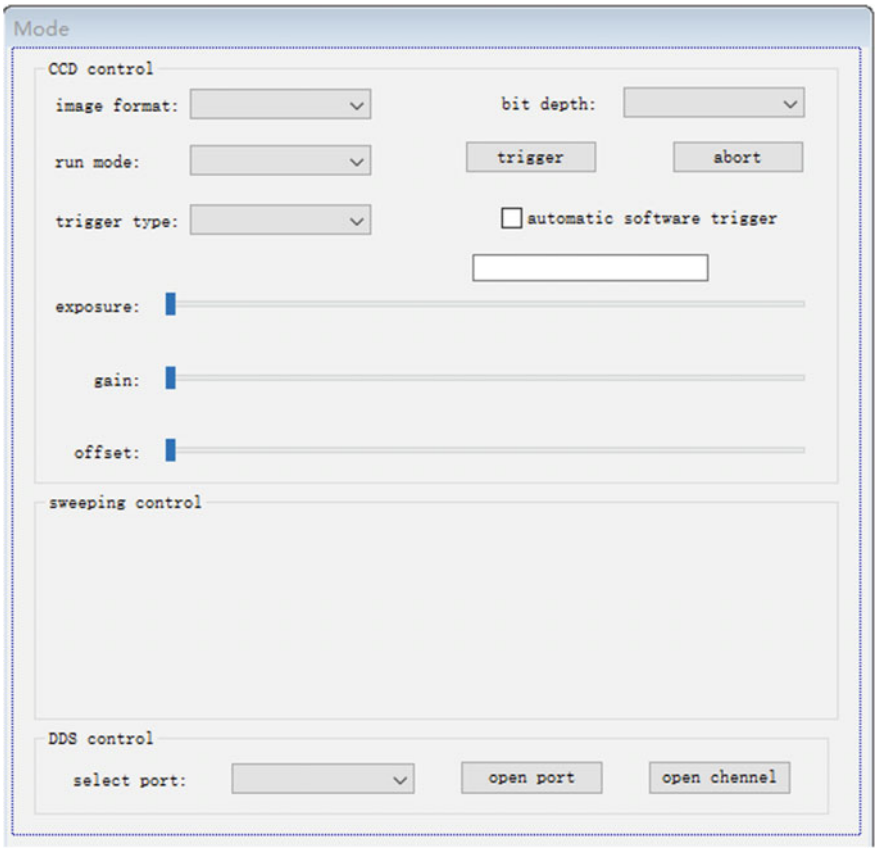

Fig. 7 MFC visualization interface

segment is shown in Fig. 8. Get f_n = 29.15 Hz f_{n+1} = 29.9 Hz, Take the Formula (4) to calculate $f_{droplets}$ = 1162.11 Hz. High-speed camera measured frequency of 1075 Hz. The experimental results are basically consistent.

5 Conclusion and Prospect

In this paper, a method for detecting the droplet frequency in a microfluidic system based on the principle of image processing is proposed in the case of no high-speed imaging device in a portable microfluidic system. By comparing the moving distance of droplets at different frequencies, find the minimum value to calculate the frequency of droplet generation.

Although the research on droplet detection in microfluidic system has achieved some results, the robustness of the program needs to be strengthened.

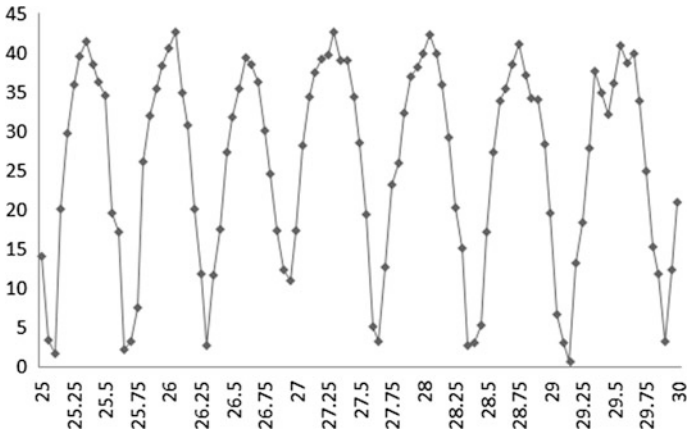

Fig. 8 Experimental data

The frequency of the droplets also changes slowly because the micro-pumps that produce droplets are unstable. In the slow frequency changes, real-time detection of droplets frequency is to be completed later.

References

1. Mazutis L, Gilbert J, Ung WL et al (2013) Single-cell analysis and sorting using droplet-based microfluidics. Nat Protoc 8(5):870
2. Cho S, Kang DK, Sim S et al (2013) A droplet-based microfluidic platform for high-throughput, multi-parameter screening of photosensitizer activity. Anal Chem 85 (18):8866–8872
3. Gasilova N, Yu Q, Qiao L et al (2014) On-chip spyhole mass spectrometry for droplet-based microfluidics. Angew Chem Int Ed Engl 53(17):4408–4412
4. Glawdel T, Elbuken C, Ren CL (2012) Droplet formation in microfluidic T-junction generators operating in the transitional regime. II. Modeling. Phys Rev E Stat Nonlinear Soft Matter Phys 85(1 Pt 2):016323
5. Hoeve WV, Dollet B, Versluis M et al (2011) Microbubble formation and pinch-off scaling exponent in flow-focusing devices. Phys Fluids 23(9):865
6. Fu T, Wu Y, Ma Y et al (2012) Droplet formation and breakup dynamics in microfluidic flow-focusing devices: From dripping to jetting. Chem Eng Sci 84(52):207–217
7. Chou WL, Lee PY, Yang CL et al (2015) Recent advances in applications of droplet microfluidics. Micromachines 6(9):1249–1271
8. Zhu Y, Fang Q (2013) Analytical detection techniques for droplet microfluidics—a review. Anal Chim Acta 787(13):24–35
9. Chao MA, Shen SF, Zhao L et al (2015) Multiscale applications of microfluidic chip in life science: from molecules to organisms. J Instrum Anal 13–22
10. Kasule JS, Maddala J, Mobed P et al (2015) Very large scale droplet microfluidic integration (VLDMI) using genetic algorithm. Comput Chem Eng 85:94–104

11. Chen AF, Huang HX (2016) Rapid fabrication of T-shaped micropillars on polypropylene surfaces with robust cassie-baxter state for quantitative droplet collection. J Phys Chem C 120 (3)
12. Soille P (2007) On genuine connectivity relations based on logical predicates. International Conference on Image Analysis and Processing, IEEE, pp 487–492
13. Jang I, Kim H, Lee H et al (2007) Height control and failsafe algorithm for closed loop air suspension control system. International conference on control, automation and systems, IEEE, pp 373–378
14. Mcdonnell MJ (1981) Box-filtering techniques. Comput Graph Image Process 17(1):65–70
15. Rosenfeld A, Vanderbrug GJ (1977) Coarse-Fine Template Matching. IEEE Trans Syst Man Cybern 7(2):104–107

Dynamics Control and Simulation of Two DOF Robot

Yanping Yang, Haisheng Yu, Songfeng Pan and Zhencheng Zhou

1 Introduction

As to the research of the robot control, it generally needs to start study respectively the driving motor control and dynamics control [1, 2] of the robot [3]. Especially, it mainly researches the uncertainty and nonlinear [4] of the robot model. It usually adopts sliding control and adaptive control [5]. This paper regards the two-degree-of-freedom robot as a research object, the position control method of the robot uses the adaptive control which has the high reliability and anti-interference capability. The adaptive controller can modify the model according to the information gathered by comparing the required performance index with the actual performance index of the system, which can improve the system model gradually. The sliding control [6] method is hardly influenced by internal parameters of the robot system and external disturbances [7]. The dynamic response of the sliding model controller is so fast that it doesn't need the online identification. So we use sliding model controller the servo control system. Although those control methods are very complex, they can meet the high performance control of the robot [8]. The motor on the robot shaft adopts three-phase permanent magnet AC synchronous motor (PMSM). PMSM makes a wide range of applications in robot joints. It is typically used in high precision servo control system [9, 10], because of its many advantages of high reliability and good performance. In industrial control, PMSM is usually controlled by the vector control method which often adopts the current control methods that include the maximum output power control, the maximum torque control, the maximum current control, and so on. So that it can be easily realized in industry.

Y. Yang · H. Yu · S. Pan (✉) · Z. Zhou
The School of Automation and Electrical Engineering,
Qingdao University, Qingdao 266000, China
e-mail: pansongfeng@163.com

Z. Deng (ed.), *Proceedings of 2017 Chinese Intelligent Automation Conference*,
Lecture Notes in Electrical Engineering 458,
https://doi.org/10.1007/978-981-10-6445-6_26

The rest of the paper is structured as follows. In Sect. 2, it describes the modeling process of the dynamics of the two-degree-of freedom robot. In Sect. 3, it introduces the design of the servo control system of the robot. In Sect. 4, the stability analysis of the system is to be submitted. In Sect. 5, the simulation results are given. This paper is completed in Sect. 6.

2 Robot Dynamics Model

The schematic structural diagram of the two-degree-of-freedom robot is shown in Fig. 1.

In Fig. 1, the point A and the point B is connected together by the connecting rod 1. And the point B and point C are connected together by the connecting rod 2. The point A means a drive motor and the same to the point B. The connecting rod 1 and the connecting rod 2 moves rotationally. The rotation angles are determined by $q_1(0^\circ \le q_1 \le 180^\circ 0^\circ \le q_1 \le 180^\circ)$ and $q_2(0^\circ \le q_2 \le 180^\circ)$. The mass of the connecting rod 1 and the connecting rod 2 is defined respectively by m_1 and m_2. The mass of the whole rod is expressed by the mass of the point which is at the end of the connecting rod.The length of the connecting rods is denoted respectively by d_1 and d_2. There is a known trajectory of the point C. According the inverse kinematics of robot, the angular displacement q can be obtained.

The Lagrangian function can be described as:

$$L = K - P \tag{1}$$

where L is the Lagrangian function, K is the kinetic energy of the system, and P is the energy of the system [10].

The system dynamics equation is as follows:

$$F_i = \frac{d}{dt}\frac{\partial L}{\partial \dot{q}_i} - \frac{\partial L}{\partial \dot{q}}, \quad i = 1, 2 \tag{2}$$

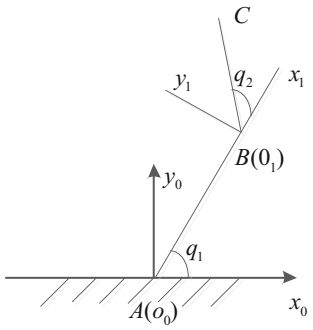

Fig. 1 The schematic structural diagram of the two-degree-of-freedom robot

where q_i represents the coordinates of kinetic energy and potential energy. $\dot{q}_i$ is the corresponding velocity. If q_i is the linear coordinate system, then F_i is the force acting on the coordinate. If q_i is the angular coordinate system, then F_i is the torque on the coordinate.

It can get the dynamic equation of the robot by Formulas (1) and (2) as follows:

$$M(q)\ddot{q} + C(q,\dot{q})\dot{q} + G(q) = \tau \tag{3}$$

where q is a rotational angle vector,$\dot{q}$ is a rotational velocity vector. The $\ddot{q}$ is a rotational acceleration vector and $M(q)$ is positive definite inertia matrix, $C(q,\dot{q})$ is the centrifugal force and Coriolis moment, $G(q)$ is weight moment vector, τ is the input torque vector.

By calculation, it can get $M(q)$,$C(q,\dot{q})$ and $G(q)$ as follow:

$$M(q) = \begin{bmatrix} (m_1+m_2)d_1^2 + m_2d_2^2 + 2m_2d_1d_2\cos q_2 & m_2(d_2^2 + d_1d_2\cos q_2) \\ m_2(d_2^2 + d_1d_2\cos q_2) & m_2d_2^2 \end{bmatrix} \tag{4}$$

$$C(q,\dot{q}) = \begin{bmatrix} -m_2d_1d_2\sin q_2\dot{q}_2 & -m_2d_1d_2\sin q_2(\dot{q}_1+\dot{q}_2) \\ m_2d_1d_2\sin q_2\dot{q}_1 & 0 \end{bmatrix} \tag{5}$$

$$G(q) = \begin{bmatrix} (m_1+m_2)gd_1\sin q_1 + m_2gd_2\sin(q_1+q_2) \\ m_2gd_2\sin(q_1+q_2) \end{bmatrix} \tag{6}$$

3 Robot Servo Control System

3.1 Mathematical Model of Servo Motor

The PMSM is selected for the servo drive motor, and the mathematical model of the PMSM in a synchronous rotating reference frame can be expressed as follows:

$$\begin{cases} L_d\dfrac{di_d}{dt} = -R_Si_d + n_p\omega L_pi_d + u_d \\ L_q\dfrac{di_q}{dt} = -R_Si_q - n_p\omega L_di_d - n_p\omega\Phi + u_q \\ J_m\dfrac{d\omega}{dt} = \tau - \tau_L = n_p\left[\left(L_d - L_q\right)i_di_q + \Phi i_q\right] - \tau_L \\ \tau = n_p\left[\left(L_d - L_q\right)i_di_q + \Phi i_q\right] \end{cases} \tag{7}$$

where u_d and u_q are the stator voltages of the d-axis and the q-axis respectively. i_d and i_q are the stator inductances of the d-axis and the q-axis.τ_L is the load torque.R_s is the stator resistance.ω is the rotor angular velocity. n_p is the number of pole pairs. J_m is the moment of inertia. τ is the electromagnetic torque.

3.2 Robot Control Principle

The drive motor of the robot joint is the PMSM (permanent magnet synchronous motor) and robot dynamics control schematic diagram is presented in Fig. 2.

3.2.1 Inverse Kinematics

Suppose the desired position of the robot is $C_d(x_d, y_d)$. According to the inverse kinematics of the robot, we can get q_d:

$$q_d = \begin{bmatrix} q_{1d} \\ q_{2d} \end{bmatrix} = \begin{bmatrix} \arctan\frac{y_d}{x_d} + \arccos\frac{x_d^2+y_d^2+L_1^2-L_2^2}{2L_1\sqrt{x_d^2+y_d^2}} \\ \arctan\frac{y_d}{x_d} + \arccos\frac{x_d^2+y_d^2+L_1^2-L_2^2}{2L_1\sqrt{x_d^2+y_d^2}} - \arccos\left(\frac{x_d^2+y_d^2-L_1^2-L_2^2}{2L_1L_2}\right) \end{bmatrix} \tag{8}$$

3.2.2 The Design of the Adaptive Controller

The adaptive controller is designed as follows:

$$\tau = \hat{M}(q)\ddot{q}_r + \hat{C}(q,\dot{q})\dot{q}_r + \hat{G}(q) - K_D s = Y(q,\dot{q},\dot{q}_r,\ddot{q}_r)\hat{\alpha} - K_D s \tag{9}$$

$$\dot{\hat{\alpha}} = -\Gamma^{-1}Y^T(q,\dot{q},\dot{q}_r,\ddot{q}_r)s \tag{10}$$

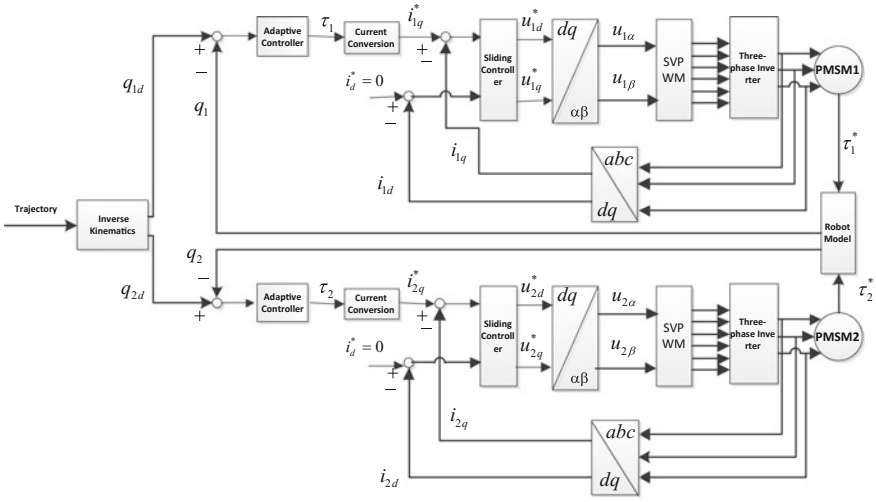

Fig. 2 Robot dynamics control schematic diagram

where $s = \dot{q} - \dot{q}_r = \dot{\tilde{q}} + \Lambda\tilde{q}, \dot{q}_r = q_d - \Lambda\tilde{q}, \ddot{q}_r = \ddot{q}_d - \Lambda\dot{\tilde{q}}, \tilde{q} = q - q_d$. α is a vector, and $\hat{\alpha}$ is an estimate of $\alpha.\tilde{q}$ is the tracking error, Λ is a constant matrix. $\hat{M}(q)$, $\hat{C}(q,\dot{q})$ and $\hat{G}(q)$ are the estimation matrix of $M(q)$, $C(q,\dot{q})$ and $G(q).K_D$ and Γ are the design parameter matrix, K_D is the positive definite matrix. Define $\tilde{M}(q) = \hat{M}(q) - M(q), \tilde{C}(q,\dot{q}) = \hat{C}(q,\dot{q}) - C(q,\dot{q}), \tilde{G}(q) = \hat{G}(q) - G(q)$ as the corresponding estimated error matrix. $\tilde{\alpha} = \hat{\alpha} - \alpha$ represents the vector of estimated parameter errors.

3.2.3 The Design of the Sliding Controller

Reference currents for the d-axis and q-axis of the permanent magnet synchronous motor on the joint i are denoted by i_{di}^* and i_{qi}^* respectively. Feedback currents for d-axis and q-axis are denoted by i_{di} and i_{qi}. The voltages for d-axis and q-axis are denoted by u_{di}^* and u_{qi}^*. On the basis of $i_{di}^* = 0$, it can design the sliding controller to check the current of PMSM. The current errors of d-axis and q-axis are denoted by $\tilde{i}_{qi} = i_{qi}^* - i_{qi}, \tilde{i}_{di} = -i_{di}$.

According to the current errors of $\tilde{i}_{qi}$ and $\tilde{i}_{di}$ of the d-axis and the q-axis, the sliding surfaces s_{1i} and s_{2i} are designed as follow:

$$s_{1i} = c_{1i}\tilde{i}_{qi}, s_{2i} = c_{2i}\tilde{i}_{di} \tag{11}$$

where c_{1i} and c_{2i} are constants.

In order to design the sliding controller, the exponential approach law with constant velocity approximation is selected as following formula:

$$\dot{s}_{1i} = -\varepsilon_{1i}\mathrm{sgn}s_{1i} - k_{1i}s_{1i} \tag{12}$$

where $-\varepsilon_{1i}\mathrm{sgn}s_{1i}$ is an isokinetic approximation term, $-k_{1i}s_{1i}$ is an exponential approach term, ε_{1i} is an isokinetic approach coefficient and k_{1i} is an exponential approach coefficient. In the exponential reaching law, by increasing k_{1i} and decreasing ε_{1i}, it can result in a faster approach and eliminate chattering from the sliding control.

According to Formulas (11) and (12), it can get the following equations:

$$\dot{s}_{1i} = c_{1i}\dot{\tilde{i}}_{qi} = c_{1i}(\dot{i}_{qi}^* - \dot{i}_{qi}) = c_{1i}(\dot{i}_{qi}^* - \frac{-R_{si}i_{qi} - n_{pi}\omega_i\phi_i - n_{pi}\omega_i L_{di}i_{di} + u_{qi}}{L_{qi}}) \tag{13}$$

$$u_{qi} = R_{si}i_{qi} + n_{pi}\omega_i\phi_i + n_{pi}\omega_i L_{di}i_{di} + L_{qi}(\frac{\varepsilon_{1i}\mathrm{sgn}s_{1i} + k_{1i}s_{1i}}{c_{1i}} + \dot{i}_{qi}^*) \tag{14}$$

Then the d-axis control law is shown as follow:

$$u_{di} = R_{si} i_{di} - n_{pi} \omega_i L_{qi} i_{qi} + L_{di} \left(\frac{\varepsilon_{2i} \mathrm{sgn} s_{1i} + k_{2i} s_{2i}}{c_{2i}} \right) \tag{15}$$

3.2.4 Torque and Current Conversion

Current conversion means to transform the moment of the robot system into the amount of current of the PMSM. When $i_{di}^* = 0$, the Eq. (7) can be replaced by $\tau_i = n_{pi} \phi_i i_{qi}^*$. The q-axis reference current of the PMSM on joint i as follows:

$$i_{qi}^* = \frac{\tau_i}{n_{pi} \phi_i} \tag{16}$$

4 System Stability Analysis

The Lagrangian function of the control system is chosen as follow:

$$V = \frac{1}{2} s^T M(q) s + \tilde{\alpha}^T \Gamma \tilde{\alpha} + \frac{1}{2} s_{1i}^2 + \frac{1}{2} s_{2i}^2 + \frac{1}{2} \tilde{i}_{qi}^2 + \frac{1}{2} \tilde{i}_{di}^2 \tag{17}$$

According to Formula (9) and linear characteristics of robot dynamics equation, it can get the following equation:

$$\dot{V} = \tilde{\alpha}^T Y^T s - s^T K_D s + \tilde{\alpha}^T \Gamma \dot{\tilde{\alpha}} + s_{1i} \dot{s}_{1i} + s_{2i} \dot{s}_{2i} + \tilde{i}_{qi} \dot{\tilde{i}}_{qi} + \tilde{i}_{di} \dot{\tilde{i}}_{di} \tag{18}$$

On the base of Formulas (12), (15) and (16), we can get the following equation:

$$\begin{aligned} \dot{V} &= \tilde{\alpha}^T Y^T s - s^T K_D s + \tilde{\alpha}^T \Gamma \dot{\tilde{\alpha}} + s_{1i} \dot{s}_{1i} + s_{2i} \dot{s}_{2i} + \frac{s_{1i} \dot{s}_{1i}}{c_{1i}^2} + \frac{s_{2i} \dot{s}_{2i}}{c_{2i}^2} \\ &= -s^T K_D s + s_{1i} \left(\frac{1 + c_{1i}^2}{c_{1i}^2} \right) (-\varepsilon_{1i} \mathrm{sgn} s_{1i} - k_{1i} s_{1i}) + s_{2i} \left(\frac{1 + c_{2i}^2}{c_{2i}^2} \right) (-\varepsilon_{2i} \mathrm{sgn} s_{2i} - k_{2i} s_{2i}) \leq 0 \end{aligned} \tag{19}$$

Since K_D is a positive definite matrix and only if $s = s_{1i} = s_{2i} = i_{qi} = i_{di} = 0$, it can get $\dot{V} = 0$. In the light of the Lyapunov stability theory, the control system is asymptotically stable.

5 Robot Simulation and Experimental Results

According to the block diagram of the control system shown in Fig. 2, it uses Simulink to the MATLAB to get a simulation. PMSM parameters of connecting rod 1 and connecting rod 2 are shown as follows:

$$\begin{aligned} &R_{s1} = R_{s2} = 2.875\,\Omega, L_{d1} = L_{q1} = L_{d2} = L_{q2} = 0.0085\,\text{H},\ \Phi_1 = \Phi_2 \\ &\quad = 0.175\,\text{Wb}, J_{m1} = J_{m2} = 0.025\,\text{kg}\,\text{m}^2, \end{aligned}$$

its power is 1.1KW, its rated voltage is 220 V, its pole pairs are 4. The mass of connecting rod 1 and connecting rod 2 is

$$m_1 = m_2 = 1kg, L_1 = L_2 = 1m.$$

The adaptive control parameter is $\Lambda = diag(6,6), K_D = diag(350,350), \Gamma = diag(1,1,1,1)$ and the input trajectory is $\begin{cases} x = -0.2t + 2 \\ (x-1.5)^2 + y^2 = 0.25 \\ y \geq 0 \end{cases}$.

The simulation results are shown in the following figures:

Figure 3 is the input trajectory, Fig. 4 is the output trajectory. We can find that if we input a semicircle to the control system we can get a same semicircle. So it can achieve the tracking control the robot by using the combination control of the adaptive controller to monitor the robot and the sliding controller to control the motor. Figure 5 is the error curve of connecting rod 1, Fig. 6 is the error curve of connecting rod 2. From Figs. 5 and 6, it can get the result that the angular displacement error of connecting rod 1 and connecting rod 2 reduces the time variation and eventually reaches zero value. So the feasibility and controllability of the control strategy that this paper proposes being verified.

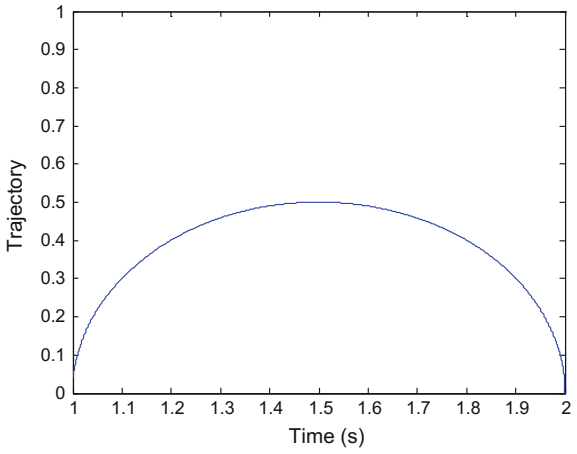

Fig. 3 The input trajectory

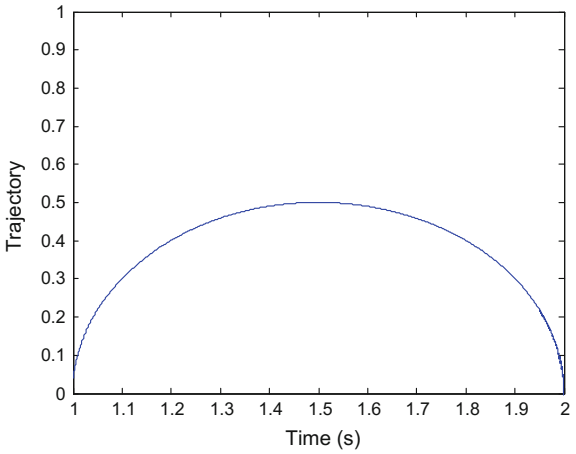

Fig. 4 The output trajectory

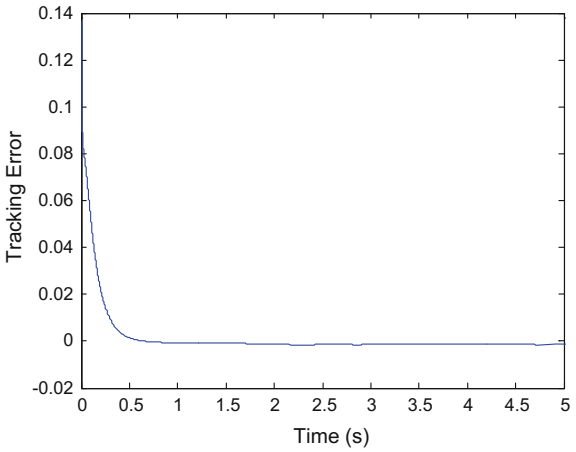

Fig. 5 Error curve of connecting rod 1

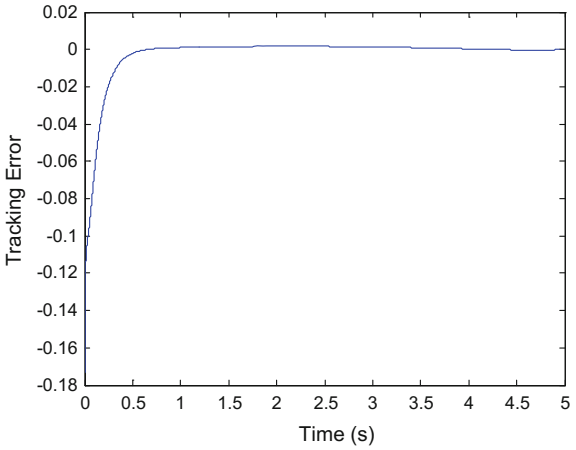

Fig. 6 Error curve of connecting rod 2

6 Conclusions

This paper has studied the dynamics control of the two-degree-of-freedom robot controlled by PMSM. The whole system is divided into 2 parts: the drive motor model and the robot model. Each connecting rod is controlled by a permanent magnet synchronous motor and the robot joint position control adopts adaptive control to establish the robot dynamics control system. The simulation of the robot system is completed by using the simulink module of the MATLAB. And the simulation results show that the robot dynamic control system can realize precisely the position tracking control in a short time. The propositional control method is simple and easy to implement and has good control effect and a good application prospect. However, many functions need to be added and many control theories need to be taken into account. For example, although adaptive control is appropriate for a class of systems where object characteristics or perturbation characteristics vary widely and are often required to maintain high performance specifications, it should be pointed out that adaptive control is more complex and costly than conventional feedback control. So how to solve this problem will be my next stage of research.

References

1. Wu C, Cao Z, Xiao Q, Fu Y (2016) Dynamics analysis of bionic parallel joint mechanism for the snake robot, control conference (CCC), 2016 35th Chinese, TCCT, pp 6301–6306
2. Jo S, Kim M, Koo Y, Won J, Kang J, Han S (2016) A study on kinematics and dynamics analysis of vertical articulated robot with 6 axies for forging process automation in high temperatures environments. J Korean Soc Indus Convergence 19(1):10–17
3. Seering W, Eppinger S (2015) On dynamic models of robot force control
4. Gazi V, Fidan B, Marques L, Ordonez R (2015) Robot swarms: dynamics and control, mobile robots for dynamic environments. ASME, pp 81–85
5. Soltanpour M, Khalilpour J, Soltani M (2012) Robust nonlinear control of robot manipulator with uncertainties in kinematics, dynamics and actuator models. Int J Innovative Comput Inf Control 8(8):5487–5498
6. Gautier M, Janot A, Vandanjon P (2013) A new closed-loop output error method for parameter identification of robot dynamics. IEEE Trans Control Syst Technol 21(2):428–444
7. Orin D, Goswami A, Lee S (2013) Centroidal dynamics of a humanoid robot. Auton Robots 35(2-3):161–176
8. Wai R, Muthusamy R (2013) Fuzzy-neural-network inherited sliding-mode control for robot manipulator including actuator dynamics. IEEE Trans Neural Netw Learn Syst 24(2):274–287
9. Ramos J, Wang A, Kim S (2016) Robot-human balance state transfer during full-body humanoid teleoperation using divergent component of motion dynamics, IEEE international conference on robotics and automation (ICRA), pp 1587–1592
10. Zhao Y, Bai Z (2011) Dynamics analysis of space robot manipulator with joint clearance. Acta Astronaut 68(7):1147–1155

Dynamic Decision Based Noncyclic Scheduling of Multi-cluster Tools

Yuanyuan Yan, Huangang Wang and Wenhui Fan

1 Introduction

Cluster tools are widely applied in semiconductor industry. A typical cluster tool consists of load locks (LL), process modules (PMs) and transport module (robot), and it is often used for processing wafers. In cluster tools, the wafers are stored in the load lock, and each wafer is transported by the robot from the load lock, and goes through PMs to finish a sequence of process steps in its recipe, and finally returns to the load lock. Each robot can only do one action at a time, and it can have single arm or dual arms, where each arm can hold only one wafer at a time. Each PM processes only one wafer at a time, and there are no buffers between PMs. Due to the structural characteristics of cluster tool, the scheduling requirements are complex. First, deadlocks often occur due to the lack of buffers. Second, the actions of robot may conflict, since the robot is public with more than one action to be carried out simultaneously. Third, there are different scheduling requirements in wafer manufacturing, such as parallel and reentrant processes. Multi-cluster tools consist of several single cluster tool, where every two cluster tools are connected with buffer modules (BMs), The BMs can also process wafers. Due to the increase of PMs and the coordination among robots, the scheduling of multi-cluster tools becomes more complex than single cluster tool. Figure 1 shows the schematic view of a multi-cluster tool.

Y. Yan · H. Wang (✉) · W. Fan
Department of Automation, Tsinghua University, Beijing 100084, China
e-mail: hgwang@tsinghua.edu.cn

Y. Yan
e-mail: yan-yy14@mails.tsinghua.edu.cn

W. Fan
e-mail: fanwenhui@tsinghua.edu.cn

Z. Deng (ed.), *Proceedings of 2017 Chinese Intelligent Automation Conference*,
Lecture Notes in Electrical Engineering 458,
https://doi.org/10.1007/978-981-10-6445-6_27

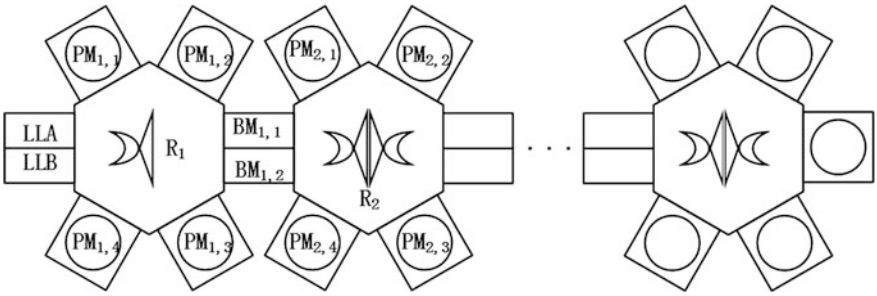

Fig. 1 The schematic view of a multi-cluster tool

There have been numerous works on multi-cluster tools scheduling, and most of them are based on cyclic scheduling. Chan et al. proposed a resource-based approach to analytically capture the dependencies between two single cluster tools, provided a polynomial-time algorithm to find the optimal schedule [1], and then they extended it to schedule tree-like multi-cluster tools [2]. Zhu et al. [3–5] focused on one-cycle scheduling, and developed a petri net model to explore the dynamic behaviour for cluster tools scheduling. And also developed algorithms to calculate the minimal cycle time in polynomial time [6]. Yi et al. [7] divided a multi-cluster tool to multiple independent single-cluster tool to analyse the steady-state throughput and robot scheduling, but they ignored the robot moving time. Cyclic scheduling is usually used in mass production, but recently, semiconductor manufacturing industry tends to reduce the wafer lot size, down to just a few, even being only 5–8 wafers. There is no cycle time in the process, thus the cyclic scheduling is not suitable for this problem. Kim et al. [8–10] developed a timed petri net model and used branch and bound approach to solve noncyclic scheduling problem in single-cluster tool. Wikborg and Lee [11] used the reachability graph to descript the state transition, and used dynamic programming to search the optimal solution. Nishi and Matsumoto [12] processed a petri net decomposition approach to deadlock-free scheduling of dual-armed cluster tools. However, all of them solved the problem in single-cluster tool, not multi-cluster tools.

Dynamic programming is able to deal with noncyclic scheduling problem, and it is an implicit enumeration method, which can obtain the optimal solution of the problem [11]. Moreover, as an implicit enumeration, deadlocks do not need to be considered and searched, since a deadlock situation is infeasible. Although the dynamic programming is efficient to single-armed single-cluster tool scheduling, it has not been applied to multi-cluster tools scheduling. The main challenge of multi-cluster tools scheduling is the coordination among the robots since there are various robots in the equipment and there exists BMs between cluster tools which affects the actions of the two robots inside. This paper construct a reachability graph model in multi-cluster tools, and adopt a dynamic decision method to solve the multi-robot coordination problem in searching.

2 Noncyclic Scheduling Problem of Multi-cluster Tools

As shown in Fig. 1, an L-cluster tool consists of L single-cluster tools, and the i-th tool is called C_i. Each single-cluster tool contains at least one PM. Each single-cluster tool has only one robot with either single arm or dual arms, and the robot in C_i is called R_i. Each pair of adjacent cluster tools is connected by BMs. The processing time in each BM ranges from zero to several seconds, and we assume that the time for robot picking up a wafer, putting down a wafer and moving are constants, and the processing time in PMs or BMs are also assumed to be constants. Each process can be conducted in more than one PM, and each PM may need to do different processes. In summary, there are three possible cases, which are the serial flow, the parallel flow, and the reentrant flow. In serial flow, each process is conducted in only one PM, while in the parallel flow, some process is carried out in more than one PM. In the reentrant flow, there exist some PMs which do different processes simultaneously and can be revisited. These three types of flows are shown in Eq. 1–3 respectively.

$$\begin{aligned} &P_0(LLA) \to P_1\left(PM_{1,1}\right) \to P_2\left(PM_{1,2}\right) \to P_3\left(BM_{1,1}\right) \to P_4\left(PM_{2,1}\right) \\ &\quad \to P_5\left(PM_{2,2}\right) \to \cdots \to P_{m-4}\left(PM_{2,3}\right) \to P_{m-3}\left(PM_{2,4}\right) \\ &\quad \to P_{m-2}\left(BM_{1,2}\right) \to P_{m-1}\left(PM_{1,3}\right) \to P_{\mathrm{m}}\left(PM_{1,4}\right) \to P_{m+1}(LLB) \end{aligned} \tag{1}$$

$$\begin{aligned} &P_0(LLA) \to P_1\left(PM_{1,1}, PM_{1,2}\right) \to P_2\left(BM_{1,1}\right) \to P_3\left(PM_{2,1}, PM_{2,2}\right) \\ &\quad \to \ldots \to P_{m-2}\left(PM_{2,3}, PM_{2,4}\right) \to P_{m-1}\left(BM_{1,2}\right) \to P_m\left(PM_{1,3}, PM_{1,4}\right) \to P_{m+1}(LLB) \end{aligned} \tag{2}$$

$$\begin{aligned} &P_0(LLA) \to P\left(PM_{1,1}\right)_1 \to P_2\left(PM_{1,2}\right) \to P_3\left(BM_{1,1}\right) \to P_4\left(PM_{2,1}\right) \\ &\quad \to P_5\left(PM_{2,2}\right) \to \cdots \to P_{m-5}\left(PM_{2,3}\right) \to P_{m-4}\left(PM_{2,4}\right) \to P_{m-3}(BM_{1,2}) \\ &\quad \to P_{m-2}\left(PM_{1,3}\right) \to P_{m-1}\left(PM_{1,4}\right) \to P_m\left(PM_{1,3}\right) \to P_{m+1}(LLB) \end{aligned} \tag{3}$$

where m is the processing number. P_i is the i-th step. $PM_{i,j}$ is the j-th PM in C_i. $BM_{i,1}$ and $BM_{i,2}$ connect C_i with C_{i+1}. We assume that $BM_{i,1}$ transport wafer from C_i to C_{i+1}, and $BM_{i,2}$ transport wafer from C_{i+1} to C_i.

Based on the above description, a unified model can be developed to represent a variety of equipment and process path for one-cluster tools, two-cluster tools, and multi-cluster tools. When the equipment structure changes or the process changes, we can quickly re-write the process flow and the formula of this unified model can be written as Eq. 4.

$$P_0(LLA) \to P_1 \to P_2 \to \ldots \to P_{m-1} \to P_m \to P_{m+1}(LLB) \tag{4}$$

3 Noncyclic Scheduling Based on Dynamic Decision

To solve the scheduling problem of dual-armed cluster tools, we divide the robot action into two parts, where the first part is picking up a wafer and moving to the correct position and the second is putting down a wafer and moving to the correct position. The wafer needs to be processed in m steps, as described in Eq. 4, so that $2m+2$ actions are required to complete a wafer processing. We define a vector z to represent the robot action, where each element in z is a logical variable to illustrate the action of picking up or putting down a wafer.

$$z = (a_1, b_1, a_2, b_2, \ldots, a_m, b_m, a_{m+1}, b_{m+1}) \tag{5}$$

where a_i denotes for the statement of picking up a wafer from P_{i-1}, and b_i is for that of putting down a wafer to P_i. $a_i, b_i = 0$ or 1. When $a_i, b_i = 1$, it means that the corresponding action happens, vice versa. For instance, $z = (1, 0, \ldots 0, 0)$ demonstrates that the robot picks up a wafer from $P_0(LLA)$. We define vector s as the state in Eq. 6, where the variables represents the corresponding numbers of wafers in robot or PMs.

$$s = (w, c_1, d_1, c_2, d_2, \ldots, c_m, d_m, c_{m+1}) \tag{6}$$

where w is the number of wafers to be processed in $P_0(LLA)$. c_i is the number of wafers in robot picking up from P_{i-1}, and d_i is the number of wafers in P_i. The sum of c_i is limited by the number of arms of the robot, while d_i is restricted by the number of PMs. For instance, when $s = (5, 1, \ldots, 0, 0)$, there are 5 wafers in $P_0(LLA)$, and the robot has a wafer picking up from $P_0(LLA)$, and no wafer in processing. When all wafers are finished and no wafer in processing, the final state is $s = (0, 0, \ldots, 0, 0)$.

A transition from one state to another is made by the action of robot, and the relationship between the state and the action is shown in Eq. 7.

$$s_k = s_{k-1} + z_k A, \quad A = \begin{pmatrix} -1 & 1 & \cdots & 0 \\ 0 & -1 & \ddots & \vdots \\ \vdots & \ddots & \ddots & 1 \\ 0 & \cdots & 0 & -1 \end{pmatrix} \tag{7}$$

Generally, in one state, there is more than one action to be performed, but the robot can only do one action at a time, thus we can choose only one of them. The chosen actions affects the following state. The choices in the whole process can varied, where we use a directed graph to represent the state transitions. Each node in the graph equals a state and the edges are denoted for the corresponding state transitions between the states. This graph is called a state transition diagram or a reachability graph, and we present Fig. 2 to show the first few steps in the

reachability graph whose initial state is $s_0 = (5, 0, 1, 0, 0, 0, 0, 0, 0, 0, 0, 0)$, and the wafer flow presented in Eq. 8.

$$P_0(LLA) \rightarrow P_1\left(PM_{1,1}, PM_{1,2}\right) \rightarrow P_2\left(BM_{1,1}\right) \rightarrow P_3\left(PM_{2,1}, PM_{2,2}, PM_{2,3}, PM_{2,4}\right) \rightarrow P_4\left(BM_{1,2}\right) \rightarrow P_5\left(PM_{1,3}, PM_{1,4}\right) \rightarrow P_0(LLA) \tag{8}$$

To choose the best sequence of the actions, Lee et al. defined resources ready time to help search, where the resource is regarded as the robots and PMs required in the process. Lee et al. also proposed a dynamic decision based on Pareto-optimal optimization to solve single-armed single-cluster tool scheduling problem [11]. When the PM is occupied with a wafer, it cannot be used before process ends, and the resource ready time is the time that resource becomes free to perform the next task. They delete the paths which is not the Pareto-optimal to get the optimal solution faster. Lee et al. proved that their approach could get the optimal solution in single-armed cluster tool.

However, in multi-cluster tools, this method cannot be fully adapted. When searching actions, every robot can possibly take actions. If we use the method in [11] to update the resources ready time and act time, the next action may occur earlier than the previous one, which contradicts with the facts. Thus, the solution may be unfeasible. Although one robot cannot do more than one action at a time, using multiple robots can achieve it. Therefore, there may be more than one action at a time, and the transfer of the states can be successive. In such case, we propose a modified dynamic decision method to solve the problem. In searching, when the act time of the next action is earlier than the previous ones, we set it equal to the previous act time, so that the action will not be disordered. When actions occur in the same time, the corresponding states do not disturb each other, since it is associated with only one robot. Thus, such cases are allowed in this paper.

To make the search faster, in multi-cluster tool, there are more than one robot, and each PM needs to wait for the robot in their own cluster tool, so that their ready time can be considered equal to their own robot. While, BM are related to two

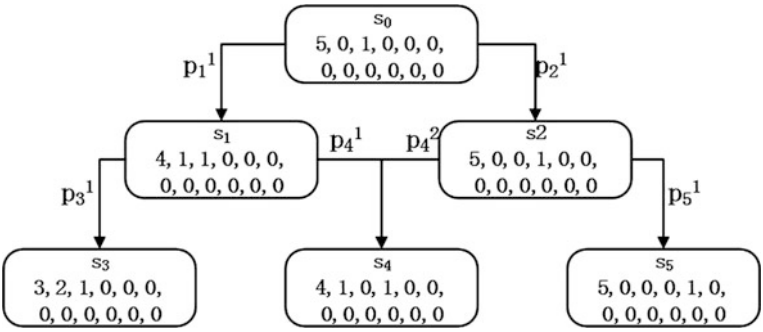

Fig. 2 The first few steps in the reachability graph

robots. If there are no wafers in BM, robot needs to put down a wafer in BM, and BM required to wait for the robot. Thus, the ready time of BM can be considered equal to that of robot. Correspondingly, if there exists wafers in BM, robot needs to pick up a wafer from BM, and BM needs to wait for the robot.

In multi-cluster tools scheduling, there may be more than one path in the final state, and the ready time of these robots can be different, thus there may be all Pareto-optimal solution. Our target is to minimize the makespan, which is the time of putting down the last wafer to the $P_{m+1}(LLB)$. Since the last action of putting down the wafer is performed by R_1, we only need to choose the path which has the minimal ready time of R_1.

The algorithm of our method is shown in Table 1.

4 Experiment

We develop a generic framework to solve the problem, and the program can solve any type of multi-cluster tools scheduling problem, including single-armed, dual-armed, hybrid-armed, serial flow, parallel flow, and reentrant flow. For different problems, we do not need to re-model it, but just modify the parameters, which takes only a few minutes. Thus it is very flexible and convenient. Algorithm 1 is implemented in MATLAB and the experiments is run on an 8 GB RAM PC with 3.40 GHz Intel Core. The configurations, process parameters and results are listed in Table 2, which robot picks up, moves, and puts down wafer's time are all set to 1 s, and the initial state are all set as $s = (5, 0, \ldots, 0, 0)$.

In Table 2, 'configurations and process parameters' gives the process flow and structures of the equipment. 'single-armed + dual-armed' means that the robot in cluster tools is single-armed or dual-armed. Results show that the proposed method can solve multi-cluster tools scheduling problem under different cases, including serial flow, parallel flow and reentrant flow. From the results, we also find that the CPU time of single-armed is less than dual-armed when the structure is the same,

Table 1 Algorithm for noncyclic scheduling based on dynamic decision

Algorithm 1
(1). Add initial state as start node in the list, pick the start node as current node s_c
(2). Find all possible actions of s_c
(3). For each action, extend the node according to $s_k = s_{k-1} + z_k A$, get a node s_{c+1}
(4). If s_{c+1} already exists, pick it, else add it to the list and then pick it
(5). Pick a path in s_c and extend it to s_{c+1}
(6). Remove all paths that are not Pareto-optimal
(7). Remove s_c
(8). Pick a node in the list as s_c, if s_c is the final node, end program, else repeat the steps (2) to (8)

Table 2 Scheduling result of multi-cluster tools

	Configurations, process parameters	Optimal (s)	CPU time (s)
1	$P_0 \to P_1(PM_{1,1}, 60) \to P_2(PM_{1,2}, 70) \to P_3(BM_{1,1}, 0) \to P_4(PM_{2,1}, 40)$ $\to P_5(PM_{2,2}, 50) \to P_6(PM_{2,3}, 50) \to P_7(PM_{2,4}, 60) \to P_8(BM_{1,2}, 0)$ $\to P_9(PM_{1,3}, 50) \to P_{10}(PM_{1,4}, 48) \to P_{11}$ dual-armed + dual-armed serial flow	757	202
2	$P_0 \to P_1(PM_{1,1}, 60) \to P_2(PM_{1,2}, 70) \to P_3(BM_{1,1}, 0) \to P_4(PM_{2,1}, 40)$ $\to P_5(PM_{2,2}, 50) \to P_6(PM_{2,3}, 50) \to P_7(PM_{2,4}, 60) \to P_8(BM_{1,2}, 0)$ $\to P_9(PM_{1,3}, 50) \to P_{10}(PM_{1,4}, 48) \to P_{11}$ single-armed + single-armed serial flow	883	16.7
3	$P_0 \to P_1(PM_{1,1}, 60) \to P_2(PM_{1,2}, 70) \to P_3(BM_{1,1}, 0) \to P_4(PM_{2,1}, 40)$ $\to P_5(PM_{2,2}, 50) \to P_6(PM_{2,3}, 50) \to P_7(PM_{2,4}, 60) \to P_8(BM_{1,2}, 0)$ $\to P_9(PM_{1,3}, 50) \to P_{10}(PM_{1,4}, 48) \to P_{11}$ single-armed + dual-armed serial flow	880	56.2
4	$P_0 \to P_1(PM_{1,1}, 60) \to P_2(PM_{1,2}, 70) \to P_3(BM_{1,1}, 0) \to P_4(PM_{2,1}, 40)$ $\to P_5(PM_{2,2}, 50) \to P_6(PM_{2,3}, 50) \to P_7(PM_{2,4}, 60) \to P_8(BM_{1,2}, 0)$ $\to P_9(PM_{1,3}, 50) \to P_{10}(PM_{1,4}, 48) \to P_{11}$ dual-armed + single-armed serial flow	757	73.8
5	$P_0 \to P_1(PM_{1,1}, PM_{1,2}, 139) \to P_2(BM_{1,1}, 0) \to P_3(PM_{2,1}, PM_{2,2}, 131)$ $\to P_4(PM_{2,3}, PM_{2,4}, 130) \to P_5(BM_{1,2}, 0) \to P_6(PM_{1,3}, PM_{1,4}, 120) \to P_7$ dual-armed + dual-armed parallel flow	828	13.6
6	$P_0 \to P_1(PM_{1,1}, PM_{1,2}, 139) \to P_2(BM_{1,1}, 0) \to P_3(PM_{2,1}, PM_{2,2}, 131)$ $\to P_4(PM_{2,3}, PM_{2,4}, 130) \to P_5(BM_{1,2}, 0) \to P_6(PM_{1,3}, PM_{1,4}, 120) \to P_7$ single-armed + single-armed parallel flow	836	2.8

(continued)

Table 2 (continued)

	Configurations, process parameters	Optimal (s)	CPU time (s)
7	$P_0 \rightarrow P_1(PM_{1,1}, 60) \rightarrow P_2(PM_{1,2}, 70) \rightarrow P_3(BM_{1,1}, 0) \rightarrow P_4(PM_{2,1}, 40)$ $\rightarrow P_5(PM_{2,2}, 50) \rightarrow P_6(BM_{2,1}, 0) \rightarrow P_7(PM_{3,1}, 50) \rightarrow P_8(PM_{3,2}, 76)$ $\rightarrow P_9(PM_{3,3}, 64) \rightarrow P_{10}(PM_{3,4}, 60) \rightarrow P_{11}(BM_{2,2}, 0) \rightarrow P_{12}(PM_{2,3}, 50)$ $\rightarrow P_{13}(PM_{2,4}, 60) \rightarrow P_{14}(BM_{1,2}, 0) \rightarrow P_{15}(PM_{1,3}, 50) \rightarrow P_{16}(PM_{1,4}, 48) \rightarrow P_{17}$ single-armed + single-armed + single-armed serial flow	1201	1807
8	$P_0 \rightarrow P_1(PM_{1,1}, PM_{1,2}, 80) \rightarrow P_2(BM_{1,1}, 0) \rightarrow P_3(PM_{2,1}, PM_{2,2}, 60)$ $\rightarrow P_4(BM_{2,1}, 0) \rightarrow P_5(PM_{3,1}, PM_{3,3=2}, 60) \rightarrow P_6(PM_{3,3}, PM_{3,4}, 66) \rightarrow P_7(BM_{2,2}, 0)$ $\rightarrow P_8(PM_{2,3}, PM_{2,4}, 70) \rightarrow P_9(BM_{1,2}, 0) \rightarrow P_{10}(PM_{1,3}, PM_{1,4}, 60) \rightarrow P_{11}$ dual-armed + dual-armed + dual-armed parallel flow	764	300
9	$P_0 \rightarrow P_1(PM_{1,1}, PM_{1,2}, 80) \rightarrow P_2(BM_{1,1}, 0) \rightarrow P_3(PM_{2,1}, PM_{2,2}, 60)$ $\rightarrow P_4(BM_{2,1}, 0) \rightarrow P_5(PM_{3,1}, PM_{3,3=2}, 60) \rightarrow P_6(PM_{3,3}, PM_{3,4}, 66) \rightarrow P_7(BM_{2,2}, 0)$ $\rightarrow P_8(PM_{2,3}, PM_{2,4}, 70) \rightarrow P_9(BM_{1,2}, 0) \rightarrow P_{10}(PM_{1,3}, PM_{1,4}, 60) \rightarrow P_{11}$ single-armed + single-armed + single-armed parallel flow	780	35.3
10	$P_0 \rightarrow P_1(PM_{1,1}, PM_{1,2}, PM_{1,3}, 200) \rightarrow P_2(BM_{1,1}, 0) \rightarrow P_3(PM_{2,1}, 60)$ $\rightarrow P_4(PM_{2,2}, 50) \rightarrow P_5(PM_{2,3}, PM_{2,4}, 130) \rightarrow P_6(PM_{2,2}, 50)$ $\rightarrow P_7(BM_{1,2}) \rightarrow P_8(PM_{1,4}, 110) \rightarrow P_9$ dual-armed + dual-armed reentrant flow	1082	47.6
11	$P_0 \rightarrow P_1(PM_{1,1}, PM_{1,2}, PM_{1,3}, 200) \rightarrow P_2(BM_{1,1}, 0) \rightarrow P_3(PM_{2,1}, 60)$ $\rightarrow P_4(PM_{2,2}, 50) \rightarrow P_5(PM_{2,3}, PM_{2,4}, 130) \rightarrow P_6(PM_{2,2}, 50)$ $\rightarrow P_7(BM_{1,2}) \rightarrow P_8(PM_{1,4}, 110) \rightarrow P_9$ single-armed + single-armed reentrant flow	1116	5.2
12	$P_0 \rightarrow P_1(PM_{1,1}, PM_{1,2}, 139) \rightarrow P_2(BM_{1,1}, 10) \rightarrow P_3(PM_{2,1}, PM_{2,2}, 131)$ $\rightarrow P_4(PM_{2,3}, PM_{2,4}, 130) \rightarrow P_5(BM_{1,2}, 10) \rightarrow P_6(PM_{1,3}, PM_{1,4}, 120) \rightarrow P_7$ dual-armed + dual-armed parallel flow	846	14.2

since the number of states in dual-armed robot is much more than single-armed. As the number of process becomes larger, the CPU time is longer, due to the increasing number of states. Our method only deletes paths in searching, but not delete the states which may contain some useless ones. Thus, the proposed algorithm still has potential to bet improved. In the future, we plan to find a method which is capable of deleting the useless states to further improve the efficiency.

5 Conclusion

This paper mainly focuses on noncyclic scheduling of multi-cluster tool, and gives a unified description for different problems with serial flow, parallel flow, and re-entrant flow. It also develops a reachability graph model based on the unified description to search the optimal solution in the reachability graph, and then give a modified dynamic decision to solve it. The numerical results proved that efficacy of the proposed method.

References

1. Chan WKV, Yi J, Ding S (2011) Optimal scheduling of multicluster tools with constant robot moving times, part i: two-cluster analysis. IEEE Transa Autom Sci Eng 8(1):5–16
2. Chan WKV, Yi J, and Ding S (2011) Optimal scheduling of multicluster tools with constant robot moving times, part ii: tree-like topology configurations. IEEE Trans Autom Sci Eng 8(1):17–28
3. Zhu Q, Wu N, Qiao Y, Zhou M (2013) Petri net-based optimal one-wafer scheduling of single-arm multi-cluster tools in semiconductor manufacturing. IEEE Trans Semicond Manuf 26(4):578–591, Nov 2013
4. Zhu Q, Wu N, Qiao Y, Zhou M (2014) Modeling and schedulability analysis of single-arm multi-cluster tools with residency time constraints via Petri nets. In: Proceedings of the IEEE international conference on automation science and engineering, Taipei, Taiwan, Aug 2014, pp 81–86
5. Zhu Q, Wu N, Qiao Y, Zhou M (2015) Scheduling of single-arm multicluster tools with wafer residency time constraints in semiconductor manufacturing. IEEE Trans Semicond Manuf 28(1):117–125, Feb 2015
6. Zhu Q, Wu N, Qiao Y, Zhou M (2016) Optimal scheduling of complex multi-cluster tools based on timed resource-oriented petri nets. IEEE Access 4:2096–2109
7. Yi JG, Ding SW, Song DZ et al. (2008) Steady-state throughput and scheduling analysis of multi-aluster tools for semiconductor manufacturing: a decomposition approach. IEEE Trans Semicond Manuf 5(2):321–336
8. Kim HJ, Lee JH, Lee TE (2015) Time-feasible reachability tree for noncyclic scheduling of timed petri nets. IEEE Trans Autom Sci Eng 12(3):1007–1016
9. Kim HJ, Lee JH, Lee TE (2015) Noncyclic scheduling of cluster tools with a branch and bound algorithm. IEEE Trans Autom Sci Eng 12(2):690–700
10. Kim HJ, Lee JH, Jung C, Lee TE (2013) Scheduling cluster tools with ready time constraints for consecutive small lots. IEEE Trans Autom Sci Eng 10(1):145–159

11. Wikborg U, Lee TE (2013) Noncyclic scheduling for timed discrete-event systems with application to single-armed cluster tools using pareto-optimal optimization. IEEE Trans Autom Sci Eng 10(3):699–709
12. Nishi T, Matsumoto I (2015) Petri net decomposition approach to deadlock-free and non-cyclic scheduling of dual-armed cluster tools. IEEE Trans Autom Sci Eng 12(1):281–293

Pattern Recognition of Artificial Legs Based on WPT and LVQ

Lei Liu, Yinmao Song, Peng Yang and Zuo Jun Liu

1 Introduction

Multi-channel Surface Electromyographic (SEMG), is a complex of subcutaneous muscle activity on the Surface of the skin in time and space after the comprehensive physiological electricity phenomenon. It has been widely used in clinical diagnosis, rehabilitation medicine and sports medicine research [1]. In the disabled prosthesis control application of SEMG, it can achieve good effect of bionic, certain achievements has been made in the study of [2] in this aspect.

Artificial leg using SEMG signal needs good recognition rate, and the recognition rate with the method of feature extraction and classifier are closely related. The time domain analysis methods of SEMG are mainly, the average absolute value (MAV Mean Absolute Value), the number of passing zero, the root mean square (Root Mean Square) and electromyographic signal regression modeling analysis, electromyographic signal (Variance) and Willison amplitude histogram, Variance, etc., simple algorithm, feature extraction is easy, but the defect is poor universality and instability [3]. The main frequency domain analysis with Fourier spectrum analysis and power spectrum analysis, because of the need to assume the SEMG signal is a random signal, the lack of rigorous scientific evidence [4]. The experimental research showed that the SEMG is essentially a non-stationary characteristics of biological electrical signals. So some time - frequency analysis method in recent years, such as (Short-Time Fourier Transform), Short time Fourier Transform (STFT), Wavelet Transform (Wavelet Transform, WT) and Wavelet Packet Transform (Wavelet Packet Transform, WPT) have been considerable attention in the SEMG signal analysis [5]. The Wavelet Transform time-frequency local

L. Liu (✉) · P. Yang · Z.L.L. Chen · Y. Geng
Department of Automation Engineering, School of Control Science and Engineering, Hebei University of Technology, Guangrongdao, Hongqiao District, Tianjin, China
e-mail: liulei2006000@126.com

Z. Deng (ed.), *Proceedings of 2017 Chinese Intelligent Automation Conference*, Lecture Notes in Electrical Engineering 458,
https://doi.org/10.1007/978-981-10-6445-6_28

Transform multi-scale decomposition characteristics, To analysis the different scales of signals, has been widely used in filtering, but it was used for feature extraction, the fixed form of time-frequency decomposition is not optimal [6], such as low resolution, in some cases, the high frequency end is a disadvantage, so it needed to be improved. WPT because the multi-scale decomposition of signals with arbitrary form, contains rich wavelet BaoJi, different wavelet BaoJi have different nature, reflect different signal characteristics, so it can provide the important features of SEMG [6], thus in the feature extraction of SEMG, it has irreplaceable advantages.

Classifier design is closely related to the feature extraction, classifier for SEMG feature can choose statistical classifier, fuzzy classifier and neural network classifier. It is needed concrete analysis according to the feature extraction method. Neural network application in the electrical pattern classification is a hot topic in recent years, and obtained some significant research results. In the neural network classifier, learning vector quantization (Learning Vector Quantization, LVQ neural network compared with BP network, ART network in structure type choice application more simple network structure, learning rate faster and more reliable recognition and better fault tolerance [7]. based on SEMG signal characteristics and advantages of LVQ, This article attempts through the characteristics of the wavelet packet transform to extract the SEMG signal vector, then using LVQ classifier for pattern classification. Methods by two SEMG signals collection, complete four motion modes (upstairs, downstairs, uphill and downhill) recognition experiment. To illustrate the wavelet packet transform feature extraction method and the LVQ network classifier combination of advantages, this paper compared based on wavelet packet transform, wavelet transform, power spectrum analysis and the regression model (AutoregressiveModel, AR), the characteristics of the coefficient using the LVQ classifier classification outcomes. Compared with the characteristics of the wavelet packet transform to extract using the LVQ network, the BP network, RBF neural network and Elman network classifier recognition effect.

2 The Wavelet Packet Transform

As a kind of multi-scale wavelet transform signal analysis method, it has good time-frequency localization features. It was used in high frequency short window. When low frequency signal is decomposed into a rough part of low frequency and high frequency detail part, and then only low frequency details were done the second decomposition. They were decomposed into low frequency part and high frequency part, without further decomposed high frequency part. The feature of wavelet transform is very suitable for non-stationary signal analysis of transient and time-varying characteristics. Compared with the wavelet transform, wavelet packet analysis can provide a more detailed analysis for signal method. It can according to the analysis of features of the signal, adaptively select band. It make it match the actual signal spectrum characteristics. It can improve the time-frequency resolution

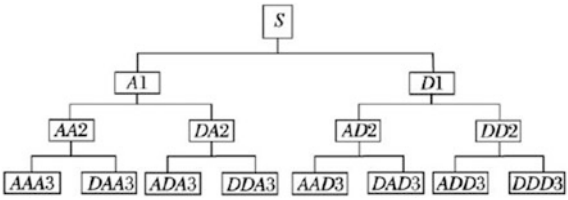

Fig. 1 Decomposition tree of WPT

[8]. The assumption for the analysis of the signal was the S, the three layer wavelet packet decomposition tree was shown in Fig. 1.

Signal S through wavelet transform, were expressed as high frequency and low frequency decomposition, such as AA2 + DA2 + D1, AA3 + DAA3 + DA2 + D1. And wavelet packet transform to allow signal S to a variety of combinations of low frequency and high frequency part, such as S = DAD3 AAD3 A1 + + + DD2. The relative wavelet transform, wavelet packet transform in the aspect of signal frequency resolution and feature extraction has a better adaptability [9].

3 The Optimal Wavelet BaoJi Decomposition

Step 1 normalized processing, for the sequence s sure to select the wavelet packet function and decomposition layers F, F layer wavelet packet decomposition, and calculate the entropy of each node.

Step 2 marked each node of the lowest layer, for other nodes in each layer does not make the mark.

Step 3 a total of 2 f each layer nodes, from left to right every two nodes constitute a group, from down to up to two adjacent layers the next layer of the sum of each group with a layer of the corresponding node entropy value comparison.

Step 4 if the two nodes of the next layer of entropy and greater than or equal to a layer of the corresponding entropy is marked on a layer of the node, and remove the next layer of the two nodes tag. Otherwise, the following a layer of the sum of the two nodes of entropy to replace a layer of the node of entropy, but not for processing of tag.

Step 5 from down to up to two adjacent layers according to the above process, step by step until all layers are processed and marked all the nodes of the wavelet packet function is to search the optimal wavelet BaoJi.

4 Feature Extraction Multi-channel Semg

Feature extraction is the key problem in pattern recognition or classification, it directly affects the design of classifier, and performance. The use of SEMG for intent recognition, with the increase of number of gesture recognition, recognition difficulty is becoming more and more big, so the effective extraction of intent recognition characteristic vector is crucial to the design of the classifier, and directly affect the accuracy of classification.

Although the intensity of the same action in different action under the SEMG in each wavelet packet decomposition energy will be different, but the relative changed little after normalization, but different actions on the same muscles of SEMG relative amplitude and energy have obvious difference, thus different modes of action of SEMG in various frequency bands after wavelet packet decomposition of the projection is different, completely can use this feature for feature extraction. Corresponding to the speed of hand gesture signal generated by the same action in each frequency band energy change is not obvious, so I can put the SEMG energy in each frequency band projection sequence was used as the characteristic of each type of motion vector, can avoid the strength of the action itself, the influence of the speed of characteristic value. Based on this idea, the steps of feature extraction.

Step1 Calculation of each frequency band energy. Signal after F layer wavelet packet decomposition, get the F layer 2^F from low frequency to high frequency band components coefficients of the characteristic signal of (j = 1, 2, …, 2^F), the corresponding frequency band characteristic signal energy.

$$E_F^j = \left| \int Q_F^j(t) \right|^2 dt = \sum_{k=1}^{M'} \left| d_{jn}^k \right|^2 \tag{1.1}$$

the first k to decompose signals; coefficients of discrete points, was to decompose the signal sequence by the number of discrete points.

Step2 to normalization processing get energy relative value:

$$\overline{E_F^j} = E_F^j \Big/ \sum_{j=1}^{2^F} E_F^j \tag{1.2}$$

Step3 tectonic feature vector

$$T = \left(\overline{E_F^1}, \overline{E_F^2}, \ldots, \overline{E_F^{2^F}} \right) \tag{1.3}$$

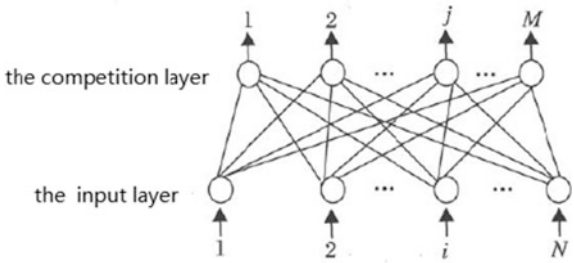

Fig. 2 Neural network structure of LVQ

5 Learning Vector Quantization Neural Network Classifier

Study of classifier based on SEMG hand motions, in previous research work, try a variety of types of neural networks, such as, the BP network, Elman network, the self-organizing competitive network, etc., are good recognition effect, but there are still certain deterrent rate. Here, try using LVQ neural network to design the classifier.

LVQ network is made up of Kohonen, and been successfully applied in many identify problems [10], LVQ network belongs to the basic competitive neural network, is composed of input layer and competition, have N input neurons, the input vector for the Competition layer M neurons, the basic structure is shown in Fig. 2. The network connection for {wij}, i = 1, 2, …, N.j = 1, 2, …, m. constraints of Cj category, j for the output neuron represents different output neurons can output the same mode.

6 The Experimental Results and Analysis

Based on WPT feature and the LVQ classifier combination mode, it including signal filtering and the selection of effective signals load-point and length, etc., then the feature extraction by wavelet packet transform. In the training phase, set the basic parameters of the classifier as the number of neurons in hidden layer, learning rate, etc.

Experiment was designed to study and verify the above structure based on WPT and the movement of SEMG and VQ neural network pattern recognition classifier. The subjects for health students, experimental muscle group for the long strands of rectus muscle and adductor, identify actions to go upstairs, downstairs, uphill and downhill four categories. Before the trial, the electromyographic signal collecting electrode paste in the subjects of rectus muscle and long adductor corresponding on the surface of the skin, at the same time also selected a place without muscle activity of skin surface as a reference point grounding, common mode signal to eliminate the body surface. Through Labview and the building of the data

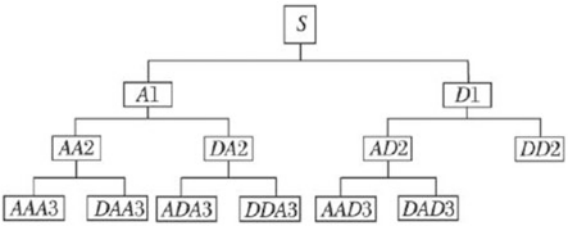

Fig. 3 Best wavelet packet decomposition tree

acquisition card signal acquisition system, set up the sampling frequency of 2.5 kHz, when the hand and wrist, wrist flexion, exhibition boxing and four kinds of action, at the same time gathering foot side wrist flexor and two road side wrist extensor muscle signals. Each action done 100 times, choose the most out of every action category specification of 30 times, a total of 120 groups of data.

In view of the SEMG movements, using Sym5 wavelet function, according to the method of optimal wavelet BaoJi fast algorithm, the preprocessing of two way electromyographic signal level 3 wavelet packet decomposition, to seek the optimal basis under the optimal wavelet packet tree consistent results as shown in Fig. 3.

According to the selection of optimal wavelet packet tree (3, 1), (3, 2), (3, 3), (3, 4), (3, 5), (3, 6), (2, 4) as a vector of the node structure characteristics, corresponding to the frequency of each node were 5–67 Hz, 67–129 Hz, 129–191 Hz, 191–253 Hz, 253–315 Hz, 315–377 Hz, 377–500 Hz. 7 per road signal is the signal frequency band energy feature, the normalized processing, characteristic vector of signal form 14 dimension.

It is listed as shown in Table 1, upstairs, downstairs, uphill and downhill four gait each type of five categories, a total of 20 typical samples by feature extraction

Table 1 Characteristic energy of 4 intent kinds based on best wavelet packet decomposition

Intent recognition		E_3^1	E_3^2	E_3^3	E_3^4	E_3^5	E_3^6	E_2^4
Upstairs	Vastus rectus	−15.7426	−502.138	16.5047	−462.387	0.5709	5.1963	355.874
	Vastus lateralis	8.5377	21.9184	8.2753	22.9371	0.2582	0.4267	32.7208
Downstairs	Vastus rectus	15.5140	30.9163	11.1703	27.3487	0.2805	0.5184	42.3289
	Vastus lateralis	−1179.62	−13,575.3	−541.80	−5630.68	−0.7254	16.0291	−5745.27
Uphill	Vastus rectus	−47.8772	−490.16	22.5125	−160.77	0.2038	2.4150	−77.6421
	Vastus lateralis	−160.823	−981.56	23.7462	−179.72	0.3012	3.0129	−78.3192
Downhill	Vastus rectus	19.3871	−200.17	26.1612	−99.017	0.2415	2.0825	−11.7548
	Vastus lateralis	−25.7054	−532.19	18.6515	−105.64	0.3315	1.8096	−70.0461

Table 2 Identification results of intent recognition using LVQ method

Intent recognition	Upstairs	Downstairs	Uphill	Downhill	Error recognition rate
Upstairs	30	0	0	0	0
Downstairs	0	30	0	0	0
Uphill	0	3	27	0	3
Downhill	0	3	0	27	3

calculated the optimal wavelet packet decomposition characteristics of each sub-band energy averages.

LVQ neural network classification recognition, each action corresponding to the two lines of SEMG 14 is a band of normalized energy as input vector of LVQ neural network, output vector [1 0 0 0] = y1, y2 = [1 0 0 0], y3 = [1 0 0 0], y4 = [0 0 0 1] respectively upstairs, downstairs, uphill and downhill four state. For each type of action samples randomly selected five times each, a total of 20 sets of data as learning samples for training. The remaining 25 each, a total of 100 groups of test samples as a signal is input into the LVQ neural network has been trained in complete identification, and the output results comparing with actual sample category, get the results in Table 2.

As can be seen from Table 2, using the LVQ classifier to go upstairs and downstairs two action recognition rate is 100%, the uphill and the downhill recognition rate is 92%, the average recognition rate reached 96%. The uphill and downhill respectively 2 times is deterrent to go upstairs, possible reason is that (1) the action of the experimenter normative enough data deviation, (2) the building of characteristic vector and remains to be perfect.

Also, with the characteristics of the wavelet packet transform to obtain and use a variety of classifiers are compared, and identifying respectively to investigate LVQ network, the BP network and RBF neural network and Elman network classifier, four kinds of gait recognition rate are shown in Table 3. We can find that, according to the characteristics of the wavelet packet transform, extract method, LVQ classifier can more accurately identify the different gait.

Table 3 recognition rate comparison among 5 recognition methods

Different classifiers	Upstairs	Downstairs	Uphill	Downhill	The average recognition rate
WPT + LVQ	100	100	93	93	96.5
WPT + BP	95	100	85	86	91.5
WPT + RBF	95	100	77	90	77.4
WPT + SVM	94	100	84	87	90.25
WPT + KNN	95	100	88	91	92.6

7 Conclusion

With long strands of rectus muscle and adductor two SEMG signals as a has four actions: upstairs, downstairs, uphill and downhill prosthetic control signal source using optimal wavelet BaoJi subband of wavelet packet transform each frequency band energy as the feature vector of each movement mode is fully display of SEMG signal under different wavelet BaoJi nature, has the characteristics of good presentation skills. When taken characteristics applied to LVQ network classifier for training and classification, obtains the excellent classification performance, shows that feature extraction method of wavelet packet transform and LVQ network classifier combination is very suitable for SEMG signal processing, targeted. The experimental results show that using this method can well identify four hands movement pattern classification, recognition rate of 96%, has a certain practical value.

Acknowledgements This work is supported by Natural Science Foundation of China (61174009) and Colleges and Universities in henan province key scientific research project, China (16B413006).

References

1. Au S, Berniker M, Herr H (2008) Powered ankle-foot prosthesis to assist level-ground and stair-descent gaits. Neural Netw 21:654–659
2. Chen LL, Yang P, Xu XY (2008) Above-knee prosthesis control based on posture recognition by support vector machine. In: IEEE international conference on robotics, automation and mechatronics, pp 307–312
3. Shen L, Yu HL (2012) Development course of prosthetics at home and abroad Chinese. J Tissue Eng Res 16(3):2451–2454 (in Chinese)
4. Gong SY, Yang P, Song L, Chen LL (2011) Simulation of swing phase dynamics in trans-femoral prostheses based on MATLAB. J Hebei univ Technol 40(2):6–9 (in Chinese)
5. Ma YL, Xu WL, Meng M, Luo ZZ, Yang JQ (2010) Adaptive control for intelligent lower limb prosthesis based on neural net work. J Zhejiang Univ Eng Sci 44(7):1373–1377 (in Chinese)
6. Yu HL, Guan SHY, Qian SHS, Zhao Zh (2008) The control method of the Knee prosthesis intelligent. Chin J Rehabil Med 23(2):145–147 (in Chinese)
7. Li WG, Huang YY, Ye XJ (2011) Feature selection based on genetic neural network and its application in classification. J Sys Simul 23(10):2094–2097 (in Chinese)
8. Li SH, Luo ZZ, Meng M (2009) Acquisition method for the lower limb motion information based on accelerometers. Mech Electr Eng Mag 26(1):5–7 (in Chinese)
9. Huihua Z, Jonathan H, Jacob R (2016) Multicontact locomotion on transfemoral prostheses via hybrid system models and optimization-based control. IEEE Trans Autom Sci Eng 13(2):502–513
10. Aaron JY, Levi JH (2016) A classification method for user-independent intent recognition for transfemoral amputees using powered lower limb prostheses. IEEE Trans Neural Syst Rehabil Eng 24(2):217–225

The Survey of Methods and Algorithms for Computer Game Go

Xiali Li, Xun Sun, Licheng Wu, Songting Deng and Qiao Gao

1 Introduction

Computer game is one of the most challenging research branches in the field of artificial intelligence. It is called drosophila in artificial intelligence [1]. In 1997, chess computer game Deep Blue developed by IBM won Kasparov, a grand master in world chess champion. This event has been an important milestone in the history of computer game research. Compared with chess computer game, go game is much more complex both in the search tree and search space. The search tree of go game is 10^{237} times the complexity of that of chess game. The search space of go game is 10^{124} times as complicated as that of chess game. Go game is much more approachable to the essence of artificial intelligence than chess. Computer go game research is of great value in artificial intelligence and cognitive science. 2016, AlphaGo beat the top human master, which is the milestone of Artificial Intelligence development history. The great success of AlphaGo makes the Go computer game receives a worldwide attention.

In early times, searching algorithm and situation evaluation algorithm for go game are mainly expert systems, Alpha-Beta search, Aspiration Search, negative maximum search. After 2003, there appeared Monte Carlo situation evaluation algorithm, UCB (Upper Confidence Bound) applied to UCT, MCTS, TD (Time Difference algorithm), AMAF (All Moves as First situation evaluation algorithm), RAVE (Rapid Action Value Estimation situation evaluation algorithm) and other algorithms based on UCT. Among which, MCTS [2] and RAVE are widely used and efficient after 2006. 2016, AlphaGo used deep convolutional neural network to reduce calculation time and improve accuracy. Darkforest effectively combined DCNN and MCTS, and achieved the communication between them.

X. Li · X. Sun · L. Wu (✉) · S. Deng · Q. Gao
Minzu University of China, Beijing 100081, China
e-mail: wulicheng@tsinghua.edu.cn

Z. Deng (ed.), *Proceedings of 2017 Chinese Intelligent Automation Conference*,
Lecture Notes in Electrical Engineering 458,
https://doi.org/10.1007/978-981-10-6445-6_29

This paper discuss go search algorithm and situation evaluation strategies including expert systems, Alpha-Beta search, Aspiration Search, negative maximum search, UCT (Upper Confidence Bound applied to Tree Search algorithm), MCTS (Monte Carlo tree searching algorithm), the algorithms used by AlphaGo and Darkforest.

The article is organized as follows. Section 2 discusses the traditional algorithms applied to go. Section 3 presents UCT, MCTS and the improvements based on them. Section 4 introduce the methods adopted by AlphaGo and Darkforest. The last section is the conclusion.

2 Traditional Algorithms

Expert system is the firstly used searching and situation evaluation algorithm in go game. In 1968, Zobrist [3–5] implemented the first computer program of go successfully with expert system algorithm. The key of its success is that it established an expert system with knowledge, regulation and reasoning capability, which can do static assessment on the chessboard and then decide the move. From then on, expert systems have been mainstream ways of computer go for a long period. However, it is output of move tend to be less ideal due to the difficulty in collecting expert knowledge accurately and applying properly. Besides, it's also hard to use mathematical methods to prove the effectiveness of those moves chosen by expert system.

Alpha-Beta searching algorithm is another important method that are widely used in early times of computer go [6–8]. This algorithm prunes mini-max tree by using searching window. During the searching process, it keeps narrowing window to improve its capability of pruning. In the beginning stage, the capability of its pruning is comparatively weak. Aiming at this problem, aspiration search [6] does improvement on Alpha-Beta search by setting a proper home window to do large pruning and return to results quickly, which shortens the time for searching. But it's hard to choose the home window and an inaccurate home window will weaken the pruning advantage of aspiration search. Negative maximum search [6] does improvement on longing for search, offering a higher pruning efficiency than Alpha-Beta searching algorithm as long as there is a proper order for child nodes. However, once child nodes are under improper order, the negative investigation algorithm will have a low efficiency when it searches certain nodes for many times.

3 UCT, MCTS and Improvements

3.1 Monte Carlo Simulation and Pruning Technologies

In 2003, Bouzy firstly applied Monte Carlo simulation to evaluate moves in computer go [9]. This method does global search without using any domain knowledge. It uses Monte Carlo simulation to do situation evaluation on leaf nodes and gets the equivalent effect to Alpha-Beta tree searching algorithm in 9 way go. But Monte Carlo simulation lacks of effective pruning. Domain knowledge of go is rarely applied in the pretreatment of Monte Carlo simulation, which goes against the acquisition for optimal solution.

In 2005, Bouzy applied gradual pruning technology in Monte Carlo simulation [10] and presented two pruning methods named MP (Miai pruning) and SP (Set Pruning) [11]. Gradual pruning can significantly increase time efficiency in choosing moves but it cannot improve chess power. Its efficiency decreases in the ending stage of go, and in the beginning stage it cannot quickly select the valuable move out of all the moves. MP randomly selects the next move from candidate set, which can increase 30% chess power when used in 19 way go, compared with those methods without pruning. SP divides candidate moves into good move set and bad move set. When the statistical result shows that the latter performs worse than the former, SP will prune the latter. This pruning method can accelerate the producing process of move in 9 way go. MP prune performs excellent in the ending stage of go, for it can shorten operating time and save resources. When used in the beginning stage of go, SP method can accelerate the producing process of optimal move. However, MP method is hard to realize under a deep searching hierarchy and time limit while SP method cannot find a satisfied balance between operating time and choice of optimal move.

3.2 UCT Algorithm and the Improvements

The year of 2006 is an important year in the history of computer go. In this year, researchers presented two famous algorithms: and Monte Carlo Tree Search algorithm.

UCT algorithm [12, 13] uses UCB algorithm to prune game tree, and applies Monte-Carlo simulation to do situation evaluation on leaf nodes. The prune process usually uses UCB1 or UCB1-Tuning formula for guidance, which gives consideration to the balance between development and adventure [14]. Branches with tree nodes that performed well in the simulation process will get more access while nodes that performed badly will be no longer visited after few accesses. This algorithm does further exploration on nodes with good performance and its output move is similar to the optimal solution. But UCT algorithm does not take domain knowledge of go into consideration.

In 2008, researchers in Jiu Ding institution of computer go (Beijing University of Posts and Telecommunications) applied pattern recognition method to extract strategies that players used as knowledge, and then use KB-UCT (knowledge-based upper confidence bound for trees) in node situation evaluation of UCT algorithm. Compared with single Monte-Carlo evaluation, this evaluation method can increase chess power of go and adaptability of game [15]. KB-UCT algorithm takes domain knowledge of go into consideration, but different nodes have different need for domain knowledge, and ignorance of this difference will cause the consequence that the searching efficiency of tree cannot increase greatly.

In 2007, Sylvain and other people proposed TD searching algorithm by adding offline and online knowledge study to UCT tree [16]. This method acquires global knowledge by offline study and acquires local knowledge by online study, which can accelerate the searching speed of UCT. But knowledge acquired online often occurs error, so the quality of its output moves tends to be bad.

3.3 Monte Carlo Tree Search and the Improvements

Monte Carlo Tree Search [17] combines Monte Carlo simulation method, mini-max tree searching method and UCT algorithm. It improves the backtracking method of evaluation value in mini-max tree, proposing a universal method that can realize gradual backtrack with the simulating times increase. This universal backtracking method of evaluation value endows Monte-Carlo Tree Search algorithm with high chess power. But the situation-evaluation method still excludes domain knowledge of go.

In 2009, D.P. Helmbold and other people used AMAF method [18] in the situation evaluation of Monte Carlo tree searching algorithm. AMAF assumes that all the moves are like the opening one, and it makes the most effective use of simulating result to allocate the benefit of a certain move to its child nodes and brothers' nodes. Under completely random chessboard, AMAF method can acquire a large number of scoring results with a few simulating times, which can accelerate the speed for situation evaluation. But, the order of go move has great influence on the result of game, and this kind of completely random evaluation may get an opposite conclusion.

In 2011, Gelly and Silver [19] used RAVE (Rapid Action Value Estimation) situation evaluation method in Monte Carlo Tree Search. RAVE applies heuristic rules of AMAF in Monte Carlo tree search, and use adjustable parameter to correct errors caused by AMAF. After certain times of simulation, this evaluation method can finally find out the optimal move. Adjustable parameter in RAVE can effectively overcome disadvantages of AMAF method and obviously increase chess power of go, so it's the generally acknowledged best situation-evaluation function at present. However, when the simulation reaches huge times, the RAVE method may face failure.

In 2012, Keh-hsun Chen and some people applied dynamic randomization and domain knowledge in Monte Carlo tree searching algorithm [20]. According to domain knowledge, this method divides move generator into different priority, and use dynamic randomization method to choose move generator in the same priority. Dynamic randomization method increases the diversity of Monte Carlo simulation, but whether it can improve efficiency still remains to be further studied.

Generally speaking, due to different chess-playing pace of go, the nodes of game tree and the searching hierarchy will also be different. Go use single searching algorithm and situation-evaluation algorithm, so the effects differ greatly under different paces and searching hierarchies. According to the experimental result of Gnu go [21], it's more effective to use pattern matching algorithm that is on basis of domain knowledge of go in the beginning and ending stages, which can save time and space resources. While in the middle stage of game, the Monte Carlo tree searching algorithm is more effective, and it can quickly get the optimal move.

4 Methods of AlphaGo and Darkforest

4.1 Methods of AlphaGo

In 2016, Google's AlphaGo team used the architecture that is DCNN for computer Go. The team introduced a new approach to the AlphaGo that use 'value networks' to evaluate board positions and 'policy networks' to select moves [22]. AlphaGo efficiently combined the policy and value networks with MCTS. The DCNN can effectively reduce the depth and breadth of the search tree. AlphaGo used multi-stage machine learning to train the neural network. First, AlphaGo trained the SL (supervised learning) police network by thousands of chess manual, including experts and amateurs. In addition, AlphaGo also trained a fast policy to reduce calculation time. Second, AlphaGo trained RL (reinforcement learning) policy network to improve policy network accuracy and optimize SL policy network. Finally, AlphaGo trained value network to predict the winning. To get the credible result, AlphaGo used MCTS to combine the policy and value network evaluated the peers and achieve the optimized result [22]. To efficiently combine MCTS with deep neural networks, AlphaGo used an asynchronous multi-threaded search that executes simulations on CPUs, and calculate policy and networks in parallel on GPUs [22]. But AlphaGo still leaves several gaps, such as ko fight.

4.2 Methods of Darkforest

Shortly after AlphaGo, Facebook published their Go program called Darkforest. Like AlphaGo program, Darkforest also combined DCNN and MCTS. By building a standard MCTS framework and study the performance of DCNN and MCTS,

Darkforest effectively achieved the communication between them. Unlike AlphaGo, Darkforest use default policy instead of the fast policy. At training, Darkforest strengthen the policy network. Darkforest use a 12-layered full convolutional network. Darkforest do not use pooling to avoid reducing performance. Darkforest only use one softmax layer to predict the black and white moves, not using two softmax output. Despite the involvement of MCTS, Darkforest still has weakness. For example, local tactics remain weak [23].

5 Conclusion

From the achievements of AlphaGo, we can get the following conclusion. The combination of deep learning, reinforcement learning and Monte Carlo tree searching is the promising future research on the computer go.

Acknowledgements This paper is supported by the National Science Foundation (Granted number is 61602539 and 51375504).

References

1. Xu X, Deng Z (2007) Various challenging issues faced to computer game research. Progress of Artificial Intelligence in China (in Chinese)
2. Browne CB, Powley E, Whitehouse D, Lucas SM, Cowling PI, Rohlfshagen P, Tavener S, Perez D, Samothrakis S, Colton S (2012) A survey of monte carlo tree search methods, IEEE Trans Comput Intell Ai Games 4(1):1–43 Mar 2012
3. Zobrist AL (1969) A new hashing method with application for game playing. Tech Rep
4. Zobrist AL (1970) Feature extraction and representation for pattern recognition and the game of go. Ph.D. Thesis, 1970
5. Zobrist AL (1971) Complex preprocessing for pattern recognition. In: Proceeding of ACM annual conference, 1971
6. Zhiqing L, Wenfeng L (2011) The basis of modern computer go. Beijing University of Posts and Telecommunications Publishing House (in Chinese)
7. Bouzy B, Cazenave T (2001) Computer go: an Ai oriented survey. Artif Intell 132(1):39–103
8. Campbell M, Marsland (1983) A comparison of minimax tree search algorithms. Artif Intell 1 (20):347–367
9. Bouzy B (2003) Associating domain-dependent knowledge and Monte Carlo approaches within a Go program. In: Proceedings of joint conference on information sciences, pp 125–136
10. Bouzy B, Helmstetter (2003) Monte carlo go developments. In: Advances in Computer Games conference (ACG-10), Graz 2003, pp 159–174
11. Bouzy B (2005) Move pruning techniques for Monte Carlo Go. In: Proceedings of 11th advance in Computer Game Conference, Taipei, pp 201–210
12. Gelly S, Wang Y (2006) Exploration exploitation in Go: UCT for Monte-Carlo go. In: Twentieth Annual Conference on Neural Information Processing Systems, Canada, pp 225–236

13. Kocsis L, Szepesvari C (2006) Bandit based monte-carlo planning. In: 15th European Conference on Machine Learning (ECML), pp 282–293
14. Auer P, Cesa-Bianchi N, Fischer P (2002) Finite-time analysis of the multi-armed bandit problem. Mach Learn 47(2):235–256
15. He S, Wang Y, Xie F, Meng J, Chen H, Luo S, Liu Z, Zhu Q (2008) Game player strategy pattern recognition and how UCT algorithm apply pre-knowledge of player's strategy to improve opponent AI. In: Proceedings of International Conference on Computational Intelligence Model. Control Autom, Vienna, Austria, pp 1177–1181
16. Gelly S, Silver D (2007) Combining online and offline learning in UCT. In: 24th International Conference on Machine Learning, pp 273–280
17. Rémi Coulom (2006) Efficient selectivity and backup operators in Monte-Carlo tree search. Submitted to CG 2006, 2006
18. Helmbold DP, Parker-Wood A (2009) All-moves-as-first heuristics in Monte-Carlo Go. In: Proceedings of International Conference on Artificial Intelligence, Las Vegas, NV, pp 605–610
19. Gelly S, Silver D (2011) Monte-Carlo tree search and rapid action value estimation in Computer Go. Artif Intell 175:1856–1875
20. Chen K-H (2012) Dynamic randomization and domain knowledge in Monte-Carlo tree search for Go knowledge-based systems, knowledge based systems, vol 34, pp 21–25
21. Xiali L, Licheng W (2015) A multi-modal searching algorithm in computer go based on test, CIAC2015, Lecture Notes in Electrical Engineering of Springer, Fuzhou, China, pp 68–72
22. Silver D, Huang A, Maddison CJ et al. (2016) Mastering the game of Go with deep neural networks and tree search. Nature 529(7587):484–489
23. Tian Y, Zhu Y (2015) Better computer go player with neural network and long-term prediction. Comput Sci

On-line Monitoring of Batch Processes Using Additive Kernel Partial Least Square

Ziang Ma, Huangang Wang and Junwu Zhou

1 Introduction

Batch processes are widely used in modern industry like biochemical, foods and medicines [3]. In Batch process, raw materials are added in batches and the whole process can be divided into a number of stages where different products are made. To ensure the safety of process, monitoring methods gain much attention. Those monitoring methods like principal component analysis (PCA) [6], support vector domain description (SVDD) [2] only utilize process variables to train the model and test abnormity. Besides process variables, we can obtain quality variables at the end of batches. Therefore, partial least square (PLS) [7] gains people's attention because it considers both process variables and quality variables.

The PLS finds a series of projection directions of both process variables and quality variables. We hope that projected vectors of process variables into projection directions have high correlation with projected vectors obtained from quality variables. Those projection directions can be found through serval times of iterations. After that projected vectors and residual vector can be obtained and both T^2 and SPE statistic can be derived. We can compare those statistics with predefined control line to judge the condition of the process. Additionally, kernel partial least square (KPLS) is introduced if we want to analyze non-linear relationship between process variables and quality variables.

Z. Ma · H. Wang (✉)
Department of Automation, Tsinghua University, Beijing, China
e-mail: hgwang@tsinghua.edu.cn

Z. Ma
e-mail: maza11@126.com

J. Zhou
State Key Laboratory of Process Automation in Mining and Metallurgy, Beijing, China
e-mail: zhou_jw@bgrimm.com

Z. Deng (ed.), *Proceedings of 2017 Chinese Intelligent Automation Conference*,
Lecture Notes in Electrical Engineering 458,
https://doi.org/10.1007/978-981-10-6445-6_30

In on-line monitoring, only data until current time point are available, which is a kind of missing data problem [5]. In order to deal with missing data, researches are made to estimate statistics when data is incomplete. One handing method is filling those missing data with predefined data, average of training data or current obtained data for instance. Another method makes use of the characteristics of monitoring method. As for PLS, we can estimate projected vectors based on the thought of least square. Then we can calculate T^2 and SPE statistics. However, if nonlinear kernel like Gaussian kernel is chosen as kernel in KPLS, we cannot use the thought of least square to estimate projected vectors because the value of kernel cannot be decomposed into sum of kernel of every time slice.

The additive kernel [4, 10] is a special kind of kernel. It considers nonlinear relationships among variables in every time slice and the value of generalized additive kernel can be decomposed into sum of kernel of every time slice. Based on characteristics mentioned above, we can continue to use the thought of least square to estimate projected vectors without filling missing data. In this paper, we will introduce additive kernel into KPLS [9] and name it AKPLS. Then we can also estimate projected vectors without filling those missing data.

2 Kernel Partial Least Square Based Batch Processes Monitoring

Sample data in batch processes are usually expressed as the three-dimensional matrix $\underline{\mathbf{X}}(I \times J \times K)$, where I denotes the number of batches, J denotes the number of variables at each time point, K denotes the number of time slices in a batch. Before using monitoring methods, the data preprocessing for batch processes is needed [8]. In data preprocessing, we unfold the three-dimensional matrix $\underline{\mathbf{X}}$ and get a two-dimensional matrix $\mathbf{X}(I \times JK)$. Figure 1 represents the process of batch-wise unfolding method. Then we centralize and normalize different variables and get process variable matrix $\mathbf{X}$ and quality variable matrix $\mathbf{Y}$.

PLS considers linear relationships between $\mathbf{X}$ and $\mathbf{Y}$, like (1) where t_i denotes projection score, $\mathbf{p}_i$ and $\mathbf{q}_i$ are loading vectors, $\mathbf{E}$ and $\mathbf{F}$ are residuals.

$$\mathbf{X} = \sum_{i=1}^{n} t_i \mathbf{p}_i^T + \mathbf{E}, \mathbf{Y} = \sum_{i=1}^{n} t_i \mathbf{q}_i^T + \mathbf{F} \tag{1}$$

For each preprocessed test sample $\mathbf{x} \in R^{m*1}$, we can derive n projected scores and residual vector. The iteration procedures to derive statistics from complete test sample using PLS are summarized as follow:

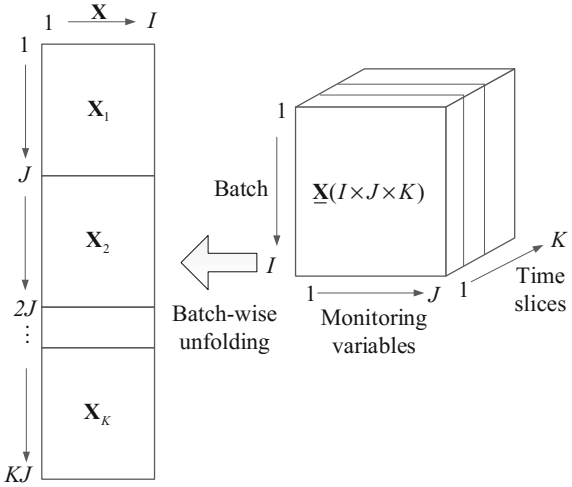

Fig. 1 Batch-wise unfolding process

1. $\mathbf{x}_1 = \mathbf{x}$, $i = 1$.
2. When $i \leq n$, do the following steps 3.
3. $t_i = \mathbf{x}_i^T \mathbf{w}_i$, $\mathbf{x}_{i+1} = \mathbf{x}_i - t_i \mathbf{p}_i$, $i = i + 1$.
4. Set $\mathbf{t} = [\, t_1 \quad t_2 \quad \ldots \quad t_n \,]^T$ as projected vector, $\mathbf{x}_{n+1}$ as residual vector.
5. Set $\mathbf{t}^T \mathbf{\Lambda}^{-1} \mathbf{t}$ as T^2 statistic ($\mathbf{\Lambda}$ denotes diagonal matrix of the variances of the projected vectors). Set SPE statistic as square of $\mathbf{x}_{n+1}$.

The control limit of T^2 can be estimated by F-distribution and the control limit of SPE can be estimated as chi-squared distribution, like (2), where N denotes the number of training samples, n denotes the number of projection directions, α denotes the significance level. m and v denote the mean and variance of SPE calculated from training data.

$$\begin{aligned} T^2 &\sim \frac{n(N^2-1)}{N(N-n)} F_{n,\, N-n,\, \alpha} \\ SPE &\sim g\chi^2_{h,\alpha}, g = \mathrm{v}/(2m), h = 2m^2/\mathrm{v} \end{aligned} \tag{2}$$

In batch process, there exists non-linear relationship among process variables and quality variables. Therefore, we introduce kernel to make it KPLS by replacing $\mathbf{X}$ with $\Phi(\mathbf{X})$ using (3).

$$\begin{aligned} \Phi(\mathbf{X}) &= [\, \Phi(\mathbf{x}_1) \quad \Phi(\mathbf{x}_2) \quad \ldots \quad \Phi(\mathbf{x}_N) \,]^T \\ Ker(\mathbf{x}_i, \mathbf{x}_j) &= \Phi(\mathbf{x}_i)^T \Phi(\mathbf{x}_j) \end{aligned} \tag{3}$$

In batch process on-line monitoring, data after current time point are unavailable. If we choose traditional nonlinear kernel like Gaussian kernel and polynomial kernel, those missing data should be filled before we calculate monitoring statistics.

Inappropriate padding may affect the monitoring result. In the next section, another special kernel called additive kernel is introduced to solve this problem.

3 Batch Process Monitoring Based on Additive Kernel Partial Least Square (AKPLS)

In this section, we introduce a kind of kernel called additive kernel (AK) and the training and monitoring procedure of AKPLS.

3.1 Additive Kernel (AK)

Additive Kernel (AK) is a special kind of kernel which is defined as (4), where K denotes K different time slices.

$$\Phi(\mathbf{x}_i) = \left[\phi(\mathbf{x}_{i,1})^T \quad \phi(\mathbf{x}_{i,2})^T \quad \ldots \quad \phi(\mathbf{x}_{i,K})^T \right]^T \tag{4}$$

Data from different time slices are mapped independently in $\Phi(\mathbf{x}_i)$. The value of the whole kernel can be decomposed into the sum of K kernels. We can select different kind of kernels at different time slices to analyze non-linear relationship among variables. If kernel at every time slice is Gaussian kernel, it is called additive Gaussian kernel, like (5).

$$\begin{aligned} Ker(\mathbf{x}_i, \mathbf{x}_j) &= \Phi(\mathbf{x}_i)^T \Phi(\mathbf{x}_j) = \sum_{k=1}^{K} \exp\left(-\left\| \mathbf{x}_{i,k} - \mathbf{x}_{j,k} \right\|^2 / r \right) \\ \phi(\mathbf{x}_{i,k})^T \phi(\mathbf{x}_{j,k}) &= \exp\left(-\left\| \mathbf{x}_{i,k} - \mathbf{x}_{j,k} \right\|^2 / r \right) \end{aligned} \tag{5}$$

3.2 Training Process of AKPLS

Additive Kernel Partial Least Square(AKPLS) is a special case of KPLS where $\Phi(\mathbf{x}_i)$ satisfied with (4) can be chosen as kernel. Then we can derive training process of AKPLS, summarized as Algorithm 1.

Algorithm 1: Training part of AKPLS
Input: $\mathbf{X}$ as process variables matrix, $\mathbf{Y}$ as quality variables matrix, n as iteration times.

1. Set $\Phi(\mathbf{X})_1 = \Phi(\mathbf{X})(\mathbf{I} - \frac{1}{h}\mathbf{1_I})$, where $\mathbf{I}$ denotes unit matrix, $\mathbf{1_I}$ denotes matrix with all elements equals to 1, h is the dimension of the matrix, the definition of $\Phi(\mathbf{X})$ is (1.3). Set $\mathbf{Y}_1 = \mathbf{Y}$ and $i = 1$.
2. If $i \leq n$ do the following 3, 4, 5, 6, else do 7.
3. Set $\mathbf{t}_i$ as the eigenvector of maximum eigenvalue of $\Phi(\mathbf{X})_i \Phi(\mathbf{X})_i^T \mathbf{Y}_i \mathbf{Y}_i^T$.
4. Calculate $\mathbf{c}_i$, $\mathbf{u}_i$, $\mathbf{w}_i$, $\mathbf{t}_i$ using $\mathbf{c}_i = \mathbf{Y}_i^T \mathbf{t}_i$, $\mathbf{c}_i = \mathbf{c}_i / \|\mathbf{c}_i\|$,$\mathbf{u}_i = \mathbf{Y}_i \mathbf{c}_i$, $\mathbf{w}_i = \Phi(\mathbf{X})_i^T \mathbf{u}_i$, $\mathbf{w}_i = \mathbf{w}_i / \|\mathbf{w}_i\|$, $\mathbf{t}_i = \Phi(\mathbf{X})_i \mathbf{w}_i$.
5. Use $\mathbf{p}_i = \frac{\Phi(\mathbf{X})_i^T \mathbf{t}_i}{\mathbf{t}_i^T \mathbf{t}_i}$, $\mathbf{q}_i = \frac{\mathbf{Y}_i^T \mathbf{t}_i}{\mathbf{t}_i^T \mathbf{t}_i}$, $\Phi(\mathbf{X})_{i+1} = \Phi(\mathbf{X})_i - \mathbf{t}_i \mathbf{p}_i^T$, $\mathbf{Y}_{i+1} = \mathbf{Y}_i - \mathbf{t}_i \mathbf{q}_i^T$ to calculate $\mathbf{p}_i$, $\Phi(\mathbf{X})_{i+1}$, $\mathbf{Y}_{i+1}$.
6. Set $i = i + 1$.
7. Get $\mathbf{w}_i, \mathbf{p}_i$ $(i = 1, 2, \ldots n)$ after n iterations.
8. Using $\Phi(\mathbf{X})_{n+1}$, $\mathbf{t}_i$ $(i = 1, 2, \ldots n)$ to calculate SPE_k, $\overline{SPE}_k$, T^2 statistics of training data and set control limits of those statistics.

Output: $\mathbf{w}_i, \mathbf{p}_i$ $(i = 1, 2, \ldots n)$. Control limit of SPE_k, $\overline{SPE}_k$, T^2.

In Algorithm 1, statistic T^2 is defined as $\mathbf{t}^T \mathbf{\Lambda}^{-1} \mathbf{t}$ in which $\mathbf{\Lambda}$ denotes diagonal matrix of the variances of the scores associated with n projected directions. SPE_k denotes sum of the square of the residual vector corresponding to time point k. $\overline{SPE}_k = \sum_{i=1}^{k} SPE_i \Big/ k$. The control limits of those statistics are shown in (2).

3.3 On-line Monitoring of AKPLS

In on-line monitoring, variables after current time slice are unknown. In this part, we will mainly discuss how to estimate monitoring statistics without filling in unknown data in AKPLS.

In AKPLS, $\Phi(\mathbf{x}_j)$ can be decomposed as (6). At time point k, $\Phi^{(1,k)}(\mathbf{x}_j)$ is known while $\Phi^{(k+1,K)}(\mathbf{x}_j)$ is unknown.

$$\begin{aligned} \Phi(\mathbf{x}_j) &= \left[\Phi^{(1,k)}(\mathbf{x}_j)^T \quad \Phi^{(k+1,K)}(\mathbf{x}_j)^T \right]^T \\ \Phi^{(1,k)}(\mathbf{x}_j) &= \left[\phi(\mathbf{x}_{j,1})^T \quad \phi(\mathbf{x}_{j,2})^T \quad \ldots \quad \phi(\mathbf{x}_{j,k})^T \right]^T \\ \Phi^{(k+1,K)}(\mathbf{x}_j) &= \left[\phi(\mathbf{x}_{j,k+1})^T \quad \phi(\mathbf{x}_{j,2})^T \quad \ldots \quad \phi(\mathbf{x}_{j,K})^T \right]^T \end{aligned} \tag{6}$$

In on-line monitoring, we can derive optimization problem (7) to estimate projection vectors of test data $\mathbf{x}_j$, with corresponding results shown in (8). $\hat{t}_i$ shows the estimated projected score. $\mathbf{w}_i^{(1,k)}$ and $\mathbf{p}_i^{(1,k)}$ show parts of $\mathbf{w}_i$ and $\mathbf{p}_i$

corresponding to times slices from 1 to k. Then we can derive $\Phi_{i+1}^{(1,k)}(\mathbf{x}_j)$ with (9). On-line monitoring of AKPLS is shown in Algorithm 2.

$$\min \left\| \Phi_i^{(1,k)}(\mathbf{x}_j)^T - \hat{t}_i \, \mathbf{w}_i^{(1,k)T} \right\|_2 \tag{7}$$

$$\hat{t}_i = \Phi_i^{(1,k)}(\mathbf{x}_j)^T \mathbf{w}_i^{(1,k)} / (\mathbf{w}_i^{(1,k)T} \mathbf{w}_i^{(1,k)}) \tag{8}$$

$$\Phi_{i+1}^{(1,k)}(\mathbf{x}_j) = \Phi_i^{(1,k)}(\mathbf{x}_j) - \hat{t}_i \mathbf{p}_i^{(1,k)} \tag{9}$$

Algorithm 2: On-line monitoring of AKPLS

Input: $\mathbf{x}^{(1,k)}$ denotes variables of $\mathbf{x}$ from time slice 1 to k. $\mathbf{w}_i, \mathbf{p}_i$ $(i = 1, 2, \ldots n)$, control limit of SPE_k, $\overline{SPE}_k$, T^2.

1. Set $i = 1$ and centralize $\Phi^{(1,k)}(\mathbf{x})$ to get $\Phi_1^{(1,k)}(\mathbf{x})$.
2. If $i \leq n$ do the following steps 3, else do 4.
3. Estimate $\hat{t}_i$ with (8), estimate $\Phi_{i+1}^{(1,k)}(\mathbf{x})$ with (9), $i = i + 1$.
4. Set $\mathbf{t} = [\hat{t}_1 \quad \hat{t}_2 \quad \ldots \quad \hat{t}_n]^T$.
5. Calculate monitoring statistics using $\Phi_{n+1}^{(1,k)}(\mathbf{x})$ and $\mathbf{t}$.
6. Compare statistics with control limit and judge whether $\mathbf{x}$ is normal.

Output: whether the sample is normal or not.

Additive kernel has characteristics that variables in different time slices are independent when mapped into feature space. $\mathbf{w}_i$ and $\mathbf{p}_i (i = 1, 2, \ldots n)$ are linear combinations of projections in feature space of training data. Therefore, $\mathbf{w}_i$ and $\mathbf{p}_i$ can also be decomposed into $\mathbf{w}_i^{(1,k)}$, $\mathbf{w}_i^{(k+1,K)}$ and $\mathbf{p}_i^{(1,k)}$, $\mathbf{p}_i^{(k+1,K)}$ respectively, similar to (6). However, some nonlinear kernels like Gaussian kernel cannot be decomposed into two parts like (6), so we cannot use methods discussed above to estimate statistics without filling unknown data.

More experiments and analysis about score estimation using the thought of least square are shown in [5], where estimation methods in PLS are discussed.

4 Case Study

A fed-batch penicillin fermentation dataset is used to evaluate the performance of methods. The dataset is simulated by a standard simulator Pensim V.2.0 [1].

In my experiments, 110 normal batches and 4 abnormal batches are generated from the simulator. Every batch lasts 400 h and the sampling rate is 30 min. The start time point of faults of 4 abnormal batches are 60, 55, 40, 30 h respectively.

Those 4 faults last until the end of batch. Training dataset includes 100 normal batches. Test dataset includes 10 normal and 4 abnormal batches. Eight variables including Aeration rate, Agitator power, Substrate feed temperature, Culture volume, Carbon dioxide concentration, pH, Bioreactor Temperature, Generated heat are selected as process variables while 3 variables including Substrate concentration, Biomass concentration, Penicillin concentration are quality variables. Every batch includes 6400 process variables and 3 quality variables because we can get quality variables only at the end of every batch.

On-line monitoring starts from the 21st time point until the end of the batch. We choose 21 because a small portion of data is necessary when we estimate test statistics. Faced with missing data problem, PLS and AKPLS uses method discussed in Algorithm 2 to estimate statistics while KPLS fills data after current time with current data before calculating monitoring statistics. $\overline{SPE}_k$ is selected to judge the test sample because it works better than other statistics.

From Table 1 we can see that $\overline{SPE}_k$ together with KPLS or AKPLS can discriminate normal batches from abnormal batches. Results in Table 2 show that AKPLS with Gaussian kernel is better than other methods because it alarms earlier than other methods in most cases after faults occur. The control charts of three methods are presented in Fig. 2, where time units are 30 minutes.

Table 1 On-line monitoring results in penicillin dataset ($\overline{SPE}_k$)

Algorithm	Number in 10 normal batches the method deems normal	Number in 4 abnormal batches the method deems abnormal
PLS	9	3
Gaussian KPLS	10	4
Gaussian AKPLS	10	4

Table 2 Alarm time (0.5 h) of 4 abnormal batches ($\overline{SPE}_k$)

Algorithm	Fault 1	Fault 2	Fault 3	Fault 4
PLS	544	Not detected	366	62
Gaussian KPLS	554	135	293	60
Gaussian AKPLS	122	123	119	68
True start time	120	110	80	60

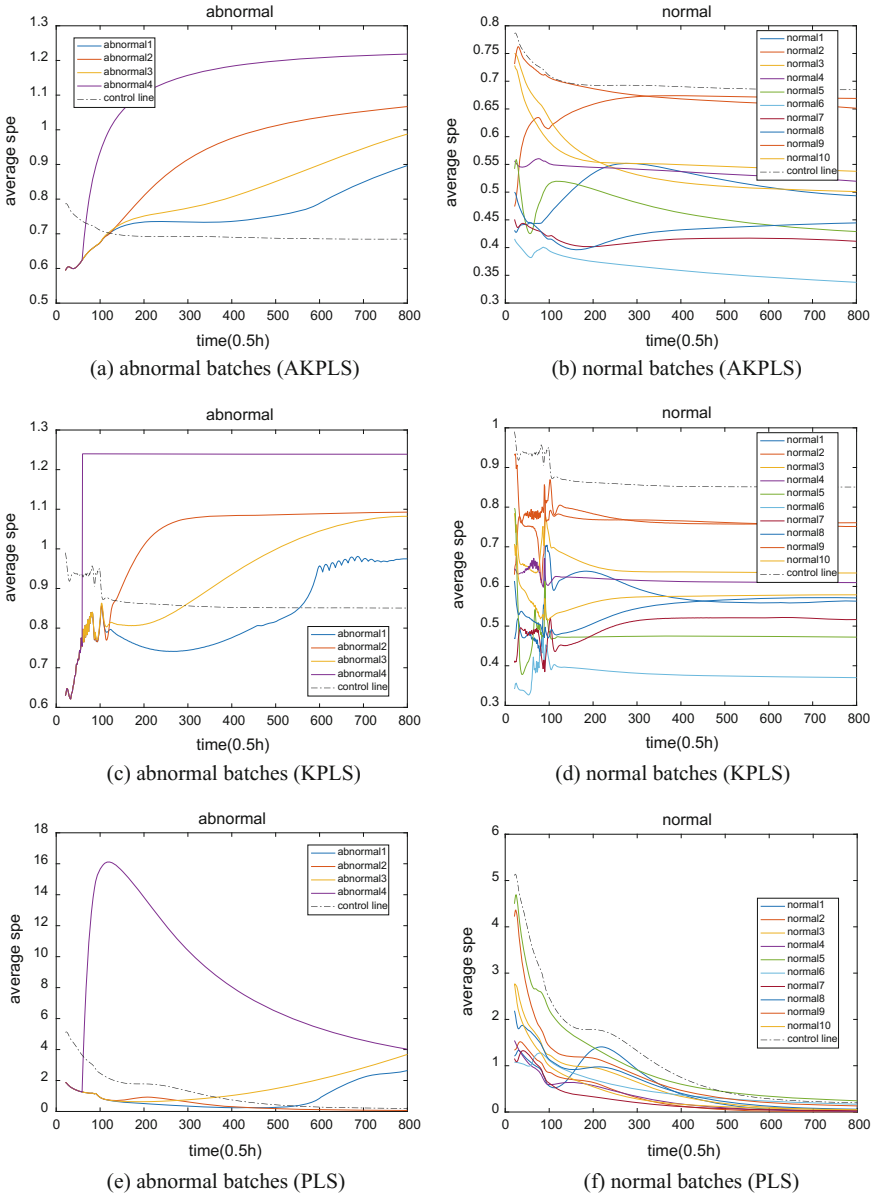

(a) abnormal batches (AKPLS)

(b) normal batches (AKPLS)

(c) abnormal batches (KPLS)

(d) normal batches (KPLS)

(e) abnormal batches (PLS)

(f) normal batches (PLS)

Fig. 2 On-line monitoring results with $\overline{SPE}_k$

5 Conclusion

In this paper, we propose a special case of kernel partial least square called additive kernel partial least square(AKPLS) and show its application in batch process on-line monitoring. AKPLS uses a special kind of kernel called additive kernel where variables in different time points are mapped independently into feature space. Using ASPLS, we can estimate statistics without filling missing data after current time point in on-line monitoring. Experiments on penicillin dataset show effectiveness of AKPLS.

References

1. Birol G, Ündey C, Cinar A (2002) A modular simulation package for fed-batch fermentation: penicillin production[J]. Comput Chem Eng 26(11):1553–1565
2. Ge Z, Gao F, Song Z (2011) Batch process monitoring based on support vector data description method. J Process Control 21(6):949–959
3. Ge Z, Song Z, Gao F (2013) Review of recent research on data-based process monitoring. Ind Eng Chem Res 52(10):3543–3562
4. Maji S, Berg AC, Malik J (2013) Efficient classification for additive kernel SVMs. IEEE Trans Pattern Anal Mach Intell 35(1):66–77
5. Nelson PRC, Taylor PA, MacGregor JF (1996) Missing data methods in PCA and PLS: score calculations with incomplete observations. Chemometr Intell Lab Syst 35(1):45–65
6. Nomikos P, MacGregor JF (1994) Monitoring batch processes using multiway principal component analysis. AIChE J 40(8):1361–1375
7. Nomikos P, MacGregor JF (1995) Multi-way partial least squares in monitoring batch processes. Chemometr Intell Lab Syst 30(1):97–108
8. Nomikos P, MacGregor JF (1995) Multivariate SPC charts for monitoring batch processes. Technometrics 37(1):41–59
9. Rosipal R, Trejo LJ (2002) Kernel partial least squares regression in reproducing kernel hilbert space. J Mach Learn Res 2:97–123
10. Yao M, Wang H (2015) On-line monitoring of batch processes using generalized additive kernel principal component analysis. J Process Control 28:56–72

Research for Path Planning in Indoor Environment Based Improved Artificial Potential Field Method

Hu Pan, Chen Guo and Zhaodong Wang

1 Introduction

In the last few decades, the service mobile robots are developing rapidly, which could be able to execute different complex works. The path planning for mobile robot in indoor environment becomes a hot and rather complicated issue in the field of mobile robot research. Its task is to find a path in the narrow space with large number of obstacles, the path is optimal and collision-free [1]. The research on path planning is divided into the two directions, one is the global path planning, another is about the local path planning [2]. At present, the commonly methods are artificial potential field method [3], fuzzy logic [4], genetic algorithm [5] and so on. They can be applied into the unknown environment. The methods for the global path planning are cell decomposition [6], A* algorithm [7], D* algorithm, and others. The artificial potential field (APF) is a mature and efficient method in path planning, and it is simple mathematical calculation and high efficiency, so it is widely used. However, the local minimum point and GNRON (goals unreachable with obstacles nearby) problems are often occurred in APF [8], and the path jitter is easily to occur in narrow environment. Although there are a variety of methods can be used to solve it, such as random escape [9], heuristic search [10], walk along the wall and Tangent bug method [11] and so on, but these methods have some disadvantages and not suit for the path planning in indoor environment [15–17].

This paper puts forward a new method to apply into the path planning in indoor environment. We analysis the problems in APF and modify the function of repulsive potential field [12]. The intermediate target points are proposed to guide the robot walking out of the local minimum point [13], A* algorithm is used to get these intermediate target points and the global optimized path [14]. Several simulation experiments are carried out to demonstrate our improved APF method.

H. Pan · C. Guo (✉) · Z. Wang
School of Information Science and Technology, DMU, Dalian 116026, China
e-mail: dmuguoc@126.com

Z. Deng (ed.), *Proceedings of 2017 Chinese Intelligent Automation Conference*,
Lecture Notes in Electrical Engineering 458,
https://doi.org/10.1007/978-981-10-6445-6_31

2 Modify the APF

2.1 The Disadvantages of APF and the Improvement Measures

When the APF method is applied to the mobile robot path planning, the following phenomena often appear:

1. If the target point is near the obstacle and located in the effective scope of the influence of obstacle. The repulsion force may be greater than the attraction force in this situation, the GNRON problem would happen.
2. If the resultant force turns to zero, and the robot has not yet reached the target point at the same time, the local minimum problem would occur and make the robot wanders or stops in a certain area.
3. If the robot walks in the narrow environment that the distance between two walls is especially short, the robot could not walk along the straight line in the narrow space and need extra times to reach the goal.

The problems in APF are analyzed in the front, and some methods are put forward to solve them. By adding the coefficient term to the function of the repulsive potential field, this could make the attractive force and the repulsive force reduce at the same time. They both reduce to zero until the robot reaches the target point, so the GNRON problem could be solved. Also the intermediate target point is introduced to guide the robot moving out of the local minima area. Last, adjust the value of the attractive force and the repulsive force, and the distribution of the potential field is modified to make sure the mobile robot can walk straightly along the wall.

2.2 The Improved Potential Field Model

According to the improvement measures are described above, the distance factor is added into the function of the repulsive potential field, the redefine function of it is shown as:

$$U_{rep} = \begin{cases} \frac{1}{2}\eta\left(\frac{1}{\rho} - \frac{1}{\rho_0}\right)^2 (X - X_g)^n, & \rho \le \rho_0 \\ 0, & \rho > \rho_0 \end{cases} \tag{1}$$

where: U_{rep} is the repulsive potential field, ρ is the Euclidean distance from the robot to the obstacles, ρ_0 is the largest impact distance of simple obstacle, η is a positive scaling factor, n is a index coefficient, and it is 2 in this paper.

The modified potential field can solve the GNRON problem, but the local minimum problem did not solve. There may be a variety of kinds of local minima in

mobile robot's path planning and it often occurs. This paper mainly discusses the following three kinds of local minimum problem, the three map models that used to descript them are shown in Fig. 1.

In Fig. 1, there is a common feature that the target point and the robot are almost in a straight line and the obstacles are located between them in three maps. And there are some special points that the attractive force and the repulsive force is equal or almost equal and collinear but on the opposite direction in these circumstances. This would make the robot to be trapped in local minima and could not reach the target point.

Two methods are adopted to solve the local minima. First, we change the direction of repulsion force to solve the local minimum problem in Fig. 1a, the force analysis after changing the direction of the repulsive force is shown in Fig. 2a. In Fig. 2a, F_{rep} is divided into F_{rep1} and F_{rep2}, the direction of F_{rep1} is changed and the new direction is set as the tangent which along the scope of maximum impact with obstacles, so the angle between the repulsive force and the attractive force is no longer greater than 90°, the resultant force turns to toward the robot and the magnitude is greater than zero, the local minimum problem can be solved. The formulas in Fig. 2a are follows as:

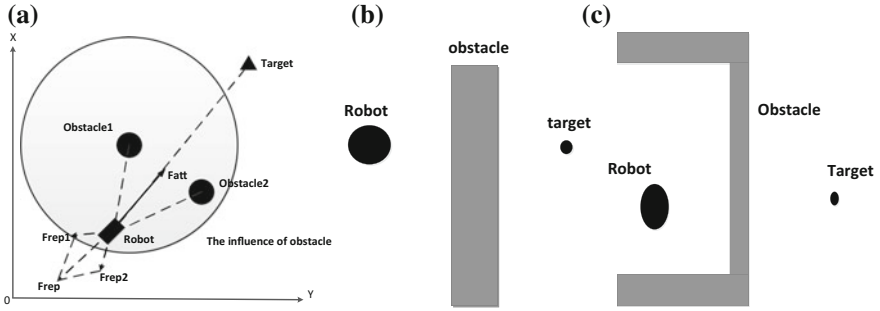

Fig. 1 Three kinds of local minimum problem

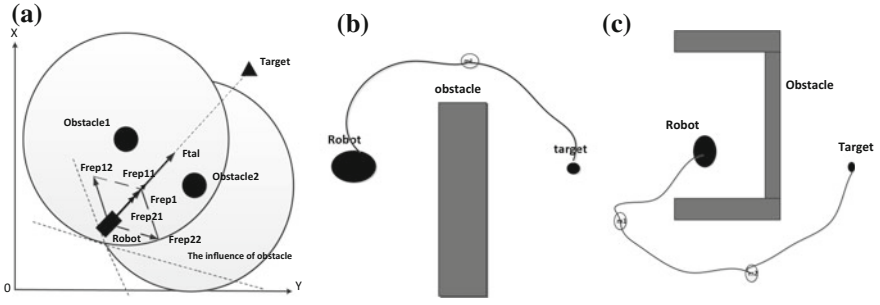

Fig. 2 Two ways of solving the three kinds of local minimum problem

$$F_{rep1} = \eta\left(\frac{1}{\rho} - \frac{1}{\rho_0}\right)\frac{1}{\rho^2}(X - X_g)^n \frac{\partial \rho}{\partial X} \tag{2}$$

$$F_{rep2} = -\frac{n}{2}\eta\left(\frac{1}{\rho} - \frac{1}{\rho_0}\right)^2 (X - X_g)^{n-1} \frac{\partial (X - X_g)}{\partial X} \tag{3}$$

The obstacles (Fig. 1b, c) are tightly connected together and form a wall or U-shaped wall. If we just change the direction of the repulsive force as above, the robot could not bypass the wall or the U-shaped wall, so we proposed the intermediate target point based method. The additional intermediate target points are needed to be set in the special circumstances that contain U-type obstacles to guide the robot out of the local minima area. The results would be like in Fig. 2b, c by using the intermediate target point based method. This method need to detect whether the robot is located in local minimum or not firstly. The next paragraph would introduce how to detect local minima.

2.3 Detect the Local Minima

In the process of robot path planning, due to the existence of various errors, the attractive force and repulsive forces are rarely possible to the same. The so-called local stability phenomena are actually the robot moves in the range of the circle of a point and wanders in it. The kind of the so-called local stability phenomena is shown in Fig. 3.

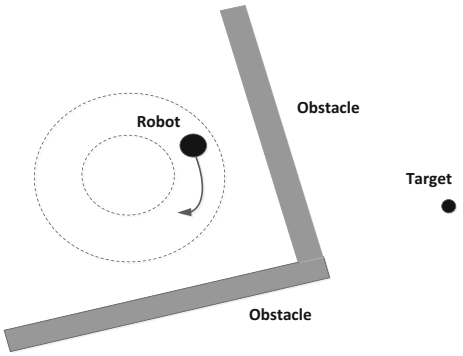

Fig. 3 The phenomenon that the robot traps in local minima

In Fig. 3, when the robot traps into the local minimum point, the robot would wandering in the range of circle and could not get out, this is the local steady status.

In this paper, we have taken some strategies to detect whether the robot is in the local steady status or not. The specific strategies are as follows:

1. According to the robot's moving step v and the scope of the repulsive force ρ_0, set the radius of the circle as R in the local stable area.
2. According to the speed of the robot to set the detection time as t (t is almost several times than the moving step), the program would detect whether the robot in the local steady statue every t time (t should be meet the required time that the robot could walk out of the radius of the circle).
3. Calculating the distance between every two points that the time interval is t time. If the distance is less than R, the program would turn to the corresponding algorithm to solve the local minima. Otherwise the robot is in normal state, taking the next cycle and making cycle detection.

The local minima can be detected by the three steps. The common method of setting the intermediate target point is mainly design from the view of geometric point, it needs for different analysis in different circumstances, so it is difficult to achieve the robot real-time path planning. In this paper, the A* algorithm is proposed to carry out the global path planning and the inflection points on the path can be set as the intermediate target points. The next section will describe A* algorithm in detail.

3 The Intermediate Target Point Based on A* Algorithm

A* algorithm is a typical heuristic search algorithm in artificial intelligence, compared with genetic algorithm, particle swarm algorithm, it has simple math function and small calculation, so that it is widely applied in real-time systems, artificial intelligence and so on. The core of the A* algorithm is composed of a valuation function. The valuation function is as follows:

$$f(n) = g(n) + h(n) \tag{4}$$

In formula (4), $f(n)$ is the valuation function of node n. $g(n)$ is the actual cost from the initial node to the n-node; $h(n)$ is the estimated cost of the best path from the n-node to the destination node. The function of $h(n)$ is closely related to what the actual environment is, the commonly used methods are Manhattan distance, diagonal distance and Euclidean distance, etc. Since the Euclidean distance can better represent the true distance between two points in the map, we adopt it as the calculation formula.

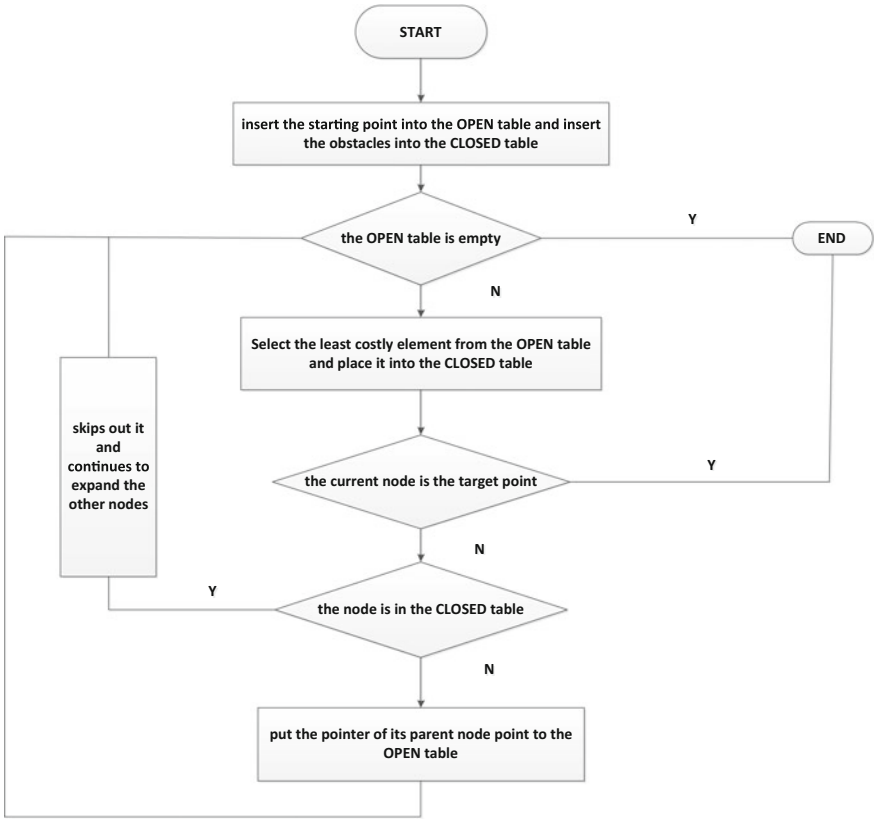

Fig. 4 The flow chart of A* algorithm

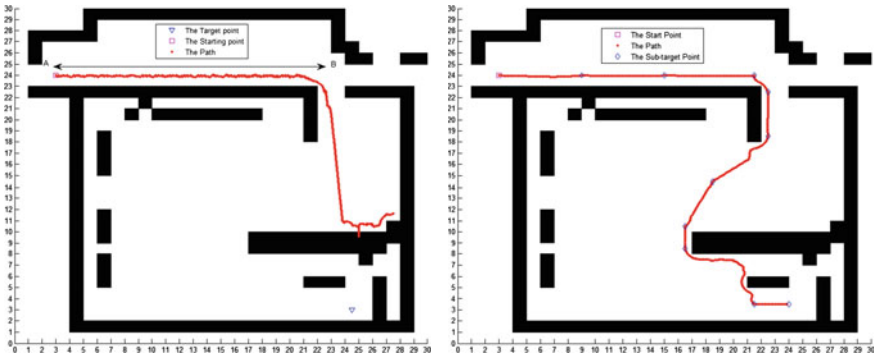

(a) Path planned by the APF method (b) Path planned by our IAPF method

Fig. 5 The planned path in indoor environment

Table 1 The list of the intermediate target points in the global path planning

The global path planning in A* algorithm	
Starting point (3, 24)	Sub-target point 3 (16.5, 10.5)
Terminal point (24, 3.5)	Sub-target point 4 (16.5, 8.5)
Sub-target point 1 (9, 24)	Sub-target point 5 (18.5, 14.5)
Sub-target point 2 (15, 24)	Sub-target point 6 (22.5, 18.5)

After understanding the basic idea of A* algorithm, the flow chart of A* algorithm is design, it is shown in Fig. 4.

According to the actual indoor environment, we build the grid map (like Fig. 5) for the global path planning, and the path nodes are obtained by using the procedure of A* algorithm. The intermediate target points are shown in Table 1.

4 Simulation Studies

In order to prove the efficient and flexibility of our optimized IAPF algorithm, some experiments have been done in MATLAB. In these experiments, the robot is set in a certain speed, and it moves forward in the direction of the resultant virtual force, experiments are under these circumstances. The experimental environment is with 30×30 room indoor environment that includes corridor and a large laboratory. The map is built and is shown in Fig. 5, which the rectangles with different sizes are set as the obstacles in the laboratory. The coordinate of starting point and the terminal point is the same in Table 1. The number of iterations is 130. The other related parameters are shown in Table 2.

The path by the traditional APF method is shown in Fig. 5a, the robot collides with some obstacles and cannot reach the target, it would wandering at some area in some steps, and it could not bypass U-type obstacles. Additionally, the path is tortuous when the robot walks in the corridor.

In order to solve these two kinds of local minima problems, the IAPF method based on the intermediate target point is proposed. We use the A* algorithm to get the intermediate target points, the sub-target points are shown in Table 1. We also change the coefficients of attraction and repulsive force, they are turn to 25 and 8 respectively, and two sub-targets are added into the corridor. All of these measures are used to solve the local minima and ensure that the robot can walk straightly in the corridor. These improvement measures are written into the procedure of the IAPF method, and the planned path is shown in Fig. 5b. Compared with the path in

Table 2 The list of parameters in the path planning

k	η	v	ρ_0	t	R
20	5	0.2	2.7	10	2

Fig. 5a, the robot can walk along the corridor straightly and bypass the U-shaped obstacles to reach the target point. The path is smooth and collision-free.

5 Conclusions

This paper adopts a new IAPF method for the path planning in indoor environment where many kinds of obstacles are located in it. The function of the repulsive potential field is redefined and the intermediate target point based method is adopted. All of them are used to solve the common problem in APF method. Additionally, in order to make a smooth and safe path in the indoor environment, the A* algorithm is proposed and used to get the required intermediate targets. The path in simulation experiments with the IAPF method is smooth and safety.

Acknowledgements This work is supported by National Natural Science Foundation of China (Nos. 51579024, 6137114) and the Fundamental Research Funds for the Central Universities (DMU no. 3132016311).

References

1. Jiang B, Bishop AN, Anderson BDO et al (2015) Optimal path planning and sensor placement for mobile target detection. Automatica 60:127–139 (in Chinese)
2. Jia YH, Mei FX (2002) Simple path planning for mobile robots in the present of obstacles. J Beijing Inst Technol 11(2):208–211 (in Chinese)
3. Khatib O (1986) Real-time obstacle avoidance for manipulators and mobile robot. Int J Robot Res 5(1):90–98
4. Ye B-Q, Zhao M-F, Wang Y (2011) Research of path planning method for mobile robot based on artificial potential field. In: international conference on multimedia technology (ICMT). IEEE 2011
5. Koren Y, Borenstein J (1991) Potential field methods and their inherent limitations for mobile robot navigation. In: IEEE international conference on robotics and automation. IEEE, pp 1398–1404
6. Li G, Yamashita A, Asama H et al (2012) An efficient improved artificial potential field based regression search method for robot path planning. In: International conference on mechatronics and automation (ICMA). IEEE, pp 1227–1232
7. Ge SS, Cui YJ (2000) New potential functions for mobile robot path planning. IEEE Trans Robot Autom 16(5):615–620
8. Yu ZZ, Yan JH, Zhao J, Chen ZF, Zhu YH (2011) Mobile robot path planning based on improved artificial potential field method. J Harbin Inst Technol 43(1):50–55 (in Chinese)
9. Liu CY, Chen YQ, Liu CG (2009) Anti-collision path planning for mobile robot based on modified potential field method. J Southeast Univ 39(supp. 1):116–120 (in Chinese)
10. Li Q, Chen B, Wang LJ, Zhang WC (2011) An improved artificial potential field method for path planning of mobile robots. In Proceedings of the 2011 international conference on management science and intelligent control
11. Zhang JY, Zhao ZP, Liu D (2006) A path planning method for mobile robot based on artificial potential field. J Harbin Inst Technol 38(8):1306–1309 (in Chinese)

12. Lee MC, Park MG (2003) Artificial potential field based path planning for mobile robots using a virtual obstacle concept. In: Proceedings of the 2003 IEEE/ASME international conference on advanced intelligent mechatronics, vol 2, pp 735–740
13. Zhang MK, Li LS (2007) A method for solving local minimization problem of artificial potential field. Comput Technol Develop 17(5):137–139 (in Chinese)
14. Nilsson NJ (2000) Problem-solving methods in artificial intelligence. In: Artificial intelligence: a new synthesis. Morgan Kaufmann Publishers, Burlington
15. Li GH (2014) Distributed task allocation and path planning in dynamic environment for multi-robot guidance system, pp 103–138
16. Yu Z, Yan J, Zhao J, Chen Z, Zhu Y (2011) Mobile robot path planning based on improved artificial potential field. J Harbin Inst Technol 43(1):50–55 (in Chinese)
17. Guo D, Sun F, Kong T, Liu H (2016) Deep vision networks for real-time robotic grasp detection. Int J Adv Robot Syst 14(1)

Active Learning Based Support Vector Data Description for Large Data Set Novelty Detection

Lili Yin, Huangang Wang, Wenhui Fan and Qingkai Wang

1 Introduction

Novelty detection is a popular problem in industry, network intrusion detection, disease diagnosis, etc. It can be seen as "one-class classification". Most of current novelty detection methods are supervised. Learning algorithms need the true labels of all the data samples. But in practical application, the obtainment of the true labels is often time-consuming and expensive. Faria et al. [6] also pointed out that a more realistic view is to ask the true label of only a subset of the examples. At present, the active learning framework is often used to solve the problem of lacking labeled samples. In the active learning situation, the learning algorithm choose the unlabeled samples containing the most information iteratively. The selected unlabeled samples will be labeled by domain specialists and then added to the training set to optimize current model. In this way, the active learning algorithm can achieve high accuracy just using as few labeled instances as possible.

L. Yin · H. Wang (✉) · W. Fan
Department of Automation, Tsinghua University, Beijing, China
e-mail: hgwang@tsinghua.edu.cn

L. Yin
e-mail: yll15@mails.tsinghua.edu.cn

W. Fan
e-mail: fanwenhui@tsinghua.edu.cn

Q. Wang
State Key Laboratory of Process Automation in Mining and Metallurgy, Beijing, China
e-mail: wang_qk@bgrimm.com

Z. Deng (ed.), *Proceedings of 2017 Chinese Intelligent Automation Conference*,
Lecture Notes in Electrical Engineering 458,
https://doi.org/10.1007/978-981-10-6445-6_32

In recent years, the active learning has been used into the novelty detection problem in many researches, such as [1, 2, 7, 9, 11, 13]. Among them, Görnitz et al. [7] propose semi-supervised data domain description (SSSVDD) method to process data set composed of labeled data and unlabeled data by combining active learning and support vector data description (SVDD). They substitute the Huber loss for the hinge loss to translate the optimization problem into an unconstraint, continuous problem which can be optimized with efficient gradient-based techniques. However, it also needs to recalculate in each iteration without using previous results. It is also time-consuming.

There are many researches on SVDD in recent years, including speeding up the decision function [10], working set selection [5], improving the robustness of SVDD for data with noise or uncertainty [4], and so on. Sequential minimal optimization (SMO) is a relatively fast algorithm to solve the dual problem of SVDD. But there is no research on the iterative implementation of SMO. In this paper, we propose a novelty detection method called active learning-based support vector data description (ALSVDD). Because the active learning is iterative, it is important to solve the problem of weak convergence performance of SVDD when combined with it. This paper proposes a simple iterative Sequential minimal optimization (SMO) strategy to improve the speed of solving ALSVDD algorithm. The experimental results on UCI data sets show the effectiveness of this strategy.

The rest of the work is organized as followed: Sect. 2 reviews the conventional SVDD algorithm. Section 3 introduces our ALSVDD novelty detection method. Section 4 presents the experimental results in several UCI data sets. Finally, Sect. 5 presents the conclusions of this work.

2 Conventional SVDD

SVDD is a popular and mature one-class classification algorithm. Its main idea is to find a minimal hyper sphere in feature space, making much normal samples but little abnormal samples surrounded by the hyper sphere. The surface of the super sphere is the decision boundary used to discriminate normal and abnormal samples. Given the dataset $X = \{x_1, x_2, \ldots, x_n\}$, y_i ($y_i \in \{+1, -1\}$) is the label of point x_i, and φ ($\mathrm{X} \rightarrow F$) is a mapping function from the input space to a high-dimensional feature space. The decision function can be written as Eq. (1).

$$f(x) = \|\varphi(x) - a\|^2 - R^2 \tag{1}$$

where a is the center and R is the radius of the hyper sphere in the feature space. The samples satisfy $f(x) \leq 0$ will be tested as normal and $f(x) > 0$ as novel. The optimization problem is constructed as Eq. (2).

$$\begin{aligned} &\min R^2 + C_1 \sum_{y_i=+1} \xi_i + C_2 \sum_{y_i=-1} \xi_i \\ &s.t.\ \|\varphi(x_i) - a\|^2 \le R^2 + \xi_i, y_i = +1 \\ &\quad \|\varphi(x_i) - a\|^2 \ge R^2 - \xi_i, y_i = -1 \\ &\quad \xi_i \ge 0,\ i = 1, 2, \ldots, n \end{aligned} \tag{2}$$

where ξ_i is the slack parameter to allow the data point x_i has a little error, $C_1 > 0, C_2 > 0$ are the penalty parameter of ξ_i. Its Lagrange dual problem is Eq. (3).

$$\begin{aligned} &\min W(\alpha) = \sum_{i=1}^{n} \sum_{j=1}^{n} y_i y_j \alpha_i \alpha_j \kappa(x_i, x_j) - \sum_{i=1}^{n} y_i \alpha_i \kappa(x_i, x_i) \\ &s.t. \sum_{i=1}^{n} y_i \alpha_i = 1 \\ &\quad 0 \le \alpha_i \le C_1, y_i = +1 \\ &\quad 0 \le \alpha_i \le C_2, y_i = -1 \end{aligned} \tag{3}$$

where $\kappa(x_i, x_j) = (\varphi(x_i), \varphi(x_j))$ is defined as the kernel function.

Because the dual problem of SVDD is a quadratic optimization problem, it can be solved by the usual quadratic programming algorithm. But the complexity of this problem is proportional to the number of training samples, which leads to large expense in practical applications. Sequential Minimal Optimization (SMO) [12] is the commonly used fast algorithm to solve the Lagrange dual problem of SVDD. SMO is an iterative algorithm, in each iteration it selects two Lagrange multipliers to optimize by fixing other multipliers. For example, Xie et al. [15] adopt training set reduction strategy and SMO algorithm based on second order approximation to accelerate the training of SVDD, Li et al. [8] propose an improved SMO used in SVDD to deal with the situation where negative samples are presented.

3 Active Learning-Based SVDD

The active learning strategy mainly composed of two parts: a selection part and an updating part. The learner repeatedly selects the most informative unlabeled samples to annotate and update the learned model. Thus, the active learning-based SVDD can be summarized as four steps:

1. Randomly select some samples from the training set to label. And calculate the preliminary SVDD model using SMO algorithm;

2. Select an unlabeled sample from data pool to label according to a certain selection rule;
3. Add the selected sample to the training set and update current SVDD model;
4. If the stop criterion is met, return the model, otherwise return to step (2).

Step 2 and step 3 are the key and difficulties to combine active learning with SVDD. The following content are carried out according to these three steps.

3.1 Solving SVDD Problem Using SMO

Here, we use the ordinary SMO algorithm to calculate the preliminary SVDD model. There are two things that need to recommend: the selection method of kernel parameter and the working set selection method.

The Gaussian RBF kernel: $\kappa(x_i, x_j) = \exp\left(-\|x_i - x_j\|^2 / s\right)$ is adopted in this paper. The parameter s ($s > 0$) is the Gaussian width parameter. Here we adopt the DFN idea proposed by Xiao et al. [14] to determine s. Note that the condition of DFN is all the samples are positive, but there may be some negative samples in the training set here. Therefore, we alter the DFN algorithm as follows:

1. If all the samples are positive in the training set, the optimized parameter s is calculated according to the traditional DFN algorithm.
2. If there are some negative samples, donate $Near(x_i) = \min_{j \neq i} \|x_i - x_j\|^2$ as the distance between each positive sample and its nearest positive neighbor, and $NNear(x_i) = \max_{j \neq i} \|x_i - x_j\|^2$ as the distance between each positive sample and its nearest negative neighbor. Select s to maximum objective function (4).

$$f_0(s) = \frac{2}{n}\sum_{i=1}^{n} \exp\left(-Near(x_i)/\sigma^2\right) - \frac{2}{n}\sum_{i=1}^{n} \exp\left(-NNear(x_i)/\sigma^2\right) \tag{4}$$

In addition, in the SMO algorithm, we use the working set strategy based on second order information proposed by Fan et al. [5]. Figure 1 is the pseudo code.

where $\kappa_{ij}=\kappa(x_i, x_j)$, $G_i = -y_i \nabla W(\alpha)_i = \kappa_{ii} - 2\sum_{t=1}^{n} \alpha_t y_t \kappa_{it}$, and two sets defined as $I_{up}(\alpha) \equiv \{t|\alpha_t < C_1, y_i = +1 \ or \ \alpha_t > 0, y_i = -1\}$, $I_{low}(\alpha) \equiv \{t|\alpha_t > 0, y_i = +1 \ or \ \alpha_t < C_2, y_i = -1\}$.

WSS (α, κ, G)

(1) Select index $i \in \arg\max_t \{G_t \mid t \in I_{up}(\alpha)\}$

(2) Select index $j \in \operatorname{argmin}_t \left\{ -\frac{(G_t - G_i)^2}{2(\kappa_{ii} + \kappa_{tt} - 2\kappa_{it})} \mid t \in I_{low}(\alpha^k), -y_t \nabla W(\alpha^k)_t < -y_i \nabla W(\alpha^k)_i \right\}$

(3) Return $B = \{i, j\}$

Fig. 1 Working set selection method using two order information

3.2 The Sample Selection Process

Obviously, the surface of the super sphere is the key of SVDD to discriminate normal and abnormal samples, it is also the most uncertain region of the SVDD model. Therefore, we use the distance in feature space between the samples and the surface of the super sphere as one of the selection rule.

Besides, the samples located at higher density region are often more important. The density can be simply measured by the distance with the nearest neighbor, which has the opposite relationship with the density. The Gauss kernel function has a property that the larger distance in the original space must corresponds to a large distance, so we simply use the distance in the original space instead of feature space distance to reduce the amount of calculation.

Here, we define r_i to be the distance between sample x_i and the center in the feature space, d_i to be the distance between sample x_i and nearest neighbor in the original space. Normalize these two criteria separately and add a coefficient $\eta\,(0 \le \eta \le 1)$, our finial active learning strategy is given as

$$t_i = (1-\eta) \times \left(\frac{|r_i - R| - \min_{x_i \in P}(|r_i - R|)}{\max_{x_i \in P}(|r_i - R|)} \right) + \eta \times \left(\frac{d_i - \min_{x_i \in P}(d_i)}{\max_{x_i \in P}(d_i)} \right) \quad (5)$$

3.3 The Updating Process of SVDD Model

In the active learning process, we have got a SVDD model before adding the new sample in each iteration. If we recalculate the parameters using SMO method, the computation expense is too much and it is not necessary. Here we use an iterative strategy. Assume the sample set is $x = [x_1, x_2, \ldots, x_n]^T$, its corresponding labels are $y = [y_1, y_2, \ldots, y_n]^T$, and the Lagrange multipliers are $\alpha^k = \left[\alpha_1^k, \alpha_2^k, \ldots, \alpha_n^k\right]^T$ after the kth iteration. In the $(k + 1)$th iteration, the selected sample is x_{n+1}, its label is y_{n+1}, Lagrange multiplier is α_{n+1}.

Obviously, there must be $\sum_{i=1}^{n} y_i \alpha_i^k = 1$ after the kth iterations. And we wish $\sum_{i=1}^{n+1} y_i \alpha_i^{k+1} = 1$ after the $(k+1)$th iteration. Thus we simply initialize $\alpha_{n+1} = 0$. The original working set selection method is to select the violating pair that most violate the KKT condition. The definition of violating pair is: If $i \in I_{up}(\alpha), j \in I_{low}(\alpha)$ and $-y_i \nabla W(\alpha)_i > -y_j \nabla W(\alpha)_j$, then $\{i, j\}$ is a violating pair. Following the above definitions, we have:

- If $y_{n+1} = +1$, then $n+1 \in I_{up}(\alpha)$. We need to find a $t \in I_{low}(\alpha)$ satisfied $-y_{n+1} \nabla W(\alpha)_{n+1} > -y_t \nabla W(\alpha)_t$;
- If $y_{n+1} = -1$, we have $n+1 \in I_{low}(\alpha)$. We need to find a $t \in I_{up}(\alpha)$ satisfied $-y_t \nabla W(\alpha)_t > -y_{n+1} \nabla W(\alpha)_{n+1}$.

We define this working set selection method as WSS_AL, its pseudo code is shown in Fig. 2.

Here we only consider the situation when $C_1 > 1/numP$. Based on the existing $\alpha^k = [\alpha_1^k, \alpha_2^k, \ldots, \alpha_n^k]^{\mathrm{T}}$, the pseudo code of SMO_AL algorithm is shown in Fig. 3.

Based on the above analysis, the whole process of the ALSVDD algorithm is shown in Fig. 4.

WSS_AL $(\alpha^{k+1}, \kappa, G^{k+1})$

(1) if $y_{n+1} = +1$, select index

$$j \in \underset{t}{\operatorname{argmin}} \left\{ -\frac{\left(G_{(n+1)} - G_t\right)^2}{2\left(\kappa_{(n+1)(n+1)} + \kappa_{tt} - 2\kappa_{(n+1)t}\right)} \mid t \in I_{low}\left(\alpha^{k+1}\right), -y_t \nabla W\left(\alpha^{k+1}\right)_t < -y_{n+1} \nabla W\left(\alpha^{k+1}\right)_{n+1} \right\}$$

else if $y_{n+1} = -1$, select index

$$j \in \underset{t}{\operatorname{argmin}} \left\{ -\frac{\left(G_{n+1} - G_t\right)^2}{2\left(\kappa_{(n+1)(n+1)} + \kappa_{tt} - 2\kappa_{(n+1)t}\right)} \mid t \in I_{up}\left(\alpha^{k+1}\right), -y_{n+1} \nabla W\left(\alpha^{k+1}\right)_{n+1} < -y_t \nabla W\left(\alpha^{k+1}\right)_t \right\}$$

(2) if j is not empty, return $B = \{n+1, j\}$

else return WSS$(\alpha^{k+1}, \kappa, G^{k+1})$

Fig. 2 WSS_AL method

SMO_AL

(1) $\{i, j\} = \text{WSS\_AL}(\alpha^{k+1}, \kappa, G^{k+1})$

(2) Calculate the lower bound L and the upper bound H of α_j

Calculate α_j^{new} and α_i^{new} to update α, G

(3) $\{i, j\} = \text{WSS}(\alpha, \kappa, G)$

(4) while($G_i - G_j > eps$){

1) $\{i, j\} = \text{WSS}(\alpha, \kappa, G)$

2) Calculate the lower bound L and the upper bound H of α_j. Calculate α_j^{new} and α_i^{new}

3) Update α, G

4) $\{i, j\} = \text{WSS}(\alpha, \kappa, G)$

}

(5) Calculate the center a and the radius R, return

Fig. 3 SMO_AL algorithm

Algorithm ALSVDD

(1) Assume data set U contains n samples. Input parameter η. And set $eps = 10^{-7}$

(2) Randomly select objects in U with a ratio of "ratio". Label these samples manually and form the original training set T, set the data pool P as the complementary set of T in U, that is, P=U-T

(3) Calculate SVDD model using SMO method based on current T. Get α, G, support vectors, center a and radius R

(4) Calculate the average value of the negative gradient of support vector on the boundary, donated as b

(5) do

1) $b_{old} = b$

2) Calculate r_i and d_i for each sample x_i in P, and get the t_i

$$t_i = (1-\eta) \times \left(\frac{|r_i - R| - \min\limits_{x_i \in P}(|r_i - R|)}{\max\limits_{x_i \in P}(|r_i - R|)} \right) + \eta \times \left(\frac{d_i - \min\limits_{x_i \in P}(d_i)}{\max\limits_{x_i \in P}(d_i)} \right)$$

3) Select the object x_s in P corresponding to the minimum value of evaluation

$x_s = \underset{x_i}{\text{argmin}} \{t_i | x_i \in P\}$

4) Label x_s manually, remove x_s from P and add it to set T. Get $B = \{i, j\}$ using WSS_AL

5) Update model using SMO_AL

6) Calculate current b

while $b_{old} - b > eps$

(6) Return set T, support vectors, center a and radius R

Fig. 4 ALSVDD algorithm

4 Experimental Result

In this section, experiments on the UCI data sets [3] are presented. First, the data set Image segmentation, Ionosphere, Landsat Satellite of UCI databases used in this paper are presented. The detailed information about these datasets is shown in Table 1. For the Image segmentation and Ionosphere data set, 90% of the normal data and 10% of the outliers were selected randomly in the training phase, and the remaining data (10% of the normal data +90% of the outliers) were used for testing. For the Landsat Satellite data set, the samples in the sat.trn file are used as training data set, and the sat.tst file as test data set.

Next, some of the measures employed during experiments are described. The True Positive Rate (TPR) is the fraction of normal objects accepted by the classifier, while the False Positive Rate (FPR) is the fraction of abnormal objects accepted by the classifier. Dually, the False Negative Rate (FNR) is the fraction of normal objects rejected by the classifier, while the True Negative Rate (TNR) is the fraction of abnormal objects rejected by the classifier. It holds that FNR = 1−TPR and FPR = 1−TNR. The ROC curve is the plot of the FNR versus the TNR (or, equally, TPR vs. FPR), and the area under the ROC curve (AUC) provides a summary to compare two classifiers.

4.1 ROC Curve

In each experiment, the amount of samples randomly selected at beginning is 20. And set parameter $C_1 = C_2 = 0.25,\ \eta = 0.2$.

In order to verify the effectiveness of the recursive SMO method, we directly use the original SVDD algorithm on the final labeled training set to compare with our recursive SMO method. In addition, in order to verify the effectiveness of the ALSVDD algorithm, we directly use the original SVDD algorithm on all the data set to compare with our ALSVDD algorithm. We donate these three methods as ALSVDD, SVDD and SVDD_ALL respectively in the following analysis.

The ROC curves in these three experiments using ALSVDD, SVDD and SVDD_ALL are shown in Fig. 5, and the AUC are shown in Table 2. It can be seen that the result of ALSVDD is the same as SVDD, demonstrating the effectiveness of

Table 1 Description of datasets used in the experiments

Dataset	Attributes	Normal (number:train + test)	Outlier (number: rain + test)
Image segmentation	19	Grass (300:270 + 30)	Path (300:30 + 270)
Ionosphere	34	Good (225:202 + 23)	Bad (126:12 + 114)
Landsat satellite	36	Red soil (1533:1072 + 461)	Others (4905:3366 + 1539)

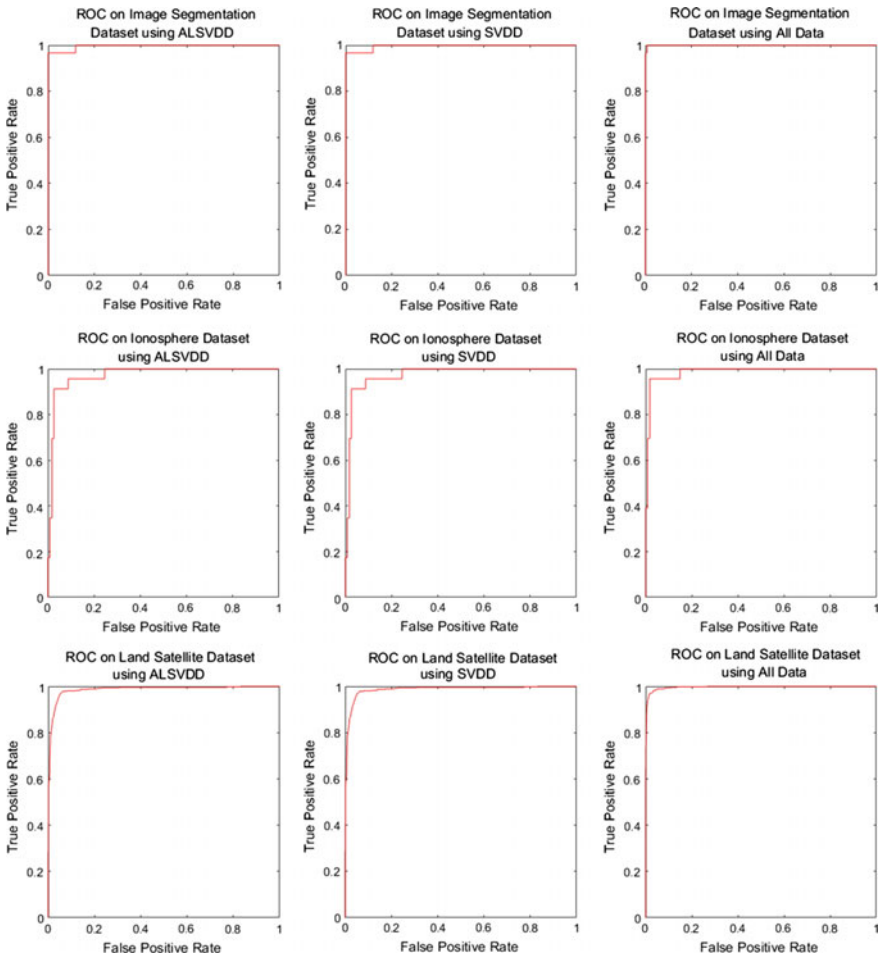

Fig. 5 The ROC curve in three experiments

the recursive SMO method. The result of ALSVDD is a little worse than SVDD_ALL, but it is within the acceptable limits.

4.2 The Final Amount of Samples in Training Set

The target of ALSVDD algorithm is to reduce the amount of samples to label and train. Obviously, the less the final size of the training set, the less iterations in ALSVDD process and the less time would be used to build the model. Thus, this is an important index to evaluate the related algorithms. Except for the data randomly

Table 2 The AUC in three experiments

Data set	ALSVDD	SVDD	SVDD_ALL
Image segmentation	0.9969	0.9969	0.9998
Ionosphere	0.9699	0.9699	0.9863
Landsat satellite	0.9723	0.9724	0.9966

Table 3 The size of finial set of ALSVDD

Data set	Finial size	Proportion (%)
Image segmentation	100	33.33
Ionosphere	100	46.72
Landsat satellite	125	2.82

selected initially, the ALSVDD algorithm will add some samples to the training set in the active learning process. So the final size of the training set T is composed of these two parts. The finial size of the training set in these three experiments are shown in Table 3. It can be seen that ALSVDD has the advantage of reducing sample amount.

5 Conclusion

In order to solve the problem of lacking of labeled samples in novelty detection problem, this paper proposed a novel scheme called ALSVDD based on active learning framework and SVDD method. In addition, this paper proposed an improved DFN method to select Gaussian kernel parameters, a recursive SMO method based on KKT condition and a working set selection strategy according to the second order information. The proposed method can not only reduce the computational expense but also keep the detection rate at the same time. The experiments on several UCI data sets also indicate its effectiveness and practicability.

References

1. Abe N, Zadrozny B, Langford J (2006) Outlier detection by active learning. In: Proceedings of the 12th ACM SIGKDD international conference on knowledge discovery and data mining. Philadelphia, PA, USA
2. Almgren M, Jonsson E (2004) Using active learning in intrusion detection. In: Proceedings 17th IEEE Computer Security Foundations Workshop
3. Blake C, Merz CJ (1998) UCI repository of machine learning databases. http://www.ics.uci.edu/∼mlearn/MLRepository.html
4. Chen G, Zhang X, Wang ZJ, Li F (2015) Robust support vector data description for outlier detection with noise or uncertain data. Know Based Sys. doi:10.1016/j.knosys.2015.09.025

5. Fan R, Chen P, Lin C (2005) Working set selection using second order information for training support vector machines. J mach learn res 6(12):1889–1918
6. Faria ER, Gonçalves IJ, de Carvalho AC, Gama J (2016) Novelty detection in data streams. Artif Intell Rev. doi:10.1007/s10462-015-9444-8
7. Görnitz N, Kloft M, Brefeld U (2009) Active and semi-supervised data domain description. Joint European Conference on Machine Learning and Knowledge Discovery in Databases. Bled, Slovenia
8. Li D, Cai J, Du M, Zhu S, Zhang J (2015) SVDD fast training algorithm based on improved SMO. China Meas Text. doi:10.11857/j.issn.1674-5124.2015.11.022
9. Li Y, Guo L (2007) An active learning based TCM-KNN algorithm for supervised network intrusion detection. Comp Secur. doi:10.1016/j.cose.2007.10.002
10. Liu Y, Liu Y, Chen Y (2010) Fast support vector data descriptions for novelty detection. IEEE Trans Neural Networks. doi:10.1109/TNN.2010.2053853
11. Pelleg D, Moore AW (2004) Active learning for anomaly and rare-category detection. NIPS, Vancouver Canada
12. Schölkopf B, Burges CJ, Smola AJ (eds) (1999) Advances in kernel methods: support vector learning. MIT press
13. Seliya N, Khoshgoftaar TM (2010) Active learning with neural networks for intrusion detection. IEEE International Conference on Information reuse and integration (IRI). Las Vegas, Nevada
14. Xiao Y, Wang H, Zhang L, Xu W (2014) Two methods of selecting Gaussian kernel parameters for one-class SVM and their application to fault detection. Knowl Based Sys. doi:10.1016/j.knosys.2014.01.020
15. Xie Y, Chen X, Yu X, Yue B, Guo J (2011) Fast SVDD-based outlier detection approach in wireless sensor networks. Chinese J Sci Instr 1:009. (in Chinese)

Modeling and Analysis of the Driving Range for Electric Passenger Vehicles Based on Robust Regression Analysis

Ting Zhang, Jun Bi, Pan Wang and Longhui Li

1 Introduction

In order to solve the "mileage anxiety", large numbers of research have been done by domestic and foreign scholars, but many are based on experimental data. The vehicle dashboard will display the remaining range when driving the EV, but which is estimated in the ideal state and is not accurate. Thus, it is necessary to establish the range model to estimate the remaining range based on the operating data of the electric passenger vehicle.

At present, there are two types of data-driven modelling methods to research of SOC and range: mathematical statistics method and intelligent optimization method. The regression analysis can explain the relationship between the independent variable and the dependent variable, which is adopted in much research. Thus, the regression analysis is used to establish the range model in this paper.

The traditional regression analysis is based on the least squares method for parameter estimation. The least squares method requires the residual is independent of each other, normal distribution, zero mean and random variables with the same variance. However, the data collected in the actual project most contains a large number of outliers, and the residual may not obey the normal distribution, but the

T. Zhang (✉) · P. Wang · L. Li
China Automotive Technology & Research Center, No. 68, East Xianfeng Road, Dongli, Tianjin 300300, China
e-mail: zt10255024@126.com

P. Wang
e-mail: wangpan2015@catarc.ac.cn

L. Li
e-mail: lilonghui@catarc.ac.cn

J. Bi
Beijing Jiaotong University, Weihait 264200, China
e-mail: jbi@bjtu.edu.cn

Z. Deng (ed.), *Proceedings of 2017 Chinese Intelligent Automation Conference*, Lecture Notes in Electrical Engineering 458,
https://doi.org/10.1007/978-981-10-6445-6_33

heavy-tailed distribution. In this case, the model is not accurate established by the least squares method. In order to solve these problems, researchers commonly deleted abnormal data, on the basis of pure data to establish model, which will lead to lack of useful information in the abnormal data, and cannot accurately describe the variation tendency of original production. Therefore, the scholars have turned to the robust regression analysis. Compared with the traditional regression analysis, the robust estimation method has the ability to resist the influence of the abnormal value due to the fact that the actual data is subject to the constraint of the assumed distribution. Thus, the model is more able to reflect the truth established by the robust regression analysis [1–5].

The main idea of robust regression analysis is to optimize the objective function in the least squares regression, which is sensitive to the outliers. The appropriate weight function is chosen to minimize the influence of outliers for parameter estimation, that is, the small residual value is given to the larger weight, and the large residual value is given to the smaller weight. The useful information contained in the outliers is extracted as much as possible to reduce the adverse effects of the abnormal values; so that the model can calculate the best estimated value [6–8].

2 Theory

2.1 SOC

State of Charge (SOC) refers to the battery charge state used to describe the battery power state, which is the ratio of battery current capacity and rated capacity. SOC is a relative amount, the value is [0, 100%], and 0% means full discharge, 100% refers to full power state. The equation is as follows:

$$SOC = \frac{Residual\ Capacity}{Rated\ Capacity} = \frac{Q_m - Q(I_n)}{Q_m} \tag{2.1}$$

in which Q_m is the battery rated capacity (Ah), $Q(I_n)$ is the battery consumed capacity (Ah).

2.2 Range

Driving range is the electric vehicle total range driving from fully charged state to the minimum safe discharge power [9]. The driven range refers to the distance traveled by any starting charge to the current power during a single discharge in this paper. Remaining range refers to the travel range that electric vehicle drives from the current power down to the minimum safe power, the minimum power threshold is 20% generally [10].

2.3 Robust Regression Analysis

The linear regression model reflects the linear relationship between the dependent variable and the independent variable. The basic model is as follows:

$$\mathrm{y} = \alpha + \beta x + \varepsilon \tag{2.2}$$

in which x is the independent variable; α and β are the parameter vector to be estimated; y is the dependent variable depends on x, α and β; ε is the random residual.

The traditional least squares method estimates the parameters by solving the minimum of the sum of squares of residuals. The objective function is as follows:

$$\min \sum_{i=1}^{n} \left(y_i - \sum \mathrm{x}_{ij} \beta_{\mathrm{j}} \right)^2 = \min \sum_{i=1}^{n} (\mathrm{E}_i)^2 \tag{2.3}$$

in which E represents the random residual.

In this paper, the parameters of the model are calculated by M-estimation in robust regression. The objective function is constructed in M-estimation as well, which is not based on minimizing the sum of residuals, but minimizing the residual function. The robustness of the estimator depends on the choice of the weight function. The objective function is defined as:

$$\min \sum_{i=1}^{n} \rho \left(y_i - \sum \mathrm{x}_{ij} \beta_{\mathrm{j}} \right)^2 = \min \sum_{i=1}^{n} \rho(\mathrm{E}_i) \tag{2.4}$$

In which, the objective function has no scale homogeneity, so the residuals must be standardized. It is necessary to uniformly remove a constant that does not vary with the scale, and the median absolute deviation (MAD) is used mostly.

$$\hat{\sigma} = \mathrm{MAD}(E_i) = median|\mathrm{y}_i - M| \tag{2.5}$$

in which median represents the function of the sequence median, M represents the median.

Then the updated formula for objective function can be expressed as:

$$\min \sum_{i=1}^{n} \rho \left(\left(y_i - \sum \mathrm{x}_{ij} \beta_{\mathrm{j}} \right) \Big/ \sigma_i \right)^2 = \min \sum_{i=1}^{n} \rho(E_i / \sigma_i) \tag{2.6}$$

Take the derivative of ρ, set $\Psi = \rho'$, then solving formula (2.6) can be transformed into solving formula (2.7).

$$\sum_{i=1}^{n} \Psi\left(\left(y_i - \sum \mathrm{x}_{ij}\beta_{\mathrm{j}}\right)\Big/\hat{\sigma}_i\right)\mathrm{x}_{i\mathrm{k}} = \sum_{i=1}^{n} \Psi(E_i/\hat{\sigma}_e)\mathrm{x}_i = 0 \tag{2.7}$$

Replace the ψ with the appropriate weight that decreases following the residuals growth. Thus, the formula (2.7) can be converted as:

$$\sum_{i=1}^{n} \omega_{\mathrm{i}}(E_i/\hat{\sigma}_e)x_i = 0 \tag{2.8}$$

To solve the M-regression of robust regression estimation must adopt the iterative procedure, because the residual cannot be known before modeling, and model parameters cannot be estimated with no residual based on M-estimation. Thus it is usually adopt weighted least squares method (IRLS) to solve the M-estimation parameters. The steps are simply described as follows:

Step 1 Set the iteration cursor $I = 0$, get the initial estimate parameters $\hat{\beta}^{(0)}$ of the regression coefficient based on the least squares linear regression.

Step 2 Calculate the initial residuals $E_i^{(0)}$ of the regression model based on $\hat{\beta}^{(0)}$, then calculate initial weight.

Step 3 Select the appropriate weight function, and calculate $\omega\left(E_i^{(0)}\right)$.

Step 4 Start the first iteration $I = 1$, minimize $\Sigma\omega_i^{(1)}\left(E_i^2\right)$ based on the weighted least squares (WLS), calculate the new parameters $\hat{\beta}^{(0)}$ Use W to represent the weight of the residual individual diagonal matrix $n \times n$, the formula of $\hat{\beta}^{(1)}$ is as follows:

$$\hat{\beta}^{(1)} = \left(X^T W X\right)^{-1} X^T W Y \tag{2.9}$$

Step 5 Calculate the next weight $w\left(E_i^{(1)}\right)$ based on the residual in step 4.

Step 6 Perform the second iteration $I = 2$, calculate the $\hat{\beta}^{(2)}$ based on the new weight $\omega\left(E_i^{(1)}\right)$

Step 7 Repeat Step 4 to Step 6 until $\hat{\beta}$ is stable on one iteration, then $\hat{\beta}^{(i)} - \hat{\beta}^{(i-1)} \cong 0$ In general, when the amount of change in the iteration results is less than 0.01%, it can be regarded as convergent.

In the verification of regression equation, the least squares regression mostly adopts F-test and t-test, but it is not applicable in robust regression analysis for the residual is not normal distribution as a result of abnormal data. Thus the fitting coefficient (R^2), square sum error (SSE), root mean square error (RMSE) is mainly used in robust regression analysis

3 Experiment

In order to study the relationship between SOC and mileage in different seasons, set January on behalf of winter, April on behalf of spring and autumn, and August on behalf of the summer. Collect monthly operating data for 10 days in January, April, and August with the Jianghuai IEV5 electric passenger vehicles. The data are modelled as training data with seven days per month, and the remaining data is used as test data. Randomly extract the one day data to draw a gap between the SOC and mileage, as shown in Fig. 1. It can be seen that with the reduction of SOC mileage increase gradually, general linear increase. It can be seen that with the decrease of SOC, the mileage increases gradually as linear increasing. Among them, the changes in April and August are similar.

The model between SOC and mileage can be designed as:

$$\mathrm{M} = aS + b + \varepsilon \tag{3.1}$$

in which M is the driven range (km); S is SOC (%); a and b represent the parameter vector to be estimated; and ε represents white Gaussian noise.

Based on parameter estimation steps in Sect. 2.3, solve the daily model estimation parameters. The Huber-estimation method, which is commonly used in the robust regression M-estimation, is established to establish the objective function and the weight function in this paper. The objective formula is as follows:

$$\rho(E_i/\sigma_i) = \begin{cases} 1/2(E_i/\sigma_i)^2 & \text{if } E_i/\sigma_i \le \mathrm{c} \\ \mathrm{c}|E_i/\sigma_i| - 1/2c^2 & \text{if } E_i/\sigma_i > \mathrm{c} \end{cases} \tag{3.2}$$

The corresponding weight function of Huber-estimation is as follows, set c = 1.345

$$\omega = \begin{cases} 1 & \text{if } E_i/\sigma_i \le \mathrm{c} \\ \mathrm{c}/|E_i/\sigma_i| & \text{if } E_i/\sigma_i > \mathrm{c} \end{cases} \tag{3.3}$$

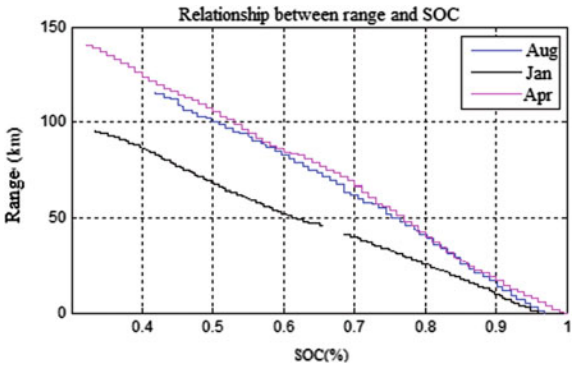

Fig. 1 The curve of SOC and driving range

This section takes the data collected on April 16, 2016 (18,775) as an example to establish the model of SOC and driven range. The parameters are identified based on the least square method. The initial model is as follows:

$$M = -213.95 \cdot S + 210.68 \tag{3.4}$$

Calculate the initial estimation of the regression coefficients. The confidence interval of the residuals and residuals value estimated by the general linear least squares method is plotted by Matlab shown in Fig. 2. It can be seen from the figure that most of the observed sequences have intersections with the horizontal lines, and between 2000 and 4000, between 6000 and 8000, there are some intersections that do not intersect the horizontal lines, as shown in the red areas in the figure. The confidence interval of the corresponding residuals does not contain 0, which is considered that these observations are abnormal data.

Thus, this paper adopts robust linear regression analysis to establish driving range model. The initial parameter $\hat{\beta}^{(0)}$ is calculated based on the Eq. (3.1). According to the robust estimation steps in Sect. 2.3, the parameters of the robust regression model are estimated and the robust regression model between SOC and mileage on April 16, which is expressed as:

$$M = -213.92 \cdot S + 212.84 \tag{3.5}$$

4 Results and Discussion

Based on the training data, the daily robust regression model parameters of SOC and the mileage are estimated respectively. The parameter estimation results are shown in Table 1.

Average the parameters a and b per month respectively as the parameters of the final model of this month.

$$\text{January: } \mathrm{M} = -150.72 \cdot \mathrm{S} + 150.32 \tag{3.6}$$

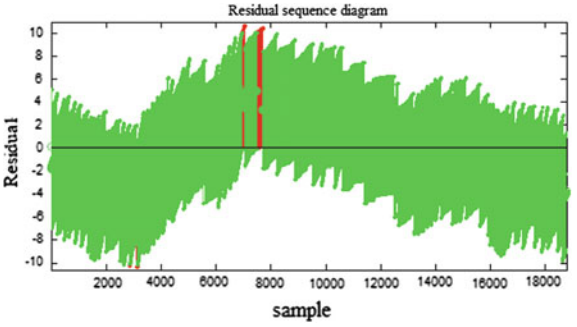

Fig. 2 Residual chart based on OLS estimation

Table 1 Performance indicators

Month	R2	RMSE
January	0.9967	1.0879
April	0.9952	0.9997
August	0.9964	1.1885

$$\text{April: M} = -213.51 \cdot S + 213.37 \tag{3.7}$$

$$\text{August: M} = -210.26 \cdot \text{S} + 209.36 \tag{3.8}$$

in which M is he driven range during a full discharging (km); S is SOC and interval is [0, 100%].

Based on the test data to verify and analysis the above models, Figs. 3 and 4 show the 16/01/2016 test results. The change trend of red line and blue line is the same, and the similarity is high, which indicates that the fitting effect of the model is

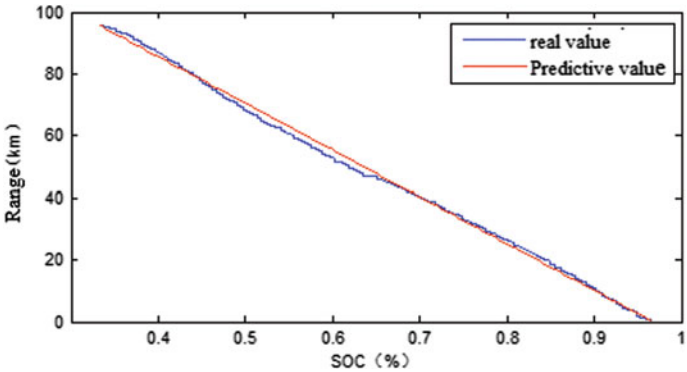

Fig. 3 Driving range estimation results (16/01/2016)

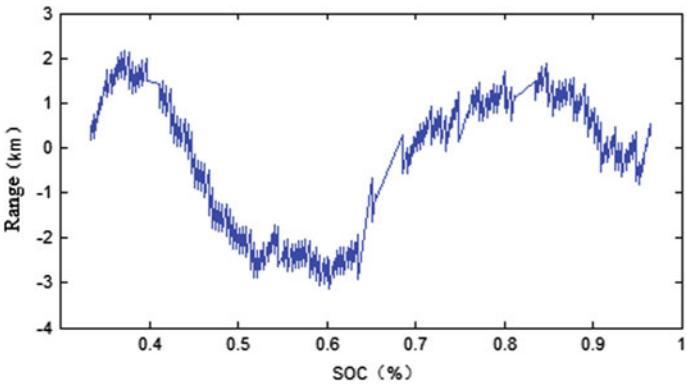

Fig. 4 Driving range estimation residual (16/01/2016)

better. As shown in Table 1, the fitting coefficient is very close to 1, and the root mean square error is small, which represents the validity and accuracy of the models established by RRS.

5 Conclusion

Based on the operation data, linear regression models of SOC and driven range in different seasons are established by robust regression analysis. The model parameters are estimated and validated based on the test data. From the validation of the indicators, the three models are accurate and effective, which indicates RRS have a good performance in modelling and analysis of the driving range for electric passenger vehicles. The study of this paper will provide a new perspective for range estimating. The next work is to consider more factors.

Acknowledge This research is supported by Key research and development project of Shandong Province (2016GGX105004).

References

1. Sun S (2008) Research and application of robust regression algorithm in software cost estimation. Hunan University, pp 5–9
2. Wibowo A, Desa MI (2015) Nonlinear robust regression using kernel principal component analysis and R-estimators. Inter J Comp Sci Issues, 8(5)
3. Minaee S, Yu H, Wang Y (2014) A robust regression approach for background/foreground segmentation. Eprint Arxiv
4. Ondruska P, Posner I (2014) Probabilistic attainability maps: efficiently predicting driver-spesific electric vehicle range. IEEE Intell Veh Symp (IV) Dearborn, June 2014
5. Wager G, Mchenry MP, Whale J et al (2013) Testing energy efficiency and driving range of electric vehicles in relation to gear selection. Renew Energy 62(62):303–312
6. Zang T, Wen G, et al (2016) Rotor system unbalance measurement based on robust regression analysis. Vibration, testing and diagnosis, 2016(1):126–130
7. Wang Gu, Guo Xiucheng (2011) Containing abnormal data resident trip stable regression analysis. J Wuhan Univ Technol (Transp Sci Eng) 35(3):509–511
8. Yuan X, Li L, Gou H et al (2015) Energy and environmental impact of battery electric vehicle range in China. Appl Energy 157:75–84
9. Liu T, et al (2011) Study on energy consumption of pure electric vehicle based on bench simulation. J Sun Yat Sen Univ 50(1):44–48
10. Zhang J (2015) Establishment and analysis of electric vehicle driving mileage model based on data driven. Beijing Jiaotong University

Variable Pitch Fault Prediction of Wind Power System Based on LS-SVM of Parameter Optimization

Tao Liang and Yingjuan Zhang

1 Introduction

Variable pitch control system is an important component of modern variable speed constant frequency wind power generator, which is of great significance to the safe and stable operation of wind turbine [1]. However, wind power system failure rate has increased, especially the pitch system, due to bad running environment and the wind wheel speed fluctuations [2–4]. Therefore, in order to ensure the safe and reliable operation of the wind turbine, it is necessary to predict the fault of the variable pitch system.

In recent years, some scholars have studied and analyzed pitch the fault prediction of wind turbine. To diagnose the fault in the pitch actuator of wind turbines, a method based on the variable forgetting factor recursive least-squares (VFF-RLS) algorithm is proposed by Wu [5]. In [6], the data of SCADA system for MW class wind turbine were analyzed, and the fault characteristics of pitch control system were extracted. Multiple linear regression analysis and BP neural network model are used to predict the fault of pitch system. In [7], based on the theory of data mining, the problem of the asymmetry of the 3 blades of the wind turbine system is studied. As the core part of the wind turbine, the variable pitch system is worth a lot of energy.

In this paper, the parameters data related to the operation of the pitch system are analyzed and processed from the SCADA system of the wind farm. Then, the PSO-Optimized least squares support vector machine is used to establish the prediction model of the pitch fault. Studies have shown that the blade pitch angle, the blade motor drive current, the generator speed and the blade IGBT temperature of these four parameters can be sensitive to reflect the pitch system failure [8].

T. Liang · Y. Zhang (✉)
School of Control Science and Engineering, Hebei University of Technology, Tianjin 300130, China
e-mail: 215751490@qq.com

Z. Deng (ed.), *Proceedings of 2017 Chinese Intelligent Automation Conference*, Lecture Notes in Electrical Engineering 458,
https://doi.org/10.1007/978-981-10-6445-6_34

Therefore, the four types of parameters in the SCADA system are chosen as the input of the model, and the output of the fault system is used as the model to establish the prediction model. The model can predict the state of fan pitch and provide a reasonable analysis for its abnormal condition, which provides a new method for fan maintenance.

2 The Classification Algorithm of Least Squares Support Vector Machine (LSSVM)

2.1 Binary LS-SVM Classifier

LS-SVM is a kind of kernel function learning machine based on the structural risk minimization (SRM) principle, which is a special type of SVM [9]. The main purpose of the LS-SVM is to transform the inequality constraint problem of support vector machine into equation constraint. As a result, LS-SVM expresses training in terms of solving a linear system instead of a quadratic programming problem, which thus reduces the computation time of model learning significantly. The specific algorithm is:

Supposing the given training data set (x_i, y_i), $i = 1, 2, \cdots, l$, where l represents the total number of training data pairs, $x \in R^d$ is the input vector, $y \in \{-1, +1\}$ is a class label of each vector, and d is the dimension of x_i. We considered that x_i belongs to class I, if $y_i = +1$ and x_i belongs to class II, if $y_i = -1$. Based on the corresponding mapping function in the feature space, the formula is used to estimate the unknown function. We can determine the optimal hyperplane $f(x)$ satisfies the condition:

$$\begin{cases} \boldsymbol{w}^T x_i + \beta \geq 1, & y_i = 1 \\ \boldsymbol{w}^T x_i + \beta \leq -1, & y_i = -1 \end{cases} \tag{1}$$

where, $\boldsymbol{w}$ represents the hyperplane normal vector, and β determines the offset amount of the separating hyperplane from the origin.

Then the optimal classification decision function is constructed:

$$y = \operatorname{sgn}\left(\boldsymbol{w}^T x_i + \beta\right) \tag{2}$$

According to the principle of structural risk minimization, the optimization problem can be expressed as:

$$\begin{aligned} \min \boldsymbol{R}(\boldsymbol{w}, e_i) &= \frac{1}{2}\boldsymbol{w}^T\boldsymbol{w} + \gamma \sum_{i=1}^{l} e_i^2 \\ y_i\left[\boldsymbol{w}^T\boldsymbol{\varphi}(x_i) + \beta\right] &= 1 - e_i (i = 1 \sim l) \end{aligned} \tag{3}$$

where, $\boldsymbol{\varphi}(x_i)$ denotes a non-linear mapping of the input from the primal space to the feature space. e_i is an error variable and γ is called the penalty coefficient.

In order to solve the problems, the constrained optimization problem is transformed into unconstrained optimization problem. Therefore we construct the Lagrangian for the problem in the dual problem, get the following formula:

$$L(\boldsymbol{w}, b, e, \alpha) = \frac{1}{2}\boldsymbol{w}^T\boldsymbol{w} + \gamma\sum_{i=1}^{l} e_i^2 - \sum_{i=1}^{l}\alpha_i[\boldsymbol{w}^T\varphi(x_i) + \beta - 1 + e_i] \tag{4}$$

where α_i are Lagrange multipliers. According to Kuhn-tucker conditions, differentiating equation with $\boldsymbol{w}, b, e$ and α the conditions for optimality of this problem can be obtained by setting all partial derivatives equal to zero. So we can get the following expression:

$$\begin{cases} \frac{\partial L}{\partial \boldsymbol{w}} = 0 \Rightarrow \boldsymbol{w} = \sum_{i=1}^{l}\alpha_i y_i \boldsymbol{\varphi}(x_i) \\ \frac{\partial L}{\partial b} = 0 \Rightarrow \sum_{i=1}^{l}\alpha_i y_i = 0 \\ \frac{\partial L}{\partial e_i} = 0 \Rightarrow \alpha_i = \gamma e_i \\ \frac{\partial L}{\partial \alpha_i} = 0 \Rightarrow y_i[\boldsymbol{w}^T\boldsymbol{\varphi}(x_i) + b - 1 + e_i] = 0 \end{cases} \tag{5}$$

After elimination of the variables $\boldsymbol{w}$ and $\boldsymbol{e}_i$, the optimization problem can be transformed into the following linear equal set:

$$\begin{bmatrix} 0 & \boldsymbol{y}^T \\ \boldsymbol{y} & \boldsymbol{Q} + \boldsymbol{I}/c \end{bmatrix}\begin{bmatrix} \beta \\ \boldsymbol{\alpha} \end{bmatrix} = \begin{bmatrix} 0 \\ \boldsymbol{I} \end{bmatrix} \tag{6}$$

where, $\boldsymbol{y} = [y_1, y_2, \ldots, y_l]^T$ is the output vector of the training samples, $\boldsymbol{\alpha} = [\alpha_1, \alpha_2, \ldots, \alpha_l]^T$, $I = [1, 1, \ldots, 1]^T$ is an N-dimension identity matrix and $\boldsymbol{Q} = \boldsymbol{\varphi}(x_i)^T\boldsymbol{\varphi}(x_i)$; $\boldsymbol{Q}$ is an $N \times N$ kernel function symmetric matrix. From the positive definite matrix, the inner product of $\boldsymbol{Q} = \boldsymbol{\varphi}(x_i)^T\boldsymbol{\varphi}(x_i)$ can be replaced by kernel function $\boldsymbol{K}(x_i, x_j)$. In conclusion, the classifier in the dual space of the LSSVM model can be expressed as:

$$f(x) = \mathrm{sgn}\left\{\sum_{i=1}^{l}\alpha_i y_i \boldsymbol{K}(x_i, x_j) + \beta\right\} \tag{7}$$

2.2 Multi-class LS-SVM Formulations

The LS-SVMs were designed intrinsically for binary classification but can be extended for multi-class classification that is common in fault prediction. Two main approaches have been considered for the multi-class classification issue. One is considering all classes at once and solving the multi-class problem in one step. The other is to break down the multi-class problem into a number of smaller binary problems. The two approaches are, however, very different in detail. With the former, the number of its variables which are used to construct and solve the optimization problem for LS-SVM, is a positive function of the number of classes. Hence, in general, it is computationally more expensive to solve a multi-class problem than a binary problem with the same number of data. In this paper, our discussion focuses on the combination of binary schemes.

In combination schemes, multi-class classification problems are solved by reformulating the multi-class problems with K classes into a set of N binary classification problems. To each class C_k, $k = 1, 2, \ldots, K$, a unique coding $c_k = \left[y_m^{(1)}; y_m^{(2)}; \ldots; y_m^{(n)}; y_m^{(n+1)}; \ldots y_m^{(N)}\right]$, $y_m^{(n)} \in \{-1, 0, 1\}$, is assigned, where each binary classifier discriminates between the corresponding output bit $y_m^{(n)}$. There are four popular ways then to construct the set of binary classifiers. In the OAO scheme, it requires the training of $K(K-1)/2$ binary classifiers, where each classifier discriminates between two opposite classes in a pairwise way. To decide the final class for OAO approach, a voting scheme is used and the final class belongs to the one with maximum number of votes. In the MOC, each class is represented by a unique binary coding using N classifiers to encode $K = 2^N$.

2.3 Select Kernel Function of LS-SVM

The type of the kernel function is the key point in constructing high-performance LSSVM. A kernel function has many types, in order to make the fault prediction effect of the turbine pitch system better, the kernel function of this model chooses the radial basis function (RBF). The RBF is as follows:

$$\boldsymbol{K}(x_i, x_j) = \exp\left(-\frac{\left\|x_i - x_j\right\|^2}{2\sigma^2}\right) \tag{8}$$

where σ denotes the width parameter.

3 Optimal LS-SVM Classification with Modified PSO

In general, when the LS-SVM model is used to predict the fault of the pitch system, the prediction results are affected by the penalty parameters γ and the kernel function parameters σ. Therefore, it is necessary to select the appropriate γ and σ to achieve the desired effect. In practice, however, it is difficult to find the optimal parameters when applying LSSVM to the fault prediction of the turbine pitch system. So they should be optimized via an optimization method. In this study, we use the particle swarm optimization (PSO) algorithm because of its proven effectiveness in heuristic search and relatively small computational time required [10].

Similar to other evolutionary computation algorithms like genetic algorithms, PSO is a swarm intelligence evolutionary algorithm based on random search and optimization process [11]. Nevertheless, particle swarm optimization, as an intelligent optimization algorithm, can easily lead to the loss of diversity in the search space, which causes premature convergence and poor local search ability and so on, resulting in poor prediction effect. In view of the deficiency of PSO algorithm, in this study, we use an improved nonlinear descent algorithm. In this way, we can not only improve the ability of local optimization of the algorithm, but also guarantee the convergence speed of the global optimization process, so that the parameter optimization effect is better.

In summary, based on the modified PSO optimization algorithm preferred LSSVM penalty parameters γ and kernel function parameters σ of the flow chart shown in Fig. 1.

The fault prediction model of turbine pitch system is roughly summarized as the following aspects:

Step 1: Fault parameter selection of variable pitch system of wind turbine. The four kinds of parameters which have great impact of the pitch system are selected as the input vector of the model, as shown in Table 1.

Pitch system failure are generally: pitch motor temperature fault, pitch cabinet capacitor fault, pitch capacitor voltage imbalance fault, blade asymmetry fault, pitch power supply fault, pitch position sensor fault, pitch speed overrun fault, et al. Overall consideration, in this paper, the above seven kinds of faults and the normal state of variable pitch system are taken as the output layer of the model.

Considering that the least squares support vector machine can only deal with the problem of two categories. However, in this paper, we need to predict the classification of pitch system failure, which belongs to the multi class classification problems, eight kinds of states included in this article. Therefore, we adopt the minimum output encoding (MOC) of the multi-class classification problem is transformed into a plurality of two classification problems [11], that is, only $\log_2 8 = 3$ second classifier can achieve the above classification, and then the 3 classifiers are binary coded.

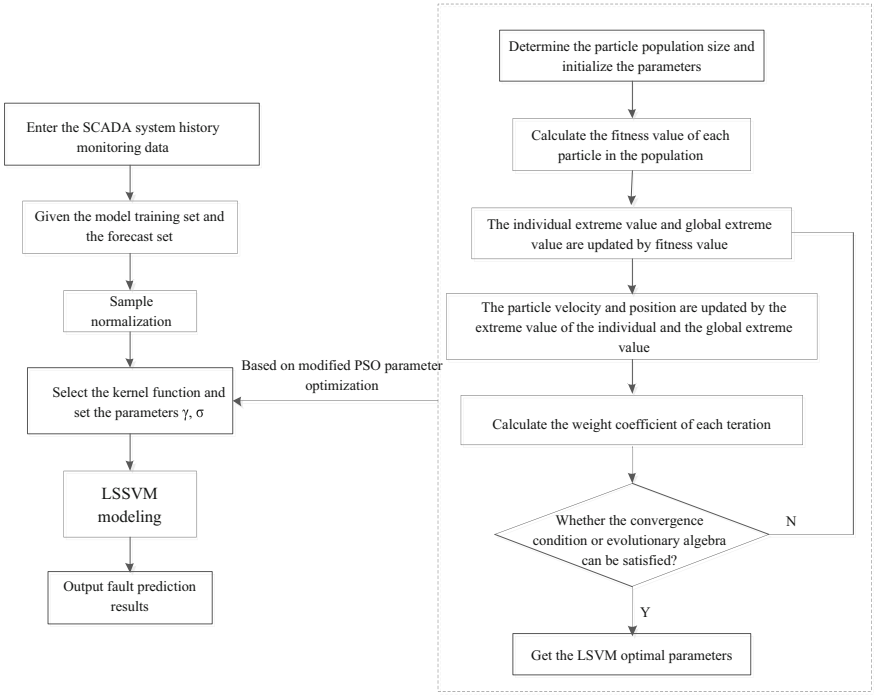

Fig. 1 Flowchart of the procedure structure based on modified PSO optimization LSSVM

Table 1 The input vector of the model

Four types of parameters that affect the fault of the pitch system		
1#blade pitch angle	1#blade motor drive current	1#blade IGBT temperature
2#blade pitch angle	2#blade motor drive current	2#blade IGBT temperature
3#blade pitch angle	3#blade motor drive current	3#blade IGBT temperature
Generator speed		

Step 2: Data preprocessing of original data. In order to reduce the influence of different values of input vectors, it is necessary to normalize the input data of the model. The normalized mapping relationship is:

$$f : x \to y = \frac{x - x_{\min}}{x_{\max} - x_{\min}} \tag{9}$$

where, $x, y \in R^n$, $x_{\min} = \min(x)$, $x_{\max} = \max(x)$, mapping the original data to [0, 1].

Step 3: Feature parameter optimization. In this study, the classification accuracy of the predicted sample cross validation is taken as the fitness function value of PSO.

Step 4: Predict the fault type of the wind turbine pitch system and output the prediction result. Train the multi-class LS-SVM classifier with the optimal parameters on the training samples. Then test the outputs on the testing samples. Finally, end the procedure and analyze the results.

4 Case Analysis and Comparison

In this paper, the effective SCADA data of 320 groups of 1.5 MW wind turbines in a wind farm are taken as the research object. The 320 sets with a clear fault category and the normal state of data before 240 groups as the training set, after the 80 group as the prediction set.

By the proposed model to predict its classification, the model and the kernel function parameters of the LS-SVM model are optimized by PSO algorithm. The parameters of the LS-SVM model are $\gamma = 75.098$ and $\sigma = 0.4672$, respectively. Taking the MOC LS-SVM classifier, the fitness curve of the modified PSO algorithm for the parameter optimization of the fault diagnosis model of LS-SVM propeller system are drawn in Fig. 2. In Fig. 2, the average fitness curve shows the average fitness of all particles in each iteration of the particle swarm, and the best fitness curve represents the maximum fitness value of all swarm in each iteration. It can be seen from Fig. 2 that the fitness curve converges quickly and then slowly, and finally the convergence degree of the fitness curve is almost the same. This process is the optimization of LSSVM parameters.

Based on the selected optimal feature parameters, the classification prediction results in training and testing phases are shown in Fig. 3. From Fig. 3, it is observed that, only 14 of the 240 training samples and 6 of the 80 testing samples are misclassified, respectively, yielding the 94.17 and 92.5% success rates. Obviously, from the above experimental results, we can conclude that the proposed multi-class LSSVM classifiers with PSO obtain very promising abilities and have good practicability in fault classification for pitch system.

In order to reflect the superiority of the model, the prediction results of BP neural network and standard SVM algorithm are compared. The main aim of this study is to compare the traditional approaches with our optimized approaches in their abilities to accurately predict faults for pitch system. To facilitate fair comparison, all approaches are based on the same training and testing samples. In the experiments, we apply a double hidden-layer network with the transfer functions of tangent sigmoid and log-sigmoid to train the BPNN classifier. The Levenberg–Marquardt optimization method is used to minimize the predetermined error goal

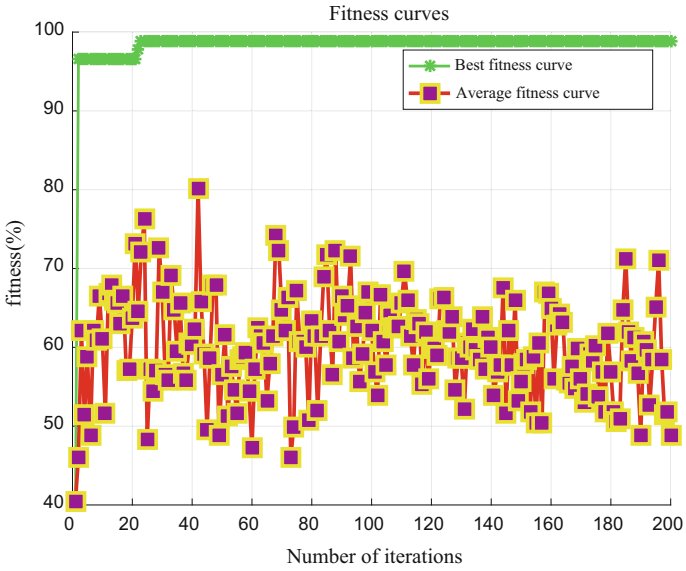

Fig. 2 Fitness curves of PSO for feature parameter optimization based upon MOC scheme

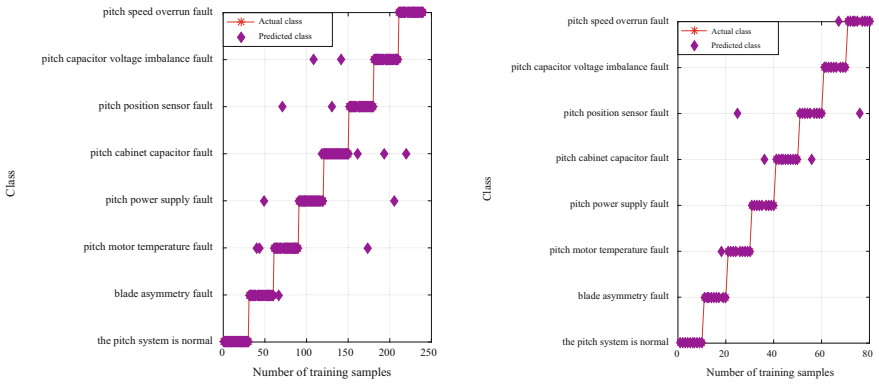

Fig. 3 Classification results in training and testing phases using MOC scheme and modified PSO

value as fast as possible. For SVM, the kernel function is still based on Gauss radial basis function. The pitch system prediction results on selected approaches are represented in Fig. 4 and Table 2. It is clear that the proposed optimized approach preserves its superiority both in terms of classification accuracy and generalization performance compared with the traditional fault prediction approaches.

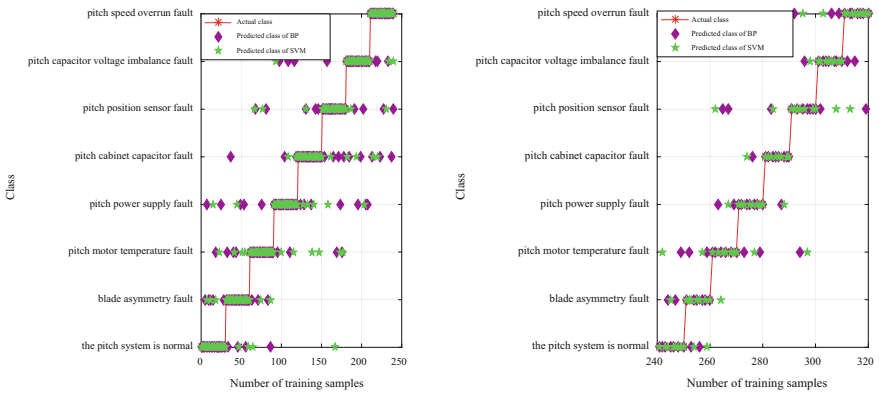

Fig. 4 Pitch system fault prediction accuracy of different algorithms

Table 2 Pitch system fault prediction accuracy of different algorithms

Fault prediction accuracy	BP neural network (%)	Standard SVM (%)	Proposed method in this paper (%)
Training	75	82.92	94.17
Testing	68.75	77.5	92.5

5 Conclusion

This paper has presented multi-class LS-SVM classifiers with modified PSO to improve the classification accuracy for turbine pitch system fault prediction. By constructing three 2-class LSSVM to achieve the operation state of pitch system. By using the improved PSO algorithm, we can get the optimal value of the penalty parameter and kernel function parameter of the LSSVM classification model. It is shown that both the multi-class classification issue and the optimal LS-SVM classification problem are settled successfully and generalized.

In addition, based on the analysis of the fault classification of fan propeller system, it is shown that compared with the BP neural network and the standard LSSVM model, the model of modified PSO optimization of the LS-SVM parameters of the wind turbine blade failure prediction model can be more effective and accurately predict the failure of the pitch system. Fault prediction is helpful to provide valuable information to a maintenance programme and serve as the basis of a preventive maintenance strategy.

Acknowledgements This work is supported by Science and Technology Program Foundation of Hebei Province (No. 16214510D).

References

1. Huawei MEI, Zengqiang MI, Junliang BAI (2014) Calculation model and method of output power loss of wind farms and wind turbines. Autom Electr Power Syst 38(2):12–16 (in Chinese)
2. Amirat Y, Benbouzid M, Ahmar EA et al (2009) A brief status on condition monitoring and fault diagnosis in wind energy conversion systems. Renew Sustain Energy Rev 13(9):2629–2636
3. Liu WY, Zhang WH, Han JG et al (2012) A new wind turbine fault diagnosis method based on the local mean decomposition. Renew Energy 48:411–415
4. Hang J, Zhang JZ, Cheng M (2016) Application of multi-class fuzzy support vector machine classifier for fault diagnosis of wind turbine. Fuzzy Sets Syst 927:128–140
5. Wu D, Song J, Shen Y (2016) Variable forgetting factor identification algorithm for fault diagnosis of wind turbines. In: Proceedings of 28th Chinese control and decision conference, pp 1895–1900
6. Cheng Xiao, Zuojun Liu, Lei Zhang (2017) Variable pitch fault prediction of wind power system based on SCADA system. Renew Energy Resour 35(2):278–284 (in Chinese)
7. Kusiak A, Verma A (2011) A data -driven approach for monitoring blade pitch faults in wind turbines. IEEE Trans Sustain Energy 2(1):87–96
8. Hui Li, Chao Yang, Xuewei Li et al (2014) Conditions characteristic parameters mining and outlier identification for electric pitch system of wind turbine. Proc CSEE 34(12):1922–1930 (in Chinese)
9. Suykens JAK, Gestel TV, Brabanter JD et al (2002) Least squares support vector machines. World Scientific, Singapore
10. Kennedy J, Eberhart RC (1995) Particle swarm optimization. In: IEEE international conference on neural networks. IEEE, Perth, Australia, pp 1942–1948
11. Hsu CW, Lin CJ (2002) A comparison of methods for multiclass support vector machines. IEEE Trans Neural Networks 13(2):415–425

Observability and Controllability Preservation for Multi-agent Systems with Time Delay and Time-Varying Topology

Xiangju Jiang, Zhijian Ji, Ting Hou and Fanggang Sun

1 Introduction

In recent years, the study of multi-agent systems has attracted more and more attention. It is known that controllability is a core concept of modern control, playing a fundamental role in analysis and synthesis of linear control systems [1–3]. For multi-agent systems, the controllability problem aims at driving follower agents to achieve any configurations from any initial states only through controlling a few leaders externally. The controllability of multi-agent systems is first proposed by Tanner [4], in which the Laplacian matrix was divided into submatrices and the controllability was acquired by taking advantage of the classical controllability concept. There are some related results e.g., leaders selection [5], switching topology [6], directed topology [7–9], time-delay [10], structural controllability [11], etc. However, the study on the preservation of controllability is at starting stage. Sufficient conditions are derived in [12] that guarantee controllability of a network system from a graph-theoretic perspective. Fraceschelli etc. presented a strategy in [13] to verify the controllability, the strategy is based on decentralized estimation of the spectrum of the Laplacian matrix. An energy function associated with the second-smallest eigenvalue of Laplacian matrix is presented in [14], that ensure the connectivity of multi-agent systems. In addition, The proposed methodology is based on a decentralized strategy presented in [15–17] for the maintenance of the connectivity of the multi-agent systems, that will be here exploited for guaranteeing structurally controllable systems.

X. Jiang · Z. Ji (✉) · F. Sun
The School of Automation Engineering, Qingdao University, Qingdao 266000, China
e-mail: jizhijian@pku.org.cn

T. Hou
Mathematics and Systems Science, Shandong University of Science and Technology, Qingdao 266590, Shandong, China

Z. Deng (ed.), *Proceedings of 2017 Chinese Intelligent Automation Conference*,
Lecture Notes in Electrical Engineering 458,
https://doi.org/10.1007/978-981-10-6445-6_35

Compared with the concept of controllability, the concept of observability is related to the possibility of observing the whole state of the systems from only a subset of the agents. In the relevant studies about the observability, Ji etc. have studied the observability of the distributed sensors from the equivalence partition and they have gotten the requirement of the system observability [18]. The observability of the multi-agent system about choosing the leaders has been studied by the literature [19]. Lozano, R. and others have studied the observability of the second-order systems in the structure of the path graph and the circle graph.

Usually, a multi-agent system is interconnected through neighbor rules and there will exist a time delayed due to finite speed of communication between two coupled agents. From a graph-theoretic perspective, Sufficient conditions are derived in [20] that guarantee controllability of multi-agent systems with interaction time delays. Liu etc. studies the controllability of a leader-follower network of dynamic agents in the presence of communication delays in [21]. In this paper, the case of time delay is also studied.

2 Preliminaries

In this section, we present some fundamental terminologies on graph theory including the system model, the formulation of controllability problem that will be used in the proof of the main results.

2.1 Graph Preliminaries

An undirected graph G is composed of three parts including a vertex set, an edge set, and an adjacency matrix with weights. And it is marked as $G = (V, \varepsilon, A)$, where the nodes are marked as $1, 2, \ldots, n$, he edge set is marked as $\varepsilon = \{(i,j) \in V \times V\}$ and $A = [a_{ij}] \in \mathbb{R}^{n \times n}$ is the adjacency matrix, where $a_{ij} > 0$ if the vertex i is adjacent with the vertex j. An edge of the graph G is denoted by $e_{ij} = (v_j, v_i)$, where the v_j is called as parent vertex of v_i and v_i is called as child vertex of v_j. We suppose there is no self-loops in this paper, namely $e_{ii} \notin \varepsilon$. If the vertex i is connected with the j by an edge e_{ij}, then those two vertexes are called the adjacency vertexes. The vertex i is adjacency directly with the edge e_{ij}. Therefore we take the adjacency vertexes set $\mathrm{N}_i = \{v_j \in V | (v_j, v_i) \in \varepsilon\}$ as the vertex set where the vertexes are all directly adjacency with the vertex i. $d(v_i) = \sum_j a_{ij}$ is on behalf of the degree of a vertex and the $D(G) = diag(d(v_i))$ is the corresponding degree matrix. The Laplacian matrix $L(G)$ of the graph G is defined as $L(G) = D(G) - A$. For an undirected graph, the Laplacian matrix is symmetrical and positive semi-definite.

2.2 Problem Formulation

With the leader-following structure of the linear system, the observability will be studied. A multi-agent system is composed of leaders and followers. The followers are under control by the neighbor agreement. But the leaders are free of such a constrain and are allowed to picked its control input arbitrarily. In this case, the leaders are regarded as control inputs and the followers are controlled by the leaders. Given leaders, the Laplacian matrix of the figure G is divided into $L = \begin{bmatrix} L_f & L_{fl} \\ L_{lf} & L_l \end{bmatrix}$ where $L_f \in \mathbb{R}^{n\times n}$ and $L_l \in \mathbb{R}^{l\times l}$ correspond to the indices of followers, leaders. L_{lf} represents the communication relation from followers to leaders. L_{fl} represents the communication relation from leaders to followers. We denote by $F \triangleq L_f, R \triangleq L_{fl}$. In the undirected graphs, $L_{lf} = L_{lf}^T$, namely $L_{lf} = R^T$. After having chosen the leaders, Laplacian matrices are completely decided by the communication topology. In this paper, the leaders are already set in advance.

3 Observability of Multi-Agent Systems with Time Delay and Time-Varying Topology

Considering $n+l$ multi-agents, the dynamic equation of the single integral is as follows:

$$\dot{x}_i(t) = u_i(t), i = 1, 2, \ldots, n+l \tag{3.1}$$

The corresponding delay control protocol is as follows:

$$u_i(t) = -\sum_{j\in N_i} a_{ij}\big(x_i(t) - x_j(t-\tau)\big) + \sum_{j\in N_i} a_{ij}\big(x_j(t) - x_i(t)\big) \tag{3.2}$$

where $x_i(t)$ represents state of the agent i. $u_i(t)$ represents the input of the system, and $\tau > 0$ represents the time delay, a_{ij} represents the weight of edge from agent v_j to agent v_i.

The state space equation of multi-agent systems with time varying topology is described as:

$$\dot{x}(t) = -(D+L)x(t) - Bx(t-\tau) \tag{3.3}$$

where

$$D = \begin{bmatrix} \sum\limits_{j\in N_1} a_{1j} & 0 & \cdots & \cdots & 0 \\ 0 & \ddots & 0 & \cdots & \vdots \\ \vdots & 0 & \sum\limits_{j\in N_n} a_{nj} & 0 & \vdots \\ \vdots & \cdots & 0 & \ddots & 0 \\ 0 & \cdots & \cdots & 0 & \sum\limits_{j\in N_n+l} a_{(n+l)j} \end{bmatrix} \quad L = [l_{ij}] \quad \text{with} \quad l_{ij} =$$

$$\begin{cases} -a_{ij}, & j \neq i \text{ and } j \in N_i \\ \sum\limits_{j\in N_i} a_{ij}, & i = j \\ 0, & \text{otherwise} \end{cases} \quad \text{and } B = [b_{ij}] \text{ with}$$

$$b_{ij} = \begin{cases} -a_{ij}, & j \neq i \text{ and } j \in N_i \\ 0, & \text{otherwise} \end{cases}$$

The dynamic equation of the followers is as follows

$$\dot{x}_f(t) = -(D_1 + F)x_f(t) - B_1 x_f(t-\tau) - R(x_l(t) + x_l(t-\tau)) \tag{3.4}$$

where

$$D_1 = \begin{bmatrix} \sum\limits_{j\in N_1} a_{1j} & 0 & \cdots & 0 \\ 0 & \sum\limits_{j\in N_2} a_{2j} & \cdots & 0 \\ \vdots & \vdots & \ddots & \vdots \\ 0 & 0 & \cdots & \sum\limits_{j\in N_n} a_{nj} \end{bmatrix} \quad B_1 = \begin{bmatrix} 0 & -a_{12} & \cdots & -a_{1n} \\ -a_{21} & 0 & \cdots & -a_{2n} \\ \vdots & \vdots & \ddots & \vdots \\ -a_{n1} & -a_{n2} & \cdots & 0 \end{bmatrix}$$

where $x_f(t) = [x_1(t) \quad x_2(t) \quad \cdots \quad x_n(t)]^T$ is the stacked vector of followers' position in the state of t. $x_f(t-\tau) = [x_1(t-\tau) \quad x_2(t-\tau) \quad \cdots \quad x_n(t-\tau)]^T$ is the stacked vector of followers' position in the state of $t-\tau$. $x_l(t) = [x_{n+1}(t) \quad x_{n+2}(t) \quad \cdots \quad x_{n+l}(t)]^T$ is the stacked vector of leaders' position in the state of t. $x_l(t-\tau) = [x_{n+1}(t-\tau) \quad x_{n+2}(t-\tau) \quad \cdots \quad x_{n+l}(t-\tau)]^T$ is the stacked vector of followers' position in the state of $t-\tau$.

According to literature [22], the controllability of multi-agent systems with time delay is usually determined by the algebraic criterion proposed for the associated auxiliary system without delay. In order to study the controllability of the system represented by (3.4), the following auxiliary equations are introduced:

$$\dot{x}_f(t) = -2Fx_f(t) - 2Rx_l(t) \tag{3.5}$$

Lemma 1 Hewer [22] If the system (3.5) is controllable, then system (3.4) is controllable for any $\tau > 0$.

Let $y \in \mathbb{R}^l$ respect the output vector, which contains all the state vectors measured by the leader. The output equation of the system is as follows:

$$y(t) = R^T x_f(t) \tag{3.6}$$

Then the equations of the time-varying multi-agent system can be written as described in the literature [14]:

$$\begin{cases} \dot{x}_f(t) = -2Fx_f(t) - 2Rx_l(t) \\ y(t) = R^T x_f(t) \end{cases} \tag{3.7}$$

Lemma 2 Dong et al. [23] For the multi-agent system (3.7), there exists all the eigenvalues can make the matrix $\begin{bmatrix} \lambda I - F \\ R^T \end{bmatrix}$ nonsingular. Namely, if $Lv = \lambda v$, then $R^T v \neq 0$, where v is the nonzero eigenvector of the L.

Theorem 1 *The system* (3.7) *is observable if and only if there is no eigenvector of* L *taking zero on the element corresponding to the leader.*

Proof The result will be shown by contradiction. From $Lv = \lambda v$, where $v = \begin{bmatrix} v_f \\ v_l \end{bmatrix}$, we can get: $Lv = \begin{bmatrix} F & R \\ R^T & E \end{bmatrix} \begin{bmatrix} v_f \\ v_l \end{bmatrix} = \lambda \begin{bmatrix} v_f \\ v_l \end{bmatrix}$

(Necessity) If the eigenvector of the matrix L corresponding to the leader node the element is zero, that is $v_l = 0$, we have

$$\begin{bmatrix} Fv_f \\ R^T v_f \end{bmatrix} = \lambda \begin{bmatrix} v_f \\ 0 \end{bmatrix} \tag{3.8}$$

The equation of (3.8) leads to $Fv_f = \lambda v_f, R^T v_f = 0$. Then, the matrix $[F, R^T]$ is not observable. So, if the system (3.7) is able to observe, the matrix L in the eigenvector and the corresponding element of the leader node is not a factor of 0.

(Sufficiency) If the system (3.7) is not observable, by the lemma 2, we see that the matrix F has a characteristic value of λ and its eigenvector is v_f, which satisfies $R^T v_f = 0$. (3.8) means that $v_l = 0$. The eigenvectors corresponding to the matrix and L and leader node elements are not 0 contradictory, so if the corresponding eigenvector matrix L and the leader node element is not 0, the system (3.7) can observe.

4 The Preservation of Controllability

For a multi-agent system with time-delay and time-varying topology, the number and lengths of the edges between different nodes will change as time goes on. The change further affects the Laplacian matrix of the system, which will give rise to a variation of algebraic connectivity that makes the whole system uncontrollable from the Theorem 1 and the reference [24]. Therefore, it will introduce a concept of structural controllability in order to ensure preservation of controllability of the systems

4.1 Structural Controllability

Definition 1 A multi-agent system is said to be structurally controllable if and only if it is controllable for almost all choices of the edge weights.
According to reference [24], a multi-agent system is structurally controllable if and only if the topology of the system is connected. It means that the algebraic connectivity $\lambda_2 > 0$.

In view of the definition of structural controllability and reference [24], Fig. 1 can be used to show the relationship between the structural controllability and the usual controllability for a multi-agent system.

4.2 The Strategy of Structural Controllable Preservation

Due to the change of the relationship between the agents, the connectivity of the corresponding topological graph of the system (1) may change at a certain time. As show in Fig. 2a, the node 1 represents the leader which is endowed an external control input. As the followers arrive at expected positions, the connection strength between the node 2 and the node 3 is weakened in Fig. 2b, because the distance

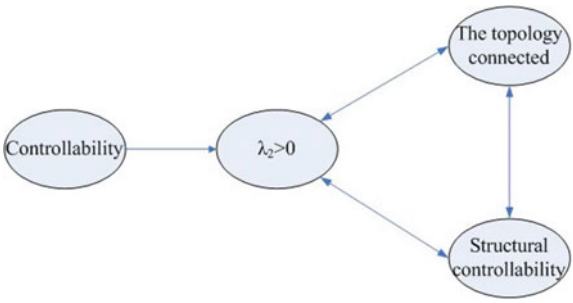

Fig. 1 Relationship between controllability and structural controllability

between them increases longer, which is inconsistent with the design requirements of the multi-agent systems.

In case of the aforesaid conditions, it will introduce a control strategy of preserving controllability:

$$u_i^c = -\frac{\partial V(\lambda_2(L_a(G)))}{\partial x_i} \tag{4.1}$$

where $L_a(G)$ is the Laplacian matrix of the graph G. The weights of the graph G are inversely proportional to the distances between agents i and j. From the formula (4.2), it can get the specific relationship between the weights and distances. It assumes the R is the maximum communication distance between any two agents, which means when $\|x_i - x_j\| \leq R$, the two agents are still connected. Therefore

$$a_{ij} = \begin{cases} e^{-\left(\|x_i - x_j\|\right)/\left(2\sigma^2\right)} & if \|x_i - x_j\| \leq R \\ 0 & \text{otherwise} \end{cases} \tag{4.2}$$

the scalar σ is chosed by the threshold condition $e^{-\left((R^2)\right)/\left(2\sigma^2\right)} = \Delta$, Δ is a minimum predetermined value.

This control protocol ensures that the value of the algebraic connectivity of the system will not be lower than the value of a given threshold ξ. From [4], the value of λ_2 will decrease with a_{ij} decreasing.

Definition 3 *Energy Function* $V(\lambda_2(\cdot))$

The energy function $V(\lambda_2(\cdot))$ has the following properties:

(P1) $\forall \lambda_2(\cdot) > \xi$ energy function is continuous and differentiable.

(P2) The energy function is non-negative.

(P3) With $\lambda_2(\cdot)$ increasing, the energy function converges to a constant value.

(P4) $\lim_{\lambda_2(\cdot)\to\xi} V(\lambda_2(\cdot)) = \infty$. (P5) $\lim_{\lambda_2(\cdot)\to\xi} \left\| \frac{\partial V(\lambda_2(\cdot))}{\partial \lambda_2(\cdot)} \right\| = \infty$.

According to the reference [9], the energy function is defined as follows:

$$V(\lambda_2(L_a(G))) = \frac{1}{(\lambda_2(L_a(G)))^3} \tag{4.3}$$

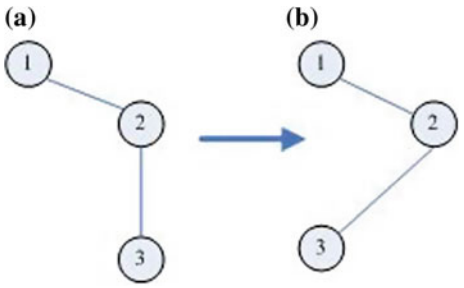

Fig. 2 Time varying topology

The dynamic model is considered by $\dot{x}_i = u_i^c$. The control protocol u_i^c is shown by (4.1).So dynamic functions are modified by the next forms:

$$\begin{cases} \dot{x}_i = -\sum_{j\in N_i} a_{ij}(x_i(t) - x_j(t-\tau)) \\ \quad + \sum_{j\in N_i} a_{ij}(x_j(t) - x_i(t)) + u_i^c & \text{if } i = 1, 2, \ldots, n \\ \dot{x}_i = u_i + u_i^c & \text{if } i = n+1, \ldots, n+l \end{cases} \tag{4.4}$$

Theorem 2 *As for the multi-agent system decorated by (4.4), it supposes the system is structurally controllable at the moment of $t = 0$.Then, the corresponding control strategy $u_i^c = -\frac{\partial V(\lambda_2(L_a(G)))}{\partial x_i}$ enables the multi-agent system preserving structural controllability.*

Proof At the moment of $t = 0$, it supposes the system is structurally controllable. So the topology is connected and $\lambda_2 > \xi$. Inspired by [17], we can get that the control strategy guarantees that, if a time-varying system is connected firstly, then the system is always connected with time varying. At this time, it is necessary to consider an energy function $V(\cdot)$ defined according to Definition 3, which does not increase with the varying of the systems. The dynamic functions decorated by the form (4.4) can be modified as the follows:

$$\dot{x}_i = u_i^c + u_i^\varepsilon \quad \forall\, i = 1, 2, \ldots, n+l \tag{4.5}$$

where external input u_i^ε is bounded. It means $\exists u_M \in \mathbb{R}$ which cause:

$$\left\| u_i^\varepsilon \right\| \le u_M, \forall\, i = 1, 2, \ldots, n+l \tag{4.6}$$

The derivative of the energy function is written as the following form:

$$\dot{V}(\cdot) = \nabla_x V(\cdot)^T \dot{x} = \sum_{i=1}^{n+l} \frac{\partial V(\cdot)^T}{\partial x_i} \dot{x}_i \tag{4.7}$$

According to the form (4.1) and (4.5), the derivative of the energy function can be transformed by follows:

$$\dot{V}(\cdot) = \sum_{i=1}^{n+l} \frac{\partial V(\cdot)^T}{\partial x_i} \left(-\frac{\partial V(\cdot)}{\partial x_i} + u_i^\varepsilon \right) \tag{4.8}$$

Considering the form (4.6) and $\frac{\partial V(\cdot)}{\partial x_i} = \frac{\partial V(\cdot)}{\partial \lambda_2(\cdot)} \frac{\partial \lambda_2(\cdot)}{\partial x_i}$. It can get the following inequality:

$$\dot{V}(\cdot) \leq -\left\|\frac{\partial V(\cdot)}{\partial \lambda_2(\cdot)}\right\|^2 \sum_{i=1}^{N}\left\|\frac{\partial \lambda_2(\cdot)}{\partial x_i}\right\|^2 + \left\|\frac{\partial V(\cdot)}{\partial \lambda_2(\cdot)}\right\| u_M \sum_{i=1}^{N}\left\|\frac{\partial \lambda_2(\cdot)}{\partial x_i}\right\| \tag{4.9}$$

So, if the inequality

$$\left\|\frac{\partial V(\cdot)}{\partial \lambda_2(\cdot)}\right\| \sum_{i=1}^{N}\left\|\frac{\partial \lambda_2(\cdot)}{\partial x_i}\right\|^2 \geq u_M \sum_{i=1}^{N}\left\|\frac{\partial \lambda_2(\cdot)}{\partial x_i}\right\| \tag{4.10}$$

is right, then $\dot{V}(\cdot) \leq 0$.

It assumes the following conditions are right:

$$\sum_{i=1}^{N}\left\|\frac{\partial \lambda_2(\cdot)}{\partial x_i}\right\|^2 \neq 0 \tag{4.11}$$

Therefore, the form (4.10) can be written by the following form:

$$u_M \frac{\sum_{i=1}^{N}\left\|\frac{\partial \lambda_2(\cdot)}{\partial x_i}\right\|}{\sum_{i=1}^{N}\left\|\frac{\partial \lambda_2(\cdot)}{\partial x_i}\right\|^2} \leq \left\|\frac{\partial V(\cdot)}{\partial \lambda_2(\cdot)}\right\| < \infty \tag{4.12}$$

According to the Property (P5) in Definition 2, $\exists \bar{\lambda} > \xi$ such that, $\forall \lambda_2(\cdot) \leq \bar{\lambda}$, the inequality (4.12) is right. This indicates that the value of $\lambda_2(\cdot)$ is always bounded away from ξ. Suppose that the form (4.11) is not satisfied, so $\dot{\lambda}_2(\cdot) = \frac{\partial \lambda_2(\cdot)}{\partial x_i}\dot{x}_i = 0$ therefore the value of the $\lambda_2(\cdot)$ is invariable $\lambda_2 > \xi$.

From the aforesaid conclusion, if the topology is connected at the initial moment, the second eigenvalue of the corresponding Laplacian matrix will forever be greater than ξ even though the topology has changed with time varying. At last, it can ensure the multi-agent be structurally controllable.

According the Fig. 3, if the structural controllable system is endowed a set of weights, then not only the structural controllability can preserve and $\lambda_2 > \xi$, but also the topology is connected.

To sum up, by the effect of the control strategy u_i^c, the controllability of the time-varying multi-agent systems can be preserved by assigning a set of weights to multi-agent systems.

5 Example Analysis

Consider a system of six agents with time-delay interaction topology as shown in Fig. 4. Let the sixth agent be the leader and the interconnection graph be defined by the matrices:

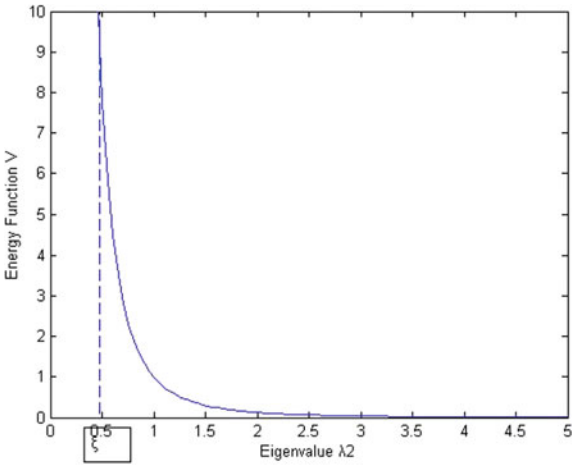

Fig. 3 The decreasing trend of energy function

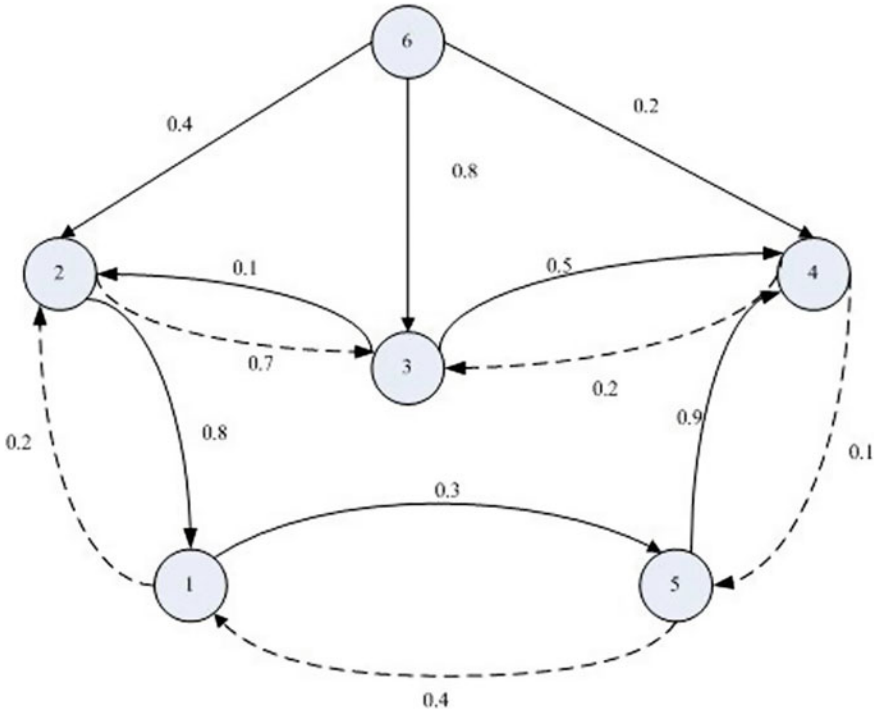

Fig. 4 A communication topology

$$D_1 = \begin{bmatrix} 1.2 & & & & \\ & 0.3 & & & \\ & & 0.9 & & \\ & & & 1.4 & \\ & & & & 0.4 \end{bmatrix}$$

$$B_1 = \begin{bmatrix} 0 & -0.8 & 0 & 0 & -0.4 \\ -0.2 & 0 & -0.1 & 0 & 0 \\ 0 & -0.7 & 0 & -0.2 & 0 \\ 0 & 0 & -0.5 & 0 & -0.9 \\ -0.3 & 0 & 0 & -0.1 & 0 \end{bmatrix}$$

and

$$F = \begin{bmatrix} 1.2 & -0.8 & 0 & 0 & -0.4 \\ -0.2 & 0.3 & -0.1 & 0 & 0 \\ 0 & -0.7 & 0.9 & -0.2 & 0 \\ 0 & 0 & -0.5 & 1.4 & -0.9 \\ -0.3 & 0 & 0 & -0.1 & 0.4 \end{bmatrix} \quad R = \begin{bmatrix} 0 \\ -0.4 \\ -0.8 \\ -0.2 \\ 0 \end{bmatrix}$$

With the above parameters, we have verified the equation of the (5):

$$-D_1 - F + B_1 = -2F, R^T = [0 \quad -0.4 \quad -0.8 \quad -0.2 \quad 0]$$

It is easy to verify that rank(Q) = 5. Therefore, the condition of Theorem 1 is satisfied and hence the given system is observable.

6 Conclusion

This paper mainly study the preservation of the controllability and observability of time delay and time-varying topology multi-agent systems with leader-following structure. We have gotten that the controllability of multi-agent systems with time-delay are related to the corresponding systems without time-delay. With respect to the selected leader agents, the observability of the multi-agent system with time delay and time-varying topology is equivalent to that of (F, R^T). In the future, it is meaningful to study the preservation of the controllability of time-varying topology and time-delay multi-agent systems with high-order dynamic agents.

Acknowledgements This work is supported by National Natural Science Foundation (NNSF) of China (No. 61374062, 61603288, 61673013), Science Foundation of Shandong Province for Distinguished Young Scholars (No. JQ201419). Natural Science Foundation of Shandong Province under Grant ZR2016JL022.

References

1. Ji ZJ, Yu H (2017) A new perspective to graphical characterization of multi-agent cotrollability. IEEE Trans Cybern 47(6):1471–1483
2. Cai N, He M, Wu Q., Khan MJ, On almost controllability of dynamical complex networks with noises. J Syst Sci Complex (arXiv:1706.00890). doi:10.1007/s11424-017-6273-7(in press)
3. Ji ZJ, Lin H, Yu H (2015) Protocols design and uncontrollable topologies construction for multi-agent networks. IEEE Trans Autom Control 60(3):781–786
4. Tanner Hg. (2004) .On the controllability of nearest neighbor interconnections. In Proceeding of 43rd IEEE conference on decision and control, Paradise Isl, Bahamas, pp 2467–2472
5. Ji ZJ, Lin H, Yu H (2012) Leaders in multi-agent controllability under consensus algorithm and tree topology. Syst Control Lett 61(9):918–925
6. Liu KE, Ji ZJ, Ren W (2016) Necessary and sufficient conditions for consensus of second-order multi-agent systems under directed topologies without global gain dependency. IEEE Trans Cybern. doi:10.1109/TCYB.2616020
7. Guan YQ, Ji ZJ, Zhang L, Wang L (2016) Controllability of heterogeneous multi-agent systems under directed and weighted topology. Int J Control 89(5):1009–1024
8. Guan YQ, Ji ZJ, Zhang L, Wang L (2017) Controllability of multi-agent systems under directed topology. Int J Robust Nonlinear Control. doi:10.1002/rnc.3798
9. Liu B, Chu TG, Wang L (2008) Controllability of a leader-follower dynamic network with switching topology. IEEE Trans Autom Control 53(4):1009–1013
10. Ji ZJ, Wang D, Lin H, Wang Z (2010) Controllability of multi-agent systems with time-delay in state and switching topology. Int J Control 83(2):371–386
11. Lou Y, Hong Y (2012) Controllability analysis of multi-agent systems with directed and weighted interconnection. Int J Control 5(10):1486–1496
12. Ji M, Egersted M (2007). A graph-theoretic characterization of controllability for multi-agent systems. In American Control Conference, pp 4588–4593
13. Franceschelli M, Martini S, Egerstedt M (2010) Observability and controllability verification in multi-agent systems through decentralized laplacian spectrum estimation. In 49th IEEE Conference on Decision and Control(CDC), pp 5775–5780
14. Sabattini L, Secchi C, Fantnzzi C (2004). Controllability and observability preservation for networked systems with time varying topologies. In Proceedings of the 19th world congress on the international federation of automatic control, Cape Town, South Africa, pp 1837–1842
15. Sabattini L, Chopra N, Secchi C (2013) Decentralized connectivity maintenance for co operative control of mobile robotic systems. Int J Robot Res (SAGE) 32(12):1411–1423
16. Sabattini L, Chpra N, Secchi C (2014) On decentralized connectivity maintenance for mobile robotic systems. In: 2011 50th IEEE conference on decision and control and European control conference, Orlando, USA, pp 1837–1842
17. Sabattini L, Secchi C, Chopra N, Gasparri A (2013) Distributed control of multi-robot systems with global connectivity maintenance. IEEE Trans Robot 29(5):1326–1332
18. Meng J, Magnus E (2007) Observability and estimation in distributed sensor networks. In Proceedings of the 46th IEEE conference on decision and control, New Orleans, LA, USA, Dec.12–14, pp 4221–4226
19. Lozano R, Spong MW, Guerrero JA, Chopra N (2008) Controllability and observability of leader-based multi-agent systems. In Proceedings of the 47th IEEE conference on decision and control, Cancun, Mexico, pp 3713–3718
20. Weiss L (1970) An algebraic criterion for controllability of linear systems with time delay. IEEE Trans Automatic Control 55:443–444
21. Liu B, Zou J, Zhang J (2008) Controllability of a leader-follower dynamic network with interaction time delays. Fifth International Conference on Fuzzy Systems and Knowledge Discovery, pp 468–473

22. Hewer GA (1972). A note on controllability of linear systems with time delay. IEEE Trans Autom Control AC-17:733–734
23. Dong J, Ji ZJ, Wang X (2015) Algebraic conditions for controllability of multi-agent networks. J Intell Sys 105:747–754 (in Chinese)
24. Fiedler M (1973) Algebraicconnectivity of graphs. Czechoslovak Math J 23(98):298–305

A Classified Access Control Model Research for Cloud Computing

Wenyi Shen, Linbo Tao, Bo Liu and Yishen Wang

1 Introduction

Cloud computing forms a huge pool of IT resources by linking a large number of IT resources, which facilitates its use and access to IT resources, together with lower cost to users. It stores user data in the cloud instead of storing them in the local by their owners. So Users do not know where their data is stored, in which server, all these are managed and maintained by the third parties. This framework can properly solve the problems of disaster recovery, sharing and scalability [1], but bring the risk of illegal access and privacy diffusion. There are three reasons, the first, the data of user may be stored together with other users' data in a same physical host with different virtual machine instances which faces the side channel attack, we need to know how to ensure them safely isolated. The second, users store their data in the cloud, facing illegal access by other users or unauthorized internal cloud service providers [2], we need to know how to identify the access identity and permission control. The third, when illegal access to data occured, how to restrict the scope of unauthorized access. All these problems present great challenges to access control.

Based on comparing the advantages and disadvantages of traditional access control and the analysis of cloud computing environment, an access control model based on object sensitivity classification and model T-RBAC is proposed, efficiency

W. Shen (✉)
Department of Computer Science and Technology,
Suzhou College of Information Technology, Suzhou 215000, China
e-mail: shenwenyi0806@163.com

L. Tao · Y. Wang
School of Arts and Sciences, Information Engineering University,
Zhengzhou 450001, China

B. Liu
NanChang High School, Shenyang 110000, China

Z. Deng (ed.), *Proceedings of 2017 Chinese Intelligent Automation Conference*,
Lecture Notes in Electrical Engineering 458,
https://doi.org/10.1007/978-981-10-6445-6_36

and dynamic property are fully considered in this model. It improves the data control ability to users, reduces the scope of illegal access, improves the authorization efficiency of access control.

2 Characteristics Analysis of Access Control

The access control system consists of three main elements: subject, object and control strategy. The subject refers to the access request initiator [3], it could be a user, application or process. The object refers to program called by subject or accessed data. The control strategy refers to a set of rules that subject how to access object. Subject and object are relative, they can be transformed into each other under certain conditions. The nature of access control is to limit the access of users to the resources based on the access control policy, only those authorized subjects allowed to access corresponding resources. Access control intend to prevent objects from invading and destroying.

The traditional access control models have DAC(Discretionary Access Control), MAC(Mandatory Access Control) and RBAC (Role-based Access Control). DAC technology is a kind of common access control technology in multiple users environment, users have absolute control of their data, they may grant other users or groups to access their data, or revoke their permissions, the authorities of each authorized subject controlled by an ACL (Access Control, List) [4]. This kind of access control model fits the small scale systems, but for large distributed systems, it is difficult to maintain the large ACL, flexible task allocation and limiting the malicious operation to authorized users. The MAC model is mainly used in military, government and other high safety requirements areas, it adds the classification to resources security attributes in the network on the basis of DAC, it sets the different subjects access permissions to different attributes. The MAC model has higher security, but less flexibility, so it can not adapt to the frequent switching between subjects and objects in the cloud environment. The role is a collection of a number of rights, refers to the rights set about access resources and operating rights assignment of a task [5]. The RBAC model introduces the concept role into access control, it associates rights with roles. Users get the authority by becoming a member of the proper role instead of getting authority directly, this can greatly simplify the rights management, reduce the complexity of authorization management, improve the flexibility of security policy. As the middle layer between user and rights, role achieves the separation of user and authority, enhances their independence, especially simplifies the large-scale network applications authority. RBAC has relatively fixed roles and corresponding permissions, but it lacks the consideration of the context, so it is not suitable for the distributed environment with complex roles and frequent changes. Due to the lack of dynamic attribute of RBAC model, Thomas et al. proposed TBAC(Task-Based Access Control) model which is a kind of active security model based on task oriented and dynamic authorization [6]. TBAC model considers the implementation of the environment

context, to determine whether to grant access to the subject [7], it considers the implementation of current task and manages authority dynamically according to the tasks state. The TBAC model is very suitable for information processing of distributed computing and multipoint access control, workflow, distributed processing [8], and transaction management system decision making etc., but it does not support passive access.

In order to give full play to the advantages of RBAC and TBAC, an access control model T-RBAC (Task-Role Based Access Control) is proposed, such as Wang and Zhao [9] proposed T-RBAC has different access control strategies for different access users, and provides hierarchical security features to improve the accuracy of access control. Huang Yi et al. proposed to improve the accuracy of access control through the classification of roles and permissions [10], all these T-RBAC solve the problem of cloud access control to a certain extent, but these models have the shortcomings of fuzzy classification, lacking the authority interaction between the objects and their owners, especially those sensitive data, privacy information who need fine-grained access control under distributed conditions. A CT-RBAC (Classified Task-Role Based Access Control) model is presented in the paper, the model will give full consideration to the role assignment, task attribute and object sensitivity, through dynamic rights assignment according to object security requirements level, it makes access control more accurate.

3 Design of CT-RBAC Model

3.1 Definitions and Rules

Cloud computing uses the third party data storage and management under distributed environment, it bases on the hypotheses that cloud service providers are believable and they have super user privileges. It is these two hypotheses that may cause potential security risks. So the CT-RBAC model are design based on the following principles.

Principle 1, the cloud service providers are not believable. Most of the T-RBAC model suppose the cloud servers as the believable third party, so it can be used as the middle transfer of authority, but the cloud server is not believable at most time.

Principle 2, the cloud service providers do not have super user privileges. The users' information are stored in the cloud server, their information storage, backup, maintenance and management are all managed by cloud service providers, but users usually do not make any restrictions for cloud service providers on privileges, so cloud service providers actually have the super user privileges on users' data management. This is contrary to the users' security needs.

Principle 3, safety and efficiency. Due to the distributed, concurrency, and dynamic nature of cloud computing, the excessive emphasis on security will affect the efficiency of access control and reduce the user experience. So the right strategy is needed to balance security and efficiency.

Principle 4, flexibility. Some RBAC models are used to group users, which can improve the simplicity of role division, but it limits the flexibility and mobility of user roles. The CT-RBAC model does not block users, it authorize all users uniformly in order to adapt to the dynamic execution of cloud computing and the characteristics of distributed access.

In order to facilitate the expression, the related concepts are expressed as follows.

Users set $U = \{u_1, u_2, \ldots u_m\}$, ($m \in N$, N is natural number set), represents the subjects of the initiate, in cloud computing environment users can be businesses, individuals or other services that apply for the cloud services.

upload() represents the operation of upload.
identity() represents the operation of identification.
grant() represents the operation of authorization.
bool() represents the Boolean function.
$\rightarrow$ represents the process of implementing related operations.
ob represents objects.
ow represents objects owners.
cs represents cloud services servers.

3.2 Architecture of CT-RBAC

The TBAC model is usually divided into high, medium and low three security levels according to the security requirements of the task. The RBAC model is also divided into high, medium and low three grades according to different roles. Whether tasks or roles, their ultimately security requirement is the object security attributes. So in order to make up for this deficiency, it is necessary to give an initial sensitive level to all objects. This value should be set by the owner of the object.

Here we divide the sensitive level of object into four grades, they are open access object, part shared object, limited shared object and the exclusive object, their sensitive level are st_1, st_2, st_3, st_4, let sensitivity set $St = \{st_1, st_2, st_3, st_4\}$, to represent the degree of resource sharing. st_4 corresponds to the open access objects, who can be accessed without the consent of the object owner. st_3 corresponds to the part shared objects, this kind of object is open or shared to certain types of objects, so its access control requires only the consideration of how to define the scope of the group and identify its members. Because this part of the object is large and commonly used, if all them are authorized by the object owner, it will inevitably lead to frequent interaction and low access efficiency, so, this type of object can be authorized by the agency, The access control authority can be done by cloud service provider's proxy servers instead of objects owners, this will reduce the authorized interactions, improve authorization efficiency, the objects owners only need to set the filtering conditions, this strategy can reduce the switching frequency of interaction, improve the efficiency of management. st_2 corresponds to limited shared

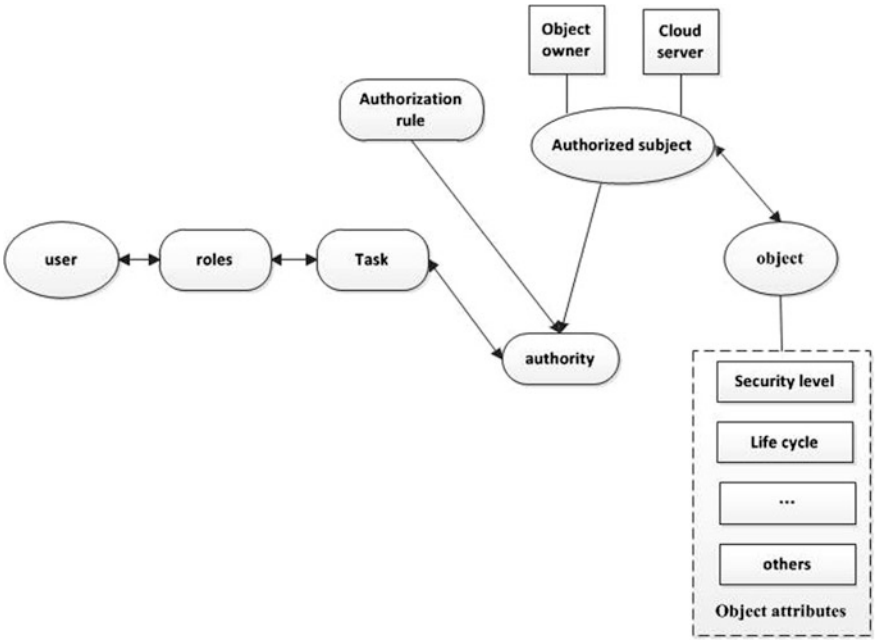

Fig. 1 CT-RBAC model structure diagram

objects which occupied by their owners only at first, not shared by a group, any applying for sharing must get the owner's authority, and the authority can not be transmitted by the authorized users, the authorization is not transitive. st_1 corresponds to the exclusive object, the object is a private information that is only required to be exclusive and will not be authorized to anyone. So any shared request is illegal except its owner.

CT-RBAC model adds the initial object security level and the authorization policy of authorized agent on the basis of the T-RBAC model, the model structure is shown in Fig. 1.

The implementation of the CT-RBAC model can be described as:

Step 1 the user sends an access request.
Step 2 the cloud server identifies the highest security level of the object in the requested task and matches the request role level, if matched, authorizes the request by the authorization policy, otherwise, submits the request to the object owner to determine whether authorized.
Step 3 create tasks, allocate resources.
Step 4 record the life cycle of the task, realize the object access.
Step 5 determine whether the task is over and recycle related resources and permissions.

There are two issues that need to be focused on in the model, one is the classification of the security level of the object and the proxy authorization strategy, and the other is the authorization transfer problem.

First, we discuss the classification of the security level of the object and the proxy authorization strategy.

The process can be described as:

1. The object owner uploads resources to the cloud server.

$$upload(ob_{ow}) \rightarrow cs$$

2. The cloud server identifies whether the object owner has marked the object sensitivity.

$$identify(ob) = value_{st}, (value_{st} \in \{st_1, st_2, st_3, st_4, \phi\})$$

3. If $value_{st} \neq \phi$, According to the value of $st_i, i = \{1, 2, 3, 4\}$ cloud server stores them correspondingly, those high sensitivity data should be blocked, marked, and encrypted.
4. If $value_{st} = \phi$, the cloud server asks the object owner to give a sensitivity level to the object, and then jump to step 2 to rejudge, if the sensitivity level has been given, process it in accordance with step 3, otherwise skip to step 5.
5. If the object owner ignores the hint and continues to upload the object to the cloud server, then assign a default value st_3 to the object. The reason is that the object owner ignore the reminder shows that there is not much sensitive information contained in the object, but from the view of resource protection, we should limit the scope of access. If a user access request is higher than the cloud server authorization level, the cloud server can submit the request to the object owner to determine whether to authorize. The object owner has the rights to change the sensitivity level of the object.

Now, the object has the original sensitivity attributes, then the user involves an efficiency issues in the following authorization strategy. The authorization strategy is as following.

The object with sensitivity level st_1 does not set other user access rights, its permissions can not be passed.

$$bool(grant(ob)) = false, \text{if } u_{ob} \neq ow_{ob}, u \in U$$

The object with sensitivity level st_2 is authorized by the object owner, and the authorization is not transitive

$$bool(ow \rightarrow grant(u_i)) = true$$
$$bool(u_i \rightarrow grant(u_j)) = false, u_i, u_j \in U, (i \neq j)$$

The object with sensitivity level st_3 is authorized by the cloud server agent, and the members of the group can pass the authorization.

$$
\begin{aligned}
&bool(ow \rightarrow grant(u_i)) = false,\\
&bool(ow \rightarrow grant(cs)) = true,\\
&bool(cs \rightarrow grant(u_i)) = true\\
&bool(u_i \rightarrow grant(u_j)) = false, u_i, u_j \in U, (i \neq j),
\end{aligned}
$$

The object with sensitivity level st_4 is authorized by the cloud server agent and the authorization can be passed.

$$
\begin{aligned}
&bool(ow \rightarrow grant(u_i)) = false,\\
&bool(ow \rightarrow grant(cs)) = true,\\
&bool(cs \rightarrow grant(u_i)) = true\\
&bool(u_i \rightarrow grant(u_j)) = true, u_i, u_j \in U, (i \neq j),
\end{aligned}
$$

This process is shown in Fig. 2.

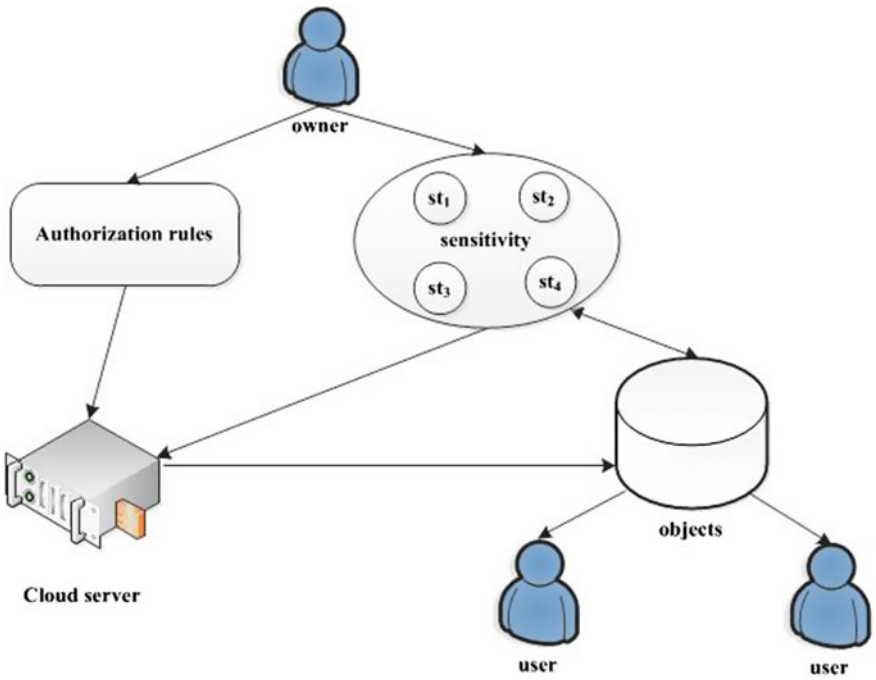

Fig. 2 Authorization policy diagram

4 Conclusion

Based on the T-RBAC model, the object owner has divided the sensitivity level related to the object, in order to avoid the security level change caused by data transfer or storage location change, the CT-RBAC formulates the authorization rules between the object owner and the cloud server. It realizes the combination of cloud server proxy authorization and the object owner authorization to those high sensitivity information. It also improves the efficiency and security of access control, realizes the fine grained access control.

References

1. Jiang Z-W, Zhao W-R, Liu Y, Liu B-X (2013) Model for cloud computing security assessment based on classified protection. Comput Sci 40(8):151–156 (in Chinese)
2. Xin Chen, Wang X-H, Huang H (2009) Research on multi-attribute information security risk assessment method based on threat analysis. Comput Eng Design 30(1):38–41 (in Chinese)
3. Fan J, Xue Y (2010) Information security risk assessment method based on traffic and classified protection. Comput Digital Eng 38(3):112–115 (in Chinese)
4. Yang H, Fong S (2013) Countering the Concept-drift Problem in Big Data Using iOVFDT. IEEE Int Congr Big Data 2013:126–132
5. Wang Y-D, Yang J-H, Xu C, Ling X, Yang Y (2015) Survey on access control technologies for cloud computing. Journal of Software 26(5):1129–1150 (in Chinese)
6. Hong C, Zhang M, Feng DG (2010) AB-ACCS: a cryptographic access control scheme for cloud storage. J Comput Res Dev 47:259–265
7. Li W-G, Zhao F-Yu (2013) RBAC permission access control model with attribute policy. J Chin Comput Syst 34(2):328–331
8. Li F-H, Su M, Shi G-Z, Ma J-F (2012) Research status and development trends of access control model. Acta Electronica Sinica 40(4):805–813 (in Chinese)
9. Wang X-W, Zhao Y-M (2012) A task-role-based access control model for cloud computing. Comput Eng 38(24):9–13 (in Chinese)
10. Yi H, Li K-L (2013) Model of cloud computing oriented T-RBAC. Application Research of Computers 30(12):3735–3737 (in Chinese)

Finite-Time Sliding Mode Control for Fractional-Order Gyroscope Systems with Unknown Parameters and Nonlinear Inputs

Xiaomin Tian and Zhong Yang

1 Introduction

Although fractional calculus is a mathematical topic with more than 300 years history, its application to physics and engineering has attracted lots of attention only in the recent years. It was found that, with the help of fractional calculus, many systems in interdisciplinary fields can be described more accurately, such as viscoelastic system [1], dielectric polarization [2], electrode-electrolyte polarization [3], finance systems and electromagnetic waves [4]. That is to say, fractional derivatives provide a superb instrument for the description of memory and hereditary properties of various materials and processes.

The gyroscope system is one of the most intriguing nonlinear systems, which has been widely studied by many researchers. Gyroscope has been applied in many fields, such as navigation, optics, aeronautical and space engineering, etc. Different types of gyro systems with linear or nonlinear damping properties has been found in recent research, these gyro systems can present rich dynamic behaviour such as sub-harmonic and chaotic motions [5]. There are many methods have been reported in synchronizing two gyroscope systems. For example, Yan [6] applied sliding mode control approach to realize the generalized projective synchronization of two gyroscope systems. Lei et al. [7] developed an active control scheme to synchronize two identical gyroscope systems. Recently, Aghababa [8, 9] investigated the problem of finite-time stabilizing/synchronizing gyroscope systems.

However, almost all of the aforementioned works have focus on the synchronization of two integer-order gyroscope systems, while, the control of fractional-order gyroscope system has been rarely involved so far. At present, input nonlinearity phenomenon is often encountered in many engineering systems, which

X. Tian (✉) · Z. Yang
Institute of Intelligence Science and Control Engineering,
Jinling Institute of Technology, Nanjing 211169, China
e-mail: tianxiaomin100@163.com

Z. Deng (ed.), *Proceedings of 2017 Chinese Intelligent Automation Conference*,
Lecture Notes in Electrical Engineering 458,
https://doi.org/10.1007/978-981-10-6445-6_37

can cause unpredictable and undesirable motion in chaotic systems. So, it is urgent to consider the effects of nonlinear inputs in analysing and implementing the synchronization control scheme. However, to the best of our knowledge, the problem of finite-time synchronizing two fractional-order gyroscope systems with unknown parameters and nonlinear inputs has not been researched so far.

The goal of this paper is to design a robust sliding mode controller to synchronize two fractional-order gyroscope systems with nonlinear inputs in finite time. The parameters of both master and slave systems are assumed to be unknown in advance. To deal with these unknown parameters, some adaption laws are proposed.

2 Preliminaries

2.1 Definitions and Lemmas

The Riemann-Liouville is one of the main definitions of fractional calculus.

Definition 1 For $n-1<\alpha\leq n$, $n\in R$, the Riemann-Liouville fractional derivative of order α of the function $f(t)$ is defined as

$$ {}_{t_0}D_t^{\alpha}f(t)=\frac{d^{\alpha}f(t)}{dt^{\alpha}}=\frac{1}{\Gamma(n-\alpha)}\frac{d^n}{dt^n}\int_{t_0}^{t}\frac{f(\tau)}{(t-\tau)^{\alpha-n+1}}d\tau=\frac{d^n}{dt^n}I^{n-\alpha}f(t) \tag{1}$$

Lemma 1 (see [10]). *Consider the system*

$$ \dot{x}(t)=f(x(t)),\quad f(0)=0,\ x(t)\in R^n \tag{2}$$

where $f:D\rightarrow R^n$ is continuous on an open neighborhood $D\subset R^n$. Suppose there exists a continuous differential positive definite function $V(x(t)):D\rightarrow R$, real numbers $p>0$, $0<\eta<1$, such that

$$ \dot{V}(x)+pV^{\eta}(x)\leq 0,\quad \forall x(t)\in D \tag{3}$$

Then the origin of system (2) is a locally finite time stable equilibrium, and the settling time, depending on the initial state $x(0)=x_0$, satisfies $T(x_0)=\frac{V^{1-\eta}(x_0)}{p(1-\eta)}$. In addition, if $D=R^n$ and $V(x(t))$ is also radially unbounded, then the origin is a globally finite time stable equilibrium of system (2).

Property 1 (see [11]) *For the Riemann-Liouville derivative, we have*

$$ {}_{t_0}D_t^{-\alpha}\left({}_{t_0}D_t^{\beta}f(t)\right)={}_{t_0}D_t^{\beta-\alpha}f(t)-\sum_{j=1}^{m}\left[{}_{t_0}D_t^{\beta-j}f(t)\right]|_{t=t_0}\frac{(t-t_0)^{\alpha-j}}{\Gamma(1+\alpha-j)} \tag{4}$$

where $m-1\leq\beta<m$.

2.2 Fractional-Order Model of Gyroscope System

A typical symmetric gyroscope system, mounted on a vibrating base is presented in Fig. 1.

The angle θ (nutation), ϕ (precess) and φ (spin) can be used to describe the system's motion. The multiple harmonic motions $\sum_{i=1}^{n} A_k \sin \omega t \sin x$ can be used to describe the vibration motion. Through letting $x_1 = \theta$, $x_2 = \dot{\theta}$, $x_3 = \phi$, we can get the system dynamic equation as follows.

$$\begin{aligned}
\dot{x}1 &= x2 \\
\dot{x}2 &= -\frac{(\beta_\phi - \beta_\varphi \cos x_1)(\beta_\varphi - \beta_\phi \cos x_1)}{I_1^2 \sin^3 x_1} - \frac{C}{I_1} x_2 \\
&\quad + \frac{Mgl}{I_1} \sin x_1 - \frac{Mg}{I_1} \sum_{k=1}^{n} A_k \sin \omega_k t \sin x_1 \\
\dot{x}3 &= -\frac{B \cos x_1}{\sin x_1} x_2 x_3 + \frac{\beta_\varphi x_2}{I_1 \sin x_1}
\end{aligned} \tag{5}$$

where I_1 represents the moment of inertia of the gyroscope systems, Mg is the gravity, l is the distance between orthocenter and the origin O. If the only first term is considered for the harmonic motion in the system (5), and set $A_1 = A$, then the normalized fractional-order model of gyroscope system is shown as follows

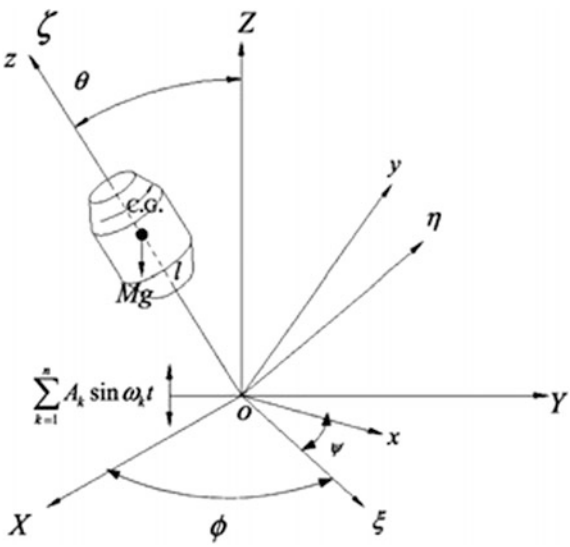

Fig. 1 The schematic diagram of a heavy symmetric gyroscope system

$$\begin{aligned} D^{\alpha}x_1 &= x_2 \\ D^{\alpha}x_2 &= -\frac{\left(\beta_{\phi}-\beta_{\varphi}\cos x_1\right)\left(\beta_{\varphi}-\beta_{\phi}\cos x_1\right)}{I_1^2\sin^3 x_1}-\frac{C}{I_1}x_2+\frac{Mgl}{I_1}\sin x_1 \\ &\quad -\frac{Mg}{I_1}\sum_{k=1}^{n}A_k\sin\omega_k t\sin x_1 \\ D^{\alpha}x_3 &= -\frac{B\cos x_1}{\sin x_1}x_2x_3+\frac{\beta_{\varphi}x_2}{I_1\sin x_1} \end{aligned} \tag{6}$$

where $\alpha \in (0,1)$ is the fractional order of system (6), $\mathrm{X}=[x_1,x_2,x_3]^T$ is the state vector of the system.

3 Main Results

In this section, on the basis of SMC approach, the problem of finite-time synchronizing two chaotic gyroscope systems with identical unknown parameters and nonlinear inputs is solved.

We take the system (6) as master system, and the slave system is described as follows

$$\begin{aligned} D^{\alpha}y_1 &= y_2+h_1(u_1(\mathrm{t})) \\ D^{\alpha}y_2 &= -\frac{\left(\beta_{\phi}-\beta_{\varphi}\cos y_1\right)\left(\beta_{\varphi}-\beta_{\phi}\cos y_1\right)}{I_1^2\sin^3 y_1}-\frac{C}{I_1}y_2+\frac{Mgl}{I_1}\sin y_1 \\ &\quad -\frac{Mg}{I_1}\sum_{k=1}^{n}A_k\sin\omega_k t\sin y_1+h_2(u_2(\mathrm{t})) \\ D^{\alpha}y_3 &= -\frac{B\cos y_1}{\sin y_1}y_2y_3+\frac{\beta_{\varphi}y_2}{I_1\sin y_1}+h_3(u_3(\mathrm{t})) \end{aligned} \tag{7}$$

where $\mathrm{Y}=[y_1,y_2,y_3]^T$ is the state vector of the slave system, $\mathrm{u(t)}=[u_1(t),u_2(t),u_3(t)]^T$ is the vector of inputs will be designed later, $h_i(u_i(t))$, i = 1, 2, 3 is continuous function inside the sector $[\rho_{i1},\rho_{i2}]$, $\rho_{i1}>0$, i.e.

$$\rho_{i1}u_i^2(t)\le u_i(t)h_i(u_i(t))\le\rho_{i2}u_i^2(t) \tag{8}$$

the presented nonlinear function of input in (8) is called sector nonlinear input.

Our goal in this section is that design a sliding mode controller to realize the finite-time synchronization between system (6) and (7) with identical unknown parameters and sector nonlinear inputs $h_i(u_i(t))$, i = 1, 2, 3. So-called finite-time

synchronization means that if there exist a constant T > 0, such that $\lim_{t\to T}||E|| = 0$ and $||E|| \equiv 0$ for $t \geq$ T, where E = Y − X is the synchronization error, $||\cdot||$ represents the Euclidean norm in R^n, then the chaos synchronization is realized in a given finite time.

Subtracting Eq. (6) from Eq. (7), we can get the synchronization error system as follows

$$\begin{aligned}
D^{\alpha}e_1 &= e_2 + h_1(u_1(\mathrm{t})) \\
D^{\alpha}e_2 &= -\frac{\beta_\phi\beta_\varphi}{I_1^2}\left(\frac{1+\cos^2 y_1}{\sin^3 y_1} - \frac{1+\cos^2 x_1}{\sin^3 x_1}\right) + \frac{\beta_\phi^2+\beta_\varphi^2}{I_1^2}\left(\frac{\cos y_1}{\sin^3 y_1} - \frac{\cos x_1}{\sin^3 x_1}\right) \\
&\quad - \frac{C}{I_1}e_2 + \frac{Mgl}{I_1}(\sin y_1 - \sin x_1) - \frac{Mg}{I_1}A\sin \omega t(\sin y_1 - \sin x_1) + h_2(u_2(\mathrm{t})) \\
D^{\alpha}e_3 &= -B\left(\frac{\cos y_1}{\sin y_1}y_2y_3 - \frac{\cos x_1}{\sin x_1}x_2x_3\right) + \frac{\beta_\varphi}{I_1}\left(\frac{y_2}{\sin y_1} - \frac{x_2}{\sin x_1}\right) + h_3(u_3(\mathrm{t}))
\end{aligned} \tag{9}$$

where $\mathrm{E} = [e_1, e_2, e_3]^T$ is the state vector of system (9). It is clear that the problem of finite-time synchronization between system (6) and system (7) is transformed to the equivalent problem of finite-time stabilizing the synchronization error system (9). Before introduce our method, we first give an assumption.

Assumption 1 We assume that the parameters β_ϕ, β_φ, I_1, Mg, l, C, ω, A and B are unknown in advance. Letting $\psi_1 = \left[\frac{\beta_\phi\beta_\varphi}{I_1^2}, \frac{\beta_\phi^2+\beta_\varphi^2}{I_1^2}, \frac{C}{I_1}, \frac{Mgl}{I_1}, \frac{Mg}{I_1}A\right]^T = [b_1, b_2, b_3, b_4, b_5]^T$, $\psi_2 = \left[B, \frac{\beta_\varphi}{I_1}\right]^T = [b_6, b_7]^T$ as the unknown vector parameters for the second, third equations of error system (9), respectively.

Generally, two steps are involved in design the sliding mode controller. The first step is to construct a proper sliding surface with desired dynamics. The second step is to determine a controller to ensure the occurrence of the sliding motion. In this paper, we propose a novel fractional-order integral type sliding surface as follows

$$s_i = D^{\alpha-1}|e_i| + \eta_i^a D^{\alpha-1}e_i + \eta_i^b \int_0^t (e_i + sgn(e_i))d\tau, \quad \mathrm{i} = 1, 2, 3 \tag{10}$$

where $\eta_i^a > 1$, $\eta_i^b > 0$, i = 1, 2, 3 are arbitrary constants.

When the system trajectories operate in the sliding mode, the following equations are satisfied

$$s_i = 0, \quad \dot{s}_i = 0 \tag{11}$$

Taking the time derivative of the fractional-order sliding surface (15), we obtain the desired sliding dynamics.

$$\dot{s}_i = D^{\alpha}|e_i| + \eta_i^a D^{\alpha} e_i + \eta_i^b (e_i + sgn(e_i)) \tag{12}$$

that is

$$D^{\alpha} e_i = -\frac{\eta_i^b (e_i + sgn(e_i))}{sgn(e_i) + \eta_i^a} \tag{13}$$

Theorem 1 *Consider the sliding mode dynamics* (13)*, the system is stable and the state trajectories converge to zero in a given finite time.*

Proof First, according to the Ref. [12], we can assume that the following inequality holds.

$$\left| \sum_{k=1}^{\infty} \frac{\Gamma(1+\alpha)}{\Gamma(1+k)\Gamma(1-k+\alpha)} D^k e_i D^{\alpha-k} e_i \right| \leq \xi_i |e_i| \tag{14}$$

where ξ_i is a positive constant.

Choosing the following Lyapunov function for system (13)

$$V_{i1}(t) = e_i^2 \tag{15}$$

it is obvious that $V_{i1}(t)$ is positive definite. Motivated by the Ref. [12], we taking α order fractional derivative from both sides of (15), one has

$$D^{\alpha} V_{i1}(t) = e_i D^{\alpha} e_i + \sum_{k=1}^{\infty} \frac{\Gamma(1+\alpha)}{\Gamma(1+k)\Gamma(1-k+\alpha)} D^k e_i D^{\alpha-k} e_i \tag{16}$$

it follows easily that

$$D^{\alpha} V_{i1}(t) \leq e_i D^{\alpha} e_i + \left| \sum_{k=1}^{\infty} \frac{\Gamma(1+\alpha)}{\Gamma(1+k)\Gamma(1-k+\alpha)} D^k e_i D^{\alpha-k} e_i \right| \tag{17}$$

substituting Eq. (14) into Eq. (17), one has

$$D^{\alpha} V_{i1}(t) \leq e_i D^{\alpha} e_i + \xi_i |e_i| \tag{18}$$

inserting Eq. (13) into Eq. (18), we have

$$D^{\alpha} V_{i1}(t) \leq e_i \left(-\frac{\eta_i^b}{sgn(e_i) + \eta_i^a} (e_i + sgn(e_i)) \right) + \xi_i |e_i| \tag{19}$$

according to $\mathrm{sgn}(e_i) \cdot e_i = |e_i|$, then

$$D^{\alpha}V_{i1}(t) \leq -l_i\left(e_i^2 + |e_i|\right) + \xi_i|e_i| \leq -(l_i - \xi_i)|e_i| \tag{20}$$

where $l_i = \frac{\eta_i^b}{sgn(e_i)+\eta_i^a}$, and satisfying $l_i > \xi_i$. According to Lemma 1, the states will converge to $e_i = 0$ asymptotically. Next, we will prove that the convergence process will finished in finite time. In other words, e_i will converge to origin in a given time.

Taking α order fractional integral of both sides of (20) from t_r to t_s, where t_r is the time of e_i reach to the sliding surface $s_i = 0$, and letting $e_i(t_s) = 0$, using the Property 1, the following inequality is holds

$$V_{i1}(t_s) - D^{\alpha-1}V_{i1}(t)|_{t=t_r}\frac{(t_s - t_r)^{\alpha-1}}{\Gamma(\alpha)} \leq -(l_i - \xi_i)D^{-\alpha}|e_i| \tag{21}$$

according to Definition 1, we can find a positive constant M_i such that $D^{-\alpha}|e_i| \geq M_i$, since $e_i(t_s) = 0$, so we have $V_{i1}(t_s) = 0$, and

$$-D^{\alpha-1}V_{i1}(t_r)\frac{(t_s - t_r)^{\alpha-1}}{\Gamma(\alpha)} \leq -(l_i - \xi_i)M_i \tag{22}$$

Through simple derivation, we can get

$$(t_s - t_r)^{\alpha-1} \geq \frac{\Gamma(\alpha)(l_i - \xi_i)M_i}{D^{\alpha-1}V_{i1}(t_r)} \tag{23}$$

further, we have

$$t_s \leq \left(\frac{D^{\alpha-1}V_{i1}(t_r)}{\Gamma(\alpha)(l_i - \xi_i)M_i}\right)^{\frac{1}{1-\alpha}} + t_r \tag{24}$$

It is obvious that e_i will converge to zero in a given time $t_s \leq \left(\frac{D^{\alpha-1}e_i^2(t_r)}{\Gamma(\alpha)(l_i-\xi_i)M_i}\right)^{\frac{1}{1-\alpha}} + t_r$, i = 1, 2, 3. Thus, the proof is completed.

Once the appropriate sliding surface has been designed, next, we will propose a control law to steer the state trajectories of the error system (9) onto the sliding surface (10) in finite time and stay on it forever. The proposed control law has the following form

$$u_i(t) = -\gamma_i\zeta_i\delta_i^{-1}sgn(s_i) \tag{25}$$

where $\gamma_i = \rho_{i1}^{-1}$ and

$$\begin{aligned}
\zeta_1 &= \delta_2|e_2| + m\left(\left\|\widetilde{\psi_1}\right\| + \left\|\widetilde{\psi_2}\right\|\right)\frac{|s_1|}{\|S\|^2} + |\Delta_1| + k_1 \\
\zeta_2 &= m\left(\left\|\widetilde{\psi_1}\right\| + \left\|\widetilde{\psi_2}\right\|\right)\frac{|s_2|}{\|S\|^2} + \delta_2\left(\left|\widehat{b_1}\right|\left|\frac{1+\cos^2 y_1}{\sin^3 y_1} - \frac{1+\cos^2 x_1}{\sin^3 x_1}\right| + \left|\widehat{b_2}\right|\left|\frac{\cos y_1}{\sin^3 y_1}\right.\right. \\
&\quad \left.\left. - \frac{\cos x_1}{\sin^3 x_1}\right| + \left|\widehat{b_3}\right||e_2| + \left|\widehat{b_4}\right||\sin y_1 - \sin x_1| + \left|\widehat{b_5}\right||\sin y_1 - \sin x_1|\right) + |\Delta_2| + k_2 \\
\zeta_3 &= m\left(\left\|\widetilde{\psi_1}\right\| + \left\|\widetilde{\psi_2}\right\|\right)\frac{|s_3|}{\|S\|^2} + \delta_3\left(\left|\widehat{b_6}\right|\left|\frac{\cos y_1}{\sin y_1}y_2y_3 - \frac{\cos x_1}{\sin x_1}x_2x_3\right|\right. \\
&\quad \left. + \left|\widehat{b_7}\right|\left|\frac{y_2}{\sin y_1} - \frac{x_2}{\sin x_1}\right| + |\Delta_3| + k_3\right)
\end{aligned} \tag{26}$$

where $\delta_i = \left(sgn(e_i) + \eta_i^a\right) > 0$, $\Delta_i = \eta_i^b(e_i + sgn(e_i))$, $k_i > 0$, m = min{k_i}, i = 1, 2, 3. $S = [s_1, s_2, s_3]^T$, $\widetilde{\psi_1} = \widehat{\psi_1} - \psi_1$, $\widetilde{\psi_2} = \widehat{\psi_2} - \psi_2$, $\widehat{\psi_1} = \left[\widehat{b_1}, \widehat{b_2}, \widehat{b_3}, \widehat{b_4}, b_5\right]^T$ and $\widehat{\psi_2} = \left[\widehat{b_6}, \widehat{b_7}\right]^T$ are the estimations for unknown parameters ψ_1 and ψ_2, respectively, if ‖S‖ = 0, then $\frac{|s_i|}{\|S\|^2} = 0$. Subsequently, the appropriate adaption laws are given to deal with the unknown vector parameters ψ_1, ψ_2

$$\begin{aligned}
\dot{\widehat{\psi_1}} &= \left[-\left(\frac{1+\cos^2 y_1}{\sin^3 y_1} - \frac{1+\cos^2 x_1}{\sin^3 x_1}\right)\delta_2 s_2, \left(\frac{\cos y_1}{\sin^3 y_1} - \frac{\cos x_1}{\sin^3 x_1}\right)\delta_2 s_2,\right. \\
&\quad \left. - e_2\delta_2 s_2, (\sin y_1 - \sin x_1)\delta_2 s_2, |\sin y_1 - \sin x_1||\delta_2 s_2|\right]^T \\
\dot{\widehat{\psi_2}} &= \left[-\left(\frac{\cos y_1}{\sin y_1}y_2y_3 - \frac{\cos x_1}{\sin x_1}x_2x_3\right)\delta_3 s_3, \left(\frac{y_2}{\sin y_1} - \frac{x_2}{\sin x_1}\right)\delta_3 s_3\right]^T
\end{aligned} \tag{27}$$

Theorem 2 *Consider the error system* (9) *with unknown parameters and sector nonlinear inputs. If the system is controlled by the control law* (25) *and the adaption law* (27)*, then the state trajectories of the system* (9) *will converge to S = 0 in a finite time.*

Proof Choosing a Lyapunov function in the following form

$$V_2(t) = \frac{1}{2}\left(||S||_2^2 + \left\|\widetilde{\psi_1}\right\|_2^2 + \left\|\widetilde{\psi_2}\right\|_2^2\right) \tag{28}$$

taking the time derivative of both sides of Eq. (28), we have

$$\dot{V}_2(t) = \sum_{i=1}^{n} s_i \dot{s}_i + \left(\widehat{\psi_1} - \psi_1\right)^T \dot{\widehat{\psi_1}} + \left(\widehat{\psi_2} - \psi_2\right)^T \dot{\widehat{\psi_2}} \tag{29}$$

inserting $\dot{s}_i$ from Eq. (12) into Eq. (29), it yields

$$\dot{V}_2(t) = \sum_{i=1}^{n} s_i \left[\delta_i D^{\alpha} e_i + \eta_i^b (e_i + sgn(e_i))\right] + \left(\widehat{\psi_1} - \psi_1\right)^T \dot{\widehat{\psi_1}} + \left(\widehat{\psi_2} - \psi_2\right)^T \dot{\widehat{\psi_2}} \tag{30}$$

substituting $D^{\alpha} e_i$ from Eq. (9) into above equation, and noting that all parameters of the gyroscope system are all positive, we have

$$\begin{aligned}
\dot{V}_2(t) \le\ & \delta_1 |s_1||e_2| + |s_1||\Delta_1| + \delta_1 s_1 h_1(u_1) + s_2\delta_2 \left(-b_1 \left(\frac{1+\cos^2 y_1}{\sin^3 y_1} - \frac{1+\cos^2 x_1}{\sin^3 x_1}\right)\right. \\
& \left. + b_2 \left(\frac{\cos y_1}{\sin^3 y_1} - \frac{\cos x_1}{\sin^3 x_1}\right) - b_3 e_2 + b_4(\sin y_1 - \sin x_1)\right) \\
& + \delta_2 b_5 |s_2||\sin y_1 - \sin x_1| + |s_2||\Delta_2| + \delta_2 s_2 h_2(u_2) \\
& + s_3\delta_3 \left(-b_6 \left(\frac{\cos y_1}{\sin y_1} y_2 y_3 - \frac{\cos x_1}{\sin x_1} x_2 x_3\right) + b_7 \left(\frac{y_2}{\sin y_1} - \frac{x_2}{\sin x_1}\right)\right) \\
& + \delta_3 s_3 h_3(u_3) + |s_3||\Delta_3| + \left(\widehat{\psi_1} - \psi_1\right)^T \dot{\widehat{\psi_1}} + \left(\widehat{\psi_2} - \psi_2\right)^T \dot{\widehat{\psi_2}}
\end{aligned} \tag{31}$$

according to the adaption law (27), we know that

$$\begin{aligned}
\psi_1^T \dot{\widehat{\psi_1}} &= s_2\delta_2 \left[-b_1 \left(\frac{1+\cos^2 y_1}{\sin^3 y_1} - \frac{1+\cos^2 x_1}{\sin^3 x_1}\right) + b_2 \left(\frac{\cos y_1}{\sin^3 y_1} - \frac{\cos x_1}{\sin^3 x_1}\right)\right. \\
&\quad \left. - b_3 e_2 + b_4(\sin y_1 - \sin x_1)\right] + \delta_2 b_5 |s_2||\sin y_1 - \sin x_1| \\
\psi_2^T \dot{\widehat{\psi_2}} &= s_3\delta_3 \left[-b_6 \left(\frac{\cos y_1}{\sin y_1} y_2 y_3 - \frac{\cos x_1}{\sin x_1} x_2 x_3\right) + b_7 \left(\frac{y_2}{\sin y_1} - \frac{x_2}{\sin x_1}\right)\right]
\end{aligned} \tag{32}$$

so, Eq. (31) can be rewritten as follow

$$\begin{aligned}
\dot{V}_2(t) \le\ & \delta_1 |s_1||e_2| + |s_1||\Delta_1| + \delta_1 s_1 h_1(u_1) + |s_2||\Delta_2| + \delta_2 s_2 h_2(u_2) \\
& + |s_3||\Delta_3| + \delta_3 s_3 h_3(u_3) + \left|\widehat{\psi_1}\right|^T \left|\dot{\widehat{\psi_1}}\right| + \left|\widehat{\psi_2}\right|^T \left|\dot{\widehat{\psi_2}}\right|
\end{aligned} \tag{33}$$

surveying (8) and (25), it is clear that

$$u_i h_i(u_i) = -\gamma_i \zeta_i \delta_i^{-1} sgn(s_i) h_i(u_i) \geq \rho_{i1} \gamma_i^2 \zeta_i^2 \delta_i^{-2} sgn^2(s_i) \tag{34}$$

since $\gamma_i = \rho_{i1}^{-1}$, $\zeta_i > 0$, $\delta_i > 0$, according to above inequality, we have

$$-\text{sgn}(s_i) h_i(u_i) \geq \zeta_i \delta_i^{-1} sgn^2(s_i) \tag{35}$$

multiply both sides of inequality (35) by $\delta_i |s_i|$, and according to $sgn^2(s_i) = 1$, $|s_i| sgn(s_i) = s_i$, we have

$$\delta_i s_i h_i(u_i) \leq -\zeta_i |s_i| \tag{36}$$

Substituting the inequality (36) into (35), it yields

$$\begin{aligned} \dot{V}_2(t) \leq\ & |s_1|(\delta_1 |e_2| + |\Delta_1| - \zeta_1) + |s_2|(|\Delta_2| - \zeta_2) + |s_3|(|\Delta_3| - \zeta_3) \\ & + \left|\widehat{\psi}_1\right|^T \left|\dot{\widehat{\psi}}_1\right| + \left|\widehat{\psi}_2\right|^T \left|\dot{\widehat{\psi}}_2\right| \end{aligned} \tag{37}$$

using the adaption law (27), we have

$$\begin{aligned} \dot{V}_2(t) &\leq -k_1 |s_1| - k_2 |s_2| - k_3 |s_3| - m\left(\left|\left|\widetilde{\psi}_1\right|\right| + \left|\left|\widetilde{\psi}_2\right|\right|\right) \\ &\leq -m\left(|s_1| + |s_2| + |s_3| + \left|\left|\widetilde{\psi}_1\right|\right| + \left|\left|\widetilde{\psi}_2\right|\right|\right) \end{aligned} \tag{38}$$

according to the fact that a_1, a_2, …, $a_n \in R$, the inequality $(|a_1| + |a_2| + \cdots + |a_n|) \geq \left(|a_1|^2 + |a_2|^2 + \cdots + |a_n|^2\right)^{1/2}$ still holds, we get

$$\dot{V}_2(t) \leq -\sqrt{2} m \left(\frac{1}{2}\left(||S||^2 + \left|\left|\widetilde{\psi}_1\right|\right|^2 + \left|\left|\widetilde{\psi}_2\right|\right|^2\right)\right)^{\frac{1}{2}} = -\sqrt{2} m V_2^{\frac{1}{2}}(t) \tag{39}$$

Based on Lemma 1, we can conclude that the state trajectories of system (9) will converge to S = 0 in a given finite time $t = \frac{\sqrt{2}}{m}\left(\frac{1}{2}\left(||S(0)||^2 + \left|\left|\widehat{\psi}_1(0) - \psi_1\right|\right|^2 + \left|\left|\widehat{\psi}_2(0) - \psi_2\right|\right|^2\right)\right)^{1/2}$. Hence, the proof is finished.

4 Simulation Examples

In this section, an example is given to verify the effectiveness and applicability of the proposed finite-time SMC scheme.

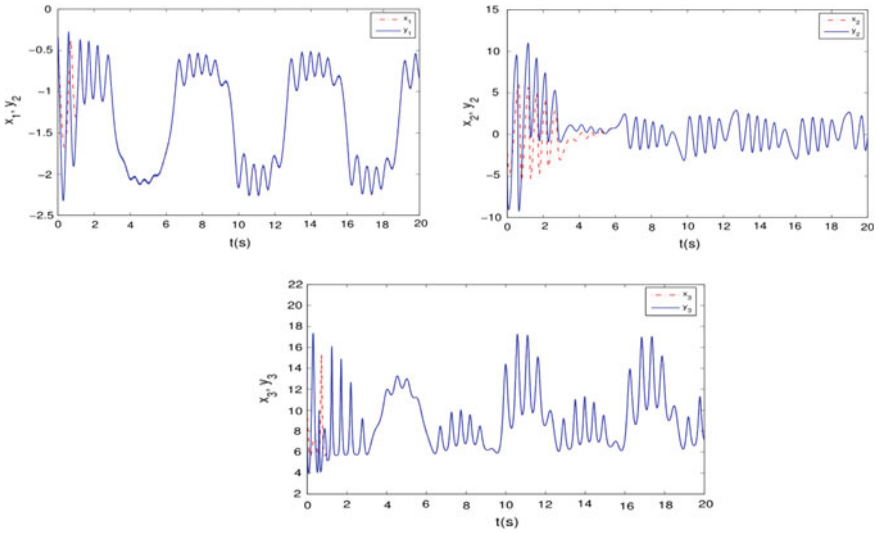

Fig. 2 Time responses of the master (6) and slave (7) systems

In this simulation, let $\alpha = 0.998$, the initial values of the master and slave systems are selected as $X(0) = [-0.5, -1.3, -10]^T$,$Y(0) = [-0.3, -2, 8]^T$, the constants $\eta_1^a = \eta_2^a = \eta_3^a = 1$, $k_1 = k_2 = k_3 = 1$, all initial conditions of $\widehat{\psi_i}$ are set to 0.5, the sector nonlinearity is defined in

$$h_i(u_i(t)) = [1 + 0.2\sin(u_i(t))]u_i(t)$$

correspondingly, $\rho_{i1} = 0.8$, $\rho_{i2} = 1.2$, $\gamma_i = 5/4$, i = 1, 2, 3. The nominal values of systems' parameters are $\beta_\phi = 2$, $\beta_\varphi = 5$, $I_1 = 1$, Mg = 4, l = 0.25, C = 0.5, ω = 2, A = 12.1 and B = 2. When the controller is activated at t = 1 s, the state trajectories of master (6) and slave (7) systems can be shown in Fig. 2.

In Fig. 2, it can be seen that even though the parameters of both master and slave systems are fully unknown, the state trajectories of the slave system (7) are approach to the state trajectories of the master system (6) in a finite time. These simulation results sufficiently demonstrate that the finite-time SMC scheme is effective in synchronizing two fractional-order gyroscope systems with identical unknown parameters and sector nonlinear inputs.

5 Conclusions

This paper proposed a novel fractional sliding mode control scheme to realize the finite-time synchronization of two gyroscope systems with identical unknown parameters. The effects of nonlinear inputs are taken into account. The finite-time

stability and convergence of the designed controller are proved, and the estimations of convergence time are given. Simulation results verified that the proposed SMC scheme work well in synchronizing two fractional-order gyroscope systems.

Acknowledgements This paper is supported by the funds of Jinling Institute of Technology (Grant No: jit-fhxm-201607 and jit-b-201706), the funds of Jiangsu Province University in Natural Science Research (Grant No: 17KJB120003) and the university-industry collaboration education funds of Ministry of Education (Grant No: 201602009006).

References

1. Bagley RL, Calico RA (1991) Fractional order state equations for the control of viscoelastically damped structure. J Guidance Control Dyn 14:304–311
2. Sun HH, Abdelwahad AA, Oharal B (1984) Linear approximation of transfer function with a pole of fractional power. IEEE Trans Autom Control 29:441–444
3. Ichise M, Nagayanagi Y, Kojima T (1971) An analog simualtion of non-integer order trasfer functions for analysis of electrode process. J Electroanal Chem Interfacial Electrochem 33:253–265
4. Heaviside O (1971) Electromagnetc theory. Cambridge University Press, New York
5. Chen HK (2002) Chaos and chaos synchronization of a symmetric gyro with linear-plus-cubic damping. J Sound Vib 255:719–740
6. Yau H (2007) Nonlinear rule-based controller for chaos synchronization of two gyro with linear-plus-cubic damping. Chaos, Solitons Fractals 34:1357–1365
7. Lei Y, Xu W, Zheng H (2005) Synchronization of two chaotic nonlinear gyros using active control. Phys Lett A 343:153–158
8. Aghababa MP, Aghababa HP (2012) Chaos synchronization of gyroscopes using an adaptive robust finite-time controller. J Mech Sci Technol 27:909–916
9. Aghababa MP, Aghababa HP (2013) The rich dynamics of fractional-order gyros applying a fractional controller. Proc Inst Mech Eng Part I: J Syst Control Eng 227:588–601
10. Bhat SP, Bernstein DS (2000) Finite-time stability of continuous autonomous systems. SIAM J Control Optim 38:751–766
11. Podlubny I (1999) Fractional differential equations. Academic Press, New York
12. Efe MO (2008) Fractional fuzzy adaptive sliding mode control of a 2-DOF direct-drive robot arm. IEEE Trans Syst Man Cybern Part B 28:1561–1570

Tracking Accuracy Research on FLL-Assisted PLL in Ultra-tightly Integrated Navigation System

Shenglan Wang and Yandong Wang

1 Introduction

Using the Inertial Measurement Unit (IMU) output to assist the tracking loop in the satellite navigation system is called ultra-tightly integrated navigation system, which is a hot research topic in domestic and abroad [1]. The autonomy of inertial navigation system (INS) can help Global Position System (GPS) gain better positioning accuracy in high dynamic and high noise conditions. A fundamental task of every GPS carrier loop is to synchronize with the satellite carrier signals. And the synchronization error determines the system operation efficiency.

In order to get data code for further navigation solution, the carrier loops aim to lock the captured signal [2], that is, keep synchronous with signals in frequency or phase. Therefore, carrier loops can be divided into two kinds: PLL to lock phase and FLL to lock frequency. In order to track satellite signals accurately, PLL bandwidth is narrower relatively, which leads to a poor dynamic stress tolerance. In signal-tracking performance, (N − 1)th-order FLL can be equivalent to Nth-order PLL. But FLL is subject to the high bit error ratio in data demodulation [3]. FLL-assisted PLL consists of a PLL and a FLL in a coupled mode, thus it incorporates the advantages of avoiding false locks and reducing locking time. But in high dynamic conditions, tracking ability of carrier loops is still limited [4]. The inertial navigation aid can calculate the Doppler shift in advance by cooperating satellite ephemeris. INS can help GPS reduce dynamic stress error and improve tracking accuracy in the high dynamic and high noise environments [5].

In the previous researches, ultra-tightly integrated navigation system usually use a single PLL alone to track signals. Unfortunately in high-dynamics environments, single PLL is easy to lose signal-locking and not suitable to high dynamic

S. Wang (✉) · Y. Wang
School of Automation Science and Electronic Engineering,
Beihang University, Beijing 100083, China
e-mail: wangshenglan@buaa.edu.cn

Z. Deng (ed.), *Proceedings of 2017 Chinese Intelligent Automation Conference*,
Lecture Notes in Electrical Engineering 458,
https://doi.org/10.1007/978-981-10-6445-6_38

environment [6]. Therefore, this paper proved that it is necessary to introduce the FLL-assisted PLL into ultra-tightly integrated navigation system, and it can improve the precision and reduce the error.

Our work is organized as follows: Sect. 2 analyses the carrier loop error introduced by FLL assistance and IMU assistance respectively. In Sect. 3, we designed the simulation scheme to verify our theory and the results are analyzed. Finally, the conclusions are presented in Sect. 4.

2 Theoretical Analysis of Carrier Loop Error

2.1 Noise Error Model of FLL-Assisted PLL

The closed loop structure of FLL-assisted PLL is shown $F_p(s)$ in Fig. 1. On the one side, the target phase $\theta_k(s)$ goes through the phase discriminator represented as $K_p(s)$ and the PLL filter represented as. On the other side, $\theta_k(s)$ after conversion goes through the frequency discriminator $K_f(s)$ and FLL filter $F_f(s)$. The filters' outputs are used to adjust the numerical control oscillator (NCO), whose transfer function represented as. In these processes, some errors are introduced inevitably. n_p and n_f represent the thermal noise caused by phase discriminator and frequency discriminator respectively; n_{dyn} is the phase vibration error introduced by inertial navigation assistance. The specific calculation is analyzed in the next section.

Based on the loop structure, the formula of phase-tracking error in FLL-assisted PLL is deduced as follows:

$$\begin{aligned}\Delta\theta(s) = \theta(s) &- K_p(s)F_p(s)N(s)[\Delta\theta(s) + n_p] \\ &- K_f(s)F_f(s)N(s)[\Delta\omega(s) + n_f]\end{aligned} \tag{1}$$

where $\Delta\omega(s)$ is the output of frequency discriminator. When the system is steady, the phase error is mainly obtained by frequency, thus $\theta(s) \approx K_f(s)F_f(s)\Delta\omega(s)$, Therefore, the phase error of FLL-assisted PLL can be obtained:

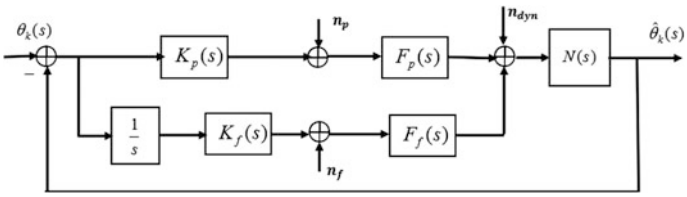

Fig. 1 Closed loop structure of FLL-assisted PLL

$$\Delta\theta(s) \approx -\frac{K_p(s)F_p(s)N(s)}{1+K_p(s)F_p(s)N(s)}n_p - \frac{K_f(s)F_f(s)N(s)}{1+K_f(s)F_f(s)N(s)}n_f \tag{2}$$

The transfer function of the PLL is defined as:

$$H_{PLL}(s) = \frac{K_p(s)F_p(s)N(s)}{1+K_p(s)F_p(s)N(s)} \tag{3}$$

The transfer function of the FLL-assisted PLL is defined as:

$$H_{FLL}(s) = [1 - H_{PLL}(s)]K_f(s)F_f(s)N(s) \tag{4}$$

Then the phase error can be written as:

$$\Delta\theta(s) \approx -H_{PLL}(s)n_p - H_{FLL}(s)n_f \tag{5}$$

2.2 Noise Error Model of Inertial Auxiliary

In the ultra-tight combination, the inertial-navigation-aid is used to estimate the Doppler shift of the current time by the IMU outputs and GPS ephemeris data. It can improve the carrier loop tracking accuracy. Feed-forward mode is used (shown in Fig. 2) which combines the INS measurement and the filter output to feed back the NCO input.

The inertial-aided noise is introduced by Doppler shift, mainly affecting phase vibration error and dynamic stress error of the carrier loop. Here the Doppler frequency auxiliary error is given as δf_d In this case, the phase tracking error with INS auxiliary is calculated as:

$$\delta\varphi(s) = [1 - H(s)] \cdot [\widehat{\theta}_k + \delta\varphi_d(s)] - H(s)\theta_k \tag{6}$$

where $\delta\phi_d(s) = 2\pi \cdot \delta\hat{f}_d \cdot F(s)/s$ represents the phase error introduced by Doppler shift, $F(s)$ is the inertial auxiliary transfer function, and $H(s)$ is the FLL-assisted PLL loop transfer function.

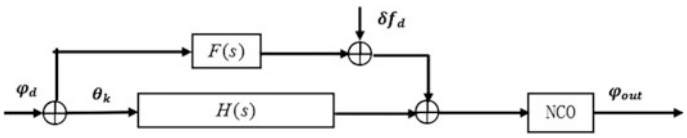

Fig. 2 A feed-forward model of INS auxiliary

According to Ref. [7], PLL phase vibration σ_d is described as follows:

$$\sigma_d^2 = \int_0^\infty |1 - H(j \cdot 2\pi f)|^2 S_d df \tag{7}$$

S_d is the first-order Markov process model of the inertial navigation auto-correlation error, written as:

$$S_d = \left(\frac{f_L}{f \cdot c}\right)^2 \left(\frac{-2\left(\frac{\ln(1-k_c)}{\Delta t}\right)\frac{k_c}{2-k_c}}{(2\pi f)^2 + \left(\frac{\ln(1-k_c)}{\Delta t}\right)^2} \right) \times 3\Delta t_{GPS} \mathrm{var}(\dot{\rho}) \tag{8}$$

where f_L is carrier frequency, Δt is the filter update time, Δt_{GPS} is the pseudo-range update time, and k_c is the filter gain. The pseudo-range error $\mathrm{var}(\dot{\rho})$ is described as:

$$\mathrm{var}(\dot{\rho}) = \left(\frac{c}{\sqrt{2}\pi f_L \Delta t_{GPS}}\right)^2 \frac{B_n}{C/N_0}\left[1 + \frac{1}{2T_{coh} \cdot C/N_0}\right] \tag{9}$$

Therefore, the FLL-assisted PLL phase vibration variance with INS auxiliary can be derived:

$$\sigma_d^2 \approx A_1^2 A_2 \mathrm{var}(\dot{\rho}) \frac{\omega_1^2 \left[\begin{array}{l} 3\omega_1^5 + 6\omega_1^2\left(\omega_1^3 + 2\sqrt{2}\omega_1^2\omega_2 + 4\omega_1\omega_2^2 + 2\sqrt{2}\omega_2^3\right) \\ + \sqrt{2}\omega_2\left(4\omega_1^4 + 2\sqrt{2}\omega_1^3\omega_2 + 5\omega_1^2\omega_2^2 + 8\sqrt{2}\omega_1\omega_2^3 + 4\omega_2^4\right) \end{array} \right]}{6\sqrt{2}\left(\begin{array}{l} \omega_1^6 + 2\sqrt{2}\omega_1^5\omega_2 + 4\omega_1^4\omega_2^2 \\ + 3\sqrt{2}\omega_1^3\omega_1^3 + 4\omega_1^2\omega_2^4 + \sqrt{2}\omega_1\omega_2^5 + \omega_2^6 \end{array} \right)} \tag{10}$$

where A_1, A_2 are considered as stationary parameters and can be described as: $A_1 = \frac{\pi f_L}{c}$; $A_2 = -\frac{6\ln(1-k_c)k_c\Delta t_{GPS}}{(2-k_c)\Delta t}$; ω_1 is the PLL angular frequency, ω_2 is the FLL angular frequency. Since the expression is too complex, we use approximate values to discuss. In previous studies [8], single PLL is used in ultra-tightly integrated navigation system, so the phase vibration error expression is only related to the PLL order, The general second-order PLL phase vibration error with inertial guidance is written as:

$$\sigma_{d,PLL}^2 = K \cdot \frac{\omega^2 + \sqrt{2}\omega + 1}{\sqrt{2}(\omega + \omega^5)} \tag{11}$$

where K is a constant factor related to carrier frequency, filter gain and i.e. In denominator, there is a ω^5 leading the phase vibration error rebounded when ω

increases. The loop bandwidth is proportional to angular frequency ω. So, using PLL alone in the ultra-tightly integrated navigation system can not reach a wide bandwidth. However, in formula (10), the maximum numerator index is larger than the maximum denominator index. Introducing FLL in ultra-tightly integrated navigation system ensures the convergence of phase vibration error.

Moreover, the dynamic stress error of the PLL is described as:

$$\sigma_{de} = \frac{1}{3} K_k \frac{d^k R/dt^k}{(B_n)^k} \cdot \frac{360 f_L}{c} \tag{12}$$

where $d^k R/dt^k$ is the relative movement in view direction between receiver and satellite, K_k is the scale factor corresponding to the kth-order PLL. This paper uses the third-order PLL and sets $K_3 = 0.4828$. In the ultra-tightly INS, the relative movement is obtained by inertial navigation and satellite ephemeris solution. In this case, the expression (12) is written as:

$$\sigma_{de} = \frac{1}{3} K_3 \frac{\delta f_{IMU}}{(B_{PLL})^k} \cdot \frac{360 f_L}{c} \tag{13}$$

where δf_{IMU} is frequency error related to IMU accuracy. The devices precision is higher, the loop dynamic stress error is smaller.

The carrier loop noise also includes the Alan variance phase noise σ_a, depending on the material and process of the receiver crystal. In this paper, σ_a is regarded as a constant value.

In summary, the FLL-assisted PLL noise variance in the ultra-tightly integrated navigation system is shown as follows:

$$\sigma = \sigma_d + \sigma_{de} + \sigma_a \tag{14}$$

3 Simulation and Results

Figure 3 illustrates the simulation for a second order FLL assisting the third order PLL in the ultra-tightly integrated navigation system:

In the figure, K_p is phase discriminator gain, K_f is frequency discriminator gain, K_0 is the NCO gain, T_s is sampling time,and f_{dyn} is Doppler shift calculated by the inertial navigation and satellite ephemeris, a_2, a_3, and b_3 are the filter parameters. ω_{n2} is the bandwidth of the second-order FLL, ω_{n3} is the bandwidth of the third-order PLL.

In order to remove High-order components due to high dynamic stress, the integrator is aim to combine the influences of different angular frequency index, and the detail structure is shown in Fig. 4.

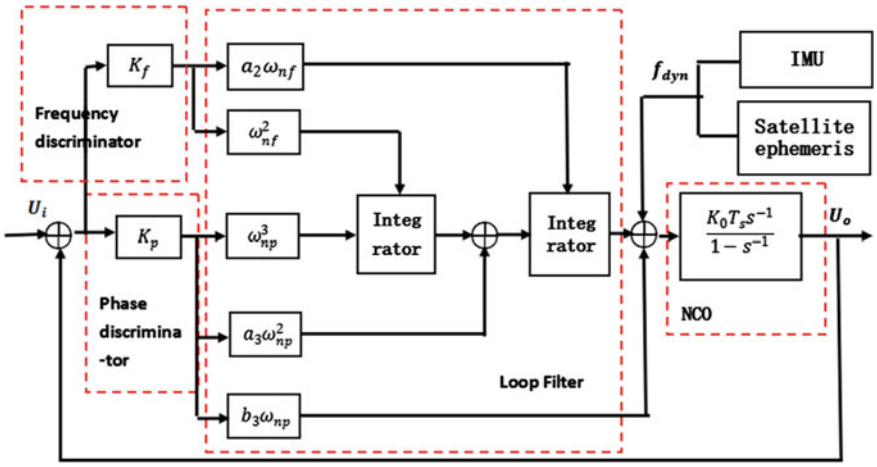

Fig. 3 The structure model of simulation

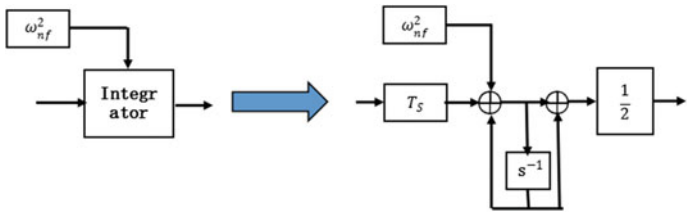

Fig. 4 Integrator structure

Simulation parameters Ref. [9], where the running time is 120 ms, the satellite intermediate frequency(IF) signal is 4.124 MHz, the phase discriminator gain is 1, the frequency discriminator gain is 0.25, and the NCO gain is 1. The filter parameters of the second-order FLL and third-order PLL picked as $a_2 = 1.414$, $a_3 = 1.1$, $b_3 = 2.4$. The bandwidth of the frequency-locked loop is $B_{L2} = 100$ Hz, angular frequency is $\omega_{n2} = \frac{B_{L2}}{0.53}$, the bandwidth of the phase-locked loop is $B_{L3} = 20$ Hz, angular frequency is $\omega_{n3} = \frac{B_{L3}}{0.7845}$, and the damping ratio is 0.707. The inertial navigation assistance transfer function is described as $F(s) = \frac{as}{s+a}$, where $a = 2\pi \times f_{dyn}$.

In order to ensure not to lose the lock of the carrier tracking loop, we select the 1σ tracking threshold 15°. Figure 5 shows the different tracking results between FLL-assisted PLL and PLL alone when they are assisted by IMU. And using FLL-assisted PLL in the ultra-tightly integrated navigation system gets better tracking accuracy.

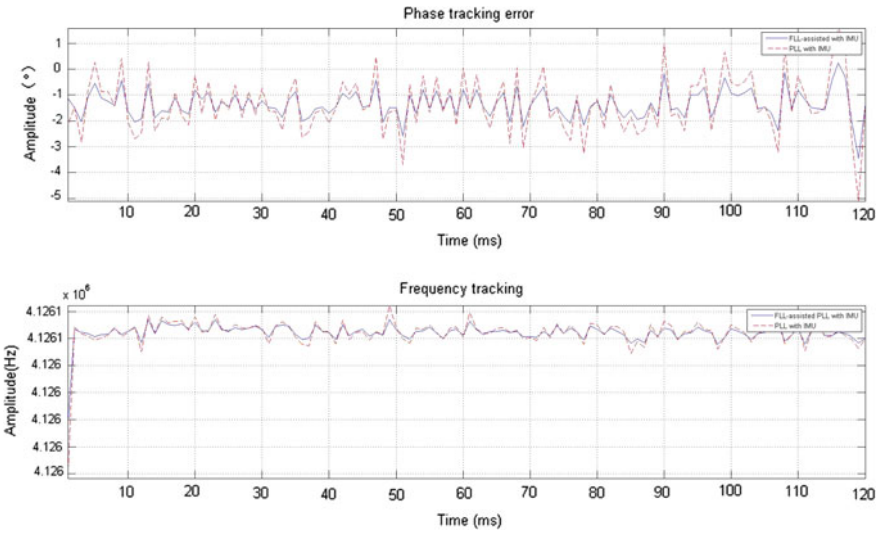

Fig. 5 Phase tracking error and frequency tracking results

Figure 6 not only compares the dynamic stress error between FLL-assisted PLL and PLL alone with IMU but also adds the FLL-assisted PLL without inertial auxiliary into comparison. However, in system without IMU assistance, the dynamic stress error is dozens times larger than that in ultra-tightly INS. Moreover, in the same system with IMU assistance, FLL-assisted PLL performs smaller dynamic stress error.

In Fig. 7, we compare the phase vibration error of FLL-assisted PLL and PLL alone in ultra-tightly integrated navigation system. In ultra-tightly INS using PLL alone, the phase vibration error rebound when the bandwidth increases to

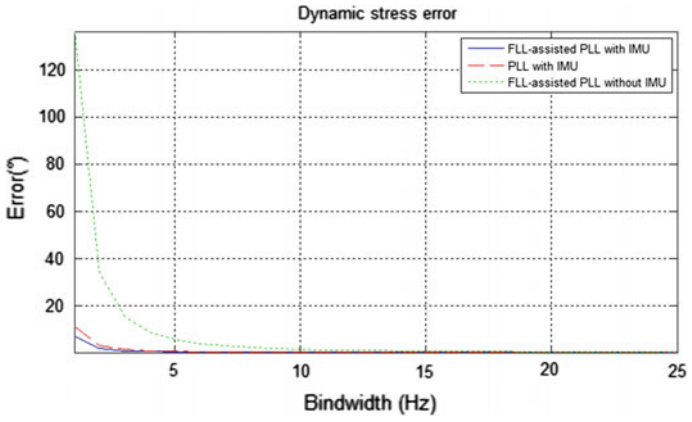

Fig. 6 Comparison of dynamic stress

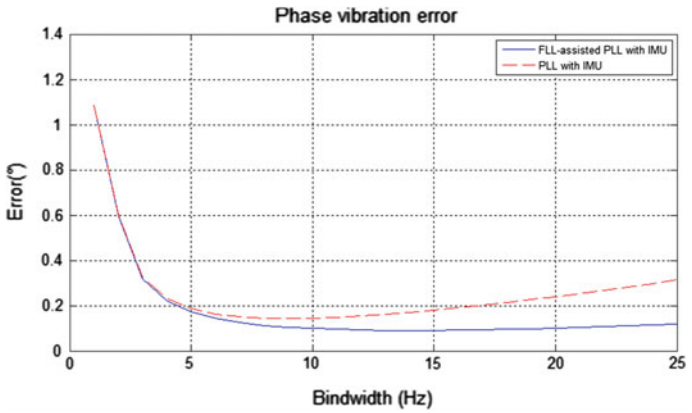

Fig. 7 Comparison of phase vibration error

approximate 15 Hz. This shortcoming is compensated by introducing the FLL assistance.

4 Conclusion

In this paper, we introduce the FLL-assisted PLL in the ultra-tightly integrated navigation system. The thermal noise and phase vibration error model are analyzed theoretically. Because of the narrow bandwidth of PLL, using PLL alone in the carrier loop can not track signals as soon as FLL. But the FLL's tracking accuracy is worse. Taking into account these two aspects, FLL-assisted PLL is a better chose in high-dynamic situations. With FLL-assisted PLL, smaller dynamic stress error and higher tracking accuracy are achieved. And it can effectively inhibit phase vibration error rebounding when the bandwidth increases to a certain extent.

References

1. Wang X, Ji X, Feng S, Calmettes V (2014) A high-sensitivity GPS receiver carrier-tracking loop design for high-dynamic applications. GPS Solut 19(2):225–236
2. Liu Y, Zhu Y (2014) A FLL-PLL cooperative GNSS weak signal tracking framework. Appl Mech Mater 551:470–477
3. Xu R, Liu Z, Chen W (2014) Improved FLL-assisted PLL with in-phase pre-filtering to mitigate amplitude scintillation effects. GPS Solut 19(2):263–276
4. Zhang T, Niu X, Ban Y, Zhang H, Shi C, Liu J (2015) Modeling and development of INS-Aided PLLs in a GNSS/INS deeply-coupled hardware prototype for dynamic applications. Sensors 15(1):733–759

5. Miura S, Kamijo S (2014) GPS error correction by multipath adaptation. Int J Intell Transp Syst Res 13(1):1–8
6. Kou Y, Zhang H (2016) Sample-wise aiding in GPS/INS ultra-tight integration for high-dynamic, high-precision tracking. Sensors 16(4):519
7. Qin F, Zhan X, Zhan L (2014) Performance assessment of a low-cost inertial measurement unit based ultra-tight global navigation satellite system/inertial navigation system integration for high dynamic applications. IET Radar Sonar Navig 8(7):828–836
8. Jiang R, Wang K, Liu S, Li Y (2016) Performance analysis of a Kalman filter carrier phase tracking loop. GPS Solutions 21(2):551–559
9. Ogaja C (2011) Applied GPS for engineers and project managers, 1st edn. ASCE, Reston

Feature-Based Monocular Real-Time Localization for UAVs in Indoor Environment

Yu Zhang, Zhihao Cai, Jiang Zhao, Zhenxing You and Yingxun Wang

1 Introduction

UAV applications in recent years have become more and more widely for its small size and excellent mobility. Most UAVs used to depend on GPS or inertial system for autonomous flight, but in the indoor or GPS denied environment it becomes a great challenge. Because of the small size and load capacity constraints, traditional sensors are not suitable for small UAV platforms, such as lasers [1, 2]. As a result, visual sensor provides a good solution as it contains a wealth of motion and environment information.

The traditional visual odometry which can be seen as pairwise and structure-less lacks robustness and easily accumulate drift. In this paper, we realize the real-time localization for UAVs in indoor environment based on the idea of the monocular visual odometry. Figure 1 shows main components of the system and we elaborates on in the paper. In addition, to improve the performance and overcome the shortcomings of traditional method, we use g2o and a map based method to optimize the estimated pose and reduce the drift of estimated trajectory in the case of prolonged motion.

Y. Zhang (✉) · Z. Cai · J. Zhao · Z. You · Y. Wang
School of Automation Science and Electrical Engineering,
Beihang University, Beijing 100191, China
e-mail: zhangyu5782@163.com

Z. Deng (ed.), *Proceedings of 2017 Chinese Intelligent Automation Conference*,
Lecture Notes in Electrical Engineering 458,
https://doi.org/10.1007/978-981-10-6445-6_39

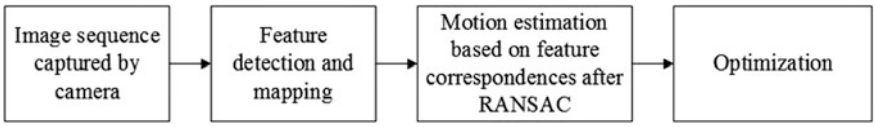

Fig. 1 Main components of the system

2 Feature Detection and Mapping

2.1 ORB Feature Detection and Description

ORB features consists of two parts: the oriented multi-scale FAST keypoints and the rotated BRIEF descriptor [3]. As a result, they are rotation invariant and it is extremely fast to compute and match ORB.

FAST corners are widely used because of its fast detection speed, but they do not have an orientation component and are not multi-scale. To overcome these weaknesses, ORB add scale and rotation description. Scale invariance is achieved by building a scale pyramids of the image and detecting corners at each level and the rotation description is added by intensity centroid. The moments of a patch are defined as:

$$m_{pq} = \sum_{x,y} x^p y^q I(x, y) \tag{1}$$

And the centroid of it can be found by the moments defined above:

$$C = \left(\frac{m_{10}}{m_{00}}, \frac{m_{01}}{m_{00}}\right) \tag{2}$$

A vector OC is get by connecting the corner's center and the centroid. The orientation of the features is defined as:

$$\theta = \arctan(m_{01}, m_{10}) \tag{3}$$

The BRIEF descriptor is a binary descriptor which describes the pixels information around the detected keypoints. The "Steer BRIEF" feature after the rotation can be calculated by using the direction information, so that the descriptor of the ORB has good rotation invariance.

According to the statistics, the calculation speed of ORB is about 10 times faster than SURF and SIFT. To compute ORB in an image of size 752 × 480, it detects 500 features in 0.011679 s. Comparing to SURF and SIFT on the same image, the time cost are as follows: 0.091570 s, 0.116692 s.

2.2 Feature Matching

The feature matching step solves the problem of data association, which is critical because it can reduce the burden for subsequent pose estimation, optimization, and so on by accurate feature matching.

We adopt FLANN (Fast Library for Approximate Nearest Neighbors) in the feature matching step as it is fast and efficient. It significantly improves matching efficiency depending on the Randomized K-d Three Algorithm and The Priority search K-means Three Algorithm. For better performance, we remove error matches based on the condition that Hamming distance is less than twice the minimum distance. In the next step, we will use random sampling consensus strategies to remove more outliers for more accurate motion estimation.

3 Motion Estimation

3.1 Motion Estimation Based on the Epipolar Constraint

After feature matching, the geometric relations between two images can be computed from feature correspondences. Furthermore, we can compute the relative motion to get real-time position information. The main property of the epipolar constraint illustrated in the below, which is the basis of 2d-2d motion estimation [4].

P2 is the corresponding feature point of P1 in the other image, and they are both normalized coordinates. The epipolar constraint between them can be formulated as:

$$p_2^T E p_1 = 0 \tag{4}$$

E is the essential matrix which describes the geometric relations between two images. In this paper, we use the classic eight-point algorithm to compute E in the following form, where u and v is the normalized coordinates:

$$\left[u_1 u_2, u_1 v_2, u_1, v_1 u_2, v_1 v_2, u_2, v_2, 1\right] \cdot E = 0 \tag{5}$$

The rotation matrix R and the translation matrix t can directly be extracted from E by SVD. And the rigid body transformation can be composed as:

$$T_{i+1,i} = \begin{bmatrix} R_{i+1,i} & t_{i+1,i} \\ 0 & 1 \end{bmatrix} \tag{6}$$

In summary, the motion estimation based on feature correspondences are as follows. Step 1: Feature detection and matching in continuous frame. Step 2:

Compute essential matrix E based on corresponding features. Step 3: Extract the rotation and translation parts R, t from E. So the current pose can be computed by the transformation T if we get the pose at last timestamp.

3.2 RANSAC Algorithm

Matched features are usually contaminated by outliers that may be caused by blur, illumination and so on. Since the motion estimation is based on matched features, the wrong data association will have a bad effect on the accuracy on estimation.

For robust estimation, in the motion estimation step we take RANSAC (random sampling consensus) algorithm as a solution to outlier removal [5, 6]. The main idea behind the RANSAC algorithm is that based on data sets that randomly sampled the model hypotheses can be computed and the hypothetical model can be verified on other data. After iterations, the hypotheses which has the highest accordance is selected as a solution.

4 Optimization

4.1 Bundle Adjustment

Since the pose and trajectory of the camera are computed incrementally, the errors of each image will increase with time gradually. To keep the drift as small as possible, we use bundle adjustment to obtain more accurate estimation. 3D point P is computed based on correspondences P1, P2 by triangulation. The projection position of point P2′ is known according to the current pose. The error distance between P2 and P2′ is reprojection error.

In bundle adjustment, the goal is to minimize the reprojection error:

$$\arg\min_{C_k} \sum_{i,k} \left\| p_k^i - g(X_i, C_k) \right\|^2 \tag{7}$$

where C_k is the camera pose in kth frame. In this paper, we use g2o to realize the bundle adjustment. G2o is a library based on graph optimization [7]. In a pose graph, the camera poses and all 3D points are presented as nodes and the image projection of all 3D points are edges between nodes. Bundle adjustment tried to optimize the poses and 3D points to minimize the reprojection error.

4.2 Map Based Visual Odometry

The traditional visual odometry computes the relative transformations T from the adjacent images and then concatenate the transformation to recover the full trajectory [8]. It can be seen as pairwise and structure-less VO, because it only concentrates the motion between two frames. In addition, it ignores the features that once used so it saves the amount of computation but losses lots of information. Another drawback of the pairwise VO is that once there is a bad estimate in one frame, the error will always effect the following estimate.

To solve the problem mentioned above and take advantage of features extracted in old frames, we can use map based visual odometry instead. The map is a collection of 3D points by triangulating features in each frame. We match points in the map and the features extracted in the current frame to compute the pose of camera directly. The benefit of this method is that we are able to maintain a constantly updated map. As long as the map is correct, even if a frame goes wrong, it is possible to estimate the correct position of following frames. Besides, only feature points that close to the current position are kept in the map and those points out of view field will be dropped for computation efficiency.

The difference between traditional VO and map based VO is described in Fig. 2 in detail.

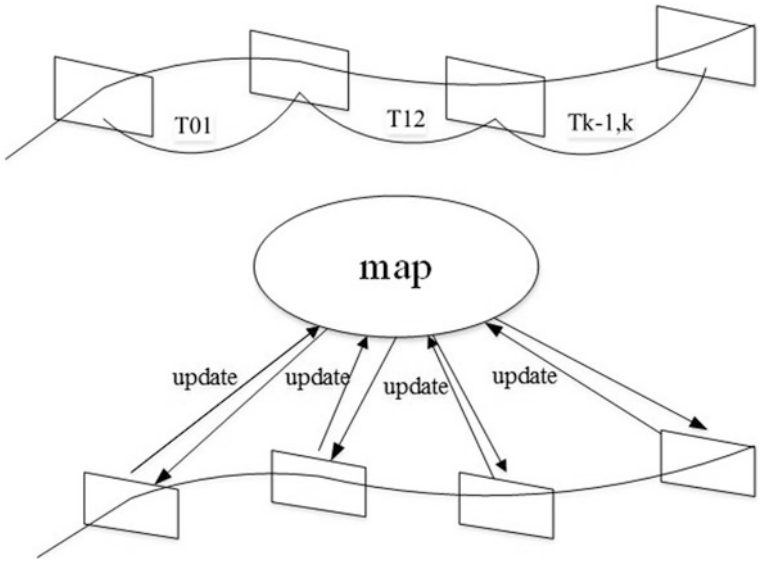

Fig. 2 The difference between the pairwise VO and map based VO

5 Results and Analysis

To test the effect of the bundle adjustment and evaluate the performance of the system, we have performed several experiments that are demonstrated in detail as follows.

The system runs with Intel Core-i7 and 16G RAM and in the platform of ROS (Robot Operating System), and the image is captured by the IDS-ueye camera at 30 fps. The resolution of the image is 752 × 480.

1. Accuracy evaluation in the TUM dataset

The TUM dataset is good for evaluating the accuracy as it provides image sequences with accurate ground_truth which is given by motion capture system. The following experiments are performed in freiburg1_xyz dataset.

In Fig. 3, the black line is the ground truth, and the blue is the estimated trajectory. The red line is the difference between them. Figure 3a shows the estimated trajectory before bundle adjustment, and Fig. 3b is the result after bundle

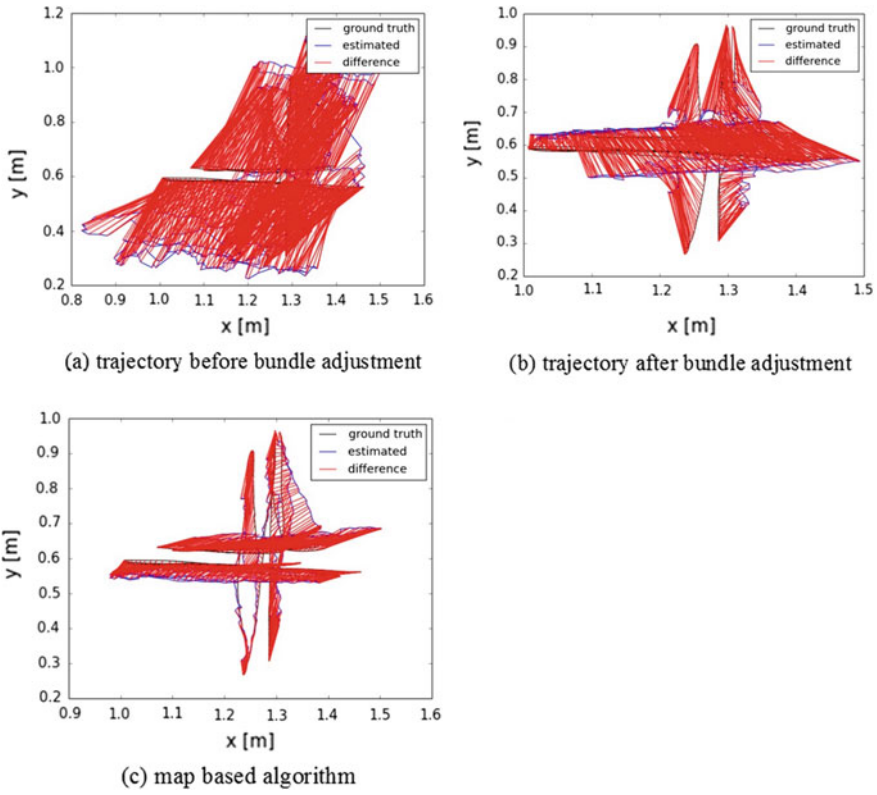

Fig. 3 Comparison of the estimated trajectory using different methods

adjustment with pairwise algorithm. Figure 3c shows the performance with map based algorithm.

- Experiment on bundle adjustment

Figure 4 shows that the reprojection error decreases a lot after bundle adjustment. In addition, from Fig. 3a, b and the first two lines in Table 1, it can be concluded that after bundle adjustment the localization error is reduced and the estimated trajectory is clearly more accurate.

- Pairwise algorithm Versus map based algorithm

Comparing Fig. 3b, c and the last two lines in Table 1, map based visual odometry obviously shows a better performance. And Fig. 5 plots the error respectively in x direction and y direction based on map based visual odometry.

2. Real-time localization experiments in indoor environment

Besides the experiments in TUM dataset, we have done the real-time localization experiments in the lab environment.

- Handheld experiment

We handheld the camera and walked around a table with a rectangular track in the lab environment. The environment and the real-time estimated trajectory is shown in Fig. 6. And from Table 2, it shows the computation speed of the system can satisfied the real-time need for UAVs.

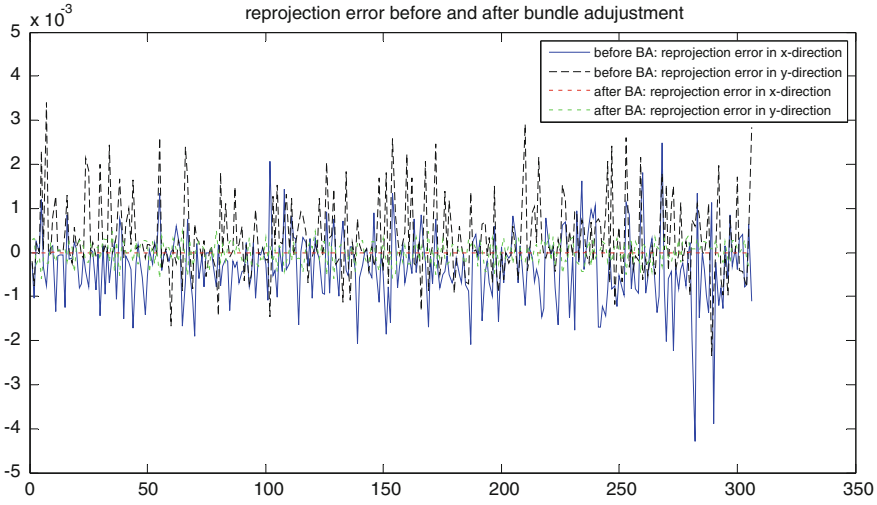

Fig. 4 Comparison of reprojection error before and after bundle adjustment

Table 1 Localization error comparison in different methods

Algorithms	Translational error min (m)	Translational error max (m)	Translational error mean (m)
Before BA	0.084973	0.413918	0.280460
After BA	0.015544	0.308868	0.109293
Map based algorithm	0.010236	0.137224	0.067179

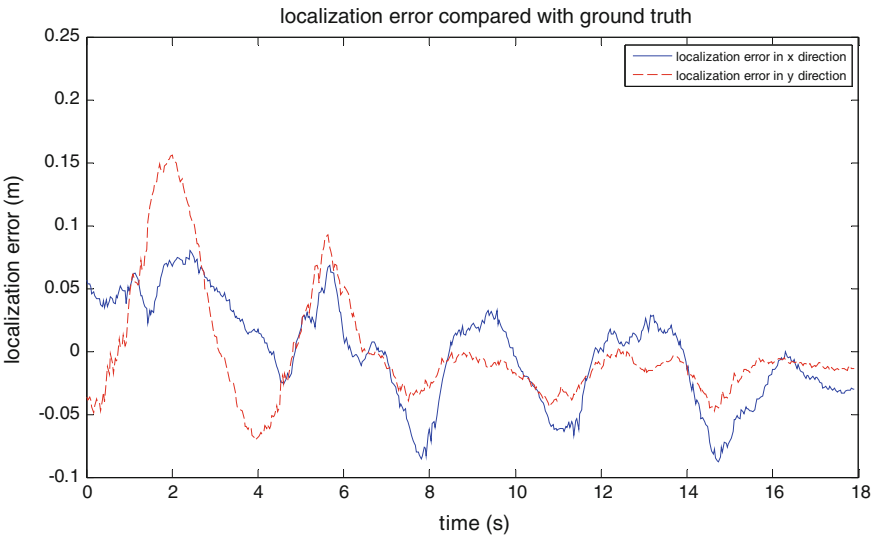

Fig. 5 Localization error

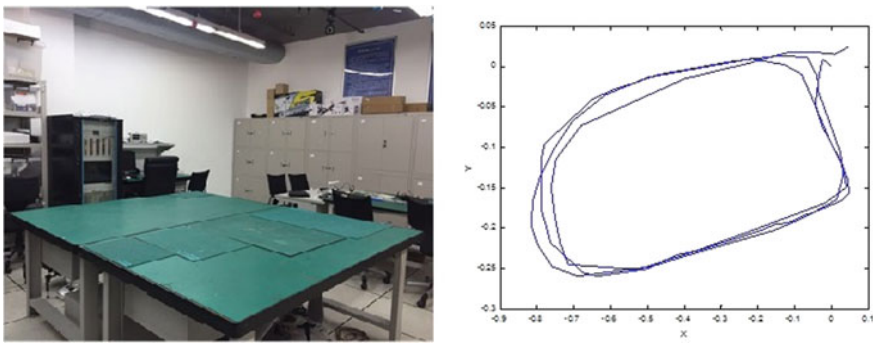

Fig. 6 Real-time rectangular trajectory around a table

Table 2 Computation time in one frame

	Feature detection	Feature matching	Motion estimation and optimization	Total
Time (s)	0.01665	0.01182	0.011342	0.039812

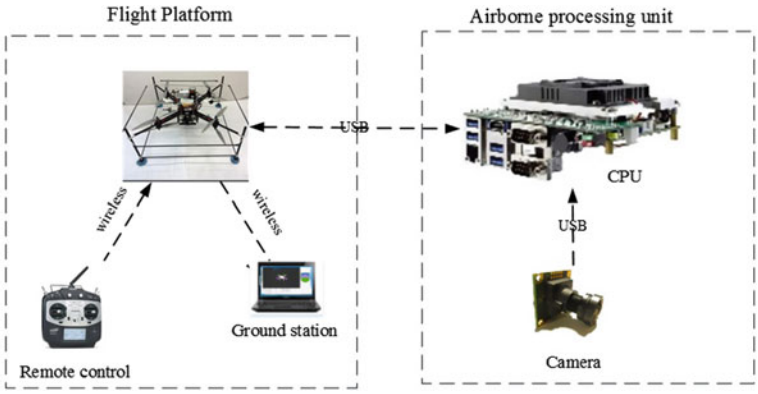

Fig. 7 The components of the system

Fig. 8 The images during the flight and the estimated trajectory

- Flight experiment

We use a small UAV with the wheelbase of 80 cm and 1 ~ 2 m/s flight speed to perform the experiments in the indoor environment. The components of the hardware is showed in Fig. 7. Figure 8 shows some images during the flight and the estimated flight trajectory.

6 Conclusion

A real-time localization method based on monocular is proposed to solve the navigation problem for UAVs in indoor environment in this paper. Several improvements have been made on traditional VO to satisfy the need of real-time and accuracy of UAVs. With the experiments carried out both in dataset and indoor environment, it turns out the method is feasible for UAV applications.

References

1. Zhang Y, Wang T, Cai Z et al (2017) The use of optical flow for UAV motion estimation in indoor environment. In: Guidance, navigation and control conference. IEEE, pp 785–790
2. Wang T, Zhang Y, Cai Z et al (2016) Visual attention based target detection and tracking for UAVs. In: IEEE chinese guidance, navigation and control conference. IEEE, pp 895–900
3. Rublee E, Rabaud V, Konolige K, Bradski G (2011) ORB: an efficient alternative to SIFT or SURF. In: IEEE international conference on computer vision (ICCV), Barcelona, Spain, pp 2564–2571
4. Fraundorfer F, Scaramuzza D (2012) Visual odometry: part II: matching, robustness, optimization, and applications. IEEE Robot Autom Mag 19(2):78–90
5. Nistér D (2005) Preemptive RANSAC for live structure and motion estimation. Mach Vis Appl 16(5):321–329
6. Chum O, Matas J, Kittler J (2013) Locally optimized RANSAC. Lect Notes Comput Sci 2781:236–243
7. Kümmerle R, Grisetti G, Strasdat H et al (2011) G2o: a general framework for graph optimization. In: IEEE international conference on robotics and automation. IEEE, pp 3607–3613
8. Scaramuzza D, Fraundorfer F (2011) Visual odometry: part i: the first 30 years and fundamentals. IEEE Robot Autom Mag 18:80

Scene Parsing with Deep Features and Per-Exemplar Detectors

Xiaofei Cui, Hanbing Qu, Xi Chen, Ziliang Qi and Liang Dong

1 Introduction

This paper addresses the problem of scene parsing, i.e., labeling each pixel in an image with its semantic category, which is a challenging task in computer vision. It involves many types of problems, e.g., object detection problems, image segmentation problems, and multi-label recognition problems. In the past few years, scene parsing had been extensively studied.

For scene parsing or many problems in computer vision, the first step is to extract features. Features are expressions of images for easy calculation and classification. Hence, extracting good features is crucial to computer vision tasks. For image representation, the conventional approaches utilize carefully designed hand-crafted features, e.g., SIFT [1], HOG [2], GIST [3], SURF [4], etc. Recently, compared with the hand-engineered features, learning image features with deep network structures have shown great potential in various computer vision recognition tasks [5–9]. Deep learning is advantageous for large image regions with complex variations, because its deep architectures can better learn the global contextual feature representation.

Another problem of scene parsing is to improve the recognition rate of the object classes. The recognition rate of some previous methods [10–12] for small objects which occupy few pixels was not very good. To improve the recognition rate of small samples, Tighe and Lazebnik [13] presented using per-exemplar detectors

X. Cui · H. Qu (✉) · X. Chen · Z. Qi
School of Computer Science and Engineering, Hebei University of Technology,
No 5340 XiPing Road, Beichen, Tianjin, China
e-mail: quhanbing@gmail.com

H. Qu · L. Dong
Beijing Institute of New Technology Applications, Beijing, China

H. Qu · L. Dong
Beijing Academy of Science and Technology, Beijing, China

Z. Deng (ed.), *Proceedings of 2017 Chinese Intelligent Automation Conference*,
Lecture Notes in Electrical Engineering 458,
https://doi.org/10.1007/978-981-10-6445-6_40

which trained all classes and SVM for classification. Yang et al. [14] expanded the retrieval set using rare class exemplars to achieve more balanced superpixel classification results. In this paper we use the exemplar-SVMs [15] which are identical to [13] to improve the accuracy rate of rare classes.

The remainder of the paper is organized as follows. In Sect. 2, we review some relevant works such as the parametric approach and nonparametric approach for scene parsing. Section 3 presents our approach. Section 4 provides the results of our experiments in two challenging datasets, and a conclusion is provided in Sect. 5.

2 Related Work

Simultaneous image segmentation and labeling are a fundamental problem in computer vision. It is a core technology of image understanding, context-based retrieval and object recognition. The goal of scene parsing is to assign each pixel in the image a class label. In recent years, several approaches for scene parsing have been proposed. The solution to this problem is basically divided into two categories: parametric approach and nonparametric approach. The following will introduce the related research work about the parametric method and the nonparametric method.

2.1 Parametric Approach

The parametric method refers to that model is trained for scene parsing in advance. Farabet et al. [5] trained a multi-scale convolutional network from raw pixels to extract dense feature vectors and computed a tree of segments according to a graph of pixel dissimilarities to extract the most consistent segmentation. In order to achieve better performance, Bu et al. [6] combined the neural network architecture with an inference layer based on a graphical model. They not only provided a powerful representation, but also learned structural performance. Pinheiro and Collobert [7] used recurrent convolution neural networks which enabled one to consider the context for scene labeling. Its advantage was that no segmentation or any task-specific features were required. Mohan [8] combined deep deconvolutional neural networks with CNNs and employed multi-patch for training which could learn spatial priors from the scenes. Zhao et al. [16] presented a large and open vocabulary for scene parsing. They put image pixels and word concepts into the parsing framework, where word concepts were connected by semantic relations. To parse a 2D image into semantic regions and recover the 3D scene structures of all regions, Liu et al. [17] proposed an attribute grammar which included a set of production rules, each of which described a type of spatial relation among planar surfaces in 3D scenes.

2.2 *Nonparametric Approach*

Compared with the parameter methods, nonparametric methods does not require any pre-training. They have simple and easy implementation. For each query image, they try to retrieve the most similar images and transfer the information from the training images to the query image. Liu et al. [10] proposed a nonparametric approach for scene parsing using dense scene alignment to label transfer. This approach used the SIFT flow algorithm to align the structures in two images, but the inference via the SIFT flow was notably complex and computationally expensive. Thus, Tighe and Lazebnik [11] presented a scalable nonparametric image parsing method with superpixels. This approach required no training, was easy to implement and established a new benchmark for image parsing. But its performance was poor for object classes.

To minimize the classification error, Eigen et al. [12] learned the per-descriptor weights. And to improve the performance on rare classes, the method used a context-driven adaptation of the training set for each query image. Tighe and Lazebnik [13] combined region-level features with per-exemplar sliding window detectors to achieve broad coverage across hundreds of object categories. To improve the accuracy of nonparametric approach, Singh et al. [18] presented the adaptive feature relevance and semantic context. Yang et al. [14] used rare class exemplars, which expanded the retrieval set, to achieve balanced superpixel classifications and incorporated the global and local semantic context information to refine the image retrieval and superpixel matching. George et al. [19] merged the likelihood scores from different probabilistic classifiers to improve the label likelihood estimates at superpixels and incorporated the semantic context in the parsing process through global label costs.

3 Our Approach

In this section, we introduce a method that combines the convolution neural network with exemplar-SVMs for scene parsing. First, we use GoogLeNet [20] to extract global image features to compute the retrieval set for query image. Then, we segment the image into superpixels and compute the superpixels features to obtain the probability of class labels for each query image, and train the exemplar detectors for each class in training set. Finally, we integrate the superpixels parsing results with the exemplar-SVMs parsing results, and use MRF fine-tuning the consistency of the label among adjacent pixels to obtain the final parsing. The general architecture of the proposed framework is presented in Fig. 1.

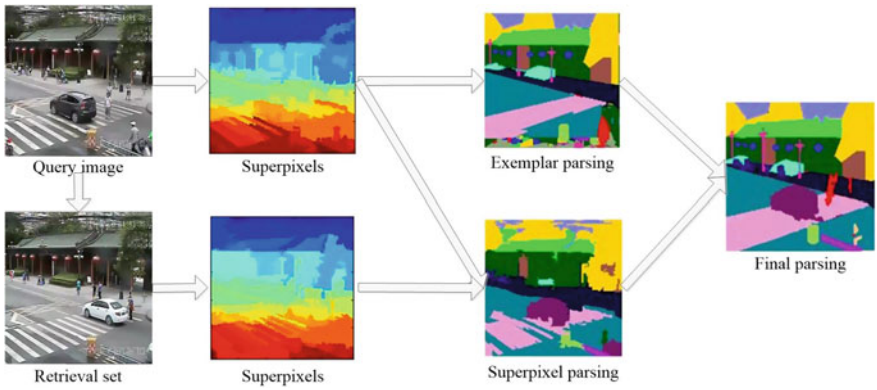

Fig. 1 Overview of our approach. Given a query image, our system uses deep features to find the most matched images from the training set. Next, we segment the query image and retrieval images to superpixels. Then, we use local features to describe the superpixels and compute the superpixel likelihood ratio scores to obtain the superpixel parsing results. Through training the exemplar detectors for each class, we obtain the exemplar parsing results. Finally, we combine the exemplar parsing results with the superpixel parsing results to obtain the final parsing results

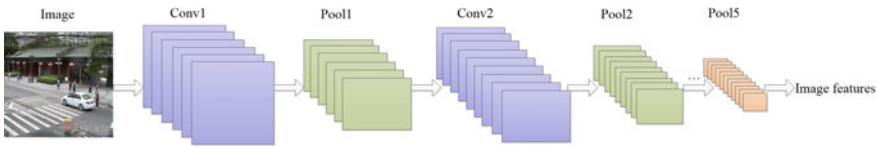

Fig. 2 Process of the convolution neural network. For an image, we extract the output of the pool5 layer in GoogLeNet as our deep features

3.1 Feature Extraction

3.1.1 Feature Extraction with CNN

The major goal of deep learning is to learn the feature representations. And it is import to comprehend what kinds of tasks are good to be used to learn features. For our system, given a query image I_q, we first extract the pool5 layer output of GoogLeNet [20] as the 1024-dimensional feature vector to find the top K similar images which will contain similar objects and spatial layouts from the training dataset. Similar to previous works, we rank the training images in increasing order of Euclidean distance from the query. Those similar images form the retrieval set. Next we process the images in the retrieval set instead of those in the training set to reduce the computational cost. The process of extracting features using a convolution neural network is presented in Fig. 2.

3.1.2 Feature Extraction with Superpixels

We assign labels to the superpixels instead of pixels to reduce the problem complexity and provide better spatial support for aggregating features that may belong to a single object. We use the fast graph-based segmentation algorithm of [21] to obtain the superpixels, and describe their appearance using 20 different features (similar to [11]). Those features produce a log-likelihood ratio score $L(r_i, y)$ for class label y at the superpixel r_i:

$$L(r_i, y) = \log \frac{P(r_i|y)}{P(r_i|\bar{y})} = \sum_k \log \frac{P(f_i^k|y)}{P(f_i^k|\bar{y})} \tag{1}$$

where $P(f_i^k|y)$ (resp. $P(f_i^k|\bar{y})$) is the likelihood of feature type k for region r_i given class y (resp. all classes but y).

3.2 *Exemplar-SVMs*

We train a per-exemplar detector for each labeled object instance in our dataset based on the per-exemplar framework of [15]. Following the detector training procedure of [15], we train all classes, which include "rare" classes and "common" classes. The detection windows are created for each exemplar-SVMs in a sliding-window fashion, and we use an exemplar co-occurrence based mechanism to suppress the redundant responses.

The SVM is trained using a leave-one-out method on the training set. We normalize each feature dimension by its standard deviation and use fivefold cross validation to find the regularization constant. The RBF kernel is used for SVM training. The resulting SVMs produce Y responses at each pixel. We define $D_{SVM} = (y_i, r_i)$ as the response of the SVM for class y_i at superpixel r_i.

3.3 *MRF Inference*

To assign labels to a set of superpixels r_i of query image I_q, we formulate the image labeling problem as minimization of a standard Markov Random Field energy function, which combines the unary potential with a pairwise potential to derive the final parsing result. The MRF energy function over the field of superpixels labels $\mathbf{y}$ is defined as:

$$\mathbf{E}(\mathbf{y}) = \sum_{r_i \in I_q} D(\mathbf{y}, r_i) + \sum_{r_i \in I_q} \max[0, M - D_{SVM}(y_i, r_i)] + \lambda \sum_{(r_i, r_j) \in A} \varphi(y_{r_i}, y_{r_j}) \tag{2}$$

where $D(\mathbf{y}, r_i)$ is the data term; $D(\mathbf{y}, r_i) = -\omega_i \log L(y, r_i)$; M is the highest expected value of the SVM response; A is the set of adjacent pixels; and λ is a smoothing constant. The pairwise potential term φ is similarly defined as in [11, 14, 22] according to the probabilities of label co-occurrences in the training set:

$$\varphi(y_{r_i}, y_{r_j}) = -\log\left[(P(y_{r_i}|y_{r_j}) + P(y_{r_j}|y_{r_i}))/2\right]\delta\left[y_{r_i} \neq y_{r_j}\right] \tag{3}$$

where $P(y_{r_i}|y_{r_j})$ in the conditional probability of the class label y_{r_i} of the pixel r_i because its adjacent pixel r_j has class label y_{r_j}.

The MRF energy function is minimized using the α-expansion algorithm [23].

4 Experiments

4.1 Dataset

We use two datasets to evaluate the system: the SIFTflow dataset [10], which included 2488 training images, 200 test images, and 33 classes; and video images collected from actual video surveillance scene, which contained 95 training images, 5 test images, and 20 classes.

4.2 The Result of Scene Parsing

We use the per-pixel accuracy (the percentage of pixels of test images that are correctly labeled) and per-class recognition rate (the average of all classes accuracy) to evaluate our system. For the SIFTflow dataset, we set the size of the retrieval set as 200. For our video images, we set the size of the retrieval set as 10. The smoothing constant λ is 1. The highest expected value of the SVM response M is approximately 10.

Our computing environment is MATLAB 2012b and a 3.4 GHz CPU with Intel Core i7-6700 and 8G of RAM. The feature dimensionality highly influences the training time and the parsing time. The higher the feature dimension is, the slower the training time and the parsing time. For the SIFTflow dataset, we parse a training image in approximately 20 s and a test image in approximately 22 s.

Table 1 shows the results of our approach in comparison with the state-of-the art methods about per-pixel and per-class accuracy on SIFTflow dataset. On SIFTflow dataset, our method acquires good performance. Our method is higher nearly 18.3% than Farabet et al. [5] and nearly 8.6% than Tighe and Lazebnick [13] about per-class accuracy.

Table 1 Comparison with the state-of-the-art approaches about per-pixel and per-class accuracy on SIFTflow dataset

Approach	Per-pixel (%)	Per-class (%)
Liu et al. [10]	74.75	N/A
Tighe and Lazebnick [11]	76.90	30.10
Eigen and Fergus [12]	77.10	32.50
Farabet et al. [5]	78.50	29.50
Tighe and Lazebnick [13]	78.60	39.20
Singh and Kosecka [18]	79.20	33.80
Yang et al. [14]	79.80	48.70
Shuai et al. [24]	81.20	45.50
Our approach	80.06	47.79

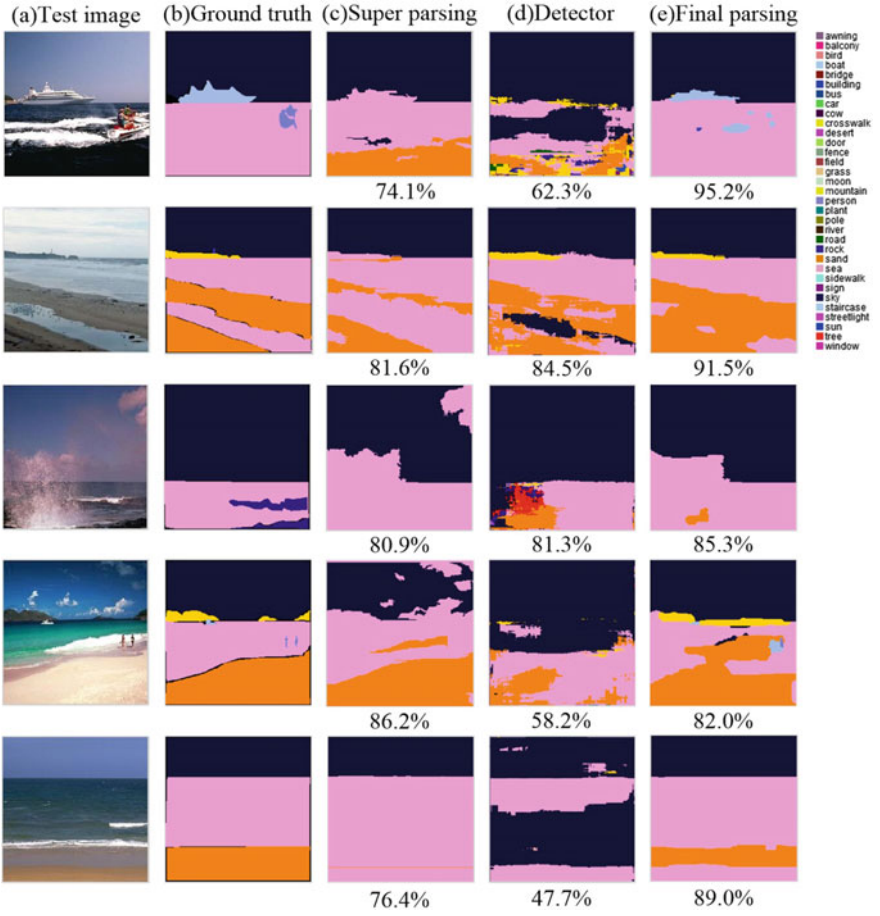

Fig. 3 The results of our approach on SIFTflow dataset. Column **a** is the test images; **b** is the ground truth; the superpixel parsing results are (**c**); **d** is the exemplar parsing results; and **e** is the final parsing results which combine (**c**) with (**d**)

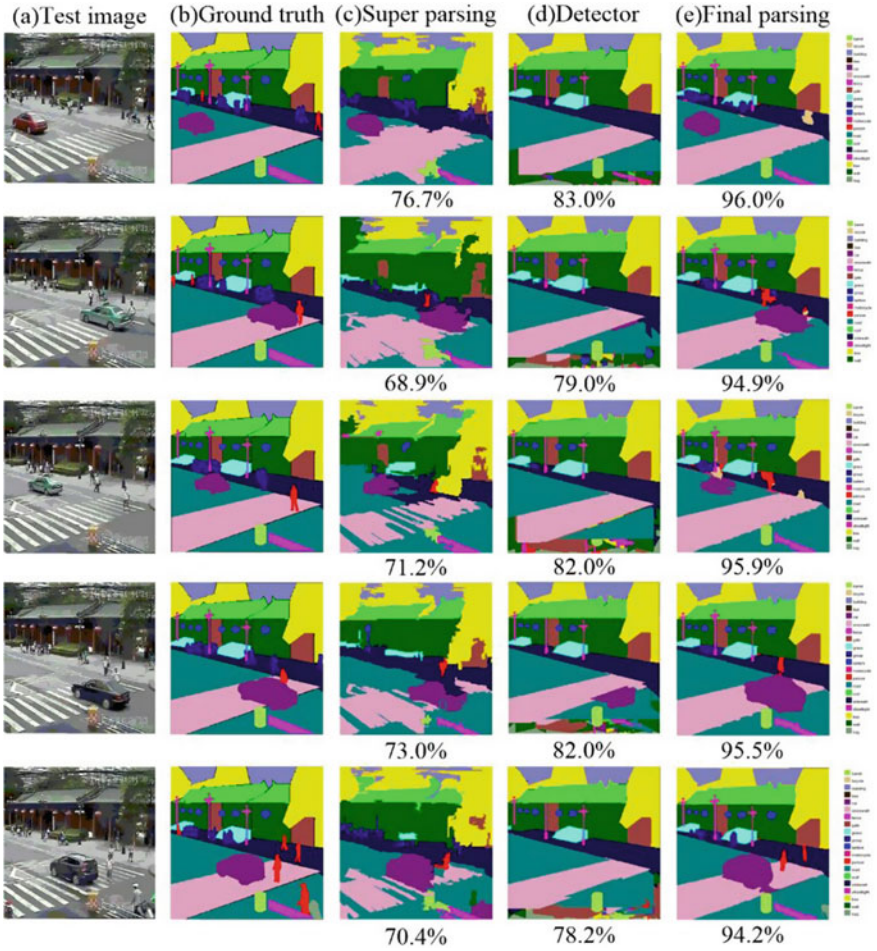

Fig. 4 The results of our approach in the video images. Column **a** is the test images; **b** is the ground truth; the superpixel parsing results are (**c**); **d** is the exemplar parsing results; and **e** is the final parsing results which combine (**c**) with (**d**)

The visual results of our approach on SIFTflow dataset and our collected video images are presented in Figs. 3 and 4, respectively. In the figures, Column (a) is the test images; (b) is the ground truth; the superpixel parsing results are (c); (d) is the exemplar parsing results; and (e) is the final parsing results which combine (c) with (d). From the visual results, we can see that the more similar of images which include the background, the space layout and the objects, the higher the recognition rate.

5 Conclusions

In this paper, we combine the convolution neural network with per-exemplar detectors for scene parsing. We use deep convolutional features to improve the quality of retrieval set and exemplar-SVMs to improve the recognition rates of objects classes with only a few pixels. In the experiments, we apply this system to an actual scene under surveillance video and obtain good parsing results.

Acknowledgements This research was supported by Beijing Municipal Special Financial Project (PXM2016_178215_000013), Beijing Urban System Engineering Research Center's Independent Project (2017C010).

References

1. Lowe DG (2004) Distinctive image features from scale-invariant keypoints. Int J Comput Vis 60(2):91–110
2. Dalal N, Triggs B (2005) Histograms of oriented gradients for human detection. In: 2005 IEEE computer society conference on computer vision and pattern recognition. CVPR 2005, vol 1. IEEE, pp 886–893
3. Oliva A, Torralba A (2001) Modeling the shape of the scene: a holistic representation of the spatial envelope. Int J Comput Vis 42(3):145–175
4. Bay H, Ess A, Tuytelaars T, Van Gool L (2008) Speeded-up robust features (SURF). Comput Vis Image Underst 110(3):346–359
5. Farabet C, Couprie C, Najman L, LeCun Y (2012) Scene parsing with multiscale feature learning, purity trees, and optimal covers. arXiv preprint arXiv:1202.2160
6. Bu S, Han P, Liu Z, Han J (2016) Scene parsing using inference embedded deep networks. Pattern Recogn 59:188–198
7. Pinheiro P, Collobert R (2014) Recurrent convolutional neural networks for scene labeling. In: International conference on machine learning, pp 82–90
8. Mohan R (2014) Deep deconvolutional networks for scene parsing. arXiv preprint arXiv:1411.4101
9. Krizhevsky A, Sutskever I, Hinton GE (2012) Imagenet classification with deep convolutional neural networks. In: Advances in neural information processing systems, pp 1097–1105
10. Liu C, Yuen J, Torralba A (2009) Nonparametric scene parsing: label transfer via dense scene alignment. In: 2009 IEEE conference on computer vision and pattern recognition. CVPR 2009. IEEE, pp 1972–1979
11. Tighe J, Lazebnik S (2010) Superparsing: scalable nonparametric image parsing with superpixels. Comput Vis ECCV 352–365
12. Eigen D, Fergus R (2012) Nonparametric image parsing using adaptive neighbor sets. In: 2012 IEEE conference on computer vision and pattern recognition (CVPR). IEEE, pp 2799–2806
13. Tighe J, Lazebnik S (2013) Finding things: image parsing with regions and per-exemplar detectors. In: Proceedings of the IEEE conference on computer vision and pattern recognition, pp 3001–3008
14. Yang J, Price B, Cohen S, Yang MH (2014) Context driven scene parsing with attention to rare classes. In: Proceedings of the IEEE conference on computer vision and pattern recognition, pp 3294–3301

15. Malisiewicz T, Gupta A, Efros AA (2011) Ensemble of exemplar-svms for object detection and beyond. In: 2011 IEEE international conference on computer vision (ICCV). IEEE, pp 89–96
16. Zhao H, Puig X, Zhou B, Fidler S, Torralba A (2017) Open vocabulary scene parsing. arXiv preprint arXiv:1703.08769
17. Liu X, Zhao Y, Zhu SC (2017) Single-view 3D scene reconstruction and parsing by attribute grammar. IEEE Trans Pattern Anal Mach Intell (99):1–1
18. Singh G, Kosecka J (2013) Nonparametric scene parsing with adaptive feature relevance and semantic context. In: Proceedings of the IEEE conference on computer vision and pattern recognition, pp 3151–3157
19. George M (2015) Image parsing with a wide range of classes and scene-level context. In: Proceedings of the IEEE conference on computer vision and pattern recognition, pp 3622–3630
20. Szegedy C, Liu W, Jia Y, Sermanet P, Reed S, Anguelov D et al. (2015) Going deeper with convolutions. In: Proceedings of the IEEE conference on computer vision and pattern recognition (pp. 1–9)
21. Felzenszwalb PF, Huttenlocher DP (2004) Efficient graph-based image segmentation. Int J Comput Vis 59(2):167–181
22. Tung F, Little JJ (2016) Scene parsing by nonparametric label transfer of content-adaptive windows. Comput Vis Image Underst 143:191–200
23. Kolmogorov V, Zabin R (2004) What energy functions can be minimized via graph cuts? IEEE Trans Pattern Anal Mach Intell 26(2):147–159
24. Shuai B, Zuo Z, Wang G, Wang B (2016) Scene parsing with integration of parametric and non-parametric models. IEEE Trans Image Process 25(5):2379–2391

Design of a Temperature and Humidity Monitoring System for Plant Growth Cabinets Based on Data Fusion

Shigang Cui, Kun Liu, Xingli Wu, Yongli Zhang and Lin He

1 Introduction

With the growing demand for green and healthy vegetables, a plant growth cabinet has drawn wide attention from the people around the world in recent years. A plant factory is an efficient production method which can use intelligent automatic control technology to control the internal temperature, humidity, light, CO_2 concentration and other environmental factors according to the demand of agricultural crops growth environment. It achieves the continuous production of annual crops, and has the characteristics of saving resources, safety and no pollution [1, 2]. The Plant growth cabinet with modern science and technology integration innovation, is a new mode of production, which provides effective technical support for the future development of intelligent agriculture.

The key technology of the plant growth cabinet is a reasonable and effective control system so that the internal environment of multiple factors are in a suitable range. Temperature and humidity play an important role in plant growth. In view of this situation, a temperature and humidity monitoring system for plant growth cabinet has been designed. The monitoring system takes STM32 microprocessor as the core controller, use the SHT11 sensor with I_2C bus interface to monitor temperature and humidity, and the realization of such control system through the performing structure. In order to solve the accuracy problem in the temperature and humidity monitoring system, the data fusion value and variance were obtained through batch estimation fusion method based on the average value. Then an

S. Cui · K. Liu (✉) · X. Wu · Y. Zhang · L. He
Tianjin Key Laboratory of Information Sensing and Intelligent Control,
Tianjin University of Technology and Education, No.1310, Dagu South Road,
Hexi District Tianjin 300222, China
e-mail: china68kun@163.com

Z. Deng (ed.), *Proceedings of 2017 Chinese Intelligent Automation Conference*,
Lecture Notes in Electrical Engineering 458,
https://doi.org/10.1007/978-981-10-6445-6_41

adaptive weighted fusion was conducted on each layer of sensor data in accordance with the optimal distribution principle of the weight to obtain accurate temperature and humidity value.

2 Overall Design Scheme

The plant growth cabinet is designed with 3 layers of integrated space, each layer is in the same control environment, which maintains the consistency of the control environment conditions. The suitable position of each layer in plant growth cabinet arrange a SHT11 temperature and humidity integrated sensor which is arranged through a long cable.

The Monitoring system is mainly composed of processor module, sensor module, display screen and actuator control module. The processor module is the control core part of the plant growth cabinet, receives the environmental data from the sensor module and displays on the LCD screen; The sensor module is used to collect the real-time data of temperature and humidity inside the plant growth cabinet; The display screen can set the parameters and display the environmental data in real time; The actuator control module maintains the internal environment of the plant growth cabinet in a suitable range by controlling the actuating mechanism be switch on and off. Structural diagram of control system was as shown in Fig. 1.

3 System Hardware Design

3.1 Processor Module

The processor module takes the STM32 microprocessor as its core controller, which is produced by the company ST. The STM32 is a micro controller based on high performance and low power consumption of the Cortex-M3 kernel, operating frequency up to 73 MHz, with 512 KB FLASH and 64 K bytes of SRAM, I^2C, USART interface module. ST company has released the function library, which reduce the development cycle and meet the design requirements of the system [3].

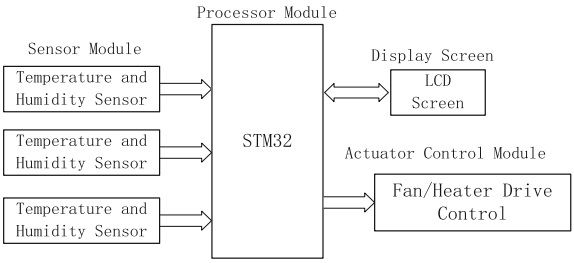

Fig. 1 Structural diagram of control system

3.2 Sensor Module

The sensor module uses SHT11 digital temperature and humidity sensor chip, it includes A/D converter and the corresponding communication interface. SHT11 digital temperature and humidity sensor chip has the advantages of quick response, strong anti-interference ability and high reliability, using the standard I^2C bus interface to connect with the STM32 to complete the corresponding monitoring work. The two I/O (P0.0, P0.1) of STM32 are connected with the SCK line and the DATA line of SHT11. SCK clock data line to complete connect with the STM32 synchronization, DATA lines to complete the acquisition of data transmission.

3.3 Display Screen

The display screen uses DGUS LCD screen as the display terminal, interface for 8Pin_2.0 mm belt lock, serial mode is TTL232, the screen resolution is 800 * 480, the normal working voltage is 12 V. In addition, the liquid crystal screen also has the characteristics of strong anti-interference and good electromagnetic compatibility.

3.4 Actuator Drive Circuit

The actuator adopts the switch quantity control system, STM32 GPIO port is not able to directly drive the actuator operation, so STM32 P1.2 and P1.3 are connected with light coupling MOC3041 and SCR, respectively. System make use of STM32 timer to output PWM wave to control the SCR trigger phase angle, which controls the opening and closing time of the actuator to achieve the STM32 GPIO port drive actuator.

4 System Software Design

The whole monitoring system is written by Keil uVision5 software, in order to facilitate the future expansion, this system uses the modular programming method, including the main task of the system, temperature and humidity data acquisition task, data processing task, communications task, actuator task and touch screen task. The main task is to set up by calling the function; temperature and humidity data acquisition task is to mainly used to control the temperature and humidity data regularly; data processing task is to collect data for data fusion; Communication

task is to achieve touch screen and MCU serial communication connection; Actuator task is to control the environment equipment; Touch screen task is to control of the actuator as well as the display of the current temperature and humidity.

4.1 Data Fusion Algorithm

The traditional single sensor monitoring technology is difficult to accurately collect the data of temperature and humidity, and the multi-sensor cooperative work must be adopted to complete the monitoring task [4]. This paper put forward a data fusion algorithm applied to plant growth cabinet monitoring system.

4.1.1 Fusion Method Based on the Average Value

According to the statistical analysis, the sample observations from the single sensor system have the characteristics of normal distribution [5]. Take the inner layer of the plant growth cabinet as an example, a series of temperature data are obtained by eighth measurements: $T_1, T_2, T_3, T_4, T_5, T_6, T_7, T_8$, the measured data was divided into 2 groups, respectively including T_1, T_3, T_5, T_7 and T_2, T_4, T_6, T_8, the average values $\bar{T}_1$, $\bar{T}_2$ and standard deviation σ_1, σ_2 of two groups were:

$$\bar{T}_1 = \frac{1}{4}\sum_{i=1}^{4} T_{2i-1} \tag{1}$$

$$\bar{T}_2 = \frac{1}{4}\sum_{i=1}^{4} T_{2i} \tag{2}$$

$$\sigma_1 = \sqrt{\frac{1}{4-1}\sum_{i=1}^{4}\left(T_{2i-1} - \bar{T}_1\right)^2} \tag{3}$$

$$\sigma_2 = \sqrt{\frac{1}{4-1}\sum_{i=1}^{4}\left(T_{2i} - \bar{T}_2\right)^2} \tag{4}$$

According to the research of literature [6], the batch estimation theory in the statistics can be used to solve the fusion value T^+ and variance σ^+ of the measured data according to formulas (1–4):

$$\mathrm{T}^{+} = \frac{\sigma_1^2 \bar{T}_2 + \sigma_2^2 \bar{T}_1}{\sigma_1^2 + \sigma_2^2} \tag{5}$$

$$\sigma^{+} = \frac{\sigma_1^2 \sigma_2^2}{\sigma_1^2 + \sigma_2^2} \tag{6}$$

4.1.2 Multi-sensor Adaptive Weighted Data Fusion

The temperature and humidity of the plant growth cabinet was the final value of fusion which was monitored by 3 sensor. The measured data in different layers had different weights W_i, so using the adaptive weighted data fusion algorithm can distinguish the measured data T_i^+ in each layer. According to the optimal condition of the minimum total mean-square error σ^2, their corresponding weights W_i were found in the adaptive form according to groups of data measured by the sensor, and finally the smaller the total variance, the higher the accuracy of data fusion [7].

Adaptive weighted fusion estimated value:

$$\hat{\mathrm{T}} = \sum_{i=1}^{N} W_i T_i^{+} \tag{7}$$

$$\sum_{i=1}^{N} W_i = 1 \tag{8}$$

the total square deviation after fusion was:

$$\sigma^2 = \sum_{i=1}^{N} W_i^2 \sigma_i^2 \tag{9}$$

According to the theory of multivariate function solving extreme values, when the weighting factor was:

$$W_i = \frac{1}{\sigma_i^2 \sum_{i=1}^{N} \frac{1}{\sigma_i^2}} \tag{10}$$

the minimum σ^2 can be calculated, and

$$\sigma_{\min}^2 = \frac{1}{\sum_{i=1}^{N} \sigma_i^2}$$

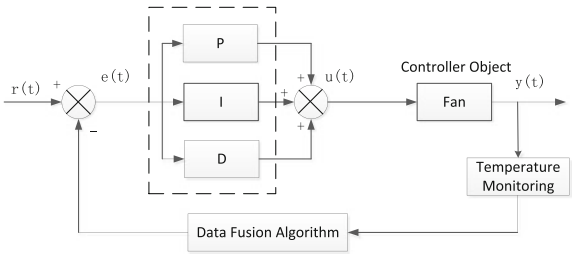

Fig. 2 System schematic diagram of PID control

4.2 PID Control Algorithm

In order to control the temperature more accurately, the paper combine multi-sensor data fusion and PID control algorithm. Firstly, the temperature is setting by the touch screen, the temperature sensor collects the environment temperature data by the sampling period, the fusion is processed by the multi-sensor data fusion technology, then calculate difference between the measured temperature and the setting temperature, and the PID operation, the temperature error and the error variation are obtained, and finally query control output query table, get the actual control output control, to achieve the control of the fan. System schematic diagram of PID control was as shown in Fig. 2.

5 Test Analysis

In order to verify the reliability and practicability of the system, the system is used to test the temperature and humidity data in the intelligent plant growth cabinet which is developed independently. The parameters of the internal environmental

Table 1 Monitoring data

Time/h	Data fusion algorithm		Arithmetic mean method	
	Temperature	Humidity	Temperature	Humidity
0	22.2	60.4	22.6	60.8
2	22	60.7	22.3	62.4
4	21.8	61.5	21.5	63.6
6	21.5	60.5	21.1	60.9
8	22.1	60.1	21.6	59.8
10	22.3	59.2	22.7	58.5
12	22.4	59.7	22.3	59.4
14	22.5	60	22.6	60.6
16	22.2	60.2	22.5	60.5
18	21.8	60.5	21.3	61.2
20	22.3	60.4	23.5	59.3
22	21.7	60.1	21.2	60.6
Average absolute error	0.27	0.46	0.65	1.13

factors are 23° with 60% humidity. Temperature and humidity monitoring data based on data fusion algorithm and arithmetic average are shown in Table 1.

Analyze of the Table 1: Data fusion algorithm results compared with arithmetic mean method is more close to the real truth, the absolute error is less than the arithmetic average, this is because the arithmetic average method with zero drift caused by the inevitable.

6 Conclusion

The design in this paper provides an effective solution for the development of plant growth cabinet monitoring systems. The monitoring system took the STM32 microprocessor as its core controller and used touch screen for human-computer interaction. To solve the accuracy problem in the temperature and humidity monitoring system, the means and variances for the fusioned temperature and humidity data were given by use of the average values based batch estimation fusion method, then the adaptive weighted fusion was conducted on each layer of sensor data in accordance with the optimal distribution principle of the weight to obtain accurate temperature and humidity values. The designed system can supply us with temperature and humidity data with small errors and therefore improves the control accuracy of plant growth cabinet.

Acknowledgements This work was supported by 863 Projects (Project No. 2015AA033303), Key technologies and systems of visible light communication (Project No. 2017YFB0400900) and the Foundation of Tianjin University of Technology and Education (Project No. KYQD12012).

References

1. He D (2016) The concept of plant factory and its development of domestic and foreign. Agric Eng Technol 10:13–15 (in Chinese)
2. Yang Q, Wei L, Liu W et al (2012) Plant factory system and practice. Chemical Industry Press (in Chinese)
3. Ai H, Wei J, Qiu Q et al (2014) Design of miniature plant factory temperature and humidity monitoring system of based on STM32. J Agric Mechanization Res 5:141–144 (in Chinese)
4. Wang H, Wang D (2015) An improved adaptive weighted fusion algorithm of wireless multi-sensor data batch estimation. Chin J Sens Actuators 8:1239–1243 (in Chinese)
5. Zhu M, Xu X, Chen Z (2010) Design of constant temperature box measurement and control system based on multi-sensor information fusion. Transducer Micro syst Technol 03:62–64 + 67 (in Chinese)
6. Zhang P, Dong W, Gao D (2014) An optimized bayesian estimation multi-sensor data fusion method. Chin J Sens Actuators 5:643–648 (in Chinese)
7. Tang Y (2015) Data processing based on adaptive weighted data fusion algorithm. Comput Technol Dev 4:53–56 (in Chinese)

Consensus of Heterogeneous Multi-agent Systems Based on Event-Triggered

Zhiqiang Yan and Ronghao Wang

1 Introduction

During the past years, the consensus control of MASs has attracted many researchers' attention. In the beginning, the consensus problems of MASs with first-order and second-order or high-order dynamics have been investigated from severally different directions, such as communication delay, switching topology, external disturbances in [1–3].

Afterwards researchers have worked out some results about heterogeneous MASs. In [4], Wang discussed linear consensus protocol and input saturated consensus protocol and obtained a sufficient condition of the system. In [5], the consensus of heterogeneous MASs under bounded communication delays were studied. The orther studies directions about consensus of heterogeneous MASs have been investigated in [6]. In view of MASs is limited to computing ability, communication ability, energy reserves and other restrictions, research on MASs based on event-triggered mechanism has attracted considerable attention. In [7], Lemmon applied event-triggered mechanism to distributed networked control systems. Meanwhile, research directions of the MASs about event-triggered mechanism have been investigated in [8, 9].

In fact, there are several research on solving the cooperation of heterogeneous MASs by event-triggered control. In [10], Huang investigated consensus problems for two different dynamics: first and second-order integrators, but zeno behavior is

Z. Yan
School of Automation, Nanjing University of Science and Technology, Nanjing, China

R. Wang (✉)
College of Defense Engineering, PLA University of Science and Technology, Nanjing, China
e-mail: wrh@893.com.cn

Z. Deng (ed.), *Proceedings of 2017 Chinese Intelligent Automation Conference*, Lecture Notes in Electrical Engineering 458,
https://doi.org/10.1007/978-981-10-6445-6_42

not excluded theoretically. In [11], Yin and Yue investigated the consensus problem for a set of discrete-time heterogeneous MASs.

Inspired by the above results, we consider a heterogeneous MASs, which compose of first-order and second-order agent, and solve consensus problem based on event-triggered mechanism. The contributions of this work are listed as follows. (i) This work propose a novel event-triggered condition different from have published articles in [10, 11] about the consensus problem of heterogeneous MASs, which can reduce the number of communication. (ii) Control protocols based on event-triggered mechanism are respectively designed for both leaderless and leader-follower heterogeneous systems. Meanwhile, the zeno phenomenon is excluded and a positive lower triggered bound will be found between two consecutive actuation updates.

2 Problem Formulation

Consider a heterogeneous MASs consisting of a group of n identical agents with a communication graph G. Assume that there are $m(m<n)$ first-order agents and $n-m$ second-order agents. The dynamics of the first-order agents can be described as follows:

$$\dot{x}_i(t) = u_i(t), i = 1, 2, \ldots, m, \tag{1}$$

where $x_i \in R, u_i \in R$, denote the position state and control input of the ith first-order agent and the second-order agents can be described as follows:

$$\begin{cases} \dot{x}_i(t) = v_i(t) \\ \dot{v}_i(t) = u_i(t) \end{cases}, i = m+1, \ldots, n, \tag{2}$$

where $x_i \in R, v_i \in R, u_i \in R$, denote the position state, velocity state and control input of the ith second-order agent.

In a leader-follower consensus problem, the dynamics of the leader is described by the following frist-order differential equation:

$$\dot{x}_0(t) = v_0 \tag{3}$$

where $x_0(t) \in R$,$v_0 \in R$ are the position state and velocity state.

3 Leaderless Consensus with Event-Triggered Control

An event-triggered heterogeneous MASs (1) and (2) consensus protocol of agent i is designed as follows:

$$\begin{cases} u_i(t) = \sum\limits_{j\in 1}^{n} a_{ij}(x_j(t_k) - x_i(t_k)), i = 1, 2, \ldots, m \\ u_i(t) = -2\mu v_i(t_k) + \mu \sum\limits_{j\in 1}^{n} a_{ij}(x_j(t_k) - x_i(t_k)), i = m+1, \ldots, n \end{cases} \tag{4}$$

for $t \in [t_k, t_{k+1}), k = \{0, 1, \ldots\}$. Where $\mu > 0$ is the control gain parameter and will be determined in sequel. The system (1) and (2) with the protocol (4) can be rewritten

$$\begin{cases} \dot{x}_i(t) = \sum\limits_{j\in 1}^{n} a_{ij}(x_j(t_k) - x_i(t_k)), i = 1, 2, \ldots, m \\ \dot{x}_i(t) = v_i(t),\ i = m+1, \ldots, n \\ \dot{v}_i(t) = -2\mu v_i(t_k) + \mu \sum\limits_{j\in 1}^{n} a_{ij}(x_j(t_k) - x_i(t_k)) \end{cases} \tag{5}$$

Suppose that the event-times of all agents are modeled as a sequence t_k for $k = \{0, 1, \ldots\}$. For agent i with dynamics (1) and (2), define measurement errors

$$\begin{aligned} e_{i,x}(t) &= x_i(t_k) - x_i(t) \\ e_{i,\tilde{v}}(t) &= \tilde{v}_i(t_k) - \tilde{v}_i(t) \end{aligned} \tag{6}$$

where $\tilde{v}_i(t) = v_i(t)/\mu + x_i(t)$. The event-times t_k are defined by the function

$f(e(t_k), x(t_k), \tilde{v}(t_k)) \geq 0$, which will be determined in sequel. Denote

$$\begin{cases} \mathrm{x_f(t) = col(x_1(t), x_2(t), \ldots . x_m(t)), x_s(t) = col(x_{m+1}(t), x_{m+2}(t), \ldots . x_n(t))} \\ \mathrm{\tilde{v}_s(t) = col(\tilde{v}_{m+1}(t), \tilde{v}_{m+2}(t), \ldots, \tilde{v}_n(t)), e_{x,f}(t) = col(e_{1,x}(t), e_{2,x}(t), \ldots . e_{m,x}(t))} \\ \mathrm{e_{x,s}(t) = col(e_{m+1,x}(t), e_{m+2,x}(t), \ldots . e_{n,x}(t)), e_{\tilde{v},s}(t) = col(e_{m+1,\tilde{v}}(t), e_{m+2,\tilde{v}}(t), \ldots . e_{n,\tilde{v}}(t))} \end{cases} \tag{7}$$

Let $\psi(t) = col[x_f(t), x_s(t), \tilde{v}_s(t)]$,$e(t) = col[e_{x,f}(t), e_{x,s}(t), e_{\tilde{v},s}(t)]$, then system (1) and (2) can be transformed into the closed-loop system as follows:

$$\dot{\psi}(t) = -F\psi(t) + Je(t) \tag{8}$$

$$F = \begin{bmatrix} L_{11} & L_{12} & 0 \\ 0 & \mu I_{n-m} & -\mu I_{n-m} \\ L_{21} & L_{22} - \mu I_{n-m} & \mu I_{n-m} \end{bmatrix}, J = -\begin{bmatrix} L_{11} & L_{12} & 0 \\ 0 & 0 & 0 \\ L_{21} & L_{22} - \mu I_{n-m} & \mu I_{n-m} \end{bmatrix} \tag{9}$$

$L_{11} \in R^{m\times m}, L_{12} \in R^{m\times(n-m)}, L_{21} \in R^{(n-m)\times m}$ and are parts of $L_{22} \in R^{(n-m)\times(n-m)}$. Laplacian matrix is $L = \begin{bmatrix} L_{11} & L_{12} \\ L_{21} & L_{22} \end{bmatrix}$.

Assume an undirected graph $G(V, E, A)$ is connected, mean that $L1_n = 0_n$, then we can get

$$\begin{aligned} 1_{2n-m}^T(-F\psi(t) + Je(t)) &= 0_{2n-m} \\ 1_{2n-m}^T\dot{\psi}(t) &= 0_{2n-m} \end{aligned} \tag{10}$$

Denote $\xi(t) = \psi(t) - \omega 1_{2n-m}$, where $\omega = (1/(2n-m))\sum_{i=1}^{2n-m}\psi_i$. From (10), it is clear that ω is a constant. Then the system (10) becomes

$$\dot{\xi}(t) = -F\xi(t) + Je(t) \tag{11}$$

We can get that $\lim_{t\to\infty}\psi(t) = \omega 1_{2n-m}$ when $\lim_{t\to\infty}\xi(t) = 0_{2n-m}$, that is mean $\lim_{t\to\infty} x_i = \omega, i = 1, 2, \ldots, n, \lim_{t\to\infty}\tilde{v}_i = \omega, i = m+1, m+2, \ldots, n.$ Because of $\tilde{v}_i(t) = v_i(t)/\mu + x_i(t)$, we can get $\lim_{t\to\infty} v_i = 0, i = m+1, m+2, \ldots, n$, the consensus problem of MASs (8) can be changed into the stability issue of system (11).

Theorem 1 *Assume that the interconnection topology G associated with multi-agent system (1)–(2) is connected. If there exist a symmetric positive definite matrix $P \in R^{(2n-m)\times(2n-m)}$, and constants $\mu > 0$ such that*

$$(F_1 + \mu F_2)^T P + P(F_1 + \mu F_2) \geq 0 \tag{12}$$

event-triggered condition $f(e(t_k), x(t_k), \tilde{v}(t_k)) = \|e\| - \sigma\frac{\lambda_{\min}(Q)\|\xi\|}{2\lambda_{\max}(P)\|J\|} \geq 0$, and the event-triggered consensus protocol (4), heterogeneous MASs (1) and (2) can achieve consensus, where $F_1 = \begin{bmatrix} L_{11} & L_{12} & 0 \\ 0 & 0 & 0 \\ L_{21} & L_{22} & 0 \end{bmatrix}, F_2 = \begin{bmatrix} 0 & 0 & 0 \\ 0 & I_{n-m} & -I_{n-m} \\ 0 & -I_{n-m} & I_{n-m} \end{bmatrix}$.

Proof For system (1) and (2), construct following Lyapunov function candidate

$$V(\xi) = \xi^T P\xi \tag{13}$$

where P is a positive definited matrix.

Consider the derivative of $V(\xi)$ and along the trajectory of (13) we can get

$$\begin{aligned} \dot{V}(\xi) &= \dot{\xi}^T P\xi + \xi^T P\dot{\xi} \\ &= -\xi^T(F^T P + PF)\xi + 2\xi^T PJe \\ &= -\xi^T Q\xi + 2\xi^T PJe \end{aligned} \tag{14}$$

where $Q = F^T P + PF$, $F = F_1 + kF_2$. Make the measurement error e to satisfy $\|e\| \leq \sigma \frac{\lambda_{\min}(Q)\|\xi\|}{2\lambda_{\max}(P)\|J\|}$, with $\sigma \in (0,1)$, from (12), Q is positive definite with k given in (13), therefore

$$\begin{aligned} \dot{V}(\xi) &\leq -\lambda_{\min}(Q)\|\xi\|^2 + 2\lambda_{\max}(P)\|J\|\|\xi\|\|e\| \\ &= -\|\xi\|(\lambda_{\min}(Q)\|\xi\| - 2\lambda_{\max}(P)\|J\|\|e\|) \\ &\leq -(1-\sigma)\lambda_{\min}(Q)\|\xi\|^2 \leq -\frac{(1-\sigma)\lambda_{\min}(Q)}{\lambda_{\max}(P)} V(\xi) \end{aligned} \tag{15}$$

From (15), we conclude that $\lim_{t\to 0} \xi(t) = 0$. In other words, under the event-triggered consensus control protocol (4), MASs (1) and (2) achieves consensus.

Theorem 2 *In MASs* (1) and (2) *based on event-trigger mechanism of consensus control protocol* (4), *and trigger function* $f(e(t_k), x(t_k), \tilde{v}(t_k))$, *let* K *satisfy the following expression* $K = \sigma \frac{\lambda_{\min}(Q)}{2\lambda_{\max}(P)\|J\|}$, *the triggered time interval* $t_{k+1} - t_k$ *are bounded by the time*

$$\Delta t_{\min} = \frac{\ln(\|F\|) - \ln(\left\|\frac{\|F\| + K\|J\|}{1+K}\right\|)}{\|F\| - \|J\|} \tag{16}$$

Proof be similar to Tabuada [12] proofs that calculate the interval lower bound. Based on measurement error $\|e\|$, we can written as follows:

$$\frac{\|e\|}{\|\xi\|} \leq \sigma \frac{\lambda_{\min}(Q)}{2\lambda_{\max}(P)\|J\|} \tag{17}$$

Let $\phi(t) = \|e(t)\|/\|\xi(t)\|$, we can get that when $\phi(t) = \sigma \frac{\lambda_{\min}(Q)}{2\lambda_{\max}(P)\|J\|}$, system will be triggered, transfer state information and update control inputs. Take derivative of $\phi(t)$, when the derivative of $\phi(t)$ become bigger, the inter event times become shorter. So we can get the minimum inter-event times, when the derivative of $\phi(t)$ reach its maximum.Take the derivative of $\phi(t) = \|e(t)\|/\|\xi(t)\|$, we can get

$$\begin{aligned} \dot{\phi} &= \frac{d}{dt}\frac{\|e(t)\|}{\|\xi(t)\|} = \frac{d}{dt}\frac{(e^T e)^{1/2}}{(\xi^T \xi)^{1/2}} = -\frac{e^T \dot{\xi}}{\|e\|\|\xi\|} - \frac{\xi^T \dot{\xi}}{\|\xi\|^2}\frac{\|e\|}{\|\xi\|} \\ &\leq \frac{\|e\|\|\dot{\xi}\|}{\|e\|\|\xi\|} + \frac{\|\xi\|\|\dot{\xi}\|\|e\|}{\|\xi\|\|\xi\|\|\xi\|} = (1 + \frac{\|e\|}{\|\xi\|})\frac{\|\dot{\xi}\|}{\|\xi\|} = (1+\phi)(\|F\| + \|J\|\phi) \end{aligned} \tag{18}$$

From the above analysis, the derivative of $\phi(t)$ reach maximum when $\dot{\phi} = (1+\phi)(\|F\| + \|J\|\phi)$. Solving the differential equations $\phi(t)$, assume $\phi(t, \phi_0)$ is the solution differential equations, we can get the solution as follows:

$$\phi(t,\phi_0)=\frac{e^{(t+C)(\|J\|-\|F\|)}-\|F\|}{\|J\|-e^{(t+C)(\|J\|-\|F\|)}} \tag{19}$$

where e is natural constant, ϕ_0 is the initial value of differential equations, C is the constant of indefinite integral solutions. Because the system start first triggered, so we can get $\phi_0=0$, and get into the equation, $C=\frac{\ln(\|F\|)}{\|J\|-\|F\|}$, we can get

$$\phi(t,\phi_0)=\frac{e^{(t+\frac{\ln(\|F\|)}{\|J\|-\|F\|})(\|J\|-\|F\|)}-\|F\|}{\|J\|-e^{(t+\frac{\ln(\|F\|)}{\|J\|-\|F\|})(\|J\|-\|F\|)}} \tag{20}$$

Let $K=\sigma\frac{\lambda_{\min}(Q)}{2\lambda_{\max}(P)\|J\|}$, solving the differential equation $\phi(t,\phi_0)$ leads to

$$\Delta\tau_{\min}=\frac{\ln(\|F\|)-\ln(\left\|\frac{\|F\|+K\|J\|}{1+K}\right\|)}{\|F\|-\|J\|}=\frac{\ln(\frac{(1+K)\|F\|}{\|F\|+K\|J\|})}{\|F\|-\|J\|}>0 \tag{21}$$

which is a positive bound due to the fact that $\|F\|>\|J\|$, the proof is now finished.

4 Leader-Following Consensus with Event-Triggered Control

Assumption 1 The state information of the leader can be measured in continuous-time by the followers. An undirected graph $G(V,E,A)$ is connected and at least one agent is connected with the leader.

A control protocol for heterogeneous MASs (1)–(3) with an active leader is designed

$$\begin{cases} u_i(t)=\sum\limits_{j\in 1}^{n}a_{ij}(x_j(t_k)-x_i(t_k))+a_{i0}(x_0(t)-x_i(t_k))+v_0(\mathrm{t}),i=1,2,\ldots,m \\ u_i(t)=\mu(v_0(t)-v_i(t_k))+\sum\limits_{j\in 1}^{n}a_{ij}(x_j(t_k)-x_i(t_k)) \\ \quad +a_{i0}(x_0(t)-x_i(t_k)),i=m+1,\ldots,n \end{cases} \tag{22}$$

denote the measurement errors

$$\begin{aligned} e_{i,x}(t)&=x_i(t_k)-x_i(t) \\ e_{i,v}(t)&=v_i(t_k)-v_i(t) \end{aligned} \tag{23}$$

for $t\in[t_k,t_{k+1}),k=\{0,1,\ldots\}$. The t_k are defined by function $f(e(t_k),x(t_k),v(t_k))\geq 0$.

Let $H = L + B$, $\tilde{x}_i(t) = x_i(t) - x_0(t)$, $\tilde{v}_i(t) = v_i(t) - v_0(t)$, based on the fact that $H\tilde{x}(t) = Hx(t) - B\vec{1}x_0(t), H\tilde{v}(t) = Hv(t) - B\vec{1}v_0(t)$, MASs (1)–(3) can changed

$$\begin{pmatrix} \dot{\tilde{x}}_f(t) \\ \dot{\tilde{x}}_s(t) \\ \dot{\tilde{v}}_v(t) \end{pmatrix} = -U \begin{pmatrix} \tilde{x}_f(t) \\ \tilde{x}_s(t) \\ \tilde{v}_s(t) \end{pmatrix} + W \begin{pmatrix} e_{x,f}(t) \\ e_{x,s}(t) \\ e_{v,s}(t) \end{pmatrix} \tag{24}$$

$$U = \begin{pmatrix} L_{11} + B_f & L_{21} & 0 \\ 0 & 0 & -I_{n-m} \\ L_{21} & L_{22} + B_s & \mu I_{n-m} \end{pmatrix}, W = -\begin{pmatrix} L_{11} + B_f & L_{21} & 0 \\ 0 & 0 & 0 \\ L_{21} & L_{22} + B_s & \mu I_{n-m} \end{pmatrix}$$

$B_f = diag(a_{10}, a_{20}, \ldots, a_{m0}), B_s = diag(a_{(m+1)0}, a_{(m+2)0}, \ldots, a_{n0})$

Let $\xi(t) = col(\tilde{x}_f(t)\, \tilde{x}_s(t)\, \tilde{v}_s(t)), e(t) = col(e_{x,f}(t)\, e_{x,s}(t)\, e_{v,s}(t))$, (23) expressed as

$$\dot{\xi}(t) = -U\xi(t) + We(t) \tag{25}$$

Theorem 3 *Assume that the leader-follower topology G associated with MASs* (1)–(3) *is connected. If there exist a symmetric positive definite matrix* $P_L \in R^{(2n-m)\times(2n-m)}$, *and constants* $\mu > 0$ *such that*

$$U^T P_L + P_L U \geq 0 \tag{26}$$

under the event-triggered condition

$$f(e(t_k), x(t_k), v(t_k)) = \|e\| - \sigma \frac{\lambda_{\min}(Q_L)\|\xi\|}{2\lambda_{\max}(P_L)\|W\|} \geq 0 \tag{27}$$

and protocol (22), *heterogeneous MASs* (1)–(3) *can achieve consensus.*

Theorem 4 *In MASs* (1)–(3) *based on event-trigger mechanism of consensus control protocol* (22), *and trigger function* (27), *the triggered time interval* $t_{k+1} - t_k$, K *satisfy the following expression* $K = \sigma \frac{\lambda_{\min}(Q_L)}{2\lambda_{\max}(P_L)\|W\|}$, *the inter-event times are bounded by the time* $\Delta t_{\min} = \frac{\ln(\|U\|) - \ln(\left\|\frac{\|U\| + K\|W\|}{1+K}\right\|)}{\|U\| - \|W\|}$.

5 Simulations

A leaderless heterogeneous MASs is showed on Fig. 1a. The communication topology G has a globally vertex 5, 1 and 2 denote the first-order agents, 3, 4 and 5 denote the second-order agents. Each agent is governed by the controller (4). The

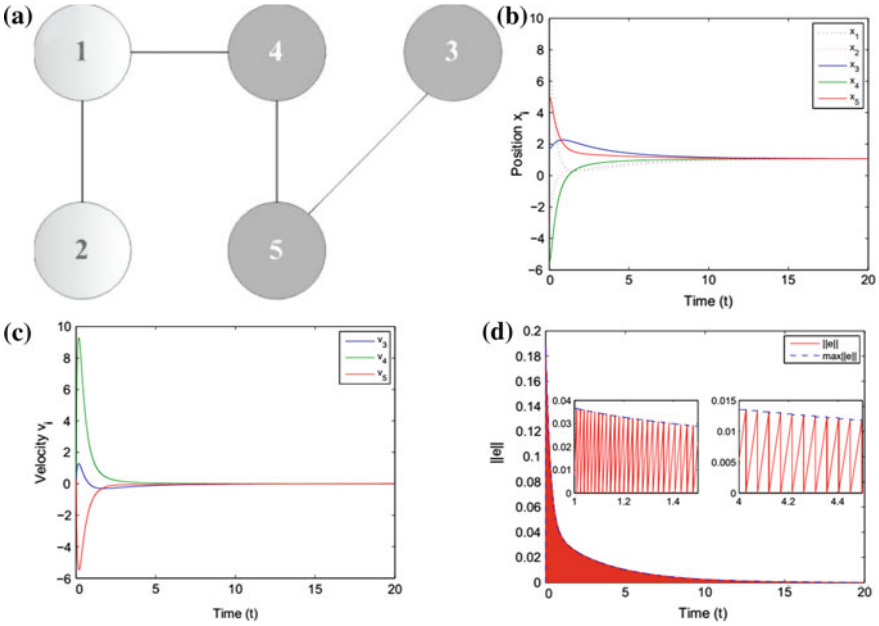

Fig. 1 **a** Leaderless heterogeneous MASs. **b** The trajectories of position x_i. **c** The trajectories of velocity v_i. **d** Evolution of error signals for agent

parameters are given by $k = 6$ and $\sigma = 0.8$ for all agents. The initial positions and velocities are randomly chosen within $[-10, 10]$ and $[0, 0.5]$.

Figure 1 we know that the leaderless heterogeneous MASs (1) and (2) with consensus protocol (4) can solve consensus problem. Figure 1d shows that curve $\|e\|$ is always in the bottom of curve max $\|e\|$,which means that the error $\|e\|$ is bounded by the threshold $\sigma \frac{\lambda_{\min}(Q)\|\xi\|}{2\lambda_{\max}(P)\|J\|}$. Figure 1d also shows consensus controllers are illustrated for the four agents, whose event-driven update frequencies are decreasing as time evolves, mean that the triggered time is getting longer as time goes by.

6 Conclusion

An event-triggered consensus problem of heterogeneous MASs with leaderless and leader-following was considered in this paper. The heterogeneous consensus controllers have been proposed for all agents based on an event-triggered control strategy. Some sufficient conditions for heterogeneous MASs consensus have been solved. Numerical examples have been presented to verify the efficiency of proposed controls. The consensus of heterogeneous MASs based on event-driven under external disturb and communication delay will be researched in the future.

Acknowledgements This work is supported by the National Natural Science Foundation of China under Grant No. 61603414.

References

1. OlfatiSaber R, Murray R (2004) Consensus problems in networks of agents with switching topology and time-delays. IEEE Trans Autom Control 49(9):1520–1533
2. Lin P, Jia Y (2009) Consensus of second-order discrete-time multiagent systems with nonuniform time-delays and dynamicallychanging topologies. Automatica 45(9):2154–2158
3. Zhang Y, Tian Y (2010) Consensus of data-sampled multi-agent systems with random communication delay packet loss. IEEE Trans Autom Control 55(4):939–943
4. Zheng Y, Zhu Y, Wang L (2011) Consensus of heterogeneous multi-agent systems. IET Control Theory Appl 15(16):1881–1888
5. Tian Y, Zhang Y (2012) High-order consensus of heterogeneous multi-agent systems with unknown communication delays. Automatica 48(6):1205–1212
6. Huang WC, Zeng JP, Sun HF (2015) Robust consensus for linear multi-agentsystems with mixed uncertainties. Syst Control Lett 76:56–65
7. Wang X, Lemmon MD (2011) Event-triggering in distributed networked control systems. IEEE Trans Autom Control 56(3):586–601
8. Lehmann D, Lunze J (2012) Event-based control with communication delays and packet losses. Int J Control 85(5):563–577
9. Hu J, Chen G, Li H (2011) Distributed event-triggered tracking control of leader-follower multi-agent systems with communication delays. Kybernetika 47(4):630–643
10. Huang N,Duan Z, Zhao Y (2014) Event-triggered consensus for heterogeneous multi-agent systems. The 33rd Chinese Control Conference, pp 1259–1264
11. Yin X, Yue D, Hu S (2013) Event-triggered consensus of heterogeneous multi-agent systems with double-integrator dynamics. J Franklin Inst 350(3):651–669
12. Ren W, Beard R (2005) Consensus seeking in multiagent systems under dynamically changing interaction topologies. IEEE Trans Autom Control 50(5):655–661

Lifetime Maximization Strategy for Wireless Sensor Network Using Cluster-Based Method

Xiaoping Ma, Honghui Dong, Limin Jia and Ruhao Zhao

1 Introduction

As the development of the wireless sensor and communication technology, the Wireless Sensor Networks (WSNs) are applied widely to detect and estimate the service condition of the equipment and devices. However, the energy capacity, processing ability and communication bandwidth of the tiny sensor nodes are all limited, in order to make full use of the limited energy and guarantee the stability and reliability of the wireless sensor network, it is necessary to design an energy-efficiency protocol to extend the lifetime of the system.

There are various wireless sensor networks adopting the cluster-based protocol to cope with energy-efficiency issues [1, 2]. In the cluster-based structures, all the sensor nodes are divided into several clusters, and select one sensor node in each cluster as the cluster head (CH). The CH received the sensor information of others in the cluster and then transmitted to the base station (BS). The CH sensor nodes will consume large more energy than No-CH nodes. The clustering and CHs selection schemes as the most important factors had become the focus of study. As one of the effective cluster-based methods, The CHs selection strategy proposed in LEACH [3] and LEACH-C [4] is based on the probabilistic model, which just consider whether the node had been selected as the CH in recent rounds and the sensors are divided into several clusters uniformly while ignoring the location information of the sensors. In the practical monitoring field, the sensors are deployed unevenly, the distances among the sensor are different from each other. To reduce the energy waste caused by the unreasonable cluster solutions, K-means [5, 6] is used to gather the sensors close to each other into one group and save the energy as more as possible. However, the selection of the initial CHs will affect the

X. Ma · H. Dong · L. Jia (✉) · R. Zhao
State Key Lab of Rail Traffic Control & Safety,
Beijing Jiaotong University, Beijing 100044, China
e-mail: jialm@vip.sina.com

Z. Deng (ed.), *Proceedings of 2017 Chinese Intelligent Automation Conference*,
Lecture Notes in Electrical Engineering 458,
https://doi.org/10.1007/978-981-10-6445-6_43

optimization solutions mostly, to avoid the local optimal result, the K-means ++ is adopted in this paper [7]. Furthermore, the number of clusters will affect the total energy consumption of the system, which is determined by the scales of the sensors and the distances to the base station, the optimization method is used to calculate the optimal number of the clusters [8]. The lifetime of the system is determined by the communicate rounds of the first sensor which fails because of energy exhaust, the balance of the energy consumption is another very important factor to be considered in this paper [9, 10].

The structure of the sensor network is shown in Fig. 1, it is consisted of sensor layer and communication layer. In the sensor layer, there are a large number of sensor nodes in charge of sensing the service condition information, while the communication layer ensuring the information could be sent to the base station successfully. The energy will be consumed in the communication process mostly.

In this paper, we proposed an effective method to optimal the clusters to minimize the energy consumption. First, we calculate the optimal number of clusters to decline the total energy consumption. Second, we divided the sensor nodes into K clusters base on K-means ++, to save the energy consumption from the No-CH nodes to CH node. The strategy proposed in this paper will extend the lifetime of the network greatly.

2 Sensor Network Energy Consumption Model

To meet energy-efficiency demands in sensor network, based on the random distribution of the sensor nodes in the monitoring region, we adopt the K-means + + strategy to divide the nodes close to each other into the same cluster. It is benefitted to minimize the energy consumption.

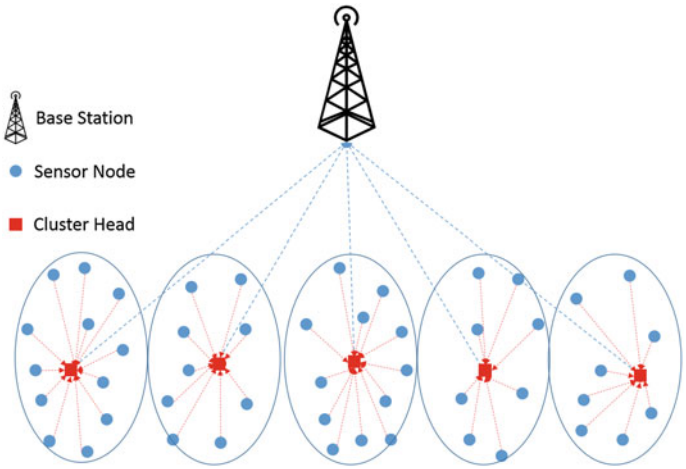

Fig. 1 The communication structure of the sensor network

There are lots of sensors deployed in the monitoring area to detect the condition. The sensor nodes are all with sufficient transmission power to communicate with the nearest base station directly. A large quantity of energy will be wasted in this direct transmission model because the transmission energy consumption is proportional to the square or four powers of the distance between source and destination nodes. The energy consumption for *l-bit* data is shown in Eq. 1:

$$E = E_R + E_D + E_T \tag{1}$$

where E_R is the energy consumption by received *l-bit* data, it is defined as:

$$E_R = L * E_{ele} \tag{2}$$

where E_{ele} is the energy consumption to process *1-bit* data, and E_D is the energy consumption to aggregate *l-bit* data, which is defined as,

$$E_D = l * E_{DA} \tag{3}$$

where E_{DA} represents the energy consumption in *1-bit* data aggregation. And E_T is the energy consumption to transmit *l-bit* data, which is defined as:

$$E_T = \begin{cases} l * E_{ele} + l * \xi_{fs} * d^2, d < d_0 \\ l * E_{ele} + l * \xi_{mp} * d^4, d > d_0 \end{cases} \tag{4}$$

where ξ_{fs} and ξ_{mp} are the energy coefficient related to the distance between the source and the destination. The reference distance d_0 is defined as:

$$d_0 = \sqrt{\frac{\xi_{fs}^2}{\xi_{mp}}} \tag{5}$$

The Eq. (4) shows that the transmission energy consumption go hand in hand with the distance, which imply that the information transmitted from the sensor nodes to the base station will waste larger number of energy, it is a wise way to select one sensor node to complete the mission on behalf of the cluster. In this paper, we divided the sensor nodes into several clusters, and then select one node in each cluster as the cluster head (CH), other sensor nodes as the cluster member called Non-CH nodes sent their information to the CHs, and then transmitted to the base station.

3 The Optimal Number of Clusters

As shown in last section, the energy consumption is mostly related to the distance, declining the valid transmitting distance is an effective way [5, 6]. Dividing the sensor nodes close to each other into the same group will be benefit to the energy efficiency of the nodes. As an effective strategy to generate the clusters based on the distance, K-means ++ would complete the objective in the paper. However, before this we should calculate the number of the clusters K.

The optimal number of the clusters k is the prerequisite to design the cluster-based protocols based on K-means ++, and the energy-efficiency is the fine criterion. We assume that the base station is located at the ordinate origin $B(0,0)$, there are N sensor nodes deployed in the monitoring region $M \times M$ following uniform distribution $S(x,y)$, where $x \in [-M/2,\ M/2]$ and $y \in [-(1+\alpha)M, -\alpha M]$, which means that nearest distance between the sensor node to the base station is αM as shown in Fig. 2.

The sensor nodes wound be given two different identities (CH nodes and Non-CH nodes), and the energy consumption of the sensor system is also generated by the two parts [7]. The Non-CH nodes just transmit their information to CH nodes, the transmission energy consumption follows the free-space model because of the small distance among them. As shown in Eq. (5):

$$E_{Non-CH} = l * E_{ele} + l * \xi_{fs} * d_{toCH}^2 \tag{6}$$

The CHs in charge of the data reception, aggregation and transmission, the energy consumed by CHs is correlated to the above parts. Due to the BS located far away from the sensor nodes, the multipath model is adopted in the transmission

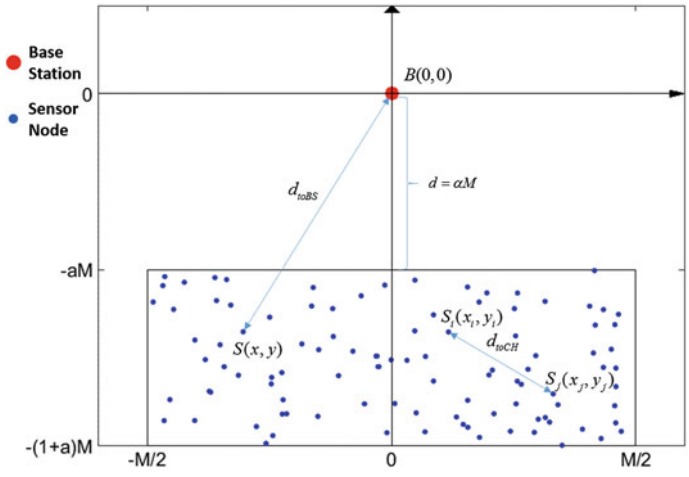

Fig. 2 The cluster structure of the sensor network

energy consumption, we assume that all the sensor nodes are divided into k clusters equally, and there are $n = N/k$ nodes in each cluster. As shown in Eq. (7):

$$\begin{aligned} E_{CH} &= (n-1) * l * E_{ele} + n * l * E_{DA} + l * E_{ele} + l * \xi_{mp} * d_{toBS}^4 \\ &= l * (n * E_{ele} + n * E_{DA} + \xi_{mp} * d_{toBS}^4) \\ &= l * (\frac{N}{k} * E_{ele} + \frac{N}{k} * E_{DA} + \xi_{mp} * d_{toBS}^4) \end{aligned} \tag{7}$$

The energy consumed in one cluster in 1 rounds is calculated as:

$$E_{Cluster} = E_{CH} + \sum_{i=1}^{n-1} E_{Non-CHi} \tag{8}$$

It means in 1 round, there is one sensor node acts as CH while other $n-1$ nodes as Non-CH. The total energy consumption in the cluster in the sum of both.

The probability density of the sensor nodes is $\rho(x, y)$, where the distribution of x and y are all uniformed. The location of the sink node is $B(0, 0)$, the distance between the CH and the base station is defined as:

$$d_{toBS} = \sqrt{x^2 + y^2} \tag{9}$$

The expected power distance from the CH to the base station is given as:

$$\begin{aligned} E[d_{toBS}^4] &= \iint (\sqrt{x^2 + y^2})^4 \rho(x, y) dx dy \\ &= \int_{-(\alpha+1)M}^{-\alpha M} \int_{-M/2}^{M/2} (x^2 + y^2)^2 \rho(x, y) dx dy \end{aligned} \tag{10}$$

We assume that the sensor nodes in the area follows a uniform distribution, the probability density is defined as:

$$\rho(x, y) = 1/M^2 \tag{11}$$

And the expectation is calculated as:

$$E[d_{toBS}^4] = (0.0125 + \frac{(\alpha+1)^3 - \alpha^3}{18} + \frac{(\alpha+1)^5 - \alpha^5}{5}) * M^4 \tag{12}$$

The distance from the Non-CH I to CH j is defined as:

$$d_{toCH} = \sqrt{(x(i) - x(j))^2 + (y(i) - y(j))^2} \tag{13}$$

The expected squared distance from the Non-CH to the CH is expressed as:

$$E[d_{toCH}^2] = \frac{1}{2}\int\int\iint (\sqrt{(x_1-x_2)^2+(y_1-y_2)^2})^2 \rho(x_1,x_2,y_1,y_2)dx_1dx_2dy_1dy_2$$
$$= \frac{1}{2}\rho(x_1,x_2,y_1,y_2) * (\int\int \int_0^{M/\sqrt{k}} \int_0^{M/\sqrt{k}} (x_1-x_2)^2 dx_1dx_2dy_1dy_2$$
$$+ \int\int \int_0^{M/\sqrt{k}} \int_0^{M/\sqrt{k}} (y_1-y_2)^2 * dy_1dy_2dx_1dx_2) \tag{14}$$

The distribution of the sensor nodes is independent to each other, so the joint probability density function is defined as:

$$\rho(x_1,x_2,y_1,y_2) = \rho(x_1) * \rho(x_2) * \rho(y_1) * \rho(y_2) = 1/(M^4/k^2) \tag{15}$$

And the expectation is calculated as:

$$E[d_{toCH}^2] = \frac{M^2}{6k} \tag{16}$$

And then the expectation of total energy consumption in one node is given as:

$$E_{cluster} = E_{CH} + (\frac{N}{k} - 1)E_{Non-CH} \approx E_{CH} + \frac{N}{k} * E_{Non-CH} \tag{17}$$

The total energy consumption of all nodes is defined as:

$$\begin{aligned} E_{total} &= k * E_{cluster} = k * E_{CH} + N * E_{Non-CH} \\ &= l * (2N * E_{ele} + N * E_{DA} + k * \xi_{mp} * d_{toBS}^4 + N * \xi_{fs} * d_{toCH}^2) \end{aligned} \tag{18}$$

The optimal number of clusters is calculated by setting the derivative to zero:

$$k_{opt} = \sqrt{\frac{\xi_{fs} * N * M^2}{6\xi_{mp} * d_{toBS}^4}} \tag{19}$$

4 Communication Protocol Base on K-Means ++

The energy consumption is related to the information transmission distance, declining the transmission distance is an effective way to decrease the energy consumption and prolong the lifetime of the sensor network. The location of each

node and the distance between the nodes are all different. The cluster-based protocol proposed in this paper based on K-means ++ select the nodes close to each other in one cluster, which could decline the energy consumption of the Non-CH nodes. The initial optimal number of clusters k is determined by the number of all the sensor nodes and the distance to the sink node as shown in (19).

4.1 The Process of K-Means ++ Based Cluster Strategy

The proposed strategy based on K-means ++ classify the sensor nodes close to each other into the same cluster. The objective function is minimizing the total distance among the Non-CH nodes to the CHs. The cluster generation method based on K-means ++ is carried out as follows.

Assume that there are N sensor nodes deployed in the monitoring region, and the optimal number of clusters is k. Due to the uniform distribution of the sensor nodes, in order to minimize the energy consumed during the communication among the Non-CH to CH, ideally, the nodes close to each other should be divided into the same cluster. To avoid obtaining partial optimal solutions only as the cluster strategy adopted K-means in, the K-means ++ method is implemented to initial the clusters as Table 1:

In step 3, in order to avoid the effect of noise, the node with larger but not largest distance will be selected as the new CH. The allocation solution by K-means + + probably not ideal enough to make full use of the energy. The clusters should be optimized in the following phases.

4.2 The Cluster Head Generation

The CHs (cluster heads) are the most important roles in the wireless network systems. First, the cluster heads as the leaders in their own cluster are in charge of collecting the information from other Non-CH nodes and transmitting forward to the sink nodes, which will consume more energy than others. Second, the clusters

Table 1 The clusters generation steps

The clusters generated based on K-means ++
Step 1: 1 node is selected from N sensor nodes as the first CH;
Step 2: Calculate the distance to the nearest selected CH for every sensor nodes D(x);
Step 3: Select a new sensor node as another new CH. The larger the D(x) the greater the probability to be selected;
Step 4: Repeat the step2 and step3 until k CHs are all selected;
Step 5: The standard K-means algorithm is operated based on the k CHs selected.

generation in this paper by the generic algorithm are mostly based on the conditions of the cluster heads. Third, the rotation of cluster heads is necessary to balance the energy consumption among all nodes. The design of cluster heads selection and rotation criterion is the vital challenges in the monitoring network. At first, we should select the first group of CHs based on the K-means ++ solution, and the nodes nearest to them will be selected as the first-round CHs.

$$CHs_{virtual} = (\frac{\sum_{i=1}^{n} x(i)}{n}, \frac{\sum_{i=1}^{n} y(i)}{n}) \tag{20}$$

where, n is the sensor number in the cluster. Once the CHs are selected, the system will communicate based on the structure. After these phases, the CHs will be updated and rotated in the new round to balance the energy consumption.

4.3 The Cluster Head Rotation

In general, the energy consumed by the CHs is far more than the Non-CH, equality of CHs duty opportunity is conducive to system harmony. However, everyone's situation is different, as we make the selection, each factor should be considered.

To decide on the CH rotation, we should synthesize each kind of factor into consider, the probability on CHs candidacy, the residual energy and the energy consumption prediction. The importance of each factor is various in different IA (Industrial Application), the weighting coefficients are introduced to adjust the impact of the above factors to the selection of CHs. The whole probability to select the CHs is defined as:

$$P = \lambda_1 p_1 + \lambda_2 p_2 + \lambda_3 p_3 \tag{21}$$

where λ_i is the weighting coefficient, the selection and rotation of the CHs based on the probability take all the factors account, the optimal solution is benefitted to generate clusters. p_1 represents the probability on CHs candidacy, which means that the nodes had not been the CHs will be selected as CHs with high probability; p_2 represents the ratio of residual energy of the nodes, which means that the nodes with more residual energy will be selected as the CHs with higher probability; p_3 represents the energy consumption prediction in the following round, the less the energy consumption the more the chance to be selected.

The system lifetime is determined by the sensor who fails at first. CHs rotation scheme could avoid the energy excessive consumption for the CHs and balance the energy consumption among all the sensors to extend the system lifetime.

5 Performance Evaluation

In this section, the validity and reliability of the communication protocols proposed in this paper are tested via computer simulation with Python. We calculate and compare the simulation results with other protocols used widely in the sensor networks.

In our simulation scenarios, there is one BS located at (x = 0, y = 0) and the sensor nodes are distributed randomly in the rectangular region between (x = −50, y = −100) and (x = 50, y = −200). The base station is in charge of collecting the sensor information in corresponding monitoring region. In the first communication phase, the sensor nodes sent the detecting information to the CHs; in the second phase, the CHs transmit the information to the base station. In the simulation phase, we assume that there are 200 sensor nodes distributed randomly in the separate monitoring area. The optimal initial number of clusters is selected as 6.

We compared the protocol proposed in this paper with other two representative methods LEACH and Single-Hop, with the same simulation initial conditions, same nodes deployment and initial energy. However, the gaps in simulation results are shown in Fig. 3, we can see that almost all the sensor nodes died at about 200 rounds in K-means ++, while in LEACH nodes died to begin at 50 rounds and decreased to 175 at 180 rounds, and then to zero quickly. Even worse in single-hop, the nodes died grandly from 60 rounds, and quickly to 100 about 110 rounds. As we all know that once the nodes are less than one-half of all, the stability of the system is destroyed. Figure 4 reveals that the variance of the residual energy is all fluctuating as the increase of communication rounds. Whereas, the variance of K-means ++ is less than the other two methods which imply that the residual energy is more balance among all sensors. It is benefited to extend the lifetime of the system.

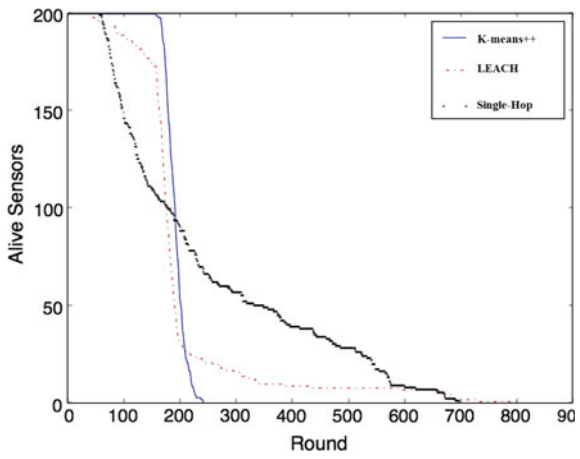

Fig. 3 The comparison of the alive sensors

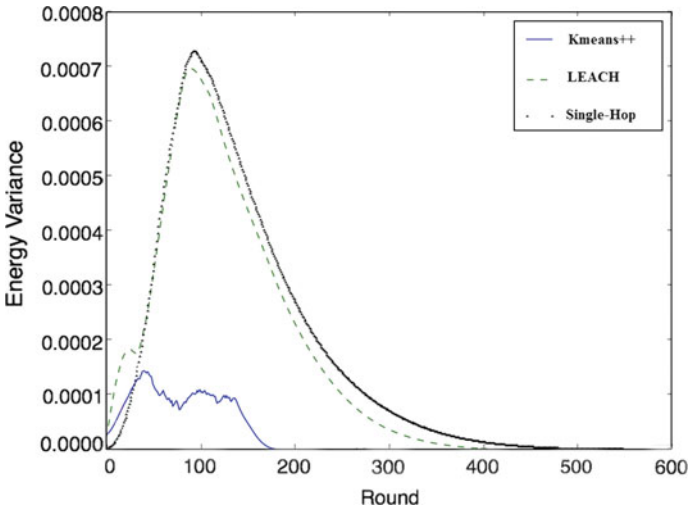

Fig. 4 The comparison of the energy variance

6 Conclusions

A lifetime maximum and energy consumption balanced protocol based on K-means ++ is proposed in this paper. The K-means ++ strategy is used to initialize the clusters to accelerate the optimal process and avoid the remaining local optima. Furthermore, the cluster heads are selected and rotated based on the energy information. The simulation results show that comparing to LEACH and Single-Hop, the K-means ++ is remarkably better at prolonging the lifetime and balancing the energy consumption. The two characteristics are of greatest importance to guarantee the stability and continuity of the wireless monitoring system. The accuracy of prediction based on the sensor information and the real-time of signal exchanges will be improved markedly, and then ensure the safety of the system.

Acknowledgements This work was supported by the National Science and Technology Major Project Grant No. 2016YFB1200100; State Key Laboratory under Grant No. RCS2016ZT018.

References

1. Wei D, Jin Y, Vural S, Moessner K, Tafazolli R (2011) An energy—efficient clustering solution for wireless sensor networks. IEEE Trans Wireless Commun 10(11):3973–3983
2. Zhang DG, Wang X, Song XD, Zhang T, Zhu Y-N (2015) A new clustering routing method based on PECE for WSN. EURASIP J Wirel Commun Networking 2015(1):1–13

3. Heinzelman WR, Chandrakasan A, Balakrishnan H (2000) Energy-efficient communication protocol for wireless micro-sensor networks, in System sciences. In: Proceedings of the 33rd annual Hawaii international conference on, IEEE, 2000, pp 1–10
4. Heinzelman WB, Chandrakasan AP, Balakrishnan H (2002) An application-specific protocol architecture for wireless micro-sensor networks. IEEE Trans Wireless Commun 1(4):660–670
5. Khan F (2012) An initial seed selection algorithm for k-means clustering of georeferenced data to improve replicability of cluster assignments for mapping application. Appl Soft Comput 12(11):3698–3700
6. Bholowalia P, Kumar A (2014) Ebk-means: a clustering technique based on elbow method and k-means in wsn. Int J Comput Appl 105(9)
7. Zimichev EA, Kazanskii NL, Serafimovich PG (2014) Spectral-spatial classification with k-means ++ particional clustering. Computer Optics 38(2):281–286
8. Liu F, Peng S (2010) On stabilization for stochastic control systems which the coefficient is time-variant. J Syst Sci Complex 23(2):270–278
9. Younis O, Fahmy S (2004) Heed: a hybrid, energy-efficient, distributed clustering approach for ad hoc sensor networks. IEEE Trans Mob Comput 3(4):366–379
10. Zhang H, Shen H (2009) Balancing energy consumption to maximize network lifetime in data-gathering sensor networks. IEEE Trans Parallel Distrib Syst 20(10):1526–1539

Reliable Static Output Feedback Guaranteed Cost Control for Uncertain Systems with Time-Delay

Shuangquan Zou, Hao Yan and Lin Zhang

1 Introduction

With the rapid development of industrial automation, people not only insure with the stability of the automatic control system, but pursuit some performance index. Where, guaranteed cost control has attracted growing interests and has produced many achievements [1–3]. Its main content is that the quadratic performance index is less than a certain upper bound under the premise of the asymptotic stability of the closed-loop system. In fact, failures of actuators often occur. Once the actuator fails, the controller in [1–3] will fail, resulting in the closed-loop system becomes unstable or losses the needed performance. Therefore, it is vital to design a reliable controller for the control system.

Generally speaking, state feedback control is the most common form [4] in the design of control systems. However, the state of the control system is often unobservable in practical engineering. The static output feedback controller is used conveniently because of simple structure. If the system can be controlled effectively under the static output feedback, it will have more application prospects [5, 6]. However, none of these studies consider the static output feedback control and the performance index of guaranteed cost at the same time when study the reliable control design of uncertain linear systems with time-delay.

The main objective of this paper is to design the static output feedback reliable controller against actuator failures for uncertain linear system with time-delay. The system remains asymptotically stable and satisfies original index of guaranteed cost under the designed reliable controller. Finally, the simulation and state response curve were made with MATLAB, showing the effectiveness of the proposed control method.

S. Zou (✉) · H. Yan · L. Zhang
College of Information and Control Engineering,
Shenyang Jianzhu University, Shenyang 110168, China
e-mail: a0020924@126.com

Z. Deng (ed.), *Proceedings of 2017 Chinese Intelligent Automation Conference*,
Lecture Notes in Electrical Engineering 458,
https://doi.org/10.1007/978-981-10-6445-6_44

2 Problem Descriptions

We consider uncertain systems with time-delay. Its model is the following form:

$$\begin{aligned} \dot{x}(t) &= (A_1 + \Delta A_1)x(t) + (A_2 + \Delta A_2)x(t-\tau) + (B + \Delta B)u(t) \\ y(t) &= Cx(t) \\ x(0) &= x_0 \end{aligned} \tag{1}$$

where $x(t) \in R^n$ is the state vector, $u(t) \in R^m$ is the control input vector, $y(t) \in R^p$ is the controlled output vector. $A_1, A_2 \in R^{n\times n}, B \in R^{n\times p}$ are independent constant matrices, $C \in R^{m\times n}$ is the row full rank matrix with appropriate dimensions. $\tau > 0$ is a time-delay. Uncertain matrices ΔA_1, ΔA_2, ΔB are defined as follows

$$[\Delta A_1, \Delta A_2, \Delta B] = DH[E_1, E_2, E_3], H^T H \le I \tag{2}$$

where D, E_1, E_2, E_3 are constant matrices with appropriate dimensions.

Static output feedback controller can be expressed as:

$$u(t) = Ky(t) \tag{3}$$

Combine (1) with (3), the normal closed-loop uncertain systems with time-delay can be expressed as follows

$$\begin{aligned} \dot{x}(t) = \ & [A_1 + \Delta A_1 + (B + \Delta B)FKC]x(t) + (A_2 + \Delta A_2)x(t-\tau) \\ y(t) &= Cx(t) \end{aligned} \tag{4}$$

When the actuator failures happen, the closed-loop system (4) can be rewritten as follows

$$\dot{x}(t) = [A + \Delta A + (B + \Delta B)FKC]x(t) + (A_2 + \Delta A_2)x(t-\tau) \tag{5}$$

where $F = diag(f_1, f_2, \ldots, f_p)$ is the matrix with actuator failures, $\underline{f}_i \le f_i \le \bar{f}_i, 0 \le \underline{f}_i \le 1, \bar{f}_i \ge 1, (i = 1, 2, \ldots, p)$ are showed that output signal of actuator failures may be not an accurate value of 0 or 1. It may be fluctuate up and down.

For the actuator fault matrix, it can be described as:

$$F = F_0(I + L) \tag{6}$$

Define the following symbol:

$$F_0 = diag\left(f_{10}, f_{20}, \ldots, f_{p0}\right) \tag{7}$$

where $f_{i0} = \frac{1}{2}\left(\underline{f}_i + \bar{f}_i\right), (i = 1, 2, \ldots, p)$

$$J = diag\left(J_1, J_2, \ldots, J_p\right) \tag{8}$$

where $j_i = \frac{\bar{f}_i - \underline{f}_i}{\bar{f}_i + \underline{f}_i}, (i = 1, 2, \ldots, p)$.

Definition 1 For system (1), if there exists the static output feedback controller (3) and a positive number M^*, the closed-loop uncertain systems with time delayer mains stable, and guaranteed cost index meets

$$M = \int_0^{+\infty} \left[x^T(t)Qx(t) + u(t)^T Ru(t)\right]dt \le M^*, M^* = x_0^T P x_0.$$

where $R > 0, Q > 0$ are known weighting matrices, x_0 is initial value of system, M^* is called performance upper bound of system (1). The controller (3) is called the guaranteed cost controller of system (1).

Lemma 1 *Given matrices Y, F with appropriate dimensions, $\sum$ is a time-varying diagonal matrix with appropriate dimensions, and $|\sum| \le \Lambda, \Lambda$ is a positive definite diagonal matrix such that the following inequality is satisfied*

$$Y\sum F + \left(Y\sum F\right)^T \le \varepsilon_1 Y\Lambda Y^T + \varepsilon_1^{-1} F^T \Lambda F$$

where $\varepsilon_1 > 0, \sum = diag(\sigma_1, \sigma_2, \ldots \sigma_r)$

Lemma 2 *For uncertain systems with time-delay (1), if there exists a symmetric positive definite matrix P, N and a matrix U, satisfying the following inequality*

$$\begin{bmatrix} PA_1 + A_1^T P + N + \Pi & PA_2 + PDHE_2 \\ (PA_2 + PDHE_2)^T & -N \end{bmatrix} < 0 \tag{9}$$

where $\Pi = Q + (KC)^T RCK + [BKC + DH(E_1 + E_3KC)]^T P + P[BKC + DH(E_1 + E_3KC)]$. *Then the static output feedback standard controller is given by $u(t) = Ky(t)$, and satisfy guaranteed cost upper bound $M^* = x_0^T P x_0$.*

3 Main Results

Theorem 1 *For uncertain systems with time-delay (1), given a symmetric positive definite matrix X, a matrix U and a ε to satisfy the following LMI*

$$\begin{bmatrix} A_1X+BUC+(A_1X+BUC)^T & A_2X & (E_1X+E_3UC)^T & X & (UC)^T \\ \quad +\varepsilon DD^T+S & & & & \\ * & -S & (E_2X)T & 0 & 0 \\ * & * & -\varepsilon I & 0 & 0 \\ * & * & * & -Q^{-1} & 0 \\ * & * & * & * & -R^{-1} \end{bmatrix} <0 \tag{10}$$

where $S = XNX$.If there exists a feasible solution (X, U, ε) to LMIs (10), the closed-loop system (4) is stable by static output feedback standard controller (3). The control gain matrix is $K = UW^{-1}$, and the guaranteed cost upper bound is M^*.

Proof Because of the limitation of length, no more proof here.

Theorem 2 *For uncertain systems with time-delay when actuator fails (5), given symmetric positive definite matrices X, J, a matrix U and some positive numbers $\varepsilon_1, \varepsilon_2$ such that the following LMIs is satisfied*

$$\begin{bmatrix} A_1X+BF_0UC & & (E_1X+E_3F_0UC)^T & & (F_0UC)^T & \\ \quad +(A_1X+BF_0UC)^T & A_2X & \quad +\varepsilon_1BJE_3^T & X & \quad +\varepsilon_1BJ & \left(F_0UCJ^{1/2}\right)^T \\ \quad +\varepsilon_2DD^T+S+\varepsilon_1BJB^T & & & & & \\ * & -S & (E_2X)^T & 0 & 0 & 0 \\ * & * & \varepsilon_1E_3JE_3^T-\varepsilon_2I & 0 & \varepsilon_1E_3J & 0 \\ * & * & * & -Q^{-1} & 0 & 0 \\ * & * & * & * & \varepsilon_1J-R^{-1} & 0 \\ * & * & * & * & * & -\varepsilon_1I \end{bmatrix} <0 \tag{11}$$

If there exists a feasible solution $(U, X, \varepsilon_1, \varepsilon_2)$ to LMIs (11), the closed-loop system (5) is stable by static output feedback reliable controller (3). The control gain matrix is $K = UW^{-1}$, and satisfy guaranteed cost upper bound M^*.

Proof Because of the limitation of length, no more proof here.

4 Example Simulation

In this section, we use a practical system about the linearized motion equation in the stage of unmanned aerial vehicle climbing. The state equation of longitudinal wing can be expressed as follows:

$$\begin{bmatrix}\dot{x}_1\\ \dot{x}_2\\ \dot{x}_3\end{bmatrix} = \left(\begin{bmatrix}0.034 & 0.122 & 0.011\\ 0.155 & 0.194 & 0.112\\ -0.031 & 0.023 & 0.086\end{bmatrix} + \begin{bmatrix}0.001 & 0 & 0\\ 0 & 0.001 & 0\\ 0 & 0 & 0.001\end{bmatrix}\right)\begin{bmatrix}x_1\\ x_2\\ x_3\end{bmatrix} + \left(\begin{bmatrix}-0.190 & -0.007 & 0.110\\ -0.198 & -0.012 & 0.111\\ -0.194 & -0.063 & -0.189\end{bmatrix} + \begin{bmatrix}0.002 & 0 & 0\\ 0 & 0.002 & 0\\ 0 & 0 & 0.002\end{bmatrix}\right)\begin{bmatrix}x_1(t-0.01)\\ x_2(t-0.01)\\ x_3(t-0.01)\end{bmatrix}\left(\begin{bmatrix}-0.045 & 0.141 & -0.134\\ -0.068 & 0.071 & -0.145\\ -0.155 & -0.074 & -0.191\end{bmatrix} + \begin{bmatrix}0.002 & 0 & 0\\ 0 & 0.002 & 0\\ 0 & 0 & 0.002\end{bmatrix}\right)u(t), y(t) = \begin{bmatrix}-0.053 & 0.087 & -0.183\\ 0.047 & 0.160 & 0.066\\ 0.061 & -0.124 & -0.064\end{bmatrix}\begin{bmatrix}x_1\\ x_2\\ x_3\end{bmatrix}$$

where $x_1(t)$ is the change of the flight speed; $x_2(t)$ is the change of the power angle; $x_3(t)$ is the change of the pitch angular velocity.

Step1: Solving the LMI in Theorem 1 by using MATLAB, the standard static output feedback guaranteed cost control gain matrix and ε can be obtained as follows:

$$K = \begin{bmatrix}0.7437 & 12.0125 & -6.8407\\ -1.8418 & 2.0899 & -1.8850\\ 4.6981 & 38.2170 & 2.9245\end{bmatrix}, \varepsilon = 0.1248$$

Figure 1 shows the state response curve, indicating the system is asymptotically stable under the standard static output feedback guaranteed cost controller.

Step2: We consider the system with actuator failures $F = diag(f_1, f_2, f_3)$, assume the failure gain range is $0 \le f_1 \le 1.2, 0 \le f_2 \le 1.2, 0 \le f_3 \le 1.2$. Via (7) and (8), we can obtain $F_0 = 0.6, J = 1$. Choose $F = diag(0, 0, 1)$. If we still use the standard controller in Step 1, the state response curve is showed by Fig. 2. Evidently, the system is unstable.

Step3: We design the reliable static output feedback guaranteed cost controller against actuator failures for the proposed practical system. Solving the LMI in Theorem 2 by using MATLAB, the control gain matrix and $\varepsilon_1, \varepsilon_2$ can be obtained as follows:

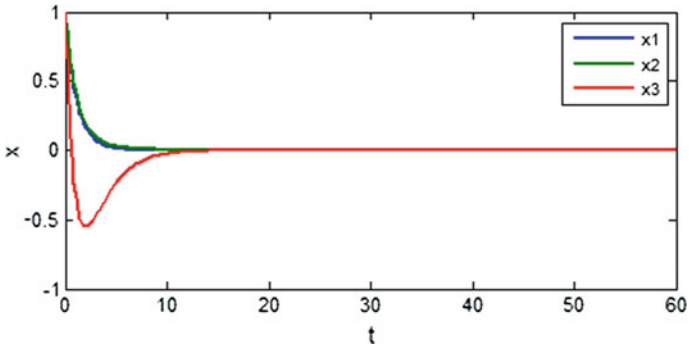

Fig. 1 Stateresponse of standard controller

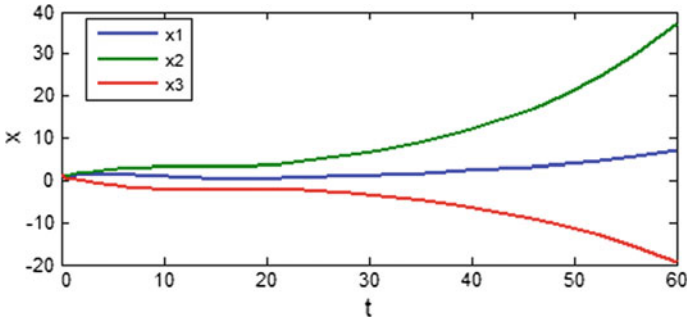

Fig. 2 Stateresponse of standard controller with failures

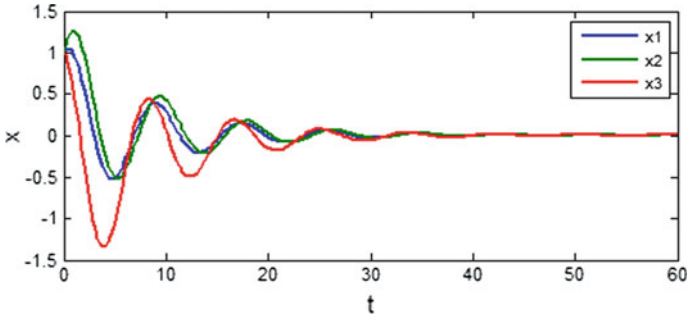

Fig. 3 State response of reliable controller with failures

$$K = \begin{bmatrix} -18.9242 & -263.1484 & -424.6037 \\ -84.8679 & -502.8614 & -768.5727 \\ 18.8994 & -148.4234 & -269.5710 \end{bmatrix}, \varepsilon_1 = 1, \varepsilon_2 = 2$$

Figure 3 shows the state response curve. Obviously, the system is asymptotically stable, demonstrating the effectiveness of the proposed reliable controller.

5 Conclusion

In this paper, the reliable static output feedback guaranteed cost control is designed by employing LMI, Lyapunov second theory and actuator failure treatment method. The uncertain system with time-delay remains asymptotically stable and satisfies original guaranteed cost index under the static output feedback reliable controller, whether the actuator is suffered with fault or not. Finally, the simulation studies and state response curve were made with MATLAB, showing the effectiveness of the proposed control design method.

References

1. Yu L, Chu J (1999) An LMI approach to guaranteed cost control of nonlinear uncertain time-delay systems. IEEE Trans Autom Control 35(6):155–159
2. Li HF, Zhou J (2007) Delay-independent robust guaranteed-cost control for uncertain linear neutral systems. J Syst Eng Electron 18(4):858–864
3. Xu GM, Zhao WQ (2016) Static output feedback guaranteed cost control for linear system. Text Dyeing Finish J 38(11):50–54 (in Chinese)
4. Yan H, Wang FZ (2016) Reliable passive control for a class of T-S fuzzy systems with time-delay. In: 28th Chinese control and decision conference 6089–6094 (in Chinese)
5. Ge D, Yao B, Wang FZ (2016) Static output feedback reliable control with uncertain systems. Comput Technol Autom 35(1):5–8 (in Chinese)
6. Xu YC, Wang FZ, Yao B (2016) Static output feedback reliable control with performance H_∞/H_2 against actuator failures. Dyn Syst Control 5(3):124–133

An Iterative Camera Pose Estimation Algorithm Based on EP*n*P

Peng Chen

1 Introduction

Vision-based pose estimation problem is to determine position and orientation between a camera and a target with a set of n control points expressed in the object frame and their 2D projections expressed in the image frame. It is one of the key problems in object recognition, visual navigation, robot localization, augmented reality and other areas.

When the correspondences between 3D object points and 2D image points are given, the pose estimation problem of a calibrated camera is also known as a perspective-n-point (PnP) problem. Since firstly proposed in 1981 [1], the PnP problem has attracted a lot of researchers to devote in it. Existing algorithms can be summarized into two categories: analytical algorithms and iterative algorithms. Analytical algorithms try to acquire the algebraic solutions of PnP problem. A large amount of researches are focused on P3P, P4P and P5P problems [2], since PnP problem can be treated as a classical Direct Linear Transformation (DLT) problem and can be solved linearly when $n > 5$ [3]. The most popular algorithms to handle arbitrary value of n are proposed in [4, 5]. Analytical solutions can achieve high precision only when the image points can be extracted accurately, and the estimation results will become unreliable when the image is noisy. Besides, the computational complexity of an analytical algorithm is usually high, which is commonly between $O(n^5)$ and $O(n^8)$.

Compared to analytical algorithms, iterative algorithms are more forward to realize and more robust to image noise. Classical iterative algorithms formulate the pose estimation problem as a nonlinear least-square problem with the constraint that the rotation matrix is orthogonal. The problem can be solved by using non-linear

P. Chen (✉)
School of Control Science and Engineering, Hebei University of Technology, Tianjin 300130, China
e-mail: holmes83@163.com

Z. Deng (ed.), *Proceedings of 2017 Chinese Intelligent Automation Conference*, Lecture Notes in Electrical Engineering 458,
https://doi.org/10.1007/978-981-10-6445-6_45

optimization algorithms, such as Levenberg-Marquadt or Gaussion-Newton algorithm [6, 7]. However, in those algorithms the structure properties of the projection model are ignored, which will finally impact the algorithm performance. The famous POSIT algorithm [8], which is based on the weak perspective projection model, has been widely applied as a built-in function in OpenCV [9]. Although the computational efficiency of POSIT is high, the objective function of the optimization process is not clearly defined, so that the convergence of the algorithm cannot be directly proofed. Orthogonal iterative (OI) algorithm is another popular iterative algorithm [10]. The most outstanding contribution of the OI algorithm is the proposition of the object space error, which can make the algorithm take full use of the structure properties of the perspective projection model, so that the orthogonality of the rotation matrix can be guaranteed naturally in the iterative process. However, OI algorithm cannot ensure the final estimation results is the real camera pose, especially when all the control points are located on the same plane.

In recent years, the EPnP algorithm has attracted much attention in various literatures [11]. The algorithm is considered to be the most efficient analytical algorithm, since its computational complexity is only $O(n)$. When image points can be extracted accurately, the estimation result of EPnP is comparable to iterative algorithms, such as POSIT and OI. However, as most analytical algorithms, EPnP is not tolerant to image noise. Therefore, we adjust the original EPnP algorithm into an iterative one, called IEPnP, in this paper to make it more robust. Simulations under different image noise levels are conducted, the results show that IEPnP is more reliable than the original EPnP algorithm with the increasing of image noise.

2 Problem Formulation

In a perspective projection model, the coordinate systems involved in the imaging process can be shown in Fig. 1. For a calibrated camera, the focal length can be denoted as f, the coordinate of the principle point in the pixel frame can be denoted as $\boldsymbol{u}_0 = [u_0, v_0]^T$, and the pixel size can be denoted as $d_u \times d_v$. If there are n control points, denoted as $\boldsymbol{P}_i$, $i = 1, 2, \ldots, n$, the corresponding coordinates of $\boldsymbol{P}_i$ in the object frame can be denoted as $\boldsymbol{P}_i^w = [X_i^w, Y_i^w, Z_i^w]^T$, and the coordinates of $\boldsymbol{P}_i$ in the camera frame can be denoted as $\boldsymbol{P}_i^c = [X_i^c, Y_i^c, Z_i^c]^T$. Furthermore, the 2D projections of $\boldsymbol{P}_i$ in the image frame can be denoted as $\boldsymbol{p}_i = [x_i, y_i]^T$, and the coordinates of $\boldsymbol{P}_i$ in the pixel frame can be denoted as $\boldsymbol{u}_i = [u_i, v_i]^T$.

By using the homogeneous coordinates, the imaging process described in Fig. 1 can be formulated as

$$\lambda_i \tilde{\boldsymbol{u}}_i = \boldsymbol{K}[\boldsymbol{R}|\boldsymbol{t}]\tilde{\boldsymbol{P}}_i^w \tag{1}$$

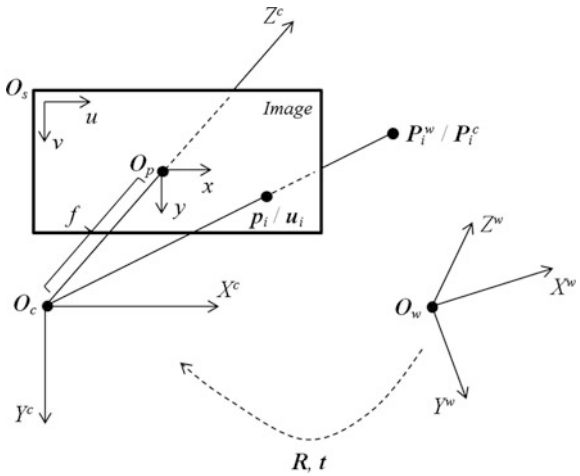

Fig. 1 The coordinate systems involved in a imaging process

where λ_i is a scale factor, $\tilde{\boldsymbol{u}}_i$ and $\tilde{\boldsymbol{P}}_i^w$ are respectively the homogeneous coordinates of $\boldsymbol{u}_i$ and $\boldsymbol{P}_i^w$. Matrix $\boldsymbol{K}$ is composed of the intrinsic camera parameters

$$\boldsymbol{K} = \begin{bmatrix} f_u & \gamma & u_0 \\ 0 & f_v & v_0 \\ 0 & 0 & 1 \end{bmatrix} \tag{2}$$

where $\gamma = 0$ usually.$\boldsymbol{R}$ and $\boldsymbol{t}$ in (1) are called the extrinsic camera parameters, where $\boldsymbol{R} \in SO(3)$, is a rotation matrix, and $\boldsymbol{t} \in \Re^{3\times 1}$ is a translation vector. The main purpose of camera pose estimation is to determine $\boldsymbol{R}$ and $\boldsymbol{t}$.

According to EP*n*P algorithm [11], 4 virtual control points are set up in 3D space, denoted as $\boldsymbol{C}_1$, $\boldsymbol{C}_2$, $\boldsymbol{C}_3$, $\boldsymbol{C}_4$. For convenience, the coordinates of the virtual control points are usually selected as $\boldsymbol{C}_1^w = [1, 0, 0]^T$, $\boldsymbol{C}_2^w = [0, 1, 0]^T$, $\boldsymbol{C}_3^w = [0, 0, 1]^T$, $\boldsymbol{C}_4^w = [0, 0, 0]^T$. For a real control point, such as $\boldsymbol{P}_i^w$, it can be represented as a linear combination of the 4 virtual control points as

$$\boldsymbol{P}_i^w = \sum_{j=1}^{4} \alpha_{ij} \boldsymbol{C}_j^w, \quad \sum_{j=1}^{4} \alpha_{ij} = 1 \tag{3}$$

Obviously, the combination coefficients in (3) can also be applied in the representation of $\boldsymbol{P}_i^c$ in the camera frame

$$\boldsymbol{P}_i^c = \sum_{j=1}^{4} \alpha_{ij} \boldsymbol{C}_j^c \tag{4}$$

Apply (3) and (4) to (1), the following equation can be obtained

$$\forall i,\ \lambda_i \begin{bmatrix} u_i \\ v_i \\ 1 \end{bmatrix} = \boldsymbol{K}\boldsymbol{P}_i^c = \boldsymbol{K}\sum_{j=1}^{4}\alpha_{ij}\boldsymbol{C}_j^c \tag{5}$$

Denote $\boldsymbol{C}_j^c = [U_j^c,\ V_j^c,\ W_j^c]^T$, then (5) can be rewritten as

$$\forall i, \quad \lambda_i \begin{bmatrix} u_i \\ v_i \\ 1 \end{bmatrix} = \begin{bmatrix} f_u & 0 & u_0 \\ 0 & f_v & v_0 \\ 0 & 0 & 1 \end{bmatrix} \sum_{j=1}^{4}\alpha_{ij} \begin{bmatrix} U_j^c \\ V_j^c \\ W_j^c \end{bmatrix} \tag{6}$$

where $f_u = f/d_u$, $f_v = f/d_v$, $\lambda_i = \sum_{j=1}^{4}\alpha_{ij}W_j^c$. Since the combination coefficients can be acquired from (3), the only unknown variables are U_j^c, V_j^c, W_j^c in (6), i.e. the coordinates of the virtual control points in the camera frame. The final equations with respect to U_j^c, V_j^c, W_j^c, can be represented as

$$\sum_{j=1}^{4}\alpha_{ij}f_u U_j^c + \alpha_{ij}(u_0 - u_i)W_j^c = 0 \tag{7}$$

$$\sum_{j=1}^{4}\alpha_{ij}f_u V_j^c + \alpha_{ij}(v_0 - v_i)W_j^c = 0 \tag{8}$$

Expanding the 12 coordinates of the 4 virtual control points in the camera frame as a column vector $\boldsymbol{c} = [\boldsymbol{C}_1^{cT}, \boldsymbol{C}_2^{cT}, \boldsymbol{C}_3^{cT}, \boldsymbol{C}_4^{cT}]^T$, 12 equations can be obtained from (7) and (8) as

$$\boldsymbol{F}\boldsymbol{c} = 0 \tag{9}$$

where $\boldsymbol{F}$ is a matrix of size $2n \times 12$. It is obvious that vector $\boldsymbol{c}$ is located in the null space of $\boldsymbol{F}$, so that it can be represented as

$$\boldsymbol{c} = \sum_{i=1}^{N_F}\beta_i \boldsymbol{w}_i \tag{10}$$

where $\boldsymbol{w}_i$, $i = 1, \ldots, N_F$, are the eigenvectors of $\boldsymbol{F}^T\boldsymbol{F}$ correspond to the zero eigenvalues. It can be implied that once the coefficients β_i, $i = 1, \ldots, N_F$, can be acquired, the vector $\boldsymbol{c}$ can be computed according to (10), furthermore, the coordinates of the real control points in the camera frame can be acquired according to (4), so that the camera pose can be evaluated from the correspondences between $\{\boldsymbol{P}_i^w\}$ and $\{\boldsymbol{P}_i^c\}$, which is known as an absolute orientation problem and solved in [10].

3 The Algorithm

To acquire the coefficients β_i, $i = 1, \ldots, N_F$, the first thing is to evaluate N_F, which is the dimension of the null space of $\boldsymbol{F}$. Given the only information lost in the imaging process is the distance from a scene point to the camera, N_F should be 1. However, with the increasing of the focal length, the imaging model will gradually transit from perspective projection to orthogonal projection, which makes the image projections of the virtual control points are gradually irrelevant to the varying of the distance to the camera, so that the dimension of the null space of $\boldsymbol{F}$, i.e. N_F, should be 4. Therefore, N_F is between 1 and 4, which can be proofed by Fig. 2.

Figure 2 is acquired by computing the eigenvalues of $\boldsymbol{F}^T\boldsymbol{F}$ 100 times for each $f = 4$, 35, 64, 100, 200 mm. As shown in Fig. 2, when the camera focal length is small, the number of zero eigenvalues of $\boldsymbol{F}^T\boldsymbol{F}$ is 1, with the increasing of the camera focal length, the number of zero eigenvalues of $\boldsymbol{F}^T\boldsymbol{F}$ gradually increases to 4.

Herein, we assume $N_F = 4$ and rewrite (10) as

$$\boldsymbol{c} = \begin{bmatrix} \boldsymbol{w}_1 & \boldsymbol{w}_2 & \boldsymbol{w}_3 & \boldsymbol{w}_4 \end{bmatrix} \begin{bmatrix} \beta_1 \\ \beta_2 \\ \beta_3 \\ \beta_4 \end{bmatrix} = \boldsymbol{W}\boldsymbol{\beta} \tag{11}$$

From the equation $\boldsymbol{C}_i^c = \boldsymbol{R}_0\boldsymbol{C}_i^w + \boldsymbol{t}_0$, the coefficient vector $\boldsymbol{\beta}$ can be acquired as

$$\boldsymbol{\beta} = \left(\boldsymbol{W}^T\boldsymbol{W}\right)^{-1}\boldsymbol{W}^T\boldsymbol{c} \tag{12}$$

where $\boldsymbol{R}_0$ and $\boldsymbol{t}_0$, is the initial value of $\boldsymbol{R}$ and $\boldsymbol{T}$ which can be acquired from weak perspective projection model to start the iteration process [10].

Furthermore, an objective function can be set up to optimize the value of $\boldsymbol{\beta}$ as

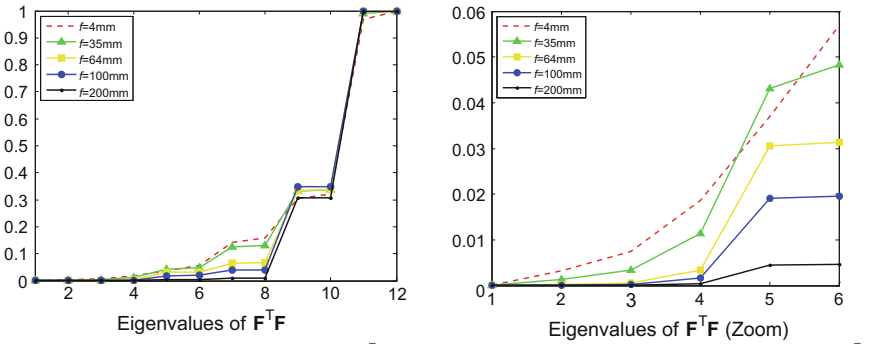

(a) The varying of the eigenvalues of $\boldsymbol{F}^T\boldsymbol{F}$ (b) The varying of the first 6 eigenvalues of $\boldsymbol{F}^T\boldsymbol{F}$

Fig. 2 The varying curves of the eigenvalues of F^TF

$$\boldsymbol{\beta} = \arg\min_{\boldsymbol{\beta}} \sum_{i,j=1,i<j}^{4} \left| \left\| \boldsymbol{C}_i^c - \boldsymbol{C}_j^c \right\|^2 - \left\| \boldsymbol{C}_i^w - \boldsymbol{C}_j^w \right\|^2 \right| \tag{13}$$

Nonlinear least square methods, such as Gauss-Newton, can be applied to find the solution of (13). After that, the coordinates of the virtual control points in the camera frame, $\{\boldsymbol{C}_i^c\}$, can be solved from (10), so that the coordinates of the real control points, $\{\boldsymbol{P}_i^c\}$, can be solved from (4). Finally the camera pose, $\boldsymbol{R}$ and $\boldsymbol{t}$, can be solved by deal with an absolute orientation problem between $\{\boldsymbol{P}_i^c\}$ and $\{\boldsymbol{P}_i^w\}$. To make it clear, the proposed IEP*n*P algorithm is described in Table 1.

4 Simulations

In this section, the proposed IEP*n*P algorithm is compared with the original EP*n*P algorithm in the following simulations. A virtual camera has been set, whose intrinsic parameters are: focal length f = 8 mm, the image size is 1200 × 1600, the pixel size is 12 × 12 μm^2, and the principle point is located in the center of the image. 5 control points are located in the object frame with the coordinates as (0.10, 0.00, 0.00), (0.00, 0.15, 0.00), (−0.18, 0.00, 0.00), (0.00, −0.08, 0.00), (0.00, 0.00, 0.16). The motion trajectories of the three Euler angles and the translation vector are subject to the following equations

$$\begin{cases} \alpha = -1 + 0.2\cos(1.5t_s) \\ \beta = -1 + 0.5\sin(1.8t_s) \\ \gamma = -1 + 0.3\cos(1.3t_s) \end{cases}, \quad \begin{cases} t_x = 1 + 0.1t_s \\ t_y = 1 + 0.15t_s \\ t_z = 1 + 0.2t_s \end{cases} \tag{14}$$

Table 1 The IEP*n*P algorithm

Step 1: Set 4 virtual control points in the object frame, denoted as C_j^w, j = 1, 2, 3, 4. Compute the combination coefficients α_{ij} according to (3)
Step 2: Compute the value of the vector c from the initial value or the estimated value of R and t
Step 3: Construct the matrix F according to (9), find the eigenvectors, w_1, w_2, w_3, w_4, corresponding to the zero eigenvalues of F^TF
Step 4: Find the initial β according to (12), then solve the optimization problem as shown in (13) to find the optimized β^*
Step 5: Find the optimized C_j^{c*}, j = 1, 2, 3, 4 from β^* according to (10), and compute P_i^{c*}, i = 1, 2, …, n, according to (4)
Step 6: Solve the absolute orientation problem defined by the correspondences of $\{P_i^{c*}\}$ and $\{P_i^w\}$ to find out the camera pose, R and t
Step 7: If R and t meets the terminal criterion, then return R and t, otherwise, go to step 2

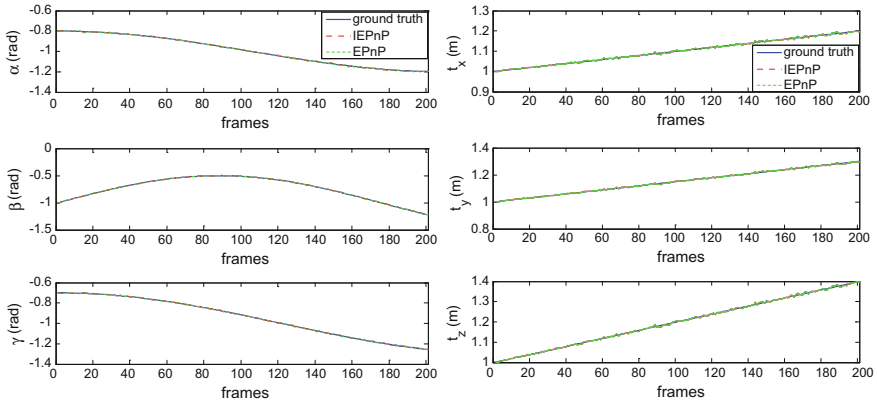

Fig. 3 The estimation results when the standard deviation of image noise is 0

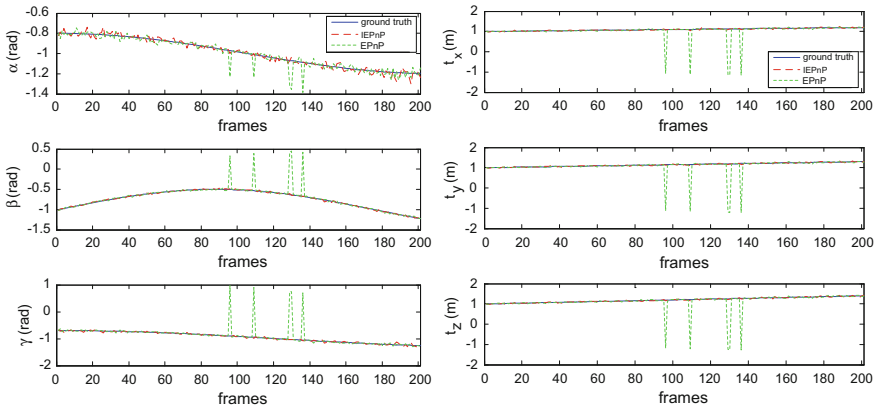

Fig. 4 The estimation results when the standard deviation of image noise is 2

where t_s is the sample instance, $\boldsymbol{t} = [t_x, t_y, t_z]^T$.

A Gaussian noise with zero mean and varying standard deviations is added to the image points in the simulations. At the beginning, the standard deviation is 0, the simulation results are shown in Fig. 3. It can be observed that there are no big differences between the estimation results of IEP*n*P and EP*n*P, which means IEP*n*P has a similar performance as EP*n*P when the image noise is low.

In the next simulation, the standard deviation of the image noise is 2, the simulation results is shown in Fig. 4. It is obvious that the estimation results of EP*n*P become unstable, while the results of IEP*n*P can still reliably reflect the real varying of the camera pose.

Similar simulation results can be acquired with even higher level of image noise. With the increasing of the standard deviation of image noise, the estimation results

of EP*n*P become more and more unstable, while the estimation results of IEP*n*P can still reliably track the varying of the real camera pose. Through those simulations, it can be concluded that the proposed IEP*n*P algorithm is more robust to image noise than the original EP*n*P algorithm.

5 Conclusion

In this paper, an iterative version of EP*n*P algorithm, called IEP*n*P, is proposed. The iterative process is started by firstly acquiring the initial rotation and translation from weak perspective projection model, then four virtual control points are set up to represent the real control points. During the iteration, the coordinates of the virtual control points in the camera frame are updated by a nonlinear least square algorithm, and finally the camera pose is estimated by solving an absolute orientation problem. Simulation results show that the proposed IEP*n*P algorithm has a similar performance compared to EP*n*P algorithm when the image noise is low, furthermore, the IEP*n*P algorithm is more robust than the original EP*n*P algorithm when the image becomes noisier.

References

1. Fischer J, Eichler M, Bartz D (2006) Model-based hybrid tracking for medical augmented reality. In: Eurographics symposium on virtual environments, EGVE 2006, Lisbon, Portugal, DBLP, pp 71–80
2. Wu FC, Hu ZY (2001) A study on the p5p problem. J Softw 12(5):768–775
3. Wu F-C, Hu Z-Y (2003) A linear method for the P*n*P problem. J Softw 14(3):683–688
4. Quan L, Lan Z (1999) Linear n-point camera pose determination. IEEE Trans Pattern Anal Mach Intell 21(8):774–780
5. Ansar A, Daniilidis K (2003) Linear pose estimation from points or lines. IEEE Trans Pattern Anal Mach Intell 25(5):578–589
6. Liu ML, Wong KH (1999) Pose estimation using four corresponding points. Pattern Recogn Lett 20(1):69–74
7. Dongkai Dai (2012) Camera calibration and attitude measurement technology based on astronomical observation. Acta Optica Sinica 32(3):0312005
8. Dementhon DF, Davis LS (1995) Model-based object pose in 25 lines of code. Int J Comput Vision 15(1):123–141
9. Kaehler A, Bradski G (2008) Learning OpenCV. O'Reilly
10. Lu CP, Hager GD, Mjolsness E (2000) Fast and globally convergent pose estimation from video images. IEEE Trans Pattern Anal Mach Intell 22(6):610–622
11. Moreno-Noguer F, Lepetit V, Fua P (2009) EP*n*P: accurate non-iterative $O(n)$ solution to the P*n*P problem. Int J Comput Vision 81:155–166

The Research on the Dynamic Performance Test Method Based on SPHS

Jun Xiao Li, Xue Mei Wang, Zhe Xu and Tong Wu

1 Introduction

Dynamic performance testing is the application of modern science and technology. The dynamic performance of the system is tested by signal acquisition, transformation, transmission and real-time processing. It combines modern sensor technology, computer technology, signal analysis and processing technology and other disciplines and applied to the test system and test process. Different from the traditional testing process, the latter is just a simple comparison of measurement. But dynamic performance testing uses signal acquisition, signal conversion and signal processing and analysis to get a more comprehensive system characteristics. The technique used to analyze the dynamic characteristics and performance index of the system is called the modern dynamic testing technology. The dynamic test is different from the simple numerical correspondence between the output and the input in the traditional test, and the corresponding relationship between the output signal and the input signal is obtained. In the dynamic test, the waveform of the input signal which can output the waveform without distortion is required [1].

This paper introduces the advantages of SPHS in system dynamic testing. Taking multi harmonic phase difference signal as an example, this paper introduces the simulation analysis of the system by MATLAB, and adopts the mirror mapping method to obtain the frequency characteristic of the signal processing. It can avoid the problem of digital ill posed by traditional least square method and reduced the requirements for the test object.

J.X. Li (✉) · X.M. Wang · Z. Xu · T. Wu
Xi'an High Tech Research Institute, Xi'an 710025, China
e-mail: ljx_22@163.com

Z. Deng (ed.), *Proceedings of 2017 Chinese Intelligent Automation Conference*,
Lecture Notes in Electrical Engineering 458,
https://doi.org/10.1007/978-981-10-6445-6_46

2 SPHS

SPHS (Schroeder Phased Harmonic Sequence) is a kind of special multi frequency signal, which was put forward by Schroeder M.R in 1970. It is a kind of periodic multi frequency signal which is formed by the superposition of several sine waves with power, period and initial phase. By adjusting the initial phase angle of the positive (or residual) components of the signal to form its own characteristics [2]. General mathematical expression is:

$$x(t) = \sum_{k=1}^{N} \sqrt{2p_k} \cos(\frac{2\pi k}{T} t + \theta_k), \quad k = 1, 2 \cdots N \tag{1}$$

In Formula (1), N is the number of harmonics contained in the signal; p_k is the relative power of the second harmonic of k; Total signal power is $P = \sum_{k=1}^{N} p_k$; T is the fundamental period of the signal; θ_k is the first phase of the first harmonic of K.

The SPHS signal is encoded by Schroeder, and its phase can be obtained by the following method:

$$\theta_k = \pi[\sum_{i=1}^{k-1} (k-i)p_i], \quad p_i = \frac{P_i}{P} \tag{2}$$

The [•] said the operation rounded to zero, When the harmonic power is evenly distributed, $P_k = \frac{P}{N}$, $(k = 1, 2 \ldots N)$, its phase $\theta_k = \pi\left[\frac{k^2}{2N}\right]$.

Set parameter N = 30,T = 0.5 s, P_k = 1 W. The waveform of the SPHS signal is shown in Fig. 1.

In the system dynamic characteristic test, the SPHS signal excitation has the following advantages:

(1) Compared with the widely used sine(cosine) point by point scanning method, the SPHS signal excitation method can be used to excite the mode of each frequency point in front, and greatly shorten the test time [3].
(2) With a low peak to peak ratio, the peak factor is relatively small, it can be used to test the system to apply a smooth, uniform excitation, especially suitable for inertial devices, servo devices and other equipment testing [4].
(3) Signal parameters can be set according to the needs, the form is more flexible, can adapt to the needs of a variety of system testing, the application field is more extensive.
(4) SPHS is a periodic signal, if the FFT method is used to analyze the data, it can be cut off for the whole week and avoid spectrum leakage [5].

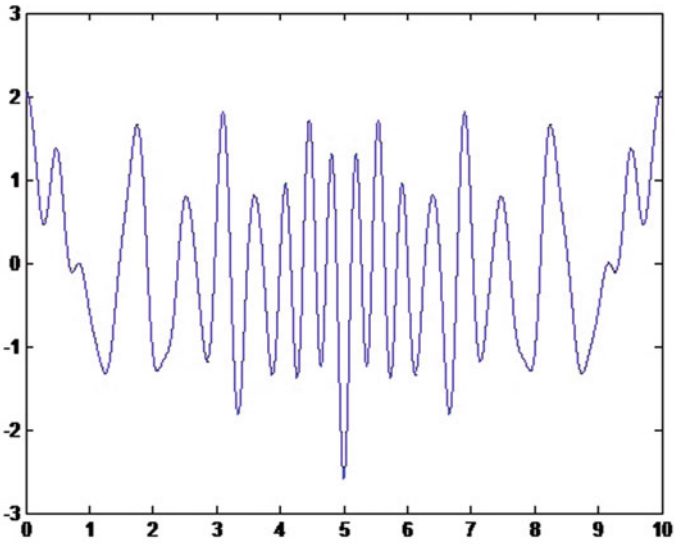

Fig. 1 SPHS signal waveform

3 System Response Signal Testing and Processing Method

3.1 Testing Process

In the process of testing, the SPHS signal is applied to the measured system firstly, and then the dynamic response of the system is obtained. Excitation signal for SPHS signal, immediate satisfaction $x(t) = \sum_{k=1}^{N} a_k \cos(\omega_k t + \theta_k)$, $\omega_k = \frac{2\pi k}{T}$, $a_k = \sqrt{2p_k}$. In general, the measured system is a linear system. According to the superposition principle and the frequency invariance of the linear system, the response of the system to $y(t)$ should satisfy the following formula [6]:

$$y(t) = \sum_{k=1}^{N} b_k \cos(\omega_k t + \theta_k + \varphi_k), \quad k = 1, 2 \ldots N \tag{3}$$

In formula (3), a_k is the amplitude of the first harmonic of the excitation signal k, θ_k is the first phase of the first harmonic of k, b_k is the response amplitude of the system, phase shift generated by φ_k as input signal of excitation signal. The amplitude φ_k and phase of each harmonic b_k in the system response can be calculated by the mathematical method. According to frequency characteristics, the amplitude ratio of the input and output harmonics to $L(\omega_k) = 20 \lg \frac{b_k}{a_k}$ is about the amplitude frequency characteristic of the measured system, which reflects the gain or attenuation of the excitation signal through the angular frequency ω_k [7]. Phase difference A and the function curve of the angular frequency B are the phase

frequency characteristics of the system under test, which reflects the hysteresis or advance of the excitation signal of the system. Amplitude frequency characteristic and phase frequency characteristic are the frequency domain index to reflect the dynamic performance of the system [8–10].

The formula (3) on the right in accordance with the cosine function and the angular formula can be obtained:

$$\begin{aligned} y(t) &= \mathrm{b}_1 \cos(\omega_1 t + \theta_1 + \varphi_1) + \cdots \mathrm{b}_N \cos(\omega_N t + \theta_N + \varphi_N) \\ &= \mathrm{b}_1 \cos(\omega_1 t + \theta_1)\cos(\varphi_1) - \mathrm{b}_1 \sin(\omega_1 t + \theta_1)\sin(\varphi_1) \\ &\quad + \cdots \mathrm{b}_N \cos(\omega_N t + \theta_N)\cos(\varphi_N) - \mathrm{b}_N \sin(\omega_N t + \theta_N)\sin(\varphi_N) \\ &= \begin{bmatrix} \cos(\omega_1 t + \theta_1) \\ -\sin(\omega_1 t + \theta_1) \\ \vdots \\ \cos(\omega_N t + \theta_N) \\ -\sin(\omega_N t + \theta_N) \end{bmatrix}^T \times \begin{bmatrix} b_1 \cos(\varphi_1) \\ b_1 \sin(\varphi_1) \\ \vdots \\ b_N \cos(\varphi_N) \\ b_N \sin(\varphi_N) \end{bmatrix} \end{aligned} \tag{4}$$

If the sampling frequency is f_s, then the time interval of sampling data is $t_s = \frac{1}{f_s}$, that is $Y^T = [y(0), y(t_s), y(2t_s), \ldots, y((n-1)t_s)]_{1\times n}$,so the corresponding expansion should be:

$$\mathrm{Y}_{n\times 1} = \begin{bmatrix} \cos(\omega_1 0 + \theta_1) & \cos(\omega_1 t_s + \theta_1) & \cdots & \cos(\omega_1 (n-1)t_s + \theta_1) \\ -\sin(\omega_1 0 + \theta_1) & -\sin(\omega_1 t_s + \theta_1) & \cdots & -\sin(\omega_1 (n-1)t_s + \theta_1) \\ \vdots & \vdots & \vdots & \vdots \\ \cos(\omega_N t + \theta_N) & \cos(\omega_N t_s + \theta_N) & \cdots & \cos(\omega_N (n-1)t_s + \theta_N) \\ -\sin(\omega_N t + \theta_N) & -\sin(\omega_N t_s + \theta_N) & \cdots & -\sin(\omega_N (n-1)t_s + \theta_N) \end{bmatrix}^T_{2N\times n} \times \begin{bmatrix} b_1 \cos(\varphi_1) \\ b_1 \sin(\varphi_1) \\ \vdots \\ b_N \cos(\varphi_N) \\ b_N \sin(\varphi_N) \end{bmatrix}_{2N\times 1}$$

The right side of the equation is denoted as matrix $A_{2N\times n}$ and $C_{2N\times 1}$ respectively, By the formula (4) was obtained:

$$Y_{n\times 1} = A^T_{n\times 2N} C_{2N\times 1} \tag{5}$$

3.2 Data Processing Based on Mirror Mapping Method

The traditional method of solving the matrix equation is the least squares method, but this method requires AA^T non-singular, and easy to encounter digital morbid problem, using the image mapping method can effectively avoid this problem. The image mapping method is characterized by the use of Householder transform to find a suitable orthogonal array $H_{n\times n}$, so that $H_{n\times n}A^T_{n\times 2N}$ is converted to the upper triangular matrix. Let the observation equation be $L = Y + \Delta$, then the residual equation $V = A^T C - L$, the sum of squared residuals is $J = ||V||^2 = ||A^T C - L||^2$, so that the sum of the squares of the residuals is the least squares solution of the contradictory Eq. (5).

Let exist in the orthogonal matrix $H_{n\times n}$, so that:

$$H_{n\times n}A^T_{n\times 2N} = \begin{bmatrix} R_{2N\times 2N} \\ 0_{(n-2N)\times 2N} \end{bmatrix} \tag{6}$$

The first 2N elements in $H_{n\times n}L$ are m, the remaining elements are denoted as g, and the residual equation is orthogonal transform:

$$HV = HA^T C - HL = \begin{bmatrix} R \\ 0 \end{bmatrix} C - \begin{bmatrix} m \\ g \end{bmatrix} = \begin{bmatrix} RC - m \\ -g \end{bmatrix} \tag{7}$$

From the formula (7) can be obtained by the sum of squares:

$$J = ||V||^2 = ||HV||^2 = ||\begin{bmatrix} RC - m \\ -g \end{bmatrix}||^2 = \sqrt{(RC - m)^T (RC - m) + g^T g} \tag{8}$$

It can be seen that in Eq. (8), $C = R^{-1}m$ reaches the minimum value $\sqrt{g^T g}$. Thus the least squares solution of the contradictory Eq. (5) is $C = R^{-1}m$. According to this, the system response amplitude ratio $L(\omega_k)$ and the phase difference $\phi(\omega_k)$ corresponding to the angular frequency ω_k of the system are:

$$L(\omega_k) = 20\lg\frac{b_k}{a_k} = 20\lg\frac{\sqrt{c_{2k-1}^2 + c_{2k}^2}}{a_k} \tag{9}$$

$$\phi(\omega_k) = -\arctan\frac{c_{2k}}{c_{2k-1}} \tag{10}$$

4 Matlab Simulation

In order to verify the effectiveness of the method in the dynamic performance test of the system, a SISO system is selected as the test object, and the simulation experiment is carried out using Matlab. The system open-loop transfer function model is:

$$G(s) = \frac{U(s)}{I(s)} = \frac{b_1 s + b_0}{a_3 s^3 + a_2 s^2 + a_1 s + a_0} \tag{11}$$

The main parameters of the system transfer function are:

$$a_3 = 0.0148,\ a_2 = 0.1701,\ a_1 = 0.74,\ a_0 = 1,\ b_1 = 0.282,\ b_0 = 2$$

The dynamic performance test is carried out in the frequency range of the system. The parameters of the SPHS signal are N = 30, T = 10 s, and the sampling interval Td = 0.002 s. Use Matlab to generate the SPHS signal shown in Fig. 2, discretize it into Simulink.

In Simulink as shown in Fig. 4 to build the system transfer function model, the output of the sampling system to get the response shown in Fig. 3.

For Eq. (5), the matrix Y (t) is obtained by sampling the system response, and the matrix A is obtained from the excitation SPHS signal parameters. Since the matrix Y (t) and A are known, the least squares fit can be obtained by using the mirror mapping method. According to Eqs. (9) and (10), the system response amplitude ratio $L(\omega_k)$ and the phase difference $\phi(\omega_k)$ corresponding to the angular frequency ω_k are obtained. As shown in Fig. 5, the abscissa is set to the frequency of every ten times the angle, and the system amplitude and frequency characteristic

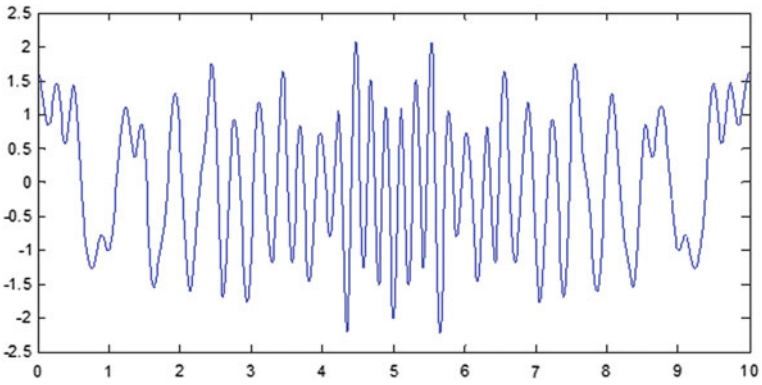

Fig. 2 SPHS excitation signal waveform

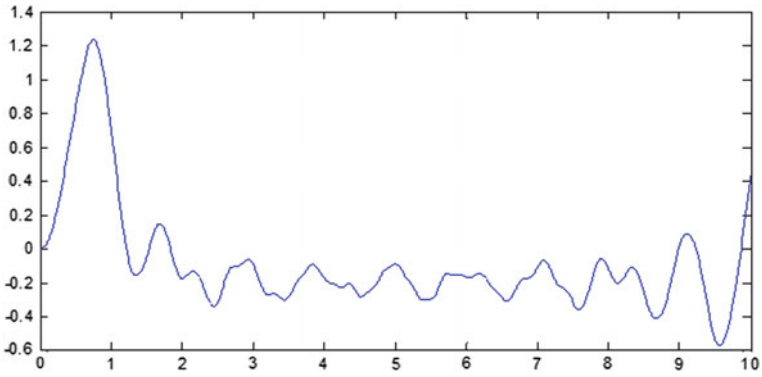

Fig. 3 System response signal waveform

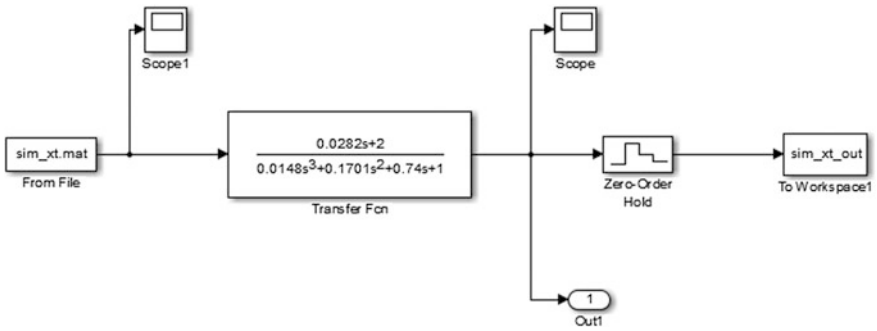

Fig. 4 Simulink build system model

graph and phase frequency characteristic graph are obtained by plotting $L(\omega_k)$ and $\phi(\omega_k)$ as the ordinate respectively. The dynamic performance of the system is analyzed and analyzed. It is necessary to pay attention to the result of the discretization of the response signal in the matrix data before the drawing. It is necessary to smooth the processing by the interpolation method before the drawing to obtain the system frequency characteristic curve.

In the above figure, the blue curve is a frequency characteristic curve directly obtained according to the transfer function of the system, and the green line is the frequency characteristic curve obtained according to the SPHS excitation. Contrast shows that the test results can better reflect the dynamic performance of the system.

According to the amplitude margin and the phase angle margin, the amplitude margin is the difference between the amplitude and the 0 dB at the phase angle crossing frequency. The phase margin is the difference between the phase angle and

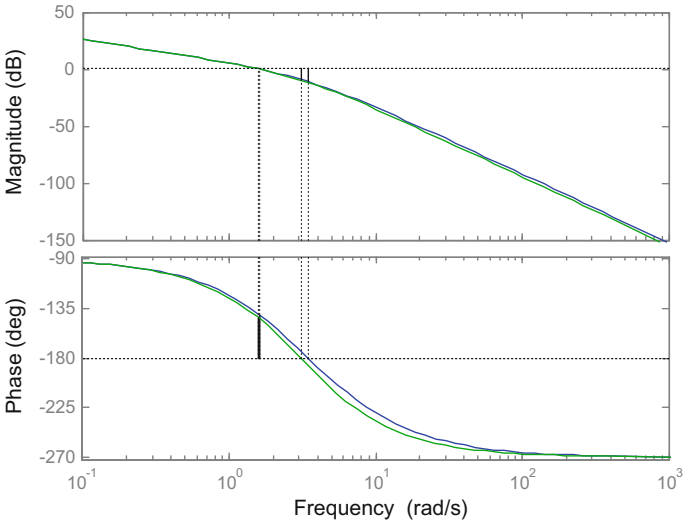

Fig. 5 System frequency characteristic curve

the $-180°$ of the amplitude crossing frequency. From the analysis of Fig. 5 available, the system amplitude margin K_g=3.5633, phase angle margin γ=38.8237°, cutoff frequency $\omega_c = 1.6108$ rad/s. And the original dynamic performance parameters of the system as follows:

	Amplitude margin	Phase margin (°)	Cut-off frequency (rad/s)
System parameters	3.5620	38.8229	1.7047
Test results	3.5633	38.8237	1.6108

5 Conclusion

Through the simulation experiment of SISO system, it can be seen that the dynamic performance test method based on SPHS signal can achieve high test precision. Using the image mapping method for data processing, effectively avoiding the digital morbid problem, expanding the scope of application of test methods. At the same time SPHS signal relative to the sine point by point scanning faster, and can be generated by the computer. Technology is easier to achieve than traditional methods.

References

1. Wang Y, Ye X, Huang Z et al (2003) Modern dynamic test technology. National Defense Industry Press, Beijing, pp 1–3, 03–31
2. Chen L, Yue R, Zhao N et al (2011) Frequency characteristic test method for multi-harmonic phase signal excitation. Foreign Electr Meas Technol 30(196 (3)):21–23, 36
3. Huang J, Xu H et al (2008) Application of multi-harmonic phase signal in missile dynamic test. Comput Meas Control 116(5):103–104, 134
4. Zhang X, Zhang S, Wang N (2009) Study on testing method of certain missile servo system based on multi-harmonic phase signals. J Proj Guidance 29(122 (3)): 83–85
5. Zhou J, Li J (2016) Test characteristic test method based on multi-harmonic phase signal. Ind Control Comput 29(11):39–41
6. Wang Y (2012) Dynamic mathematical model test modeling method. Xi'an University of Electronic Science and Technology Press, Xi'an, pp 50–53
7. Hao W, Li F, Xu H (2005) Frequency domain modeling method and MATLAB simulation based on multi-harmonic phase signal excitation. Chinese J Test Technol 31(6):123–125
8. Zhou Shenglong, Miao Dong (2001) System parameter identification under multi-harmonic coherent modulation signal excitation. Shanghai Aerosp 3:32–35
9. Zhou L (2004). Research on the dynamic test system of modern measurement and control platform. Nanjing University of Aeronautics and Astronautics, Nanjing, pp 28–32
10. Xu B, Zhou Y (2015) The small tactical missile dynamic testing technology research—Xu Baolian. Missiles Guidance J 35(164(4)):165–167, 172

A New Tuning Approach to Second-Order Active Disturbance Rejection Control

Xudong Shen, Wei Wei, Yanjie Shao and Min Zuo

1 Introduction

Active disturbance rejection control (ADRC) is proposed by Han in 1998 [1]. It is able to actively estimate and compensate total disturbance in real time. ADRC has been applied in numerous industrial processes and achieved desired performance, such as superconducting cavity control [2], flywheel energy storage system [3], tracking of IPSRU [4], hysteresis compensation [5], piezoelectric beam control [6], pneumatic force control system [7] and internal permanent-magnet synchronous motor control [8].

But in practice, parameter tuning of ADRC is somewhat difficult. Reasons are as follows. Firstly, many parameters have to be determined. Secondly, experience is indispensable. In order to reduce the difficulty of determining parameters, numerous approaches have been proposed. Genetic algorithms [9], neural networks [10] have been utilized to optimize the ADRC's parameters and tuning processes, but those algorithms are time-consuming, which may not be practical in engineering. In general, *n*th-order controllers are designed to control *n*th-order plants, and bandwidth parameterization approach is proposed for linear ADRC (LADRC) [11]. However, it is costly to identify the exact order of a given plant and bandwidth parameterization approach is also not optimized for a specified performance index.

Generally, for simplification, second order controller, including velocity and acceleration information, is enough for control engineering. For getting a simple, effective and optimal controller parameter tuning approach and for applying ADRC to a wider range, just like PID, it is necessary to fix the order of ADRC and optimize the parameters of ADRC. Researchers have discussed cases that second order ADRC controllers for non-second-order plants [12], but it is only used for

X. Shen · W. Wei (✉) · Y. Shao · M. Zuo
School of Computer and Information Engineering, Beijing Technology and Business University, Beijing 100048, China
e-mail: weiweizdh@126.com

Z. Deng (ed.), *Proceedings of 2017 Chinese Intelligent Automation Conference*,
Lecture Notes in Electrical Engineering 458,
https://doi.org/10.1007/978-981-10-6445-6_47

first to third order systems and authors did not give out a clear parameter tuning approach.

Integral of time-multiplied absolute-value of error (ITAE), one of the general performance indexes for evaluating the performance of a closed-loop system, is taken for single parameter optimal control and adaptive control [13–15]. Since ITAE is an index that describes system performance form the point of fast and accuracy, a set of normalized transfer function coefficients have been obtained by minimizing ITAE values [16]. Scholars have taken such idea to optimize PID tuning rules [17].

In this paper, we also use ITAE index to refine the second order ADRC tuning rule, and an ITAE optimal bandwidth parameterization method is proposed. For the approach proposed in this paper, only three parameters are needed to be tuned, which does make the tuning processes easier and guarantee fast and accurate system response.

2 Second Order Active Disturbance Rejection Control

In this paper, following second order system is considered

$$\ddot{y} = f + b_0 u \tag{1}$$

where y is the system output, f is the total disturbance of the system, u is the control signal, and b_0 is the coefficient of u.

A closed-loop system by second order ADRC is shown in Fig. 1.

where r is the set value, y is the output, u represents the control input, k_p and k_d are control parameters, G_p represents the controlled plant.

Extended state observer (ESO) takes the form as follows

$$\begin{cases} \dot{z}_1 = z_2 + \beta_1(y - z_1) \\ \dot{z}_2 = z_3 + \beta_2(y - z_1) + b_0 u \\ \dot{z}_3 = \beta_3(y - z_1) \end{cases} \tag{2}$$

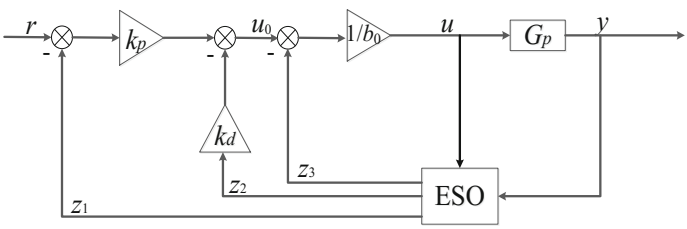

Fig. 1 Structure of closed-loop system by second order ADRC

where β_1, β_2, β_3 are observer parameters, b_0 is the coefficient of control input, z_1 is the estimation of system output, z_2 and z_3 represent the estimation of the velocity and total disturbance of the system, respectively.

Control law can be designed as

$$\begin{cases} u_0 = k_p(r - z_1) - k_d z_2 \\ u = (u_0 - z_3)/b_0 \end{cases} \tag{3}$$

If ESO works well, i.e. $z_1 \to y, z_2 \to \dot{y}, z_3 \to f$, we have

$$\ddot{y} = f + b_0 u \approx u_0 \tag{4}$$

i.e.

$$\ddot{y} \approx k_p(r - y) - k_d \dot{y} \tag{5}$$

Then we have the transfer function of the closed-loop system

$$G_{cl}(s) = \frac{y(s)}{r(s)} = \frac{k_p}{s^2 + k_d s + k_p} \tag{6}$$

where s is the Laplace operator.

3 ITAE Optimal Bandwidth Parameterization Approach

Here, ITAE optimal bandwidth parameterization approach is proposed. Firstly, the bandwidth parameterization approach is briefly introduced and then the new approach will be described.

Let controller bandwidth be ω_c and define [11]

$$k_p = \omega_c^2, \quad k_d = 2\omega_c \tag{7}$$

Also, let the bandwidth of ESO be ω_o and define

$$\beta_1 = 3\omega_o, \ \ \beta_2 = 3\omega_o^2, \ \ \beta_3 = \omega_o^3 \tag{8}$$

One can choose ω_c, ω_o and b_0 to get desired system response.

Based on above bandwidth parameterization approach, ITAE optimal bandwidth parameterization approach can be described as follows.

Let $k_p = \omega_n^2, S = s/\omega_n$, then Eq. (6) becomes

$$G_{clopt}(s) = \frac{\omega_n^2}{s^2 + k_d s + \omega_n^2} = \frac{1}{S^2 + \frac{k_d}{\omega_n} S + 1} \tag{9}$$

According to Graham [16], the second-order ITAE optimal transfer function can be written as

$$G_{opt}(s) = \frac{1}{S^2 + 1.41S + 1} \tag{10}$$

Then, we have

$$k_p = \omega_n^2, \quad k_d = 1.41\omega_n \tag{11}$$

For the parameters of ESO, we also take Eq. (8).

Therefore, for the ITAE optimal bandwidth parameterization approach, its adjustable parameter becomes ω_n, ω_o, b_0. By such approach, we can adjust the un-damped natural oscillation frequency and obtain the ITAE optimal response.

4 Simulation Results

Assuming that step signal is the desired output. Four typical plants have been considered. Numerical results are shown in Table 1.

Table 1 shows the system responses by bandwidth parameterization approach and ITAE optimal bandwidth parameterization approach. Both time and frequency domain responses have been given to show the difference. From the time domain responses, it can be seen that the responding speed of the ITAE optimal bandwidth parameterization approach is faster than the bandwidth parameterization approach and such fact is also confirmed by the comparison between frequency responses. In order to depict the difference much clearer, closed-loop bandwidth ω_b, gain margin G_m, phase margin P_m and ITAE values have been listed in Table 2.

From Table 2, we can see that ω_{b2} is greater than ω_{b1} in all cases. It means that the system response got by ITAE optimal bandwidth parameterization approach is faster. Furthermore, G_{m1} and G_{m2} are generally close to each other, P_{m1} is slightly bigger than P_{m2}, which means that a small part of the stability is sacrificed by taking ITAE optimal method. Obviously, $ITAE_2$ is less than $ITAE_1$, which confirms the proposed approach is optimal in ITAE.

In summary, although sacrificing a little stability margin, the new tuning approach is able to improve the dynamic performance of the system.

Table 1 Comparisons of system responses by two tuning approaches

Plants		Bandwidth parameterization	ITAE optimal bandwidth parameterization
$G_{p1}(s) = \frac{e^{-5s}}{(s+1)^3}$	Parameters	$b_0 = 12, \omega_c = 1, \omega_o = 4$	$b_0 = 1, \omega_n = 0.8, \omega_o = 1$
	Time domain response	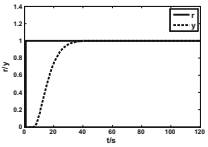	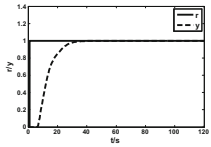
	Frequency domain response	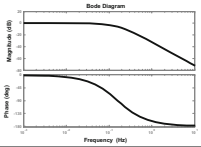	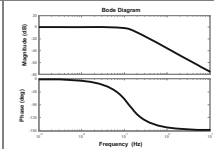
$G_{p2}(s) = \frac{1-2s}{(s+1)^3}$	Parameters	$b_0 = 4.5, \omega_c = 1, \omega_o = 4$	$b_0 = 6, \omega_n = 200, \omega_o = 1$
	Time domain response	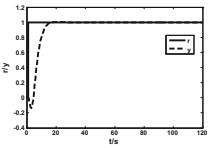	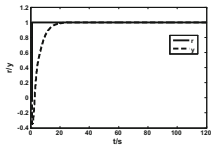
	Frequency domain response	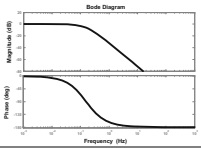	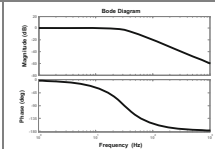
$G_{p3}(s) = \frac{1}{s(s+1)^3}$	Parameters	$b_0 = 0.58, \omega_c = 0.4, \omega_o = 1.6$	$b_0 = 6, \omega_n = 0.3, \omega_o = 60$
	Time domain response	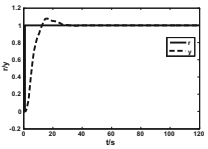	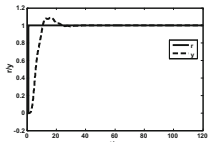
	Frequency domain response	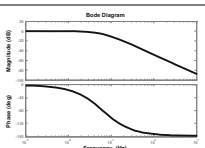	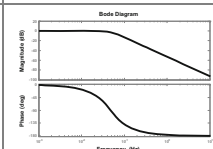
$G_{p4}(s) = \frac{1}{(s+1)^6}$	Parameters	$b_0 = 8, \omega_c = 1, \omega_o = 4$	$b_0 = 1, \omega_n = 1.1, \omega_o = 1$
	Time domain response	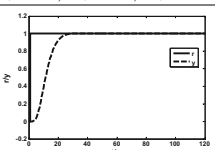	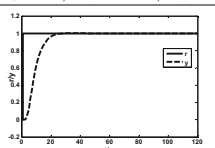
	Frequency domain response	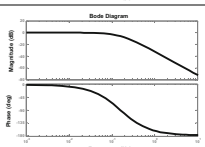	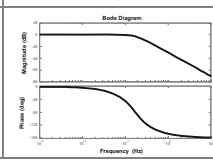

Table 2 Comparisons of indexes by two tuning approaches

Plants	Bandwidth parameterization				ITAE optimal bandwidth parameterization			
	ω_{b1}	G_{m1}	P_{m1}	ITAE_1	ω_{b2}	G_{m2}	P_{m2}	ITAE_2
$G_{p1}(s) = \frac{e^{-5s}}{(s+1)^3}$	0.642	92	180	160	0.801	94.5	171.180	110
$G_{p2}(s) = \frac{1-2s}{(s+1)^3}$	0.642	72.5	180	35	200.360	83.7	171.152	31
$G_{p3}(s) = \frac{1}{s(s+1)^3}$	0.257	92	180	40	0.301	76.7	171.077	35
$G_{p4}(s) = \frac{1}{(s+1)^6}$	0.642	92	180	88	1.102	91	171.152	58

5 Conclusion

In this paper, a new tuning approach, i.e. ITAE optimal bandwidth parameterization approach, has been proposed for second order active disturbance rejection control. Four different controlled plants are considered to confirm the proposed approach. Both bandwidth parameterization tuning approach and ITAE optimal bandwidth parameterization approach are taken in the simulations. By comparing time domain responses, the frequency domain responses and the ITAE values, we can arrive at that the new tuning approach is able to improve the system dynamic performance effectively. It provides another practical tuning approach for LADRC.

Acknowledgements This work is supported by National Science Technology Support Plan Projects 2015BAK36B04.

References

1. Han JQ (1998) Auto-disturbances-rejection controller and its applications. Control Decis 13 (1):19–23 (in Chinese)
2. Geng ZQ (2017) Superconducting cavity control and model identification based on active disturbance rejection control. IEEE Trans Nucl Sci 64(3):951–958
3. Chang XY, Li YL, Zhang WY et al (2015) Active disturbance rejection control for a flywheel energy storage system. IEEE Trans Ind Electron 62(2):991–1000
4. Li HS, Yang YY, Jia P et al (2016) Application of active disturbance rejection control in tracking problem of IPSRU. IEEE ICCA 2016:616–620
5. Goforth FJ, Zheng Q, Gao ZQ (2012) A novel practical for rate independent hysteretic systems. ISA Trans 51(3):477–484
6. Zheng QL, Richter H, Gao ZQ (2013) On active vibration suppression of a piezoelectric beam. ACC 2013:6613–6618
7. Liu FC, Jia YF, Liu SS (2015) Integral-linear active disturbance rejection controller for pneumatic force control system. Control Theory Appl 32(8):1090–1097 (in Chinese)
8. Du BC, Wu SP (2016) Application of linear active disturbance rejection controller for sensorless control of internal permanent-magnet synchronous motor. IEEE Trans Ind Electron 63(5):3019–3027

9. Liu D, Liu XL, Yang YX (2006) Uncalibrated robotic hand-eye coordination based on genetically optimized ADRC. Robot 28(05):510–514 (in Chinese)
10. Liu Z, Guo H, Wang DY et al (2010) Active-disturbance rejection control of brushless DC motor based on BP neural network. IEEE ICECE 2010:3253–3256
11. Gao ZQ (2003) Scaling and bandwidth-parameterization based controller tuning. Denver, CO, United States, pp 4989–4996
12. Yao XM, Wang QL, Liu WL et al (2002) Two-order ADRC control for general industrial plants. CEC 9(05):59–62 (in Chinese)
13. Sehuliz WC, Rideout CV (1961) Control system performance measures: past: present and future. AIEE Trans AC 6(1):22–35
14. Maurya AK, Bongulwar MR, Patre BM (2015) Tuning of fractional order PID controller for higher order process based on ITAE minimization. In: IEEE India conference, pp 1–5
15. Feng XU, Li DH, Xue YL (2003) Comparing and optimum seeking of PID tuning methods base on ITAE index. CSEE 23(8):207–211 (in Chinese)
16. Graham D, Lathrop RC (1953) The synthesis of 'Optimum' transient response: criteria and standard forms. AIEE Trans 72(5):273–288
17. Ala EAA, Rosbi BM (2010) Refine PID tuning rule using ITAE criteria. IEEE ICCAE 2010:171–176

RBF-ADRC Based Intelligent Course Control for a Twin Podded Ship

Zaiji Piao and Chen Guo

1 Introduction

Podded electric propulsion ship is different from the conventional ship, because its power and steering is provided by the propulsion motor. Due to the cancellation of the rudder, we can establish a relationship between the speed and steering angle of POD propeller and the conventional rudder angle, namely equivalent rudder angle analysis method.

Mentioned in the literature [1], Ship Manoeuvrability Research and Training Centre (SMRTC) in Poland Get the following conclusion on test of POD type ship: in all cases, POD promote rotary capacity of the ship was very good, the main problems existing is the ability to keep the ship heading stability. The stability of twin podded ship is better than single. So it is very necessary to design the course controller for the problem [2]. Neural network technology is a major bright spot in the field of artificial intelligence, which can achieve a lot of functions and have a successful application in the field of control, becoming a powerful branch of intelligent control. ADRC has strong robustness and wide adaptability, it has the ability to estimate and compensate the uncertain external disturbance, without depending on the mathematical model, it can learn advantages from PID technology and many advanced control technology in process control. The design of the RBF-ADRC course control combines the advantages of both, in order to provide a method for further optimizes the podded ship control problem.

Z. Piao · C. Guo (✉)
School of Information Science and Technology, Dalian Maritime University, Dalian 116026, China
e-mail: dmuguoc@126.com

Z. Deng (ed.), *Proceedings of 2017 Chinese Intelligent Automation Conference*, Lecture Notes in Electrical Engineering 458,
https://doi.org/10.1007/978-981-10-6445-6_48

2 The Pod Thrust Vector Model and Equivalent Rudder Angle Analysis Method

2.1 The Pod Thrust Vector Model

The pod thrust vector model can be calculated according to the following formula:

$$\begin{cases} X_P = (1-t_p)(T_P\cos\theta_P + T_s\cos\theta_s) \\ Y_P = (1-t_p)(T_P\sin\theta_P + T_s\sin\theta_s) \\ N_P = (1-t_p)(T_P\cos\theta_P - T_s\cos\theta_s)0.5\mathrm{L}_{PS} + Y_P\mathrm{L}_{OP} \end{cases} \tag{1}$$

θ is steering Angle for pods; L_{PS} is the lateral distance between the two propeller; L_{OP} is the distance from the center of the ship to the pods; T_P and T_s respectively represent left and right pod propeller thrust; t_p is the thrust deduction coefficient [3].

$$T_P = \rho n_P^2 D^4 K_T(J_P) \tag{2}$$

In formula (2) ρ is for the density of sea water; n_P is the left screw rotational speed; D is the propeller diameter; $J_P = U_P/(n_P D)$ is the speed ratio; K_T is based on pod propeller open water performance of the map which was used curve fitting and interpolation methods find out the thrust coefficient, the specific formula see (3). T_s was calculated in the same way as T_P.

$$K_T = 0.7 + 0.3589J_P + 0.1875{J_P}^2 \tag{3}$$

2.2 Equivalent Rudder Angle Analysis Method

Without consideration of the influence of the roll motion of the ship, the force F_δ generated by the conventional rudder is decomposed into the components of the Surge X, the sway Y, and the yaw N [4–6], X_R, Y_R, N_R:

$$\begin{cases} X_R = (1-t_R)F_\delta\sin\delta \\ Y_R = (1+d_{1R})F_\delta\cos\delta \\ N_R = (1+d_{2R})x_G F_\delta\cos\delta \end{cases} \tag{4}$$

In the formula, $F_\delta = 0.5\rho \mathrm{f}_a A_P U_P^2 \sin(a_P)$, A_P is rudder area, U is the flow velocity of rudder blade; f_a Is the lift coefficient C_L in the slope Angle of attack is equal to zero, a_P is angle of attack.

Combined formula (1) and formula (4), this formula can be obtained:

$$\begin{aligned} &0.5\rho \mathrm{f}_a A_P U_P^2 \sin(a_P)(1+d_{2R})x_G \cos\delta \\ &\quad = (1-t_p)(T_P \cos\theta_P - T_s \cos\theta_s)0.5\mathrm{L}_{PS} \\ &\qquad + (1-t_p)(T_P \sin\theta_P + T_s \sin\theta_s)\mathrm{L}_{OP} \end{aligned} \tag{5}$$

The formula (2) is brought into the above formula:

$$\begin{aligned} &0.5\rho \mathrm{f}_a A_P U_P^2 \sin(a_P)(1+d_{2R})x_G \cos\delta \\ &\quad = (1-t_p)(\rho n_P^2 D^4 K_T(J_P)\cos\theta_P - \rho n_S^2 D^4 K_T(J_S)\cos\theta_s)0.5\mathrm{L}_{PS} \\ &\qquad + (1-t_p)(\rho n_P^2 D^4 K_T(J_P)\sin\theta_P + \rho n_S^2 D^4 K_T(J_S)\sin\theta_s)\mathrm{L}_{OP} \end{aligned} \tag{6}$$

We set a_P=δ, in the case of the rotation angle is not large, and it can be similar that $\sin a = a, \cos a = 1 - a^2/2$, and then the formula can be changed into:

$$\begin{aligned} \delta = [&(1-t_p)(\rho n_P^2 D^4 K_T(J_P)(1-\theta_P^2/2) \\ &- \rho n_S^2 D^4 K_T(J_S)(1-\theta_S^2/2)0.5\mathrm{L}_{PS} \\ &+ (1-t_p)(\rho n_P^2 D^4 K_T(J_P)\theta_P \\ &+ \rho n_S^2 D^4 K_T(J_S)\theta_s)\mathrm{L}_{OP}]/0.5\rho \mathrm{f}_a A_P U_P^2(1+d_{2R})x_G \end{aligned} \tag{7}$$

We set $(1-t_p)\rho D^4/0.5\rho \mathrm{f}_a A_P U_P^2(1+d_{2R})x_G = \mathrm{A}$, $n_P^2 K_T(J_P) = N_1$, $n_S^2 K_T(J_S) = N_2$, The above formula can be simplified as:

$$\begin{aligned} \delta = \mathrm{A}[&(N_1(1-\theta_P^2/2) - N_2(1-\theta_S^2/2))0.5\mathrm{L}_{PS} \\ &+ (N_1\theta_P + N_2\theta_s)\mathrm{L}_{OP}] \end{aligned} \tag{8}$$

3 Twin Pod of Ship Maneuverability Analysis in Different Working Conditions

In this paper, the simulation is carried out by taking the "Taian port" as an example [7], which used two sets of SSP electric propulsion system. Its main parameters are shown in Table 1.

Table 1 Ship's main dimensions

Total length L *OA* (m)	156
Beam B (m)	32.2
Draft d (m)	7.5
Square coefficient C_b	0.755
Displacement m (Ton)	26,426
Prismatic coefficient C_p	0.8315

According to relevant information, the movement of twin podded ship is divided into the following four conditions [8]:

(1) The propeller rotation angle is equal, and the rotate speed is same, namely two pods by linkage control. This condition is normal operation in the ocean of the twin podded ship. Applying the equivalent rudder angle method, the given podded propeller rotate speed is 144 r/min, steering angle is 10°, and operate in the MATLAB simulation, we can get the following results (Fig. 1).
(2) Twin podded propellers rotate speed is same, only a single rotary paddle. This condition is ship's approaching and leaving docks, or correcting the state in special locations. The given left and right POD propeller rotate speed is 144 r/min, the left steering angle is 0°, the right steering angle is 10°, and we can get the following results in MATLAB (Fig. 2).
(3) Single pod function. This condition is when one pod in failure situation. The steering angle and rotate speed of left pod was set zero. The given right podded propeller rotate speed is 144 r/min, and the right steering angle is 10°. The following simulation results can be obtained in MATLAB (Fig. 3).
(4) The twin pods were not turned, but the rotate speeds are different. Because of the particularity of podded propulsion mode, in this case it can still generate torque. It is also well reflect the advanced nature of this propulsion mode. The twin pod steering angle is 0°, given the right podded propeller rotate speed 60 r/min, left the podded propeller rotate speed is 144 r/min. The following simulation results can be obtained in MATLAB (Fig. 4).

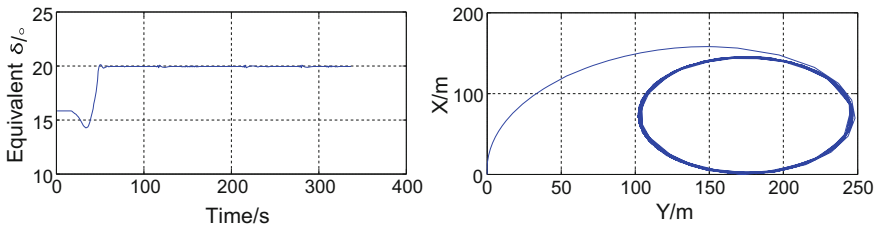

Fig. 1 Equivalent rudder angle and turning circle in first work condition

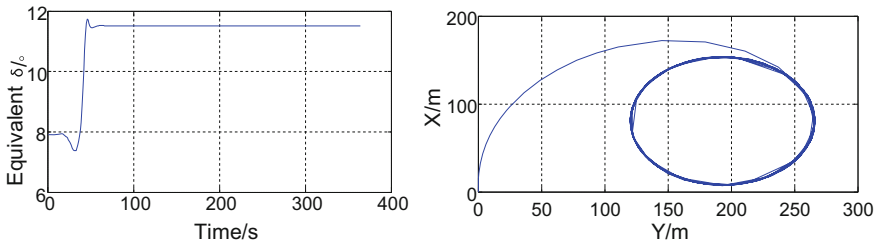

Fig. 2 Equivalent rudder and turning circle angle in second work condition

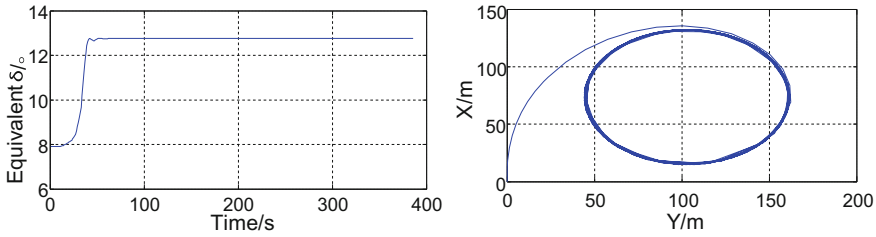

Fig. 3 Equivalent rudder angle and turning circle in third work condition

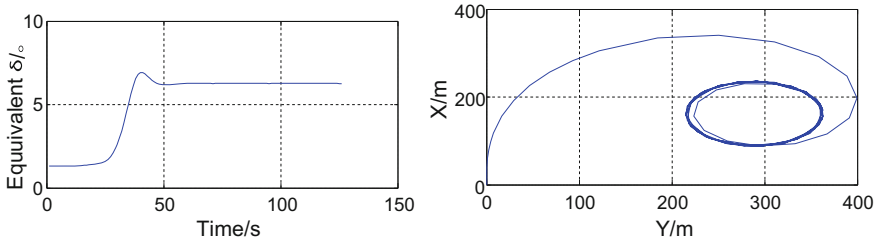

Fig. 4 Equivalent rudder angle and turning circle in fourth work condition

3.1 RBF-ADRC Control Principle

The so-called RBF-ADRC course control is the combination of RBF neural network and auto disturbance rejection controller in the course control. RBF neural network which is a feed-forward neural network is composed of three layers, it is nonlinear structure, but the second hidden layer to the third output layer is linear, so accelerating effectively without the local minimum problem of learning speeds.

The ADRC is mainly composed of tracking differentiator (TD), the nonlinear state error feedback control law (NLSEF) and the expansion of state observer (ESO) three parts [9, 10].

The general steps of the design of RBF-ADRC are summarized as follows:

(1) By selecting the appropriate parameters, the auto disturbance rejection controller can control the basic course of podded propulsion ship.
(2) The outputs z_1, z_2, z_3 were taken from the state observer and save them. The practice of this paper is to import the MATLAB state variable space, in this way to save the data.
(3) Train the neural network, using RBF neural network, z_1, z_2 for the input, z_3 for the expect output. In the course of training, the training parameters and termination conditions are given.

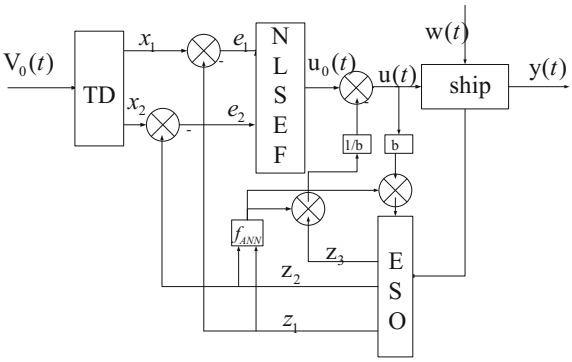

Fig. 5 The structure of RBF-ADRC

(4) The trained neural network is embedded into the corresponding position in Fig. 5 in the form of nonlinear function f_{ANN}, and then the result of course control is observed.

3.2 Simulation Studies of Course Control

Simulation experiment in this paper using the "Taian port" POD electric propulsion ship as the control object [11, 12]. In order to compare the control effect, the RBF-PID controller [13, 14] as a contrast objects. Target course are 10° and 20°, and initial speed is 15.3 km, ship engine speed 140 r/min.

The simulation curve of course control in the MATLAB is shown below (Figs. 6 and 7).

When a given course angle is 10°, the RBF-PID controller takes about 200 s to reach a stable value, and has an overshoot about ten percent, while the RBF-ADRC takes only about 70 s. When a given course angle is 20°, the RBF-PID controller takes about 150 s to reach a stable value, while the RBF-ADRC takes only about 60 s. The simulation results show that the two controllers were able to reach the

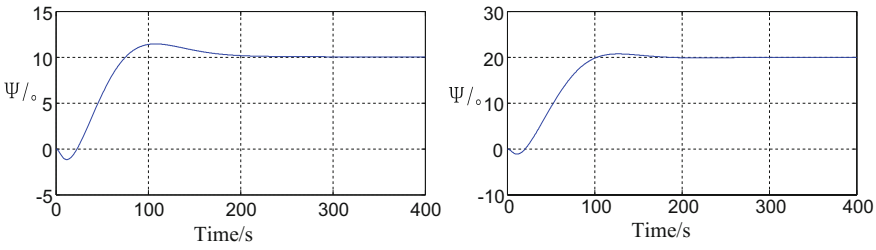

Fig. 6 Simulation results of RBF-PID course control

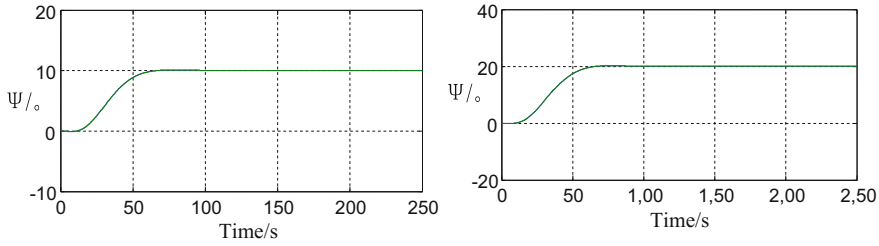

Fig. 7 Simulation results of RBF-ADRC course control

control requirement, but the RBF-ADRC course controller reached the expected course more quickly, and in accordance with the expected steady driving, greatly shorten the adjustment time.

4 Conclusions

This article started with the structure of twin podded propulsion ship, using the equivalent rudder method to study the ship maneuverability and course control problem. the "Taian port" ship was as example to simulate in the MATLAB, mainly completed the following work:

(1) The thrust vector model of the pod is established, which the mathematical model of ship motion based on.
(2) By using the method of equivalent rudder effect, the functional relationship between the two twin podded propeller rotate speed, two rotation angle and conventional rudder angle has been established, and four work conditions for ship maneuverability have been analyzed.
(3) Through the analysis the advantages of RBF neural network and ADRC, the RBF-ADRC course controller has been designed, and compared the control effect with RBF-PID controller, and simulated in the MATLAB. Lay a foundation for further study the control of twin podded ship.

Acknowledgements The authors are very grateful to the editors and reviewers for their valuable comments and suggestions. This work is supported by National Natural Science Foundation of China (Nos. 51579024, 6137114) and the Fundamental Research Funds for the Central Universities (DMU No. 3132016311).

References

1. Ma C (2007) Podded propulsion technology. Shanghai Jiaotong University Press (in Chinese)
2. Xian Y, Nie WT (2008) Present situation and prospects of podded rotary electric propulsion systems. Jiangsu Ship 24(6):28–29 (in Chinese)

3. Gou TT (2012) The research of control system of podded electric propulsion. Jiangsu University of Science and Technology (in Chinese)
4. Jia XL, Yan YS (1999) Mathematical model of ship motion: the mechanism modeling and ferreting modeling. Dalian Maritime University Press (in Chinese)
5. Heinke HJ (2004) Investigation about the forces and moments at podded drives. In: Proceedings of the 1st international conference on technological advances in podded propulsion. Newcastle University, UK, April 2004, pp 305–320
6. Woodward MD, Clarke D, Atlar M () On the manoeuvring prediction of POD driven ship. In: International conference on marine simulation and ship maneuverability (MARSIM 2003), vol 2. Kanazawa, Japan. 25th–28th Aug 2003
7. Chen XX, Jian D et al (2013) Modeling and simulation of power system for semi submersible ship of Taian (in Chinese)
8. Huang H, Zhu JX et al (2016) Rotary sculls ship equivalent rudder model. J Harbin Eng Univ (Engl Ed) 37(2):168–173 (in Chinese)
9. Hui ZG (2009) Semi-submerged ship maneuvering motion simulation. Dalian Maritime University (in Chinese)
10. Gao Z (2002) From liner to nonlinear contol means: a practical progression. ISA Trans 4 (41):177–189 (in Chinese)
11. Zhang R, Han JQ (2000) A neural network based active disturbance rejection controller. Syst Simul J 12(2):141–151 (in Chinese)
12. Pan JX (2014) Research on intelligent control for large ship course. Dalian Maritime University (in Chinese)
13. Xi QC (2014) Research on ship course control based on the ADRC. Dalian Maritime University (in Chinese)
14. Liu JK (2011) Advanced PID control MATLAB simulation. Electronic Industry Press (in Chinese)

Human Action Recognition with Skeleton Data Using Extreme Learning Machine

Ying Li, Xiong Luo, Weiping Wang and Wenbing Zhao

1 Introduction

Action recognition is a popular research topic all the time due to its wide range of applications. Compared with 2D image data, the human skeleton data is robust to sophisticated environment and provides more meaningful skeletal information. Considering the superiority of skeleton data, in this paper the recognition algorithm is studied through the use of the 3D coordinates of skeleton joints.

On account of distinct performing speed and lengths of various video sequences, we first select several key frames for each action sequence using K-means clustering algorithm. It can also help to remove the redundant information, thus reducing the computational complexity and improving the learning speed. In addition, we combine the joint-based and body part-based features to represent action sequences. Then extreme learning machine (ELM) algorithm is used to recognize the actions. It can achieve a rapid training speed compared with other classifiers, and is suitable for online recognition system.

Y. Li · X. Luo (✉) · W. Wang (✉)
School of Computer and Communication Engineering, University of Science and Technology Beijing (USTB), 30 Xueyuan Road, Haidian District, Beijing 100083, China
e-mail: xluo@ustb.edu.cn

W. Wang
e-mail: weipingwangjt@ustb.edu.cn

Y. Li · X. Luo · W. Wang
Beijing Key Laboratory of Knowledge Engineering for Materials Science, 30 Xueyuan Road, Haidian District, Beijing 100083, China

W. Zhao
Department of Electrical Engineering and Computer Science, Cleveland State University, Cleveland, OH 44115, USA

Z. Deng (ed.), *Proceedings of 2017 Chinese Intelligent Automation Conference*, Lecture Notes in Electrical Engineering 458,
https://doi.org/10.1007/978-981-10-6445-6_49

2 Related Work

In the past decades, the topic on human action recognition has attracted many researchers' interest. There are various kinds of features that can be extracted from skeleton data, and these features are mainly divided into two categories: features based on the 3D coordinates of joints and features based on the angular characteristics of body parts [1].

On one hand, Müller et al. proposed the concept of motion templates as a feature and extracted the geometric relations between the significant joints of human skeleton [2]. Shimada et al. treated the 3D coordinates of joints as features and trained them directly without any preprocessing [3].

On the other hand, Deng et al. calculated the angles of each joint and then combined the angle feature vectors of all frames [4]. Ofli et al. also extracted all the joints' angles for each frame and then segmented these feature sequences into temporal windows [5].

On the basis of the above work, we can combine the joint-based and body part-based features to represent action sequences.

3 The Proposed Approach

3.1 Key Frames Selection Using K-Means

In this paper, the classical K-means clustering algorithm [6] is used to extract a few cluster centers of similar data. Then the key frames are selected based on these cluster centers. In our approach, we cluster the coordinates of skeleton 3D joints at each frame in an action sequence. 20 skeleton joints' positions can be obtained from Kinect, and each joint has three coordinates representing x-, y-, and z-axis positions, respectively. Therefore, the coordinates comprise a 60-dimensional vector at each time frame. The details of K-means algorithm are given below.

Let $\mathbf{X} = \{\mathbf{x}_1, \ldots, \mathbf{x}_N\}$ ($\mathbf{x}_i \in \mathbf{R}^d$, $i = 1, \ldots, N$) be the set of N vectors to be clustered, where N is the total frames of an action sequence. And $\mathbf{x}_i$ is the i-th frame's joints vector with d-dimension where $d = 60$ here. Let $C = \{c_1, \ldots, c_K\}$ ($K \leq N$) be the set of K clusters. Then, we can select K key frames of an action sequence as follows.

(1) Select initial K cluster centroids randomly as $\boldsymbol{\mu}_1, \ldots, \boldsymbol{\mu}_K \in \mathbf{R}^d$.
(2) Compute the distances between $\mathbf{x}_i$ and each cluster center. Then assign the sample to its closest cluster center. The distance can be obtained as

$$D = \arg\min_{j} \sum_{i=1}^{N} \sum_{j=1}^{K} \left\| \mathbf{x}_i - \boldsymbol{\mu}_j \right\|^2 . \tag{1}$$

(3) For each cluster j, compute new cluster center again as follows:

$$\boldsymbol{\mu}_j = \left(\sum_{i=1}^{N} r_{ij}\mathbf{x}_i\right) \Big/ \left(\sum_{i=1}^{N} r_{ij}\right) \tag{2}$$

where $r_{ij} = 1$ when the sample $\mathbf{x}_i$ belongs to the j-th cluster, otherwise it equals to 0.

(4) Repeat steps (2) and (3) until the cluster centers nearly stay the same.

(5) For each cluster center $\boldsymbol{\mu}_j$, compute the Euclidean distance between each joint in $\boldsymbol{\mu}_j$ and the same joint at each frame. Then we can get an $N \times 20$ matrix $\mathbf{M}_j$, where the matrix element $m_{p,\ q}$ ($p = 1, \ldots, N$; $q = 1, \ldots, 20$) represents the distance between the q-th joint at the p-th frame and the same joint in cluster center $\boldsymbol{\mu}_j$. Therefore we will obtain K matrixes $\mathbf{M}_j$ ($j = 1, \ldots, K$).

(6) For each matrix $\mathbf{M}_j$, find the minimum of each column, then let it equals to 1 and others equals to 0.

(7) Combine K matrixes $\mathbf{M}_j$ ($j = 1, \ldots, K$) and then extract K frames which have the most number of value 1. As a result, these frames are the key frames.

3.2 Feature Extraction

Feature extraction is a crucial procedure in action recognition. Here, we extract the distance features between a fixed human center point, which is the hip center, and other joints. The skeleton structure captured from the Kinect sensor is illustrated in Fig. 1. In addition, we incorporate the angles of critical joints as features [7]. These features can help us understand the distinct importance of each body part and make it more accurate on action recognition.

Let $\mathbf{F}_t$ be the feature vector at time t for each key frame, and it is denoted as:

$$\mathbf{F}_t = [D_{\text{HipCenter}}, \theta] \tag{3}$$

where $D_{\text{HipCenter}}$ is the distance between each joint and the hip center, and θ represents the angles of the important joints, which are shoulder, elbow, wrist, hip, knee and ankle in the left and right sides, respectively. Formally, these features can be represented as follows:

- Let P be the skeleton 3D joints. The distance $D_{\text{HipCenter}}$ between joint $P_i = (x_i, y_i, z_i)$ and the hip center $P_c = (x_c, y_c, z_c)$ for each frame is calculated as [7]:

$$D_{\text{HipCenter}} = \sqrt{(x_i - x_c)^2 + (y_i - y_c)^2 + (z_i - z_c)^2} \tag{4}$$

- We define each body part as a vector $\mathbf{V}$ formed by two adjacent joints. The angle of a joint $\theta_{(\mathbf{V}1,\ \mathbf{V}2)}$ between two body parts $\mathbf{V}_1$ and $\mathbf{V}_2$ can be computed as:

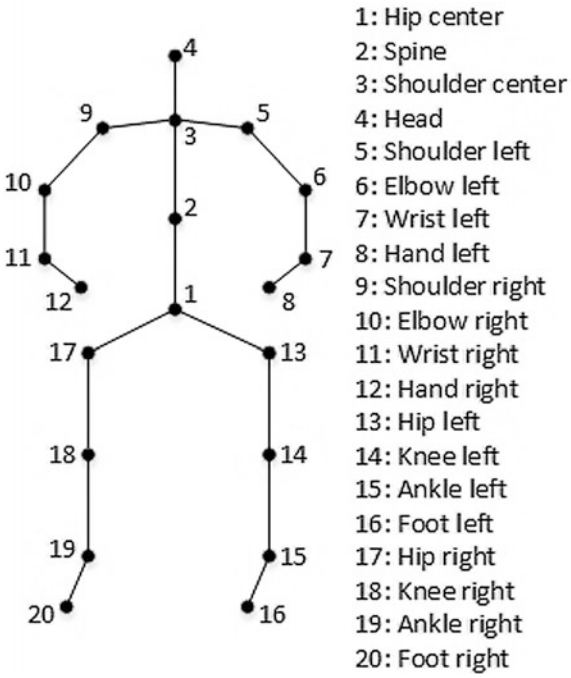

Fig. 1 Skeleton joints captured by the Kinect sensor

$$\theta_{(\mathbf{V}_1,\mathbf{V}_2)} = \arccos((\mathbf{V}_1 \cdot \mathbf{V}_2)/(|\mathbf{V}_1| \cdot |\mathbf{V}_2|)) \tag{5}$$

where $\theta_{(\mathbf{V}1,\ \mathbf{V}2)}$ is the angle of joint P_i, $\mathbf{V}_1$ is represented with joints P_i and P_j, and similarly, $\mathbf{V}_2$ is represented with joints P_i and P_k ($i \neq j \neq k$).

3.3 Classification Using Extreme Learning Machine

ELM was first proposed by Huang et al. [8] as a kind of learning algorithm for single-hidden layer feedforward neural networks (NN). It is with satisfactory computational performance for some tasks [9], among some popular learning methods, e.g., kernel learning algorithm [10–12], other NN-based methods [13]. The hidden node parameters of ELM network, including input weights and hidden layer biases, are initialized randomly and need not be adjusted manually. So it can obtain very fast learning speed with low computational cost.

Given M arbitrary distinct samples ($\mathbf{x}_i$, $\mathbf{y}_i$) (i = 1, …, M), where $\mathbf{x}_i \in \mathbf{R}^n$ is the training data vector and $\mathbf{y}_i \in \mathbf{R}^s$ is the label of output for each sample. The standard ELM network with L hidden nodes can be expressed as follows:

$$\mathbf{y}_i = \mathrm{f}(\mathbf{x}_i) = \sum_{j=1}^{L} \beta_j \mathrm{g}(\mathbf{w}_j \cdot \mathbf{x}_i + b_j), \quad 1 \le i \le M,\ \mathbf{w}_j \in \mathbf{R}^n,\ \beta_j, b_j \in \mathbf{R} \tag{6}$$

where $\mathrm{g}(\cdot)$ denotes the activation function for hidden nodes, β_j is the output weight, $\mathbf{w}_j$ is the input weight vector connecting the input neurons to the j-th hidden neuron and b_j is the bias of the j-th hidden neuron.

Then, (6) can be written compactly in the matrix form as

$$\mathbf{H}\boldsymbol{\beta} = \mathbf{Y} \tag{7}$$

where $\mathbf{H} = [\mathbf{h}(\mathbf{x}_1), \ldots, \mathbf{h}(\mathbf{x}_M)]^{\mathrm{T}}$ is the hidden layer output matrix, and $\mathbf{h}(\mathbf{x}_i) = [h_1(x_i), \ldots, h_L(x_i)]^{\mathrm{T}}$ ($i = 1, \ldots, M$). In addition, $\boldsymbol{\beta} = [\beta_1, \ldots, \beta_L]^{\mathrm{T}}$ is the output weight matrix from the hidden layer to the output layer.

When the number of input samples is much larger than the dimensionality of the hidden layer, that is $N \gg L$, the output weight $\boldsymbol{\beta}$ can be calculated as [8]

$$\boldsymbol{\beta} = \left(C^{-1}\mathbf{I} + \mathbf{H}^{\mathrm{T}}\mathbf{H}\right)^{-1}\mathbf{H}^{\mathrm{T}}\mathbf{Y} \tag{8}$$

where C represents the regularization parameter.

4 Experiments and Discussions

We evaluate the performance of our proposed approach on the Kintense action dataset, which contains 4 different actions and about 13,000 action sequences. All the experiments are performed on MATLAB R2012a, Intel-i5 2.3G CPU, 16G RAM, Windows 7.

4.1 The Selection of Hyperparameters

For ELM network, only the number of hidden nodes L and the regularization parameter C are required to be tuned. Moreover, we need choose the number of key frames k of an action sequence first. We use 75% of all the Kintense action instances for training and the rest 25% for testing. Considering that each action instance has around 50–80 frames, one will be able to find the best k by conducting the search from 4 to 10. According to the experiments, we set k as 6.

In the experiments, L is set as $\{500, 600, \ldots, 7500\}$ and C is set as $\{2^{-20}, 2^{-19}, \ldots, 2^{9}, 2^{10}\}$ to choose the best parameters. As shown in Fig. 2a, the testing accuracy first increases rapidly and then converges gradually with the increase of L when C is prefixed. It is the same with the variation tendency when L is decided in advance and C grows exponentially as shown in Fig. 3a. Furthermore, from Fig. 2b, we can

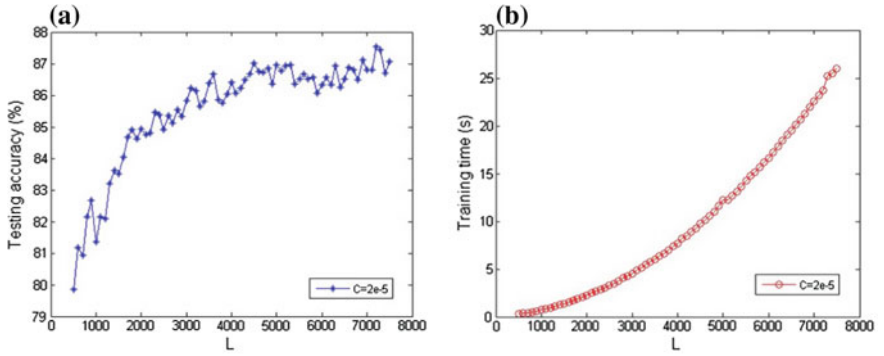

Fig. 2 Relationship between the number of hidden nodes L versus testing accuracy and training time. **a** Testing accuracy and **b** training time

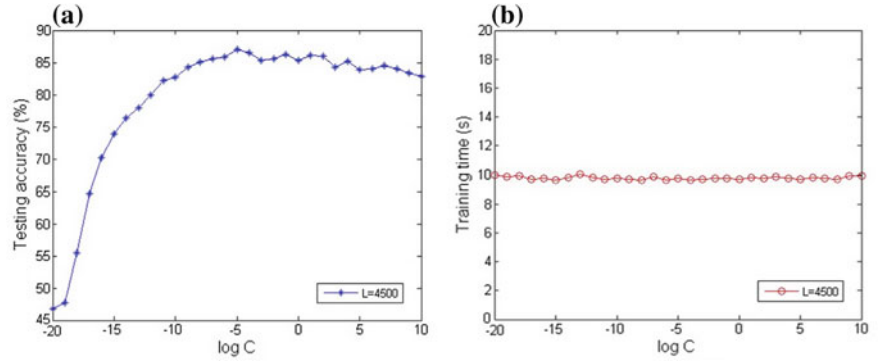

Fig. 3 Relationship between the regularization parameter C versus testing accuracy and training time. **a** Testing accuracy and **b** training time

also observe that the training time grows all the time when L goes up. This is because that the ELM network becomes large when L increases, resulting in a high computational cost. When C grows, the training time almost stays the same due to the fixed factor L as illustrated in Fig. 3b. In consideration of the classification accuracy, training time, and computational cost, we set L as 4500 and C as 2^{-5} in the experiments below.

4.2 Comparison with Other Methods

To evaluate our results, we first compare the recognition accuracy of our proposed approach with the frame-level method without any preprocessing. Figures 4a, b show the testing accuracy and training time, respectively, and indicate that the

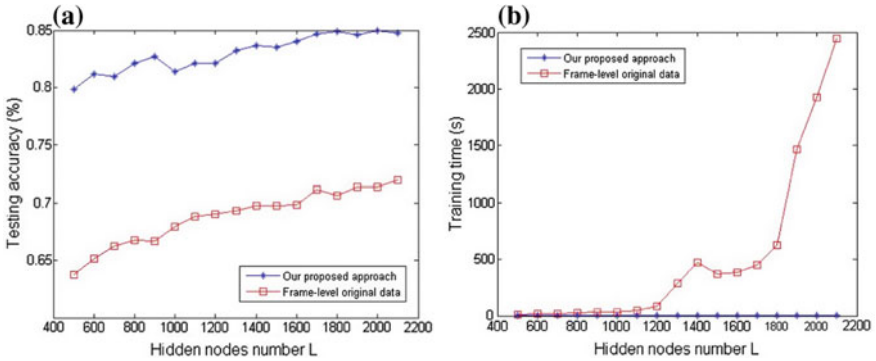

Fig. 4 Comparison between our approach and the frame-level method without preprocessing in testing accuracy and training time. **a** Testing accuracy and **b** training time

Table 1 Performance comparison of our approach and BP classifier

Method	ELM	BP
Accuracy (%)	87.31	80.50
Training time (s)	13.92	54
Hidden nodes	5500	90

recognition performance of our approach is much better than another. Moreover, the training time of our approach is several orders of magnitude lesser than the raw data. So compared with a high time cost in frame-level method, the learning time in our approach is nearly close to zero. This is due to the extracted key frames and the corresponding distance and angle features. Thus, our approach can perform a strongly fast training process without losing the recognition accuracy.

Finally, we compare the performance of ELM with Backpropagation (BP) classifier in the Kintense dataset. Both of the two methods are trained with the same preprocessing ways for the action instances. Table 1 shows the comparison results of ELM and BP. It is obvious that our approach not only remarkably decreases the computational cost but also improves the classification accuracy. So it is an effective method in the field of human action recognition.

5 Conclusion

In this paper, we propose an effective method for fast action recognition using 3D skeleton data. We select key frames through K-means clustering algorithm and then extract the features of both joint-based and body part-based ones. Finally, we use ELM classifier to perform action recognition. The experimental results indicate that our proposed approach outperforms other methods with a relatively high recognition accuracy and a fast training speed. So it is suitable for online recognition application.

Acknowledgements This work was jointly supported by the National Natural Science Foundation of China (Grant Nos. 61174103, 61603032), the National Key Technologies R&D Program of China (Grant No. 2015BAK38B01), the National Key Research and Development Program of China (Grant Nos. 2016YFB0700502, 2016YFB1001404, 2017YFB0702300), and the University of Science and Technology Beijing - National Taipei University of Technology Joint Research Program under Grant TW201705.

References

1. Chen X, Koskela M (2015) Skeleton-based action recognition with extreme learning machines. Neurocomputing 149:387–396
2. Müller M, Röder T (2006) Motion templates for automatic classification and retrieval of motion capture data. Proc Comput Anim Conf 137–146
3. Shimada A, Taniguchi RI (2008) Gesture recognition using sparse code of hierarchical SOM. Proc Int Conf Pattern Recognit 4761795
4. Deng L, Leung H, Gu N et al (2010) Automated recognition of sequential patterns in captured motion streams. Lect Notes Comput Sci 6184:250–261
5. Ofli F, Chaudhry R, Kurillo G et al (2013) Berkeley MHAD: a comprehensive multimodal human action database. Proc IEEE Workshop Appl Comput Vis 53–60
6. Lloyd SP (1982) Least squares quantization in PCM. IEEE Trans Inform Theory 28(2):129–137
7. Chikhaoui B, Ye B, Mihailidis A (2016) Feature-level combination of skeleton joints and body parts for accurate aggressive and agitated behavior recognition. J Ambient Intell Humaniz Comput 1–20
8. Huang GB, Zhou HM, Ding XJ et al (2012) Extreme learning machine for regression and multiclass classification. IEEE Trans Syst Man Cybern Part B Cybern 42(2):513–529
9. Luo X, Chang XH, Ban XJ (2016) Regression and classification using extreme learning machine based on L1-norm and L2-norm. Neurocomputing 174:179–186
10. Luo X, Zhang DD, Yang LT et al (2016) A kernel machine-based secure data sensing and fusion scheme in wireless sensor networks for the cyber-physical systems. Future Gener Comput Syst 61:85–96
11. Luo X, Liu J, Zhang DD et al (2016) A large-scale web QoS prediction scheme for the industrial Internet of Things based on a kernel machine learning algorithm. Comput Networks 101:81–89
12. Xu Y, Luo X, Wang WP et al (2017) Efficient DV-HOP localization for wireless cyber-physical social sensing system: a correntropy-based neural network learning scheme. Sensors 17(1):135
13. Luo X, Luo H, Chang XH (2015) Online optimization of collaborative web service QoS prediction based on approximate dynamic programming. Int J Distrib Sens Netw 2015:452492

An Adaptive Dynamic Programming Control Scheme Using Tunable Radial Basis Function

Jianzhong Bi, Xiong Luo and Weiping Wang

1 Introduction

Recent years have witnessed a growing interest in the intelligent learning and optimization in the machine intelligence community. Adaptive dynamic programming (ADP) as an effective way of solving "curse of dimension" has attracted much attention [1]. More recently, ADP related schemes have been applied to various realistic and complex systems [2]. Although ADP methods have been used for optimization purpose for well, there are also some limitations. To cope with the obstacle, some methods were proposed to improve the performance. For example, a Laguerre neural network (NN) was also integrated into the design of ADP to achieve tracking control [3]. Furthermore, some advanced intelligent optimization techniques, such as fuzzy NN, have been used in ADP [4], and it achieves satisfactory performance compared with some popular learning method, e.g., kernel learning algorithm [5–7].

However, improving the performance of ADP still remains a challenging problem in some complex systems. In response to this issue, we propose a novel ADP scheme, through the integration of a tunable node radial basis function (RBF) into the action NN which is a key module in ADP. Here, this tunable RBF is a concise NN with less computation and faster learning speed [8]. Specifically, the RBF-based ADP is to optimize the system parameters of characteristic model

J. Bi · X. Luo (✉) · W. Wang (✉)
School of Computer and Communication Engineering,
University of Science and Technology Beijing (USTB),
30 Xueyuan Road, Haidian District, Beijing 100083, China
e-mail: xluo@ustb.edu.cn

J. Bi · X. Luo · W. Wang
Beijing Key Laboratory of Knowledge Engineering for Materials Science,
30 Xueyuan Road, Haidian District, Beijing 100083, China
e-mail: weipingwangjt@ustb.edu.cn

Z. Deng (ed.), *Proceedings of 2017 Chinese Intelligent Automation Conference*,
Lecture Notes in Electrical Engineering 458,
https://doi.org/10.1007/978-981-10-6445-6_50

(CM) based adaptive controller. Generally, the CM-based controller could achieve satisfactory performance in dynamic environment [9].

2 Background

2.1 Characteristic Model-Based Adaptive Processing Method

On the basis of CM theory, the mathematical representation of a controlled system can be shown as a 2-order slowly time-varying difference equation [9]:

$$y(t+1) = f_1(t)y(t) + f_2(t)y(t-1) + g_0(t)v(t) \tag{1}$$

where $y(t)$ and $v(t)$ are the input and output of controlled system at time t, respectively. In addition, f_1, f_2, g_0 as the key parameters for the above CM should be slowly time-varying. Here, the golden-section control law could be used in the design of CM-based adaptive controller. It is represented as follows

$$v_g(t) = -(l_1 f_1(t)e(t) + l_2 f_2(t)e(t-1))/g_0(t) \tag{2}$$

where $l_1 = 0.382$, $l_2 = 0.618$, and $e(t) = y(t) - y_{in}(t)$. Moreover, $y_{in}(t)$ is the expected signal. Furthermore, the final CM-based adaptive controller could be designed by using (2) and some other control law. In this paper, the controller is defined as $v(t) = v_g(t) + v_i(t)$, where $v_i(t) = v_i(t-1) - k_i e(t)$, and we have

$$k_i = \begin{cases} k_{i1}, & e(t)[e(t) - e(t-1)] > 0 \\ k_{i2}, & e(t)[e(t) - e(t-1)] \leq 0 \end{cases} \tag{3}$$

Here, k_{i1} and k_{i2} are positive.

Then, the parameters we need to optimize for CM-based adaptive processing method in our RBF-based ADP is $\mathbf{k}(t) = [f_1(t), f_2(t), g_0(t), k_i(t)]$.

2.2 The Tunable RBF NN

As a local approximation network, RBF spends less leaning time than some global approximation networks. In this paper, we employ a tunable RBF NN proposed in [8], to reconstruct ADP. There are M hidden layer nodes. At time t, the input vector of the RBF network is denoted as $\mathbf{x}(t) = [x_1(t), x_2(t), \ldots, x_m(t)]^T$, where m is the

number of input variables, and $x_i(t)$ ($i = 1,\ldots, m$) is the input value at time t. The RBF network output is given by

$$f(\mathbf{x}(t)) = \sum_{i=1}^{M} \omega_i(t-1) g_i(\mathbf{x}(t)) \tag{4}$$

where $g_i(\mathbf{x}(t))$ and $\omega_i(t-1)$ are the output and weight coefficient of the i-th node.

Without loss of generality, we assume that the RBF is Gaussian. Then

$$\mathrm{g}_i(\mathbf{x}(t)) = \exp\Big(-(\mathbf{x}(t) - \mathbf{c}_i)^{\mathrm{T}} \mathbf{H}_i (\mathbf{x}(t) - \mathbf{c}_i)\Big) \tag{5}$$

where $\mathbf{c}_i = [c_i(1), \ldots, c_i(m)]^{\mathrm{T}}$ and $\mathbf{H}_i = \mathrm{diag}\{\delta_i^2(1), \ldots, \delta_i^2(m)\}$ is the center vector and the diagonal covariance matrix of the i-th node, $c_i(j)$ and $\delta_i^2(j)$ are the j-th center and variance of the i-th RBF node, respectively.

The residual error of RBF NN is expressed as $e(t) = y(t) - f(\mathbf{x}(t))$, where $y(t)$ is the ideal output.

The gradient descent is used for RBF NN. So the weight updating is defined as

$$\boldsymbol{\omega}(t+1) = (\boldsymbol{\omega}(t) + l[-\partial e(t)/\partial \boldsymbol{\omega}(t)])/\|(\boldsymbol{\omega}(t) + l[-\partial e(t)/\partial \boldsymbol{\omega}(t)])\|_1 \tag{6}$$

where l is the learning rate, $\|\cdot\|_1$ represents the 1-norm, and $\boldsymbol{\omega}(t-1) = [\omega_1(t-1), \ldots, \omega_M(t-1)]^{\mathrm{T}}$. When the weight updating is no longer able to handle the residual error, the node that makes the least contribution is replaced through the following rule.

$$W_i = \|\omega_i(t-1)\mathbf{g}_i\|^2, \quad i = 1, \ldots, M \tag{7}$$

where $\mathbf{g}_i = [g_1(\mathbf{x}(t)), g_1(\mathbf{x}(t-1)), \ldots, g_M(\mathbf{x}(t-s+1))]^{\mathrm{T}}$, and s is the innovation length which determines the number of past errors used for weight adaptation.

For all hidden layer nodes, the one with least W is replaced by a new node.

3 The RBF-Based ADP Control Scheme

3.1 ADP Learning Method

Let $r(t) = (e(t))^2/2$ be the instantaneous cost function at time t. The cost-to-go function is given by

$$J(t) = \sum_{i=1}^{\infty} \alpha^{i-1} r(t+i), \quad 0 < \alpha < 1 \tag{8}$$

where α is the discount factor.

Here, the proposed ADP learning method is developed in accordance with the actor-critic architecture, including the critic NN and the action NN. The critic NN output is the estimate of cost-to-go function as follows

$$\hat{J}(t-1) = r(t) + \alpha \hat{J}(t) \tag{9}$$

Therefore, the Bellman residual is defined as

$$e_c(t) = \alpha \hat{J}(t) - [\hat{J}(t-1) - r(t)] \tag{10}$$

The action NN is used to reduce the difference between the cost-to-go and the target objective. The approximation error is expressed as $e_a(t) = \hat{J}(t) - U_c$, where U_c is defined as the target objective and is set to 0 in this paper.

Here, let $\mathbf{u}(t) \in \mathbf{R}^4$ be the output of action NN, and it is employed to update key parameters of the CM-based adaptive controller by $\mathbf{k}(t+1) = \mathbf{k}(t) + \mathbf{u}(t)$.

3.2 Online Learning Implementation of RBF-Based ADP

In our implementation, we adopt the feed forward NN with one hidden layer to optimize the approximation error $e_a(t)$ and $e_c(t)$. In the hidden layer, a hyperbolic tangent threshold function is used by $L(x) = (1 - e^{-x})/(1 + e^{-x})$.

The action NN is shown in Fig. 1, where $\mathbf{x}(t) = \mathbf{e}(t)$ is the input, and $\mathbf{u}(t) = [\Delta f_1(t), \Delta f_2(t), \Delta g_0(t), \Delta k_i(t)]$ is the output. We have

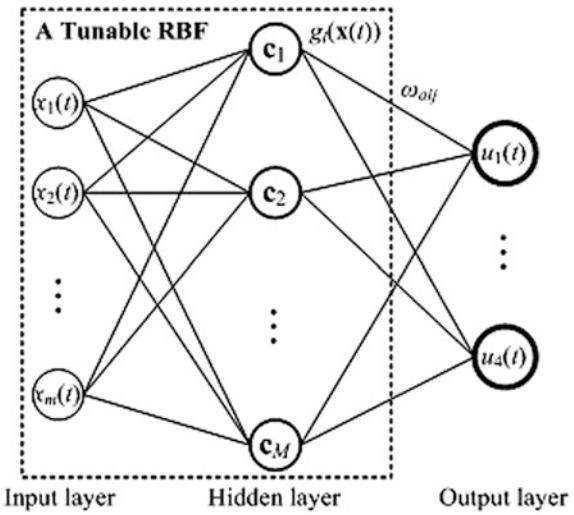

Fig. 1 The action neural network

$$u_j(t) = \sum_{i=1}^{n} \omega_{aij}(t) g_i(t), \quad j = 1, 2, 3, 4 \tag{11}$$

$$g_i(t) = \exp\Big(-(\mathbf{x}(t) - \mathbf{c}_i)^{\mathrm{T}} \mathbf{H}_i (\mathbf{x}(t) - \mathbf{c}_i)\Big), \quad i = 1, \ldots, M \tag{12}$$

$$\mathbf{H}_i = \mathrm{diag}\{\delta_i^2(1), \ldots, \delta_i^2(m)\}, \quad i = 1, \ldots, M \tag{13}$$

The critic NN is shown in Fig. 2, where ($\mathbf{x}(t)$, $\mathbf{u}(t)$) are the inputs and $J(t)$ is the output which can be defined as

$$J(t) = \sum_{i=1}^{N_{hc}} \omega_{ci}^{(2)}(t) p_i(t) \tag{14}$$

$$p_i(t) = L(q_i(t)), \quad i = 1, \ldots, N_{hc} \tag{15}$$

$$q_i(t) = \sum_{k=1}^{m} \omega_{cik}^{(1)}(t) x_k(t) + \sum_{k=m+1}^{m+4} \omega_{cik}^{(1)}(t) u_{k-m}(t), \quad i = 1, \ldots, N_{hc} \tag{16}$$

where N_{hc} is the number of hidden layer nodes.

The rule of the weight online updating for the action NN and the critic NN is a gradient-based adaptation. However, for the action NN in RBF-based ADP, there is only the weight between the hidden layer and output layer to be updated.

The rule of node online updating for the action NN is shown in (7). And W for all nodes are ordered as

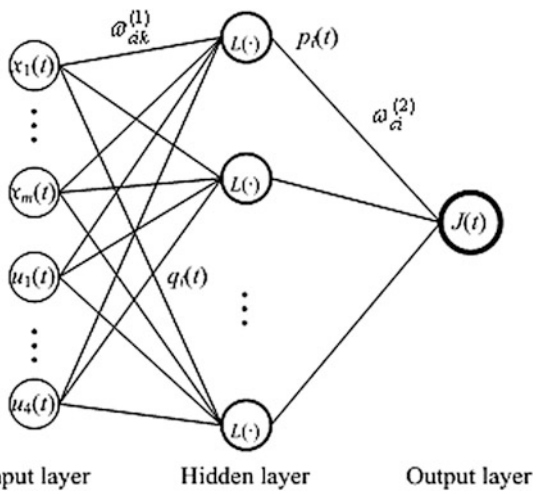

Fig. 2 The critic neural network

$$W_1 \leq W_2 \leq \cdots \leq W_M \tag{17}$$

where W_i is the i-th smallest value for all M nodes. Then, according to (17), the node 1 is the one to be replaced.

4 Simulation

The proposed scheme is tested on a complex system, i.e., the generic hypersonic vehicle system [10].

4.1 The Controlled System Model

In cruise and gliding stages, the system can be described by a series of differential equations by means of the forward velocity V, the flight-path angle γ, the altitude h, the angle of attack α, and the pitch rate q [10].

$$\dot{V} = (T\cos\alpha - D)/m - (\mu\sin\gamma)/r^2 \tag{18}$$

$$\dot{\gamma} = (L + T\sin\alpha)/(mV) - \left((\mu - V^2 r)\cos\gamma\right)/\left(Vr^2\right) \tag{19}$$

$$\dot{h} = V\sin\gamma \tag{20}$$

$$\dot{\alpha} = q - \dot{\gamma} \tag{21}$$

$$\dot{q} = M_y/I_y \tag{22}$$

where m, μ, and I_y represent the mass, the moment of inertia, and the gravity constant, respectively. And L, M_y, D, T, and r represent the lift, the pitching moment, the drag, the thrust, and the radial distance from Earth's center. Their definitions can be found in [10].

4.2 Simulation Results

(1) Case 1. The ideal signal is defined as $y_{\text{in}}(t) = 5\sin(1\pi t) + k_1 t + k_2 t + b$. Here, the initial state is $k_1 = 0$, $k_2 = 0$, and b is a constant. To test the stability of the proposed scheme, k_1 is changed to -0.015 at the time of 50 s and k_2 is changed

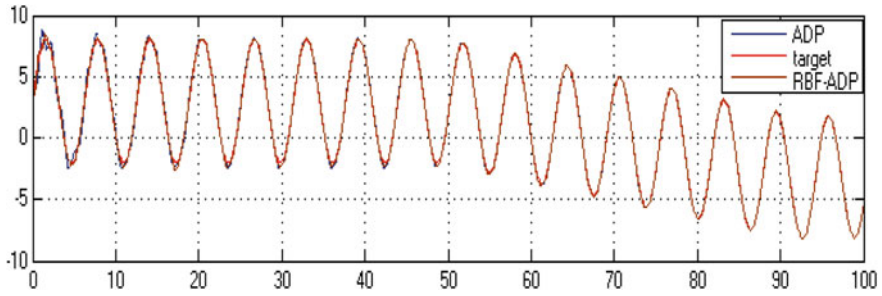

Fig. 3 Tracking result

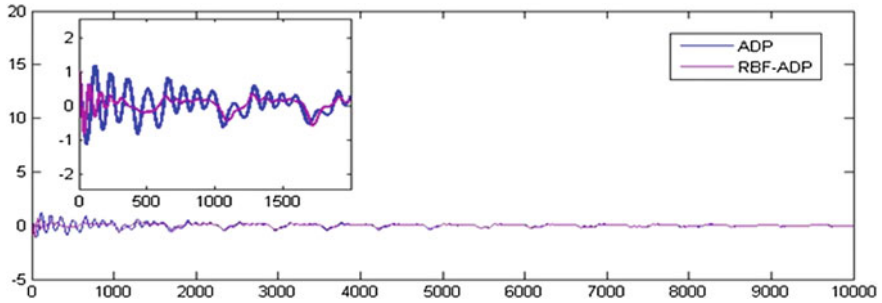

Fig. 4 Tracking error

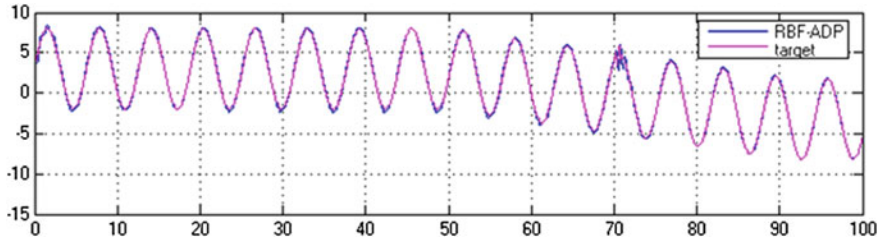

Fig. 5 Tracking curve with disturbed signal

to 0.1 at the time of 90 s. The tracking result of RBF-based ADP control scheme and the ADP are shown in Fig. 3. The difference of learning speed is shown in Fig. 4.

(2) Case 2. To verify the robustness of our scheme, we add a disturbed signal, which is a series of Gaussian random variables, and it occurs from 70 s. The tracking curve is shown in Fig. 5. We can find that the controlled signal converges very quickly after a sudden change.

5 Conclusion

In this paper, we propose a RBF-based ADP control scheme using the fast convergence of tunable RBF, and apply it to update those key parameters of CM-based adaptive controller. Generally, due to the use of tunable node in RBF, its convergent time is less than that of traditional ADP. Hence, the learning performance of RBF-based ADP is better than that of ADP. The proposed scheme is employed to the controller design for a generic hypersonic vehicle system. The results show that our scheme is faster than the ADP method in terms of the computational time.

Acknowledgements This work was jointly supported by the National Natural Science Foundation of China (Grant Nos. 61174103, 61603032), the National Key Technologies R&D Program of China (Grant No. 2015BAK38B01), the National Key Research and Development Program of China (Grant Nos. 2016YFB0700502, 2016YFB1001404, 2017YFB0702300), and the University of Science and Technology Beijing—National Taipei University of Technology Joint Research Program under Grant TW201705.

References

1. Lewis FL, Liu DR (2012) Reinforcement learning and approximate dynamic programming for feedback control. Wiley-IEEE, Hoboken
2. Luo X, Luo H, Chang XH (2015) Online optimization of collaborative web service QoS prediction based on approximate dynamic programming. Int J Distrib Sens Netw 2015:452492
3. Luo X, Lv YX, Zhou M et al (2016) A Laguerre neural network-based ADP learning scheme with its application to tracking control in the internet of things. Pers Ubiquitous Comput 20 (3):361–372
4. Luo X, Lv YX, Li RX et al (2015) Web service QoS prediction based on adaptive dynamic programming using fuzzy neural networks for cloud services. IEEE Access 3:2260–2269
5. Luo X, Zhang DD, Yang LT et al (2016) A kernel machine-based secure data sensing and fusion scheme in wireless sensor networks for the cyber-physical systems. Future Gener Comput Syst 61:85–96
6. Luo X, Liu J, Zhang DD et al (2016) A large-scale web QoS prediction scheme for the industrial Internet of Things based on a kernel machine learning algorithm. Comput Netw 101:81–89
7. Xu Y, Luo X, Wang WP et al (2017) Efficient DV-HOP localization for wireless cyber-physical social sensing system: a correntropy-based neural network learning scheme. Sensors 17(1):135
8. Chen H, Gong Y, Hong X et al (2016) A fast adaptive tunable RBF network for nonstationary systems. IEEE Trans Cybern 46(12):2683–2692
9. Wu HX, Hu J, Xie YC (2007) Characteristic model-based all-coefficient adaptive control method and its applications. IEEE Trans Syst Man Cybern C Appl Rev 37(2):213–221
10. Wang Q, Stengel RF (2000) Robust nonlinear control of a hypersonic aircraft. J Guid Control Dyn 23(4):577–585

Efficient Hidden Danger Prediction for Safety Supervision System: An Advanced Neural Network Learning Method

Zhigang Zhao, Yongfeng Wei, Xinyan Wang, Ruixin Li and Jing Deng

1 Introduction

Safety production of enterprises is an important issue for sustainable development. Hidden danger prediction plays an important role in ensuring the safety and efficient development of enterprises [1]. By providing effective prediction method for hidden danger data, enterprises can know their future safety production situation and possible changes in advance, so as to take measures to control [2]. And safety supervision department can evaluate the hidden danger management ability of enterprises by predicting the trend of hidden danger situation. Aiming at the influence of the relevant management index on the trend of hidden danger, this paper proposes a new learning algorithm based on management index for the number of hidden danger.

Generally, the prediction methods of the number of hidden danger can be divided into two categories. One is specialist analytical prediction according to the artificial experience. Such methods can play a positive role in some special occasions, but the efficiency will decreases rapidly when the number of hidden danger index becomes larger. Another is automatic prediction based on model driven or data driven methods. This kind of methods is less used in practical situations

Z. Zhao · Y. Wei · X. Wang
Communication and Information Center, State Administration of Work Safety, Beijing 100013, China

R. Li · J. Deng (✉)
School of Computer and Communication Engineering, University of Science and Technology Beijing (USTB), 30 Xueyuan Road, Haidian District, Beijing 100083, China
e-mail: informationscience@126.com

R. Li · J. Deng
Beijing Key Laboratory of Knowledge Engineering for Materials Science, 30 Xueyuan Road, Haidian District, Beijing 100083, China

Z. Deng (ed.), *Proceedings of 2017 Chinese Intelligent Automation Conference*, Lecture Notes in Electrical Engineering 458,
https://doi.org/10.1007/978-981-10-6445-6_51

because of their complex prediction models. Aiming at hidden danger data source, the automatic prediction based on data driven method can be widely used because it carries out optimal learning through some artificial intelligence methods without accurate mathematical model [3].

Different artificial intelligence algorithms can be used flexibly in data driven prediction methods [4, 5]. Recently, the prediction learning method based on neural network (NN) has witnessed a growing interest [6, 7]. This paper mainly implements hidden danger prediction using an advanced NN learning algorithm. The main contributions are as follows.

(1) At present, hidden danger prediction is mainly applied to coal chemical industry and other special industries. However, in some small-medium cities, the hidden danger prediction accuracy of medical treatment and other tertiary industries does not require as high as coal chemical industry, so there may exist some inaccurate data. Data driven hidden danger prediction algorithms for such industries is still scarce. This paper proposes an advanced algorithm to predict hidden danger for these tertiary industries.
(2) In the hidden danger prediction applications, the existing NN prediction algorithm is mainly implemented on the basis of Back-propagation (BP) algorithm [3]. In practice, there exist a lot of problems, such as over fitting and low learning precision. Recently, researchers have proposed various ways to improve the efficiency, e.g., extreme learning machine (ELM) [8], and achieved good results. Motivated by it, this paper discusses the application for the above areas using ELM.

2 Backgrounds

2.1 Theoretical Basis of Hidden Danger Prediction

Safety supervision is to avoid the occurrence of accidents and the damage caused by the accident. Only by fully understanding the causes and rules of the accident, can we make the production reach a safe state. Accident-causing theory is a kind of theory to grasp the law of accident occurrence [9]. By analyzing the original data, we can find out the potential impact of the hidden danger and the law of its development, so as to provide a favorable protection for safety production.

Accident-causing theory is of great significance to the study of the mechanism of accident, analysis and elimination of hidden danger, accident prevention and so on. At present, there are more than ten kinds of theories related to accident-causing theories, and the typical accident-causing theories include the accident causation sequence theory, the human error model, the orbit intersecting theory, the energy transfer theory and so forth [10]. Modern accident-causing theory is the model of action mechanism extracted from many typical accidents [10]. It reveals a certain rule of the accident, provides an effective and scientific reference basis to perfect

and improve the work of safety management, and is helpful to enhance the ability of enterprise's hidden danger investigation and governance.

In this paper, the application of ELM based hidden danger prediction method can be regarded as a novel practice of accident-causing theory.

2.2 ELM

ELM is a learning algorithm for single-hidden layer feedforward NN, and its schematic diagram is shown in Fig. 1 [8].

The output function of a single hidden layer feedforward NN with L hidden layer neurons is:

$$f_L(x) = \sum_{i=1}^{L} \beta_i G(a_i, b_i, x) \tag{1}$$

where a_i and b_i are hidden node parameters, β_i is the output weight vector between the i-th hidden layer node and the output nodes, $G(a_i, b_i, x)$ is a nonlinear output function of the i-th hidden layer node corresponding to the sample x. For the additive type hidden layer nodes, $G(a_i, b_i, x) = g(a_i x + b)$, where g: $\mathbf{R} \rightarrow \mathbf{R}$ denotes activation function, $a_i\, x$ denotes the inner product of the inner weight vector a_i and sample x in $\mathbf{R}^n$.

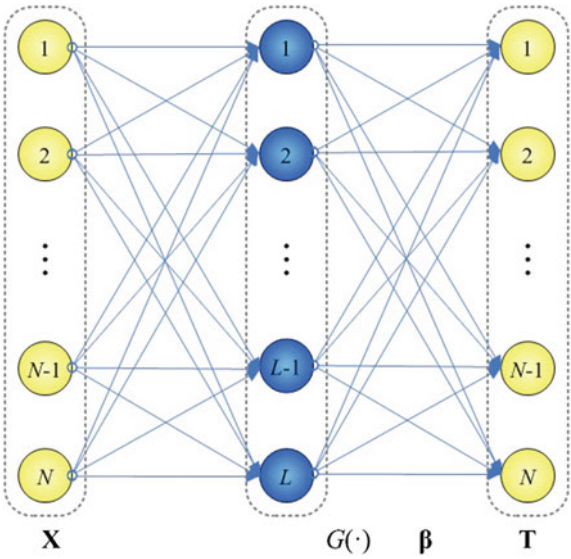

Fig. 1 The schematic diagram of ELM for a single hidden layer feedforward NN

For radial basis function (RBF) NN type hidden layer nodes, $G(a_i, b_i, x)$ can be expressed as $G(a_i, b_i, x) = g(b_i\|x - a_i\|)$, where a_i and b_i ($b_i > 0$) represent the center and influence factors of the i-th RBF node, respectively.

Considering N different data samples $\{(x_i, t_i)\}_{i=1}^{N} \subset \mathbf{R}^n \times \mathbf{R}^m$, if there is a single hidden layer NN with L hidden layer neurons, which can approximate the N different data samples with zero error, i.e., there exist a_i, b_i, β_i ($i = 1,2,\ldots, L$), making

$$f_L(x_j) = \sum_{i=1}^{L} \beta_i G(a_i, b_i, x_j) = t_j, \quad j = 1, \ldots, N \tag{2}$$

Here, (2) can be simplified as $\mathbf{H}\boldsymbol{\beta} = \mathbf{T}$, where

$$\mathbf{H}(a_1, \ldots, a_L, b_1, \ldots, b_L, x_1 \ldots, x_N) = \begin{bmatrix} G(a_1, b_1, x_1) & \cdots & G(a_L, b_L, x_1) \\ \vdots & \ddots & \vdots \\ G(a_1, b_1, x_N) & \cdots & G(a_L, b_L, x_N) \end{bmatrix}_{N \times L} \tag{3}$$

$$\boldsymbol{\beta} = \left(\left[\beta_1^{\mathrm{T}}, \ldots, \beta_L^{\mathrm{T}} \right]^{\mathrm{T}} \right)_{L \times m} \text{and} \quad \mathbf{T} = \left(\left[t_1^{\mathrm{T}}, \ldots, t_N^{\mathrm{T}} \right]^{\mathrm{T}} \right)_{N \times m} \tag{4}$$

Here, $\mathbf{H}$ is called the hidden layer output matrix, the i-th column of $\mathbf{H}$ represents the output of the i-th hidden layer neuron corresponding to the input sample x_1, x_2, …, x_N, and the j-th row indicates the output of all hidden layer neurons corresponding to the input sample x_j.

But in most cases, the number of hidden layer neurons is far less than the number of training samples ($L \ll N$). It is difficult to achieve the objective of making the single hidden layer NN with L hidden layer neurons approximate the N different data samples with zero error. In this case, (2) can be further rewritten as $\mathbf{H}\boldsymbol{\beta} = \mathbf{T} + \mathbf{E}$, where $\mathbf{E} = \left(\left[e_1^{\mathrm{T}}, \ldots, e_N^{\mathrm{T}} \right]^{\mathrm{T}} \right)_{N \times m}$.

Define the square loss function

$$J = \sum_{i=1}^{L} \left(\beta_i G(a_i, b_i, x_j) - t_j \right) \tag{5}$$

Then, (5) can be rewritten as $J = (\mathbf{H}\boldsymbol{\beta} - \mathbf{T})^{\mathrm{T}}(\mathbf{H}\boldsymbol{\beta} - \mathbf{T})$.

The training problem of network parameters is transformed into the problem of minimizing the square loss function. It is to find the least squares solution, making

$$\left\| \mathbf{H}\hat{\boldsymbol{\beta}} - \mathbf{T} \right\| = \min_{\boldsymbol{\beta}} \|\mathbf{H}\boldsymbol{\beta} - \mathbf{T}\| \tag{6}$$

If the output matrix of the hidden layer has full column rank, by utilizing Moore-Penrose generalized inverse, we can obtain

$$\hat{\boldsymbol{\beta}} = \arg\min_{\boldsymbol{\beta}} \|\mathbf{H}\boldsymbol{\beta} - \mathbf{T}\| = \mathbf{H}^{\dagger}\mathbf{T} \tag{7}$$

where $\mathbf{H}^{\dagger} = (\mathbf{H}^{\mathrm{T}}\mathbf{H})^{-1}\mathbf{H}^{\mathrm{T}}$[8].

If the output matrix of the hidden layer does not have full column rank, the weight vector β_i can be obtained via singular value decomposition (SVD) method.

In the parameter training process of ELM, the parameters of hidden layer nodes are determined randomly. In practice, the samples should be normalized, and the hidden layer node parameter values are selected randomly in the interval [−1, 1].

3 Hidden Danger Prediction Using ELM

According to the above analysis, the ELM algorithm framework for the prediction of special industry hidden danger can be described in Table 1 [8]. Here, the activation function of additive type hidden layer nodes in single hidden layer NN can be chosen as an arbitrary bounded nonlinear piecewise continuous function. But for the single hidden layer NN with RBF type hidden layer nodes, the activation function can be chosen as an arbitrary piecewise continuous integrable function.

4 Experimental Results and Discussions

4.1 Dataset

From nationwide enterprise hidden danger data provided by the State Administration of Work Safety, we find that the hidden danger investigation in some small-medium cities mainly aims at tertiary industries, and there may exist some inaccurate data because of the lack of high accuracy requirements. For example, Fig. 2 gives a summary of hidden danger data of a city in August 2014.

Table 1 The ELM algorithm framework for the prediction of special industry hidden danger

Input	Training set $\{(x_i, t_i)\}_{i=1}^{N} \subset \mathbf{R}^n \times \mathbf{R}^m$, activation function $G(x)$, the number of hidden layer nodes L
Output	Optimal the outer weight vector $\boldsymbol{\beta}$
(1)	Randomly generate input weight vector a_i and bias b_i
(2)	Calculate the output matrix $\mathbf{H}$ of hidden layer
(3)	Compute the optimal the output weight vector $\boldsymbol{\beta}$:$\boldsymbol{\beta} = \mathbf{H}^{\dagger}\mathbf{T}$

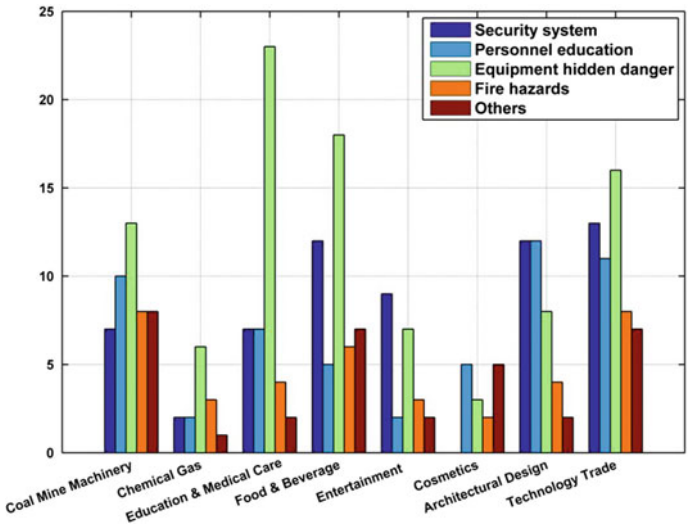

Fig. 2 The summary of hidden danger data of a city in August 2014

The experimental data is the spot check result of hidden danger of catering industry in a city from January to September 2014. We predict the total number of hidden danger in the following month according to historical data. Data obtained from the first 8 months and the 9th month constructs the training set and test set, respectively. The input terms are the inspection items of different locations, including offices, workshops, kitchens, and warehouses; the inspection items of hidden danger are security standard, personnel education, equipment hidden danger, and fire hidden danger. Thus, the input of training set is a high-dimensional numerical matrix.

4.2 Case 1

In the absence of some data, Fig. 3 gives a comparison of the prediction result between BP algorithm and ELM after running 5 times. It is obvious that ELM has higher prediction accuracy than BP. Moreover, in practice, ELM spends less time than BP. It illustrates the feasibility of ELM algorithm in practice.

4.3 Case 2

In order to further verify the robustness of algorithm, the experimental data are processed by partial perturbation.

Safety supervision personnel may make mistakes in statistics because of the huge amount of data and the complex relationship between hidden danger items and

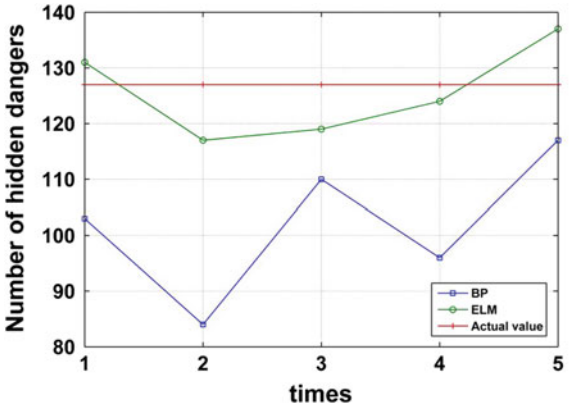

Fig. 3 The prediction results of ELM and BP neural network

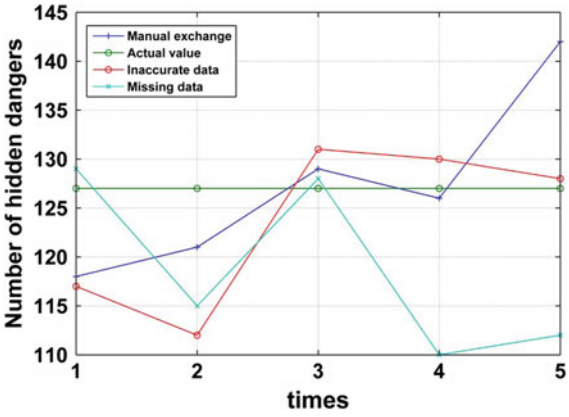

Fig. 4 The prediction results of ELM under different artificial intervention

locations in the actual production. In view of the fact that the data is not accurate in the actual production, 5% of the original input data is added or subtracted in a certain range to simulate the inaccurate statistics. For data missing case, 5% of the original input data is changed to 0 to simulate the situation of missing data.

In this case, we also conduct experiments 5 times, and the data are processed randomly before each experiment. As can be seen from Fig. 4, ELM still has a good prediction result in the case of data error, data missing and inaccurate.

5 Conclusion

Aiming at the application of safety supervision hidden danger prediction in education, medical treatment, restaurant, and other tertiary industries, this paper combines ELM algorithm to achieve application of hidden danger prediction.

Compared with the traditional BP learning algorithm for NN, the single hidden layer feedforward NN oriented ELM has the advantages of fast learning speed and high generalization performance [8, 11]. The experimental results verify the advantages of the method used in this paper. The method developed here is a novel practice of modern accident-causing theory. In the future, we will combine more effective ELM algorithm to further improve the prediction performance.

Acknowledgements This work was supported by the National Key Technologies R&D Program of China (Grant No. 2015BAK38B01).

References

1. Wei LJ, Fang LH (2014) Study on safety supervision law enforcement and hidden trouble inspection system based on mobile internet and cloud service. J Saf Sci Technol Supp 136–140 (in Chinese)
2. Shi H (2008) The risk early-warning of hidden danger in coal mine based on rough set-neural network. Proc Int Conf Risk Manag Eng Manag 314–317
3. Xiao HF, Tian YL (2011) Prediction of mine coal layer spontaneous combustion danger based on genetic algorithm and BP neural networks. Procedia Eng 26:139–146
4. Luo X, Zhang DD, Yang LT et al (2016) A kernel machine-based secure data sensing and fusion scheme in wireless sensor networks for the cyber-physical systems. Future Gener Comput Syst 61:85–96
5. Luo X, Liu J, Zhang DD et al (2016) A large-scale web QoS prediction scheme for the industrial internet of things based on a kernel machine learning algorithm. Comput Netw 101:81–89
6. Luo X, Luo H, Chang XH (2015) Online optimization of collaborative web service QoS prediction based on approximate dynamic programming. Int J Distrib Sens Netw 452492
7. Xu Y, Luo X, Wang WP et al (2017) Efficient DV-HOP localization for wireless cyber-physical social sensing system: a correntropy-based neural network learning scheme. Sensors 17(1):135
8. Huang GB, Zhu QY, Siew CK et al (2006) Extreme learning machine: theory and applications. Neurocomputing 70(1–3):489–501
9. He QX (2000) Safety engineering. China University of Mining and Technology Press, Xuzhou (in Chinese)
10. Jin Z (2011) Study on support vector machine classification algorithm and its application in safety evaluation of human accident in coal mine. China University of Mining and Technology Press, Xuzhou (in Chinese)
11. Luo X, Chang XH, Ban XJ (2016) Regression and classification using extreme learning machine based on L1-norm and L2-norm. Neurocomputing 174:179–186

A Domain Ontology Construction Method with Ontology Modification Effort Assessment

Yuehua Yang, Yuan Ping, Junping Du and Hui Ma

1 Introduction

With the rapid development of semantic Web technology, ontology technology has been widely concerned [1, 2]. For specific domains, most existing ontology lack domain words and semantic relationships between them. When these ontology are applied to specific domains, the application effect is not ideal. Therefore, in many cases, it is necessary to construct new ontology according to the situation of the domain itself [3, 4]. Therefore, it is essential to study and propose an effective domain ontology construction method.

In the construction of domain ontology, successful projects mostly refer to the software engineering approach, and some domain ontology construction methods are summed up according to the construction process. But these methods don't consider fully, and seldom consider the ontology modification efforts assessment [5, 6]. So they are not always applicable to other domain or applications.

In view of the above problems, in this paper a domain ontology construction method (DOCM) is proposed. This method divides the ontology construction process into ontology requirements analysis, domain knowledge analysis, ontology

Y. Yang (✉) · Y. Ping (✉) · H. Ma
School of Information Engineering, Xuchang University, Xuchang 461000, China
e-mail: yyh0504@126.com

Y. Ping
e-mail: pyuan.lhn@xcu.edu.cn

H. Ma
e-mail: xcmahui@qq.com

J. Du
Beijing Key Laboratory of Intelligent Telecommunications Software and Multimedia, School of Computer Science, Beijing University of Posts and Telecommunications, Beijing 100876, China
e-mail: junpingdu@126.com

Z. Deng (ed.), *Proceedings of 2017 Chinese Intelligent Automation Conference*, Lecture Notes in Electrical Engineering 458,
https://doi.org/10.1007/978-981-10-6445-6_52

establishment, ontology evaluation, and ontology modification effort assessment. In order to determine whether it is necessary to modify the ontology, an evaluation method based on ontology modification effort and elements importance is proposed. When updating the ontology, we can use this method to evaluate the modification effort to avoid the loss outweighs the gain in ontology use and modification.

2 DOCM

In recent years, a large number of domain ontology has been established, but few is really used in the practical applications. The problems mainly include: requirement analysis is not sufficient; ontology construction process is completed very casually; ontology is rarely evaluated and modified; the usability of the constructed ontology is generally poor. In order to ensure that the ontology construction process is relatively normal, and the ontology is easy to expand, a new domain ontology construction method DOCM is proposed. The framework of DOCM is shown in Fig. 1.

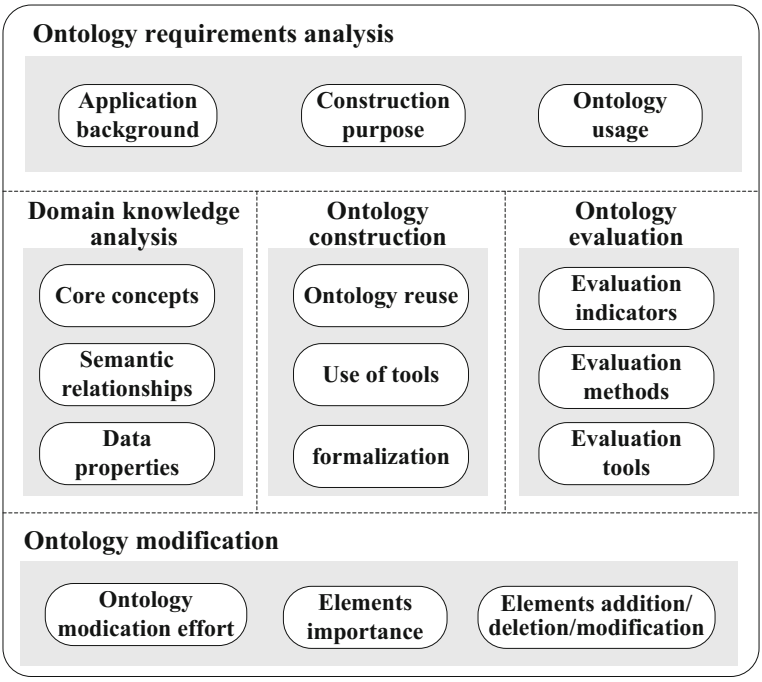

Fig. 1 Framework of DOCM

(1) Ontology requirements analysis: to understand and define the specific application background, construction purpose and usage of ontology. In order to combine the construction requirements of ontology and specific applications tightly, we need to have a certain understanding of the specific functional requirements of the application itself. Many following steps of ontology construction are corresponding to the requirements. Therefore, the more detailed the requirements description of ontology is, the clearer the content that the domain ontology should contain and the following construction steps are.
For example, an emergency domain ontology is constructed to provide semantic support for emergency information retrieval. Users' queries can be optimized with the rich semantic relationships and reasoning mechanism of the emergency domain ontology, thus making up for the shortcoming that users' queries expressions are not sufficient. The ontology can also be used to index the documents, and filter out the language ambiguity of the text when extracting the features of the text content.

(2) Domain knowledge analysis: to analyze and extract the knowledge based on the application requirements, such as core concepts, semantic relationships and data properties. After all, the understanding of domain knowledge from different perspectives is different, and the application demands are diversified.
In emergency information retrieval, the domain ontology needs to include more comprehensive emergency knowledge so that it can provide better semantic support. After analyzing the emergency domain knowledge, we can conclude that it need to include the core concepts about the classes of emergencies, the emergency evolution process, the emergency actions and decisions; semantic relationships between emergency concepts, such as classification, causality, coupling and sequence relationships. etc.; data properties that describe the concepts, for example, emergencies can be described with properties such as time, place, level, hazard, controllability, victim, influence scope, nature, characteristics, and precautionary methods, so these data properties need to be added into the ontology.

(3) Ontology construction: to use ontology building tools to add domain concepts, data properties, semantic relationships between the concepts and axioms for the domain ontology, or use a formal language to describe the content clearly. Besides reuse and integration of the existing ontology are also need to do. For example, the emergency domain ontology can be built by using Protégé tool and formalized in OWL language. Then it can be applied into emergency information retrieval.

(4) Ontology evaluation: to evaluate the quality of ontology after it is constructed to ensure that ontology meets the demands. It can also help the user to quickly find the appropriate ontology to support the application, so as to ensure the quality of the application system. In the evaluation process we need to select the appropriate evaluation indicators and evaluation methods or evaluation tools.
For example, OntoQA method proposed by LSDIS laboratory of computer science department of Georgian University is used to evaluate emergencies

domain ontology. The classes richness, the properties richness, the relationship richness, the inheritance richness and the average distribution of instances are selected as the evaluation indicators to evaluate the ontology quality. According to the indicators calculation results we can know the quality of the emergency domain ontology to a great extent.

(5) Ontology modification: to modify the ontology appropriately in the practical application, such as add new concepts, modify or delete the inaccurate concepts in the ontology. Before modification we should evaluate the ontology modification effort and the importance of the elements to be modified. The importance of the assessment, because there are usually some associations between ontology elements, changing an element will affect other elements. If the modification effort is too large, modification is not so necessary.

3 Ontology Modification Effort Assessment Method

The number of concepts, properties and semantic relationships between concepts, which are the three main elements of ontology, will affect the complexity of an ontology comprehensively. Only considering one of the elements is not sufficient to fully assess the efforts of modifying the ontology. The more concepts covered in the ontology, the richer the entity knowledge ontology can express is. Properties can describe some internal features of the concepts. The number of properties indicates the completeness and complexity of the concepts in an ontology. The more the relationships, the more work to do when modify a concept, because the associated sub classes or parent classes need to be checked.

Therefore, a method used to evaluate the effort of modifying a given ontology is presented. This method considers the concepts, properties and semantic relationships in modification effort assessment. Here, the number of concepts is represented by c, the number of semantic relationships is represented by r, and the number of properties is represented by p, hence forming a point (c, r, p). So this method is also called a three-dimensional modification assessment method.

For a given ontology with the higher complexity, the farther the point (c, r, p) is away from the origin (0, 0, 0), the more the modification effort is, and vice versa. Similarly, after adding new elements to the ontology, the farther the corresponding point is away from point (c, r, p), the more the modification effort is. In addition, the more complex the given ontology, that is, the ontology contains more concepts, properties, or relationships, the more the effort of adding new elements is. So in order to better measure the ontology modification effort, the case above should also be considered. Thus the following formula is proposed to evaluate the effort of adding new elements to the ontology:

$$e = k\sqrt{(c_2 - c_1)^2 + (r_2 - r_1)^2 + (p_2 - p_1)^2} \quad (k = c_1 + r_1 + p_1 + 1) \qquad (1)$$

In formula (1), c_2, r_2, p_2 represent the number of concepts, relationships and properties respectively after adding new ontology elements. c_1, r_1 and p_1 represent the number of concepts, relationships and properties of the original ontology. k is a coefficient. It is used to ensure that when adding the same number of elements into the ontology, the more the original elements, the greater the effort estimate of adding new elements.

For example, a domain ontology originally contains 50 concepts, 25 semantic relationships, and 8 properties. Through evolution, more domain concepts, relationships and properties can be obtained. If the number of concepts, relationships and properties is increased to 55, 28, 10 respectively, according to the formula (1) the ontology modification effort estimate is:

$$e_1 = (50 + 25 + 8 + 1) \times \sqrt{(55 - 50)^2 + (28 - 25)^2 + (10 - 8)^2} = 517.8$$

If the concepts, relationships and properties are increased to 60, 31, 12 respectively, according to the formula (1) the modification effort estimate of the ontology is:

$$e_2 = (60 + 31 + 12 + 1) \times \sqrt{(60 - 50)^2 + (31 - 25)^2 + (12 - 8)^2} = 1282.2$$

According to e_1 and e_2 we can understand the ontology modification effort and complexity that is measured based on the three factors: the number of concepts, the number of relationships and the number of properties.

If the concepts, relationships and properties are increased from 50, 25, 8 to 55, 28, 10 respectively, the concepts, relationships and properties are increased by 5, 3 and 2 respectively, the ontological modification effort estimate e_1 is 511.6. On this basis the concepts, relationships and properties are increased to 60, 31, 12 respectively, also increased by 5, 3, 2. According to formula (1) the modification effort estimate e_3 is:

$$e_3 = (55 + 28 + 10 + 1) \times \sqrt{(60 - 55)^2 + (31 - 28)^2 + (12 - 10)^2} = 579.5$$

As the results show, $e_3 > e_1$. This indicates that the more the original ontology concepts, relationships and properties, the more the modification effort. Thus, a three-dimensional modification assessment method can also be used to assess whether a given ontology is worth modifying for reuse. In addition, the three-dimensional modification assessment method plays an important role in many other aspects of the ontology. In order to clarify some actual situations, the following tests and comparison are done on some real ontology. These ontology are very large, so we will need to do a lot of work to modify them. The results is shown in Table 1.

Table 1 Results of testing on real world ontologies

Ontology name	No. of concepts	No. of relationships	No. of properties	Modification effort estimate
BCGO	1882	117	3644	2.3×10^7
PO	1691	10	2687	1.4×10^7
SO	936	1	840	2.2×10^6
EO	906	90	1114	3.0×10^6
HDO	8946	15	6918	1.8×10^8

Results from Table 1 on these real world ontology show that using the three dimensions ontology modification effort assessment method can assist in providing general understanding about an ontology. That is, when using the proposed method to calculate the modification effort estimate results, ontology modification effort and complexity can be estimated. This can be significantly beneficial when a decision is about to be made concerning an ontology. If modifying the ontology need more effort, we should consider to divide it into several ontology.

Assume that in some scenarios ontology about "Places" is needed. And the ontology SWETO covers the concepts, relationships and properties of some topics including person, places, academic department, event, organization, etc. So SWETO ontology offers the modeling that is needed about "Places". Table 2 shows the modification effort estimate before and after extracting the concepts and relationships about place from SWETO. Before applying the proposed method, it is a little vague that how detailed this ontology is, and what these numbers mean.

It can be seen from Table 2 that the modification effort estimate before extracting the concepts and relationships about place is large. Therefore, after considering the modification effort estimate, the expected effort can be grasped when using SWETO ontology, so that the place module can be independently selected and extracted. To modularize the ontology, we can use a Web-based OWL extractor to separate an ontology based on user-specified feature words and options. After extracting the place module we calculate the modification effort estimate again with formula (1) and find that the estimate becomes smaller. And the relevant concepts and relationships of place become relatively rough.

The three-dimensional modification effort assessment method can also be used when the ontology owner needs to adjust the ontology size in order to ensure that the ontology is easy to understand and update. Through this assessment method, the ontology owner can track the ontology development process. In order to ensure that the ontology modification effort estimate is small, we can perform frequent tests based on this assessment method when updating the ontology, and then determine whether new elements are all added to the ontology. If not, we need to determine which new elements should be retained, which is mainly determined by the

Table 2 Modification effort estimate before and after testing

Ontology	No. of concepts	No. of relationships	No. of properties	Modification effort estimate
Before	114	69	111	5.1×10^4
After	8	14	7	5.3×10^2

Table 3 The importance

Candidate ontology elements	Weighted percentage	Importance (%)
Fire hazard	3.91	49.06
Fire control	1.13	14.18
Scene	0.95	11.92
Cause	0.82	10.29
Casualty	0.43	5.40
Fire behavior	0.40	5.02
Accident	0.33	4.14
Total	7.97	100

importance of the elements. For a set of elements (assuming the number of the elements is n), the importance of each element c is determined according to the following formula:

$$I_c = \frac{w_c}{\sum_{i=1}^{n} w_i} \tag{2}$$

where I_c is the importance of concept c in the group; w_c is the weight of concept c among all the concepts while the denominator represents the sum of weights of the concepts in the group. The weighted percentage of each word has been identified by the content analysis software NVivo (http://www.qsrinternational.com/) comparing the frequency of each word in the corpus of data with other words.

For example, use "query"—"word frequency" function of NVivo software to obtain the weighted percentage of a group of ontology elements from the corpus, as shown in Table 3, and then calculate the importance of each element according to the formula (2).

4 Conclusion

A new domain ontology construction method DOCM is proposed to perfect the domain ontology construction process provide semantic support for multiple domain applications. In addition to the ontology requirements analysis, domain knowledge analysis, ontology establishment and ontology evaluation, ontology

modification effort assessment is also included in this method to determine whether it is worth modifying the ontology. And a three-dimensional modification assessment method is proposed. In the modification effort assessment the changes of three main elements of ontology including concepts, properties and the semantic relationships between concepts are all considered. If the modification effort estimate is too large, the ontology will be no longer modified. Therefore, based on the assessment method, the ontology owner can track the ontology development process. Besides, the knowledge in the ontology can be extracted and reused so that the effort estimate for ontology modification and use can be reduced. Domain ontology constructed with the proposed method will include more domain terms and semantic relationships and can also get better application effect when applied to the domain applications.

Acknowledgements This work was supported by National Natural Science Foundation of China (No. 61320106006), Foundation of He'nan Educational Committee (No. 17A520013, No. 15A520096, 18A520047), Program for Science &Technology Innovation Talents in Universities of He'nan Province (18HASTIT022), Foundation for University Key Teacher of He'nan Province (No. 2016GGJS-141), Outstanding Young Teacher Project of Xuchang University, and Xuchang Science and Technology Development Program (No. 1504017).

References

1. Yang YH, Du JP, Ping Y (2015) Ontology-based intelligent information retrieval system. J Softw 26(7):1675–1687
2. Zhitomirsky-Geffet M, Erez ES, Judit BI (2017) Toward multiviewpoint ontology construction by collaboration of non-experts and crowd sourcing: the case of the effect of diet on health. J Assoc Inf Sci Technol 68(3):681–694
3. Liu LZ, Zhao XL, Wang HS et al (2015) Constructing domain affective ontology based on product features. Trans Beijing Inst Technol 35(5):538–544
4. Azam E, FarookhKhadeer H, Elizabeth C (2013) University social responsibility ontology. Eng Intell Syst 21(4):271–281
5. Yu XL, Wang XP (2016) A construction method of emergency domain ontology based on scenario. ICIC Express Lett B Appl 7(4):947–953
6. Abdulelah AA, Austin CM (2016) Three dimensions ontology modification matrix. In: International conference on information management, pp 77–83

Adaptive Generalized Function Projective Synchronization of Colored Networks in Finite Time

Guoliang Cai, Wenjun Shi, Yuxiu Li, Zhiyin Zhang and Gaihong Feng

1 Introduction

Various control and synchronization of complex networks have been widely studying, which have many potential applications in many areas such as biology system, physics, communication, traffic and so on [1–3]. In view of the ubiquitous synchronization phenomena, the studies of synchronization and control have been attracted increasing attention [4–6]. Many works mainly study the outer relationship between the nodes. However the inner relationship ignored in many literatures plays important roles for the study of the whole networks.

In many realistic systems, another relationship may exist in the social networks consisting of N individuals, e.g., schoolmates, relatives and collaborative relationship. For individuals i and j, they may be either schoolmate or relatives but have no collaborative relationship, while for individual i and k ($k \neq j$), they may only have collaborative relationship. To depict this phenomenon more clearly, the graph theory in mathematics is introduced to solve such problem [7, 8]. In the colored networks, nodes with different color signify that they have different properties, and a pair of nodes connected by different color edges means that they have different mutual interactions. In particular, networks of coupled nonidentical dynamical systems with identical inner coupling matrixes can be deem as node colored networks, while networks of coupled identical dynamical systems with nonidentical inner coupling matrixes can be regarded as edge colored networks. Figure 1 shows a colored networks consisting of 6 colored nodes and 9 colored edges.

G. Cai (✉) · W. Shi · Y. Li · Z. Zhang · G. Feng
Institute of Applied Mathematics, Zhengzhou Shengda University of Economics, Business and Management, Zhengzhou 451191, China
e-mail: 1013801022@qq.com; glcai@ujs.edu.cn

G. Cai · Y. Li
Nonlinear Scientific Research Center, Jiangsu University, Zhenjiang 212013, China

Z. Deng (ed.), *Proceedings of 2017 Chinese Intelligent Automation Conference*,
Lecture Notes in Electrical Engineering 458,
https://doi.org/10.1007/978-981-10-6445-6_53

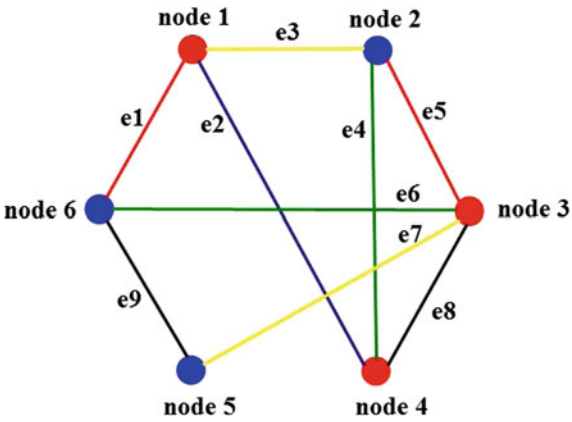

Fig. 1 A colored networks consisting of 6 colored nodes and 9 colored edges

To our knowledge, the research of colored networks synchronization was concerned with asymptotical or exponential synchronization of networks through impulsive control, intermittent control to reduce the synchronization time [9, 10]. However, in reality, it needs a faster rate to achieve in engineering area. For achieving synchronization quickly, an effective method is to use finite time synchronization control technique [11, 12]. There are few works involved in the synchronization of colored networks in finite time.

This paper investigates the problems of adaptive generalized function projective synchronization of colored networks in finite time. By using finite time synchronization control technique, one considers a complex networks consisting of N linearly and diffusively coupled identical nodes, which in many papers only consider the general synchronization of drive-response networks. Particularly, the parameter identification is considered in this paper, and the finite time considers the unknown parameters identification. Based on Lyapunov stability theory, sufficient conditions for ensuring the synchronization of colored networks are derived through designing appropriate controllers.

This paper is organized as follow: In Sect. 2, a general colored networks consisting of N linearly and diffusively coupled identical nodes is considered. At the same time, assumption and lemma are stated. In order to reach the generalized function projective synchronization with general colored networks, a sufficient criterion is presented in Sect. 3. In Sect. 4, several simulations are illustrated to verify the effectiveness of the theory proposed. Finally, conclusions are gained in Sect. 5.

2 Problem Formulation and Preliminaries

In this section, one considers a general colored networks consisting of N linearly and diffusively coupled identical nodes described as follows:

$$\dot{x}_i(t) = F_i(t, x_i(t), \alpha_i) + \varepsilon \sum_{j=1, j\neq i}^{N} a_{ij} H_{ij}\big(x_j(t) - x_i(t)\big), \quad i = 1, 2, \ldots, N. \tag{1}$$

where $x_i(t) = (x_{i1}(t), x_{i2}(t), \ldots, x_{in}(t))^{\mathrm{T}} \in R^n$ is the state variable of the ith node, $F_i(t, x_i(t), \alpha_i)$ representing the local dynamic of node i, which is continuous differentiable, can be rewritten in the following form: $F_i(t, x_i(t), \alpha_i) = f_i(t, x_i(t)) + g_i(t, x_i(t)) \cdot \alpha_i$, $f_i(\cdot)$ and $g_i(t, x_i(t)) : R^n \to R^n$ is a nonlinear vector-valued function. The matrix $A = (a_{ij})_{N\times N}$ is outer-coupling matrix, which denotes the networks topology. If there is a connection between node i and node j $(i \neq j)$, then $a_{ij} > 0$, otherwise $a_{ij} = 0$, and the entire diagonal element $a_{ii} = 0$. $H_{ij} = \mathrm{diag}(h_{ij}^1, h_{ij}^2, \ldots, h_{ij}^n)$ is the inner coupling matrix, which represents the mutual interactions between nodes i and j, which is defined as the following: if the ζth component of node i is affected by that of node j, then $h_{ij}^{\xi} \neq 0$, otherwise $h_{ij}^{\xi} = 0$.

Figure 1 indicates that $F_1 = F_3 = F_4$, $F_2 = F_5 = F_6$, $H_{16} = H_{23}$, $H_{12} = H_{35}$, $H_{24} = H_{36}$. When $n = 3$, and $H_{16} = \mathrm{diag}\{1,1,0\}$ and $H_{56} = \mathrm{diag}\{1,0,1\}$, then the first and second components of node 1 are affected by those of node 6, and the first and third components of node 6 are affected by that of node 5, which is shown by Fig. 2.

Let $c_{ij} = diag(c_{ij}^1, c_{ij}^2, \ldots, c_{ij}^n)$, where $c_{ij}^k = a_{ij} h_{ij}^k$ for $i \neq j$ and $c_{ii}^k = -\sum_{j=1, j\neq i}^{N} c_{ij}^k$,

Then, the colored networks (1) can be rewritten as follows:

$$\dot{x}_i(t) = F_i(t, x_i(t), \alpha_i) + \varepsilon \sum_{j=1}^{N} c_{ij} x_j(t), \quad i = 1, 2, \ldots, N \tag{2}$$

Let $C_{\xi} = (c_{ij}^{\xi}) \in R^{N\times N}$, $\xi = 1, 2, \ldots, N$, then we regard the colored networks (2) as a combination of n component sub-networks with a topology determined by $C_{\xi}, \xi = 1, 2, \ldots, n$.

A general response colored networks, which can be response edged-colored networks or colored networks, is given to achieve adaptive generalized function projective synchronization with the colored networks (2), which is shown as

$$\dot{y}_i(t) = F_i(t, y_i(t), \alpha_i) + \varepsilon \sum_{j=1}^{N} c_{ij} y_j(t) + u_i(t), \quad i = 1, 2, \ldots, N \tag{3}$$

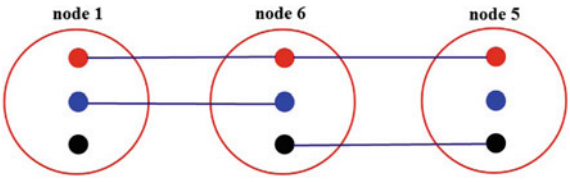

Fig. 2 The *red*, *blue* and *black* stand for the first, second, and third components of each individual node, respectively

where $y_i(t) = (y_{i1}(t), y_{i2}(t), \ldots, y_{in}(t))^{\mathrm{T}} \in R^n$ stands for the state vector of the ith node, $f_i(t, y_i(t))$ and $g_i(t, y_i(t)):R^n \to R^n$ is a nonlinear vector-valued function, u_i is the adaptive controller.

Next, one introduces definitions assumptions, lemmas that will be required in this paper.

Definition 1 (*GFPS*) For the colored networks (3), it is said that achieve adaptive generalized function projective synchronization (GFPS) with the colored networks (2), if there exist the continuous function $\varphi(x_i(t))$ such that

$$\lim_{t\to\infty}\|e_i(t)\| = \lim_{t\to\infty}\|y_i(t) - \varphi(x_i(t))\| = 0, \quad i = 1, 2, \ldots, N.$$

where $\varphi(x_i(t))$ are nonzero scaling functions and continuously differentiable functions.

Assumption 1 Suppose that there exist a constant $L_i > 0$ satisfying

$$\|F_i(t, y_i(t), \alpha_i) - F_i(t, x_i(t), \alpha_i)\| \le L_i\|y_i(t) - x_i(t)\| \tag{4}$$

Lemma 1 *Let* $x_1, x_2, \ldots, x_n > 0$ and $0 < r < p$. *Then*

$$\left(\sum_{i=1}^{n} x_i^p\right)^{1/p} \le \left(\sum_{i=1}^{n} x_i^r\right)^{1/r} \tag{5}$$

Lemma 2 *Cai et al.* [12]. *Assume that a continuous, positive-definite function V(t) satisfy the following differential inequality*:

$$\dot{V}(t) \le -pV^{\xi}(t) \quad \forall t \ge t_0,\ V(t_0) \ge 0 \tag{6}$$

where p > 0, 0 < ξ < 1 are two constants. Then, for any given t_0, $V(t)$ satisfies the following inequality: $V^{1-\xi}(t) \le V^{1-\xi}(t_0) - p(1-\xi)(t-t_0)$, $t_0 \le t \le t_1$ and $V(t) = 0\ \forall t \ge t_1$ with t_1 given by $t_1 = t_0 + \frac{V^{1-\xi}(t_0)}{p(1-\xi)}$.

3 Main Results

In this section, the colored networks (2) achieve generalized function projective synchronization with general colored networks (3).

For simplicity sake, we define $\varphi(x) = Px + Q$, where P and Q is constant matrix. The error dynamic networks can be calculated in the following:

$$\begin{aligned}\dot{e}_i(t) &= \dot{y}_i(t) - P\dot{x}_i(t) \\ &= f_i(t, y_i(t)) - Pf_i(t, x_i(t)) + (g_i(t, y_i(t)) - Pg_i(t, x_i(t))) \cdot \alpha_i \\ &\quad + \sum_{j=1}^{N} c_{ij}(y_i(t) - Px_i(t)) + u_i \quad i = 1, 2, \ldots, N\end{aligned} \tag{7}$$

For achieving the main focus, the nonlinear controllers are designed as

$$\begin{aligned}u_i = Pf_i(t, x_i(t)) - f(t, \varphi(x_i(t))) - (g_i(t, y_i(t))) - Pg_i(t, x_i(t))\hat{\alpha} - \sum_{j=1}^{N} c_{ij}Q \\ - d_i(t)e_i - \omega sign(e_i(t))|e_i(t)|^{\theta}\end{aligned} \tag{8}$$

where $d_i(t) > 0$, $i = 1,2,\ldots,N$ are the time-varying adaptive control gains that can be suitably chosen by the generalized function projective synchronization system and satisfy the following conditions: $\dot{d}_i(t) = k_i e_i^{\mathrm{T}}(t)e_i(t) > 0$

Theorem 1 *Suppose the Assumption 1 and Lemma 2 holds. If the following condition holds:*

$$\eta = -\lambda_{\max}((L_i + C - d^*)I \otimes I) > 0 \tag{9}$$

when using the above controller (8) and the parameter identification:

$$\dot{\hat{\alpha}} = \beta_i e_i^{\mathrm{T}}(t)[g_i(y_i(t)) - Pg_i(x_i(t))] \tag{10}$$

then the drive system (2) and response system (3) can achieve synchronization in finite time $t_1 = t_0 + \frac{V(t_0)^{(1-\theta)/2}}{2\omega(1-\theta)}$ *for any given* t_0.

Proof Construct a Lyapunov function as the following

$$V(t) = \frac{1}{2}\sum_{i=1}^{N} e_i^{\mathrm{T}}(t)e_i(t) + \sum_{i=1}^{N}\frac{1}{2\beta_i}(\alpha - \hat{\alpha})^2 + \sum_{i=1}^{N}\frac{1}{2k_i}(d_i - d^*)^2 \tag{11}$$

Then the derivation of $V(t)$:

$$\begin{aligned}\dot{V}(t) &= \sum_{i=1}^{N} e_i^{\mathrm{T}}(t)\dot{e}_i(t) - \sum_{i=1}^{N}\frac{1}{\beta_i}\dot{\hat{\alpha}}(\alpha - \hat{\alpha}) + \sum_{i=1}^{N}\frac{1}{\alpha}\dot{d}_i(d_i - d^*) \\ &= \sum_{i=1}^{N} e_i^{\mathrm{T}}(t)[f_i(t, y_i(t)) - Pf_i(t, x_i(t)) + (g_i(t, y_i(t) - Pg_i(t, x_i(t)))) \cdot \alpha_i \\ &\quad + \sum_{j=1}^{N} c_{ij}(y_i(t) - Px_i(t)) + U_i\Big] + \sum_{i=1}^{N}\frac{1}{\beta_i}\dot{\hat{\alpha}}(\hat{\alpha} - \alpha) + \sum_{i=1}^{N}\frac{1}{k_i}\dot{d}_i(d_i - d^*)\end{aligned} \tag{12}$$

From the above calculations, one has

$$\sum_{i=1}^{N}\sum_{j=1}^{N} e_{ij}^{\mathrm{T}}\omega sign\big(e_{ij}(t)\big)\big|e_{ij}(t)\big|^{\theta} = \omega\sum_{i=1}^{N}\sum_{j=1}^{N}\big|e_i^{\mathrm{T}}(t)\big||e_i(t)|^{\theta} = \omega\sum_{i=1}^{N}\sum_{j=1}^{N}|e_i(t)|^{\theta+1}$$

By Lemma 1, $\left(\sum_{i=1}^{N}\sum_{j=1}^{N} e_{ij}^2\right)^{1/2} \le \left(\sum_{i=1}^{n} e_{ij}^{1+\theta}\right)^{1/(1+\theta)}$

Hence,

$$\sum_{i=1}^{N}\sum_{j=1}^{N}|e_i(t)|^{\theta+1} \ge \left(\sum_{i=1}^{N}\sum_{j=1}^{N}\big|e_{ij}(t)\big|^2\right)^{(\theta+1)/2} = \left(\sum_{i=1}^{N}\sum_{j=1}^{N} e_{ij}^{\mathrm{T}}(t)e_{ij}(t)\right)^{(\theta+1)/2}. \tag{13}$$

According to (3), (5) and (6), the derivation of $V(t)$ can be calculated as follows:

$$\begin{aligned}\dot{V}(t) &\le \sum_{i=1}^{N} e_i^{\mathrm{T}}[(L_i + C - d^*)I \otimes I]e_i - \omega\left(\sum_{i=1}^{N}\sum_{j=1}^{N} e_{ij}^{\mathrm{T}}(t)e_{ij}(t)\right)^{(\theta+1)/2} \\ &\le -\eta\sum_{i=1}^{N} e_i^{\mathrm{T}}(t)e_i(t) - \omega\left(\sum_{i=1}^{N}\sum_{j=1}^{N} e_{ij}^{\mathrm{T}}(t)e_{ij}(t)\right)^{(\theta+1)/2} \\ &\le -4\omega(V(t))^{(\theta+1)/2}\end{aligned} \tag{14}$$

From Lemma 2, Theorem 1 and on the basis of the Lyapunov stability theorem, one has $e(t) \to 0$ $(t \to \infty)$, which means the drive system (1) can achieve the generalized function projective synchronization with response system (2) in finite time $t_1 = t_0 + \frac{V(t_0)^{(1-\theta)/2}}{2\omega(1-\theta)}$ for any given t_0. That completes the proof.

Based on Theorem 1, one gives the procedure of complex networks finite time's calculation methods: Firstly, according to the Theorem 1, calculate the parameters d^*. Secondly, determine the system initial values, especially the unknown parameters' ones. Next step is to calculate the $V(t_0)$ when $t_0 = 0$. At the last, in line with the equation $t_1 = t_0 + \frac{V(t_0)^{(1-\theta)/2}}{2\omega(1-\theta)}$, obtain the finite time scheme t_1.

Remark 1 It should emphasized that finite time synchronization control techniques are adopted to guarantee generalized function projective synchronization of colored networks in finite time, while little of form paper has been done about this work, which can applied to many practical areas.

4 Numerical Simulations

In this section, two illustrative examples are adopted to demonstrate the validity and reduce conservatism of the above theory.

Example 1 Consider a edge-colored networks with 10 coupled Lorenz systems.

$$f(t,x(t)) = \begin{pmatrix} 0 \\ -x_1x_3 - x_2 \\ x_1x_2 \end{pmatrix} \text{and } g(t,x(t)) = \begin{pmatrix} x_2 - x_1 & 0 & 0 \\ 0 & 0 & x_1 \\ 0 & -x_3 & 0 \end{pmatrix}$$

and in view of the error system defined, one sets

$$P = \begin{bmatrix} 2 & -1 & 0 \\ 0 & -1 & 0 \\ 0 & 0 & 1 \end{bmatrix}, Q = (0,0,0)^{\mathrm{T}}.$$

In numerical simulation, the initial values of drive-response system are chosen as $x_i(0) = (0.3+0.1i, 0.3+0.1i, 0.3+0.1i)^{\mathrm{T}}$, For brevity, one always sets Γ=diag(1, 1, 1), $\|\Gamma\|$=1, L = 1, θ=0.5, $\beta_1 = \beta_2 = \beta_3 = 1$, $\omega_1 = \omega_2 = \omega_3 = 5$ the estimated parameters have initial conditions: $\hat{a} = 0, \hat{b} = 0, \hat{c} = 0$. According to procedure of complex networks finite time's calculation methods, one can obtain

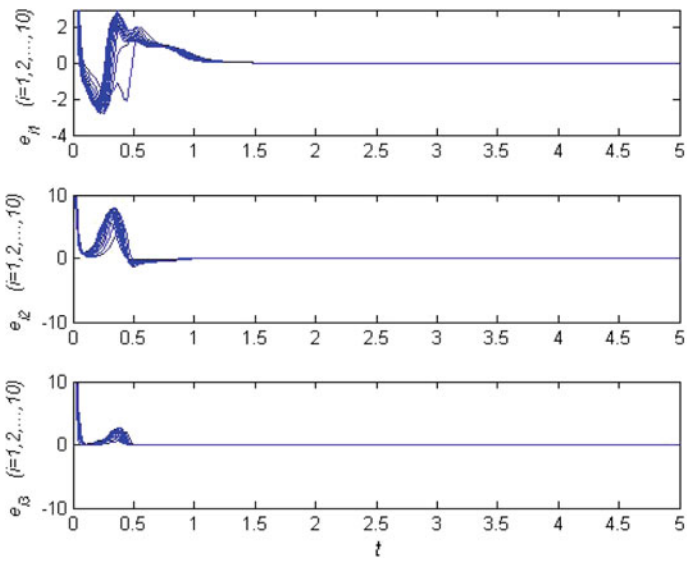

Fig. 3 Synchronization errors of the edge-colored networks coupled with 10 Lorenz systems

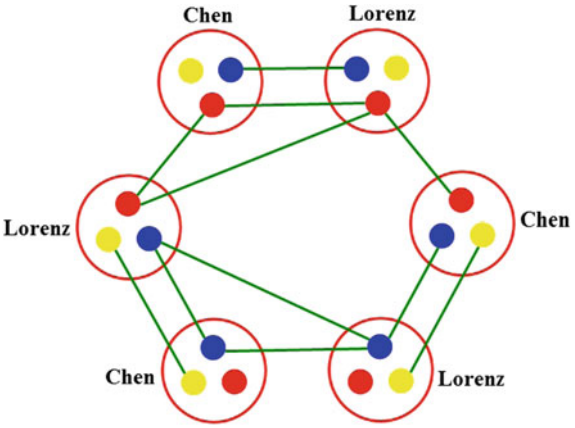

Fig. 4 The topology of the colored networks coupled with 3 Chen systems and 3 Lorenz systems

and give the parameter $d^*= 5$.Then the finite time is $t_1 = t_0 + \frac{V(t_0)^{(1-\theta)/2}}{2\omega(1-\theta)} = 2.41$ s. The Fig. 3 shows the synchronization errors of the edge-colored networks.

Example 2 Two general colored networks, whose topology coupled with 3 Chen systems and 3 Lorenz systems shown in Fig. 4, are considered.

$$f(t,x(t)) = \begin{pmatrix} 0 \\ -x_1x_3 \\ x_1x_2 \end{pmatrix} \text{ and } g(t,x(t)) = \begin{pmatrix} x_2 - x_1 & 0 & 0 \\ -x_1 & 0 & x_1 + x_2 \\ 0 & -x_3 & 0 \end{pmatrix}.$$

The initial values of drive-response system are chosen as the Example 1 except the $\omega_1 = \omega_2 = \omega_3 = 2$. So the finite time is $t_1 = t_0 + \frac{V(t_0)^{(1-\theta)/2}}{2\omega(1-\theta)} = 7.17$ s. The synchronization error of the general colored networks is shown in Fig. 5.

Remark 2 General synchronization of colored networks has been extensively studied, in which all the nodes synchronized each other in a common manner. However, in real complex networks, different communities usually synchronize with each other in a different manner. So in this paper, one considers generalized function projective synchronization. If $P = \phi_i$, $Q = 0$, the general projective synchronization can be realized.

Remark 3 In the existing research of synchronization of the colored networks, certain networks are often considered. However, information may be not available in many practical cases. The uncertain networks (1) can be seen as the special case of the colored networks.

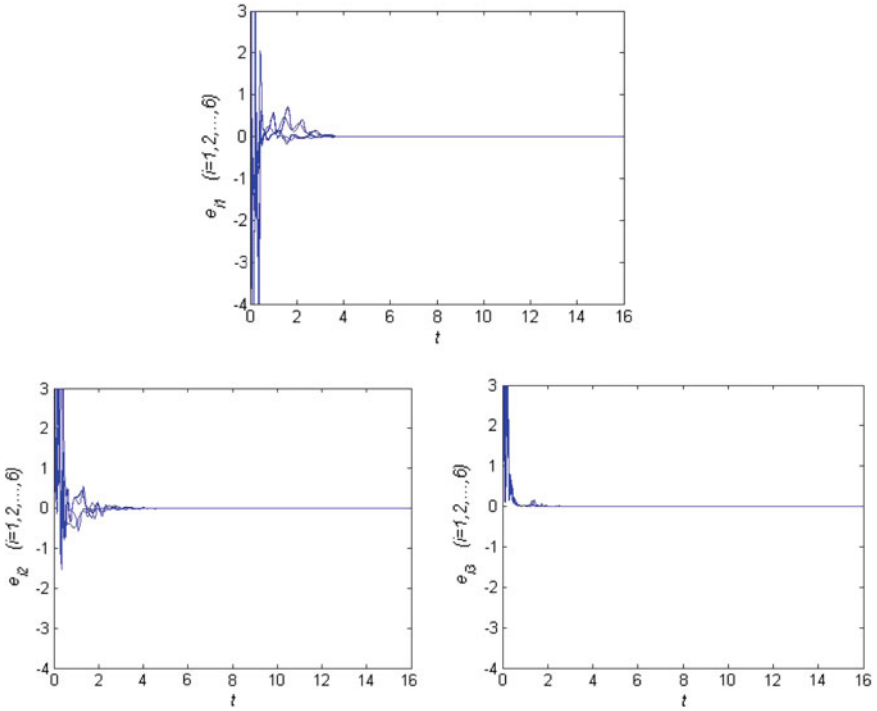

Fig. 5 Synchronization errors of the colored networks coupled with 3 Chen systems and 3 Lorenz systems

5 Conclusions

In this paper, adaptive generalized function projective synchronization of the colored networks in finite time has been investigated. A uncertain colored networks is considered as many practical cases. Specially, instead of using impulsive control, intermittent control to reduce the synchronization time, an effective method—finite time synchronization control techniques, is applied to achieve the colored networks' synchronization. Based on Lyapunov stability theorem, simple and useful criteria for the colored networks have been established. The corresponding numerical simulations have been presented to verified effectiveness and correctness of the theoretical results.

Acknowledgements This work was supported by the National Nature Science foundation of China (No. 61603157), the Society Science Foundation from Ministry of Education of China (No. 15YJAZH002), the Society Science Foundation of Henan Province (No. 2018BJJ008), the Key Technologies R&D Program of Henan Province (No. 172102210553), the Key Scientific Research Projects of Higher Education Institutions of Henan Province (No 18A120013), and the

Advanced Talents' Foundation of Zhengzhou Shengda University of Economics, Business & Management (No. 2016SDKY001). Especially, thanks for the support of Zhengzhou Shengda University of Economics, Business & Management.

References

1. Zhang HG, Wang ZS, liu D (2007) Global asymptotic stability of delayed cellular neural networks. IEEE Trans Neural Netw 18(3):947–950
2. Cai GL, Yao Q, Shao HJ (2012) Global synchronization of weighted cellular neural network with time-varying coupling delays. Commun Nonli Sci Numer Simul 17(10):3843–3847
3. Li YX, Cai GL (2015) Adaptive cluster synchronization for weighted cellular neural networks with time-varying delays. Lect Notes Elec Eng 338:21–28
4. Ding W (2009) Synchronization of delayed fuzzy cellular neural networks with impulsive effects. Commun Nonli Sci Numer Simul 14:3945–3952
5. Jiang SQ, Cai GL, Cai SM, Tian LX, Lu XB (2015) Adaptive cluster general projective synchronization of complex dynamic networks in finite time. Commun Nonli Sci Numer Simul 28(10):194–200
6. Zhu QX, Cao JD (2010) Adaptive synchronization of chaotic Cohen-Crossberg neural networks with mixed time delays. Nonlinear Dyn 61(3):517–534
7. Cai GL, Yao Q, Fan XH, Ding J (2012) Adaptive projective synchronization in an array of asymmetric neural networks. J Comput 7(8):2024–2030
8. Cai GL, Jiang SQ, Cai SM, Tian LX (2015) Cluster synchronization of overlapping uncertain complex networks with time-varying impulse disturbances. Nonlinear Dyn 80(1):503–513
9. Li T, Wang T, Yang X (2012) Cluster synchronization in hybrid coupled discrete-time delayed complex networks. Commun Theor Phys 56(5):686–696
10. Wu XJ, Lu HT (2011) Cluster anti-synchronization of complex networks with nonidentical dynamical nodes. Phys Lett A 375(14):1559–1565
11. Cai SM, Hao JJ, He QB, Liu ZR (2012) New results on synchronization of chaotic systems with time-varying delays via intermittent control. Nonlinear Dyn 67:393–402
12. Cai GL, Jiang SQ, Cai SM, Tian LX (2016) Finite-time analysis of global projective synchronization on coloured networks. Pramana J Phys 86(3):545–554

The Comparative Study of Mars Entry Phase's Guidance Methods

Maomao Li and Jun Hu

1 Introduction

As one of the closest planets to earth, Mars is similar to earth in many ways [1]. Therefore, it has become one of the most important planets for deep space exploration [2]. Considering that the Mars atmosphere's density is only 1% of the earth's atmosphere, so compared with the spacecraft return to earth, weak control capability and parameter uncertainty should be considered, and the adaptive ability of guidance method has become a hot spot in the field of Mars Exploration [3]. So far, the world has conducted 39 Mars Exploration, but only 7 landing missions are successful [4, 5].

The guidance methods of entry phase are generally divided into the method of tracking nominal trajectory and predictor-corrector method. The former one has the advantages of simple control law, easy realization, but it is sensitive to the initial entry conditions. In order to improve the accuracy, the first one is to study the trajectory tracking method with robust performance and adaptive ability, and the second one is to study the trajectory planning algorithm online. Such as, the sliding mode variable structure control (SMC) is adopted, which can obtain better guidance accuracy [6]. However, this method is difficult to be used in engineering practice because of the buffet. Benito and Mease use nonlinear model predictive control which can achieve high guidance accuracy. The predictor-corrector guidance method uses numerical or analytical methods for predicting the placement of entry phase's final point and the final conditions. The correctional step is to get the instructions of bank angle to nullify the final errors in real-time. Now, with the rapid development of the aerospace computer, it provides the basis for the application of numerical prediction guidance method.

M. Li (✉) · J. Hu
Beijing Institute of Control Engineering, Beijing 100190, China
e-mail: limaobuaa@163.com

Z. Deng (ed.), *Proceedings of 2017 Chinese Intelligent Automation Conference*,
Lecture Notes in Electrical Engineering 458,
https://doi.org/10.1007/978-981-10-6445-6_54

Foreign scholars commonly use the predictor corrector guidance method based on iterative numerical correction to get the instructions of bank angle. The all-coefficient adaptive predictor-corrector guidance method which is proposed by Hu Jun is different from the traditional predictor-corrector guidance method [7]. In this method, the characteristic model which describes the relationship between guidance increment and the error of generalized predictive range is established. The guidance law calculates the characteristic increment based on the range error from the predictor step, and then the new range error is predicted with the new guidance instructions. Compared with the traditional predictor-corrector guidance method, this method is a non-iterative method which relieves the calculation burden of computer, so it can be used in engineering practice problems.

In this paper, the all-coefficient intelligent adaptive predictor-corrector guidance method is used. The first-order characteristic model is used which is different from the traditional second order characteristic model in [7]. What's more, the method is compared with the traditional predictor-corrector guidance method based on iteration and the robust guidance method of tracking nominal trajectory, so the method which is more suitable for engineering application can be found.

2 The Formulation of Mars Entry Guidance Problem

The entry guidance problem for the Mars detector is to determine bank angle commands such that the Mars detector can meet the final constraints. In this paper, the entry guidance model is given as follows:

$$\dot{r} = v \sin\gamma \tag{1}$$

$$\dot{\theta} = \frac{v \cos\gamma \ \sin \ \psi}{r\cos\phi} \tag{2}$$

$$\dot{\phi} = \frac{v \cos\gamma \cos\psi}{r} \tag{3}$$

$$\dot{v} = -D - g \sin\gamma \tag{4}$$

$$\dot{\gamma} = \frac{1}{v}\left[L\cos\sigma + \left(\frac{v^2}{r} - g\right)\cos\gamma\right] \tag{5}$$

$$\dot{\psi} = \frac{1}{v}\left[\frac{L\sin\sigma}{\cos\gamma} + \frac{v^2}{r}\cos\ \gamma\ \sin\ \psi \tan\phi\right] \tag{6}$$

where r is radial distance from the center of the Mars, θ and ϕ are the longitude and latitude, v is the velocity, γ is the flight path angle, ψ is the velocity azimuth angle

and σ is the bank angle. L and D are the acceleration of aerodynamic lift and drag. The aerodynamic lift and drag forces are given by

$$L = \frac{0.5\rho v^2 C_L S}{m} \tag{7}$$

$$D = \frac{0.5\rho v^2 C_D S}{m} \tag{8}$$

3 The Guidance Methods of Mars Entry Guidance

In this section, the all-coefficient intelligent adaptive predictor-corrector guidance method based on the first-order characteristic model is introduced. The traditional predictor-corrector guidance method based on iteration is also introduced simply.

3.1 The All-Coefficient Intelligent Adaptive Predictor-Corrector Guidance Method

During every period of guidance, the actual landing point is predicted with the Eqs. (1)–(6) using the fixed step 4th order Runge-Kutta method, and then the predicted range error can be obtained. With the range error, the guidance method calculates the modification value of bank angle. In the all-coefficient intelligent adaptive predictor-corrector guidance method, the guidance method of integral type is used. In other words, the modification value is added on the guidance instructions of last guidance period, so the integrator must be used in the guidance method. In this method, the elimination of the error is evenly distributed from the current point to the terminal point of the whole interval.

In the correction step, the relation between the variation of lift characteristic quantity and range change must be known. Measured from the nominal terminal time, if the bank angle changes earlier, the amount of range change is larger. A special situation is researched that the detector is always in a nominal flight state before the adding of the increment of lift characteristic variable. Although it is a special case, it can be seen that the relationship between the increment and the range error. From the Fig. 1, we can see that the range change $D_1(t)$ when the increment is 0.1 and -0.1. The definition is given that $D(t) = D_1(t)/0.1$ is the time-varying dynamic amplification factor between the increment of the lift characteristic variable and the range change [7].

Although the above dynamic amplification factor is the nominal situation, it has great significance for the guidance, because the time-varying dynamic factor for the non-nominal situation can be divided into two parts artificially. The two parts are

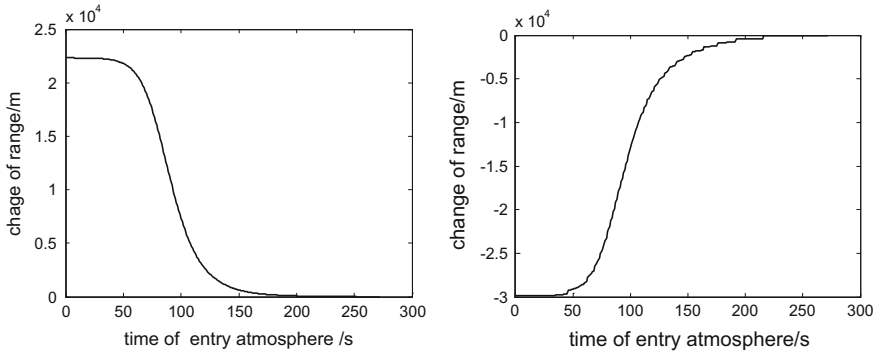

Fig. 1 The change value of range when the increment is 0.1 and −0.1

the known $\bar{D}(t)$ and the unknown $\Delta D(t)$ [8]. The unknown $\Delta D(t)$ is calculated by the following intelligent adaptive algorithm.

In the guidance method, the relationship between the range error and the increment is represented by the time-varying dynamic system based on first-order characteristic model, and the coefficients of the first-order characteristic model are estimated online. The all-coefficient intelligent adaptive theory is built on the sum of all coefficients is 1. In order to use the all-coefficient adaptive theory, input and output conversion is done using the time-varying dynamic factor. The known $\bar{D}(t)$ will be added to the controlled system as the transformation coefficient, and then the magnification of the transformed system is around 1, so the adaptive predictor-corrector guidance method can use the all-coefficient adaptive theory [7]. Through analysis, the relationship between the predicted range error after the input conversion and the increment of lift characteristic variable can be described by the following first order difference equation with variable coefficients. It is different from the traditional second order characteristic model

$$y(k+1) = f(k)y(k) + g(k)u(k) \tag{9}$$

where $y(k)$ represents the predicted range error after the input conversion, and $u(k)$ represents the increment of lift characteristic variable.

Based on the all-coefficient adaptive theory, the unknown time-varying parameters $f(k)$ and $g(k)$ are identified using gradient method, and then the estimated parameter values are projected into their respective ranges because there are estimated parameter values constraints using the adaptive control.

Define the regression vectors

$$\boldsymbol{\alpha}(k) = [y(k-1), u(k-1)]^{\mathrm{T}} \tag{10}$$

The parameter vectors

$$\boldsymbol{\beta}(k) = [f(k), g(k)]^{\mathrm{T}} \tag{11}$$

The estimated parameter vectors are represented as $\hat{\boldsymbol{\beta}}(k) = \left[\hat{f}(k), \hat{g}(k)\right]^{\mathrm{T}}$.

The gradient method to identify the time-varying parameters is

$$\hat{\boldsymbol{\beta}}(k) = \hat{\boldsymbol{\beta}}(k-1) + \frac{\lambda_1 \boldsymbol{\alpha}(k)}{\boldsymbol{\alpha}^{\mathrm{T}}(k)\boldsymbol{\alpha}(k) + \lambda_2}\left[y(k) - \boldsymbol{\alpha}^{\mathrm{T}}(k)\hat{\boldsymbol{\beta}}(k-1)\right] \tag{12}$$

where λ_1 and λ_2 are positive constants.

Then the values are projected into the following respective ranges

$$f(k) \in [f_{\min}, f_{\max}], \quad g(k) \in [g_{\min}, g_{\max}] \tag{13}$$

So the gradient method can be reformulated as

$$\hat{\boldsymbol{\beta}}(k) = \pi_D\left\{\hat{\boldsymbol{\beta}}(k-1) + \frac{\lambda_1 \boldsymbol{\alpha}(k)}{\boldsymbol{\alpha}^{\mathrm{T}}(k)\boldsymbol{\alpha}(k) + \lambda_2}\left[y(k) - \boldsymbol{\alpha}^{\mathrm{T}}(k)\hat{\boldsymbol{\beta}}(k-1)\right]\right\} \tag{14}$$

where π_D represents the orthogonal projection on set D. The set D is obtained by the formula (13). And then the increment $u(k)$ of bank angle can be obtained by the following linear feedback control

$$u(k) = -L \cdot \hat{f}(k) y(k) / (\hat{g}(k) + \lambda) \tag{15}$$

where L is the parameter of controller, and the sign of λ is same as $g(k)$.

The adaptive predictor-corrector guidance method is a non-iterative method and the adaptive control is used only once during each guidance period.

Because the all-coefficient guidance method is the guidance method of integral type, the total control value $u_1(k)$ is obtained by

$$u_1(k) = u_1(k-1) + u(k) \tag{16}$$

where $u_1(k-1)$ is the bank angle of the last guidance period.

The lateral guidance isn't discussed too much in this paper. The sign of bank angle is determined by a lateral logic that the crossrange threshold is used.

3.2 *The Predictor Corrector Guidance Method Based on Iteration*

In this section, the predictor corrector guidance method based on iteration will be introduced simply, and the detailed content can be found in the paper [8]. In this method, the bank angle magnitude at any range-to-go is

$$|\sigma_s| = \sigma_f + \frac{S_s - S_f}{S_{togo} - S_f}\left(\sigma_c - \sigma_f\right) \tag{17}$$

where σ_f represents the bank angle of terminal time, S_f represents the range-to-go of terminal time, σ_s and S_s represent the bank angle and the range-to-go of the current interval point, and σ_c and S_{togo} represent the bank angle and the range-to-go of the current position.

Using the above bank angle strategy, the predicted range error can be obtained. And then the correction step is done. The traditional predictor corrector guidance method uses the iteration technique which can be achieved as follows:

$$\cos\ \sigma_{n+1} = \cos\sigma_n - \frac{\cos\sigma_n - \cos\sigma_{n-1}}{\Delta s(\sigma_n) - \Delta s(\sigma_{n-1})}\Delta s(\sigma_n) \tag{18}$$

where $\Delta s(\sigma_n)$ is the range error of the current guidance period.

4 Numerical Simulation

First of all, the all-coefficient intelligent adaptive predictor-corrector guidance method is compared with the traditional predictor-corrector guidance method based on iteration. The nominal values and ranges of variation are given in Table 1.

Given the same and biggest errors in the initial position, and aerodynamic coefficients uncertainty, such as the drag and lift coefficient increase by 20%, the simulation is done. The Figure 2 shows the simulation results. The bank angle range of all-coefficient intelligent adaptive method is smaller than the method based on iteration, and this can leave some margin for the bank angle. In addition, the bank angle of terminal time is zero in the all-coefficient intelligent adaptive method which can create good condition for opening the parachute.

In order to see the results clearly, the third figure gives the change of longitude and latitude for the final 30 s, the actual landing points and the expected landing point. We can see that the all-coefficient intelligent adaptive method has higher

Table 1 Initial states and dispersion ranges

States	Initial values	Ranges of variation
Height (km)	125	[−3.5, 3.5]
Velocity (m/s)	5505	[−100, 100]
Flight path angle	−14.5°	[−0.3°, 0.3°]
Longitude	−90.072°	[−1°, 1°]
Latitude	43.88°	[−0.5°, 0.5°]
Velocity azimuth angle	85.01°	[−0.2°, 0.2°]

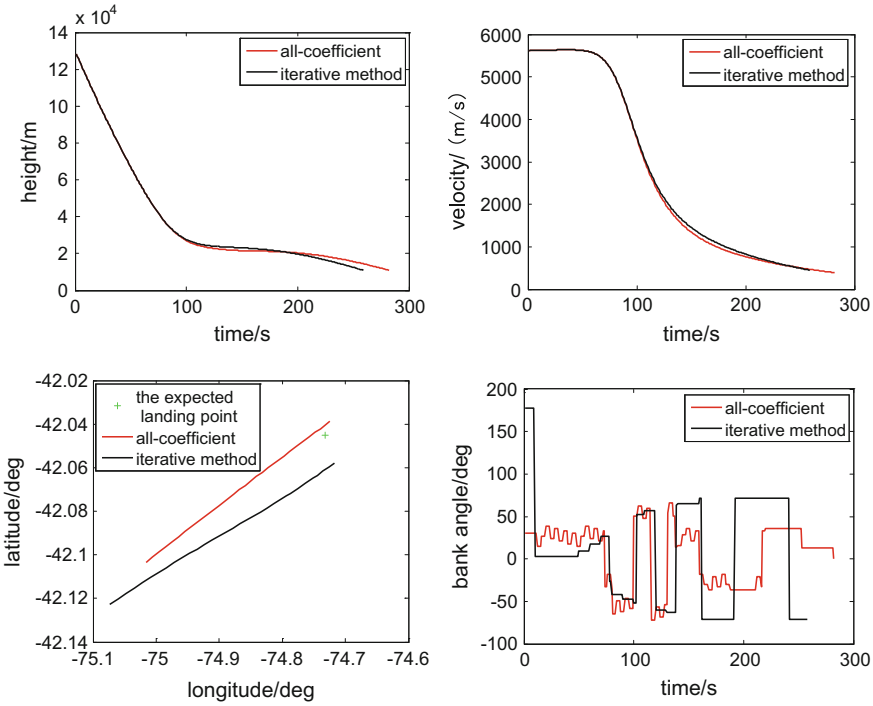

Fig. 2 The comparison charts of two predictor-corrector guidance methods

accuracy than the iterative method. Taking the above simulation condition as an example, the time of all-coefficient intelligent adaptive method is 0.31 s, and the time of iterative method is 1.19 s, so the former is easier to implement in the engineering and the property of the real time can be guaranteed.

Then the Monte Carlo simulation using the all-coefficient intelligent adaptive predictor-corrector guidance method is done with random variations in the initial states. The Fig. 3 shows the 40 guided trajectory charts of intelligent adaptive predictor-corrector guidance method. In the third chart of Fig. 3, the red points represent the entry points of detector and the cyan point represents the expected landing point. The method can guide the detector to the expected landing point accurately. The height and velocity can also satisfy the terminal conditions.

A 300-run Monte Carlo simulation is done. From Fig. 4 we can see that the range errors are all within 1.6 km, so the method has high accuracy.

Finally the two predictor-corrector methods are compared with the robust guidance method in [9]. The results show that the maximum point radius is not more than 1.5 km using the all-coefficient intelligent adaptive predictor-corrector guidance method, and the maximum point radius is not more than 3 km using the predictor-corrector guidance method based on iteration. If the initial states errors are big, the reference trajectory can't be tracked using the robust reference trajectory

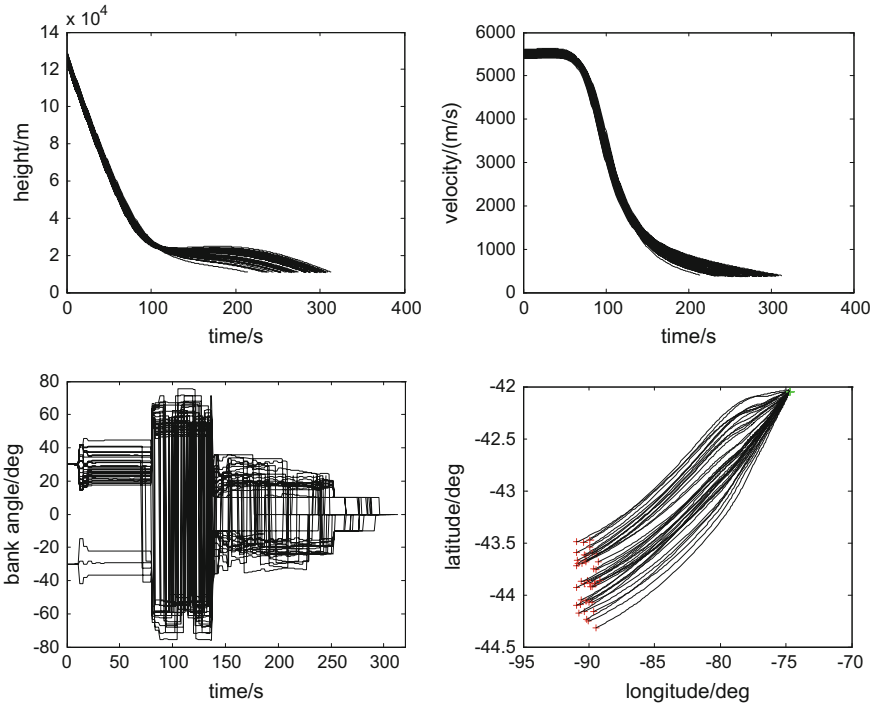

Fig. 3 The 40 guided trajectory charts of adaptive predictor-corrector guidance methods

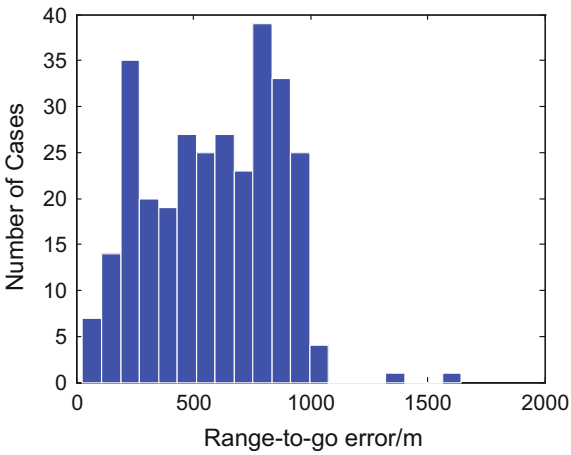

Fig. 4 The range errors of 300-run Monte Carlo simulation

Table 2 Initial states errors

States	Initial values	Ranges of variation
Height (km)	125	[−1.2, 1.2]
Velocity (m/s)	5505	[−50, 50]
Flight path angle	−14.15°	[−0.1°, 0.1°]
Longitude	−90.072°	[−0.2°, 0.2°]
Latitude	43.898°	[−0.1°, 0.1°]
Velocity azimuth angle	85.01°	[−0.1°, 0.1°]

guidance method. Table 2 shows the initial states errors that the robust reference trajectory guidance method can be tolerant. We can see the initial errors are smaller than the ones in Table 1. The tracking reference trajectory guidance method is sensitive to the initial reentry conditions.

5 Conclusion

Aiming at the problem of Mars entry guidance, the all-coefficient intelligent adaptive predictor-corrector guidance method based on the first-order characteristic model is proposed. And it is compared with the predictor-corrector guidance method based on iteration and robust tracking reference trajectory method. It can be seen that the all-coefficient intelligent adaptive predictor-corrector guidance method is more suitable for the problem of Mars entry guidance.

Acknowledgements This work was supported by the National Nature Science Foundation of China (61333008).

References

1. Scheeres DJ (1998) Interactions between ground-based and autonomous navigation for precision landing at small soler-system bodies. Tele Data Acqui Prog Rep 42–132
2. Braun RD, Manning RM (2007) Mars exploration entry, descent and landing challenges. J Spa Roc 44(2):310–323
3. Topcu U, Casoliva J, Mease KD (2007) Minimum-fuel powered descent for Mars pinpoint landing. J Spa Roc 44(2):324–331
4. Shen H, Seywald H, Powell RW (2010) Desensitizing the Minimum-fuel powered descent for Mars pinpoint landing. J Guid Control Dyn 33(1):108–115
5. Leavitt JA, Mease KD (2007) Feasible trajectory generation for atmospheric entry guidance. J Guid Control Dyn 30(2):473–481
6. Restrepo C, Valasek J (2008) Structured adaptive model inversion controller for Mars atmospheric flight. J Guid Control Dyn 31(4):937–957

7. Hu J (1998) All coefficients adaptive reentry lifting control of manned spacecraft. J Astonaut 19(1):8–12 (in Chinese)
8. Brunner CW, Lu P (2008) Skip entry trajectory planning and guidance. J Guid Control Dyn 31 (5):1210–1219
9. Wu HN, Li MM (2015) Finite-horizon approximate optimal guaranteed cost control of uncertain nonlinear systems with application to mars entry guidance. IEEE Trans Neur Net Learning Sys 26(7):1456–1467

Feature Level Information Fusion Based Deep Learning

Kejun Wang, Xuesen Hao and Xianglei Xing

1 Introduction

Feature level information fusion has been attracted widely attention. It can be considered that we extract feature then combine them. Feature level fusion can retain features and decrease amount of calculation. It can realize real time processing. In early years, they detect key points from images. Then they calculate the distance between two images. Burt PJ proposed to make fusion by Laplace pyramid. In 1995, Li H proposed wavelet method [1]. As a promising direction, Linas and Waltz analysis fusion technology delicately. Additionally, information fusion used to solve robot obstacle avoidance problem.

In recent years, facial recognition has two main methods. One of them is extract feature vector, another one is PCA(Principal Component Analysis) method [8]. These two methods base on features. Classification and identification based combine characteristic vector. Similarly, feature fusion methods also widely used in gait recognition [11], face recognition [12] and people identification [13]. It has a merit that if one tensor had problem or poor quality it would lead to low accuracy. From this point of view fusion theory and fuzzy neural network has satisfactory result [4]. It has stronger anti-interference skills. With the development of neural network [9], it is widely used to solve problems [10]. As for many other computer vision tasks, in the last few years significant performance gains have been achieved thanks to approaches based on deep networks [2, 5–7]. In 2005, Yan Lecun firstly proposed verify facial based Siamese [3]. It is different from common network. It has more than one channel as input in Siamese. It is significant to design a stable and effective system.

K. Wang · X. Hao · X. Xing (✉)
College of Automation, Harbin Engineering University,
No.145 Nantong Street, Harbin City, China
e-mail: xingxl@hrbeu.edu.cn

Z. Deng (ed.), *Proceedings of 2017 Chinese Intelligent Automation Conference*,
Lecture Notes in Electrical Engineering 458,
https://doi.org/10.1007/978-981-10-6445-6_55

Given the observations above, this paper introduces an approach based deep learning to realize feature level fusion. Our method is inspired by Siamese network. We add another channel to make fusion in facial recognition. We improve Siamese network in facial comparison. Experimental results on datasets, demonstrate the advantages of our approach over previous methods. Improved Siamese network has been proved to be useful in other dataset. In facial recognition and comparison, our method has good generalization.

Our main contributions:

1. Firstly,we establish a new dataset. We add samples to extend dataset. We set one image as a basic image and compare with remain images. If there is a result shows that they belong to the same person. We consider it as a positive sample. By contrast, we consider it as a negative sample. There are 6,848,920 positive samples and 9,910,668 negative samples.
2. Then, we crop regions of eye, nose and mouth regions. This purpose is increasing proportion of feature in an image. We train these features and face region together, and hence it is able to utilize the information of given features and improve recognition performance. We verify the effectiveness on several datasets and achieve state-of-the-art performance.
3. Moreover, an improved Siamese network is proposed to compare two images. We analyze both traditional Siamese network and improved Siamese network. Specifically, we add Spatial Transformer Network to Siamese work. We transfer single branch to seven channels.
4. Without training again when you want to compare two images. You can select two images, it will give you result.

2 The Proposed Approach

In this section we present to proposed network. We first provide an overview of our approach and we describe in details the architectures we design to realize fusion. In this paper, we propose a new deep learning framework with multiply channels as shown in Fig. 1. In traditional methods, there adapt to send all features once a time. This will lead high dimension and not unified of each feature vector. To solve these

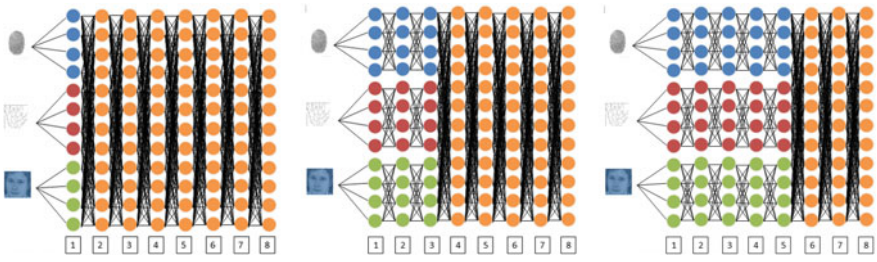

Fig. 1 Setting three channels and making fusion at different layers

problems, we adapt to set three channels as input. We try to make fusion at different layers to evaluate effectiveness of our method.

The most expensive part in terms of facial recognition is to detect the features. Despite significant progress in the past few years, facial recognition and comparison is still challenging due to the following two unanswered questions. The first one is face region has low proportion in an image. Secondly, there are more than one faces in an image. Solving these two difficulties will bring performance gain over traditional methods.

To solve the first problem, we crop face, eyes, nose and mouth regions. The process is illustrated in Fig. 2. We crop face regions by Haar algorithm. Furthermore, we detect key points by SDM algorithm. At last, we crop the other regions. The aim of crop regions is to avoid missing face region.

2.1 *Feature Level Information Fusion Based Deep Learning Test on Facial Recognition*

In traditional methods, they determine recognition by only one image. We propose to increase feature proportion. When we get eyes, nose and mouth regions, these features carry information, while there is no shelter. However, when sheltered in

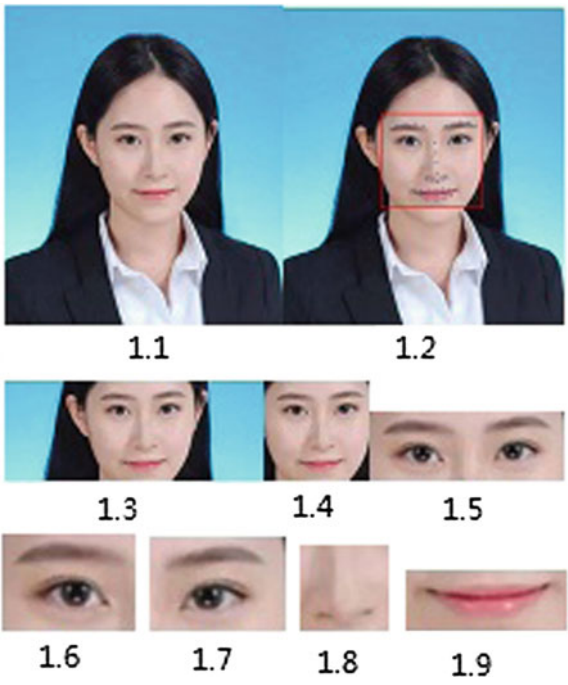

Fig. 2 Process of crop regions (Original image 1.1, detect face region 1.3, crop face region 1.4, detect eye region 1.6 and 1.7, crop nose region 1.8, crop mouth region 1.9, 1.2 and 1.5 are produced in processing)

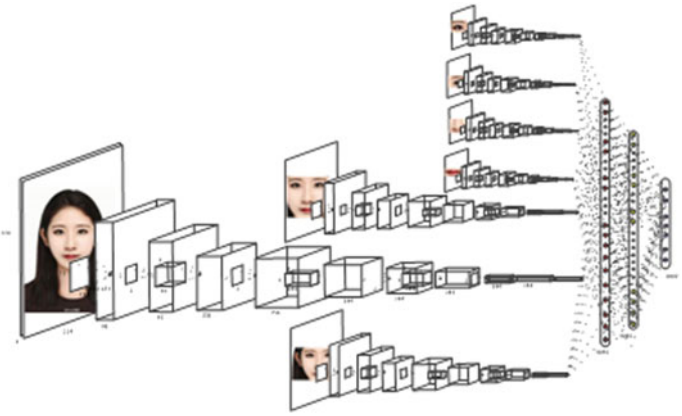

Fig. 3 Proposed fusion method for one channel

some regions, it cannot recognize efficiently. Without face region, there will be fluctuation. Furthermore, to improve accuracy, we combine face and the other parts to make fusion. It is more appropriate to achieve better result and generalization as shown in Fig. 3.

Inspired by previous works demonstrating the importance of considering feature level information in facial recognition, we propose to add another channel as shown in Fig. 4. This is specifically designed to perform facial recognition by adding another channel. If one image has low quality, we can get features from another image. In the network, it will combine these features which from two images. This will improve rate of recognition and generalization.

2.2 Feature Level Information Fusion Based Deep Learning Test on Facial Comparison

Facial comparison also called facial similarity comparison. As shown in Fig. 5, this method utilizes two channels as input. We can see the two images are the same person. The first step is detecting face region. The second step is extracting features. At last, we compare them and give the result.

Traditional neural network is widely used. However, there are problems such as low recognition and convergent slowly. These problems have effect on accuracy in practice. Through detailed analysis, we demonstrate how two channels can benefit from this network to overcome these problems in experiments. We adapt Siamese loss function in the proposed network. It can be calculated by the following formula (1):

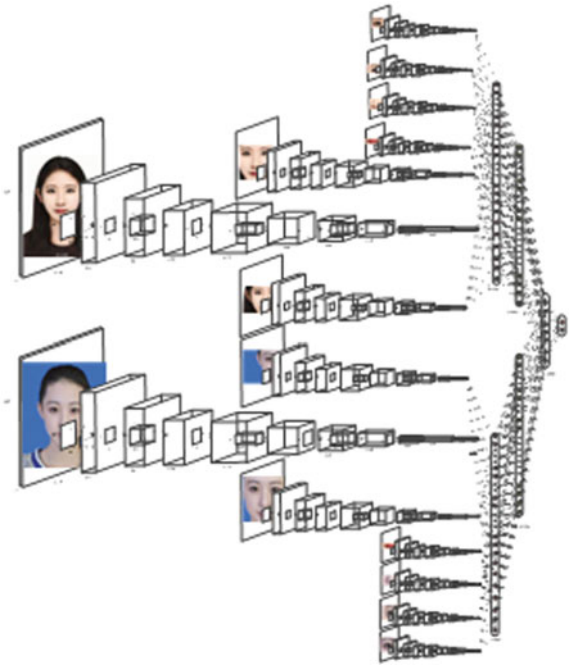

Fig. 4 Overview of our framework. Two channels with the same structure are used in facial recognition and comparison

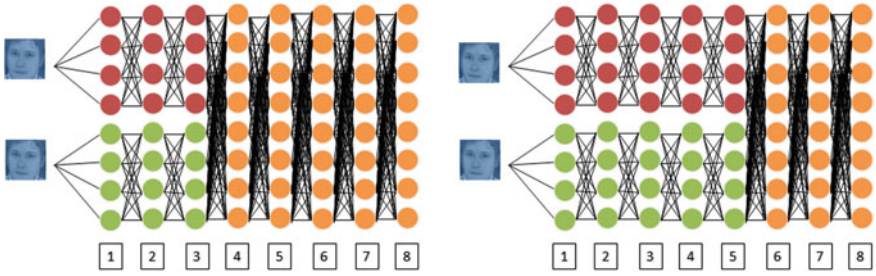

Fig. 5 Process of facial comparison. Two images belong to one person. We make fusion at different layers

$$E_W(X_1, X_2) = \|G_W(X_1) - G_W(X_2)\| \tag{1}$$

We propose to split single branch to seven channels in the middle of network as shown in Fig. 4. These features are connected in series one by one up. Previous works have not considered invariance in network. In order to have better

performance, we add Spatial Transformer Networks. It has robust to translation and rotation.

3 Experiments

In this section, we present experimental evaluations and in-depth analysis of the proposed method on the new dataset. Firstly, we introduce our dataset. Then we compare our framework with the state-of-art method on LWF dataset in Table 2. Our framework is implemented under digits, and our evaluation is conducted on a NVIDIA TeslaK40 GPU. In the experiments, we show the effectiveness of our proposed method. At last, we present the result on an interface.

3.1 Prepare Datasets

Before delving into our experiments, we describe our dataset. We combine some datasets and add new samples to build new dataset. It contains LFW and CASIA-maxpy-clean dataset and our new samples. LFW dataset contains 5749 persons (13,233 images). CASIA-maxpy-clean dataset contains 10,575 persons. In this dataset, each person has 100–769 images. We add samples to our datasets. Firstly, we select 790 persons as basic images. Second, we compare each person with remain images in this dataset. If there are two images belong to one person, we regard it as a positive sample. By contrast, we regard it as a negative sample. And so on, we get 14,582 positive samples, 598,096 negative samples. Considering image size has effect on recognition. Therefore, we change images to 28*28, 56*56, 128*128 and 256*256. Then we introduce CelebFaces dataset to increase capacity. In total, we have 12,000 persons, 390,000 images. We get 6,848,920 positive samples and 9,910,668 negative samples.

3.2 Test on Facial Recognition and Analysis

It is different from usual deep learning network because of we add another input to our framework. As shown in Fig. 1. In fully connection layer, class number equal to neuron number. We compare shallow network and deep network to evaluate effective of deep network.

We evaluate the performance of four types of images and four types of network. Table 1 shows the result of our comparison. From the table, it is clear that in deep network with 256*256 images outperforms, confirming the fact that deep framework improves the recognition accuracy.

Table 1 Comparison of performace based on different network

Pixel of image	Shallow network (image undisposed) (%)	Shallow network (image preprocess) (%)	Deep network (image undisposed) (%)	Deep network (image preprocess) (%)
28*28	60.19	69.13	66.25	70.75
56*56	78.14	82.24	80.01	86.49
128*128	85.90	93.58	92.37	97.64
256*256	90.94	96.58	93.39	98.94

Table 2 Comparisons of detecting performance on LWF dataset

Method	LBP	Joint Bayesian	GMM	Original network	Single input	Our proposed
Accuracy (%)	95.17	96.33	96.52	95.71	97.13	97.98

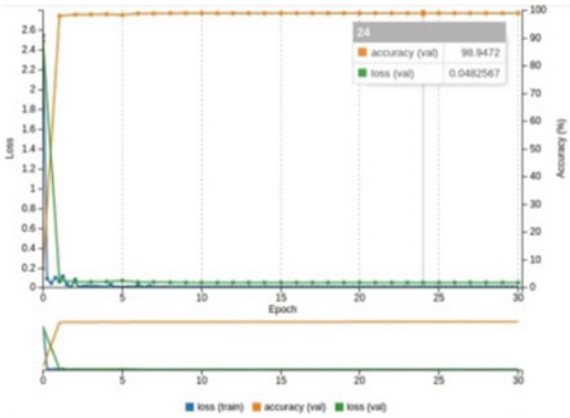

Fig. 6 Result of our proposed method on the new dataset (*blue line* is loss value of training, *orange line* is accuracy value)

We compare our approach with conventional methods. The results are summarized in Table 2. On LWF dataset, our approach outperforms all of the compared approaches. It is remarkable that our method achieves 97.98% accuracy. As shown in Table 2, it is easy to observe that different detectors affect the performance significantly. We directly using a detector may not be a good choice when applying existing method in the real world. Otherwise the detector may lose some valuable data when there is complex background.

Observing Fig. 6, we notice that it convergent quickly and stability. We can see the accuracy reach to 98.94%. In training process, it needs 18 h on NVIDIA Tesla K40 GPU. Then we evaluate 20,000 images base on this network, it needs 1 h and 20 min on CPU(Inteli76700).

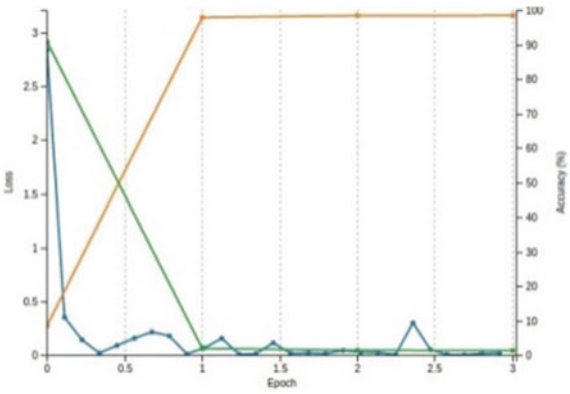

Fig. 7 Result of our approach on another dataset we select about 10,000 images to test our approach

To further demonstrate that the performance with the proposed network is not simply suit for only one dataset, we test this network by another dataset as shown in Fig. 7. It is clear that it also convergent in short time and has high accuracy. We analyze the performance of our approach on the other dataset. It assumes that this network has strong generalization ability.

3.3 Test on Facial Comparison and Analysis

Two kinds of network result are visualized in Fig. 8. We respectively evaluate the effect of improved Siamese network. It is clear that there is fluctuate in Fig. 8a. From Fig. 8a, we can see there are failed results. Compared with traditional Siamese network, the improved Siamese network has good stability and convergence as shown in Fig. 8b. Because of traditional Siamese network has few layers, and also has bad robust performance. However, it is not enough if we only add layers to network. In addition, we make the network complicated, it achieved by improved Siamese network.

We train our dataset base on improved Siamese network. We can find that it has high accuracy and stability as shown in Fig. 9. Bringing Spatial Transformer Networks, it also has effect on stability.

Furthermore, we develop interface based our proposed methods as shown in Fig. 10. These are planted to C# and Winform platform. You can select two images from your own datasets at random. It will detect regions of face and eyes. At last, there output the result of similarity without train network again. This method not only has stability but also useful in practice.

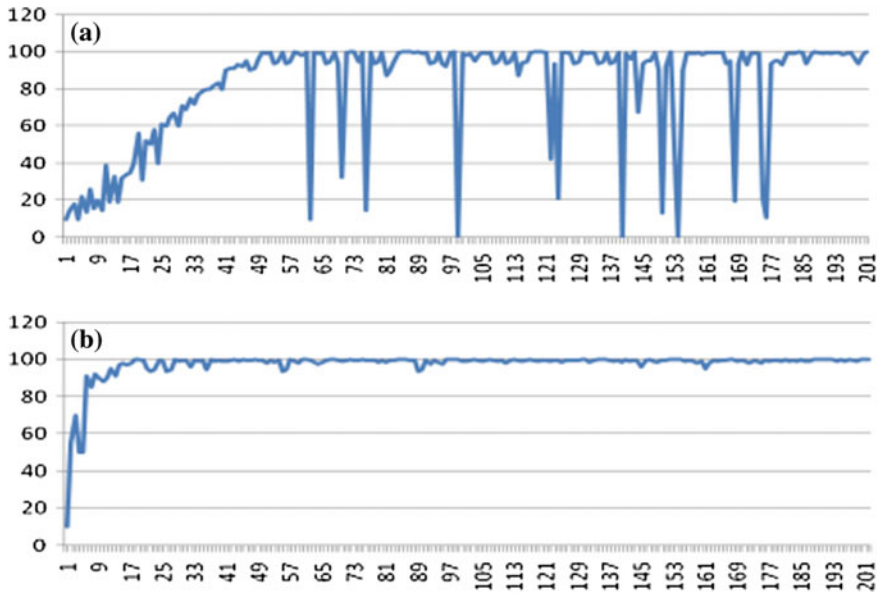

Fig. 8 Comparison of training result between Siamese and improved Siamese network. The *blue line* is result of accuracy

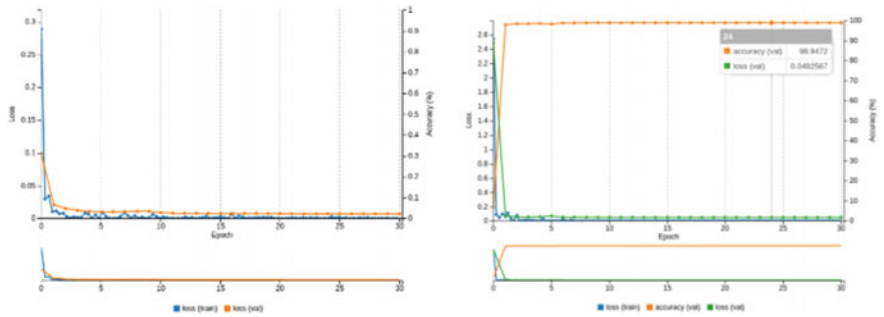

Fig. 9 Loss function and accuracy of improved Siamese network

4 Conclusion

In this paper, we propose to add channel to network. Our experiments show the proposed method can achieve satisfactory performance. Commonly used hand craft features, as they do not have good robustness. Differently from previous methods, the proposed method is possible to learn features from the improved network. We show that by increasing feature proportion and adding another input to network, it is possible to improve rate of recognition. An improved Siamese network is proposed

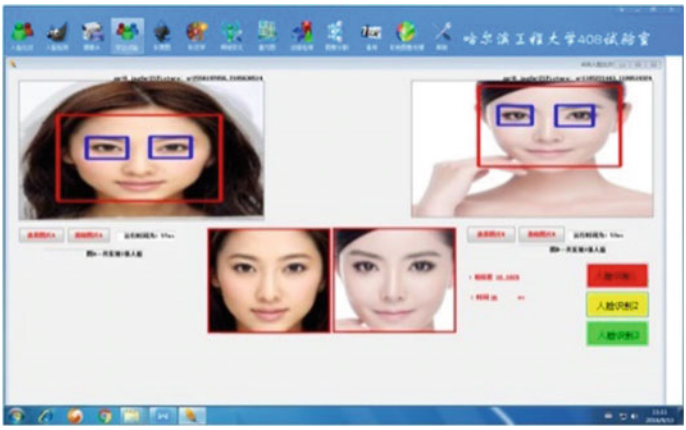

Fig. 10 Interface of facial detection and comparison result

by adding Spatial Transformer Networks. It is validated through series of experiments that our method has generalization ability. Hence, relevant application areas and topics with potential for further research.

Acknowledgement This work was supported by the Fundamental Research Funds for the Central Universities of China, Natural Science Foundation of China, and Natural Science Fund of Heilongjiang Province of China under Grand No HEUCFJ170404, 61573114, 61703119, F2015033 and QC20170702.

References

1. Li H, Nozaki T (1995) Wavelet analysis for the plane turbulent jet: analysis of large eddy structure. Jsme Int J 38(4):525–531
2. LeCun Y, Bengio Y, Hinton G (2015) Deep learning. Nature 521(7553):436–444
3. Chopra S, Hadsell R, LeCun Y (2005) Learning a similarity metric discriminatively, with application to face verification. IEEE computer society conference on computer vision and pattern recognition, vol 1, pp 539–546
4. Yuan X, Zhu QD, Lan H (2006) Multi-sensor information fusion based on rough set theory. J Harbin Inst Tech 38(10):1669–1672
5. Krizhevsky A, Sutskever I, Hinton GE (2012) ImageNet classification with deep convolutional neural networks. International conference on neural information processing systems, vol 25. Curran Associates Inc., pp 1097–1105
6. Zbontar J, LeCun Y. (2014) Computing the stereo matching cost with a convolutional neural network. In: Proceedings of the IEEE conference on computer vision and pattern recognition, pp 1592–1599
7. Ahmed E, Jones M, Marks TK (2015) An improved deep learning architecture for person re-identification. Computer vision and pattern recognition, pp 3908–3916
8. Moore B (2003) Principal component analysis in linear systems: controllability, observability, and model reduction. IEEE Trans Autom Contr 26(1):17–32

9. Sun Y, Wang X, Tang X (2015) Deeply learned face representations are sparse, selective, and robust. Computer vision and pattern recognition, pp 2892–2900
10. Zhang C-L, Zhang H, Wei X-S, Wu J (2016) Deep bimodal regression for apparent personality analysis. J Eur Conf Comput Vision
11. Xing X, Wang K, Yan T, Lv Z (2016) Complete canonical correlation analysis with application to multi-view gait recognition. Pattern Recognit 50:107–117
12. Xing X, Wang K (2016) Couple manifold discriminant analysis with bipartite graph embedding for low-resolution face recognition. Sig Process 125:329–335
13. Xing X, Wang K, Yan T, Lv Z (2015) Fusion of gait and facial features using coupled projections for people identification at a distance. IEEE Sig Process Lett 22(12):2349–2353

Study on Optimal Setting of Decomposing Furnace Temperature Based on Soft Measurement

Hong Liang Yu, Guo Dong Lian and Xiao Hong Wang

1 Preface

In the production process, when the cement raw meal (the main ingredient is limestone) through the kiln hoist into the preheater, it would exchange heat with high temperature flue gas, and the pre decomposition process occurs, then the mixture was sent into the claimer. At the same time, the coal was sprayed into the decomposition furnace, with the assist of tertiary air, the mixture combustion violent; when majority of limestone was decomposed, raw meal was dropped from the decomposing furnace and getting into rotary kiln been calcined and decomposition rate of kiln was one of the important control targets, which refers to the percentage of carbonate decomposed during the raw meal throughing decomposing furnace and lower preheater, before entering the kiln. Generally the range of decomposition rate is 90–95%. If the decomposition rate is too low, it will increase the final energy consumption of cement clinker and if the decomposition rate is too high, it is very prone to bring sintering blockage disastrous. In cement production process, the decomposition rate is determined by the temperature of decomposition furnace.

But at this stage, the temperature's control of decomposition furnace finished by artificial, few cement production lines were achieved automatic control, seen the literature [1–5]. However the temperature's setting of decomposing furnace is still completed by operator, which refers to the interval value of decomposition rate about raw meal given by laboratory, this can't ensure the science and real time of setting value, There is a certain gap between the level of automation and the international advanced cement production line, and this situation cannot meet the increasing quality and energy consumption control requirements of cement enter-

H.L. Yu (✉) · G.D. Lian · X.H. Wang
School of Electrical Engineering, University of Jinan, Jinan, China
e-mail: ziliao_yhl@163.com

Z. Deng (ed.), *Proceedings of 2017 Chinese Intelligent Automation Conference*,
Lecture Notes in Electrical Engineering 458,
https://doi.org/10.1007/978-981-10-6445-6_56

prises. for this reason, this paper has been carried on the related research, and proposed the corresponding solution.

2 Study on the Soft Measurement of the Decomposition Rate of the Kiln

In present period the decomposition rate of raw meal; cannot be detected online sampling and testing at intervals in most companies (once a day or eight hours a day) and The detection value of this kind of method is obviously not conducive to the automatic temperature optimization of the decomposition furnace. And the literature [6] has made a preliminary study on the online soft measurement of the decomposition rate of raw meal (The same research group), To this end, this paper carried out some reference. But this thesis is based on the production process of Shandong cement plant, cement production line process and document the differences, and in order to further improve the versatility of raw meal decomposition rate of soft measuring method, we improved the selection of dominant parameters and specific algorithm.

2.1 Selection of Dominant Parameters

(1) Enhance mechanical and electrical flow into the kiln: The enhance mechanical and electrical flow into the kiln can not only reflect the number of raw material into the kiln in real-time Through the current fluctuations, and the distance of preheater closer, better real-time, therefore, this paper selects one of the variables as auxiliary variables.
(2) Decomposition furnace temperature and pressure: decomposition furnace should provide enough heat to support the decomposition of raw materials, ensure the kiln before raw meal decomposition rate in more than 90%, so the decomposition furnace temperature and pressure is the main parameters of soft measurement.
(3) Three wind temperature: the three wind is a part of the decomposition furnace combustion with wind, and the temperature is higher, so the stability of the furnace temperature and the temperature of the tertiary air has a great relationship.
(4) Five stage preheated cone inlet temperature and pressure: according to field technology, from the decomposition of the furnace to the smoke room still need three minutes, the three minutes is through the time of the 5 stage preheated, in addition, through the off-line laboratory data, the 5 stage preheated sometimes B and A decomposition rate of the sample gap is larger, so it can be determined that the 5 stage preheated has a greater impact on the decomposition rate.

2.2 Data Preprocessing

(1) Abnormal data elimination

AS the decomposition rate based on cement plant was sampled and tested at 6 PM, therefore, the first three minutes of 6 PM per day the data was selected and Pull the Rule was used to eliminate.

(2) Mean filter

After eliminating the abnormal data, through the mean filter to further improve the smoothness of the data, Average three minutes before six pm every night to remove outliers.

(3) Data standardization

And then through the data standardization, all of the parameters to select the appropriate range of transformation, data processing for the [−1,1] range of the data.

The above three types of methods are more common, so the specific algorithm is no longer described.

2.3 The Soft Measurement Model of the Decomposition Rate of the Kiln

Least squares support vector machine (LS_SVM) has many advantages, for example, it does not have the local minimum, which causes the phenomenon of excessive learning, and the convergence rate is faster than that of the neural network. So the LS_SVM method is used to build the model of the soft sensor of the kiln decomposition rate. The main need to determine the two parameters, one for the penalty factor, and the other for the parameter of the kernel function.

After repeated trials and selection, the final punishment factor $C = 50$, Kernel function using radial basis function, the Kernel width is $\sigma = 3.0$. Based on these two variables, the estimated function is $\alpha = \begin{bmatrix} 26.9273 \\ -32.8816 \\ \vdots \\ -4.5123 \end{bmatrix}_{45\times 1}$, $b = -0.1487$, modeling the data to get the modeling results and test results as shown in Fig. 1.

As can be seen from the figure, even in the case of substandard data, it can be very good to follow, and the forecast is more accurate.

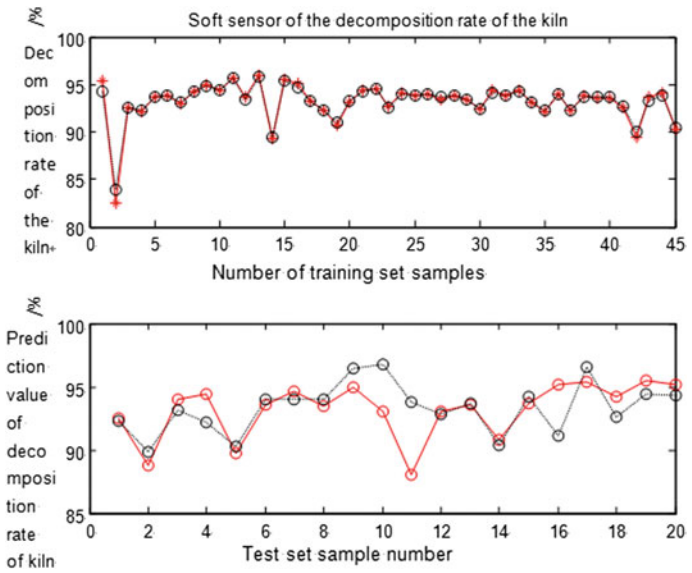

Fig. 1 Least squares support vector machine learning and test results

3 Control System of Kiln Decomposition Rate Based on Fuzzy Control

After realizing of the online soft measurement of the decomposition rate of the kiln, we give the automatic control system of the decomposition rate of raw meal. The plan is shown in Fig. 2.

Decomposition rate optimal control system is divided into two parts, the first part is through the OPC to exchange data between database and the DCS of cement site, the data in the database will be flitted and estimated model by the algorithm system, then evaluating the raw material pre decomposition rate of raw material related to this time, The other part is to calculate the burn index of the raw material through the three rate values from laboratory.

3.1 Burn Ability Index Calculation

The burn ability index adopt the format proposed by H.N.Banerjee:

$$LSF = \frac{100 \times CaO}{2.8 \times SiO_2 + 1.65 \times Al_2O_3 + Fe_2O_3} \tag{3.1}$$

$$BF = LSF + 6 \times (SM - 2) - (MgO + K_2O + Na_2O) \tag{3.2}$$

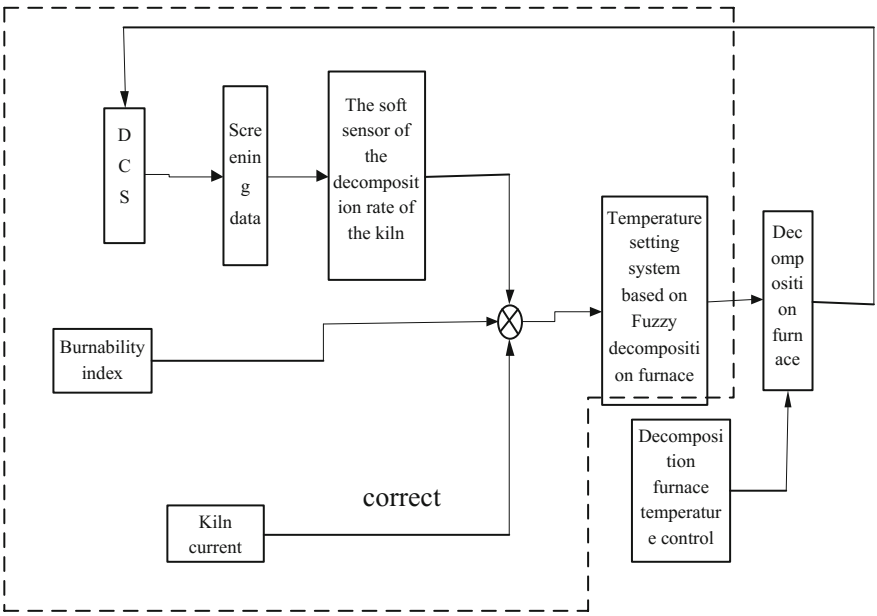

Fig. 2 The block diagram of the control system of the kiln decomposition rate

Among them, BF is the burn ability index.

In the actual production, the three rate values of raw material will be inputted into DCS (once per hour), automatic acquisition, so, we need to change the above formula, using the three rate values of raw materials, the expression will replace the above chemical expression about three rate values

$$LSF = \frac{100 \times [KH \times SM \times (IM + 1) \times 2.8 + 1.65 \times IM + 0.35]}{2.8 \times (IM + 1) + 1.65 \times IM + 1} \tag{3.3}$$

$$BF = LSF + 6 \times (SM - 2) - Q \tag{3.4}$$

the Q is the default value, because of the raw material, the contents of Na_2O, K_2O, MgO are very few, so in this paper, the default value is 2 for all this can instead.

3.2 *The Fuzzy Control System of Decomposition Furnace Temperature Setting*

After completing of online estimation of the decomposition rate and calculation of burn ability index, based on the fuzzy rules, the automatic control of the temperature setting value of the decomposition furnace is realized, and then the automatic

control of the decomposition rate of the kiln is finally realized through the automatic control of the decomposition rate temperature.

3.2.1 Fuzzy Input

In the decomposition rate control system, the burn ability index and the value of decomposition rate as the input of the two-dimensional fuzzy controller to characterize the different raw materials real time decomposition, and defined as D1, D2. D1, D2 both contain 3 fuzzy subsets, in {N, O, P} representation, D1 means {difficult to burn, normal, easy to burn}, D2 means {decomposition low, decomposition normal, decomposition high}. The basic domain sets to [80, 99] and [−1, 1]. In order to ensure that the setting value does not change, the incremental output is used and domain temporary is located [−7, 7]. 5 fuzzy subsets are included, representing [Negative major adjustment, Negative minor adjustment, keep, positive major adjustment, positive minor adjustment].

At the same time, in order to ensure the stability of the control, the value of the setting value should not be changed frequently, so the trapezoidal membership function which is not changed within a certain range and at special points on the fast change is adopted.

In summary, the formulas of decomposition rate membership degree are:

$$f_1(x) = \begin{cases} 1, & 80 \le x \le 89, \\ \frac{90-x}{90-89}, & 89 \le x \le 90, \\ 0 & x \ge 90 \end{cases} \tag{3.5}$$

$$f_1(x) = \begin{cases} 0, & x \le 89, \\ \dfrac{x-89}{90-89} & 89 \le x \le 90 \\ 1, & 90 \le x \le 94, \\ \dfrac{95-x}{95-94} & 94 \le x \le 95 \\ 0 & x \ge 95 \end{cases} \tag{3.6}$$

$$f_1(x) = \begin{cases} 0, & x \le 94, \\ \frac{95-x}{95-94}, & 94 \le x \le 95, \\ 1 & x \ge 95 \end{cases} \tag{3.7}$$

Burn ability of membership formulas are similar to these. The formulas are as follows.

$$f_2(x) = \begin{cases} 1, & x \le -0.5, \\ \frac{-0.3-x}{0.2}, & -0.5 \le x \le -0.3, \\ 0 & x \ge -0.3 \end{cases} \tag{3.8}$$

$$f_2(x) = \begin{cases} 0, & x \leq -0.5, \\ \dfrac{x-(-0.5)}{0.2} & -0.5 \leq x \leq -0.3 \\ 1, & -0.3 \leq x \leq 0.3, \\ \dfrac{0.5-x}{0.2} & 0.3 \leq x \leq 0.5 \\ 0 & x \geq 0.5 \end{cases} \tag{3.9}$$

$$f_2(x) = \begin{cases} 0, & x \leq 0.3, \\ \frac{0.5-x}{0.2}, & 0.3 \leq x \leq 0.5, \\ 1 & x \geq 0.5 \end{cases} \tag{3.10}$$

3.2.2 Fuzzy Rules

According to the experience of the excellent operator and the relevant cement production process, we summary the forms of control rules are as follows: if A and B then C, $f1$ is the fuzzy value for decomposition rate, $f2$ is the fuzzy value of burn ability. The fuzzy handwriting of them respectively correspond to the digital 1, 2, 3, the Settled values of the 5 fuzzy subsets corresponding to the digital 1, 2, 3, 4, 5.

If $f1$ is 1 and $f2$ is 1 then U is 5
If $f1$ is 2 and $f2$ is 1 then U is 3
IF $f1$ is 3 and $f2$ is 1 then U is 2
If $f1$ is 1 and $f2$ is 2 then U is 4
If $f1$ is 2 and $f2$ is 2 then U is 3
If $f1$ is 3 and $f2$ is 2 then U is 2
If $f1$ is 1 and $f2$ is 3 then U is 4
If $f1$ is 2 and $f2$ is 1 then U is 2
If $f1$ is 3 and $f2$ is 3 then U is 1

3.3 The Correction Module Design of the Rotary Kiln Motor

In the actual production, because of the model mismatch, there is a certain degree of deviation in soft measurement of the kiln decomposition rate and fuzzy rules, therefore the kiln motor current is adopted to modify. If the kiln motor current drops, then increases the setting value of decomposition furnace temperature, and vice versa. By analyzing the historical data of cement plant, the kiln motor current about 490 is normal, 470 is lower and 510 is higher.

In the actual production, according to the operation experience, If the kiln motor current is low in long term, this kind of situation is very harmful to the quality of clinker. What is more, operator's operating experience is generally to improve the

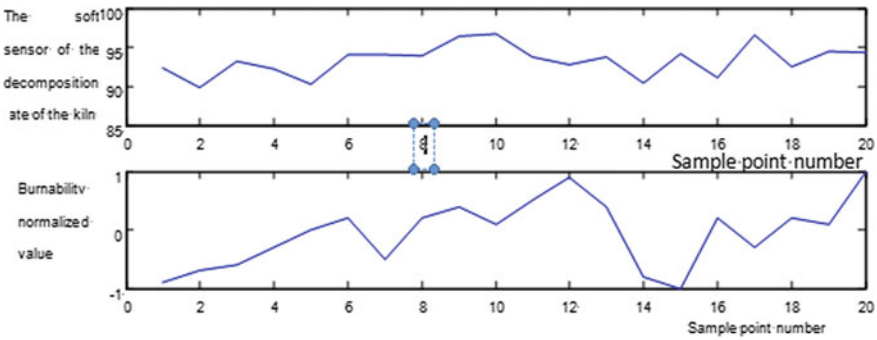

Fig. 3 The kiln decomposition rate and the normalized value of burn ability according to the model prediction

decomposition furnace temperature setting value and increase the decomposition rate. Therefore, when the kiln motor current is low, the temperature of decomposition furnace setting value is increased. Two mean filter is used by kiln motor current, each time is 150 s.

4 Conclusion

4.1 System Simulation

After the design of the main parts of the system, according to the historical data of the cement plant, the setting system of pre-decomposition temperature was validated. According to the normalization of burning resistance and the value of soft measurement of the decomposition rate, the Fig. 3 was obtained.

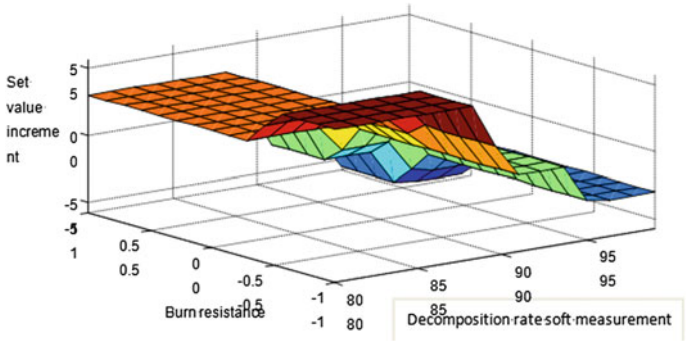

Fig. 4 Three dimensional control chart based on the output of fuzzy controller

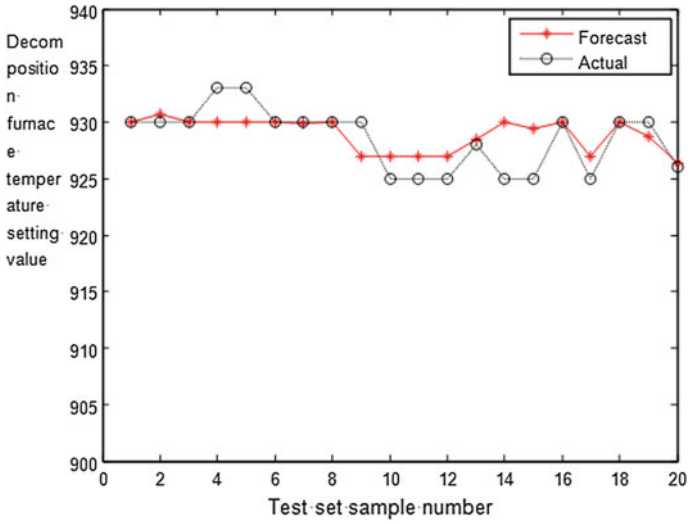

Fig. 5 Comparison of simulation and actual value

According to the design of the fuzzy controller to get three-dimensional graphics, as shown in Fig. 4.

According to the fuzzy output, comparison with actual output is shown in Fig. 5.

As can be seen from the graph, the trend of the system output and operator's manual setting is basically t same. The practicability of the system is verified.

Acknowledgements This work has been transformed into major projects of independent innovation achievements in Shandong province and central and small and medium enterprises in China and the small and medium enterprises in energy conservation and emission reduction research and cooperation funding project funding, the project approval number: 2014CGZH0601, SQ2013ZO600003.

References

1. Qian ZL (2005) Reflection on several problems in the development of new dry process kiln. China Cement 7:8–11
2. Jie W, Zhenliang Y (2011) Semi supervised fuzzy clustering modeling method for quality grade of cement clinker. Comput Meas Control 10:2507–2510
3. Wang Z, Yuan M, Wang H, Wang T (2006) Research on soft sensor modeling of cement clinker quality index. Chem Autom Instrum (6):53–58
4. Zhang Y (2011) Study on optimal control of cement rotary kiln, University of Jinan
5. Zeng LS (2012) Study on optimal control of decomposition furnace in the process of cement production. University of Jinan, Liu Hui (2010) Soft-sensing research on kiln tail decomposition rate of new dry process cement production, University of Jinan
6. Yao C, Chen H (2009) Automated retinal blood vessels segmentation based on simplified PCNN and fast 2D-Otsu algorithm. J Central South Univ Technol (4)

Safe Diagnosis of Stochastic Discrete Event Systems by Constructing Safe Verifier

Fuchun Liu and Pengbiao Yang

1 Introduction

Due to the practical and theoretical importance, failure diagnosis, which aims to timely identify and exactly characterize the occurrence of incipient faults, has received considerable attention in recent years (for example, [1–4] and the references, therein). In particular, Sampath et al. [3] proposed an approach for failure diagnosis of discrete event system (DES), in which a diagnoser was constructed to perform the on-line detection and off-line verification of the diagnosability properties of the system. Thorsley et al. [4] extended the framework of [3] to stochastic DESs. For the decentralized systems, Qiu and Kumar [2] and Liu et al. [5] investigated the failure diagnosis issue of the decentralized classical and stochastic DESs by constructing the local diagnosers.

Motivated by the fact that the complexity of constructing such diagnosers in above references is exponential in the cardinality of the states of the system, Yoo and Lafortune [6] presented a polynomial-time verification for the diagnosability of partially observed DESs. In [7, 8], two polynomial test methods for stochastic diagnosability of DESs were developed by constructing different diagnosis models. Moreira et al. [9] proposed a polynomial-time failure diagnosis approach for decentralized DESs. In our prior work [10], the diagnosability and safe diagnosability of fuzzy DESs were studied, respectively, in both of which the complexity of constructing the models for failure diagnosis are polynomial-time.

This paper aims to present a new approach to deal with the safe diagnosis problem for stochastic DESs by constructing the safe verifier, which was investigated in our previous work by constructing the safe diagnosers [11]. More specifically, after formalizing the notion of safe diagnosability of stochastic DESs,

F. Liu (✉) · P. Yang
School of Computers, Guangdong University of Technology,
Guangzhou 510006, China
e-mail: fliu2011@163.com

Z. Deng (ed.), *Proceedings of 2017 Chinese Intelligent Automation Conference*,
Lecture Notes in Electrical Engineering 458,
https://doi.org/10.1007/978-981-10-6445-6_57

we construct a non-fault automaton to represent the specification language. Then, a recognizer of the illegal language is introduced to distinguish the forbidden strings from the system behaviors, and a safe verifier is constructed to realize the safe diagnosis of the system. In particular, a necessary and sufficient condition for the verification of safe diagnosability of stochastic DESs is proposed. It is worth noting that the construction of the safe verifier is polynomial-time in the number of states and events of the system.

2 Notations and Preliminaries

A stochastic DES is modeled by a stochastic automaton $G = (X, \Sigma, \eta_G, x_0)$, where X is a set of states with the initial state x_0, Σ is the set of events, $\eta_G : X \times \Sigma \times X \to [0, 1]$ is a partial state transition probability function.

Define a partial transition function $\delta_G : X \times \Sigma \to X$ as: $\delta_G(x, \sigma) = x'$ if and only if $\eta_G(x, \sigma, x') > 0$, where $x, x' \in X$ and $\sigma \in \Sigma$. The event set Σ is partitioned into the observable event set Σ_o and the unobservable event set Σ_{uo}, $\Sigma_f \subseteq \Sigma_{uo}$ is the failure event set. Generally, Σ_f is partitioned into a set of failure types $\Sigma_f = \Sigma_{f1} \cup \Sigma_{f2} \ldots \cup \Sigma_{fm}$.

For convenience, we introduce the notations from [1, 3, 4, 11]: Let $s \in L$, denote $pre\,(s)$ and $suf\,(s)$ as the prefixes and suffixes of s, respectively. $L_\sigma(G, x) = \{u\sigma : \Pr(u\sigma|x) > 0, u \in \Sigma_{uo}^*, \sigma \in \Sigma_o\}$, and $L/s = \{t \in \Sigma^* : st \in L\}$ represents the post-language. $\Psi(\Sigma_{fi}) = \{s \in L : s_l \in \Sigma_{fi}\}$, where s_l is the final event of s. $P : \Sigma^* \to \Sigma_o^*$ is the projection defined in the usual manner.

As mentioned in [11], the purpose of safe diagnosis is to prevent local faults developing into failures that can lead to serious hazards. So we should prevent the system executing a forbidden string from Γ_i after a failure of type f_i, where $\{\Gamma_i \subseteq \Sigma^* : i = 1, 2, \ldots m\}$ is a class of forbidden string sets. The set of such illegal strings is called illegal language, denoted by $\Re_f^i$, which is defined as $\Re_f^i = \{\omega \in L/s : s \in \Psi(\Sigma_{fi}), \Gamma_i \in \omega\}$, where $\Gamma_i \in \omega$ represents that there is $t \in \Gamma_i$ such that t is a substring of ω.

Definition 1 [11]: A language L generated by a stochastic automaton $G = (X, \Sigma, \eta_G, x_0)$ is said to be safe diagnosable if for any $\varepsilon > 0$,

$$(\exists n_0 \in N)\,(\forall s \in \Psi(\Sigma_{fi}))\,(\forall t \in L/s \wedge ||t|| \geq n_0)\,(\exists v \in pre(t))\,(pre(v) \cap \Re_f^i = \varnothing)$$

and, at least one of the following conditions holds:

1. $\omega \in P^{-1}[P(sv)] \Rightarrow \Sigma_{fi} \in \omega$, i.e., $D(sv) = 1$,
2. $\Pr(t : D(sv) = 0|v \in pre(t)) < \varepsilon$.

where the diagnosability function $D : \Sigma^* \to \{0, 1\}$ is defined as follows:

$$D(sv) = \begin{cases} 1, & \text{if } \omega \in P^{-1}[P(sv)] \Rightarrow \Sigma_{fi} \in \omega, \\ 0, & \text{otherwise.} \end{cases} \quad (1)$$

3 Construction of Safe Verifier of Stochastic DESs

Let $G = (X, \Sigma, \eta_G, x_0)$ be a stochastic DES, $\Re_f^i$ be the illegal language and Γ_i be the set of forbidden strings. In order to construct the recognizer G_r, we first define a label set of forbidden strings from Γ_i as $LB = \{N, F, B\}$, where the label N represents that the failure does not occur in the behavior of system, F represents that the system executes the failure but does not execute any forbidden string from Γ_i after the occurrence of that failure, and B means that the behavior of system containing a forbidden string from Γ_i after the occurrence of a failure.

Algorithm 1: Construction of safe verifier of stochastic DESs Step 1: Construct a non-fault automaton $H = (X', \Sigma_N, \eta_H, \delta_H, x_0')$ to generate the sublanguage of L without fault events, where $\Sigma_N = \Sigma - \Sigma_f$, X' is a set of finite states with the initial state $x_0' = x_0$, for any $x' \in X$, if there exists $\omega \in \Sigma^*$ satisfying $\Sigma_f \notin \omega$ and $\eta_G(x_0, \omega, x') > 0$, then $x' \in X'$, the state transition probability function $\eta_H : X' \times \Sigma \times X' \to [0, 1]$ is defined as $\eta_H(x, \sigma, x') = \eta_G(x, \sigma, x')$, for $\forall x, x' \in X'$, $\sigma \in \Sigma_N$ satisfying $\eta_G(x, \sigma, x') > 0$, the state transition function, $\delta_H : X' \times \Sigma \to X'$ is defined as $\delta_H(x, \sigma) = x'$ if and only if $\eta_H(x, \sigma, x') > 0$.

Step 2: Construct the recognizer of the illegal language $\Re_f^i$ as a stochastic automaton $G_r = (Q_r, \Sigma, \eta_r, \delta_r, p_0)$, where $Q_r \subseteq X \times LB$ is a set of finite states with the initial state $p_0 = (x_0, N)$, η_r and δ_r are defined in the following Definitions 2 and 3, respectively.

Step 3: Construct the safe verifier G_v based on the recognizer G_r, the $G_v = (Q_v, \Sigma_o, \delta_v, \eta_v, q_0)$ is a finite state automaton, where Q_v is a set of finite states with the initial state $q_0 = (x_0, N, y_0)$, $Q_v \subseteq X \times LB \times Y$, where $Y = X' \cup \{E\}$, E represents empty, η_v and δ_v are defined in the following Definitions 4 and 5, respectively.

Definition 2 The partial state transition probability function of recognizer G_r is defined as $\eta_r : Q_r \times \Sigma \times Q_r \to [0, 1]$: for $p_i = (x_i, lb_i)$, $p_j = (x_j, lb_j) \in Q_r$ and $\sigma \in \Sigma$, $\eta_r(p_i, \sigma, p_j) = \eta_G(x_i, \sigma, x_j)$.

Definition 3 The partial state transition function of recognizer G_r, is defined as $\delta_r : Q_r \times \Sigma \to Q_r$: for $p_i = (x_i, lb_i) \in Q_r$, $lb_i \in LB$ and $\sigma \in \Sigma$,

$$\delta_r(p_i, \sigma) = \begin{cases} (\delta_G(x_i, \sigma), N), & \text{if } \sigma \notin \Sigma_f, lb_i = N, \\ (\delta_G(x_i, \sigma), F), & \text{if } (\sigma \in \Sigma_f, lb_i = N) \vee lb_i = F, \\ (\delta_G(x_i, \sigma), B), & \text{if } (suf(s_2) \cap \Gamma_i \neq \varnothing, \text{where} \\ & s\sigma = s_1\sigma_f s_2, \sigma_f \in \Sigma_f) \vee lb_i = B. \end{cases} \quad (2)$$

Definition 4 The state transition probability function $\eta_v : Q_v \times \Sigma_o \times Q_v \to [0,1]^2$ of safe verifier G_v is defined as: for any $q_1 = (x_1, lb_1, y_1)$, $q_2 = (x_2, lb_2, y_2) \in Q_v$, $\sigma \in \Sigma_o$, $\eta_v(q_1, \sigma, q_2) = (\theta, \theta') > 0$ holds, where

$$\theta' = \sum_{s \in L_\sigma(H, y_1)} \eta_H(y_1, s, y_2), \quad \theta = \sum_{s \in L_\sigma(G, x_1)} \eta_G(x_1, s, x_2).$$

Definition 5 The state transition function of $\delta_v : Q_v \times \Sigma_o \to Q_v$ is defined as:

$$\delta_v(q_1, \sigma) = \begin{cases} (\delta_r(p_1, s), E), & \text{if } \delta_H(y_1, \sigma) \text{ is undefined or } y_1 = E, \\ (\delta_r(p_1, s), \delta_H(y_1, \sigma)), & \text{otherwise,} \end{cases} \tag{3}$$

where for any $q_1 = (x_1, lb_1, y_1) \in Q_v$, $\sigma \in \Sigma_o$, $s \in L_\sigma(G, x_1)$, $p_1 = (x_1, lb_1) \in Q_r$, state E means that there is no transition originate from state y_1 with the event of σ.

Remark It is worth noting that the construction of the safe verifier is polynomial-time in the number of states and events of the system.

4 Necessary and Sufficient Condition of Safe Diagnosability

Before proposing the necessary and sufficient condition, we introduce some concepts about the safe verifier.

Definition 6 For state $q_i = (x_i, lb_i, y_i) \in Q_v$, if $lb_i = N$, then q_i is called a normal state. The set of all normal states is denoted as Q_v^N, if $lb_i = B$, then q_i is called a B state, and the set of all B states is denoted as Q_v^B, if $lb_i = F \wedge y_i \neq E$, then q_i is called a fault state, and the set of all fault states is denoted as Q_v^F, where $Q_v^N, Q_v^B, Q_v^F \subseteq Q_v$.

Definition 7 If there exists the sequence of states $q_k, q_{k+1}, q_{k+2}, \ldots q_l \in Q_v$ and events $\sigma_k, \sigma_{k+1}, \sigma_{k+2}, \ldots \sigma_l \in \Sigma_o$, $0 \leq k \leq l$ such that

$$q_k \xrightarrow{\sigma_k, (\theta_k, \theta'_k)} q_{k+1} \xrightarrow{\sigma_{k+1}, (\theta_{k+1}, \theta'_{k+1})} q_{k+2} \ldots q_l \xrightarrow{\sigma_l, (\theta_l, \theta'_l)} q_k, \tag{4}$$

then the sequence of states $q_k, q_{k+1}, q_{k+2}, \ldots q_l \in Q_v$ forms a state cycle, denoted as $cl = (q_k, q_{k+1}, \ldots q_l)$, and the set of the states in the cycle cl is denoted as cl'.

Definition 8 Assume that $cl = (q_k, q_{k+1}, q_{k+2}, \ldots q_l)$ is a state cycle of safe verifier G_v, and its probability of transition is $(\vartheta, \vartheta') = (\theta_k \theta_{k+1} \ldots \theta_l, \theta'_k \theta'_{k+1} \ldots \theta'_l)$, if $q_i \in Q_v^B$, $(k \leq i \leq l)$ and $\vartheta = 1$, then the state cycle cl is called a recurrent B state cycle, denoted as $cl^B_{recurrent}$.

Theorem 1 *Let L be the generated language of stochastic DES* $G = (X, \Sigma, \eta_G, x_0)$ *and* $G_v = (Q_v, \Sigma_o, \delta_v, \eta_v, q_0)$ *be the safe verifier. L is safe diagnosable, if and only if,* G_v *satisfies the following condition: There does not exist the states* $q_1 \in Q_v^F \vee Q_v^N$, $q_2 \in Q_v^B$, $q_3 \in cl^{B\prime}_{recurrent}$ *such that* $\delta_v(q_1, \sigma) = q_2$ *and* $\delta_v(q_2, \alpha) = q_3$, where $\sigma \in \Sigma_o$, $\alpha \in \Sigma^*$.

Due to the limitation of space, the proof is omitted. Next, some examples are provided to illustrate Algorithm 1 and Theorem 1.

Example 1 For comparison with the method proposed in [11], we consider the same stochastic system $G_1 = (X, \Sigma, \eta_G, x_0)$ as that in [11] (Example 3 in [11]), which is shown in Fig. 1, where $\Sigma_0 = \{a, b\}$, $\Sigma_f^i = \{\sigma_f\}$ and $\Gamma_i = \{b\}$. In [11], it has been proved that G_1 is not safe diagnosable by constructing the safe diagnoser.

In the following, we verify this result by constructing the safe verifier proposed in this paper (i.e., by using Algorithm 1 and Theorem 1).

According to Algorithm 1, we construct the non-fault automaton H_1 shown in Fig. 2 by Step 1 and the recognizer G_{r1} shown in Fig. 3 by Step 2.

Then we construct the safe verifier G_{v1} shown in Fig. 4 by Step 3.

Note that in Fig. 4, $\delta_v((0, N, 0), b) = (3, B, E)$,$\delta_v((3, B, E), b) = (3, B, E)$ and $\delta_v((2, F, 1), b) = (3, B, E)$, $\delta_v((3, B, E), b) = (3, B, E)$ where $(3, B, E) \in cl^{B\prime}_{recurrent}$. By Theorem 1, G_1 is not safe diagnosable, which coincides with the result in [11].

Example 2 Consider the stochastic system $G_2 = (X, \Sigma, \eta_G, x_0)$ shown in Fig. 5, which is the same example as that in [11] (Example 4 in [11]), where

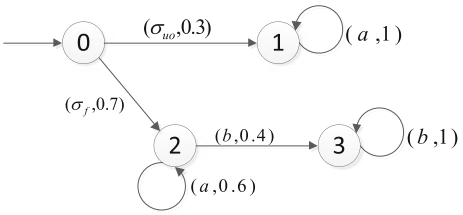

Fig. 1 Stochastic system G_1

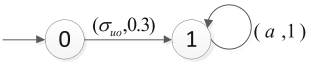

Fig. 2 Non-fault automaton H_1

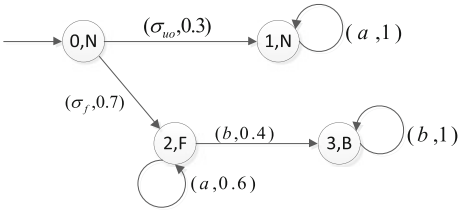

Fig. 3 Recognizer G_{r1}

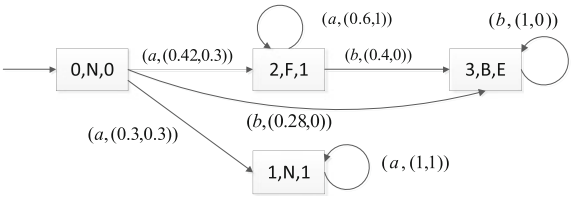

Fig. 4 Safe verifier G_{v1}

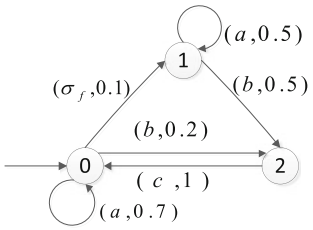

Fig. 5 System G_2

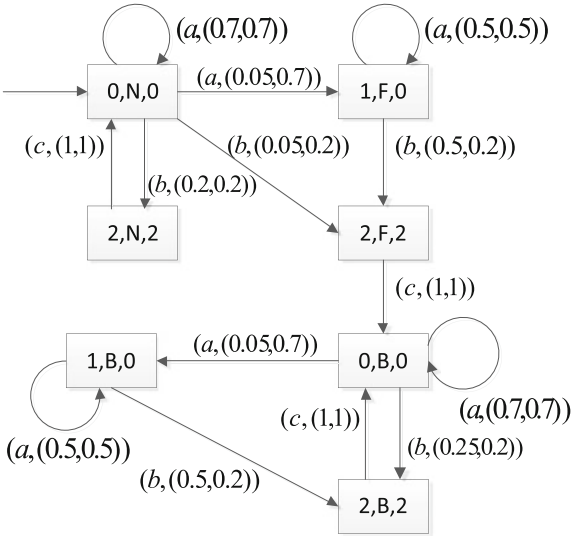

Fig. 6 Safe verifier G_{v2}

$\Sigma_0 = \{a, b, c\}$, $\Sigma_f^i = \{\sigma_f\}$ and $\Gamma_i = \{c\}$. In [11], it is proved that G_2 is safe diagnosable. Next, we verify the result by using the methods proposed in this paper.

Similar to Example 1, the safe verifier G_{v2} is constructed as that shown in Fig. 6. Note that G_{v2} satisfies the conditions of Theorem 1. Therefore, we conclude G_2 being safe diagnosable, which coincides with the result obtained in [11].

5 Conclusion

Motivated by the fact that the complexity of constructing safe diagnosers to deal with safe diagnosability of stochastic DESs in [11] is exponential, a new algorithm is proposed by constructing the safe verifier to realize safe diagnosis of stochastic DESs, which is polynomial-time in the number of states and events of the system.

Acknowledgements This work is supported by the National Natural Science Foundation (61673122, 61273118), the Public Welfare Research and Capacity Building Project of Guangdong Province (2015A030402006), the Provincial Major Program of Guangdong Province (2014KZDXM033), the Major Award Training Program of School of Computers of GDUT (2016PY01) of China.

References

1. Paoli A, Lafortune S (2005) Safe diagnosability for fault-tolerant supervision of discrete-event systems. IEEE Trans Autom Control 41(8):1335–1347
2. Qiu W, Kumar R (2006) Decentralized failure diagnosis of discrete event systems. IEEE Transaction on Systems, Man, and Cybernetics-part A: Systems and Humans 36(2):384–395
3. Sampath M, Sengupta R, Lafortune S, Sinnamohideen K, Teneketzis D (1995) Diagnosability of discrete-event systems. IEEE Trans Autom Control 40(9):1555–1575
4. Thorsley D, Teneketzis D (2005) Diagnosability of stochastic discrete-event systems. IEEE Trans Autom Control 50(4):476–492
5. Liu F, Qiu D, Xing H, Fan Z (2008) Decentralized diagnosis of stochastic discrete event systems. IEEE Trans Autom Control 53(2):535–546
6. Yoo T, Lafortune S (2002) Polynomial-time verification of diagnosability of partially observed discrete-event systems. IEEE Trans Autom Control 47(9):1491–1495
7. Chen J, Kumar R (2012) Polynomial test for stochastic diagnosability of discrete-event systems. IEEE Trans Autom Sci Eng 10(4):969–979
8. Luo M, Sun F, Li Y (2011) A polynomial algorithm for testing diagnosability of stochastic discrete event systems. In: 8th Asian Control Conference (ASCC). pp 1048–1053
9. Moreira MV, Jesus TC, Basilio JC (2011) Polynomial time verification of decentralized diagnosability of discrete event systems. IEEE Trans Autom Control 56(7):1679–1684
10. Liu F (2015) Safe Diagnosability of fuzzy discrete-event systems and a polynomial-time verification. IEEE Trans Fuzzy Syst 23(5):1534–1544
11. Liu F, Qiu D (2008) Safe diagnosability of stochastic discrete event systems. IEEE Trans Autom Control 53(5):1291–1296

An Example for Extension Strategy of Tourism Industry Integration in Guizhou Province

Qiaoxing Li and Hongyan Zhao

1 Introduction

Industrial integration is always the focus of industrial study at home and abroad. About the tourism industry integration, explored the strategic mechanism of development and innovation of tourism industry, and integrated the cultural tourism industry by using the APH method [1]; Zhang and Yue-Hua [2] believed that the integration of tourism with cultural industry can expand the value chain of cultural industry and the life cycle of cultural products; Wang and Xu [3] analyzed the relationship between tourism and agriculture in Beijing, and pointed out that the correlation both of them was gradually improved but their integration between them was still relatively low. Zhao and Yu [4] gave a review on the integration between the rural tourism industry and the culture and creation industry at home and abroad, and proposed some suggestion to explore Chinese tourism industry integration. On the other hand, Extenics is an original disciplinary subject, which utilized the formal and intelligent model to explore the laws and methods of innovation and then solve the contradiction problems [5]. Sun et al. [6] utilized the extension innovation method to analyze and transform the contradiction and then solved the problem of the urban power grid planning. Huang and Mai [7] established an extension evaluation model and then proposed the adjustment suggestion of forestry industry structure in order to promote the employment and the sustainable development of forestry in Yunnan.

Guizhou Province has rich resources of tourism, but the Karst landscape led the ecological environment be more fragile. The local tourism industry is small but it

Q. Li (✉) · H. Zhao
The Research Center of Development Strategy in Karst Region, Guizhou University, Guiyang, People's Republic of China
e-mail: qxli@gzu.edu.cn

Q. Li · H. Zhao
School of Management, Guizhou University, Guiyang, People's Republic of China

Z. Deng (ed.), *Proceedings of 2017 Chinese Intelligent Automation Conference*, Lecture Notes in Electrical Engineering 458,
https://doi.org/10.1007/978-981-10-6445-6_58

was developed quickly. On the other hand, the road traffic is convenient, and the industrial integration among the tourism industry, the historic culture industry and others has been developed but its scale is still in the initial stage. In order to promote the integration degree among the industries and increase the income and employment of local residents, we need to plan the local economy.

2 Extension Process of Health Tourism Industry Integration

According to the Ref. [8], we list the extension process of tourism industry integration in Guizhou Province under the big health background.

(1) Define a contradictory issue. According to the actual development need of local economy in Guizhou Province, we propose a total target material element B_0 and a condition matter-element l_0 of tourism industry integration in Guizhou province. Under the condition, the total target can not be realized, then the matter-element model $P = B_0 l_0$ of contradictory problem has been established.
(2) Do extension analysis on overall goal of matter-element B_0 and condition matter-element l_0 of the contradictory problems, which includes the analysis of divergence, correlation, implication, conjugate and scalability. For the specific process, the readers can see the Ref. [9].
(3) Obtain and evaluate the innovation ideas. Through the extension of matter elements, a variety of ideas generated, and then some solutions of the contradiction are obtained. We also should evaluate the creative ideas according to the current conditions of the local society, economy, technology and feasibility.
(4) According to the best creative idea, we draw up the specific planning proposal. The planning scheme can help decision-makers and implementers make better decisions to achieve more satisfactory results.
(5) Implement and improve the scheme. During the process of implement the best solution, the deficiencies may be found and corrected in time. Finally, further modifications are made to obtain the most satisfactory results.

3 Case Analysis

In Extenics, the basic-element B includes matter-element M, affair-element A and relationship-element R. It is expressed as an ordered three tuple $B = (N, c, v)$, which N represents the corresponding description objects, and c represents the features of the object N, and $v = c(N)$ represents the quantity of the features c. Apparently, $B = (N, c, v)$ is the one-dimensional basic-element. When object N has multiple features $c_1, c_2, \ldots, c_n$, and the corresponding values of each feature

are $v_1, v_2, \ldots, v_n$, respectively, we can define the multidimensional basic-element below:

$$B = \begin{bmatrix} N, & c_1 & v_1 \\ & c_2 & v_2 \\ & \vdots & \vdots \\ & c_n & v_n \end{bmatrix} = (N, C, V), \text{or } B = \begin{bmatrix} N & c_1 & \cdots & c_n \\ & v_1 & \cdots & v_n \end{bmatrix},$$

and B is n-dimensional basic element [5].

According to the 2030 program of Health China and the 13th Five-Year Plan of Guizhou province, the government proposed to integrate the tourism industry in order to improve the level of regional economy. According to the tourism development plan of China and Guizhou province, we establish the matter-element B_0 of the regional total target and the matter-element l_0 of the regional conditions as follows.

$$B_0 = \begin{bmatrix} \textit{Tourism Industry } N, & \textit{The number of fused industries } c_1, & 4 \\ & \textit{Resource development level } c_2, & \textit{perfect} \\ & \textit{Number of industry practitioners } c_3, & 500 \end{bmatrix}$$

and $l_0 = \begin{bmatrix} \textit{An ancient town } D, & \textit{GDP } d_1, & 20 \textit{ billion} \\ & \textit{Location } d_2, & \textit{preferably} \\ & \textit{Traffic Conditions } d_3, & \textit{general} \\ & \textit{Service Level } d_4, & \textit{lower} \\ & \textit{Policy Guidance } d_5, & \textit{support} \end{bmatrix}$.

Obviously, the tourism industry can not achieve the target under the current conditions, and it forms the contradiction between them. Therefore, we analyze the contradiction in order to achieve the overall goal.

3.1 Extension Analysis of Matter-Element

Extension analysis on total matter-element B_0 and condition matter-element l_0 is to conduct the analysis of divergence, correlation, conjugate and implication, and then we can obtained the matter-element of specific squired industries by improving the condition matter-element. The discussed process is bellow:

3.1.1 Divergence Analysis of Target Matter-Element and Condition One

According to the Guizhou global tourism policy, the local government decided to construct the integrated development model of Travel +, i.e., to integrate the

tourism industry with modern leisure agriculture industry, culture one, health and sport one, and so on. The actions may boost the rapid development of culture and tourism industry which is the core of modern service industry. According to the actual situation, the researchers should investigate the local industries that can be integrated with the tourism industry, and they mainly include the culture industry, leisure agriculture, health care industry, mountain sports and other health-related industries. Therefore, in accordance with the current develop policy of the tourism industry and the actual development situation in this area, we can assign the value v1 = 4 (i.e., there has four industries of culture, leisure agriculture, health industry and mountain sports) for c_1, and get the value range of c_2 is {perfect, good, general, poor, worst}. The value of characteristic c_3 can be obtained according to the current employment. Since we utilized one specific area as a case, the condition matter-element (see l_0) is set according to local situations.

3.1.2 Correlation Analysis on the Matter-Elements of Target and Condition

By using the correlation analysis, the present value of department scale c_4 for the tourism can be set as $c_4 \in \{big, medium, small\}$ (note: the characteristic value can be broken down and it is the same below). When the tourism industry N_1 is integrated with other industries, the new industries c_5 can be generated. The new integrated industry includes the cultural tourism N_2, agricultural tourism N_3, health tourism N_4, mountain sports tourism N_5, and so on.

3.1.3 Conjugate Analysis on the Matter-Elements of Target and Condition

By using the conjugate analysis, the well-known degree c_6 of the industries at home and abroad can be obtained and its value v_6 is within {high, medium, low}; and the personal quality c_7 of the industry employers, which value v_7 is {high, middle, low}; and the regional economy influence c_8 of the industry, which value v_8 is {big, general, small}; and the development prospect c_9, also namely profitability, of the tourism industry, which value v_9 is {strong, medium, low}. On the other hand, we also should greatly review the impact of integration and development of the tourism industry on the ecological environment in the region, and reasonably control the visitor number in order to promote the sustainable development and management of the tourism industry.

3.1.4 Contain Analysis on Matter-Elements

The internal motive force of the integrated development of tourism industry is to increase the consumer demand. When consumers put forward higher requirement

for the local services and infrastructure, the development of local tourism industry may be greatly improved. Therefore, the contain analysis on the industry may induce the consumer demand c10, and its value is {high, general, low}. Then a lot of measures are used to stimulate the consumption demand, such as food, shelter, transportation, tourism and consumption ability, and to actively improve the quality of reception facilities and services, and explore the specialty products.

3.1.5 Expansion Analysis on Matter-Elements

The expansion of matter elements includes the additive, integrative and divisible qualities of the thing and its characteristics and quantities. According to the additive quality of matter-element, different industries can be integrated. Many forms of different industries can be achieved and some of them may get better results, for example, to create more economic, environmental and social benefits. Through the expansion analysis on the target and condition matter-elements, we can get the expected object matter-element (see Table 1) as follow:

3.2 Conjugate Analysis of Environmental Resources

For the point view of physical quality of things, the real part of the region includes land resources, buildings, residents, fresh air, and so on. On the other hand, the topography of this area belongs to the hilly valley basin, which is about 1100–1300 m above the sea level, and the climate is subtropical monsoon humid, where is not very cold in winter and not very heat in summer and has fresh air. For the point view of imaginary quality of things, the region has its specific nature landscape and

Table 1 Industrial expected object matter-elements

	c1	c2	c3	c4	c5	c6	c7	c8	c9	c10
B1	4	preferably	100	bigger	Culture, agriculture, health, mountain	higher	higher	higher	high	higher
B2	1	preferably	60	bigger	Cultural tourism	higher	higher	higher	high	higher
B3	1	preferably	80	bigger	Agricultural tourism	higher	higher	higher	high	higher
B4	1	preferably	60	bigger	Wellness tourism	higher	higher	higher	high	higher
B5	1	preferably	50	bigger	Mountain tourism	higher	higher	higher	high	higher

local customs and practices. There are a lot of festivals in this region in the first month of every year, such as dragon dance, jump lanterns, Miao jump field, as well as other folk activities. It also has a unique religious culture and a lot of tourism resources.

For the point view of system, the region is an old town in history and culture in Guizhou Province. It is very convenient at the city traffic, such as buses and passenger car. However, it is relative poor at the out-province traffic. For the point view of dynamic, the tourism industry in this area developed rapidly, which greatly improved some industries, such as leisure agriculture, culture and others. However, the integration degree among these industries is not very big and it is still at the initial stage of development, and its popularity is not also big in China. So it is necessary to further promote to integrate tourism industry with other industries. For the point view of opposition, we should pay more attention to protect the environmental resources while exploring local tourism resources, and decreased to damage the ecological environment.

3.3 Generate the Creative Ideas

Doing the extension transformation to the matter-element of industrial target can generate the creative ideas of extension, and different transformation can generate different ideas, so we can adjust it according to specific conditions. However, the generated creation scheme to transform the matter-element is not always feasible, and it needs to be evaluated and selected. Because it is limited to the length of this article, we does not discussed in detail.

4 Conclusions

By using extension method, we got a formal approach to integrate the tourism industry with others in Guizhou province. During the development process of the tourism industry integration, we took into account the local eco-environment and the reasonable economy development; secondly, we also selected the appropriate industry to integrate with tourism according to the local policy; finally, the method also took into account to create more jobs by the industrial integration and paid more attention to improve the living standard of local residents. By using the extension planning, the idea of industrial integration may be more clarified. The method considers both qualitative and quantitative approaches, and provides a good direction to promote the integration of tourism industry in Guizhou province.

Acknowledgements The work is supported by Guizhou Soft Science Project (No. [2016]1532-1 of Qiankehe Foundation) and The Humanities Society and Science Research Project of colleges of education department in Guizhou Province (2016ssd07).

References

1. Xiao Y (2013) Development strategy of tourism industry based on innovation mechanism. Proc Int Conf Inform Eng Appl 217:745–752
2. Zhang M, Yue-Hua JI (2014) The tourism industry and cultural industry integration research on implementation mechanism and path of development-take Chengde City as an example. Econ Res Guide 30:223–227
3. Wang Q and Xu L (2013) Research on the integration of tourism and agriculture in Beijing based on the perspective of industrial correlation. Tourism Tribune 28(8):102–110 (in Chinese)
4. Zhao H, Yu J (2015) Research on the fusion development of rural tourism and cultural creative industries under the new normal. Econ Issue 4:50–55 (in Chinese)
5. Yang C, Cai W (2014) Extenics. Science Press, Beijing (in Chinese)
6. Sun X, Yang L, Wang Z (2015) Extension analysis and transformation of contradictory problems in urban power grid planning. Electr Meas Instrum 52(8):23–29 (in Chinese)
7. Huang Y, Mai Q (2015) Evaluation of forestry sustainable development in Yunnan Province Based on extension method. For Resour Manage 5:139–144 (in Chinese)
8. Yang C, Zhang Y (2001) Planning research based on extension method. Ind Eng 4(2):29–33 (in Chinese)
9. Li Q, Liu S, Dang Y (2006) Extension analysis of industrial structure adjustment of urban and rural economy in China. J Harbin Inst Technol, 38(7):1205–1208 (in Chinese)

An Evolutionary Algorithm for Optimal Tracking Gate Based on Hybrid Encoding

Han Zhao, Cheng Zhang and Jiajun Lin

1 Introduction

Tracking gate is the first step of data association. Appropriate tracking gate is helpful to reduce the number of false correlations and improve the performance of the target tracking algorithm. Data association algorithms has been a topic of extensive study, but there are few studies on tracking gate. Literature review reveals that most related research on tracking gate focuses much more on gate size than the shapes. Several adaptive design approaches have been proposed in [1–4]. In this paper, hybrid coding genetic algorithm is used to the tracking gate parameters optimization, without dependency of prior knowledge.

2 Overview of Tacking Algorithm

2.1 Target Motion Model

This research focuses on maneuvering target tracking, accordingly, Jerk model is adopted. The components of state vector $X = [x, \dot{x}, \ddot{x}, \dddot{x}]'$, denote respectively the position, velocity, acceleration, and jerk of the target [5]. The model fully considers the jerk of the target, which can better reflect the mobility of the target.

$$X(k+1) = F(k+1,\, k)X(k) + U(k) \tag{2.1}$$

H. Zhao (✉) · C. Zhang · J. Lin
School of Information Science and Engineering, East China University of Science and Technology, 286 No. 130 Meilong Road, Shanghai 200237, Xuhui District, China
e-mail: lotus@ecust.edu.cn

Z. Deng (ed.), *Proceedings of 2017 Chinese Intelligent Automation Conference*, Lecture Notes in Electrical Engineering 458,
https://doi.org/10.1007/978-981-10-6445-6_59

The measurement function is:

$$Z_x(k) = H(k)X(k) + W(k) \tag{2.2}$$

where $H(k) = [1, 0, 0, 0]$ is the system measurement matrix, and W(k) is the measurement noise vector, assumed uncorrelated to the process noise.

2.2 Kalman Filtering and Data Association

The Kalman filtering [6] and probabilistic data association algorithm (PDA) [7, 8] are adopted. The prediction covariance and the observation vector can be described as follow:

$$P(k|k-1) = F(k-1)P_x(k-1|k-1)F^T(k-1) + Q(k-1) \tag{2.3}$$

$$\hat{Z}(k|k-1) = H(k-1)\hat{X}(k|k-1) \tag{2.4}$$

The Kalman gain matrix is given by (2.5), while $S_i(k) = H(k)P(k|k-1)H^T(k) + R(k)$.

$$W_{k|k-1} = P_{k|k-1}H^T_{k|k-1}S^{-1}_{k|k-1} \tag{2.5}$$

The estimate function of i-th candidate measurement is:

$$\hat{X}_i(k|k) = \hat{X}(k|k-1) + K_i(k)V_i(k) \tag{2.6}$$

Assuming that there are m_k candidate measurements are fall into the gate, after all candidates weighted and association probabilities $\beta_i(\mathrm{k})$ are summed together, the final updated state function can be described as follows:

$$\hat{X}(k|k) = \sum_{i=0}^{m_k} \beta_i(\mathrm{k})\hat{X}_i(k|k) \tag{2.7}$$

where $V(k) = \sum_{i=1}^{m_k} \beta_i(\mathrm{k})V_i(k)$ is combined innovation, $\beta_i(\mathrm{k})$ can be defined as: $\beta_i(\mathrm{k}) \triangleq \Pr\{\theta_i(\mathrm{k})|Z^k\}$, where $\theta_i(\mathrm{k}) \triangleq \{Z_i(k)\}$, Z^k is the set of candidate measurements up to time k.

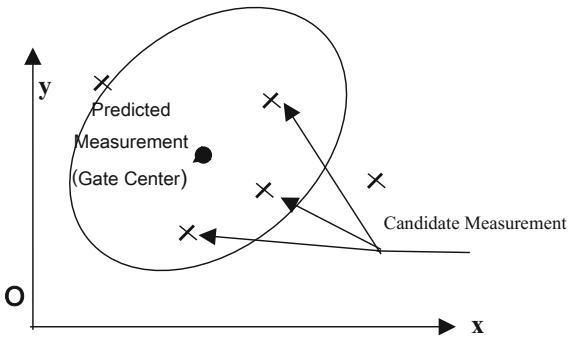

Fig. 1 Elliptical gate schematic diagram

2.3 Tracking Gate

The tracking gate is an area by a center point of predicted measurement. It is used to reduce the number of candidate measurements to be considered for further data association [9]. General tracking gates include elliptical gate, rectangular gate and sector gate etc. [10]. If $Z_i(k)$ the i-th measurement at time k meets the following criteria: $\mathrm{D}\left(Z_i(k), \hat{Z}_j(k|k-1)\right) \leq K_G$, it will be candidated. Where $\hat{Z}_j(k|k-1)$ is the predicted measurement and the gate center point. D is distance function, K_G is the tracking gate constant. Elliptical gate as Fig. 1. The gate size can be tuned by constant K_G, hence K_G can be take as the optimation parameter.

3 Gate Optimization Based on Genetic Algorithm

3.1 Hybrid Encoding

The parameters of tracking gate include shape and size, which are belonged to different data types. Hybrid encoding scheme is applied to ensure both precision and efficiency of algorithm. The gate shapes are represented in binary and the size decoded by float encoding. The individuals contain two components, i.e. $G = [G_S, G_L]$. Where G_S represents shapes, while G_L reflects size. Only rectangular gate and elliptical gate are discussed in this work, set "0" and "1" represent them respectively. Similarly, gate size relates to tracking gate constant which decoded by float encoding [11].

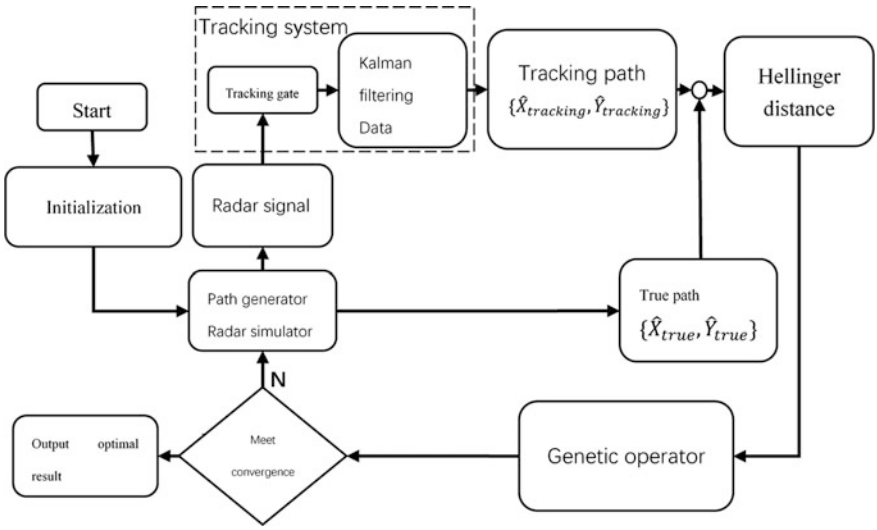

Fig. 2 Flow chart of tracking gate optimization based on hybrid coding genetic algorithm

3.2 Algorithm Description

Obviously, the hybrid encoding genetic algorithm and the tracking system constitute a closed-loop optimization system. Genetic algorithm is adopted for one tache optimization of tracking system, and its optimization objective represents whole system's. The fitness value for genetic operator is more than an algebraic value simply get by arithmetic operations, but obtained by the error of the dynamics tracking system. Therefore, multi-objective optimization problem can be transformed into single-objective problem. This will provide reference for further research of tracking optimization (Fig. 2).

3.3 Hellinger Distance and Fitness Function

There are several metrics currently used to evaluate performance of tracking system, such as position root mean square error (PRMSE), Mahalanobis distance, Hellinger distance, etc. It is difficult to distinguish the true path and the tracking path using PRMSE when the state estimations are same with different uncertainties. Hellinger distance takes more account of covariance to overcome it and has higher appropriate accuracy and sensitivity. It is selected to evaluate the error of the tracking system.

There are two probability distribution $m = N(m, \sum m)$, $n = N(n, \sum n)$ obey Gaussian distribution, Hellinger distance between them is defined as following formula

$$d_H(m, n) = 1 - \sqrt{\frac{\sqrt{\det(\sum m \sum n)}}{\det[0.5(\sum m + \sum n)]}} \exp(\delta) \tag{3.1}$$

Hellinger distance ranging from 0 to 1, which means when the two probability distributions are exactly the same, Hellinger distance get the minimum value of 0. On the contrary, if two sets have no overlapping regions, 1 can be defined as maximum Hellinger distance.

In the tracking system, $m = N(m, \sum m)$ can be regarded as true state vector $\{\hat{X}_{true}(k), \hat{Y}_{true}(k)\}$, where $\sum m$ is uncertainty of true state vector, which can be presented by Cramér-Rao lower bounds $\{P_{true|x}(k), P_{true|y}(k)\}$. $n = N(n, \sum n)$ can be regarded as the estimated state vectors $\{\hat{X}_{tracking|G}(k), \hat{Y}_{tracking|G}(k)\}$ where $\sum n$ represents corresponded error covariance matrix $\{P_{tracking|x,G}(k), P_{tracking|y,G}(k)\}$. Hellinger distance between true path and tracking path can be represented as follows:

$$\begin{aligned} &d_{H|G}\left(\{\hat{X}_{true}(k), \hat{Y}_{true}(k)\}, \{\hat{X}_{tracking|G}(k), \hat{Y}_{tracking|G}(k)\}\right) \\ &= 1 - \sqrt{\frac{\sqrt{\det\left(\{P_{true|x}(k), P_{true|y}(k)\}\{P_{tracking|x,G}(k), P_{tracking|y,G}(k)\}\right)}}{\det\left[0.5\left(\{P_{true|x}(k), P_{true|y}(k)\} + \{P_{tracking|x,G}(k), P_{tracking|y,G}(k)\}\right)\right]}} \exp(\delta) \end{aligned} \tag{3.2}$$

Fitness function is:

$$f_{fitness}(G) = 100\left(1 - \frac{\sum_{k=0}^{t} d_{H|G}\left(\{\hat{X}_{true}(k), \hat{Y}_{true}(k)\}, \{\hat{X}_{tracking|G}(k), \hat{Y}_{tracking|G}(k)\}\right)}{t}\right)^2 \tag{3.3}$$

Accordingly, the optimal tracking gate problem can be transformed into:

$$G = arg_G \max f_{fitness}(G) \tag{3.4}$$

$$\text{s.t. } G = [G_s, G_L]\, G_s \in \{0, 1\}\, B_L \le G_L \le B_U\, G_L, B_L, B_U \in R$$

3.4 Genetic Operator

The best individual may be lost at any generation. This can be overcome by employing a heuristic termed elitist selection, which simply always retains the best individual in the population. The population subjected to roulette wheel selection. With this select operator, each chromosome is assigned a probability of being copied into the next generation that is proportional to its fitness relative to all other individual in the population. Successive trials are conducted in which an individual is selected, until all available positions are filled [12].

Two different crossover operators are applied, the bit crossover for binary encoding and the nonuniform arithmetical crossover for float encoding. Similarly, two different encodings also employ the bit mutation and the nonuniform mutation respectively.

4 Simulation Studies

The simulation studies are based on highly maneuvering single target tracking. The initial state of the target is [4.92 km, −79.4 m/s, 0, 0; 0.891 km, 94.6 m/s, 0, 0]. Let an initial population of 20 individuals be selected with the probabilities of crossover and mutation ($P_{crossover} = 0.6\, and\, P_{mutate} = 0.01$), respectively. During simulation, the iteration steps are set as 114, sampling interval is 1 s, and the number of simulation is 50. Setting the detection probability as 0.98, the false alarm is generated randomly and uniformly in an area centered on the true measurement. The total number of false alarm is $n_c = \lambda A_v$, λ is the clutter density, A_v is the square of the clutter area. Two scenarios' simulation is given in this research, "light" and "heavy" clutter, with $\lambda = 2$ and $\lambda = 20$ respectively.

Table 1 Statistics table of tracking gate parameter and tracking accuracy

Sparse clutter environment		Dense clutter environment	
Gate parameter	Hellinger distance	Gate parameter	Hellinger distance
Elliptical gate $K_G = 4.217$	0.1782	Elliptical gate $K_G = 6.145$	0.2089
Rectangle gate $K_G = 4.217$	0.1755	Rectangle gate $K_G = 6.145$	0.2024
Elliptical gate $K_G = 4$	0.1790	Elliptical gate $K_G = 7$	0.2059
Elliptical gate $K_G = 5$	0.1776	Elliptical gate $K_G = 5$	0.2129

4.1 Simulation Results and Analysis

With "light" clutter, the parameter converges to 014.217, which means choosing the elliptic gate with gating constant of 4.217 is the optimal result. The Hellinger distance is 0.1708. With "heavy" clutter, the parameter converges to 016.145, optimal tracking gate is elliptic gate too, with gating constant of 6.145 and Hellinger distance is 0.2008.

When the detection probability is given, due to the clutter density increased, the gate size also need to enlarge, the simulation result is in agreement with it. On the other hand, if the tracking gate size is excessively enlarged, it will lead to more false alarms and decreased tracking accuracy. Table 1 shows corresponding tracking accuracy in different cluttered environments and with different tracking gate parameters. Consequently, the proposed tracking gate optimization can ensure high tracking accuracy.

4.2 Discussion About Adaptability of Tracking Gate Optimization

In practical, the disturbances are variable. In this section, simulation studies to test the adaptability of variable disturbances. Apply the optimal result which obtained with clutter density of 20 to the scenario with different clutter density. There is only

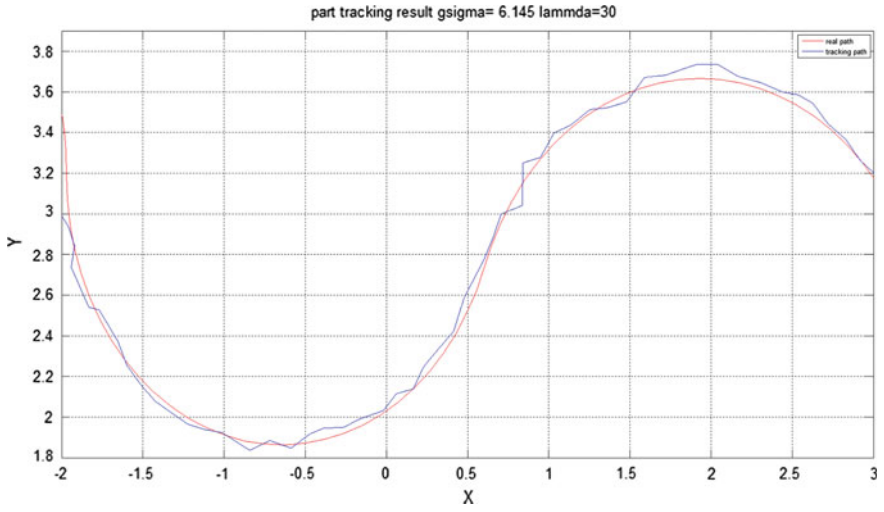

Fig. 3 Tracking with clutter density of 30

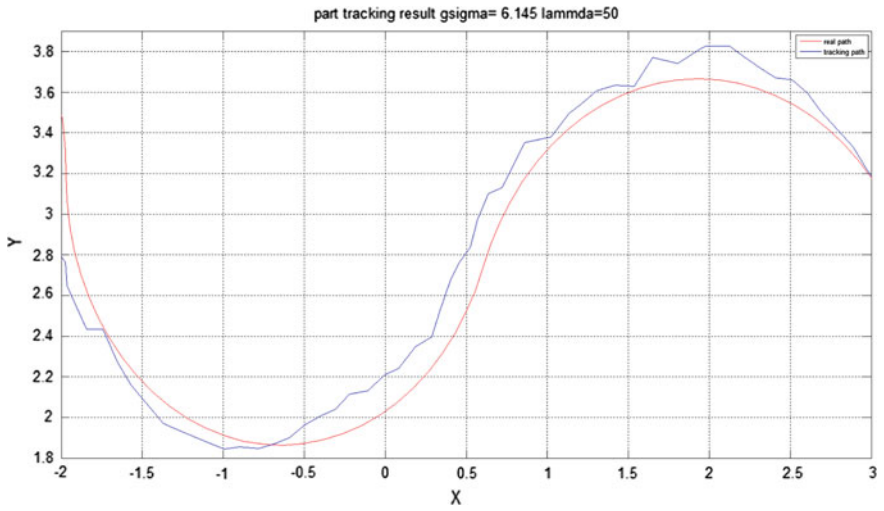

Fig. 4 Tracking with clutter density of 50

a little inconsistency between the truth path and the tracking path with clutter density 30, shown as Fig. 3. With the clutter density increase to 50, obvious deviation is appeared, especially in high maneuvering such as the target makes a bend, shown as Fig. 4.

5 Conclusion

A hybrid encoding genetic algorithm is proposed for the tracking gate optimization in this work. Simulation proved that this algorithm presented prospective tracking performance. Also, certain adaptability can assure during disturbances.

There are still many other factors correlated to the tracking performance, from fine-grain perspective, such as maneuvering frequencies, measurement noise, process noise etc., from coarse-grained viewpoint, there are data association algorithms, maneuvering models, filtering algorithms etc. Obviously, further research can focus on other tracking optimization. In addition, the optimal value is off-line obtained of single target in this paper. How to achieve real-time optimization of multi-target tracking system is also another issue need to be explored.

References

1. Guo D, Sanchuang Y (2012) Study on the relevant gates in track pretreatment. doi:10.16652/j.issn.1004-373x.2012.13.034 (in Chinese)
2. Biao J, Bo J, Tao S et al (2014) A method to design adaptive correlation gate for maneuvering target tracking in clutter. doi:10.7652/xjtub201410006 (in Chinese)
3. Minghui W, Zhisheng Y, Chunrong Z et al (2000) A performance optimized tracking gate algorithm. Acta Electr sinaca 28:13–15 (in Chinese)
4. Huihui M (2017) An improved tracking gate for reverse solution based on performance evaluation function. doi:10.3969/j.issn.2095-5839.2017.02.009 (in Chinese)
5. Kishore M, Pravas R (1997) A jerk model for tracking highly maneuvering targets. IEEE Trans Aerosp Electron Syst. doi:10.1109/7.624345
6. Charles k, Guantong C (2009) Kalman filtering. In: Springer series in information sciences. Springer, Berlin
7. Grosche J (2013) Tracking and sensor data fusion. Springer, Berlin
8. Grewal MS, Andrews AP (2008) Kalman filter theory and practice using matlab, 3rd edn. Wiley, New York, pp 283–284
9. Jie Z, Jiajun L, Xiaowei C (2006) The Effect of tracking gate on the performance of multi—target tracking system. J East China Univ Sci Technol (Nature Science Edition). doi:10.14135/j.cnki.1006-3080.2006.12.022 (in Chinese)
10. Xuezhi W, Challa S, Evans R (2002) Gating techniques for maneuvering target tracking in clutter. IEEE Trans Aerosp Electron Syst. doi:10.1109/taes.2002.1039426
11 Yinzhen Y, Jinyin F, Huanghong W et al (2017) Evolutionary polynomial regression based modelling of clay compressibility using an enhanced hybrid real-coded genetic algorithm. doi:10.1016/j.enggeo.2016.06.016
12. David B (1994) An introduction to simulated evolutionary optimization. IEEE Trans Neural Network. doi:10.1109/72.265956

Study on Extension Design of Business Model

Qiaoxing Li and Tunhua Jiang

1 Introduction

At the era of Internet, the enterprises may often change their strategies. In response to the diversification, complication and net of business, the enterprises are forced to change their business model in order to keep their sustainable competition advantages [1]. The famous manage specialist named Peter Drucker once viewed that the business competition is no longer to get a pure service or product, and however, the business model may be more important in the future.

Scholars have made abundant achievements to research on the design and innovation of business model. Most of them utilized the empirical description and qualitative form to study it [1–3]. These patterns established the basic concept and theory system of business model, and it also gave rise to a lack of practical and reliable judgment, then the innovation and design methods are difficult to be a tool for easy operation. Extension design method is based on the basic principle of Extenics and it is a both qualitative and quantitative design method. Extenics avoids the issue that mathematical modeling often abandons the real background of problems, and the most current design methods are lack to be formalized and quantified, so Extenics may improve the artificial intelligence [4–7]. On the basis of the theories of business model and extension design, we proposed the formalized and quantified method of extension design of business model, which can improve computer decision efficiency of business model in the near future. At last, an example of community hospital showed the process of business model design.

Q. Li (✉) · T. Jiang
The Research Center of Development Strategy in Karst Region, Guizhou University, Guiyang, People's Republic of China
e-mail: qxli@gzu.edu.cn

Q. Li · T. Jiang
School of Management, Guizhou University, Guiyang, People's Republic of China

Z. Deng (ed.), *Proceedings of 2017 Chinese Intelligent Automation Conference*, Lecture Notes in Electrical Engineering 458,
https://doi.org/10.1007/978-981-10-6445-6_60

2 The Extension Design of Business Model

2.1 Build Extension Model of Business Model

In Extenics, the object N, characteristic c as well as the value v of c about N can order a triple $R = (N, c, v)$ and it called one-dimensional basic-element (including matter-element M, Event-element A and relationship-element R) [4]. In particular, when the object has multiple characteristics and the corresponding values, we get n-dimensional Basic-element [4].

According to the nine elements of business model, we adopts the matter-element R to describe the business model of enterprise N and its partial matter-element R_i $(i = 1, 2, \ldots, 9)$ of business model as follows:

$$R = \begin{bmatrix} N, & \text{products and services } c_1, & v_1 \\ & \text{customer groups } c_2, & v_2 \\ & \text{resource allocation } c_3, & v_3 \\ & \text{core resources } c_4, & v_4 \\ & \text{cost structure } c_5, & v_5 \\ & \text{source of income } c_6, & v_6 \\ & \text{customer relations } c_7, & v_7 \\ & \text{the channel pathway } c_8, & v_8 \\ & \text{partner cooperation } c_9, & v_9 \end{bmatrix} = \begin{bmatrix} R_1 \\ R_2 \\ R_3 \\ R_4 \\ R_5 \\ R_6 \\ R_7 \\ R_8 \\ R_9 \end{bmatrix}$$

When the value of Matter-element R, it is the Compound Basic-element. For example, the value of products and services c_1 of enterprise N is the product O with function v_{01} can be expressed as

$$\mathrm{R}_1 = (N, \text{product and service } c_1, (\text{product, function } c_{01}, v_{01}))$$

The characteristic value of above the matter-element R can be assigned according to the current situation of the enterprise.

Business model design and innovation has been the necessary management means to obtain core of competitive ability. Then we get the basic element $\mathrm{G} = (\text{Enhance, Dominant object, Core competence})$ of general goal of the enterprise.

Supposing that the enterprise cannot improve the core competitiveness under the current business model, which forms an incompatible problem, then we get the extension model of the contradictory problem: $\mathrm{P} = \mathrm{G} \uparrow \mathrm{R}$, which means that G can not be achieved under the condition R. By the means of extended analysis on goal matter-element G, i.e., extension innovation of business model, we obtain the new business model, which may make the controversial issue transform to the compatible problem, then it can be solved.

2.2 Extension Analysis of Basic Element

The extension analysis is to carry out the analysis, which includes the divergence relevance, implication and scalability, on the basic element from different angle. The technology may extend the element to be many ones, and the decision-makers can constantly adjust the basic element to enrich its features and values, so many methods that may be possible to solve contradiction problems are provided. Then, we firstly utilized the extension analysis to analyze the goal matter-element of enterprise and the part matter-element of business model, and get the schemes to realize the goal of enterprises and extension value set of characteristics below:

$$V_E(v_i) = \{v_{i1}, v_{i2}, \ldots, v_{ij}) \ (i = 1, 2, \ldots, 9)$$

.

(1) Implication Analysis

The implication analysis of matter-element aims to consider another goal matter-element and make the original goal to be realized when the goal cannot be achieved under the original conditions [4]. Supposing that there are two basic elements B_1 and B_2, and that B_2 should be realized when B_1 is achieved, then we called that B_1 implicates B_2 and denoted it as $B_1 \Rightarrow B_2$ [4].

The basic way to enhance the core competition ability of enterprises is to increase the profit margin and expand the core resources of enterprises. The cost and income of enterprises is an important part of profit margin, and the enterprises may increase its profitability by reducing costs and expanding incomes. To expand the enterprise incomes can be achieved by the approach to enlarge the consumers. When we use implication analysis to enlarge the consumer group, the approaches to improve customer satisfaction, increase the sales of products and services as well as optimize sales channels are usually considered. Under the condition of limited resources of enterprises, to enhance the cooperation among enterprises is a highly

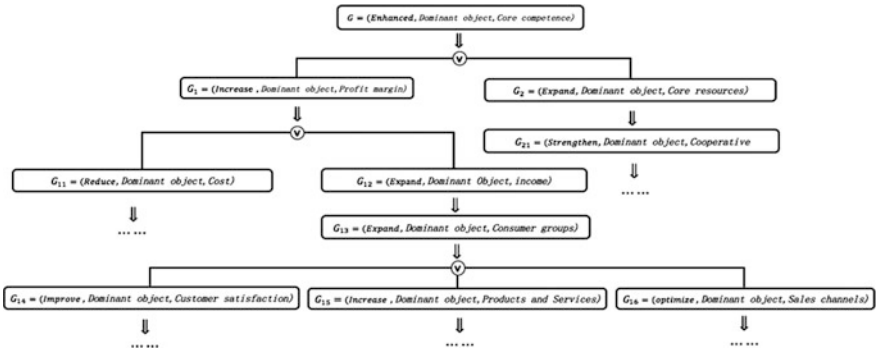

Fig. 1 Implication analysis

efficient and convenient path to expand the core resources of enterprises. The implication analysis is shown in Fig. 1.

(2) Correlation Analysis

In order to let people clearly understand the relation and function among things in a formal way, we analyze the relationship between the basic elements according to the relevance quality of matter, affair and relationship [4]. That is to say, for the given two basic element sets $\{B_1\}$ and $\{B_2\}$, if the element $B_1 \in \{B_1\}$ holds, there exists at least one $B_2 \in \{B_2\}$ which makes B_1 be correspond with B_2, then $\{B_1\}$ and $\{B_2\}$ are related with each other and we denote it as $\{B_1\} \sim \{B_2\}$ [4].

In order to improve customer satisfaction, we should meet their consumption demand, and get t element $G_{17} = (\text{Meet}, \text{Dominant object}, \text{Customer Demand})$. However, the customer demand is varied and it includes product price t_{18}, product function t_{19}, service quality t_{20}, and so on. Through the market survey, we get the following matter-element $G_{18} = (\text{Demand}, t_{18}, w_{18})$, $G_{19} = (\text{Demand}, t_{19}, w_{19})$ and $G_{20} = (\text{Demand}, t_{20}, w_{20})$.

Because the customer demand is related with the price, function and cost of products, we can get the conditional matter-element according to the existing condition of enterprise below: $R_{01} = (\text{Product O}, \text{Function}\, c_{01}, v_{10})$, $R_{02} = (\text{O}, \text{Price}\, c_{02}, v_{02})$, $R_{03} = (\text{O}, \text{Cost}\, c_{03}, v_{03})$.

Obviously, the products and services R_1 of the enterprise is restricted by the allocation efficiency t_3 of the core resources R_4 of enterprise. And the business partner R_9 is a highly effective supplement for enterprise resources. Then the pointed enterprise can expand the core resources R_4 if it forms a strategic alliance with the relevant enterprises. At the same time, R_1 is also related with R_2 of corporate customer. Under the traditional economy, the enterprises often promote the functions and values of their products through the technological innovation, and the customers evaluated and selected their products during the utilization. In this mode, the sovereignty of producers occupies a dominant position. However, Internet economy makes the communication between customers and enterprises become easier and closer, and the products and services of enterprises are more in line with customer demands, and it provides a more convenient path to meet the personal demand of costumers.

(3) Expanded Analysis

The combination, decomposition and enlargement possibility of matter, affair and relationship can provide a new way to solve the contradiction problems [4].

The function of any products has the diversity, and the different customer demand leads to the different utilization of the product function. On the basis of decomposition analysis of Extenics, we analyze the product function R_{01} and get

$R_{01} = (O, \text{Function } c_{01}, v_{01}) \,//\, \{(O, c_{01}, v_{011}), (O, c_{01}, v_{012}), \ldots, (O, c_{01}, v_{01j})\} = \{R_{01}\}$, where v_{01j} represents the jth function of product O.

Similarly, according to the customer group R_2, cost structure R_5 and income source R_6, we do the decomposition analysis and get the elements of business model, which are represented as $\{R_{20}\}, \{R_{50}\}, \{R_{60}\}$, and so on, where $\{R_{i0}\} = \{(N, c_i, v_{0i1}), (N, c_i, v_{0i2}), \ldots, (N, c_i, v_{0ij})\}$ and v_{0ij} represents the element value of the enterprise business model, and $\sum_{p=1}^{j} v_{0ip} = v_i$.

(4) Divergence Analysis

By using the divergent quality of matter, affair and relation, we can expand many basic-element sets, which may provide more approaches to solve a problem or analyze the object. The merit of this method can formalize the process of creative thinking and it has some forms, such one thing with more characters, one character with more values, and one character with more things, etc.

According to one character with more values, we do the divergence analysis for the partial matter-element R_i of business model and get ($\dashv$ represents divergence):

$$R_i \dashv \{R_{i1}, R_{i2}, R_{i3}, \ldots, R_{in}\}; \quad (i = 1, 2, \ldots, 9).$$

where $R_{ij} = (N, c_i, v_{ij})$ $(j = 1, 2, \ldots, n)$, and v_{ij} represents the value of the jth characteristic of R_i, and the value includes baby, young, middle-aged, old, men, women, etc.

According to the definition of characteristic element in Extenics, we denote the partial matter-element sets of business model as extension value-sets of characteristic element which is $V_E(v_i) = \{v_{i1}, v_{i2}, \ldots, v_{ij})$ $(i = 1, 2, \ldots, 9)$, for example, $V_E(v_2) = \{\text{babies, children, middle aged, older, males, females, } \ldots\}$.

It should be pointed that it is not the only for the process of above expansion analysis. We only provide a extension thought and our readers can do further adjustment according to the actual situation.

2.3 *Extension Transformation of Business Model*

The tool to solve the contradiction problem is the extension transform. By using a certain extension transform, we can make the unknown issue be a known one, and the unfeasible problem be a feasible one, and the false proposition be a true one, and so on [4]. We do a series of related extension transformation to the extension analysis results of the partial matter-elements and may get many new business models, and then we evaluate them and can select the final design scheme.

Suppose that there has a object R and we do a transformation to R, then we get another similar object R_1 or object set $\{R_1, R_2, \ldots, R_n\}$, which can be referred as

$TR = R_1$ or $TR = \{R_1, R_2, R_3, \ldots, R_n\}$ [4]. The extension transformation has many kinds of basic forms below:

(1) Displacement Transformation:

$T_1R = R'$, which is to replace one or more elements of basic element and the new one can be obtained [4].

During the innovation process of business model design, we can obtain a variety of innovative ideas by replacing the element values of business model. The formal representation is described below:

For the ith partial matter-element $R_i = (N, c_i, v_i)$ of business model, we take $R_{ij} = (N, c_i, v_{ij})$ and do $T_1R_i = R_{ij}$ $(i = 1, 2, \ldots, 9)$, where $v_{ij} \in V_E(v_i)$. For example, $T_1(N, \text{The Channel pathway } c_8, \text{Offline retail }) = (\text{N}, c_8, \text{Online retail})$. That is to say, the enterprise do the displacement change to the elements of the channel pathway by using the Internet advantages, and then the retail offline model of store is changed into the retail online model of electricity.

(2) Addition and subtraction transformation

The addition and subtraction transformation is to increase or reduce the characteristic value of basic-element and then get a new one, which includes the addition transformation and the subtraction one [4].

The addition and subtraction transformation of business model design is to change the results of extension transformation above, and it is as follows:

Firstly, addition transformation: $T_2R = R \oplus R'$. The specific process is below:

For the ith partial matter-element $R_i = (N, c_i, v_i)$ of business model, we get $R_{ij} = (N, c_i, v_{ij})$ and do $T_2R_i = R_i \oplus R_{ij} = (N, c_i, v_i \oplus v_{ij})$ $(i = 1, 2, \ldots, 9)$, $v_{ij} \in \text{V}_\text{E}(v_i)$. For example,

$$\begin{aligned} &T_2(N, \text{customer group } \text{c}_2, \text{female}) \\ &\quad = (N, \text{customer group } \text{c}_2, \text{female}) \\ &\qquad \oplus (N, \text{customer group } \text{c}_2, \text{chileren}) \\ &\quad = (N, \text{customer group } \text{c}_2, \text{female} \oplus \text{children}) \end{aligned}$$

Secondly, subtraction transformation: $T_3R = R \ominus R'$. The process is below:

For the ith partial matter-element $R_i = (N, c_i, v_i)$ of business model, we get $R_{ij} = (N, c_i, v_{ij})$ and do $T_2R_i = R_i \ominus R_{ij} = (N, c_i, v_i \ominus v_{ij})$ $(i = 1, 2, \ldots, 9)$, $v_{ij} \in \text{V}_\text{E}(v_i)$.

For example, if we let $R_1 = (N, c_1, (\text{Mobile phone } O, \text{function } c_{01}, v_{01}))$ and delete some functions of the mobile phone, then it can be denoted as follows:

$$
\begin{aligned}
&T_3(O, c_{01}, \text{phone} \oplus \text{surfing} \oplus \text{send message} \oplus \text{play games}) \\
&\quad = (O, c_{01}, \text{phone} \oplus \text{surfing} \oplus \text{send message} \oplus \text{play game}) \\
&\qquad \ominus (O, c_{01}, \text{surfing} \oplus \text{play games}) \\
&\quad = (O, c_{01}, \text{phone} \oplus \text{send message})
\end{aligned}
$$

(3) Scalability transformation: $T_4R = \alpha R$

When the value of basic-element can be enlarged or narrowed, we can do the scalability transformation to it. During the innovation process of business model design, we often utilize the scalability transformation to change the values of the basic-element, so the core competitiveness of enterprise is to be improved. The specific process is below:

For the ith partial matter-element $R_i = (N, c_i, v_i)$ of business model, we do $T_4R_i = (N, c_i, \alpha v_i) = \alpha R_i$ $(i = 1, 2, \ldots, 9)$. The form is a enlargement transformation when $\alpha > 1$ and a narrow one when $0 < \alpha < 1$. For example, if we do the change $T_4(\text{mobile phone } O, Maximum \text{ font}, v_0) = (\text{mobile phone } O, \text{Maximum font}, 2v_0)$ for $R_1 = (N, \text{product and services } c_1, (\text{mobile phone } O, \text{Maximum font}, v_0))$, then the market of mobile phone can be enlarged to the old people from the young and the mobile is fit for the elders.

Please note that the extension transformation has the conductive quality. Because there are many kinds of relationship among things, it may cause other basic-elements to be changed if we do extension transformation for one element. For example, if we do the extension transformation T_jR_i to the partial matter-element R_i, it may lead R_n to be changed, i.e., $T_{T_j}R_n = R_n'$. So we fully consider the conduction transformation from this change and remedy the negative effect from these conductions when we do the extension transformation of business model.

To do extension transform to the matter-element of business model means that there has some kinds of transformation ways for the partial one because there has a number of value sets, and then we can get a set of new matter-elements R^*, namely $TR = R^*$. Finally, we should evaluate the new business model R^* from the aspects of market, economy and society, and then select the optimal one to form the final design plan.

3 Modified Design of Business Model of Community Hospital

As important support for medical health system, community hospital guarantees the basic need for the people health demand, so to innovate the business model of community hospital has great significance to develop the health service.

(1) Extension model to construction business model

According to the current operation situation of business model of community hospital, we build the matter-element R of business model and establish the goal matter-element G, and then get the extension model as $P = G \uparrow R$, where

$$R = \begin{bmatrix} N, & \text{products and services } c_1, & \textit{health } v_1 \\ & \text{customer groups } c_2, & \text{community patient } v_2 \\ & \text{resource allocation } c_3, & \text{medical rehabilitation } v_3 \\ & \text{core resources } c_4, & (\text{physician}, \text{quantity}, d) \\ & \text{cost structure } c_5, & \text{device maintenance}, \text{the salary of physician } v_5 \\ & \text{source of income } c_6, & \text{treated patients } v_6 \\ & \text{customer relations } c_7, & \text{doctor}-\text{patient relationship } v_7 \\ & \text{the channel pathway } c_8, & \text{outpatient department}, \text{hospitalization } v_8 \\ & \text{Partner cooperation } c_9, & \text{pharmaceutical factory } v_9 \end{bmatrix}$$

$$= \begin{bmatrix} R_1 \\ R_2 \\ R_3 \\ R_4 \\ R_5 \\ R_6 \\ R_7 \\ R_8 \\ R_9 \end{bmatrix}$$

$$G = (Enhance, Dominantobject, Corecompetence)$$

(2) Expansion Analysis

According to the former of this article, we do expansion analysis to the basic-elements of enterprise goal and business model, and then construct the extension value set of matter-element of business model as follows:

$$V_E(v_1) = \{\text{health}, \text{recovered}, \text{aged service}, \text{Physical examination}, \text{physical exercise}, \ldots)$$

$$V_E(v_2) = \{\text{Community patients}, \text{Aged}, \text{children}, \text{youth}, \text{middle aged}, \ldots)$$

$$V_E(v_3) = \{\text{physician}, \text{equipment}, \text{beds}, \ldots)$$

$$V_E(v_4) = \left\{ \begin{matrix} \text{Community platform Senior physician, Medical equipment,} \\ \text{social policies, High quality of service}, \ldots \end{matrix} \right)$$

$$V_E(v_5) = \left\{ \begin{array}{r} \text{Physician salaries, equipment maintenance,} \\ \text{Infrastructure construction Drugs,} \ldots \end{array} \right)$$

$$V_E(v_6) = \{\text{health, recovered, aged service, Drug sales, Physical examination,} \ldots)$$

$$V_E(v_7) = \{\text{doctor}-\text{patient relationship, Platform service, aged service,} \ldots)$$

$$V_E(v_8) = \{\text{Community platform, Network sale, Retail agent,} \ldots)$$

$$V_E(v_9) = \left\{ \begin{array}{r} \text{pharmaceutical factory,superior medical institutions,} \\ \text{Medical device manufacturers,} \ldots \end{array} \right)$$

.

(3) Extension Transformation of Business Model

With improvement of people living standards and health consciousness, as well as the senior doctor is gradually reduced in community hospitals, the medical function is gradually gathered by the large hospitals. Then we can strengthen the cooperation with the superior hospital through the network platform in order to solve the loss problem of senior physicians. Through the network platform, the physicians can do the diagnosis and treatment to the community patients, and finally solve the optimization problem of core resources. At the same time, to adjust the function of community hospitals can help to improve the management. That is to say, if we take $R_1 = (N, c_1, health)$ and $V_E(v_1) = \{recovered, aged\ service, physical\ examination, \ldots)$, and do the addition and subtraction transformation to it, i.e., $T_2R_1 = R_1 \oplus R_{ij} = (N, c_1, health \oplus recovered \oplus aged\ service \oplus physical\ examination)$. Because the extension transformation has the conduction effect, the customer group should be changed according to the changes of the products and services of community hospital, which is expressed by the form below:

$$T_{T_2}R_2 = \left(\begin{array}{r} N, c_2, Community\ patients \oplus \\ Rehabilitation\ peoples \ \oplus \ Community\ elders \oplus Healthy\ population \end{array} \right).$$

Therefore, to make extension transformation for the partial matter-element of business model can induce a series of new matter-elements R^* of business model. Subsequently, we evaluate R^* from the aspects of environment, economy and society, and then select the optimal one to form the final design scheme, such as:

$$R' = \begin{bmatrix} N, & \textit{products and services } c_1, & \textit{health, aged service } v_1 \\ & \textit{customer groups } c_2, & \textit{community patient, community elders } v_2 \\ & \textit{resource allocation } c_3, & \textit{medical rehabilitation, aged service } v_3 \\ & \textit{core resources } c_4, & (\textit{physician},\ \textit{quantity}, \alpha d) \\ & \textit{cost structure } c_5, & \textit{device maintenance, the salary of physician } v_5 \\ & \textit{source of income } c_6, & \textit{treated patients, aged service } v_6 \\ & \textit{customer relations } c_7, & \textit{health} - \textit{nursing relationship } v_7 \\ & \textit{the channel pathway } c_8, & \textit{outpatient department, hospitalization/aged service } v_8 \\ & \textit{partner cooperation } c_9, & \textit{pharmaceutical factory, superior medical institutions } v_9 \end{bmatrix}$$

The matter-element R′ means that the products and services of community hospital is expanded by the model of Medical + pension, and the model can strengthen the cooperation with the higher medical institutions and use the Internet platform to realize the rational flow of senior physicians and strengthen the allocation of core resources. The significance of this scheme is that the people demand for health care and pension increased as the coming of old age. As the grass-root of medical institutions, the community hospital should establish a sound collaboration mechanism with the medical and pension institutions. It not only has highly realistic significance for the old, the ill and the disable to provide pension, nursing and medical services, but also enhances the profit and survival ability of community hospital. At the same time, the rational flow of senior physicians improves the efficiency of human resources within entire medical industry and proposes the development way for community hospital.

4 Conclusions

On the basis of the extension design method, we proposed a method to design the business model. The method provides a new formalized path to innovate business model, as well as give an effective mode to do intelligent decision-making of business model innovation. we only offer the design method of business model in this paper, and it should be further researched on subsequent evaluation for the business model innovation.

Acknowledgements The work was supported partially by the Project of Humanities Society and Science Research Base of colleges of education department in Guizhou Province (NO. 2016JD020), and partially by the Major Project Fund for Social Science & Humanities of Guizhou University (NO. GDZT201604).

References

1. Moser K, Muller M, Piller FT (2006) Transforming mass customisation from a marketing instrument to a sustainable business model at Adidas. Int J Mass Customisation 1(4):463–479
2. Osterwalder A, Pigneur Y, Tucci CL (2005) Clarifying business model: origins, present, and future of the concept. Commun AIS 15:1–40
3. Wei H, Zhu W, Lin G (2008) The business model theory based on the transaction structure of stakeholders. Manage World 12:125–131
4. Chunyan Y, Wen C (2014) Extenics. Science Press, Beijing
5. Cai W, Yang C (2013) Basic theory and methodology on extenics. Chin Sci Bull 58(13):1190–1199
6. Zhao Y, Zhou J (2015) Overview and prospects of extension design methodology. Comput Integr Manuf Syst 21(5):1157–1167
7. Yang C, Luo L (2016) Application of extension innovation method in product design. Packaging Eng 37(24):7–10

Adaptive Sliding Mode Control for an Active Gravity Offload System

Jiao Jia, Yingmin Jia and Shihao Sun

1 Introduction

Various methods of reducing gravity have been used such as parabolic flight, air-bearing, neutral buoyancy and suspension system [1–5]. These methods may be beneficial in some ways but are limited in others. Among them the suspension method [5–7] is superior on practicality, economy and reliability. There are two types of suspension methods passive suspension [5] and active suspension [6, 7]. The active suspension gravity offload method performs much better than the passive one. The offload accuracy of the active suspended system depends on the mechanical structure and the controller. Generally, a wire rope is one necessary part of the upright subsystem. However, the rope is flexible and easy to swing. To solve this problem, a buffer is developed. Besides, a creative suspension structure is developed to insure the object to rotate freely. The dynamic model of the system is deduced based on Lagrange equation. It's a nonlinear coupling system with disturbances, uncertainties and control input uncertainties. To ensure the system robust stability, an adaptive sliding mode controller is developed [8, 9].

2 Active Gravity Offload System (AGOS)

The AGOS is a servo platform consisting of a suspension structure, a buffer, a universal joint, a gantry robot, a tilt sensor, a tension sensor. The work flow chart is presented in Fig. 1. The specific connection relationship is shown in Fig. 2. The

J. Jia · Y. Jia (✉) · S. Sun
The Seventh Research Division and the Center for Information and Control,
School of Automation Science and Electrical Engineering,
Beihang University (BUAA), Beijing 100191, China
e-mail: ymjia@buaa.edu.cn

Z. Deng (ed.), *Proceedings of 2017 Chinese Intelligent Automation Conference*,
Lecture Notes in Electrical Engineering 458,
https://doi.org/10.1007/978-981-10-6445-6_61

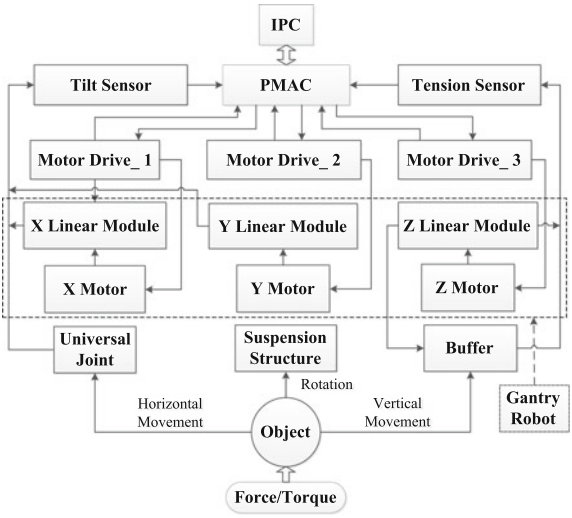

Fig. 1 The work flow chart

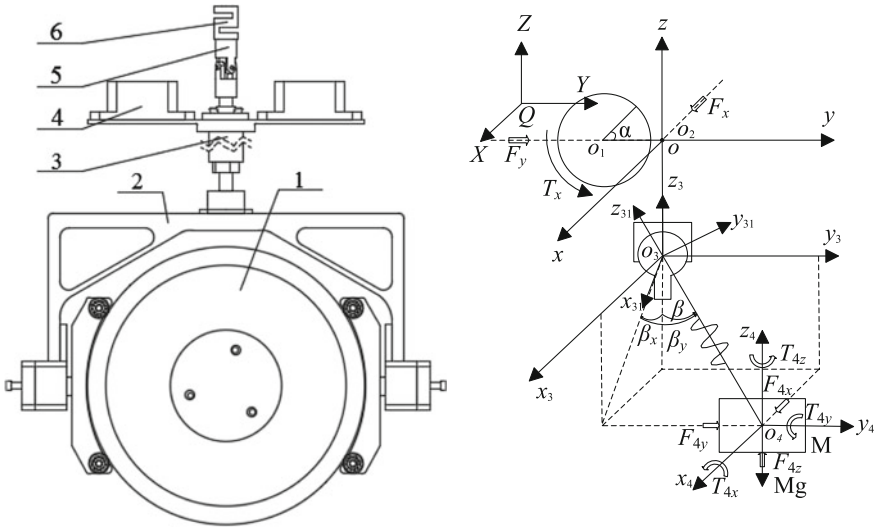

Fig. 2 The connection relationship and the coordinate system of AGOS. *1* object, *2* suspension structure, *3* buffer, *4* tilt sensor, *5* universal joint, *6* tension sensor

suspension structure is composed of rolling bearings and the corresponding fixations, which guarantees the equivalent suspension point to coincide with the centroid of the object. Hence, the object can maintain balance at any attitude.

According to Figs. 1 and 2, when the object is driven to move along the horizontal plane, the buffer swings around the universal joint and the tilt sensor can measure the swing angles. Then the X and Y linear modules will be driven by the X motor and Y motor to eliminate the swing angle to maintain the buffer vertically. When the object is driven to move vertically, the tension sensor will detect the variation of the buffer and then the Z linear module will be actuated by the Z motor to eliminate the variation as required. The control inputs are determined by the PMAC and the IPC. Then the variable gravity field is built for the object.

The AGOS coordinate system is shown in Fig. 2. The buffer is equivalent to a spring and the suspension structure is equivalent to a rope linked to the centroid of the object. The meaning of each part is as below.

- m_{0x}, m_{0y}, the load of X motor and the load of Y motor respectively,
- m_1, m_2, the pinion and the rack mass,
- M, the object mass,
- α, the pinion rotation angle
- $Q - XYZ$, the static coordinate system
- O, m_{0x} centroid
- O_1, O_2, O_4, centroids of m_1, m_2, M respectively,
- O_3, the universal joint centroid,
- F_x, F_y, X motor and Y motor equivalent driven force on X and Y linear modules
- T_x, Z motor output torque on the pinion
- F_{4x}, F_{4y}, F_{4z}, the object driven force
- T_{4x}, T_{4y}, T_{4z}, the object driven torque
- β, swing angle between spring buffer and upright
- β_x, β_y, orthogonal decomposition of β
- $O - xyz$, coordinate moves with O,
- $O_i - x_i y_i z_i, i = 3, 4$, coordinates move with O_3 and O_4,
- $O_3 - x_{31} y_{31} z_{31}$, coordinate rotates with the buffer.

According to the definition above, the coordinates of O, O_1, O_2 are $(x, y, 0)$, $(x, y - R, 0)$ and $(x, y, \alpha R)$ respectively.

The velocities of O, O_1, O_2 are $(\dot{x}, \dot{y}, 0)$, $(\dot{x}, \dot{y}, 0)$ and $(\dot{x}, \dot{y}, \dot{\alpha} R)$ respectively.

Denote $l_1 = Mg/k, d = l_0 + l_1 + l$ where l_0 is the free length of the spring. And O_4 is $(x + d \sin \beta_x \cos \beta_y, y + d \sin \beta_y, \alpha R - 0.5h_0 - d \cos \beta_x \cos \beta_y)$ where h_0 presents the length of the rack. O and O_2 are coincident at the initial position. The variation of the spring length is denoted by l. Define $l = 0$, when spring force is equal to the object.

When $\beta \leq 5°$, let $\sin \beta \approx \beta, \cos \beta \approx 1$. The position and velocity of O_4 are

$$\left(x + d\beta_x, y + d\beta_y, \alpha R - 0.5h_0 - d\right), \left(\dot{x} + \dot{l}\beta_x + d\dot{\beta}_x, \dot{y} + \dot{l}\beta_y + d\dot{\beta}_y, \dot{\alpha} R - \dot{l}\right)$$

The object attitudes will be changed along with T_{4x}, T_{4y}, T_{4z}, and therefore the angular velocity is time-varying. But when x, y, α, l, β_x and β_y are choose as the system generalized coordinates, they are independent of the object rotational kinetic energy. Hence, when we calculate the system kinetic energy the object rotational kinetic energy could be ignored.

The system kinetic energy is

$$T = 0.5(0.5m_1R^2)\dot{\alpha}^2 + 0.5m_2(\dot{\alpha}R)^2 + 0.5m_{0x}v_{m0x}^2 + 0.5m_{0y}v_{m0y}^2 + 0.5M(v_{Mx}^2 + v_{My}^2 + v_{Mz}^2)$$

The pinion and rack move with the X and Y linear modules at the horizontal plane, so their kinetic energy is included in $0.5m_{0x}v_{m0x}^2 + 0.5m_{0y}v_{m0y}^2$.

Choose xOy plane as zero potential energy surface. Then the system potential energy is

$$V = m_2g\alpha R + 0.5k(l + l_1)^2 + Mg(\alpha R - 0.5h_0 - d)$$

$$L = T - V \tag{1}$$

The Lagrange equation

$$\frac{d}{dt}\left(\frac{\partial L}{\partial \dot{q}}\right) - \frac{\partial L}{\partial q} = Q_j \quad (j = 1, 2, \ldots) \tag{2}$$

Substitute Eq. (1) into Eq. (2) and define $m = 0.5m_1 + m_2 + M, \eta_x = (M + m_{0x})/M, \eta_y = (M + m_{0y})/\quad .M, \eta = m/M, \varsigma = k/M, \eta_2 = (m_2 + M)/M, \rho = 1/M$, $\beta^2 = \beta_x^2 + \beta_y^2, \beta_x^y = \beta_x\dot{\beta}_x + \beta_y\dot{\beta}_y, \boldsymbol{q}_1 = [x, y, \alpha]^T$, $\boldsymbol{q}_2 = [l, \beta_x, \beta_y]^T$. We get

$$\boldsymbol{M}_1\ddot{\boldsymbol{q}}_1 + \boldsymbol{M}_2\ddot{\boldsymbol{q}}_2 + \boldsymbol{C}_1\dot{\boldsymbol{q}}_1 + \boldsymbol{C}_2\dot{\boldsymbol{q}}_2 + \boldsymbol{G}_1 = \boldsymbol{F}_1 \tag{3}$$

$$\boldsymbol{M}_2^T\ddot{\boldsymbol{q}}_1 + \boldsymbol{M}_3\ddot{\boldsymbol{q}}_2 + \boldsymbol{C}_3\dot{\boldsymbol{q}}_1 + \boldsymbol{C}_4\dot{\boldsymbol{q}}_2 + \boldsymbol{G}_2 = \boldsymbol{F}_2 \tag{4}$$

Obviously, M_2 is invertible as follow

Let Eq. (3) $-M_1M_2^{-T}$ Eq. (4) and because of $C_1 = C_3 = 0$ we gain Eq. (5)

$$\boldsymbol{M}_m(\boldsymbol{q}, \dot{\boldsymbol{q}})\ddot{\boldsymbol{q}}_2 + \boldsymbol{C}(\boldsymbol{q}, \dot{\boldsymbol{q}})\dot{\boldsymbol{q}}_2 + \boldsymbol{G}(\boldsymbol{q}) = \boldsymbol{F}_1 - \boldsymbol{M}_1\boldsymbol{M}_2^{-T}\boldsymbol{F}_2 \tag{5}$$

$$\boldsymbol{M}_m = \boldsymbol{M}_2 - \boldsymbol{M}_1\boldsymbol{M}_2^{-T}\boldsymbol{M}_3, \boldsymbol{C} = \boldsymbol{C}_2 - \boldsymbol{M}_1\boldsymbol{M}_2^{-T}\boldsymbol{C}_4, \boldsymbol{G} = \boldsymbol{G}_1 - \boldsymbol{M}_1\boldsymbol{M}_2^{-T}\boldsymbol{G}_2$$

$$\boldsymbol{M}_1 = \begin{bmatrix} \eta_x & 0 & 0 \\ 0 & \eta_y & 0 \\ 0 & 0 & \eta R^2 \end{bmatrix}, \boldsymbol{M}_2 = \begin{bmatrix} \beta_x & d & 0 \\ \beta_y & 0 & d \\ -R & 0 & 0 \end{bmatrix}, \boldsymbol{M}_3 = \begin{bmatrix} \beta^2 + 1 & d\beta_x & d\beta_y \\ d\beta_x & d^2 & 0 \\ d\beta_y & 0 & d^2 \end{bmatrix}, \boldsymbol{F}_1 = \begin{bmatrix} F_x \\ F_y \\ T_x \end{bmatrix}$$

$$\boldsymbol{C}_2 = \begin{bmatrix} 2\dot{\beta}_x & 0 & 0 \\ 2\dot{\beta}_y & 0 & 0 \\ 0 & 0 & 0 \end{bmatrix}, \boldsymbol{C}_4 = \begin{bmatrix} 2\beta_x^y & 0 & 0 \\ 2d\dot{\beta}_x & 0 & 0 \\ 2d\dot{\beta}_y & 0 & 0 \end{bmatrix}, \boldsymbol{G}_1 = \begin{bmatrix} 0 \\ 0 \\ \eta_2 g R \end{bmatrix}, \boldsymbol{G}_2 = \begin{bmatrix} \zeta l \\ 0 \\ 0 \end{bmatrix}, \boldsymbol{F}_2 = \begin{bmatrix} F_{4z} \\ F_{4x} \\ F_{4y} \end{bmatrix}$$

3 Adaptive Sliding Mode Controller

For Eq. (5), define $\boldsymbol{M}(\boldsymbol{q}, \dot{\boldsymbol{q}}) = \boldsymbol{M}_m, \boldsymbol{F} = \boldsymbol{F}_1, \boldsymbol{F}_d = -\boldsymbol{M}_1 \boldsymbol{M}_2^{-T} \boldsymbol{F}_2$, and we obtain

$$\boldsymbol{M}(\boldsymbol{q}, \dot{\boldsymbol{q}})\ddot{\boldsymbol{q}} + \boldsymbol{C}(\boldsymbol{q}, \dot{\boldsymbol{q}})\dot{\boldsymbol{q}} + \boldsymbol{G}(\boldsymbol{q}) = \boldsymbol{F} + \boldsymbol{F}_d \tag{6}$$

Then $\ddot{\boldsymbol{q}}_2 = \boldsymbol{M}^{-1}(\boldsymbol{F} + \boldsymbol{F}_d - \boldsymbol{C}\dot{\boldsymbol{q}} - \boldsymbol{G})$. Define $\boldsymbol{x}_1 = \boldsymbol{q}_2 = \boldsymbol{q}$, we gain $\dot{\boldsymbol{x}}_1 = \boldsymbol{x}_2, \dot{\boldsymbol{x}}_2 = \boldsymbol{M}^{-1} \times (\boldsymbol{F} + \boldsymbol{F}_d - \boldsymbol{C}\dot{\boldsymbol{q}} - \boldsymbol{G})$. Define $\dot{\boldsymbol{x}} = [\dot{\boldsymbol{x}}_1, \dot{\boldsymbol{x}}_2]^T, \boldsymbol{u} = \boldsymbol{F}_1 = \boldsymbol{F}$, we gain Eq. (7)

$$\dot{\boldsymbol{x}} = \boldsymbol{f}(\boldsymbol{x}) + \boldsymbol{b}(\boldsymbol{x})\boldsymbol{u} + \boldsymbol{d} \tag{7}$$

where $\boldsymbol{f}(\boldsymbol{x}) = [\boldsymbol{x}_2, \boldsymbol{M}_m^{-1}(-\boldsymbol{C}\boldsymbol{x}_2 - \boldsymbol{G})]^T$, $\boldsymbol{b}(\boldsymbol{x}) = [\boldsymbol{0}, \boldsymbol{M}_m^{-1}]^T, \boldsymbol{g} = \left[\boldsymbol{0}, -\boldsymbol{M}_m^{-1}\boldsymbol{G}_1\right]^T$, $\boldsymbol{d} = [\boldsymbol{0}, -\boldsymbol{M}_m^{-1}\boldsymbol{M}_1\boldsymbol{M}_2^{-T}\boldsymbol{F}_2]^T$.

Due to external disturbances and parameters uncertainties, rewrite the dynamical model as below

$$\dot{\boldsymbol{x}} = \boldsymbol{f}_0(\boldsymbol{x}) + \boldsymbol{b}_0(\boldsymbol{x})\boldsymbol{u} + \boldsymbol{\omega} \tag{8}$$

$\boldsymbol{f}(\boldsymbol{x}) = \boldsymbol{f}_0(\boldsymbol{x}) + \Delta\boldsymbol{f}(\boldsymbol{x}), \boldsymbol{b}(\boldsymbol{x}) = \boldsymbol{b}_0(\boldsymbol{x}) + \Delta\boldsymbol{b}(\boldsymbol{x}),$ $\boldsymbol{\omega} = \Delta\boldsymbol{f}(\boldsymbol{x}) + \Delta\boldsymbol{b}(\boldsymbol{x})\boldsymbol{u} + \boldsymbol{d}$ is bounded.

The control objectives of the system are to keep the object vertically and the gravity of the object is partly or completely compensated as demanded. When the reference input is given as $\boldsymbol{x}_{d1} = [l_d, 0, 0]^T$, then we have $\boldsymbol{x}_d = [\boldsymbol{x}_{d1}, \dot{\boldsymbol{x}}_{d1}]^T$, $\boldsymbol{e} = \boldsymbol{x} - \boldsymbol{x}_d$. Choose the sliding surface as Eq. (9).

$$\boldsymbol{s} = \boldsymbol{\psi e} = 0 \tag{9}$$

where $\boldsymbol{s} = [s_1, s_2, s_3]^T \in \boldsymbol{R}^3$, $\boldsymbol{\alpha} = diag(\alpha_1, \alpha_2, \alpha_3)$, $\boldsymbol{\beta} = diag(\beta_1, \beta_2, \beta_3)$, $\boldsymbol{\psi} = [\boldsymbol{\alpha}, \boldsymbol{\beta}]^T$. The constant $\alpha_1, \alpha_2, \alpha_3, \beta_1, \beta_2, \beta_3$ and are chosen to be positive to make sure the relative polynomial is Hurwitz.

Theorem 1 *For the AGOS (8), if the sliding function is defined as (9), the controller is designed as*

$$\begin{aligned} \boldsymbol{u} = \boldsymbol{u}_e + \boldsymbol{u}_d, \boldsymbol{u}_e = & -(\boldsymbol{\psi}^T \boldsymbol{b}_0(\boldsymbol{x}))^{-1}(\boldsymbol{\psi}^T \boldsymbol{f}_0(\boldsymbol{x}) \\ & - \boldsymbol{\psi}^T \dot{\boldsymbol{x}}_d), \boldsymbol{u}_d = -(\boldsymbol{\psi}^T \boldsymbol{b}_0(\boldsymbol{x}))^{-1} diag(\hat{\boldsymbol{\lambda}}) sign(\boldsymbol{s}) \end{aligned} \tag{10}$$

the sliding mode is guaranteed to be reached in finite time.
$\hat{\boldsymbol{\lambda}} = \left[\hat{\lambda}_1, \hat{\lambda}_2, \hat{\lambda}_3\right]^T$ *is an adjustable parameter, and the adaptive law is*

$$\dot{\hat{\boldsymbol{\lambda}}} = (\frac{1}{\rho_1}\|s_1\|, \frac{1}{\rho_2}\|s_2\|, \frac{1}{\rho_3}\|s_3\|)^T \tag{11}$$

where ρ_1, ρ_2, ρ_3 *are positive.*

Proof Assume that $\boldsymbol{\lambda}_d$ is the terminal solution of $\hat{\lambda}$ which satisfies $\omega_1 < \lambda_{d1}, \omega_2 < \lambda_{d2}, \omega_3 < \lambda_{d3}$ respectively.

Choose the adaption error as:

$$\tilde{\boldsymbol{\lambda}} = \hat{\boldsymbol{\lambda}} - \boldsymbol{\lambda}_d \tag{12}$$

Consider a Lyapunov candidate function as:

$$V = \frac{1}{2}\boldsymbol{s}^T \boldsymbol{s} + \frac{1}{2}\tilde{\lambda}^T diag(\rho_1, \rho_2, \rho_3)\tilde{\lambda} \tag{13}$$

By differentiating V with respect to time, substituting Eqs. (9)–(12) into it, we have

$$\begin{aligned} \dot{V} &= \boldsymbol{s}^T(\boldsymbol{\psi}^T \boldsymbol{f}_0(\boldsymbol{x}) - \boldsymbol{\psi}^T \dot{\boldsymbol{x}}_d + \boldsymbol{\psi}^T \boldsymbol{b}_0(\boldsymbol{x})\boldsymbol{u} + \boldsymbol{\omega}) + \tilde{\lambda}^T diag(\rho_1, \rho_2, \rho_3)\dot{\tilde{\boldsymbol{\lambda}}} \\ &= \boldsymbol{s}^T(\boldsymbol{\omega} - \hat{\boldsymbol{\lambda}} sign(\boldsymbol{s})) + \tilde{\boldsymbol{\lambda}}^T diag(\boldsymbol{s}) sign(\boldsymbol{s}) \\ &= s_1\omega_1 + s_2\omega_2 + s_3\omega_3 - |s_1|\lambda_{d1} - |s_2|\lambda_{d2} - |s_1|\lambda_{d3} < 0 \end{aligned}$$

In order to reduce the input chattering caused by the $sign(\boldsymbol{s})$, the function $\boldsymbol{s}./(|\boldsymbol{s}|+\varepsilon)$ is used.

4 Simulation

The nominal values are $\hat{m}_1 = 0.5\,\text{kg}, \hat{m}_2 = 4\,\text{kg}, \hat{m}_{0x} = 16\,\text{kg}, \hat{m}_{0y} = 40\,\text{kg}, \hat{M} = 10\,\text{kg}, \hat{k} = 500\,\text{N/m}, \hat{l}_0 = 1\,\text{m}, \hat{g} = 10\,\text{m/s}^2, \hat{R} = 0.02\,\text{m}$. The parameter values are $m_1 = 0.55\,\text{kg}, m_2 = 4.4\,\text{kg}, m_{0x} = 17.6\,\text{kg}, m_{0y} = 44\,\text{kg}, M = 11\,\text{kg}, k = 550\,\text{N/m}, l_0 = 1.1\,\text{m}, g = 9.8\,\text{m/s}^2, R = 0.022\,\text{m}$.

The reference signals are given by $\boldsymbol{x}_{d1} = [l_d, 0, 0]^T$ according to the simulation mechanism of AGFS and l_d represent offload quantity of the object gravity. When $l_d = 0$ the object's gravity is compensated completely and when $l_d = -0.2$ the object's gravity is at normal situation. When the value of l_d is between $(0, -0.2)$, the object's gravity is partly compensated and when l_d is positive, the object's gravity is greater than earth's gravity.

Fig. 3 shows the object driven inputs. For the control objectives we consider them as disturbances.

For the uncertain system with bounded disturbances and noises, the control parameters of the controller parameters are chosen as

$\boldsymbol{\alpha} = diag(120, 200, 200), \quad \boldsymbol{\beta} = diag(2, 1, 1), \quad \rho_1 = 0.5, \rho_2 = \rho_3 = 1, \hat{\boldsymbol{\lambda}}_0 = [80, 10, 10]^T$

The boundary layer $\|\boldsymbol{s}\| \leq 6.2 \times 10^{-3}$ is reached in the finite time and the settling time $t \leq 0.3\,\text{s}$ and $\|\boldsymbol{e}\| \leq 2.0 \times 10^{-4}$ as shown in Figs. 4 and 5.

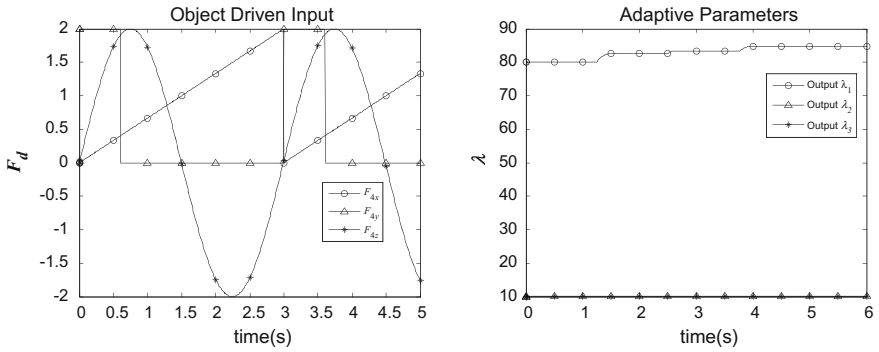

Fig. 3 The object driven input and adaptive parameters $\hat{\lambda}$

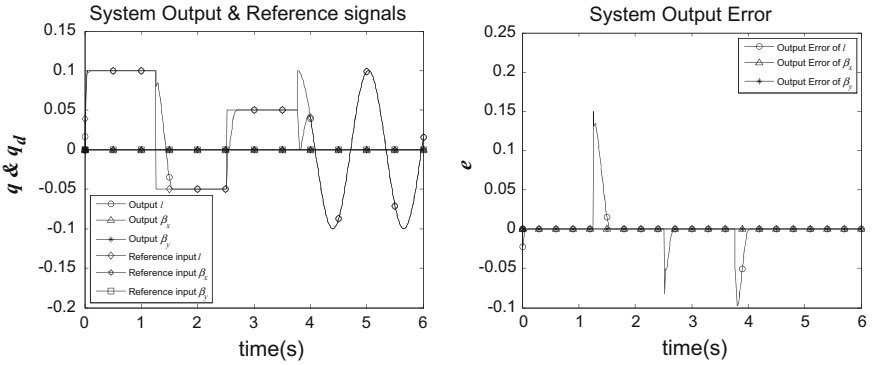

Fig. 4 The system outputs and reference inputs, system output errors

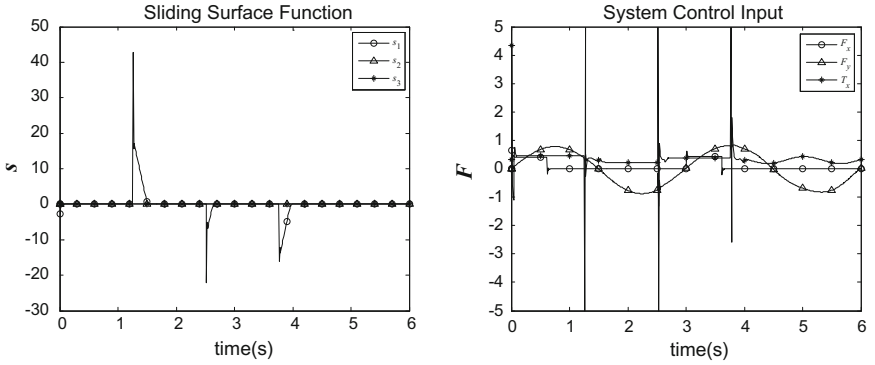

Fig. 5 The sliding surfaces and system control inputs

5 Conclusions

In this paper, an active gravity offload system is introduced in details. It's a servo platform consisting of a suspension structure, a buffer, a universal joint, a gantry robot, a tilt sensor and a tension sensor. A variable gravity field is built by the gravity offload system with the adaptive sliding mode controller.

Acknowledgment This work was supported by the NSFC (61327807, 61521091, 61520106010, 61134005) and the National Basic Research Program of China (973 Program: 2012CB821200, 2012CB821201).

References

1. Watanabe Y (1988) Microgravity experiments for a visual feedback control of a space robot capturing a target. In: International conference on IEEE, vol 3, pp 1993–1998
2. Sawada H (2004) Micro-gravity experiment of a space robotic arm using parabolic flight. Adv Robot 18(3):247–267
3. Menon C (2007) Issues and solutions for testing free-flying robots. Acta Astronaut 60(12): 957–965
4. Robertson A (1999) Spacecraft formation flying control design for the Orion mission. In: AIAA guidance, navigation, and control conference, pp 1562–1575
5. Kienholz AD (1989) Very low frequency suspension systems for dynamic testing. In: Proceedings of the 30th structures, structural dynamics and materials, pp 327–336
6. White GC (1994) Active vertical-direction gravity compensation system. IEEE Trans Instrum Meas 43(6):786–792
7. Han O (2010) Gravity-offloading system for large-displacement ground testing of spacecraft mechanisms. In: Proceedings of 40th aerospace mechanisms symposium, pp 119–132
8. Huang YJ (2008) Adaptive sliding-mode control for nonlinear systems with uncertain parameters. IEEE Trans Syst Man Cybern 38(2):534–539
9. Duan M (2016) Adaptive sliding mode control for A 2 DOF magnetic levitation system with uncertain parameters. J Rob Networking Artif Life 2(4):263–267

Four Quadrant Operation and Regenerative Braking Control of PMSM Drive Systems

Xinxin Cheng, Haisheng Yu and Jinpeng Yu

1 Introduction

PMSM control systems are widely used electrical drives and servo systems and usually holds two operating modes, motor and regenerative [1–3]. PWM rectifiers with IGBT have many advantages compared to diodes, the striking advantage is bidirectional power flow [4]. The NN direct MRAC can achieve online application of AC [5]. PCH control has been used widely due to real-time energy optimization [6, 7]. SMC has good real-time, robust, and simple realization [8].

In this paper, the RBFNN to totally substitute conventional PI constitute RBFNN direct MRAC in grid-side to ensure bus voltage is controllable. The SMC is used as the signal controller to get the fast speed tracking control. The PCH is used as energy controller to achieve the real-time energy optimization. The load torque observer is proposed to evaluate the unknown load torque.

2 The Mathematical Model of System

The drive systems is a back-to-back structure consists of the grid-side converter, the motor-side converter, PMSM and other components.

The mathematical model of the grid-side can be expressed as [8]

X. Cheng · H. Yu (✉) · J. Yu
School of Automation and Electrical Engineering,
Qingdao University, Qingdao 266071, China
e-mail: yu.hs@163.com

Z. Deng (ed.), *Proceedings of 2017 Chinese Intelligent Automation Conference*,
Lecture Notes in Electrical Engineering 458,
https://doi.org/10.1007/978-981-10-6445-6_62

$$\begin{cases} L_g \, \mathrm{d}i_{gd}/\mathrm{d}t = e_{gd} - Ri_{gd} + \omega_g L_g i_{gq} - \mu_{gd} u_{dc} \\ L_g \, \mathrm{d}i_{gq}/\mathrm{d}t = e_{gq} - Ri_{gq} - \omega_g L_g i_{gd} - \mu_{gq} u_{dc} \\ C \, \mathrm{d}u_{dc}/\mathrm{d}t = i - i_L = (\mu_{gd} i_{gd} + \mu_{gq} i_{gq}) - i_L \end{cases} \tag{1}$$

where, $e_{gd} = \sqrt{3/2}E_m, e_q = 0, E_m = 80\,\mathrm{V}, L_g = 15\,\mathrm{mH}, R = 2.875\,\Omega, C = 2200$ μF, $\omega_g = 50\,\mathrm{Hz}$, i_{gd} and i_{gq} are input current in d-q frame, i_L is the load current, u_{dc} is link voltage, μ_{gd} and μ_{gq} are the PWM duty ratio in d-q frame.

The mathematical model of motor-side can be written as [9]

$$\begin{cases} L_d \, \mathrm{d}i_{md}/\mathrm{d}t = u_{md} - R_s i_{md} + n_p \omega_m L_q i_{mq} \\ L_q \, \mathrm{d}i_{mq}/\mathrm{d}t = u_{mq} - R_s i_{mq} - n_p \omega_m L_d i_{md} - n_p \omega_m \Phi \, , \tau = n_p[(L_d - L_q) i_{md} i_{mq} + \Phi i_{mq}] \\ J_m \, \mathrm{d}\omega_m/\mathrm{d}t = \tau - \tau_L \end{cases} \tag{2}$$

where, $J_m = 0.8\,\mathrm{g\,m^2}, L_d = L_q = 85\,\mathrm{mH}, R_s = 2.875\,\Omega, \Phi = 0.175\,\mathrm{Wb}, n_p = 4$, u_{md}, u_{mq} and i_{md}, i_{mq} are the d-q axes voltage and stator currents, ω_m is the mechanical velocity, τ and τ_L are the electromagnetic and load torque.

3 The Control Principle of the Grid-Side

This side converter control targets are as follows. The actual u_{dc} tracks precisely V_{dc}. The power unity of the grid-side is equal to one.

3.1 Controller Design of Grid-Side Converter

According to $i_{gq}^* = 0$ and equation (1), reference model selected as $a_1 \dot{u}_{rdc} + a_0 u_{rdc} = V_{dc}, a_0 = 540, a_1 = 6.67$ [10], so output $u_{rdc}(t) = \frac{V_{dc}(t)}{a_1} e^{-\frac{a_0 t}{a_1}}$. The enhanced error function $E_g = \frac{e_g^2}{2} = \frac{[(u_{rdc} - u_{dc}) + KD(\dot{u}_{rdc} - \dot{u}_{dc})]^2}{2}, KD = 0.025$. The $X = [x_1 \quad \ldots \quad x_m], i_{gd}^* = h_1 w_1 + \cdots + h_j w_j + \cdots + h_m w_m$ as input and output vector of RBFNN, where h_j is Gaussian function and w_j is weight coefficient, and existing

$$W = [w_1 \quad \ldots \quad w_j \quad \ldots \quad w_m], h_j = \exp\left(-\|x - c_j\|/2b_j^2\right) \quad j = 1, \ldots n \tag{3}$$

where c_j is the center vector of the j-th neuron.

The control target is E_g converges to zero. The learning algorithm of w_j is $\Delta w_j = -\eta \, \partial E_g/\partial w_j = \eta e_g \left(\partial u_{dc}/\partial i_{gd}^* + KD \, \partial \dot{u}_{dc}/\partial i_{gd}^*\right) h_j$, where $\eta \in [0, 1]$, by replacing, we get

$$\Delta w_j = \eta e_g \left[\operatorname{sgn}\left(\partial u_{dc} / \partial i_{gd}^* \right) + KD \operatorname{sgn}\left(\partial \dot{u}_{dc} / \partial i_{gd}^* \right) \right] h_j \tag{4}$$

The momentum factor α ($\alpha \in [0, 1]$) is added to the equation

$$w_j(k) = w_j(k-1) + \Delta w_j(k) + \alpha \Delta w_j(k) \tag{5}$$

The current controller is designed as

$$\begin{aligned} u_{gd}^* &= K_{p1}\left(i_{gd}^* - i_{gd} \right) + K_{i1} \int_0^t \left(i_{gd}^* - i_{gd} \right) dt, \\ u_{gq}^* &= K_{p2}\left(i_{gq}^* - i_{gq} \right) + K_{i2} \int_0^t \left(i_{gq}^* - i_{gq} \right) dt \end{aligned} \tag{6}$$

where K_{p1}, K_{i1} and K_{p2}, K_{i2} are coefficients of d-q axes current controller.

3.2 Stability Analysis of the Grid-Side

Define Lyapunov function and variation as

$$V_g(k) = E_g(k) = \frac{1}{2} e_g^2(k), \Delta V_g(k) = \frac{1}{2} \left[\Delta e_g^2(k) + 2 e_g(k) \Delta e_g(k) \right] \tag{7}$$

$\Delta W(k) = e_g \eta \operatorname{sgn}\left(\frac{\partial u_{dc}}{\partial i_{gd}^*} + KD \frac{\partial \dot{u}_{dc}}{\partial i_{gd}^*} \right) \frac{i_{gd}^*}{\partial W}$ got by given $\Delta e_g(k) = \Delta W_g(k) \left[\frac{\partial e_g(k)}{\partial W_g(k)} \right]^T$. Let $A = \frac{\partial e_g(k)}{\partial W(k)}$ and then $\Delta e_g(k) = -\eta A A^T e_g(k)$. Combined $\Delta e_g(k)$, have $\Delta V_g(k) = -e_g^2(k)(AA^T)[2\eta - \eta^2(AA^T)]/2$, the converter is stable when $0 < \eta < 2(AA^T)^{-1}$.

4 The Control Principle of the Motor-Side

The regulative targets of the motor-side converter are achieving smooth speed control, the four quadrant operation and regenerative braking.

4.1 Sliding Mode Controller Based on Signal

The SMC based on exponential function is developed to reduce the chattering. Assuming the given speed is ω_m^*, define error and sliding mode surface are

$$e_m = \omega_m - \omega_m^*, s = ce_m + \dot{e}_m \tag{8}$$

where c is the coefficient. The exponential reaching law is given by

$$\dot{s} = -f(x,s) \cdot sign(s), f(x,s) = {}^{k|x|}\!/_{\delta + (1-\delta)e^{-\varepsilon|s|}} \tag{9}$$

where $k > 0, \varepsilon > 0, 0 < \delta < 1, f(x,s) > 0$. From (2) and (9), it can be gotten as

$$i_{mq}^* = {}^{J_m}\!/_{cn_p\Phi}[-f(x,s)sign(s) + {}^{c\tau_L}\!/_{J_m} + c\dot{\omega}_m - c\dot{e}_m - \ddot{e}_m] \tag{10}$$

Define current errors $\tilde{i}_{msd} = i_{msd}^* - i_{md}, \tilde{i}_{msq} = i_{msq}^* - i_{mq}$, $\dot{\tilde{i}}_{msd} = -k_1\tilde{i}_{msd}$, and $\dot{\tilde{i}}_{msq} = -k_2\tilde{i}_{msq}$. From (2), $i_{msd}^* = 0$, and $L_d = L_q = L$, the controller $(k_1 > 0, k_2 > 0)$

$$\begin{cases} u_{msd} = R_s i_{md} - n_p\omega_m L i_{mq} + k_1 L\tilde{i}_{msd} \\ u_{msq} = L\dot{i}_{msq}^* + R_s i_{mq} + n_p\omega_m L i_{md} + n_p\Phi\omega_m + k_2 L\tilde{i}_{msq} \end{cases} \tag{11}$$

The Lyapunov function is defined as $V_s = {}^{\left(s^2 + \tilde{i}_{msd}^2 + \tilde{i}_{msq}^2\right)}\!/_2$, we can get $\dot{V}_s = -f(x,s)|s| - k_1\tilde{i}_{msd}^2 - k_2\tilde{i}_{msq}^2 < 0$, the SMC subsystem is asymptotically stable.

4.2 PCH Controller Based on Energy

The optimization control of input energy and output energy is achieved via the state error PCH control. In [6, 7], the nonlinear systems will be written as

$$\begin{cases} \dot{\boldsymbol{x}} = [\boldsymbol{J}(\boldsymbol{x}) - \boldsymbol{R}(\boldsymbol{x})]\partial\boldsymbol{H}(\boldsymbol{x})/\partial\boldsymbol{x} + \boldsymbol{g}(\boldsymbol{x})\boldsymbol{u} \\ \boldsymbol{y} = \boldsymbol{g}^T(\boldsymbol{x})\partial\boldsymbol{H}(\boldsymbol{x})/\partial\boldsymbol{x} \end{cases} \tag{12}$$

where $\boldsymbol{J}(\boldsymbol{x},\mu) = -\boldsymbol{J}^T(\boldsymbol{x},\mu)$ and $\boldsymbol{R}(\boldsymbol{x}) = \boldsymbol{R}^T(\boldsymbol{x}) \geq 0$ represent the interconnection and damping matrices, $\boldsymbol{g}(\boldsymbol{x})$ is ports features. The state and input vectors are defined as

$$\begin{aligned} \boldsymbol{x_{me}} &= [\, x_{me1} \quad x_{me2} \quad x_{me3} \,]^T = [\, L_d i_{med} \quad L_q i_{meq} \quad J_m\omega_{me} \,]^T, \\ \boldsymbol{u_m} &= [\, u_{med} \quad u_{meq} \quad -\tau_L \,]^T \end{aligned} \tag{13}$$

Given Hamiltonian function $\boldsymbol{H}_m(\boldsymbol{x_{me}}) = \frac{1}{2}\left[L_d {i_{med}}^2 + L_q {i_{meq}}^2 + J_m {\omega_{me}}^2\right]$, then the system (2) can be expressed in the shape of PCH (12) with

$$\boldsymbol{J_m}(\boldsymbol{x_{me}}) = \begin{bmatrix} 0 & 0 & n_p x_{me2} \\ 0 & 0 & -n_p(x_{me1}+\Phi) \\ -n_p x_{me2} & n_p(x_{me1}+\Phi) & 0 \end{bmatrix}, \boldsymbol{R_m} = \begin{bmatrix} R_s & 0 & 0 \\ 0 & R_s & 0 \\ 0 & 0 & 0 \end{bmatrix},$$
$$\boldsymbol{g_m} = \begin{bmatrix} 1 & 0 & 0 \\ 0 & 1 & 0 \\ 0 & 0 & 1 \end{bmatrix} \tag{14}$$

According to $L_d = L_q$ and MTPA rule [6], the desired equilibrium point is $\boldsymbol{x_{me0}} = [\,0 \quad L_q\tau_{L0}/n_p\Phi \quad J_m\omega_m^*\,]^{\mathrm{T}}$. The closed-loop Hamilton system designed as

$$\dot{\boldsymbol{x}} = [\boldsymbol{J}_{md}(\tilde{\boldsymbol{x}}_{me}) - \boldsymbol{R}_{md}(\tilde{\boldsymbol{x}}_{me})]\partial \boldsymbol{H}_{md}(\tilde{\boldsymbol{x}}_{me})/\partial \tilde{\boldsymbol{x}}_{me} \tag{15}$$

Selecting the desired Hamilton function ($\boldsymbol{H}_{md}(\tilde{\boldsymbol{x}}_{\boldsymbol{me}}) > 0$ and $\boldsymbol{H}_{md}(0) = 0$)

$$\boldsymbol{H}_{md}(\tilde{\boldsymbol{x}}_{\boldsymbol{me}}) = \frac{1}{2}\left[L_d(i_{med} - i_{med0})^2 + L_q\left(i_{meq} - i_{meq0}\right)^2 + J_m(\omega_{me} - \omega_{me0})^2\right] \tag{16}$$

Let $J_{md}(\tilde{\boldsymbol{x}}_{\boldsymbol{me}}) = J_m(\tilde{\boldsymbol{x}}_{\boldsymbol{me}}) + J_a = -J_{md}^T(\tilde{\boldsymbol{x}}_{\boldsymbol{me}}), \boldsymbol{R}_{md}(\tilde{\boldsymbol{x}}_{\boldsymbol{me}}) = \boldsymbol{R}_m(\tilde{\boldsymbol{x}}_{\boldsymbol{me}}) + \boldsymbol{R}_a = \boldsymbol{R}_{md}^T(\tilde{\boldsymbol{x}}_{\boldsymbol{me}}) \geq 0$ and selecting $(\tau_L = \tau_{L0}, J_{13} = n_p x_{me20} - n_p L_d i_{meq0}, J_{23} = n_p L_q i_{med0} - n_p(x_{me10} + \Phi))$

$$\boldsymbol{J_{ma}} = \begin{bmatrix} 0 & 0 & J_{13} \\ 0 & 0 & -J_{23} \\ -J_{13} & J_{23} & 0 \end{bmatrix}, \mathbf{R_{ma}} = \begin{bmatrix} r_1 & 0 & 0 \\ 0 & r_2 & 0 \\ 0 & 0 & 0 \end{bmatrix} \tag{17}$$

The controller of PMSM drive system is

$$\begin{cases} u_{med} = -r_1(i_{md} - i_{med0}) + R_s i_{med0} - n_p L_d i_{meq0}(\omega_m - \omega_0) - n_p L_q i_{mq}\omega_0 \\ u_{meq} = -r_2(i_{mq} - i_{meq0}) + R_s i_{meq0} + n_p L_q i_{med0}(\omega_m - \omega_0) + n_p(L_d i_{md} + \Phi)\omega_0 \end{cases} \tag{18}$$

According to [10], the observer error equation has the form

$$\begin{bmatrix} \dot{\tilde{\omega}}_m \\ \dot{\tilde{\tau}}_L \end{bmatrix} = \begin{bmatrix} -k_3 & -1/J_m \\ -k_4 & 0 \end{bmatrix} \begin{bmatrix} \tilde{\omega}_m \\ \tilde{\tau}_L \end{bmatrix} \tag{19}$$

where, $\tilde{\omega}_m = \omega_m - \hat{\omega}_m, \tilde{\tau}_L = \tau_L - \hat{\tau}_L$. The observer is asymptotically stable when $k_3 > 0, k_4 < 0$. The poles of the observer can be solved from $s_{1,2} = -k_3/2 \pm \sqrt{k_3^2 + 4k_4/J_m}/2$. All the poles are assigned at $s_1 = s_2 = -k_m$ by

selecting $k_3 = 2k_m, k_4 = -J_m k_m^2$. The load estimation errors $\tilde{\tau}_L$ decay exponentially to zero by the pole placement.

Replace i_{meq0} of (18) with $\hat{i}_{meq0} = \frac{\hat{\tau}_L}{n_p \Phi}$, the new controller is expressed as

$$\begin{cases} u_{med} = -r_1(i_{md} - i_{med0}) + R_s i_{med0} - n_p L_d \hat{i}_{meq0}(\omega_m - \omega_0) - n_p L_q i_{mq}\omega_0 \\ u_{meq} = -r_2(i_{mq} - \hat{i}_{meq0}) + R_s \hat{i}_{meq0} + n_p(L_d i_{md} + \Phi)\omega_0 + n_p L_q i_{med0}(\omega_m - \omega_0) \end{cases} \tag{20}$$

According to [7], equilibrium point is asymptotically stable when τ_L is not given.

4.3 The Coordination Control Strategy Design

The coordination functions are designed as

$$\begin{cases} u_{md} = c_{sd}(t) \cdot u_{msd} + c_{ed}(t) \cdot u_{med} \\ u_{mq} = c_{sq}(t) \cdot u_{msq} + c_{eq}(t) \cdot u_{meq} \end{cases}, \begin{cases} c_{sd}(t) = e^{-(t-t_i)/T_c} \\ c_{ed}(t) = 1 - e^{-(t-t_i)/T_c} \end{cases} \begin{cases} c_{sq}(t) = e^{-(t-t_i)/T_c} \\ c_{eq}(t) = 1 - e^{-(t-t_i)/T_c} \end{cases}, \tag{21}$$

where, $T_c = 1$, t_i is the start time when $|\omega_m - \omega_m^*| < 0.6\,\text{rad/s}$, $c_{sd}(t), c_{ed}(t), c_{sq}(t), c_{eq}(t) \in [0, 1]$ are the d-q axes coefficient of signal controller and energy controller, respectively.

4.4 Stability Analysis of the Motor-Side

Choose $V = V_s + V_e + \frac{\left(e^{-(t-t_i)/T_c}\right)^2}{2}$ as the Lyapunov function of motor-side, and

$$\dot{V} = \dot{V}_s + \dot{V}_e - \frac{\left(e^{-(t-t_i)/T_c}\right)^2}{T_c} < 0 \tag{22}$$

So, the motor-side of system is asymptotically stable.

5 Simulation Experiment Results

The grid-side is only run in 0.0−0.2 s, the grid-side and motor-side are run in 0.2−2.0s. The controller parameters: $W(0) = 0.5, \eta = 0.5, \alpha = 0.05, k_{p1} = k_{p2} = 1$, $k_{i1} = k_{i2} = 0.01$, $k_1 = k_2 = 10{,}000$, $c = 350, \delta = 0.2, \varepsilon = 2, r_1 = r_2 = 0.01$, $k =$

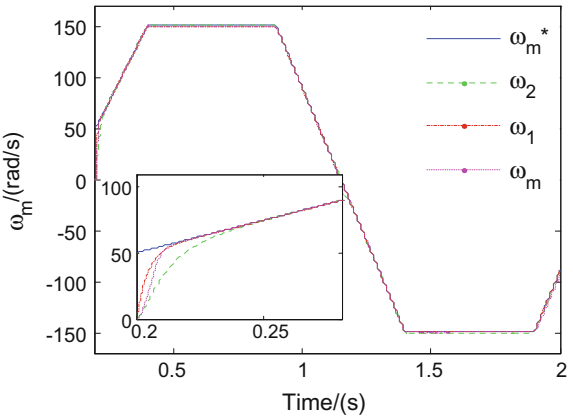

Fig. 1 Motor speed ω_m curve

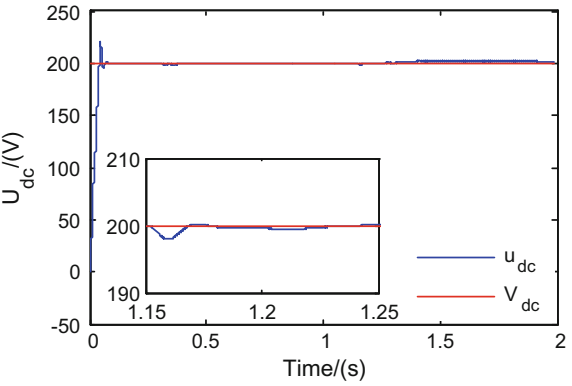

Fig. 2 DC bus voltage u_{dc} curve

$k_m = 500$. The $V_{dc}, \tau_L, \omega_m^*$ are given, $\omega_1, \omega_2, \omega_m$ are speed of SMC, PCH and coordination control.

Figures 1 and 3 show that the $\tau - \tau_L$ and ω_m have the same direction in 0.2−0.4 s, the motor operates in quadrant I. From 0.9−1.15 s, $\tau - \tau_L$ and ω_m have the contrary direction, the motor operates in quadrant II. Similarly, the motor runs in the III and IV quadrants in 1.15−1.4 s and 1.9−2.0 s. From Figs. 1 and 4, the coordination control has fast dynamic response and lower energy consumption combined the advantages of SMC and PCH. Figure 2 shows u_{dc} is controllable and energy is bidirectional flow.

A load disturbance is added at $t = 0.6$ s.The ω_3 is speed without observer. Figure 5 shows the system also has favorable speed tracking property with observer.

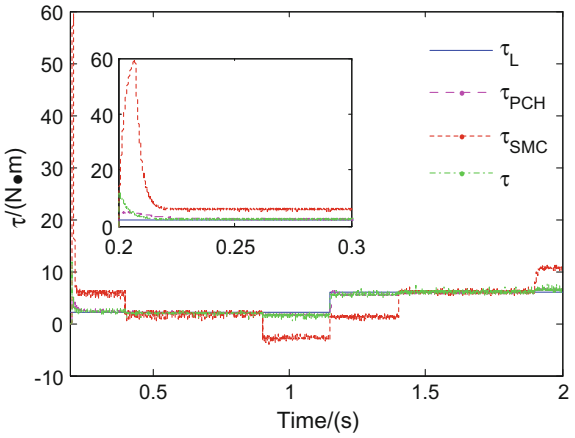

Fig. 3 Torque curve of PMSM

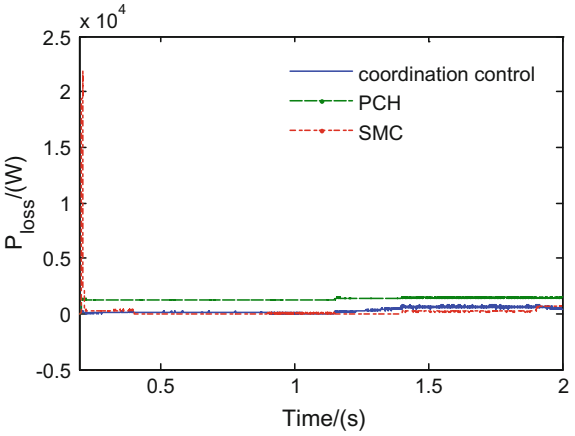

Fig. 4 Curves of the energy loss

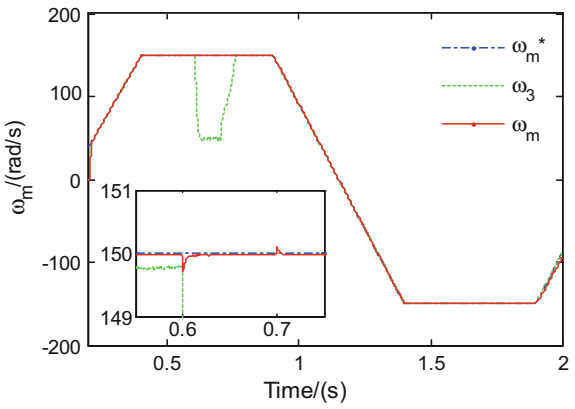

Fig. 5 Motor speed curve with load observer

6 Conclusions

Four quadrant operation and regenerative braking control of PMSM drive systems are presented in this paper. The RBFNN direct MRAC controller is designed to control DC bus voltage. The coordination controller improves the dynamic and steady state properties and achieves the energy optimization in motor-side. The SMC strategy based on signal has good dynamic performances, the PCH control strategy based on energy reaches its minimum loss. Regenerative braking transforms kinetic energy into electrical energy and decreases the loss of energy. The controller ensures that the motor achieves four quadrant operation, energy is bidirectional flow, and bus voltage is controllable.

Acknowledgement This work is supported by the Natural Science Foundation of China (61573203).

References

1. Pillay P, Krishnan R (1989) Control characteristics and speed controller design for a high performance permanent magnet synchronous motor drive. IEEE Trans Power Electron 5 (2):151–159
2. Kaynak O, Erbatur K, Ertugrul M (2001) The fusion of computationally intelligent methodologies and sliding-mode control—a survey. IEEE Trans Ind Electron 48(1):4–17
3. Pan C, Chen L, Jiang H et al (2016) Research on motor rotational speed measurement in regenerative braking system of electric vehicle. Mech Syst Signal Proc 66–67(2):829–839
4. Zhou D, Zhou J, Li Y (2016) Model-predictive control scheme of five-leg AC-DC-AC converter-fed induction motor drive. IEEE Trans Ind Electron 63(7):4517–4526
5. Gadoue SM, Giaouris D, Finch JW (2008) A neural network based stator current MRAS observer for speed sensorless induction motor drives. IEEE Int Symp Ind Electron 10 (1109):650–655
6. Ortega R, Schaft AVD, Mschobar B et al (2002) Interconnection and damping assignment passivity-based control of port-controlled hamiltonian systems. Automatica 38(4):585–596
7. Yu H, Yu J, Liu J, Song Q (2013) Nonlinear control of induction motors based on state error PCH and energy-shaping principle. Nonlinear Dyn 72:49–59
8. Li S, Zhang W (2017) An adaptive sliding-mode observer with a tangent function-based PLL structure for position sensorless PMSM drives. Int J Electr Power Energy Syst 88:63–74
9. Turker T, Buyukkeles U, Bakan AF (2016) A robust predictive current controller for PMSM drives. IEEE Trans Ind Electron 63(6):3906–3914
10. Yu H, Zhao K, Wang H, Guo L (2006) Energy shaping control of PM synchronous motor based on load torque observer. Syst Eng Electron 28(11):1740–1742

CMAC and NISM Integrated Controller for Twin-Rudder Twin-Propeller Ship Course Tracking

Hongxin Wu, Chen Guo and Yingkai Lou

1 Introduction

With the rapid development of the world economy, economic globalization has greatly promoted the international economic exchanges. Container ship as carrier of sea transport is becoming increasingly busy. Large-scale, high-speed become main trend. The twin-rudder twin-propeller system can set different speeds for the two main engines, so that the propeller produces different thrust to produce transshipment torque [1]. However, with limited data available for the twin-rudder twin-propeller ship, it's difficult to estimate parameters for a given position of the ship. The theory of manipulation of twin-rudder twin-propeller ship is not very mature at present, and the research institutions include Dalian Maritime University, Shanghai Jiaotong University, Harbin Engineering University.

The cerebellar model controller (CMAC) neural network is widely used due to good generalization capability. And the sliding-mode controller has a strong robustness. In Ref. [2–4], the NISM is not only apt to design, but also can be directly applied to the nonlinear model of ship. The paper explores the intelligent control method of ship course control, designs the NISM controller and combines with the CMAC control algorithm for twin-rudder twin-propeller ship system, which avoids the estimation of the uncertain term and the interference term of the model, effectively suppresses the chattering problem. What's more, the Maersk Triple E ship is taken as the research object, and the simulation result is compared with the PID control.

H. Wu · C. Guo (✉) · Y. Lou
Dalian Maritime University, Dalian 116026, Liaoning, China
e-mail: guoc@dlmu.edu.cn

H. Wu
e-mail: 2267995616@qq.com

Z. Deng (ed.), *Proceedings of 2017 Chinese Intelligent Automation Conference*,
Lecture Notes in Electrical Engineering 458,
https://doi.org/10.1007/978-981-10-6445-6_63

2 Mathematical Mode for Twin-Rudder Twin-Propeller Ship

The mathematical model is the core of ship simulation and motion control. The model for twin-rudder twin-propeller ship will be described based on the MMG model and the wind, wave and current disturbances are added into the model. It's worth noting that this paper only studied the plane motion. The effect of the heave, pitching and rolling of the ship is very tiny and can be ignored, so the ship is simplified to three degrees of freedom. The model is given as follows:

$$\left.\begin{aligned}
\dot{\delta}_p &= (\delta_{Ep} - \delta_p)/T_{Ep} \\
\dot{\delta}_s &= (\delta_{Es} - \delta_s)/T_{Es} \\
\dot{u} &= [(m + m_y)vr + X_H + X_P + X_R + X_{wind} + X_{wave} + X_{current}]/(m + m_x) \\
\dot{v} &= [-(m + m_x)ur + Y_H + Y_P + Y_R + Y_{wind} + Y_{wave} + Y_{current}]/(m + m_y) \\
\dot{r} &= (N_H + N_p + N_R + N_{wind} + N_{wave} + Z_{current})/(I_{zz} + J_{zz}) \\
\dot{\varphi} &= r \\
\dot{x}_0 &= u\cos\varphi - v\sin\varphi \\
\dot{y}_0 &= v\cos\varphi + u\sin\varphi
\end{aligned}\right\} \quad (2.1)$$

where X, Y, N are external forces and moment, u, v, r are the surge velocity, the sway velocity and the yaw rate respectively, ψ, δ_p, δ_s are the heading angle and rudder angle, x_0, y_0 is the position of the ship's gravity center in the fixed coordinate system. The subscripts 'H' 'P' 'R' 'wind' 'wave' 'current' refer to hull, propeller, rudder wind, wave and current respectively, I_{zz} is the yaw moment of inertia, J_{zz} is added yaw moment of inertia, δ_E is command rudder angle, T_E is time constant.

3 CMAC and NISM Integrated Controller

3.1 Nonlinear Iterative Sliding Mode Description

The iterative sliding mode design idea is to obtain the tracking error of the system through a series of first order low pass filter via the sliding mode surface, until the iterative access to the final filter output. At this time, the high order tracking problem of the system is transformed into a series of iterations of low order stabilization problem [5].

The system state variable $f(r, \delta_{p,s}, t)$ is a smooth unknown continuous function with a continuous partial derivative of $\delta_{p,s}$. $d(\psi, t)$ is the influence of uncertain term and interference term, the ship course nonlinear control system can be simplified as follows:

$$\left.\begin{aligned}\dot{\psi} &= r \\ \dot{r} &= (N_H + N_p + N_R + N_{wind} + N_{wave} + N_{current})/(I_{zz} + J_{zz}) \\ &= f(r, \delta_{p,s}, t) + d(\psi, t) \\ y &= \psi\end{aligned}\right\} \tag{3.1}$$

According to the iterative sliding mode design idea, aiming at the tracking error ψ_e of the actual ship course, a nonlinear sliding mode controller is designed with strictly bounded hyperbolic tangent nonlinear function tanh (x).

$$\left.\begin{aligned}s_1(\psi_e) &= k_2 \tanh(k_1\psi_e) + \dot{\psi}_e \\ s_2(s_1) &= k_4 \tanh(k_3 s_1) + \dot{s}_1 \\ \psi_e &= \psi - \psi_d\end{aligned}\right\} \tag{3.2}$$

where $k_i \in \mathrm{R}^+ (i = 1, 2, 3, 4)$, ψ_d is desired heading angle. From the above formula, when s_1 tends to zero, the $\dot{\psi}_e$ tends to $-k_2 \tanh(k_1\psi_e)$. According to the characteristics of the hyperbolic tangent function, in order to ensure that the s_2 close to 0 when the s_1 tends to 0, the formula should meet $k_4 \geq k_2$.

The sliding mode surface feedback value s_2 is used to obtain an easy-to-implement sliding mode feedback control law [5]:

$$\dot{\delta}_{p,s} = -k_p s_2 - \varepsilon \operatorname{sgn}(s_2) \quad (k_p, \varepsilon \in R^+) \tag{3.3}$$

3.1.1 Stability Analysis

Make the following assumptions for the system:

(1) The system is controllable;
(2) $f(r, \delta_{p,s}, t)$ and $d(\psi, t)$ is a continuous bounded function.

Based on Lyapunov stability theory and twin-rudder twin-propeller ship mathematical model, the Lyapunov function is constructed:

$$V = \frac{1}{2} s_2^2 \tag{3.4}$$

The derivative of the function is:

$$\dot{V} = s_2 \dot{s}_2 = s_2 \frac{\partial s_2}{\partial \delta_{p,s}} \dot{\delta}_{p,s} \tag{3.5}$$

Combined with the ship model the s_2 can be expressed as:

$$s_2 = k_3 \tan \mathrm{h}(k_2 s_1) + \frac{k_1 k_0 \dot{\psi}_e}{\cos \mathrm{h}^2(k_0 \psi_e)} + \ddot{\psi}_e \tag{3.6}$$

From the ship model we can see that only $\ddot{\psi}_e$ derivation of $\delta_{p,s}$ is not zero, and only N_R is related to the rudder angle, so the sign of $\frac{\partial s_2}{\partial \delta_{p,s}}$ depends on the sign of $\frac{\partial N_R}{\partial \delta_{p,s}}$. *NR* is described as [6]:

$$\begin{aligned} N_R = &-[(x_R + \alpha_H x_H)\left(F_{N(s)} \cos \delta_{(s)} + F_{N(p)} \cos \delta_{(p)}\right)] \\ &- \frac{b_r}{2}(1 - t_R)\left(F_{N(p)} \sin \delta_{(p)} - F_{N(s)} \sin \delta_{(s)}\right) \end{aligned} \tag{3.7}$$

When the twin-rudder twin-propeller ship is under oceanic navigation conditions, in other words, ship is under double rudders linkage control condition, $\frac{\partial N_R}{\partial \delta_{p,s}} \geq 0$. Then the sign of $\dot{V}$ depends on the sign of $\dot{\delta}_{p,s}$ and s_2 based on Eq. (3.5):

$$s_2 \dot{\delta}_{p,s} = -k_p (s_2)^2 - \varepsilon |s_2| \leq 0 \tag{3.8}$$

Therefore,

$$\dot{V} = s_2 \dot{s}_2 = s_2 \frac{\partial N_R}{\partial \delta_{p,s}} \dot{\delta}_{p,s} \leq 0 \tag{3.9}$$

According to the Lyapunov stability theorem, it can be seen that the tracking error of the ship heading angle ψ_e under the sliding mode controller is asymptotically stable.

3.2 CMAC Neural Network Control

CMAC is a learning structure that mimics the human cerebellum. It's table inquiry self-adapting neural network used to express complex nonlinear function, which has rapid study and local generalization capacity and it can change the contents of a table by learning algorithms. Though the unit weights are also adjusted, but it doesn't have the neural network structure of the connection level and the dynamic behavior, but just a nonlinear mapping [7]. CMAC is recognized as an important part of a class of associative memory neural networks, which can learn any multi-dimensional nonlinear mapping. CMAC algorithm can be effectively used for nonlinear function approximation, dynamic modeling, control system design.

The structure of the CMAC is summarized Fig. 1.

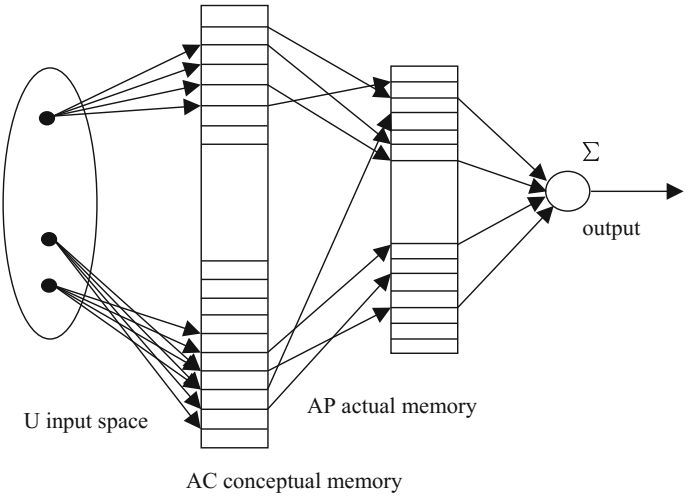

Fig. 1 The architecture of CMAC network

3.3 CMAC and NISM Integrated Controller

CMAC controller is suitable as a feed forward controller which can achieve the inverse dynamic model of the controlled object, while the nonlinear iterative sliding mode controller (NISM) is as a feedback control. Combining the two algorithms above can embody their advantages and overcome their shortcomings. The CMAC and NISM integrated controller is shown in Fig. 2.

In this chapter, the CMAC controller uses a learning algorithm of tutor. At the end of each control cycle, the corresponding output $u_n(k)$ of the CMAC is calculated and compared with the total control input $u(k)$, then correct the weights and enter into the learning process. The purpose of learning is to minimize the

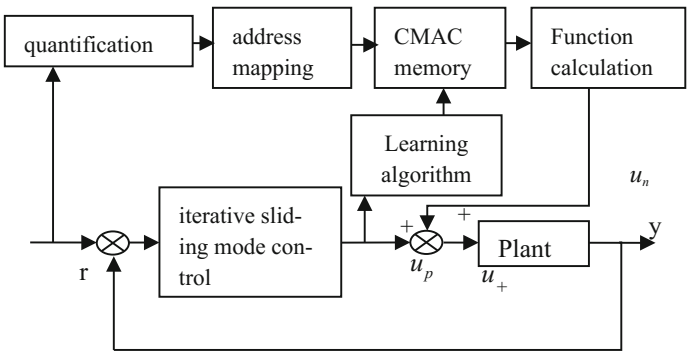

Fig. 2 Block diagram of CMAC and NISM integrated controller

difference between the total control input and the CMAC output [8]. After CMAC learning, the total control output of the system is generated by CMAC. In other word, in the early stage, the system is controlled by iterative sliding mode algorithm, after the end of learning, the system is mainly controlled by CMAC control algorithm. The control algorithm of the system is shown as below:

$$\begin{aligned} u_n(k) &= \sum_{i=1}^{c} w_i a_i \\ u(k) &= u_n(k) + u_p(k) \end{aligned} \tag{3.10}$$

where c refers to network generic parameters, a_i refers to the selected vector of system, $u_n(k)$ refers to the output produced by CMAC, $u_p(k)$ refers to the output of NISM controller. The adjustment indicators are as follows:

$$\begin{aligned} E(k) &= \frac{1}{2}(u_n(k) - u(k))^2 . \frac{1}{c} \\ \Delta w(k) &= -\eta \frac{\partial E(k)}{\partial w} = \eta \frac{u_p(k)}{c} a_i \\ w(k) &= w(k-1) + \Delta w(k) + \alpha(w(k) - w(k-1)) \end{aligned} \tag{3.11}$$

During the entire simulation system is running, assume $w = 0$, so $u_n = 0$, $u = u_p$. The system is controlled by iterative sliding mode controller, then gradually make the output $u_p(k)$ approaches zero, and the value of control variable $u_n(k)$ produced by CMAC will be gradually closed to the $u(k)$.

3.4 Simulation Studies

At this point the simulation state of ship is listed as follows: given course angle is 15°, initial speed is 23 km, propeller speed is 76.5 r/min. The parameters of environmental interference are shown as follows: wind speed is 10 m/s, wind direction angle is 30°, wave height is 2 m/s, wave direction is 10°, flow rate is 2 m/s, flow direction is 10°.

The simulation is given as follows:

Figures 3 and 4 show the curves of the ship's course angle and the rudder angle under the setting environment and working conditions. It can be seen from the simulation diagram that the curve of the rudder angle is smoother and there is no obvious chattering. The CMAC and NISM integrated controller is stable at about 500 s, while the PID is stable at 400 s. In addition, the peak of the rudder angle of the former controller is about 14°, which meets safety requirements and extends the service life of the steering engine. But the peak of the PID controller rudder angle is about 24°. The course angle can reach the expected value, but the PID controller is faster.

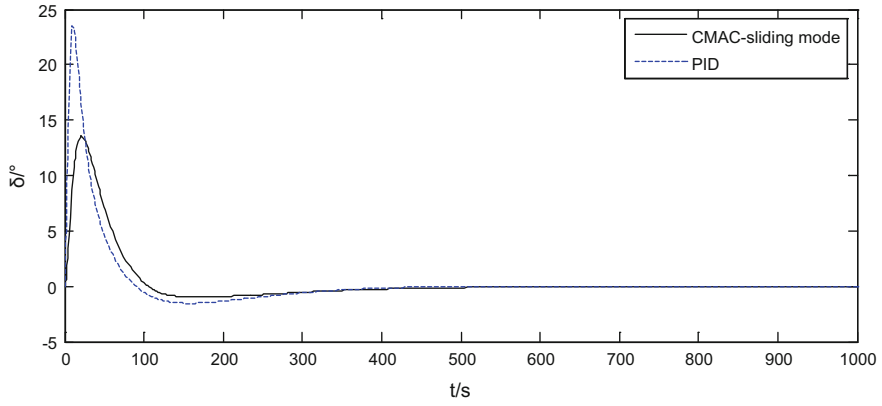

Fig. 3 Rudder angle curve

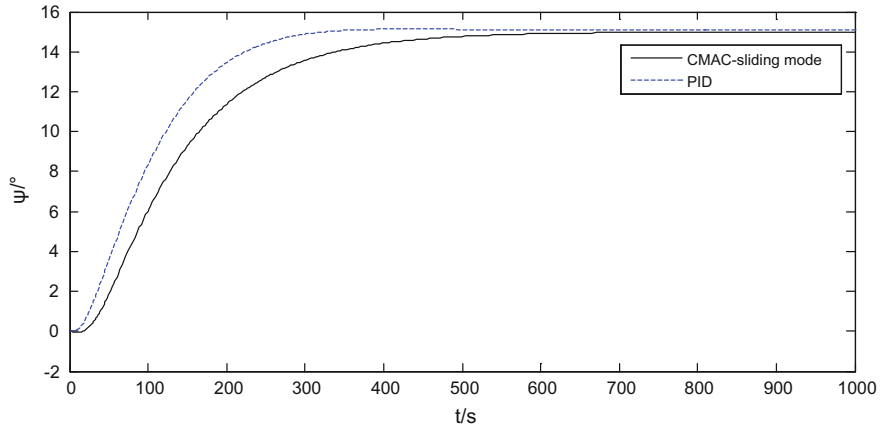

Fig. 4 Course angle curve

4 Conclusions

In this chapter, the mathematical model of the twin-rudder twin-propeller ship with interference is established by using MMG model. In order to overcome the disturbances, a nonlinear iterative sliding mode controller based on CMAC algorithm is illustrated and applied, which can effectively improve the performance and reduce the consumption. Nonlinear iterative sliding mode controller is designed with strictly bounded hyperbolic tangent nonlinear function tan h(x). And the stability of the algorithm is proved by the Lyapunov theory. In addition, the performance of the CMAC and NISM integrated controller scheme is compared with that of PID controller according to course tracking, stability and robustness. The

simulation results demonstrate that the curves of ship rudder angle and course angle are both smooth, and the controller has strong robustness for interference, therefore, stability can be achieved.

Acknowledgements The authors are very grateful to the editors and reviewers for their valuable comments and suggestions. This work is supported by National Natural Science Foundation of China (Nos. 51579024, 6137114) and the Fundamental Research Funds for the Central Universities (DMU No. 3132016311).

References

1. Wang ZW (2014) The simulation of maneuverability and intelligent control of large twin-propeller twin-rudder. Dalian maritime university, Dalian (in Chinese)
2. Hashem A, Kenneth R et al (2008) Sliding-mode tracking control of surface vessels. IEEE Trans Industr Electron 55(11):4004–4012
3. Bu RX, Liu ZJ et al (2008) Path following of underactuated surface ships with uncertain forward speed. In: Proceedings of the Chinese control and decision conference, IEEE, pp 4053–4058
4. Dai CS, Jang N, Shen ZP (2016) An adaptive nonlinear iterative sliding mode controller based on heuristic critic algorithm. In: International conference on information and automation, IEEE, pp 419–424
5. Jia HM, Zhang LJ et al (2012) Three dimensional path following control for an underactuated UUV based on nonlinear iterative. ACTA Autom Sinca 38(2):308–314 (in Chinese)
6. Jia XL, Yang YS (1999) Mathematical model of ship movement. Dalian maritime University Press, Dalian (in Chinese)
7. Wang L, Guo C (2010) CMAC-PID integrated controller used in marine propulsion plant. In: International conference on intelligent control and information processing, pp 367–370
8. Liu FR, Chen H (2008) Motion control of intelligent underwater robot based on CMAC-PID. In: International conference on information and automation, pp 1308–1311

A Method for Topic Classification of Web Pages Using LDA-SVM Model

Yuliang Wei, Wei Wang, Bailing Wang, Bo Yang and Yang Liu

1 Introduction

The fast developments on the computer and networking technologies have made the Internet become the largest medium of information in the word at present. While raw materials on Internet are massive, we often use some search engines, like Google, Baidu, for finding the required information. For most companies, they need collect government policies, competitors' marketing strategy and other industry-specific information. But the filtering of result from search engines and other input sources become a challenge. Man need check all of the web pages re-trieved from keywords and find the really websites he needed. The problem here is we need classify a set of web pages form different websites to different kinds, like government official site, finance company site.

In this problem, we can get many web pages form different source including search engine, third part input and manual input. The raw web pages don't have any label or classification. We need classify these web pages to some special types. In order to get right classification, manual classification is needed, but the sign work is heavy without creativity. There is very small signed samples can be used in here.

Many machine learning techniques, like Bayesian, neural networks, support vector machines (SVM), have been proposed for several classification problems. Among these methods, SVM is based on the structural risk minimization and VC dimension theory, and it is able to handle a small sample of data and has good

Y. Wei · W. Wang · B. Wang (✉) · Y. Liu
Harbin Institute of Technology, Culture West Road 2,
264209 Weihai, China
e-mail: wbl@hit.edu.cn

Y. Wei · W. Wang · B. Yang · Y. Liu
Coordination Center of China, Chaoyang District Yumin Road No. 3,
100029 Beijing, China
e-mail: yangbo@cert.org.cn

Z. Deng (ed.), *Proceedings of 2017 Chinese Intelligent Automation Conference*,
Lecture Notes in Electrical Engineering 458,
https://doi.org/10.1007/978-981-10-6445-6_64

generalization ability [1]. Considering the data attributes we use Latent Dirichlet Allocation (LDA) for the vectorization of documents [2]. The reason we chose these model are discussed in de-tail in the following sections. The result shows our method is efficient in this problem.

This paper is organized as follows: In Sect. 2, we give the definition of our webpages classification problem, and discuss the relate work. Section 3 introduce the detail about our LDA based classification. And the experimental results and discussion on the results are presented in Sect. 4. Finally, Sect. 5 concludes the study and gives some future work.

2 Relate Work

At first, we introduce the web pages classification problem, and then we describe the relate work.

2.1 Web Classification

Web page classification problem has been divided into more specific problems such as detection of pornographic web pages [3], finding phishing web pages [4], optimizing the crawler strategy [5] and some Web pages recommendation systems [6]. Unlike pure text, web page contains a number of elements. Many features can be extracted from the web pages, like contextual, visual, label and domain features. Some applications may use part of features while the other want use comprehensive information. Pornographic Web pages classification problem is more likely using both contextual and visual features while some search engine spam classification systems only use the url information [7]. The choice of features is ba*sed on the goal of application.*

In our problem, we are more focus on the company's properties of the website, such as decide whether the Web page is a "bank homepage", or a "finance web site", or a "P2P Lending platform". This kind of classification problem exists especially in focused the contextual features. Different categories may have same Web page structure and these features are useless in our problem. We only use the contextual feature in the Web pages. The problem is more likely a content classification.

Due to this big amount of data, web page classification becomes crucial since users encounter difficulties in finding what they are seeking, even though they use search engines. Many studies are focus on search engine results classification. In [8], Abdelbadie use implicit links-based techniques improve K-Nearest Neighbors and Naive Bayes algorithm. They consider the clicked list by a user through a query from search engine. The web pages clicked by one query are more likely similarity. Results show that: the implicit links-based similarity helps improve results. Thabit

and Ali are focus on terrorist activities, propose a feature set hybridization method, based on feature selection and extraction methods, for accurate content classification in Arabic dark web pages. It's turn out Web page classification problem has been divided into more specific problems.

2.2 SVM-LDA Model

Latent Dirichlet Allocation (LDA) was proposed by Blei et al. in 2003 [2]. The algorithm belongs to unsupervised clustering method. The input of LDA is only a topic number K and documents with word segmentation. Then LDA can output two matrix, word-topic and document-topic matrix. In our problem, we use the document-topic matrix as the SVM inputting vectors. LDA is a method to reduce the dimension of data so many application use LDA as data preprocessing.

Limeng et al. use SVM-LDA for news classification. The experimental data comes from the news data of 2013 issued by NCNA (New China News Agency), covering domestic news data from various news portals, containing 700 thousand news pages [9]. They randomly divided the corpus into five parts and used 5-fold validation to verify the theory. The results show LDA-SVM is qualified for the classification. In [10], Chen et al. put forward descriptive LDA which performs dataless text classification with only category description words and unlabeled documents. Their work is suitable for a given keyword unsupervised clustering. The LDA algorithm is often used in dimension reduction problem. Text classification is one of them.

In our problem, we discuss the influence of different K to the classification, and then we try sign the terms in web pages directly using word-topic matrix rather than re-training LDA model. The result show only the value of K is data set dependency.

3 Method Introduction

We define the collection of web pages is $H = \{h_1, h_2, \ldots, h_n\}, |h| = n$. And the content of h_i is $c_i, C = \{c_1, c_2, \ldots, c_n\}$. While the input of LDA algorithm is term list, we make segmentation processing to each c_i, and we get $S = \{s_1, s_2, \ldots, s_n\}, s_i = \{t_1, t_2, \ldots, t_m\}, t_i \in W$, W is the word dictionary. S and a topic number K is the parameter of LDA algorithm. And we can get word-topic matrix WT and document-topic matrix DT. $DT[s_i] = p_i$ means the probability of document i belong to each topic, $p_i = \{p_{i1}, p_{i2}, \ldots, p_{ik}\}$. $P = \{p_1, p_2, \ldots, p_k\}$ is the input of SVM classification.

1. Web pages H convert to document C. There are two kinds of strategies to achieve the transformation of web page to the content. One is extract all the text in web page and the other is only extract the main content without navigation

menus and other symbol text. For news classification, the latter one is more suitable. But in our problem, the web pages are the portal of websites, there is nearly no main content but many shot descriptive text and the main features are focus on these shot text. We use the all text in web page. Combine all text to one document in a web page as the web documents.

2. We use "jieba" module for text segmentation. "jieba" is a chinese text segmentation module for Python [11]. This library includes new word discovery and part-of-speech tagging. The final term list s_i is removal of stop words.
3. LDA algorithm has two priori parameters 'a' and 'b'. These two parameters affect the density of *WT* and *DT* topics, respectively. If the parameter is close to 0, the topics will be scattered. For example, assume we have five words and three topics, if the parameter is close to 0, the probability of each word belong to each topic tend to high variance. It's means little of topics' probability are high and others' are low. Contrary the results will be smoother. In text classification, we general take a small 'a' and a big 'b', that means we want one word is as little as possible belong to topics, and one document may content multiple topic. So here we set the 'a = 0.1' and 'b = 10'.
4. We use Libsvm as classifier module. Libsvm supply some easy script with which we can easily adjust the parameters including Kernel function selection [12].

4 Method Introduction

Test data set includes three categories, show in Table 1.

We can see that the number of P2P lending Platform sample is more than ten times of Bank Homepage. The reason is obvious, ordinary people can't open a bank but a P2P Lending company. The sample size disparity is a challenge.

We get document term list *S* after preprocessing. Then the LDA algorithm can process and we get the *WT* and *DT* matrixes. Each web page can find a K length vector in *DT* expressing the probity of each topic. For the sake of simplicity, let $B = \{b_1, b_2, \ldots, b_{139}\}$ be the vectors of Bank Homepage category, the vectors of Finance Website category be $F = \{f_1, f_2, \ldots, f_{375}\}$ and $L = \{l_1, l_2, \ldots, l_{1753}\}$ be the vectors of P2P Lending Platform category.

For different values of K, we calculate the average of each category vectors. The calculate formula show as below.

Table 1 Test data set

Categories	Number
Bank homepage	139
Finance website	375
P2P lending platform	1753

$$\bar{P} = \frac{\sum_{i=0}^{|P|} p_i}{|P|}, (\bar{P} = \{\bar{p}_1, \bar{p}_2, \ldots, \bar{p}_K\}) \quad (1)$$

And then we can get $\bar{B}$, $\bar{F}$, $\bar{L}$. We made a ladder to choose K value as an example, show in Fig. 1. In Fig. 2 only the topics who has probability greater than 0.02 are shown in the picture. Through these picture, we can see:

1. Different categories are focus one different topics. This attribute shows the data is separable. Different categories have different features.
2. The blue one is always focus on one topic. At first, we thought this is a good feature for classification. But we soon find it is not quite well.
3. With increasing K, the maximal probability is depressed. In Fig. 3 we can see more directly. The phenomenon is easy understanding. The number of documents and terms is stability, as the K increasing, each term belong to one topic

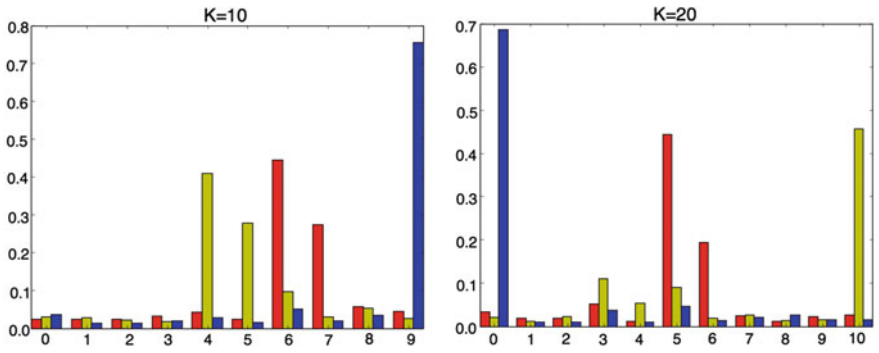

Fig. 1 K = 10, 20 $\bar{B} = blue$, $\bar{F} = yellow$, $\bar{L} = red$

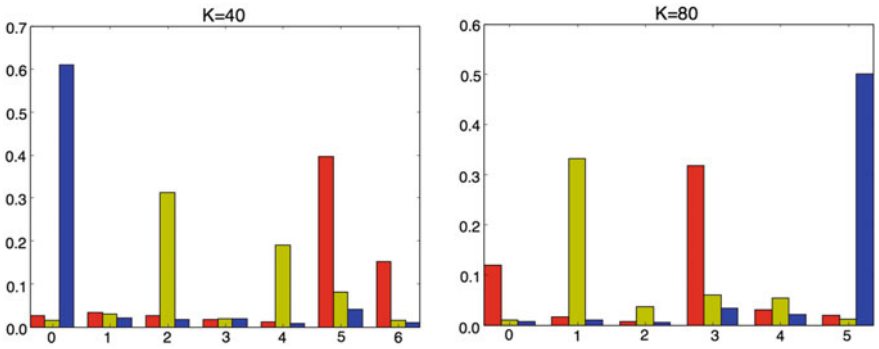

Fig. 2 K = 40, 80 $\bar{B} = blue$, $\bar{F} = yellow$, $\bar{L} = red$

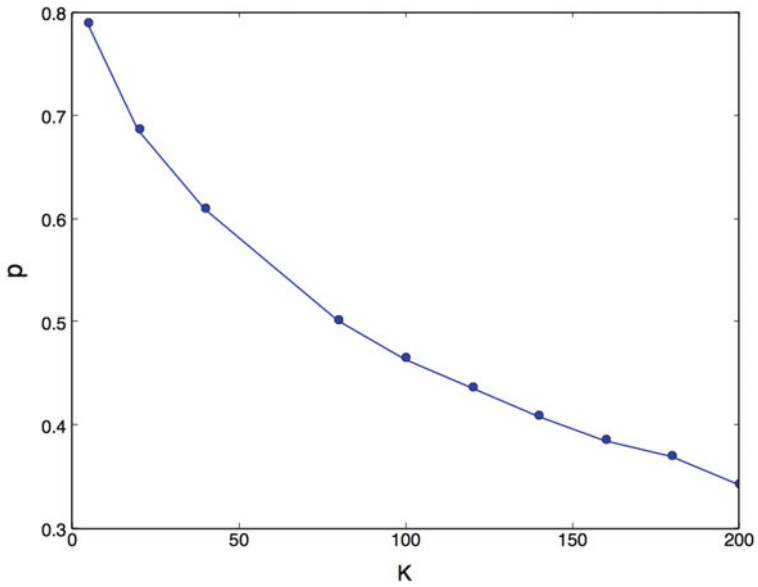

Fig. 3 The maximal probability of differnet K values

becomes more random. The characteristics is not very friendly to single peak category $\bar{B}$.

In our experiment, we can only use a tiny amount of samples. So we randomly selected 20 samples for SVM training. The samples are not enough to support Bayesian algorithm, so there is no contrast test with traditional algorithm. The result is show in Figs. 4 and 5. When K is between 10 and 50, the accuracy and recall is stability. We example the volatility $\bar{F}$ and find the wrong classification due to the poor web pages content. The many pages have too little text to get a right classification. When K is beyond 60, the recall of blue one is plummeting. To explain this, let's see the Fig. 3. When the K = 50, the maximal probability is nearly 0.5. Consider the feature 2), blue one is single peak. We can say that the highest probability topic determines a page whether belongs to blue. LDA is a probability model. A term's topic is random base on *WT* matrix. If the maximal probability is less than 0.5, a word can have a high possibility marked as other topic rather than the maximal probability. This is very bad for the single peak category. Because the key words are signed wrong with a high possibility. So the final prediction is wrong.

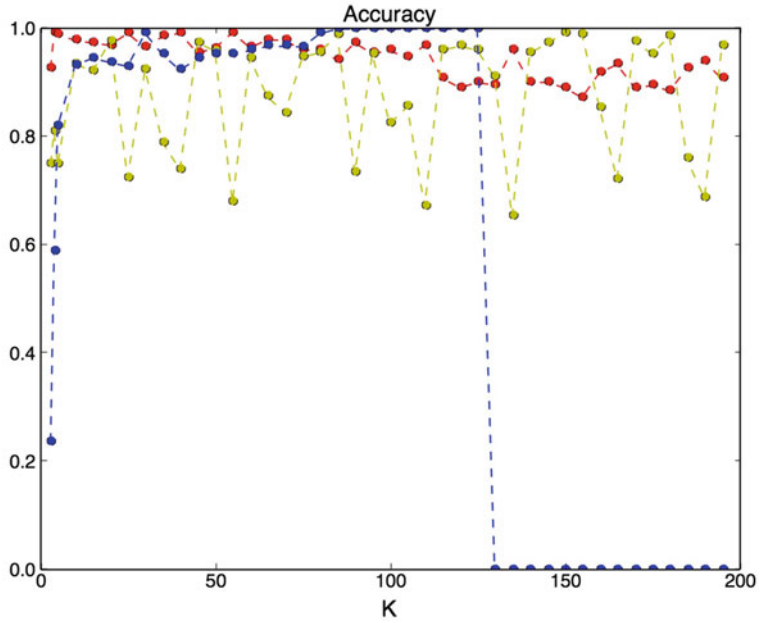

Fig. 4 SVM accuracy, $\bar{B} = blue, \quad \bar{F} = yellow, \quad \bar{L} = red$

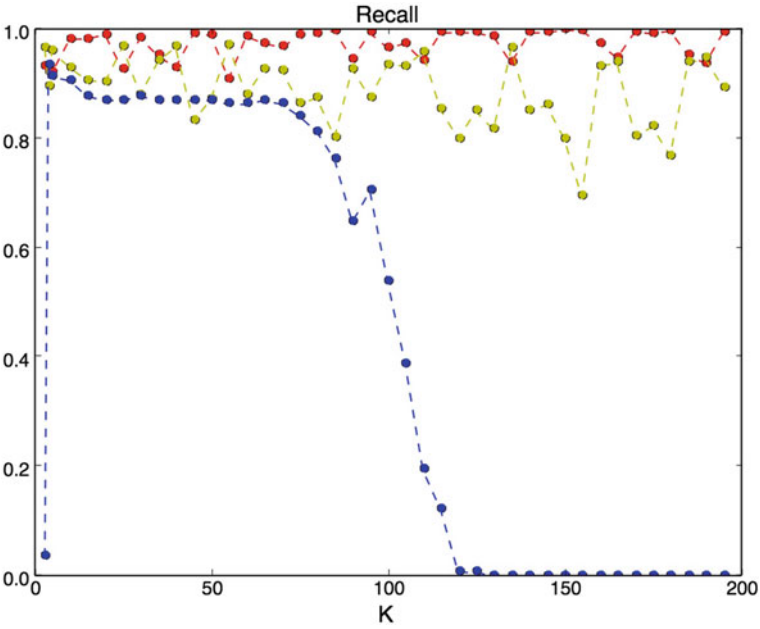

Fig. 5 SVM recall, $\bar{B} = blue, \quad \bar{F} = yellow, \quad \bar{L} = red$

5 Conclusion

Using the model we propose in this paper, we can use little signed samples for web pages classification. This will greatly reduce the manual work. Through the analyze of experiments, we find the connection between topic number K and data set. Further testing is needed for finding accurate correlation.

Another, we get 90 thousand poor classification data set, some of the classification is wrong and some web page is outdated or change. We want to build a flexible and effective system for unknown web pages classification. This work is focus on sophisticated category, and our next work will expand the data set and categories. Wrong data filtering and hierarchical classification is both challenge.

Acknowledgements Project supported by the National Natural Science of China undergrant No. 61371177.

References

1. Cortes Corinna, Vapnik Vladimir (1995) Support-vector networks. Mach Learn 20(3):273–297
2. Blei DM, Ng AY, Jordan MI (2003) Latent dirichlet allocation. J Mach Learn Res 3
3. Ahmadi A, Fotouhi M, Khaleghi M (2011) Intelligent classification of web pages using contextual and visual features. Appl Soft Comput 11(2)
4. Abdelhamid N, Ayesh A, Thabtah F (2014) Phishing detection based associative classification data mining. Expert Syst Appl 41(13):5948–5959
5. O ̈zel SA (2011) A web page classification system based on a genetic algorithm using tagged-terms as features. Expert Syst Appl: Int J 38(4)
6. Nguyen TTS, Lu HY, Lu J (2014) Web-page recommendation based on web usage and domain knowledge. IEEE Trans Knowl Data Eng 26(10):2574–2587
7. Hern´andez I, Rivero CR, Ruiz D, Corchuelo R (2014) CALA: an unsupervised URL-based web page classification system. Knowl-Based Syst 57
8. Belmouhcine A, Benkhalifa M (2016) Implicit links-based techniques to enrich k-nearest neighbors and naive bayes algorithms for web page classification. In Proceedings of the 9th international conference on computer recognition systems CORES 2015. Springer International Publishing
9. Cui L, Meng F, Shi Y, Li M, Liu A (2014) A hierarchy method based on LDA and SVM for news classification. In 2014 IEEE international conference on data mining workshop, pp 60–64
10. Chen X, Xia Y, Jin P, Carroll J (2015) Dataless text classification with descriptive LDA. In AAAI'15: Proceedings of the twenty-ninth AAAI conference on artificial intelligence. Leshan Teachers College, AAAI Press, New York
11. fxsjy. "jieba" chinese text segmentation. https://github.com/fxsjy/jieba, 2012
12. Chang CC, Lin CJ (2011) A library for support vector machines.http://www.csie.ntu.edu.tw/cjlin/libsvm/, 2001

Adaptive Robust Control for a Class of Singular Systems with Actuator Saturation

Zhuang Cai, Hai-tao Song and Qi Tian

1 Introduction

Singular systems, also known as descriptor systems, implicit systems and differential algebraic systems, are widely used in the fields of electric power, economy, aviation and chemical industry systems. In recent years, many scholars have carried out research on the control problems of singular system [1, 2]. The robust H_∞ control problem for a class of singular systems was studied in [3]. First, the sufficient condition for solving the H_∞ control problem is given by using the state feedback and the output feedback control method. Then, based on two Hamilton-Jacobi inequalities and a weak coupling condition, the necessary condition of H_∞ control for a class of singular systems by output feedback is given. In [4], two adaptive robust control approaches are proposed for structural and non-structural uncertainty respectively, the first control method achieves asymptotical stability and robustness of the closed-loop singular system, the second approach aims at a more general case where the stability of the system is obtained while avoiding the influence of potential problems such as parametric drift caused by un-modeled dynamics. The robust dissipative control problem was researched in [5], firstly, the sufficient conditions for the strict dissipation of the system are given based on the Lyapunov stability theory, and a state feedback controller is designed to achieve the asymptotic stability of closed-loop systems.

Actuator saturation is a common physical phenomenon in practical systems. In recent years, the analysis and design problems of systems with actuator saturation have attracted the attention of many researchers [6, 7]. However, in the case of actuator saturation, little work has been done for singular systems, especially nonlinear singular systems. Different from [6], we give the existence condition of the stabilization controller based on the Lyapunov indirect method. In [7], the

Z. Cai (✉) · H. Song · Q. Tian
Xi'an High-Tech Research Center, Xi'an 710025, China
e-mail: caiz_summer@163.com

Z. Deng (ed.), *Proceedings of 2017 Chinese Intelligent Automation Conference*,
Lecture Notes in Electrical Engineering 458,
https://doi.org/10.1007/978-981-10-6445-6_65

control design of a class of affine singular systems with actuator saturation is studied. State feedback stabilization controller, robust controller and adaptive controller are designed respectively. It should be pointed out that the theorem 4 in [7] cannot be established according to Schur complement lemma.

Adaptive robust control method has been applied to many uncertain systems [8, 9]. In [8], an adaptive robust control method is applied to nonlinear systems with parametric uncertainties and external disturbances, where the system disturbance has an upper bound which can be determined by a known function. In [9], adaptive variable structure control is applied to a nonlinear system with uncertain input-output linearization, in which the uncertainty bound is considered to be known and can be expressed as a product of a known function and a positive constant, and the objective of the adaptive design is to estimate the unknown constants within the system. In this paper, in order to enhance the robustness of the system and the practicality of control method, the system uncertainties are considered to be represented by the product of a known functions set and an unknown adaptive parameter.

In this paper, we study the stabilization and adaptive robust control problem for a class of singular systems with actuator saturation. The Lyapunov stability theory is used to derive the stablizable condition of the system. For the nonlinear uncertainties which exist widely in practical systems, an adaptive compensation controller is designed for matching nonlinear uncertainties, the LMI conditions and control parameter conditions for the system to be robust is derived. Finally, the simulation experiment is carried out for the singular system with disturbance, and the simulation results show the correctness and validity of the proposed method.

2 System Description

We consider the following singular system with nonlinear uncertainty:

$$E\dot{x}(t) = Ax(t) + Bsat(u) + g(x,p,t) \tag{1}$$

where, $x \in R^n$ is state vector, $u \in R^m$ is control input vector, $g(x,p,t)$ is nonlinear uncertainty, $p \in P$ is unknown parameter vector, P is the admissible set of the system. $E \in R^{n\times n}$ is singular matrix, i.e. $rank\ E = r < n$, matrix A and B are real matrices with appropriate dimension. $sat(u) = [sat(u_1), sat(u_2), \cdots, sat(u_m)]^{\mathrm{T}}$, $sat(\cdot)$ is nonlinear saturation function, defined as:

$$sat(u_i) = \begin{cases} s_i, & u_i > s_i \\ u_i, & -s_i \le u_i \le s_i, \ , i = 1,2,\cdots,m. \\ -s_i, & u_i < -s_i \end{cases}$$

Definition 1 [1]

(1) If there exist a complex number s such that $\det(sE - A) \not\equiv 0$, then matrix pencil (E, A) is called to be regular;
(2) If $^{\circ}(\det(sE - A)) = rank(E)$, then matrix pencil (E, A) is called to be impulse-free;
(3) If matrix pencil (E, A) is regular, stable and impulse-free, then it is admissible.

Lemma 1 [10] *Matrix pencil* (E, A) *admissible, if and only if there exists matrix* $X \in R^{n\times n}$ *such that*

$$E^{\mathrm{T}}X = X^{\mathrm{T}}E \geq 0$$
$$A^{\mathrm{T}}X + X^{\mathrm{T}}A < 0.$$

3 Adaptive Robust Control

The stabilization problem of singular system with actuator saturation can be described as follows:

For the nominal system of system (1):

$$E\dot{x}(t) = A\,x(t) + B\,sat(u) \tag{2}$$

Finding a state feedback control law

$$u(t) = Kx(t) \tag{3}$$

Such that the closed-loop system is asymptotic stable.

Lemma 2 [11] *Let* $\eta = u - sat(u)$, *there exists a real constant* $\varepsilon \in (0, 1)$ *such that*:

$$\eta^{\mathrm{T}}\eta \leq \varepsilon u^{\mathrm{T}}u.$$

The adaptive robust control problem of system (1) can be described by designing the controller $u(t) = \alpha(x, \theta)$ and the parameter adaptive law $\dot{\hat{\theta}} = \beta\left(x, \hat{\theta}\right)$, such that the closed loop system achieves asymptotic stability under the nonlinear uncertainty $g(x, t)$. $g(x, t)$ is a time varying nonlinear perturbation with $g(0, t) = 0$ and satisfies the following Lipschitz condition:

$$\|g(x_1) - g(x_2)\| \leq \varsigma\|M_i(x_1 - x_2)\| \tag{4}$$

In this article, the nonlinear uncertainty $g(x, p, t)$ is approximated by an RBF neural networks model

$$\hat{g}(\hat{x},p,t) = \xi^{\mathrm{T}}(\hat{x},t)\hat{\theta}(p)$$
$$\xi(\hat{x},t) = diag(\xi_1,\xi_2,\cdots,\xi_m)$$
$$\hat{\theta} = \left[\hat{\theta}_1,\hat{\theta}_2,\cdots,\hat{\theta}_m\right]^{\mathrm{T}}$$

where, $\hat{\theta}(p)$ is unknown adaptive parameter vector, $\xi(\hat{x},t)$ is known Gaussian basis function.

It is assumed that there is an optimal weight matrix θ such that the approximation error is minimized, i.e.

$$\theta \triangleq \arg\min_{\hat{\theta}} \|g(x,p,t) - \hat{g}(\hat{x},p,t)\|$$

and this optimal weight matrix is assumed to be piecewise constant, or slow time-varying, i.e. $\dot{\theta} = 0$.

It is shown in [9, 10] that, if $\hat{x}$ is restricted to a compact set $X \subset R^n$, for a large enough number hidden layer neurons in neural network, there always exist a constant θ such that any nonlinear function can be estimated accurately by an RBF networks model.

Theorem 1 *For the singular system* (1) *with actuator saturation and nonlinear uncertainty, if there exists positive definite matrix P such that the following conditions are satisfied:*

$$E^{\mathrm{T}}P = P^{\mathrm{T}}E \tag{5}$$

$$P^{\mathrm{T}}A + \frac{1}{2}P^{\mathrm{T}}BB^{\mathrm{T}}P < 0 \tag{6}$$

then the adaptive robust control problem of system (1) can be solved by the following control law $u(t)$ which is numerical solutions of the following equation

$$au^{\mathrm{T}}u + bu + c = 0 \tag{7}$$

and the adaptive law

$$\dot{\hat{\theta}} = -\rho^{-1}\xi B^{\mathrm{T}}Px \tag{8}$$

where, a,c,λ,ρ, are real constants, b is real vector, $a = 0.5\varepsilon$, $b = x^{\mathrm{T}}P^{\mathrm{T}}B$, $c = x^{\mathrm{T}}P^{\mathrm{T}}B\xi^{\mathrm{T}}\hat{\theta}$.

Proof Using the Lipschitz condition (4), we can always achieve $u(t)$ from Eq. (7). Select the Lyapunov candidate function

$$V = \frac{1}{2}x^{\mathrm{T}}P^{\mathrm{T}}Ex + \frac{1}{2}\tilde{\theta}^{\mathrm{T}}\rho\tilde{\theta}$$

where $\tilde{\theta} = \theta - \hat{\theta}$, the derivative of V is

$$\begin{aligned}\dot{V} &= x^{\mathrm{T}}P^{\mathrm{T}}Ax - x^{\mathrm{T}}P^{\mathrm{T}}B\eta + x^{\mathrm{T}}P^{\mathrm{T}}Bu + x^{\mathrm{T}}P^{\mathrm{T}}B\xi^{\mathrm{T}}\theta + \tilde{\theta}^{\mathrm{T}}\rho\dot{\tilde{\theta}} \\ &\leq x^{\mathrm{T}}P^{\mathrm{T}}Ax + \frac{1}{2}x^{\mathrm{T}}P^{\mathrm{T}}BB^{\mathrm{T}}Px + \frac{1}{2}\eta^{\mathrm{T}}\eta + x^{\mathrm{T}}P^{\mathrm{T}}Bu + x^{\mathrm{T}}P^{\mathrm{T}}B\xi^{\mathrm{T}}\theta + \tilde{\theta}^{\mathrm{T}}\rho\dot{\tilde{\theta}}\end{aligned}$$

Using lemma 2 and Eq. (7), we obtain

$$\dot{V} \leq x^{\mathrm{T}}P^{\mathrm{T}}Ax + \frac{1}{2}x^{\mathrm{T}}P^{\mathrm{T}}BB^{\mathrm{T}}Px + x^{\mathrm{T}}P^{\mathrm{T}}B\xi^{\mathrm{T}}\tilde{\theta} + \tilde{\theta}^{\mathrm{T}}\rho\dot{\tilde{\theta}}$$

Using the adaptive law (8), we obtain

$$\dot{V} \leq x^{\mathrm{T}}P^{\mathrm{T}}Ax + \frac{1}{2}x^{\mathrm{T}}P^{\mathrm{T}}BB^{\mathrm{T}}Px$$

Therefore, the asymptotic stability can be achieved under control law $u(t)$.

Remark In order to obtain matrix P, we need the following transformation:

$$\bar{P} = U^{-\mathrm{T}}PM = \begin{bmatrix}\bar{P}_{11} & \bar{P}_{12} \\ \bar{P}_{21} & \bar{P}_{22}\end{bmatrix}, \quad \bar{E} = UEM = \begin{bmatrix}I_r & \\ & 0\end{bmatrix}$$

where, U and M are invertible matrices.
From Eq. (5), we obtain

$$\begin{aligned}&\bar{E}^{\mathrm{T}}\bar{P}{=}M^{\mathrm{T}}E^{\mathrm{T}}U^{\mathrm{T}}U^{-\mathrm{T}}PM = M^{\mathrm{T}}P^{\mathrm{T}}U^{-1}UEM = \bar{P}^{\mathrm{T}}\bar{E} \\ &\bar{E}^{\mathrm{T}}\bar{P} = \bar{P}^{\mathrm{T}}\bar{E} \geq 0 \Rightarrow \bar{P}_{11} = \bar{P}_{11}^{\mathrm{T}} \geq 0, \bar{P}_{12} = 0 \Rightarrow \bar{P} = \begin{bmatrix}\bar{P}_{11} & 0 \\ \bar{P}_{21} & \bar{P}_{22}\end{bmatrix} \\ &P = U^{\mathrm{T}}\begin{bmatrix}\bar{P}_{11} & \\ & 0\end{bmatrix}UU^{-1}\begin{bmatrix}I_r & \\ & 0\end{bmatrix}M^{-1} + U^{\mathrm{T}}\begin{bmatrix}0 & \\ & I_{n-r}\end{bmatrix}Q^{-1}Q[\bar{P}_{21} \quad \bar{P}_{22}]M^{-1} \\ &= ZE + LY\end{aligned}$$

where, $Z = U^{\mathrm{T}}\begin{bmatrix}\bar{P}_{11} & \\ & 0\end{bmatrix}U$, $Y = N[\bar{P}_{21} \quad \bar{P}_{22}]V^{-1}$. Matrix L satisfies $E^{\mathrm{T}}L = 0$, and $L = U^{\mathrm{T}}\begin{bmatrix}0 \\ I_r\end{bmatrix}Q^{-1}$. To obtain matrix P, we just need matrix Z and matrix Y.

4 Simulation Example

In this section, we propose the adaptive robust controller for nonlinear singular systems with actuator saturation based the conclusion in Sect. 3.

To validate the effectiveness of this paper, in this section, we give a simulation example, where the parameters are:

$$E = \begin{bmatrix} 1 & 0 \\ 0 & 0 \end{bmatrix}, \quad A = \begin{bmatrix} -3 & 2 \\ 1 & -3 \end{bmatrix}, \quad B = \begin{bmatrix} 0.5 & 0 \\ 0 & 0.5 \end{bmatrix},$$

Using the LMI toolbox in Matlab, the following matrix can be obtained:

$$Z = \begin{bmatrix} 5.8556 & 16.7656 \\ 16.7656 & 0 \end{bmatrix}, \quad P = \begin{bmatrix} 5.8556 & 0 \\ -1.1940 & 13.9666 \end{bmatrix},$$

$$Y = \begin{bmatrix} -17.9596 & 13.9666 \end{bmatrix}$$

The initial state is $x(0) = [-1 \quad 0]^{\mathrm{T}}$. Nonlinear uncertain function is $g(t) = \sin(t)$.

The curve of uncertainty g and its estimation $\hat{g}$ are shown in Fig. 1, the response of the state x_1 is shown in Fig. 2, and the control signal curve is shown in Fig. 3.

It can be observed from Fig. 1 that the output of neural network converges to the uncertainty, therefore, in Fig. 2 that the system state converges to the origin quickly under the effect of nonlinear uncertainty. Simulation results show that the system controller works very well in attenuating external uncertainty.

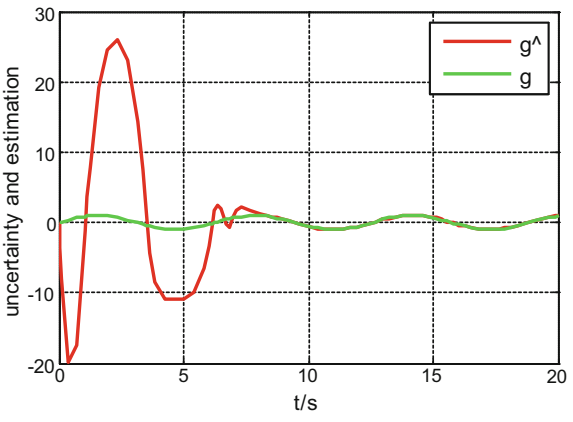

Fig. 1 Uncertainty g and its estimation $\hat{g}$

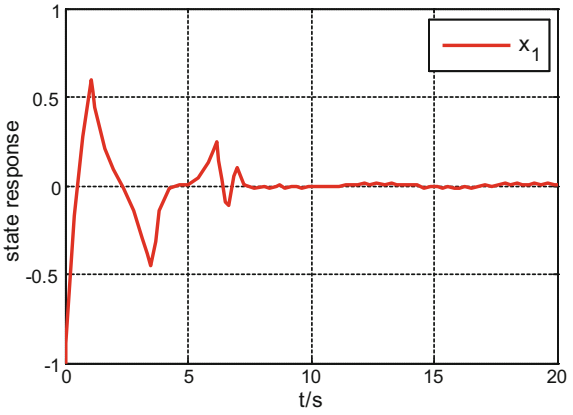

Fig. 2 Response of the state x_1

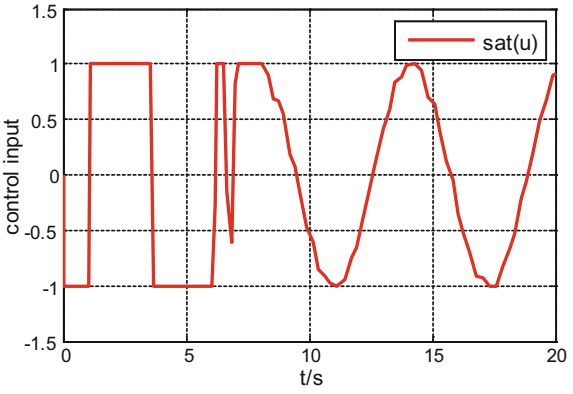

Fig. 3 Control input curve $sat(u)$

5 Conclusions

In this article, a class of singular systems with nonlinear uncertainties and actuator saturation is studied, an adaptive robust controller is designed for the nonlinear uncertainties of the system. The asymptotic stability of the closed-loop system is proved based on the Lyapunov stability theory, and the correctness of the method is proved by the simulation experiment. The method of this paper enriches the adaptive robust control of singular systems, which can be regarded as a supplement and perfection under the condition of actuator saturation.

References

1. Dai L (1989) Singular control systems. Springer, Berlin, Germany
2. Duan GR, Yu HH, Wu AG, Zhang X (2012) Analysis and design of descriptor linear systems. Science Press, Beijing
3. Wang HS, Yung CF, Chang FR (2002) H_∞ control for nonlinear descriptor systems. IEEE Trans Autom Control 47(11):1919–1925
4. Xu JX, Jia QW, Lee TH (2000) Adaptive robust control schemes for a class of nonlinear uncertain descriptor systems. IEEE Trans Circ Syst-I: Fundam Theory Appl 47(6):957–962
5. Zhou J, Zhang QL, Li J, Men B, Ren J (2014) Dissipative control for a class of nonlinear descriptor dystems. Int J Syst Sci 1–12
6. Lan W, Huang J, Semiglobal stabilization and output regulation of singular linear systems with input saturation. IEEE Trans Autom Control 48(7):1274–1280
7. Sun LY, Wang YZ, Feng G (2015) Control design for a class of affine nonlinear descriptor systems with actuator saturation. IEEE Trans Autom Control 60(8):2195–2200
8. Xu JX, Lee TH, Jia QW, An adaptive robust control scheme for a class of nonlinear uncertain systems (1997). Int J Syst Sci 28(4):429–434
9. Liao TL, Fu LC, Hsu CF (1990) Adaptive robust tracking of nonlinear systems and with an application to a robotic manipulator. Syst Control Lett 15:339–348
10. Masubuchi I, Kamitane Y, Ohara A (1997) H_∞ Control for Descriptor systems: a matrix inequalities approach. Automatica 33(4):669–673
11. Wei AR, Wang YZ (2010) Stabilization and H_∞ control of nonlinear port-controlled Hamiltonian systems subject to actuator saturation. Automatica 46:2008–2013

Trajectory Tracking Control for Omnidirectional Mobile Robots with Full-State Constraints

Wenhao Zheng and Yingmin Jia

1 Introduction

During recent few years, omnidirectional mobile robots have been widely applied in different fields of society, such as the mobile platform, factory automation, logistics transportation, military affairs and environmental exploration. Comparing with the nonholonomic robots such as car-like mobile robots, the omnidirectional mobile robot have the ability of three degree-of-freedom motion in the plane, which can provide the superior maneuvering capability. Tracking control problems of omnidirectional mobile robots, which have attracted the interest of many researchers, are significant in the practical application.

Many control methods have been proposed such as sliding mode control [1], fuzzy control [2], adaptive control [3], model predictive control [4] and their combinations. Due to the ideal assumptions and the complex environment, model uncertainties and external disturbances are significant factors which have effects on the tracking performance, and these factors should be considered during designing the control strategy. An adaptive fuzzy terminal sliding-mode tracking controller for omnidirectional mobile robots with system uncertainties and external disturbances was presented in [5], in which the adaptive estimation scheme was used to adjust parameter vector and the switching law of sliding mode with fuzzy logic was given to constitute the control strategy. Alakshendra [6] proposed an adaptive higher-order sliding mode controller for the trajectory tracking based on dynamics with unknown bounded uncertainties, and the adaptive law was designed. Comparing with the PID controller and the adaptive robust sliding mode controller, this control strategy had better tracking performance. Moreover, system parameters

W. Zheng · Y. Jia (✉)
The Seventh Research Division and the Center for Information and Control,
School of Automation Science and Electrical Engineering,
Beihang University (BUAA), Beijing 100191, China
e-mail: ymjia@buaa.edu.cn

Z. Deng (ed.), *Proceedings of 2017 Chinese Intelligent Automation Conference*,
Lecture Notes in Electrical Engineering 458,
https://doi.org/10.1007/978-981-10-6445-6_66

of dynamics are assumed unknown, and the adaptive sliding mode controller with smooth switching law was designed to handle structured and unstructured uncertainties in [7], in which this controller was able to improve tracking behaviors and avoid the singularity of control inputs. In practical engineering applications, in order to guarantee the safety or meet requirements of the operating environment, state constraints of omnidirectional mobile robots should be taken into account. A novel adaptive control strategy was proposed for nonlinear pure-feedback systems in [8], and the BLF with tracking errors was introduced to avoid violating the state constraints. In [9], an adaptive neural network was employed to approximate dynamic model of the uncertain robot system, and the control method was given based on barrier Lyapunov method to ensure the boundedness of all signals, thus, state constraints held all the time and the tracking error would be tuned into a sufficiently small compact set with suitable parameters of controller.

This paper mainly focuses on the tracking problem of omnidirectional mobile robots with state constraints. The adaptive law is designed for unknown bounded disturbances caused by simplified assumptions of dynamics and complex environment, so that the reliability, stability, robustness and safety of trajectory tracking are improved. And the controller based on barrier Lyapunov function guarantees the full-state constraints which indicates that the states will never exceed the limitations. All signals in the closed-loop system are proved to be uniformly bounded and stability of tracking is guaranteed. Comparing with existing results, this paper contributes to the novel solution of states constraints of omnidirectional mobile robots with disturbances.

The rest of the paper is organized as follows. The Sect. 2 introduces the kinematic model and the dynamic model of the three-wheel omnidirectional mobile robots with model uncertainties and external disturbances. In the Sect. 3, the controller with the adaptive law based on barrier Lyapunov function is given, and the stability of tracking system is analyzed. The simulation is presented to show the validity of the control strategy in Sect. 4. In the end, the Sect. 5 summarizes the whole paper and draws the conclusions.

2 Kinematics and Dynamics of Omnidirectional Mobile Robots

As shown in Fig. 1, the three-wheel omnidirectional mobile robot, which is composed of three omnidirectional wheels, servo driving systems, and the control motion control card, is considered in this paper. The kinematic model is shown as Eq. (1).

$$\begin{pmatrix} \dot{x} \\ \dot{y} \\ \dot{\theta} \end{pmatrix} = \begin{pmatrix} \cos\theta & -\sin\theta & 0 \\ \sin\theta & \cos\theta & 0 \\ 0 & 0 & 1 \end{pmatrix} \begin{pmatrix} v_x \\ v_y \\ \omega \end{pmatrix} \tag{1}$$

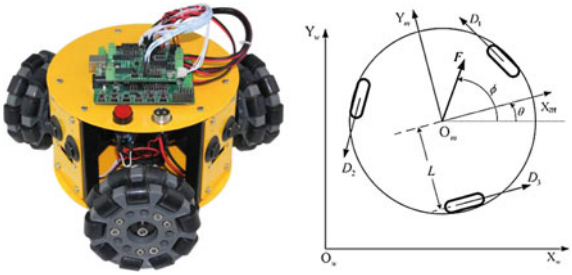

Fig. 1 The structure of three-wheel structure of the robot (*left*) and the force analysis (*right*)

X_wOY_w represents the world coordinate and $X_mO_mY_m$ is the coordinate system of the mobile robot. The position of the center of the robot in Cartesian coordinates is (x, y) and θ is the robot orientation in world coordinate. (v_x, v_y) here denotes robot's longitudinal velocity and transverse velocity, and ω represents the rotate speed of the robot. L is the plane distance from the center of the robot to the center of the omnidirectional wheel. The driving force from the driving wheel can be described as $D_i(i = 1, 2, 3)$. F is the resultant force of driving forces and ϕ is the direction angle of the resultant force. As a matter of fact, the kinematics of all kinds of omnidirectional robots can be expressed as Eq. (1).

The dynamics of this kind of three-wheel omnidirectional mobile robot can be derived by using Newton' Second Law. The Eq. (2) can be obtained with similar derivation process in [6].

$$\begin{pmatrix} \dot{v}_x \\ \dot{v}_y \\ \dot{\omega} \end{pmatrix} = \begin{pmatrix} a_1 v_x \\ a_1 v_y \\ a_3 \omega \end{pmatrix} + \begin{pmatrix} a_2 \omega v_y \\ -a_2 \omega v_x \\ 0 \end{pmatrix} + \begin{pmatrix} -b_1 & -b_1 & 2b_2 \\ \sqrt{3}b_1 & -\sqrt{3}b_1 & 0 \\ b_2 & b_2 & b_2 \end{pmatrix} \begin{pmatrix} \tau_1 \\ \tau_2 \\ \tau_3 \end{pmatrix} \tag{2}$$

According to the kinematics (1) and dynamics (2), we can describe the motion of omnidirectional mobile robots as

$$\begin{aligned} \dot{x}_1 &= J(\theta) x_2 \\ \dot{x}_2 &= A x_2 + a_2 S(x_2) + B\tau \end{aligned} \tag{3}$$

where the variables and parameters are defined as follows:

$$x_1 = (x, y, \theta)^T,\ x_2 = (v_x, v_y, \omega)^T,\ S(x_2) = (\omega v_y, -\omega v_x, 0)^T, \tau = (\tau_1, \tau_2, \tau_3)^T,$$
$$A = diag\{a_1, a_1, a_3\},\ a_1 = -3c/(3I_\omega + 2mr^2),\ a_2 = 2mr^2/(3I_\omega + 2mr^2),$$
$$a_3 = -3cL^2/(3I_\omega L^2 + I_v r^2),\ b_1 = kr/(3I_\omega + 2mr^2),\ b_2 = krL/(3I_\omega L^2 + I_v r^2),$$

$$J(\theta) = \begin{pmatrix} \cos\theta & -\sin\theta & 0 \\ \sin\theta & \cos\theta & 0 \\ 0 & 0 & 1 \end{pmatrix}, \quad B = \begin{pmatrix} -b_1 & -b_1 & 2b_2 \\ \sqrt{3}b_1 & -\sqrt{3}b_1 & 0 \\ b_2 & b_2 & b_2 \end{pmatrix}$$

Assume that each wheel has the same property and the same size. m is the mass of the robot and I_v is the moment of Inertia of the robot. The moment of each wheel can be defined as I_w, and r is the radius of the wheel. Besides, c denotes the viscous friction factor of the wheel and k represents the gain factor of the driving wheel. The input torques are described as τ_i.

Considering the model uncertainties and external disturbance, we can get the dynamics as $\dot{x}_2 = (A + \Delta A)x_2 + (a_2 + \Delta a_2)S(x_2) + (B + \Delta B)\tau + w(x,t)$. In order to deal with this problem, we define $d(x,t) = \Delta A x_2 + \Delta a_2 S(x_2) + \Delta B\tau + w(x,t)$ where $d(x,t) = (d_1, d_2, d_3)^T$ and the boundedness d of $d(x,t)$ is unknown with $|d_i| \le d_t$. Thus, the robot system with model uncertainties and external disturbance can be expressed as (4).

$$\begin{aligned} \dot{x}_1 &= J(\theta)x_2 \\ \dot{x}_2 &= Ax_2 + a_2 S(x_2) + B\tau + d(x,t) \end{aligned} \tag{4}$$

The tracking control problem with full-state constraints is that suitable control law should be designed to track the desired trajectory (x_d, y_d, θ_d) and the state constraints $|x| < k_x$, $|y| < k_y$, $|\theta| < k_\theta$, $|v_x| < k_{vx}$, $|v_y| < k_{vy}$, $|\omega| < k_\omega$ are not violated, where $k_{c1} = (k_x, k_y, k_\theta)^T$, $k_{v1} = (k_{vx}, k_{vy}, k_\omega)^T$ are positive constants. Assume that the desired trajectory satisfies $|x_d| \le k_{xd} < k_x$, $|y_d| \le k_{yd} < k_y$, $|\theta_d| \le k_{\theta d} < k_\theta$,

$|v_{xd}| \le k_{vxd} < k_{vx}$, $|v_{yd}| \le k_{vyd} < k_{vy}$, $|\omega_d| \le k_{\omega d} < k_\omega$, where $k_{c2} = (k_{xd}, k_{yd}, k_{\theta d})^T$, $k_{v2} = (k_{vxd}, k_{vyd}, k_{\omega d})^T$ are positive constants.

3 Controller Design

Consider the kinematics and dynamics of the robot (4). An adaptive controller based on barrier Lyapunov method is given to handle the full-state constraints and disturbances. Two inequalities are given as follows.

$$0 \le |x| - x \tan h(\varepsilon x) \le \frac{l}{\varepsilon} \quad (\varepsilon > 0, l = e^{-(l+1)}) \tag{5}$$

$$\log \frac{k^2}{k^2 - x^2} \le \frac{x^2}{k^2 - x^2} \quad (|x| < k) \tag{6}$$

Denote $z_{11} = x - x_d$, $z_{12} = y - y_d$, $z_{13} = \theta - \theta_d$, $z_{21} = v_x - \alpha_{11}$, $z_{22} = v_y - \alpha_{12}$, $z_{23} = \omega - \alpha_{13}$, which also can be expressed as $z_1 = x_1 - x_{1d}$, $z_2 = x_2 - \alpha_1$. Choose a barrier Lyapunov function as

$$V_1 = \frac{1}{2}\sum_{i=1}^{3} \log \frac{k_{1i}^2}{k_{1i}^2 - z_{1i}^2} \tag{7}$$

where $k_1 = (k_{11}, k_{12}, k_{13})^T = |k_{c1}| - |k_{c2}|$ are positive constants. Differentiating Eq. (7) will lead to $\dot{V}_1 = \sum_{i=1}^{3} \frac{z_{1i}\dot{z}_{1i}}{k_{1i}^2 - z_{1i}^2}$ and $\dot{z}_1 = J(\theta)(z_2 + \alpha_1) - (\dot{x}_d, \dot{y}_d, \dot{\omega}_d)^T$. Design the auxiliary variables as $\alpha_1 = J^T(\theta)[(\dot{x}_d, \dot{y}_d, \dot{\theta}_d)^T - (k_{a1}z_{11}, k_{a2}z_{12}, k_{a3}z_{13})^T]$, where $k_{ai}(i = 1, 2, 3)$ are positive constants, thus we can obtain

$$\dot{V}_1 = \sum_{i=1}^{3} \frac{z_{1i}\dot{z}_{1i}}{k_{1i}^2 - z_{1i}^2} = -\sum_{i=1}^{3} \frac{k_{ai}z_{1i}^2}{k_{1i}^2 - z_{1i}^2} + \sum_{i=1}^{3} \frac{z_{1i}J_i(\theta)z_2}{k_{1i}^2 - z_{1i}^2} \tag{8}$$

In order to deal with the disturbances, we denote the unknown boundary as $d = d_t$, and the estimate error is described as $\tilde{d} = \hat{d} - d$. Then we choose a barrier Lyapunov function based on (7).

$$V_2 = V_1 + \frac{1}{2}\sum_{i=1}^{3} \log \frac{k_{2i}^2}{k_{2i}^2 - z_{2i}^2} + \frac{1}{2}\tilde{d}^2 \tag{9}$$

It is obviously to get $\dot{z}_2 = Ax_2 + a_2S(x_2) + B\tau + d(x,t) - \dot{\alpha}_1$ by differentiating z_2. And we get $\dot{\alpha}_1 = \dot{J}^T(\theta)[(\dot{x}_d, \dot{y}_d, \dot{\theta}_d)^T - (k_{a1}z_{11}, k_{a2}z_{12}, k_{a3}z_{13})^T] + J^T(\theta)[(\ddot{x}_d, \ddot{y}_d, \ddot{\theta}_d)^T - (k_{a1}\dot{z}_{11}, k_{a2}\dot{z}_{12}, k_{a3}\dot{z}_{13})^T]$. Design the input torques as follows.

$$\begin{aligned}
\tau &= -B^{-1}[K_b z_2 + Ax_2 + a_2S(x_2) + \hat{d}\tanh(\varepsilon z_2) + (h_1, h_2, h_3)^T - \dot{\alpha}_1] \\
h_1 &= (k_{21}^2 - z_{21}^2)\left(\frac{z_{11}\cos\theta}{k_{11}^2 - z_{11}^2} + \frac{z_{12}\sin\theta}{k_{12}^2 - z_{12}^2}\right) \\
h_2 &= (k_{22}^2 - z_{22}^2)\left(-\frac{z_{11}\sin\theta}{k_{11}^2 - z_{11}^2} + \frac{z_{12}\cos\theta}{k_{12}^2 - z_{12}^2}\right) \\
h_3 &= \frac{z_{13}(k_{23}^2 - z_{23}^2)}{k_{13}^2 - z_{13}^2}
\end{aligned} \tag{10}$$

$K_b = diag\{k_{b1}, k_{b2}, k_{b3}\}$ and $k_{bi} > 0 (i = 1, 2, 3)$. Differentiate the Eq. (9) and substitute (10) into $\dot{V}_2$. We can obtain the (11) following $|d_i| \le d$ and the inequality (5).

$$\dot{V}_2 \le -\sum_{i=1}^{3} \frac{k_{ai}z_{1i}^2}{k_{1i}^2 - z_{1i}^2} - \sum_{i=1}^{3} \frac{k_{bi}z_{2i}^2}{k_{2i}^2 - z_{2i}^2} - \sum_{i=1}^{3} \frac{\tilde{d}z_{2i}\tanh(\varepsilon z_{2i})}{k_{2i}^2 - z_{2i}^2} + \frac{l}{\varepsilon}\sum_{i=1}^{3} \frac{d}{k_{2i}^2 - z_{2i}^2} + \tilde{d}\dot{\hat{d}} \tag{11}$$

The adaptive law is designed for unknown boundary as Eq. (12).

$$\dot{\hat{d}} = \sum_{i=1}^{3} \frac{z_{2i} \tan h(\varepsilon z_{2i})}{k_{2i}^2 - z_{2i}^2} - \gamma_d \hat{d} \tag{12}$$

Substituting the adaptive law (12) and the inequality (6) into (11) will lead to the inequality (13) with the equation $\tilde{d}\hat{d} = (\tilde{d}^2 + \hat{d}^2 - d^2)/2$.

$$\dot{V}_2 \leq -\sum_{i=1}^{3} [\log \frac{k_{ai} k_{1i}^2 z_{1i}^2}{k_{1i}^2 - z_{1i}^2} + \log \frac{k_{bi} k_{2i}^2 z_{2i}^2}{k_{2i}^2 - z_{2i}^2}] - \frac{\gamma_d}{2} \tilde{d}^2 + \frac{l}{\varepsilon} \sum_{i=1}^{3} \frac{d}{k_{2i}^2 - z_{2i}^2} + \frac{\gamma_d}{2} d^2 \tag{13}$$

Therefore, (13) can be expressed as (14), and we can draw the theorem.

$$\begin{aligned} &\dot{V}_2 \leq -\rho V_2 + C \\ &\rho = \min\{2k_{ai}k_{1i}^2, 2k_{bi}k_{2i}^2, \gamma_d\} (i = 1, 2, 3) \\ &C = \frac{l}{\varepsilon} \sum_{i=1}^{3} \frac{d}{k_{2i}^2 - z_{2i}^2} + \frac{\gamma_d}{2} d^2 \end{aligned} \tag{14}$$

Theorem 1 *For the system* (4) *of omnidirectional mobile robots with full-state constraints, if the initial conditions satisfy* $z_{1i}(0) \in \overline{\Omega}_1 \triangleq \{|z_{1i}| < k_{1i},\ i = 1, 2, 3\}$ *and* $z_{2i}(0) \in \overline{\Omega}_2 \triangleq \{|z_{2i}| < k_{2i},\ i = 1, 2, 3\}$, *all signals* $\{z_{1i}, z_{2i}, d, i = 1, 2, 3\}$ *will be uniformly bounded with the controller* (10) *and the adaptive law* (12). *And the state constraints will never be violated with suitable parameters, which means* $|x_1| < k_{c1}$, $|x_2| < k_{v1}$. *The tracking error will converge to a sufficiently small compact set to zero with large* ε *and small* γ_d.

4 Simulation Results

The parameter values of the system model are $I_v = 11.25\,\mathrm{kgm}^2$, $I_w = 0.02108\,\mathrm{kgm}^2$, $m = 9.4\,\mathrm{kg}$, $c = 5.983 \times 10^{-6}\,\mathrm{kgm}^2/\mathrm{s}$, $k = 1.0$, $L = 0.178\,\mathrm{m}$, $r = 0.0245\,\mathrm{m}$. Initial positions of robot are $(x(0), y(0), \theta(0) = (-0.5, 0.2, 0.1)$ and the desired trajectory can be described as $x_d = 0.75 \sin(2\pi t/45) y_d = \sin(4\pi t/45)$ and $\theta_r = \pi \cos(\pi t/16)/4$. Besides, the parameters are chosen as $k_1 = (0.2, 0.5, \pi)^T$, $k_2 = (0.2, 0.4, 0.2)^T$, $k_{ai} = 1.5$, $k_{bi} = 2.0$, $\hat{d}_0 = 0.2$, $\varepsilon = 3.0$, $l = 0.2785$, $\gamma_d = 4, k_{11} = 0.6$, $k_{12} = 0.3, k_{13} = 0.8$, $k_{21} = k_{22} = k_{23} = 1.2$. The disturbance is expressed as $d_i(x, t) = 0.05 \cos(t/50)$.

Figure 2 shown that the z_{1i} and z_{2i} will are bounded. z_{1i} will converge to a enough small compact set, which means the tracking errors will be sufficiently

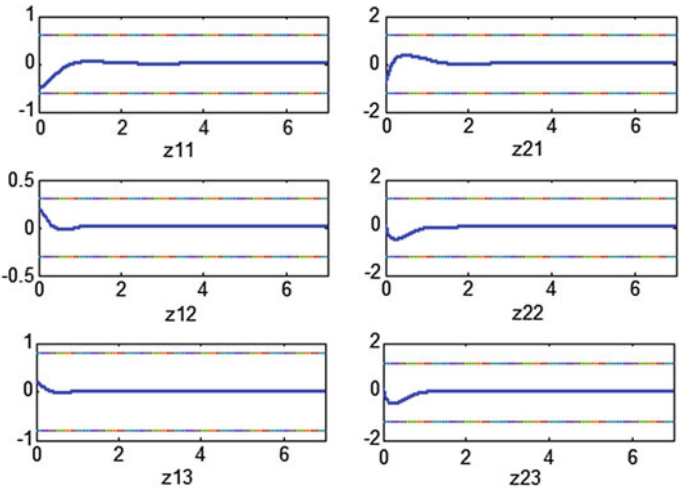

Fig. 2 Tracking errors of z_{1i} and z_{2i} using the proposed controller with the adaptive law

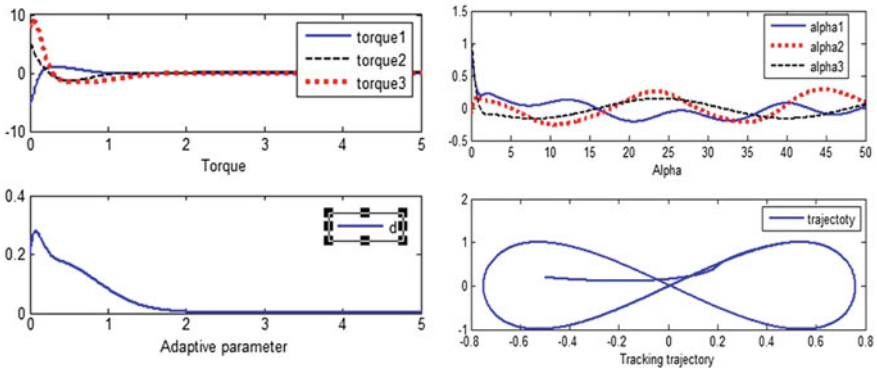

Fig. 3 Tracking trajectory, input torques, the adaptive parameter and the tendency of α_{1i}

small. The tracking trajectory, input torques, the adaptive parameter are shown in Fig. 3. Simulation results validate the effectiveness of the proposed method.

5 Conclusions

In this paper, trajectory tracking of omnidirectional mobile robots with full-state constraints was considered. The control scheme combined the barrier Lyapunov function with adaptive technique to achieve the great tracking performance subject

to state constraints. An adaptive estimation law was proposed for disturbances of dynamics in practical systems to improve the robustness of control systems. Meanwhile, the stability of the closed-loop system was analyzed. And simulation results demonstrated the efficiency and availability of the proposed control strategy. In future work, input saturations of robots should be considered to satisfy the real system, and more complicated situations, such as time delay and time-varying state constraints, can be researched to achieve superior tracking performance.

Acknowledgements This work was supported by the NSFC (61327807, 61521091, 61520106010, 61134005) and the National Basic Research Program of China (973 Program: 2012CB821200, 2012CB821201).

References

1. Viet TD, Doan PT, Hung N, Kim HK, Kim SB (2012) Tracking control of a three-wheeled omnidirectional mobile manipulator system with disturbance and friction. J Mech Sci Technol 26(7):2197–2211
2. Hashemi E, Jadidi MG, Jadidi NG (2011) Model-based PI–fuzzy control of four-wheeled omni-directional mobile robots. Robot Auton Syst 59(11):930–942
3. Huang HC, Tsai CC (2008) Adaptive trajectory tracking and stabilization for omnidirectional mobile robot with dynamic effect and uncertainties. IFAC Proc Volumes 41(2):5383–5388
4. Teatro TA, Eklund JM, Milman R (2014) Nonlinear model predictive control for omnidirectional robot motion planning and tracking with avoidance of moving obstacles. Can J Electr Comput Eng 37(3):151–156
5. Liu CH, Hsiao MY (2012) Adaptive fuzzy terminal sliding-mode controller design for omni-directional mobile robots. Adv Sci Lett 8(1):611–615
6. Alakshendra V, Chiddarwar SS (2016) Adaptive robust control of Mecanum-wheeled mobile robot with uncertainties. Nonlinear Dyn 87(4):2147–2169
7. Huang JT, Van Hung T, Tseng ML (2015) Smooth switching robust adaptive control for omnidirectional mobile robots. IEEE Trans Control Syst Technol 23(5):1986–1993
8. Liu YJ, Tong S (2016) Barrier Lyapunov functions-based adaptive control for a class of nonlinear pure-feedback systems with full state constraints. Automatica 64:70–75
9. He W, Chen Y, Yin Z (2016) Adaptive neural network control of an uncertain robot with full-state constraints. IEEE Trans Cybern 46(3):620–629

An Improved Extreme Learning Machine Model and State-of-Charge Estimation of Single Flow Zinc-Nickle Battery

Xiaofeng Lin, Yang Guo, Jie Cheng, Zhenbang Guo and Xinglong Yan

Redox flow battery was first funded by NASA. In 1974, Thaller proposed this new type of battery and applied for a patent on it. After several decades of development, the researchers have developed a variety of double-flow battery systems. However, the double-flow battery uses two kinds of electrolyte, which requires expensive ion-exchange membrane. Therefore, there are many disadvantages in those battery systems, such as cross-contamination of electrolyte high cost, large volume and low specific energy.

In 2004, Pletcher's team developed a single-flow lead-acid battery with no ion-exchange membrane [1]. This battery requires only one tank and one pump compared to the double-flow battery. Therefore, this kind of single-flow battery reduces the cost and simplifies the structure of the flow battery. It also provides a new idea for the development of flow battery. In 2007, Yang Yusheng and Cheng Jie's team developed a new single-flow zinc-nickel battery [2].

Since the single-flow zinc-nickel battery was proposed, many scholars have studied it from different angles: Beijing Research Institute of Chemical Defense studied the effects of electrolyte and electrode materials on the cell performance. And according to the internal reaction mechanism of the battery, they established a mechanism model of charge and discharge processes in battery electrode [3]. Beijing University of Chemical Technology [4] studied the relationship of electrolyte flow rate, current density and zinc deposition area capacity. After that, the effects of them on single-flow zinc-nickel battery charge and discharge performance has been studied. Dalian Institute of Chemical Physics [5, 6] studied battery performance from the temperature and shape of the electrode material. Internationally, single-flow zinc-nickel batteries have been studied by the Energy Institute of New York City University, which in 2014 successfully increase capacity of single battery to 555Ah, and assembled a 25kWh single-flow zinc-nickel battery pack.

X. Lin (✉) · Y. Guo · J. Cheng · Z. Guo · X. Yan
School of Electrical Engineering, Guangxi University, Nanning, China
e-mail: gxulinxf@163.com

Z. Deng (ed.), *Proceedings of 2017 Chinese Intelligent Automation Conference*,
Lecture Notes in Electrical Engineering 458,
https://doi.org/10.1007/978-981-10-6445-6_67

The experimental results show that, after 1000 cycles of 100% Depth of Discharge (DoD) tests, battery pack still keep energy efficiency above 80% [7]. This is a breakthrough of single-flow zinc-nickel battery application.

1 Model of Single Flow Znic-Nickle Baterry

Battery as large energy storage device needs a accurate model to describe its charge/discharge status and voltage characteristics. The existing battery model could be divided into electrochemical model, equivalent circuit model and neural network model. The electrochemical model establishes a positive and negative electrode model by analyzing the electrode dynamics, diffusion and mass transfer processes. This kind of model has high accuracy, but it is too complex and difficult to be applied in actual application. Equivalent circuit model uses voltage source, resistance and capacitance components to establish a battery model. This kind of model can simulate the change of battery terminal voltage during charge/discharge process and the analysis method of this model is clearer and can be deduced from the theoretical basis of the circuit. Therefore, this modeling method is widely used in research on external characteristic and dynamic response of battery.

Artificial Neural Network (ANN) model is based on the battery variable parameters of charge/discharge process, such as voltage, current, internal resistance, temperature etc. By self-learning and parallel processing capabilities of neural network, this kind of model can obtain non-linear mapping relation between battery data and establish battery model. At present, the widely used neural network models include BP network model, RBF network model [8] and Extreme Learning Machine (ELM) model [9].

However, because the inputs of ELM are based on the voltage of previous time, SoC and current of present moment, so when a great change occurred in current, ELM often cannot accurately track the instant step change of battery voltage. In this article, based on the advantages of ELM network and the equivalent circuit model, an improved Extreme Learning Machine model of data driven and equivalent circuit is established, and compared this proposed model with simple ELM network model, the superiority of improved ELM model is verified.

1.1 Extreme Learning Machine

The algorithm process of ELM will be described below. The training set is defined as $x_i = (x_{i,1}, x_{i,2} \ldots, x_{i,N})^T \in R^N$, $t_i \in R$. Here, N is the input-output sample number of the training set. The activation function g(x) which is differentiable on arbitrary

interval is determined before training. For the standard Single-hidden layer feed forward neural network with L hidden nodes, the output model of the network is

$$\sum_{i=1}^{L} \beta_i(\alpha_i x_i + b_i) = t_j \quad j = 1 \ldots N \quad b_i, t_j \in R, \quad \alpha_i \in R^N \tag{1}$$

where α_i is input weight vector $\alpha_i = (\mathrm{a}_{i1}, a_{i2} \ldots, \mathrm{a}_{iN})^T$, b_i is hidden layer bias and i represents the ith hidden node. β_i is the output weight connecting the I th hidden node and output node; $\alpha_i x_i$ is the inner product of α_i and x_i; t_j is the jth input-output sample; (1) can be written in the equivalent form $H \cdot \beta = T$, where

$$H = \begin{bmatrix} g(\alpha_1, b_1, \mathrm{x}_1), & \cdots, & g(\alpha_L, b_L, \mathrm{x}_1) \\ \vdots & \cdots & \vdots \\ g(\alpha_1, b_1, \mathrm{x}_N), & \cdots, & g(\alpha_L, b_L, \mathrm{x}_N) \end{bmatrix}$$

$$\beta = [\beta_1, \beta_2 \ldots \beta_L]^T, \quad T = [t_1, t_2, t_3]^T$$

H is the hidden layer output matrix. The input weights of network parameters and the biases of hidden layer neurons are given randomly. Therefore β is the only parameter which needs to be calculated in network. This means it is necessary to find $\hat{\beta}$ which make

$$\left\| H\hat{\beta} - T \right\| = \min_{\beta} \|H\beta - T\| \tag{2}$$

Huang et al. [10] has shown that the least squares solution of above equation is

$$\hat{\beta} = \mathrm{H}^{+} T \tag{3}$$

where H^{+} is the Moore-Penrose generalized inverse of H.

It can be seen that the ELM network does not need to iteratively adjust parameters of network, only need to solve the network output weight matrix once by the number of hidden neurons and the neuron activation function. It means great improvement in network learning speed and obtaining the global optimal solution of network parameters.

2 The Proposed Model of Single Flow Zinc-Nickel Battery

As shown in Fig. 1, the single-flow zinc-nickel battery model in this paper is an improved ELM model which consists of voltage source, resistance and data-driven ELM model.

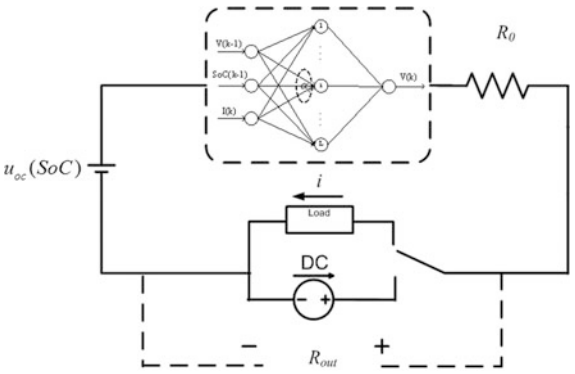

Fig. 1 Improved ELM model of single flow zinc-nickel battery

This model can simulate the variation of terminal voltage during charge and discharge process. In this model, the voltage source $U_{OC}(\mathrm{SoC})$ describes the relationship between battery open-circuit voltage U_{OC} and battery SoC. R_0 is ohmic resistance which describes the losses caused by electrodes, electrolytes, and contact resistance. This resistor can also explain the step change in battery terminal voltage when a large change occurred in battery current. Open-circuit voltage and ohmic resistance can be obtained by the method of Ref. [11]. ELM model is used to describe the changes in polarization voltage when SoC and battery current changed. To establish the ELM model of single flow zinc-nickel battery, first need to determine the network input and output variables. The following is commonly used battery equivalent circuit model expression:

$$V_{out}(k) = f(Soc(k)) + I(k)R_0 + U_{R_1C_1}(k) + U_{R_2C_2}(k) \tag{4}$$

$$U_{R_1C_1}(k) = U_{R_1C_1}(k-1)\mathrm{e}^{-T/R_1C_1} + I(k)R_1(1-\mathrm{e}^{-T/R_1C_1}) \tag{5}$$

$$U_{R_1C_1}(k) = U_{R_1C_1}(k-1)\mathrm{e}^{-T/R_1C_1} + I(k)R_1(1-\mathrm{e}^{-T/R_1C_1}) \tag{6}$$

It can be seen that there is a non-linear relationship in battery output voltage $V_{out}(k)$ at time k with battery State-of-Charge $SoC(k)$, battery current $I(k)$, battery polarization voltage ($U_{R_1C_1}(k)$, $U_{R_2C_2}(k)$) and other factors at same time. As shown in Eqs. (5) and (6), the polarization voltage of the battery at each sampling time is affected by polarization voltage ($U_{R_1C_1}(k-1)$, $U_{R_2C_2}(k-1)$) at time $(k-1)$ and battery current $I(k)$ at same time. Therefore this paper selects polarization voltage $V(k)$ of cell at time k as the ELM network output variable $t(k) = V(k)$ and selects current $I(k)$ and $SoC(k-1)$ at time k, polarization voltage $V(k-1)$ at time $(k-1)$ as the network input vector $x(k) = [V(k-1)SoC(k-1)I(k)]^T$.

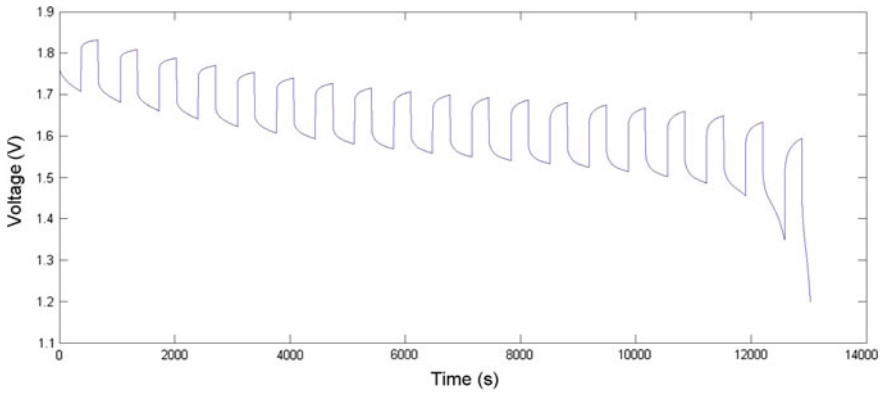

Fig. 2 Voltage curves of pulsed discharge

3 Obtain Training Data

The test battery is 200 Ah single flow zinc-nickel battery. In order to make experimental data as much as possible to cover the working scope of battery and make battery model more accurate, this paper uses the intermittent discharge test on battery. The test system records battery terminal voltage, current and battery capacity during discharge process to obtain training data and test data of the network. Figure 2 is voltage curves of pulsed discharge.

4 Establishment and Verification of Model

Based on the experimental data obtained in the previous section, all training samples and test samples were normalized to reduce the adverse effect of data variation on network training. The activation function $g(x)$ was selected as sigmoid function:

$$g(x) = \frac{1}{e^{-x} + 1} \tag{7}$$

The number of hidden layer neurons, L was set to 100. In order to verify the superiority of proposed model, a simple ELM model of single flow zinc-nickel battery was also established and trained by same data sample. The number of hidden layer neurons in simple ELM model was also set to 100 to ensure consistency with ELM network part of proposed model. Finally, another group of discharge current was used to verify the generalization performance of the two models.

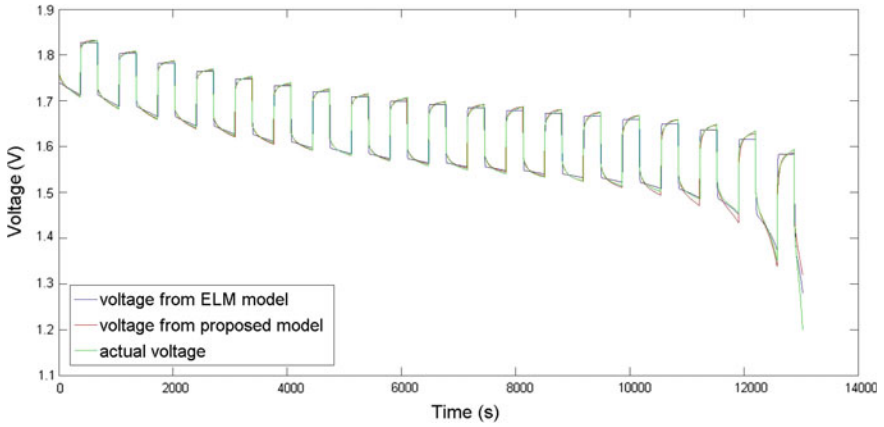

Fig. 3 Actual voltage and output voltage of model

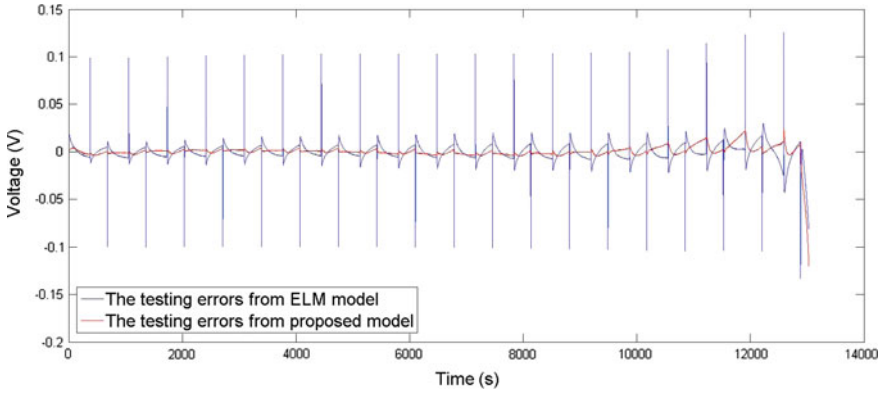

Fig. 4 Output voltage error of two models

Figures 3 and 4 are comparisons between output voltage and actual voltage and output error curves of two models at two different discharge currents. It can be seen that proposed model is more accurate in simulating actual voltage variation of battery during standing time. And when current changes greatly, simple ELM model can not accurately track the variation of battery output voltage which would increase the error of model. But because of ohmic resistance, the proposed model can react more quickly than simple ELM model. The root mean square error (RMSE) of improved ELM model is 0.0077 V, which is less than 0.0106 V of simple ELM model. So it can be said that the proposed model is more accurate than simple ELM model.

5 State-of-Charge Estimation Strategy of Single Flow Zinc-Nickel Batteryssas

SoC is an important state variable in battery operation. It directly describes the remaining capacity of battery, and is also an important guarantee for battery safe operation. However, the SoC of battery can not be directly measured, and affected by many factors, so it has been a hot and difficult subject in the research of energy storage.

In this section, based on improved ELM model model established in Sect. 2, the adaptive unscented Kalman filter which is based on covariance matching is used to estimate the SoC variation of single flow zinc-nickel battery under intermittent discharge test. By comparing with AUKF based on simple ELM model, the superiority of AUKF based on proposed model is verified.

5.1 Battery State-of-Charge Estimation Based on Adaptive Unscented Kalman Filter

In this paper, Adaptive Unscented Kalman Filter are not described in detail.the state space equation and output equation of battery must be established when using AUKF algorithm to estimate battery SOC. According to improved ELM model of battery established in Sect. 2, the expressions of battery model can be obtained as:

$$V(k) = \sum_{i=1}^{L} \beta_i \frac{1}{\left(\mathrm{e}^{-(\alpha_i [V(k-1) Soc(k-1) I(k)]^T + b_i}\right) + 1} \tag{8}$$

$$R(k) = \sum_{j=1}^{10} A_{(j)} SoC^{(j)}(k) + A_{(j+1)} \tag{9}$$

$$V_{OCV}(k) = \sum_{j=1}^{10} B_{(j)} SoC^{(j)}(k) + B_{(j+1)} \tag{10}$$

$$V_{out}(k) = V(k) + R(k) I(k) + V_{OCV}(k) \tag{11}$$

where α_i is input weight vector, b_i is hidden layer bias, β_i is output weight and i represents the ith hidden node. $R(k)$ and $V_{OCV}(k)$ are the values of the ohmic resistance and the open circuit voltage at time k fitted with 10th order equations, respectively. $I(k)$ and $V_{out}(k)$ are current excitation and terminal voltage of the battery at time K, respectively.

According to the current integration method, the calculation equation of battery SoC can be obtained as:

$$SoC = SoC(0) + \int_0^t \frac{\eta I(t)}{C_n} dt \tag{12}$$

where η is battery charge and discharge efficiency. It is generally assumed that $\eta = 1$ in charge process and $0 < \eta < 1$ in discharge process. $SoC(0)$ is initial value of SoC. C_n is battery rated capacity, for 200Ah single flow zinc-nickel battery, $C_n = 200$ Ah. And $i(t)$ represents the real-time current of battery and it is positive in charge, negative in discharge. The discretization of (12) is:

$$SOC(k) = SOC(k-1) + \eta \frac{I(k-1)T}{C_n} \tag{13}$$

Combining battery model and current integration method expression, taking battery model output voltage $V(k-1)$ and $SOC(k-1)$ at time $k-1$ as state variables, and model output voltage $V_{out}(k)$ at time k is taken as output variable. The state equation and output equation of battery model can be obtained as:

$$\begin{bmatrix} V(k) \\ SOC(k) \end{bmatrix} = \begin{bmatrix} \sum_{i=1}^{L} \beta_i \frac{1}{\left(e^{-(\alpha_i [V(k-1) SoC(k-1) I(k)]^T + b_i)} + 1\right)} \\ SOC(k-1) + \eta \frac{I(k)T}{C_n} \end{bmatrix} + w_{1,k} \tag{14}$$

$$V_{out}(k) = V(k) + (\sum_{j=1}^{10} A_{(j)} SoC^{(j)}(k) + A_{(j+1)}) I(k) + \sum_{j=1}^{10} B_{(j)} SoC^{(j)}(k) + B_{(j+1)} v_{1,k} \tag{15}$$

where $w_{1,k}$ and $v_{1,k}$ are process noise and measurement noise, respectively.

6 Experimental Verification and Analysis

In order to verify the estimation ability of above algorithms, AUKF algorithm based on proposed model and AUKF based on simple ELM model are used to estimate the variation of battery SoC under pulsed discharge as described in Sect. 2. In most cases, the initial value of SoC can not be accurately obtained and this is one of the reasons why current integration method can not accurately estimate battery SoC. Therefore, a good estimation algorithm should have good anti-jamming ability for initial SoC error. In order to verify the robustness of above algorithms to initial error, the initial SoC value is set to 80%, but actual initial value is 100%. Figure 5 and Fig. 6 are estimation results and estimation errors of two algorithms. Both AUKF based on proposed model and AUKF based on simple ELM model show strong ability to correct initial error of SoC. But under same ELM network

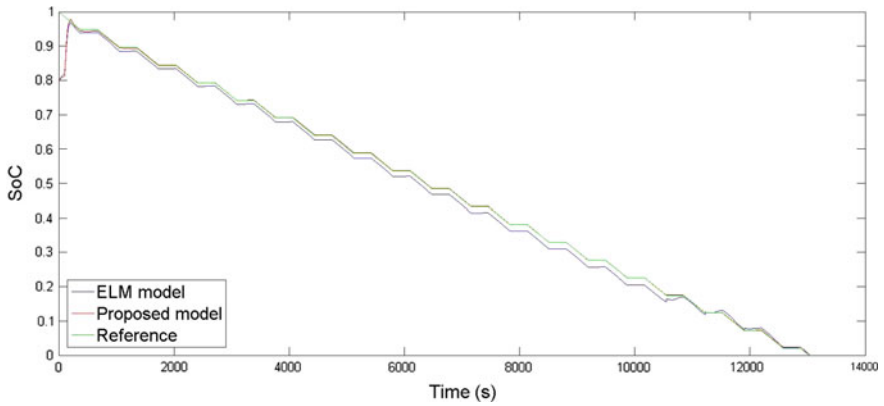

Fig. 5 Estimated SoC of AUKF based on proposed model and AUKF based on simple ELM model

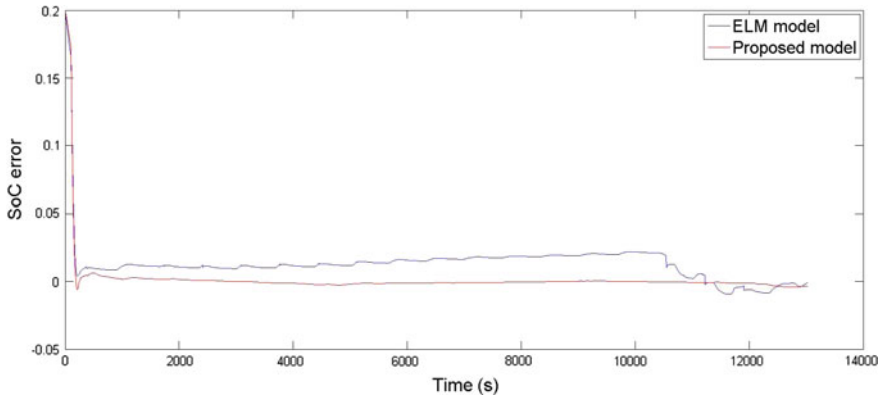

Fig. 6 Estimated SoC of AUKF based on proposed model and AUKF based on simple ELM model

model, the RMSE of AUKF based on proposed model is 0.0178, and RMSE of AUKF based on simple ELM model is 0.0222. Therefore, it can be said, AUKF based on proposed model improves the accuracy of estimation.

7 Conclusion

A novel redox flow battery–single flow Zinc-Nickle battery is introduced in this paper. Based on battery simple ELM model, this paper proposes a improved ELM model model combined with equivalent circuit and ELM for the problem that

simple ELM model can not track the variation of voltage rapidly when current changes greatly. It is proved that the proposed model can simulate the variation of battery terminal voltage during discharge process with higher precision. Finally, based on this improved ELM model model, AUKF algorithm is used to estimate battery SOC, which proves that the proposed algorithm can converge quickly and has higher precision compared with AUKF based on simple ELM model. The study provides a basis for the control, optimization and energy conversion of single flow Zinc-Nickle battery energy storage system, and also provides a reference for its further research and application.

Acknowledgements The project supported by the National Natural Science Foundation of China No. 61364007.

References

1. Pletcher D, Wills R (2005) A novel flow battery—a lead acid battery based on an electrolyte with soluble lead (II): III. The influence of conditions on battery performance. J Power Sources 149:96–102
2. Cheng J, Zhang L, Yang YS, Wen YH, Cao GP, Wang XD (2007) Preliminary study of single flow zinc–nickel battery. Electrochem Commun 9(11):2639–2642
3. Liu X, Cheng J, Xie Z, Cao G (2011) Process in mathematical models of the nickel hydroxide electrode. Mater Rev 3:024
4. Shiye S, Junli P, Yuehua W, Jie C, Junqing P, Gaoping C (2014) Effects of electrolyte flow speed on the performance of Zn-Ni single flow batteries. Chem J Chin Univ 35(1):134–139
5. Cheng Y, Zhang H, Lai Q, Li X, Zheng Q, Xi X, Ding C (2014) Effect of temperature on the performances and in situ polarization analysis of zinc–nickel single flow batteries. J Power Sources 249:435–439
6. Cheng Y, Zhang H, Lai Q, Li X, Shi D, Zhang L (2013) A high power density single flow zinc–nickel battery with three-dimensional porous negative electrode. J Power Sources 241:196–202
7. Turney DE, Shmukler M, Galloway K, Klein M, Ito Y, Sholklapper T, Banerjee S (2014) Development and testing of an economic grid-scale flow-assisted zinc/nickel-hydroxide alkaline battery. J Power Sources 264:49–58
8. Charkhgard M, Farrokhi M (2010) State-of-charge estimation for lithium-ion batteries using neural networks and EKF. IEEE Trans Industr Electron 57(12):4178–4187
9. Du J, Liu Z, Wang Y (2014) State of charge estimation for Li-ion battery based on model from extreme learning machine. Control Engineering Practice 26:11–19
10. Huang GB, Zhu QY, Siew CK (2006) Extreme learning machine: theory and applications. Neurocomputing 70(1):489–501
11. Kim T, Qiao W (2011) A hybrid battery model capable of capturing dynamic circuit characteristics and nonlinear capacity effects. IEEE Trans Energy Convers 26(4):1172–1180

A Unified Framework for Age Invariant Face Recognition and Age Estimation

Changhong Wu and Jianbo Su

1 Introduction

Human facial appearances change substantially over time, resulting in great challenges for the face recognition task. On the other hand, the age estimation task expects to catch the age related information. To some extent, the two tasks can be considered as competing with each other. Most existing researches investigate the two tasks independently, while in this paper we explore the coordination between them.

Existing researches on age invariant face recognition (AIFR) fall into two categories: the generative methods and the discriminative methods. The generative methods [1–3] focus on generating an aging pattern which relies on accurate age estimation and the model is computationally expensive. The discriminative methods focus on extracting age invariant features for face recognition [4–7]. However, they ignore the aging effects on facial appearance.

The age estimate task usually performs by two steps: feature extraction and classification (or regression). Most existing methods extract the geometry and texture features and combine with the AAM to simultaneously model the shape and texture of face images [1, 8]. Nevertheless, it is difficult to design effective features for age estimation due to the unclear mechanism of the ageing effect on face images [9].

The method proposed in [10] considers the two tasks with conflicting goals can help inhibit irrelevant features for each task and hence improve the performance. Since the age invariant face recognition expects to extract age insensitive features while the age estimation expects the age sensitive features, it is desired to improve one of them by incorporating information from the other. Gong et al. [11, 12] propose a probabilistic model with the two latent factors and learn an identity space

C. Wu · J. Su (✉)
Department of Automation, Research Center of Intelligent Robotics,
Shanghai Jiao Tong University, Shanghai 200240, China
e-mail: jbsu@sjtu.edu.cn

Z. Deng (ed.), *Proceedings of 2017 Chinese Intelligent Automation Conference*,
Lecture Notes in Electrical Engineering 458,
https://doi.org/10.1007/978-981-10-6445-6_68

and an age space at the same time. But the model is based on the assumption that the latent factors and random noise follow the Gaussian distribution. The method proposed in [13] consider that the face image can be decomposed into a class specific part and a common part and a dictionary can be split into two corresponding dictionaries. However, they ignore the discrimination ability of the coding coefficients.

In this paper, a novel unified framework is proposed for face recognition and age estimation. The two tasks are modeled together in a joint framework. Identity and age dictionaries are introduced to encode the identity and age parts of a face image onto two separated subspaces. The learned identity subspace only catches the identity information of the face images, which can be used for face recognition. The age subspace catches the age sensitive features which can be used for age estimation.

2 The Joint Model for Face Recognition and Age Estimation

2.1 Face Images Decomposition

Firstly, Suppose the training set is composed of c classes, then the training samples of the i-th class $F_i = [f_1, \ldots, f_{n_i}] \in R^{d \times n_i}$, where $f_j \in R^d, j = 1, \ldots, n_i$. Let $F = [F_1, \ldots, F_c] \in R^{d \times n}$, $n = n_1 + \cdots + n_c$ be the training samples matrix. Each training sample $f_j \in R^{d \times 1}, j = 1, \ldots, n$ can be decomposed into four parts: the person specific part $I_j \in R^{d \times 1}$, the age related part $A_j \in R^{d \times 1}$, the mean face feature $m_j \in R^{d \times 1}$ and the random noise part $\varepsilon_j \in R^{d \times 1}$. The face image decomposition can be formulated as:

$$f_j = m_j + I_j + A_j + \varepsilon_j, \quad j = 1, \ldots n \tag{1}$$

2.2 Collaboration Coding with Identity and Age Dictionaries

In this paper, two dictionaries are introduced to encode the identity part and age part of face features: the identity dictionary $U = [U_1, U_2 \ldots U_i, \ldots U_c] \in R^{d \times p}$, $U_i \in R^{d \times p_i}$ and the age dictionary $V = [V_1, \ldots V_s, \ldots V_t] \in R^{d \times q}$, $V_s \in R^{d \times q_s}$. The coding coefficients $X_i = \left[x_i^1, \ldots, x_i^j, \ldots x_i^{n_i}\right] \in R^{p \times n_i}$ denotes the identity component of the i-th class training samples $I_i \in R^{d \times n_i}$ coded over the identity dictionary $U \in R^{d \times p}$, where $x_i^j \in R^{p \times 1}$ denotes the identity coding efficient of f_i^j. Similarly, $Y_i = \left[y_i^1, \ldots, y_i^j, \ldots y_i^{n_i}\right] \in R^{q \times n_i}$ denotes the age component of the i-th class training

samples $A_i \in R^{d\times n_i}$ coded over the age dictionary $V \in R^{d\times q}$, where $y_i^j \in R^{q\times 1}$ denotes the age coding efficient of f_i^j.

In our model, over-complete dictionary is difficult to acquire since the number of training images per class is limited. Here, we introduce collaboration coding [15] and combine it with the reconstruction error to form a unified objective function:

$$\min\|F - M - UX - VY\|_F^2 + \lambda_1\|X\|_F^2 + \lambda_2\|Y\|_F^2, \tag{2}$$

where UX and VY denote the person specific component I and age related component A. The first term $\|F - m - UX - VY\|_F^2$ is based on the idea of data reconstruction. The mean face can be calculated by: $M = [m, m, \ldots, m] \in R^{d\times n}$, $m = \frac{1}{n}\sum_{i=1}^{c} f_i \in R^{d\times 1}$, where n is the size of the total training set. λ_1, λ_2 are introduced to balance the reconstruction error and the collaboration constraints.

2.3 Discriminative Coefficients

The collaboration coefficient of one face image can be regarded as a feature vector representing the data in a new space, which should be discriminant for each class. Here, two label supervised constraints are introduced [14]. Identity label supervised term $\|H_1 - AX\|_F^2$ ensures that the samples from the same identity get the similar identity coding coefficient x. $\|H_2 - BY\|_F^2$ ensures that the samples from the same age group get the similar age coding coefficient y . The unified objective function is given as follows:

$$\begin{aligned}\min\|F - M - UX - VY\|_F^2 + \|H_1 - AX\|_F^2 + \beta\|H_2 - BY\|_F^2 \\ + \lambda_1\|X\|_F^2 + \lambda_2\|Y\|_F^2,\end{aligned} \tag{3}$$

where $H_1 \in R^{c\times p}$ and $H_2 \in R^{a\times p}$ denote the identity and age label matrixes. If the l-th training sample belongs to the k-th identity class, $H_1(k, l)$ equals 1, otherwise $H_1(k, l)$ equals 0, which is similar to the definition of $H_2(m, n)$.

2.4 Optimization of the Joint Model

The objection function in formula (3) is not convex for U, V, X, Y, A, B jointly. While it is convex with respect to each of them when the other ones are fixed.

- *Firstly, fix V, B, X, Y and update U, A.* Formula (3) can be rewritten as:

$$J_{U^*,A^*} = \arg\min_{U,A} \left\| \begin{bmatrix} F - M - VY \\ \sqrt{\alpha} H_1 \end{bmatrix} - \begin{bmatrix} U \\ \sqrt{\alpha} A \end{bmatrix} X \right\|_F^2, \tag{4}$$

Let $D = \begin{bmatrix} U \\ \sqrt{\alpha} A \end{bmatrix}$, D can be updated class by class according to [16].

- *Secondly, fix U, A, X, Y and update V, B.*

The update process of V, B is similar to the optimization of U, A;

- *Thirdly, fix U, V, A, B, Y and update X.* Formula (3) can be rewritten:

$$J_{X^*} = \arg\min_{X} \left\| \begin{bmatrix} F - M - VY \\ \sqrt{\alpha} H_1 \end{bmatrix} - \begin{bmatrix} U \\ \sqrt{\alpha} A \end{bmatrix} X \right\|_F^2 + \lambda_1 \|X\|_2, \tag{5}$$

X can be calculated directly in formula (6).

$$X = \left(\begin{bmatrix} U^T & \sqrt{\alpha} A^T \end{bmatrix} \begin{bmatrix} U \\ \sqrt{\alpha} A \end{bmatrix} + \lambda_1 I \right)^{-1} \begin{bmatrix} U^T & \sqrt{\alpha} A^T \end{bmatrix} \begin{bmatrix} F - M - VY \\ \sqrt{\alpha} H_1 \end{bmatrix}. \tag{6}$$

- *Fourthly, fix U, V, A, B, X and updated Y.*

The update process of Y is similar to the optimization of X.

2.5 Face Matching

In the testing, with the learned two dictionaries U, V, any unseen face $f \in R^d$ can be encoded as follow (assume $\lambda_1 = \lambda_2$):

$$J_{x^*,y^*} = \arg\min_{x,y} \left\| f - m - \begin{bmatrix} U & V \end{bmatrix} \begin{bmatrix} x \\ y \end{bmatrix} \right\|_F^2 + \lambda_1 \left\| \begin{bmatrix} x \\ y \end{bmatrix} \right\|_2. \tag{7}$$

The coding coefficient x can be directly used as an age invariant feature descriptor for face recognition. The coding coefficient y can be used for age estimation. Cosine distance and the Nearest Neighbor (NN) algorithm are used for both tasks.

3 Experiment

3.1 Implementation Details

Follows the settings in [12], HOG feature is used as feature descriptor. Feature slicing and PCA are used for dimension reduction. The PCA feature dimension d, the number of slices p, label parameters α, β and regularization parameters λ_1, λ_2 are set as follows: d = 900, $p = 6$, $(\alpha, \beta, \lambda_1, \lambda_2)$ = (2.3, 1.2, 0.005, 0.005) for MORPH database, $(\alpha, \beta, \lambda_1, \lambda_2)$ = (2.3, 0.01, 0.002, 0.002) for FGNET database.

3.2 Experiment on the FGNET Database

The FGNET database contains1002 face images with 82 different individuals. Each one has 13 images on average collected at ages in the range of 0 to 69. To train the joint model, the face images in FGNET database is divided into 9 age groups every 5 age gap.

Following the training and testing split scheme used in [5, 11], the leave-one-person-out (LOPO) scheme is used for validation. Table 1 records the rank-1 recognition rate of these methods. It shows that our method can achieve an accuracy higher than the best published result (76.2%). Moreover, the proposed model outperforms the HOG feature baseline method by a clear margin.

3.3 Experiment on the MORPH Database

The MORPH Album2 database contains 55,134 facial images of 13,618 subjects. Following the experimental settings in [17], we randomly select 10,000 subjects from the MORPH Album2. For each subject, the images with the youngest age is

Table 1 Comparison of age invariant face recognition methods on FGNET database

	Database (subjects, images) in probe and gallery	Face recognition accuracies (%)	Age estimation accuracies (%)
Geng et al. [1]	FGNET(10,10)	38.1	–
Park et al. [2]	FGNET(82,1002)	37.4	–
Li et al. [5]	FGNET(82,82)	47.5	–
Gong et al. [11]	FGNET(82,82)	69.0	–
Gong et al. [15]	FGNET(82,82)	76.2	–
HOG only	FGNET(82,82)	53.7	–
The joint model	FGNET(82,82)	79.8	74.4

Table 2 Performance of different methods on the MORPH database

Algorithms	Rank-1 face identification (%)	Rank-1 age estimation (%)
Park et al. [2]	79.80	–
Li et al. [5]	83.90	–
Du et al. [3]	79.24	–
Klare et al. [4]	79.08	–
Otto et al. [7]	81.27	–
HOG + HFA (2013)	91.14	–
HLBP + CARC(2014)	92.80	–
HOG + IFA (2015)	92.26	–
Method (2015) in [18]	87.13	–
HOG only	43.65	–
The proposed method	89.57	83.19

Fig. 1 Some failed age estimation results in MORPH Album2

selected as gallery set and the images with the oldest age is used as probe set. Then another 1000 subjects are randomly selected from the dataset as the training set.

The experiment results are shown in Table 2. One thing to note is that the age span of one subject on the MORPH dataset is relative small and face images contain more expression and pose variations. Nevertheless, our approach still achieves a good result on both two tasks. Some failed examples of age estimation are shown in Fig. 1. Some failed results of face matching are shown in Fig. 2.

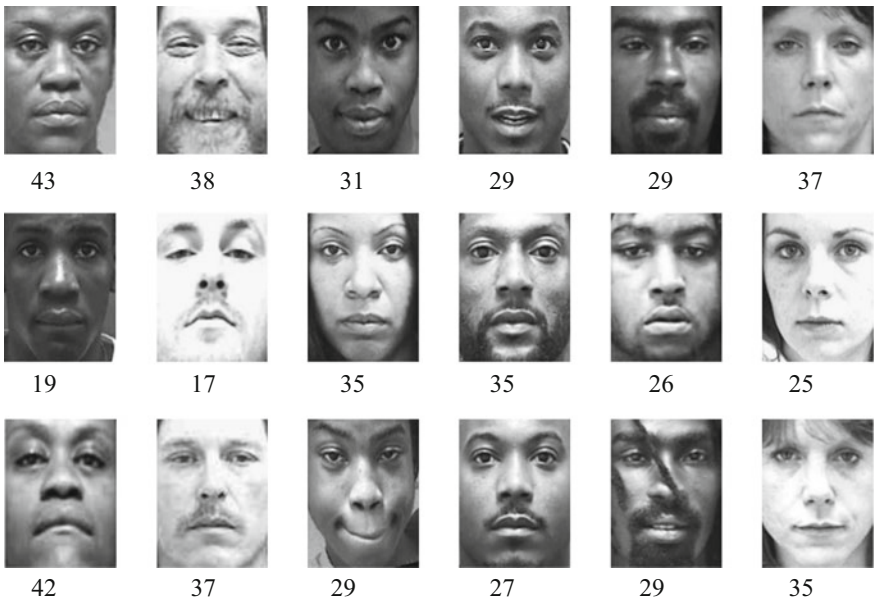

Fig. 2 Some failed retrieve results in MORPH Album2. The *first row* shows the probe images and the *second row* is the incorrect rank-1 matching results using the proposed model. The *third* shows the correct match in the gallery

4 Conclusions

In this paper, we develop a joint model to tackle age invariant face recognition and age estimation at the same time. The result of the experiments on the MORPH and FGNET databases indicate the effectiveness of the proposed method.

Acknowledgements This paper is partially financially supported by the National Science Foundation of China (NSFC) under grants 61533012 and 61521063.

References

1. Geng X, Zhou ZH, Smith-Miles K (2007) Automatic age estimation based on facial aging patterns. IEEE Trans Pattern Anal Mach Intell 29(12):2234–2240
2. Park U, Tong Y, Jain AK (2010) Age-invariant face recognition. IEEE Trans Pattern Anal Mach Intell 32(5):947–954
3. Du JX, Zhai CM, Ye YQ (2013) Face aging simulation and recognition based on NMF algorithm with sparseness constraints. Neurocomputing 116:250–259
4. Klare B, Jain AK (2011) Face recognition across time lapse: on learning feature subspaces. In: International joint conference on biometrics (IJCB). IEEE, pp 1–8

5. Li Z, Park U, Jain AK (2011) A discriminative model for age invariant face recognition. IEEE Trans Inf Forensics Secur 6(3):1028–1037
6. Ling H, Soatto S, Ramanathan N, Jacobs DW (2010) Face verification across age progression using discriminative methods. IEEE Trans Inf Forensics Secur 5(1):82–91
7. Otto C, Han H, Jain A (2012) How does aging affect facial components? In: Computer Vision_ECCV 2012. Workshops and demonstrations. Springer, Berlin, pp 189–198
8. Lanitis A, Draganova C, Christodoulou C (2004) Comparing different classifiers for automatic age estimation. IEEE Trans Syst Man Cybern 34(1):621–628
9. Niu Z, Zhou M, Wang L, Gao X, Hua G (2016) Ordinal regression with multiple output cnn for age estimation. In Proceedings of the IEEE conference on computer vision and pattern recognition, pp 4920–4928
10. Du L, Ling H (2015) Cross-age face verification by coordinating with cross-face age verification. In: Proceedings of the IEEE conference on computer vision and pattern recognition, pp 2329–2338
11. Gong D, Li Z, Lin D, Liu J, Tang X (2013) Hidden factor analysis for age invariant face recognition. In: Proceedings of the IEEE international conference on computer vision, pp 2872–2879
12. Gong D, Li Z, Tao D, Liu J, Li X (2015) A maximum entropy feature descriptor for age invariant face recognition. In: Proceedings of the IEEE conference on computer vision and pattern recognition, pp 5289–5297
13. Sun Y, Liu Q, Tang J, Tao D (2014) Learning discriminative dictionary for group sparse representation. IEEE Trans Image Process 23(9):3816–3828
14. Jiang Z, Lin Z, Davis LS (2013) Label consistent K-SVD: Learning a discriminative dictionary for recognition. IEEE Trans Pattern Anal Mach Intell 35(11):2651–2664
15. Zhang L, Yang M, Feng X (2011) Sparse representation or collaborative representation: which helps face recognition? In: IEEE international conference on computer vision (ICCV). IEEE, pp 471–478
16. Yang M, Zhang L, Yang J, Zhang D (2010) Metaface learning for sparse representation based face recognition. In: 17th IEEE international conference on image processing (ICIP). IEEE, pp 1601–1604
17. Chen BC, Chen CS, Hsu WH (2014) Cross-age reference coding for age-invariant face recognition and retrieval. In: European conference on computer vision. Springer International Publishing, Berlin, pp 768–783
18. Li Z, Gong D, Li X, Tao D (2015) Learning compact feature descriptor and adaptive matching framework for face recognition. IEEE Trans Image Process 24(9):2736–2745

Optical Flow Based Obstacle Avoidance and Path Planning for Quadrotor Flight

Huiqi Miao and Yan Wang

1 Introduction

Visual navigation of UAVs is recently one of the most challenging problems in the fields of robot vision and computer vision [1]. In the field of UAVs research, the term "navigation" typically includes the ability of path planning and obstacle avoidance. Its primary objective is to derive a path from the starting point to the destination without collision with obstacles in the configuration space.

The path planning problem can be classified into the global and the local path planning [8]. The global path planning requires complete knowledge about the environment and then generates a collision-free path from the start configuration to the goal configuration according to the mission of the mobile robot. Different from the global path planning, the local path planning does not need complete knowledge about the environment, but rather relies on sensors such as sonar and scanning laser to first detect obstacles in the environment and then generate collision-free paths in real-time during the flight [2].

Many vision-based methods have been proposed for local path planning in the past. Huang et al. demonstrated a vision guided local navigation method that describes a potential field with the information of headings to the destination and to the obstacles over the robot. However, in some cases, the robot will be trapped into a local minimum [4]. Yu et al. proposed a method for local path planning that uses a single camera to measure the bearing to obstacles only and estimates the time to collision (TTC) with Extended Kalman Filter (EKF), but the camera is specialized and the obtained vision information is not suitable for general situation [10]. Eresen et al. presented an autonomous navigation technique in urban streets where the global position information is available through Google Earth [3]. Ohnishi et al.

H. Miao (✉) · Y. Wang
School of Automation Science and Electrical Engineering,
Beihang University, Beijing 100191, China
e-mail: 18811409162@163.com

Z. Deng (ed.), *Proceedings of 2017 Chinese Intelligent Automation Conference*,
Lecture Notes in Electrical Engineering 458,
https://doi.org/10.1007/978-981-10-6445-6_69

demonstrated a homography based navigation algorithm which detects the planar ground plane using a downward-looking camera mounted on a mobile robot, however, this method is just appropriate for simple environments [7]. Although many methods have been proposed for vision sensor based robot's local path planning, they rather rely more or less on the information besides vision, or the algorithms are only available in specific environments.

In this paper, we use Lucas-Kanade algorithm to compute the optical flow, and further to build a visual potential field. The basic idea is to first sense the obstacles in the environment and then determine a yaw angel according to visual potential field to offer a collision-free path. Object boundaries appear as regions with significant optical flow, and thus as regions to be avoided. The obstacles in the image generate a repulsive force using their gradient vectors to push the quadrotor away in horizontal direction. Meanwhile the relative depth indicated by TTC provides a repulsive force contrary to the heading. The destination is provided to create attraction potential field. The reference yaw angle for traversing an appropriate path is determined from visual potential field and is supplied to the control loop of the dynamic of the quadrotor. The proposed method is tested in virtual environments to evaluate our method. The experimental results show that our method is effective for UAV obstacle avoidance and path planning in unknown environment.

The rest of this paper is organized as follows. Section 2 presents the details of the approach and the specific implementation steps. Section 3 shows the results of our approach and the conclusion of this paper is given in Sect. 4.

2 Visual Potential Field for Autonomous Navigation

This approach is divided into three major components: obstacle detection of environment, path planning and control of quadrotor. The optical flow is calculated first using Lucas-Kanade algorithm for obstacle detection. Then we combine the gradient vectors and TTC of obstacles to create a repulsive potential field of obstacles. The desired yaw angle is achieved by computing the resultant force from attraction force of destination and repulsive force of obstacles.

2.1 Obstacle Detection of Environment

Detection of obstacles is the first step of autonomous navigation for UAVs. Scientific research has found that flying insects can perceive the surrounding environment through optical flow. Optical flow gives information about motion caused by the observer and objects, and this information makes it possible to detect obstacles and positions of the objects in simple working environments. Lucas-Kanade algorithm is chosen to determine the optical flow in our autonomous flight applications [6].

It is known that magnitudes of optical flow velocities for obstacles located at different distances away from observer are different, so it is a feasible method to distinguish the background and obstacles from the image according to the optical flow field. The proposed algorithm utilizes the Otsu threshold segmentation method to extract the obstacles from obtained optical flow field. We note *O(x, y, t)* the image which has detected obstacles at time t.

2.2 Path Planning Using Visual Potential Field

The artificial potential field method was proposed by Khatib [5] in 1986. It forms a virtual artificial potential field through the obstacles' repulsion field and the at-traction field of the target position, and then searches for a downward trend in the potential function, thus it finds a collision-free optimal path. Researches for bionics found that many creatures carry out navigation and obstacle avoidance through the time to contact (TTC), which is depth in terms of time. TTC is significant information to support for determination of vehicle motion [9]. Therefore, we combine the gradient vectors and TTC information of the obstacles in the image as the repulsive field from obstacle.

Since the obstacles detected map is a binary image sequence, the computation of the gradient is numerically unstable and not robust. Therefore, as a preprocess to the computation of the gradient, we smooth the obstacles detected map *O(x, y, t)* by convolution with Gaussian $G*$, that is, we adopt g such that

$$g(x,y,t) = \nabla(G * O(x,y,t)) = \left(\frac{\partial}{\partial x} G * O(x,y,t) \quad \frac{\partial}{\partial y} G * O(x,y,t)\right) \tag{1}$$

as the potential generated by obstacles. *G*O(x, y, t)* is given as

$$G * O(x,y,t) = \int_{-\infty}^{\infty}\int_{-\infty}^{\infty} \frac{1}{2\pi\sigma} e^{-\frac{(u-x)^2+(v-y)^2}{2\sigma^2}} O(x,y,t)\, dudv \tag{2}$$

As an example, Fig. 1 shows a captured image *I(x, y, t)*, and the corresponding obstacles detected image *O(x, y, t)*, the image after Gaussian operation *G*O(x, y, t)* and the gradient vectors field *g(x, y, t)*.

The TTC can be computed from the optical flow as

$$TTC_i = \frac{\sqrt{(x_i - c_x)^2 + (y_i - c_y)^2}}{\sqrt{u_i^2 + v_i^2}} \tag{3}$$

where the numerator on the right side of the Eq. 3 is the distance of the considered point (x_i, y_i) on the image plane from the focus of expansion (FOE), the u_i and v_i

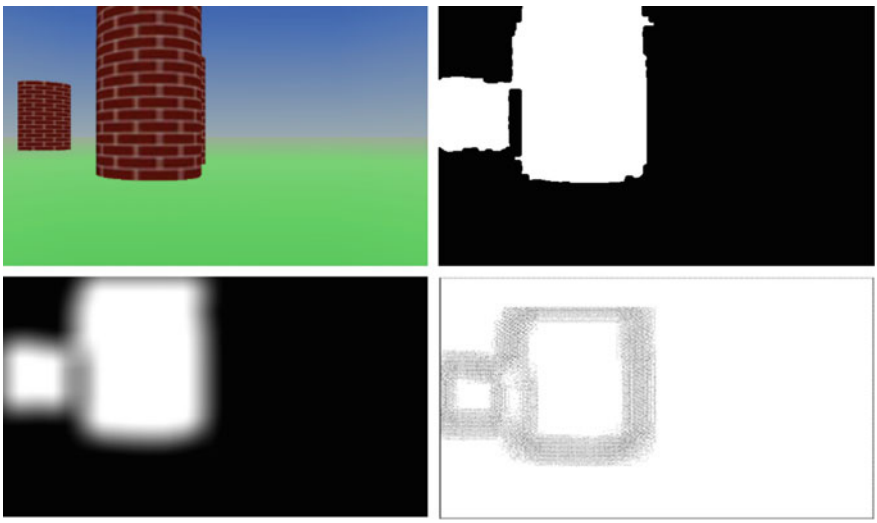

Fig. 1 An example of repulsive potential field. From *left* to *right* and *top* to *bottom* are the captured image *I(x, y, t)*, the obstacles detected image *O(x, y, t)*, the image after Gaussian operation *G*O(x, y, t)* and the gradient vector field *g(x, y, t)*

are the optical flow of horizontal direction and vertical direction for corresponding point, respectively.

Theoretically, all the optical flow vectors pass through the FOE point, so here we use the Least Squares method considering all the points to seek FOE, that is, the coordinates (c_x, c_y) of the FOE, and the specific derivation process is presented as follows:

$$(c_x, c_y)^T = (A^T A)^{-1} A^T b \tag{4}$$

matrices A and b are given as

$$A = \begin{pmatrix} v_1 & v_2 & \cdots & v_n \\ -u_1 & -u_2 & \cdots & -u_n \end{pmatrix}^T \tag{5}$$

$$b = \begin{pmatrix} v_1 x_1 - u_1 y_1 & v_2 x_2 - u_2 y_2 & \cdots & v_n x_n - u_n y_n \end{pmatrix}^T \tag{6}$$

where (x_i, y_i) is the coordinate of the point in the image plane.

We define the repulsive force F_{rep} using the gradient vector field *g(x, y, t)* and TTC information as

$$F_{rep} = \begin{pmatrix} F_x \\ F_y \end{pmatrix} = k_{rep} \frac{1}{|B|} \begin{pmatrix} \int_{(x,y)^T \in A} g(x, y, t) dx \\ \sum\limits_{(x_i, y_i)^T \in A} TTC_i \end{pmatrix} \tag{7}$$

where $|B|$ is the region of interest in an image captured by the camera mounted on the UAV, here we select the region that covers the columns between 50 and 270, the gain parameter k_{rep} modulates the strength of repulsive force.

The other force is generated by the target and it can be represented as a source of attractive potential. It is directly proportional with the Euclidean distance away from the robot and can be computed as:

$$U_{att} = \frac{1}{2} k_{att} \left\| \sqrt{\left(x - x_{goal}\right)^2 + \left(y - y_{goal}\right)^2} \right\| \tag{8}$$

The goal term pulls the robot towards the goal. Its strength increases proportionally with goal distance $\sqrt{\left(x - x_{goal}\right)^2 + \left(y - y_{goal}\right)^2}$. The parameter k_{att} modulates the strength of this component. The attraction force is the gradient of the potential field.

$$F_{att} = \nabla U_{att} = k_{att} \sqrt{\left(x - x_{goal}\right)^2 + \left(y - y_{goal}\right)^2} \tag{9}$$

Using the visual potential, we introduce a mechanism for guiding the robot to the destination. The sum of control forces can be presented as follow:

$$\begin{cases} Fx = F_{att} \sin\left(\theta_{goal}\right) - Fx_{rep} \\ Fy = F_{att} \cos\left(\theta_{goal}\right) - Fy_{rep} \end{cases} \tag{10}$$

where $y = (0, 1)^T$ is the unit vector for y axis and θ_{goal} is the angle between the attraction force and y axis.

Since the control force F is applied to the quadrotor, we require that the control force is transformed into the yaw angel guiding navigation for our flight.

$$\psi = \arctan\left(Fx / Fy\right) \tag{11}$$

2.3 Control of the Quadrotor UAV

The control of the flight is implemented utilizing cascade PID controllers. We simulate the quadrotor in Matlab/Simulink with the Virtual Reality Modeling Language (VRML). Such a high level behavioral goal is obtained via generating the necessary control sequences from the PID controllers, which receive the yaw angle ψ produced by the vision based path planning scheme. The diagram for autonomous UAV motion is shown in Fig. 2.

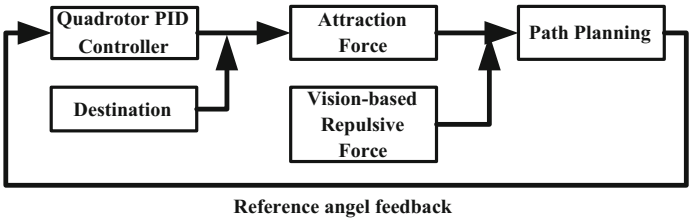

Fig. 2 Autonomous UAV motion diagram

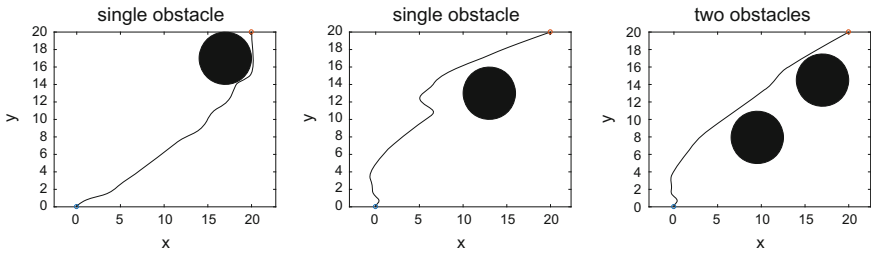

Fig. 3 *Experimental results* simple trails to illustrate the paths taken by our method. The *blue circle* indicates the start position, the *red circle* indicates the destination and the *black regions* are obstacles

3 Experimental Evaluation

To evaluate the performance of the proposed method, we create virtual environments with obstacles distributed unevenly using VRML, where the UAV is able to encounter some obstacles if it manoeuvres straight from the starting point to the destination. Several tests are conducted within different environments. The velocity of the vehicle is set to 1 m/s. There are a number of trials with varying complexity to show that the model works for different numbers of obstacles.

Figure 3 shows some trials designed to test basic obstacle avoidance behavior. Note that the paths are all smooth and take reasonably efficient paths through the field of obstacles.

The experiments shown in Fig. 3 illustrate the effect of visual repulsive potential for obstacles on the robot's path. The visual sensor can perceive the obstacles on start to avoid them in advance. There are, however, situations such as the first image of Fig. 3, in which the UAV almost collides with the obstacle due to the destination is too close to the obstacle.

Figure 4 shows experiments to test the behavior of the quadrotor UAV avoiding obstacles in complex environment. In the first image of Fig. 4, the resulting obstacle potential causes the robot to steer completely around the cluster, as in the second image of Fig. 4, the vehicle chooses a path through a gap between two obstacles when we increase the ratio of attraction potential gain to repulsive potential gain.

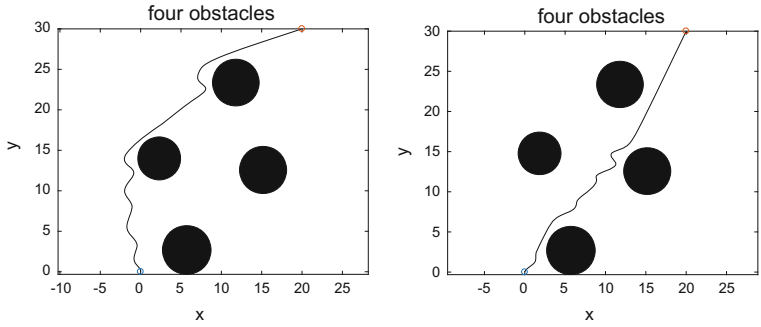

Fig. 4 Experimental results for navigation in complex environment with different gain ratio

4 Conclusion

This paper demonstrates the use of optical flow for navigating UAV to the destination without collision with obstacles. Optical flow information is utilized in detecting obstacles and the repulsive potential field is generated by gradient vectors and TTC of detected obstacles. One of the key parameters is discovered to be the gain ratio of attraction force to repulsive force. Small ratio will result in longer, more circuitous routes, while appropriate ratio will lead the UAV to pass through the obstacles safely and quickly. We implement our approach in virtual environments and conducted experiments with multiple obstacles. Our method has been demonstrated to be effective for real time obstacle avoidance and path planning.

Acknowledgements This work is supported by the National Basic Research 973 Program of China [Grant number 2012CB720003], and the National Nature Science Foundation of China [Grant numbers 61320106010, 61573019, 61627810].

References

1. Chao H, Gu Y, Napolitano M (2013) A survey of optical flow techniques for UAV navigation applications. International Conference on Unmanned Aircraft Systems (Vol.73, pp. 710–716)
2. Dolgov D, Thrun S, Montemerlo M, Diebel J (2010) Path planning for autonomous vehicles in unknown semi-structured environments. Int J Robot Res 29(5):485–501
3. Eresen A, İmamoğlu N, Efe MÖ (2012) Autonomous quadrotor flight with vision-based obstacle avoidance in virtual environment. Expert Syst Appl 39(1):894–905
4. Huang WH, Fajen BR, Fink JR, Warren WH (2006) Visual navigation and obstacle avoidance using a steering potential function. Robot Auton Syst 54(4):288–299
5. Khatib O (1986) Real-time obstacle avoidance for manipulators and mobile robots. IEEE international conference on robotics and automation, vol 2, pp 500–505
6. Lucas BD, Kanade T (1981) An iterative image registration technique with an application to stereo vision. International joint conference on artificial intelligence, vol 73, pp 674–679. Morgan Kaufmann Publishers Inc

7. Ohnishi N, Imiya A (2008) Visual navigation of mobile robot using optical flow and visual potential field. Robot Vis. Springer, Berlin Heidelberg, 412–426
8. Sedigh KH, Ashenayi K, Manikas TW, Wainwright RL (2004) Autonomous local path planning for a mobile robot using a genetic algorithm. Evolutionary Computation CEC2004, Vol 2, pp 1338–1345
9. Souhila K, Karim A (2007) Optical flow based robot obstacle avoidance. Int J Adv Rob Syst 4 (1):2
10. Yu H, Sharma R, Beard RW, Taylor CN (2013) Observability-based local path planning and obstacle avoidance using bearing-only measurements. Robot Auton Syst 61(12):1392–1405

Opinion Leader Mining of Social Network Combined with Hierarchical Sentiment Analysis

Hang Ye and Junping Du

1 Introduction

Nowadays, with the booming of internet, social networks are more and more popular in daily communications around the world. Everyone can post ideas and be the source of information at any time in anywhere on the social network. It is of great value to do research about social networks with mass data. However, because of the unrestraint and anonymity, the authenticity of the information on social networks can't be easily judged compared with the traditional official media. A huge challenge related to personal safety and social stability appears in public. Hence, it is meaningful to discuss about mining opinion leaders related with national security in social network.

Currently the methods of opinion leaders mining are divided into three patterns: the analysis of user's attributes, the analysis of information exchange and the analysis of network structure.

Considering bloggers' attributes, Zhang et al. [1] use the Markov networks to analyze the relevance of the intrinsic attributes of each user. The methods concerned with information interaction excavate opinion leaders by analyzing the propagation properties of the microblogs. Agarwal et al. [2] consider forwarding number, comment number and other attributes. To finding influential users, Li et al. [3] assess the quality of the bloggers in calculation. However, such methods have shortcomings in different aspects.

The last strategies become mainstream gradually because of exploiting graph models to represent the data structure and the better results can be obtained. There are two directions among these methods. One is complex network and the other is

H. Ye · J. Du (✉)
Beijing Key Laboratory of Intelligent Telecommunication Software and Multimedia, School of Computer Science, Beijing University of Posts and Telecommunications, Beijing 100876, China
e-mail: junpingdu@126.com

Z. Deng (ed.), *Proceedings of 2017 Chinese Intelligent Automation Conference*, Lecture Notes in Electrical Engineering 458,
https://doi.org/10.1007/978-981-10-6445-6_70

topology analysis. Cho [4] measures the user's influence by intimacy, sociality and centrality in the network. Microblog-Rank algorithm [5] pays attention on comments from the microblogs. Twitter-Rank algorithm [6] focus on the social relationship between the user and their theme similarity.

This paper mainly utilizes the method that combines network structure and microblog's attributes. Besides, we adopt the emotional analysis method of hierarchical structure to identify the malicious users who are possible threat to national security from the set of opinion leaders.

2 Expression of Mining Opinion Leaders of Social Network

Providing a microblog's dataset with specific topic, how can we find the set of leading users, how can we discover the dubious ones among the set? Our main target is to answering these questions. The solution is based on the algorithm provided by Subbian et al. [7] associated with Yu et al.'s [8]. The process is composed of two parts, the first step is to calculate each user's influence score, the second is to pick up the ones who are probably harmful to social stability.

2.1 Construction of Information-Flow Tree

The construction can be divided into two process which are building a tree and calculating. With communication networks, we need an accessible and computable pattern to represent the connections. Under this circumstance, we use the information-flow tree to save interactions and attributes of texts and users without taking textual information into consideration. Imitating from the creation of frequent pattern tree, the information-flow tree is constructed based on the behaviors like forwarding and commenting, and each node stands for a user.

2.2 Attributes of Nodes and Calculation of Users' Influence

As we discuss in Sect. 3.1, the nodes' weight is determined by social and users' properties. The users' attribute is composed of the quantities of microblogs, followers as well as followings. As for the social attribute, we take account for the number of posting and the number of comments for the formulas. The calculations are given by:

$$wi = \beta_1 N_1 + \beta_2 N_2 + \beta_3 N_3 \tag{1}$$

$$p_i = \lambda N_4 + (1 - \lambda) N_5 \tag{2}$$

Besides, it is noticeable that the overall path weight from root to a particular node is equal to the node's weight itself.

After completing the construction of information-flow tree, it comes to the calculation of each node's influence score. The influence between two nodes is obtained by calculating the sum of the information flows in the two pairs of nodes. The information flows between paired nodes is defined as the sum of the flows of all paths between two nodes for a certain keyword for some time.

The flows between paired nodes are given by following:

$$V(a_j, a_k, K_i, t_c) = \sum_{P \in S_{jk}} A(P, K_i, t_c) = \sum_{P \in S_{jk}} \sum_{a_i \in P} w(a_i, K_i, t_c) \tag{3}$$

w is determined by weight of each node.

Next, we can acquire each node's influence score by Influence Function which is shown as below:

$$\alpha(a_j, Q, t) = \frac{I(a_j, *, Q, t)}{I(*, *, Q, t)} = \frac{\sum_{K_i \in Q} V(a_j, *, K_i, t)}{\sum_{K_i \in Q} V(*, *, K_i, t)} \tag{4}$$

The nodes are ranked by the influence scores. If one user get a high influence score, he is more likely to become an opinion leader of relevant topics.

2.3 Sentiment Analysis of Users

Assumed that we obtain the ordered set of conceivable leading users, it's time to take sentiment analysis into account, where we use the method called hierarchical emotional analysis. The microblog is separated into three parts which are sentence, sub-sentence and phrase. According to the bottom-up rule, each phrase sentiment score is calculated and then to the level of sentences.

When we concentrate on the sentiment of one word, the PMI has been used to calculate semantic similarity in accordance with sentiment dictionary.

Next, the emotional vector of the phrase focus on the structure and dependencies between these different words. In the sub-sentence level, the whole text is divided by punctuations like "、", ",", ";", and relations among this short sentences become a significant feature to calculate. Finally, we reach the top level which consists of long sentences. With effect of different punctuations, we can make a result of a sentence.

$$Sen(a_i) = \frac{1}{N}\sum_{a_i \in V} Sen(tweet_i) = \frac{1}{N}\sum \frac{1}{N_i}\sum_{j=1}^{N_i} \beta_{ij} \cdot \left(\frac{\overrightarrow{p_{v_{ij}}} \cdot (\overrightarrow{\varphi_{v_{ij}}} \circ \overrightarrow{\eta_{v_{ij}}})}{n_{v_{ij}}} + \frac{\overrightarrow{p_{a_{ij}}} \cdot (\overrightarrow{\varphi_{a_{ij}}} \circ \overrightarrow{\eta_{a_{ij}}})}{n_{a_{ij}}} \right), \tag{5}$$

The formula (5) presents the integration of all three levels. From it, we can arrive at the sentiment score of a microblog.

2.4 Integration of Users' Influence Score and Emotion Score

In this section, each user's degree of threatened in a certain period can be elicited on basis of influence score and sentiment score. The user list facilitates further tracking of the relevant users. The combination process is shown as below:

$$D(a_i) = \delta \times \alpha(a_i, Q, t_i) + (1 - \delta) \times Sen(a_i) \tag{6}$$

Due to the dimension between the results of α and Sen, it is essential to normalize data before formula (7).

3 Experiments on Real Data Set

This section is an application to our procedure and empirical valuation. We set the same weights of the social attributes and the combination factor as following in all experiments:

$$\beta_1 = \beta_2 = \beta_3 = 0.33, \quad \alpha = 0.6 \tag{7}$$

3.1 Data Set of Sina Weibo

We gather two datasets from Sina Weibo for assessing several aspects of our method. The total number of microblogs is 2.25 million. The period is from 2011 to 2014. Among them, we concentrate on the pieces related to national security. Therefore, some keys are used to filter to get truly meaningful contents. The keys contains The"Xiao Yueyue" Event, Bullet Train Rear-End Collision, Ya'an Earthquake, MH370 Accident etc. After pretreatment, we finally get nearly 30 thousand microblogs with 7 thousand users.

3.2 Results and Evaluation

To illustrate the advantages of our methods (Information-Flow Tree with Attributes), we introduce some influence evaluation techniques as the comparisons. They are TopicLeaderRank (LR) [9], ProfileRank (PRF) [11], Repuser (SD, SS3) [10] and PageRank (PR). The former two methods are supplements and improvements of PageRank. The Repuser algorithm is to maximize objective function by stratified sampling and diversity sampling. All this comparative methods are set with default parameters. The standard list adopted is the sequence of users that only takes the number of forwarding and comment as the sorting index.

Figure 1 shows the core rate of four methods. The core rate measures the ability of interaction of an opinion leader. The core rate of a user is determined by the number of posting and the number of comments associated with the user's microblogs. Figure 2 shows the assessments of single coverage rate. From the point view of network topology, coverage rate measures the dominant power by calculating the number of affected users. Single-step coverage only consider the direct touched neighbors of each user. As expected, our IFwA method achieve better than others in terms of the two metrics. It is a obvious fact that the IF method performs outstandingly in top-150 users.

Table 1 shows more details for this experiment with Tables 2 and 3.

Table 1 is the mean average precision of all algorithms under different chosen ranges. It is clear to observe that IFwA achieves a better result than other baseline methods.

Table 2 is the results of accuracy, which means we concern about involvement rather than sequence within measurements. Moreover, the IFwA algorithm has more advantage of NDCG in Table 3.

It is probably owing to the IF tree not only rely on the communications among users, but also consider user attributes and interaction attributes, rather than only take the number of forwarding for the construction of IF tree. This procedure is learnt from the principle of LeaderRank algorithm to complement the original influence calculation. Compared with the sampling strategy in the SD and SS3

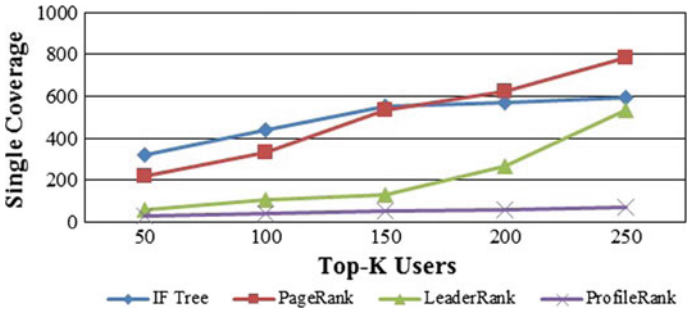

Fig. 1 Single coverage of the PageRank, LeaderRank, IF tree with attributes and ProfileRank

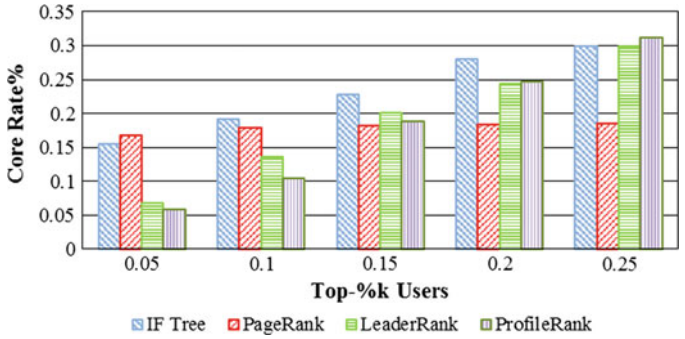

Fig. 2 Core rate of the PageRank, LeaderRank, IF tree with attributes and ProfileRank

Table 1 Evaluation of the PageRank, LeaderRank, IF tree, ProfileRank in terms of MAP

MAP	PR	LR	IFwA	PFR
@50	0.50	0.01	0.71	0.32
@100	0.51	0.02	0.72	0.33
@200	0.56	0.15	0.60	0.34
@300	0.59	0.23	0.55	0.20
@400	0.61	0.26	0.53	0.30
Avg.	0.54	0.17	0.57	0.31

Table 2 Evaluation of the PageRank, LeaderRank, IF tree, ProfileRank, SS3, SD in terms of accuracy (without sequence)

Accuracy	PR	LR	IFwA	SSD	S3	PRF
@50	0.48	0.0	0.86	0.16	0.2	0.02
@100	0.62	0.0	0.83	0.19	0.22	0.01
@150	0.72	0.006	0.83	0.17	0.17	0.01
@200	0.72	0.04	0.67	0.15	0.15	0.005
@400	0.73	0.235	0.38	0.15	0.19	0.02

Table 3 Evaluation of the methods of NDCG (Top-100)

NDCG	PR	LR	IFwA	SSD	S3	PRF
@50	0.557	0.0	0.640	0.193	0.379	0.002
@100	0.554	0.0	0.644	0.192	0.377	0.002
@200	0.601	0.0001	0.650	0.193	0.380	0.0004
@300	0.600	0.105	0.649	0.167	0.379	0.003
@400	0.604	0.096	0.648	0.153	0.379	0.003

algorithm, the IFwA method pays more attention to the specific behavior of the users. Hence, for the chosen baseline as the evaluation, the IFwA improves superiorly.

Next, we evaluate the complete proposed procedure using 2500 randomly chosen data because of the limitation of runtime. The comparisons are the combination of hierarchical sentiment analysis with PR as well as with LR. The baseline

Table 4 MAP of performance by integration of influence score and emotional score

MAP	PR_Sentiment	LR_Sentiment	IFwA_Sentiment
@50	0.06	0.03	0.27
@100	0.11	0.37	0.34
@150	0.36	0.33	0.38
@200	0.39	0.41	0.41
@500	0.40	0.38	0.39

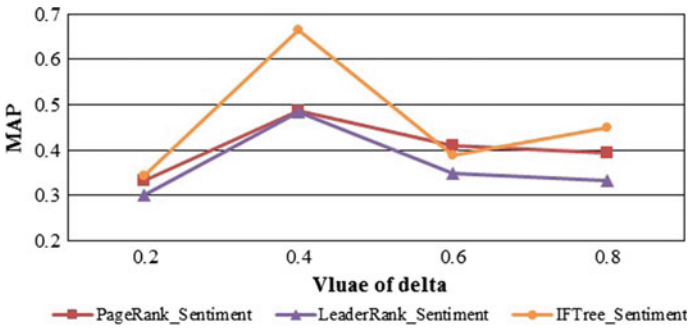

Fig. 3 Evaluation of MAP about the integration with different values of delta

of the sentiment analysis is the array only considering the number of sentiment words. δ in formula (10) is identified as 0.5. The evaluation displays in Table 4.

We can find that the Information-Flow tree with Attributes with hierarchical emotional method is slightly better than the other two integration.

Figure 3 presents the impact of the value of δ on MAP. The greater the δ value is, the more dominant the emotional factor is. Therefore, we can figure it out that the integration of our procedure perform outstandingly under most conditions. And when the δ reaches nearly 0.5, this three methods all have greater effect.

4 Conclusions and Future Work

We propose to tackle the problem of mining opinion leaders related to national security by quantizing the leading degree and threat degree of each user. The two-step procedure is used to realize our goal: an Information-Flow tree is first constructed for the calculation of influence score. Furthermore, we apply a Hierarchic Emotional analysis to discover the radicalness from microblogs. The experiment results show our procedure meet the requirement in real dataset. Quantitative analysis on synthetic data demonstrates our method performs more excellent than other baseline algorithms.

In the future, we could extend our procedure in source trustworthiness analysis besides improvement in influence calculation. Moreover, it would be possible to produce a more fine-grained word-level analysis in sentiment evaluation.

Acknowledgements This work was supported by the National Natural Science Foundation of China (No. 61532006, No. 61320106006, No. 61502042).

References

1. Zhang WZ, Li XQ, He H et al (2014) Identifying network public opinion leaders based on Markov logic networks. Sci World J 435–444
2. Agarwal N, Liu H, Tang L et al (2010) Identifying the influential bloggers in a community. In: International conference on web search and web data mining, Palo Alto, California, pp 207–218
3. Li F, Du TC (2011) Who is talking? An ontology-based opinion leader identification frame00work for word-of-mouth marketing in online social blogs. Decis Support Syst 51 (1):190–197
4. Cho Y, Hwang J, Lee D (2012) Identification of effective opinion leaders in the diffusion of technological innovation: a social network approach. Technol Forecast Soc Chang 79(1):97–106
5. Lin Y, Li HX, Liu XQ et al (2013) Hot topic propagation model and opinion leader identifying model in microblog network. Abstr Appl Anal 6:1–13
6. Weng J, Lim EP, Jiang J et al (2010) Twitterrank: finding topic-sensitive influential twitters. In: Proceedings of the third ACM international conference on Web search and data mining, New York City, pp 261–270
7. Subbian K, Aggarwal CC, Srivastava J (2016) Querying and tracking influencers in social streams. In: ACM international conference on web search and data mining, San Francisco
8. Yu ZW, Wang ZT, Chen LM et al (2016) Featuring, detecting, and visualizing human sentiment in Chinese micro-Blog. ACM Trans Knowl Discov Data 10(4):48
9. Wu XH, Zhang H, Zhao X (2015) Mining algorithm of microblogging opinion leaders based on user-behavior network. Appl Res Comput 9:2678–2683 (in Chinese)
10. Tang J, Chenhui Z, Keke C et al (2015) Sampling representative users from large social networks. In: 2015, Association for the Advancement of Artificial Intelligence, Austin
11. Silva A, Meira W, Zaki M (2013) ProfileRank: finding relevant content and influential users based on information diffusion. The Workshop on social network mining and analysis, pp 1–9

Cloud Model Based Intelligent Control for Marine Hydraulic Steering Gear System

Yongfeng Huang, Chen Guo, Jianbo Sun and Yutong Huo

1 Introduction

The steering gear is a control device which used to realize the change of navigation direction of a ship, such as ship course-changing, turning, direct navigation, etc. The cloud model is founded on the traditional fuzzy set theory, the introduction of probability statistics theory, will expand the accuracy of the membership function with the statistical distribution of uncertainty, but also has realized transformation of uncertainty between the qualitative and quantitative characteristics [1, 2], therefore, the cloud model method is applied to the marine hydraulic steering control positive significance.

2 Modeling of Hydraulic Steering Gear System

The mathematical model of marine hydraulic steering gear system includes the system pipeline mathematical model, hydraulic pump model, steering gear model and rudder regulator model [3].

Y. Huang · C. Guo (✉) · Y. Huo
School of Information Science and Technology, DMU, Dalian 116026, China
e-mail: dmuguoc@126.com

Y. Huang
e-mail: hyf_ol@qq.com

J. Sun
School of Marine Engineering, DMU, Dalian 116026, China
e-mail: vrsjb@dlmu.edu.cn

Z. Deng (ed.), *Proceedings of 2017 Chinese Intelligent Automation Conference*,
Lecture Notes in Electrical Engineering 458,
https://doi.org/10.1007/978-981-10-6445-6_71

2.1 Hydraulic Pump Model

In this paper, the swash plate axial piston pump is used. The pipeline mathematical model can be expressed as:

$$Q = \frac{\pi}{4} d^2 \cdot D \tan\beta \cdot z \cdot n \cdot \eta_v \tag{1}$$

Here D is the center circle diameter of the piston, m; d is the diameter of the piston, m; z is the number of the piston; n is the pump speed, r/min; η_v is the volumetric efficiency of pump.

We can get the tilt angle of swash plate from:

$$\dot{\beta} + k_1\beta = k_2 u \tag{2}$$

Here k_1 and k_2 is proportion coefficient.

2.2 Steering Gear Model

The steering gear in this paper is the four cylinder double ram structure. The hydraulic cylinder static force balance equation is:

$$A\Delta P = Jy'' + B_c y' + F_l \tag{3}$$

Here A is the sum of the ram acreage, m^2; J is the rotational inertia of moving parts; B_c is the viscous damping coefficient; y' is the velocity of the ram; y'' is the accelerated velocity of the ram.

The actual rudder is:

$$\alpha = \arctan\frac{y}{R} \tag{4}$$

Here y is the displacement of the ram when the rudder angle equals α; R is the distance between the rudder center and the cylinder center line.

2.3 Pipeline Mathematical Model

The pipeline mathematical model can be expressed as

$$Q = \lambda \Delta P + \frac{V_t}{4B_c'} d\Delta P/dt + Ay' \tag{5}$$

Here λ is the leakage coefficient; V_t is the cylinder volume; B_c' is the Elastic modulus of hydraulic oil.

2.4 Rudder Regulator Model

In the hydraulic steering gear system, the rudder angle regulator uses the rudder angle feedback error signal to change the output signal. The rudder angle control schematic is shown in Fig. 1.

3 Cloud Model

3.1 Cloud Theory

Cloud is defined as follows, suppose that $U = \{x\}$ is the qualitative universe of discourse, and A is a linguistic term associated with U. If the quantitative value x is one of the random values of A belongs to U and the certainty degree μ of x to A is a random number with stable tendency, then the distribution of x in the universe of discourse U is called a cloud model [4], and (x, μ) is a cloud drop.

3.2 Cloud Model Inference Rule

The inference rules of cloud model contain two parts: the X conditional cloud model and the Y conditional cloud model [5, 6].

In the universe of discourse, if the cloud model (Ex, En, He) consists a specific input conditions $x = x_0$, then it is also called X conditional cloud model, noted as

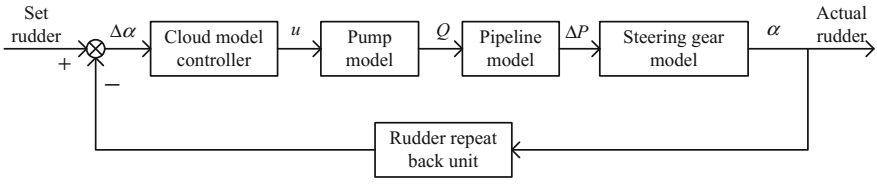

Fig. 1 Block diagram of the steering gear control system

CGx. If the specific condition $\mu(x) = \mu(x_0)$, then it is called Y conditional cloud model, noted as *CGy* [7].

One-dimensional X conditional cloud model:

$$P_i = R_1(En, He) \tag{6}$$

$$\mu_i = \exp[-0.5(x - Ex)^2 / P_i^2] \tag{7}$$

Here the expected value Ex, entropy En and hyper entropy He are the characteristics of the X conditional cloud model.

One-dimensional Y conditional cloud model:

$$P_i = R_1(En, He) \tag{8}$$

$$y_i = Ey \pm \sqrt{-2\ln(\mu)} \cdot P_i \tag{9}$$

Here the expected value Ey, entropy En and hyper entropy He are the characteristics of the Y conditional cloud model.

The single rule inference structure of one-dimensional cloud model is shown in Fig. 2. And the inference rules can be expressed as: If X then Y.

Figure 3 is a cloud model mapping structure, this composed of one-dimensional multi-rule inference structure consist of N one-dimensional rules, the inference rules is: If $X = X_i$ then $Y = Y_i$.

Similarly, the introduction of two-dimensional cloud model inference process is shown in Figs. 4 and 5.

Two-dimensional X conditional cloud model:

$$(P_{A1i}, P_{A2i}) = R_2(En_{A1}, En_{A2}, He_{A1}, He_{A2}) \tag{10}$$

$$\mu_i = \exp[-0.5(x_1 - Ex_{A1})^2 / P_{A1i}^2 - 0.5(x_2 - Ex_{A2})^2 / P_{A2i}^2] \tag{11}$$

Here x_1, x_2 are two quantitative input values; $(Ex_{A1}, En_{A1}, He_{A1})$ is a digital feature of fuzzy subset A1; $(Ex_{A1}, En_{A1}, He_{A1})$ is a digital feature of fuzzy subset A2; μ is the output of the X conditional cloud.

Two-dimensional Y conditional cloud model:

$$P_i = R_1(En, He) \tag{12}$$

$$y_i = Ey \pm \sqrt{-2\ln(\mu)} \cdot P_i \tag{13}$$

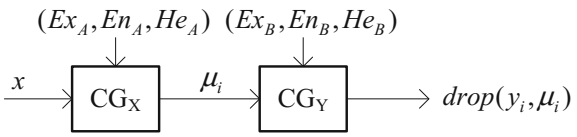

Fig. 2 Single rule inference by one-dimensional cloud model

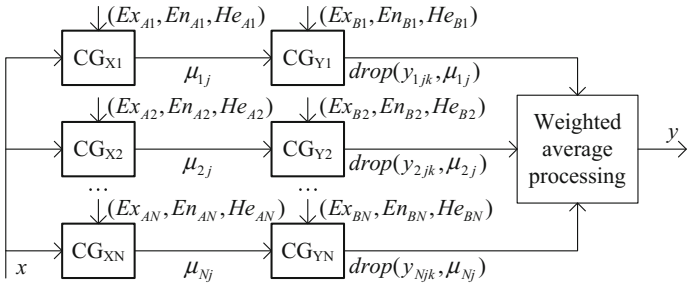

Fig. 3 One-dimensional cloud model mapping processor

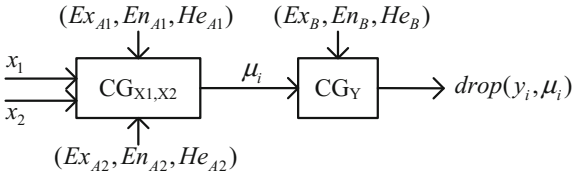

Fig. 4 Single rule inference by two-dimensional cloud model

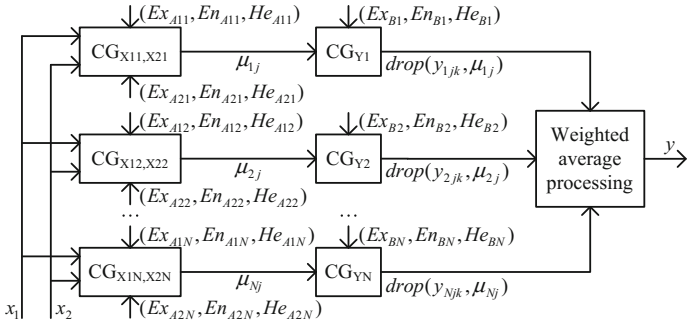

Fig. 5 Two-dimensional cloud model mapping processor

Here the expected value Ey, entropy En and hyper entropy He are the characteristics of the Y conditional cloud model.

Two-dimensional cloud model inference rule is If X_{1i}, X_{2j}, then Y_k, $k = R_{ij}$.

3.3 Cloud Model Controller

Cloud model controller is shown in Fig. 6. The controller is composed of one-dimensional I cloud model controller and two-dimensional PD cloud model controller, known as PD + I cloud model intelligent controller.

Among them, the error integral e_i is the input of one-dimensional cloud model mapper. And the deviation e and the deviation change rate e_c are the input of the two-dimensional cloud model mapper. K_1, K_2, K_3 are the quantization factor, K_4 is the driving factor, K_{U1}, K_{U2} are the control of the output regulation parameters, the output:

$$u = K_4(K_{U1}y_1 + K_{U2}y_2) \tag{14}$$

The input and output cloud model digital characteristics of one-dimensional cloud model controller are shown in Table 1. The input and output cloud model digital characteristics of two-dimensional cloud model controller are shown in Table 2.

Here the parameters setting are: $K_1 = 3/35$, $K_2 = 3/350$, $K_3 = 1/70$, the driving factor $K_4 = 35$; the control output parameters $K_{U1} = 0.8$,$K_{U2} = 0.002$.

One-dimensional rule is: If $X = X_i$ then $Y = Y_i$, $i = 1{-}7$.

Since $i, j, k = 1{-}7$, there are 49 two-dimensional rules as shown in the matrix $R_k^{7\times7}$.

$$R_k^{7\times7} = \{R_{ij}\} = \begin{bmatrix} 1 & 1 & 1 & 2 & 3 & 3 & 4 \\ 1 & 2 & 2 & 3 & 3 & 4 & 5 \\ 2 & 2 & 2 & 3 & 4 & 5 & 5 \\ 2 & 3 & 3 & 4 & 5 & 5 & 6 \\ 3 & 3 & 3 & 5 & 5 & 6 & 6 \\ 3 & 4 & 4 & 5 & 5 & 6 & 6 \\ 4 & 5 & 5 & 6 & 6 & 7 & 7 \end{bmatrix}$$

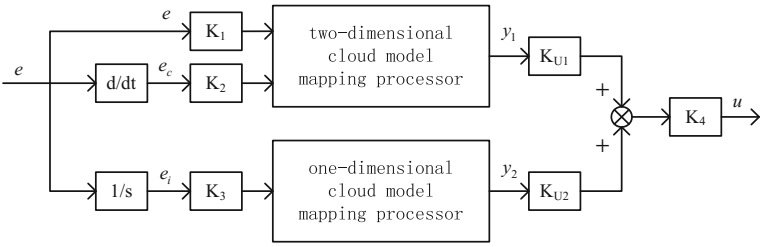

Fig. 6 Structure of cloud model controller

Table 1 Parameters of one-dimensional cloud model mapping processor

i	1	2	3	4	5	6	7
X_i	(−1, 0.3, 0.01)	(−0.67, 0.3, 0.01)	(−0.33, 0.3, 0.01)	(0, 0.3, 0.01)	(0.33, 0.3, 0.01)	(0.67, 0.3, 0.01)	(1, 0.3, 0.01)
Y_i	(−1, 0.3, 0.01)	(−0.67, 0.3, 0.01)	(−0.33, 0.3, 0.01)	(0, 0.3, 0.01)	(0.33, 0.3, 0.01)	(0.67, 0.3, 0.01)	(1, 0.3, 0.01)

Table 2 Parameters of two-dimensional cloud model mapping processor

i,j,k	1	2	3	4	5	6	7
X_{1i}	(−6, 0.3, 0.01)	(−4, 0.3, 0.01)	(−2, 0.3, 0.01)	(0, 0.3, 0.01)	(2, 0.3, 0.01)	(4, 0.3, 0.01)	(6, 0.3, 0.01)
X_{2j}	(−6, 0.3, 0.01)	(−4, 0.3, 0.01)	(−2, 0.3, 0.01)	(0, 0.3, 0.01)	(2, 0.3, 0.01)	(4, 0.3, 0.01)	(6, 0.3, 0.01)
Y_k	(−6, 0.3, 0.01)	(−4, 0.3, 0.01)	(−2, 0.3, 0.01)	(0, 0.3, 0.01)	(2, 0.3, 0.01)	(4, 0.3, 0.01)	(6, 0.3, 0.01)

4 Simulation Results and Analysis

Simulation experiments are conducted based on the MATLAB software. The control effect of the cloud model controller is compared with traditional PID controller. The parameters of traditional PID controller are: $k_p = 0.8$, $k_i = 0.002$, $k_d = 0.01$. In this paper, we use positive value to represent the port action, the negative value the starboard action. Set the rudder angle, the control effect is shown in Fig. 7.

In Fig. 7, the solid line is the cloud model controlling curve, the dotted line is the PID controlling curve. It is clear to see that cloud model controller obtained rudder angle curve without overshot. The stability error of cloud model controller is limited to 2×10^{-2}, and the stability error of PID controller is limited to 4×10^{-2}. The cloud model controller obtained a fast stability speed and a better control accuracy.

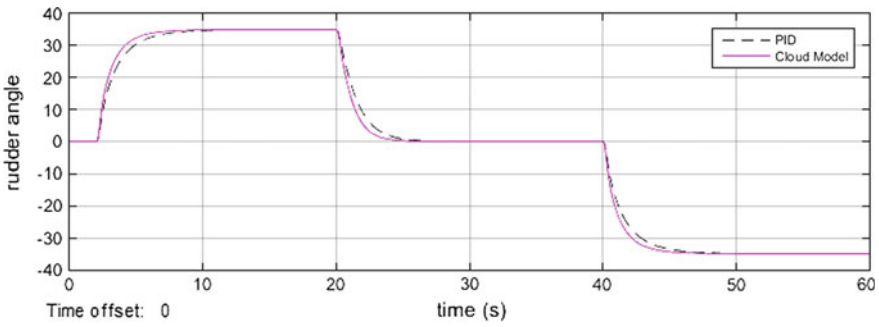

Fig. 7 Simulation curve of rudder angle

5 Conclusion

In this paper a mathematical model of the ship hydraulic steering gear is established, and the PD + I cloud model intelligent controller is designed and applied to control the marine hydraulic steering gear. The simulation results demonstrate that the controller is simple and intuitive, and the control performance is suitable and acceptable. It has better control quality than the conventional PID controller. The cloud model controller significantly possesses a high practical application value with simple structure.

Acknowledgements The authors are very grateful to the editors and reviewers for their valuable comments and suggestions. This work is supported by National Natural Science Foundation of China (Nos. 51579024, 6137114) and the Fundamental Research Funds for the Central Universities (DMU No. 3132016311).

References

1. Gao J, Jiang C, Li Z (2006) A novel design of controller based on the cloud model. Inf Control 34(2):157–162 (in Chinese)
2. Gao J, Li Z (2006) Study on design and application of one-dimension cloud model mapping processor. J Syst Simul 18(7):1861–1865 (in Chinese)
3. Liu Y, Ji X (2009) Simulation of cavitation in rotary valve of hydraulic power steering gear. Sci China 52(11):3142–3148 (in Chinese)
4. Li DY, Meng HJ, Shi XM (1995) Membership clouds and membership clouds generators. Comput Res Develop 32(6):15–20 (in Chinese)
5. Liu S, Chang X-C (2012) Synchro-control of twin-rudder with cloud model. Int J Autom Comput 9(1):98–104
6. Gao J, Zhou A, Li Z (2008) Study on cloud model control for ship course-keeping system. J Jiang su Univ Sci Technol (Nat Sci Ed) 22(5):11–16 (in Chinese)
7. Li DY, Cheung D, Shi XM, Ng V (1998) Uncertainty reasoning based on cloud models in controllers. Comput Math Appl 35(3):99–123

Tourism Information Search Based on Dynamic Attraction Topic Distribution

Lingfei Ye, Junping Du and Zijian Lin

1 Introduction

With the development of Internet technologies and economics, tourism has become more and more important for people, and there is an increasing demand for tourism information services. More and more people choose to plan their travels by themselves, through the texts and images of attractions on the Internet. And they also tend to share their own travel itineraries and travel experiences. Therefore, the study of tourism information search has become a research hotspot [1–3].

In order to speculate the search intents of tourists, there has been a lot of work on retrieval modeling. There are the early Boolean model, space vector model, the probability model, language model and sorting learning technology. The traditional search engine does not consider the search intents of users, and the search method based on the user's preferences has become a popular research direction.

Through the speculation of the user's intents, the search service provides users with better search results according to their search habits and background. Song et al. [4] used a probabilistic topic model to mine topics from users' search history and regard the topics as the users' search intents. Xue et al. [5] employed named entities and topic model to understand users' major search intents and considered the relation of entities, categories and topics. Santos et al. [6] proposed a new method of search result diversification and learned the intent distribution for each intent aspect by LTR. Hu et al. [7] and Wang et al. [8] employed clustering algorithms to extract subtopics of query terms from search logs or surrounding texts in returned results and the subtopics can further be used in result ranking. In view of the shortcomings of query response mechanism based on keyword matching, a lot

L. Ye · J. Du (✉) · Z. Lin
Beijing Key Laboratory of Intelligent Telecommunication Software and Multimedia, School of Computer Science, Beijing University of Posts and Telecommunications, Beijing 100876, China
e-mail: junpingdu@126.com

Z. Deng (ed.), *Proceedings of 2017 Chinese Intelligent Automation Conference*, Lecture Notes in Electrical Engineering 458,
https://doi.org/10.1007/978-981-10-6445-6_72

of scholars have carried out extensive research on the needs of dealing with complex user information. The related technologies are query expansion and topic model.

In this paper, we propose a method of tourism information search based on attraction dynamic topic distribution. We train the dynamic topic model with tourism comments of different time periods to get the topic distribution of attractions in time dimension. In this way, we can speculate user's search intents by the topic distribution of the query and improve the search accuracy of tourism information search. This method can be used in tourism search systems to get better search results to satisfy different users' search needs.

2 Tourism Information Search Based on Attraction Dynamic Topic Distribution

In this paper, we employ the dynamic topic model [9] to handle attraction comments, and mine the attraction topic information at different time periods. We make the following assumption of attraction comments: There are T themes in each comment, each topic corresponds to a word distribution, and each attraction comment has a most representative topic. There exists a topic distribution for each attraction and the topic distribution evolves in time.

2.1 Construction of Dynamic Attraction Topic Model

First of all, according to the time information of attraction comments, we divide them into text-time sets of different time periods. Then we apply LDA to extract the topic distribution of texts in each time slice on T topics. By using the incremental Gibbs sampling, we get the probability distribution relation of the attraction documents and topics, that is, the topic-word distribution φ and document-topic distribution θ of attraction comments. And then we use the topic-word distribution φ_{t-1} of the comment text set of the former time slice as the prior probability of the topic-word distribution φ_t of the current time slice to get the probability distribution relation of the attraction documents and topics of the current time slice, and then ultimately get the evolution of attraction topics in time. The generation model of attraction comments based on dynamic topic model is shown in Fig. 1.

The dynamic Gibbs sampling formula for dynamic topic model is shown as Eqs. (1)–(3).

$$P_t(z_i = j | z_{-i}, \omega_i, d_i, \cdot) = \frac{P_t(z_i = j, z_{-i}, \omega_i, d_i, \cdot)}{P_t(z_{-i}, \omega_i, d_i, \cdot)} \tag{1}$$

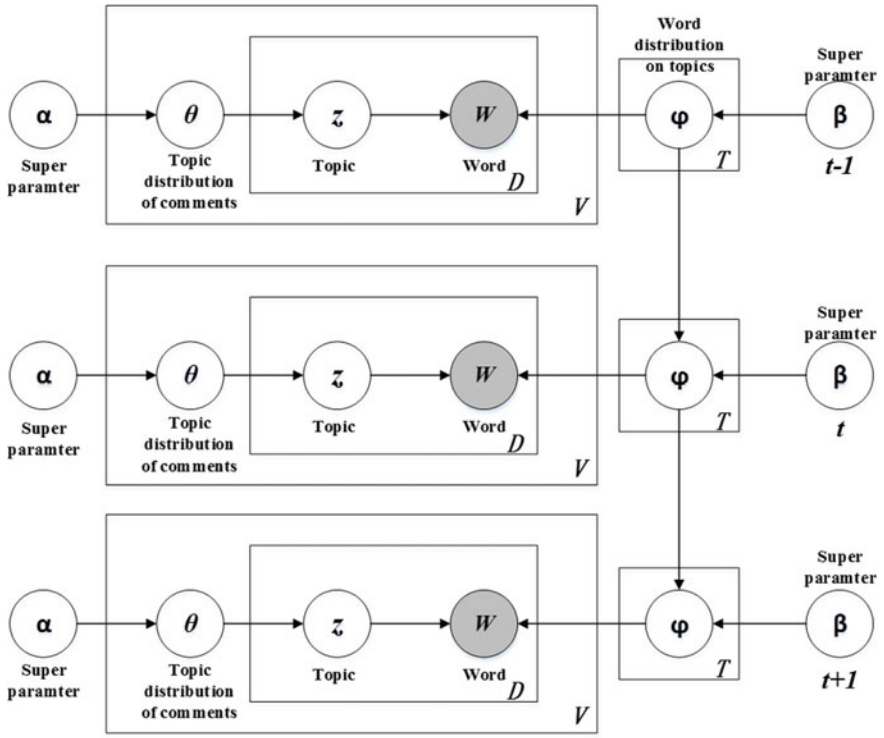

Fig. 1 The generation model of attraction comments based on dynamic topic model

$$P_t(z_i = j, z_{-i}, \omega_i, d_i, \cdot) = \frac{(n_{-i,j}^{(\omega_i)})_t + v(n_{-i,j}^{(\omega_i)})_{t-1} + \beta}{(n_{-i,j}^{(\cdot)})_t + v(n_{-i,j}^{(\cdot)})_{t-1} + V\beta} * \frac{(n_{-i,j}^{(d_i)})_t + \alpha}{(n_{-i,\cdot}^{(d)})_t + T\alpha} \tag{2}$$

$$P_t(z_{-i}, \omega_i, d_i, \cdot) = \sum_{j=1}^{T} \frac{(n_{-i,j}^{(\omega_i)})_t + v(n_{-i,j}^{(\omega_i)})_{t-1} + \beta}{(n_{-i,j}^{(\cdot)})_t + v(n_{-i,j}^{(\cdot)})_{t-1} + V\beta} * \frac{(n_{-i,j}^{(d_i)})_t + \alpha}{(n_{-i,\cdot}^{(d)})_t + T\alpha} \tag{3}$$

where t represents the time slice, V represents the number of words, $z_i = j$ means that topic j is assigned to word ω_i as its topic, $\cdot$ represents all other known information, z_{-i} represents the topic assignment z_k of words except the current word, $v(n_{-i,j}^{(\omega_i)})_{t-1}$ represents the times that word ω_i appears in topic z_i except the current counting of word ω_i of the former time slice, $v(n_{-i,j}^{(\cdot)})_{t-1}$ represents the number of words in all the documents appear in topic z_i in the former time slice, $(n_{-i,j}^{(d_i)})_t$ is the number of words in d_i allocated to topic z_i.

Then use Gibbs sampling and determine the initial state of the Markov chain based on the previous time slice and cycle for each word ω_i from 1 to V according

to Eq. (1), and assign topic z_i to word ω_i as its topic, then get the next state of the Markov chain and constantly iterate until the state is steady.

2.2 Information Search Based on Dynamic Attraction Topic Model

The user's query contains their implied search intents. In this paper, we use the topic-word distribution of attraction comments in different time periods to generate the topic distribution of the user search query, and calculate the similarity between user search query and local comment texts to realize the information search based on dynamic topic distribution.

Use the topic-word distribution φ_t of different time slice to calculate the topic distribution Q_t of the current query q at each time slice by Gibbs sampling and iteration, and the calculation process of the sampling is shown as Eq. (4) and the topic distribution Q_t of the query is shown in Eq. (5).

$$P(z_i = j|z_{-i}, w) = \frac{n_{k,-i}^{(j)} + \alpha_j}{\sum_{j=1}^{T}(n_{k,-i}^{(j)} + \alpha_j)} * \frac{n_{j,-i}^{(t)} + \beta_t}{\sum_{t=1}^{V}(n_{j,-i}^{(t)} + \beta_t)} \tag{4}$$

$$Q_t = (z_1, z_2, z_3, \ldots, z_m) \tag{5}$$

Using the calculated document-topic matrix θ_t and the topic distribution Q_t of the current query in different time slice, the similarity between the topic distribution of the query text and the topic distribution of local texts is calculated. The search results are sorted by the similarity scores. The higher the similarity score is, the more related the document is to the user's query. Use KL-Divergence to calculate the similarity between the query distribution Q_t and the document distribution $\theta_{t,i}$. The formula is shown in Eq. (6).

$$D(Q_t||\theta_{t,i}) = \sum_{\omega \in V} p(\omega|Q_t) \log \frac{p(\omega|Q_t)}{p(\omega|\theta_{t,i})} \tag{6}$$

The search system is implemented based on Lucene. Lucene can segment the search query, combining with the "and" operation between keywords to search in the local text database and return search results with theirs similarity scores *LScore*. Using our proposed method, we can get the topic similarity *TScore* for each document. After normalized the two scores, the sort weight factor λ is used to combine Lucene with our method, and the final score of the document is calculated by Eq. (7).

$$ComScore = (1 - \lambda) * LScore' + \lambda * TScore' \quad (7)$$

The search results are reordered according to the ComScore value of the document to obtain the final search results.

3 Experiments and Analysis

We obtained around 60 thousand attraction comments of more than 10 attractions in Beijing from microblog and travel sites as experimental data. And we use ICTCLAS API to do word segmentation on attraction comments and retain nouns, adjectives, verbs to represent users' interests and activities, and also introduce the stop word list to filter the meaningless nouns and adjectives. We encode the documents after word segmentation and remove of meaningless word and also get the word dictionary, which can be used as the input of dynamic LDA. In this way, we finish the preprocessing of attraction comments.

3.1 Attraction Topic Evolution Analysis

After training the model, we get the document-topic distribution θ of attraction comments. Then combining with the functional category dictionary constructed by keywords from travel websites and a classifier, we can gain the classification of attractions, and the attraction topic changes in time. As for the dynamic topic model, the number of topics T is set to 20, and $\alpha = T/50$, $\beta = 0.01$.

Based on the comment data of Beijing from April to July, 2016, combined with dynamic topic model, the time slice interval is 7-day, and the topic distribution of each attraction is obtained. Use 60% of the data as the training set to train the LambdaMART classifier and 40% as the test set. The classification results of shopping, eating and entertainment category are shown in Table 1.

As can be seen from Table 1, based on dynamic topic model and category dictionary, the average precision of topic classification is 0.7, meaning that the dynamic topic distribution of attractions can represent the function of attractions well, where shopping, eating and entertainment are three main function of attractions.

Table 1 The topic classification results

Category	Precision	Recall	F value
Shopping	0.6785	0.7037	0.6909
Eating	0.6875	0.8461	0.7586
Entertainment	0.75	0.7058	0.7272
Average	0.7053	0.7519	0.7256

Based on the comment data of Xidan from May 1 to 20, 2016, the time slice interval is set to 1 day, and the distribution of three representative functions of Xidan during 20 days is shown in Fig. 2.

As can be seen from the trend of the curves of Fig. 2, the function theme of Xidan is not static, but changes with time. The theme of Xidan on Saturday is mainly shopping, the main theme of Sunday is eating, and entertainment is not the main theme of Xidan relatively. The experimental results show that the topics of an attraction do change over time and the dynamic topic distribution can represent the theme or function of attractions well. So we can use it to speculate user's search intents for more accurate and relevant search results.

3.2 *Results and Analysis of Tourism Information Search*

NDCG is the ratio of the actual sorted DCG to the ideal sorted DCG value. The ideal order is that the document is sorted by the correlation from large to small. We calculate the NDCG@K for all test queries and evaluate the overall performance of the search system.

We set the number T of topics of dynamic topic model to $20, 30, 40, 50, 60, 70$, $\alpha = T/50$, $\beta = 0.01$, and the number of iteration is set to 300 times, the sort weight factor is set to 0.5. We designed 10 travel queries in Chinese used as query cases to test the search system: see cherry blossoms, one day trip to Forbidden City, climb the Great Wall, bars, Beijing souvenirs, the history of Yuanmingyuan Palace, Beijing Sanlitun, Wangfujing Street, Buddha, snow scenes. We recorded NDCG@K for each test case, and then got the average values as the final test results. In order to test the effectiveness of our proposed method, experiments were carried out on the method only based on Lucene and our method, noted as L + DLDA. The search results are shown in Table 2 and Fig. 3.

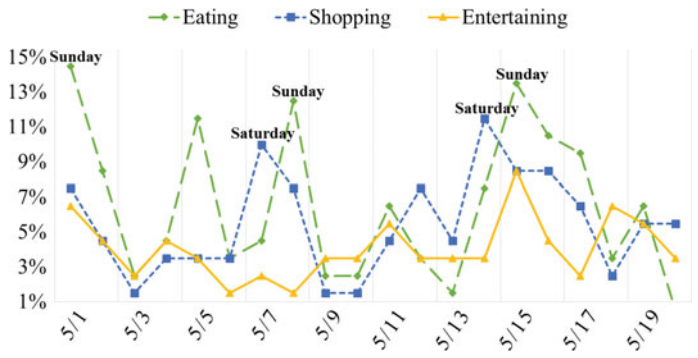

Fig. 2 Xidan function distribution results in May

Table 2 Search capabilities based on Lucene and L + DLDA

NDCG	Lucene	L + DLDA
NDCG@5	0.401	0.630
NDCG@10	0.412	0.648
NDCG@15	0.415	0.652
NDCG@30	0.435	0.670
NDCG@50	0.452	0.724

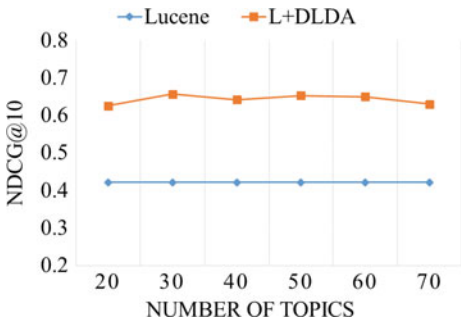

Fig. 3 Sorting ability of different number of topics

As can be seen from Table 2, our proposed method L + DLDA is better than Lucene-based method on NDCG, which verifies that our method can effectively improve the sorting ability, meaning that it can gain better tourism search results to help users get more related information by entering a search query in a search system.

As can be seen from Fig. 3, L + DLDA works best when the number of topics is 30 and 50, meaning that the dynamic topic model is relatively good with the number of topics as 30 and 50. L + DLDA always outperforms the method only based on Lucene, meaning that the dynamic topic model can get good topic distribution of attractions and it helps speculate users' search intents in our search system and return more relative search results.

4 Conclusions

In this paper, a search method of tourism information based on attraction dynamic topic distribution is proposed. We constructed the attraction dynamic topic model and trained the model with tourism comments of different time period to get the topic distribution of attractions in time dimension. In this way, we can speculate user's search intents by topic distribution of the query. Based on experiments on tourism comments of Beijing attractions crawled from websites, we verified the dynamic change of attraction topics and the accuracy of our proposed search method. In the future, we plan to consider more of users' personalized factors, and

establish a more optimized user search intent model to achieve better travel information search.

Acknowledgements This work is supported by the National Natural Science Foundation of China (No. 61320106006, No. 61532006, No. 61502042).

References

1. Azizan A, Bakar ZA, Noah SA (2014) Analysis of retrieval result on ontology-based query reformulation. In: International conference on computer, communications, and control technology, Langkawi, pp 244–248
2. Kliman-Silver C, Hannak A, Lazer D et al (2015) Location, location, location: the impact of geolocation on web search personalization. In: ACM conference on internet measurement conference, Tokyo, pp 121–127
3. Yu ZW, Xu H, Yang Z et al (2016) Personalized travel package with multi-point-of-interest recommendation based on crowdsourced user footprints. IEEE Trans Human-Machine Syst 46 (1):151–158
4. Song W, Zhang Y, Liu T, Li S (2010) Bridging topic modeling and personalized search. In: International conference on computational linguistics, pp 1167–1175
5. Xue XB, Yin XX (2011) Topic modeling for named entity queries. In: Proceedings of the 20th ACM international conference on information and knowledge management, Glasgow, pp 2009–2012
6. Santos RLT, Macdonald C, Ounis I (2011) Intent-aware search result diversification. In: Proceedings of the 34th international ACM SIGIR conference on research and development in information retrieval, Beijing, pp 595–604
7. Hu YH, Qian YN, Li H, Jiang DX, Pei J, Zheng QH (2012) Mining query subtopics from search log data. In: International ACM SIGIR conference on research and development in information retrieval, Beijing, pp 305–314
8. Wang QL, Qian YN, Song RH, Dou ZC, Zhang F (2013) Mining subtopics from text fragments for a web query. Inf Retrieval J 16(4):484–503
9. Hu JM, Chen G (2014) Mining and evolution of content topics based on dynamic LDA. Librar Inf Serv 58(2):138–142 (in Chinese)

Motion Transition Based on Bézier Quaternion Curve

Yancai Lu and Shuling Dai

1 Introduction

Virtual human is a digital representation of the geometric and behavioral property of human beings in the virtual environment generated by computer [1]. It is demanded by numerous applications ranging from military simulation, education, aerospace and movie special effects, to human factors analysis, etc. With the development of motion capture technology, data-driven [2] virtual human motion control method has become prevalent in recent years. It has been a successful technique for creating realistic virtual human motions, in large part because of the availability of motion editing methods [3]. As an important method of motion editing, motion translation can create seamless transitions between motions, allowing one to build lengthy, complicated motions out of simpler actions. It can improve the reuse of motion capture data and meet the demands of a particular situation.

Making a transition between two motions of virtual human has been a known problem with various authors solving it in different ways. Linear interpolation of keyframes can produce discontinuities at keyframe transitions [4]. To create fluent motion between motion clips, cubic bézier quaternion curve is introduced. We use four control points to determine the shape of the bézier quaternion curve and De Casteljau's algorithm to calculate interpolation points. We chose quaternion spherical linear interpolation as the interpolation method. Because it has a significant advantage over other interpolations.

Y. Lu (✉) · S. Dai
State Key Lab Virtual Reality Technology and Systems, Beihang University, Beijing 100191, China
e-mail: luyc_2014@163.com

S. Dai
e-mail: sldai@buaa.edu.cn

Z. Deng (ed.), *Proceedings of 2017 Chinese Intelligent Automation Conference*, Lecture Notes in Electrical Engineering 458,
https://doi.org/10.1007/978-981-10-6445-6_73

2 Quaternion Spherical Linear Interpolation

Gimbal lock (the loss of one degree of freedom in a three-dimensional) inevitably occurs when using Euler angles to represent rotation. Therefore, we choose quaternions instead. Quaternions express rotation is a more natural way to perceive rotation than Euler angles. In this paper, all we use for rotation are unit quaternions since they possess a range of desirable properties.

2.1 Conversions Between Quaternions and Euler Angles

Before our connecting work, we should convert the Euler angles of the motion data to quaternions. The quaternions are converted to Euler angles when all the connection work is done.

Any given Euler angle $[\varphi, \theta, \psi]$,φ is the rotation angle about the X-axis, θ is the rotation angle about the Y-axis and ψ is the rotation angle about the Z-axis. The following Eq. (1.1) [5] shows how Euler angle converted to quaternion $q = [w, x, y, z]$.

$$q = [w, x, y, z] = \begin{bmatrix} \cos\frac{\psi}{2}\cos\frac{\theta}{2}\cos\frac{\varphi}{2} - \sin\frac{\psi}{2}\sin\frac{\theta}{2}\sin\frac{\varphi}{2} \\ \cos\frac{\psi}{2}\cos\frac{\theta}{2}\sin\frac{\varphi}{2} + \sin\frac{\psi}{2}\sin\frac{\theta}{2}\cos\frac{\varphi}{2} \\ \cos\frac{\psi}{2}\sin\frac{\theta}{2}\cos\frac{\varphi}{2} - \sin\frac{\psi}{2}\cos\frac{\theta}{2}\sin\frac{\varphi}{2} \\ \cos\frac{\psi}{2}\sin\frac{\theta}{2}\sin\frac{\varphi}{2} + \sin\frac{\psi}{2}\cos\frac{\theta}{2}\cos\frac{\varphi}{2} \end{bmatrix}^T \tag{1}$$

Equation (1.2), the conversion of quaternions into Euler angles [6, 7], can simply be achieved through rotation matrix (convert the quaternion to a matrix, then the matrix to the Euler angles).

$$\varphi = \begin{cases} \arctan 2\left(yz + wx, \frac{1}{2} - x^2 - y^2\right) & if\ \cos\ \delta \neq 0 \\ \arctan 2\left(xy - wz, \frac{1}{2} - x^2 - z^2\right) \end{cases}$$

$$\beta = \arcsin 2(wy - xz) \tag{2}$$

$$\gamma = \begin{cases} \arctan 2\left(xy + wz, \frac{1}{2} - y^2 - z^2\right) & if \cos\delta \neq 0 \\ 0 \end{cases}$$

where δ is the rotation angle of quaternion about rotation axis.

2.2 Interpolation Method

The spherical linear interpolation [7, 8], abbreviated as Slerp, is the optimal interpolation curve between two rotations. Given two unit quaternions q_0,q_1 to be the start position and end position of the interpolation, the Slerp is defined by

$$q(t) = Slerp(t, q_0, q_1) = \frac{q_0 \sin((1-t)\theta) + q_1 \sin(t\theta)}{\sin(\theta)} \tag{3}$$

where $\theta = \arccos \frac{dot(q_0, q_1)}{|q_1||q_2|}$, t is the parameter, $t \in [0, 1]$, and $q(t)$ is the interpolation result. The interpolation curve for Slerp forms a great arc on the quaternion unit sphere (shown in Fig. 1). As t uniformly varies between 0 and 1, the values $q(t)$ are uniformly vary along the circular arc from q_0 to q_1.

3 Cubic Bezier Quaternion Curve

The technique of using piecewise bézier quaternion curves to construct smooth interpolants between key-points in space is well-known. Less well-known is their application in virtual human to construct smooth transitions between keyframes.

A cubic bézier curve is the path traced by the function $B(t)$, given points P_0, P_1, P_2 and P_3.

$$B(t) = (1-t)^3 P_0 + 3(1-t)^2 t P_1 + 3(1-t)t^2 P_2 + t^3 P_3 \tag{4}$$

where t is a parameter with a value of 0 to 1. Figure 2 shows a simple cubic bézier quaternion curve with four control points P_0, P_1, P_2, P_3.

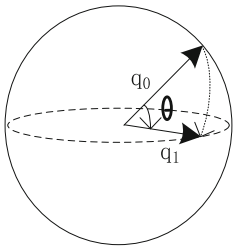

Fig. 1 The quaternion spherical linear interpolation

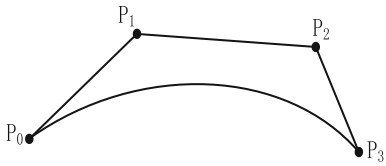

Fig. 2 Cubic Bézier quaternion curve

3.1 Four Control Points Computation

From Fig. 2 we can see that the first and last control points are always the start and end points of the curve. However, the intermediate control points generally do not lie on the curve. So the control points that needs to be calculated are the inner control points.

Typically, any given segment S_i runs from keyframe K_i (in the following equations represents unit quaternions of the joint points in this keyframe) to keyframe K_{i+1}. K_{i-1} is the keyframe before K_i and K_{i+2} is the keyframe after K_{i+1}. The inner control point $C1_i$ is constructed as follows

$$\begin{aligned} R_i &= Slerp(2, K_{i-1}, K_i) \\ T_i &= Slerp(1/2, R_i, K_{i+1}) \\ C1_i &= Slerp(1/3, K_i, T_i) \end{aligned} \tag{5}$$

Similarly, $C2_i$ is calculated as follows

$$\begin{aligned} R_{i+1} &= Slerp(2, K_i, K_{i+1}) \\ T_{i+1} &= Slerp(1/2, R_{i+1}, K_{i+2}) \\ C2_i &= Slerp(-1/3, K_{i+1}, T_{i+1}) \end{aligned} \tag{6}$$

Figure 3 shows the construction of inner control points for a bézier segment in 2-dimensional vector space [9].

3.2 De Casteljau's Algorithm for Interpolation Points

De Casteljau's algorithm is a recursive method to evaluate the bézier curve at any point along its length. We use it to find the interpolation points $B_i(u)$ on the bézier

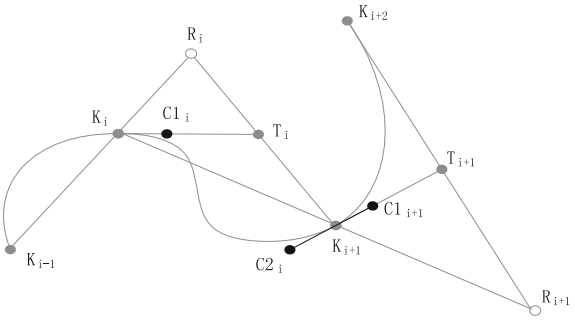

Fig. 3 Bézier's construction of inner control points

curves, where u runs from 0 to 1 along the length of the segment. It is defined as follows

$$p_i^k = \begin{cases} P_i & k = 0 \\ (1-u)P_i^{k-1} + uP_{i+1}^{k-1} & k = 1, 2, \ldots, n;\ i = 0, 1, \ldots, n-k \end{cases} \tag{7}$$

where $P_i^0 = P_i$ is the control point defined on the bézier curve, P_i^k is the point $B_i(u)$ on the bézier curve with a parameter u.

The geometric interpretation of De Casteljau's algorithm is straightforward. Subdivide each line segment between control points of this polygon with the ratio $u : (1-u)$ and connect the points you get. Repeat the process until you arrive at the single point. This process for a cubic bézier curve is shown in Fig. 4.

4 Transition Period Construction

The end period of a motion and the beginning period of another play a key role in computing the transition motion. Figure 5 shows the connection method we choose in our experiment.

The posture (frame) of virtual human is defined by the position of the root segment, its orientation, and the other joint angles [10]. The root in the skeleton structure records the offset of the human body in the world coordinate, whereas the

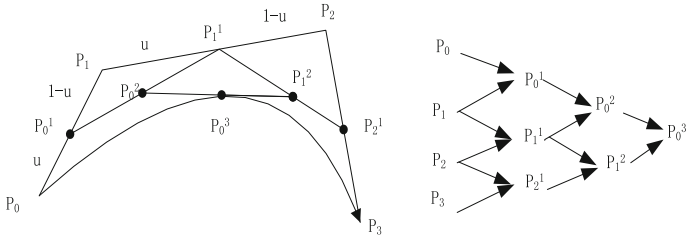

Fig. 4 De Casteljau's algorithm

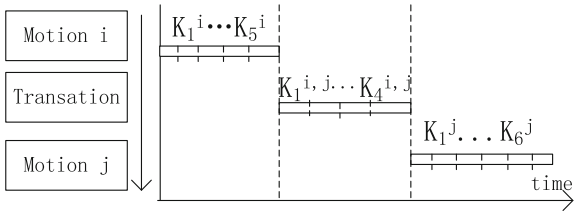

Fig. 5 Generating a transition motion between motions

other joints record their translation and rotation information with respect to their parent joint [11]. So we blend not only the joint angles but also the root positions and orientations to obtain the posture between motions.

5 Implementation and Results

5.1 Experimental Setup

The experimental data is from CMU Graphics Lab Motion Capture Database in the format of ASF/AMC. The ASF file, which encodes the skeleton kinematics including lengths of bones, degrees of freedom, etc. The skeleton which is shown in Fig. 6 is represented using a hierarchy, composed of a root node and several children nodes, corresponding to the various joints. The AMC file, which stores the motion (translation, joint angles) in time (at 120 frames per second) and contains the translation of the root node (xyz coordinates), rotation of the root node (in Euler angles).

Experiments were performed on a lenovo PC, Intel(R) Core(TM) i5-2450 M CPU 2.50 GHz with 4 GB main memory. The described solution was implemented in C++ on VS2010.

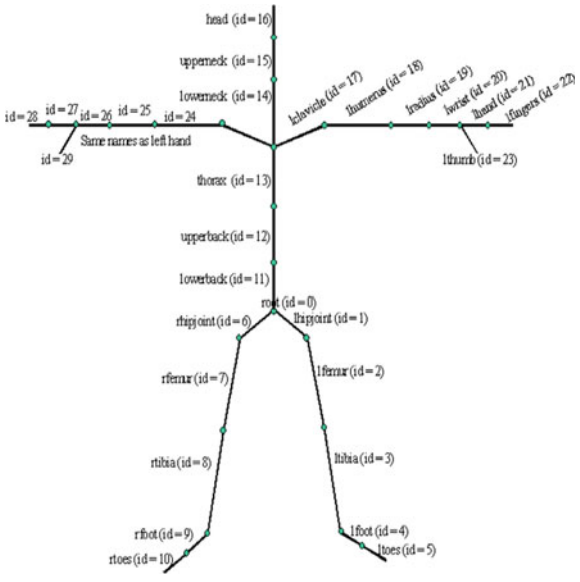

Fig. 6 The skeleton hierarchy, in particular name and id for each bone as defined in a representative ASF file [12]

5.2 Experimental Results

We tested our proposed solution from walking to running. Experimental Result is shown in Fig. 7. In order to show transition movements more intuitively, we have selected 5 keyframes in Fig. 8. We first do the preliminary processing of motion data, and then extract the keyframes from motion clips. The transition section runs from the last keyframe of the previous motion to the first keyframe of the latter.

At present, there is no uniform evaluation standard for motion synthesis, except for human observation. We did the comparison experiment between linear and the bézier quaternion curve method. The result is shown in Fig. 9. The red skeleton corresponds to the linear method and the green one to ours. We can easily see that the green skeleton behaved slower than the red one near the walking clip and gradually they became similar near the running clip. Which is more reasonable in human movement.

The results show that our algorithm has successfully synthesized a long natural-looking motion smoothly from one motion to another by using the bézier

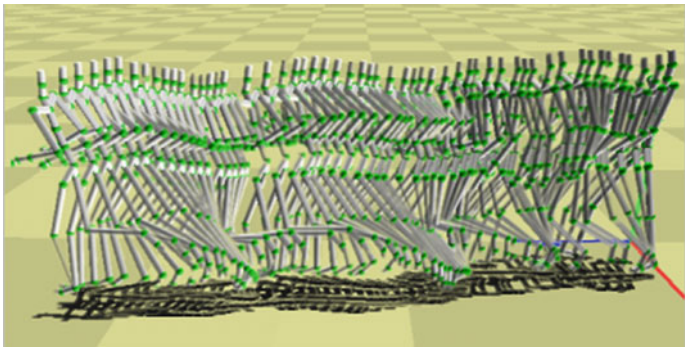

Fig. 7 Experimental result (Motion from walk to run)

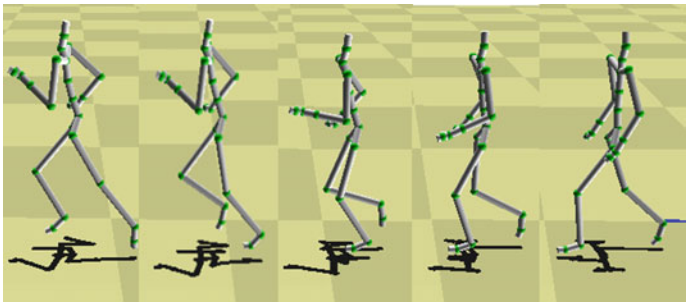

Fig. 8 Keyframes in transition movements

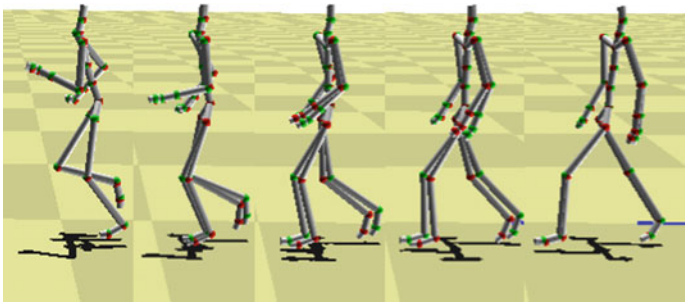

Fig. 9 The comparison between linear and the bézier quaternion curve

quaternion curve. The synthesized human motion sequence looks realistic and real-time. The experiment demonstrated the validity of our proposed motion transition solution well.

6 Conclusion

In this paper, we propose to transfer between motions smoothly by using bézier quaternion curve. We addressed three issues:quaternion spherical linear interpolation, control and interpolation points calculation, motion transition. The experimental results show that our proposed solution works well. For future research, we are planning to develop an automatic scheme for motion blending.

Acknowledgements The experimental motion capture data and the basic code were obtained from mocap.cs.cmu.edu. Access to these data and basic code provided valuable insight for the progress of this project and usage of them in this study is acknowledged by the authors.

References

1. Xia S, Wang Z (2009) Recent advances on virtual human synthesis. Sci China Ser F Inf Sci 52 (5):741–757
2. Du H, Manns M, Herrmann E et al (2016) Joint angle data representation for data driven human motion synthesis. Procedia CIRP 41:746–751
3. Kovar L, Gleicher M (2003) Flexible automatic motion blending with registration curves. In Proceedings of the 2003 ACM SIGGRAPH, Eurographics symposium on Computer animation. Eurographics Association, pp 214–224
4. Guay M, Ronfard R, Gleicher M et al (2015) Space-time sketching of character animation. ACM Trans Graph (TOG) 34(4):118
5. Fangt YC, Hsieh CC, Kim MJ et al (1998) Real time motion fairing with unit quaternions. Comput Aided Des 30(3):191–198
6. Diebel J (2006) Representing attitude: Euler angles, unit quaternions, and rotation vectors. Matrix 58(15–16):1–35

7. Shoemake K (1985) Animating rotation with quaternion curves. ACM SIGGRAPH Comput Graph ACM 19(3):245–254
8. Dam EB, Koch M, Lillholm M (1998) Quaternions, interpolation and animation. Copenhagen Universitet, Datalogisk Institut
9. Buckley C (1994) Bézier curves for camera motion. Trinity College, Department of Computer Science
10. Park SI, Shin HJ, Kim TH et al (2004) On-line motion blending for real-time locomotion generation. Comput Anim Virtual Worlds 15(3–4):125–138
11. Wang X, Chen Q, Wang W (2014) 3D human motion editing and synthesis: a survey[J]. Comput Math Methods Med 2014
12. http://run.usc.edu/cs520-s12/assign2/

RBF Based Integrated ADRC Controller for a Ship Dynamic Positioning System

Fangfang Yang, Chen Guo and Yunbiao Jiang

1 Introduction

Dynamic Positioning (DP) Systems use sensors to measure the movement states and positions of ships and provide the propeller systems with a certain control amount by a controller, which can resistance the environmental interferences and maintain the lateral, longitudinal positions and heading angle [1, 2]. However, because of their strong dependence on the model and the complexity of the theory and the algorithm, many methods only stay in the theoretical simulation stage, having many shortcomings in practice [3]. Active Disturbance Rejection Controller (ADRC) doesn't depend on an exact model of the controlled object [4, 5].

However, there are many adjustable parameters in nonlinear ADRC, which seriously affected the application of ADRC in the project. In order to solve this problem, RBF neural network control is used to improve ADRC in this paper. We uses RBF neural network to do online identification for the controlled object and design RBF Neural Network Identifier (RBFNNI). Then, use RBFNNI to adjust the controller's parameters of NLSEF in real time. Compared with the traditional ADRC, this method greatly reduces the number of adjustable parameters, improves the control accuracy, and increases the anti-disturbance range of the control system.

F. Yang (✉) · C. Guo (✉) · Y. Jiang
Dalian Maritime University, Dalian 116026, China
e-mail: 739059100@qq.com

C. Guo
e-mail: dmuguoc@126.com

Z. Deng (ed.), *Proceedings of 2017 Chinese Intelligent Automation Conference*,
Lecture Notes in Electrical Engineering 458,
https://doi.org/10.1007/978-981-10-6445-6_74

2 Problem Formulation

2.1 Mathematical Model of Ship Manoeuvring

Generally, low frequency motion model is used in DP systems of ships [5]:

$$\begin{cases} \dot{\eta} = R(\psi)v \\ M\dot{v} + Dv = \tau \end{cases} \tag{2.1}$$

where, $\eta = [x\ y\ \psi]^T$ expresses a ship's position, $v = [u\ v\ r]^T$ is the velocity vector. $R(\psi)$ is the conversion matrix of the inertial coordinate system and the ship coordinate system. M is the inertial matrix. D is the damping matrix. $\tau = \tau_T + \tau_W + \cdots$ is the total force of the ship's motion. $\tau_T = [X_T\ Y_T\ N_T]^T$ is the force calculated by the controller. τ_W is the total interferences force and torque, generated by Wind, wave, flow and other environmental interference.

2.2 Mathematical Model of Disturbances

2.2.1 Wind, Wave and Flow

Marine environmental disturbances that can affect the location of the ship include second-order wave force, flow and average wind. The model is described as following [6]:

$$\begin{cases} X_W = F_e \cos(\beta_e - \psi) \\ Y_W = F_e \sin(\beta_e - \psi) \\ N_W = l_x \sin(\beta_e - \psi) - l_y \cos(\beta_e - \psi) \end{cases} \tag{2.2}$$

where, F_e is the constant force, β_e is the average direction of disturbance change, (l_x, l_y) is the position of the interference force acting on the ship.

2.2.2 System's Unmodeled Dynamics

Considering the unmodeled dynamics of the system, the ship dynamic positioning linear model given by Formula (2.1) can be rewritten as:

$$M\dot{v} + Dv = \tau_{\mathrm{T}} + \tau_{\mathrm{M}} + w \tag{2.3}$$

where, $w = [w_1, w_2, w_3]^T$ is the unmodeled dynamics.

$$\begin{cases} w = J^T(\eta)b \\ \dot{b} = -T_b^{-1}b + E_b\omega_b \end{cases} \tag{2.4}$$

where, $b \in R^3$ is the deviation force and torque. $E_b = diag\{E_{b1}, E_{b2}, E_{b3}\}$ and ω_b are Gaussian white noise vectors, T_b is a diagonal matrix.

Then, the ship's motion model can be described as:

$$\begin{cases} \dot{\eta} = J(\eta)v = R(\psi)v \\ M\dot{v} + Dv = \tau_{\mathrm{T}} + \tau_{\mathrm{M}} + w \end{cases} \tag{2.5}$$

3 Controller Design

3.1 ADRC

ADRC includes Tracking Differentiator (TD), Extended State Observer (ESO) and Nonlinear State Error Feedback (NLSEF).

1. Tracking Differentiator (TD).

$$\mathrm{TD}\begin{cases} \dot{x}_1 = x_2 \\ \dot{x}_2 = fhan(x_1 - v, x_2, r, h_0) \end{cases} \tag{3.1}$$

2. Extended State Observer (ESO).

$$\begin{cases} e = z_1 - y \\ \dot{z}_1 = z_2 - \beta_1 e \\ \dot{z}_2 = z_3 - \beta_2 fal(e, \alpha_1, \delta) + bu \\ \dot{z}_3 = -\beta_3 fal(e, \alpha_1, \delta) \end{cases} \tag{3.2}$$

3. Nonlinear State Error Feedback (NLSEF).

$$u_0 = \beta_1 fal(e_1, \alpha_1, \delta) + \beta_2 fal(e_2, \alpha_2, \delta) \tag{3.4}$$

Then, the final control is:

$$u = u_0 - \frac{z_3}{b} \tag{3.5}$$

3.2 RBF and ADRC Integrated Controller

There are many parameters in nonlinear ADRC, which is quite inconvenient to adjust. In this paper, RBF Neural Network Identifier (RBFNNI) is designed to identify the controlled object and adjust the controller parameters of NLSEF in real time, as shown in Fig. 1.

3.2.1 RBF Neural Network

RBF neural network is a three-layer feed forward network of local approximation [7]. The mapping from the input layer to the output layer is non-linear and the mapping from the hidden layer to the output layer is linear, which can track any continuous function with arbitrary precision [7, 8].

In this chapter, the function of RBF neural network is Gaussian basis function. Then the output of the neurons in the hidden layer is:

$$h_j = \exp\left(-\frac{||X - C_j||^2}{2b_j^2}\right) \tag{3.5}$$

where, $X = [x_1, x_2, \ldots, x_n]^T$ is the input vector for the network. C_j is the center vector of node j, $C_j = [c_{j1}, c_{j2}, \ldots, c_{ji}, \ldots, c_{jn}]^T$, $j = 1, 2, \ldots, m$. b_j is the base width parameter of node j, $b_j > 0$.

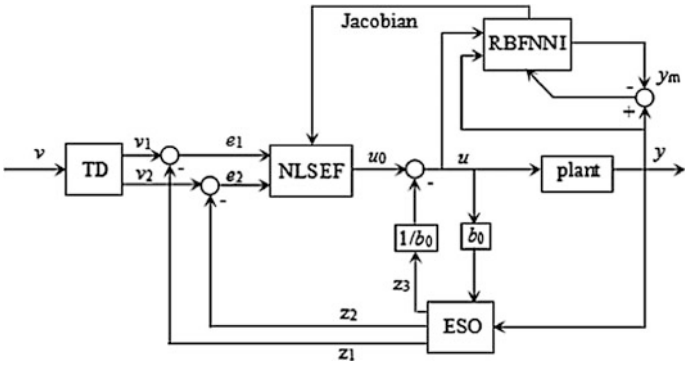

Fig. 1 The structure of RBF neural network based on ADRC

Weight vector of the network is:

$$W = \left[w_1, w_2, \ldots, w_j, \ldots, w_m\right]^T \tag{3.6}$$

The output of the network identification at time k is:

$$y_m(k) = w_1 h_1 + w_2 h_2 + \cdots + w_j h_j + \cdots + w_m h_m \tag{3.7}$$

3.2.2 Design of RBFNNI and Parameters Setting for NLSEF

Select $X = [u(k), y(k), y(k-1)]^T$ as input vector of RBFINN, in which, $u(k)$ and $y(k)$ are the control and output of the system respectively.

The performance index function of the identifier is:

$$E(k) = \frac{1}{2}e(k)^2 = \frac{1}{2}(y(k) - y_m(k))^2 \tag{3.8}$$

According to the gradient descent method, the iterative algorithm of output weight vector, node center vector and node base width parameters are:

$$\Delta w_j(k) = \eta(y(k) - y_m(k))h_j$$

$$\omega_j(k) = \omega_j(k-1) + \Delta w_j(k) + \alpha\big(\omega_j(k-1) - \omega_j(k-2)\big)$$

$$\Delta b_j(k) = \eta(y(k) - y_m(k))\omega_j h_j \frac{||X - C_j||^2}{b_j^3}$$

$$b_j(k) = b_j(k-1) + \Delta b_j + \alpha\big(b_j(k-1) - b_j(k-2)\big)$$

$$\Delta c_{ji}(k) = \eta(y_k(k) - y_m(k))\omega_j \frac{x_i - c_{ji}}{b_j^2}$$

$$c_{ji}(k) = c_{ji}(k-1) + \Delta c_{ji}(k) + \alpha\big(c_{ji}(k-1) - c_{ji}(k-2)\big)$$

where, η is for the learning rate; α is for the momentum factor.

Jacobian matrix from RBFNNI is as following

$$\frac{\partial y(k)}{\partial u(k)} \approx \frac{\partial y_m(k)}{\partial u(k)} = \sum_{j=1}^{m} w_j h_j \frac{c_{ji} - x_1}{b_j^2} \tag{3.9}$$

where, $x_1 = u(k)$.

Gradient descent method is used to adjust β_1 and β_2:

$$\Delta\beta_1(k) = -\eta\frac{\partial E}{\partial \beta_1} = -\eta\frac{\partial E}{\partial y}\frac{\partial y}{\partial u}\frac{\partial u}{\partial \beta_1} = \eta e(k)\frac{\partial y}{\partial u}fal(e_1, \alpha_1, \delta)$$

$$\beta_1(k) = \beta_1(k-1) + \Delta\beta_1(k)$$

$$\Delta\beta_2(k) = -\eta\frac{\partial E}{\partial \beta_2} = -\eta\frac{\partial E}{\partial y}\frac{\partial y}{\partial u}\frac{\partial u}{\partial \beta_2} = \eta e(k)\frac{\partial y}{\partial u}fal(e_2, \alpha_2, \delta)$$

$$\beta_2(k) = \beta_2(k-1) + \Delta\beta_2(k)$$

4 Simulation Studies

In this paper, the controlled object is a rescue ship, named as Beihaijiu115. Its DP system with RBF-ADRC Controller gradient descent method is simulated in MATLAB. Combined with ADRC control, we conducted a comparative study in lower disturbance and higher disturbance of sea conditions environment, respectively.

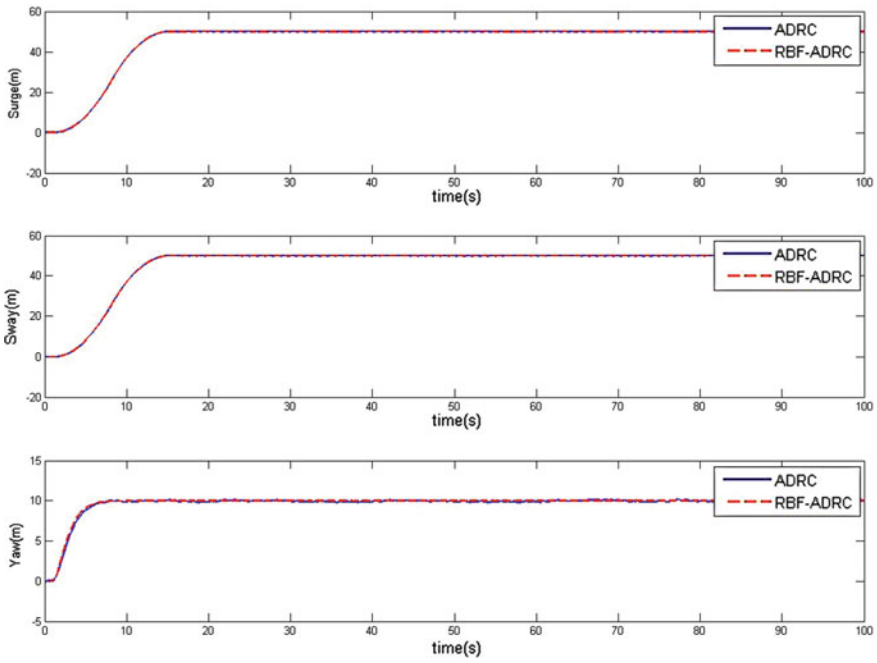

Fig. 2 Simulation result in lower disturbance of sea conditions

The initial state of the ship is $[x, y, \psi]^T = [0\text{m}\ 0\text{m}\ 0\text{rad}]^T$, the expected state is $[x_d, y_d, \psi_d]^T = [50\text{m}\ 50\text{m}\ 10\text{rad}]^T$ and the total time is 100 s.

1. Under lower disturbance of sea conditions.

The parameters of the external slow disturbance simulated in Formula (2.2) are set as:

$$F_e = 10,\ \beta_e = 120\sin(0.3t),\ \left(l_x, l_y\right) = (20m, 5m);$$

The parameters of unmodeled dynamic simulated in formula (2.4) are set as:

$T_b = diag\{1000, 1000, 1000\}$, $E_b = diag\{1, 1, 1\}$, The variance of ω_b is 0.01. The simulated results are shown in Fig. 2

2. Under higher disturbance conditons.

Set the external slow disturbance as $F_e = 100$ to increase disturbance force of sea conditions. The simulated results are shown in Fig. 3.

From Figs. 2 and 3, it can be seen that, in lower disturbance of sea conditions, ADRC controller and RBF-ADRC controller have the same result and can control the ship to maintain the desired position. In higher disturbance of sea conditions,

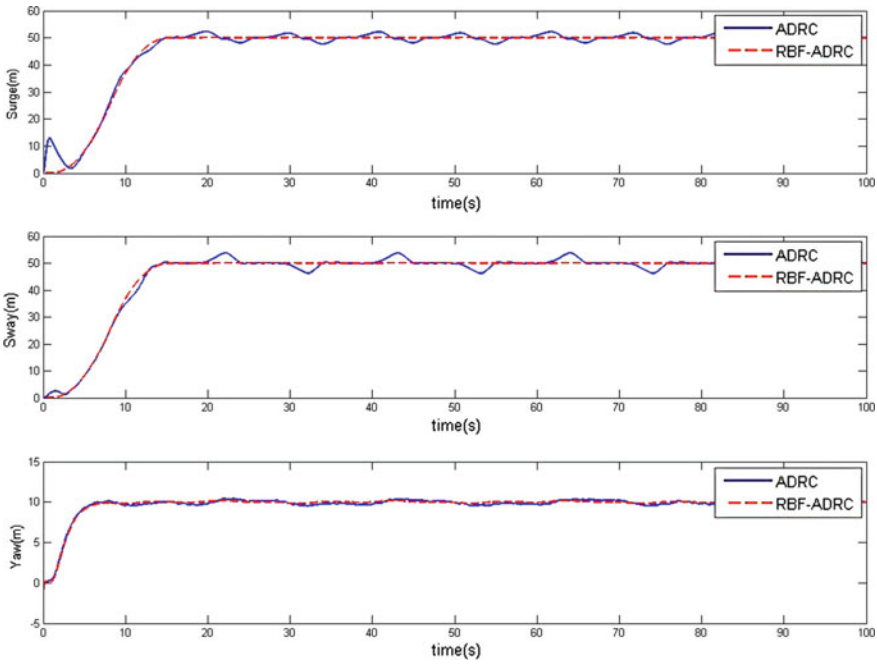

Fig. 3 Simulation result in higher disturbance of sea conditions

RBF-ADRC controller still has a good result, the simulation curve is not change. However, the simulation curve of the ADRC controller has a large oscillation, the ship deviates from the desired position is 5 m, and the curve in the bow control is unstable. It can be seen that improved ADRC with RBF neural network has excellent control performance, which can increase the range of interference suppression of ADRC and improve the control accuracy, when the ship suffered a large disturbance.

5 Conclusions

RBF based ADRC control method is used to locate the low-frequency model of the ship with strong non-linear characteristics. When the system is disturbed, ADRC can automatically compensate for the disturbance, which has strong anti-interference ability. However, it is difficult to adjust so many parameters in ADRC and the suppression of interference intensity of ADRC is limited. Using RBF Neural Network Identifier to set the parameters of ADRC can reduce the number of adjustable parameters. What's more, the simulation results demonstrate that RBF-ADRC can increase the range of interference suppression and improve the control accuracy of ship dynamic positioning system.

Acknowledgements The authors are very grateful to the editors and reviewers for their valuable comments and suggestions. This work is supported by National Natural Science Foundation of China (Nos. 51579024, 6137114) and the Fundamental Research Funds for the Central Universities (DMU No. 3132016311).

References

1. D Zhao, Bian XQ, Ding FG (2010) Nonlinear controller based ADRC for dynamic positioned vessels. Dalian Maritime University, Harbin, pp 1367–1371 (in Chinese)
2. Fossen TI (2002) Marine control systems guidance, navigation and control of ships, rigs and underwater vehicles. Marine Cyernetics AS, Trondheim, Norway
3. Xiong HJ, Liu JY, Chen YP (2015) Research and simulation of ADRC on ships dynamic positioning control under strong disturbance, pp 1671–4431. 03. 010 (in Chinese)
4. Han JQ (2007) Active disturbance rejection control technique-the technique for estimating and compensating the uncertainties. National Defence Industry Press. ISBN 978-7-05795-9 (in Chinese)
5. Lei ZL (2014) Active disturbance rejection control on ship dynamic positioning system. Dalian Maritime University, Dalian, China (in Chinese)
6. Yang YSH (1998) Mathematical model of ship motion. Dalian Maritime University, Dalian, China (in Chinese)
7. Liu JK (2011) Advanced PID control and MATLAB simulation. Publishing House of Electronics Industry, Beijing (in Chinese)
8. Jiang T (2016) ADRC for ship steering based on RBF neural network. Dalian Maritime University, Dalian, China (in Chinese)

Research of Localization Method Based on Virtual Reference Points in Robot Auditory System

Shuopeng Wang, Peng Yang, Hao Sun, Jing Xu and Xiaomeng Zhang

1 Introduction

With the development of signal processing and artificial intelligence, voice interaction gains extensive attention in area of robot research and application [1]. During the process of human-robot voice interaction, sound source localization technology can provide reference for robot pose adjustment to promote the effect of HR interaction [2]. As a kind of scene analysis method, position fingerprint can effectively solve the problems of high model dependence and environmental impaction of conventional methods [3]. Generally, grid map method is adopted in the construction of reference points of position fingerprint method [4]. Usually, high density of the reference points is helpful to the localization precision, but the computing load will increase in the matching process, and location efficiency will reduce at the same time [5]. Therefore, on the premise of positioning precision, decreasing the quantity of reference points to reduce the computational burden of the feature matching can effectively improve the applicability of the mobile robot.

In this paper, according to the low rank feature of the sound source location indoor, a novel robot auditory localization method based on virtual reference points constructed by the method of linear interpolation is put forward to solve the contradiction between positioning accuracy and efficiency of robot auditory system.

S. Wang · P. Yang (✉) · H. Sun · J. Xu · X. Zhang
School of Control Science and Engineering, Hebei University of Technology,
No 8 Guangrong Road, Hongqiao District, Tianjin City, China
e-mail: yphebut@163.com

Z. Deng (ed.), *Proceedings of 2017 Chinese Intelligent Automation Conference*,
Lecture Notes in Electrical Engineering 458,
https://doi.org/10.1007/978-981-10-6445-6_75

2 Research Method

Position based on location fingerprint can be generally divided into two independent phases: offline sampling phase and online positioning phase [6]. As shown in Fig. 1, a distributed microphone array sound localization system with 4 array elements is chosen as an example to introduce the location process.

The aim of offline sampling phase is to build the location database, First, divide the target area into rules grids according to the requirements of positioning accuracy, then choose the grid angular points (blue dots of target area in Fig. 1) as the positioning reference points, where feature information acquisition will be taken through the microphone array (M0, M1, M2, and M3), and database will be constructed based on the location coordinates and its feature information obtained.

Online positioning phase: in the working area, when the robot releases a sound signal needed location, the positioning system will capture the sound signals and extract the feature information, which will be taken for matching with the location fingerprint database to find out the most similar reference points for location estimation, and got the sound source location coordinates through specific algorithm.

2.1 *Offline Sampling Phase*

The main purpose of the offline sampling phase is construction of the location fingerprint database. First, determine the coordinates of reference points according to the application requirements. Then, drive mobile robot to each reference point, release location sound and collect the sound signal by the distribute microphone

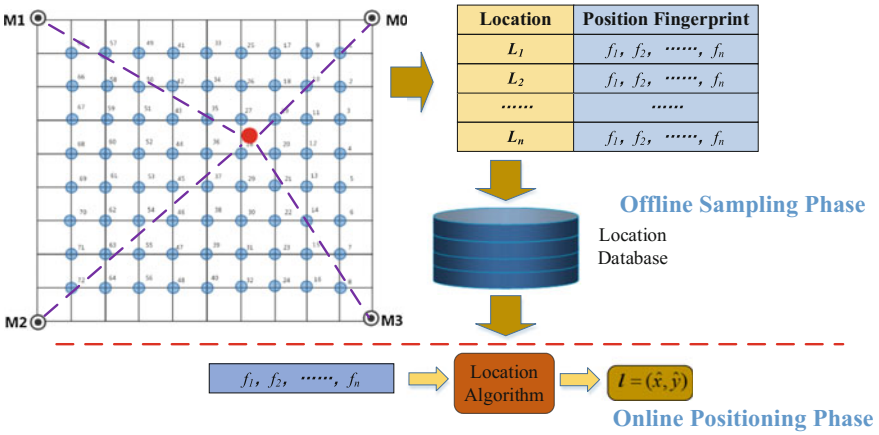

Fig. 1 Position process of fingerprint positioning system

array. Finally, the features of the collected signals and the coordinates of acquisition points will form a set of fingerprints, as

$$\boldsymbol{Data}_n = [x_n, y_n, f_1^n, f_2^n, \ldots, f_M^n]^T$$

where $\boldsymbol{Data}_n$ ($n = 1, 2 \ldots, N$) corresponding to the fingerprint data collected in the n_{th} reference point, N is the total quantity of the reference points; M is the total number of the features, f_m ($m = 1, 2 \ldots, M$) means the m_{th} feature; x_n and y_n means the 2D coordinates of n_{th} reference point. Collect all the ***Data*** in each sampling site and store them together to establish the location fingerprint database as $\boldsymbol{D}$

$$\boldsymbol{D} = [\boldsymbol{Data}_1 \quad \boldsymbol{Data}_2 \quad \ldots \quad \boldsymbol{Data}_N]^T$$

Usually, in order to improve the reliability of the database and ensure the position precision, multi collection to get the average of the result is need in each sampling process. The methods such as median filtering, gaussian filter are also needed to deal with feature information acquisition.

2.2 Online Positioning Phase

2.2.1 Adjacent Reference Points

In online positioning phase, when the robot moves to a unknown position and releases a sound, then the signal acquisition system will capture the sound signal and transmit it to the central processing platform for feature vector extraction as $\boldsymbol{F} = [f_1, f_2, \ldots, f_m]^T$, then the central processing platform will match the feature information captured $\boldsymbol{F}$ with database information $\boldsymbol{D}$, and the adjacent reference points will be chosen according to the matching result based on the distance between feature vector information. The adjacent reference points will be the reference points with minimum distances to $\boldsymbol{F}$.

The distance between $\boldsymbol{F}$ and each fingerprint $\boldsymbol{F_n}$ of database $\boldsymbol{D}$ is given by

$$dis_i = \left(\sum_{j=1}^{M} (f_j - f_{ij})^q\right)^{\frac{1}{q}}, \quad i = 1, 2, \ldots, n. \tag{1}$$

where $f_j \in \boldsymbol{F}, f_{ij} \in \boldsymbol{F_n} \in \boldsymbol{D}$. The adjacent reference points will be chosen through

$$\arg\min dis_i \quad i = 1, 2, \ldots, n. \tag{2}$$

2.2.2 Virtual Reference Points

In online positioning process, adjacent reference points $\boldsymbol{D}_{\mathrm{a}} = [\boldsymbol{data\_a}_1, \boldsymbol{data\_a}_2, \boldsymbol{data\_a}_3, \boldsymbol{data\_a}_4]$, and $\boldsymbol{data\_a}_n = [\boldsymbol{F}_n, \boldsymbol{L}_n]$, where n means the order of the adjacent reference points. The first group recent reference points $\boldsymbol{D}_{\mathrm{r}} = \boldsymbol{D}_{\mathrm{a}}$. then the recent reference points $\boldsymbol{D}_{\mathrm{r}}$ will refresh by the new virtual reference points in each iteration process. The coordinates and feature of virtual reference points of t_{th} are

$$\boldsymbol{D}_{\mathrm{v}}^{t} = [\boldsymbol{data\_v}_1^{t}, \boldsymbol{data\_v}_2^{t}, \boldsymbol{data\_v}_3^{t}, \boldsymbol{data\_v}_4^{t}]$$

where $\boldsymbol{data\_v}_n^{t} = [\boldsymbol{F}_n^{t}, \boldsymbol{L}_n^{t}]$,where n means the order of the virtual reference points, and t means the times of total iteration. $\boldsymbol{data\_v}_n^{\mathrm{t}+1}$ can be calculated by

$$\begin{cases} \boldsymbol{data\_v}_n^{t+1} = \omega_n^{t}\boldsymbol{data\_r}_n + \omega_{n+1}^{t}\boldsymbol{data\_r}_{n+1} & n < N \\ \boldsymbol{data\_v}_n^{t+1} = \omega_n^{t}\boldsymbol{data\_r}_n + \omega_{n+1}^{t}\boldsymbol{data\_r}_1 & n = N \end{cases} \tag{3}$$

where $\omega_n^{t} = \begin{cases} \frac{1/(dis_n^{t}+e)}{1/(dis_n^{t}+e)+1/(dis_{n+1}^{t}+e)}, & n < N \\ \frac{1/(dis_n^{t}+e)}{1/(dis_n^{t}+e)+1/(dis_1^{t}+e)}, & n = N \end{cases}$, and dis means the euclidean distance of features vectors between recent virtual reference points and target needed location. e is a small random value for avoiding the denominator to be zero.

2.2.3 Location Estimation

Position estimation results of sound source can be calculated by KNN (K nearest neighbors algorithm)as type 4, as follow [7]

$$l = (\widehat{x}, \widehat{y}) = \sum_{n=1}^{k} \omega_n \times (x_n, y_n) \tag{4}$$

where $(\widehat{x}, \widehat{y})$ is the location result, (x_n, y_n) is the coordinate of n_{th} virtual reference points, ω_n is the weight of n_{th} virtual reference point, which can be calculated by type 5 as follow

$$\omega_n = \frac{1/(dis_n + \varepsilon)}{\sum_{j=1}^{k} 1/(dis_j + \varepsilon)} \tag{5}$$

where $dis_i = (\sum_{j=1}^{M} (f_j - f_{ij})^q)^{\frac{1}{q}}, \quad i = 1, 2, \ldots, n$. Here $q = 2$, and the dis_i means the euclidean distance between latest virtual reference points and pending sites.

The location process based on virtual reference points is shown as Fig. 2.

input: database $\boldsymbol{D}$;
features vector of target $\boldsymbol{F}$;
maximum iterations times T
threshold value E;
number of adjacent reference points k.
process:
1: For all $\boldsymbol{Fn} \in \boldsymbol{D}$ do $dis_n = \|\boldsymbol{F} - \boldsymbol{Fn}\|^2$, according to type (1);
2: k adjacent reference points selected, according to type (2);
repeat
3: $\boldsymbol{D}_{\mathrm{v}}^{t+1}$ generation according to type (3);
4: $\boldsymbol{l}_{k+1}$ according to type (4) and (5);
5: $\Delta \boldsymbol{l} = |\boldsymbol{l}_k - \boldsymbol{l}_{k-1}|$;
6: end for
7: until $\Delta \boldsymbol{l} < E$ **or** $t > T$
8: $\boldsymbol{l} = \boldsymbol{l}_k$, $t = t+1$
output: $\boldsymbol{l}$

Fig. 2 Positioning method based on virtual reference points

3 Simulation and Implementation Results

3.1 Simulation and Verification

Simulation experiment of the novel localization method based on virtual reference points was designed. The number of adjacent reference points was set to 4, and the maximum times of iterations was set as 5. Three representative positions, at the top right corner, the middle lower part and the center of the location area was be taken in the simulation respectively.

The generating process of virtual reference points, positioning results, and change of the position error is shown as Fig. 3.

Through 5 times generation process, as shown in the Fig. 3a, the position error of the test point of the top right corner reduces from 0.8010 to 0.0474 m and as shown in Fig. 3b, the position error of the test points in the middle lower part reduces from 1.3318 to 0.0801 m, from Fig. 3b, the position error of the center test point reduces from 0.1264 to 0.0917 m. Even in various location areas the effect of virtual reference points method with a certain extent different, the positioning accuracy are all obtained significant improvement.

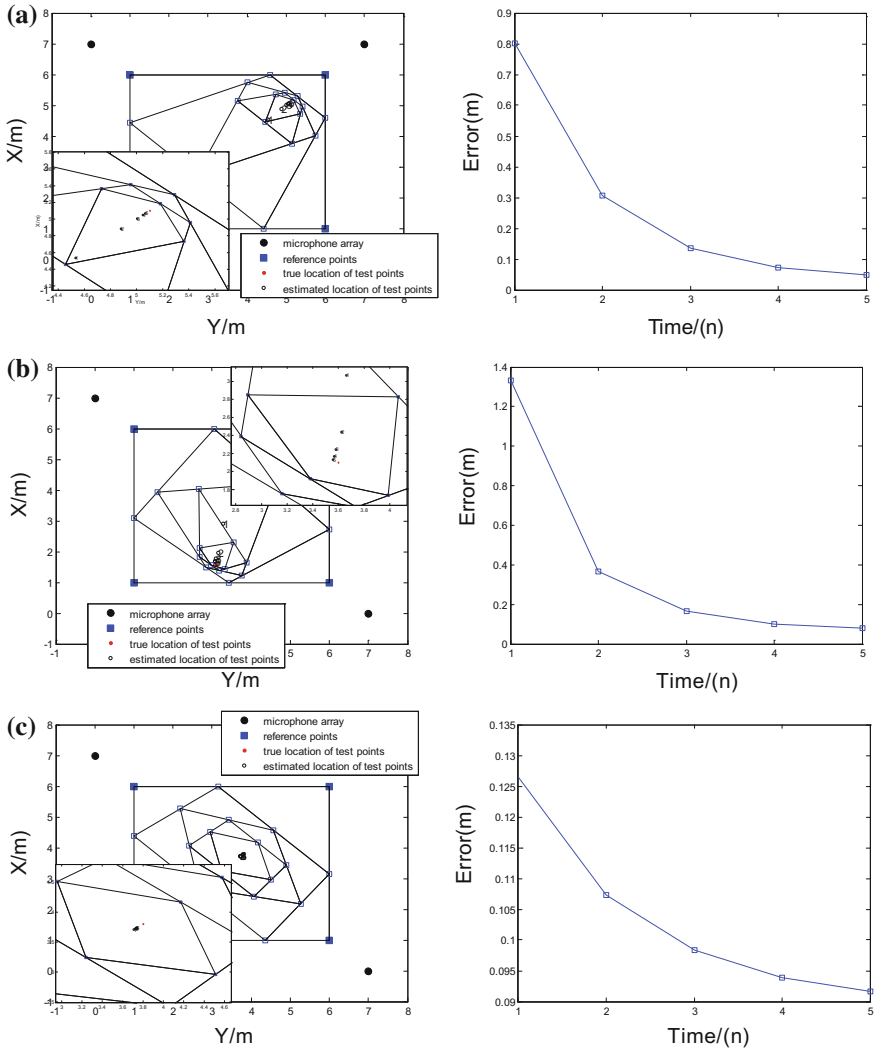

Fig. 3 Location results in different areas

3.2 Online Positioning Stage

Location experiments is carried out in a laboratory room with noisy about 40 dB, and the wall without soundproof treatment. 4-channel microphone array is arranged in the region of the positioning of the four vertices, 136 cm height. Sound source is a small Bluetooth stereo. As shown in Fig. 4, the location area was a rectangle, about 6 m $\times$ 5 m.

Fig. 4 Auditory system and experiment scene

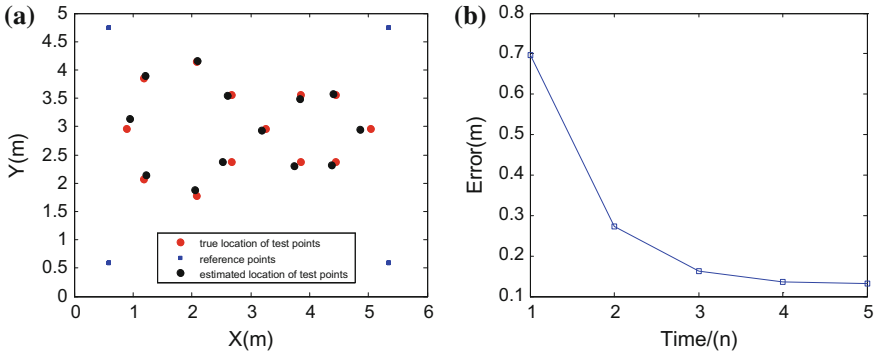

Fig. 5 Global positioning results

Four positioning adjacent reference points was selected and 13 positioning test points was also chosen in the location area in primary. The global positioning results was defined as the mean value of the test points positioning errors.

As shown from Fig. 5a, the novel method can reduce the global location error from 0.6667 to 0.0950 m without increasing the number of reference points. Compare with the result of conventional method (the distance between reference points is 0.6 m, and mean error is 0.0945 m, this result mentioned in the paper [8]), the distance between reference points of the method of virtual reference points is 5 m, and the means error is 0.0950 m similar with the results in paper [8] which needs about 20 times reference points to the novel method. This demonstrates that a more efficient auditory localization system that requires less reference points can be developed.

4 Conclusion

A robot auditory localization method based on virtual reference points is proposed in this paper. Virtual reference points are generated by iterative interpolation method based on adjacent reference points. Simulation and experimental results show that this method can effectively reduce the number of location reference points on the premise of the location accuracy. Compared with the traditional auditory localization method, the novel method based on virtual reference points has better efficiency of positioning, and significantly enhance the applicability of the auditory localization robot.

Acknowledgements This work is supported by National Nature Science Foundation of China (61305101) and Graduate Student Innovation Funding Project of Hebei Province (220056).

References

1. Zhen J, Aoki H, Sato-Shimokawara E, Yamaguchi T (2011) Interactive system for sharing objects information by gesture and voice recognition between human and robot with facial expression. IEEE/SICE International Symposium on System Integration, Tokyo, pp 293–298
2. Li XF, Liu H (2012) A survey of sound source localization for robot audition. CAAI Trans Intell Syst 7(1):9–20
3. Yin J, Yang Q, Ni LM (2008) Learning adaptive temporal radio maps for signal-strength-based location estimation. IEEE Trans Mob Comput 7(7):869–883
4. He S, Ji B, Chan SHG (2016) Chameleon: survey-free updating of a fingerprint database for indoor localization. IEEE Pervasive Comput 15(4):66–75
5. Borenovic M, Neskovic A, & Neskovic N (2011) Impact of varying reference points density on performances of fingerprinting based GSM positioning system. Int Symp Appl Sci Biomed Commun Technol 92
6. Dawes B, Chin KW (2011) A comparison of deterministic and probabilistic methods for indoor localization. J Syst Softw 84(3):442–451
7. Huang CN, Chan CT (2011) ZigBee-based indoor location system by k-nearest neighbour algorithm with weighted RSSI. Procedia Comput Sci 5:58–65
8. Wang SP, Sun H, Yang P (2017) Indoor sound-position fingerprint method based on scenario Analysis. J Beijing Univ Technol 02:224–229

Vehicle Tracking Based on Structured Output SVM Using Retinex and Mutual Information

Longqi Wang, Xinyang Li, Guanyu Lin, Wei Pei and Guanrong Wang

1 Introduction

As the core issue of video analysis, target tracking is a challenging problem in the field of computer vision. It has a wide application prospect in the security monitoring, intelligent transportation, man-machine interactive, sports events and other fields. At present, the vehicle target tracking algorithms based on video are roughly divided into three categories: The vehicle target tracking algorithms based on filter, kernel and classification.

The algorithms based on filter [1–6] and kernel [7–15] only rely on foreground target information and ignore the background information, although some tracking algorithms also take the background into account, but the focus is still the foreground target. Avidan [16] proposed the offline learning firstly and adopted offline support vector machine (SVM) to improve the vehicle tracking. Later, Li et al. [17] used subsection Blob and Snack Blob feature and the neural network offline classification method to vehicle detection and tracking research. In 2006, Grabner, etc. put forward a method which could separate the target from the background of online Boost with adaptive feature selecting. Xie and Zhang etc. [18] proposed discriminative object tracking via sparse representation and online dictionary learning method. Hare et al. [19] proposed structured output SVM tracking algorithm based on kernel (struck) using a structured output SVM to predict the target location. It can avoid labeling sample and transforming the sample to the target

L. Wang · X. Li (✉) · G. Lin · G. Wang
Changchun Institute of Optics, Fine Mechanics and Physics,
Chinese Academy of Science, Changchun 130033, China
e-mail: Lixynx@126.com

W. Pei
Environmental Science and Engineering College, Dalian Maritime University Dalian,
Liaoning Province, China

Z. Deng (ed.), *Proceedings of 2017 Chinese Intelligent Automation Conference*,
Lecture Notes in Electrical Engineering 458,
https://doi.org/10.1007/978-981-10-6445-6_76

location manually. The algorithm has a perfect tracking effect on the clear video image tracking.

Although domestic and foreign scholars have put forward a large number of target tracking algorithms, the target tracking is still very challenging, such as severe occlusion, illumination change, attitude change, mutation movement and so on. The model updating and identification based on discriminative classifier need accurate sampling results, and the existing tracking strategies need to be adjusted to adapt to the complex scene. Based on the above considerations, this paper adopts struck [20], enhances video with multi-scale Retinex algorithm of fuzzy enhancement, and deals with occlusion through the template matching algorithm based on the mutual information. A large number of experiments are used to verify the tracking accuracy and robustness of this algorithm.

2 Retinex Image Enhancement Algorithm

Retinex is the abbreviation of Retina and Cortex. It is a kind of image enhancement theory based on human visual system and color constancy features. The theory called color was proposed by Edwin Land and McCann in 1870s [21]. The advantage of Retinex image enhancement algorithm is to balance dynamic range compression, edge enhancement and color constancy, and it can enhance different types of images adaptively [22]. This makes the Retinex algorithm is widely used in many fields.

An image can be regarded as made up of the incident light and the reflected light from the object, as shown in Fig. 1. The dynamic range of the pixel is determined by the incident light, and the intrinsic property of the image is determined by the reflected light. Therefore, the enhanced image should eliminate or weaken the heterogeneous light reflect from the object.

Single Scale Retinex [23, 24] (SSR) is improved obviously in computing speed and has more explicit physical meanings. Its operation process mimics the human visual system. It uses difference of Gaussians function to simulate the perception of the cerebral cortex neurons to the object. The method has the characteristics of high color fidelity and large dynamic range compression.

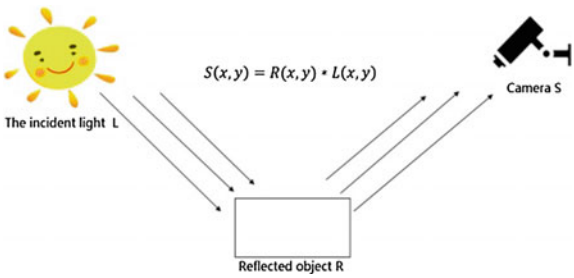

Fig. 1 The imaging model

Mutli-Scale Retinex [20, 25] (MSR) is the improvement of SSR. The single Gaussian convolution function in SSR cannot estimate image brightness accurately. In MSR multiple Gauss convolution function are weighted sum to improve the enhancement effect. Its formula is as follows.

$$r(x,y) = \sum_{k=1}^{K} W_k\{\log S(x,y) - \log[F_k(x,y) * S(x,y)]\} \tag{1}$$

where W_k represents related weights of the Gauss's function which corresponding to K different Gaussian convolution functions (Gaussian filtering). In general, the most classical algorithm is to guarantee the advantages of low, middle, high three dimensions of MSR. The value of K is 3, that is $W_1 = W_2 = W_3 = 1/3$. It can not only achieve the dynamic range compression of image, but also maintain the consistency of color sense. In order to ensure the image saturation, the mean square error (MSE) is introduced to determine maximum and minimum of the image. Compared with SSR, the image contrast has been improved obviously as shown in Fig. 2.

In the reality of the vehicle tracking process,the target vehicle will inevitably be occluded by other background such as buildings, trees, bridges and other vehicles in the traffic road. If the occlusion cannot be resolved, it is easy to make the tracking results drift, and finally lose the target. Handling process of occlusion mainly

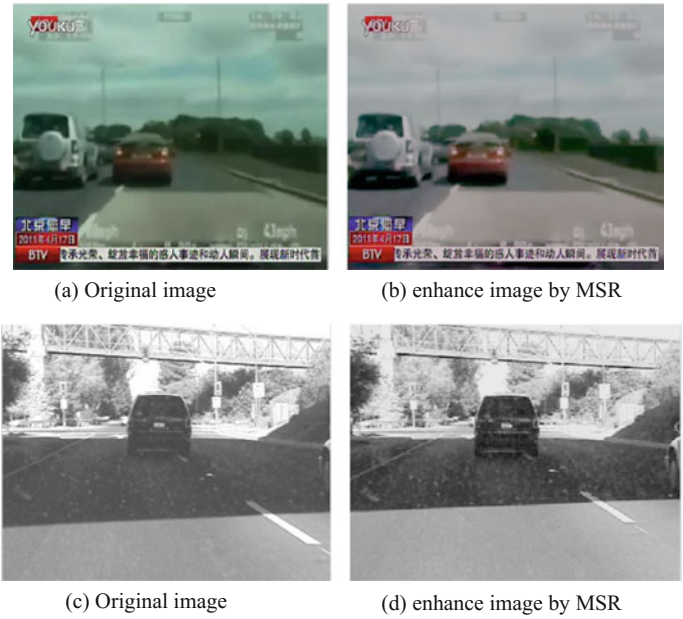

(a) Original image (b) enhance image by MSR

(c) Original image (d) enhance image by MSR

Fig. 2 Effect of mutli-scale Retinex algorithm

includes finding shelter and tracking vehicles after leaving shelter. Only when the problem is solved, can vehicle tracking have better application in reality.

3 Occlusion Handling Strategy Based on Mutual Information

In order to detect whether the target is occluded, the optimal sampling and tracking template are matched. Whether the target was occluded or not is judged through the similarity indirectly. The optimal sampling and templates are both derived from the target image, and the geometric correction and normalization are already carried out, as shown in Fig. 3.

The following are the process of the template matching algorithm based on mutual information.

1. Defining a two-dimensional array S with length of 256 both in horizontal and vertical coordinates, and the gray level is 0–255.
2. The relative position of the two pictures with pixels M × N (The optimal sampling image A and template image B) is read circularly. The pixel gray value pairs $(a(i,j), b(i,j))$ is generated which corresponding array element position $S[(a(i,j), b(i,j))]$ plus 1. That is, the elements of the array saves the total disappear times of the gray value pairs.
3. This step is normalization. All the elements in the array S are divided by the total disappear times of the gray values n to get the probability of each gray value pair.
4. Adding the elements of each row in the array S can generate a column vector H_A which is the pixel gray value probability of image A. Adding the elements of each column in the array S can generate a row vector H_B which is the pixel gray value probability of image B.
5. For the non-zero elements in H_A, H_B and S, the entropies of H_A and H_B are calculated as S_A and S_B respectively, and the corresponding joint information entropy of S is S_AB.
6. The mutual information coefficient is derived from the mutual information formula. MuInf = abs (S_A + S_B−S_AB)/(S_A + S_B).

Fig. 3 Vehicle template

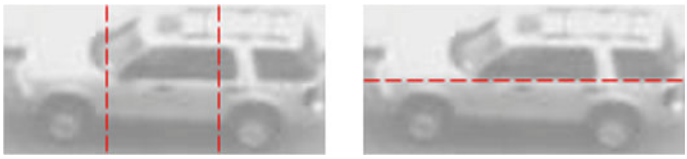

Fig. 4 Block-matching

Due to partial occlusion of the target, the appearance of the target can be changed greatly. Therefore, this paper combines block matching c with global matching. The template obtained in different tracking video in the experiment is shown in Fig. 3. First of all, the whole template matching based on mutual information is used. If it is less than the threshold, it is considered that the occlusion occurs directly. Then the block is handled. When it is larger than the threshold, the template and the optimal sampling are divided into blocks, as shown in Fig. 4. The optimal sampling samples and templates are both divided into five parts to match respectively, which two parts are in vertical direction and three are in horizontal direction. If the similarities are all larger than the threshold, it is considered that there is no occlusion. The current optimal sampling can be used as a new template to match the next frame and update classifier discriminant model. If the match-degree of the partial block is less than the threshold, it is considered that the occlusion occurs, and the template and classifier discriminant model will no longer be updated.

The target position is tagged manually in the initial frame, and is taken as the initial template to track the second frame. Each frame is used to match the optimal sampling and template. When the matching degree is greater than the threshold, the optimal sampling is saved as the target template of the next fame. With the deepening of the track and the changing of tracking scene, the method can ensure that the sample matches with the latest template each time. When occlusion occurs, the target template is not updated.

4 Experiment Analysis

Experiment platform is Lenovo PC which is equipped I3 3.3 GHz Intel CPU with Win7 × 64. Visual Studio C++ 2010 and OpenCV visual library are selected as programming tools.

For car4 data sets, the overlap ratio and center distance of the original Struck tracking algorithm and the improved Struck tracking algorithm which is added with image enhancement preprocessing are shown in Fig. 5 and Table 1.

For car4 video set, the tracking process is affected by noise and shadow, so the feature information extracted is weakened, and the recognition accuracy is reduced. Therefore the tracking center of the original Struck algorithm offsets gradually

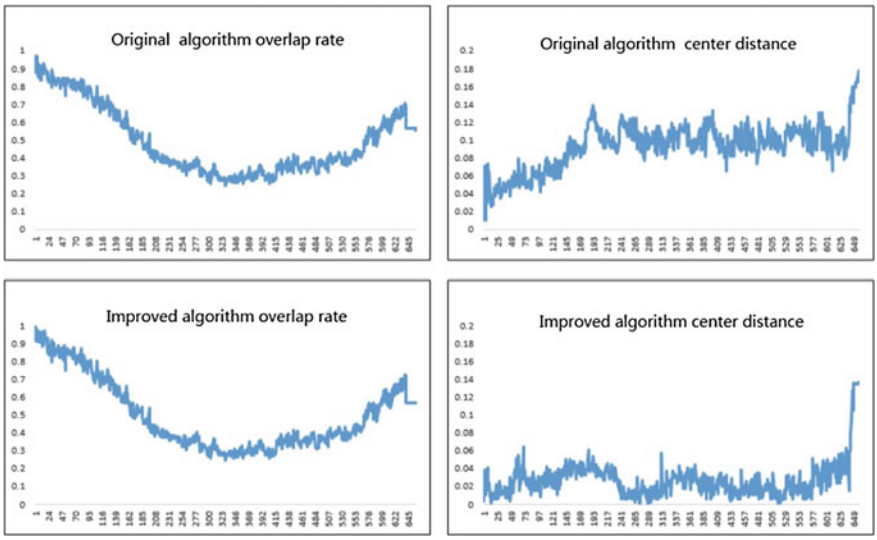

Fig. 5 Original and improved algorithm tracking results

Table 1 Original and improved algorithm overlap ratio table

	Average overlap ratio	Frame number	Overlap ratio sum	Improved ratio
Original algorithm	0.4904	659	323.2014	
Improved algorithm	0.4944	659	325.8218	0.8%

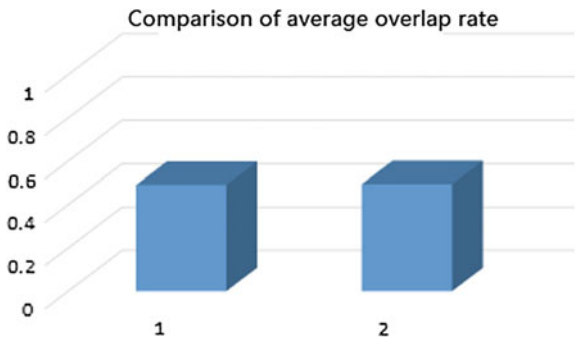

Fig. 6 Comparison of average overlap rate between the original algorithm and the improved algorithm

larger compare to the real target center. As shown in Table 1 and Fig. 6, the average overlap rate of the improved Struck algorithm improves 0.8% than the original one. As shown in Table 2 and Fig. 7, the average migrant center distance of the improved Struck algorithm improves 71.3% than the original one, which has

Table 2 The average center distance of the original algorithm and the improved algorithm

	Average center distance	Frame number	Sum center distance	Improved ratio
Original algorithm	0.0930	659	61.3040	
Improved algorithm	0.0267	659	17.6592	71.3%

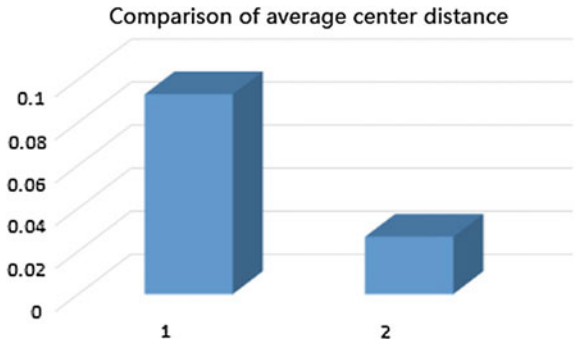

Fig. 7 Comparison of the average center distance between the original algorithm and the improved algorithm

shortened about 7 pixels than the real distance. The experimental results show that the improved multi-scale Retinex algorithm has a perfect effect on the overall process of video vehicle tracking.

5 Summary

This paper proposes the improved tracking algorithm based on the research of the structured output SVM tracking algorithm. In order to improve the tracking accuracy, the multi-scale Retinex image enhancement preprocessing and the mutual information based occlusion processing strategy are intruded to the original algorithm. The experimental results show that the improved structured output SVM algorithm can cope with the blur, occlusion and other conditions, and the accuracy and robustness of the original algorithm are improved.

References

1. De WC, Proctor AA, Johnson EN (2003) Vision-only aircraft flight control. The 22nd digital avionics systems conference vol 2, pp 8.B.2-81–11
2. Davidson C, Blake A (1998) Error-tolerant visual planning of planar grasp. Sixth international conference on computer vision, pp 911–916

3. Ayache N, Cohen I, Herlin I (1992) Medical image tracking. Active Vision MIT Press
4. Angella F, Reithler L, Gallesio F (2007) Optimal deployment of cameras for video surveillance systems. In: IEEE Conference on Advanced Video and Signal Based Surveillance, pp 388–392
5. Wang X, Fang L, Chong Z-H (2010) Research on video vehicle tracking algorithm based on Kalman and particle filter.J Image Graph 15(11):615–1622
6. Wei LK, Wei YK, Yit KC, Mei YC, Teo KTK (2012) Enhancement of particle filter resampling in vehicle tracking via genetic algorithm. In: Sixth UKSim/AMSS European Symposium on Computer Modeling and Simulation (EMS), pp 243–248, 14–16 Nov 2012
7. Singer RA (1970) Estimating optimal tracking filter performance for manned Maneu-vering Targets. IEEE Trans Aerosp Electron Syst AES 6(4):473–483
8. Candamo J, Shreve MA, Goldgof DB, Sapper DB (2010) Understanding transit scenes: a survey on human behavior-recognition algorithms. IEEE Trans Intell Transp Syst 11(1):206–224
9. Malladi R, Sethian JA (1996) Level set and fast marching methods in image processing and computer vision. Int Conf Image Processing 1:489–492
10. Michael K, Andrew W, Demetri T (1988) Snakes: active contour models. Int J Comput Vision 1(4):321–331
11. Zhang H, Dong Y, Xia Y (2007) Vehicle tracking algorithm based on modified GVF-snake model. PR AI 20(3):388–393
12. Roya R, Mansour J (2005) Real time classification and tracking of multiple vehicles in highways. Pattern Recogn Lett 26(10):1597–1607
13. Tao G, Zheng-guang L, Junetc Z (2010) Traffic vehicle contour tracking and its engineering application. J Basic Sci Eng 18(2):343–351
14. Horn BKP, Schunck BG (1981) Determining optical flow. Artif Intell 17(1–3):185–203
15. Comaniciu D, Ramesh V, Meer P (2000) Real time tracking of non-rigid objects using mean shift. Comput Vision Pattern Recogn 2:142–149
16. Avidan S (2004) Support vector tracking. Pattern Anal Mach Intelligence IEEE Trans 26 (8):1064–1072
17. Li X, Yao X, Murphey YL et al (2004) A real-time vehicle detection and tracking system in outdoor traffic scenes. In: IEEE Conference on Pattern Recognition, Cambridge, pp 761–764
18. Xie Y, Zhang W (2014) Discriminative object tracking via sparse representation and online dictionary learning. Cybern IEEE Trans 44(4):539–553
19. Hare S, Saffari A, Torr PHS (2011) Struck: structured output tracking with kernels. International conference on computer vision (ICCV), 2011. In: IEEE international conference pp 263–270
20. Jobson DJ, Rahman Z, Woodell GA (1997) A multi-scale Retinex for bridging the gap between color images and the human observation of scenes. IEEE Trans Image Processing 6 (7):965–976
21. Land E (1964) The Retinex. Amer Scient 52(2):247–264
22. Bin R (2009) Research and implementation of image enhancement algorithm based on Retinex. Master's degree thesis of Nanjing University of Science and Technology 5:6–7
23. Jobson DJ, Rahman Z-U, Woodell GA (1997) Properties and performance of a center/surround Retinex. IEEE Trans Image Processing 6(3):451–462
24. Wang M, Zhou S (2011) The study of color image defogging based on wavelet transform and single scale Retinex. Advances in imaging detectors and applications. In: Proceedings of SPIE, vol 8194, pp 1–5
25. Barnard K, Funt B (1999) Investigations into multi-scale Retinex in colour imaging. Vision and Technology, New York, pp 9–17

Neural Network-Based Self-triggered Attitude Control of a Rigid Spacecraft

Shuai Sun, Mengfei Yang and Lei Wang

1 Introduction

Modern spacecrafts are typical Cyber-Physical Systems (CPSs) which are tight integrations between onboard cyber systems (e.g. processing, communication) and physical elements (e.g. platform structure, sensing, actuation, and environment) [1, 2]. Tasks implement on the onboard cyber systems of spacecrafts include attitudes and orbit control, onboard planning and scheduling, onboard data acquiring and analyzing et al. For the limit of onboard digital resource, saving communication bandwidth and power from the basic function like control tasks mean providing more resource to payloads onboard, which may implement a sufficient use of spacecrafts.

Classic spacecraft attitude control problem is always developed in continuous framework [3–5], and their implementation on the digital platform is traditionally in a periodic fashion due to the ease of design and analysis. However, periodic sampling is sometimes less preferable from a resource utilization point of view. When the system states almost keep constant and no disturbances are acting, the systems are operating desirably is a waste of digital resources. To overcome these limitations, some resource-aware control laws like anytime control [6] event-triggered control (ETC) [7–9] self-triggered control (STC) [10, 11] and so on are developed. In anytime control, consisting in a hierarchy of controllers for the same plant, will switch between different order control algorithms to adopt the cyber resource of the onboard system. In ETC, the classic event triggered mecha-

S. Sun (✉) · L. Wang
Beijing Institute of Control Engineering, Beijing 100081, China
e-mail: sunshuai_hitsa@163.com

L. Wang
e-mail: Wangl01@mails.tsinghua.edu.cn

M. Yang
China Academy of Space Technology, Beijing 100190, China
e-mail: yangmf@bice.org.cn

Z. Deng (ed.), *Proceedings of 2017 Chinese Intelligent Automation Conference*,
Lecture Notes in Electrical Engineering 458,
https://doi.org/10.1007/978-981-10-6445-6_77

nisms are detecting the system output or states varying. The main idea of STC is to select the next controller update instant based on the knowledge of the dynamics and the latest measurements of the plant state. While the ETC depending on the continuous supervision of the plant, the STC will reduce more cyber resource than ETC theoretically.

In recent years, many work addressed on STC and its applications in CPSs. In [9], the theoretical foundation rendering control system Input-to-State Stable (ISS) is introduced. Based on this framework, many STC mechanisms are proposed for linear and nonlinear systems. In [10–15], the basic self-triggered strategies for linear system are presented and a trade-off between performance and cyber resource utilization is making. However, the most expensive part of the realization of STC is the derivation of the trigger function. The above work is extremely complex so that the calculating of the trigger functions requires a lot of computing resources. From this point of view, the use of NN as a model of trigger behavior is presented in this paper.

The Neural Network is usually performed to estimate the system that transforms inputs into outputs, where a set of examples of input-output pairs are given in [16]. Furthermore, the NN was demonstrated as a universal smooth function approximator, extensive studies have been conducted for diverse applications, especially pattern recognition, identification, estimation, and time series prediction [17]. In [18], the NN is designed to predict the time delay induced in the networked control systems, which shows that the NN can alleviate the influence of time delay and improve the performance of the networked control system.

The main contribution of this paper is the design of a neural network based self-triggered control (NN-STC) strategy for the spacecraft attitude stabilization problem. The attitude motion dynamics equations are derived and a STC algorithm is proposed to ensure attitude stability. Furthermore, simulation results demonstrate the proposed approach guarantees a high control performance and a large reduction of sampling times.

2 Space Attitude Dynamics

The dynamics equations of motion of a rigid spacecraft are given by [4]

$$\mathbf{J}\dot{\boldsymbol{\omega}} = -\boldsymbol{\omega}^{\times}\mathbf{J}\boldsymbol{\omega} + \boldsymbol{u} + \boldsymbol{T} \tag{1}$$

where $\mathbf{J} = \mathbf{J}^T \in \mathbb{R}^{3\times 3}$ is the inertia matrix, $\boldsymbol{\omega} = \boldsymbol{\omega}(t) \in \mathbb{R}^3$ denotes the body angular velocity of the spacecraft body-fixed frame B with respect to the inertial frame I. $\boldsymbol{u} \in \mathbb{R}^3$ is the actuator torque calculated by the onboard computer and $\boldsymbol{T} \in \mathbb{R}^3$ is the external disturbance torques.

To describe the orientation of B respect to the inertial frame I in terms of three Euler angles: roll angle φ, pitch angle θ, and yaw angle ψ. In the rigid body

three-axis stability control problem, the Euler angles are all small. Therefore, the linearized kinematic differential equations can be found as

$$\omega_1 = \dot{\varphi} - \omega_o\psi, \quad \omega_2 = \dot{\theta} - \omega_o, \quad \omega_3 = \dot{\psi} + \omega_o\varphi \tag{2}$$

We consider the attitude motion about its pitch axis, assume the effect of the attitude motion on the orbital motion with a constant angular velocity ω_o.

In such case, the dynamics equations (1) with small attitude errors and small products of inertial become [19]

$$\begin{aligned} &J_x\ddot{\varphi} + (J_y - J_z)\omega_o^2\varphi + (J_y - J_z - J_x)\omega_o\dot{\psi} = u_x + T_x, \quad J_y\ddot{\theta} = u_y + T_y \\ &J_z\ddot{\psi} + (J_y - J_z)\omega_o^2\psi - (J_y - J_z - J_x)\omega_o\dot{\varphi} = u_z - \omega_o h_x + T_z \end{aligned} \tag{3}$$

Also, the external disturbance torques include the gravity gradient torque, and it can be expressed in the body frame B as

$$T_{gx} \approx -3\omega_o^2(J_y - J_z)\varphi, \quad T_{gy} \approx -3\omega_o^2(J_x - J_z)\theta, \; T_{gz} \approx 0 \tag{4}$$

Generally, from the equations above, we can see that the pitch equation is uncoupled from the roll/yaw equations. It is a Single Input & Single Output system (SISOs), which is easy to design a classical PD controller. However, if we take three dynamics equations into consideration with the self-triggered control design, the size of the state space is large, which will provide more pressure on the real time calculation on the embedded system. Therefore, we only consider roll & yaw coupled system in this paper.

The dynamics and kinematic equations can be realized in state space form as

$$\dot{\boldsymbol{x}} = \mathbf{A}\boldsymbol{x} + \mathbf{B}\boldsymbol{u}, \quad \boldsymbol{x} = \begin{pmatrix} \varphi & \psi & \dot{\varphi} & \dot{\psi} \end{pmatrix}^T \tag{5}$$

$$\mathbf{A} = \begin{pmatrix} 0 & 0 & 1 & 0 \\ 0 & 0 & 0 & 1 \\ -\frac{1}{J_{11}}a & 0 & 0 & \frac{1}{J_{11}}b \\ 0 & -\frac{1}{J_{33}}c & \frac{1}{J_{33}}b & 0 \end{pmatrix}, \quad \mathbf{B} = \begin{pmatrix} 0 & 0 \\ 0 & 0 \\ \frac{1}{J_{11}} & 0 \\ 0 & \frac{1}{J_{33}} \end{pmatrix}$$

3 Neural Network Based Self-triggered Control Strategy Design

3.1 Problem Formulation

The attitude control system on the spacecraft is shown in Fig. 1. The control signal $\boldsymbol{u}$ and states signal $(\boldsymbol{x}, \dot{\boldsymbol{x}})$ is transferred over the network. In a periodic implementation, this system is usually in the following form

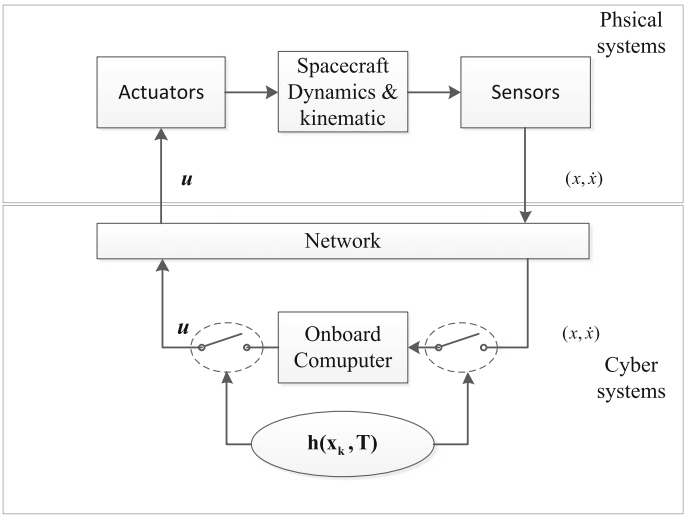

Fig. 1 CPSs on the spacecrafts

$$\begin{aligned} \dot{\boldsymbol{x}} &= \mathbf{A}\boldsymbol{x}(t) + \mathbf{B}\boldsymbol{u}(t) \\ y(t) &= \mathbf{C}\boldsymbol{x}(t) \end{aligned} \tag{6}$$

where $\mathbf{A} \in \mathbb{R}^{n\times n}$, $\mathbf{B} \in \mathbb{R}^{n\times r}$, $\mathbf{C} \in \mathbb{R}^{m\times n}$ are the characteristic matrices and $x(t) \in \mathbb{R}^n$, $u(t) \in \mathbb{R}^r$ and $y(t) \in \mathbb{R}^m$ the state, input and output vectors respectively. If the pair $(\mathbf{A}, \mathbf{B})$ is stabilizable, then a linear feedback controller $\boldsymbol{K} : \mathbb{R}^n \to \mathbb{R}^m$ rendering the closed-loop asymptotically stable can be found:

$$\boldsymbol{u}(t) = \boldsymbol{K}(\boldsymbol{x}(t)) \tag{7}$$

where $\mathbf{A} + \mathbf{BK}$ is Hurwitz.

The controller will implement on the embedded system, and a sampled-data system implementation is in a classical periodic time-triggered way:

$$\begin{aligned} &\dot{\boldsymbol{x}} = \mathbf{A}\boldsymbol{x}(t) + \mathbf{B}\boldsymbol{u}(t_k) \quad t \in [t_k, t_{k+1}) \\ &y(t) = \mathbf{C}\boldsymbol{x}(t) \\ &\boldsymbol{u}(t) = \boldsymbol{K}(\boldsymbol{x}(t_k)), \quad t \in [t_k, t_{k+1}),\ k \in \mathbb{Z}_+ \end{aligned} \tag{8}$$

where t_k represents the sampling time satisfying $t_{k+1} - t_k = T$. For some specified period $T > 0$, it means $h(\boldsymbol{x}_k, T)$ in Fig. 1 equals a constant T. In discrete control aspect, T is generally chosen as small as technology and network load permit to achieve a desired performance. This strategy is easy to implemented, however, it may produce unnecessary overload on the network and power consumption.

We design the Performance Index (PI) ΔJ

$$\Delta J = 100\left[\int_0^\infty \left(\boldsymbol{x}^T\mathbf{Q}_{lqr}\boldsymbol{x} + \boldsymbol{u}^T\mathbf{R}_{lqr}\boldsymbol{u}\right)dt - J^*\right] \tag{9}$$

when any control $\boldsymbol{u}(t)$ is implemented digitally, the system performance will depend on the sampling period. As the sampling period increasing, the PI will increase and the system tends to unstable.

To extend the sampling periods without sacrificing performance, we apply self-triggered control to the system. Moreover, the longer mean sampling period means the lower network loaded.

The STC scheme can be defined in following form

$$\begin{aligned}
&\dot{\boldsymbol{x}} = \mathbf{A}\boldsymbol{x}(t) + \mathbf{B}\boldsymbol{u}(t_k) \quad t \in [t_k, t_{k+1}) \\
&\boldsymbol{y}(t) = \mathbf{C}\boldsymbol{x}(t) \\
&\boldsymbol{u}(t_k) = \boldsymbol{K}(\boldsymbol{x}(t_k)), \quad t \in [t_k, t_{k+1}),\ k \in \mathbb{Z}_+ \\
&t_{k+1} = t_k + h(\boldsymbol{x}_k)
\end{aligned} \tag{10}$$

A general STC scheme usually means two functions: A feedback control $\boldsymbol{u}(t_k)$ is used as in the classical frame and the triggered function $h(\boldsymbol{x}(t_k), T) : \mathbb{R}^m \times \mathbb{R}_0^+ \to \mathbb{R}_0^+$, determining the sampling time t_{k+1} as a function of the state $\boldsymbol{x}(t_k)$ at the time t_k. The design of these two functions is the main problem in the STC study. Moreover, a positive minimal inter-sample time is also required to fulfill, to avoid the Zeno phenomenon.

3.2 Feedback Controller Design

An LQR design technique is usually applied to the spacecraft attitude control problem. The cost function and weighting matrices used in the LQR design are

$$\begin{aligned}
&J^* = \min(J(\boldsymbol{u})) = \int_0^\infty \left(\boldsymbol{x}^T\mathbf{Q}_{lqr}\boldsymbol{x} + \boldsymbol{u}^T\mathbf{R}_{lqr}\boldsymbol{u}\right)dt \\
&\mathbf{Q}_{lqr} = \begin{bmatrix} \mathbf{I}_{2\times 2} & \\ & 5\mathbf{I}_{2\times 2} \end{bmatrix} \quad \mathbf{R}_{lqr} = 10\mathbf{I}_{2\times 2}
\end{aligned} \tag{11}$$

The consideration of selecting weighting matrices in this paper is increasing system dumpling and preventing the actuators saturation.

we can solve the Riccati equation to get the unique positive definite solution $\mathbf{P}$

$$\mathbf{A}^T\mathbf{P} + \mathbf{PA} - \mathbf{PB}^{-1}\mathbf{R}_{lqr}\mathbf{B}^T\mathbf{P} + \mathbf{Q}_{lqr} = \mathbf{0} \tag{12}$$

The optimal feedback policy $\boldsymbol{K}$ is given by

$$\boldsymbol{K} = -\boldsymbol{R}_{lqr}^{-1}\mathbf{B}^T\mathbf{P} \tag{13}$$

The true cost of continuous LQR is

$$J^* = \boldsymbol{x}_0^T\mathbf{P}\boldsymbol{x}_0 \tag{14}$$

3.3 NN Based Triggered Condition Design

Under certain conditions, it has been proved that the neural networks have function approximation abilities and have been frequently used as function approximators. In this section, the NN is used to approximate the function $h(\boldsymbol{x}_k, T)$ in Fig. 1, $h(\boldsymbol{x}_k, T)$ determines the next sampling time based on the states sampled before, so it is a mapping between state space and time space. And a neural network model can be derived from measured input/output data of the original triggered conditions.

As one of the classical neural networks, BP feedforward neural network has a simple topology and strong generalization ability. We use a four-layered feedforward neural network and adopt the BP learning algorithm to determine the sampling time.

Figure 2 shows the specific configuration of the BP feedforward network for approximating the triggered function. The BP network consists of four layers: input layer with four neurons presenting the four input states of dynamics systems (5). The neuron numbers of the two hidden layers are 12 and 4, which greatly improve the accuracy of the network. The output layer which has only one neuron for the triggered time is one dimension. The number of hidden layers and neurons are varied, but in this problem the above choice is enough.

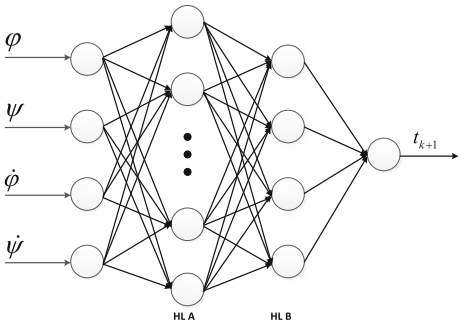

Fig. 2 BP network configuration for triggered time prediction

In order to make the NN perform the desired mapping performance, the connection weights will be trained by so-called training algorithms. The detail of this algorithm is given in [20] which is no longer mentioned here. Moreover, the training data generation is another important issue.

We acquire a training set which is generated by the system under closed-loop and the specified triggered condition. The input sets with four states $(\varphi, \psi, \dot{\varphi}, \dot{\psi})$ are generated randomly within $(-5, 5)$ deg and $(-5, 5)$ deg/s which ensure the linearized model is effective. And a triggered time is calculated from a input sets by the original triggered function. Finally, a training sample with five elements $(\varphi, \psi, \dot{\varphi}, \dot{\psi}, t_k)$ is acquired.

4 Simulation

In this section, an example is presented to validate the proposed STC strategy for spacecraft attitude control problem. The inertia matrix of spacecraft **J** is assumed to be as follows

$$\mathbf{J} = \begin{bmatrix} 10.5 & & \\ & 8 & \\ & & 6.75 \end{bmatrix} \text{kg m}^2$$

The control authority is limited by the maximum torque provided by the actuators is ± 0.15 N m, orbit angle velocity is $\omega_o = 0.0612$ deg/s.

The time of simulation is 80 s, the initial attitude and angular velocity is

$$[\varphi_0 \quad \psi_0]^T = [5 \quad -3]^T \text{ deg}, \quad [\dot{\varphi}_0 \quad \dot{\psi}_0]^T = [2 \quad 1]^T \text{ deg/s}$$

The disturbance is given by:

$$\begin{pmatrix} d_{ex} \\ d_{ez} \end{pmatrix} = \begin{pmatrix} 0.0015 + 0.0012\sin(0.263t) \\ 0.0015 + 0.0012\sin(0.245t) \end{pmatrix}$$

The triggered function is given by

$$t_{k+1} = \sup\{t < t_{\max} | h(\boldsymbol{x}(t_k), t) < 0\}$$
$$h(\boldsymbol{x}(t_k), t) := \boldsymbol{x}(t_k + t)^T \mathbf{P} \boldsymbol{x}(t_k + t) - \boldsymbol{x}(t_k)^T \mathbf{P} \boldsymbol{x}(t_k)^T \exp(-\lambda t)$$

P is calculated by (14), $\lambda = 1.0524$, the detail is given in [9–11].

From Table 1, we have compared the performance between the NN with one and two hidden layers. The results show the two hidden layers of NN has better

Table 1 Performance of the NN

Two hidden layers (neurons: 12.4)		One hidden layer (neurons: 18)	
Performance (MSE)	Iterations	Performance (MSE)	Iterations
0.01 (t1)	6	0.01	4
0.001 (t2)	9	0.001	45
0.0005 (t3)	58	0.0005	Failed

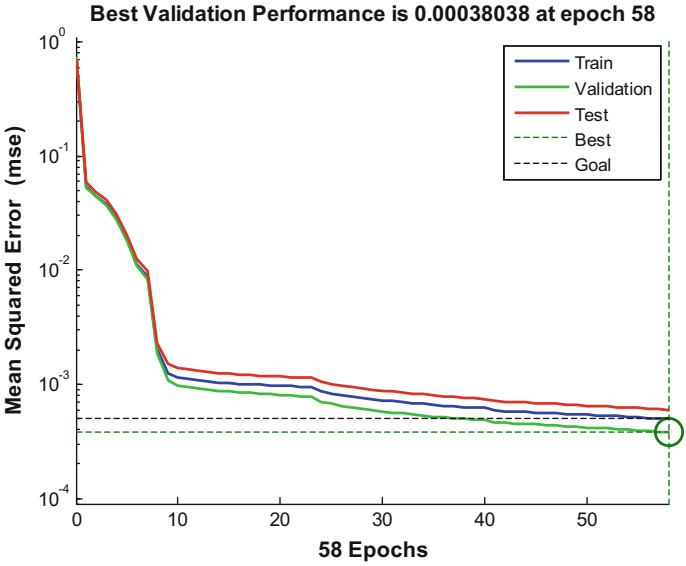

Fig. 3 Training curve of the NN

performance. Figure 3 is the training curve of the NN, it shows that the training progress becomes very slow after 10 iterations.

From Fig. 4, we can see the Performance Index (PI) ΔJ is increasing with the sampling period increases in the scheme of periodic time triggered LQR. Moreover, with the performance of NN increasing, the mean sampling times increases in the scheme of the NN-STC. But the PI is much lower than periodic time triggered control with the same mean sampling period. It means the control performance of NN-STC is better than the periodic time triggered control using the same use of network resource.

The attitude angle and angular velocity errors, by using STC and classical nonlinear controller are shown in a, b of Fig. 5. Roughly speaking, the errors converge to a small level. From c of Fig. 5, it can be seen that the sampling interval continuous increases and it keeps constant after 30 s. It means when the states

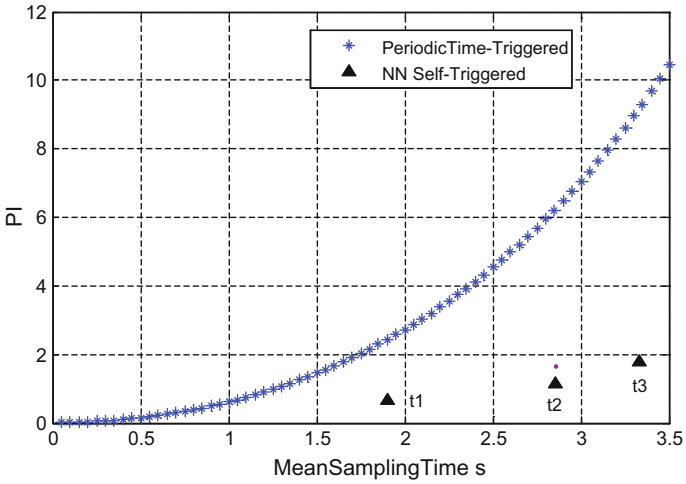

Fig. 4 Performance comparison between PTTC and NN-STC

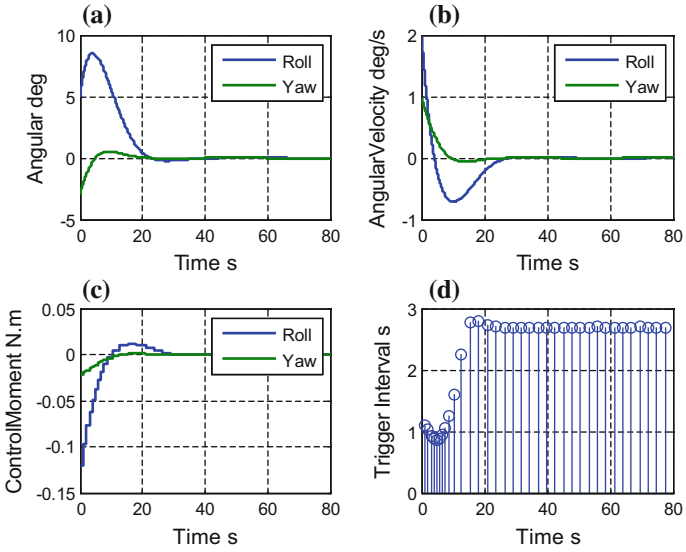

Fig. 5 States responses and triggered intervals using NN-STC

convince to the steady equilibrium, the controller will entry a salient periods, which is advantageous to save the cyber resources onboard. During 0–10 s, sampling intervals changes with the states overshoot. It means the NN-STC scheme works when the system quits steady process immediately.

5 Conclusion

The main contribution of this paper is the development and implementation of a neural network based self-triggered control for the attitude stabilization of a rigid spacecraft. The control law ensures the system stability of the closed-loop system to the desired attitude. The approach is validated in the simulation and it shows the proposed NN-STC strategy reduces sampling times without degrading the control system performance. The overall performance of the spacecraft is improved by this CPS aspect design.

Acknowledgements The research is supported by National High Technology Research and Development Program of China (No. 2015AA7046306).

References

1. Lee EA (2008) Cyber physical systems: design challenges. In: IEEE International symposium on object oriented real-time distributed computing, pp 363–369
2. Yang M, Wang L, Gu B, Zhao L (2012) The application of CPS to spacecraft control system. Aerosp Control Appl 38(5):8–13
3. Tayebi A (2008) Unit quaternion-based output feedback for the attitude tracking problem. IEEE Trans Autom Control 53(6):1516–1520
4. Hu Q (2009) Robust adaptive backstepping attitude and vibration control with L2-gain performance for flexible spacecraft under angular velocity constraint. J Sound Vib 327 (3):285–298
5. Wu B (2015) Spacecraft attitude control with input quantization. J Guid Control Dyn 39:1–5
6. Bhattacharya R, Balas GJ (2004) Anytime control algorithm: model reduction approach. J Guid Control Dyn 27(5):767–776
7. Årzén KE (1999) A simple event-based pid controller. In: Proceedings of IFAC world congress
8. Åström KJ, Bernhardsson B (2002) Comparison of Riemann and Lebesgue sampling for first order stochastic systems. In: Proceedings of the IEEE conference on decision and control, 2002, vol 2, 2011–2016
9. Tabuada P (2007) Event-triggered real-time scheduling of stabilizing control tasks. IEEE Trans Autom Control 52(9):1680–1685
10. Jr MM, Anta A, Tabuada P (2010) An ISS self-triggered implementation of linear controllers. Automatica 46(8):1310–1314
11. Mazo M, Tabuada P (2010) Input-to-state stability of self-triggered control systems. In: Proceedings of the, IEEE conference on decision and control, 2009 held jointly with the 2009, Chinese control conference. CDC/CCC 2009, vol 54, pp 928–933
12. Gommans TMP, Heemels WPMH (2015) Resource-aware MPC for constrained nonlinear systems: a self-triggered control approach. Syst Control Lett 79:59–67
13. Wang X, Lemmon MD (2009) Self-triggered feedback control systems with finite-gain stability. IEEE Trans Autom Control 54(3):452–467
14. Gommans T, Antunes D, Donkers T, Tabuada P, Heemels M (2014) Self-triggered linear quadratic control. Automatica 50(4):1279–1287
15. Santos C, Mazo M Jr, Espinosa F (2014) Adaptive self-triggered control of a remotely operated p 3-dx robot: simulation and experimentation. Rob Auton Syst 62(6):847–854

16. Poggio T, Girosi F (1990) Networks for approximation and learning. Proc IEEE 78(9): 1481–1497
17. Hornik K., Stinchcombe M., White H. (1989) Multilayer feedforward networks are universal approximators. Elsevier Science Ltd
18. Yi J, Wang Q, Zhao D, Wen JT (2007) Bp neural network prediction-based variable-period sampling approach for networked control systems. Appl Math Comput 185(2):976–988
19. Tu S (2011) Attitude dynamics and control of spacecraft. China Astronautic Publishing House, Beijing
20. Sun Z, Deng Z, Zhang Z (2011) Intelligent control theory and technology. Tsinghua University Press, Beijing

Target Locating and Tracking Based on the Azimuth and the Change Rate of Doppler Frequency

Qingshan Fu, Shuaihu Tian and Xiaoyan Mao

1 Introduction

With the development of science and technology and the upgrading of electronic warfare technology, passive location technology has drawn more and more attention. The target location technique, which the observation platform uses the targets' radiation signals or other radiation signals that targets reflect, has developed by leaps and bounds.

In the very beginning, the main positioning method is Direction of Arrival (DOA), but the accuracy is low. With the increasingly improvement of positioning accuracy's requirements, the precise electronic reconnaissance and positioning system theory appeared in the early 1970s, which mainly uses the Time Difference of Arrival (TDOA) and the Difference of Doppler Frequency (DFOA or DD) to measure and position, and the typical application is the PLSS system of the United States. At present, the existing passive positioning systems mainly use the targets' self-radiation signals to locate the targets. In addition to the traditional positioning technology, these systems has introduced a number of new single observer rapid positioning technologies, such as passive ranging, phase changing rate technology, and "out-of-plane" multi-path reflection signal positioning technology, which consists of infrared passive positioning and differential Doppler localization. For the target tracking technique, the scholar Kalman in 1960 and his colleague Bucy proposed the Kalman filtering algorithm [1], and this algorithm is the most basic

Q. Fu
School of Automation, Beijing Institute of Technology, Beijing 100081, China

S. Tian
Harbin Institute of Technology, Harbin 150001, China

X. Mao (✉)
Beijing Institute of Control Engineering, Beijing 100094, China
e-mail: cicely_mao@163.com

Z. Deng (ed.), *Proceedings of 2017 Chinese Intelligent Automation Conference*,
Lecture Notes in Electrical Engineering 458,
https://doi.org/10.1007/978-981-10-6445-6_78

and most widely used. In 1985, T.L. Song and J.L. Speyer proposed the Modified Gain Extended Kalman Filter (MGEKF) [2]. By the end of 20th century, some scholars proposed several nonlinear filtering algorithms such as Bayesian filtering based on nonparametric Monte Carlo simulation and Particle Filtering (PF) [3]. In 2002, Julier proposed the Unscented Kalman Filtering method of non-linear mapping transformation, and this algorithm directly uses the non-linear function to filter.

Since the traditional positioning method is azimuth intersection positioning, and the accuracy is low, so in this paper, we choose to add the change rate of Doppler frequency to the target positioning and tracking process; And in the meantime, the IMM_UKF (Intersecting Multiple Model) will increase the accuracy of tracking the maneuvering targets.

2 Positioning of Maneuvering Target

2.1 Observability Analysis

For the unobservable object, there must be a set of target trajectories corresponding to a same measurement value. In other words, for any trajectory in this set, the observer can exactly get an identical observation value. From another point of view, the target is observable means that a set of observation values can be used to determine the solution and the solution is unique. In this paper, we locate and track the maneuvering targets by the azimuth and the change rate of Doppler frequency. Compared with azimuth tracking, the addition of the change rate of Doppler frequency is supposed to improve the observability of targets to some degree. But, whether it can improve observability of targets in any case should be further studied. According to the principle of particle kinematics, the measurement value can be expressed as follows:

$$\begin{cases} \theta(t_k) = \arctan\left(\frac{x_p(t_k)-x_e(t_k)}{y_p(t_k)-y_e(t_k)}\right) \\ \dot{f}_d(t_k) = -\frac{\ddot{r}(t_k)}{c} f \\ \ddot{r}(t_k) = \frac{v_t^2(t_k)}{r(t_k)} - a_r(t_k) \\ r(t_k) = -\frac{v_t(t_k)}{\dot{\theta}(t_k)} \end{cases} \tag{1}$$

In the above equations, $\theta(t_k)$ represents the measurement value of azimuth angle at time t_k, $\dot{\theta}(t_k)$ represents the change rate of azimuth angle at time t_k, $x_p(t_k)$ represents the abscissa of the observation platform at time t_k, $x_e(t_k)$ represents the abscissa of the target at time t_k, $y_p(t_k)$ represents the ordinate of the observation platform at time t_k, $y_e(t_k)$ represents the ordinate of the target at time t_k, $\dot{f}_d(t_k)$ represents the measurement value of the change rate of Doppler frequency at time t_k, $r(t_k)$ represents the radial distance between the target and the platform at time t_k,

$\ddot{r}(t_k)$ represents the radial acceleration of the target relative to the platform at time t_k, $v_t(t_k)$ represents the tangential velocity of the target relative to the platform at time t_k, $a_r(t_k)$ represents the acceleration component of the target caused by the force to which it's subjected in the direction between the target and the platform at time t_k, f represents the coming frequency of the target, c represents the velocity of light in vacuum. So we can get from above equations:

$$\begin{aligned} x_e(t_k) &= \frac{-c \cdot \dot{f}_d(t_k) + a_r(t_k) \cdot f}{f \cdot \dot{\theta}^2(t_k)} \cos(\theta(t_k)) + x_p(t_k) \\ y_e(t_k) &= \frac{-c \cdot \dot{f}_d(t_k) + a_r(t_k) \cdot f}{f \cdot \dot{\theta}^2(t_k)} \sin(\theta(t_k)) + y_p(t_k) \end{aligned} \tag{2}$$

Obviously we can see, the positioning solution is dependent on the value of $\dot{\theta}^2(t_k)$ and $\dot{f}_d(t_k)$. Considering the existing measurement error in practice, a larger measurement error of azimuth angle will decrease the observability of the target because $\dot{\theta}^2(t_k)$ will be affected by the measurement error of azimuth angle, either.

2.2 Target Initial Positioning

Under the circumstance of passive location of maneuvering targets, although there is the radial distance between the target and the platform that we can get from the change rate of Doppler frequency, and we can locate the target just by the combination of the azimuth angle and the change rate of Doppler frequency, but the existing measurement error may cause a huge error on the positioning of targets, and the filtering performance won't be assured unless we optimize the results of target positioning.

Figure 1 indicates the geometric relation between platform trajectory and radiation source. At time t_k, the azimuth angle $\theta(x_e(t_k), y_e(t_k), t_k)$ and the change rate of Doppler frequency $\dot{f}_d(x_e(t_k), y_e(t_k), t_k)$ that the radar measures can be expressed respectively as follows:

$$\begin{cases} \theta(t_k) = \arctan\left(\frac{y_e(t_k) - y_p(t_k)}{x_e(t_k) - x_p(t_k)}\right) + \sigma_\theta \\ \dot{f}_d(t_k) = -\frac{\dot{\theta}^2(t_k) \cdot r(t_k) + a_r(t_k)}{\lambda} + \sigma_{\dot{f}_d} \end{cases} \tag{3}$$

In which, σ_θ and $\sigma_{\dot{f}_d}$ represent the measurement error of the azimuth of target and the change rate of Doppler frequency respectively, and they are often considered as priori information; $r(t_k)$ represents the radial distance between the target and the observation platform at time t_k, $a_r(t_k)$ represents the radial acceleration of the target, λ represents the wavelength of target emitter signal. Obviously, we can see that the

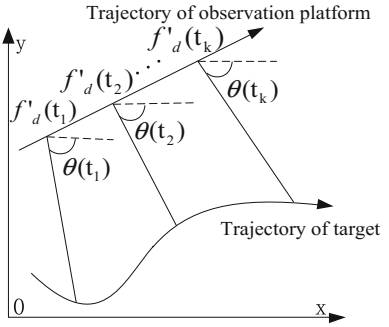

Fig. 1 Geometric relation between platform trajectory and radiation source

accuracy of $\theta(t_k)$ and $\dot{f}_d(t_k)$ depends on the measurement error and the geometric relation between the platform trajectory and the radiation source.

The main idea of initial positioning is as below: As to the target concerned, it's assumed that the target is not maneuvered at the initial time, then the positioning result in a period of time will be calculated, and each individual positioning point will be smoothed to the latest time, and the mean values of smoothed results will be the initial positioning results.

In the above process, we calculate the wavelength λ by the detected target's radiation source signal frequency f instead of signal carrier frequency f_c, but due to the Doppler frequency, f and the real frequency f_c are different. So in this case, we define:

$$f = f_c + f_d = \left(1 - \frac{\dot{r}}{c}\right) f_c \tag{4}$$

The relative frequency error caused by it is: $\frac{\Delta f}{f_c} = \frac{f_d}{f_c} = -\frac{\dot{r}}{c}$, due to $|\dot{r}/c| \ll 1$, the bias can be neglected.

2.3 *Tracking Maneuvering Targets*

Because tracking targets is a nonlinear filtering process, so in this paper, we choose the Unscented Kalman Filter, and there is no need to linearize the nonlinear system. And we choose the intersecting multiple model (IMM) algorithm to track targets due to the changing motion form of maneuvering targets. From time k − 1 to k, The recursive process of the intersecting multiple model (IMM) algorithm which contains N models is as follows:

1. The intersection of state estimation
   Let the transition probability from model i to model j be $P_{t_{ij}}$

$$P_{t_{ij}} = \begin{bmatrix} P_{t_{11}} & P_{t_{12}} & \cdots & P_{t_{1N}} \\ P_{t_{21}} & P_{t_{22}} & \cdots & P_{t_{2N}} \\ \vdots & \vdots & \ddots & \vdots \\ P_{t_{N1}} & P_{t_{N2}} & \cdots & P_{t_{NN}} \end{bmatrix} \tag{5}$$

   Let $\hat{X}^j(k-1|k-1)$ be the state estimation of filter j at time k − 1, and $P^j(k-1|k-1)$ be the corresponding state covariance, and $u_{k-1}(j)$ be the probability of model j at time k − 1, and $i, j = 1, 2 \ldots, N$. So after intersection, the input of each filter at time k is:

$$\hat{X}^{oj}(k-1|k-1) = \sum_{i=1}^{N} \hat{X}^i(k-1|k-1) u_{k-1|k-1}(i|j) \tag{6}$$

   In which, $\begin{cases} u_{k-1|k-1}(i|j) = \frac{1}{\bar{C}_j} P_{t_{ij}} u_{k-1}(i) \\ \bar{C}_j = \sum_{i=1}^{N} P_{t_{ij}} u_{k-1}(i) \end{cases}$

$$P^{oj}(k-1|k-1) = \sum_{i=1}^{N} \left\{ P^i(k-1|k-1) + \left[\hat{X}^i(k-1|k-1) - \hat{X}^{oj}(k-1|k-1)\right] \times \left[\hat{X}^i(k-1|k-1) - \hat{X}^{oj}(k-1|k-1)\right]^T \right\} u_{k-1|k-1}(i|j)$$

2. Model updating
   Let the state vector $\hat{X}^{oj}(k-1|k-1)$ and its variance $P^{oj}(k-1|k-1)$ and the observed value $Z(k)$ as the input of model j at time k; by means of the selected filters, we can calculate the output of each model, which are $\hat{X}^j(k|k)$, $P^j(k|k)$, $j = 1, 2, \ldots, N$.
3. Model possibility calculation
   If the filtering residual of model j is v_k^j, and the corresponding covariance is S_k^j, and assumed to obey the Gauss distribution in the meantime, then the possibility of model j is:

$$\Lambda_k^j = \frac{1}{\sqrt{|2\pi S_k^j|}} \exp\left[-\frac{1}{2}(v_k^j)'(S_k^j)^{-1} v_k^j\right] \tag{7}$$

   In which, $\begin{cases} v_k^j = Z(k) - H^j(k)\hat{X}^j(k|k-1) \\ S_k^j = H^j(k)P^j(k|k-1)H^j(k)' + R(k) \end{cases}$

4. Model probability updating

$$u_k(j) = \frac{1}{C}\Lambda_k^j \bar{C}_j \tag{8}$$

In which, $C = \sum_{i=1}^{N} \Lambda_k^i \bar{C}_i$

5. Model output

Let $\hat{X}(k|k)$ and $\hat{X}(k|k)$ be the output of the intersecting model respectively at time k, and we can get:

$$\hat{X}(k|k) = \sum_{i=1}^{N} \hat{X}^i(k|k) u_k(i) \tag{9}$$

$$\begin{aligned} P(k|k) = \sum_{i=1}^{N} u_k(i) \Big\{ & P^i(k|k) + \left[\hat{X}^i(k|k) - \hat{X}(k|k)\right] \\ & \times \left[\hat{X}^i(k|k) - \hat{X}(k|k)\right]^T \Big\} \end{aligned} \tag{10}$$

As we can see from the algorithm above, since the measurement information is used in the filtering estimation and the model probability calculation, the adaptive adjustment model can be used to track the maneuvering target, and tracking maneuvering targets without maneuver detection, tracking without time lag.

3 Simulation Test and Experiment

3.1 Observability Analysis of Target

Experiment 1: There are 3 targets to be observed in order to verify the observability. The observation platform is stationary at the coordinate (10 km, 20 km), and all three targets' initial point is at the coordinate (50 km, 50 km) and their initial location is all the same. One of their motion forms is uniform rectilinear, and the trajectory line and the line between the target and the platform is at a 45° angle; One is the radial motion along the path between target and platform; The other is uniform circular motion around the platform. The azimuth angle error is 0.1°, the change rate error of Doppler frequency is 1 Hz/s. Three targets' motion forms are corresponding to three states as follows: Both of the change rate of Doppler frequency and the azimuth angle are observable; The change rate of Doppler frequency is observable and the azimuth angle is not; Only the azimuth angle is observable. And the results of simulation are demonstrated in Fig. 2.

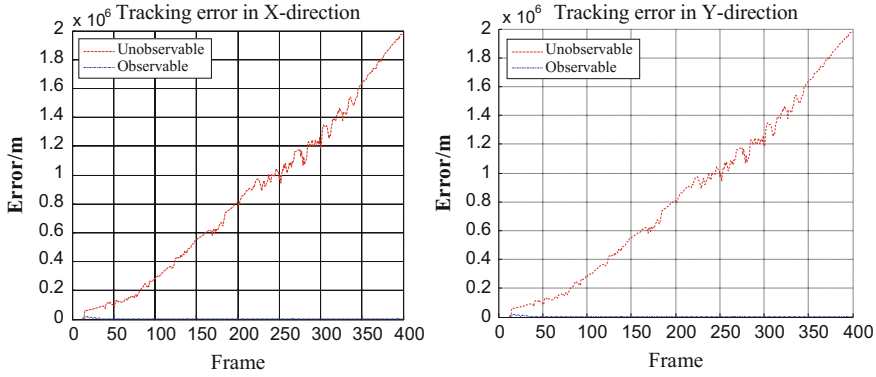

Fig. 2 Observability positioning error

The results shows that when the change rate of Doppler frequency is observable and the azimuth angle is not, the location error is far greater than that when only the azimuth angle is observable. As for that, increasing one-dimensional information of Doppler frequency change rate does not necessarily improve the observability of the target. If and only if the both observability of them is good, we can improve the tracking effects through improving observability.

3.2 Initial Analysis of Target

Experiment 2: The simulation environment is the same as that in Experiment 1, and the purpose is to find the influence of target's observability on initial positioning; 300 times Monte Carlo simulation will be carried out, and the results are shown in Table 1.

Experiment 3: The measurement error of azimuth angle is 0.05°, 0.1°, 0.2° respectively; The measurement error of change rate of Doppler frequency is 0.5, 1, 3 Hz/s respectively; and the results are shown in Table 2.

The above results shows, with the worse observability of the target, the initial positioning accuracy will decrease. In addition, Experiment 3 shows, with larger

Table 1 Influence of target's observability on initial positioning

Target's motion form	Observability	RMS error of positioning	
		X direction	Y direction
45°	Good	8.42×10^3	8.89×10^3
Along between target and platform	Not	2.73×10^8	2.73×10^8
Circular around the platform	Weak	1.006×10^5	1.001×10^5

Table 2 Influence of measurement error on initial positioning

Measurement error of azimuth (°)	Measurement error of change rate of Doppler frequency (Hz/s)	RMS error of positioning	
		X direction	Y direction
0.05	0.5	3.30×10^3	3.64×10^3
	1	3.41×10^3	3.76×10^3
	3	5.99×10^3	6.57×10^3
0.1	0.5	7.15×10^3	7.51×10^3
	1	7.75×10^3	8.17×10^3
	3	7.86×10^3	8.34×10^3
0.2	0.5	2.97×10^4	3.04×10^4
	1	2.98×10^4	2.97×10^4
	3	3.44×10^4	3.62×10^4

measurement error of the azimuth angle and the change rate of Doppler frequency, the positioning accuracy decreases greatly.

3.3 Tracking Analysis of Target

Experiment 4: the observation platform is at the coordinate (0 km, 0 km), and in uniform rectilinear motion at 550 km/h; the azimuth angle is −60°, and its measurement error is 0.1°, and the change rate of Doppler frequency is 1 Hz/s, and the data updating rate is 1 Hz. The starting point of target is at the coordinate (100 km, 100 km), and the target is set as uniform rectilinear motion at a speed of 300 m/s and the azimuth angle is 135°; UKF tracking purely by azimuth angle and UKF

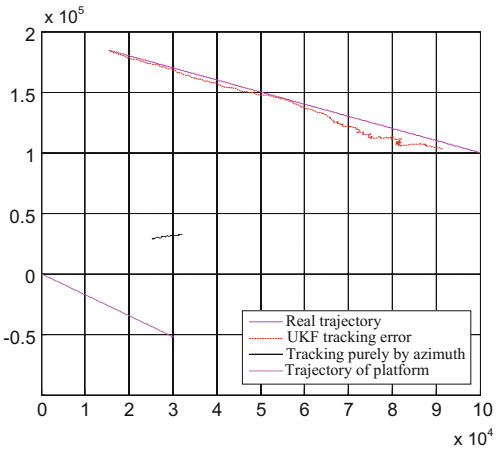

Fig. 3 Tracking results

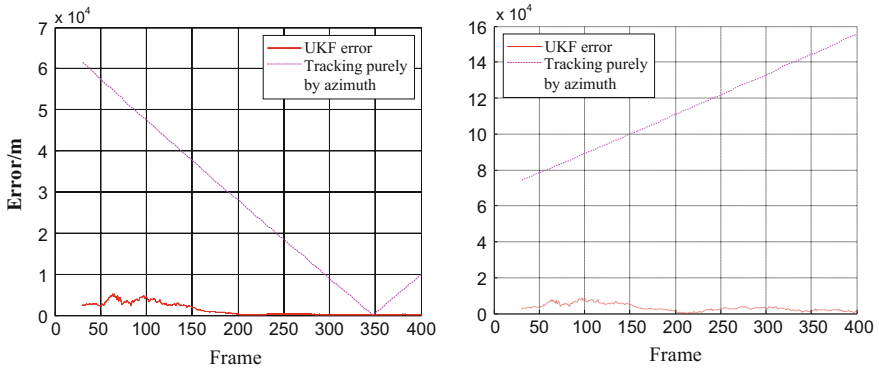

Fig. 4 Tracking error in X-direction and Y-direction respectively

tracking by both of azimuth angle and change rate of Doppler frequency will be carried out respectively (Figs. 3 and 4).

As is shown above, compared with tracking purely by azimuth angle, the effect of tracking by the addition of the change rate of Doppler frequency is more good and satisfactory.

Experiment 5: the environment is set as same as that in Experiment 4. The starting point of target is at the coordinate (100 km, 100 km). In the first, the target is set as uniform rectilinear motion for a period of time at a speed of 300 m/s and the azimuth angle is 135°, then the target turns and move as uniform rectilinear motion again. UKF tracking purely by azimuth angle, UKF tracking by both of azimuth angle and change rate of Doppler frequency and IMM_UKF tracking by

Fig. 5 Tracking results

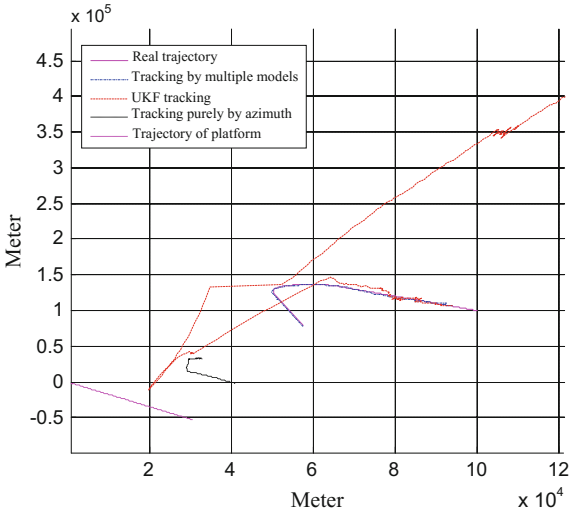

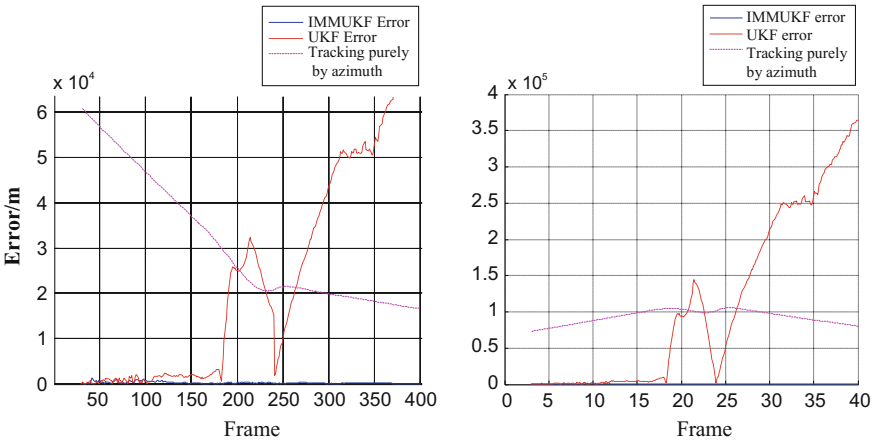

Fig. 6 Tracking error in X-direction and Y-direction respectively

both of azimuth angle and change rate of Doppler frequency will be carried out respectively (Figs. 5 and 6).

The Experiment 5 shows that, in the initial phase of uniform rectilinear motion, the tracking effects of UKF and IMM_UKF with the addition of the change rate of Doppler frequency are good and satisfactory, but when the target maneuvers, the IMM_UKF can quickly converges, but the algorithms which don't use intersecting multiple model (IMM) distinctly diverge.

4 Conclusions

This paper mainly studied the positioning and tracking maneuvering targets in observability, initial positioning and tracking; Compared with tracking purely by azimuth, the addition of the change rate of Doppler frequency, if both of them are well observable in the meantime, would increase the accuracy of initial positioning greatly, then improve the tracking performance. The experiments also shows that the intersecting multiple model (IMM) would achieve real-time tracking for maneuvering targets.

Acknowledgements This work is supported by National Natural Science Foundation (NNSF) of China under Grant 61473039.

References

1. Liu C, Yang J, Wang F (2013) Joint TDOA and AOA location algorithm. J Syst Eng Electron 24(2):183–188
2. Jwo DJ, Wang SH (2007) Adaptive fuzzy strong tracking extended Kalman filtering for GPS navigation. IEEE Sens J 7(5):778–789
3. Kuo CM, Chung SC, Shih PY (2006) Kalman filtering based rate-constrained motion estimation for very low bit rate video coding. IEEE Trans Circuits Syst Video Technol 16(1): 3–18

The Embedded Implementation of Millimeter Wave Radar Signal Processing System

Xingbo Ren, Zhiyuan Liu and Tengfei Fu

1 Introduction

The high rate of traffic accidents seriously threats the safety of people's lives. So the intelligent automobile which can improve the traffic safety is more and more concerned by the automobile manufacturers and the public [1]. One of the biggest problems with intelligent automobile is how to accurately identify the environment around the automobile [2]. In the aspect of environmental perception, millimeter-wave radar has been widely used because of its wide range of measurement, less susceptible to environmental factors and moderate price.

In foreign countries, such as the United States, Japan and Germany, the major automobile manufacturers began the millimeter-wave radar technology research from the sixties of last century [3]. At present, some countries even have products that can be used in the car. However, in China, the research on millimeter-wave radar started lately. And most colleges that study millimeter-wave radar are still in the stage of theoretical research and experimental testing [4]. At present, there is no reliable product in China that can be used in the car [5, 6].

In this paper, We designed a hardware platform of radar signal processing and a algorithm of radar signal calculation using the K-MC3 millimeter-wave radar sensor from RFbeam company. The system can realize the recognition of the distance, velocity and direction of the objects in front of the radar.

X. Ren (✉) · Z. Liu · T. Fu
Department of Control Science and Engineering, Harbin Institute of Technology, Harbin Heilongjiang Province, China
e-mail: renxingboya@163.com

Z. Deng (ed.), *Proceedings of 2017 Chinese Intelligent Automation Conference*, Lecture Notes in Electrical Engineering 458,
https://doi.org/10.1007/978-981-10-6445-6_79

2 Measurement Principle of Radar

The K-MC3 radar used in this paper is a frequency modulated continuous wave radar. Its working principle is as follow: the modulation signal whose amplitude is in the form of triangular wave controls radar transmitting millimeter wave signal whose frequency is changed in the form of triangular wave. Then, if there is an obstacle, the millimeter wave signal will be reflected. Next, the millimeter wave signal is received by the receiver of the radar. Finally, the intermediate frequency signal is generated by subtracting the transmitted signal and the received signal [7]. The principle of the intermediate frequency signal generation is shown in Fig. 1.

In Fig. 1a, the vertical axis is the frequency, and the horizontal axis is the time. The solid line is the frequency with time curve of radar transmitting wave. And the dotted line is the frequency with time curve of radar receiving wave. The difference frequency signal in Fig. 1b can be got by subtracting the transmitted signal and the received signal. According to the principle of Doppler Effect and the principle of electromagnetic wave we can get the formulas for calculating the distance and velocity:

$$R = \frac{c_0}{2}\frac{f_{b+} + f_{b-}}{2f_M}\frac{T_M}{2} \tag{1}$$

$$v = \frac{c_0}{f_0}\frac{f_{b+} - f_{b-}}{4} \tag{2}$$

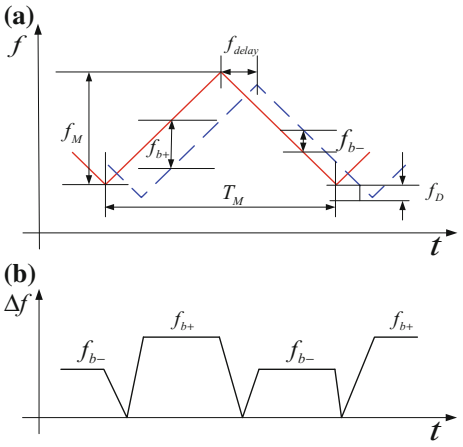

Fig. 1 The schematic diagram of IF signal generation

3 System Hardware Structure

The overall structure of the hardware circuit is shown in Fig. 2. The hardware circuit includes the main control unit, the communication module, the modulation signal generation module and the radar signal processing module.

The system chose TMS320F28335 from TI as the main control chip. TMS320F28335 is a 32 bit floating point DSP whose frequency can reach 150 MHz. And the DSP integrates a wealth of peripheral resources [8]. In the signal processing algorithm, a large amount of data needs to be stored. So the RAM space of F28335 was expanded using IS64LV12816 chip.

The CAN Communication Module is mainly used to send out the results of radar signal processing algorithm.

3.1 Modulation Signal Generation Module Design

In order to produce transmitting wave whose frequency changes like the shape in Fig. 1a, we must give the radar a input signal like shown in Fig. 3.

The modulation signal generation module is composed of DSP, DAC and amplifier. First of all, the modulation signal data is sent to the DAC chip through the DMA channel of DSP. Then, the DAC chip transforms the data into analog signal. Finally, we can get the modulation signal after a 2.5 fold amplifier.

3.2 Radar Signal Processing Module Design

When the radar works, the output signal of the sensor is like Fig. 4. It can be seen from the figure that there are two obvious problems in the original signal. One is that the output signal is mixed with the 100 Hz leaky wave signal. And the

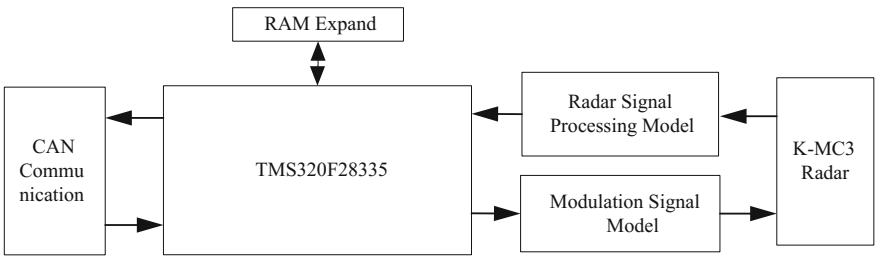

Fig. 2 The structure of hardware circuit

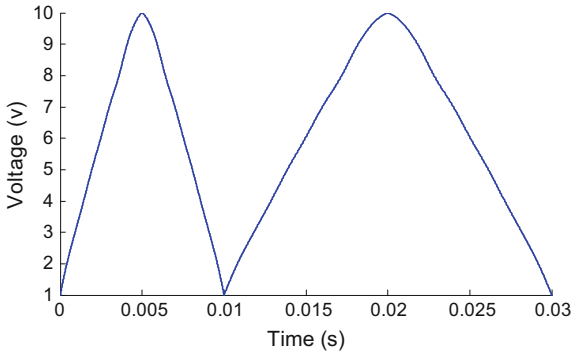

Fig. 3 Modulation signal

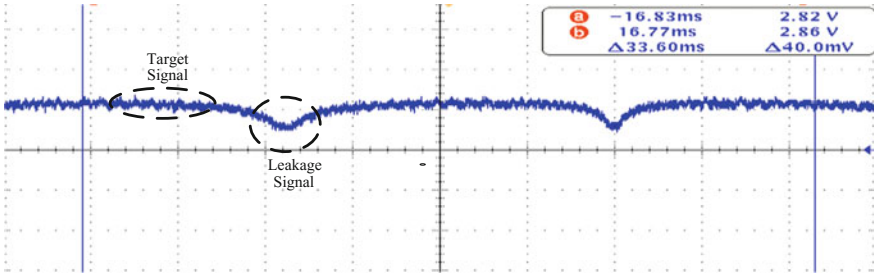

Fig. 4 The output signal of radar

amplitude of leaky signal is much larger than the amplitude of target signal. The other is that the amplitude of target signal is very small, which is not conducive to the ADC.

In order to solve the above two problems, it is necessary to design the radar signal processing circuit. The function includes two parts: filter and amplification.

The filter circuit is used to filter the low frequency leaky signal and the high frequency interference signal. So it is necessary to design a band-pass filter. The high cutoff frequency is determined by the frequency range of the target signal. According to formula (1) and (2), We can get the formula (3) to calculate the target signal frequency.

$$f_{b+} = \frac{4Rf_M}{c_0 T_M} + \frac{2vf_0}{c_0} \tag{3}$$

It can be seen from the formula (3) that the maximum frequency of the target signal can be obtained when the distance and velocity are taken to the maximum. The target measurement range of radar in this paper is as follows: the distance is less than 120 m, the speed is less than 110 km/h. Then we can get that the highest frequency of the target signal is about 40 kHz. So the high cutoff frequency was

taken as 40 kHz. On the other hand, the low cutoff frequency is determined by the leaky wave signal and the target signal. The frequency of the leaky wave signal is about 100 Hz. And the target signal frequency is from 0 to 40 kHz. So when filtering out the leaky wave signal, we are filtering out some useful target signal. Then we can get the selection principle of low cutoff frequency. The principle is that the frequency should be as small as possible when it can filter out the leaky wave signal. After the simulation in Pspice, we chose the low frequency 400 Hz. Above all, the pass-band of the band-pass filter is 400 Hz–40 kHz. In this paper, we used LM2904 of TI to design the band-pass filter.

The purpose of the amplifier is to amplify the target signal to the range of ±1 V. The function consists of two parts: a fixed gain amplifier circuit and an adjustable gain amplifier circuit. The fixed gain amplifier was designed 30 times enlarge the signal using LM2904 chip. The amplitude of the target signal is related to material, size and distance of the target. So it is necessary to design an adjustable gain amplifier circuit that can adjust the output signal automatically to the range of ±1 V according to the amplitude of the input signal. In this paper, the AD603 chip was used as the amplifier chip, and the half wave detection circuit was used as the negative feedback circuit to design the adjustable gain amplifier circuit.

4 Radar Signal Processing Algorithm Design

The radar's output signal was processed by the hardware circuit and then sampled by the ADC module. After sampling the radar signal, DSP needs to deal with a series of data to get the information of the targets.

First of all, in order to further eliminate the interference caused by high frequency signal, a low-pass digital filter was designed. Then, we need to design algorithm to separate the signal corresponding to every target, and accurately identify the exact frequency of every target signal. Finally, it is easy to appear false alarm and missing alarm when recognize targets. So it is necessary to design algorithm to eliminate some of the interference, so as to avoid the phenomenon of false alarm and missing alarm.

A low-pass digital filter was designed using FIR. The maximum frequency of the pass-band was set to 40 kHz. And the minimum frequency of the stop-band was set to 60 kHz.

4.1 Peak Frequency Determinate

It can be seen from the formulas (1) and (2) that we need to identify the peaks' frequency of the targets in order to calculate the targets' information. In this paper, FFT and Chirp-z algorithm were used to determine the peaks' frequency.

The output signal of radar is the mixture of multiple targets' signal. So the output signal cannot be separated until we transform the data into frequency domain. For the purpose of improving the speed of calculation, this paper used the Fast Fourier Transform (FFT) algorithm to realize the Discrete Fourier Transform algorithm. Firstly, we must determine the sampling frequency. According to the sampling theorem, the sampling frequency should be at least two times as much as the highest target frequency 40 kHz. But when using, we always choose the sampling frequency at least four times as much as the highest target frequency. So the ADC sampling frequency was chose as 187,500 Hz. Then, we must determine the points' number of FFT transform. If the ADC work as 187,500 Hz, It can sample 937 points during the rising segment of the 100 Hz modulation signal. Removing about 200 points that at the beginning and at the end, we can only use about 700 points to calculate the FFT. On the other hand, there is fence effect error in FFT. The error is:

$$\Delta f = \frac{f_s}{n} \tag{4}$$

From the formula (4), we can see that we must increase the number of FFT in order to reduce the fence effect. Therefore, the sampling points n was finally taken as 512. The error brought by the fence effect was 366.21 Hz.

In order to further reduce the error caused by the fence effect, the Chirp-z transform was used in this system. In theory, the Chirp-z transform of m point can reduce the error of FFT by m times [9]. Therefore, from the point of view of error analysis, the 16 point Chirp-z transform can reduce the error of the fence effect to 22.89 Hz. At this time, the error of the fence effect on the measurement results can be small enough to meet the requirements. However, in practical application, it was found that the result of 16 point Chirp-z transform was always different from the result of FFT. That is because 16 point is only a small part of the sampling point. It is easy to be influence. so we must further increase the number of Chirp-z transform. It was found that when the number of points is 128, it can achieve a good amplification effect. Finally, the points of Chirp-z was taken as 128.

4.2 False Targets Exclude

False alarm is that the number of solved targets is more than that of actual targets. While the missing alarm is that the number of solved targets is less than that of actual targets. The false alarm phenomenon will cause the vehicle frequently braking. And the missing alarm will seriously affect the safety of the vehicle. So the elimination of false alarm and missing alarm is very important during recognizing targets that in front of radar. In this paper, we used CFAR algorithm to remove the interference of environmental factors firstly. Then, the peaks match algorithm and false targets exclude algorithm were used to avoid false alarm and missing alarm.

There is not only the targets' information, but also the interference of the surrounding environment information in the radar's output signal. And it is generally considered that the interference signal of the environment obeys Rayleigh. In order to eliminate the false targets caused by environmental disturbance, a SO-CFAR algorithm was designed based on arithmetic average value [10]. The algorithm used the average value of the signal intensity near the target signal to estimate the intensity of the environmental disturbance at the target signal.

From the formula (1) and (2), it can be seen that we need the frequency of peak in the ascending branch and the frequency of peak in the descending branch to calculate the information of the targets. When there are many targets, there will be multiple peaks in ascending branch and descending branch. So we need to design a peaks match algorithm to match different peaks. The principle that we can use is that the power of the corresponding peak in the ascending and descending branch should be the same. In order to avoid the missing targets, every peak in ascending branch is matched with two peaks in descending branch.

When we matched peaks, some false targets were introduced. In order to eliminate these false targets, this paper designed false targets exclude algorithm. It can be proved that when the frequency of the modulation signal changed, the results of real targets will not change, but the results of false targets will change. According to this principle, we inputted modulation signal like Fig. 3 to the radar. Then we compared the two groups of results. If the distance, velocity and direction were the same, the target was a real one. Then we outputted the information of the target.

5 Experiment

In order to verify the effect and accuracy of the designed system on the distance, velocity and direction information calculation of a single target,this paper built a test environment like Fig. 5. The target signal of the radar sensor was processed and calculated in the hardware circuit, and the result was sent to the PC through the CAN module.

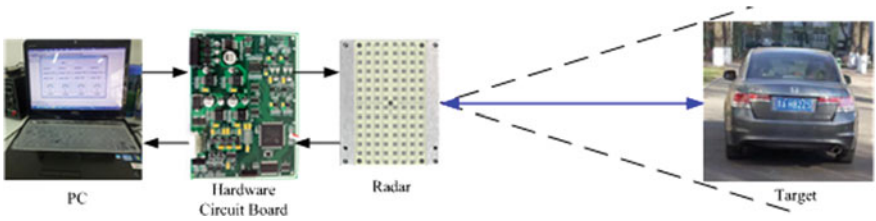

Fig. 5 The experimental environment

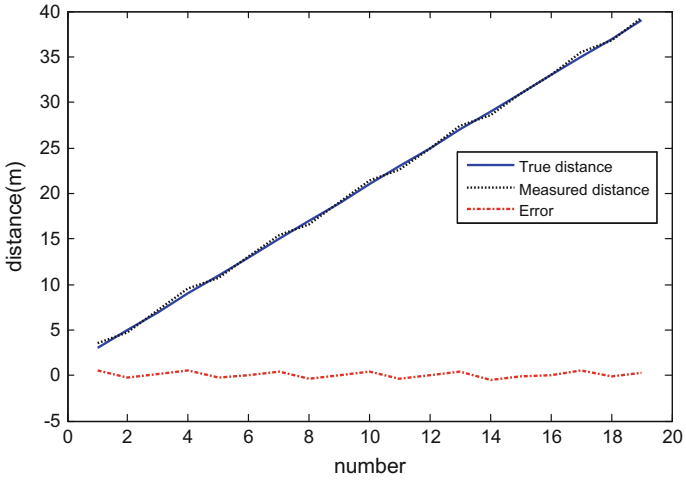

Fig. 6 The experimental results of single target's distance

First, let the car rest and measured its distance. A series of tests were carried out by changing the relative distance between the target vehicle and the radar. The measured distance, the true distance and the test error were represented in Fig. 6.

It can be seen from Fig. 6 that the measurement error is within ± 0.6 m.

Then we tested the velocity of the moving car. The car moved deceleration away from the target, deceleration toward to the target, acceleration away from the target and acceleration toward to the target. In this paper, the test results of the Delphi product radar were taken as the reference value, and compared with the test results of the radar signal processing system designed by ourselves. The reference velocity, test velocity and velocity error were expressed in the same graph. The test results of four processes were shown in Fig. 7.

As can be seen from Fig. 7, the direction of the reference movement and the test movement are always consistent. And in speed value, the change rule of the test speed is consistent with the reference speed, and the error of the velocity is always in the range of ± 1 m/s.

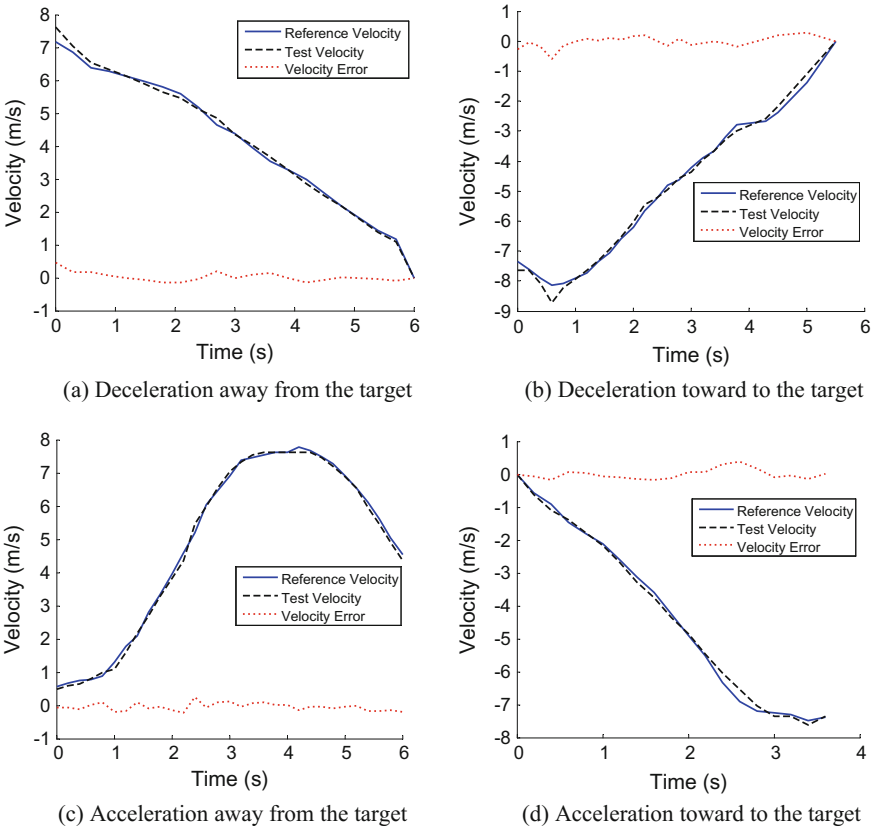

(a) Deceleration away from the target

(b) Deceleration toward to the target

(c) Acceleration away from the target

(d) Acceleration toward to the target

Fig. 7 The experimental results of single target's velocity

6 Conclusion

The paper designed a radar signal processing hardware circuit and radar signal calculation algorithm based on the K-MC3 mm wave radar. Then the algorithm was programmed in C language and downloaded to the hardware circuit to do some test. The test results show that the millimeter wave radar signal processing system designed in this paper successfully realizes the calculation of the distance, velocity and direction of the targets. What is more, the error of the distance identification is within ± 0.6 m, the error of speed identification is within ± 1 m/s.

Acknowledgements This work is supported by China Automobile Industry Innovation and Development Joint Fund (No. U1564213), and National Natural Science Foundation of China (No. 61403105).

References

1. Sai S, Altintas O, Kenney J et al (2013) Current and future ITS. IEICE Trans Inf Syst E96.D (2):176–183
2. Becker J, Colas MBA, Nordbruch S et al (2014) Bosch's vision and roadmap toward fully autonomous driving. Road Veh Autom, pp 49–59
3. Grimes DM, Jones TO (1974) Automotive radar: a brief review. Proc IEEE 62(6):804–822
4. Zheng X (2007) Study on signal processing key technology of millimeter wave automobile anti-collision radar system. National University of Defense Technology, Changsha (in Chinese)
5. Xu J (2015) Investigations on some key technologies of 77 GHz automative radars. Southeast University, Nanjing (in Chinese)
6. Chen T (2016) The design of A 24 GHz FMCW vehicle ranging radar system. Appl Electron Tech 42(12):37–40 (in Chinese)
7. Bredendiek C, Pohl N (2012) A 24 GHz wideband single-channel SiGe bipolar transciver chip for monoststic FMCW radar systems. In: Proceedings of the 7th european microwave integrated circuits conference, pp 309–310
8. Zhang Q, Xu Y (2015) Teach you DSP hand by hand-about TMS320F28335. Beijing University of Aeronautics and Astronautics Press, Beijing, pp 26–30 (in Chinese)
9. Xu F, Wang Y (2011) Application of Chirp-z transform in radar signal processing. Modern Electron Tech 34(9):28–30 (in Chinese)
10. Fan X (2014) A study of adaptive constant false alarm rate detection. Xidian University, Xian (in Chinese)

Monitoring System Design and Realization for Unmanned Mobile Robot Based on Web

Yuchao Wang, Tianlong Huang, Guang Zou and Huixuan Fu

1 Introduction

At present, unmanned mobile robots are widely used in industry, agriculture, medicine, construction, military and other fields. It used to replace human accomplish some dangerous or difficult task. The research and development, manufacture and application of robots are the important symbols to measure a country's scientific and technological innovation and high-end manufacturing level [1, 2]. But the users and enterprises do not have the ability to handle fault of the robot. There is also a lack of effective methods for early warning and intelligent fault diagnosis. Therefore, it put forward the requirements for the after-sales service of robot manufacturers. ABB is a well-known industrial robotics company in foreign countries. ABB has developed a "remote service" platform [3]. In 2013, Shenyang SIASUN robot cooperation with the Dalian University of Technology developed a remote monitoring and diagnosis service platform. SIASUN robot remote monitoring service platform is limited for the type of robot, versatility should be improved. There are more universities and research institutions to start research on the remote monitoring system based on application requirements and achieved some results. In this paper, the unmanned mobile robot remote monitoring system based on Web [4]. Using 4G DTU to realize data transmission, with the advantages of fast speed and large amount of data transmission. The Web server based on JavaEE can satisfy the principle of open and close, good scalability and high network security.

Y. Wang · T. Huang · G. Zou · H. Fu (✉)
College of Automation, Harbin Engineering University,
Nantong Street 145, Harbin, China
e-mail: fuhuixuan@hrbeu.edu.cn

Z. Deng (ed.), *Proceedings of 2017 Chinese Intelligent Automation Conference*,
Lecture Notes in Electrical Engineering 458,
https://doi.org/10.1007/978-981-10-6445-6_80

2 System Design

The monitoring system for unmanned mobile robot based on Web is composed of three parts which are data acquisition and controller, data monitoring center and client. As shown in Fig. 1. The ARM11S3C6410 main controller obtains real-time running data of unmanned mobile robot through the gyroscope, accelerometer, tachometer module, GPS and other sensors (The number of unmanned mobile robot, time, roll angle, pitch angle, yaw angle, latitude and longitude, the speed of the four wheels). The Data Monitoring Center consists of two parts, database servers and application servers. The database server receives real-time data uploaded by the main controller through 4G DTU (Data Transfer unit). The database server writes the data to MySQL database. The application server connect to the database and published on the Web for the client to view. The client accesses the application server remotely through the Web browser. The application server accomplish the functions of real-time data monitoring, historical data query, upload and remote control. The system is relatively independent of each part, with low coupling, good scalability, operability and practicality [5].

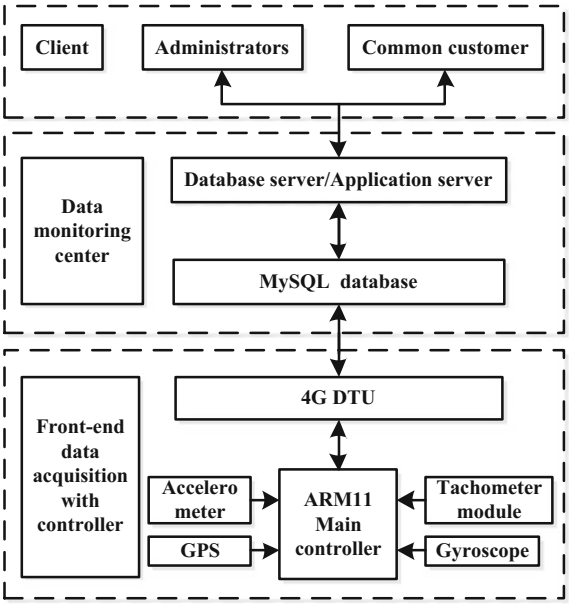

Fig. 1 Structure diagram of system

3 System Realization

3.1 Front-End Data Acquisition with Controller

The main controller of the system is the OK6410 development board made by Flying Ling embedded company. The S3C6410 processor is a 16/32-bit RSIC ARM111176JZF-S kernel with low-cost and low-power, which is launched by Samsung. The performance of this processor is the frequency of 533 MHz/667 MHz, 128M bytes of MobileDDR memory, 1G bytes of NAND Flash (MLC). S3C6410 has an excellent external memory interface which can meet the needs of broadband communications services [6].

Using 4G DTU named USR-G780 developed by People Network company as the wireless communication. This module supports 4G high-speed access for China Mobile, China Unicom and China Telecom, while supporting 3G and 2G access for China Mobile and China Unicom. It has three mode of operations which are transparent transmission, HTTPD and FTP, and supports TCP/UDP/NDS/HTTP/FTP network communication protocols. It also supports the maximum 4 TCP and 4-channel socket connections, each one supports 10 KB serial port data caching, though connection exceptions the optional cache data is not lost. It has three user configuration ways which are serial at commands, network at commands and SMS at directives. It supports two simple pass through methods which are TCP client and UDP client.

The main controller collects data through three line TTL level serial port by gyroscope, accelerometer, GPS and tachometer module. It connects the 4G wireless communication module through the RS-232 serial port. It controls the 4G wireless communication module to access Internet. The 4G wireless communication module and main controller realize two-way transparent transmission of network data through RS-232 serial port [7].

3.2 Data Monitoring Center

The structure design of data monitoring center is to separate the database server and application server. This design is conducive to the security of the data, also facilitates the upgrading and maintenance of the application server. Using Java programming language for the development of data monitoring center. Using relational database MySQL to store data and Tomcat as a Web server. The combination of this three makes up a good foundation for system development.

The database server stores the data to the database table in real-time. The application server reads the data from the database tables as Webs for Web remote clients to view and use. There are four data tables in the database which are userdata, monitordata, controldata and logdata [8].

The application server of data monitoring center to provides data access service to remote clients. Figure 2 is the structure diagram of the application server.

The B/S (Browser/Server) mode is the architecture of the application server. The remote client accesses the application server through the browser. The client sends the request and the business logic processing is done on the application server. The permissions of common customer are monitoring real-time data and querying historical data. The administrator could download the historical data file and select the export format for txt, Excel and CSV. Also it can send control commands to operate the unmanned mobile robot and get the positioning information of unmanned mobile robot in real time.

4 Design and Realization of Web Application

The design and realization of Web application is a concrete manifestation of the function of monitoring system for unmanned mobile robot. It is the basic requirement of this paper to build a system with good practicability, safe, reliable and highly scalable.

Using SSH (Struts + Spring + Hibernate) framework to achieve the application of the system. The MVC design pattern of Struts2 realizes the separation of model layer, view layer and control layer. The Spring container and control inversion solve the dependencies between components, modules and hierarchies in the system. Hibernate technology implements a lightweight package for JDBC access to the database. Therefore, use three advanced framework technologies of struts, spring and hibernate. Making the system has a good scalability and maintainability.

This system utilizes the most popular web development technology (HTML, CSS, jQuery, Ajax). Realizing the functions of system login, monitoring, data querying and exporting, remote control and so on. The system of the interface is simple, the function is reasonable and the user experience is good.

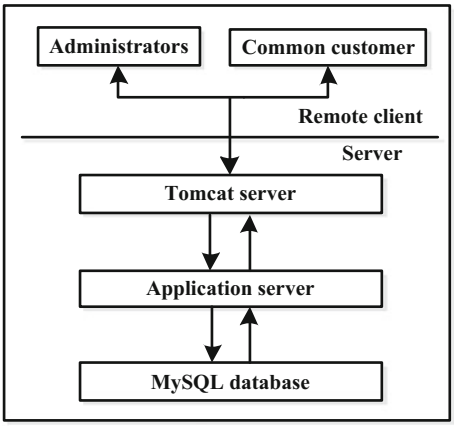

Fig. 2 Structure diagram of the application server

4.1 System Login

The system users are divided into common customer and administrators. The permissions of common customer are real-time monitoring and historical data viewing. The privileges of the administrator are real-time monitoring, historical data querying with exporting and remote control.

4.2 Real-Time Monitoring

The real-time monitoring interface is shown in Fig. 3. The running data of the unmanned mobile robot are arranged in reverse order by time. The latest data is shown at the top. The display page refreshes once per second, and the client sends access request to the server every second to ensure that the latest data is available in real time.

At the top right of the Real-time monitoring page, click the button of the velocity curve. Shows the real-time velocity curve of the four motors, as shown in Fig. 4. The real-time curves adopts the Highcharts graph library which are written in JavaScript. It is easy to analyze the change trend of motor velocity in the form of graphics.

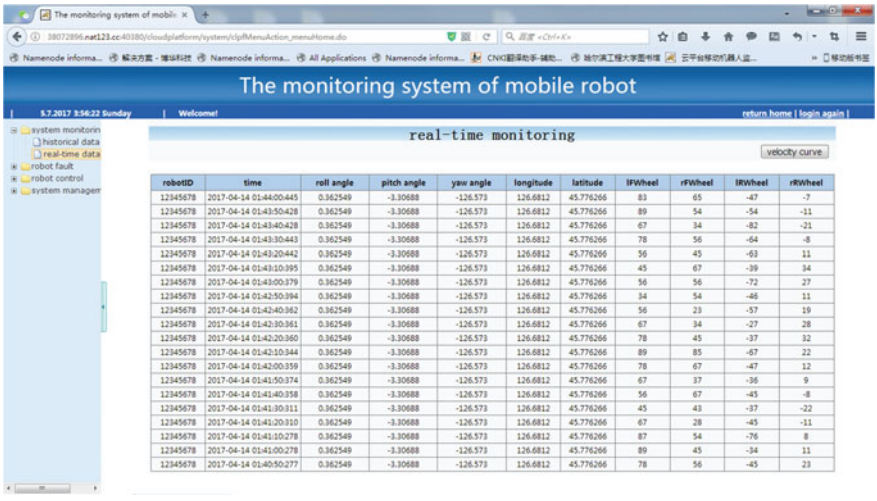

Fig. 3 Real-time monitoring

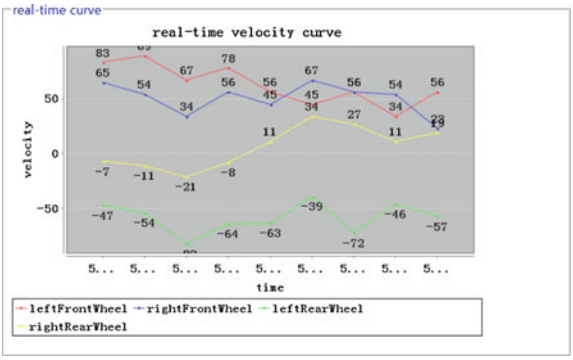

Fig. 4 Real-time velocity curve

4.3 Historical Data

There are three features in the historical data page, which are historical data display, query and output. Select the unmanned mobile robot number, time interval and data type. The system will display the real-time running data of unmanned mobile robot through a graph, shown in Fig. 5.

4.4 Remote Control

The remote control is one of the core function for unmanned mobile robot. In this paper, the unmanned mobile robot application is to complete the airport runway

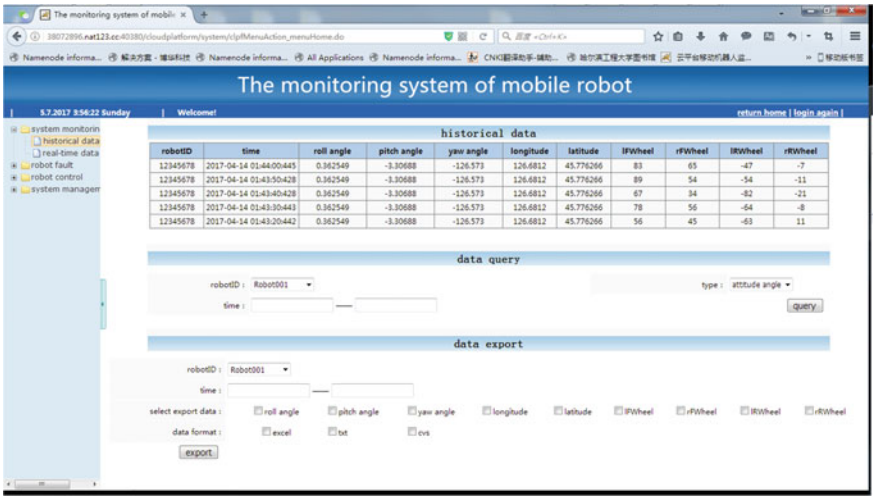

Fig. 5 Historical data interface

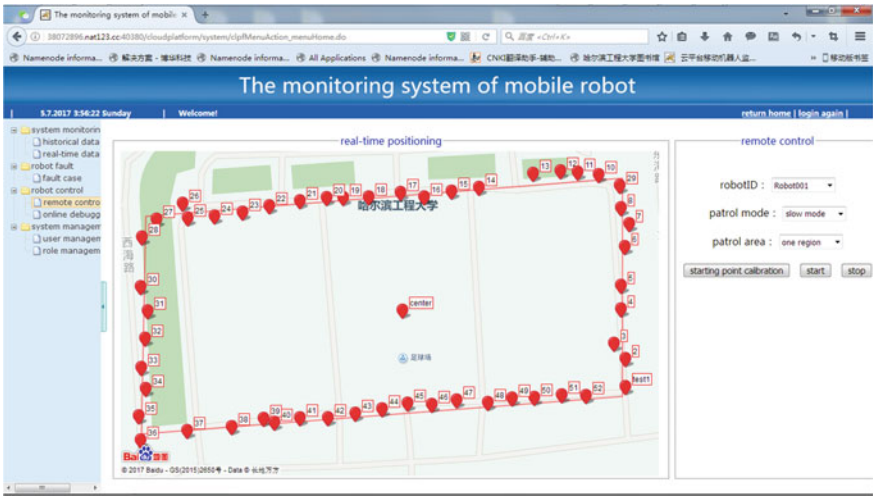

Fig. 6 Remote control interface

cracks and foreign substance detection. The implementation of the function is fixed-point movement and automatic cruise. The remote control interface of the unmanned mobile robot as shown in Fig. 6.

In this paper, on the left side of the remote control page is the location information of unmanned mobile robot. Obtaining real-time latitude and longitude of unmanned mobile robot by using GPS modules. Development based on Baidu Map to realize the real-time positioning of unmanned mobile robots. On the right side of the page is the setting of the automatic cruise parameters for the unmanned mobile robot. Set up the mode and cruise area of the unmanned mobile robot cruise to realize automatic inspection of the designated area of the runway. The remote client can monitor the running state of the unmanned mobile robot and view the position information in real time. In the event of failure, the field engineers conduct artificial intervention.

5 Conclusions

This paper describes a monitoring system for unmanned mobile robot based on Web, and provides the design and implementation of the system.

(1) In this paper, combine with the application and the needs of remote monitoring for unmanned mobile robot. Designed and realization the remote monitoring system for unmanned mobile robot based on the framework of internet. The monitoring system for unmanned mobile robot is composed of three parts that are front-end data acquisition with controller, data monitoring center and client.

This design effectively reduces the coupling between the parts to improve the scalability and maintainability of the system.

(2) The front-end data acquisition with controller collect information of the unmanned mobile robot. Including the number of unmanned mobile robot, data time, longitude, latitude, attitude angle and the velocity for four motor. Using 4G DTU as data transmission module to meet the basic requirements of real-time and security for data transmission.

(3) According to the requirement, the application server of the data monitoring center designed many kinds of functions, such as system login, real-time monitoring, historical data and remote control. To achieve the monitoring of the unmanned mobile robot anytime and anywhere, as well as the full utilization of historical data. Realizing real-time positioning of unmanned mobile robot based on the development of Baidu API. Setting the inspection parameters online to meet the basic requirements of remote control for unmanned mobile robot.

Through operation and testing, the system is stable, the function is set reasonable, the data transmission is reliable and the response of the application server is quickly. This system could meet the basic needs of remote monitoring for unmanned mobile robot, so that engineers could control and interfere with the unmanned mobile robot anytime and anywhere.

In addition, the security of the remote control system needs to be improved. High-definition video camera installed on the unmanned mobile robot. It is more intuitive to monitor the unmanned mobile robot through real-time images. To ensure that the unmanned mobile robot complete the runway crack and foreign substance detection.

Acknowledgements This work is supported by the National Natural Science Foundation of China (Grant No. 51409064).

References

1. Jianling L, Lingling Q, Chun S (2013) Design and implementation of remote monitoring and control system for modern greenhouse based on Web. In: The 32nd China control conference, pp 6660–6663
2. Ali Buldu (2011) A web-based controlled greenhouse system and monitoring the system's data. Inter Rev Comp Softw 6(5):856–861
3. Dandan Y (2015) Implementation of bridge monitoring system based on cloud intelligence technology. Beijing University of Posts and Telecommunications
4. Jianling L, Lingling Q, Chun S (2015) Design of greenhouse intelligent monitoring system based on internet of things. Trans Chin Soc Agric Mach 46(3):261–267
5. Zhongfu S, Hongtai C, Hongliang L (2013) Realization of greenhouse environment information collection system based on GPRS and WEB. Trans Chin Soc Agric Eng 22 (6):131–134 (2013)

6. Chen Xiao W, Haihong YH (2008) Design of greenhouse remote monitoring system based on web service. Mech Eng 25(8):8–10
7. Tao P (2015) Design and implementation of supervision project management system based on SSH framework. Beijing University of Posts and Telecommunications
8. Wang FY, Liu DR (2008) Networked control system: theory and application. Springer, London

Visual-Inertial Tightly Coupled Fusion and Nonlinear Optimization for UAVs Navigation

Zhenxing You, Zhihao Cai, Jiang Zhao, Yu Zhang and Yingxun Wang

1 Introduction

Unmanned aerial vehicles (UAVs) have turn out to be potential platforms for numbers of applications in various environments due to their small size, superior mobility, and hovering capacity. Autonomous level of UAVs can be defined by the ability of taking on challenging tasks and the key of classification is the levels of vehicle's environment perception [1]. On the other hand, Motion estimation by on-board sensors gets rid of dependence on outer signals such as satellite which may be inaccessible indoors and can be more reliable in exploring complex surroundings [2]. Among the on-board sensors, the combination of Visual-Inertial sensors gives a cheap but expressive solution. Cameras provides abundant information of the environments and we can recover the 3D geometry exactly but will fail in simple surroundings without enough features, IMU measures the self-motion of vehicles which we can get a well estimation of the motion of camera, which recovers the metric scale of monocular and gives the direction of gravity for cameras.

Approaches of vision inertial fusion can be classified into loosely coupled fusion and tightly coupled fusion according to how to combine the data of images and IMU [3]. Loosely coupled fusion methods use the results of IMU self-motion estimation to correct the measurements of cameras, which is easy to establish, the tightly coupled methods fusion use the raw measurements of IMU and cameras by optimizing same states variates, which is more complex but gives more optimal results and become an active research topic in recent years.

Z. You (✉) · Z. Cai · J. Zhao · Y. Zhang · Y. Wang
School of Automation Science and Electrical Engineering,
Beihang University, Beijing 100191, China
e-mail: youzx163@163.com

Z. Deng (ed.), *Proceedings of 2017 Chinese Intelligent Automation Conference*,
Lecture Notes in Electrical Engineering 458,
https://doi.org/10.1007/978-981-10-6445-6_81

2 Notations and Definition

2.1 Frames

Throughout this work, we denote the IMU frame as F_B, camera frames as F_C, and the word frame as F_W. We ignore the Mechanical error between UAVs coordinate frame and IMU frame and express the kinematics parameter in F_B with respect to the world frame. The coordinate frames set up schematically are depicted in Fig. 1.

2.2 States

In general, we regard the problem of UAVs navigation as the problem of estimation of 6-DOF rigid body which can be express as by three dimensions of position and three dimensions of rotation. The IMU, measuring the acceleration and angular velocity of grid body, affected by additional noises which are modelled as white noises and slowly varying biases which are modelled as Gaussian random walk. The sates x to be estimates include the position, rotation and velocity between continuous images and the biases of IMU sensors. We rewrite the states as Eq. (1).

$$x^j = [\mathrm{R}^j_{WB}, \mathrm{p}^j_{WB}, \mathrm{v}^j_{WB}, \mathrm{b}^j_a, \mathrm{b}^j_g] \tag{1}$$

where x^j are states linked to the image j, R^j_{WB} refers to the rotation between image j and the last reference image, p^j_{WB} and v^j_{WB} are position and velocity of j, expressed in the world frame. b^j_a and b^j_g are biases of accelerometer and gyroscope with the time of image j.

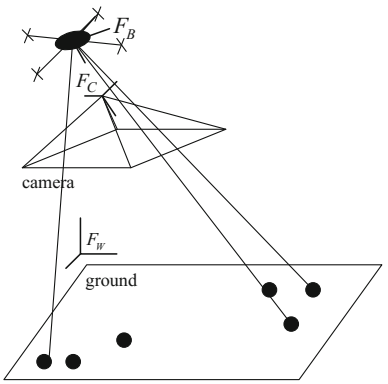

Fig. 1 Coordinate frames involved in this work

3 IMU Measurements Model and Kinematics

The uncertainty of IMU sensors can be divided into two parts, one is white noises created by measurement process, and the other is bias created by inertial physical process modelled as Gaussian random walk [7]. The measurements of IMU with additional uncertainties are expressed in (2–3) with continuous-time form noises.

$$\tilde{\omega}_B(\mathrm{t}) = \omega_B(\mathrm{t}) + b_g(\mathrm{t}) + \eta_g(\mathrm{t}) \tag{2}$$

$$\tilde{a}_B(\mathrm{t}) = \mathrm{R}_{WB}^{T}(\mathrm{t})(a_W(\mathrm{t}) - g_W) + b_a(\mathrm{t}) + \eta_a(\mathrm{t}) \tag{3}$$

where the $\tilde{\omega}_B(\mathrm{t})$ and $\tilde{a}_B(\mathrm{t})$ are measurements of accelerometer and gyroscope at time t expressed in the IMU frame, $\omega_B(\mathrm{t})$ and $a_B(\mathrm{t})$ are the nominal value of the measurements at time t, $b_g(\mathrm{t})$ and $b_a(\mathrm{t})$ are biases in continuous-time form, $\eta_a(\mathrm{t})$ and $\eta_a(\mathrm{t})$ are white noise of the measurements. g_W is the gravity vector expressed in the world frame.

By assuming the measurement of IMU are constant during the sampling period, and write the acceleration and angular rate are functions of measurements, we get the first-order approximate IMU kinematic incremental function:

$$\begin{aligned} R_{WB}(t+\Delta t) &= R_{WB}(t)exp((\tilde{\omega}_B(\mathrm{t}) - b_g(\mathrm{t}) - \eta_{gd}(\mathrm{t}))\Delta t)^{\wedge} \\ v_{WB}(t+\Delta t) &= v_{WB}(t) + \mathrm{g}_W\Delta t \\ &\quad + R_{WB}(\tilde{a}_B(\mathrm{t}) - b_a(\mathrm{t}) - \eta_{ad}(\mathrm{t}))\Delta t \\ p_{WB}(t+\Delta t) &= p_{WB}(t) + v_{WB}\Delta t + \frac{1}{2}g_W\Delta t^2 \\ &\quad + \frac{1}{2}R_{WB}(\tilde{a}_B(\mathrm{t}) - b_a(\mathrm{t}) - \eta_{ad}(\mathrm{t}))\Delta t^2 \end{aligned} \tag{4}$$

where Δt is data sample rate, the η_{gd} is discrete form of continuous noise η_g, with relationship $\mathrm{cov}(\eta_{gd}) = \frac{1}{\Delta t}\mathrm{cov}(\eta_g)$, the same to η_{ad}. $()^{\wedge}$ is the skew symmetric matrix.

4 Visual-Inertial Fusion

4.1 Simultaneous Localization and Mapping

SLAM (Simultaneous Localization and Mapping) realizes a robot explores in unknown environments and find its position at the same time, which is considered a crown problem for robot navigation.

A detailed survey of the SLAM algorithm is proposed in literature [3], Numbers of works have been done to increase robustness of visual SLAM, and one of them,

fusing IMU data turn out to be a good choice for data fusion to make visual SLAM work better.

4.2 Camera-IMU Calibration and Initialisation

For multi-sensor fusion, the first important determining accuracy is to get a well estimation of the temporal and spatial information of each other sensor [11, 12]. Generally, in UAVs or other robots, CPU get sensors data in streams by fixed rate, and the delay between different sensors results from communication delay and inertial sensor delay introduced by filters or logic. In this lecture, we use the work [9], which proposes a novel algorithm to estimate the time-offset and transpose of sensors using batch, continuous-time, and max-likelihood estimation.

It is pointed out that monocular visual has no observability about scale, and optimization will benefit from a good initial guess of the estimated variable. Thus, we use methods introduced in literature [7], which incorporates IMU data and visual estimated pose to estimate initial value of scale, gravity vector, velocity, and biases.

4.3 Pose Tracking and Optimization

As depicted in Fig. 2, the main idea of fusing IMU and visual data for pose estimation is using IMU data to predict pose of camera frame and using visual measurements to correct it, predicting process can reduce searching area for feature matching and increase accuracy in less features or fast motion environment, while correcting process uses visual measurements to decrease estimation errors. As the data rate of IMU are far faster than camera frame rate, there are numbers of IMU samples between consecutive frames. We introduce preintegration approach descripted in literature [6, 7] which computes incremental motion term ΔR, Δv and Δp in between consecutive frames to avoid re-computation when the estimated pose of frames are changed because of subsequent optimization.

We use IMU preintegration term to predict next frame pose, as described in (5). Where R_{WB}^{i+1}, v_{WB}^{i+1} and p_{WB}^{i+1} are predicted motion of next frame, R_{WB}^{i}, v_{WB}^{i} and p_{WB}^{i} are estimated motion of current frame, $J_{\Delta p}^{g}\mathrm{b}_{g}^{i}, J_{\Delta p}^{a}\mathrm{b}_{a}^{i}$ accounts for the change of biases during computing preintegration.

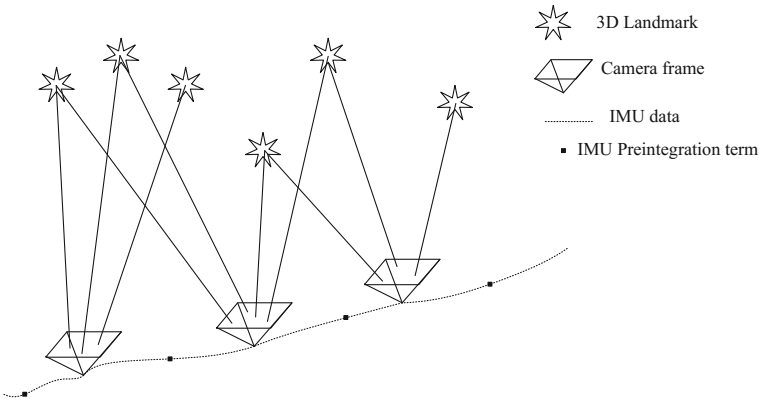

Fig. 2 Evolution of visual-inertial fusion for camera poses tracking and optimization

$$\begin{aligned} R_{WB}^{i+1} &= R_{WB}^{i}\Delta R_{i,i+1}\exp(J_{\Delta R}^{g}\mathrm{b}_{g}^{i})^{\wedge} \\ v_{WB}^{i+1} &= v_{WB}^{i} + g_{W}\Delta t_{i,i+1} \\ &\quad + R_{WB}^{i}(\Delta \mathrm{v}_{i,i+1} + J_{\Delta v}^{g}\mathrm{b}_{g}^{i} + J_{\Delta v}^{a}\mathrm{b}_{a}^{i}) \\ p_{WB}^{i+1} &= p_{WB}^{i} + v_{WB}^{i}\Delta t_{i,i+1} + \frac{1}{2}g_{W}\Delta t_{i,i+1}^{2} \\ &\quad + R_{WB}^{i}(\Delta p_{i,i+1} + J_{\Delta p}^{g}\mathrm{b}_{g}^{i} + J_{\Delta p}^{a}\mathrm{b}_{a}^{i}) \end{aligned} \tag{5}$$

In this way, we get the predicted pose of next frame, By using the predicted motion; we get a fast feature matching and get another estimated pose by visual feature matching and triangulation. Then the estimated poses will be transited to the back end for global bundle adjustment to get more accurate results.

Considering two consecutive frames i, j, the motion of i is well estimated by initialization or optimization, using related IMU data to create preintegration term, we get the predicted motion of frame j. We get optimization function as described in (6)

$$\begin{aligned} \theta &= [\mathrm{R}_{WB}^{j}, \mathrm{p}_{WB}^{j}, \mathrm{v}_{WB}^{j}, \mathrm{b}_{a}^{j}, \mathrm{b}_{g}^{j}] \\ \theta &= \underset{\theta}{\mathrm{argmin}}(\sum E_{proj}(\mathrm{j}) + \mathrm{E}_{IMU}(\mathrm{j})) \end{aligned} \tag{6}$$

where reprojection error term $E_{proj}(\mathrm{j})$ is given by features matching:

$$E_{proj}(\mathrm{j}) = (\mathrm{x} - \mathrm{H}(\mathrm{X}_{C}))^{T}\Sigma_{x}(\mathrm{x} - \mathrm{H}(\mathrm{X}_{C})) \tag{7}$$

where x is the pixel coordinate in the image j of the 3D landmark of which coordinate is X_C in the camera frame. Σ_x is the information matrix associated with the landmark.

The IMU error term $E_{IMU}(j)$ is defined as:

$$\begin{aligned} E(i,j) &= \rho(e_R^T e_v^T e_p^T \Sigma_I (e_R^T e_v^T e_p^T)^T) + \rho(e_b^T \Sigma_R e_b) \\ e_R &= \log(\Delta R_{i,j}(\exp(J_{\Delta R}^g b_g^i)^\wedge)^T R_{BW}^i R_{WB}^j)^\vee \\ e_v &= R_{BW}^i(v_{WB}^j - v_{WB}^i - g_W \Delta t_{i,j}) \\ &\quad - (\Delta v_{i,j} + J_{\Delta v}^g b_g^j + J_{\Delta v}^a b_a^j) \\ e_p &= R_{BW}^i(p_{WB}^j - p_{WB}^i - v_{WB}^i \Delta t_{i,j} - \frac{1}{2} g_W \Delta t_{i,j}^2) \\ &\quad - (\Delta p_{i,j} + J_{\Delta p}^g b_g^j + J_{\Delta p}^a b_a^j) \\ e_b &= b^j - b^i \end{aligned} \tag{8}$$

where Σ_I is the information of preintergation, Σ_R is the information of bias random walk, $()^\vee$ is process function to get the vector of creating corresponding skew matrix. ρ is Huber robust function to decrease the influence of some very large errors in error function. The optimization process can be well solved by g2o library [5].

5 Experiments

In this section, we will introduce the experiments we make to evaluate the visual-inertial algorithms we describe above. Firstly, Camera-IMU calibration is carried on to estimate the pose, time offset between two sensors. Use initialization algorithm to get a good initial guess of the optimized states. To assess the accuracy of the visual-inertial fusion algorithm, we test the algorithm in EuRoc flying dataset [10] and compare the results with state-of-the-art ORBSLAM [4]. Then a real flying experiment is carried on indoor, using our own multi-rotor flying platform. All these experiments will be described in detail below.

5.1 Hardware Overview

We use our own designed flying platform to make algorithm tests as depicted in Fig. 3. Some parameters of the platform related to this work is that we use a global shutter UI122xLE-C camera whose frame rate is set to 30 Hz, and an Xsens MTI100 IMU with 200 Hz data rate. We use Intel NUC6i7KYK as on-board computing unit with 4-core 3.5Ghz CPU, 16 GB RAM and 128 GB SSD. Calibration and initialization of camera-IMU are performed using the approaches in literature [9], with results of mean reprojection error 0.245 pixel, and a scale recovery accuracy of 0.988.

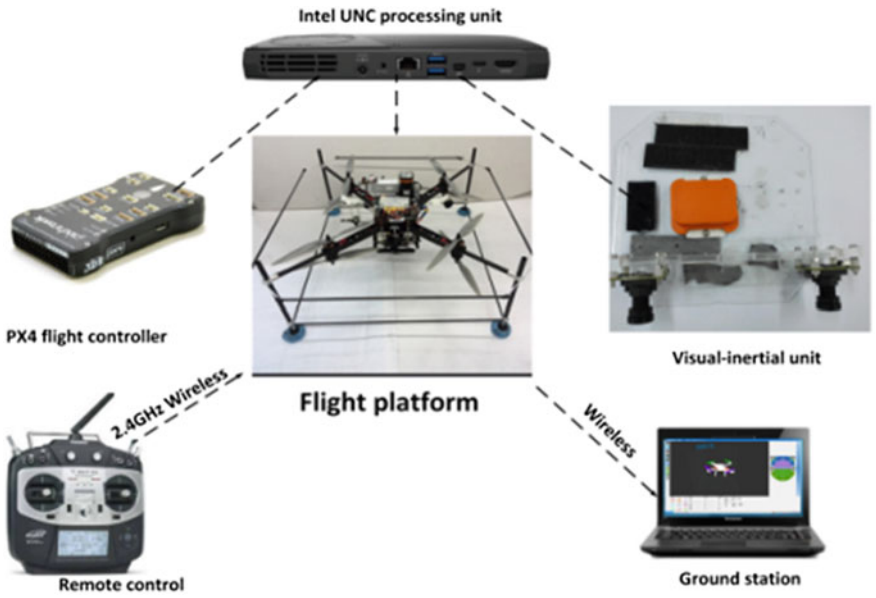

Fig. 3 Flying platform we use to evaluate the visual-inertial algorithm. EuRoC dataset experiment

We test our visual-inertial fusion method in EuRoC flying datasets with groundtruth to access states accuracy, and compare the results with ORBSLAM which is the state of art visual navigation approach. Firstly, we consider the influence of estimated scales, as depicted in Fig. 4, although the shape of trajectory estimated by ORBSLAM is similar to the groundtruth trajectory, the size of it is far from fitting to the groundtruth because monocular visual is ambiguous to metric scale. While the trajectory estimated by our visual-inertial fusion method fits the grountruth well, as we data from IMU can recover the metric scale for monocular.

Next, In order to compare the pose estimation accuracy, we ignore the influence of scale by using the similarity transformation introduced by literature [8] to compute the optimal scale to fit the gorundtruth. The results are depicted in Fig. 5. We find that, in smoothing motion condition, the two methods act exactly the same, as visual can give detailed information of the environment; but in fast motion, fuzzy images and little transition will increase estimation error by sole visual approach, and our visual-inertial method acts better as we use IMU to predict the rotation of the camera, which increase the robustness of estimated algorithms.

5.2 Real Time UAV Flying Experiment

After evaluating performances using flying datasets, we implemented our method in our own designed flying platform and carried on real experiments in indoor

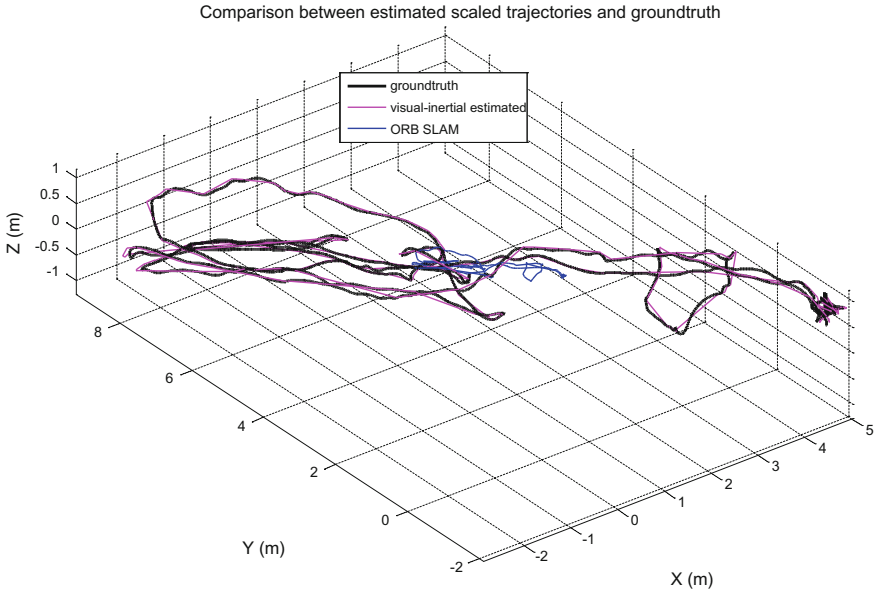

Fig. 4 Comparison between trajectories estimated by our method, state-of-art ORBSLAM and the EuRoC grountruth

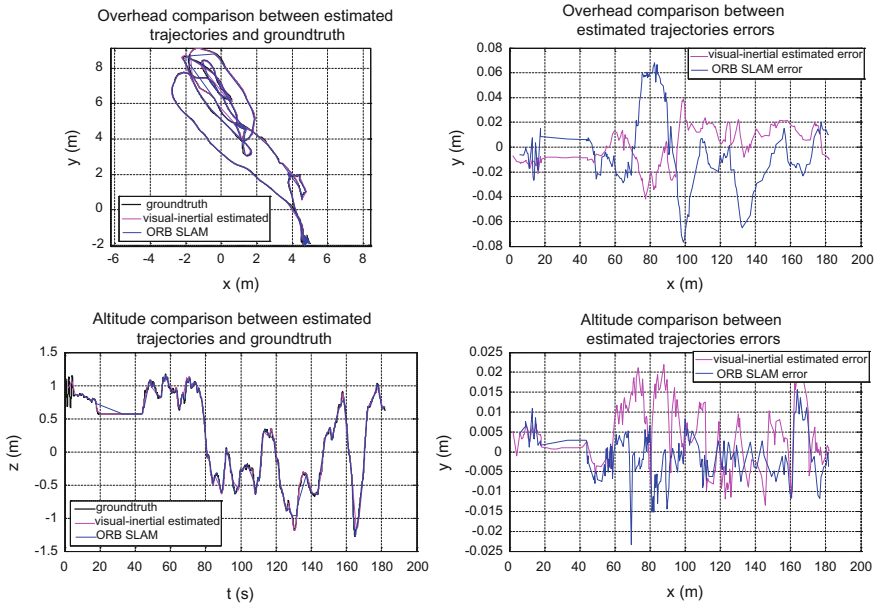

Fig. 5 Comparison of pose estimated accuracy by our visual-inertial method and the state-of-art monocular ORBSLAM ignoring the influence of scale

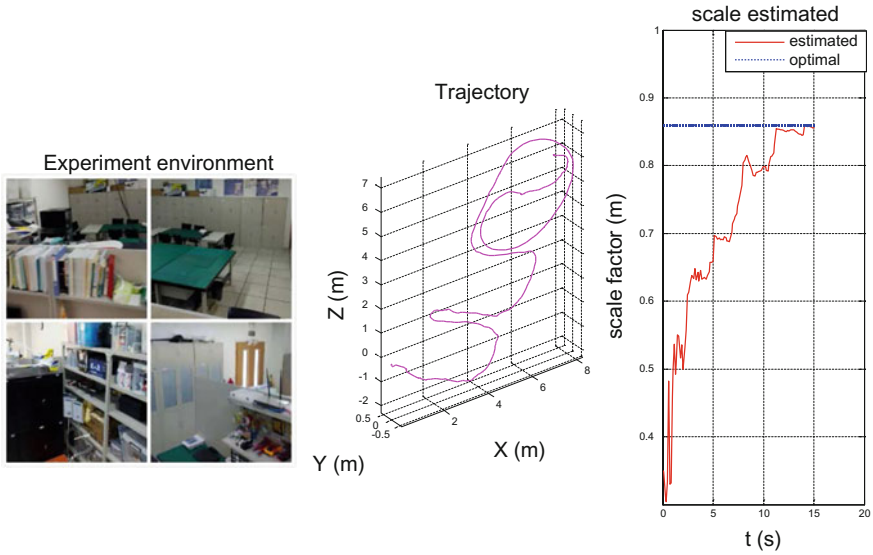

Fig. 6 Environment, trajectory and scale estimation results of real indoor flying

environment, the results depicted in Fig. 6 show that the method we proposed can give accurate state estimation to satisfy the need of UAVs navigation.

6 Conclusions

We proposed a visual-inertial fusion and nonlinear optimization approach for UAVs navigation, the detailed theory is discussed in this paper. The results compared to the state-of-the-art visual SLAM approach show that fusing IMU data can increase the robustness of the algorithms, and real flying experiments indicate that the proposed method can give an accurate state estimation for UAVs navigation.

References

1. Kendoul F (2012) Survey of advances in guidance, navigation, and control of unmanned rotorcraft systems. J Field Robot 29(2):315–378
2. Cadena C, Carlone L, Carrillo H et al (2016) Past, present, and future of simultaneous localization and mapping: toward the robust-perception age. IEEE Trans Rob 32(6):1309–1332
3. Donavanik D, Hardtstremayr A, Gremillion G, et al (2016) Multi-sensor fusion techniques for state estimation of micro air vehicles. SPIE Defense + Security 98361
4. Murartal R, Tardos JD (2016) ORB-SLAM2: an open-source SLAM system for monocular, stereo and RGB-D cameras

5. Strasdat H (2011) g2o: a general framework for graph optimization. PLoS ONE 7(8):e43478
6. Forster C, Carlone L, Dellaert F, et al. (2016) On-manifold preintegration for real-time visual–inertial odometry. IEEE Trans Robot 99:1–21
7. Mur-Artal R, Tardós JD (2017) Visual-inertial monocular SLAM with map reuse. IEEE Robot Autom Lett 2(2):796–803
8. Horn BKP (1987) Closed-form solution of absolute orientation using unit quaternions. J Opt Soc Am A 4(4):629–642
9. Furgale P, Rehder J, Siegwart R (2014) Unified temporal and spatial calibration for multi-sensor systems. In: IEEE/RSJ international conference on intelligent robots and systems. IEEE, 2014, pp 1280–1286
10. Burri M, Nikolic J, Gohl P et al (2016) The EuRoC micro aerial vehicle datasets. Int J Robot Res 35(10):1157–1163
11. Kelly J, Sukhatme GS (2011) Visual-inertial sensor fusion: localization, mapping and sensor-to-sensor self-calibration. Sage Publications, Inc.
12. Shen S, Michael N, Kumar V (2015) Tightly-coupled monocular visual-inertial fusion for autonomous flight of rotorcraft MAVs. In: IEEE international conference on robotics and automation. IEEE, 2015, pp 5303–5310

Model and Attitude Control of a Miniature Hybrid Autogyro

Ziwei Song, Zhihao Cai, Kunpeng Li, Jiang Zhao and Ningjun Liu

1 Introduction

Hybrid layout UAV is a new direction of the future development of UAV, which has several flight patterns and is different from the traditional aircraft. This kind of UAV has the abilities of both short takeoff and landing and cruising on high speed through the conversion between different flight patterns.

As we know, autogyro can fly at very low speeds, and have good short takeoff and landing (STOL) performance [1]. But at the same time, the rotor structure is also limited its flight performance in high-speed regimes. During high-speed flight, high autorotation speeds cause such problems as retreating blade stall, blade tip shock waves and excess vibration, similar to those experienced in helicopters [2]. A way of improving the autogyro's high-speed flight performance is to use a hybrid autogyro configuration, in which fixed wings are added to the autogyro. At low flight speeds, the rotor provides most of the lift, thus retaining the autogyro's STOL performance. At high flight speeds, some of the lift is generated by the fixed wings, and rotor load is reduced [3].

In short, the hybrid autogyro has excellent overall performance. However, domestic and foreign research on such hybrid autogyro is rare, the study of its flight control is rarely reported. In this paper, for the strong coupling, nonlinear and time-varying characteristics of the system, we designed attitude controller based on back-stepping strategy.

Z. Song (✉) · Z. Cai (✉) · K. Li · J. Zhao · N. Liu
School of Automation Science and Electrical Engineering, Beihang University, 100191 Beijing, China
e-mail: szwer1015@163.com

Z. Cai
e-mail: czh@buaa.edu.cn

Z. Deng (ed.), *Proceedings of 2017 Chinese Intelligent Automation Conference*,
Lecture Notes in Electrical Engineering 458,
https://doi.org/10.1007/978-981-10-6445-6_82

2 Aircraft Dynamics Modelling

2.1 The Structure of the Hybrid Autogyro

The hybrid autogyro is built based on a Hobbyking Super-G RC autogyro. Wings from an RC glider are attached to the autogyro's fuselage, as shown in Fig. 1.

The main structure to obtain the lift of the hybrid autogyro is the non-powered rotating rotor (relies on the relative flow of the rotor to rotate the rotor, which is different from the way of the helicopter to drive the rotor) and the wing. The rotating rotor also could be tilted left and right for roll control. Pitch and yaw controls are achieved via the elevator and rudder. At this stage, the role of the wing is only to provide lift, using aileron for hybrid control does not be involved [4].

The establishment of a reasonable and accurate mathematical model is the basis for the design of the control law. In the paper, the rotor model, the fixed-wing model are estimated respectively, and then we can get the motion equation of the UAV. Aircraft parameters are shown in Table 1.

2.2 Establish the Mathematical Model for the Hybrid Autogyro

In the paper, we use the model structure shown in Fig. 2, calculate the force and moment of each part separately and the aerodynamic interference between the various parts should be considered.

Fig. 1 Hybrid autogyro

Table 1 Parameters of the aircraft

Parameters	Value	Unit
Mass	1.823	kg
Length	1.223	m
Rotor diameter	1.08	m
Blade length	0.518	m
Blade chord length	0.05	m
Wing span	0.74	m
Wing chord length	0.11	m
Horizontal tail area	0.08	m^2
Vertical tail area	0.075	m^2
I_x	0.0646	kg m^2
I_y	0.134	kg m^2
I_z	0.1265	kg m^2
I_{xz}	−0.017	kg m^2

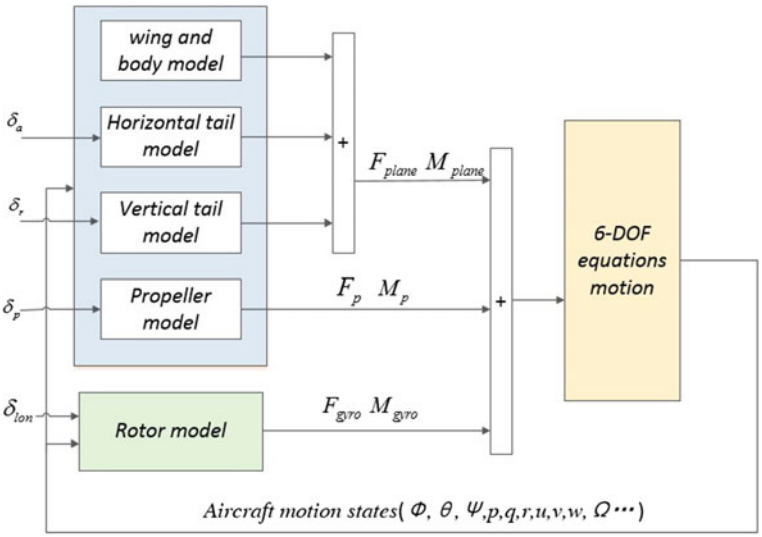

Fig. 2 Aircraft dynamics model structure

2.2.1 Rotor Model

When the hybrid autogyro flies forward, the paddle tilt backward, the flow relative to the UAV flow from the bottom up to the paddle, shown in Fig. 3.

In the diagram, α_R is the angle of the plane of the rotor. In order to establish the mathematical model of the rotor, we first use the leaf element theory to analyse the rotor's dynamics characteristic. The coordinate system used in this paper is

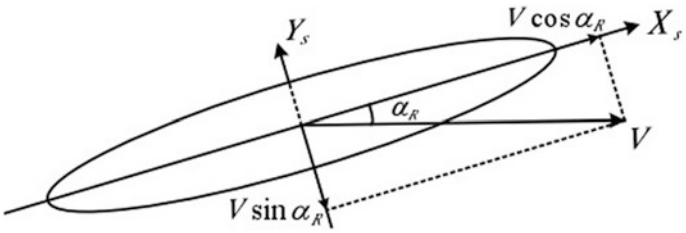

Fig. 3 Relative flow to the rotor when the aircraft flies forward

American coordinate system, and then we can get the force and moment of the rotor in the body coordinate system [5, 6].

$$\begin{cases} F_{xb-gyro} = -H\cos(\alpha_{1s}+\alpha_0) - T\sin(\alpha_{1s}+\alpha_0) \\ F_{yb-gyro} = T\sin b_{1s} - H\sin\beta \\ F_{zb-gyro} = -T\cos(\alpha_{1s}+\alpha_0) + H\sin(\alpha_{1s}+\alpha_0) \\ L_{gyro} = (T\sin b_{1s} - H\sin\beta)l_z + Q\sin(\alpha_{1s}+\alpha_0) \\ \qquad + [-T\cos(\alpha_{1s}+\alpha_0) + H\sin(\alpha_{1s}+\alpha_0)]l_y \\ M_{gyro} = (-H\cos(\alpha_{1s}+\alpha_0) - T\sin(\alpha_{1s}+\alpha_0))l_z \\ \qquad -(-T\cos(\alpha_{1s}+\alpha_0) + H\sin(\alpha_{1s}+\alpha_0))l_x - Q\sin b_{1s} \\ N_{gyro} = (T\sin b_{1s} - H\sin\beta)l_x - (-H\cos(\alpha_{1s}+\alpha_0) \\ \qquad -T\sin(\alpha_{1s}+\alpha_0))l_y + Q\cos(\alpha_{1s}+\alpha_0)cosb_{1s} \end{cases} \tag{1}$$

In the Eq. (1), T, H, Q are the lift force, the horizontal force and the anti-torque produced by the rotor, shown in Eq. (2). α_0 is the initial chamfering angles of the rotor paddle; α_{1s}, b_{1s} are the rotor longitudinal paddle inclination and horizontal paddle inclination, respectively. l_x, l_y, l_z is the coordinate of the center of the rotor paddle in the body coordinate system.

$$\begin{aligned} T &= C_T\rho S_{rotor}(\Omega R)^2 \\ H &= C_H\rho S_{rotor}(\Omega R)^2 \\ Q &= C_Q\rho S_{rotor}(\Omega R)^2 R \end{aligned} \tag{2}$$

The rotor speed can also reflect the flight status of the aircraft, so we also take the rotor speed as a state, the dynamic equation of the rotor rotation is:

$$\dot{\Omega} = -Q/J_{rotor} \tag{3}$$

2.2.2 Fixed-Wing Model

The fixed-wing part of the hybrid autogyro is essentially a fixed-wing aircraft, and can be modelled using well-established methods [7]. The forces and moments (in the aircraft body axes) of the entire fixed-wing part of the hybrid autogyro are:

$$\begin{aligned}
\begin{bmatrix} F_{x_fw} \\ F_{y_fw} \\ F_{z_fw} \end{bmatrix} &= \begin{bmatrix} C_{x_b} \\ C_{y_b} \\ C_{z_b} \end{bmatrix} q_b S_b + R_{b/a} \begin{bmatrix} C_{x_w} \\ C_{y_w} \\ C_{z_w} \end{bmatrix} q_w S_w \\
&\quad + R_{b/ht} \begin{bmatrix} -C_{x_\delta_e} \\ 0 \\ C_{y_\delta_e} \end{bmatrix} S_{ht} q_{ht} + R_{b/vt} \begin{bmatrix} -(C_{d_vt} + C_d^{\delta_r}) \\ C_{l_vt} + C_l^{\delta_r} \\ 0 \end{bmatrix} S_{vt} q_{vt} \\
\begin{bmatrix} L_{fw} \\ M_{fw} \\ N_{fw} \end{bmatrix} &= \begin{bmatrix} C_{L_b} \\ C_{N_b} \\ C_{M_b} \end{bmatrix} q_b S_b l_b + \begin{bmatrix} C_{L_w} \\ C_{N_w} \\ C_{M_w} \end{bmatrix} q_w S_w c_w \\
&\quad + \begin{bmatrix} 0 & -z_{ht} & y_{ht} \\ z_{ht} & 0 & -x_{ht} \\ -y_{ht} & x_{ht} & 0 \end{bmatrix} \begin{bmatrix} X_{ht} \\ Y_{ht} \\ Z_{ht} \end{bmatrix} + \begin{bmatrix} 0 & -z_{vt} & y_{vt} \\ z_{vt} & 0 & -x_{vt} \\ -y_{vt} & x_{vt} & 0 \end{bmatrix} \begin{bmatrix} X_{vt} \\ Y_{vt} \\ Z_{vt} \end{bmatrix}
\end{aligned} \tag{4}$$

The left side of the formula represents the force and moment provided by the body, wing, Horizontal tail, vertical tail of the aircraft in the body coordinate system.

The aircraft's kinetic equation vector is described below:

$$\begin{aligned}
\dot{V}_b &= -\omega_{b/n}^b \times V_b + \frac{F_b}{m} + \frac{F_{b,g}}{m} \\
\dot{\omega}_{b/n}^b &= J^{-1}\left[M_b - \omega_{b/n}^b \times \left(J\omega_{b/n}^b\right)\right]
\end{aligned} \tag{5}$$

$$\begin{cases} F_b = F_{gyro} + F_{fw} + F_{pr} \\ M_b = M_{gyro} + M_{fw} + M_{pr} \end{cases} \quad F_{b,g} = \begin{bmatrix} -mgs_\theta \\ mgs_\phi c_\theta \\ mgc_\phi c_\theta \end{bmatrix} \tag{6}$$

3 Attitude Control by Back-Stepping

As a result of the hybrid autogyro model is a strong nonlinear system, we tried PID method, but did not reach the ideal effect. So this paper uses nonlinear control method back-stepping control strategy to design attitude controller and perform the simulation analysis. Back stepping control has the ability of dealing with

mismatched, uncertainties, nonlinear systems [8]. It already showed a great deal of flexibility and superior performance in the design of the robust control of uncertain systems and adaptive control.

In order to use the back-stepping method to control the design, the model of the hybrid autogyro represented by Eq. (5) will be simplified, expressed as a strict feedback form attitude subsystem as shown below:

$$\begin{cases} I_x\ddot{\phi} = \dot{\theta}\dot{\psi}(I_y - I_x) + I_{zx}(\ddot{\psi} + \dot{\theta}\dot{\phi}) + U_2 \\ I_y\ddot{\theta} = \dot{\phi}\dot{\psi}(I_z - I_x) + I_{zx}(\dot{\psi}^2 - \dot{\theta}^2) + U_3 \\ I_z\ddot{\psi} = \dot{\phi}\dot{\theta}(I_x - I_y) + I_{zx}(\ddot{\theta} - \dot{\phi}\dot{\psi}) + U_4 \end{cases} \tag{7}$$

U_2 (roll), U_3 (pitch), U_4 (yaw) are the control variables of three channels. U_1 is the control variable of throttle [9]. By keeping the speed of the aircraft at trim, the throttle control variable U_1 can be obtained. In order to calculate U_2,U_3, U_4, suppose:

$$x_1 = \phi, x_2 = \dot{x}_1 = \dot{\phi}, x_3 = \theta, x_4 = \dot{x}_3 = \dot{\theta}, x_5 = \psi, x_6 = \dot{x}_5 = \dot{\psi},$$
$$x_7 = \dot{x}_4 = \ddot{\theta}, x_8 = \dot{x}_6 = \ddot{\psi}$$

We can get:

$$S_1 : \begin{cases} \dot{x}_1 = x_2 \\ \dot{x}_2 = x_4x_5a_1 + (x_8 + x_2x_4)a_4 + b_1u_2 \\ \dot{x}_3 = x_4 \\ \dot{x}_4 = x_2x_6a_2 + (x_6^2 - x_2^2)a_5 + b_2u_3 \\ \dot{x}_5 = x_6 \\ \dot{x}_6 = x_2x_4a_3 + (x_7 - x_4x_6)a_6 + b_3u_4 \end{cases} \tag{8}$$

where:

$$a_1 = \frac{I_y - I_z}{I_x}, a_2 = \frac{I_z - I_x}{I_y}, a_3 = \frac{I_x - I_y}{I_z}, a_4 = \frac{I_{zx}}{I_x}, a_5 = \frac{I_{zx}}{I_y},$$
$$a_6 = \frac{I_{zx}}{I_z}, b_1 = \frac{1}{I_x}, b_2 = \frac{1}{I_y}, b_3 = \frac{1}{I_z}$$

The first step: define error variable $z_1 = x_{1d} - x_1$, then:

$$\dot{z}_1 = \dot{x}_{1d} - \dot{x}_1 = \dot{x}_{1d} - x_2 \tag{9}$$

Choose Lyapunov function:

$$\dot{V}(z_1) = z_1\dot{z}_1 = z_1(\dot{x}_{1d} - x_2) \tag{10}$$

To stabilize z_1, x_2 is considered a virtual input, express by v_1:

$$v_1 = \dot{x}_{1d} + \alpha_1 z_1 \quad \alpha_1 > 0 \tag{11}$$

Define the error variable: $z_2 = x_2 - v_1$, then:

$$\dot{V}(z_1) = z_1\dot{z}_1 = z_1(\dot{x}_{1d} - x_2) = z_1(\dot{x}_{1d} - z_2 - v_1) = -z_1 z_2 - \alpha_1 z_1^2 \tag{12}$$

The coupling part $-z_1 z_2$ will be elimination in the second step.
The second step:

$$z_2 = x_2 - v_1 = x_2 - \dot{x}_{1d} - \alpha_1 z_1 \tag{13}$$

We can get:

$$\dot{z}_1 = -\alpha_1 z_1 - z_2 \tag{14}$$

$$z_2 = x_2 - \dot{x}_{1d} - \alpha_1 z_1 = x_4 x_6 a_1 + (x_8 + x_2 x_4)a_4 + b_1 u_2 - x_{1d} - \alpha_1(-\alpha_1 z_1 - z_2) \tag{15}$$

Choose Lyapunov function:

$$V(z_1, z_2) = V(z_1) + \frac{1}{2} z_2^2 \tag{16}$$

$$\begin{aligned} \dot{V}(z_1, z_2) &= z_1\dot{z}_1 + z_2\dot{z}_2 = -z_1 z_2 - \alpha_1 z_1^2 + z_2[x_4 x_6 a_1 + (x_8 + x_2 x_4)a_4 \\ &\quad + b_1 u_2 - \ddot{x}_{1d} - \alpha_1(-\alpha_1 z_1 - z_2)] \\ &= -\alpha_1 z_1^2 + z_2[-z_1 + x_4 x_6 a_1 + (x_8 + x_2 x_4)a_4 \\ &\quad + b_1 u_2 - \ddot{x}_{1d} - \alpha_1(-\alpha_1 z_1 - z_2)] \end{aligned} \tag{17}$$

We can design u_2 to make $\dot{V}(z_1, z_2) < 0$:

$$u_2 = \frac{1}{b_1}[-\alpha_2 z_2 + z_1 - x_4 x_6 a_1 - (x_8 + x_2 x_4)a_4 + \ddot{x}_{1d} - \alpha_1(\alpha_1 z_1 + z_2)] \quad \alpha_2 > 0 \tag{18}$$

Could make:

$$V(z_1, z_2) = -\alpha_1 z_1^2 - \alpha_2 z_2^2 < 0$$

In the same way, we can get:

$$\begin{aligned} u_3 &= \frac{1}{b_2}\left[-\alpha_4 z_4 + z_3 - x_2 x_6 a_2 - (x_6^2 - x_2^2)a_5 + \ddot{x}_{3d} - \alpha_3(\alpha_3 z_3 + z_4)\right] \\ u_4 &= \frac{1}{b_3}\left[-\alpha_6 z_6 + z_5 - x_2 x_4 a_3 - (x_7 - x_4 x_6)a_6 + \ddot{x}_{5d} - \alpha_5(\alpha_5 z_5 + z_6)\right] \end{aligned} \tag{19}$$

4 Simulation and Result Analysis

Give each channel 5°, 10°, −5° step input signal separately, get the response curves as shown in Fig. 4:

It can be seen that the response time of around 0.6 s for θ and 0.4 s for ψ, but the response time of ϕ is a little bigger. Overshoot is not apparent and the steady state error $e_{ss} = 0$ for each channel.

Next, in order to verify that the controller we designed can achieve the desired control effect near the actual flight, we enter the input signal in the actual manual flight test into the simulation model, and each channel's respond as shown in Fig. 5.

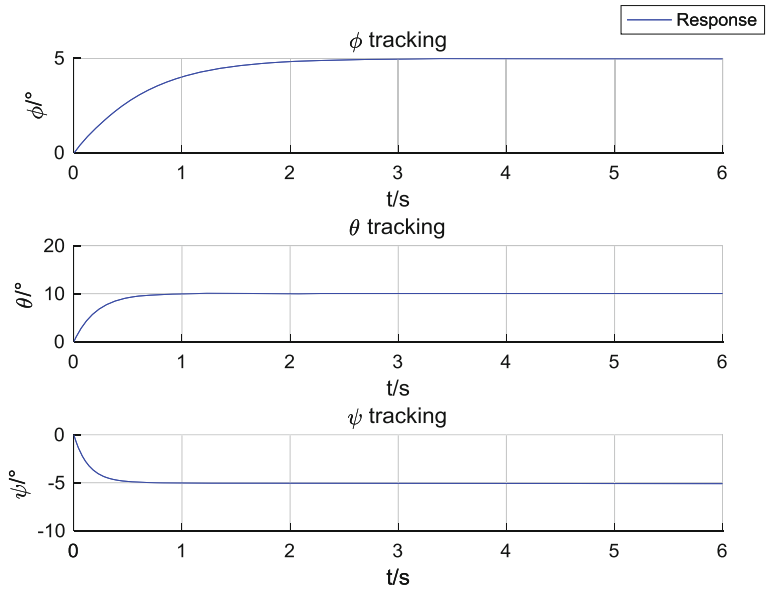

Fig. 4 Step response curve of back-stepping control

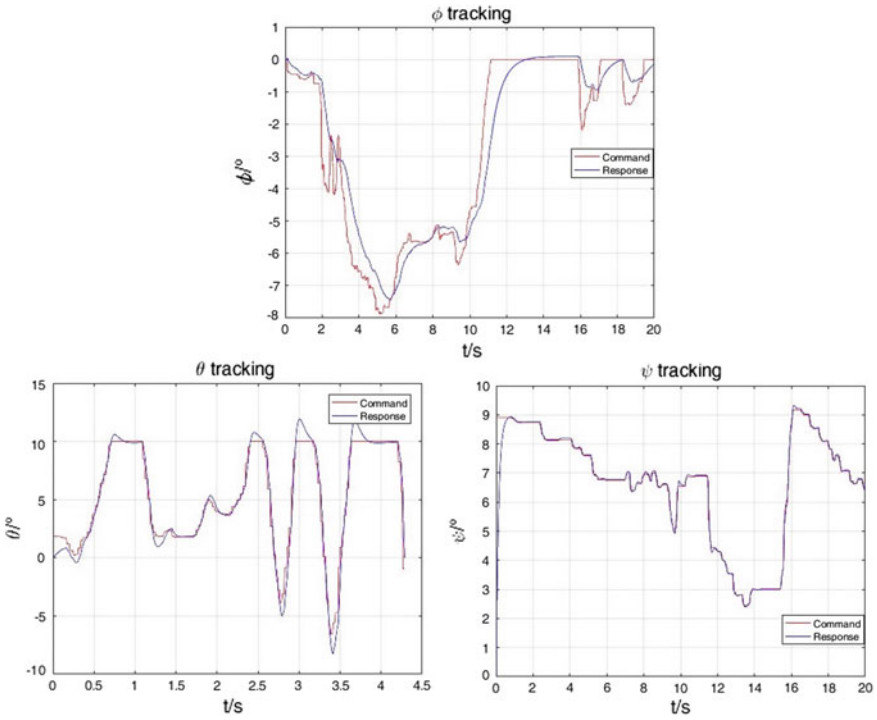

Fig. 5 Roll, pitch and yaw angle tracking curves

The first figure is the roll angle response curve, it can be seen that the controller can successfully track desired roll angles, although it has a command response delay of about 0.5 s. The reason of the response delay should be the adjusting time of ϕ is a little bigger. It may because the relationship between the control amount of roll U_2 to rotating rotor tilted angle does not accurately reflect the actual situation of the aircraft.

For the pitch and roll channel, we can see the response speed in both curves is very fast and there is no steady-state error or θ response delay, the controller can successfully track desired attitude angles. Compared to the simulation results, the pitch channel has a little overshoot, the parameter of this channel should be improved.

5 Conclusion

In this paper, we focus on the hybrid autogyro, which is a newer type UAV rather than the common UAV. Because the model is more complex, involving the coupling of rotor and fixed-wing, so the modeling encountered a relatively large

difficulty. Finally we use back-stepping control method to design the attitude controller. The controller can successfully control the hybrid autogyro's roll, pitch and yaw angles. Tracking is quick and largely satisfactory, with good stability. There are also some problems in the model and the controller, such as the function between control amount and rotating rotor tilted angle should be improved and the anti-interference ability for the model is poor. So these are the direction of our efforts in the future.

References

1. Leishman JG (2004) Development of the autogiro: a technical perspective. J Aircr 41(4): 765–781
2. Prouty RW (2003) Helicopter performance, stability, and control, chapters 1–3. Krieger, London
3. Lin Q (2016) Multi-mode flight control for hybrid V/STOL unmanned aerial vehicle with rotor and wing. PhD Dissertation, School of Automation Science and Electric Engineering, Beihang University, Beijing (in Chinese)
4. Yan K (2016) Research on flight control for hybrid gyroplane UAV. Master's Thesis, School of Automation Science and Electric Engineering, Beihang University, Beijing (in Chinese)
5. Lopez CA, Wells VL (2004) Dynamics and stability of an autorotating rotor/wing unmanned aircraft. J Guid Control Dyn 27(2):258–270
6. Mettler B (2003) Identification modeling and characteristics of miniature rotorcraft. Kluwer Academic Publisher
7. Etkin B, Reid LD (1995) Dynamics of flight: stability and control, 3rd edn. John Wiley & Sons, Hoboken, Chapters 2–6
8. Mian AA (2008) Modeling and backstepping-based nonlinear control strategy for a 6 DOF quadrotor helicopter. Chin J Aerinautics 03:261–268
9. Das A, Lewis F, Subbarao K (2009) Backstepping approach for controlling a quadrotor using lagrange form dynamics. J Intell Rob Syst 56(1–2):127–151

Receding Horizon Control for Lateral Collision Avoidance of Intelligent Vehicles

Siyu Lin, Zhiyuan Liu and Songyan Wang

1 Introduction

The increase of the car ownership makes the traffic safety problem even more prominent. The lateral collision of the urban traffic accidents account for up to 27%, which is one of the main types of accidents [1]. Therefore, in recent years, the vehicle lateral collision avoidance problem has been paid more attention and many people have done a lot of researches. In the literature [2], a predictive control method based on the robust model for host vehicle is given in the absence of the control of the other vehicles and without communication between the vehicles. In the literature [3], the changes of the vehicle speed are extracted from the Event Data Recorder (EDR) of the accident vehicle, and the vehicle collision model is constructed and introduced into the I-ADAS to enable lateral collision warning or automatic avoidance function. References [4, 5] propose the vehicle collision avoidance system based on the vehicle and the infrastructure integration. The literature [6, 7] based on DSRC do the research for collision avoidance algorithm.

This paper presents an algorithm using the receding horizon control strategy to achieve the lateral collision avoidance. The structure of this paper is: in the second section, the paper proposes the lateral collision prediction algorithm obtained by the coordinate transformation and the trajectory prediction. In the third section, the paper introduces the receding horizon control algorithm to avoid the coming collision. In the fourth section, we gives the simulation results of this method.

S. Lin (✉) · Z. Liu · S. Wang
Department of Control Science and Engineering, Harbin Institute of Technology, Harbin, Heilongjiang, China
e-mail: linsiyu_hit@163.com

Z. Deng (ed.), *Proceedings of 2017 Chinese Intelligent Automation Conference*, Lecture Notes in Electrical Engineering 458,
https://doi.org/10.1007/978-981-10-6445-6_83

2 Predictive Algorithm for Lateral Collision of Vehicles

At present, the vehicles' lateral collision avoidance control strategy can be attributed to three categories. The first is to prevent collisions by emergency braking when it is about to crash [6, 8]. The second is to predict the possibility of collision in the future position, by way of early deceleration to avoid it [2, 4]. Unlike the second category, the third category avoids the collision through deceleration and steering [7, 9]. The first strategy is relatively simple to implement for the driver of the mandatory intervention conditions. The second strategy can take into account the driving safety and driving comfort. The driving operation of the second strategy is similar to the operation of the drivers, but it is necessary to predict the trajectory of the other vehicle. The third can be adapted to a more complex driving environment, but it is difficult to achieve. The second type take into account the feasibility and control performance, so we choose the second strategy. To predict the other vehicles' trajectory, we assume that the host vehicle loads the millimeter-wave radar and GPS, the other vehicles load GPS. And the other vehicles transmit its location and driving direction to the host vehicle through V2V.

The location of the host vehicle and the other vehicles are shown in Fig. 1.

The centroids of the host vehicle and the other vehicle are defined as the origins of the coordinate. The x-axis is the driving direction of the vehicle, the y-axis is perpendicular to the x-axis and it points to the drivers' side. Then, the host vehicle and the other vehicle coordinate systems are established. The relative distance S between the two vehicles and the angle α between the other vehicle and the x-axis of the host vehicle are measured by the host vehicle's radar. The translational relationship between the two vehicle coordinate systems is obtained. The origin of the other vehicle relative to the host vehicle coordinate system is (x_2, y_2).

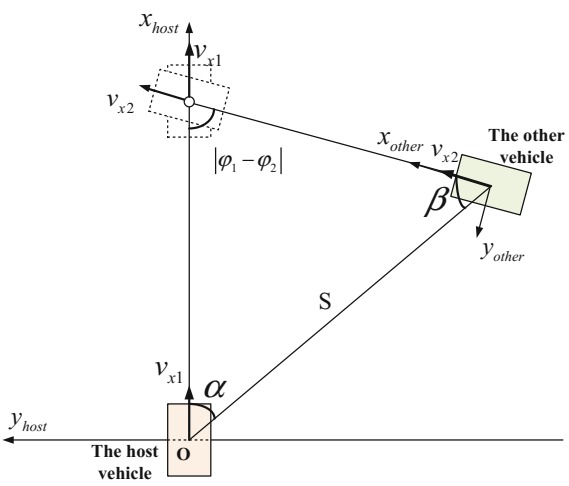

Fig. 1 The coordinate location of the two vehicles

$$\begin{cases} x_2 = S\cos\alpha \\ y_2 = -S\sin\alpha \end{cases} \tag{1}$$

The coordinate relationship between the two vehicles is determined by the GPS positioning direction. The x-axis direction of the host vehicle and the other vehicle are φ_1, φ_2 got by their loaded GPS [10]. The angle between their x-axis is $\theta = |\varphi_1 - \varphi_2|$. We can get the angle of the host vehicle relative to the x-axis of the other vehicle.

$$\beta = \pi - \alpha - \theta = \pi - \alpha - |\varphi_1 - \varphi_2| \tag{2}$$

Since the other vehicle transmits the longitudinal speed of it through V2V, it is necessary to convert the speed of the other vehicle to the host vehicle coordinate system in order to predict its trajectory relative to the host vehicle. We assume that v_{x2} is the longitudinal velocity of the other vehicle in its own coordinate system and v'_{x2}, v'_{y2} are the speed components of v_{x2} along the x-axis and the y-axis.

$$\begin{bmatrix} v'_{x2} \\ v'_{y2} \end{bmatrix} = \begin{bmatrix} \cos\theta & -\sin\theta \\ \sin\theta & \cos\theta \end{bmatrix} \begin{bmatrix} v_{x2} \\ 0 \end{bmatrix} \tag{3}$$

The other vehicle speed is converted into the speed in the host vehicle coordinate through (3) and we assume it's unchanged in the prediction horizon. Then we can get the other vehicle's motion equation in the host vehicle coordinate system.

$$\begin{cases} x_2(k+1) = x_2(k) + v'_{x2}(k)T \\ y_2(k+1) = y_2(k) + v'_{y2}(k)T \end{cases} \tag{4}$$

The host vehicle's motion equation is as follow.

$$\begin{cases} x_1(k+1) = x_1(k) + v_{x1}(k)T \\ y_1(k+1) = y_1(k) \end{cases} \tag{5}$$

where T is the sampling period, v_{x1} is the speed of the host vehicle. As the speed of the other vehicle at k + 1 is relevant to $\alpha(k+1)$ and $\beta(k+1)$, we can calculate these two angles at any time from Fig. 1.

$$\begin{aligned} \alpha(k+1) &= arctan\frac{|y_2(k) - y_1(k)|}{|x_2(k) - x_1(k)|} \\ \beta(k+1) &= arctan\frac{|x_2(k) - x_1(k)|}{|y_2(k) - y_1(k)|} + \frac{\pi}{2} - |\varphi_1 - \varphi_2| \end{aligned} \tag{6}$$

According to (4)–(6), the distance at $0 \le i \le T_p$ (T_p is the prediction horizon) between the center of mass of the two vehicles is:

$$\Delta S(k+i) = \sqrt{[(x_1(k+i) - x_2(k+i)]^2 + [(y_1(k+i) - y_2(k+i)]^2} \tag{7}$$

We compare the distance between the vehicles $\Delta S(k+i)$ with the safe distance S_{def}. If $\Delta S(k+i) \geq S_{def}$ $(0 \leq i \leq T_p)$, there is no collision in the prediction horizon, or the collision will occur. If these two vehicles do not collide in the prediction horizon, there is no need to control the speed of the host vehicle. If two vehicles will collide in the prediction horizon, the longitudinal speed of the host vehicle need to be adjusted to avoid the coming collision.

3 Receding Horizon Control Algorithm

If two vehicles are predicted to have a collision according to the method given in Sect. 2, the host vehicle speed should be adjusted for collision avoidance. This section discusses the purpose of adjusting the longitudinal speed of the host vehicle based on the receding horizon control strategy to realize the collision avoidance. Since there is a speed item of the host vehicle to be adjusted in (5), it is necessary to predict the speed of the host vehicle. In this regard, considering the following longitudinal dynamic equation of the host vehicle.

$$m\dot{v}_x = \frac{T}{R} - F_{aero} - F_r - F_s \tag{8}$$

where, m is the mass of the host vehicle, T is the total torque of the host vehicle, R is the wheel radius, v_x is the longitudinal velocity of the center of mass. F_{aero} is the host vehicle's air resistance and F_r is the host vehicle's rolling resistance. We can get:

$$\dot{v}_x = \frac{T}{mR} - \frac{\rho C_d A_F v_x^2}{2m} - [f_{R0} + f_{R1}\frac{v_x}{100} + f_{R2}(\frac{v_x}{100})^4]g \tag{9}$$

The sampling interval is $\Delta T = 0.05$ s. The torque T is the control quantity and the longitudinal velocity of the host vehicle v_x is the state quantity. Then, we have: $u = T$, $v = v_x$. We Taylor expand formula (9) at point v_x (k) and collate to get:

$$\begin{aligned} v(k+1) = \{1 - [(&\frac{\rho C_d A_F x^*}{m} + \frac{f_{R1} g}{100} + \frac{4 f_{R2} g (x^*)^3}{100^4})\Delta T]\}v(k) + \frac{\Delta T u(k)}{mR} \\ &+ (\frac{\rho C_d A_F (x^*)^2}{2m} + \frac{3 f_{R2} g (x^*)^4}{100^4} - f_{R0} g)\Delta T \end{aligned} \tag{10}$$

We define: $\Delta v(k) = v(k) - v(k-1)$, $\Delta u(k) = u(k) - u(k-1)$. Then (10) can be written in the form of the following incremental model.

$$\Delta v(k+1) = A\Delta v(k) + B\Delta u(k) \tag{11}$$

where, $A = 1 - [(\frac{\rho C_d A_F x^*}{m} + \frac{f_{R1} g}{100} + \frac{4 f_{R2} g (x^*)^3}{100^4})\Delta T]$, $B = \frac{\Delta T}{mR}$.

Based on formula (11), the host vehicle speed prediction model can be obtained.

$$\Delta V(k+1|k) = S_v(k)\Delta v(k) + S_u(k)\Delta U(k) \tag{12}$$

where,

$$\Delta V(k+1|k) = [\,\Delta v(k+1|k) \quad \Delta v(k+2|k) \quad \cdots \quad \Delta v(k+p|k)\,]^T$$
$$\Delta U(k) = [\,\Delta u(k) \quad \Delta u(k+1) \quad \cdots \quad \Delta u(k+p-1)\,]^T$$
$$S_v(k) = \begin{bmatrix} A \\ A^2 \\ \vdots \\ A^p \end{bmatrix}, S_u(k) = \begin{bmatrix} B & 0 & \cdots & 0 \\ AB & B & \cdots & 0 \\ \vdots & \vdots & \vdots & \vdots \\ A^{p-1}B & A^{p-2}B & \cdots & B \end{bmatrix}$$

Figure 2 is the illustration of the collision avoidance between two vehicles. In the figure, A is the position of the collision between two vehicles at k + p when the host vehicle is traveling at the original speed. The point B is the expected position of the host vehicle collision with the other vehicle at time k + p by the use of the control method in this paper.

The safety distance of collision avoidance between two vehicles at k + p (i.e., the distance between A and B) is s*(k + p). According to (12), by adjusting the speed of the host vehicle to avoid the collision can be described as the following problem.

The optimization problem 1:

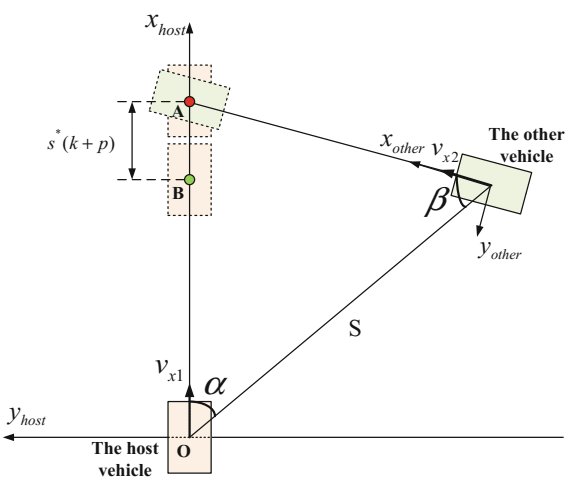

Fig. 2 The illustration of the collision avoidance between the two vehicles

$$\begin{aligned} &Find \quad \min_{\Delta u(k),\Delta u(k+1)\cdots\Delta u(k+p-1)} \quad J \\ &with \quad J = \sum_{i=0}^{p} \|\Delta v(k+i)\|_Q^2 + \sum_{i=0}^{p} \|\Delta u(k+i)\|_R^2 \\ &\qquad + L_p \left| \sum_{i=0}^{p} \Delta v(k+i)\Delta T - s^*(k+p) \right| \end{aligned} \tag{13}$$

s.t.

$$\Delta V(k+1|k) = S_v(k)\Delta v(k) + S_u(k)\Delta U(k) \tag{14}$$

$$\Delta u_{\min}(k+i) \le \Delta u(k+i) \le \Delta u_{\max}(k+i) \tag{15}$$

$$u_{\min}(k+i) \le u(k+i) \le u_{\max}(k+i) \tag{16}$$

The objective function J of the optimization problem 1 consists of three terms: the first term is weighting term of the speed change; the second term is weighting term of the driving torque change, and the third term is weighting term of the error between the host vehicle actual position and desired position at k + p, it is used to constrain the error of the actual position and the desired position. In order to get the optimal solution of problem 1, the problem is written as follow.

$$\begin{aligned} \min_U J = {} & \Delta V(k+1|k)^T Q \Delta V(k+1|k) + \Delta \mathrm{U}^T(k) R \Delta U(k) + L_p[s^*(k+p)]^2 \\ & + \Delta T_m \Delta V(k+1|k) L_p \Delta V(k+1|k)^T \Delta T_m^T - 2[\Delta V(k+1|k)^T \Delta T_m^T + \Delta v(k)\Delta T \cdot s^*] \end{aligned} \tag{17}$$

We can get the next formula from (17).

$$\min_U J \overset{\text{Equivalent}}{\Rightarrow} \tilde{J} = \Delta \mathrm{U}^T(k) H \Delta U(k) + 2F^T \Delta U(k) \tag{18}$$

where, $\begin{cases} H = R + S_u^T Q S_u + S_u^T \Delta T_m^T L_p \Delta T_m S_u \\ F = -L_p s^* S_u^T \Delta T_m^T \end{cases}$, $\Delta T_m = [\,\Delta T \quad \cdots \quad \Delta T\,]_{1*T_p}$.

Obviously, the optimization problem described by (18) can obtain the optimal solution by QP algorithm. For the sake of clarity, the vehicle lateral collision avoidance control method is summarized as follows.

Step 1 We measure the relative position and angle of the other vehicle through the host vehicle's radar and we get the heading angle of two vehicles through the GPS.

Step 2 At the moment of k, through the V2V to obtain the other vehicle's speed and heading angle, we converse the positions, speeds and relative angles to the host vehicle's coordinate system.

Step 3 The trajectory prediction model of the vehicles in the host vehicle coordinate is established at k, and we determine whether the two vehicles may crash based on it.

Step 4 For the case of possible collision, we use the receding horizon control algorithm to control the host vehicle. According to the principle of receding optimization, we get the driving torque sequence at time k by solving the optimization problem 1: $\Delta U(k) = [\Delta u(k) \quad \Delta u(k+1) \cdots \Delta u(k+p-1)]^T$. We use $\Delta u(k)$ to control the host vehicle so that the collision between the vehicles can be avoided. Repeat the above process, by optimizing the control of each moment to achieve the collision avoidance between the host vehicle and other vehicles.

4 Simulation Results and Analysis

Host vehicle parameters and simulation parameters used in the simulation experiment are shown in Table 1.

The internal time of the drawing cars in the following figures are 0.5 s.

Simulation condition 1: the other vehicle speed is constant.

This simulation condition is used to examine the feasibility and effectiveness of the host vehicle collision avoidance algorithm when the vehicle speed is kept constant. The initial speed of the host vehicle is 17 m/s and the initial speed of the other vehicle is 16 m/s. The time of the prediction is 3 s, and the internal time is 0.05 s. Then we can get the length of the prediction horizon T_p=60. It is known that the initial distance between two vehicles is 80 m, and the angle of two vehicles' heading direction is $\alpha(k) = 45°, \beta(k) = 47°$ (Fig. 1). According to formula (1), the

Table 1 Host vehicle and simulation parameters

Variable	Numerical value (dimension)
m	1550 (kg)
R	0.310 (m)
ρ	1.25 (kg/m^3)
C_d	0.4 (−)
A_F	1.586 (m^2)
g	9.8 (m/s^2)
f_{R0}	0.01
f_{R1}	0.03
f_{R2}	0.035
ΔT	0.05 (s)

coordinate of the other vehicle in the coordinate system of the host vehicle can be shown as:

$$[x_2(k), y2(k)]' = [56.57, -56.57]'$$

The simulation supposes that the safe distance between the two vehicles is S_{def} = 30 m, and the relative distance to avoid the collision between them is s*(k + p) = 15 m. According to the collision avoidance algorithm in the Sect. 2 of this paper, if the host vehicle is not controlled, the distance between two vehicles is 1.15 m at 3.5 s as shown in Fig. 3a and the other vehicle is in the collision risk area (which is shown in red). Figure 3b shows that the two vehicle trajectories got through the receding horizon control method given in the third section. The figure shows that the adjustment of the longitudinal speed of the host vehicle by the receding horizon control algorithm can make the other vehicle avoid being in the collision area of the host vehicle to realize the collision avoidance.

Figure 4 shows how the host vehicle speed changes with time. From Fig. 4, we can know that the host vehicle speed rapidly reduces to 8 m/s in the initial 3 s, when the other vehicle is in the collision risk area. After 3.5 s, the other vehicle drives away from the collision risk area, and the host vehicle speed begins to gradually return to 17 m/s until about 10 s. Figure 5 shows how the host vehicle acceleration changes with time. In the deceleration process, the maximum acceleration is about −0.6 g. 2.5 s later, the acceleration begins to gradually increase and 3.5 s later, it returns to a positive value. After the other vehicle drives away from the collision risk area, the host vehicle begins to speed up.

Simulation condition 2: the other vehicle speed changes.

The simulation condition 2 is used to test the feasibility and effectiveness of the algorithm in this paper in the case that the vehicle speed changes. It is supposed that S_{def} and s^* (k + p) are the same as the simulation condition 1. And the initial speed, relative position and other parameters of the host vehicle and the other vehicle are

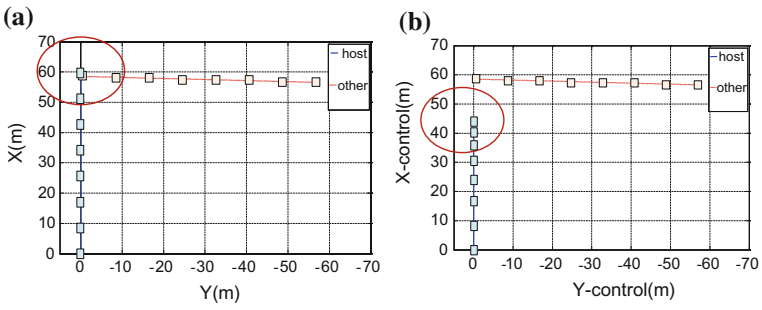

Fig. 3 **a** The host vehicle is not in control. **b** The host vehicle is in control

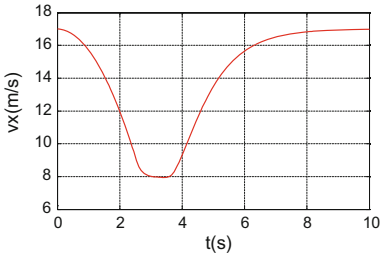

Fig. 4 The speed changes with time

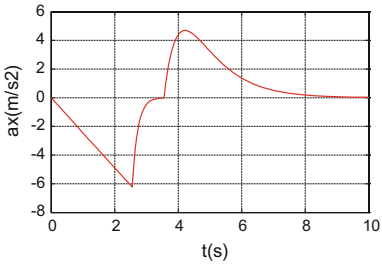

Fig. 5 The acceleration changes with time

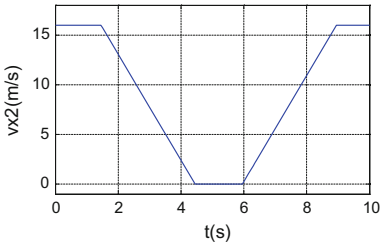

Fig. 6 The speed change of the other vehicle

also the same as the condition 1. It is supposed that the other vehicle speed changes as shown in Fig. 6: from 0 to 1.5 s, v_{x2} = 16 m/s; from 1.5 to 4.5 s the speed decelerates; at the time of 4.5 s, the speed reduces to 0; from 6 to 9 s, the other vehicle accelerates until the speed increases to 16 m/s at 9 s.

The collision avoidance algorithm in the Sect. 2 of this paper shows: if the host vehicle is not controlled, the distance between the two vehicles is 11.57 m at 3.5 s and it is in the collision risk area (which is shown in red). Figure 7b shows that the adjustment of the longitudinal speed of the host vehicle by the receding horizon control algorithm can make the other vehicle avoid being in the collision area of the host vehicle to realize the collision avoidance.

Figure 8 shows how the host vehicle speed changes with time. It shows that the host vehicle speed in the initial 4 s quickly reduces to about 2 m/s. 4 s later, the other vehicle drives away from the collision area and the host vehicle speed increases gradually. Figure 9 shows how the host vehicle acceleration changes with time. In the process of host vehicle speed reduction, the maximum acceleration is about −0.8 g. 3.5 s later, the acceleration began to gradually increase. 4 s later, it

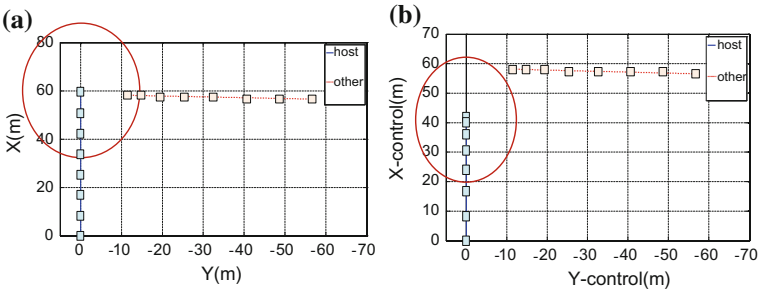

Fig. 7 **a** The host vehicle is not in control. **b** The host vehicle is in control

Fig. 8 The speed changes with time

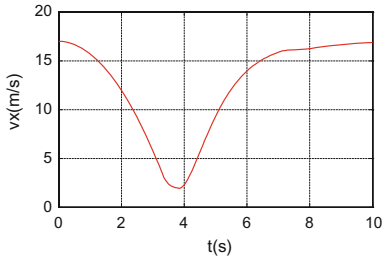

Fig. 9 The acceleration changes with time

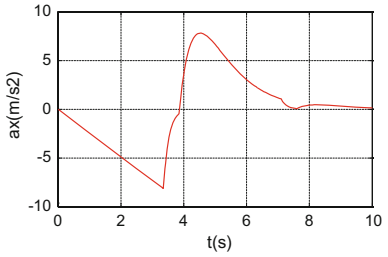

returns to a positive value. After the other vehicle drives away from the collision area, the host vehicle begins to speed up.

5 Conclusion

In this paper, the collision recognition algorithm and the receding horizon optimization algorithm make the other vehicle always be outside the collision risk area of the host vehicle. After judging there is no collision risk of two vehicles, the host vehicle returns to the normal speed, while ensuring the safety of vehicles and their driving performance at the same time. The simulation results show that when the

other vehicle is in the collision risk area, the host vehicle speed decreases to avoid the collision between the two vehicles according to the receding horizon strategy. When the other vehicle drive away from the collision risk area, the host vehicle speed increases incrementally and eventually returns to normal.

Acknowledgements This work is supported by China Automobile Industry Innovation and Development Joint Fund (No. U1564213) and National Natural Science Foundation of China (No. 61403105).

References

1. Li FZ (2005) Research on virtual test technology of vehicle lateral collision. Wuhan University of Technology
2. Schildbach G, Soppert M, Borrelli F et al (2016) A collision avoidance system at intersections using Robust model predictive control. In: IEEE intelligent vehicles symposium, pp 233–238
3. Scanlon JM, Page K, Sherony R et al (2016) Using event data recorders from real-world crashes to investigate the earliest detection opportunity for an intersection advanced driver assistance system. In: SAE 2016 world congress and exhibition
4. Hafner MR, Cunningham D, Caminiti L et al (2013) Cooperative collision avoidance at intersections: algorithms and experiments. IEEE Trans Intell Trans Syst 14(3):1162–1175
5. Basma F, Tachwali Y, Refai HH (2011) Intersection collision avoidance system using infrastructure communication. In: International IEEE conference on intelligent transportation systems. IEEE, pp 422–427
6. Maile M, Chen Q, Brown G et al (2015) Intersection collision avoidance: from driver alerts to vehicle control. In: Vehicular technology conference. IEEE, pp 1–5
7. Lin CF, Juang JC, Li KR (2014) Active collision avoidance system for steering control of autonomous vehicles. IET Intel Transport Syst 8(6):550–557
8. Savino G, Brown J, Rizzi M et al (2015) Triggering algorithm based on inevitable collision states for autonomous emergency braking (AEB) in motorcycle-to-car crashes. Intelligent vehicles symposium. IEEE, pp 1195–1200
9. Soudbakhsh D, Eskandarian A (2015) Steering control collision avoidance system and verification through subject study. IET Intel Transport Syst 9(10):907–915
10. Chen GR (2016) Research and application of vehicle running distance calculation based on GPS positioning technique. Southwest JiaoTong University

Research on Cross Platform Model Display Technology of BIM

Junjie Huang, Jia Wang and Xiaoping Zhou

1 Introduction

BIM (Building Information Modeling) is a kind of information management technology which runs through the whole life cycle of the building [1]. This is the first construction information model application engineering standard, put forward the basic requirements of the construction information model application, will lay the foundation for the improvement of the national construction industry information technology ability [2].

At present, application development and use are faced with legal, technical, cost and other aspects of the risks and challenge [3]. How to reduce the implementation cost of application services [4], so that BIM service consumers at the cost of economic input BIM technology implementation benefits [5], and reduce the difficulty of using the application, reduce the BIM software user learning pressure, software Developers should consider the important issue [6], is also the starting point of this study.

2 Building Information Model Based on IFC Standard

2.1 Introduction to IFC Standards

In order to realize the sharing and exchange of building information, the Building SMART Alliance has established the current general IFC standard data format [7]. As an open international standard, IFC has a relatively complete

J. Huang (✉) · J. Wang · X. Zhou
School of Electrical and Information Engineering, Beijing University of Civil Engineering and Architecture, Beijing 100044, China
e-mail: junjie@stu.bucea.edu.cn

Z. Deng (ed.), *Proceedings of 2017 Chinese Intelligent Automation Conference*,
Lecture Notes in Electrical Engineering 458,
https://doi.org/10.1007/978-981-10-6445-6_84

Table 1 IFC certified software and vendor

Supplier name	Application name
Autodesk	Revit
Bentley	ABD
Cad Line Ltd	ARCH Line.XP
Graphisoft	Archi CAD
NEMETSCHEK	Allplan
Tekla	Tekla Structures
Glodon Software	Glodon Takeoff

Table 2 Model file statistics table

File name	.rvt file (MB)	.ifc file (MB)
B01structure	74.7	25.2
B02structure	65.4	23.0
B03structure	59.1	15.5
Foundation structure	12.7	6.2

information classification and data structure, which can exchange data and information between many BIM applications Shared provides a uniform specification [8].

The official website lists the certified and certified software vendors and application name list, including the import and export of data to guide the two-way process, as shown in Table 1, this article statistics and lists the two-way through IFC V2.0 certified software vendors and Software Products. Which includes Revit and ABD and other commonly used BIM design software.

The IFC standard file is implemented in EXPRESS language, and the text has the advantages of clear structure, easy to understand and machine-friendly. In addition, this paper through the modeling experiment comparison, the same model case, IFC format file size is. Rvt file about 1/4, as shown in Table 2, Fig. 1 corresponds to the four models of the three-dimensional view. In addition, IFC data standards have a complete description of norms and implementation guidance, to facilitate the extraction of information and related application development, data delivery and information sharing is a good medium.

2.2 IFC Standard Scene Organization Structure

The IFC file specifies the architectural structure of the building project, by defining the spatial structure elements and the relationships between them. Spatial structure elements include the site (Site), building (Building), floor (Storey) and space (Space) and so on. An IFC file has and can only define a project object as a container for all project objects. Most of the building components are associated with the space that the floor or floor is split to determine the dependencies and their coordinates in the entire 3D model.

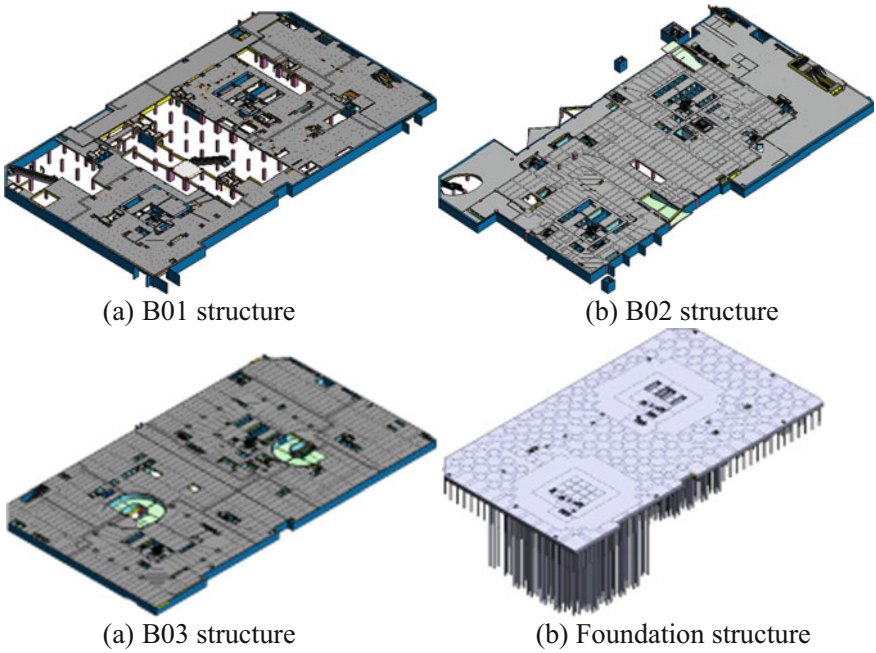

Fig. 1 Three dimensional view of experimental model

The scene organization structure describes the hierarchical framework of the building information model, and also provides a spatial topological relation for 3D rendering visualization of the model through computer graphics processing.

2.3 Parametric Component Definition

IFC standard not only establishes the macro scene organization structure, but also defines the comprehensive information of the professional building components. The IFC standard is mainly from the geometric information, attribute information and relation information on three aspects of this kind of component information description and data storage, so according to the geometry information of components is analyzed.

The IFC file uses a geometric entity representation method when describing the geometric model of the component. As shown in Fig. 2, this paper excludes the IFC file content of a wall from the experimental model data. It can be seen that the IFC file uses the Swept Solid description method when describing the geometric information of the wall. The data processing part of the data is transformed into the three-dimensional rendering data of the computer. 3D visualization.

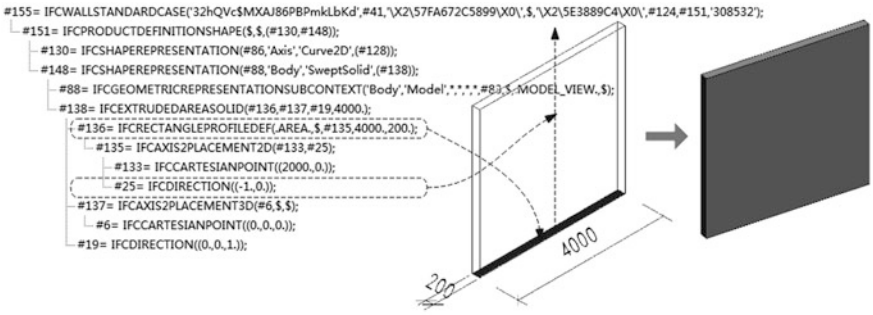

Fig. 2 Geometric representation of components

3 Data Processing

In computer graphics processing, discrete data is required to represent geometries. For example, curves need to be approximated by straight segments, and surfaces are mostly approximated by polygons or triangles. Using a triangular mesh to represent surfaces is often used in graphical processing, and the density and quality of the mesh can be adjusted according to the application accuracy requirements. This process is also known as triangular meshing in computer graphics. Using a triangular mesh to represent surfaces requires triangulation, sheet traversal, data compression, and so on. The rendering data generated by the model presentation technique described in this paper is the triangular mesh data of the geometric model.

After the above steps, the geometric data defined by the IFC standard in Fig. 3 is converted into the triangular mesh data shown in Fig. 4. As can be seen from Fig. 4, the triangular mesh data generated by the object is stored as a JSON object, Such an object storage method for network transmission and database storage [9]. Is currently the most commonly used network application data format.


```
{
  "positions": [
4000,100,0,4000,100,4000,0,100,0,0,100,4000,0,100,0,0,100,40000,-100,0,0,-100,4000,0,-100,0,0,-100,
          4000,4000,-100,0,4000,-100,4000,4000,-100,0,4000,-100,4000,4000,100,0,4000,100,4000,4000,100,0,0,
          100,0,0,-100,0,4000,-100,0,4000,100,4000,0,100,4000,0,-100,4000,4000,-100,4000]
   "indices": [ 1,0,3,3,0,2,5,4,6,7,5,6,9,8,10,11,9,10,13,12,14,
          15,13,14,17,19,18,17,16,19,22,23,21,23,20,21],
  "normals": [ 0,1,0,0,1,0,0,1,0,0,1,0,-1,0,0,-1,0,0,-1,0,0,-1,0,0,
          0,-1,0,0,-1,0,0,-1,0,0,-1,0,1,0,0,1,0,0,1,0,0,1,0,0,
          0,0,-1,0,0,-1, 0,0,-1,0,0,-1,0,0,1,0,0,1,0,0,1,0,0,1],
    "matrix": [ 1,0,0,0,0,1,0,0,0,0,1,0,0,0,0,1],
    "colors": [0.5019608,0.5019608,0.5019608,1],
 "materials": [ 0,0,0,0,0,0,0,0,0,0,0,0 ],
      "type": "IfcWallStandardCase"
      "guid": "32hQVc$MXAJ86PBPmkLbKd",
}
```


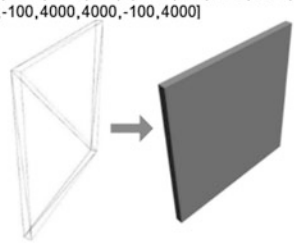

Fig. 3 Geometric representation of the rendering data

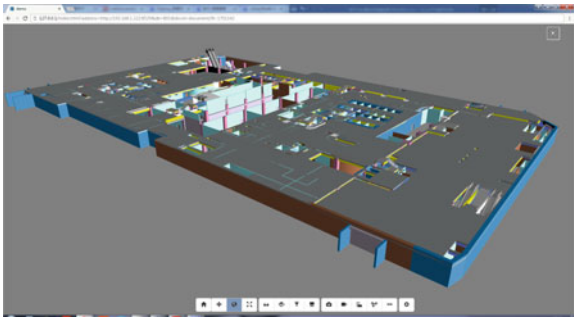

(a) PC browser

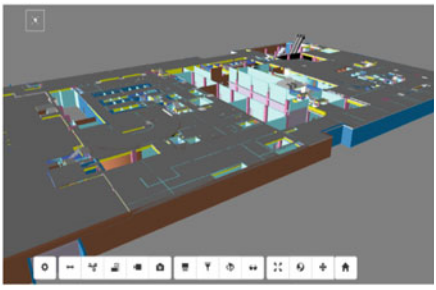

(b) Iphone6 browser

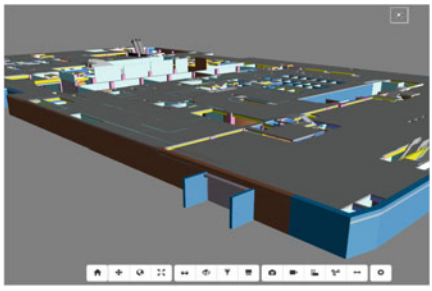

(c) Xiao Mi 2 generation

Fig. 4 Shows the effect of the model

4 Model Display

4.1 Web GL-Based Model Display

Web GL is a set of JavaScript APIs developed by KHRONOSGROP that allows developers to embed embedded 3D graphics that support hardware acceleration directly in the browser. As an open WEB standard, Google, Apple and other companies are involved in the development and promotion of the standard. Tencent, Baidu as the representative of the Internet companies are working on Web GL research and application. The <canvas> tag in HTML5 provides the context for the Web GL element. Web GL is a subset of Open GL ES 2.0 that can run on different hardware devices such as desktops, tablets, phones, or smart TVs. The application of the technology provides the browser to achieve human-computer interaction, games, data visualization, 3D modeling and physical simulation and other technical support.

4.2 Model Show Effect

In this paper, we introduce the BIM model of B01 structure as an example to introduce the model display effect of building information model display system. First, we use Revit software to build the BIM model of the building and export the model file in IFC format and upload it to the server. The parsing service parses the IFC file and stores it in the database. The database then responds to the data request of the model browser and sends the data to the front end application. Front-end application to complete the model rendering and display in the web browser, the cross-platform terminal actual test, PC, MAC, iPad, iPhone, Android phone, Android tablet device can achieve smooth model display and interactive operation, as shown in Fig. 4 Visualization of three typical devices.

4.3 Model Interaction Function

The BIM model presentation system introduced in this paper also designs a variety of functional extensions for model interaction to meet the user's need for detailed analysis of the model. First, the component selection function, the application

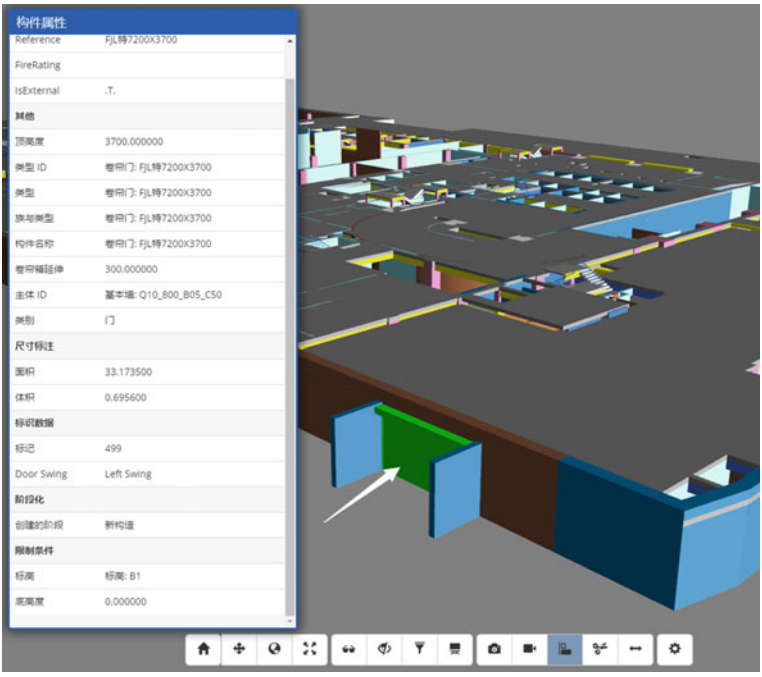

Fig. 5 Component selected effect

Fig. 6 Roaming effect map

design is selected for the green highlight state, and when the property display window is called to read the selected member of the property information, as shown in Fig. 5. In addition, by controlling the camera position and angle changes in the scene, you can achieve the first person perspective in the model of simulation roaming, roaming effect shown in Fig. 6. In order to realize the model analysis, the model is designed to cut the bounding box. The six faces of the moving bounding box can be cut from six directions. The cutting effect is shown in Fig. 7.

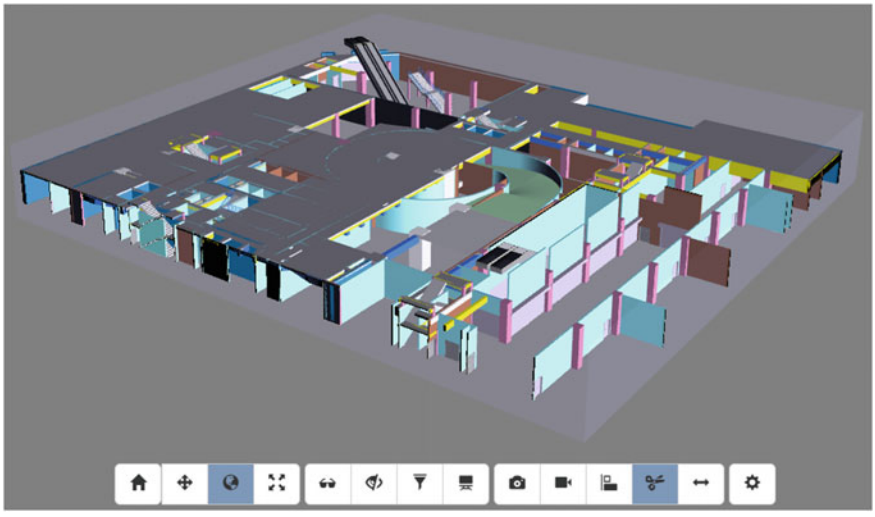

Fig. 7 Cut the effect of figure

5 Design of BIM Application Architecture Based on HTML5 Technology

In October 2014, the HTML5 standard was developed by the World Wide Web Consortium (W3C). Native Web GL technology was able to provide a three-dimensional model of web-based applications without plug-ins, providing a model for BIM applications. BIM application based on HTML5 technology has the advantages of short development period, easy cloud deployment and strong autonomy in the application of the construction information model presentation technology proposed in this paper.

6 Conclusion

In order to solve the problem that BIM application data sharing is poor, equipment hardware requirements are high, application service is not flexible, this paper presents a low cost, cross platform and easy expansion of building information model display technology application method. On the basis of the model display system introduced in the text, it can easily expand the peripheral application system integration, quickly realize the development of the network application platform in the construction field, plan the discussion of the planning stage, the calculation of the drawings at the design stage, the progress of the construction, The three-dimensional visualization of the operation and fire emergency and other construction applications to provide model display services. The application of this technology not only extends the BIM model to use the scene, but also a lot of savings in hardware input costs and user learning costs. In the subsequent study, data compression, information security, interactive features of the rich will be the focus of the study.

References

1. Wang Y, Wang J, Yu H (2016) Application of BIM technology in construction engineering management. Civil Eng Inf Technol 8(4):89–93
2. Gao X, Wang J, Yi J (2016) Study on the evacuation path of buildings based on bim technology. J Archit Sci 32(2):143–146
3. Cai W (2015) BIM application, risk and challenge. Constr Technol 46(2):134–137
4. Mi J, Zhang X, Zhao X et al (2016) Comparison of BIM application between China and Britain. Constr Technol 47(8):689–691
5. Bi Z, Wang H, Pan W et al (2013) Application of BIM in cloud computing model. Build Technol 44(10):917–919
6. Liu Z, Zhao M, Xu R (2013) BIM technology in China's research and development and engineering applications. Constr Technol 44(10):893–897

7. Lin T, Wang J, Zhou X (2015) Study on visual fire management platform based on BIM. Build Sci 31(6):152–155
8. Wang J, Ren Y, Zhou X (2013) Application of BIM technology based on IFC standard in fire protection of large public buildings. Civil Eng Archit Inf Technol 5(1):45–48
9. Chen Z, Luo F (2016) Revised 3D reconstruction of revit based on WebGL. J Zhejiang Univ Technol 44(6):608–613

Hand Detection from Cluttered Images Based on a Hierarchical Strategy

Jing Qi, Kun Xu and Xilun Ding

1 Introduction

As one of body language, hand gesture is often used for communication and interaction [1]. Vision-based hand gesture recognition may provide a natural computer interface. It is widely used in many applications. Hand detection (localization/segmentation) is the initial step for hand gestures recognition [2–4]. However it is difficult to detect hands in one image, since of the deformable shape of hands, complicated background and variable illumination of the images [5]. As a result, hand detection in complicated scenarios is still a challenging task [6].

Researchers used skin, shape, motion and multimodal information to detect hands. Skin detection is one of the most common methods to detect hands. Girondel et al. [7] proposed an adaptive skin detection method working in the YCbCr colour space and an adaptive thresholding in the Cb and Cr channel. They utilized position information to localize face and hands. Ghidary et al. [8, 9] assumed that user wore long-sleeved clothes and the robot was static while observing. They employed a statistical skin colour classifier to detect skin colour regions. Furthermore, they used the position of segmented skin areas to differentiate head and hands. Some scholars made use of shape information to detect hands. Thangali and Sclaroff [10] used Support Vector Machine (SVM) which incorporated a distance measure to detect hands to improve hand detection accuracy. Wu and Huang [11] put forward the Discriminant-EM algorithm to alleviate the difficulty of the insufficiency of labelled training data by adding a large unlabelled training set, and then employed Discriminant-EM algorithm and skin information to detect hands. In addition, some scholars utilized context information to detect hands. Kim et al. [12] utilized the head information to generate effective hand region of interest to improve the hand detection accuracy. Although many approaches have been proposed for hand

J. Qi · K. Xu (✉) · X. Ding
Robotics Institute, Beihang University, Beijing 100191, China
e-mail: xk_sea@163.com

Z. Deng (ed.), *Proceedings of 2017 Chinese Intelligent Automation Conference*,
Lecture Notes in Electrical Engineering 458,
https://doi.org/10.1007/978-981-10-6445-6_85

detection, they mainly focus on the conditions without assumption of the whole human body and large skin-color backgrounds in field of view. However, sometimes it is necessary to detect hand from these images, which include the whole human body with large approximate skin colour backgrounds in the field of view.

In order to remove the influences of cluttered background, a method based on hierarchical strategy to detect hands from cluttered images is proposed. The method consists of three hierarchies: upper body detection hierarchy, skin colour detection hierarchy and hand detection hierarchy. In the first hierarchy, upper body is detected from the whole-body image with cluttered backgrounds, to exclude approximate skin colour background. In the second hierarchy, a new approach for skin colour detection, which combines samples threshold with experiential threshold, is proposed to detect skin/skin-like colour regions from the image of upper body. In last hierarchy, HOG features of the skin patches are extracted, and then SVM is used to generate hand detection model. Finally, the hand detection model is utilized to detect hand. Some experiments are carried out to verify the effectiveness of the method.

The organization of this paper is as follows, Sect. 2 introduces the hand detection approach base on hierarchical strategy. Some experiments based on this method are carried out and the results are presented in Sect. 3. Finally conclusions are given in Sect. 4.

2 Hand Detection Based on a Hierarchical Strategy

The hand detection method based on a hierarchical strategy (Fig. 1) consists of three hierarchies: upper body detection hierarchy, skin colour detection hierarchy and hand detection hierarchy. In the first hierarchy, first of all, the original images taken by camera are processed by bilateral filtering. Because there are large skin-like colour regions in the image, in order to exclude the approximate skin colour regions, upper body is detected from the whole-body image from cluttered backgrounds. In the second hierarchy, combination of samples threshold and experiential threshold is used to detect skin/skin-like colour region from image of the upper body. In last hierarchy, HOG features of the skin patches are extracted, and then SVM is used to generate hand detection model. Finally, the hand patches are obtained by the hand detection model.

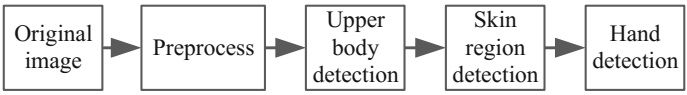

Fig. 1 The framework of the hand detection approach based on a hierarchical strategy

2.1 Upper Body Detection

In the first hierarchy, extended Haar wavelets are extracted from the upper body image, and then the classifiers are trained using Gentle Adaboost to detect the upper body from the cluttered image [13].

2.2 Skin Region Detection

Although different individuals coming from different ethnic groups and regions have different skin colors, skin colors are clustered in the color space [14]. Hence one of the common methods is to define decision boundary to detect skin regions. In this paper, multiple decision boundaries in RGB color space are defined to detect skin regions.

First of all, we labeled hand region in self-building dataset manually, and calculated the following statistical data:

$$\begin{cases} r_i^L = \min(p_i) \\ r_i^U = \max(p_i) \end{cases} \tag{1}$$

where $i \in \{R, G, B\}$, R, G and B are the R channel, G channel and B channel of RGB color space respectively. p_i presents hand pixel values in RGB color space. r_i^L and r_i^U are the minimum pixel values and maximum pixel values of hand skin samples in channel i respectively.

$$\begin{cases} r_{ii'}^L = \min\limits_{i \neq i'}(p_i - p_{i'}) \\ r_{ii'}^U = \max\limits_{i \neq i'}(p_i - p_{i'}) \end{cases} \tag{2}$$

where $r_{ii'}^L$ and $r_{ii'}^U$ are the minimum differences and maximum differences of pixel values of hand skin samples in two channels in RGB color space respectively.

Using the methods in Refs. [15–17] for reference, we propose our decision criterion, which is shown as Eqs. (3) and (4).

$$\begin{cases} Th_i^U = r_i^U \\ Th_i^L = \min\left(r_i^L, \quad n_i\right) \\ Th_{ii'}^U = \min\limits_{i \neq i'}\left(r_{ii'}^U, m_{ii'}^U\right) \\ Th_{ii'}^L = \min\limits_{i \neq i'}\left(r_{ii'}^L, m_{ii'}^L\right) \end{cases} \tag{3}$$

where n_i and $m_{ii'}$ are subjective parameters. Th_i^U,Th_i^L,$Th_{ii'}^U$ and $Th_{ii'}^L$ are the maximum threshold of pixel values, minimum threshold of pixel values, maximum differences threshold of pixel values and minimum differences threshold of pixel

values. In this paper, we set $n_R = 95$,$n_G = 40$, $n_B = 20$, $M_{RG}^L = 30$, $M_{GB}^L = 10$, $M_{RG}^U = 80$, $M_{GB}^U = 80$ and $M_{RB}^U = 120$.where M_{RG}^L,M_{GB}^L,M_{RG}^U,M_{GB}^U and M_{RB}^U are minimum threshold of R and G channel, minimum threshold of G and B channel, maximum threshold of G and B channel and maximum threshold of R and B channel respectively. And thus skin pixel is defined as:

$$S = \begin{cases} 1, & Th_i^L \le s_i \le Th_i^U, Th_{ii'}^L \le s_i - s_{i'} \le Th_{ii'}^U \\ 0, & otherwise \end{cases} \tag{4}$$

Skin regions are extracted after detecting the upper body. We proposed a new method of skin detection. Combination of samples threshold and experiential threshold is used to detect the skin patches. After that, each pixel is compared with hand regions labeled manually. If its value falls in the range of the mean and variance of the hand region, then it is defined as skin pixel. Furthermore, the small area of the connected component is removed. After that, the holes in the binary image are filled. Next, the connected component is labelled, in addition, the threshold of area and length-width ratio of the connected component is used to filter the skin region; Skin region is finally segmented from the image.

2.3 Hand Detection

After skin detection, hand detection model is established to detect hand using the train dataset. Finally, hand is detected using the trained hand detection model.

The SVM is a fundamental two-class classifier based on small sample statistical study theory. The SVM classifier is not likely to occur over-fitting [18]. Because we need to classify the skin regions into hand/non-hand regions using the small samples, SVM classifier is adopted. There are three steps to train hand detection model, as follows:

1. The segmented skin region is resized to 90×90 pixels.
2. HOG features are extracted from the resized skin region.
3. Two-class SVM classifier is used to train the hand detection model.

The skin regions, which are normalized in size, are used as samples to train hand detection model. Furthermore, the skin regions including hands are used as positive samples, while the skin regions which do not include hands, are used as negative samples. The training dataset consists of negative and positive samples. The images in training dataset are extracted HOG features, followed by SVM classifier to train the hand detection model. Two hand detection models are proposed in this paper, the difference between the two hand detection models is that they use different hand regions to train hand detection model: Skin regions segmented (see Sect. 2.2) are input into one hand detection model, while hand regions manually annotated are input into the other hand detection model. The hand regions are normalized in size,

followed by HOG features are extracted from these skin patches, and two-class SVM classifier is finally used to train hand detection model, which is used to detect hand.

3 Experiments

The images in our dataset used in this paper is captured by ourselves. There are five persons, nine kinds of hand postures and three kinds of distances (1.8, 3 and 4.2 m) between the camera and the human. Each person made nine kinds of hand posture in the indoor environment. Three photos, in which the human is in the middle, left and right fields of view respectively, were captured for each posture at each distance. There are 486 pictures in the dataset, as shown in Fig. 2. The captured images are 24 bit, JPG, resolution 3120 × 4208. The hardware used in this experiment: Intel(R) Core(TM) i5-4590 CPU, dual core 3.30 GHz CPU, 4 GB internal memory.

In the first hierarchy, the method in [13] is used to detect upper body. One of pictures in the dataset is shown in Fig. 3a, which is input to detect the upper body, and the upper body is detected, as shown in Fig. 3b.

3.1 Skin Detection

In the second hierarchy, the detected upper body image is used as input, which is shown in Fig. 3b. Then a method which combines samples threshold with experiential threshold (see Sect. 2.2. The experiential threshold in Ref. [15–17] is used for reference.), is used to detect skin pixel, the detection result is shown in Fig. 3c. The skin constraint $R > G > B$ in Ref. [19] is utilized to detect skin pixel, as shown in Fig. 3d. Figure 3c gets better result than Fig. 3d. The mean and variance of the manual annotated hand regions are calculated. The result of the skin pixel detection, which fell in the range of mean and variance of the manual annotated hand regions, is shown in Fig. 3e. Figure 3f shows detection result of skin regions.

3.2 Hand Detection

In the third hierarchy, there are two steps in hand detection, including the training of hand detection model and hand detection test using trained hand detection model. The training process of hand detection model is as follows.

The skin regions detected are used as dataset 1. The training set 1 consists of 838 positive samples and 5991 negative samples, while the testing set 1 includes 194 positive samples and 539 negative samples. HOG features are extracted from the

Fig. 2 Nine types of hand postures in the dataset

images in the training set, and then SVM hand/not-hand classifier is trained using the HOG features. After that, a hand detection model is established. Hand detection result is shown as Table 1. Hand regions, which are annotated manually and then

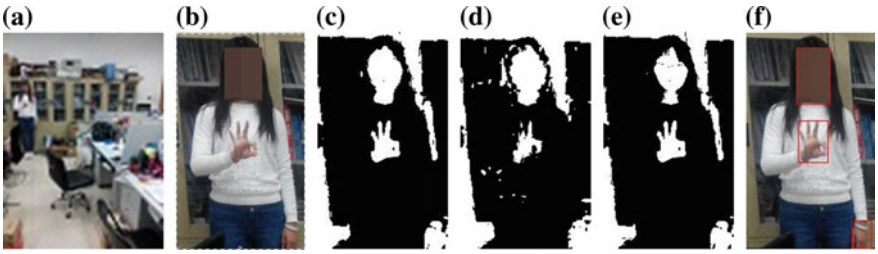

Fig. 3 An image in the dataset and its detection results of upper body and skin region

Table 1 Hand detection results of different hand posture models

Testing set	True positive rate (%)	False negative rate (%)	False positive rate (%)
1	90.72	0.19	9.28
2	95.10	0.56	4.90

Table 2 Detection result of different strategy hand posture model detection

Structure	Computing time (s)	Number of skin region	Number of false positive skin region	False positive rate (%)
Hierarchical	2.2349	3	0	0
Nonhierarchical	6.4765	138	7	4.90

normalized in size, are used as positive samples. Negative samples in dataset 1 are used in dataset 2. The training set 2 includes 1264 positive samples and 5991 negative samples, and 539 negative samples and 733 positive samples comprise testing set 2. The hand detection model was trained and tested in different dataset, hand detection result is listed in Table 1.

As shown in Table 1, the hand detection model which was trained using manual annotated samples as a training set, gets higher false negative rate and true positive rate, but lower false positive rate, than hand detection model which was trained using detected skin region as a training set.

To study the difference between hierarchical and nonhierarchical strategy better, we used the same training set, hand detection model and so on. The detection results of different structure are shown in Table 2.

As shown in Table 2, compared with nonhierarchical strategy, hand detection based on hierarchical strategy costs less computing time and gets lower false negative rate. Because there are large skin color-like areas in the background, hierarchical strategy based hand detection costs less computing time on detecting skin region and extracting HOG features and gets lower false negative rate.

4 Conclusions

Hand detection is the initial step in hand gesture recognition. A hierarchical strategy based on hand detection approach was presented in this paper. In the first hierarchy, extended Haar wavelets and a boosted classifier cascade were used to detect upper body, so that the large approximate skin color background is excluded. In the second hierarchy, a skin color model, which combines the statistical and empirical threshold in RGB color space, is presented to distinguish skin regions from non-skin regions. For hand detection, HOG features from the resized hand patches are extracted, and then SVM is used for hand/non-hand classification. Experiments show that: Using annotated hands as training set to train classifier gets higher false negative rate and true positive rate, but lower false positive rate than using detected skin patches as training set. Hierarchical strategy based hand detection, which costs less computing time and gets lower false negative rate, is superior to nonhierarchical strategy in our dataset.

Acknowledgements This work is supported by the Beijing Municipal Science and Technology Project (Grant No. D16110400130000) and National Natural Science Foundation of China (Grant No. 51305009).

References

1. Pisharady PK, Saerbeck M (2015) Recent methods and databases in vision-based hand gesture recognition: a review. Comput Vis Image Underst 141:152
2. Erol A, Bebis G, Nicolescu M, Boyle RD, Twombly X (2007) Vision-based hand pose estimation: a review. Comput Vis Image Underst 108(1):52
3. Badi HS, Hussein S (2014) Hand posture and gesture recognition technology. Neural Comput Appl 25:871
4. Zaki MM, Shaheen SI (2011) Sign language recognition using a combination of new vision based features. Pattern Recogn Lett 32(4):572
5. Kang SK, Nam MY, Rhee PK (2008) Color based hand and finger detection technology for user interaction. In: International conference on convergence and hybrid information technology: IEEE
6. Zhao Y, Song Z, Wu X (2012) Hand detection using multi-resolution HOG features. In: IEEE international conference on robotics and biomimetics (ROBIO). IEEE, Guangzhou, China
7. Girondel V, Bonnaud L, Caplier A (2006) A human body analysis system. Eurasip J Appl Signal Proc
8. Ghidary SS, Nakata Y, Saito H, Hattori M, Takamori T (2002) Multi-modal interaction of human and home robot in the context of room map generation. Auton Robots 13(2):169
9. Ghidary SS, Nakata Y, Takamori T, Hattori M (2000) Human detection and localization at indoor environment by home robot. In: IEEE international conference on systems, man, and cybernetics. IEEE, Tennessee, USA
10. Thangali A, Sclaroff S (2009) An alignment based similarity measure for hand detection in cluttered sign language video. In: IEEE computer society conference on computer vision and pattern recognition workshops. IEEE, FL, United States
11. Wu Y, Huang TS (2000) View-independent recognition of hand postures. In: IEEE conference on computer vision and pattern recognition. IEEE, South Carolina

12. Kim J, Baek J, Kim E (2013) A part-based rotational invariant hand detection. In: International conference on fuzzy theory and its applications (iFUZZY). IEEE, Taipei, Taiwan
13. Kruppa H, Castrillon-Santana M, Schiele B (2003) Fast and robust face finding via local context. In: Joint IEEE international workshop on visual surveillance and performance evaluation of tracking and surveillance (VS-PETS)
14. Yang J, Lu W, Waibel A (1998) Skin-color modeling and adaptation. In: Asian conference on computer vision. Springer, Berlin
15. Peer P, Solina F (1999) An automatic human face detection method
16. Solina F, Peer P, Batagelj B, Juvan S (2002) 15 Seconds of fame-an interactive, computer-vision based art installation. In: 7th International conference on control, automation, robotics and vision (ICARCV). IEEE
17. Chen W-C, Wang M-S (2007) Region-based and content adaptive skin detection in color images. Int J Pattern Recogn Artif Intell 21(05):831–853
18. Chen FS, Fu CM, Huang CL (2003) Hand gesture recognition using a real-time tracking method and hidden Markov models. Image Vis Comput 21(8):745–758
19 Duda RO, Hart PE, Stork DG (2012) Pattern classification. Wiley, NJ